

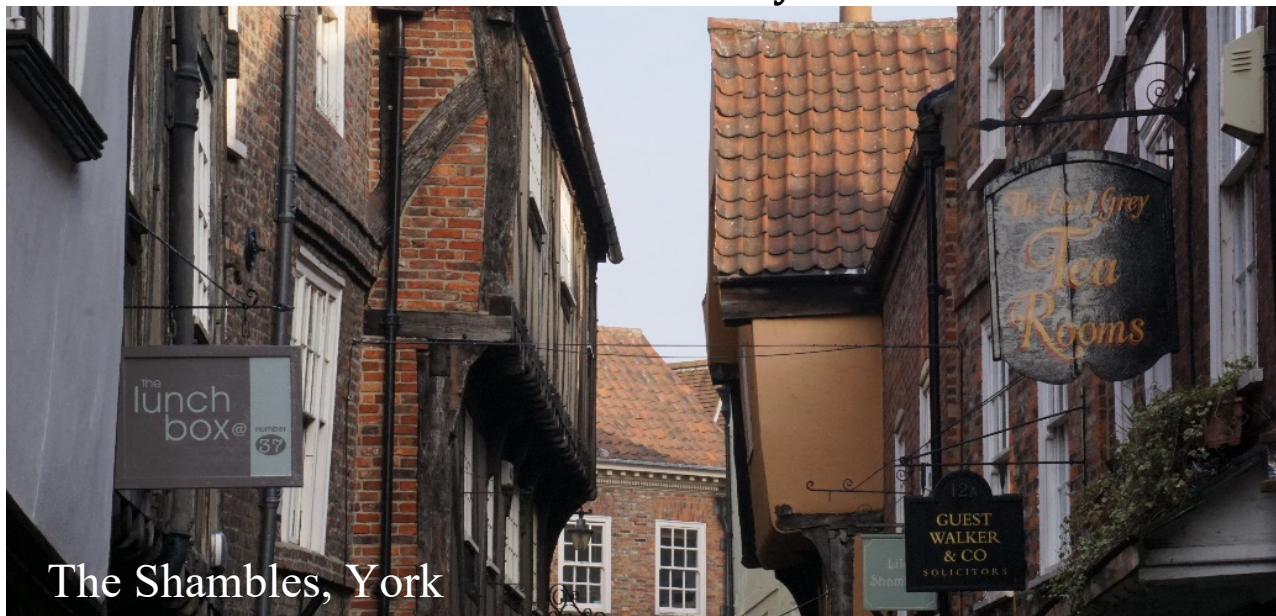
Proceedings for the European Frequency and Time Forum 2016 (EFTF 2016) held at the University of York from 4 – 7 April 2016

Finding papers: These proceedings include the 93 full papers which were submitted to the conference. These are also available on IEEE Xplore. To view the papers please select the highlighted paper number in the timetable. The papers can also be found by:

- Searching author names (CTRL- f) on a PC and (CMD-f) on a Mac.
- Clicking on paper numbers #XXXX# to jump to the full papers; **Note that you may be able to use:** <Alt> + <left arrow> to jump back.
- The original paper numbers can also be found using the bookmarks.
- An author index is available, starting on page 85.

Note that the full papers are at the end of this document. If you wish to see the long abstracts of the other papers these are included in the electronic version of the programme booklet which is available on the conference web sites.

Welcome to EFTF-2016 at the University of York



We are delighted to welcome you to the 30th European Frequency and Time Forum (EFTF), being held, for the first time, at the University of York in the UK from 4th to 7th April, 2016. This continues the series of successful meetings that started in 1987.

The tutorials, technical sessions, keynote presentations, invited speakers and exhibits will cover the many aspects of the very active field of Time & Frequency.

As usual, the three Committees have joined their efforts to organise the event: the Local Organising Committee (LOC), the Scientific Committee (SC) and the Executive Committee (EC).

The **Local Organising Committee** of EFTF-2016 includes representatives from the University of York, the UK National Physical Laboratory (NPL), the UK and France. We acknowledge the strong support from NPL for funding the EFTF awards and many companies for taking on Exhibitor Stands which are essential for an event that will bring together over 300 people for scientific, social and friendly meetings during the whole week.

The **Scientific Committee** of EFTF-2016 has arranged a rich scientific programme resulting from 228 submitted abstracts. The schedule includes three parallel sessions of lectures, poster sessions

on Tuesday and Wednesday afternoons and a short presentation from each exhibitor on Wednesday morning. The poster papers will be displayed during the whole duration of the conference

This year, we are very pleased to announce, that the two Tuesday morning plenary talks will be given by **Professor Andrew Lyne**, Emeritus Professor of Physics at the University of Manchester and former director of the Jodrell Bank Observatory and **David Rooney**, Curator of Time, Navigation and Transport at the Science Museum.

Professor Lyne's talk is entitled: 'The formation, life and uses of pulsars - nature's finest cosmic clocks' and David Rooney's talk is entitled: 'Selling time: Stories from the Greenwich Observatory'.

We are indebted to all the members of the SC and in particular the six group chairs: Alexandre Reinhardt, Jean-Pierre Aubry, Stefan Weyers, Svenja Knappe, Pierre Waller and Helen Margolis.

The **Executive Committee** of EFTF is very pleased that scientists, students and professionals meet once more and take this unique opportunity to learn, to exchange and to present their latest scientific and technological achievements to the community. We are particularly grateful to our members who organised the tutorials (Gaetano Mileti), the EFTF awards (Pierre Waller), the exhibits (Wolfgang Schäfer), the student poster competition (François Vernotte) and to the sponsors who have enabled a strong student travel support programme once again this year. We are also pleased that EFTF represents an occasion for several other committees, working groups and project consortia, from CCTF, EURAMET, and other organisations, to convene in splinter and satellite meetings. We would like to wish you a motivating and inspiring forum. Kind regards,

Jeremy Everard

Pascale Defraigne

Ekkehard Peik

Chair of the
EFTF 2016 LOC

Chair of the
EFTF 2016 SC

Chair of the
EFTF 2016 EC



Supporters

We are pleased to acknowledge the University of York, the UK National Physical Laboratory and the IEEE for being the key supporters of this conference.

UNIVERSITY *of York*



Contents

Welcome to EFTF-2016 at the University of York	1
Finding papers	1
Supporters	2
Contents	3
GENERAL CONFERENCE SCHEDULE.....	4
Useful Information.....	6
Presenter Information.....	7
Session Chairs	7
Oral Presenters	7
Poster Presentations	8
Conference Lab	8
Opening and plenary session.....	9
EFTF 2016 Awards.....	10
Sponsors of the student travel support programme.....	11
Student Finalists	13
Local Organising Committee	16
EFTF 2016 Executive Committee.....	16
EFTF 2016 Scientific Committee	17
Social Programme	19
Tutorial schedule: Monday 4th April.....	20
Detailed Conference Programme	25
Tuesday 5 th April.....	25
Wednesday 6 th April	50
Thursday 7th April.....	73
Satellite Workshop, Friday 8 th April.....	84
Authors Index.....	85
Exhibitors	90
Exhibition Centre Map.....	95
2017 Joint Conference of the European Frequency and Time Forum & IEEE International Frequency Control Symposium	96

GENERAL CONFERENCE SCHEDULE

Sunday Apr 3rd

17:00 - 19:00 Registration – James College Reception

Monday Apr 4th

08:00 - 18:00 Registration - Exhibition Centre

08:30 - 18:00 Tutorials in P/L001 and P/L005

18:00 - 20:00 Welcome Reception - Exhibition Centre

Tuesday Apr 5th

08:00 - 18:00 Registration

08:40 - 10:40 Invited Plenary Speakers, P/X001

Andrew Lyne

'The formation, life and uses of pulsars - nature's finest cosmic clocks'

David Rooney

'Selling time: Stories from the Greenwich Observatory'

10:40 - 11:10 Coffee / tea break

11:10 - 12:30 Lecture Sessions A1

A1L-A: Timescales and SI Second, Room P/X001

A1L-B: Cold Atoms for Sensors and Clocks, Room P/L001

A1L-C: Piezoelectric Resonators I, Room P/L002

12:30 - 14:00 Lunch Break

14:00 - 15:40 Poster Sessions A2

A2P-D: Student Paper Competition, P/L005

A2P-E: Frequency References and Measurements, Poster Area

A2P-F: Piezoelectric Resonators II, Poster Area

A2P-G: Microwave Frequency Standards & Applications I, Poster Area

A2P-H: Timekeeping, Time & Freq Transfer, GNSS Apps I, Poster Area

A2P-J: Optical Frequency Standards & Applications I, Poster Area

15:40 - 16:00 Coffee / tea break

16:00 - 17:40 Lecture Sessions A3

A3L-A: Lattice Clocks I, Room P/X001

A3L-B: Space Applications, Room P/L001

A3L-C: Sensors, Room P/L002

Wednesday Apr 6th

08:00 - 18:00 Registration

08:40 - 10:00 Lecture Sessions B1

B1L-A: Quantum Measurement, Room P/X001

B1L-B: GNSS and Applications, Room P/L001

B1L-C: Cross Correlation, Room P/L002

10:00 - 10:40 Exhibitors' Presentation (P/X001)

10:40 - 11:10 Coffee / tea break

11:10 - 12:30 Lecture Sessions B2

B2L-A: Applications of Optical Frequency Standards, P/X001

B2L-B: Atomic Magnetometers and Their Applications, P/L001

B2L-C: Advances in TWSTFT, P/L002

12:30 - 14:00 Lunch Break

14:00 - 15:40 Poster Sessions B3

B3P-E: Oscillators and Synthesizers, Poster Area

B3P-F: Sensors & Transducers, Poster Area

B3P-G: Microwave Freq Standards & Applications II, Poster Area

B3P-H: Timekeeping, Time & Freq Transfer, GNSS Apps II, Poster Area

B3P-J: Optical Frequency Standards & Applications II, Poster Area

15:40 - 16:00	Coffee / tea break
16:00 - 17:40	Lecture Sessions B4 B4L-A: Ion Clocks, Room P/X001 B4L-B: Timing Networks and Applications, Room P/L001 B4L-C: Atom Interferometers, Room P/L002
19:00 - 23:00	Conference Dinner
Thursday Apr 7th	
08:00 - 18:00	Registration
08:40 - 10:20	Lecture Sessions C1 C1L-A: Frequency Combs, Room P/X001 C1L-B: Caesium Frequency Standards, Room P/L001 C1L-C: Low Noise Synthesis, Room P/L002
10:20 - 10:50	Coffee / tea break
10:50 - 12:30	Lecture Sessions C2 C2L-A: Lattice Clocks II, Room P/X001 C2L-B: CPT Cell Standards, Room P/L001 C2L-C: Opto-electronics and Microwave Oscillators, Room P/L002
12:30 - 14:00	Lunch Break
14:00 - 15:40	Lecture Sessions C3 C3L-A: Optical Oscillators and Spectroscopy, Room P/X001 C3L-B: Optical Fibre Frequency Transfer, Room P/L001 C3L-C: Microwave Frequency Standards, Room P/L002
15:40	Coffee / tea
15:40 -	Lab Tours
Friday Apr 8th	
08:30 - 16:00	Satellite Workshop: Optical clocks: quantum engineering and international timekeeping

The Conference Laboratory will run in P/L006, Tuesday to Thursday from 09.00 – 17.00

Useful Information

Venue

The Exhibition Centre
University of York
Heslington, York
YO10 5NA, UK

Please ensure that you wear your badge at all times as admission to sessions, events, refreshments and lunches is by badge.

If you have any queries do not hesitate to ask any of the people manning the registration desk or wearing green badges

Tutorials on Monday 4th April will be held in P/L001 and P/L005 in the exhibition centre

If you wish to enter a session after it has started please enter via the back door if possible. In P/L001 and P/L002 the rear entrance is located at the top of the stairs in the corridor outside the lecture theatres. In P/X001 the rear door is located up the steps outside.

Welcome reception and conference dinner

The welcome reception will be in the exhibition area from 6pm until 8pm on Monday. A selection of light refreshments will be provided.

The Conference Dinner is to be held in the National Railway Museum on Wednesday 6th April at 7.00 pm. Coach transport will be supplied from outside the Exhibition area at 6.30pm and will return between 10.30 and 11pm. Guests staying in hotels within the city centre will find that the NRM is a short walk from there. Initially follow signs for the station and then for the NRM. It will also be possible to travel on the supplied coaches to the Museum.

Please note that the floor is uneven at the railway museum and therefore high heels are discouraged.

Emergency numbers

For any emergency dial 999, the call handler will ask which service you require. Alternatively dial 9999 from an internal phone. University security is 3333 and University emergency 4444.

Registration and information desk

On Sunday the registration desk will be located in James college reception area from 17.00 to 19.00.

Monday – Thursday registration will be in the exhibition area and open from 08.00-18.00

Internet Services

Complimentary WiFi will be available. There are two options to connect.

1. If you already have access to EDUROAM please select that network and if required give your normal user name and password.
2. Otherwise select CityConnectWiFi and follow the instructions. This network is also available in many places across York city centre.

Food

All lunches will be held in the Galleria Restaurant next to the exhibition centre (exit near P/X001 and reception).

For evening meals, guests are free to make their own arrangements. There are two pubs which serve food in Heslington village: 'The Charles' is popular with the students, offering a range of

value meal and drink deals; 'The Deramore Arms is more popular with mature students and academic staff, offering a good range of real ales and home cooked food.

For those guests who wish to venture into York, there is a wide range of establishments to choose from. Particular streets containing restaurants are: Walmgate, Fossgate, Goodramgate, Rougier Street, Micklegate and Lendal; but there are also many others. Many of the pubs serve food and most of the hotels also have their own restaurants. There are relatively few places to eat on the main shopping streets of Coney Street, Davygate and Parliament Street.

Breakfast for those staying in campus accommodation will be served in the Galleria restaurant, Roger Kirk Centre, on most days. Guests will be informed of any changes to the breakfast location when they collect their room keys.

Camera and Filming Policy

Please refrain from taking any video or photographs during any of the conference sessions or poster presentations.

Cell Phones and Alarms

As a courtesy to others please ensure that all phones and other alarms are turned off during all presentations.

Smoking

All public buildings (including all the University buildings and the National Railway Museum are strictly **No Smoking**.

Tipping and Taxes in the UK

Prices in restaurants do not always include a tip (or gratuity) but it should be stated on the menu if this is the case. If it is not included it is common to leave 10% to 15% for good service. VAT (20%) is included in the displayed price of any item for which it is charged.

Bus stop and Sign posts

The best bus stop for the University is 'University Library' which is located under the first bridge that the bus passes after leaving the city centre or railway station. If you arrive by bus, the best signs to follow are those for the Physics and Electronics Departments which share the building with the exhibition centre but have better signage. The colleges are also relatively well signed from the bus stop. For Alcuin, walk up the steps around the corner from the bus stop. For Vanburgh and James, cross the road and join the walkway from the bridge.

Presenter Information

Session Chairs

Please ensure that you meet your presenters before the start of the session and that you know who is presenting each paper. Ensure the presentations have been loaded onto the computer. You will be provided with a timer and are expected to ensure that the session keeps to good time to allow people to switch between sessions with minimal disruption if necessary. Laser pointers will be provided. Please ensure that these are returned at the end of each presentation.

If a speaker is absent, please do not change the session schedule which may cause people to miss a presentation they had intended to listen to.

Oral Presenters

The duration of a presentation slot is 20 minutes (40 minutes for invited speakers). You will have about 15 minutes for the presentation itself and about 5 minutes for questions from the audience (35 minutes for presentation and 5 minutes Q&A for invited speakers). Since most speakers spend

an average of one minute per slide, it would probably be best if the number of slides in your presentation is around 15 (or 30-35 for invited speakers).

LCD projectors and computers (MS PowerPoint & Adobe Acrobat Reader) will be available in every session room for regular presentations. Overhead projectors, 35mm slides projectors and VHS videotape players are NOT available.

If you have special requests please let us know well in advance. An AV technician will be available should any assistance be needed.

All presentations must be pre-loaded in the talks upload area (close to the registration desk). Please do this the previous day (for those giving presentations on Tuesday this can be done during the welcome reception). Please bring a memory stick containing your presentation.

To avoid software compatibility problems (MS PowerPoint), speakers are advised to save their PowerPoint presentation in "pack-n-go" format AND bring a backup PDF version of their presentation. "Pack-n-go" format is used when burning a presentation to a CD for use on another computer that may or may not have your current version of PowerPoint installed. It installs a viewer capability. The file should be saved as "Package for CD" under the "File" tab in PowerPoint 2003, under the "File > Publish" tab in PowerPoint 2007, under "File > Save & Send > Package Presentation for CD" in PowerPoint 2010, and under "File > Export > Package Presentation for CD" in PowerPoint 2013.

Poster Presentations

Poster boards will be available for presenters to put up their poster presentations. The size of each poster board is 100 cm (wide) by 250 cm (tall). Your poster will be attached using the fixings which will be provided.

The recommended format is **A0 portrait**: 84.1 cm x 118.9 cm (33.1 inch x 46.8 inch).

The location of your poster will be noted on each board in accordance with the corresponding number listed in the Programme Book given out at registration. You will be required to be present at your poster presentation during the hours listed in the Programme Book for the Poster Session, but your poster can remain in place all the time.

There will be a dedicated area for the student poster competition finalists in P/L005.

Conference Lab

The conference lab (located in P/L006) provides hands-on experience in key areas of time and frequency metrology, including:

Frequency stability and phase noise of sources

Oscillator lab kits enabling modelling and measurement of the key parameters of oscillators

Inside a CPT atomic clock

Residual phase noise measurements of amplifiers and two-port devices

Operation of high performance test equipment with capability up to 7 GHz.

Test samples will be from major manufacturers.

Attendees are invited to bring their own devices, preferably with own connectors and power supply.

The lab will be open for the 3 conference days (9.00 – 17.00).

Staff will be available to assist at all times.

Contact persons: Wolfgang Schäfer (TimeTech) and Simon Bale (York)

Opening and plenary session

The EFTF 2016 Scientific Committee is pleased to announce the following plenary session.

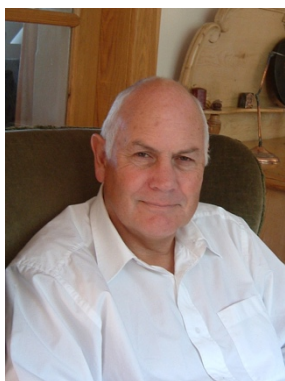
Location P/X001

Date Tuesday 5th April 2016

Time 8.40 - 10.40

Chairs Pascale Defraigne, Jeremy Everard and Ekkehard Peik

Professor Andrew Lyne



Emeritus Professor of Physics, University of Manchester and former Director of the Jodrell Bank Observatory

'The formation, life and uses of pulsars - nature's finest cosmic clocks'

Pulsars are rapidly rotating neutron stars and are some of the most exotic objects in the universe. They are mostly only observable using radio telescopes. In this talk, I will provide an introduction to pulsars and how they are formed in the violence of the supernova collapse of large stars. I will describe how these massive cosmic flywheels can make superb clocks which can be used to conduct unique experiments in gravitation. In particular, they can be used to explore some of the fundamental laws of physics that determine how the universe evolved.

David Rooney



Curator of Time, Navigation and Transport at the Science Museum

'Selling time: Stories from the Greenwich Observatory'

What time is it? We are surrounded today by accurate time. We can hear time signals on the radio or look at automatically corrected kitchen clocks. Our home computers are synchronised by the internet or we can pick up the telephone and call the speaking clock. But how did people check the time before all this existed? In this lively illustrated talk, David Rooney tells the tale of how precise Greenwich time has increasingly been distributed around Britain, Europe and the world from humble local beginnings in the early nineteenth century. It includes stories of scientists and telephonists, terrorists and horologists, poets and paupers, bombers and bell-ringers, from millionaires and murderers to the Greenwich Time Lady and the Girl with the Golden Voice. Rooney reveals the human faces behind the remorseless tick of the clock.

EFTF 2016 Awards

Two awards, sponsored by the UK National Physical Laboratory, will be presented at EFTF 2016 to recipients selected by the Executive Committee of the EFTF.

European Frequency and Time Award 2016



Harald Schnatz

“for his seminal contributions to different but interrelated fields of most accurate time and frequency measurements and dissemination in particular the first phase coherent measurement of a frequency standard in the visible and the dissemination of stable and accurate frequencies via optical fibre networks”

EFTF Young Scientist Award 2016



Nils Huntemann

"for the development and evaluation of an optical clock based on the octupole transition in a single $^{171}\text{Yb}^+$ ion with an uncertainty at the 10^{-18} level"

Sponsors of the student travel support programme

The EFTF 2016 Organising committee gratefully acknowledges the support of the following companies and institutions.



CSEM Centre Suisse d'Electronique et de Microtechnique



First-TF



FSRM

Fondation Suisse pour la recherche en microtechnique



HELMHOLTZ
FONDS e.V.

Helmholtz Fonds e.V.

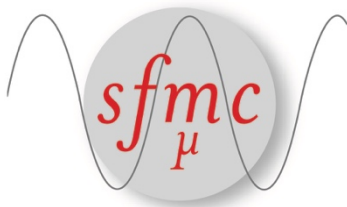


Meinberg Funkuhren



QUARTZ OSCILLATORS, FILTERS, CRYSTALS AND BLANKS
MORION, INC.

Morion



Société Française des Microtechniques et de Chronométrie
(SFMC)



Spectratime



T4Science

TIMETECH



TimeTech



TOPTICA Photonics AG

unine

UNIVERSITÉ DE
NEUCHÂTEL

Université de Neuchâtel

Student Finalists

The following papers were selected as finalists by the EFTF 2016 Scientific Committee for the Student Poster Competition. This year, the student poster awards are sponsored by the UK National Physical Laboratory.

Date and Time Tuesday 5th April, 14.00 – 15.40

Location P/L005

Posters will remain up for the whole conference

Papers marked with an L are also being given as lectures

Paper ID	Group	Title
(L) #1061#	1 & 4	Elimination of Spurious Modes in Zinc Oxide Resonators <i>Ossama Mortada, Matthieu Chatras, Abdel Halim Zahr, Pierre Blondy, Aurelian Crunteanu, Jean-Christophe Orlianges</i>
(P) #1109#	1 & 4	Mapping Acoustic Field Distributions of VHF to SHF SAW Transducers Using a Scanning Electron Microscope <i>Aurelien Godet, Jean-Michel Friedt, Soukalo Dembele, Nadine Piat, Abdelkrim Khelif, Pascal Vairac, Joel Agnus, Pierre Yves Bourgeois, Gwenhael Goavec-Merou</i>
(L) #1125#	1 & 4	S0 Lamb Wave Resonators for in-Liquid Sensing: Promising Alternative to Shear Bulk Acoustic Wave Devices <i>Teona Mirea, Ventsislav Yantchev, Enrique Iborra</i>
(P) #1206#	1 & 4	Build-Up Detection and Level Monitoring by Using Capacitive Global Technique <i>Fovad Ali Khan, Adnan Yousaf, L.M. Reindl</i>
(L) #1043#	2	Frequency Synthesis from Cryogenic Sapphire Oscillator <i>Etienne Vaillant, Fabrice Sthal, Joël Imbaud, Yannick Gruson, Christophe Fluhr, Serge Grop, Vincent Giordano, Enrico Rubiola, François-Xavier Esnault, Gilles Cibiel</i>
(P) #1177#	2	Digital Electronics Based on Red Pitaya Platform for Coherent Fiber Links <i>Andrea Carolina Cardenas Olaya, S. Micalizio, M. Ortolano, Enrico Rubiola, Jean-Michel Friedt, Claudio Eligio Calosso, (Cecilia Clivati, Alberto Mura, Matteo Frittelli)</i>
(P) #1227#	2	Optical to Microwave Synchronization with Sub-Femtosecond Daily Drift, <i>Aram Kalaydzhyan, Michael Peng, Min Xin, Kemal Shafak, Wenting Wang, Franz Kaertner</i>
(L) #1234#	2	Low Phase Noise 10MHz Crystal Oscillators <i>Tsvetan Burtichelov, Jeremy Everard</i>
(L) #1235#	2	Brillouin lasing in a LiF whispering-gallery mode resonator and application to microwave generation <i>Souleymane Diallo, Guoping Lin, Jean Pierre Aubry, Yanne K. Chembo</i>

(L) #1048#	3	A High-Performance CPT-Based Cs Vapor Cell Atomic Clock Using Push-Pull Optical Pumping <i>Moustafa Abdel Hafiz, Rodolphe Boudot</i>
(P) #1099#	3	Light Shifts Studies in CW and Ramsey Double Resonance Vapor Cell Frequency Standards <i>Mohammadreza Gharavipour, Ivan S Radojičić, Florian Gruet, Christoph Affolderbach, Aleksandar J Krmpot, Brana M Jelenkovi, Gaetano Mileti</i>
(P) #1112#	3	Non-Destructive MEMS Atomic Vapor Cells Characterization by Raman Spectroscopy and Image Analysis <i>Sylvain Karlen, Jean Gobet, Thomas Overstolz, Jacques Haesler</i>
(L) #1139#	3	Progress on the CPT Clock: Reduction of the Main Frequency Noise Sources <i>Francois Tricot, Peter Yun, Bruno Francois, Sinda Mejri, Jean-Marie Danet, M. Lours, Stephane Guerandel, Emeric De Clercq</i>
(L) #1156#	3	Toward Self Spin-Squeezing in a BEC Atom Clock <i>Theo Laudat</i>
(P) #1008#	5	Using Known Ground Station Clock Offsets to Improve Tropospheric Delay Estimates at NIMT Timing Station <i>Chaiyaporn Kitpracha, Thayathip Thongtan, Pornchanit Moonaksorn, Rata Suwanton, Chalermchon Satirapod</i>
(P) #1057#	5	Multi-Clock Dissemination via One Ring-Like Fiber Network <i>Wei Chen, Qin Liu, Jialiang Wang, Nan Cheng, Youzhen Gui, Haiwen Cai</i>
(P) #1089#	5	Time Transfer Over a White Rabbit Network <i>Namneet Kaur, Philip Tuckey, Paul-Eric Pottie,</i>
(P) #1095#	5	Synchronous Mode-Locked Laser Network with Sub-fs Drift and Multi-km Distance <i>Kemal Shafak, Ming Xin, Michael Y Peng, Franz X Kaertner</i>
(P) #1208#	5	Optimized 1f-2f Actively Compensated Frequency Synchronization <i>Xi Zhu, Bo Wang, Chao Gao, Yibo Yuan, Jingwen Dong, Lijun Wang</i>
(L) #1027#	6	Quantum Logic State Detection for Molecular Ions <i>Fabian Wolf, Yong Wan, Jan Heip, Florian Gebert, Chunyan Shi, Piet Schmidt</i>
(L) #1070#	6	Carrier-Envelope Offset Characterization in a Semiconductor Modelocked Laser Without f-to-2f Interferometry <i>Pierre Brochard, Nayara Jornod, Valentin Wittwer, Stéphane Schilt, Dominik Waldburger, Sandro Link, Cesare Alfieri, Matthias Golling, Laurent Devenoges, Jacques Morel, Ursula Keller, Thomas Südmeyer</i>

(L) #1158#	6	Atomic Quadrupole Moment Measurement Using Dynamic Decoupling Ravid Shaniv , <i>Nitzan Akerman, Roee Ozeri</i>
(L) #1163#	6	87Sr and 88Sr Optical Lattice Clocks at NPL <i>Ian Hill, Richard Hobson, William Bowden, Marco Menchetti, Antoine Rolland, Fred Baynes, Helen Margolis, Patrick Baird, Kai Bongs, Patrick Gill</i>
(L) #1171#	6	State-of-the-Art Ultra-Low Phase Noise Photonic Microwave Generation Romain Bouchand , <i>Xiaopeng Xie, Daniele Nicolodi, Pierre-Alain Tremblin, Giorgio Santarelli, Christophe Alexandre, Michele Giunta, Matthias Lezius, Wolfgang Haensel, Ronald Holzwarth, Datta Shubhashish, Joshi Abhay, Yann Le Coq</i>

Local Organising Committee

Jeremy Everard (Chair)	University of York
Simon Bale	University of York
Tsvetan Burtichelov	University of York
Linda Dawson	University of York
Matthew Kilburn	University of York
Helen Margolis (vice-chair)	National Physical Laboratory
Sundeep Bhandari	National Physical Laboratory
Patrick Gill	National Physical Laboratory
Rachel Godun	National Physical Laboratory
Leon Lobo	National Physical Laboratory
Krzysztof Szymaniec	National Physical Laboratory
Peter Whibberley	National Physical Laboratory
Mike Underhill	Underhill Research
Joël Petetin	Observatoire de Besançon

EFTF 2016 Executive Committee

Elected Members

- Ekkehard Peik - Physikalisch-Technische Bundesanstalt, Germany (Chair)
- Gaetano Mileti - Laboratoire Temps-Frequence, Switzerland (Tutorial Chair)
- Wolfgang Schaefer - TimeTech, Germany (Exhibition Chair)
- Patrizia Tavella - Istituto Nazionale di Ricerca Metrologica, Italy (Vice Chair)
- François Vernotte - Université de Franche-Comté, France (Academic Chair)
- Pierre Waller - European Space Agency, The Netherlands (Awards Chair)
- Bernard Dulmet - ENSMM, France
- Jeremy Everard - University of York, United Kingdom
- Helen Margolis - National Physical Laboratory, United Kingdom
- Pascal Rochat - Spectratime SA, Switzerland

Ex Officio Members

- Sébastien Thibaud - SFMC, France
- Pascale Defraigne - Royal Observatory of Belgium (Scientific Committee Chair)
- Michael Driscoll - Northrop Grumman Electronic Systems, USA (IEEE-IFCS Standing Committee Chair)
- Lute Maleki - OEwaves, USA (EFTF/IFCS 2017 Co-General Chair)

EFTF 2016 Scientific Committee

Chair: Pascale Defraigne - Royal Observatory of Belgium

Group 1: Materials, Resonators, & Resonator Circuits

Alexandre Reinhardt - CEA-LETI, France (Vice chair)

Thomas Baron - FEMTO-ST, France

Emmanuel Defay - Luxembourg Institute of Science and Technology, Luxembourg

Marc Faucher - IEMN, France

Songbin Gong - University of Illinois at Urbana-Champaign, USA

Olivier Le Traon - ONERA, France

Matteo Rinaldi - Northeastern University, USA

Ashwin Seshia - University of Cambridge, UK

Dana Weinstein - MIT, USA

Ventsislav Yantchev - Uppsala University, Sweden

Group 2: Oscillators, Synthesizers, Noise, & Circuit Techniques

Jean-Pierre Aubry - Aubry Conseil, Switzerland (vice chair)

Claudio Calosso - INRIM, Italy

Gilles Cibiel - CNES, France

Jeremy Everard - York University, UK

David Howe - NIST, USA

Olivier Lopic - LAAS, France

Enrico Rubiola - Femto-ST, France

Fabrice Sthal - Femto-ST, France

Michael Tobar - University Western Australia, Australia

Mike Underhill - Underhill Research, UK

Group 3: Microwave Frequency Standards

Stefan Weyers - PTB, Germany (Vice chair)

Marco Belloni - ESA, Italy

Kurt Gibble - Penn State University, USA

John Kitching - NIST, USA

Motohiro Kumagai - NICT, Japan

Arnaud Landragin - SYRTE, France

Salvatore Micalizio - INRIM, Italy

Gaetano Mileti - Universite de Neuchatel, Switzerland

Krzysztof Szymaniec - NPL, UK

Qinghua Wang - Spectratime, Switzerland

Group 4: Sensors & Transducers

Svenja Knappe - NIST, USA (Vice chair)

Ventsislav Yantchev - Uppsala Observatory, Sweden

Sylvain Ballandras - Frecnsys, France

Ralf Lucklum - University of Magdeburg, Germany

Paul Muralt - EPFL, Switzerland

Leonhad Reindl - Uni Freiburg, Germany

Victor Plessky - GVR Trade SA, Switzerland

Holger Fritze - TU Clausthal, Germany

Diethelm Johannsmann - TU Clausthal, Germany

Alfred Binder - CTR AG, Austria

Group 5: Timekeeping, T&F Transfer, Telecom and GNSS applications

Pierre Waller - ESA-ESTEC, The Netherlands (Vice chair)

Anne Amy-Klein - LPL (CNRS, UP13), France

Andreas Bauch - PTB, Germany

Laurent-Guy Bernier - METAS, Switzerland

Jerome Delporte - CNES, France

Miho Fujieda - NICT, Japan

Gesine Grosche - PTB, Germany

Per Olof Hedekvist - SP, Sweden

Judah Levine - NIST, US

Huang-Tien Lin - NTFSL - TL, Taiwan

Xiao Chun Lu - NTSC, China

Nathan Newbury - NIST, US

Vitaly Pal'chikov - VNIIFTR, Russia

Ed Powers - USNO, US

Maria Ramos - ESA-ESOC, Germany

Wolfgang Schaefer - TimeTech, Germany

Amitava Sen Gupta - NPLI, India

Patrizia Tavella - INRIM, Italy

Philip Tuckey - LNE-SYRTE OP, France

Pierre Urich - LNE-SYRTE OP, France

Hongbo Wang - BIRM, China

Peter Whibberley - NPL, UK

Michael Wouters - NMI, Australia

Aimin Zhang - NIM, China

Victor Zhang - NIST, US

Group 6: Optical Frequency Standards and Applications

Helen Margolis - NPL, UK (Vice chair)

Luigi Cacciapuoti - ESA, The Netherlands

Davide Calonico - INRIM, Italy

Roman Ciuryło - Nicolaus Copernicus University, Poland

Pierre Dubé - NRC, Canada

Patrick Gill - NPL, UK

Kazumoto Hosaka - AIST/NMIJ, Japan

Tetsuya Ido - NICT, Japan

Steve Lecomte - CSEM, Switzerland

Yann Le Coq - LNE-SYRTE, France

Christian Lisdat - PTB, Germany

Jérôme Lodewyck - LNE-SYRTE, France

Andrew Ludlow - NIST, USA

Andre Luiten - University of Adelaide, Australia

Long-Sheng Ma - East China Normal University, China

Mikko Merimaa - MIKES Metrology, VTT Technical Research Centre of Finland Ltd,

Jacques Morel - METAS, Switzerland

Ekkehard Peik - PTB, Germany

Thomas Südmeyer - LTF-UNINE, Switzerland

Alexey Taichenachev - Institute of Laser Physics, Russia

Social Programme

Monday 4th April **Welcome reception in exhibition centre**

18:00 – 20:00

Join us for a welcome drink and a selection of light food.

Wednesday 6th April Conference Dinner at the National Railway Museum

18:30 Coach

19:00 – 23:00 Reception and dinner

Take this opportunity to visit this fascinating museum with its large range of engines and railway coaches. Coaches will depart from outside the exhibition centre at 18.30 and will return between 22.30 and 23.00. EFTF and Student awards will be presented during the dinner.

Thursday 7th April, Lab Tours

15:40 onwards

If you are interested in visiting some of the laboratories within the Department of Electronics, University of York, please sign up for the tours which will take place after the conference has ended. Sign-up sheets will be located at the reception desk.

Coach Tours

Wednesday 6th April Day trip to Fountains Abbey world heritage site

09:30 - ~16:30

A coach will leave the exhibition centre at about 09.30 and will return at about 16.30. This visit is intended primarily for the partners of conference attendees. The coach is provided free of charge but guests are expected to pay for their own admittance.

Thursday 7th April Day trip to Castle Howard

09:30 - ~16:30

A coach will leave the exhibition centre at about 09.30 and will return at about 16.30. This visit is intended primarily for the partners of conference attendees. The coach is provided free of charge but guests are expected to pay for their own admittance.

Tutorial schedule: Monday 4th April

	Tutorials - Track 1 (Room: P/L001)	Tutorials - Track 2 (Room: P/L005)
08:30 - 10:00	K Szymaniec, NPL 'Cs Primary frequency standards'	P Tavella, INRIM 'Precise Time Scales and Navigation Systems, the Ultimate Challenge to Time Metrology'
10:00	Coffee / tea break	
10:15 - 11:45	S Micalizio, INRIM 'Vapor cell frequency standards'	P Defraigne, ROB 'Global Navigation Satellite Systems'
11:45	Lunch break	
13:00 - 14:30	E Peik, PTB 'Optical clocks'	C Nelson, NIST 'Phase noise measurements'
14:30	Coffee / tea break	
14:45 - 16:15	S Webster, M2L 'Lasers for optical frequency standards'	E Rubiola, FEMTO-ST 'Phase noise and jitter in digital electronics'
16:15	Coffee / tea break	
16:30 - 18:00	G Grosche, PTB 'Frequency and time transfer using optical fibers'	B Neubig, AXTAL 'Measurement techniques for piezoelectric resonators'

Welcome Reception 18.00 – 20.00 Exhibition Centre

Krzysztof Szymaniec - Cs Primary frequency standard

In 2015, the metrology community celebrated 60 years of the atomic clock. Seminal works of Rabi, Ramsey, Essen and others initiated a disruptive change in timekeeping and led to a new definition of the second based on atomic rather than astronomical phenomena. Decades of subsequent development improved the accuracy of atomic clocks and frequency standards by orders of magnitude with measurement uncertainties currently left at the sixteenth decimal place. In particular, the introduction of laser cooling and construction of atomic fountains have boosted these improvements. Nowadays, more than two decades after its first demonstration, fountain technology appears quite mature and calibrations of the global timescale TAI/UTC rely almost entirely on the fountain standards. In addition, atomic fountains are often used to discipline clocks forming local timescales. A cold atom clock similar to a fountain, but designed to operate in a microgravity environment, will soon be launched and installed on board of the International Space Station for stringent tests of general relativity. On the ground, atomic fountains give important input into the search for a possible time variation of fundamental constants of nature. These devices are also invaluable tools in the development of optical clocks, the anticipated next generation of primary frequency standards.

In this tutorial, I will begin with presenting the basic principle of an atomic clock and a description of a generic atomic fountain set-up. The focus of the lecture will then be on discussing the noise effects limiting short-term stability and systematic effects affecting the accuracy of atomic fountain clocks. The presentation will be given from a 'practitioner' point of view and will conclude with discussing applications of the fountain standards and prospects for further development.

Salvatore Micalizio - Vapor cell frequency standards

Since their first realization in the 1960s, vapour-cell frequency standards have been considered extremely attractive devices in all those applications where good frequency stability performances joined with small sizes, reliability, reduced power consumption and costs are required. These applications include telecommunication, defence, energy, space and radio-navigation. The passive rubidium frequency standard with state selection performed by the incoherent light of a lamp is still nowadays widely adopted in many measurement systems, as well as in advanced technological sectors, such as GPS and GALILEO.

The development of single mode semiconductor laser diodes in the 1980s opened new perspectives in the field of gas cell frequency standards, thanks to the replacement of the discharge lamp with a coherent optical source. In terms of frequency stability, the expected performance improvement was theoretically estimated to be 2-3 orders of magnitude, predicting a white frequency noise limit in the $10^{-14} \tau^{-1/2}$ region, τ being the integration time. However, laser noise transferred to the clock signal via the light-shift effect prevented this result from being reached. In the last twenty years, innovative schemes have been considered with the aim of approaching the expected theoretical limit and new concept laser-pumped frequency standards have been developed. These clocks are the object of this tutorial.

After resuming the main features of the traditional lamp-pumped Rb clock, the tutorial will focus on several interesting approaches that have been envisaged not only to get close to the fundamental stability limit, but also to reduce at the same time the requirements on the laser noise. These techniques include coherent population trapping, light-shift compensated schemes and pulsed optical pumping. The tutorial will describe these proposals, their main advantages and limitations and the most significant results obtained by various research groups.

Ekkehard Peik - Optical clocks

Optical clocks based on laser cooled and trapped atoms (in optical lattices at the 'magic' wavelength) and ions (in radiofrequency Paul traps) have made fast progress in recent years, with the most advanced systems now reaching an instability of 10^{-16} in only 10 s of averaging time and a systematic uncertainty in the low 10^{-18} range. This lecture will discuss the principles, experimental requirements and methods that have enabled these performances. Emphasis will be placed on the different atomic systems and types of 'forbidden' reference transitions, and on the spectroscopic methods that provide the required control of systematic frequency shifts, especially those associated with the interaction with external electric and magnetic fields. I will also discuss the conceivable future directions for the reliable evaluation and for scientific applications of atomic frequency standards with an uncertainty below that of Cs clocks.

Stephen Webster - Lasers for optical frequency standards

Over the past 50 years, atomic clocks have been based on microwave frequencies and primary standards have demonstrated uncertainties at the level of a few parts in 10^{16} . Optical clocks are a new generation of atomic clock, in which the frequency of light is the signal used for timing. They are based on 'forbidden' atomic transitions for which light is absorbed over a very narrow range of frequencies. Depending on the particular atomic species and transition used, the ratio of the frequency to the frequency width (Q-factor) ranges from 10^{14} - 10^{23} , thus, these transitions constitute

very precise frequency references. They are also insensitive to external electromagnetic fields and can be highly reproducible with uncertainties at the level of parts in 10^{18} . Further, given that the frequency of light is $\sim 100,000$ times higher than that of microwaves, the same level of precision as a microwave atomic clock may be reached in a much shorter time. As optical clocks come of age and prove the stability and reproducibility predicted of them, the prospect will open up for a redefinition of the second in terms of an optical frequency.

The atomic absorber in an optical clock takes one of two forms: it is either a single ion confined in an electro-dynamic trap (Paul trap), or an ensemble of neutral atoms held in an electric dipole force trap (optical lattice). The atomic absorbers are laser cooled so that they are nearly at rest and, to first order, do not experience a Doppler shift on interaction with the light used to probe the atomic transition. To make use of the high-Q of the atomic transition, the probe light must also have a very narrow frequency width and this is achieved by stabilizing a laser to a secondary reference, a high-finesse Fabry-Pérot etalon. A mode-locked femtosecond-pulsed laser (femtosecond comb) converts the very rapid oscillations of the light from some 100s of THz down to a radio frequency so that the output of the optical clock can be counted by commercial electronics and compared to the SI second and the outputs of other optical clocks.

This tutorial will give an overview of the essential elements of an optical clock: the atomic reference, the ultra-stable laser and the femtosecond comb. It will describe how each of these elements is realized in practice and the experimental challenges involved in operating such an apparatus. In particular, a review will be made of the laser sources required for operation of an optical frequency standard, the techniques employed in their stabilisation and the characterization of their noise.

Gesine Grosche - *Frequency and time transfer using optical fibers*

Ever more accurate clocks and frequency references are being developed in dedicated laboratories around the world, reaching astonishingly low instability and high accuracy, currently near 1 part in 10^{18} . Making the ultra-stable output of these powerful instruments available beyond the walls of the metrology laboratory, to enable physics experiments, remains a challenge. In the wake of the optical telecommunication revolution, transfer techniques that make use of optical fibre have greatly developed: within one decade, improvements of more than three orders of magnitude in precision have been achieved.

Recently, long-distance frequency transfer with an uncertainty of 2 parts in 10^{20} , and, for 1 km-scale links, synchronisation at the level of femto-seconds has been reported. Fibre based transfer of frequency has been achieved over distances exceeding 1000 km, which enables international comparisons of clocks and other joint experiments.

In this tutorial I will illustrate advantages and challenges of using optical fibre as a transmission medium for precision metrology. This will cover basic concepts, techniques and limitations, focussing on optical telecommunication fibre (1.55 μm), which is both cheap and optimised for low loss, making it suitable for long-distance transfer. The tutorial will give an overview and comparison of different transfer techniques centred on methods using the optical carrier phase.

Patrizia Tavella - *Precise Time Scales and Navigation Systems, the Ultimate Challenge to Time Metrology*

Today, atomic clocks enable precision estimates of time and position. Through the use of ultra-precise atomic frequency standards, we can form time scales, such as the international time standard Universal Coordinated Time (UTC), capable of dating events with nanosecond accuracy. Similarly, Global Navigation Satellite Systems (GNSS), provide location all over the world with sub-meter accuracy.

In timekeeping, as well as in navigation systems, the questions may be similar, but the answers are frequently dissimilar, due to different goals, requirements, technology availability and constraints. In both cases precision clocks, measuring systems, and a reference time scale are required; in both cases we need to estimate how often the clocks are to be resynchronized and what is the acceptable time error that a clock may accumulate without compromising system performance. We require a mathematical model to predict clock behaviour in order to maintain agreement with another reference clock or to ensure updated navigation messages. We need to understand the 'normal' behaviour of a clock to be able to quickly identify anomalies which can lead to incorrect estimates.

This lecture presents the needs of precise Timing and Navigation, explaining the current international timekeeping architectures and the timing systems of the current GNSS, giving insight to the most demanding topics that still challenge Time Metrology.

Pascale Defraigne - *Global Navigation Satellite Systems*

GNSS and Time have a bi-directional relationship. On the one hand, GNSS also relies on time: everything is based on the measurements of the signal travel time between the satellite and the receiver. GNSS therefore needs a reference timescale maintained by the operators and broadcast by the satellites. On the other hand, the satellite navigation systems offer a wonderful tool for time and frequency metrology, as these flying atomic clocks on board the satellites can be used as a reference for the comparison of ground time and frequency standards.

This tutorial will raise both aspects of the link between GNSS and TIME. After showing concretely the need for accurate time scales for the GNSS, the 'GNSS time transfer' technique will be detailed. Code and carrier phase measurements will be presented and the procedure to get a precise and accurate clock comparison will be explained, both from the instrumental point of view and in terms of data analysis. GNSS Common View (or All in View) as well as Precise Point Positioning will be detailed in the presentation. The different error sources on the measurements will be studied and hence an ideal station set-up will be presented.

Craig Nelson - *Phase noise measurements*

Noise is everywhere. Its ubiquitous nature interferes with or masks desired signals and fundamentally limits all electronic measurements. Noise in the presence of a carrier is experienced as amplitude and phase modulation noise. Modulation noise will be covered from its theory, to its origins and consequences. The effects of signal manipulation such as amplification, frequency translation and multiplication on spectral purity will be examined. Practical techniques for measuring AM and PM noise, from the simple to complex will be discussed. Typical measurement problems, including the cross-spectrum anti-correlation, will also be covered.

Enrico Rubiola - *Phase noise and jitter in digital electronics*

Digital electronics is progressively replacing analog electronics, even in applications where low noise is critical. When the analog signal cannot be avoided, the world is still going digital, with analog-to-digital and digital-to-analog conversion as the natural complement. The reasons are obvious: simplicity, reproducibility, cost, and no or minimal calibration. Additionally, youngsters are trained to digital, not to analog, and the digital hardware benefits from the Moore law.

Having said that, we go through phase noise in digital electronics and in the analog-digital interface, focusing on frequency applications, synthesis, and measurement. This tutorial will cover the following topics, deriving most of the concepts from examples.

- Review of definitions and principles. Phase noise spectrum, Allan deviation, jitter, quantization noise, and aliasing.

- Simplified model of a digital circuit. Front-end, sin-to-square conversion, aliasing, and clock distribution. The Egan model for frequency synthesis.
- Basic noise types found in digital electronics. Phi-type noise (regular and aliased), X-type noise (regular and aliased), chattering (multi-bouncing), and thermal effects.
- The volume law, which states the unfortunate fact that big cell size is better.
- On-chip PLL and clock frequency multiplication.
- Noise in digital chips. Model, examples, and analysis of a few phase noise spectra (FPGA, SoC, CPLD, TTL). VHF and microwave digital dividers. The classical Π (regular) scheme and the de-aliased Λ scheme.
- Direct Digital Synthesizer (DDS). Principles. Noise from truncation and non-linearity. Examples, and analysis of a few phase noise spectra.
- Phase noise in analog-to-digital converters.

This is a new tutorial, mostly based on material not available in the general literature. The author owes gratitude to P. Y. Bourgeois, C. E. Calosso, J. M. Friedt, G. Goavec-Merou, Y. Gruson, and the Go Digital Working Group at the FEMTO-ST Institute.

Bernd Neubig - *Measurement techniques for piezoelectric resonators*

This tutorial covers the measurement techniques for piezoelectric resonators in a wide frequency range, from low-frequency (tuning fork) resonators in the kHz range, over AT- and SC-cut resonators in the MHz range to HFF and SAW resonators up to the GHz range. Special emphasis will be given to the relevant IEC standards.

In this tutorial, I will discuss the following measurement techniques with their pros and cons:

- Classical Zero-Phase measurement technique (IEC 60444-1 and 60444-2)
- Measurement of resonator parameters up to >1 GHz by using modern network analysers with error correction (IEC 60444-5, EIA-512)
- Direct measurement of load resonance (IEC 60444-4 and 60444-11)
- Test fixtures for THD and SMD resonators (IEC 60444-1, 60444-5 and 60444-8)
- Measurement on low-frequency resonators (kHz) (IEC 60689)
- Drive Level Dependency (DLD) measurement to identify irregular non-linear resonator behaviour (IEC 60444-6 Ed 2)
- Characterization of activity dips and frequency jumps occurring over a narrow temperature interval (IEC 60444-7)
- Measurement of spurious resonances and their parameters (IEC 60444-9)
- Determination of frequency aging (IEC 60122-1, MIL-PRF-3098)

Detailed Conference Programme

Tuesday 5th April

P/X001			
Opening session and plenary lectures			
8.40-10.40	<p>Professor Andrew Lyne The formation, life and uses of pulsars - nature's finest cosmic clocks</p> <p>David Rooney Selling time: Stories from the Greenwich Observatory</p> <p>Chairs: Pascale Defraigne, Jeremy Everard and Ekkehard Peik</p>		
10:40	Coffee/tea break		
	Lecture sessions		
	P/X001	P/L001	P/L002
11:10-12.30	<p>A1L-A <u>Timescales and SI Second</u> Chr: Victor Zhang Track: Timekeeping, Time and Frequency Transfer, GNSS Applications</p>	<p>A1L-B <u>Cold Atoms for Sensors and Clocks</u> Chr: Franck Pereira dos Santos Track: Microwave Frequency Standards</p>	<p>A1L-C <u>Piezoelectric Resonators I</u> Chr: Alexandre Reinhardt Track: Materials, Resonators, & Resonator Circuits</p>
12.30	Lunch		
14.00-15.40	Poster session 1 Exhibition Centre, Student poster finalists P/L005		
15.40	Coffee / tea break		
16:00-17:40	<p>A3L-A <u>Lattice Clocks I</u> Chr: Ekkehard Peik Track: Optical Frequency Standards and Applications</p>	<p>A3L-B <u>Space Applications</u> Chr: Marco Belloni Track: Timekeeping, Time and Frequency Transfer, GNSS Applications</p>	<p>A3L-C <u>Sensors</u> Chr: Svenja Knappe Track: Sensors & Transducers</p>

A1L-A Timescales and SI Second

Chair Victor Zhang

P/X001

11:10 Towards Redefining the SI in 2018 (Invited paper)

#1019#

Luc Erard
LNE, France

During its 25th session held in November 2014 in Versailles, The General Conference on Weights and Measures (CGPM) re-confirmed its intention to adopt new definition for the the following base units: the kilogram, the ampere, the kelvin and the mole, leaving the present definition of the second, meter and candela unchanged. The new definition of the units should be based on fixed numerical values of fundamental constants respectively: the Planck constant h , the elementary charge e , the Boltzmann constant k and the Avogadro constant N_A . The new definitions are chosen to maintain continuity, so that the magnitude of the four redefined units in the “new SI” will be essentially identical to their magnitude at the moment of adoption. The limits of the present system will be presented first, then the choice that have been made to arrive at these proposals, and further details of the change involved in the “new SI”.

11:50 National Time Scale and Primary Frequency Standard of VNIIFTRI: Current Status

#1230#

Sergey Golubev^{2}, Sergey Donchenko^{1}, Igor Blinov^{1}, Vitaly Palchikov^{1}, Aleksander Goncharov^{1}, Leilya Gerieva^{2}
^{1}FGUP VNIIFTRI, Russia; ^{2}Rosstandart, Russia

The national time scale of the Russian Federation is reproduced and maintained based on the State standard of time and frequency operated at a facility located in Mendeleevo, Moscow Region. The aim of the VNIIFTRI system of primary frequency standards, comprising two caesium fountains, is to perform regular calibrations of the international time-scale TAI/UTC at the highest accuracy and to provide a stable reference for the construction and steering of UTC(SU), the local representation of UTC in Russia.

12:10 Incorporating Optical Clocks Into UTC(k) Time-Scales

#1159#

Peter Whibberley, Helen Margolis, Patrick Gill
NPL, United Kingdom

Improvements in the performance of optical clocks have led to increasing interest in their use for steering UTC(k) time-scales. During the ITOC campaign of European optical clock comparisons in June 2015, the NPL Sr lattice and Yb⁺ ion trap clocks were measured against the H-maser generating UTC(NPL) over 26 days, with availabilities in excess of 70%. We have used the data to simulate steering UTC(NPL) to one or both of the optical clocks, investigated strategies for dealing with the dead times, and compared the results with the BIPM Circular T.

A1L-B Cold Atoms for Sensors and Clocks

Chair Franck Pereira dos Santos

P/L001

11:10 Towards Self Spin-Squeezing in a BEC Atomic Clock

#1156#

Theo Laudat^{1}, Vincent Dugrain^{2}, Jakob Reichel^{2}, Peter Rosenbusch^{1}
^{1}Observatoire de Paris - SYRTE, France; ^{2}UPMC, France

State-of-the-art microwave-frequency standards have reached the quantum projection noise limit, and using spin-squeezing is an appealing approach to overcome this fundamental boundary. Spin squeezed states are quite hard to produce in the case of ⁸⁷Rb spinor condensate as they require to greatly modify the interstate atomic interaction $g\uparrow\downarrow$. We present a new method where the system reduces $g\uparrow\downarrow$ by itself without user intervention, leading to spontaneous spin squeezing in a BEC clock.

11:30 The Matter-Wave Laser Interferometric Gravitation Antenna (MIGA) Project: New Perspectives for High Precision Gravity Measurements

#1093#

 Arnaud Landragin
 CNRS-Observatoire de Paris-UPMC, France

The Matter-wave laser Interferometric Gravitation Antenna (MIGA) project aims at demonstrating precision measurements of gravity with cold atom sensors in a large scale under-ground instrument and at studying the associated powerful applications in geosciences and fundamental physics

11:50 Atomic Sources for Gravitational Wave Detectors

#1130#

 Christian Schubert, Sven Abend, Holger Ahlers, Wolfgang Ertmer, Naceur Gaaloul, Sina Loriani,
 Dennis Schlippert, Ernst Rasel
 Institut für Quantenoptik, Leibniz Universität Hannover, Germany

Gravitational wave detectors based on atom interferometry were proposed in earth bound setups and space borne configurations. The latter may feature a baseline exceeding few kilometres and consequently require an atomic species with an optical clock transition to suppress laser frequency noise. This contribution will present a trade-off for several atomic species considering the flux, residual expansion rates and other parameters affecting the performance.

12:10 Diffractive Optics for a Compact, Cold-Atom Microwave Clock

#1127#

 James Patrick McGilligan, Rachel Elvin, Paul F. Griffin, Erling Riis, Aidan S. Arnold
 University of Strathclyde, United Kingdom

Laser cooled atomic samples have resulted in profound advances in frequency metrology, however the technology is typically complex and bulky. In recent literature [1] we describe a micro-fabricated optical element that greatly facilitates miniaturisation of ultra-cold atom technology. Portable devices should be feasible with accuracy vastly exceeding that of equivalent room-temperature technology, with a minimal footprint. These laser cooled samples are ideal for atomic clocks. Here we will discuss next generation diffractive optical elements (DOE) that have been optimised for implementation in cold atom apparatus. Furthermore, we will demonstrate our work towards building a robust, compact cold atom clock based on a Raman-Ramsey interrogation of the cold atomic sample.

A1L-C Piezoelectric Resonators I
Chair Alexandre Reinhardt

P/L002

11:10 Advances in RF SAW Devices: What Are Demanded? (Invited paper)

#1014#

 Ken-ya Hashimoto
 Chiba University, Japan

A large number of surface acoustic wave (SAW) filters are embedded in a current smart phone, and their annual production is several tens of billions. Since total performances of current mobile communications are often limited by those of SAW devices, drastic enhancement of their performances is still strongly demanded in addition to further reduction of physical size and price. This talk reviews current status and future prospect of radio frequency (RF) SAW devices used in mobile communications. Then a survey is given to demands necessary for realization of near future communication systems.

11:50 Elimination of Spurious Modes in Zinc Oxide Resonators

#1061#

 Ossama Mortada^{2}, Matthieu Chatras^{2}, Abdel Halim Zahr^{2}, Pierre Blondy^{2}, Aurelian
 Crunteanu^{2}, Jean Christophe Orlianges^{1}
^{1}SPCTS UMR 7513, University of Limoges/CNRS, France; ^{2}XLIM UMR 7252, University of Limoges/ CNRS, France

We report on the design, simulation, fabrication and test results of micro-resonators integrating piezoelectric ZnO layers. The micro-resonators are built on top of 2 μ m silicon membranes of SOI-type wafers. We analyze several possibilities of increasing the quality factor Q and the electromechanical

coupling coefficient kt_2 of the devices, for different numbers and different lengths of inter-digitated (IDTs) electrodes by eliminating the plurality of resonance modes which are mixed together at the main mechanical resonance. IDTs of different finger numbers ($N=25, 40, 50$ and 80) and lengths ($L=25\lambda, 35\lambda, 42\lambda$ and 50λ) were designed and fabricated. The measured extracted Q confirms that reducing the length and the number of IDTs fingers enables to reach better electrical performances at 700 MHz. Our results show that for an optimized micro-resonator device having a IDTs length of 25λ and 40 finger electrodes, we obtained a Q of 1180 and a kt_2 of 7.4%

12:10 Transparent Thin Film Bulk Acoustic Wave Resonators

#1189#

Mario DeMiguel-Ramos^{2}, Girish Rughoobur^{2}, Teona Mirea^{1}, Bárbara Díaz-Durán^{1}, Jimena Olivares^{1}, Marta Clement^{1}, Enrique Iborra^{1}, Andrew Flewitt^{2}
^{1}Universidad Politécnica de Madrid, Spain; ^{2}University of Cambridge, United Kingdom

Transparent electronics have interesting applications in the field of electronic consumables. In this work we present fully transparent AlN-based FBARs with a solidly mounted resonator (SMR) structure, fabricated on a glass substrate. The obtained devices display a good performance while keeping a good transparency when placed on a retro-illuminated display.

A2P-D Student Paper Competition P/L005**Poster Area****Chair Francois Vernotte****14:00 – 15:40****Using Known Ground Station Clock Offsets to Improve Tropospheric Delay Estimates at NIMT****Timing Station**

#1008#

Chaiyaporn Kitpracha^{1}, Thayathip Thongtan^{3}, Pornchanit Moonaksorn^{1}, Rata Suwanton^{2}, Chalermchon Satirapod^{1}
^{1}Chulalongkorn University, Thailand; ^{2}Geo-Informatics and Space Technology Development Agency, Thailand; ^{3}National Institute of Metrology Thailand, Thailand

GPS satellite clocks are used as time references for time comparison with receiver clock by a direct measurement of signals from visible satellites. The timing receiver is in a fixed location by applying the Precise Point Positioning algorithm using the Position and Navigation Data Analyst (PANDA) software. When the clock offsets are estimated, the correlations between the estimated station height and the estimated troposphere are existed. This paper shows the estimated tropospheric delay is averagely at 2.5 meters. The repeatability of the station position is at 1 cm vertically.

Quantum Logic State Detection for Molecular Ions

#1027#

Fabian Wolf^{1}, Yong Wan^{1}, Jan Heip^{1}, Florian Gebert^{1}, Chunyan Shi^{1}, Piet Schmidt^{2}
^{1}Physikalisch-Technische Bundesanstalt, Germany; ^{2}Physikalisch-Technische Bundesanstalt, Universität Hannover, Germany

Molecules offer fascinating possibilities for fundamental research due to their rich internal structure. The lack of a cycling transition for cooling and detection in most molecules has limited wide-spread applications. While the development of quantum logic techniques for atomic ions has enabled spectroscopy of previously inaccessible species, the application of these techniques to molecular ions is still infeasible. Here, we present the first implementation of non-destructive state detection using quantum logic operations between a molecular and an atomic ion. This result establishes a technique enabling quantum information processing and high-precision spectroscopy for tests of fundamental physics with cold molecular ions.

Multi-Clock Dissemination via One Ring-Like Fiber Network

#1057#

Wei Chen, Qin Liu, Jialiang Wang, Nan Chen, Fei Yang, Youzhen Gui, Haiwen Cai
Shanghai Institute of Optics and Fine Mechanics, CAS, China

Fiber-based time and frequency dissemination have been developed rapidly to satisfy a higher precision of atomic clocks. In particular, some “multi-users” solutions have been demonstrated to expend its applications. But problem still leaves in multi-clock dissemination and comparison in one simple fiber link. In this paper, we present a novel scheme to distribute ultra-stable frequency signals from different locations with only one active compensation structure. Relative frequency stabilities of 3×10^{-14} @1s and 5×10^{-14} @1s for master and slave clock are obtained. This scheme opens the way to simplify a continental clocks comparison network.

Elimination of Spurious Modes in Zinc Oxide Resonators

#1061#

Ossama Mortada², Matthieu Chatras², Abdel Halim Zahr², Pierre Blondy², Aurelian Crunteanu²,
Jean Christophe Orlianges^{1}
{1}SPCTS UMR 7513, University of Limoges/CNRS, France; ²XLIM UMR 7252, University of Limoges/ CNRS, France

We report on the design, simulation, fabrication and test results of micro-resonators integrating piezoelectric ZnO layers. The micro-resonators are built on top of $2 \mu\text{m}$ silicon membranes of SOI-type wafers. We analyze several possibilities of increasing the quality factor Q and the electromechanical coupling coefficient kt^2 of the devices, for different numbers and different lengths of inter-digitated (IDTs) electrodes by eliminating the plurality of resonance modes which are mixed together at the main mechanical resonance. IDTs of different finger numbers ($N=25, 40, 50$ and 80) and lengths ($L=25 \lambda, 35 \lambda, 42 \lambda$ and 50λ) were designed and fabricated. The measured extracted Q confirms that reducing the length and the number of IDTs fingers enables to reach better electrical performances at 700 MHz. Our results show that for an optimized micro-resonator device having a IDTs length of 25λ and 40 finger electrodes, we obtained a Q of 1180 and a kt^2 of 7.4%

Frequency Synthesis from Cryogenic Sapphire Oscillator

#1043#

Etienne Vaillant^{2}, Fabrice Sthal^{2}, Joël Imbaud^{2}, Yannick Gruson ^{2}, Christophe Fluhr^{2},
Serge Grop^{2}, Vincent Giordano^{2}, Enrico Rubiola^{2}, François-Xavier Esnault^{1}, Gilles Cibiel ^{1}
{1}CNES, France; {2}FEMTO-ST, France

To characterize ultra-stable resonators, the passive technique with carrier suppression is used to measure the inherent phase stability of the ultra-stable resonators. This kind of bench usually uses both identical resonators inserted in each arm in order to suppress the noise of the source [2]. To operate with only one resonator, the driving source must have a phase noise lower than the best resonators that are measured. At 5 MHz, the power spectral density of phase fluctuations of these best quartz crystal resonators is expected around -140 dBc/Hz . In these conditions, the driving source cannot be an ultrastable 5 MHz quartz oscillator. Cryogenic sapphire oscillators present a very low phase noise. Thus in this paper, first results of frequency synthesis chain from cryogenic sapphire oscillator are presented. A 100 MHz signal is divided until 5 MHz in order to get the best phase noise. Several divider combinations are presented and discussed. The limits of commercial dividers are shown and best results have been obtained using regenerative dividers. Further investigations are proposed in order to improve these results.

High-Performance CPT-Based Cs Vapor Cell Atomic Clock Using Push-Pull Optical Pumping

#1048#

Moustafa Abdel Hafiz, Rodolphe Boudot
FEMTO-ST, France

This paper presents a high-performance CPT Cs vapor cell atomic clock using the push-pull optical pumping technique. A fractional frequency stability of 2×10^{-13} up to 100 s has been demonstrated. Latest results will be presented at the conference.

Carrier-Envelope Offset Characterization in a Semiconductor Modelocked Laser Without f-to-2f Interferometry **#1070#**

Pierre Brochard^{2}, Nayara Jornod^{2}, Valentin Wittwer^{2}, Stéphane Schilt^{2}, Dominik Waldburger^{1}, Sandro Link^{1}, Cesare Alfieri^{1}, Matthias Golling^{1}, Laurent Devenoges^{3}, Jacques Morel^{3}, Ursula Keller^{1}, Thomas Südmeyer^{2}
^{1}ETH Zurich, Switzerland; ^{2}Laboratoire Temps-Fréquence, Switzerland; ^{3}METAS, Switzerland

We measured for the first time the noise properties and the modulation response of the free-running carrier-envelope offset (CEO) frequency in a semiconductor modelocked laser. We used a novel characterization method that does not involve standard f-to-2f interferometry, but makes use of an appropriate combination of signals obtained from the comb and a reference continuous-wave laser. We first present a validation of the method in an Er: fiber comb, where the achieved results are in excellent agreement with reference data obtained by f-to-2f interferometry. Then we present an implementation of the method with a modelocked vertical external-cavity surface-emitting laser.

Time Transfer Over a White Rabbit Network**#1089#**

Namneet Kaur^{2}, Paul-Eric Pottie^{2}, Philip Tuckey^{1}
^{1}LNE-SYRTE, Observatoire de Paris, France; ^{2}SYRTE, Observatoire de Paris, France

A very promising direction for precise time transfer through optical fibers is the implementation of White Rabbit PTP (Precision Time Protocol) technology on wide area networks. This novel technology is based on Synchronous Ethernet and other techniques to achieve high performance. It demonstrates sub-nanosecond time stability and synchronization of arrays of instruments over 10-km scale networks. In view of time dissemination on active telecommunication networks, we are exploring uni-directional configurations for White Rabbit links. Our objective is the development of a scalable and compatible network time transfer approach providing multiple user dissemination, competitive with GNSS-based time distribution.

Synchronous Mode-Locked Laser Network with Sub-fs Drift and Multi-km Distance **#1095#**

Kemal Safak^{1}, Ming Xin^{2}, Michael Y. Peng^{2}, Franz X. Kärtner^{1}
^{1}Deutsches Elektronen-Synchrotron, Germany; ^{2}Massachusetts Institute of Technology, United States

Long-term stable timing transfer between three mode-locked lasers over a multi-km fiber network is reported. Two slave lasers are synchronized to the master laser via a 4.7-km fiber link network using balanced optical cross-correlators. The out-of-loop jitter between the slave lasers shows only 1.4-fs RMS total jitter over 40 hours. This results proves the feasibility of a mode-laser network with 10^{-20} relative timing instability.

S0 Lamb Wave Resonators for in-Liquid Sensing: Promising Alternative to Shear Bulk Acoustic Wave Devices**#1125#**

Teona Mirea^{2}, Ventsislav Yantchev^{1}, Enrique Iborra^{2}
^{1}Chalmers University of Technology and Q-Arts Consulting Ltd, Bulgaria; ^{2}Universidad Politécnica de Madrid, Spain

S0 Lamb wave resonators (S0-LWR) have shown great potential for in-liquid operation. They can be used on a dual quantity sensor platform since they are sensitive to both, mechanical (density and viscosity) and electrical (dielectric permittivity) properties of the liquid. Here we present extensive theoretical and experimental studies on their in-liquid sensing mechanisms. Additionally, we compare them to the commonly used solidly mounted shear mode bulk acoustic wave devices and show their comparable in-liquid performance. This places S0-LWR as promising alternative with the advantage of using commercial c-oriented AlN deposition.

Progress on a pulsed CPT Clock: Reduction of the main noise sources contributions #1139#

Francois Tricot^{2}, Sinda Mejri^{2}, Peter Yun^{2}, Bruno Francois^{1}, Jean-Marie Danet^{3}, Stephane Guerandel^{2}, Emeric De Clercq^{2}, M. Lours

^{1}INRIM, Italy; ^{2}LNE-SYRTE, France; ^{3}SYRLINKS, France

Clocks based on coherent population trapping (CPT) represent promising candidates for on-board space and industrial applications thanks to their simple scheme and high stability performance. Indeed in our CPT clocks the microwave frequency is optically carried into a vapor cell of cesium. We present here the main frequency noise sources for the clock stability, now $\sigma_y(1s) = 3.2 \times 10^{-13}$; and what we are doing to decrease the frequency noise contributions.

Towards Self Spin-Squeezing in a BEC Atomic Clock #1156#

Theo Laudat^{1}, Vincent Dugrain^{2}, Jakob Reichel^{2}, Peter Rosenbusch^{1}

^{1}Observatoire de Paris - SYRTE, France; ^{2}UPMC, France

State-of-the-art microwave-frequency standards have reached the quantum projection noise limit, and using spin-squeezing is an appealing approach to overcome this fundamental boundary. Spin squeezed states are quite hard to produce in the case of 87Rb spinor condensate as they require to greatly modify the interstate atomic interaction $g \uparrow \downarrow$. We present a new method where the system reduces $g \uparrow \downarrow$ by itself without user intervention, leading to spontaneous spin squeezing in a BEC clock.

Optimized 1f-2f Actively Compensated Frequency Synchronization #1208#

Xi Zhu^{1}, Bo Wang^{2}, Chao Gao^{2}, Yibo Yuan^{1}, Jingwen Dong^{2}, Lijun Wang^{2}

^{1}Department of Physics, Tsinghua University, China; ^{2}State Key Laboratory of Precision Measurement Technology and Instruments, Tsinghua University, China

To satisfy the Square Kilometre Array (SKA) radio telescope requirements on frequency synchronization, we proposed a 1f-2f actively compensated frequency synchronization system. In the trial test at SKA South Africa site, we found that there is a bump on the Allan variance plots of dissemination stability at the averaging time between 10s and 100s. It is caused by the nonlinear effect of RF components in the system. We optimized the scheme and performed a comparing test of the original and optimized schemes on 50 km fibre spool. In the optimized scheme, the bump on the Allan variance plot almost diminished.

Light Shifts Studies in CW and Ramsey Double Resonance Vapor Cell Frequency Standards

#1099#

Mohammadreza Gharavipour^{2}, Ivan S. Radojicic^{1}, Florian Gruet^{2}, Christoph Affolderbach^{2}, Aleksandar J. Krmpot^{1}, Brana M. Jelenkovic^{1}, Gaetano Miletic^{2}

^{1}Institute of Physics, University of Belgrade, Serbia; ^{2}Laboratoire Temps-Fréquence, Institut de Physique, Université de Neuchâtel, Switzerland

We report our investigations on the compact high-performance rubidium (Rb) vapor-cell clock based on microwave-optical double-resonance (DR). These studies are done in both DR continuous-wave (CW) and Ramsey-DR schemes, using the same clock physics package. Light-shift effects (intensity and frequency) are studied for different laser frequency detuning, in both CW and Ramsey scheme. In the Ramsey scheme, thanks to the separation of light and microwave interactions in the time domain, light-shift effects are suppressed by more than one order of magnitude. This allows improving the long-term clock stability in the case of Ramsey-DR scheme as compared to CW-DR.

Non-Destructive MEMS Atomic Vapor Cells Characterization by Raman Spectroscopy and Image Analysis #1112#

Sylvain Karlen, Jean Gobet, Thomas Overstolz, Jacques Haesler
CSEM SA, Switzerland

The UV decomposition of rubidium azide (RbN_3) in metallic Rb and nitrogen (N_2) is a very promising approach for wafer-level microfabrication of alkali vapor cell. We report on the use of three innovative and non-destructive methods to characterize the decomposition yield and the buffer gas partial pressures (N_2 and Ar) of cells made with this technique: Raman spectroscopy is used as a quantitative method to estimate the N_2 pressure inside the cavity; image analysis is used to quantify the amount of metallic Rb in the cell; Raman is used to identify potential residues in the cavities after the decomposition.

Mapping Acoustic Field Distributions of VHF to SHF SAW Transducers Using a Scanning Electron Microscope #1109#

Aurelien Godet, Jean-Michel Friedt, Soukalo Dembele, Nadine Piat, Abdelkrim Khelif, Pascal Vairac, Joel Agnus, Pierre Yves Bourgeois, Gwenhael Goavec-Merou
FEMTO-ST, France

Scanning Electron Microscopy (SEM) is used for mapping the electric field associated with acoustic wave propagation in acoustic resonators and delay lines. Shear wave acoustic field mapping is thus accessible, making SEM a complementary technique to the classical optical mapping restricted to out-of-plane displacement.

Atomic Quadrupole Moment Measurement Using Dynamic Decoupling #1158#

Ravid Shaniv, Nitzan Akerman, Roe Ozeri
The Weizmann Institute, Israel

We present a method that uses dynamic decoupling of a multi-level quantum probe " a single $88Sr^+$ ion " in order to measure electric quadrupole energy shift in the $D_{(5/2)}$ level. In contrast with typical two-level dynamic decoupling schemes, here we take advantage of the six-fold $D_{(5/2)}$ Zeeman manifold of equidistant levels and reduce the effect of magnetic field noise. By using our measurement scheme, we were able to measure the quadrupole moment of the $D_{(5/2)}$ level in $88Sr^+$ with precision better than that of the previous measurement by an order of magnitude.

Build-Up Detection and Level Monitoring by Using Capacitive Glocal Technique #1206#

Fovad Ali Khan, Adnan Yousaf, L.M. Reindl
IMTEK, University of Freiburg, Germany

This paper presents an innovative proof of concept of level monitoring capacitive sensor and build-up detection by using the "Glocal" (global and local) E-fields. The change in the sensitivity of the sensor to detect the build-up on the sensor probe is increased by using local E-fields. An initial prototype sensor with the length of 89.5 mm is developed and tested on various fluids. Finite element method (FEM) analysis is also performed in order to investigate the sensitivity of the proposed sensor in different liquids with various dielectric constants. An analytical model is also presented which estimates the electric field strength between the capacitive elements as a function of level for a single segment.

Digital Electronics Based on Red Pitaya Platform for Coherent Fiber Links #1177#

Andrea Carolina Cárdenas-Olaya^{3}, S. Micalizio^{2}, M. Ortolano^{2,3}, Enrico Rubiola^{1}, Jean-Michel Friedt^{1}, Claudio Eligio Calosso^{2}, (Cecilia Clivati^{2}, Alberto Mura^{2}, Matteo Frittelli^{2})
^{1}FEMTO-ST Institute, France; ^{2}INRIM, Italy; ^{3}Politecnico di Torino - INRIM, Italy

The work present here continues the work developed by Calosso et al. [2] where tracking direct digital synthesizer (DDS) technique for coherent optical links is introduced, using the flexibility of digital implementation. The proposed system implements the tracking DDS and additional DDSs for

compensation and monitoring completely digital. In that way, the limitation of the system bandwidth caused by the delay between the components interaction is reduced and therefore the cycle slips are minimized. The system implementation is performed in Red Pitaya, a platform driven by a system on chip (SoC) from Xilinx.

Optical to Microwave Synchronization with Sub-Femtosecond Daily Drift

#1227#

Aram Kalaydzhyan^{1}, Michael Peng^{2}, M. Xin ^{1,2}, K. Shafak ^{1}, W. Wang ^{1}, Franz Kärtner^{1}
^{1}Center for Free-Electron Laser Science, Germany; ^{2}Massachusetts Institute of Technology, United States

In this paper we demonstrate that balanced optical-microwave phase detectors (BOMPD) are able to provide a robust long-term optical-RF synchronization with sub-femtosecond residual timing drift over 24 hours in laboratory conditions without active temperature control of optical and electronic paths. Moreover, 10.833 GHz Sapphire-loaded cavity oscillator (SLCO) was successfully disciplined by 216.66 MHz laser oscillator using the BOMPD which resulted in a sub-femtosecond RMS jitter integrated from 1 Hz to 1 MHz.

Low Phase Noise 10MHz Crystal Oscillators

#1234#

Tsvetan Burtichelov, Jeremy Everard
University of York, United Kingdom

This paper describes the design and implementation of low phase noise 10MHz Crystal Oscillators which are being used as part of the chain of a local oscillator for use in compact atomic clocks. The design considerations and phase noise measurements are presented. This paper is based on a previous design [1] but now demonstrates significantly improved phase noise performance and now includes the key circuit descriptions. The latest measurements of the 10MHz crystal oscillator's performance demonstrates a phase noise of -123dBc/Hz at 1 Hz and -148dBc/Hz at 10 Hz. The results compare well with the best 5MHz BVA oscillators when 6dB (+2) is subtracted.

Brillouin lasing in a LiF whispering-gallery mode resonator and application to microwave generation

#1235#

Souleymane Diallo, Guoping Lin ^{2}, Jean Pierre Aubry, Yanne K. Chembo
Femto-ST Institute, France. ^{2} Centre for Gravitational Experiments, China

We report Brillouin lasing in a monofluoride crystalline resonator for the very first time. While Raman scattering results from the interaction between a laser beam and an optical phonon providing a frequency shift in the THz range, Brillouin scattering results from the interaction between a strong laser beam and an acoustic phonon leading to a frequency shift of few GHz, which makes it more suitable for microwave generation. We present a time do-main model which tracks the dynamics of the Stokes and pump waves and finally, with the help of a stability analysis, we determine analytically the threshold power. Such a laser has great potential for ultra-pure microwave and multi-wavelength generation.

87Sr and 88Sr Optical Lattice Clocks at NPL

#1163#

Ian Hill^{1}, Richard Hobson^{1}, William Bowden^{1}, Marco Menchetti^{1}, Antoine Rolland^{1}, Fred Baynes^{1}, Helen Margolis^{1}, Patrick Baird^{2}, Kai Bongs^{3}, Patrick Gill^{1}
^{1}NPL, United Kingdom; ^{2}Oxford, United Kingdom; ^{3}University of Birmingham, United Kingdom

We present an evaluation of the NPL 87Sr optical lattice clock. The evaluation is aided by an improved stability of the clock, provided by an ultra-stable laser at 1064 nm delivered across a fibre comb-based transfer oscillator scheme to 698 nm. We also present progress towards an accurate 88Sr clock and show the elimination of probe induced shifts using a modified-hyper-Ramsey spectroscopy.

State-of-the-Art Ultra-Low Phase Noise Photonic Microwave Generation and Characterization

#1171#

Romain Bouchand^{3}, Xiaopeng Xie^{3}, Daniele Nicolodi^{3}, Pierre-Alain Tremblin^{4}, Giorgio Santarelli^{4}, Christophe Alexandre^{2}, Michele Giunta^{5}, Matthias Lezius^{5}, Wolfgang Haensel^{5}, Ronald Holzwarth^{5}, Datta Shubhashish^{1}, Joshi Abhay^{1}, Yann Le Coq^{3}
^{1}Discovery Semiconductors, Inc., United States; ^{2}LNE-CNAM, France; ^{3}LNE-SYRTE, France; ^{4}LP2N, France; ^{5}Menlo Systems GmbH, Germany

Many applications such as telecommunication, radar, deep-space navigation systems and pre-cision microwave spectroscopy are calling for ultra-stable microwave signals. Photonic generation of such signals is of particular interest because it allows transferring the unsurpassed spectral purity of ultra-stable continuous wave lasers to the microwave domain. The conversion from optical to micro-wave is done by synchronization of the repetition rate of a femto-second laser with an ultra-stable optical frequency reference. The microwave signal is further extracted via fast photo-detection of the optical pulse train. However, the photo-detection process itself introduces excess phase noise hereby limiting the stability of the optically generated microwave signal. The main limits on the purity of the microwave signal generated are the amplitude-to-phase conversion (APC) combined with intensity noise of the femto-second laser and the shot and thermal noise from the photodetector.

**A2P-E
Chair****Frequency References and Measurements
Fabrice Stahl****Poster Area****Recent Development on a Cryogenic Superconducting Cavity Stabilized Oscillator in China**

#1005#

Nuan-Rang Wang^{1}, Zhi Li^{2}, Zhen-Wei Zhang^{1}, Ren-Fu Yang^{1}, Huan Zhao^{1}, Lian-Shan Gao^{1}
^{1}Beijing Institute of Radio Metrology & Measurement, China; ^{2}Second Academy of China Aerospace, China

The design of cryogenic superconducting cavity stabilized oscillator is achieved based on theory analysis and computer simulation. It includes the design of superconducting cavity with high quality factor, cryogenic environment, PLL and so on. The quality factor of cavity reaches $2E9$ and the temperature is 1.6K and the temperature stability is better than 0.001K in experiment. The experiment result is achieved through system debug and optimization that the stability of 1s reaches $4.6E-15$ which is the best in ever reported superconducting cavity stabilized oscillator.

High Precision Time Interval Measurement Based on Temperature Compensation

#1067#

Xiangwei Zhu, Ke Zhang, Zhibin Xiao, Zhicheng Lv, Guangfu Sun
NUDT, China

Time is one of the basic physical quantities which can be measured with high accuracy, especially, the time interval measurement usually possesses accuracy within sub-nanosecond level. Such measurement techniques are widely used in atomic time, satellite navigation, space tracking and control, quantum physics and instruments, etc. It is difficult to perform time interval measurement directly in engineering since system clocks with very high accuracy are required. Hence, several indirect measurement techniques are developed, the most representative approaches are analog interpolation, vernier method and time to amplitude conversion, etc.

System of Formation of Reference Frequency for Modern Data Conversion

#1182#

Anatoly Kosykh, Konstantin Murasov, Sergey Zavyalov, Rodion Fakhrutdinov, Ruslan Wolf
Omsk State Technical University, Russia

In this paper the system generate a set of reference frequencies required to clock functional blocks of data conversion investigation. The basis of the unit for generating reference frequency is phase-locked loop (PLL), which includes a voltage controlled oscillator on delay lines, phase-frequency detector, the output

frequency of the VCO divider, reference divider and loop filter containing the software-configurable system leakage current compensation.

On Temporal Correlations in High Resolution Frequency Counting

#1200#

Tim Dunker^{2}, Harald Hauglin^{2}, Ole Rønningen^{1}
^{1}ICTEC AS, Norway; ^{2}Justervesenet, Norway

We analyse the autocorrelation of time series of gapless frequency data from different high resolution counters. We find that the high resolution ('CONT') frequency counting process of the 53230A type counter imposes long term correlations in the output data. We show how such correlations may be due to smoothing processes with long term memory. Finally, we demonstrate how alternative finite window smoothing filters may be applied to a stream of raw (i.e. not smoothed) continuous frequency data, yielding resolution enhanced frequency estimates without spurious long term correlations.

A2P-F Piezoelectric Resonators II Chair Marc Faucher

Poster Area

Gold Thin Film Viscoelastic Losses of a Length Extension Mode Resonator

#1046#

Beatrice Bourgeteau-Verlhac, Pierre Lavenus, Raphael Levy, Thomas Perrier, Jean Guerard,
Olivier Le Traon, ONERA, France

We presented in a previous paper a new length extension mode (LEM) piezoelectric micro-resonator. We demonstrated that thanks to a specific design anchor losses were very low, showing the $Q \cdot f$ product could be maximized. Assuming viscous fluid damping and thermoelastic damping are negligible, it appears that viscous damping arising from the gold electrodes is the only remaining limiting loss. Assuming a Kelvin Voigt viscoelastic behavior of gold the quality factor expected is lower than previous LEM resonators. From this consideration a study is being carried out on new electrode designs to reduce viscoelastic damping finding a compromise between motional resistance and quality factor and to improve the viscoelastic modeling of electrodes.

In-situ Characterization of AlN-Solidly Mounted Resonators at High Temperature

#1186#

Teona Mirea, Jimena Olivares, Marta Clement, Bárbara Díaz-Durán, Jesús Sangrador, Enrique Iborra
 Universidad Politécnica de Madrid, Spain

Surface acoustic wave devices are widely investigated for high temperature applications. However they still present the drawback of using long and narrow metallic strips for their IDT, which are subjected to destructive agglomeration. In a previous work we proved that solidly mounted resonators (SMR) are promising alternative standing temperatures as high as 700°C in vacuum without degradation in performance after annealing. Here we present in-situ measurements of AlN-based SMR for temperatures up to 400°C. We show that devices maintain a constant temperature coefficient of frequency and their performance is almost preserved with a series resistance degradation due to measurement fixtures.

Behavior of Quartz Crystal Resonators at Liquid Helium Temperature

#1217#

Serge Galliou^{1}, Philippe Abbé^{1}, Maxim Goryachev^{2}, Eugene Ivanov^{2}, Michael Tobar^{2},
 Roger Bourquin^{1}
^{1}FEMTO-ST Institute, France; ^{2}UWA, Australia

Quartz resonators working at cryogenic temperature are an exciting topic of interest because of their very high quality-factors. As a consequence they are good candidates to various applications ranging from frequency references to fundamental physics. A brief reminder is first provided regarding Q-factor properties of BAW SC-cut resonators within 3K - 12K. The A, B and C mode behaviors are also examined in terms of frequency versus temperature. As unpublished data, the frequency dependence with the excitation power is particularly highlighted. Finally recent measurements on noise are discussed.

A2P-G Microwave Frequency Standards & Applications I Poster Area
Chair Patrick Berthoud

Development of an Atomic Interferometer Utilizing the Stimulated Raman Transition #1006#
Sangkyung Lee, Tae Hyun Kim, Sin Hyuk Yim, Hee Sook Ro, Kyu Min Shim
Agency for Defense Development, Korea, South

We demonstrate an atomic interferometer utilizing cold atoms and the stimulated Raman transition to measure acceleration of gravity. To improve performance of an atomic interferometer, the optical pumping to populate the free-falling atoms in the magnetic insensitive state and normalization of atomic population by using the three pulsed probe scheme are applied. The interference fringes are obtained as a function of linear chirp rates of Raman detuning. We also introduce our progresses on development of an atomic interferometer for rotation measurement.

Coherent Population Trapping Ramsey Resonance in Slow Rubidium Beam #1015#
Igor Sokolov
Peter the Great St. Petersburg Polytechnic University, Russia

We calculate the coherent population trapping (CPT) resonance in slow beam of rubidium 87 atoms caused by their interaction with bichromatic electromagnetic field in two separated spatial domains. We study the influence of the atomic beam angular divergence and residual beam velocity spread on the parameter of CPT resonance. The dependence of the profile of the resonance on principal parameters of the system is analyzed.

Effects of Microwave Leakages on the Frequency Shift of Compact Magnetic Selection State Cesium Atom Clock #1039#
Liangyu Huang, Ji Wang, Hongwei Zhu, Ning Zheng, Dapeng Cheng, Jiang Chen, Jun Yang
Lanzhou Institute of Space Technology and Physics, China

This paper discusses the relationship between the microwave leakages in the different positions and frequency shifts. The theoretical results show that the leakage taken place outside the interaction area is the one of key reasons to the frequency shift. With the same parameters, the influence of the leakage occurred inside of the interaction area is three order of magnitude smaller than the outside.

A Novel Alkali Vapor Microcell Architecture for Miniature Atomic Clocks #1050#
Vincent Maurice^{1}, Ravinder Chutani^{1}, Nicolas Passilly^{1}, Rodolphe Boudot^{2}, Serge Galliou^{1}, Moustafa Abdel Hafiz^{1}, Philippe Abbé^{1}, Emeric De Clercq^{3}, Christophe Gorecki^{1}
^{1}FEMTO-ST, France; ^{2}FEMTO-ST - CNRS, France; ^{3}LNE-SYRTE, France

This work presents a new and original architecture of microfabricated alkali vapor cell designed for miniature atomic clocks. The cell combines diffraction gratings with anisotropically etched single crystalline silicon sidewalls to route a normally-incident beam in a cavity oriented along the substrate plane.

Preparation of High Purity Cesium by Molecular Distillation #1055#
Yinguang Ma, Jiang Chen, Ji Wang, Liangyu Huang, Hongwei Zhu, Jun Yang
Lanzhou Institute of Physics, China

A novel technique was developed to purify 99.5% cesium by molecular distillation to meet the stringent requirement of Cesium-Atomic-Clock. The results show that depending on the purification conditions, most impurities of K and Rb were removed. We suggest that the molecular distillation may outperform the conventional vacuum distillation because of a lower temperature and a shorter time.

Study of the Misalignment Between Electromagnetic Fields Interacting with Rb Atoms in a Cavity with Losses **#1072#**

Anton E. Ivanov^{1}, Christoph Affolderbach^{2}, Gaetano Miletì^{2}, Anja K. Skrivervik^{1}
^{1}École Polytechnique Fédérale de Lausanne, Switzerland; ^{2}University of Neuchâtel, Switzerland

In this study we investigate the impact of misalignment of the static and/or microwave magnetic fields from the laser propagation direction. Our analysis is suitable to reveal how the geometry of the cavity and the losses influence the resonance transitions and is relevant in line with newly developed cavity characterization techniques based on field imaging.

Research of Cesium Atom Clock Beam Intensity Associated with Collimator Structure **#1081#**

Hongwei Zhu, Jiang Chen, Ji Wang, Yinguang Ma, Liangyu Huang, Jun Yang
Lanzhou Institute of Space Technology Physics, China

Beam intensity of cesium atom emanated from collimator directly affected performance of cesium atom clock. This thesis analyzed the process of cesium atom emanated from collimator, established theoretical beam distribution model based on reflection of the atom from the walls of the collimator tube, beam distribution related with structure and dimension of collimator. The thesis adopted simulative calculation method and experiment to prove theoretical model. The investigation guided collimator design to improve cesium atom beam intensity and short term stability of cesium atom clock.

High-Contrast Bright-Type Magneto-Optical Resonances in Buffer-Gas or Antirelaxation-Coated Vapour Cells **#1092#**

Denis Brazhnikov^{2}, Maxim BasalaeV^{4}, Alexey Novokreshchenov^{2}, Alexey Taichenachev^{2}, Valeriy Yudin^{4}, Christina Andreeva^{1}, Vasiliy Entin^{3}, Igor Ryabtsev^{3}
^{1}Institute of Electronics, Bulgaria; ^{2}Institute of Laser Physics SB RAS, Russia; ^{3}Institute of Semiconductor Physics SB RAS, Russia; ^{4}Novosibirsk State University, Russia

New method for observing magneto-optical electromagnetically induced absorption resonance (EIA) is theoretically and experimentally studied. We propose new scheme that allows us using buffer gas or antirelaxation-coated cells for dramatically improving properties of the resonance in contrast to the standard schemes. Under the special conditions contrast of EIA resonance can reach value of about 95% and kHz or even sub-kHz width. In the new scheme EIA effect resulted from the coherent population trapping phenomenon (CPT), which regularly leads to electromagnetically induced transparency (EIT). It opens new opportunities for applying the scheme in nonlinear optics, quantum magnetometry and optical communications.

Recent Results of an Atomic Gravimeter Developing at KRISS **#1111#**

Sang-Bum Lee, Taeg Yong Kwon, Sang Eon Park, Myoung-Sun Heo, Hyun-Gue Hong, Chang Yong Park, Won-Kyu Lee, Dai-Hyuk Yu
KRISS, Korea, South

We will introduce recent results of an atomic gravimeter developing at KRISS and also discuss about limiting elements affecting the sensitivity of our gravimeter at this conference.

Quantum Tests of the Universality of Free Fall **#1132#**

étienne Wodey, Henning Albers, Hendrik Heine, Christian Meiners, Logan L. Richardson, Dipankar Nath, Dennis Schlippert, Christian Schubert, Wolfgang Ertmer, Ernst M. Rasel
Institut für Quantenoptik, Leibniz Universität Hannover, Welfengarten 1, 30167 Hannover, Germany

The universality of free-fall (UFF) is at the foundation of our current understanding of gravity through Einstein's general relativity theory. However, theoretical attempts to reconcile general relativity with quantum field theory allow for violations of the UFF. We report on a quantum test of the UFF at the 100 ppb level by performing atom interferometry with two chemically different species. We also present our

strategies to advance quantum tests of the UFF to the level of the best classical tests and beyond using very long baseline atom interferometers.

Hydrogen Plasma Simulation for Atomic Clock Lifetime Assessment

#1134#

Eleonie van Schreven, Marco Belloni
ESA (European Space Agency), Netherlands

Passive Hydrogen Masers are currently embarked onboard of Galileo constellation and are showing outstanding performances. However, given the lack of statistic over lifetime, parallel activities are ongoing for analyzing possible failure mechanisms and improve the robustness. The present work presents a simulation model based on COMSOL Multiphysics, investigating the wear-out effects experienced by the hydrogen gas dissociator.

Optimization of Laser Radiation for CPT-Based Miniature Frequency Standard

#1147#

Konstantin Barantsev, Andrey Litvinov, Evgeniy Popov, Igor Sokolov
Peter the Great St.Petersburg Polytechnic University, Russia

In this work we investigate dependence of stability of the CPT-based miniature frequency standard on parameters of the laser radiation such as total intensity, ratio between sideband intensities, polarization and tuning of each sideband, width of the spectrum and correlation of sidebands.

VNIIFTRI Primary Frequency Standard: Current Status

#1213#

Igor Blinov, Alexandr Boyko, Yuri Domnin, Dmitrii Kupalov, Olga Kupalova
FGUP VNIIFTRI, Russia

National Frequency Standard of Russia, SU-CsFO₂, has been in use since 2012 [1]. CsFO₂ is used for the local representation of the UTC maintained by SU. To date, 18 calibrations of the International Atomic Time (TAI) have been reported to BIPM with a relative frequency agreement of $(-0.7 \pm 4.5) \cdot 10^{-16}$, between CsFO₂ and the average of the other fountains operated in the world in the reference periods. Accuracy evaluations have enabled its type B uncertainty to be reduced to $2.5 \cdot 10^{-16}$, taking into account improved evaluation of the microwave power dependence shift, the distributed cavity phase shift and collision shift. Our conference paper will update our progress towards the SU-CsFO₂ accuracy evaluation.

The Optical Feedback Spatial Phase Driving Perturbations of DFB Laser Diodes in an Optical Clock

#1219#

Roman Schmeissner^{2}, Nicolas von Bandel^{1}, A. Douahi^{2}, O. Parillaud^{1},
Michel Garcia^{1}, Michel Krakowski^{1}, Michel Baldy^{2}
^{1}III-V Lab, France; ^{2}Thales Electron Devices, France

It is shown that the sensitivity of DFB laser diodes to low-level back-reflections significantly depends on the spatial phase of the reflected beam, i.e. the surface roughness of the reflecting element. Laser diodes of different suppliers are compared. Impacts on optical clock operation are studied based on the optical hyperfine pumping principle.

**A2P-H Timekeeping, Time & Freq Transfer, GNSS Apps I Poster Area
Chair Peter Whibberley****Characterization of the Frequency Transfer Over 300 km of Aerial Suspended Fiber**

#1009#

Lukasz Sliwczynski^{1}, Przemyslaw Krehlik^{1}, Krzysztof Turza^{2}, Artur Binczewski^{2}
^{1}AGH University of Science and Technology, Poland; ^{2}Poznań Supercomputing and Networking Center, Poland

In this paper we are reporting on the experiments with a 300 km long suspended fiber running inside the safety wire of the power grid and carrying the 10 MHz frequency signal. Basing on performed measurements we determined diurnal delay changes, maximum slope of delay change as well as the dynamics of the fluctuation changes within the day.

Real-Time Performance Monitoring of Fiber Optic Long-distance Time and RF Frequency Transfer Links

#1010#

Lukasz Sliwczynski, Przemyslaw Krehlik, Karol Salwik
AGH University of Science and Technology, Poland

In this paper we propose the new idea based on monitoring of the performance of bidirectional fiber link in a real time. The key element for this is a circuit for measuring the jitter of RF the signal. The operation and parameters of developed circuit that is able to measure accurately the jitter in the full bandwidth of interest will be presented. Using proposed idea and developed circuits it will be possible to realize the distributed control system to trim the gains of SPBAs automatically to into the optimum operation, even when the parameters of the fiber path changes (e.g. due to fiber break or other modifications).

Fiber-Optic Time Distribution with the Autonomous Calibration of Dispersion-Induced Offset

#1013#

Przemyslaw Krehlik, Lukasz Sliwczynski
AGH University of Science and Technology, Poland

In this work we will describe a new and precise method of determining the dispersion-caused offset in fiber-optic time distribution system ELSTAB. Obtained results will be compared with dispersion estimation based on the fiber vendor's data, and measured with standard dispersion measurement devices used in optical tele-communication. As will be proved, application of this new method allows obtaining absolute calibration of the timescale delay with uncertainty less than 20 ps.

Comparison of Different Amplification Concepts for Multiple Point Frequency Dissemination

#1026#

Alexander Kuhl, Thomas Waterholter, Jan Froh, Gesine Grosche
Physikalisch-Technische Bundesanstalt, Germany

We present a comparison of different amplification concepts for the dissemination of an ultra stable frequency to different sites simultaneously. We extend an already available fiber link to provide an optical signal at 3 institutes located at a distance of about 73 km. At each site a fraction of the signal power is extracted from the link. Since the increased loss due to the modification of the link setup requires a different amplification scheme, we will investigate and compare different approaches by using either bidirectional erbium-doped fiber amplifiers or fiber Brillouin amplification.

Pilot Comparison of Time Interval Measurements with High Speed Oscilloscopes - Initial Results

#1044#

Albin Czubla^{1}, Piotr Szterk^{1}, Przemysław Krehlik^{2}, Łukasz Śliwczyński^{2}, Mesut Yogun^{3},
Ramiz Hamid^{3}, Khaled AlDawood^{4}, Fahad Almuhlaki^{4}, Ahmed Aljawan^{4}, Ibrahim
Alboraih^{4}, Borut Pinter^{5}, Michał Marszałec^{6}, Marzenna Lusawa^{6}

^{1} Electricity Department, Central Office of Measures (GUM), Warsaw, Poland

^{2} Department of Electronics, AGH University of Science and Technology, Krakow, Poland

^{3} Ulusal Metroloji Enstitüsü (UME), TÜBİTAK, Gebze, Kocaeli, Turkey

^{4} National Measurement and Calibration Center (NMCC), SASO, Riyadh, Saudi Arabia

^{5} Metrology Department, Slovenian Institute of Quality and Metrology (SIQ), Ljubljana, Slovenia

^{6} Central Chamber for Telecommunications Measurements, National Institute of Telecommunication (NIT), Warsaw, Poland

In this paper we present the initial results of the pilot comparison of time interval measurements with high speed oscilloscopes being the part of the EURAMET Project #1288. This comparison is aimed to better characterise the electronic based Time Interval Generator as a time interval standard for a new Inter-Laboratory Comparison planned as a Supplementary Comparison in the KCDB. The results are matched very well and contained within the range better than ± 10 ps around each measured value of time interval up to about 12 us precise time interval, comparison, picosecond resolution.

Remote Atomic Clock Delivery to the VLBI Station in Torun

#1058#

Przemyslaw Krehlik{1}, Waldemar Adamowicz{5}, Artur Binczewski{6}, Wojbor Bogacki{6}, Lukasz Buczek{1}, Bob Campbell{3}, Roman Ciurylo{4}, Piotr Dunst{2}, Jacek Kolodziej{1}, Dariusz Lemanski{2}, Marcin Lipinski{1}, Andrzej Marecki{4}, Jerzy Nawrocki{2}, Paweł Nogas{2}, Tadeusz Pawszak{5}, Eugeniusz Pazderski{4}, Janusz Pieczerak{5}, Maciej Stroinski{6}, Lukasz Sliwczynski{1}, Krzysztof Turza{6}, Michał Zawada{4}

{1}AGH University of Science and Technology, Poland; {2}Astrogeodynamic Observatory (AOS), Borowiec, Poland; {3}Joint Institute for VLBI ERIC Radiosterrenwacht, Netherlands; {4}Nicolaus Copernicus University, Poland; {5}Orange Polska S.A., Poland; {6}Poznan Supercomputing and Networking Center, Poland

On 26th Nov. 2015 Toruń Radio Astronomy Observatory (based in Piwnice near Toruń, Poland) was connected to Polish fiber optic network distributing time and frequency (T&F) signals from UTC(PL) and UTC(AOS) laboratories. The first proof-of-concept VLBI observation using remote synchronization via optical fiber link was successfully performed and will be reported.

OPTIME - Final Release

#1068#

Przemyslaw Krehlik{1}, Waldemar Adamowicz{5}, Artur Binczewski{6}, Wojbor Bogacki{6}, Lukasz Buczek{1}, Piotr Dunst{2}, Jacek Kolodziej{1}, Dariusz Lemanski{2}, Marcin Lipinski{1}, Jerzy Nawrocki{2}, Paweł Nogas{2}, Tadeusz Pawszak{5}, Janusz Pieczerak{5}, Maciej Stroinski{6}, Lukasz Sliwczynski{1}, Krzysztof Turza{6}, Michał Zawada{4}, A. Czubla {7}, P. Ostapowicz {6}, J. Igalson {5,}

{1}AGH University of Science and Technology, Poland; {2}Astrogeodynamic Observatory (AOS), Borowiec, Poland; {3}Joint Institute for VLBI ERIC Radiosterrenwacht, Netherlands; {4}Nicolaus Copernicus University, Poland; {5}Orange Polska S.A., Poland; {6}Poznan Supercomputing and Networking Center, Poland.,{7} Central Office of Measures, GUM, Warsaw, Poland

The document describes the final stage of OPTIME project which created a self-calibrating, high precision disseminating system for time and frequency reference signal based on optical fiber links. The OPTIME system reached in Poland about 800 km.

Optical Two-Way Time Transfer with Picoseconds Accuracy Over Telecommunication Fiber

#1077#

Jan Kodet{3}, Petr Panek{1}, Ivan Prochazka{2}, Ulrich Schreiber{3}

{1}Academy of Sciences of the Czech Republic, Institute of Photonics and Electronics, Czech Rep.; {2}Czech Technical University in Prague, Czech Rep.; {3}Technische Universität München, Germany

We have developed a new Two-Way Time Transfer (TWTT) system implementing standard optical telecommunications Small Form-factor Pluggable (SFP) transceivers to transfer timing information between two or more terminals with the accuracy of the order of 1 ps via optical fibers of the length up to several tens of kilometers. The heart of the measurement technique is an event timing device using a surface acoustic wave filter as a time interpolator, which allows registration of the times-of-arrival of pulses with sub-picosecond timing resolution, linearity and stability. These pulses are derived from the optical signal which is used for communication between the terminals.

Verification of Time Signals

#1080#

Matthias Schneider, Christoph Ruland
University of Siegen, Germany

In every data network the current system time has to be available in any devices. Most time signals are transmitted via continuous simplex terrestrial broadcast radio links. Such a continuous time signal data stream can also be generated or manipulated by "man-in-the-middle" attacks. This paper describes a method to verify received time signals for different existing time transmission systems. The existing transmission protocols of the time signal transmitter have not to be changed for the integration of this verification approach, because the verification of the time signals will only take place in the receiver.

WR-ZEN: Ultra-Accurate Synchronization SoC Based on Zynq Technology

#1082#

Miguel Jimenez-Lopez{2}, Emilio Lopez-Marin {1}, Rafael Rodriguez{1}, Javier Diaz{2},
Jose Luis Gutierrez-Rivas {2} {1}Seven Solutions, Spain; {2}University of Granada, Spain

Recently, the White-Rabbit technology has been proposed as alternative to provide deterministic sub-nanosecond synchronization using Gigabit Ethernet standard. In this contribution, we present a new synchronization node based on the Zynq Technology. It allows sub-nanosecond time transfer using a SoC with Linux OS support, providing improved debugging and management capabilities. We describe in detail a new clocking scheme, aspects of the OS customization, kernel modules, user-space tools and the support of additional FMC cards, clearly stating the benefits of the presented approach compared with previous FPGA based WR platforms. Finally, we present experimental results and validation of the timing features.

Avoiding Aliasing in Fiber Link Data Analysis

#1143#

Claudio Eligio Calosso, Cecilia Clivati, Salvatore Micalizio
INRIM, Italy

In optical fiber link ultrastable frequency transfer, signals are affected by phase noise up to bandwidths of kilohertz and a careful data processing is required to properly estimate the uncertainty. This aspect is often overlooked and a number of approaches have been proposed to implicitly deal with it. Here, we face this issue in terms of aliasing and show how typical tools of signal analysis can be adapted to the evaluation of optical fiber links performance. In this way, it is possible to use the Allan variance as estimator of stability and there is no need to introduce other estimators.

Sequential Measurement of Optical Frequency Difference of Semiconductor Lasers for Time Transfer System

#1215#

Łukasz Buczek
AGH University of Science and Technology, Poland

The stability and accuracy of optical time transfer system (OTTS) depends, among other factors, on optical frequency difference between forward and backward direction laser transmitters. This document describes the concept of precise measuring the difference of optical frequency of two semiconductor lasers spaced 100 GHz apart and more. This method exploits two auxiliary adjustable semiconductor lasers and three high-speed photodiodes.

Local Clocks Quality Evaluation Subsystem

#1233#

Ryszard Szplet, Krzysztof Rózycki, Paweł Kwiatkowski, Zbigniew Jachna
Military University of Technology, Poland

We propose a novel Clocks Evaluation Subsystem (CES) for continuous verification of parameters of local clocks. The main aim of the CES is to gather information about time drift of the clocks, then to evaluate their stability, and finally to select the most stable one as a local reference clock. In this paper we present the design and operation of the CES, as well as test results that include, among others, the TIC precision evaluation and clocks drift.

**A2P-J
Chair**

**Optical Frequency Standards & Applications I
Helen Margolis**

Poster Area

UV Laser System for Rydberg Spin-Squeezing in a Strontium Optical Lattice Clock

#1045#

Elizabeth Bridge, Niamh Keegan, Alistair Bounds, Ryan Hanley, Riccardo Faoro, Paul Huillery,
Danielle Boddy, Daniel Sadler, Matthew Jones
Durham University, United Kingdom

Spin-squeezing in an optical lattice clock has the potential to reduce the instability below the limit imposed by standard quantum projection noise. We have previously presented a proposal for using the interactions

between Rydberg atoms to provide a high degree of spin-squeezing. Here we present the design and characterisation of a UV laser system for Rydberg spin-squeezing in a strontium optical lattice clock.

The Optical 88Sr Lattice Clocks and Stabilized Fibre Links: a Frequency Reference for the VLBI System Over 15.5 km Link and an Absolute Measurement of the Clock Transition Over 330 km Link #1059#

Piotr Morzynski^{3}, Marcin Bober^{3}, Przemyslaw Krehlik^{1}, Lukasz Sliwczynski^{1}, Marcin Lipinski^{1}, Eugeniusz Pazderski^{3}, Andrzej Marecki^{3}, Jerzy Nawrocki^{2}, Piotr Ablewski^{3}, B. Campbell^{4}, P. Maśłowski^{3}, A. Cygan^{3}, P. Nogas, D. Lisak^{2}, R. Ciurylo^{3}, Michal Zawada^{3}
^{1}AGH University of Science and Technology, Poland; ^{2}Astrogeodynamical Observatory of Space Research Center, Poland; ^{3}Nicolaus Copernicus University, Poland; ^{4}Joint Institute for VLBI ERIC, Netherlands

The 15.5 km-long stabilized fibre optic link between KL FAMO and Toruń Centre for Astronomy made possible to use the strontium optical lattice clocks as a frequency reference for the 32 m radio telescope participating in the VLBI networks. The absolute frequency of the 88Sr clock transition was with reference to the UTC(AOS) via the 330 km-long stabilized fibre optic link of the OPTIME network. We present current status of the KL FAMO optical lattice clocks, including their frequency stability of 7×10^{-17} , the uncertainty budget and the measured absolute frequency of the 1S0-3P0 clock transition.

An EOM with Ultra-Low Residual Amplitude Modulation #1084#

Zhaoyang Tai, Lulu Yan, Yanyan Zhang, Long Zhang, Haifeng Jiang, Shougang Zhang
NTSC, China

We present a new approach to make an electro-optic modulator (EOM) with ultra-low residual amplitude modulation (RAM). Compared with commonly-used methods of actively control RAM with complicated feedbacks, this approach is simple, reliable and easy to realize. We evaluate the performance of such an EOM by setting it into a standard PDH frequency-stabilization system, and compare with that of a commercial one. Error signals of the setup using the home-made EOM is more stable than the other under same measurement conditons, and its Allen deviation is one order in magnitude lower at 1s.

High-Bandwidth Large-Dynamic Frequency Control of an Optical Comb by Tuning Polarization State #1086#

Yanyan Zhang^{2}, Lulu Yan^{1}, Songtao Fan^{2}, Maoqiang Chen^{2},
Wenge Guo^{3}, Shougang Zhang^{1}, Haifeng Jiang^{1}

^{1}Key Laboratory of Time and Frequency Primary Standards, National Time Service Center, China; ^{2}National Time Service CenterGraduate University of Chinese Academy of Sciences, China; ^{3}School of Science, Xi'an Shiyou University, China

We report a servo control method to stabilize comb's frequencies by changing polarization with a home-made intra-cavity electro-optic modulator (EOM). The EOM is inserted right after the PBS of a well-known nonlinear polarization rotation mode-locked laser's loop. The EOM rotates state of polarization about 1.2×10^{-4} rad/V in ellipticity. The frequency con-trol dynamic range of the frequency comb is two orders of magnitude larger than the tradi-tional intro-cavity EOM method, because it benefits from birefringence of the whole cavity instead of only index change of an EOM crystal driven by tunable electric-field. No side effect is observed during experiments.

Design of Clock Laser with 10^{-16} Frequency Stability for Rapid Uncertainty Evaluation of Yb Lattice Clock #1107#

Won-Kyu Lee, Chang Yong Park, Sang Eon Park, Myoung-Sun Heo, Huidong Kim, Dai-Hyuk Yu
Korea Research Institute of Standards and Science, Korea, South

A clock laser system with 10^{-16} relative frequency stability is designed to enable rapid uncertainty evaluation of KRISS Yb optical lattice clock. A ULE cuboid-type 30-cm-long cavity is adopted with fused silica mirrors and mirror coating material with low thermal noise. The vertical, longitudinal, transverse vibration sensitivity is calculated by finite element analysis to determine the optimum support position.

A Cryogenic Lattice Clock at PTB

#1121#

S. Dörscher, A. Al-Masoudi, S. Häfner, R. Schwarz, U. Sterr, Ch. Lisdat
Physikalisch-Technische Bundesanstalt, 38116 Braunschweig, Germany

We report on the implementation of a cryogenic optical lattice clock based on the $1S_0 - 3P_0$ transition of Sr-87 at PTB in order to overcome the limitation to systematic uncertainty of $2E-17$ due to our knowledge of the effective blackbody radiation (BBR) field. Several groups have already demonstrated approaches to control the BBR-induced frequency shifts to the level of few $1E-18$ and less. We present an upgrade of our existing clock with a separate cryogenic interrogation environment and a revised physics package designed to enable systematic uncertainties below $1E-18$.

Sensitivity to a Variation of m_e/m_p from Splittings Between $^{12}C^{2}HD$ Reference Frequencies

#1126#

Florin Lucian Constantin
CNRS, France

A small frequency splitting between acetylene reference lines have an enhanced sensitivity coefficient to a variation of μ . The absolute measurement of a temporal drift of a splitting with potentially smaller systematic uncertainties may probe unambiguously a variation of μ . The sensitivities to a variation of μ of $^{12}C^{2}HD$ reference transitions are calculated within the Born-Oppenheimer approximation using a four-level effective rovibrational Hamiltonian. The sensitivities to a variation of μ of the molecular parameters, issued from experimental data, are discussed. Pairs of transitions splitted by GHz-level frequency gaps with sensitivity coefficients in the range of $\pm 10^3$ are identified.

Design, Modelling and Characterization of a Single-Ion Endcap Trap with Minimized Ion-Environment Interaction

#1144#

Charles Baynham^{5}, Peter Nisbet-Jones^{3}, Steven King^{3}, Jonathan Jones^{4}, Rachel Godun^{3},
Kai Bongs^{1}, Miroslav Doležal^{2}, Petr Balling^{2}, Patrick Gill^{3}, Patrick Baird^{6}
^{1}Birmingham University, United Kingdom; ^{2}Czech Metrology Institute, Czech Rep.; ^{3}National Physical
Laboratory, United Kingdom; ^{4}National Physical Laboratory / Birmingham University, United Kingdom; ^{5}National
Physical Laboratory / Oxford University, United Kingdom; ^{6}Oxford University, United Kingdom

A single-ion endcap trap has been designed, built and tested with the demanding needs of cutting edge optical frequency metrology in mind. FEM modelling and subsequent characterisation show that trap exhibits a high quadrupole efficiency, low ion heating rate and well defined BBR environment. Due to the trap's strong environmental isolation and low perturbations, the ion's environment closely approximates an ideal, isolated quantum system. When interrogating a trapped Yb⁺ ion on its forbidden electric octupole transition for use as a frequency standard, the trap-based contributions to the transition's fractional frequency uncertainty total 3.5×10^{-19} for typical operating conditions.

Testing a Temperature-Stabilized Spectroscopy Chamber for an Optical Lattice Clock Suppressing the Uncertainty of Blackbody Radiation Shift

#1153#

Chang Yong Park, Won-Kyu Lee, Dai-Hyuk Yu, Myoung-Sun Heo, Huidong Kim
KRISS, Korea, South

In this presentation we will introduce the preliminary test result of a (^{171}Yb) optical lattice clock adopting the blackbody-like spectroscopy chamber near room temperature for reducing BBR shift uncertainty, however the temperature of it will be controlled actively. The chamber was designed to have temperature sensors and a heater mounted outside of vacuum chamber for the convenience of calibration of RTD sensors and ultra-high vacuum operation. We have made a test with a copper dummy chamber for temperature homogeneity of it during its temperature was stabilized.

Active Optical Standards Using Cold Atoms: Lasing Regimes and Instabilities

#1165#

Georgy Kazakov, Thorsten Schumm
Vienna University of Technology, Austria

The bad cavity regime of laser operation is characterized by the gain profile being narrower than the linewidth of the cavity mode. The frequency of the emitted radiation of such lasers is robust with respect to fluctuations of the cavity length, which opens the possibility to create a highly stable active optical frequency reference on the basis of such a bad cavity laser. Such a laser may have mHz linewidth and short-term frequency stability better than achievable with modern ultrastable cavity-based frequency references. We investigate the bad cavity laser signal for various configuration. We study how the multi-level structure of real atoms and various inhomogeneous effects influence the main properties of the bad cavity lasers, such as the cavity pulling coefficient, output power and the linewidth. We investigate also the stability domains for cw lasing for various atomic configurations in the presence of different inhomogeneous effects.

Stabilization of a SESAM Mode-Locked Erbium Laser Frequency Comb with an Integrated Electro-Optic Modulator to an Optical Reference

#1166#

Sebastian Schweyer{3}, Philipp Putzer{1}, Eder Bastian{1}, Andreas Kölnberger{1}, Maximilian Breuer{1}, Norbert Lemke{1}, Alexander Sell{5}, Armin Zach{5}, Reinhard Kienberger{4}, Ulrich Schreiber{2}, Urs Hugentobler{2}

{1}OHB System AG, Germany; {2}Technische Universität München, FESG, Germany; {3}Technische Universität München, FESG, Physik Department E11, Germany; {4}Technische Universität München, Physik Department E11, Germany; {5}TOPTICA Photonics AG, Germany

Intra-cavity electro-optic modulators (EOM) show a high performance for stabilizing fiber frequency combs to a narrow linewidth laser. Here a polarization maintaining (PM) SESAM mode-locked all in fiber Erbium laser frequency comb oscillator with an integrated waveguide EOM is stabilized to a HeNe laser leading to a significant linewidth narrowing. In another experiment the EOM comb oscillator was stabilized to a low noise femtosecond oscillator at 1560 nm using the balance optical cross correlator technique. Hereby the timing jitter between the optical pulse trains of both femtosecond lasers was reduced below the 1 fs area.

An Optical Lattice Clock Based on 24Mg

#1183#

Dominika Fim, Steffen Rühmann, Klaus Zipfel, Nandan Jha, Steffen Sauer, André Kulosa, Wolfgang Ertmer, Ernst Maria Rasel
Leibniz Universität Hannover, Germany

We will report on the determination of the magic wavelength which is 468.46(21) nm and the quadratic magnetic Zeeman shift of $-206.6(2.0)$ MHz/T² [1], which will be our main systematical shift. We also give an report on the current status of the experiment with an, in terms of power, enhanced lattice and thereby reduced clock transition linewidth by at least two orders of magnitude. [1] A.P. Kulosa et al., Phys. Rev. Lett. 115, 240801 (2015)

Towards an Yb⁺ Optical Clock with a BBR Uncertainty Below 1×10^{-18}

#1197#

Jonathan Jones{1}, Rachel Godun{1}, Steven King{1}, Peter Nisbet-Jones{1}, Charles Baynham{1}, Thomas Fordell{4}, Tuomas Hieta{4}, Thomas Lindvall{4}, Kai Bongs{2}, Patrick Baird{3}, Patrick Gill{1}

{1}National Physical Laboratory, United Kingdom; {2}University of Birmingham, United Kingdom; {3}University of Oxford, United Kingdom; {4}VTT Technical Research Centre of Finland, Finland

The authors will present recent measurements of the differential polarizability of the Yb⁺ clock transitions. The measurements are made by measuring the Stark shift of the clock transition while the ion interacts with off resonant IR light, at a number of wavelengths. Once analysis is completed, this should reduce the BBR uncertainty of the E3 transition to well below $1E-17$ - in line with the other systematics of this system.

Blackbody-Radiation Shifts of Ytterbium Optical Lattice Clocks

#1202#

Yilin Xu, Min Zhou, Xiaohang Zhang, Qi Gao, Chengyin Han, Peng Xu, Shangyan Li, Shuang Zhang, Xinye Xu
East China Normal University, China

Recently, the rapid developments of the optical lattice clocks make us concern about the blackbody-radiation (BBR) shift, which is resulted from the residual electric field around the cold atoms. Here we propose a new method for estimating blackbody-radiation shift and uncertainty in the ^{171}Yb optical lattice clocks by numerically simulating the temperature distribution around the cold ytterbium atoms based on the measured temperatures on the surface of the vacuum chamber. This new method will be very helpful for precisely evaluating the BBR shift and uncertainty of the optical lattice clocks without the sensors inside the chamber.

Optical Quenching of Bosonic Magnesium

#1212#

Steffen Sauer, Steffen Rühmann, Dominka Fim, Klaus Zipfel, Nandan Jha, André Kulosa, Wolfgang Ertmer, Ernst Rasel
Institut für Quantenoptik, Leibniz Universität Hannover, Germany

We report on the progress towards optical quenching of the narrow $3^1\text{S}_0 \rightarrow 3^3\text{P}_1$ intercombination line in ^{24}Mg . The two-photon process couples the 3^3P_1 state to the energetically higher state 4^1S_0 , followed by spontaneous decay to the 3^1S_0 ground state. This gives rise to a quasi two-level-system with faster decay rate of the 3^3P_1 state, adjusted via the quench laser intensity at 462 nm. With this technique applied to optically trapped magnesium atoms, we expect to demonstrate cooling temperatures of a few μK .

New Insights on the Determination of the Linewidth of Low-Noise Signals with the Emergence of a Coherent Peak

#1220#

Pierre Brochard, Stéphane Schilt, Thomas Südmeyer
Laboratoire Temps-Fréquence, Switzerland

We present a detailed investigation of the transition between a finite- and zero-linewidth with the appearance of a coherent peak for signals with a low frequency noise power spectral density (FN-PSD) approaching the B-separation line. This is important to achieve a tight phase-lock, e.g., for frequency comb stabilization. We studied this transition both experimentally and by simulations using different types of frequency noise spectra. The integrated phase noise $\Delta\phi_{\text{rms}}$ is shown to be the relevant parameter for the occurrence of a coherent peak, which can be achieved even for values higher than 1-rad and if the FN-PSD exceeds the B-separation line.

Robustness Testing of a Compact Auxiliary Laser for an Optical Atomic Clock Under Space Conditions

#1223#

Bastian Eder^{3}, André Kulosa^{2}, Stéphane Schilt^{4}, Laurent Balet^{1}, Steve Lecomte^{1}, Martin Hutterer^{3}, Laura Pedrosa Rodríguez^{3}, David Parker^{5}, Yeshpal Singh^{5}, Kai Bongs^{5}, Ernst Rasel^{2}
^{1}CSEM, Switzerland; ^{2}Leibniz Universität Hannover, Germany; ^{3}OHB Systems AG, Germany; ^{4}Université de Neuchâtel, Switzerland; ^{5}University of Birmingham, United Kingdom

We present robustness tests of a compact external cavity diode laser performed as a first step towards the use of this laser technology in a future space optical clock. Operation of the laser in environmental conditions representative of the International Space Station (ISS) have been characterized. Continuous measurements of the laser output power and emission wavelength during thermal-vacuum cycles are presented. Furthermore, the laser survived to gamma and protons irradiations at a total dose corresponding to the cumulated dose simulated for a 2-year mission on the ISS, with no significant change of its performance, such as threshold current and slope efficiency.

Development of a Strontium Optical Lattice Clock for the SOC Mission on the ISS #1231#
Sruthi Viswam{9}, Lyndsie Smith{9}, Stefano Origlia{1}, Wei He{9}, Dariusz Sweirad{9}, Josh Hughes{9}, Ole Kock{9}, Yeshpal Singh{9}, Kai Bongs{9}, Soroosh Alighanbari{1}, Stephan Schiller{1}, Stefan Vogt{6}, Uwe Sterr{6}, Christian Lisdat{6}, Rudolphe Le Targat{5}, Jèrôme Lodewyck{5}, David Holleville{5}, Bertrand Venon{5}, Sébastien Bize{5}, Geoffrey P Barwood{3}, Patrick Gill{4}, Ian Hill{4}, Yuri B Ovchinnikov{4}, Nicola Poli{8}, Guglielmo Tino{8}, Jürgen Stuhler{7}, Wilhelm Kaenders{7}, Ernst Rasel{2}
{1}Heinrich-Heine-Universität Düsseldorf, Germany; {2}Leibniz Universität Hannover, Germany; {3}National Physical Laboratory, United Kingdom; {4}National Physical Laboratory Teddington, United Kingdom; {5}Observatoire de Paris, France; {6}Physikalisch-Technische-Bundesanstalt, Germany; {7}TOPTICA Photonics AG, Germany; {8}Università di Firenze, Italy; {9}University of Birmingham, United Kingdom

Transportable optical lattice clock targeted for space applications.

A3L-A Lattice Clocks I P/X001
Chair Ekkehard Peik

16:00 Yb Optical Lattice Clock with 10^{-18} -Level Standard Uncertainty #1103#
Tai Hyun Yoon, Nathan Hinkley, William McGrew, Marco Schioppo, Roger Brown, Kyle Beloy, Robert Fasano, Nathaniel Phillips, Jeffery Sherman, Christopher Oates, Andrew Ludlow
NIST, Time and Frequency Division, United States

Recently, optical lattice clocks have demonstrated fractional instability at the 10^{-18} level. Here, we report efforts for improving stability of the NIST Yb optical lattice clock with $\leq 1 \times 10^{-16}/\sqrt{\tau}$ level, for averaging time in seconds. Furthermore, we provide an update on recent work extending the systematic uncertainty evaluation to the 10^{-18} level. We have carried out a detailed investigation into residual Doppler shifts which could otherwise compromise accuracy of a lattice clock. Additionally, we describe optical lattice tunneling considerations, and recently implemented sideband cooling mechanisms yielding axial atomic temperatures < 1 μ K, which can significantly suppress tunneling frequency shifts. We also highlight detailed studies of Stark shifts due to the optical lattice, yielding a precise characterization of lattice polarizability, hyperpolarizability, vector Stark, and M1/E2 contributions. In addition, we have improved measurements of the probe AC Stark shift and second-order Zeeman shift, and report our current total systematic uncertainty in the low 10^{-18} level.

16:20 A Magnesium Optical Lattice Clock #1129#
André P. Kulosa, Steffen Rühmann, Dominika Fim, Klaus Zipfel, Nandan Jha, Steffen Sauer, Wolfgang Ertmer, and Ernst M. Rasel
Institut für Quantenoptik, Leibniz Universität Hannover, Hannover, Germany

We report on the progress towards a highly-accurate optical lattice clock with bosonic ^{24}Mg . Recently, we measured the frequency of the magnetically enhanced $1S_0 \rightarrow 3P_0$ clock transition at 458 nm to be 655 058 646 691(101) kHz and determined its magic wavelength of 468.46(21) nm. The quadratic Zeeman shift of the clock transition was found to be $-206.6(2.0)$ MHz/T². All values are in agreement with previous calculations.

16:40 Comparison of a Mercury Optical Lattice Clock with Primary and Secondary Frequency Standards #1162#
Maxime Favier, Rinat Tyumenev, Slawomir Bilicki, Eva Bookjans, Daniele Nicolodi, Michel Abgrall, Jocelyne Guéna, Yann Le Coq, Rodolphe Le Targat, Jerome Lodewyck, Luigi De-Sarlo, Sebastien Bize
SYRTE, France

We will also present an absolute frequency measurement of the mercury clock transition, obtained by comparing the Hg optical lattice clock with the atomic fountain FO2-Cs at SYRTE. This measurement has an uncertainty of 4.3×10^{-16} , close to the limit imposed by atomic fountains and, to our knowledge, the best

uncertainty to date for the direct measurement of Hg vs Cs. Furthermore, we will report on the first direct determination of the frequency ratio between neutral mercury and Rb obtained through comparison with the atomic fountain FO2-Rb, as well as a direct optical to optical comparison of the mercury and strontium optical lattice clocks at SYRTE. The value of the Hg/Sr frequency ratio that we obtain as an uncertainty of 1.8×10^{-16} limited by Hg and is in good agreement with the value reported by RIKEN/UT. This is to our knowledge the only frequency ratio that was measured by two independent groups with an uncertainty beyond that of the SI second. These kinds of comparisons are relevant for tests of the variation of fundamental constants, as well as for assessing the reliability of optical frequency standards in view of a redefinition of the SI second.

17:00 Operational Strontium Optical Lattice Clocks

#1222#

Jérôme Lodewyck, Slawomir Bilicki, Eva Bookjans, Grégoire Vallet, Rodolphe Le Targat
LNE-SYRTE, France

We demonstrate that an optical lattice clock with strontium atoms can be reliably operated over time periods of several weeks, with a time coverage larger than 80%. These performances are compatible with the realization of robust time scales with optical clocks. We take advantage of these long integration times to report repeated and consistent comparisons of one of our strontium clocks with two atomic fountains with a statistical uncertainty below 10^{-16} .

17:20 Higher-Order and Non-Linear Effects on Precision of Clocks of Neutral Atoms in Optical Lattices

#1225#

Vitaly Ovsiannikov^{3}, Sergey Marmo^{3}, Vitaly Palchikov^{1}, Hidetochi Katori^{2}
^{1}FGUP VNIIFTRI, Russia; ^{2}University of Tokyo, Japan; ^{3}Voronezh State University, Russia

The results of numerical evaluations presented in this paper determine fundamental restrictions to various strategies of reducing uncertainties on optical lattice clocks of the group II atoms. Detailed considerations of the use of strictly forbidden transition $3P_0 \rightarrow 1S_0$ for the time and frequency standard indicate possible methods of eliminating or accounting for the multi-polar and higher-order dipole shifts of the clock levels. In particular, the difference between spatial distributions of electric-dipole (E1) and multipolar (M1 and E2) atom-lattice interaction is presented explicitly for an attractive red-detuned lattice. The case of repulsive blue-detuned lattice for Sr atoms is also considered in the paper.

**A3L-B Space Applications
Chair Marco Belloni**

P/L001

**16:00 Data Timing and Clock Monitoring in the Gaia Astrometric Mission
(Invited paper)**

#1155#

Sergei Klioner
Technische Universität Dresden, Germany

Gaia is an ESA space mission with the main goal to provide astrometric and spectro-photometric measurements of over one billion celestial objects. The accuracy of astrometric parameters should reach the level of about 10 microarcseconds. This level of accuracy requires in particular high-accuracy timing information for the observational data. To meet this requirement the spacecraft has a Rubidium clock, for which a special one-way time synchronization is organized. The presentation will review all ingredients of the data timing and clock monitoring process used in Gaia.

16:40 Impact of Turbulence on High Precision Ground-Satellite Frequency Transfer with Two-Way Coherent Optical Links #1160#Clélia Robert^{1}, Jean-Marc Conan^{1}, Peter Wolf^{2}^{1}ONERA, the French Aerospace Lab, F-92322 Châtillon, France, France; ^{2}SYRTE, Observatoire de Paris, CNRS, LNE, France

We provide statistics on heterodyne efficiency for different turbulence strengths and system parameters. We show that to avoid large fluctuations in signal to noise ratio with frequent extinctions we need to correct at least for tip-tilt. Second, we present examples of temporal phase noise evolution for both up and downlink. Finally, we quantify the two-way partial compensation of the phase noise and its impact on the frequency stability of space to ground clock comparisons in terms of Allan variance.

17:00 Optical Two-Way Timing System for Space Geodesy Applications #1079#Jan Kodet^{4}, Ulrich Schreiber^{4}, Petr Panek^{1}, Ivan Prochazka^{2}, Benjamin Männel^{3}, T Schuler^{1}Academy of Sciences of the Czech Republic, Institute of Photonics and Electronics, Czech Rep.; ^{2}Czech Technical University in Prague, Czech Rep.; ^{3}ETH Zurich, Zurich, Switzerland; ^{4}Technische Universität München, Germany

Until now time itself is not an observable in space geodesy. The major reason for this fact is the considerable difficulty to keep track of the phase of the clock oscillation between the point of origin and the point of the measurement. However, if geodesy will attempt to provide a reference frame fully based on general relativity, a proper treatment of time is mandatory. The Geodetic Observatory Wettzell is currently in the process to modernize the timing system such that the phase of the master clock can be established at all times. The ultrashort pulses of an optical frequency comb are transporting both time and frequency from the master clock of the observatory to the individual space geodetic techniques, namely Very Long Baseline Interferometry (VLBI), Satellite Laser Ranging (SLR) and Global Navigation Satellite System (GNSS), using a two-way approach, which is in the literature known as the Einstein Synchronization.

17:20 Deep Space Navigation Using X-Ray Pulsar Timing with a High Performance Space Atomic Clock #1188#Setnam Shemar^{2}, George Fraser^{3}, Lucy Heil^{1}, David Hindley^{2}, Adrian Martindale^{3}, Philippa Molyneux^{3}, John Pye^{3}, Robert Warwick^{3}, Andrew Lamb^{2}^{1}Anton Pannekoek Institute for Astronomy, University of Amsterdam, Netherlands; ^{2}National Physical Laboratory, United Kingdom; ^{3}University of Leicester, United Kingdom

We describe a recent study for ESA on the feasibility of deep space navigation using X-ray pulsar timing. The potential technique would allow increased spacecraft autonomy and improved position accuracies in certain scenarios. Simulations of navigation errors based on possible X-ray instrumentation show that the pulsar PSR B1937+21 has the potential to allow a positioning accuracy of order 2 km in the direction of the pulsar, for ranges up to 30 AU. This could be achieved autonomously on the spacecraft using a ~10 hour observation of the pulsar by the X-ray instrument together with a high performance atomic clock.

A3L-C Sensors P/L002
Chair Svenja Knappe**16:00 Using GaN for MEMS: from Material to Resonators and Sensors #1096#**
(Invited paper)Marc Faucher^{2}, Paul Leclaire^{2}, Christophe Morelle^{2}, Isabelle Roch^{2}, Bertrand Grimbert^{2}, Eric Frayssinet^{1}, Virginie Brandli^{2}, Lionel Buchaillot^{2}, Didier Theron^{2}, Yvon Cordier^{1}
^{1}CNRS CRHEA, France; ^{2}CNRS IEMN, France

We will present an overview of our work toward high performance MEMS resonators and sensors. First, we will show that developing specific epitaxial growth enables MEMS designer to go beyond the current limitations of commercially available material. In particular, we were able to demonstrate ultrathin buffers under 1 μ m thickness where the AlGaIn/GaN heterostructure properties, Young modulus, and careful

tuning of stress distribution are validated for device processing. We will report on our design and process of resonators with integrated transducers on these epilayers. The study of piezoelectric actuation, 2DEGs piezo-amplified detection in 3 terminal or 2 terminal transducers will be described and in particular the understanding of frequency variations upon bias conditions. In conclusion, we will assess the capability of GaN for MEMS accelerometers operating with wide range and resolution under 5mg/Hz^{1/2}.

16:40 Stability and Durability of Resonant SAW Strain Sensors

#1016#

Victor Kalinin, Arthur Leigh, Alexander Stopps
Transense Technologies plc, United Kingdom

Resonant SAW strain sensing elements used in non-contact torque, force and vibration sensors are investigated from the point of view of their stability and durability. Results of fatigue testing of the SAW sensing elements bonded to metal shafts with a stiff adhesive are presented. They demonstrate the sensor durability and stability of the strain sensitivity up to 13 million strain cycles. Stability of the frequency of the SAW differential resonant sensing elements is also investigated showing the sensor zero drift of approximately 0.14...0.62% FS per year at 90°C.

17:00 Experimental Procedure to Design Stressed HBAR Devices When the Third-Order Elastic Constants Are Not Known

#1114#

Thomas Baron^{2}, Ludovic Bebon^{2}, Valérie Petrini^{2}, Gilles Martin^{2}, Jean-Marc Lesage^{1},
Bernard Dulmet ^{2} {1}DGA, France; {2}FEMTO-ST, France

Third-order elastic constants are mandatory requirements to compute stress sensitivity. Experimental procedure to design stressed devices when the third-order elastic constants are not known are described. We use HBAR based on LiNbO₃ (YXl)/163 piezoelectric layer on LiTaO₃ Z-cut substrate as example of this approach. Vibration sensitivity of HBAR oscillators are measured for different package configurations. These configurations allow the computation of the six stress sensitivity coefficients of HBAR. So, an oscillator and a pressure sensor design optimization can be done although the involved nonlinear elastic constants have not been determined yet.

17:20 S0 Lamb Wave Resonators for in-Liquid Sensing: Promising Alternative to Shear Bulk Acoustic Wave Devices

#1125#

Teona Mirea^{2}, Ventsislav Yantchev^{1}, Enrique Iborra^{2}
^{1}Chalmers University of Technology and Q-Arts Consulting Ltd, Bulgaria; ^{2}Universidad Politécnica de Madrid, Spain

S₀ Lamb wave resonators (S₀-LWR) have shown great potential for in-liquid operation. They can be used on a dual quantity sensor platform since they are sensitive to both, mechanical (density and viscosity) and electrical (dielectric permittivity) properties of the liquid. Here we present extensive theoretical and experimental studies on their in-liquid sensing mechanisms. Additionally, we compare them to the commonly used solidly mounted shear mode bulk acoustic wave devices and show their comparable in-liquid performance. This places S₀-LWR as promising alternative with the advantage of using commercial c-oriented AlN deposition.

Wednesday 6th April

	P/X001	P/L001	P/L002
8.40-10.00	B1L-A <u>Quantum Measurement</u> Chr: Patrick Gill Track: Optical Frequency Standards and Applications	B1L-B <u>GNSS and Applications</u> Chr: Per Olof Hedekvist Track: Timekeeping, Time and Frequency Transfer, GNSS Applications	B1L-C <u>Cross Correlation</u> Chr: Claudio Calosso Track: Oscillators, Synthesizers, Noise, & Circuit Techniques
10.00-10.40	Exhibitors presentations Chr: Wolfgang Schaefer		
10.40	Coffee / tea break		
11:10-12.30	B2L-A <u>Applications of Optical Frequency Standards</u> Chr: Philip Tuckey Track: Optical Frequency Standards and Applications	B2L-B <u>Atomic Magnetometers and Their Applications</u> Chr: Gaetano Mileti Track: Microwave Frequency Standards	B2L-C <u>Advances in TWSTFT</u> Chr: Miho Fujieda Track: Timekeeping, Time and Frequency Transfer, GNSS Applications
12.30	Lunch		
14.00-15.40	Poster session 2		
15.40	Coffee / tea break		
16:00-17.40	B4L-A <u>Ion Clocks</u> Chr: Tai Hyun Yoon Track: Optical Frequency Standards and Applications	B4L-B <u>Timing Networks and Applications</u> Chr: Patrizia Tavella Track: Timekeeping, Time and Frequency Transfer, GNSS Applications	B4L-C <u>Atom Interferometers</u> Chr: Arnaud Landragin Track: Microwave Frequency Standards

Dinner at National Railway Museum 19.00 – 23.00 coaches depart from outside exhibition centre 18.30.

B1L-A Quantum Measurement**P/X001****Chair Patrick Gill****08:40 Hofstadter Optical Lattice for Ultracold Ytterbium Atoms (Invited paper)****#1157#**

Fabrice Gerbier, Quentin Beauvils, Jérôme Beugnon, Manel Bosch Aguilera, Raphaël Bouganne, Alexandre Dureau, Daniel Döring, Matthias Scholl
LKB, France

This talk will describe new experiments probing and manipulating many-body properties of ultracold quantum gases using ultra-narrow “clock” transitions. I will focus on our experimental project, which aims at engineering a special kind of optical lattice realizing an effective magnetic field coupling to the atomic motion - the Hofstadter optical lattice. Our specific experimental scheme uses an ultra-narrow optical

transition linking the ground state to a metastable excited state in bosonic Ytterbium. (also used as "clock" transition in Yb-based optical atomic clocks). I will present the current status of the experiment, including spectroscopy of Bose-Einstein condensates (BEC) on the clock transition, and the observation of coherent Rabi oscillations between a BEC in the ground state and in the excited state.

09:20 Atomic Quadrupole Moment Measurement Using Dynamic Decoupling #1158#

Ravid Shaniv, Nitzan Akerman, Roe Ozeri
The Weizmann Institute, Israel

We present a method that uses dynamic decoupling of a multi-level quantum probe " a single 88Sr^+ ion " in order to measure electric quadrupole energy shift in the $D_{5/2}$ level. In contrast with typical two-level dynamic decoupling schemes, here we take advantage of the six-fold $D_{5/2}$ Zeeman manifold of equidistant levels and reduce the effect of magnetic field noise. By using our measurement scheme, we were able to measure the quadrupole moment of the $D_{5/2}$ level in 88Sr^+ with precision better than that of the previous measurement by an order of magnitude.

09:40 Quantum Logic State Detection for Molecular Ions #1027#

Fabian Wolf^{1}, Yong Wan^{1}, Jan Heip^{1}, Florian Gebert^{1}, Chunyan Shi^{1}, Piet Schmidt^{2}
^{1}Physikalisch-Technische Bundesanstalt, Germany; ^{2}Physikalisch-Technische Bundesanstalt, Universität Hannover, Germany

Molecules offer fascinating possibilities for fundamental research due to their rich internal structure. The lack of a cycling transition for cooling and detection in most molecules has limited wide-spread applications. While the development of quantum logic techniques for atomic ions has enabled spectroscopy of previously inaccessible species, the application of these techniques to molecular ions is still infeasible. Here, we present the first implementation of non-destructive state detection using quantum logic operations between a molecular and an atomic ion. This result establishes a technique enabling quantum information processing and high-precision spectroscopy for tests of fundamental physics with cold molecular ions.

B1L-B GNSS and Applications P/L001
Chair Per Olof Hedekvist

08:40 Towards Operational Sub 10^{-16} Frequency Transfer with IPPP #1040#

Gerard Petit^{1}, Sylvain Loyer^{2}, Felix Perosanz^{3}
^{1}BIPM, France; ^{2}CLS, France; ^{3}CNES, France

Precise Point Positioning (PPP) is the technique of choice for GPS time and frequency transfer, with a typical uncertainty for frequency comparisons of order 1×10^{-15} at 1-day averaging and a few 10^{-16} at 5 to 10 day averaging. One approach to overcome the limitations of "classical PPP" is to consider the integer nature of phase ambiguities and the CNES-GRGS group has been a pioneer in applying integer ambiguity resolution to PPP. We show that this IPPP technique reaches a frequency transfer accuracy of 1×10^{-16} at ~ 3 to 5-day averaging for regional links. We present steps taken towards the operational use of IPPP along with some recent results.

09:00 Highly Dynamic Distance Measurement for GNSS Using the Frequency Domain Distance Measurement, for Time and Frequency Transfer #1140#

Bastian Eder^{2}, Martin Hutterer^{1}, Thomas Unterholzer^{1}, Sebastian Lindner^{2}, Andreas Fischer^{1}, Philipp Putzer^{1}, Sebastian Schweyer^{2}, Norbert Lemke^{1}, Reinhard Kienberger^{2}, Ulrich Schreiber^{2}, Urs Hugentobler^{2}
^{1}OHB System AG, Germany; ^{2}Technische Universität München, Germany

A new approach of distance measurement promises a very compact, robust, simple and fast application. The Frequency Domain Distance Measurement (FDDM) is hereby not only for absolute distance

measurements, but for highly dynamic measurements as well. This system is capable of measuring static systems as well as highly dynamic systems with speeds > 10 km/sec, and velocity resolution < 1 cm/sec. The combination of FDDM and a balanced optical cross correlation promises time and frequency transfer between largest distances with stabilities better than optical clock performances, which can be used for future Global Navigation Satellite System scenarios.

09:20 Performance of the NeQuick G Iono Model for Single-Frequency GNSS Timing**Applications**

#1032#

Ricardo Píriz^{1}, Pedro Roldán^{1}, Rafal Golcz^{1}, Carlos Moriana^{1}, Julia Leute^{2},
(Andreas Bauch^{2})
^{1}GMV, Spain; ^{2}PTB, Germany

GNSS timing is currently used worldwide in critical real-time systems that require precise synchronisation or time-stamping at geographically dispersed sites. For applications where multiple timing equipment needs to be deployed, it is desirable to use low-cost (normally single-frequency) receivers. GPS provides the simple, low-accuracy Klobuchar ionospheric model. For Galileo, the Euro-pean Union has recently published a detailed description and implementation guidelines for the NeQuick G user model [1]. In this paper we analyse the single-frequency timing accuracy using the NeQuick G model. The study is based on data from two GNSS receivers, located at PTB and connected to the highly stable UTC(PTB) timescale.

09:40 Experimental Time Dissemination Services Based on European GNSS Signals: the H2020 DEMETRA Project

#1151#

Patrizia Tavella
Istituto Nazionale di Ricerca Metrologica, Italy

The DEMETRA project, funded by the European Union in the frame of the Horizon 2020 program, aims at developing and experimenting time dissemination services based on the European GNSS, adding particular features like certification, calibration, or integrity, that could be of interest to a wide range of users as traffic control, energy distribution, finance, telecommunication, and scientific institutions. The project has a 6 month experimentation campaign starting next March 2016 and the paper will report the first results showing potentialities and limits of the proposed time dissemination services, aiming to foster the exploitation of the European GNSS for timing applications.

**B1L-C Cross Correlation
Chair Claudio Calosso****P/L002****08:40 A 1 MHz to 50 GHz Direct Down-Conversion Phase Noise Analyzer with Cross Correlation**

#1012#

Gregor Feldhaus, Alexander Roth
Rohde & Schwarz, Germany

A new instrument for phase noise test covers a frequency range from 1 MHz up to 50 GHz with direct down-conversion analog I/Q mixers and sampling of the baseband signal. The traditional PLL is replaced by a digital FM demodulator as a phase detector and for frequency tracking. An additional AM demodulator enables concurrent measurement of phase noise and amplitude noise. Phase noise as low as -183 dBc/Hz at 100 MHz carrier frequency and 10 kHz offset can be measured within two minutes.

09:00 Cross-Spectral Collapse from Anti-Correlated Thermal Noise in Power Splitters #1051#

Craig Nelson, Archita Hati, Dave A. Howe
National Institute of Standards and Technology, United States

We discuss the effect of anti-correlated thermal noise of various reactive and resistive power splitters on the cross-spectrum phase noise measurement of thermally-limited oscillators.

- 09:20 On a Conceptual Error in Cross Spectrum PM Noise Measurements #1056#**
Yannick Gruson^{1}, Vincent Giordano^{1}, Ulrich L. Rohde^{2}, Enrico Rubiola^{1}
^{1}CNRS Femto-ST Institute, France; ^{2}Synergy Microwave Corporation, United States

Modern instruments use two equal channels and cross PSD to average out the single-channel background. The loss-free power splitter at the input is actually a directional coupler. We learn from thermometry that the cross PSD is $k(T_c - T_d)$, where kT_c and kT_d are the thermal energy of the oscillator and of the dark port. The latter is generally not accounted for, which results a systematic error. We provide the formal derivation, and the experimental evidence using an audio-frequency mockup. This choice is for full control on crosstalk. Our measurement are done in a Faraday cage with additional magnetic shielding.

- 09:40 Memory-Efficient High-Speed Algorithm for Multi-Tau PDEV Analysis #1141#**
Magnus Danielson^{2}, François Vernotte^{3}, Enrico Rubiola^{1}
^{1}CNRS FEMTO-ST Institute, Dept Time and Frequency, France; ^{2}Net Insight AB, Sweden; ^{3}Observatory THETA/UTINAM, UBFC/UFC and CNRS, France

The Omega counter was introduced to improve phase noise rejection by using a least square algorithm. The associated variance is the PVAR which is more efficient than MVAR to separate the different noise types. However, unlike AVAR and MVAR, the decimation of PVAR estimates for multi-tau analysis is not possible if each counter measurement is a single scalar. This paper gives a decimation rule based on two scalars, the processing blocks, for each measurement. For the Omega-counters, this implies the definition of an output standard as well as hardware requirements for performing high-speed computations of the blocks.

B2L-A Applications of Optical Frequency Standards P/X001
Chair Philip Tuckey

- 11:10 Cold Highly Charged Ions for Highest Precision Spectroscopy #1198#**
(Invited paper)
Lisa Schmöger^{4}, Oscar Versolato^{4}, Maria Schwarz^{4}, Matthias Kohnen^{5}, Alexander Windberger^{3}, Baptist Piest^{3}, Stefanie Feuchtenbeiner^{3}, Jofre Pedregosa^{2}, Tobias Leopold^{5}, Peter Micke^{4}, Anders Hansen^{1}, Thomas Baumann^{3}, Michael Drewsen^{1}, Thomas Pfeifer^{3}, Joachim Ullrich^{5}, Piet Schmidt^{5}, José Crespo López-Urrutia^{3}
^{1}Aarhus University, Denmark; ^{2}Aix-Marseille University, France; ^{3}Max-Planck-Institut für Kernphysik, Germany; ^{4}Max-Planck-Institut für Kernphysik / Physikalisch-Technische Bundesanstalt, Germany; ^{5}Physikalisch-Technische Bundesanstalt, Germany

Cold, strongly localized highly charged ions (HCIs) are of particular interest for frequency metrology (development of novel optical clocks) and the search for physics beyond the Standard Model. We have successfully Coulomb crystallized highly-charged Ar¹³⁺ ions in a cryogenic Paul trap through sympathetic cooling with co-trapped, continuously laser-cooled Be⁺ ions. This constitutes a significant step forward for high-precision spectroscopy of HCIs.

- 11:50 Frequency Combs for Astronomical Precision Spectroscopy #1228#**
Rafael Probst^{2}, Yuanjie Wu^{2}, Tilo Steinmetz^{1}, Sebastian Stark^{1}, Theodor Hänsch^{2}, Thomas Udem^{2}, Ronald Holzwarth^{1}
^{1}Menlo Systems GmbH, Germany; ^{2}MPI für Quantenoptik, Germany

In recent years, laser frequency combs (LFCs) have found their way from precision laboratory spectroscopy into astronomy, as calibrators for astronomical spectrographs. Here we present a frequency combs with a flat spectrum covering most of the visible part of the optical spectrum with a 25 GHz mode spacing, perfectly suited for the calibration of astronomical spectrographs.

12:10 Searching for Dark Matter with Atomic Clocks and Laser Interferometry

#1062#

Yevgeny Stadnik, Victor Flambaum
University of New South Wales, Australia

We propose new schemes for the direct detection of low-mass bosonic dark matter, which forms an oscillating classical field, using atomic clocks and laser interferometers. We have recently shown that such dark matter can induce both a 'slow' cosmological evolution and oscillating variations in the fundamental constants. Oscillating variations in the fundamental constants produce oscillating shifts in the transition frequencies of atomic clocks and other atomic systems. Using recent atomic dysprosium spectroscopy data, we have derived limits on the quadratic interaction of dark matter with the photon that improve on existing constraints by up to 15 orders of magnitude.

B2L-B Atomic Magnetometers and Their Applications

P/L001

Chair Gaetano Mileti

11:10 Precision Measurements and Navigation with Frequency Measurements at the pHz

Level (Invited paper)

#1237#

Michael Romalis
Princeton University, United States

In this talk I will describe recent progress in using polarized nuclear spins for precision tests of fundamental physics as well as for practical applications, such as inertial rotation sensing. Nuclear spin polarized gases have particularly long spin coherence times, allowing for frequency measurements with precision down to the pHz level.

11:50 Frequency-Tunable Microwave Field Imaging in an Atomic Vapor Cell

#1087#

Andrew Horsley, Philipp Treutlein
University of Basel, Switzerland

We present a frequency tunable atomic vapor cell magnetometer operating at microwave frequencies from GHz to tens of GHz, a four orders of magnitude extension of the frequency tunable range of atomic magnetometers. Potential applications include near-field characterisation of microwave circuitry and devices, and medical microwave sensing and imaging.

12:10 Dual Frequency Spin-Polarized Pumping

#1083#

Dmitri L. Boiko
CSEM, Switzerland

Progress towards efficient and stable spin-polarized pumping for chip-scale atomic magnetometers and gyroscopes is reported. Typically, such devices utilize moderate pressure Rb cells containing several hundred torr of Xe and N₂ buffer that yield strong overlap of hyperfine absorption lines in Rb. Nevertheless we find that magnetic precession reveals large sensitivity to the pump-probe laser frequency. To overcome it, a dual frequency (DF) spin-polarized optical pumping for reduction of the laser frequency sensitivity is proposed. In addition, DF interrogation narrows the width of magnetic resonance and reduces bias.

11:10 Remote Optical and Fountain Clock Comparison Using Broadband TWSTFT and GPS PPP #1136#

Franziska Riedel
 Physikalisch-Technische Bundesanstalt, Germany

Various Yb ion, Sr lattice and Cs fountain clocks at INRiM, LNE-SYRTE, NPL and PTB had been compared simultaneously over a 3-week campaign using satellite-based techniques. With full 20 MChip/s modulation bandwidth TWSTFT links and PPP/iPPP analysis of GPS link data, instabilities of a few $1E-16$ could be achieved for both techniques. For the calculation of the clock-to-clock ratios and their uncertainties, gap-tolerant weighted averaging with different optimized weighting functions was employed.

11:30 A Study on Reducing the Diurnal in the Europe-to-Europe TWSTFT Links #1098#

Victor Zhang, Thomas Parker, Shengkang Zhang
 NIST, United States

In this study, we report that the diurnal in the Europe-to-Europe TWSTFT links can be reduced by using the triangle difference of the transatlantic TWSTFT differences. Notice that the triangle difference also reduces the short-term transfer noise observed in the direct difference. We will examine the triangle difference for several Europe-to-Europe links and analyze where the improvement comes from.

11:50 The 2015 TWSTFT Calibration for UTC and Related Time Links #1047#

Zhiheng Jiang^{1}, Dirk Piester^{4}, Christian Schlunegger^{2}, Erik Dierikx^{7}, Victor Zhang^{3},
 Javier Galindo^{5}, Demetrios Matsakis^{6}, (Jonathan Hirschauer ^{6})
^{1}BIPM, France; ^{2}METAS, Switzerland; ^{3}NIST, United States; ^{4}PTB, Germany; ^{5}ROA, Spain; ^{6}USNO, United States; ^{7}VSL, Netherlands

TWSTFT is one of the primary time transfer techniques for UTC generation. Calibration is one of its key strengths, but it requires considerable investment in staffing, time, and funding. As a practical matter, only the UTC links need to be calibrated. Some laboratories make use of TW time comparisons for applications other than UTC computation and the Triangle Closure Calibration (TCC) technique is used for the calibration.

12:10 TWSTFT Results by Using Software-Defined Receiver Data #1024#

Yi-Jiun Huang^{3}, Wen-Hung Tseng^{3}, Shinn-Yan Lin^{3}, Sung-Hoon Yang^{1}, Miho Fujieda^{2}
^{1}Korea Research Institute of Standards and Science, Korea, South; ^{2}National Institute of Information and Communications Technology, Japan; ^{3}Telecommunication Laboratories, Chunghwa Telecom, Taiwan

The accuracy of TWSTFT is currently limited due to instabilities of signal arrival time. We use a software-defined receiver (SDR) to accurately measure the arrival time of code signal transmitted by SATRE modem, and then we found it exhibits the capacity against the TWSTFT diurnal variations. The SDR systems have been successfully installed at TL, NICT and KRISS since 2015. For data of the KRISS-TL link, the TDEV plot of SATRE modem shows a peak of 134 ps at 8 hours, where the TDEV of SDR is only 32 ps.

B3P-E Oscillators and Synthesizers
Chair Jean-Pierre Aubry**Poster Area****An Ultra Stable Oscillator for the 3GM Experiment of the Juice Mission****#1021#**

Aviv Shapira, Avinoam Stern, Shemi Prazot, Ronny Mann, Yefim Barash, Edoardo Detoma, Benny Levy
AccuBeat LTD, Israel

An Ultra Stable Oscillator (USO) is being developed by AccuBeat for the 3GM radio occultation experiment of the ESA JUICE mission. The USO, 15x13x10cm³, will provide a highly stable reference signal for the one way (space to ground) radio link to investigate the structure of the neutral atmospheres and ionospheres of Jupiter and its moons. A partial engineering model of the USO (PEM) was built and tested in thermal vacuum. It has demonstrated a frequency stability below 2E-13 for a 5MHz output, at an averaging time 1s to 1000s, thus meeting the requirements for technology readiness level 5 (TRL5).

High Performance Miniature Integrated OCXO Solution**#1118#**

Karl Ward
Rakon UK Ltd, United Kingdom

Traditional OCXO devices have been around for many years offering frequency stabilities superior to those of smaller, lower power TCXO devices. In today's world where size constraints and power conscious systems require exacting performance, this paper presents a unique solution that addresses these challenges. Based upon a TCOCXO topology, the single chip (ASIC) solution described requires only a crystal and optional capacitors to meet frequency versus temperature stabilities down to ± 2 ppb over -40/85°C with an oven size of only 5x3.2 mm.

Long-Term Frequency Stability Improvement of OCXO Using CSAC**#1191#**

Tomáš Bagala^{1}, Adam Fibich^{1}, Vladimír Stofanik^{2}
^{1}FEEI SUT Bratislava, Slovakia; ^{2}FEEI SUT Bratislava, IP SAS Bratislava, Slovakia

Our attention is dedicated to ways of stabilizing the frequency of the OCXO using CSAC module. From our research will be proposed stabilization system using two mentioned oscillator with guaranteed properties in the long term frequency stability of output signals that will have lower phase noise, than origin CSAC module.

Theory of VCO Phase Noise Reduction Using Parallel Varactor Diodes**#1226#**

Michael Underhill
Underhill Research Limited, United Kingdom

Significant noise reduction has been observed by Rohde and Poddar using several parallel varactor or capacitor switching diodes in a Voltage Controlled Oscillator (VCO) in place of single larger diodes. We theorize that the noise is correlated over the area of a single semi-conductor diode by electromagnetic coupling, whereas the noise from discrete diodes is not correlated. For n equal discrete diodes the maximum reduction is n times. We investigate whether the effective noise temperature of the combined diode resistance has been reduced, or whether the Q has actually been increased, when applied in a Leeson oscillator model.

Quartz Orientations for Optimal Power Efficiency in Wireless SAW Temperature Sensors#1173#Alexander Shvetsov^{2}, Sergei Zhgoon^{2}, Ivan Antcev^{1}, Sergei Bogoslovsky^{1}, Gennadiy Sapozhnikov^{1}^{1}JSC "Radar mms", Russia; ^{2}National Research University MPEI, Russia

The present work is dedicated to a detailed discussion of the relation between the required value of K₂ and the maximum available TCF difference on separate substrates as well as on a single substrate. Orientations with maximum difference of TCF are described for different requirements to the K₂ level. Selected orientations have been studied experimentally and the comparison of calculated and measured results is given.

Influence of Induced Stress on AlN-Solidly Mounted Resonators

#1201#

Alvaro Delicado, Marta Clement, Teona Mirea, Bárbara Díaz-Durán, Jimena Olivares, Enrique Iborra

Universidad Politécnica de Madrid, Spain

The frequency response of AlN-based solidly mounted resonators built on rectangular silicon strips silicon is assessed as a function of the mechanical deformation exerted on the substrates, which is assessed with a strain gauge glued on their surface. The electrical behaviour of the resonators is also assessed under DC-polarisation to investigate the influence of the different materials apart from the AlN layer. Simulations of the deformation enable to assess the non-uniform stress in the silicon strip. It is found that longitudinal modes shift to lower frequencies whereas shear modes shift to higher frequencies as the silicon strip is strained.

Stress-Sensitivity of Wafer-Level Packaged SAW Delay Lines

#1137#

Lilia Arapan, Guillaume Wong, Bernard Dulmet, Thomas Baron, Jean-Michel Friedt, Vincent Placet, Sebastien Alzuaga ^{2} FEMTO-ST, France, ^{2} SENSEOR, France

We investigate the stress-sensitivity of Wafer-Level Packaged SAW delay lines aimed to wireless stress sensing. The WLP is achieved by soft polymer in order to favor the level of stresses at the SAW surface. We investigate both theoretically and experimentally the influence of this packaging onto the stress-sensitivity of the delay lines micro-machined on Lithium Niobate substrate.

High Coupling Phononic SH-SAW Resonators for in-Liquid Operation

#1146#

Ventsislav Yantchev^{2}, Teona Mirea^{3}, Enrique Iborra^{3}, Aldo Jesorka^{1}^{1}Chalmers University of Technology, Sweden; ^{2}Chalmers University of Technology and Q-Arts Consulting Ltd, Bulgaria; ^{3}Universidad Politécnica de Madrid, Spain

We present integrated IDT-phononic resonators with X-propagating SH-SAW for in-liquid operation. These devices are built on Y-cut LiNbO₃ and provide a wave velocity slower than the bulk modes and the RSAW in the structure, hence being well trapped to the surface with very high K_{eff2} (12%). The latter together with the high dielectric permittivity of the structure allows non-conductive liquid measurement directly over the IDT. Experimental measurements using ethylene glycol-water mixtures demonstrate very high sensitivity of the antiresonant frequency to the liquids densities and viscosities. Moreover very high K_{eff2} is still preserved in liquid (11.7% - 13.5 %).

Planar Angle Metrology: G-LAS, the INRIM - INFN Ring Laser Goniometer

#1207#

Jacopo Belfi^{1}, Nicolo' Beverini^{3}, Angela Di Virgilio^{1}, Enrico Maccioni^{3}, Milena Astrua^{2},
Marco Pisani^{2}, Marco Santiano^{2}
^{1}INFN- Sezione di Pisa, Italy; ^{2}INRIM, Italy; ^{3}Universita' di Pisa, Italy

In a collaboration between INRIM and INFN, we are building a new kind of laser goniometer with a target accuracy is 10 nrad. The angles are measured counting the fringes generated by interference between the two counter-propagating laser beams in a ring laser (Sagnac effect) when the ring cavity is mounted on a rotating platform. The laser cavity, a square of 0.50 m in side, makes use of the last generation dielectric super-mirrors.

B3P-G Microwave Frequency Standards & Applications II Poster Area
Chair Stefan Weyers**2D Mot Vacuum Chamber Based on Zerodur**

#1004#

Sin Hyuk Yim^{1}, Tae Hyun Kim^{1}, Sangkyung Lee^{1}, Heesook Roh^{1}, Kyu Min Shim^{1}, Taeg
Yong Kwon^{2}, Sang Eon Park^{2}, Sang-Bum Lee^{2}
^{1}ADD, Korea, South; ^{2}KRISS, Korea, South

We construct a vacuum chamber for 2-dimensional magneto-optical trap (2D MOT) based on Zerodur block for producing slow atomic beam [2]. This atomic beam will be used for cold atom interferometer experiment in near future.

The NAC - a Miniature CPT Rubidium Clock

#1020#

Avinoam Stern, Benny Levy, Chagai Levy, Uriel Arad, Yefim Barash, Ronny Mann, Alex Gorelik
AccuBeat LTD, Israel

We report of the design and characterization of a miniaturized rubidium clock based on coherent population trapping (CPT). The paper describes the atomic standard key design and performance characteristics, the size of which is 41x35x22mm³ and its power consumption is 1.2W. The clock has demonstrated a frequency stability (ADEV) of $8 \cdot 10^{-12}$ at 1000s averaging time, and an aging (drift) of $3 \cdot 10^{-10}$ per month.

**Study of Ion Beam Detection in Cesium Beam Frequency Standard with Feedback Ammeter
Circuit**

#1028#

Ji Wang, Yinguang Ma, Liangyu Huang, Dapeng Chen, Hongwei Zhu, Pei Ma, Jiang Chen
lanzhou institute of physics, China

The paper describes a new scheme adopting the feedback ammeter circuit to amplify ion beam flux generated by physical package of cesium beam frequency standard with magnetic state selection. The feedback ammeter circuit is classic current to voltage converter circuit. The value of the feedback resistance is 100GΩ. Guard shield is included in the feedback circuit. With the feedback circuit, the ion signal from cesium beam tube with 1.0pA can be amplified to 75mV. The cesium beam tube with feedback circuit is currently locked with frequency standard circuit and short term stability of $2E-13@10000s$ is achieved.

Magnetic State Selection Impact on Double Resonance Effect in H-Maser

#1029#

Michael Aleynikov
FGUP VNIIFTRI, Russia

It is well known double resonance effect in a hydrogen maser appears in a two-photon process in which the Zeeman sublevels of the hydrogen atom ground state hyperfine structure are involved when applying transverse magnetic field near the Zeeman frequency. In this paper new modified Bloch equations intended for arbitrary state selection system have been obtained and calculated. As a result an analysis of state selection performance impact on double resonance in H-maser is produced.

The Raman Laser System for Mach-Zehnder Atom Interferometry

#1030#

Nan Li, Kaikai Huang, Xuanhui Lu
Zhejiang University, China

We produced two Raman-laser beams with a frequency offset of 6.834GHz by injection-locking of a master diode-laser to a slave diode-laser. The master laser was phase-modulated at 6.834 GHz with an Electro-Optic Modulator and then injected into the slave laser that was oscillating around one of the side-bands. The relative linewidth of the two lasers was less than 1 Hz. Utilizing these laser beams, we realized the coherent manipulation of atomic wave packets in an Mach-Zehnder type atom interferometry.

Improvements of the NPL Primary Frequency Standards System

#1034#

Filip Ozimek^{2}, Weiliang Chen^{1}, Jochen Kronjaeger^{2}, Piotr Dunst^{3}, Rich Hendricks^{2},
Krzysztof Szymaniec^{2}
^{1}National Institute of Metrology, China; ^{2}National Physical Laboratory, United Kingdom; ^{3}Space Research
Centre, Astrogeodynamical Observatory, Poland

The system consists of two caesium fountain standards to be fully integrated with the NPL time and frequency infrastructure. We report on upgrades to the mature setup of NPL-CsF2 and on the accuracy evaluation of the new fountain NPL-CsF3. In addition, we show improvement in the signal-to-noise ratio and short-term stability achieved by using a laser based local oscillator. In order to avoid a systematic frequency shift due to possible, micro-radian size, microwave phase transients, which might be synchronous with the fountain cycle we have built a triggered phase analyser based on a commercial lock-in amplifier.

Investigation on Porous Materials for Cesium Beam Frequency Standard in Space Environment

#1038#

Jun Yang, Dixin Zhang, Jiang Chen, Ji Wang, Liangyu Huang, Hongwei Zhu, Yinguang Ma, Dapeng
Cheng, Ning Zheng
Lanzhou Institute of Space Technology and Physics, China

Porous materials inside cesium oven play a significant role in enhancing performance of cesium beam frequency standard, such as working lifetime of cesium beam tube, frequency stability of cesium atomic clock and so on. In this paper (for the sake of high quality of cesium atomic beam) the function characteristic about three kinds of porous materials inside cesium oven were investigated in theories and experiments respectively based on design principle of spill-resistant oven.

Recent Advances in Compact Rubidium Frequency Standards at KRISS

#1063#

Hyun-Gue Hong^{2}, Sang Eon Park^{3}, Sangmin Lee^{3}, Myoung-Sun Heo^{2}, Sang-Bum Lee^{2},
Taeg Yong Kwon^{2}, Sin Hyuk Yim^{1}, Chang Bok Lee^{2}
^{1}ADD, Korea, South; ^{2}KRISS, Korea, South; ^{3}KRISS/UST, Korea, South

We report on recent advances in the laser-pumped Rb vapor cell clock based on a magnetron-type microwave cavity at KRISS. The stability at the current stage marks 4×10^{-13} at 1 s and stays 10^{-13} level for integration time up to 10000 s in the presence of linear drift compensation.

Microwave Cavity Characterization for Rubidium Frequency Standards

#1101#

Mohammadreza Gharavipour^{2}, Anton E. Ivanov^{1}, Christoph Affolderbach^{2}, Anja
Skrivervik^{1}, Gaetano Miletì^{2}
^{1}Laboratoire d'Électromagnétisme et d'Acoustique (LEMA), École Polytechnique Fédérale de Lausanne, Switzerland;
^{2}Laboratoire Temps-Fréquence, Institut de Physique, Université de Neuchâtel, Switzerland

We report our studies on the new designed magnetron-type microwave cavity operating in the TE011-like mode, at the rubidium hyperfine ground-state frequency of about 6.835 GHz. The properties of the cavity resonance were studied as a function of cavity temperature. Numerical FEM simulations were performed

and compared to the experimental results. They shed light on the influence of different design parameters on temperature-dependent behavior of the cavity.

Light-Shift Coefficient in GPS Rubidium Clocks: Estimation Methods Using Lamplight/Frequency Correlations **#1133#**

Valerio Formichella^{1}, James Camparo^{2}, Patrizia Tavella^{1}
^{1}Istituto Nazionale di Ricerca Metrologica, Italy; ^{2}The Aerospace Corporation, United States

The frequency of the Rubidium Atomic Frequency Standards (RAFS) flying on GNSS satellites is affected by the light-shift effect, which is a change in clock frequency arising from a change in the RAFS' lamplight. We study this effect in GNSS RAFS by estimating the RAFS' light shift coefficient and its possible variation in time using two different methods: a lamplight-induced frequency jump method, and a lamplight/frequency correlation method. We present analyses using GPS Block IIR clock frequency and lamplight telemetry data, and evaluate the light shift's impact on GNSS by showing the influence of lamplight behavior on RAFS frequency stability.

Development and Spectral Characterisation of Ridge DFB Laser Diodes for Cs Optical Pumping at 894 nm **#1145#**

Renaud Matthey^{3}, Florian Gruet^{3}, Christoph Affolderbach^{3}, Nicolas Von Bandel^{1}, Michel Garcia^{1}, Michel Krakowski^{1}, Patrick Berthoud^{2}, Gaetano Mileti^{3}
^{1}III-V Lab, France; ^{2}Oscilloquartz SA, Switzerland; ^{3}Université de Neuchâtel, Switzerland

A number of research fields like time and frequency or magnetometry make use of lasers to prepare and interrogate caesium atoms. Distributed-feedback diode (DFB) lasers with sub-MHz linewidth operating at 894 nm at the caesium D1 resonance line are barely available. We report on the development and spectral characterisation of 894-nm DFB lasers with Al-free active region, which demonstrate linewidth between 640 kHz and 1.0 MHz.

"Second Order Magic" RF Dressing for Trapped Alkali Atoms **#1167#**

Georgy Kazakov, Thorsten Schumm
Vienna University of Technology, Austria

Using magnetically trapped ensembles of cold atoms in microwave clocks allows to enhance the interrogation time. To mitigate the perturbing effects of the magnetic trap, "magic field" configurations are employed, where the involved clock transitions becomes independent of the atoms potential energy to first order. Still, higher order effects remains and contribute to dephasing. We propose to add the technique of magic radiofrequency dressing to selectively modify the potential landscape experienced by the two clock states in a static magnetic trap. We demonstrate that weak RF dressing can be used to cancel the relative energy shift between the clock states to both, first and second order with respect to the magnitude of the DC magnetic field in the trap. We identify and characterize these "second-order magic" conditions for ⁸⁷Rb atoms trapped in a RF-dressed Ioffe-Pritchard-type trap, compare such trap with conventional ones, and characterize the robustness of this second-order-magic potential to deviations of magnitude and polarization of the involved fields.

Recent Progress in the Development of a Hydrogen Maser in the TE₁₁₁ Mode **#1185#**

Emeline Van der Beken^{2}, Daniel Léonard^{1}, Arnaud Counet^{1}, Thierry Bastin^{2}
^{1}Gillam-FEi, Belgium; ^{2}University of Liège, Belgium

We present the recent progress in the development of a hydrogen maser in the unusual TE₁₁₁ mode. In contrast to standard hydrogen maser that exploits the TE₀₁₁ mode, the TE₁₁₁ mode allows one to design hydrogen masers with significant reduced dimensions which represents a huge benefit for space applications and in particular for the global positioning system. We present in details the different parts of our model: cavity with a thin Teflon sheet, magnetic shielding, thermal control of the maser.

Calculation of Quadratic Zeeman Shift by Regularization Method for an Atomic Fountain Clock

KRISS-F1

#1209#

Young-Ho Park{1}, Sang Eon Park{3}, Myoung-Sun Heo{2}, Taeg Yong Kwon{2}, Hyun-Gue Hong{2},
Sangmin Lee{3}, Sang-Bum Lee{2}
{1}IBS, Korea, South; {2}KRISS, Korea, South; {3}KRISS,UST, Korea, South

We present quadratic Zeeman shift by regularization method for an atomic fountain clock KRISS-F1. We were able to deduce a reasonable field map with an approach of solving an inverse problem using Zeeman frequencies against various launching heights. Relative uncertainty due to the spatial inhomogeneity was estimated to be less than 10^{-18} from the field map.

Optical Phase Locking of DBR Laser for Atomic Gravimeter

#1211#

Sangmin Lee{2}, Sang Eon Park{2}, Sang-Bum Lee{1}, Hyun-Gue Hong{1}, Myoung-Sun Heo{1},
Taeg Yong Kwon{1}
{1}KRISS, Korea, South; {2}KRISS,UST, Korea, South

We present OPL of two DBR lasers to be used for an Rb atomic gravimeter developing at KRISS. Frequency difference of two lasers is 6.9 GHz which is the frequency near 87Rb ground hyperfine splitting. The OPL loop bandwidth is approximately 10 MHz, and the integrated phase variance is 0.29 rad^2 .

On Efficiency of Laser Pumping for Selective Hyperfine-Level Population in Cesium and Rubidium Atoms

#1232#

Vitaly Palchikov, Aleksander Magunov
FGUP VNIIFTRI, Russia

The optical pumping of the ground state hyperfine magnetic sublevels of 87Rb and 133Cs atoms is studied theoretically. Explicit expressions for the stationary populations of the "clock" sublevels during $F_g \leftrightarrow F_e = F_g$ and $F_f \leftrightarrow F_e = F_f$ transitions of corresponding D2 lines in linearly polarized laser fields are obtained versus the initial values

B3P-H Timekeeping, Time & Freq Transfer, GNSS Apps II Poster Area
Chair Peter Whibberley

The Method of Establishing and Maintaining the Interstellar Time Reference During Autonomous Operation of Satellites

#1002#

Xiang-Lei Wang, Wen-Jun Zhao
Beijing satellite navigation center, China

In order to improve the viability of satellite navigation system, we need to establish autonomous operation of interstellar satellite time reference; Because of the complex environmental conditions of space, the interstellar time system that needing to build itself has the capacity of discovering, rejecting outliers and repairing, in order to provide a continuous clock bias sequence for the establishment of satellite time reference. For establishing and maintaining the interstellar time reference based on autonomous operation of satellites, this paper propose that first detecting, rejecting and repairing outliers with the Kaman algorithm in real time, then using the repaired GPS satellite clock bias to establish the time scale with the KPW algorithm. It is found that the interstellar time reference has a good long-term stability and short-term stability, which established with the above method by experiments.

The Method on Determining Invisible Satellite-Ground Clock Difference with Inter-Satellite-Link

#1007#

Wei-Jin Qin, Pei Wei, Xu-Hai Yang
National Time Service Center, China

When the satellite elevation is 10° , visible arcs last about 7 hours, invisible arcs last about 17 hours. However, satellite-ground clock difference of invisible arc is obtained by predicting. Satellite-ground clock

difference is limited to the prediction precision. Inter-satellite link is a new operation mode, operating on a few stations or no station. Due to the limitation of station layout, this paper proposes determining satellite-ground clock difference of invisible arc by way of inter-satellite link, using target satellite connecting station with relay satellite. Satellite-ground link are composed of target satellite and station. Inter-satellite link are composed of target satellite and relay satellite. It analyzes range of relay-satellite angle. In fact, there exist more relay-satellites. In order to use all the relay-satellites, clock difference of invisible arc is determined with weight. The weight criterion: the inverse square of STD of relative clock difference. The result shows: time-synchronization precision of satellite-ground is less than 0.3ns, std is less than 0.3ns.

Research on the Zoom Technique of GNSS Timing Signal Granularity

#1011#

Jianfeng Wu, Yonghui Hu, Zaimin He, Hongchun Lv, Wenhe Yan, Lulu Yan, (Fei Chen, Jian Xu)
National Time Service Center, CAS, China

The 1PPS signal is the standard output of GNSS timing receiver. 1PPS means one pulse per second. The pulse is used to synchronize the device to Universal Time Coordinated (UTC) or the GNSS system time, and it is the recovery of GNSS system time or UTC in the local timing receiver. In a typical design, 1PPS signal is locked with the signal recovery of GNSS 1PPS. In order to correct the sawtooth error of 1PPS signal, we study the zoom technique of GNSS timing signal granularity, and propose an improved scheme. The programmable delay line technology is introduced in the improved scheme. The granularity of the programmable delay line device can reach 0.25ns. We propose a control algorithm which can realize the zoom of GNSS 1PPS's granularity by the combined with the programmable delay line device. This scheme allows for real-time correction of the quantization error and reduces the residual noise to about 1~2 nanoseconds peak to peak (pk-pk), and improves the instantaneous and short-term timing accuracy of GNSS 1PPS. References.

A Paper Clock Prediction Model for UTC(TL)

#1037#

Shinn Yan Lin
TL, Taiwan

A modified paper clock timescale weighted after removing the linearized frequency drift of each cesium clock in a 12-cesium-clock ensemble was used to be the mid-term prediction reference before the announcement of the BIPM Circular T. To get a stable paper clock time scale, we investigated the noise patterns of each cesium clock in ensemble and found their noise were dominated by white noise when the average time was less than 30~40 days. A steering strategy using both proportional and derivative control algorithm would let UTC(TL) toward the paper clock time scale.

Design of a New Calibration Device for Two-Way Satellite Time and Frequency Transfer Station

#1054#

Xueyun Wang, Hang Yu, Shengkang Zhang, Liang Wang, Chao Wang, Haifeng Wang, Peng Wang
Hongbo Wang, Hang Yi, Fan Shi, Dongliang Yan Beijing Institute of Metrology and Measurement, China

A new calibration device for TWSTFT has been developed recently at Beijing Institute of Radio Metrology and Measurement (BIRMM). The signal paths inside calibration device is bidirectional which allow both the transmission and receiving signal passed, so the delay difference of the transmission and receiving inside calibration device almost be zero. The calibration device works on Ku-band. To evaluate the performance of the BIRMM calibration device, a local TWSTFT experiments was done with SATRE modem. The measurement results show that the time delay difference was quite small instability with standard deviation (1σ) equal to 0.17ns.

Application of New Time Receivers in GLONASS

#1066#

Alexandr Bandura, Peter Bogdanov, Maksim German
Russian Institute of Radionavigation and Time, Russia

Till recently, time scale comparisons between GLONASS Central Synchronizers (CS) and State Time and Frequency Reference (STFR) have been performed with using Reference Equipment at CS and TTS-3 receiver at STFR. At the end of 2014 new equipment for time scale comparisons was additionally installed at CS and STFR: Time Transfer Unit TTU-1 developed at RIRT on the basis of 36-channel GLONASS/GPS receiver for SP signals in L1/L2 frequency bands " at the Main CS and a new GTR-51 time receiver for SP and P signals in L1/L2 frequency bands " at STFR. In 2015 the new equipment at CS and STFR was tested and the new accuracy results were obtained.

A Method to Verify the P1-P2 Hardware Calibration in GNSS Receiving Systems Dedicated to Time Transfer

#1091#

Wei Huang, Pascale Defraigne
Royal Observatory of Belgium, Belgium

The measurements from Global Navigation Satellite Systems (GNSS) are widely used for accurate time transfer and time dissemination, but first the hardware delays of the signals across the GNSS receiving system (antenna, cables and receiver) have to be determined by calibration. In this study we propose a strategy to verify the consistence between the hardware calibrations for the different frequencies (GPS P1 and P2 in this case) and to monitor the stability of these inter-frequency hardware delays.

Carrier-Phase Two-Way Satellite Frequency Transfer Between OP and PTB

#1104#

Miho Fujieda^{2}, Joseph Achkar^{1}, Franziska Riedel^{3}, Hiroshi Takiguchi^{2}, Erik Benkler^{3},
Michel Abgrall^{1}, Jocelyne Guéna^{1}, Stefan Weyers^{3}, Dirk Piester^{3}
^{1}LNE-SYRTE, France; ^{2}NICT, Japan; ^{3}PTB, Germany

We demonstrate advanced two-way satellite frequency transfer using the carrier-phase information (TWCP) between OP and PTB. In this report, the evaluation of TWCP system configuration and comparison results of atomic fountain frequency standards are presented.

The Development of GPS/BDS Time Transfer System

#1105#

Hongbo Wang, Hang Yi, Shengkang Zhang, Haifeng Wang, Fan Shi, Xueyun Wang
Beijing Institute of Radio Metrology and Measurement, China

BIRM has developed a GNSS time transfer system which supports both GPS and Beidou system. This paper describes the development of the hardware system and the data processing software of the system. CGTTS V3 file and Rinex 3.02 file including Beidou and GPS could be generated, and all the GPS/BDS satellite observations could be updated in real-time. The time transfer results from GPS and Beidou system are compared.

Determination of Differential Delays of Earth Stations in Paris and Torino from the Calibrated OP-IT TWSTFT Link

#1106#

Joseph Achkar^{2}, Ilaria Sesia^{1}, Daniele Rovera^{2}, Patrizia Tavella ^{1}
^{1}INRIM, Italy; ^{2}LNE-SYRTE, France

Two-Way Satellite Time and Frequency Transfer (TWSTFT) technique is used in most of the metrology institutes as the primary link method for time-scales comparisons. A major advantage of this technique is direct comparisons of time-scales in almost real time using remote earth stations in microwave links through a geostationary satellite. Four earth stations implemented in LNE-SYRTE and INRIM are used. The differential delays of each pair of stations are thus determined from measurements of the various two-way links, relying the measurements taken by the calibrated OP01-IT02 TWSTFT link.

Remote Time and Frequency Transfer Experiment Based on BeiDou Common View #1108#

Hang Yi, Hongbo Wang, Shengkang Zhang, Haifeng Wang, Fan Shi, Xueyun Wang
Beijing Institute of Radio Metrology and Measurement, China

BeiDou navigation satellite system (BDS) is now offering an independent regional service for the Asia-Pacific region and it is going to offer global positioning service by 2020. And BDS will be another choice for remote precise time and frequency transfer. In this paper, we made some remote time and frequency transfer experiment based on BD common view and checked the results by the TWSTFT experiment. Also the common view precision results using GPS and BD are compared in this paper.

Relativistic Effect Correction for Clock Transport #1116#

Hiroshi Takiguchi, Tadahiro Gotoh, Miho Fujieda, Fumimaru Nakagawa, Hideki Narita, Kensuke Matsubara, Kuniyasu Imamura, Hiroyuki Ito, Jun Amagai, Yuko Hanado
National Institute of Information and Communications Technology, Japan

NICT carried out the first calibration of the GPS link between Koganei and Kobe by using GPS, TWSTFT and Clock Transport (CT). We presented the result of the calibration in last EFTF. The obtained differential correction of GPS link by GPS, TWSTFT and CT were 102.5, 102.1 and 104.9 ns respectively. The CT result showed a discrepancy of 2 ns, and we concluded that the reason of this discrepancy is the uncertainty of the CT technique. This time, we applied the relativistic effect correction for CT and we confirmed a good agreement of the results obtained by their three techniques.

Generation of a Time Scale at ESO #1135#

Steffen Braun^{1}, Simon de Fine Licht^{2}, Maria Ramos^{3}, Erik Schönemann^{1}
^{1}ESOC, Germany; ^{2}None, Sweden; ^{3}SERCO / ESO, Germany

In April 2013, an activity for generating a time scale at ESO using the three available AHM was started. The scale is compared to existing UTC time scales using the IGS Rapid orbit and clock products, the PPP-based time transfer results are obtained with ESA's GNSS data processing software package NAPEOS. Proprietary software has been developed for the steering, monitoring, post-processing and generation of the BIPM files. The time scale will be used by the ESO Navigation Office for the enhancement of their clock products, and by the ESO Ground Systems Division for time transfer to the ESTRACK Deep Space Stations.

First Steps Towards a Time Integrity Service for EGNSS Systems, in the DEMETRA Project

#1150#

Ilaria Sesia^{2}, Patrizia Tavella^{2}, Giovanna Signorile^{2}, Alice Cernigliaro^{1}, Franco Fiasca^{1},
Pascale Defraigne^{3}, Lorenzo Galleani^{4}
^{1}AIZOON, Italy; ^{2}Istituto Nazionale di Ricerca Metrologica, Italy; ^{3}Observatoire Royal de Belgique, Belgium;
^{4}Politecnico di Torino, Italy

DEMETRA (DEMONstrator of EGNSS services based on Time Reference Architecture) is a research project co-funded by the European Union through the Horizon 2020 program, aiming to develop and experiment time dissemination services based on the European GNSS. An important aspect that will be analysed in the frame of this project is the capability to deliver a time integrity service to the GNSS users, providing integrity information to improve user timing accuracy as well as positioning. The DEMETRA Time Integrity Service is intended as a first step to test the concepts and performance of a Galileo time integrity system.

Interference Detection and Countermeasures in a GPS- Disciplined Chip-Scale Atomic Clock

#1199#

Aril Schultzen^{1}, Harald Hauglin^{1}, Tim Dunker^{1}, Sverre Holm^{2}
^{1}Justervesenet, Norway; ^{2}University of Oslo, Norway

We describe a smart clock controller (SMACC) intended to complement a commercial disciplined clock so that it becomes 'spooft proof', i.e. hardened against several classes of GPS jamming and spoofing attacks.

The controller uses a multi receiver, multifactorial approach to evaluate the validity/integrity of received GPS signals based on a number of observables as well as clock correction modelling.

GNSS Disciplined Oscillators: an Approach Based on Real-Time Steering Over the Internet with Certification

#1205#

Nilufer Ozdemir^{2}, Pascale Defraigne^{2}, Giancarlo Cerretto^{1}, Elena Cantoni^{1}, Patrizia Tavella^{1}
^{1}Istituto Nazionale di Ricerca Metrologica, Italy; ^{2}Royal Observatory of Belgium, Belgium

GPS disciplined oscillators based on the Common-View approach have already been proposed and implemented. In this work, we propose another system architecture: the local oscillator will be slaved to a remote reference time scale by means of time and frequency corrections streamed over the Internet in real time. Moreover, a certificate will be issued to the user, giving the time and frequency offset of the local oscillator with respect to the remote reference time scale. If such a reference time scale is a local realization of UTC, the certification allows the user to trace its clock to UTC.

A Rotating Fan-Beam Radiation Model for the Pulse Duration and Frequency Spectrum of Pulsar Radiation

#1214#

Michael Underhill
Underhill Research Limited, United Kingdom

The assumption of a rotating fan beam of broadband RF radiation would appear to give a good fit to the observed pulse length to period ratio and pulse amplitude statistics of pulsars. The radiation pattern is assumed to arise from standing waves in multiple radiating layers of (ionospheric) plasma above and around the equator of the pulsar. The frequencies of the multiple layers form a comb spectrum with components spaced at the pulsar rotation frequency. The pulse length to period ratio is found to be inversely proportional to the number layers, typically being about 40 in number.

B3P-J Chair Optical Frequency Standards & Applications II Poster Area
Helen Margolis

Narrow-Linewidth, Micro-Integrated UV Laser System for Precision Spectroscopy Applications

#1033#

Ahmad Bawamia^{1}, Mandy Krüger^{1}, Christian Kürbis^{1}, Andreas Wicht^{1}, Günther Erbert^{1},
Guenther Tränkle^{1}, Stephan Hannig^{3}, Piet Schmidt^{3}, Sana Amairi Pyka^{2}, Achim Peters^{2}
^{1}Ferdinand-Braun-Institut, Leibniz-Institut fuer Hoechstfrequenztechnik, Germany; ^{2}Humboldt Universitaet zu
Berlin, Germany; ^{3}Physikalisch-Technische Bundesanstalt, Germany

As part of the effort to realize portable and space qualified optical atomic clocks, a miniaturized laser system that suits the requirements for deployment in an optical atomic clock is being developed. Designed for an operating wavelength around 267 nm, the laser system consists of a diode-based local oscillator emitting in the NIR and two cascaded frequency doubling stages, with the last one based on a resonant cavity. Each stage is built into a packaged module with a maximum volume of 125 x 75 x 22.5 mm³ and is connected to the next stage via an optical fiber.

A Preliminary Prototype of Laser Frequency Stabilization for Space-Borne Interferometry Missions

#1052#

Yingxin Luo, Hongyin Li, Yurong Liang, Hui-Zong Duan, Jingyi Zhang, Hsien-Chi Yeh
Huazhong University of Science and Technology, China

A prototype of laser frequency stabilization system for inter-satellite laser ranging is presented. This system used Pound-Drever-Hall (PDH) method to stabilize the laser frequency and hydroxide-catalysis bonding to manufacture the Fabry-Pérot (FP) cavity and its mode-matching optical layout on a quasi-monolithic ULE optical bench. All-fiber devices were applied for the PDH optical link, and an in-house-designed digital controller was developed for automatic laser frequency locking and re-locking, which can

benefit autonomous operations on board. Preliminary result shows the frequency noise of this prototype less than $30 \text{ Hz}/\text{Hz}^{1/2}$ from 0.7 Hz to 10 Hz.

Interrogating Optical Clocks Beyond the Coherence Limit of the Clock Laser

#1065#

Marcin Bober^{1}, Ali Al-Masoudi^{2}, Sören Dörscher^{2}, Sebastian Häfner^{2}, Christian Lisdat^{2},
Uwe Sterr^{2}

^{1}Nicolaus Copernicus University, Poland; ^{2}Physikalisch-Technische Bundesanstalt, Germany

We will present a novel interrogation scheme that will allow building a compound clock using different species with probe times longer than the coherence time of the clock laser. The proposed technique utilizes a correlated interrogation sequence of two atomic clocks with one clock laser to resolve the phase ambiguity apparent in Ramsey interrogation beyond the coherence limit of the interrogation laser.

Rb-Stabilized Optical Frequency Reference at 1572 nm

#1073#

William Moreno, Renaud Matthey, Florian Gruet, Pierre Brochard, Stephane Schilt, Gaetano Miletì
Université de Neuchâtel, Laboratoire Temps-fréquence, Switzerland

In the framework of an onboard optical reference laser system, a DFB laser emitting at 1572 nm is offset-locked to a frequency stabilized optical frequency comb. The comb is generated from the radiation of a DFB laser emitting at 1560 nm that frequency-doubled and stabilized to a sub-Doppler Rb absorption using a 2-cm long vapor glass cell. At 1572 nm, a relative frequency stability of $1 \cdot 10^{-11}$ at 1 s has been obtained, reaching $< 4 \cdot 10^{-12}$ from 3,000 s up to 3 days. The accuracy and reproducibility of the locking point to the 87Rb D2 line is also presented.

A Highly Tunable Low-Drift Laser Referenced to an Atomic Transition#

#1075#

Tobias Leopold^{2}, Lisa Schmöger^{1}, Stefanie Feuchtenbeiner^{1}, Christian Grebing^{2}, Peter Micke^{2}, Nils Scharnhorst^{2}, Ian Leroux^{2}, Steven Anthony King^{2}, José Ramon Crespo López-Urrutia^{1}, Piet Oliver Schmidt^{2}

^{1}Max-Planck-Institut für Kernphysik, Germany; ^{2}Physikalisch-Technische Bundesanstalt, Germany

We present a laser system for the resolution of an atomic transition line broadened to ~ 100 kHz in Ar⁽¹³⁺⁾ with a lifetime of 10 ms. A frequency reference with fractional instability below 10^{-10} is achieved by modulation transfer spectroscopy in a rubidium vapour cell. We transfer the absolute frequency stability of a reference laser to the spectroscopy laser via an evacuated transfer cavity. Resulting linewidth and frequency fluctuations are kept below 50 kHz over time scales up to 10^5 seconds. We observe no linear drift on the kHz level over 90 h of continuous operation.

New Approaches in Deep Laser Cooling of Magnesium Atoms for Quantum Metrology #1076#

Oleg Prudnikov^{2}, Denis Brazhnikov^{1}, Anatoly Bonert^{1}, Andrey Goncharov^{1}, Alexey Taichenachev^{1}, Valeriy Yudin^{2}

^{1}Institute of Laser Physics SB RAS, Russia; ^{2}Novosibirsk State University, Russia

Laser cooling and trapping of neutral magnesium atoms have been theoretically analyzed in details. We have proposed two ways for overcoming long-standing problem on getting large number of ultracold magnesium atoms for metrological purposes. Our theory is based on widely used semiclassical approximation as well as on quantum treatment with full account for the atomic recoil effect. Significant differences between the results of two approaches explain many existing problems with deep cooling of magnesium atoms by means of laser radiation. Both of the proposed solutions can allow getting $\sim 10^6$ of Mg atoms owning temperature at the level of 10 microK.

An Yb Optical Lattice Clock at KRISS: Current Status

#1078#

Huidong Kim, Dai-Hyuk Yu, Chang Yong Park, Won-Kyu Lee, Myoung-Sun Heo, Sang Eon Park, Sang-Bum Lee, Hyun-Gue Hong, Taeg Yong Kwon
Korea Research Institute of Standards and Science, Korea, South

We report the current status of an Yb optical lattice clock at Korea Research Institute of Standards and Science (KRISS), Korea. We are making efforts to evaluate the lattice laser induced shifts with uncertainty at or below 10^{-18} level by developing a build-up cavity to enhance the optical lattice depth. The finesse of the cavity is about 155 and trap depth of up to 2000 recoil energy is expected to be reached. To reduce blackbody radiation (BBR) shift, we are developing a thermal shield with minimized temperature distribution.

Transferring Frequency Stability Simultaneously to Multiple Wavelengths with an Optical Frequency Comb

#1085#

Fred Baynes, Antoine Rolland, Steven King, Ross Williams, Stephen Kyriacou, Patrick Gill, Helen Margolis
National Physical Laboratory, United Kingdom

Many applications, such as atomic clocks and long distance optical fibre links will benefit from a local oscillator with improved frequency stability. Here we report using an optical frequency comb to simultaneously transfer the stability of a 1064 nm ultra-stable optical cavity to 4 independent optical atomic clock-relevant wavelengths ranging from 674 nm to 934 nm, a telecom laser at 1542 nm and a microwave signal at 9.2 GHz.

Development of Optical Clocks Based on Strontium Atoms: First Observed Clock-Transition Spectrum

#1088#

Sergey Strelkin, Oleg Berdasov, A. Galyshev, A. Gribov, K. Khabarova, N. Kolachevsky, S. Slyusarev
FSUE VNIIFTRI, Russia

We report about first results in clock transition spectroscopy of SR88 in FSUE VNIIFTRI lab. We have about 10^4 atoms in optical lattice and we have reached linewidth of clock transition about 100Hz.

All Fiber Coupled Ion Trap for Metrology

#1120#

Callan Jobson, Willian Groom, Matthias Keller
University of Sussex, United Kingdom

We present an ion trap system with integrated optics for delivering laser radiation to single trapped ions and to collect their fluorescence. Utilizing this compact system we develop a low volume (< few liters), low power (<100W), portable atomic clock based on trapped calcium ions.

PTB's Transportable Strontium Lattice Clock

#1124#

Jacopo Grotti, Silvio Koller, Stefan Vogt, Sebastian Häfner, Sofia Herbers, Uwe Sterr, Christian Lisdat
Physikalisch-Technische Bundesanstalt, Germany

We want to present the progress on our transportable lattice clock, which has been evaluated at the low 10^{-16} level. A comparison measurement to a stationary strontium clock has been performed. We also report the results of the first transportation of the lattice clock.

Phase Lock and Laser Characterization for the Probing of Trapped Ca+ Ions

#1131#

M. Collombon, R. Khayatadeh, Gaetan Hagel, M. Houssin, C. Champenois, M. Knoop
Université d'Aix-Marseille, France

Phase locking of three different laser involved in the Ca+ ion spectroscopy by using a frequency comb.

Cavity-Assisted Non Destructive Detection in a Strontium Optical Lattice Clock #1142#Grégoire Vallet, Eva Bookjans, Slawomir Bilicki, Rodolphe Letargat, Jérôme Lodewyck
LNE-SYRTE, Observatoire de Paris, PSL Research University, CNRS, Sorbonne Universités, UPMC Univ. Pa, France

Here we report progress on the experimental implementation and theoretical evaluation of a cavity-assisted non destructive detection on one of our strontium clock. This detection will help taking the clock towards, and eventually beyond, the QPN limit. Such a scheme permits to recycle the atoms from an interrogation to another, reducing the duty cycle of the clock. Moreover beating the QPN means entering the quantum realm, enabling quantum weak measurement and cavity spin squeezing via Quantum Non Demolition measurements (QND).

First Results for the Offset Frequency Stabilization via Opto-Optical Modulation of an All-in Fiber Single Walled Carbon Nanotube Erbium Femtosecond Laser #1169#Sebastian Schweyer^{2}, Khanh Kieu^{5}, Philipp Putzer^{1}, Eder Bastian^{1}, Andreas Kölnberger^{1},
Norbert Lemke^{1}, Reinhard Kienberger^{3}, Ulrich Schreiber^{4}
^{1}OHB System AG, Germany; ^{2}Technische Universität München, FESG, Physik Department E11, Germany;
^{3}Technische Universität München, Physik Department E11, Germany; ^{4}Technische University München, FESG,
Germany; ^{5}University of Arizona, College of Optical Sciences, United States

The opto-optical modulation (OOM) technique was recently demonstrated for the stabilization of a solid state SESAM modelocked femtosecond frequency comb. In the here presented work the OOM technique for an all in fiber tapered carbon nanotube femtosecond laser is investigated, which can be used whether to stabilize the laser's repetition rate or carrier envelope offset frequency.

Compact Self-Referenced Femtosecond Er-Doped Fiber Laser Oscillator Without External Power Amplification #1176#Jin-Long Peng, Tze-An Liu, Yuh-Chuan Cheng
Center for Measurement Standards, Taiwan

A femtosecond Er-doped fiber laser oscillator with repetition rate of 100 MHz is employed to directly drive a highly nonlinear optical fiber, which generates an octave-spanning supercontinuum spectrum without using external power amplification. Compact self-referenced fiber laser comb is realized with the f-to-2f interferometer to detect the carrier-envelope-offset frequency.

Metrological Characterization of the INRIM Yb Lattice Clock #1180#Benjamin Rauf, Marco Pizzocaro, Pierre Thoumany, Gianmaria Milani, Filippo Bregolin, Michele Gozzelino, Filippo Levi, Davide Calonico, Giovanni Costanzo, Cecilia Clivati, (Giacomo Bolognesi)
INRIM, Italy

We present INRIM's optical lattice clock based on neutral ¹⁷¹Yb atoms. The clock is currently under operation and we evaluated the first metrological characterization. We completed the set-up adding an efficient spin-polarization. The results for the uncertainty budget and the clock's stability will be described and the perspectives of the full metrological characterization together with future experiments.

Sympathetic Cooling Al⁺ Ion with Ca⁺ Ion for Optical Clock #1184#Junjuan Shang, Kaifeng Cui, Shaomao Wang, Sijia Chao, Jian Cao, Hualin Shu, Xueren Huang
Wuhan Institute of Physics & Mathematics of Chinese Academy of Sciences, China

In this work, We use one laser cooled Ca⁺ to sympathetic cool a Al⁺ in linear Paul trap. In order to increase loading aluminum ion efficiency, Compare to using laser ablation atom producing ion, we got a much lower velocity atoms sprayed from a home-made atom oven, which will make the sympathetic cooling much easier. By the method of precisely measuring the RF resonance frequency of the ion pair, finally We proved we obtained the Al⁺-Ca⁺ ion pair which will be used to QLS optical frequency standard. by sideband cooling method we succeed in cooling the Ca⁺ to the ground state with more than possibility 95%. The Quantum-logic-Spectroscopy experiment is in progress.

Very High Sensitivity Laser Gyroscope for General Relativity Tests in a Ground Laboratory

#1210#

J. Belfi{2}, F. Bosi {2}, N. Beverini{7}, G. Carelli{7}, U. Giacomelli {7}, A. Di Virgilio{2}, E. Maccioni{7}, A. Simonelli {7}, A. Beghi{6}, D. Cuccato{6}, A. Donazzan{6}, G. Naletto{6}, A. Ortolan{3}, A. Porzio{1}, Carlo Altucci{5}, Raffaele Velotta{5}, A. Tartaglia{4}. M. Pelizzo {8}

{1}CNR-SPIN Napoli, Italy; {2}INFN- Sezione di Pisa, Italy; {3}INFN-Lab. Naz. Legnaro, Italy; {4}Politecnico di Torino, Italy; {5}Universita' di Napoli, Italy; {6}Universita' di Padova, Italy; {7}Universita' di Pisa, Italy, {8} CNR-IFN & INFN, Italy

Observation of the metric frame dragging predicted by General Relativity, produced by the Earth rotating mass (Lense-Thirring effect) in a ground laboratory is the final goal of INFN GINGER project. Two laser gyroscopes have been developed. The first is a square gyroscope of 1.60 m of side devoted to test the procedure to optimize the control of the ring geometry in order to achieve the required sensitivity. The second, 3.60 m of side, is located in INFN Gran Sasso underground laboratory, beneath 1000 meters of rock in the Apennine mountains. The aim is to verify the noise quality of the site, in view of an installation of a future large GINGER apparatus.

Iodine Absorption Cells Quality Measurements

#1221#

Hrabina Jan{1}, Zucco Massimo{2}, Acef Ouali{3}, Du-Burck Frederic{4}, Sarbort Martin{1}, Hola Miroslava{1}, Cip Ondrej{1}, Lazar Josef{1}

{1}Institute of Scientific Instruments, Czech Academy of Sciences, Brno, Czech Republic
 {2}Istituto Nazionale Di Ricerca Metrologica, Torino, Italy
 {3}LNE-SYRTE, Observatoire de Paris, Paris, France
 {4}Laboratoire de Physique des Lasers, Universite Paris 13, Sorbonne Paris Cite, Paris

This work is oriented to comparison of methods for iodine absorption cells quality evaluation. Optical frequency references based on molecular iodine represent one of the most used references for stabilization of laser standards working at visible spectral range. Molecular iodine offers rich spectra of strong and narrow absorption lines, but it is a media with high sensitivity for contamination the purity of iodine cells must be precisely controlled. This contribution compares traditional methods for iodine cells quality evaluation (laser induced fluorescence, frequency shifts) with proposed alternative method of linewidth measurement and summarizes the suitability of these methods for practical using.

Turn-Key 1 GHz Ti:Sapphire Frequency Comb with Enhanced Off-Set Locking Bandwidth #1236#

Matthias Beck, Alan Cox, Tobias Plötzing, Marcel Indlekofer, Tushar Mandhyan, Philipp Leiprecht, Albrecht Bartels
 Laser Quantum GmbH, Germany

In the early days of the frequency comb mode-locked Ti:Sapphire lasers were the dominant light sources serving this ground-breaking technology. Amongst them, those with a repetition rate (fR) around 1GHz were often favored over systems nearer 100MHz due to their larger mode spacing, higher average power coherent super-continuum output and consequently higher power per mode.

B4L-A Ion Clocks

P/X001

Chair Tai Hyun Yoon**16:00 Progress Towards a Strontium Single-Ion Optical Clock with mHz Uncertainty**

#1100#

Pierre Dubé{1}, Bin Jian{1}, Alan Madej{2}

{1}National Research Council Canada, Canada; {2}York University, Canada

The Sr⁺ ion optical clock at NRC has an evaluated fractional uncertainty of 1.2×10^{-17} . The dominant source of uncertainty is currently the part of the blackbody radiation (BBR) shift that depends on the thermal field evaluation. The BBR shift uncertainty caused by the polarizability parameter has been reduced to below 1×10^{-18} recently. We will present advances made in controlling the systematic shifts of the Sr⁺ clock transition, including progress towards a new determination of the BBR field. An improved BBR field evaluation is expected to reduce the Sr⁺ uncertainty to the low 10^{-18} level.

16:20 Optical Atomic Clock Measurements in 171Yb+**#1097#**

Peter Nisbet-Jones^{1}, Rachel Godun^{1}, Steven King^{1}, Jonathan Jones^{1}, Charles Baynham^{1}, Kai Bongs^{2}, Patrick Baird^{3}, Patrick Gill^{1}
^{1}NPL, United Kingdom; ^{2}University of Birmingham, United Kingdom; ^{3}University of Oxford, United Kingdom

Clocks based on singly-ionised ytterbium are strong candidates for an optical redefinition of the SI second. We report on advances in the understanding and control of all systematic perturbations, along with advances in the stability, robustness, and reliability of the clock.

16:40 Improved Uncertainty Evaluations of the 171Yb+ Single-Ion Optical Clocks of PTB**#1122#**

Nils Huntemann, Christian Sanner, Sergey Kuznetsov, Burghard Lipphardt, Christian Tamm, Ekkehard Peik
Physikalisch-Technische Bundesanstalt, Germany

171Yb+ provides two reference transitions that are adequate for the realization of an optical frequency standard: an electric quadrupole (E2) transition at 436 nm and an electric octupole (E3) transition at 467 nm. We report on a comparison of two independently operating single-ion clocks that use the E2 transition as the reference and a measurement of the ratio of the E3 and the E2 transition frequency. To avoid the light shift of the E3 transition frequency, coherent composite pulse sequences were proposed over the last years. We present a conceptually different approach leading to a universal pulse-defect immunity.

17:00 Frequency Comparison of Two 40Ca+ Optical Clocks with an Uncertainty at the 10⁻¹⁷ Level**#1174#**

Yao Huang, Hua Guan, Wu Bian, Kelin Gao
Wuhan Institute of Physics and Mathematics, Chinese Academy of Sciences, China

Based upon an over-one-month frequency comparison of two 40Ca+ optical clocks, the frequency difference between the two clocks is measured to be 3.2×10^{-17} with a measurement uncertainty of 5.5×10^{-17} , considering both the statistic (1.9×10^{-17}) and the systematic (5.1×10^{-17}) uncertainties. This is the first performance of a 40Ca+ clock better than that of Cs fountains. A fractional stability of 7×10^{-17} in 20 000 s of averaging time is achieved. The evaluation of the two clocks shows that the shift caused by the micromotion in one of the two clocks limits the uncertainty of the comparison. By carefully compensating the micromotion, the absolute frequency of the clock transition is measured to be 411 042 19 129 776 401.7(1.1) Hz.

17:20 Frequency Ratio of a 171Yb+ Single Ion Clock and a 87Sr Lattice Clock with 2 x 10⁻¹⁷ Uncertainty**#1123#**

Nils Huntemann, Sören Dörscher, Ali Al-Masoudi, Stephan Falke, Nathan Lemke, Sebastian Häfner, Christian Grebing, Burghard Lipphardt, Christian Sanner, Christian Tamm, Uwe Sterr, Christian Lisdat, Ekkehard Peik
Physikalisch-Technische Bundesanstalt, Germany

We report on a direct comparison of two very different optical clocks. One is based on the $2S_{1/2}-2F_{7/2}$ electric octupole transition of a single 171Yb+ ion stored in a radio-frequency Paul trap and the other clock realizes the $1S_0-3P_0$ transition of many 87Sr atoms confined in an optical lattice near the magic wavelength. More than eighty hours of acquired data result in a statistical uncertainty of $1.3E-17$, and yield the frequency ratio of the two clocks with a total fractional uncertainty of $2.4E-17$, which is the smallest uncertainty achieved for clocks of different type to date.

16:00 Network Time Security Specification: Protecting Network-Based Time Synchronization (Invited paper) #1074#

Dieter Sibold, Kristof Teichel
Physikalisch-Technische Bundesanstalt (PTB), Germany

We present the Network Time Security specification (NTS), which is designed to protect time synchronization protocols, especially the Network Time Protocol (NTP) but also the Precision Time Protocol (PTP). Apart from common security requirements, such as protection of integrity and authenticity, NTS also meets specific security requirements formulated for time synchronization protocols by the IETF in RFC 7384. The specification work to apply NTS to NTP is done within the IETF, whereas the aspects of NTS in the context of PTP are considered by IEEE's P1588 working group.

16:40 Sub-Nanosecond Synchronization Accuracy for Time-Sensitive Applications on Industrial Networks #1094#

José Luis Gutiérrez{2}, César Prados{1}, Javier Díaz{2}
{1}GSI Helmholtz Centre for Heavy Ion Research, Germany; {2}University of Granada, Spain

This contribution proposes a change of approach for the White Rabbit technology to become a timing solution with strong focus on Smart Grid. It includes a new design following IEC 61850, where new developments make possible for WR devices to work as Transparent Clocks (TCs) and hence, maximizing the interoperability with other industrial devices. Moreover, the utilization of TCs offers better synchronization results since PTP messages include the entire network delay considering all TCs as a unique fiber. In addition, it eases the development of redundancy protocols like HSR or PRP to guarantee the delivery and reception of critical services such as timing and substation events.

17:00 Towards Sub-Nanosecond Synchronization of a Telecom Network by Fiber Optic Distribution of UTC(K) #1041#

Lukasz Sliwczynski{1}, Przemyslaw Krehlik{1}, Helmut Imlau{2}, Horst Ender{2}, Harald Schnatz{3}, Dirk Piester{3}, Andreas Bauch{3}
{1}AGH University of Science and Technology, Poland; {2}Deutsche Telekom Technik GmbH, Germany; {3}Physikalisch-Technische Bundesanstalt, Germany

We present the results of our four-months long experiments performed between PTB in Braunschweig and Deutsche Telekom center in Bremen with sending time and frequency signals via fiber. The purpose is synchronization and monitoring of enhanced Primary Reference Time Clocks (ePRTC) that are required to assure continuous and robust operation of telecom network. The measurements were performed in parallel using the methods and means typical for telecom operators, and common in the T&F metrology domain. The results show that the synchronization significantly below 1 nanosecond between a UTC laboratory and a telecom center may be obtained.

17:20 Development of an Ultra-Stable Frequency Transfer in a Commercial Fiber-Optic WDM-Network #1119#

Per Olof Hedekvist{2}, Sven-Christian Ebenhag{2}, Martin Zelan{2}, Magnus Karlsson{1}, Börje Josefsson{3}
{1}Chalmers, Sweden; {2}SP, Sweden; {3}SUNET, Sweden

A technique to enable actively stabilized optical frequency transfer and dissemination over deployed communication fiber networks is developed and implemented between SP and Chalmers, a 60 km distance in the Swedish University Computer Network. The stability and achievable performance of the transfer when utilizing two-way transfer in duplex fibers is characterized and evaluated with respect to requirements.

B4L-C Atom Interferometers
Chair Arnaud Landragin**P/L002****16:00 The LNE-SYRTE Cold Atom Gravimeter (Invited paper)****#1195#**Franck Pereira Dos Santos, Pierre Gillot, Bing Cheng, Sébastien Merlet, A. Imanaliev
LNE-SYRTE, France

I will present the absolute Cold Atom Gravimeter (CAG) which has been developed in the frame of the LNE watt balance project. This instrument has been operational since 2009, and participated successfully since then to three international comparison campaigns. It uses atom interferometry to perform an absolute measurement of the gravitational acceleration g , with a best sensitivity as low as $5.7 \cdot 10^{-9} \text{g/Hz}$, a high cycling rate of about 3 Hz and a relative accuracy of 4 parts in 10^9 .

16:40 Continuous Cold-Atom Inertial Sensor without Deadtime**#1036#**Bess Fang, Indranil Dutta, Denis Savoie, Bertrand Venon, Carlos Leonardo Garrido Alzar, Remi Geiger, Arnaud Landragin
LNE-SYRTE, France

We report the operation of a cold atom inertial sensor in a joint interrogation scheme, where we simultaneously prepare a cold atom source and operate an atom interferometer (AI) to eliminate the dead times. We show that such continuous operation improves the short term sensitivity of AIs, by demonstrating a record rotation sensitivity of $90 \text{ nrad/s}/\sqrt{\text{Hz}}$ in a cold atom gyroscope of 11 cm^2 Sagnac area. We also demonstrate a rotation stability below 1 nrad/s after 10^4 s of integration time, which improves previous results by more than an order of magnitude. We expect that the continuous operation of cold atom inertial sensors will allow to benefit from the full sensitivity potential of large area AIs, determined by the quantum noise limit.

17:00 Extended Source Interferometry in the Compact Regime**#1018#**Bruno Pelle, Gregory Hoth, Stefan Riedl, John Kitching, Elizabeth Donley
National Institute of Standards and Technology, United States

An atom interferometer scheme that allows a simultaneous measurement of 2-axis rotations and 1-axis acceleration in a 1 cm^3 volume will be presented. To decouple phase shifts induced by rotation and acceleration with a single atomic source, we extend the Point-Source-Interferometry technique to the compact regime. Then the atom cloud can no longer be treated as a point source, introducing a bias in the scale factor from the point-source limit. After obtaining spatial interference fringes for short free-fall durations, we explored the scale factor deviation with different initial cloud sizes and observed the transition from the point-source to finite-size situations.

Thursday 7th April

	P/X001	P/L001	P/L002
8.40-10.20	C1L-A <u>Frequency Combs</u> Chr: Harald Schnatz Track: Optical Frequency Standards and Applications	C1L-B <u>Caesium Frequency Standards</u> Chr: Krzysztof Szymaniec Track: Microwave Frequency Standards	C1L-C <u>Low Noise Synthesis</u> Chr: Mike Underhill Track: Oscillators, Synthesizers, Noise, & Circuit Techniques
10.20	Coffee / tea break		
10:50-12.30	C2L-A <u>Lattice Clocks II</u> Chr: Jérôme Lodewyck Track: Optical Frequency Standards and Applications	C2L-B <u>CPT Cell Standards</u> Chr: Salvatore Micalizio Track: Microwave Frequency Standards	C2L-C <u>Opto-electronics and Microwave Oscillators</u> Chr: Gilles Cibiel Track: Oscillators, Synthesizers, Noise, & Circuit Techniques
12.30	Lunch		
14:00-15.40	C3L-A <u>Optical Oscillators and Spectroscopy</u> Chr: Thomas Südmeyer Track: Optical Frequency Standards and Applications	C3L-B <u>Optical Fibre Frequency Transfer</u> Chr: Paul-Eric Pottie Track: Timekeeping, Time and Frequency Transfer, GNSS Applications	C3L-C <u>Microwave Frequency Standards</u> Chr: Christoph Affolderbach Track: Microwave Frequency Standards
15.40	Coffee / tea break		
16.00	Laboratory Tours (see sign-up sheets at reception if interested)		

C1L-A Frequency Combs**P/X001****Chair Harald Schnatz****08:40 Ultra Low Noise Er: fiber Frequency Comb Comparison****#1224#**

W. Hänsel^{1}, M. Giunta^{1,2}, K. Beha^{1}, M. Fischer^{1}, M. Lezius^{1}, R. Holzwarth^{1,2}
^{1}Menlo Systems GmbH, Martinsried, Germany

^{2}Max-Planck-Institute of Quantum Optics, Garching, Germany

We have developed a new generation of fiber based frequency combs with ultra high stability based on all pm fibers and NOLM mode locking. An integrated phase noise below 60 mrad (100 Hz " 2 MHz) is reached for the full frequency comb. The locked beat signals exhibit an Allan deviation (ADEV) below 10⁻¹⁶ at 1s. For a full evaluation of short and long term performance we have built and compared two such systems. Both systems are locked to the same 1542nm optical reference laser and the two combs are compared via a direct beat signal at 1µm. In the direct comparison we reach an ADEV of 1 x 10⁻¹⁶ at 1 sec and the 10⁻²⁰ range after 20000 sec, by far surpassing current optical clocks.

09:00 State-of-the-Art Ultra-Low Phase Noise Photonic Microwave Generation and Characterization

#1171#

Romain Bouchand^{3}, Xiaopeng Xie^{3}, Daniele Nicolodi^{3}, Pierre-Alain Tremblin^{4}, Giorgio Santarelli^{4}, Christophe Alexandre^{2}, Michele Giunta^{5}, Matthias Lezius^{5}, Wolfgang Haensel^{5}, Ronald Holzwarth^{5}, Datta Shubhashish^{1}, Joshi Abhay^{1}, Yann Le Coq^{3}
^{1}Discovery Semiconductors, Inc., United States; ^{2}LNE-CNAM, France; ^{3}LNE-SYRTE, France; ^{4}LP2N, France; ^{5}Menlo Systems GmbH, Germany

Many applications such as telecommunication, radar, deep-space navigation systems and pre-cision microwave spectroscopy are calling for ultra-stable microwave signals. Photonic generation of such signals is of particular interest because it allows transferring the unsurpassed spectral purity of ultra-stable continuous wave lasers to the microwave domain. The conversion from optical to micro-wave is done by synchronization of the repetition rate of a femto-second laser with an ultra-stable op-tical frequency reference. The microwave signal is further extracted via fast photo-detection of the optical pulse train. However, the photo-detection process itself introduces excess phase noise hereby limiting the stability of the optically generated microwave signal. The main limits on the purity of the microwave signal generated are the amplitude-to-phase conversion (APC) combined with intensity noise of the femto-second laser and the shot and thermal noise from the photodetector.

09:20 Carrier-Envelope Offset Characterization in a Semiconductor Modelocked Laser Without f-to-2f Interferometry

#1070#

Pierre Brochard^{2}, Nayara Jornod^{2}, Valentin Wittwer^{2}, Stéphane Schilt^{2}, Dominik Waldburger^{1}, Sandro Link^{1}, Cesare Alfieri^{1}, Matthias Golling^{1}, Laurent Devenoges^{3}, Jacques Morel^{3}, Ursula Keller^{1}, Thomas Südmeyer^{2}
^{1}ETH Zurich, Switzerland; ^{2}Laboratoire Temps-Fréquence, Switzerland; ^{3}METAS, Switzerland

We measured for the first time the noise properties and the modulation response of the free-running carrier-envelop offset (CEO) frequency in a semiconductor modelocked laser. We used a novel characterization method that does not involve standard f-to-2f interferometry, but makes use of an appropriate combination of signals obtained from the comb and a reference continuous-wave laser. We first present a validation of the method in an Er: fiber comb, where the achieved results are in excellent agreement with reference data obtained by f-to-2f interferometry. Then we present an implementation of the method with a modelocked vertical external-cavity surface-emitting laser.

09:40 Efficient Carrier Envelope Offset Frequency Stabilization Through Gain Modulation via Stimulated Emission

#1064#

Lauriane Karlen, Gilles Buchs, Erwin Portuondo-Campa, Steve Lecomte
CSEM, Switzerland

A novel scheme for intra-cavity control of the carrier- envelope offset frequency (fCEO) of a modelocked Er:Yb:glass diode-pumped solid state laser based on the modulation of the laser gain via stimulated emission is demonstrated.

10:00 DFG Comb Showing Quadratic Scaling of the Phase Noise with Frequency

#1128#

Russell Kliese, Thomas Puppe, Alexander Sell, Nazanin Hoghooghi, Felix Rohde, Armin Zach, Wilhelm Kaenders
TOPTICA Photonics AG, Germany

We characterize a passively carrier envelope phase-stable Er: fiber difference frequency comb at 1550 nm. Phase noise of single comb lines over nearly an optical octave is measured via a delayed self-heterodyne beat of a cw clean-up laser. Repetition-rate stabilization achieves a RF-reference limited line-width. A lock to a low-noise optical reference shows Hz level out-of-loop line-widths. The measured phase noise is in excellent agreement with the elastic tape model with a fix point at zero frequency.

08:40 First Accuracy Evaluation of the METAS-FoCS2 Primary Frequency Standard #1069#
 Antoine Jallageas^{2}, Laurent Devenoges^{1}, Michael Petersen^{2}, Laurent-Guy Bernier^{1}, Jacques Morel^{1}, Pierre Thomann^{2}, Thomas Südmeyer^{2}
^{1}Institute of Metrology METAS, Switzerland; ^{2}Laboratoire Temps-Fréquence, Université de Neuchâtel, Switzerland

Microwave leakages induced by spurious surface currents were eliminated with the installation of a graphite cylinder around the free evolution zone in FoCS-2. This improvement is a significant step toward the full metrological evaluation. We present here the latest measurements for the residual microwave leakages, the collisional shift and the microwave cavity-related frequency shifts and a first uncertainty budget for FoCS-2 with a total uncertainty at the 10^{-15} level.

09:00 Improvements of the Statistical and Systematic Uncertainty Contributions of PTB's Fountain Clocks #1031#
 Stefan Weyers^{3}, Vladislav Gerginov^{3}, Michael Kazda^{3}, Burghard Lipphardt^{3}, Georgi Dobrev^{2}, Kurt Gibble^{1}
^{1}Department of Physics, The Pennsylvania State University, United States; ^{2}Faculty of Physics, Sofia University, Bulgaria; ^{3}Physikalisch-Technische Bundesanstalt, Germany

For both PTB caesium fountain clocks CSF1 and CSF2 new systematic uncertainty evaluations have been undertaken. Particular attention has been concentrated on a more rigorous evaluation of frequency shifting effects due to microwave leakage, the distributed cavity phase and cold collisions. Because the necessary measurements for such investigations strongly benefit from improved frequency stability, an optically stabilized microwave source has been developed at PTB and now operates routinely. For the fountains we obtain overall systematic uncertainties at the low 10^{-16} level. We will report about details of the setups and evaluations.

09:20 Development of a High Performance Optical Cesium Beam Clock for Ground Applications #1138#
 Patrick Berthoud, Manuel Haldimann, Christophe Ducommun, Frederic Lefebvre, Radoslav Pantic, Luc Schneller, Fabiano Kroll, Nicolas Voirol, Alain Michaud
 Oscilloquartz SA, Switzerland

Oscilloquartz SA, Switzerland is developing a ground cesium beam clock for ground applications. Thanks to optical pumping rather than magnetic deflection, the useful atomic beam flux will be largely increased without compromising the clock lifetime. The aim is to get a transportable clock fitting in a standard frame (19" width, 3U high), providing an output signal frequency stability of $3 \times 10^{-12} \text{ t}^{-1/2}$ with a 10 years lifetime. Clock integration results will be presented at the conference together with frequency stability measurements and a signal-to-noise budget analysis.

09:40 Towards an Engineering Model of Optical Space Cs Clock #1218#
 R. Schmeissner^{2}, A. Douahi^{2}, I. Barbereau^{2}, P. Dufreche^{2}, Arnaud Brechenmacher^{2}, Klaus Kudielka^{1}, Frederic Loiseau^{1}, Andreas Romer^{1}, Christoph Roth^{1}, Willem Coppoolse^{1}, Nicole Mestre^{2}, Michel Baldy^{2}, N. von Bandel^{3}, O. Parillaud^{3}, M. Garcia^{3}, M. Krakowski^{3}
^{1}RUAG, Switzerland; ^{2}Thales Electron Devices, France, ^{3}III-V Lab, France

Thales Electron Devices and RUAG currently develop the engineering model of the Optical Space Cs Clock. Recent progress of the project is reported. Emphasis is put on the test and comparison of new laser sources, the implementation of an isolator free optics subsystem and the space evaluation of the laser and the photodiode.

C1L-C Low Noise Synthesis
Chair Mike Underhill

P/L002

08:40 Suppressing LO-Induced Instabilities in Passive Frequency Standards by Quantum Control (Invited paper)

#1003#

Michael Biercuk
 University of Sydney, Australia

The physical correspondence between quantum bits and the atomic transitions employed in many passive frequency standards provides an opportunity to explore how new quantum control techniques designed to suppress qubit error for large-scale quantum information may be brought to bear in the precision metrology community. We report new theoretical developments in noise filtering and quantum state estimation and how they can be applied to the stabilization of passive frequency standards suffering from LO noise. We treat a range of system parameters but focus on the challenging case of LO noise that contains spectral weight near the inverse cycle time in the presence of large dead time. We experimentally demonstrate that embedding quantum optimal estimation techniques within the feedback loop of a Ytterbium-ion microwave standard can improve both correction accuracy and long-term stability (assuming a perfect atomic reference). Our experiments provide quantitative validation of our theoretical insights and suggest new "software-only" approaches to improve passive frequency standard performance in tight-SWAP applications where LO stability is performance limiting.

09:20 Frequency Synthesis from Cryogenic Sapphire Oscillator

#1043#

Etienne Vaillant^{2}, Fabrice Sthal^{2}, Joël Imbaud^{2}, Yannick Gruson^{2}, Christophe Fluhr^{2}, Serge Grop^{2}, Vincent Giordano^{2}, Enrico Rubiola^{2}, François-Xavier Esnault^{1}, Gilles Cibié^{1}
^{1}CNES, France; ^{2}FEMTO-ST, France

To characterize ultra-stable resonators, the passive technique with carrier suppression is used to measure the inherent phase stability of the ultra-stable resonators. This kind of bench usually uses both identical resonators inserted in each arm in order to suppress the noise of the source [2]. To operate with only one resonator, the driving source must have a phase noise lower than the best resonators that are measured. At 5 MHz, the power spectral density of phase fluctuations of these best quartz crystal resonators is expected around -140 dBc/Hz. In these conditions, the driving source cannot be an ultrastable 5 MHz quartz oscillator. Cryogenic sapphire oscillators present a very low phase noise [3]. Thus in this paper, first results of frequency synthesis chain from cryogenic sapphire oscillator are presented. A 100 MHz signal is divided until 5 MHz in order to get the best phase noise. Several divider combinations are presented and discussed. The limits of commercial dividers are shown and best results have been obtained using regenerative dividers. Further investigations are proposed in order to improve these results.

09:40 A HBAR-Oscillator-Based 4.596 GHz Frequency Source: Design, Characterization and Application to a Cs Microcell Atomic Clock

#1049#

Rodolphe Boudot^{2}, Gilles Martin^{1}, Jean-Michel Friedt^{1}
^{1}FEMTO-ST, France; ^{2}FEMTO-ST - CNRS, France

This paper presents a HBAR-oscillator based 4.596 GHz frequency source. This source is used as a local oscillator in a CPT-based laboratory-prototype Cs vapor cell atomic clock.

10:00 Low Phase Noise 10MHz Crystal Oscillators

#1234#

Tsvetan Burtichelov, Jeremy Everard
 University of York, United Kingdom

This paper describes the design and implementation of low phase noise 10MHz Crystal Oscillators which are being used as part of the chain of a local oscillator for use in compact atomic clocks. The design considerations and phase noise measurements are presented. This paper is based on a previous design [1] but now demonstrates significantly improved phase noise performance and now includes the key circuit descriptions. The latest measurements of the 10MHz crystal oscillator's performance demonstrates a

phase noise of -123dBc/Hz at 1 Hz and -148dBc/Hz at 10 Hz. The results compare well with the best 5MHz BVA oscillators when 6dB (+2) is subtracted.

C2L-A Lattice Clocks II

P/X001

Chair Jérôme Lodewyck

10:50 Realization of a Timescale with an Optical Clock

#1042#

Christian Grebing, Ali Al-Masoudi, Sören Dörscher, Sebastian Häfner, Vladislav Gerginov, Stefan Weyers, Burghard Lipphardt, Fritz Riehle, Uwe Sterr, Christian Lisdat
Physikalisch-Technische Bundesanstalt, Germany

We demonstrate how PTB's strontium lattice clock (overall availability: $\approx 30\%$) in combination with a continuously running conventional maser flywheel is able to maintain a local timescale with a time error of less than 200 ps compared to an ideal reference over about 12 days, or 1.6×10^{-16} in fractional frequency. Thus, the optical timescale surpasses the performance of a timescale referenced to a continuously running primary clock by more than a factor of two.

11:10 Months-Long Evaluation of Maser Frequency by a Lattice Clock Toward the Steering of Time Scales

#1154#

Tetsuya Ido, Hidekazu Hachisu, Fumimaru Nakagawa, Yuko Hanado
NICT, Japan

With reference to a 87Sr lattice clock, the frequency of a hydrogen maser (HM) was evaluated intermittently for a few months. The result of the calibration was utilized for the most accurate TAI-based absolute frequency measurement of 10^{-16} level. The result was also used for the feasibility study of "optical" steering of time scales. Taking account the calibration data as well as the record of the HM frequency stored in Japan Standard Time system, it is realized that calibrations by an optical clock once in two weeks are sufficient to maintain a HM-based time scale in a few ns level.

11:30 Precise Frequency Comparison of Clocks Considering the Dead Time Uncertainty of Frequency Link

#1161#

Takehiko Tanabe^{1}, Daisuke Akamatsu^{1}, Takumi Kobayashi^{1}, Akifumi Takamizawa^{1}, Shinya Yanagimachi^{1}, Takeshi Ikegami^{1}, Tomonari Suzuyama^{1}, Hajime Inaba^{1}, Sho Okubo^{1}, Masami Yasuda^{1}, Feng-Lei Hong^{2}, Atsushi Onae^{1}, Kazumoto Hosaka^{1}
^{1}National Metrology Institute of Japan (NMIJ), Japan; ^{2}Yokohama National University, Japan

We have developed Yb and Sr optical lattice clocks at NMIJ. So far the uncertainties of the absolute frequencies of the clock transitions were mainly limited by the uncertainty of a comparison with UTC(NMIJ). Recently, we carefully evaluate the uncertainties of the link between the Sr optical lattice clock and TAI via UTC(NMIJ) using a caesium fountain atomic clock located at NMIJ as a transfer oscillator. In this way, we could reduce the final uncertainty to one third that of our previous measurement.

11:50 87Sr and 88Sr Optical Lattice Clocks at NPL

#1163#

Ian Hill^{1}, Richard Hobson^{1}, William Bowden^{1}, Marco Menchetti^{1}, Antoine Rolland^{1}, Fred Baynes^{1}, Helen Margolis^{1}, Patrick Baird^{2}, Kai Bongs^{3}, Patrick Gill^{1}
^{1}NPL, United Kingdom; ^{2}Oxford, United Kingdom; ^{3}University of Birmingham, United Kingdom

We present an evaluation of the NPL 87Sr optical lattice clock. The evaluation is aided by an improved stability of the clock, provided by an ultra-stable laser at 1064 nm delivered across a fibre comb-based transfer oscillator scheme to 698 nm. We also present progress towards an accurate 88Sr clock and show the elimination of probe induced shifts using a modified-hyper-Ramsey spectroscopy.

12:10 Recent Advances in Precision Spectroscopy of Ultracold Atoms and Ions #1113#Alexey Taichenachev^{1}, Valeriy Yudin^{2}, Sergey Bagayev^{1}
^{1}Institute of laser physics SB RAS, Russia; ^{2}Novosibirsk State University, Russia

New methods and approaches in precision spectroscopy of ultracold atoms and ions are discussed with an emphasis on contributions of Institute of Laser Physics SB RAS.

C2L-B CPT Cell Standards**P/L001****Chair Salvatore Micalizio****10:50 A High-Performance CPT-Based Cs Vapor Cell Atomic Clock Using Push-Pull Optical Pumping #1048#**Moustafa Abdel Hafiz, Rodolphe Boudot
FEMTO-ST, France

This paper presents a high-performance CPT Cs vapor cell atomic clock using the push-pull optical pumping technique. A fractional frequency stability of $2 \cdot 10^{-13}$ up to 100 s has been demonstrated. Latest results will be presented at the conference.

11:10 A compact setup for double-modulation Coherent Population Trapping Clock #1168#Peter Yun, Francois Tricot, David Holleville, Emeric de Clercq, Stephane Guérandel, (Sinda Mejri)
Observatoire de Paris, France

We demonstrate a setup for a high performance coherent population trapping (CPT) atomic clock based on the double-modulation scheme, i.e., the synchronous modulation of the light polarization and of the phase between the two components of the bichromatic laser beam. With the help of a current modulated DFB laser diode to generate the bichromatic beam and a liquid crystal polarization rotator to realize the polarization modulation, it is possible to implement a very compact, robust and high performance atomic clock.

11:30 Progress on the CPT Clock: Reduction of the Main Frequency Noise Sources #1139#Francois Tricot^{2}, Sinda Mejri^{2}, Peter Yun^{2}, Bruno Francois^{1}, Jean-Marie Danet^{3}, Stephane
Guerandel^{2}, Emeric De Clercq^{2}, M Lours
^{1}INRIM, Italy; ^{2}LNE-SYRTE, France; ^{3}SYRLINKS, France

Clocks based on coherent population trapping (CPT) represent promising candidates for on-board space and industrial applications thanks to their simple scheme and high stability performance. Indeed in our CPT clocks the microwave frequency is optically carried into a vapor cell of cesium. We present here the main frequency noise sources for the clock stability, now $\sigma_y(1s) = 3.2 \cdot 10^{-13}$; and what we are doing to decrease the frequency noise contributions.

11:50 Back Ground Noise Suppression in CPT Based Atomic Clock by Differential Detection**#1017#**Huifang Lin^{1}, Bozhong Tan^{2}, Yuan Tian^{2}, Sihong Gu^{2}
^{1}Huazhong University of Science and Technology, China; ^{2}Wuhan Institute of Physics and Mathematics, Chinese
Academy of Sciences, China

The conventional CPT atomic clock uses VCSEL as the light source, and the obtained CPT signal is with strong background noise which deteriorates frequency stability of the clock. We present a scheme which extracts Faraday effect CPT signal by means of differential detection technique. The strong background noise can be considerably depressed and our experimental study result reveals that it is promising to improve frequency stability by two orders of magnitudes compared with the conventional scheme, at same time the size and power consumption of the CPT atomic clock can be kept at the same level.

12:10 Investigation of High SNR Ramsey Spectrum with Dispersion Detection in the CPT**Atomic Clocks****#1172#**

Xiaolin Sun, Pengfei Cheng, Chi Xu, Jianwei Zhang, Lu Zhao, Lijun Wang
Tsinghua University, China

The lin-par-lin Ramsey coherent population trapping 87Rb clock using dispersion detection technique has a promising performance. We theoretically and experimentally investigate the signal-to-noise ratio of the Ramsey spectrum signal by varying the relative angle of the polarizer and analyzer as well as the magnetic field. Based on the experimental results, the optimized relative angle and magnetic field are determined. This kind of atomic clock is attractive for the development of high performance and compact vapor clock based on CPT.

C2L-C Opto-electronics and Microwave Oscillators**P/L002****Chair Gilles Cibiel****10:50 Photonic Oscillators: Beyond the State of the Art (Invited paper)****#1196#**

Lute Maleki
OEwaves, Inc., United States

Photonic oscillators are based on generation of RF (microwave/mm-wave) signals by beating equally spaced coherent harmonics of light produced by one, or multiple lasers on a fast photodiode. The frequency of the RF signal corresponds to the equally spaced interval between the harmonics, and thus it can be readily selectable. The phase noise of the RF signal corresponds to the phase noise of the optical signal that generated it.

11:30 Low Phase Noise 10GHz Bragg Resonator Oscillator**#1229#**

Pratik Deshpande, Simon Bale, Jeremy Everard
University of York, United Kingdom

This paper describes the theory and design of a 10GHz low noise oscillator which uses a Bragg resonator. The resonator utilizes an aperiodic arrangement of low loss alumina plates mounted in a cylindrical metal waveguide (Resonator Q0 ~ 200,000). The oscillator demonstrates a phase noise performance of -123 dBc/Hz at 1kHz offset and -153 dBc/Hz at 10kHz offset. Extensive optimization of different transistors operating at different power levels has taken place. The gain, noise figure and residual phase noise of these amplifiers is reported. This enables a suitable choice for a given oscillator frequency. The power requirements are 6V at 52mA.

11:50 Brillouin lasing in a LiF whispering-gallery mode resonator and application to microwave generation**#1235#**

Souleymane Diallo, Guoping Lin {2}, Jean Pierre Aubry, Yanne K. Chembo
Femto-ST Institute, France, {2} Centre for Gravitational Experiments, China

We report Brillouin lasing in a monofluoride crystalline resonator for the very first time. While Raman scattering results from the interaction between a laser beam and an optical phonon providing a frequency shift in the THz range, Brillouin scattering results from the interaction between a strong laser beam and an acoustic phonon leading to a frequency shift of few GHz, which makes it more suitable for microwave generation. We present a time domain model which tracks the dynamics of the Stokes and pump waves and finally, with the help of a stability analysis, we determine analytically the threshold power. Such a laser has great potential for ultra-pure microwave and multi-wavelength generation.

12:10 Ultra-Low-Noise Optoelectronic Oscillator at 10 GHz Based on a Short Fiber Delay

#1204#

Oriane Lelièvre^{3}, Vincent Crozatier^{3}, Ghaya Baili^{3}, Perrine Berger^{3}, Loic Morvan^{3}, Grégoire Pillet^{3}, Daniel Dolfi^{3}, Olivier Llopis^{2}, Fabienne Goldfarb^{1}, Fabien Bretenaker^{1}
^{1}Laboratoire Aimé Cotton, CNRS, France; ^{2}Laboratoire d'Analyse et d'Architecture des Systèmes, CNRS, France; ^{3}Thales Research and Technology, France

We report on an optoelectronic oscillator (OEO) at 10 GHz based on a single 1 km long fiber delay, and exhibiting simultaneously an ultra-low close-in phase noise (-94 dBc/Hz @100 Hz) and a low spurious level (below -110 dBc/Hz). These results are well predicted by a model taking into account the frequency and intensity noise from the laser source that are converted into phase noise.

C3L-A Optical Oscillators and Spectroscopy**P/X001****Chair Thomas Südmeyer****14:00 Direct Comparison of Two Optical Cryogenic Silicon Resonators**

#1216#

Dan Gheorghita Matei^{2}, Thomas Legero^{2}, Wei Zhang^{1}, Robin Weyrich^{2}, Christian Grebing^{2}, Sebastian Häfner^{2}, Christian Lisdat^{2}, Fritz Riehle^{2}, Lindsay Sonderhouse^{1}, John Michael Robinson^{1}, Jun Ye^{1}, Uwe Sterr^{2}
^{1}JILA, United States; ^{2}Physikalisch-Technische Bundesanstalt, Germany

We discuss the fundamental and technical limits to the stability of an optical resonator made of single-crystal silicon. By directly comparing two identical systems we measure the effect of seismic perturbations, residual amplitude modulation, temperature stability and vacuum pressure fluctuations on the overall stability. We present the measures taken to reduce their influence below the thermal noise limit.

14:20 Temperature and Current Dependence of 1/F Frequency Noise in Narrow-Linewidth**Discrete-Mode Lasers**

#1090#

Stefan Kundermann^{1}, John O'Carroll^{2}, Diarmuid Byrne^{2}, Lina Maigyte^{2}, Brian Kelly^{2}, Richard Phelan^{2}, Dmitri L. Boiko^{1}
^{1}CSEM, Switzerland; ^{2}Eblana Photonics Ltd, Ireland

Wavelength tunable lasers for coherent optical communications systems and atomic spectroscopy need to meet stringent requirements on narrow linewidth emission. For the majority of semiconductor lasers, the integral noise features such as the linewidth and RIN are defined by flicker (1/f) noise contribution, which is believed to be due to generation-recombination processes through recombination centers in defects (e.g. dislocations). In this talk we will report on 1/f noise dependence on the cavity length as well as driving current and temperature of the narrow linewidth Discrete Mode Laser Diodes (DMLD) and discuss the possible origin of these effects.

14:40 Frequency tripled 1.5 μm telecom laser diode stabilized to iodine hyperfine line in the 10¹⁴-15 range

#1178#

C. Philippe^{1}, R. Le Targat^{1}, D. Holleville^{1}, M. Lours^{1}, T. Minh-Pham^{3}, J. Hrabina^{3}, F. Du Burck^{2}, P. Wolf^{1}, O. Acef^{1}
^{1}Observatoire de Paris - SYRTE, France; ^{2}Université Paris 13-Sorbonne Paris - LPL, France, ^{3}Institute of Scientific Instruments, Czech Academy of Sciences, Brno, Czech Republic

Molecular iodine represents one of the most interesting atomic references for the realization of a frequency standard in the range of telecom laser wavelength. We have developed effective, compact and original third harmonic generation setup delivering up to 300 mW of green radiation at 514 nm with an optical conversion efficiency of $P_{3w}/P_w \sim 36\%$. Well known frequency modulation transfer is used to interrogate molecular iodine, in a compact laboratory optical setup. A preliminary evaluation of the frequency stability is reported as $\text{Sigma}(y)(\text{Tau}) = 6 \cdot 10^{-14} \text{ Tau}^{-1/2}$.

15:00 Phase Locking an Atom Interferometer

#1149#

Andrea Bartoldi {3}, Ralf Kohlhaas {4}, Etienne Cantin {3}, Alain Aspect {1}, Arnaud Landragin {2},
Philippe Bouyer {3}
{1}IOGS, France; {2}LNE - SYRTE, France; {3}LP2N - IOGS, France; {4}SRON Netherlands Institute for Space Research,
Netherlands

In atom interferometry the phase evolution of a quantum superposition state is measured with respect to a reference signal. The measurement has a limited unambiguous interval, since not the phase but its projection is measured as a population unbalance on two energetic levels. Resolving phase wrapping brings to a longer interrogation interval and hence instrument sensitivity. We extended the unambiguous probe interval using coherence preserving measurements and phase corrections, and demonstrated the phase lock of the clock oscillator to an atomic superposition state. On this basis we implemented a protocol to improve atomic clocks limited by local oscillator noise.

15:20 Absolute Frequency of the Inter-Combination Line in 171Yb with Use of the Clock Transition

#1023#

Liam Salter, John McFerran
University of Western Australia, Australia

We report on the absolute frequency measurement of the $6s^2\ 1S_0\ (F=1/2) - 6s6p\ 3P_1\ (F=3/2)$ transition in ^{171}Yb . Knowledge of this frequency will aid those searching for the $1S_0\ (F=1/2) - 3P_0\ (F=1/2)$ clock transition without access to highly accurate frequency standards. The mean frequency is 539 390 405 430 (190) (16) kHz. An absolute frequency for the same line can be inferred from a result in Pandey et al, PRA, 80, 022518, 2009. We find our frequency to be higher by 39.4MHz. We are unable to resolve the $^{171}\text{Yb}\ (F=1/2-3/2)$ and $^{173}\text{Yb}\ (F=5/2-3/2)$ lines, which have previously been reported to be closer than 2MHz. The latter we estimate to be weaker in strength by approximately a factor of ten.

C3L-B Optical Fibre Frequency Transfer

P/L001

Chair

Paul-Eric Pottie

14:00 Validating Frequency Transfer via a Stabilised Fibre Link for Optical Clock Comparisons

#1187#

Sebastian Koke, Christian Grebing, Alexander Kuhl, Gesine Grosche
Physikalisch-Technische Bundesanstalt (PTB), Germany

Comparisons of remote optical clocks with uncertainty $\sim 1\text{E-}18$ require careful validation of the frequency transfer carried out via phase-stabilised fibre links connecting them. This differs from assessing the performance of the link itself. Here, we present link data analysis, validation and selection in a recent comparison of two Sr clocks located at SYRTE and at PTB separated by 700 km line-of-sight. Using a looped link set-up, we validate each 1000s data segment requiring that the frequency offset is below $5\text{E-}18$ (5sigma). The overall uncertainty contribution of the fibre link is two orders of magnitude below the uncertainty of the clocks.

14:20 Towards an International Optical Clock Comparison Between NPL and SYRTE Using an Optical Fiber Network

#1035#

J. Kronjäger{4}, G. Marra{4}, O. Lopez{2}, N. Quintin{2}, A. Amy-Klein{2}, W. Lee{1}, P. Pottie{3}, H. Schnatz{5}

{1}Korea Research Institute of Standards and Science, Korea, South; {2}Laboratoire de Physique des Lasers, France; {3}Laboratoire National de Métrologie et d'Essais–Système de Références Temps-Espace, France; {4}National Physical Laboratory, United Kingdom; {5}Physikalisch-Technische Bundesanstalt, Germany

We aim at performing an international comparison of the optical clocks developed at SYRTE and NPL using optical frequency transfer through a long haul fiber link between London and Paris. Our experimental setup employs a novel hybrid topology combining active compensation and two-way technology, and a new implementation using a repeater laser station at the pivot point. We present a characterization of the residual phase noise using loop-back measurements over the fiber pair and demonstrate ultra-stable laser

comparisons between NPL and SYRTE. Together with the link between France and Germany, the London-Paris link will allow simultaneous multiple clock comparisons.

14:40 Transfer of Stable Optical Frequency for Sensory Networks via 306 km Optical Fiber**Link****#1152#**

Martin Cizek^{2}, Lenka Pravdova^{2}, Vaclav Hucl^{2}, Simon Rerucha^{2}, Jan Hrabina^{2}, Bretislav Mikel^{2}, Vladimir Smotlacha^{1}, Josef Vojtech^{1}, Josef Lazar^{2}, Ondrej Cip^{2}
^{1}CESNET, z. s. p. o., Czech Rep.; ^{2}Institute of Scientific Instruments of the CAS, Czech Rep.

The remote calibration of interrogators of Fiber Bragg Grating strain sensory networks may be one of future industrial applications employing highly-stable optical frequency dissemination from optical frequency standards. We present a 306 km long optical fiber link established in the Czech Republic where a coherent transfer of a stable optical frequency has been demonstrated. The link between ISI CAS Brno and CESNET Prague uses an internet communication fiber where a DWDM window of 1540-1546 nm is dedicated for the coherent transfer and 1PPS signal. The link is equipped with 6 bidirectional EDFA amplifiers. The optical frequency standard at 1540.5 nm is used for the coherent transfer where compensation with AOM of the Doppler shift induced by the optical fiber is done. The output frequency of the VCO driving the AOM is continuously measured and logged by a RF counter for computing changes in the transport delay introduced by external influences on the optical line. To compare with a different measuring method a setup for analysing the transport delay of a 1 PPS signal is connected to the same DWDM mux/demux at both sides. This comparison is a subject of results of the paper.

15:00 Absolute Frequency Measurement of the 173Yb Clock Transition via a 642-km Fiber**Link****#1115#**

Cecilia Clivati^{2}, Giacomo Cappellini^{6}, Lorenzo Livi^{6}, Francesco Poggiali^{6}, Mario Siciliani de Cumis^{3}, Marco Mancini^{7}, Guido Pagano^{7}, Matteo Frittelli^{2}, Alberto Mura^{2}, Giovanni Costanzo^{4}, Filippo Levi^{2}, Davide Calonico^{2}, Leonardo Fallani^{8}, Jacopo Catani^{1}, Massimo Inguscio^{5}

^{1}INO-CNR, LENS, Italy; ^{2}INRIM, Italy; ^{3}INRIM, INO-CNR, Italy; ^{4}INRIM, Politecnico di Torino, Italy; ^{5}INRIM, University of Florence, LENS, Italy; ^{6}LENS, Italy; ^{7}University of Florence, Italy; ^{8}University of Florence, LENS, Italy

We report on high-precision frequency measurement of the 173Yb clock transition using a long-haul optical fiber link. We transfer a narrow-linewidth telecom laser along 642 km of optical fiber and use it as a remote frequency reference for long-term, SI-traceable spectroscopy of an ultracold gas of 173Yb. Our results improve the accuracy reported in literature by two orders of magnitude and demonstrate the link as a tool for high-precision spectroscopy at a level which cannot be obtained with standard techniques.

15:20 Geodetic VLBI Field-Test of Lift: a 550 km Long Optical Fiber Link for Remote Antenna Synchronization**#1181#**

Davide Calonico^{2}, Cecilia Clivati^{2}, Matteo Frittelli^{2}, Alberto Mura^{2}, Filippo Levi^{2}, Massimo Zucco^{2}, Federico Perini^{1}, Claudio Bortolotti^{1}, Mauro Roma^{1}, Roberto Ambrosini^{1}, Giuseppe Maccaferri^{1}, Monia Negusini^{1}, Matteo Stagni^{1}, Mauro Nanni^{1}, Alessandra Bertarini^{3}

^{1}INAF - Osservatorio di Radioastronomia, Italy; ^{2}INRIM, Italy; ^{3}Institut für Geodäsie und Geoinformation der Universität Bonn, Germany

We present a geodetic VLBI field-test of LIFT, the Italian fiber link. In September 2015, the Medicina VLBI antenna participated to the Eur137 experiment, in tag along mode, using as reference systems both the local H maser and a remote H maser hosted at the INRIM labs in Turin, disseminated to Medicina via a 550 km fiber link. We describe the set-up, the measurement campaign, the results and their analysis together with the perspectives of the activity.

14:00 Main Features of Space Rubidium Atomic Frequency Standard for BeiDou Satellites
(Invited paper) #1110#

Ganghua Mei, Da Zhong, Shaofeng An, Feng Zhao, Feng Qi, Fang Wang, Gang Ming, Wenbin Li, Pengfei Wang
 Wuhan Institute of Physics and Mathematics, Chinese Academy of Sciences, China

Wuhan Institute of Physics and Mathematics (WIPM), Chinese Academy of Sciences has been developing the space borne rubidium atomic frequency standard (RAFS) for BeiDou navigation satellite system since late 1990's. The day frequency stability of the RAFS's employed in Bei-Dou regional system is within $2\sim 5 \times 10^{-14}$. A new prototype of RAFS developed for BeiDou global system has been realized, and a day frequency stability of 3×10^{-15} , obtained. In this paper we outline main features of the space RAFS designed by WIPM.

14:40 Relaxation Time Measurements in a Rb Vapor Cell #1102#

Mohammadreza Gharavipour^{2}, Ivan S. Radojicic^{1}, Florian Gruet^{2}, Christoph Affolderbach^{2}, Aleksandar J. Krmpot^{1}, Brana M. Jelenkovic^{1}, Gaetano Mileti^{2}
^{1}Institute of Physics, University of Belgrade, Serbia; ^{2}Laboratoire Temps-Fréquence, Institut de Physique, Université de Neuchâtel, Switzerland

We are studying the physics of compact atomic frequency standards (atomic clocks) based on Rb vapor cells, in view of the development of novel high-performance atomic clocks for applications such as satellite navigation systems or industrial metrology applications. Here we report on measurements of the T1 and T2 relaxation times in the Rb vapor cell of our clock, using and comparing several different methods such as relaxation in the dark, Ramsey scheme, and continuous-wave laser-microwave double resonance.

15:00 Precision Test of the ac-Stark Shift in a Vapor-Phase System #1071#

Salvatore Micalizio^{2}, James Camparo^{1}, Filippo Levi^{2}, Bruno Francois^{2}, Claudio Eligio Calosso^{2}, Aldo Godone^{2}
^{1}Aerospace Corporation, United States; ^{2}INRIM, Italy

In this work, we present a new methodology for measuring the ac-Stark shift in a Rb cell with a high level of accuracy. Specifically, we take advantage of the pulsed optical pumping technique and of the Ramsey interaction scheme. A low power perturbing laser pulse tuned to the D1 absorption resonance is applied to the atoms during their free evolution phase. In this way we were able to verify the AC Stark shift theory for a perturbing laser tuned over a broad optical frequency range (18 GHz). In our experiments we test both the frequency dependence of the scalar and, for the first time, tensor components of the light shift.

Satellite Workshop, Friday 8th April

P/L001 Lectures

P/L005 Posters

Optical clocks: quantum engineering and international timekeeping

The workshop is organised by two EMRP project consortia: International timescales with optical clocks (ITOC) and Quantum Engineered States for Optical Clocks and Atomic Sensors (QESOCAS). Complementing the scientific programme of EFTF, it will address recent developments related to the use of quantum engineered states to enhance the stability of optical clocks, as well as progress made towards using optical clocks for international timekeeping. Two invited talks from leading experts in the field will be followed by presentations from members of the two project consortia. Poster presentations from all participants are welcomed for the afternoon session.

8:30 - 09:00 Registration

09:00 - 09:45 **Fritz Riehle, PTB**

'Towards a redefinition of the SI second by optical clocks: achievements and challenges'

09:45 - 10:30 **Augusto Smerzi, Istituto Nazionale di Ottica, Trento**

'Witnessing entanglement with the Fisher information: from metrology to Bell nonlocality'

10:30 - 11:00 Coffee / tea break

11:00 - 11:30 **Helen Margolis, NPL**

'Overview of ITOC project'

11:30 - 12:00 **Sébastien Bize, LNE-SYRTE**

'Overview of QESOCAS project'

12:00 - 12:30 ITOC highlight talk

12:30 - 13:00 QESOCAS highlight talk

13:00 - 14:00 Lunch break

14:00 - 16:00 Posters

16:00 End of meeting

Contact Person: Helen Margolis (NPL)

Organising committee: Helen Margolis (NPL, UK), Sébastien Bize (LNE-SYRTE, France), Davide Calonico (INRIM, Italy), Christian Lisdat (PTB, Germany).

Authors Index

Abbé	35, 36	Bawamia.....	65	Buchaillet	48
Abend	27	Baynes	15, 33, 67, 77	Buchs	74
Abgrall.....	46, 63	Baynham.....	43, 44, 70	Buczek.....	40, 41
Abhay	15, 34, 74	Beaufils.....	50	Burtichelov	13, 33, 76
Ablewski.....	42	Bebon	49	Byrne	80
Acef	80	Beck	69	Cai	14, 29
Achkar	63	Beghi	69	Calonico	68, 82
Adamowicz.....	40	Belfi	58, 69	Calosso	13, 24, 32, 41, 83
Affolderbach.....	14, 31, 37, 59, 60, 83	Belloni	38	Camparo	60, 83
Agnus.....	13, 32	Beloy	46	Campbell	40
Aguilera	50	Benkler	63	Cantin	81
Ahlers	27	Berdasov.....	67	Cantoni	65
Akamatsu.....	77	Berger	80	Cao	68
Akerman	15, 32, 51	Bernier	75	Cappellini	82
Albers	37	Bertarini.....	82	Cárdenas-Olaya	32
Alboraih.....	39	Berthoud.....	60, 75	Carelli	69
AlDawood	39	Bertoldi.....	81	Catani	82
Alexandre	15, 34, 50, 74	Beugnon	50	Cernigliaro.....	64
Aleynikov	58	Beverini	58, 69	Cerretto.....	65
Alfieri	14, 30, 74	Bian	70	Champenois.....	67
Alighanbari.....	46	Biercuk	76	Chao	14, 31, 62, 68
Aljawan	39	Bilicki	46, 47, 68	Chatras.....	13, 27, 29
Al-Masoudi.....	43	Binczewski	38, 40	Chembo	33, 79
Almuhlaki.....	39	Bize.....	46	Chen	14, 29, 36, 37, 42, 58, 59, 62
Altucci	69	Blinov	26, 38	Cheng	14, 36, 59, 68, 72, 79
Alzar	72	Blondy	13, 27, 29	Chutani	36
Amagai	64	Bober	42, 66	Cibiel.....	13, 29, 76
Ambrosini.....	82	Boddy	41	Cip	82
An	83	Bogacki.....	40	Ciurylo.....	40, 42
Andreeva	37	Bogdanov	63	Cizek.....	82
Antcev	57	Bogoslovsky	57	Clement	28, 35, 57
Arad	58	Boiko	54, 80	Clivati	13, 32, 41, 82
Arapan	57	Bolognesi.....	68	Collombon.....	67
Arnold.....	27	Bonert	66	Conan	48
Aspect.....	81	Bongs.....	15, 33, 43, 44, 45, 46, 70, 77	Constantin.....	43
Astrua	58	Bookjans.....	46, 47, 68	Coppoolse.....	75
Aubry.....	13, 33, 79	Bortolotti	82	Cordier.....	48
Bagala.....	56	Bouchand.....	15, 34, 74	Costanzo	82
Bagayev	78	Boudot	14, 29, 36, 76, 78	Counet	60
Baili	80	Bouganne.....	50	Cox	69
Baird	15, 33, 43, 44, 70, 77	Bounds.....	41	Crozatier	80
Baldy	38, 75	Bourgeois	13, 24, 32	Crunteanu	13, 27, 29
Bale.....	79	Bourgeteau-Verlhac.....	35	Cuccato.....	69
Balet.....	45	Bourquin.....	35	Cui	68
Balling	43	Bouyer	81	Czubla.....	39
Bandura	63	Bowden.....	15, 33, 77	Danet	14, 31, 78
Barantsev	38	Boyko	38	Danielson.....	53
Barash	56, 58	Brandli.....	48	Dareau	50
Barbereau.....	75	Braun	64, 65	de Clercq	78
Baron	49, 57	Brazhnikov	37, 66	De Clercq.....	14, 31, 36, 78
Bartels.....	69	Brechenmacher.....	75	de Cumis.....	82
Barwood	46	Bregolin.....	68	de Fine Licht.....	64
Basalaev.....	37	Bretenaker	80	Defraigne	17, 20, 23, 63, 64, 65
Bastian	44, 45, 51, 68	Breuer	44	Delicado	57
Bastin.....	60	Bridge	41	Dembele	13, 32
Bauch.....	52, 71	Brochard.....	14, 30, 45, 66, 74	DeMiguel-Ramos	28
Baumann.....	53	Brown	46	De-Sarlo	46

Deshpande	79	Francois	14, 31, 78, 83	Gutiérrez.....	71
Detoma	56	Fraser.....	48	Hachisu.....	77
Devenoges	14, 30, 74, 75	Frayssinet	48	Haensel.....	15, 34, 74
Di Virgilio	58, 69	Frederic.....	69	Haesler.....	14, 32
Diallo	13, 33, 79	Friedt	13, 24, 32, 57, 76	Hafiz.....	14, 29, 36, 78
Diaz	41	Frittelli.....	13, 32, 82	Häfner.....	43, 66, 67, 70, 77, 80
Díaz	28, 35, 57, 71	Froh	39	Hagel	67
Díaz-Durán	28, 35, 57	Fujieda.....	55, 63, 64	Haldimann	75
Dierikx.....	55	Gaaloul	27	Hamid	39
Dobrev	75	Galindo	55	Han	45
Doležal.....	43	Galleani	64	Hanado	64, 77
Dolfi.....	80	Galliou.....	35, 36	Hanley	41
Domnin.....	38	Galyshev.....	67	Hannig	65
Donazzan	69	Gao	14, 31, 34, 45, 70	Hänsch	53
Dong	14, 31	Garcia	38, 60	Hansen.....	53
Donley	72	Gebert.....	14, 28, 51	Hashimoto	27
Döring.....	50	Geiger	72	Hati.....	52
Dörscher	43, 66, 70, 77	Gerbier.....	50	Hauglin	35, 64
Dos Santos.....	72	Gerginov.....	75, 77	He	46, 62
Douahi	75	German.....	63	Hedekvist.....	71
Drewsen.....	53	Gharavipour.....	14, 31, 59, 83	Heil.....	48
Du Burck	80	Gibble.....	75	Heine	37, 46
Dubé	69	Gill.....	15, 26, 33, 43, 44, 46, 67, 70, 77	Heip	14, 28, 51
Ducommun	75	Gillot.....	72	Hendricks	59
Dufreche	75	Giordano.....	13, 29, 53, 76	Heo	37, 42, 43, 59, 61, 67
Dugrain.....	26, 31	Giunta	15, 34, 74	Herbers	67
Dulmet	57	Goavec-Merou.....	13, 24, 32	Hieta	44
Dunker	35, 64	Gobet	14, 32	Hill.....	15, 33, 46, 77
Dunst	40, 59	Godet	13, 32	Hindley	48
Dutta	72	Godone	83	Hinkley	46
Ebenhag	71	Godun	43, 44, 70	Hirschauer	55
Eder	44, 45, 51, 68	Golcz	52	Hobson	15, 33, 77
Elvin	27	Goldfarb	80	Hoghooghi.....	74
Ender	71	Golling.....	14, 30, 74	Holleville.....	46
Entin	37	Goncharov	26, 66	Holm.....	64
Erbert.....	65	Gorecki.....	36	Holzwarth.....	15, 34, 53, 74
Ertmer	27, 37, 44, 45, 46	Gorelik.....	58	Hong.....	37, 59, 61, 67, 77
Esnault	13, 29, 76	Goryachev	35	Horsley	54
Everard	13, 33, 76, 79	Gotoh.....	64	Hosaka.....	77
Fakhrutdinov	34	Gozzelino.....	68	Hoth.....	72
Falke	70	Grebing.....	66, 70, 77, 80, 81	Houssin.....	67
Fallani.....	82	Gribov.....	67	Howe	52
Fan	42	Griffin.....	27	Hrabina.....	82
Fang.....	72, 83	Grimbert	48	Hu	62
Faoro.....	41	Groom.....	67	Huang	36, 37, 55, 58, 59, 63, 68, 70
Fasano.....	46	Grop.....	29, 76	Hucl	82
Faucher	48	Grosche.....	20, 22, 39, 81	Hugentobler.....	44, 51
Favier.....	46	Grotti	67	Hughes.....	46
Feldhaus.....	52	Gruet.....	14, 31, 60, 66, 83	Huillery.....	41
Feuchtenbeiner	53, 66	Gruson	24, 53	Huntemann	70
Fiasca.....	64	Gu	78	Hutterer.....	45, 51
Fibich.....	56	Guan	70	Iborra.....	13, 28, 30, 35, 49, 57
Fim.....	44, 45, 46	Guéna	46, 63	Ido.....	77
Fischer	51	Guerandel	14, 31, 78	Ikegami.....	77
Flambaum.....	54	Guérandel	78	Imamura	64
Flewitt.....	28	Guerard.....	35	Imbaud.....	13, 29, 76
Fluhr	13, 29, 76	Gui.....	14, 29	Imlau.....	71
Fordell	44	Guo	42	Inaba	77
Formichella.....	60				

EFTF 2016 Programme

Indlekofer	69	Kronjaeger	59	Ludlow	46
Inguscio	82	Krüger.....	65	Luo	65
Ito.....	64	Kudielka	75	Lusawa	39
Ivanov	35, 37, 59	Kuhl.....	39, 81	Lv	34
Jachna	41	Kulosa.....	44, 45, 46	Ma.....	36, 37, 58, 59
Jallageas.....	75	Kundermann	80	Maccaferri	82
Jan.....	69	Kupalov	38	Maccioni.....	58, 69
Jelenkovic.....	31, 83	Kupalova	38	Madej.....	69
Jesorka	57	Kürbis	65	Magunov.....	61
Jha.....	44, 45, 46	Kuznetsov	70	Maigyte.....	80
Jian.....	62, 68, 69	Kwiatkowski.....	41	Maleki.....	79
Jiang.....	36, 37, 42, 55, 58, 59	Kwon	37, 58, 59, 61, 67	Mancini.....	82
Jimenez-Lopez.....	41	Kyriacou	67	Mandhyani.....	69
Jobson	67	Lamb.....	13, 30, 48, 49	Mann.....	56, 58
Jones	41, 44, 70	Landragin.....	27, 72, 81	Männel.....	48
Jornod	14, 30, 74	Laudat.....	14, 26, 31	Marecki.....	40, 42
Josef.....	69	Lavenus	35	Margolis	15, 26, 33, 67, 77
Josefsson.....	71	Lazar	82	Marmo	47
Kaenders	46, 74	Le Coq.....	15, 34, 46, 74	Marszalec	39
Kalaydzhyan.....	13, 33	Le Targat	46, 47, 80	Martin.....	45, 49, 51, 69, 76
Kalinin	49	Le Traon	35	Martindale	48
Karlen	14, 32, 74	Leclair.....	48	Masoudi.....	66, 70, 77
Karlsson.....	71	Lecomte.....	45, 74	Massimo	69
Kärtner.....	30, 33	Lee	36, 37, 42, 43, 58, 59, 61, 67	Matei.....	80
Katori.....	47	Lefebvre	75	Matsakis	55
Kaur	14, 30	Legero.....	80	Matsubara	64
Kazakov	44, 60	Leigh.....	49	Matthey.....	60, 66
Kazda.....	75	Leiprecht.....	69	Maurice.....	36
Keegan.....	41	Lelièvre.....	80	McFerran	81
Keller	14, 30, 67, 74	Lemanski	40	McGilligan	27
Kelly	80	Lemke.....	44, 51, 68, 70	McGrew.....	46
Khabarova	67	Léonard.....	60	Mei	83
Khan	13, 32	Leopold.....	53, 66	Meiners.....	37
Khayatzadeh	67	Leroux	66	Mejri.....	14, 31, 78
Khelif.....	13, 32	Lesage.....	49	Menchetti.....	15, 33, 77
Kienberger.....	44, 51, 68	Letargat.....	68	Merlet	72
Kieu	68	Leute.....	52	Mestre.....	75
Kim.....	36, 42, 43, 58, 67	Levi.....	68, 82, 83	Micalizio.....	20, 21, 41, 83
King.....	43, 44, 66, 67, 70	Levy.....	35, 56, 58	Michaud.....	75
Kitching	72	Lezius	15, 34, 74	Micke.....	53, 66
Kitpracha	14, 28	Li	34, 45, 59, 83	Mikel	82
Kliese.....	74	Lin	33, 55, 62, 78, 79	Milani	68
Klioni.....	47	Lindner	51	Mileti ...	14, 31, 37, 59, 60, 66, 83
Knoop	67	Link	30, 74	Ming	83
Kobayashi.....	77	Lipinski.....	40, 42	Mirea	13, 28, 30, 35, 49, 57
Kock	46	Lipphardt	70, 75, 77	Miroslava.....	69
Kodet	40, 48	Lisdat ...	43, 46, 66, 67, 70, 77, 80	Molyneux	48
Kohlhaas	81	Litvinov	38	Moonaksorn.....	14, 28
Kohnen	53	Liu	14, 29, 68	Morel	14, 30, 74, 75
Koke	81	Livi	82	Morelle	48
Kolachevsky	67	Llopis.....	80	Moreno	66
Koller.....	67	Lodewyck.....	46, 47, 68	Moriana	52
Kölnberger.....	44, 68	Loiseau	75	Mortada	13, 27, 29
Kolodziej	40	Lopez.....	41	Morvan	80
Kosykh.....	34	López-Urrutia	53, 66	Morzynski.....	42
Krakowski	38, 60	Loriani	27	Mura	13, 32, 82
Krehlik.....	38, 39, 40, 42, 71	Loyer	51	Murasov.....	34
Krmpot.....	14, 31, 83	Lu	59	Nakagawa.....	64, 77
Kroll.....	75			Naletto	69

Nanni	82	Plötzing	69	Sanner	70
Narita	64	Poggiali	82	Santarelli	15, 34, 74
Nath	37	Poli	46	Santiano	58
Nawrocki	40, 42	Popov	38	Sapozhnikov	57
Negusini	82	Portuondo-Campa	74	Satirapod	14, 28
Nelson	52	Porzio	69	Sauer	44, 45, 46
Nicolodi	15, 34, 46, 74	Pottie	14, 30	Savoie	72
Nisbet-Jones	43, 44	Prados	71	Scharnhorst	66
Nogas	40	Pravdova	82	Schiller	46
Novokreshchenov	37	Prazot	56	Schilt	14, 30, 45, 66, 74
Oates	46	Probst	53	Schioppo	46
O'Carroll	80	Prochazka	40, 48	Schlippert	27, 37
Okubo	77	Prudnikov	66	Schlunegger	55
Olivares	28, 35, 57	Puppe	74	Schmeissner	38, 75
Onae	77	Putzer	44, 51, 68	Schmidt	14, 28, 51, 53, 65, 66
Ondrej	69	Pye	48	Schmöger	53, 66
Origlia	46	Pyka	65	Schnatz	71
Orlianges	13, 27, 29	Qi	83	Schneider	40
Ortolan	69	Qin	14, 29, 61	Schneller	75
Ouali	69	Radojicic	31, 83	Scholl	50
Ovchinnikov	46	Ramos	64	Schönemann	64
Overstolz	14, 32	Rasel	27, 37, 44, 45, 46	Schreiber	40, 44, 48, 51, 68
Ovsiannikov	47	Rauf	68	Schubert	27, 37
Ozdemir	65	Reichel	26, 31	Schultzen	64
Ozeri	15, 32, 51	Reindl	32	Schumm	44, 60
Ozimek	59	Rerucha	82	Schwarz	43, 52, 53
Pagano	82	Richardson	37	Schweyer	44, 51, 68
Palchikov	26, 47, 61	Riedel	55, 63	Sell	44, 74
Panek	40, 48	Riedl	72	Sesia	63, 64
Pantic	75	Riis	27	Shang	68
Park	37, 42, 43, 58, 59, 61, 67	Ro	36	Shaniv	15, 32, 51
Parker	45, 55	Robert	46, 48	Shapira	56
Passilly	36	Robinson	80	Shemar	48
Pawszak	40	Roch	48	Sherman	46
Pazderski	40, 42	Rodriguez	41	Shi	28, 51, 63, 64
Pedregosa	53	Rodríguez	45	Shim	36, 58
Peik	20, 21, 70	Roh	58	Shu	68
Pelle	72	Rohde	52, 53, 56, 74	Shubhashish	15, 34, 74
Peng	13, 14, 30, 33, 45, 62, 68	Roldán	52	Shvetsov	57
Perini	82	Rolland	15, 33, 67, 77	Sibold	71
Perosanz	51	Roma	82	Singh	45, 46
Peters	65	Romalis	54	Skrivervik	37, 59
Petersen	75	Romer	75	Sliwczynski	38, 39, 40, 42, 71
Petit	51	Rønningen	35	Śliwczyński	39
Petrini	49	Rosenbusch	26, 31	Slyusarev	67
Pfeifer	53	Roth	52, 75	Smith	46
Phelan	80	Rovera	63	Smotlacha	82
Philippe	80	Rózyc	41	Sokolov	36, 38
Phillips	46	Rubiola	13, 20, 23, 29, 32, 53, 76	Sonderhouse	80
Piat	13, 32	Rughoobur	28	Stadnik	54
Pieczerek	40	Rühmann	44, 45	Stagni	82
Piest	53	Rühmann	46	Stark	44, 46, 53
Piester	55, 63, 71	Ruland	40	Steinmetz	53
Pillet	80	Ryabtsev	37	Stern	56, 58
Pinter	39	Sadler	41	Sterr	43, 46, 66, 67, 70, 77, 80
Píriz	52	Safak	30	Sthal	13, 29, 76
Pisani	58	Salter	81	Stofanik	56
Pizzocaro	68	Sangrador	35	Stopps	49
Placet	57			Strelkin	67

EFTF 2016 Programme

Stroinski.....	40	Udem	53	Wu	53, 62
Stuhler	46	Ullrich.....	53	Xiao	34
Südmeyer.....	14, 30, 45, 74, 75	Underhill.....	56, 65	Xie	34, 74
Sun.....	34, 37, 42, 43, 59, 61, 67, 79	Unterholzer	51	Xin.....	14, 30
Suwantong	14, 28	Vaillant	13, 29, 76	Xu	45, 62, 79
Suzuyama	77	Vairac	13, 32	Yan	42
Sweirad	46	Vallet	47, 68	Yanagimachi.....	77
Szplet.....	41	Van der Beken.....	60	Yang	29, 34, 36, 37, 55, 59, 61
Szterk.....	39	van Schreven	38	Yantchev.....	13, 30, 49, 57
Szymaniec	20, 59	Velotta	69	Yasuda.....	77
Tai.....	42	Venon	46, 72	Ye	80
Taichenachev.....	37, 66, 78	Vernotte.....	53	Yeh	65
Takamizawa.....	77	Versolato	53	Yi.....	63, 64
Takiguchi.....	63, 64	Viswam.....	46	Yim.....	36, 58, 59
Tamm.....	70	Vogt.....	46, 67	Yogun.....	39
Tan.....	78	Voirol	75	Yoon.....	46
Tanabe	77	Vojtech	82	Yousaf	13, 32
Tartaglia.....	69	von Bandel.....	38	Yu	37, 42, 43, 62, 67
Tavella	20, 22, 52, 60, 64, 65	Von Bandel.....	60	Yuan	14, 31, 78
Teichel	71	Waldburger.....	14, 30, 74	Yudin.....	37, 66, 78
Theron	48	Wan	28, 51	Yun.....	31, 78
Thomann.....	75	Wang	14, 29, 31, 34, 36, 37, 58, 59, 61, 62, 63, 64, 68, 79, 83	Zach.....	44, 74
Thongtan.....	14, 28	Ward	56	Zahr	13, 27, 29
Thoumany.....	68	Warwick	48	Zavyalov.....	34
Tian.....	78	Waterholter.....	39	Zawada	40, 42
Tino	46	Wei	61	Zelan.....	71
Tobar	35	Weyers.....	63, 75, 77	Zhang.....	34, 42, 45, 55, 59, 62, 63, 64, 79, 80
Tränkle.....	65	Weyrich	80	Zhao.....	34, 61, 79, 83
Tremblin	15, 34, 74	Wicht	65	Zheng.....	36, 59
Treutlein	54	Williams	67	Zhgoon	57
Tricot	14, 31, 78	Windberger.....	53	Zhong	83
Tseng	55	Wittwer.....	14, 30, 74	Zhou	45
Tuckey	14, 30	Wodey	37	Zhu	14, 31, 34, 36, 37, 58, 59
Turza.....	38, 40	Wolf.....	14, 28, 34, 48, 51	Zipfel	44, 45, 46
Tyumenev	46	Wong	57	Zucco.....	82

Exhibitors



Oscilloquartz is a pioneer in time and frequency synchronization. We design, manufacture and deploy end-to-end synchronization systems that ensure the delivery and assurance of highly precise timing information over next-generation packet and legacy networks. As an ADVA Optical Networking company, we're creating new opportunities for tomorrow's networks. For more information, please visit us at: www.oscilloquartz.com and www.advaoptical.com.



Noise XT is one of the most experienced company in the world regarding Phase Noise. Being about frequency synthesizers or Phase Noise analyzers, our expertise can certainly help you achieve performance goals or solve issues.

Since 1992, our continuous innovation on low phase noise design made us the highest performance provider on the market. Our customers are typically in the Defense, Space, Telecommunication or Time and Frequency community. <http://www.noisext.com/>



GuideTech's newest product-line includes the **GT9000**, scalable from 2 to 24 channel "CTIA" Continuous Time Interval Analyzer & "TIC" Time Interval Counter with Integrated 3D touch screen display, **GT9001P-USB3**, a 2 channel Portable "CTIA" & "TIC" USB3 controlled, **GT9000R**, 19" Rack-Mount scalable from 2 to 24 channel "CTIA" & "TIC". Since 1988, A world leader in the design, development and manufacturing of High-Precision 0.9pS resolution, 4M m/s, Zero dead time Continuous Time & Frequency measurement instruments for Scientific Laboratories, Research and Automated Test Applications. GuideTech's products are used in commercial, education, research, government and military systems/applications worldwide. <http://www.guidetech.com/>



SpectraDynamics, Inc. (SDI) is a Colorado, USA-based company. Founded in 1994, specializing in high performance time and frequency distribution systems. In association with the National Institute of Standards and Technology, SpectraDynamics participates in the research and development of technology to provide the low noise electronics needed to support atomic time and frequency standards.

SpectraDynamics main products are Time and Frequency Distribution Amplifiers and Low Noise Frequency Synthesizers. Our featured items are the HROG series, high performance frequency and phase micro-steppers with under 1 fs resolution, and the HPDA-15RMi series, ultra low noise frequency distribution amplifiers. In addition to the standard products, SpectraDynamics has the ability to deliver custom solutions engineered to meet your specific needs.

<http://www.spectradynamics.com/>



For more than 80 years, Rohde & Schwarz has stood for quality, precision and innovation in all fields of wireless communications. The privately owned company is strategically based on four pillars: test and measurement, broadcast and media, secure communications, cybersecurity, radiomonitoring and radiolocation. The electronics group, headquartered in Munich (Germany), has a global presence and is among the world market leaders in all of its business fields.

<https://www.rohde-schwarz.com/>



Laser Quantum is a world-class manufacturer of revolutionary solid-state and ultrafast laser systems. Our products lead the industry in performance specifications, reliability, compactness and operational lifetime. They have been used in ground-breaking research, and continue to push the boundaries of science. You will find Laser Quantum lasers in laboratories worldwide and used in diverse applications including attosecond physics, forensics and genomics

due to the wide range of wavelengths and powers we offer. Our wealth of experience, together with our passionate team, mean we are committed to providing you with a service and laser system that exceeds your expectations.

We have recently launched our first complete 1GHz frequency comb, an exceptional supercontinuum typ.1uW per mode with easy access to VIS and NIR ranges, and will be showcasing its capabilities at the European Time and Frequency Forum. For more information, please visit our website: www.laserquantum.com



M Squared Lasers research, design and manufacture world-class lasers and advanced photonic systems for use in a myriad of academic, commercial and industrial applications. Its high performance systems are critical enablers in fundamental physics research and behind a number of 'world firsts' from the first demonstration of 'teleportation' to the first stable ultra-cold molecules. Its technology is also being used to enable advances in the commercial world, most

recently in the detection and classification of gases in the oil and gas industry and threat detection for the security sector.

Constantly covering new ground, M Squared is dedicated to innovation, actively involved in collaborative research projects and working on next generation quantum technologies. Founded in 2006, by laser experts Dr Graeme Malcolm, OBE and Dr Gareth Maker, the company is now considered a leader in its field. <http://www.m2lasers.com/>



MOG Laboratories Pty Ltd (MOGLabs) offers tunable cateye and Littrow lasers, laser electronics, optical amplifiers, RF-synthesizers, AOM drivers and sub-picometer wavemeters. We develop scientific

instrumentation from a user perspective, aimed at being a pleasure to use with performance to meet your expectations. We support our products, with a solid guarantee: we don't want unhappy customers.

MOGLabs is an offshoot of an experimental atom optics laboratory at the University of Melbourne. MOGLabs Europe based in Berlin was opened in 2012.

We are a company of in-the-lab scientists and engineers, people that know what you need because they've come from labs like yours. We bring you products which balance outstanding performance, superb features, high-quality design, excellent ergonomics and moderate cost.

<http://www.moglabs.com/>



Lange Electronic GmbH, founded in 1977, develops, manufactures and distributes high precision time & frequency systems worldwide.

Besides this we represent the Positioning Technology branch of Spirent Communications Plc. in the field of GNSS simulation, Masterclock (precision timing and network synchronisation solutions) and Oktal-SE, a leading mathematical company doing 3D simulation via ray-tracing and several other methods in the areas of RF and radar simulation.

Our products are used in aerospace and on board of ships, in scientific experiments, in time laboratories and testing facilities e. g. the Aviation Gate in Braunschweig as well as in banks and insurance companies. The products on display are found in research and science as well as in development and testing of GNSS receivers/systems. <http://www.lange-electronic.de/>



Microsemi

Power Matters.™

Microsemi, the world leader in precise time solutions, sets the world's standard for time by offering solutions to generate, distribute and apply precise time for communications, aerospace/defence, IT infrastructure and metrology industries. Customers use Microsemi's advanced timing algorithms, atomic clocks and frequency reference technologies to build more reliable and highly efficient networks. <http://www.microsemi.com/>



Excitement is not measureable. Light is.

Menlo Systems, a leading developer and global supplier of instrumentation for high-precision metrology, was founded in 2001 as a spin-off of the Max Planck Institute for Quantum Optics, with the foremost aim to commercialize optical measurement technologies and make it available to newly emerging application fields. Menlo Systems maintains a strong bond to co-founder Theodor W. Hänsch, who pioneered precision laser techniques.

Known for the Nobel Prize-winning optical frequency comb technology, the Munich-based company offers complete solutions based on ultrafast lasers and synchronization electronics. Applications for our products and solutions span from research laboratories to truly industrial tasks. The patented technology is recognized by global laser manufacturers to whom we deliver OEM solutions for integration into cutting-edge products. <http://www.menlosystems.com/>



Muquans is a young company who project consists in developing a new generation of high precision instruments based on laser trapping/cooling/manipulation of cold atoms.

Muquans is working on the development of the following products:

- An absolute quantum gravimeter capable of measuring gravity with a relative accuracy of 10^{-9} , dedicated to various applications in geophysics.
- An atomic clock, which provides time reference signal offering relative stability and accuracy close to 10^{-15} and dedicated to time metrology applications.
- Integrated laser systems dedicated to trapping/cooling/manipulation of Rubidium atoms.

Muquans is a spin-off from two academic laboratories (LP2N and SYRTE) specialised in high precision measurements based on quantum manipulation of cold atoms. The technology developed by Muquans therefore benefits from all the experience and know how resulting from more than 15 years of academic research. <http://www.muquans.com/Stand12>



For over seventy years, SAES Group has been the leading supplier of UHV and XHV solutions based on the Non-Evaporative Getter (NEG) technology for a variety of industrial and research applications. These solutions include compact NEG pumps with a large pumping speed for active atmospheric gases and, in particular, hydrogen, without generating vibrations or magnetic fields. In 2011, SAES Group introduced the PATENTED NEXTor[®] pump, a revolutionary product that combines the NEG and sputtering ion pump technologies on one single flange. These pumps are widely used in a variety of UHV and XHV systems, particularly in the Atom Trap segment and in atomic clocks. <http://www.saesgroup.com/>



TOPTICA is the world leader in diode laser and ultrafast technology for industrial and scientific markets. We offer the widest range of single mode tunable light in the 190 to 2900 nm and 0.1 to 2.7 THz spectral region with various accessories to measure, characterize, stabilize and analyze light. We recently extended this portfolio by introducing a frequency comb based on difference frequency generation.

A key point of the company philosophy is the close cooperation between development and research to meet our customers' demanding requirements for sophisticated customized system solutions and their subsequent commercialization.

TOPTICA is an active partner in clock-related projects: SOC2 - Space Optical Clocks, QTea - Quantum Technology Sensors and Applications and nuClock - Nuclear Clock with Thorium.

With our Passion for Precision, TOPTICA delivers!

<http://www.toptica.com/>



Stable Laser Systems is the premier provider of laser frequency stabilization hardware, systems, and accessories. Our expertise is the production and dissemination of Hz-level linewidths and low frequency drift. Our mounting and temperature control of high-finesse Fabry-Perot cavities provides high-performance, off-the-shelf solutions that can save hundreds of hours in the design and setup of narrow frequency and low-drift laser systems. Drawing on decades of combined expertise and research in laser frequency stabilization, we can assist you in choosing and characterizing the right cavity, provide you with an optimized mount and vacuum housing (including customized temperature controllers), as well as fiber-to-cavity coupling optics and associated electronics and services.

Our close partnership with Advanced Thin Films allows us to design matched housings for their world-class cavities. We also offer turnkey frequency stabilized laser systems based on high quality lasers, both at standard wavelengths and customized to your application. Our complete systems reliably deliver exceptional performance without compromising ease of use. Whether you need 1 Hz linewidth in the laboratory, or 1 kHz in the field, we can help you get there (and stay there) quickly. <http://www.stablelasers.com/>



TimeTech GmbH was set up in 1990 as a spin off from the University of Stuttgart's Institute for Navigation. The team here specialises in intercontinental time transfer and very precise satellite positioning services.

TimeTech is a reliable provider of high-tech space systems and ground stations equipment and instruments for precise frequency and time transfer. TimeTech is mainly export-oriented with customers in Europe, North America, Asia and Australia. TimeTech's business areas are subdivided into project Business and Products. Since November 2012, TimeTech has embarked upon providing systematic and regular two-way link calibration service to our customers primarily the national metrological laboratories.

Project business encompasses scientific studies as well as hardware projects, related to Galileo, Aces, Rosetta, Venus Express and other space projects and ground stations. The Product Business takes care of development, production, testing and installing equipment and complex systems for orbit determination and positioning as well as high precision synchronization and transmission of time and frequency. <http://www.timetech.de/>



Piktime Systems – satellite techniques and precise time sector company, established in 2007.

We concentrate on development and manufacturing equipment for precise, long-distance atomic clocks comparison.

We are a worldwide leader in our field.

What we do:

- Designing and manufacturing equipment for a precise atomic clocks comparison (time transfer systems),
- Development of time based products and services (navigation, security, data and document exchange, time stamping),
- Advisory on precise time and time scales,
- Time & frequency software and algorithms,
- Time & frequency counters and generators,
- Designing and execution of time laboratories on a turn-key basis.

<http://www.piktime.com/>



Founded in 2006 in Neuchatel, Switzerland, T4Science is a leading designer and manufacturer of a full range of advanced, cost-effective and high-performance maser clock solutions. Its products are used in a wide variety of scientific applications and in the time and frequency industry.

Products

The iMaser™ is a high-performance, compact Active Hydrogen MASER. It features advanced phase noise and short term stability for high-precision Frequency & timing applications like VLBI, Deep space tracking, National Timing/Frequency Station, Navigation ...

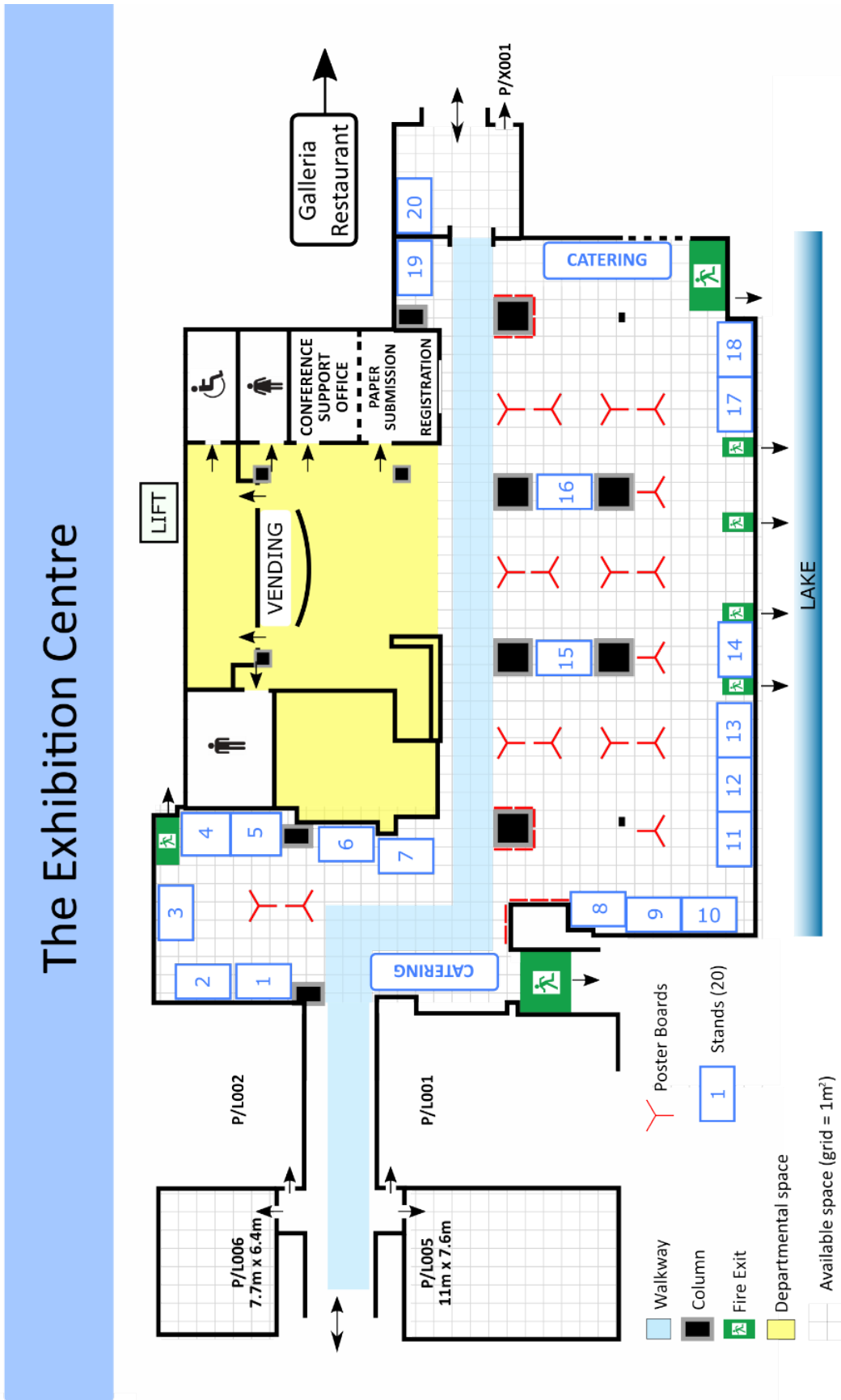
Passive Hydrogen Maser offers long term reference with excellent stability and price.

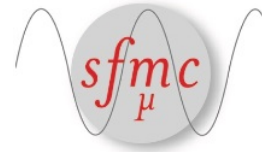
Services

We offer a complete set of first-class services over the product lifecycle for total customer satisfaction. These services include: Supply & Installation, Training, Remote & On-Site Maintenance and On-Site Support.

<http://www.t4science.com/>

Exhibition Centre Map





2017 Joint Conference of the European Frequency and Time Forum & IEEE International Frequency Control Symposium

July 9–13, 2017

Micropolis, Besançon, France

EFTF and IFCS are pleased to announce that the next joint conference of their long-established cooperation will take place at Micropolis, Besançon, the city that hosted the first European Frequency and Time Forum in 1987 and the first joint conference EFTF-IFCS in 1999. Micropolis Convention Center is now connected to Besançon historic downtown by a direct line of modern tramway and offers all equipment and amenities to host the plenary and parallel sessions of this new exciting event.

Lute Maleki and Bernard Dulmet will be the General Co-Chairs of the 2017 Joint Conference. Elizabeth Donley and Jérôme Delporte will be the Technical Program Co-Chairs. The Joint Program Committee will gather valued scientists from EFTF and IFCS Scientific Committee. The topics of the Conference will cover the following areas:

Group 1: Materials, Filters, and Resonators

Group 2: Oscillators, Synthesizers, Noise, and Circuit Techniques

Group 3: Microwave Frequency Standards

Group 4: Sensors and Transducers,

Group 5: Timekeeping, Time and Frequency Transfer, GNSS and Applications

Group 6: Optical Frequency Standards.

We expect the Conference Website eftf-ifcs2017.org to be on line by July 2016, with the first Call for papers to be issued by November 2016. Please consider submitting your abstracts by February 2017.

All members of Local Organizing Committee, brought together under the banner of The Société Française des Microtechniques et de Chronométrie, are eager to welcome you to renew the success of the two previous EFTF-IFCS Joint Meetings held in our city.

Characterization of the frequency transfer over 300 km of aerial suspended fiber

Śliwczyński Ł., Krehlik P.

Department of Electronics
AGH University of Science and Technology
Krakow, Poland
sliwczyn@agh.edu.pl

Turza K., Binczewski A.

Poznań Supercomputing and Networking Center
Poznań, Poland
kturza@man.poznan.pl

Abstract—In this paper we are reporting on the experiments with a 300-km-long suspended fiber running inside the safety wire of the power grid and being a part of large optical wavelength division multiplexing telecom network. We used this fiber to carry the 10 MHz frequency signal and investigated the influence of heavy environmental conditions on the stability of the transfer. We were able to find the evidence that the transmission in the aerial fiber is affected, apart from rapidly varying external temperature, by the wind and by the 50 Hz pickup from the power grid. However, the general result of our investigations is that the true stability-limiting factor is not the fiber and various environmental conditions, but the time-dependent asymmetry of the telecom equipment, like e.g. reconfigurable optical add-drop multiplexers.

Keywords—frequency transfer; fiber optics; delay stabilization; fiber network; optical transport network; wavelength division multiplexing

I. INTRODUCTION

Optical fibers allow obtaining very good stability parameters when used to transfer frequency and time signals over large distances. Among the factors that limit the ultimate performance of the transfer system, the phase noise introduced by an optical fiber is a key one. Published results of evaluation of various in-the-field installations were usually performed with underground [1] or submarine [2] fibers. Such fibers are well isolated from any rapid changes of temperature and from other environmental factors. However, when migrating from various experimental setups to more service-oriented time/frequency distribution links it may be necessary to exploit not only the most favorable dark, underground fibers, but aerial suspended fiber cables and dense wavelength division multiplexing (DWDM) infrastructure as well. It is thus essential to know what is the impact of such alternative transmission media on the stability of the fiber optic frequency transfer and to learn the character and behavior of related fluctuations of the propagation delay occurring in the fiber. The results presented herein are the continuation of our previous works aimed at characterizing the frequency transfer in optical DWDM networks [3].

II. METHODOLOGY AND MEASUREMENT SETUP

The aerial suspended fiber that was the object of our

This work was supported in parts by Polish National Science Centre under decision DEC-2014/15/B/ST7/00471 and by the Faculty of Computer Science, Electronics and Telecommunications, AGH University of Science and Technology.

measurements was a part of the longer fiber path forming a loop with the total length of about 1012 km, whereas the length of the suspended fiber was equal to about 300 km. Entire loop used a telecom infrastructure of Polish optical internet network PIONIER, operated by Poznań Supercomputing and Networking Center (PSNC). We also used a second fiber route of similar length that used only underground fibers. The purpose of using this second route was to have a reference, because accessing only the aerial fiber was technically impossible. By comparing the signals from both routes we were able to differentiate between the fluctuations of the propagation delay resulting from the aerial fiber and the background noise of telecom equipment and underground

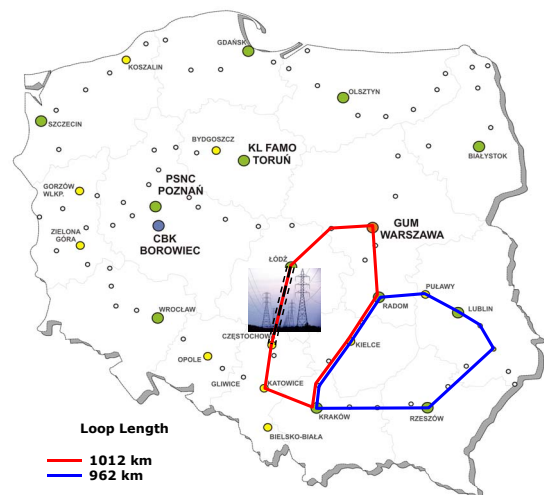


Fig. 1. A map showing the fiber optic routes investigated during the experiments.

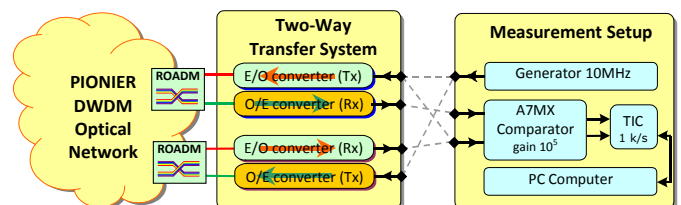


Fig. 2. A block diagram showing used measurement setup.

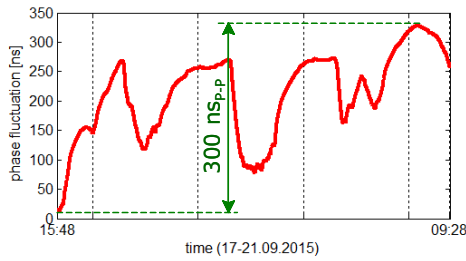


Fig. 3. One-way fluctuations of the propagation delay measured in the fiber link including 300 km of aerial fiber.

fibers. The map showing tested optical routes is presented in Fig. 1 – the red curve follows the route including the aerial fiber and the blue one shows the path of the reference link.

The block diagram showing the measurement setup is presented in Fig. 2. The 10 MHz signal from the oven controlled crystal oscillator (OCXO), after transmission through the optical fiber, was supplied to the A7MX (Quartzlock) frequency comparator, working as a multiplier of the phase noise. The gain of this setup was high enough (10^5) allowing to use an ordinary time interval counter (TIC) to

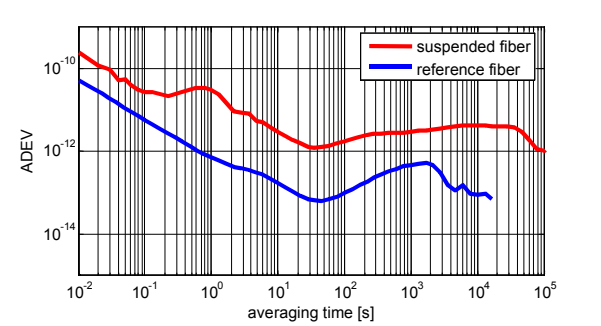


Fig. 4. ADEV for one-way transmission in the suspended and reference links.

sample and record the phase fluctuations for further analysis.

We set up a number of measurement sessions, lasting from about 10 hours to a few days and tested the transmission of the 10 MHz signal through the fiber in one direction, through the pair of the fibers running in opposite directions (differential transmission) and through the pair of the fibers running in the same directions.

III. MEASUREMENT RESULTS

The plot showing the fluctuations of the propagation delay measured in a one-way configuration is shown in Fig. 3. It may be observed that the aerial suspended fiber is very sensitive to the changes of external conditions (mostly temperature), resulting in large diurnal amplitude of the fluctuations, reaching 200 ns. Fluctuations observed in a shorter term are also very high, being around 80 ns/h and 2 ns/min.

Hugh influence of external conditions on the transmission in the aerial fiber results in relatively poor frequency stability – see a red curve in Fig. 4. The corresponding Allan deviation (ADEV) levels around 10^{-12} for averaging times greater than

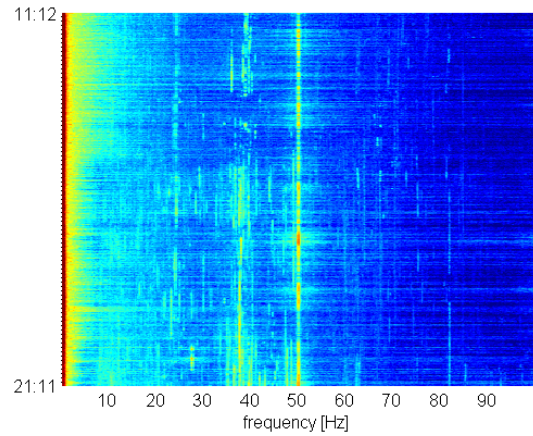


Fig. 5. Short-term spectra of the fluctuations of the propagation delay for one-way transfer in aerial fiber.

about 10 s. However, the measurements performed in the reference link also show relatively poor ADEV, typically not exceeding $2\text{-}3 \cdot 10^{-13}$ for averaging times greater than a dozen of seconds.

Apart from these relatively large effects we were also able to identify a more subtle, fine details, like e.g. the pickup from the 50 Hz frequency signal distributed through power grid and fiber swinging by the wind. These effects may be identified in the map showing the short-term spectra of fluctuations, shown in Fig. 5 as a clearly visible spectral line at 50 Hz and as a component located in a sub-hertz range close to about 0.6 Hz.

To determine the influence of the fluctuations of the propagation delay on the stability of the frequency transfer in a two-way structure we performed a series of measurements

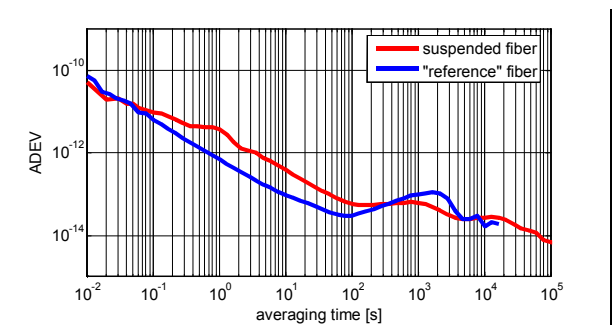


Fig. 6. ADEV calculated for differential transmission.

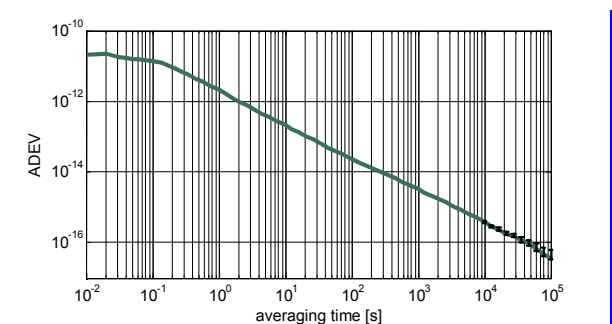


Fig. 7. Predicted stability of the frequency transfer in the link with removed asymmetry of telecom networking equipment.

using two parallel fibers running in the same cable and transmitting signals in opposite directions. Resulting ADEV curves are shown in Fig. 6. In such configuration it is possible to reach a level close to 10^{-14} , however there is no substantial difference between the link including the aerial fiber and the reference one. This suggests that the stability of the transfer is not limited by the fluctuations in the fiber (that may be expected to be closely matched between the fibers running in the same fiber cable) but by the time-dependent asymmetry of the networking equipment (like reconfigurable optical add-drop multiplexers – ROADMs) that are used to route the optical signals in the DWDM network.

To check this hypothesis we set up the link, where the signals were transmitted in parallel fibers in the same direction – although this configuration is an artificial one, it allowed us to create the conditions where both signals were affected in the same way by the fluctuations of the phase occurring in the fibers as well as in the networking equipment. We stabilized the propagation delay in this link using ELSTAB system [4]. The results are presented in Fig. 7 and suggest that our initial hypothesis is true – by reducing the asymmetry of the link we were able to reach the stability that is close to the noise floor of the ELSTAB system.

IV. CONCLUSION

The stability of the frequency transfer that may be obtained in modern optical DWDM networks using a pair of the fibers

transmitting the signals in opposite directions seems to be fundamentally limited by the time-varying asymmetry of networking equipment to the levels around a few times 10^{-14} for long averaging times. Nevertheless, obtained stability is adequate for exploiting such optical DWDM networks to distribute the frequency signals from commercial caesium clocks (like e.g. 5071A) in cases where no dark fiber is available.

REFERENCES

- [1] O. Lopez, A. Kanj, P.E. Pottie, D. Rovera, J. Achkar, C. Chardonnet, A. Amy-Klein, G. Santarelli, "Simultaneous remote transfer of accurate timing and optical frequency over a public fiber network," *Appl. Phys.*, vol. 110, pp. 3–6, 2012.
- [2] M. Amemiya, M. Imae, Y. Fujii, T. Suzuyama, S. Ohshima, "Simple time and frequency dissemination method using optical fiber network," *IEEE Trans. Instr. Meas.*, vol. 57, pp. 878-883, 2008.
- [3] Ł. Śliwczyński, P. Krehlik, M. Lipiński, K. Turza, A. Binczewski, "Frequency distribution in delay-stabilized optical DWDM network over the distance of 3000 km," *Proceedings of Joint IEEE International Frequency Control Symposium & the European Frequency and Time Forum*, pp. 761–764, Denver, Colorado, 2015.
- [4] P. Krehlik, Ł. Śliwczyński, Ł. Buczek, J. Kołodziej, M. Lipiński, "ELSTAB - fiber optic time and frequency distribution technology - a general characterization and fundamental limits," *IEEE Trans. Ultrason., Ferroelect., Freq. Control*, DOI 10.1109/TUFFC.2015.2502547.

Real-time performance monitoring of fiber optic long-distance time and RF frequency transfer links

Śliwczynski Łukasz, Krehlik Przemysław, Salwik Karol

Department of Electronics
AGH University of Science and Technology
Krakow, Poland
Email: sliwczyn@agh.edu.pl

Abstract— In a long-distance fiber optic time and frequency distribution link, operating bi-directionally over a single fiber, gains of the optical amplifiers must be judiciously chosen to minimize various undesirable effects resulting from backscattered signals and other sources of noise. In this paper we propose to monitor the performance of the link continuously during its operation and to use these information for a real-time optimization of the parameters of transferred time and frequency signals. The design of the subsystem intended to measure the jitter of the frequency signal is discussed together with the evaluation results.

Keywords— time and frequency transfer; fiber optics; bidirectional optical amplifier, jitter measurement

I. INTRODUCTION

Long-distance fiber optic time and RF frequency distribution links require using optical amplifiers to compensate the loss of optical fibers. The best performance concerning the stability of transmitted signals is assured in fully symmetric approach that calls for a dark fiber and bi-directional amplification scheme. In such a link the gains of the optical amplifiers must be judiciously chosen to minimize undesirable effects resulting from backscattered signals and other sources of noise, like e.g. amplified spontaneous emission of optical amplifiers, laser phase noise into intensity noise conversion via fiber chromatic dispersion, stimulated Brillouin scattering (SBS) etc. All these phenomena result in a non-additive broadband noise (extending to a few GHz), that converts into a jitter degrading the performance of the system. Excessive noise may also cause total system malfunction by triggering false signal pulses. In principle the optimal gains of the amplifiers, that minimizes unwanted effects, may be deduced using the model of the link [1]. This approach, however, requires substantial amount of data that are very difficult to obtain (see e.g. [2]).

II. THE IDEA OF REAL-TIME PERFORMANCE MONITORING AND OPTIMIZATION

The idea proposed herein is to perform the optimization of the gains of the bidirectional optical amplifiers in a real-time in order to maximize the signal to noise ratio (SNR) at both ends of the link. A key component to implement such an idea is a

performance monitor allowing to estimate the SNR. A direct measurement of the SNR is difficult, however measuring the jitter of frequency signal may be used to obtain equivalent information, useful for performing optimization. Under optimal settings of the gains of the optical amplifiers the jitter will shows its minimum that corresponds to the maximum value of the SNR.

The general scheme of the proposed solution is shown in Fig. 1. The jitter measurement circuits are added at both sides of the link, and the amplifiers gains are controlled accordingly to the actual jitter values. According to our investigations using computer models of the bidirectional fiber optic link and algorithms for global optimum searching the gains optimization seems to be a unimodal problem, that may be relatively easy solved even for a large number of amplifiers. Thanks to the remote supervision and management facilities incorporated in both the local and remote modules, and also in

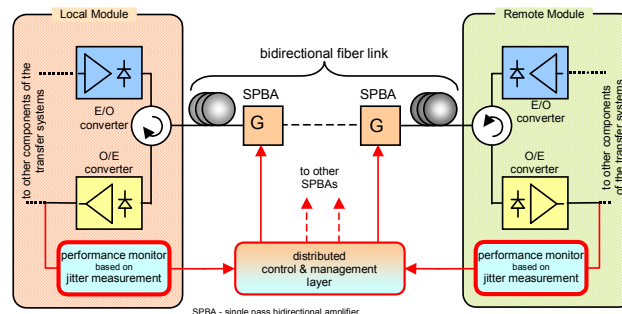


Fig. 1. General scheme of the proposed solution for real-time monitoring and optimization.

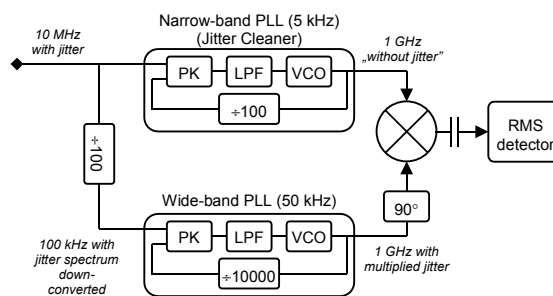


Fig. 2. Jitter measurement circuit.

This work was supported by Polish National Science Center under the decision DEC-2014/15/B/ST7/00471.

optical amplifiers, the performance optimization would be carried out on-line in a real-time.

III. JITTER MEASUREMENT CIRCUIT

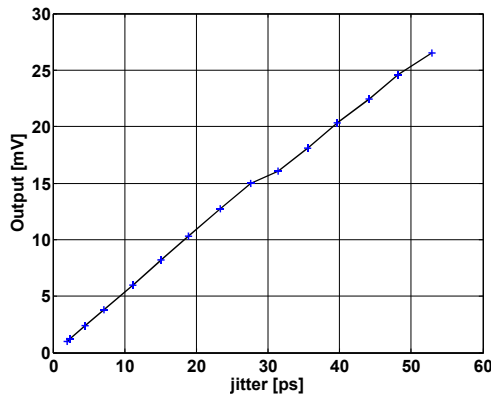


Fig. 3. Transfer characteristic of the jitter measurement circuit.

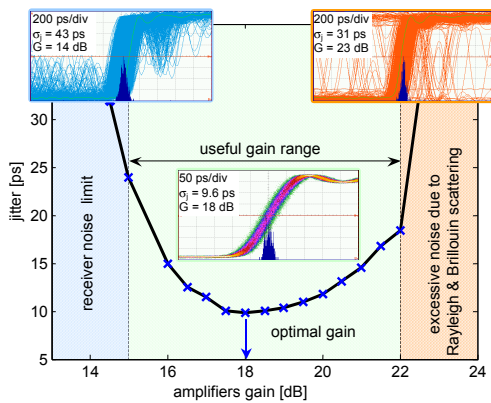


Fig. 4. Jitter optimization example. (Description in the text.)

Fig. 2 presents the jitter measurement circuit proposed and examined herein. The jitter-corrupted signal is processed in parallel by two phase locked loops (PLLs). The tracking bandwidth of the first one is small (about 5 kHz), thus the large amount of the wideband jitter is removed. In opposite to the first loop, the second PLL is intended to track the jitter in its full bandwidth. The output frequency of PLLs is multiplied up to 1 GHz, and the two signals are provided to a phase comparator (mixer), which convert the relative phase noise into a baseband signal with the magnitude proportional to the jitter. As there is difficult to build a PLL with a large enough tracking bandwidth, the input signal frequency is divided prior entering

the second PLL. Thanks to this the jitter bandwidth is down-converted, but its magnitude (in time units) is unaffected.

The initial evaluation of the practically constructed jitter measurement circuit is presented in Fig. 3. Good measurement linearity was observed in a range from 2 ps (a noise floor of the developed circuit) up to 50 ps. Such a range is adequate to accurately measure the jitter in practical installations of fiber optic T&F transfer systems, where the jitter in the range of 4-10 ps may be expected under optimal gain settings.

IV. EXAMPLE OF A LINK PERFORMANCE OPTIMIZATION

In the next stage of the evaluation the developed jitter measurement circuits were installed in a T&F distribution system. The arranged optical path consisted with three 100 km-long fiber spans with two bidirectional optical amplifiers in between. Fig. 4 presents the jitter (measured with the developed circuit) versus amplifiers gain (equal for both units). Additionally, the jitter was measured with high-speed digital oscilloscope, and the results agree within 10% tolerance.

The insets in the figure show minimum jitter for optimal gain (middle), and excessive noise conditions (upper left and right). One may notice that a few decibels deviation from an optimum gain results in a drastic degradation of the frequency signal quality, or even system malfunctioning (multiple transitions in upper right inset).

V. CONCLUSION

The developed jitter measurement circuit allows performance monitoring and on-line optimization of the bidirectional fiber optic link for T&F distribution. In contrast to a simulation-based approach, the direct jitter measurement reflects the actual situation in a particular optical path and does not suffers from inaccurate or incomplete knowledge about various link parameters. In addition, some problems very difficult for being simulated accurately, as e.g. SBS or phase noise to intensity noise conversion, are in a natural way taken into account in proposed approach. This paves the way to automated maintenance of long-distance T&F distributing networks.

REFERENCES

- [1] Ł. Śliwczynski, J. Kołodziej, "Bidirectional optical amplification in long-distance two-way fiber-optic time and frequency transfer systems," *IEEE Trans. Instr. Meas.*, vol. 62, pp. 253–262, 2012.
- [2] P. Krehlik, Ł. Śliwczynski, "Precise method of estimation of semiconductor laser phase-noise-to-intensity-noise conversion in dispersive fiber," *Measurement*, vol. 65, pp 54–60, 2015

Research on the Zoom Technique of GNSS Timing Signal Granularity

Wu Jianfeng^{1,2,3}, Hu Yonghui^{1,2,3}, Lv Hongchun^{1,2,3,4}, He Zaimin^{1,2,3}
Yan wenhe^{1,2,3} Yan Lulu^{1,3}

1.National Time Service Center, CAS, Xi'an 710600,China

2.Key Laboratory of Precision Navigation and Timing Technology, National Time Service Center, CAS, Xi'an 710600,China

3.Key Laboratory of Time and Frequency Primary Standards, National Time Service Center, CAS, Xi'an 710600,China

4.University of Chinese Academy of Sciences, Beijing 100039,China

Abstract—1PPS signal is the standard output of GNSS timing receiver. The pulse is used to synchronize the device to Universal Time Coordinated(UTC) or the GNSS system time, and it is the recovery of GNSS system time or UTC in the local timing receiver. 1PPS signal of GNSS timing receiver is often phase calibrated in discrete steps with an uncorrected frequency error present. If such a calibration was used in GNSS timing receiver, we would observe the 1PPS signal phase error progressing at the uncorrected frequency error. When the phase error grows to the phase step size, a calibration will be done and we will observe a phase step in the 1PPS signal phase. This phase step is GNSS Timing signal granularity. This phenomenon is called the sawtooth behavior of the GNSS 1PPS signal. In order to correct the sawtooth error of 1PPS signal, we study the zoom technique of GNSS timing signal granularity, and propose an improved scheme. The programmable delay line technology is introduced in the improved scheme. The granularity of the programmable delay line device can reach 0.25ns. Combining with the programmable delay line device, we propose a control algorithm which can realize the zoom of local 1PPS signal's granularity. This scheme allows for real-time correction of the quantization error and reduces the residual noise to about 1~2 nanoseconds peak to peak (pk-pk), and improves the instantaneous and short-term timing accuracy of GNSS 1PPS.

Keywords—1PPS, timing, granularity

I. THE PRINCIPLE OF THE PULSE GENERATING

1PPS signal is the standard output of GNSS timing receiver. 1PPS means one pulse per second. The pulse is used to synchronize the device to Universal Time Coordinated (UTC) or the GNSS system time, and it is the recovery of GNSS system time or UTC in the local timing receiver. In a typical design, 1PPS signal is locked with the recovery signal of GNSS 1PPS. The principle of the pulse generating based on the numeric controlled oscillator (NCO) is shown in Figure 1^[1].

As shown in Figure 1, 1PPS signal is generated by the local NCO's divided frequency. The counter is used to measure the time difference between NCO 1PPS signal and GNSS 1PPS recovery signal. The microprocessor receives the time difference data, and generates the NCO frequency control word and the NCO phase control word. According to the NCO frequency control word or the NCO phase control word, the output of NCO is tuned. The real-time 1PPS phase calibrations

are realized, and its errors with respect to GNSS system time are reduced.

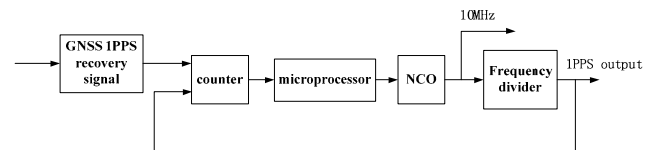


Figure 1. The principle diagram of GNSS 1PPS generating

II. THE SAWTOOTH BEHAVIOR

GNSS timing receiver gets the time phase difference between the 1PPS of local receiver and that of GNSS system time. The phase offset's adjustment often be realized as below^[2].

To calibrate 1PPS phase, we can increase or decrease the value of frequency divider's division factor. In other words, if local 1PPS signal is ahead of GNSS 1PPS signal, we will increase the value of frequency divider's division factor of local 1PPS. When the time calibration occurs, this cycle length (Δt_{local}) of local 1PPS signal will be longer than the cycle length of GNSS 1PPS signal (Δt_{GNSS}). If local 1PPS signal is behind of GNSS 1PPS signal, we will decrease the value of frequency divider's division factor of local 1PPS signal. When the time calibration occurs, this cycle length (Δt_{local}) of local 1PPS signal will be less than the cycle length of GNSS 1PPS signal (Δt_{GNSS}). It is shown in Figure 2.

More typically, this type of calibration is only applied to the 1 PPS signal phase while the frequency error is left uncorrected. 1PPS signal of GNSS timing receiver is often phase calibrated in discrete steps with an uncorrected frequency error present. If such a calibration is used in GNSS timing receiver, we will observe the 1PPS signal phase error progressing at the uncorrected frequency error. When the phase error grows to the phase step size, a calibration will be done and we will observe a phase step in the 1PPS signal phase. This phase step is GNSS Timing signal granularity. This phenomenon is called the sawtooth behavior of the GNSS 1PPS signal^[3,4].

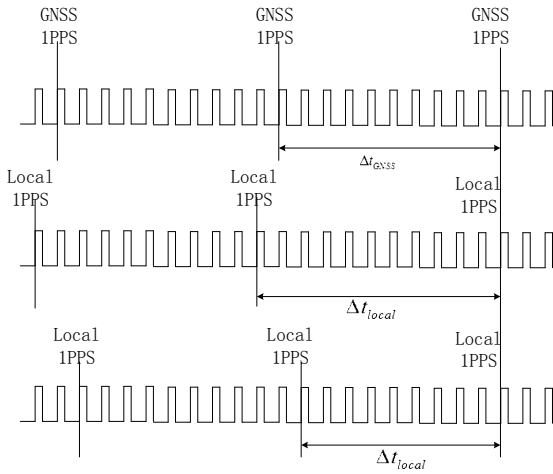


Figure 2. Calibration of Local 1PPS phase

Assuming the local crystal oscillator's frequency is f Hz, the cycle is $1/f$ second. The 1PPS signal granularity is $1/f$ second. As known from the previous principle, we can only do the $1/f$ seconds' integral cycles adjustments step by step. This phase step-by-step granularity will effect on 1PPS signal, and produce sawtooth phenomenon. The sawtooth amplitudes can reach $1/2f$ second. The receiver clock's frequency is often less than 100MHz. The sawtooth error is Gaussian, a long term average of the pulse output is not biased by the sawtooth error. But it will affect the instantaneous and short-term timing accuracy. Figure 3 is a small section of the data showing the sawtooth behavior of the raw timing receiver's 1PPS signal. The raw 1PPS shows the expected noise dominated by the quantization of the samples is nearly the cycles of the frequency twice of 9.54MHz, thus $1/(2 \times 9.54\text{MHz})$, equally 52ns.

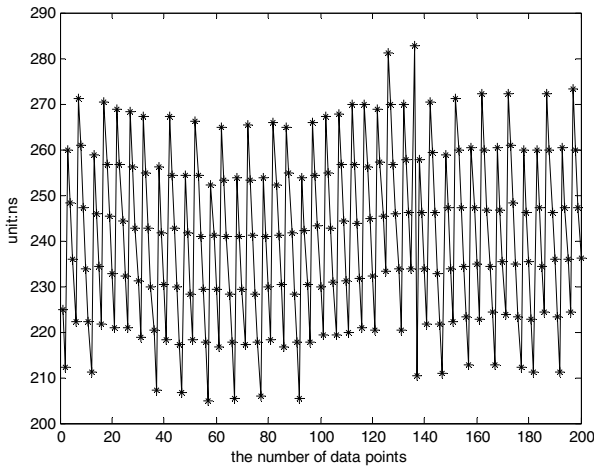


Figure 3. The sawtooth behavior of GNSS 1PPS

III. THE ZOOM TECHNIQUE

In order to correct the influence of the sawtooth error on synchronizing accuracy to UTC, a programmable delay line technique is introduced^[5,6].

As is shown in Figure 4, the receiver gets the difference between the local 1PPS signal and GNSS 1PPS signal before the arrival of the next second pulse. This difference is divided into two parts named by T1 and T2. T1 will be used to control GNSS receiver, and the local 1PPS signal will be ahead by T1 cycles of the receiver. T2 will be send to the microprocessor through the serial port, and T2 is within one clock cycle. The microprocessor achieves fine adjustment by the programmable delay line.

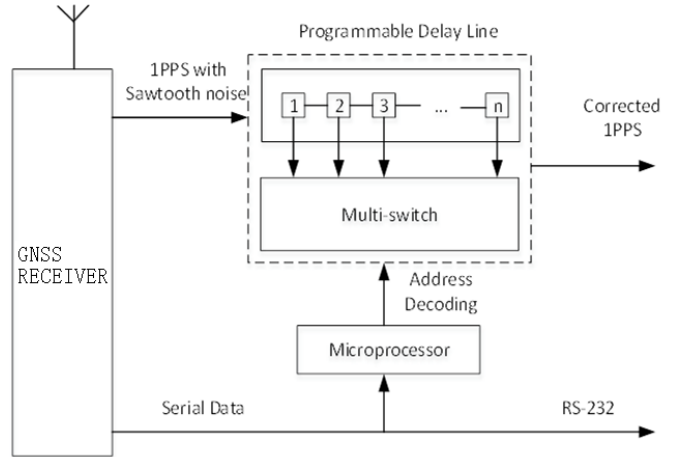


Figure 4. Block diagram of sawtooth error calibration by programmable delay line technique

The adjustment precision is determined by the minimum step of the programmable delay line. For example, Maxim's delay device DS11231-25 is an 8-bit programmable delay line, and can reach the 0.25ns delay step.

(1). Processing Mode of The Traditional Timing Receiver 1PPS Signal

The local clock frequency is assumed to be f MHz, then the half cycle is Amp , $\text{Amp} = 1/(2 \times f)$.

1) The receiver local 1PPS signal is ahead of GNSS 1PPS signal by $dT1$ (positive value), there are three kinds of situations:

Situation 1: If $(dT1 < \text{Amp})$, there will be no adjustment. The local 1PPS signal is still ahead of GNSS system by $dT1$, as is shown in Fig5.

Situation 2: If $(\text{Amp} \leq dT1 < 2 \times \text{Amp})$, the local 1PPS will lag 1 cycle for adjustment. After that, the local 1PPS signal will be behind of GNSS 1PPS signal by $(dT2 = 2 \times \text{Amp} - dT1)$, as is shown in Fig6.

Situation 3: If $(dT1 \geq 2 \times \text{Amp})$, we'll adjust in two steps: Firstly, the local 1PPS will be adjusted to lag $\text{fix}(dT1/(2 \times \text{Amp}))$ cycles, the residuals will be obtained by $\text{mod}(dT1, 2 \times \text{Amp})$. And then, according to the value of $\text{mod}(dT1, 2 \times \text{Amp})$ it can decide whether to return to the previous two situations. Where, $\text{mod}(x, y)$ is modulus after division, and $\text{fix}(X)$ rounds the elements of X to the nearest integers towards zero.

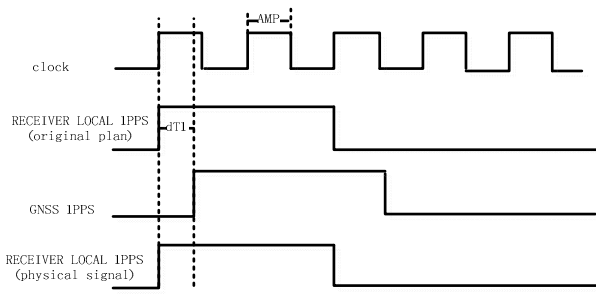


Figure 5. Advance Situation 1 of the traditional

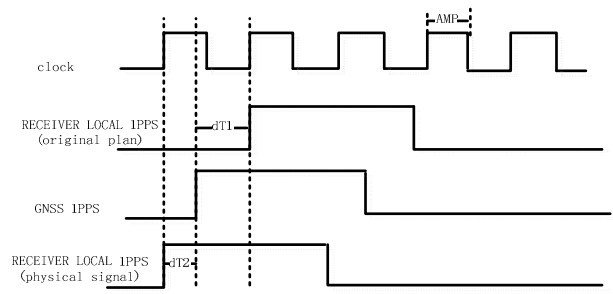


Figure 8. Lag Situation 2 of the traditional

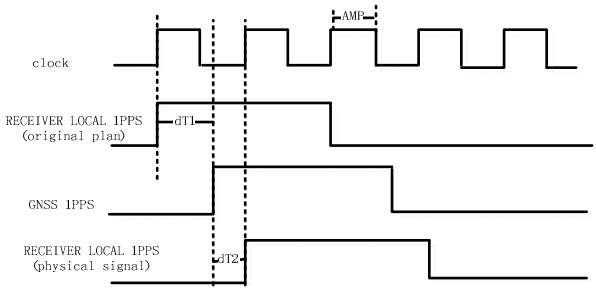


Figure 6. Advance Situation 2 of the traditional

2) The lag between the receiver local 1PPS signal and the GNSS 1PPS signal is about $dT1$ (negative value), in three situations:

Situation 1: If $(dT1 < \text{Amp})$, there will be no adjustment. The local 1PPS signal is still behind of GNSS system by $dT1$, as is shown in Fig7.

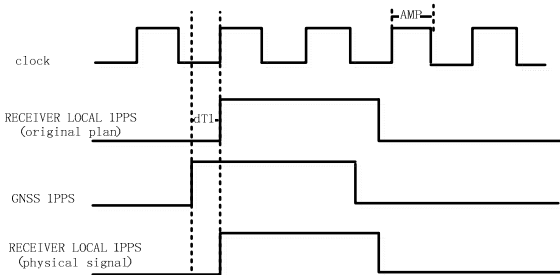


Figure 7. Lag Situation 1 of the traditional

Situation 2: If $(\text{Amp} \leq dT1 < 2 \times \text{Amp})$, the local 1PPS will advance 1 cycle for adjustment. After that, the local 1PPS signal will be ahead of GNSS 1PPS signal by $(dT2 = 2 \times \text{Amp} - dT1)$. It is shown in Fig8.

Situation 3: If $(dT1 \geq 2 \times \text{Amp})$, we'll adjust in two steps: First, the local 1PPS will be adjusted to advance $\text{fix}(dT1 / (2 \times \text{Amp}))$ cycles, the residuals are to obtained by $\text{mod}(dT1, 2 \times \text{Amp})$. And then, according to the value of $\text{mod}(dT1, 2 \times \text{Amp})$ it can decide whether to return to the previous two situations.

(2). Processing Mode of The Zoom Granularity

1) The local 1PPS signal is ahead of GNSS system time by $dT1$ (positive value), there are two kinds of situations:

Situation 1: If $0 < dT1 < 2 \times \text{Amp}$, the local 1PPS will not be adjusted. $T2$ is equal to $dT1$, and will be sent directly to the microprocessor. The delay line will be controlled by microprocessor to complete the time delay. After the adjustment, the residual is determined by the granularity of delay line and the time difference calculation precision; As is shown in Figure 9.

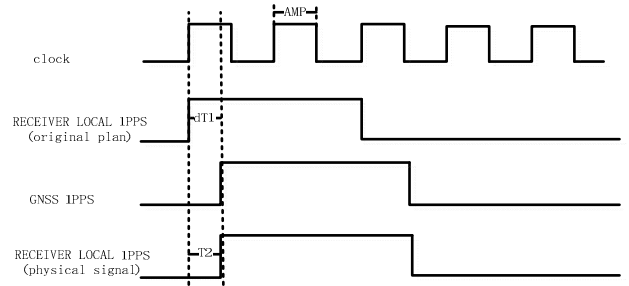


Figure 9. Advance Situation 1 of the Zoom granularity

Situation 2: If $dT1 \geq 2 \times \text{Amp}$, $T1$ is equal to $\text{fix}(dT1 / (2 \times \text{Amp}))$, and $T2$ is equal to $\text{mod}(dT1, 2 \times \text{Amp})$. We'll adjust in two steps. First, the local 1PPS will be adjusted to lag $T1$ clock cycles; The delay line will be controlled by microprocessor to complete the time delay of $T2$, as is shown in Figure 10.

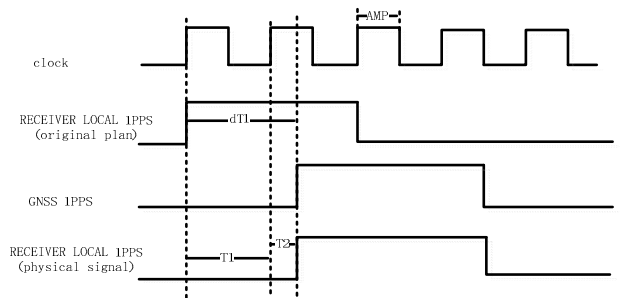


Figure 10. Advance Situation 2 of the Zoom granularity

2) The local 1PPS signal is behind of the GNSS system time by $dT1$ (positive value), in two cases:

Situation 1: If $0 < dT1 < 2 \times \text{Amp}$:
 $T1 = 1$ (clock cycle)
 $T2 = (2 \times \text{Amp} - dT1)$.

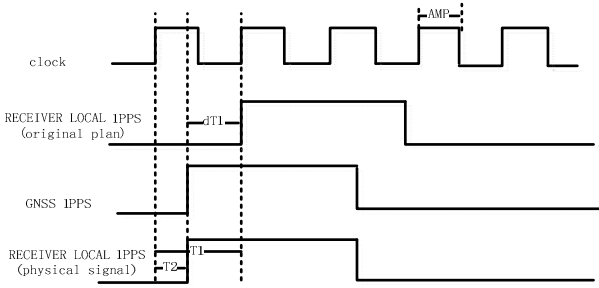


Figure 11. Lag Situation 1 of the Zoom granularity

Situation 2: If $dT1 \geq 2 \times \text{Amp}$:
 $T1 = \text{fix}(dT1 / (2 \times \text{Amp})) + 1$ (clock cycles)
 $T2 = (2 \times \text{Amp} - \text{mod}(dT1, 2 \times \text{Amp}))$.

Where, $\text{mod}(x, y)$ is modulus after division, and $\text{fix}(X)$ rounds the elements of X to the nearest integers towards zero.

IV. SIMULATION AND VERIFICATION

We accomplished the error calibration by both processing modes of traditional and the zoom granularity. As is shown in Figure 12, a small section of the data shows the sawtooth behavior of the raw timing receiver's 1PPS signal. The raw 1PPS shows the expected noise dominated by the quantization of the section reaching to about pk-pk 52ns. The pk-pk value of the high precision zoom granularity's output error is 1.57ns, and the Standard deviation is 0.25ns.

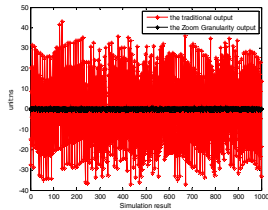


Figure 12. Errors of traditional and zoom granularity output

V. CONCLUSION

In order to correct the sawtooth error of 1PPS signal, we study the zoom technique of GNSS timing signal granularity, and propose an improved scheme. The programmable delay line technology is introduced in the improved scheme. The granularity of the programmable delay line device can reach 0.25ns. Combining with the programmable delay line device, we propose a control algorithm which can realize the zoom of local 1PPS signal's granularity. This scheme allows for real-time correction of the quantization error and reduces the residual noise to about 1~2 nanoseconds peak to peak (pk-pk), and improves the instantaneous and short-term timing accuracy of local 1PPS signal.

ACKNOWLEDGMENT

I would like to express my gratitude to all those who helped me during the writing of this paper.

This paper is supported by West Light Foundation of The Chinese Academy of Sciences (No: 2013YB06; 2012YB04).

REFERENCES

- [1] Elliott D.Kaplan, Christopher J.Hegarty 著. Understanding GPS Principles and Application, Second Edition. 寇艳红 译. 北京: 电子工业出版社, 2008.
- [2] Pratap Misra, Per Enge 著. Global Positioning System: signals, Measurement, and performance, second Edition. 罗鸣, 曹冲, 肖雄兵等译. 北京: 电子工业出版社, 2008
- [3] Dieter Hocht, Ulrich Schmid. Long-Term Evaluation of GPS Timing Receiver Failures. The 29th Annual Precise Time and Time Interval (PTTI) Meeting, 1998
- [4] Richard M. Hambly. Critical Evaluation of the Motorola M12+ GPS Timing Receiver vs. the Master Clock at the United States Naval Observatory, Washington DC. PTTI, 2002
- [5] Thomas A. Clark, Richard M. Hambly, Reza Abtahi. Low-cost, High Accuracy GPS Timing, ION, 2000.
- [6] G. Jeffrey Geier T. Michael King, Howard L. Kennedy, Russell D. Thomas, Brett R. McNamara. Prediction of the time accuracy and integrity of gps timing .IEEE International Frequency Control Symposium, 1995.

A 1 MHz to 50 GHz Direct Down-Conversion Phase Noise Analyzer with Cross-Correlation

Gregor Feldhaus and Alexander Roth

Rohde & Schwarz GmbH & Co. KG

Munich, Germany

gregor.feldhaus@rohde-schwarz.com, alexander.roth@rohde-schwarz.com

Abstract— A new phase noise test instrument covers the frequency range from 1 MHz to 50 GHz with direct down-conversion analog I/Q mixers and baseband signal sampling. The traditional PLL has been replaced by a digital FM demodulator for phase detection and frequency tracking. An additional AM demodulator enables concurrent measurement of phase and amplitude noise. The instrument can measure phase noise as low as -183 dBc/Hz with a 100 MHz carrier frequency and 10 kHz offset within two minutes.

Keywords— phase noise; pulsed phase noise; I/Q mixer; cross-correlation; FPGA

I. INTRODUCTION

Traditional phase noise analyzers use an analog phase-locked loop (PLL) to recover the phase difference between a local reference oscillator and the device under test (DUT). Setting up the loop bandwidth and phase detector characteristics correctly requires deep knowledge of the DUT's frequency drifting characteristics. The frequency response of the analog PLL must be known or calibrated to correct the final measurement result. Furthermore an analog PLL achieves only a rather poor rejection of amplitude modulation to the phase output, an effect that has recently gained attention as a cause of cross-spectrum collapse [1].

The relocation of the phase detector into the digital domain promises a much easier setup and improved measurement accuracy. The characteristics of the digital components are predefined and can be compensated with absolute precision. In [2] the RF waveforms of the local oscillator and DUT are sampled, and the phase difference of both is calculated digitally. However, the carrier frequencies are limited to the Nyquist band of the analog-to-digital converter. Additional mixers for the reference oscillator and DUT can extend this method to the microwave range [3].

The alternative approach presented in this paper employs a low phase noise local oscillator for direct down-conversion of the DUT signal. A second independent receive path enables cross-correlation to suppress uncorrelated noise in both paths. The methods described in this paper are implemented in the commercially available R&S[®]FSWP phase noise analyzer which is designed for phase noise and VCO measurements of continuous waveform (CW) and pulsed sources from 1 MHz up to 50 GHz [4].

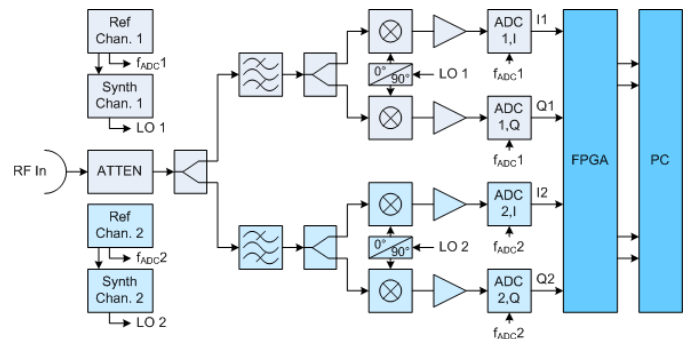


Fig. 1. Overall block diagram of the phase noise analyzer.

II. ANALOG SIGNAL PATH

Fig. 1 shows the components of the phase noise analyzer equipped with two channels for cross-correlation measurements.

The RF signal at the input connector is split into two separate paths behind the adjustable attenuator. Each path contains an analog in-phase / quadrature (I/Q) mixer to convert the RF signal into two analog low frequency signals with 90° phase shift. The local oscillators (LO) of channel 1 and channel 2 are derived from two different reference clocks. The reference of channel 2 is loosely coupled to the reference of channel 1 by a PLL with a bandwidth of less than 0.1 Hz. This allows true cross-correlation down to frequency offsets of 0.1 Hz.

The choice between the LO frequency and the DUT frequency depends on the frequency offsets to be measured. In general, the lower the intermediate frequency (IF) of the resulting I/Q signal, the better the noise performance of the subsequent analog-to-digital converters, i.e. choosing a zero IF appears to be advantageous. For free running oscillators, on the other hand, there will always be a deviation between the true RF frequency and the LO frequency, and this causes harmonics of the difference frequency. With this in mind, a zero IF is used only for measurements above the 1 MHz frequency offset where the harmonics of the remaining frequency deviation drop to the point where they no longer disturb the measurement. Measurements below the 1 MHz frequency offset use an IF slightly above 1 MHz, and their harmonics fall outside the measurement range.

Consideration must be given to the imperfections of analog I/Q mixers as shown in Fig. 2. A deviation of the desired 90°

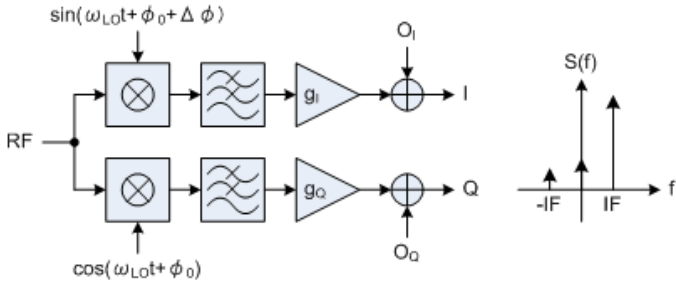


Fig. 2. Model of the I/Q mixer impairments and the resulting spectrum.

phase shift and gain differences between the I and the Q paths cause an I/Q imbalance, which also produces AM/PM conversion. In the frequency domain, a spectral line occurs at the mirrored IF frequency. LO feedthrough adds a DC offset to the I/Q signal. Gain and phase deviations are factory-calibrated over the instrument’s frequency range, while the DC offset is calibrated prior to each measurement. Compensation of these effects is carried out in the digital signal processing path of the FPGA.

This receiver concept typically achieves an AM suppression of 40 dB compared with 15 to 30 dB of traditional analog PLLs, which reduces the likelihood of a cross-spectrum collapse due to anti-correlated AM/PM conversion.

III. DIGITAL SIGNAL PATH

The choice of the analog-to-digital converter (ADC) is crucial to the performance of a fully digital phase detector. A system with an analog PLL suppresses the carrier before sampling the phase signal, i.e. it must only consider the noise dynamic range outside the loop bandwidth. With direct down conversion and carrier sampling, the ADC must cover the complete dynamic range of the input signal.

Each of the four ADCs in Fig. 1 contains four parallel channels with 16-bit resolution running at 100 MSamples/s. Each channel achieves a signal-to-noise ratio (SNR) of about 84 dB relative to full scale. The four channels are averaged, which adds an additional 6 dB to the SNR. The noise power is equally split between phase and amplitude noise. Therefore, for a signal with full scale level at the ADC input, the contribution of the white ADC noise to the phase noise without further cross-correlation gain is

$$L_{\text{ADC}} = (-\text{SNR} - 10 \cdot \log_{10}(f_{\text{sample}}) - 3) \text{ dBc/Hz}. \quad (1)$$

Inserting the numbers above a phase noise contribution of -173 dBc/Hz can be expected for an optimum leveled input signal. The external clock inputs of the first ADC pair and the second ADC pair are derived from different reference frequencies. The cross-correlation process further reduces the phase noise caused by ADC clock jitter.

Fig. 3 shows the digital signal processing chain behind I/Q sampling. This structure is implemented two times on an FPGA for cross-correlation measurements. The equalizer at the input of the signal chain has two functions. First, it compensates the frequency response of the filters in the analog signal path separated for the I- and the Q parts. Second, it compensates the I/Q imbalance and DC offset introduced by the analog I/Q

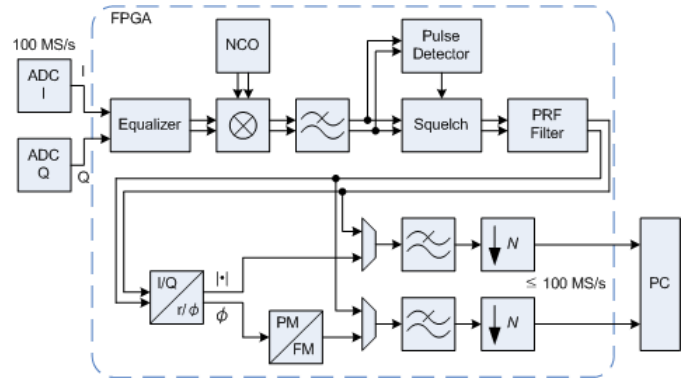


Fig. 3. Digital signal processing for one receive path.

mixer. The equalized signal can be shifted via an arbitrary frequency offset, which is set in the numerical controlled oscillator (NCO). This is used to center the spectrum on the carrier frequency. A subsequent low-pass filter removes signal parts that fall outside the spectrum of interest.

The pulse detector, squelch and pulse repetition frequency (PRF) filter allow measurements on pulsed sources and are bypassed for standard CW measurements. This functionality is explained in detail in section IV.

While the signal processing chain up to this point is similar to a standard digital radio concept, the following AM and FM demodulators are specific to the new approach, which allows concurrent measurement of amplitude and phase noise up to a frequency offset of 30 MHz. A CORDIC algorithm (Coordinate Rotation Digital Computer) is employed to separate the complex baseband I/Q signal into its magnitude and phase components. The magnitude signal is used directly to calculate the amplitude noise spectrum whereas the phase signal must be converted to a frequency signal before further processing steps (see Fig. 4).

In general, a free running oscillator will drift against the LO. The unavoidable frequency offset causes a linearly increasing phase, which wraps at the limits of $\pm\pi$. The wrapping phase signal is inappropriate for further down-sampling and FFT processing. Implementing a feedback to the preceding NCO to keep the IF at zero would be an obvious solution. However, digital feedback loops tend to be problematic due to high time constants and difficult bit growth requirements. The approach presented here uses instead a phase derivation block as a reliable feed-forward structure and converts the PM signal into a non-wrapping FM signal. Slow DUT frequency drift is converted into a low- or zero frequency component of the FM signal, which does not impede the subsequent filtering and FFT processing.

Analog FM demodulators are known to be insensitive for phase noise measurements close to the carrier, as the frequency response of the demodulator decreases at a rate of 20 dB per decade toward DC. This slope must be compensated on the final measurement trace so that any white noise occurring after the demodulator, e.g. from amplifiers or a subsequent ADC, increases by 20 dB per decade. However, a digital FM demodulator shows the same characteristics toward DC. But unlike its analog counterpart, the resources of advanced FPGAs

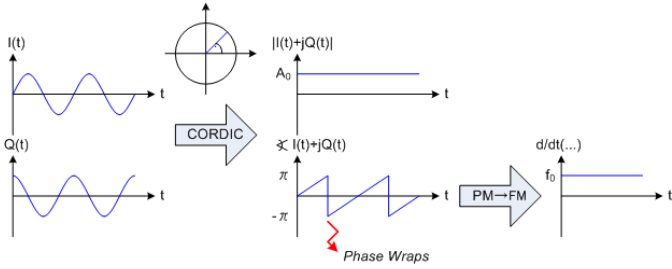


Fig. 4. AM and FM demodulation of an ideal CW source.

can handle the required increase of dynamic range. The digital decimation filters following the FM demodulator in the approach presented achieve a stopband attenuation of 220 dB. This covers the slope of the FM demodulator over 11 decades! The signal bit width increases accordingly to ensure that any quantization noise lies well beyond the FM demodulated phase noise.

The digital AM and FM demodulators require the carrier and the full two-sided measurement range to be present within the Nyquist bandwidth of the I/Q signal. The maximum frequency offset to be measured over the demodulator path is therefore limited to 30 MHz. For higher frequency offsets, only the sum of amplitude and phase noise is measured. In this case, the digital signal path allows the demodulator to be bypassed and transfers the I/Q data directly to the subsequent processor unit for standard spectrum calculation.

IV. PULSED PHASE NOISE MEASUREMENT

The AM and FM demodulator approach is also suitable for measuring the phase noise of pulsed sources without an additional test setup. A premeasurement determines the pulse parameters, i.e. pulse level, pulse width and pulse repetition interval. Pulsing a signal source generates a comb spectrum in the frequency domain with repetitions at the inverse pulse period as shown in Fig. 5. Meaningful phase noise measurements can be made up to half of the pulse repetition frequency. The block diagram in Fig. 3 contains a pulse repetition frequency (PRF) filter to cut off all repetition spectra except the main lobe. The output signal of the filter equals a CW signal and can be processed likewise by the AM and FM demodulator.

Before the PRF filter, an optional pulse detector and squelch block set all noise during pulse pauses to zero. This offers a remarkable advantage over analog pulse repetition filters, which add the noise power of the pulse pauses to their output signal. The difference between main lobe carrier power when pulsed and not pulsed is often referred to as the pulse desensitization factor

$$\text{Pulse desensitization} = 20 \cdot \log_{10} (T_{\text{width}} / T_{\text{rep}}) \text{ dB.} \quad (2)$$

In the absence of countermeasures, the SNR behind the PRF filter decreases by this factor and moves the phase noise measurement closer to the instrument's noise floor. On the other hand, setting the pulse pauses to zero reduces the noise power by

$$\text{Noise reduction} = 10 \cdot \log_{10} (T_{\text{width}} / T_{\text{rep}}) \text{ dB.} \quad (3)$$

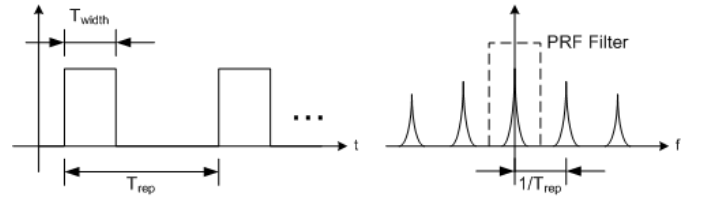


Fig. 5. Pulsed source in time and frequency domains.

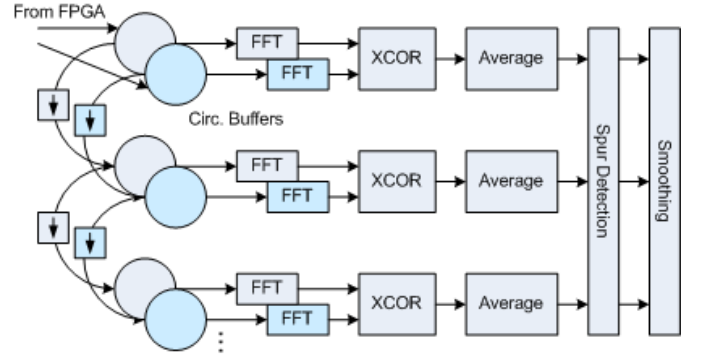


Fig. 6. FFT and Cross-Correlation.

If both effects are combined, the sensitivity of the pulse measurement approach presented here decreases by $10 \cdot \log_{10} (T_{\text{width}} / T_{\text{rep}})$, which is only half of the complete pulse desensitization factor from (2).

V. CROSS-CORRELATION

The cross-correlation and the result trace calculation is done on a standard PC processor connected to the FPGA via PCI Express. The frequency range is logarithmically divided into segments covering approximately half a decade, e.g. from 1 Hz to 3 Hz, 3 Hz to 10 Hz, and so on. Fig. 6 shows the various processing steps. The AM and FM signals from the FPGA are fed into circular buffers. The signals are continuously decimated further down to allow parallel processing of several frequency segments with different resolution bandwidths. Each segment is converted to the frequency domain via FFT. Complex conjugate multiplication of the FFT results and the following averaging block is used for the actual cross-correlation between the two independent signal paths. The estimated power density spectrum for N correlations between the FFT of the first channel X and the FFT of the second channel Y can be expressed as

$$\hat{S}_{YX} = \frac{1}{N} \cdot \left| \sum_{i=0}^{N-1} Y_i \cdot \text{conj}(X_i) \right| \quad (4)$$

Cross-correlation reduces the phase noise contribution of uncorrelated noise signals, i.e. the instrument noise arising behind the RF input splitter, by $5 \cdot \log_{10}(N)$ dB, where N is the number of correlations. As long as the uncorrelated instrument noise outweighs the correlated DUT noise, the result of (4) will drop accordingly. If the correlated noise from the DUT starts to dominate over the averaged uncorrelated noise, the result of (4) settles to the true measurement result.

VI. INSTRUMENT PERFORMANCE

The performance of a cross-correlation phase noise analyzer is defined by its inherent instrument noise contributions and measurement speed in carrying out a certain number of cross-correlations. The internal local oscillators of the analyzer presented outperform most of the available generators and sources in respect to phase noise. Fig. 7 shows the typical system noise floor with 10 seconds of measurement time.

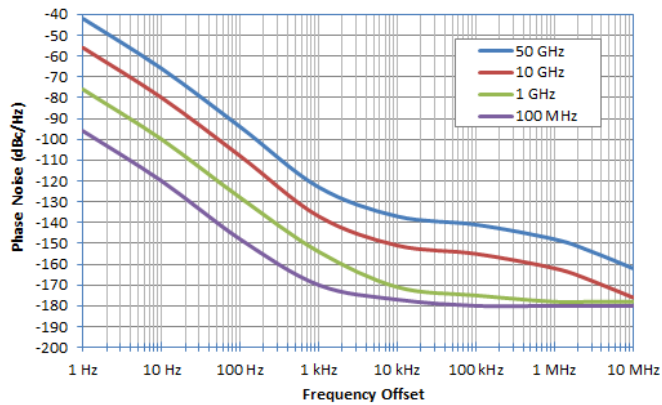


Fig. 7. Typical noise floor with a measurement time of 10 seconds and 10% measurement bandwidth.

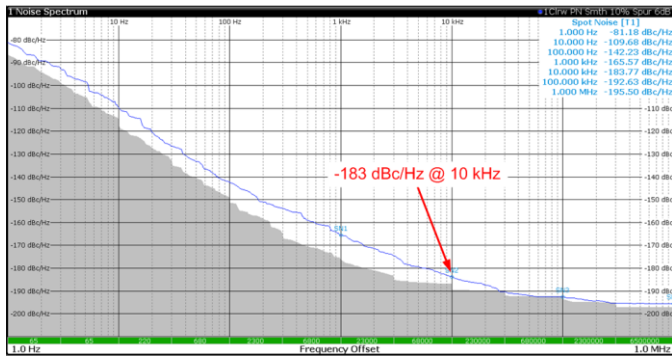


Fig. 8. Two-minute phase noise measurement of a Wenzel 100 MHz-SC Golden Citrine crystal oscillator with a 19 dBm output level.

The instrument can stop the measurement automatically if a certain distance is achieved between the settled result of (4) and the theoretical maximum drop for uncorrelated input signals. This eliminates unnecessary measurement time for cross-correlations that do not further improve the final result.

For frequency offsets up to 1 MHz, measurement speed is mainly determined by the physical capture time required to achieve a specific resolution bandwidth (RBW) with a given number of cross-correlations. With a Blackman-Harris window for the FFT and an overlap factor of 0.75, the capture time can be expressed by

$$T_{\text{capture}} = 2.0 / \text{RBW} \cdot (1 + 0.25 (N_{\text{XCORR}} - 1)). \quad (5)$$

Captured data from higher frequency segments are used for concurrent calculation of subjacent segments. Combining the excellent RF performance and intelligent signal processing makes it possible to achieve unrivaled measurement speed. Fig. 8 is the result of a phase noise measurement of a top-class oscillator, which was completed in just two minutes. This oscillator was also calibrated at the United States National Institute of Standards and Technology (NIST) to verify the precision of the measurement result.

REFERENCES

- [1] Nelson, C.W.; Hati, A.; Howe, D.A., "A collapse of the cross-spectral function in phase noise metrology", *Rev. Sci. Instrum.*, vol. 85, 2014
- [2] Grove, J. et al., "Direct-digital phase-noise measurement", *Proc. of Frequency Control Symposium and Exposition*, 2004, pp.287-291, 23-27 Aug. 2004.
- [3] Parker, S.R.; Ivanov, E.N.; Hartnett, J.G., "Extending the Frequency Range of Digital Noise Measurements to the Microwave Domain," *IEEE Transactions on Microwave Theory and Techniques*, vol.62, no.2, pp.368-372, Feb. 2014.
- [4] Rohde & Schwarz, "R&S®FSWP Phase Noise Analyzer and VCO Tester", Product Brochure, 2015.

Fiber-optic time distribution with the autonomous calibration of dispersion-induced offset

Krehlik Przemysław, Śliwczyński Łukasz
 Department of Electronics
 AGH University of Science and Technology
 Krakow, Poland
 Email: krehlik@agh.edu.pl

Abstract— In the fiber-optic time distribution a bidirectional (two-way) transmission in a single fiber is often used, as it guarantees superior forward-backward symmetry and thus accurate time transfer calibration. However, the chromatic dispersion present in optical fibers may cause noticeable difference between forward and backward propagation delay, which should be taken into account during system calibration. In this paper we describe the idea of autonomous calibration of dispersion-induced offset, and present experimental verification of the proposed solution.

Keywords— time and frequency distribution; time transfer calibration; fiber optics; chromatic dispersion

I. INTRODUCTION

To obtain high stability of the time transfer and to make possible autonomous calibration of time offset (delay) of an output 1 PPS signal, a bidirectional transmission in single fiber is commonly used. However, even in this situation the forward and backward propagation is not strictly symmetrical, which affects calibration considerably [1]. One of the main reasons of this asymmetry is the chromatic dispersion occurring in optical fibers, causing that speed of the light is slightly different for forward and backward signals, which are transmitted with deliberately detuned wavelengths.

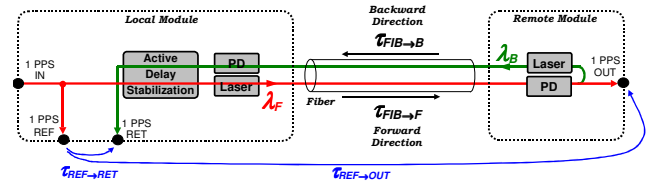
In our time and frequency distribution technology ELSTAB, the calibration of the output timescale offset is performed basing on the round-trip delay of the 1PPS signal and necessary corrections, which are: constant asymmetry of propagation delays in our hardware, correction for Sagnac effect, and asymmetry caused by the dispersion of particular fiber path – see Fig. 1. As we demonstrated in our previous works, the term related to chromatic dispersion has a dominant contribution to the calibration uncertainty, especially in long-haul links [2].

Our experience with in-field installations shows however, that it is often impossible to obtain reliable data concerning dispersion of particular path, and even to be allowed to perform measurements. Additionally, relatively frequent cable damages and path rerouting may influence the dispersion. Thus we proposed and evaluated the method of self-calibration of dispersion-induced offset in bidirectional time transfer.

This work was supported by Polish National Science Center (NCN) under project no. 2015/17/B/ST7/03628.

II. THE IDEA OF AUTONOMOUS DISPERSION MEASUREMENT

The proposed solution is based on a simple observation that changing the wavelength of the local laser (λ_F) results in variation of the round-trip delay of 1PPS pulses, proportional to the accumulated dispersion of the optical path - see Fig. 2. (During this measurement the active delay stabilization should be temporarily deactivated.) In our solution the wavelength shift is realized by temperature control of the laser chip and its amount is ± 0.15 nm. As all required actions and measurement are performed around the local module of the time distributing system, and basically do not need human activity, the functionality of dispersion measurement may be realized by additional hardware and software blocks connected (or integrated) with the local module of the system - see Fig. 3.



$$\tau_{REF \rightarrow OUT} = \frac{1}{2} [\tau_{REF \rightarrow RET} + (\tau_{FIB_F} - \tau_{FIB_B}) + \tau_C]$$

$$\tau_{FIB_F} - \tau_{FIB_B} = D(\lambda_F - \lambda_B)$$

τ_C - hardware term, D - dispersion; Sagnac term omitted for simplicity.

Fig. 1. Time transfer calibration in a system with bidirectional transmission.

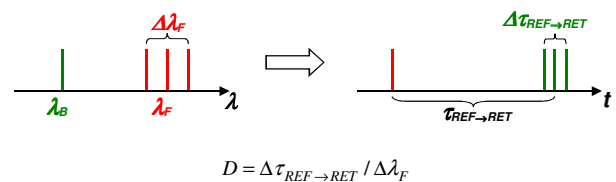


Fig. 2. Proposed method for dispersion assessment.

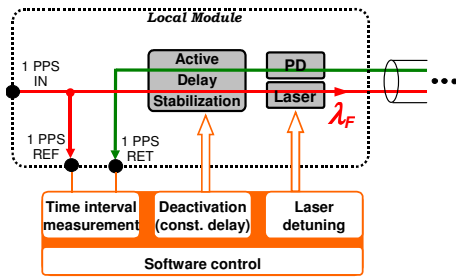


Fig. 3. Local module with additional blocks (functions) needed for autonomous dispersion assessment.

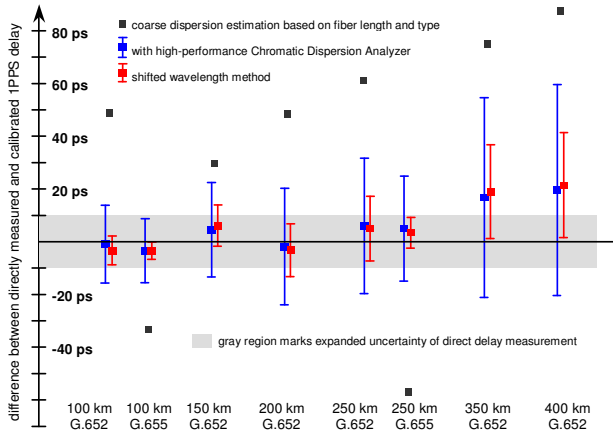


Fig. 4. Accuracy of time transfer calibration for different approaches of dispersion assessment. (For coarse dispersion estimation the uncertainty bars are omitted as they exceed the vertical axis range.)

III. EXPERIMENTAL VERIFICATION

Verification of the time transfer delay calibration was performed by direct delay measurement from 1PPS REF point to 1PPS OUT, and comparing the results with the delay calculated from calibration formulas (given in [3]), with different approaches for dispersion estimation. In the first one the dispersion was coarsely estimated basing on known fiber length and typical values of the dispersion coefficient for G.652 and G.655 fibers. In the second approach the dispersion

was measured with high-end chromatic dispersion analyzer, and finally our method with wavelength shifts was applied. The delay was measured with a high-speed digital oscilloscope and dedicated stepper, as described in [3]. Up to 400 km of fiber on spools was used, both G.652 and G.655 type, with necessary number of bidirectional optical amplifiers in between.

Fig. 4 summarizes the results of the experiment. One may notice that the calibration based on proposed method agrees very well with approach based on dispersion analyzer. The discrepancy between directly measured and calibrated 1PPS delay do not exceed 22 ps, and results are consistent with the uncertainty analysis.

IV. CONCLUSION

In long-haul links, the accumulated chromatic dispersion appears to be a major factor influencing the time transfer uncertainty. Our experience with various in-the-field installation shows that usually it is impossible to obtain accurate measurement data describing dispersion of the particular optical path designated for the time transfer. Thus we proposed the autonomous measurement method based on shifted laser wavelength. Theoretical analysis and experimental verification show that by means of this method, the time transfer uncertainty related to fiber dispersion may be reduced to values well below 20 ps, for fiber length as long as 500 km. The describe solution is not restricted to our ELSTAB technology, but may be use also within other approaches, as classical two-way time transfer over fiber.

REFERENCES

- [1] Ł. Śliwczyński, P. Krehlik, M. Lipiński, "Optical fibers in time and frequency transfer," *Meas. Sci. Technol.*, vol. 21, pp. 075302- 075312, 2010.
- [2] P. Krehlik et al., "ELSTAB - fiber optic time and frequency distribution technology - a general characterization and fundamental limits", *IEEE Trans. Ultrason., Ferroelect., Freq. Control*, DOI 10.1109/TUFFC.2015.2502547, 2015.
- [3] P. Krehlik, Ł. Śliwczyński, Ł. Buczek and M. Lipiński, "Fiber optic joint time and frequency transfer with active stabilization of the propagation delay," *IEEE Trans. Instrum. Meas.*, vol. 61, pp. 2844–2851, 2012.

aggregation (CA) introduced to the latest LTE-Advanced. Currently, the CA is used only to the downlink, but is going to apply also to the uplink. For non-CA, signals in different bands can be separated by an RF switch. However for CA, the separation must be performed by a combination of DPXs called the multiplexer (MPX). The MPX must possess good isolation for all combinations of Tx and Rx channels in addition to original DPX performances. Furthermore, linearity improvement is necessary because MPX is exposed to multiple Tx signals with high power and different frequencies.

III. REQUIREMENTS AND ATTEMPTS

A. Residual Losses

Although current SAW devices exhibit extremely high performances, there still remain unknown excess losses. One possible mechanism is energy leakage to surroundings.

Figure 2 shows representative leakage paths. Although energy leakage from both ends are often observable, it can be suppressed well when proper design is given. On the other hand, lateral energy leakage is troublesome. Although SAW energy can be confined in the resonator structure by designing the side edges to cause the total SAW reflection, this may result in generation of additional resonances called transverse mode resonances. Their modelling are one of the most important remaining tasks for theoreticians like the author. So accurate simulation tool(s) are necessary not only for device design but also for finding appropriate tricks to solve complicated problems like lateral leakage.

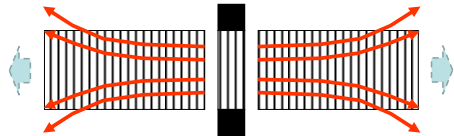


Fig. 2 SAW energy leakage from sides and ends

The piston mode operation was proposed[3,4], where the side edges are designed to behave like mechanically free. This makes all the transverse modes except the fundamental one not excitable and detectable by the interdigital transducer (IDT). It was demonstrated that high Q and spurious free are simultaneously realizable by the use of this technology.

Laser probe is quite effective to investigate such leakage in SAW/BAW devices[5]. The authors developed a phase-sensitive and fast-scanning laser probe based on the Sagnac interferometer[6]. Fig. 3 shows the measured SAW field at the resonance frequency of 5,186 MHz[7]. It took 10 min. for capturing this image. A high Q SAW resonator with 0.5 μm line width on the AlN/single-crystal diamond (SCD) structure[8] was used as a specimen. The resonance pattern is clearly visible. SAW energy penetrates to the bus-bar region while SAW energy concentrates in the IDT region.

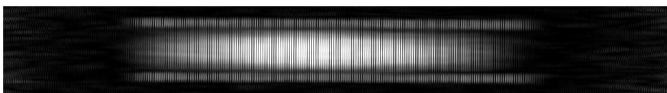


Fig. 3 Visualized vibration pattern of one-port SAW resonator on AlN/SCD structure resonator

B. Temperature Stability

For efficient use of spectrum, frequency separation between Tx and Rx bands (the DPX gap) tends to be narrow. For the use, SAW resonators must be temperature stable and high Q .

Most of all materials become soft with the temperature T . Then the filter passband shifts downward with T . Its cancellation called the temperature compensation (TC) is realized by the use of amorphous SiO_2 , which becomes stiff with T . Since SiO_2 is not piezoelectric, thinner SiO_2 is better.

It is known that SiO_2 properties including the temperature coefficient of elasticity (TCE) change drastically with the material preparation. Nevertheless, no systematic investigation was reported on the relation between TCE and SiO_2 properties.

Matsuda, et al, pointed out that the Fourier transform infrared (FTIR) spectra can be used as a guideline to search "excellent" SiO_2 films for SAW devices[9]. Fig. 4 shows the relation between the measured TCF and the full width of half maxima (FWHM) of the bending mode ω_3 peak in the FTIR spectra of SiO_2 films prepared by various techniques under various deposition conditions. The FWHM is linearly correlated with TCF with small fluctuation. This might be explained by the fact that with an increase in FWHM, disorder or non-uniformity of the SiO_2 molecular structure becomes obvious, and the elastic properties may become non-uniform.

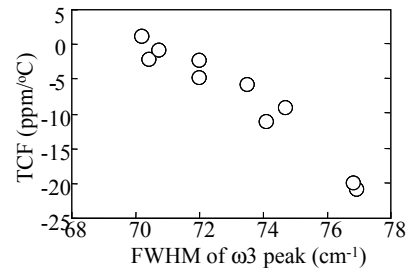


Fig. 4 Relationship between TCF and FWHM of ω_3 peak

From the FTIR measurement, fluorine-doped silicon oxide was expected to offer better TCE than pure SiO_2 [10]. This was experimentally verified, and no obvious deterioration was observed in the resonance Q when fluorine content is less than 8.8 atomic%[10].

The wafer bonding is another technique for TC. After a piezoelectric wafer such as LiTaO_3 (LT) is bonded with a stiff substrate like sapphire, the piezoelectric wafer is thinned by polishing. Due to stress caused by the bimorph effect, TCE is improved. In contrast to the SiO_2 deposition, the wafer bonding scarcely influences to the other performances.

Fig. 5 shows measured TCF of a SAW resonator fabricated on a 42°YX-LT directly bonded with a polycrystalline spinel wafer[11]. The horizontal axis is the thickness ratio r between LT and spinel. It is seen that TCF was improved from -42 to -18 ppm/°C by using the 42-LT/spinel structure at $r=15$.

C. Nonlinearities

Compared with the third-order nonlinearity, second-order one has not been paid much attention for SAW devices because it was not so obvious for SAW devices in contrast to BAW devices[12]. However, very weak second-order signals

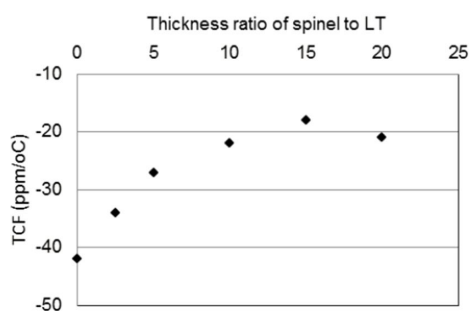


Fig. 5 Measured TCF as a function of the thickness ratio

are still detectable.

Nakagawa, et al, investigated how second-order nonlinearity occurs in SAW devices, and revealed that following two mechanisms are dominant: (a) self-mixing of the electrostatic field and (b) mixing of the electrostatic field with the strain field associated with laterally propagating modes[13]. Both of them mainly occur at the gaps between electrode tip and dummy electrode in an IDT.

They also proposed a device structure called the “parallelly divided and reversely connected (PDRC)”[13], where the IDT is sub-divided into two portions laterally, and they are electrically connected in parallel with polarity inversion. Since the second-order nonlinearity is originated from crystallographic asymmetry of the 42-LT substrate, it will be cancelled out owing to lateral mirror symmetry of the PDRC structure.

Fig. 6 shows the measured second harmonics (H2). It is seen that the H2 is suppressed well, and the H2 level is improved by circa 10 to 25 dB. In addition, the steep peak at 1.69 GHz mostly disappears. A small peak exists at 1.72 GHz. Its origin has not been identified yet.

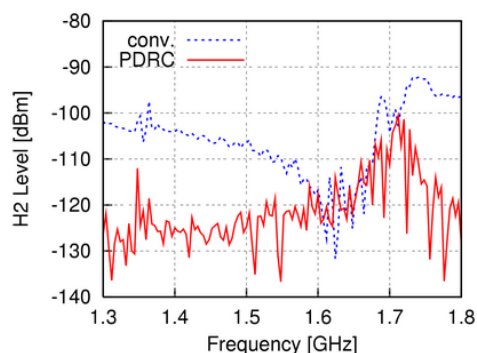


Fig. 6 Measured H2 of a one-port SAW resonator with and without the PDRC structure.

Fig. 7 shows the measured third harmonics (H3) for three SAW resonators using Al electrodes with different Al quality[14]. Note their linear performance are almost the same. The horizontal axis is the H3 frequency. The H3 changes dramatically with the Al quality. It is interesting that Al films with better quality generate stronger nonlinearity, but it is hard to explain why. Namely, sample A (single crystal) is the worst, sample B (<111> oriented) is next, and sample C (poly crystal) is the best for the third order non-linearity. Anyway, this result indicates that the Al layer is one of the major causes of the third-order nonlinearity in this kind of SAW devices.

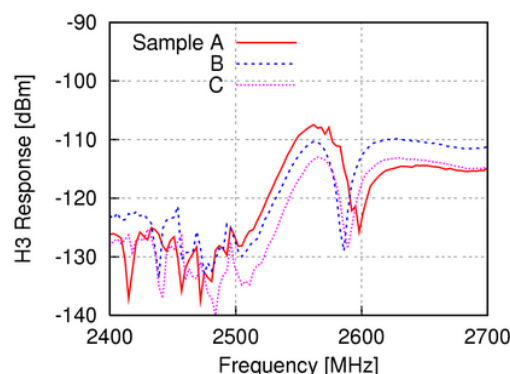


Fig. 7 Variation of measured H3 with Al quality

Since non-linear signals are very weak and very sensitive to impedance of peripheral circuits, their measurement is not so simple. The authors studied this issue in collaboration of SAW industries all over the world, and completed as an international standard of the IEC[15,16].

D. Power Durability

High power applications such as pico-cell duplexers may expand applicability of SAW devices. For such application, not only the linearity but also the power durability are critical.

Where and how does the failure occur after exposure to high RF power? The main mechanism is called the acoustic-migration[17]. Namely, acoustic vibration assists migration of Al atoms, and creates damages such as hillock and void. Various efforts have been made for finding the best electrode design by each SAW company. A review of the electrode design can be seen in [17].

How do we measure the mean time to failure of these devices? We are now studying this issue again in collaboration of SAW industries all over the world so as to establish an international standard as the IEC activity[18].

E. New Materials

Achievable performances of SAW/BAW devices are inherently limited by choice of the piezoelectric material. From this aspect, the author’s group pays much attention on paraelectric $\text{Sc}_x\text{Al}_{1-x}\text{N}$ (ScAlN) films[19,20] which offer anomalously strong piezoelectricity and low acoustic and dielectric losses in the GHz range. ScAlN films can be deposited to a large area by reactive sputtering. Thus ScAlN seems to be applicable to wideband and low loss SAW devices operating over 3 GHz, where current SAW technologies may not be feasible.

Fig. 7 shows measured impedance of a fabricate SAW resonator on a ScAlN/SCD structure with the line width of 0.7 μm [21]. Resonance and anti-resonance are seen at 2.87 GHz and 2.94 GHz, respectively. The resonance Q was 630. This high Q value confirms low SAW propagation loss in this frequency. From the fitting, K^2 was estimated as 3.77%. Weak satellite resonances are seen. They are due to transverse mode resonances. Although the SCD and SiC have been used as a base substrate[21,22] because of their very high acoustic wave velocities. Recently Gongbin, et al, indicated that conventional

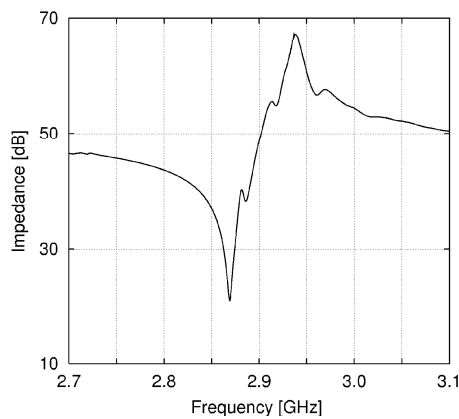


Fig. 7 Impedance characteristics of a one port SAW resonator with line width of 0.7 μm on the ScAlN/SCD structure.

Si can be also used under proper structural design[23].

The author's group is also investigating uniform deposition of high quality ScAlN films with large Sc content in large area[24].

IV. CONCLUSIONS

This paper reviewed current status and future prospect of RF SAW devices used in mobile communications.

Here, only the research directions where academia can contribute are discussed. Of course, there are other requests. For example, industries always need new technologies for reducing device area and height. Design of MPXs described in II and co-design with active circuitry are also crucial. Anyway, it is clear that our goal is far beyond the horizon.

ACKNOWLEDGMENT

The author would like to express his deepest appreciation to former and current lab members in Chiba University and industrial partners for their supports and discussions.

REFERENCES

- [1] S.Takahashi, H.Hirano, T.Kodama, F.Miyashiro, B.suzuki, A.Onoe, T.Adachi, and K.Fujimura, "SAW IF Filter on LiTaO₃ for Color TV Receivers," *IEEE Trans. Consumer Electronics*, **CE-24**, 3 (1978) pp. 337-346
- [2] L.Maurer, C.Ruppel, R.Vazny, and R.Weigel, "Future of SAW/BAW Devices in Mobile Radio A Brief Overview," *Proc. 5th International Symposium on Acoustic Wave Devices for Future Mobile Communication Systems (2012)* pp.61-64
- [3] M.Solal, J.Gratier, R.Aigner, K.Gamble, B.Abbott, T.Kook, A.Chen and K.Steiner, "Transverse modes suppression and loss reduction for buried electrodes SAW devices," *Proc. IEEE Ultrason. Symp.* (2010) pp. 624-628
- [4] B.Abbott, R.Aigner, A.Chen, K.Gamble, T.Kook, J.Kuypers, M.Solal, and K.Steiner, "High Q TCSAW," *Proc. 6th International Symposium on Acoustic Wave Devices for Future Communication Systems (2015)* 2A-3
- [5] V.Knuutila, P.T.Tikka, and M.M.Salomaa, "Scanning Michelson Interferometer for Imaging Surface Acoustic Wave Fields", *Optics Lett.*, **25**, 9 (2000) pp. 613-615.
- [6] K.Hashimoto, N.Wu, K.Kashiwa, T.Omori, M.Yamaguchi, O.Takano, S.Meguro, and K.Akahane, "A Laser Probe Based on Sagnac Interferometer with Fast Mechanical Scan for RF Surface and Bulk Acoustic Wave Devices", *IEEE Trans. Ultrason., Ferroelec., and Freq. Contr.*, **58**, 1 (2011) pp.187-194.
- [7] K.Hashimoto, S.Kawachi, A.Takahashi, S.Sakamoto, and T.Omori, "Laser Probe System for 5 GHz SAW/BAW Devices," *Proc. IEEE Freq. Contr. Symp.* (2014) pp.321-324
- [8] S.Fujii, H.Yamada, T.Omori, K.Hashimoto, H.Torii, H.Umezawa, and S.Shikata, "One-port SAW Resonators Fabricated on Single Crystal Diamond", *Tech. Digest, IEEE Microwave Symp.* (2013) TU-1D6
- [9] S.Matsuda, M.Hara, M.Miura, T.Matsuda, M.Ueda, Y.Satoh, and K.Hashimoto, "Correlation between temperature coefficient of elasticity and Fourier transform infrared spectra of silicon dioxide films for surface acoustic wave devices," *IEEE Trans. Ultrason., Ferroelec., and Freq. Contr.*, **58**, 8 (2011) pp.1684-1687
- [10] S.Matsuda, M.Hara, M.Miura, T.Matsuda, M.Ueda, Y.Satoh, and K.Hashimoto, "Use of fluorine doped silicon oxide for temperature compensation of radio frequency surface acoustic wave devices," *IEEE Trans. Ultrason., Ferroelec., and Freq. Contr.*, **59**, 1 (2012) pp. 135-138
- [11] K.Geshi, K.Teraoka, S.Kinoshita, M.Nakayama, Y.Imagawa, S.Nakayama, K.Hashimoto, S.Tanaka, K.Totsu, and H.Takagi, "Wafer bonding of polycrystalline spinel with LiNbO₃/LiTaO₃ for temperature compensation of RF surface acoustic wave devices," *Proc. IEEE Ultrason. Symp.* (2012) pp. 2726-2729
- [12] M.Ueda, M.Iwaki, T.Nishihara, Y.Satoh, and K.Hashimoto, "Nonlinear distortion of acoustic devices for radio-frequency front-end circuit and its suppression," *Jpn. J. Appl. Phys.*, **49**, 7 (2010) 07HD12
- [13] R.Nakagawa, H.Kyoya, H.Shimizu, T.Kihara, and K.Hashimoto, "Study on Generation Mechanisms of Second-Order Non-linear Signals in SAW Devices and Their Suppression," *Jpn. J. Appl. Phys.*, **54**, 7 (2015) 07HD12.
- [14] R.Nakagawa, T.Suzuki, H.Shimizu, H.Kyoya, and K.Hashimoto, "Influence of Electrode Structure to Generation of Third-Order Non-linearity in SAW Devices," *Jpn. J. Appl. Phys.*, **54**, 7 (2015) 07HD11
- [15] Y.Wang, F.Thalmayr, N.Wu and K.Hashimoto, "Considerations on Measurement Setup for Second-Order Nonlinearity in Radio-Frequency Bulk Acoustic Wave Duplexers," *IEEE Trans. Ultrason., Ferroelec., and Freq. Contr.*, **57**, 8 (2010) pp.1854-1859
- [16] IEC Standard 62761, "Guidelines for the measurement method for surface acoustic wave (SAW) and bulk acoustic wave (BAW) devices in radio frequency (RF)," 2014
- [17] R.Takayama, H.Nakanishi, and K.Hashimoto, "Impact of Composition and Structure of Al Alloy Electrodes to Power Durability of SAW Devices," *Proc. IEEE Ultrason. Symp.* (2014) pp. 886-892
- [18] T.Omori, S.Ohara, C.J.Ahn, and K.Hashimoto, "Study of Power Durability Measurement of RF SAW Devices for IEC Standardization," *Proc. IEEE Ultrason. Symp.* (2015) 90-1~4
- [19] M.Akiyama, T.Kamohara, K.Kano, A.Teshigahara, Y.Takeuchi, and N.Kawahara, "Enhancement of piezoelectric response in scandium aluminum nitride alloy thin films prepared by dual reactive cosputtering," *Adv. Mater.*, **21**, 5 (2009) p. 593-596
- [20] M.Akiyama, K.Kano, and A.Teshigahara, "Influence of Growth Temperature and Scandium Concentration on Piezoelectric Response of Scandium Aluminum Nitride Alloy Thin Films," *Appl. Phys. Lett.*, **95**, 16 (2009) 162107
- [21] K.Hashimoto, T.Fujii, S.Sato, T.Omori, C.Ahn, A.Teshigahara, K.Kano, H.Umezawa, and S. Shikata "High Q Surface Acoustic Wave Resonators in 2-3 GHz Range Using ScAlN/Single Crystalline Diamond Structure," *Proc. IEEE Ultrason. Symp.* (2012) pp. 1926-1929
- [22] K.Hashimoto, S.Sato, A.Teshigahara, T.Nakamura, and K.Kano, "High Performance Surface Acoustic Wave Resonators in the 1 to 3 GHz Range Using a ScAlN/6H-SiC Structure," *IEEE Trans. Ultrason., Ferroelec., and Freq. Contr.*, **60**, 3 (2013) pp. 637-642
- [23] G.B.Tang, T.Han, A.Teshigahara, T.Iwaki, and K.Hashimoto, "Enhancement of effective electromechanical coupling factor by mass loading in layered SAW device structures," *Jpn. J. App. Phys.*, **55**, 7 (2016). [to be published]
- [24] M.Sumisaka, K.Yamazaki, S.Fujii, G.Tang, T.Han, Y.Suzuki, S.Otomo, T.Omori and K. Hashimoto, "Sputter Deposition of ScAlN Using Large Size Alloy Target with High Sc Content and Reduction of Sc Content in Deposited Films," *Jpn. J. App. Phys.*, **54**, 7 (2015) 07HD06.

Coherent Population Trapping Ramsey Resonance in Slow Rubidium Beam

Igor M. Sokolov

Department of Theoretical Physics, Peter the Great St.-Petersburg Polytechnic University, St.-Petersburg, 195251, Russia

Email: ims@is12093.spb.edu

Abstract—We calculate the coherent population trapping (CPT) resonance in slow beam of rubidium 87 atoms caused by their interaction with laser bichromatic electromagnetic field in two separated spatial domains. We study influence of the finite width of the atomic beam, its angular divergence and residual beam velocity spread on the parameters of CPT-Ramsey resonance. We analyze properties of the CPT resonance depending on intensity of electromagnetic field, applied magnetic field strength and on width of the laser light beams.

I. INTRODUCTION

Quantum frequency standards are widely adopted in such systems of navigation as GLONASS, GPS, GALILEO. For this reason creation of compact frequency standards having, at the same time, high accuracy remains an important problem in modern quantum electronics. One of the most promising ways to solve this problem is to use the coherent population trapping (CPT) effect [1], [2]. In the simplest case CPT can be observed for three level atomic systems interacting with bichromatic laser field. Under conditions of two-photon resonance, atoms transit into so called dark state, and stop absorbing laser radiation.

The width of CPT resonance can be much less than natural linewidth and it makes for successful utilization of this resonance in metrology and frequency standardization [3]-[5]. Even more narrow resonance is observed if CPT is registered by means of Ramsey method [6]. For the first time CPT-Ramsey fringe was experimentally registered for thermal atomic beam of nitrogen atoms in [7]. In a series of subsequent experiments the spatial separation of two areas of interaction of atoms with bichromatic radiation was replaced by time domain separation [8], [9]. In [10], [11] such experiments were performed with cold atoms confined in atomic traps. The resonances with several Hertz width were observed. Narrowing of CPT resonance in the case of spatial-zone pumping in atomic cells which is analog of Ramsey method was demonstrated in [12]-[14].

In [15] a scheme of a mobile slow-beam microwave atomic clock is proposed. This scheme does not assume usage of a bulky atomic trap. The slow atomic beam is generated from thermal one by means of a modified Zeeman slower [16]. Utilization of the CPT resonance with Ramsey registration technique allows one to refuse from the microwave cavity and thus to decrease the size of the clock and its power consumption.

In papers [17], [18] we analyzed the formation of a CPT-Ramsey signal in this standard for the model case of a single-velocity narrow atomic beam. We calculated time dynamics of atomic internal states in the beam and studied the shape of the CPT resonance depending on the specific type of working transitions and polarization scheme. An influence of the main setup parameters such as light intensity, magnetic field intensity and thickness of laser beams on amplitude and width of the resonance was studied in this case.

In real experimental setups an atomic beam has finite width and velocities of different atoms are different. The main goal of the present work is to study the influence of the finite width of the atomic beam, its angular divergence and residual beam velocity spread on the parameters of CPT-Ramsey resonance. Particularly we calculate the shape of the CPT resonance, its amplitude and width depending on intensity of electromagnetic field, applied magnetic-field strength and on size of laser light beams.

II. BASIC ASSUMPTIONS AND APPROACH

Signal of a frequency discriminator based on the CPT effect is determined by changes in total population of atomic excited states in registration area caused by variation of two-photon detuning. To calculate this population in the present paper we use the density matrix formalism. This formalism allows us to describe the interaction between atoms and laser radiation taking into account main factors responsible for generation the CPT-Ramsey signal.

We solve nonstationary equations for atomic density matrix and determine time evolution of population of different atomic sublevels. Under typical conditions (see [15]) the density of atoms in the beam does not exceed $3 \times 10^7 \text{cm}^{-3}$. Velocities of relative atomic motion are also very small. It gives us opportunity to neglect interatomic collisions. Resonance dipole-dipole interatomic interaction which causes noticeable shifts and distortion of atomic transitions in cold gases can also be neglected [19]-[21]. Thus when depicting the dynamics of atoms in the beam we can completely neglect interatomic interaction and consider evolution of separate atoms in the beam.

It is convenient to describe internal atomic dynamics in the co-moving frame of reference. The atomic motion for typical velocities can be considered classically. Momentum transmitted to the atom from the light in the result of their interaction is essentially smaller than both initial atomic longitudinal and

transverse momentum in the beam [17]. It allows us not to consider recoil effect.

In the co-moving frame of reference the atom is motionless. Its dynamic in external laser field is described by the following equation

$$\frac{\partial \rho}{\partial t} = -\frac{i}{\hbar} [H_0 + V, \rho] + \Gamma \rho. \quad (1)$$

Here Γ is spontaneous decay relaxation operator; H_0 is the Hamiltonian of free atom; V is the operator of atom-light interaction. In the dipole approximation

$$V = -\mathbf{dE} = -\mathbf{d}(\mathbf{e}_1 E_{01}(t) \exp(-i\omega_1 t) + \mathbf{e}_2 E_{02}(t) \exp(-i\omega_2 t) + c.c.)/2. \quad (2)$$

Here we take into account that atomic ensemble interacts with two mode of the field which generally have different polarizations (\mathbf{e}_1 and \mathbf{e}_2) and different frequencies (ω_1 and ω_2). Spatial profile of the laser field is assumed to be Gaussian so in considered reference frame the fields are essentially nonstationary. We indicate it explicitly by argument t in field amplitudes E_{01} and E_{02} . Further we consider the case when the parameters of electromagnetic radiation in two spatially separated interaction domains are similar. The intensities of the two spectral components are also taken equal.

We assume also that the spectrum of both components of laser radiation is narrow enough and each mode of bichromatic field causes transitions only from one hyperfine sublevel of the ground state $F_1 = I - 1/2$ and/or $F_2 = I + 1/2$ of considered alkali atom (here I is the nuclear angular momentum).

In rotating wave approximation with regard to approximations discussed above the Eq. (1) has the following matrix form

$$\begin{aligned} \frac{\partial \rho_{gg'}}{\partial t} &= i(-\omega_{gg'} - (\omega_g - \omega_{g'}))\rho_{gg'} + \\ &+ \frac{i}{\hbar} \sum_e \left(-\tilde{V}_{ge}\rho_{eg'} + \rho_{ge}\tilde{V}_{eg'} \right) + (\Gamma\rho)_{gg'}, \\ \frac{\partial \rho_{ee'}}{\partial t} &= -i\omega_{ee'}\rho_{ee'} + (\Gamma\rho)_{ee'} + \\ &+ \frac{i}{\hbar} \sum_e \left(-\tilde{V}_{eg}\rho_{ge'} + \rho_{eg}\tilde{V}_{ge'} \right), \\ \frac{\partial \rho_{eg}}{\partial t} &= i(-\omega_{eg} + \omega_g)\rho_{eg} - \frac{i}{\hbar} \sum_e \tilde{V}_{eg'}\rho_{g'g} + (\Gamma\rho)_{eg}. \end{aligned} \quad (3)$$

$$\tilde{V}_{eg} = \langle F_e M_e | d_\mu | F_g M_g \rangle e_g^\mu E_{0g}(t). \quad (4)$$

Here \tilde{V}_{eg} are time-dependent matrix elements of the operator of interaction of the atom with radiation; \mathbf{d} is operator of atomic dipole moment; $\omega_{ji} = (E_j - E_i)/\hbar$; ρ_{ij} are matrix elements of slow varying amplitudes of the density operator. Indexes g and e correspond to ground and excite states respectively. These states are characterized by quantum numbers F and M . The frequency with one index ω_i denotes the frequency of that mode which causes transition from corresponding ground sublevel.

The set of equations (3) allows us to take into account all fine and hyperfine structure of atomic excited states. Further

in calculation we restrict ourself by considering all hyperfine sublevel of only one D line. Corresponding equations are solved numerically. As opposed to paper [17], [18] in the present work we allow for the finite width of atomic beam, its angular divergence and residual beam velocity spread. In such a case different atoms in the atomic beam cross the laser rays with different velocities and with a different impact parameters. This difference leads to different dependencies $E_{01}(t)$ and $E_{02}(t)$ for each atom.

The calculation is performed by the Monte-Carlo method. We solve equations (3) many times for different atoms. Obtained solution give us information about atomic state at any instant of time. Transforming this solution into laboratory system of coordinates we get information about atomic state at a given space point. Obtained results are averaged according to specific atomic velocity and space distribution. In the following section we analyze the results of calculation for the case of rubidium 87 atomic beam.

III. RESULTS AND DISCUSSION

Choice of the working transitions and polarization scheme of registration strongly influence on the figure of merit of the CPT based standard. As it was shown in [17], [18] the best choice is to use mutually orthogonal linearly polarized components of bichromatic field and to tune them at transition to the $F_e = 2$ level of the D1 line. In the present paper we consider only this case. For this most promising geometry we analyze the dependence of the CPT-Ramsey resonance on the conditions of observations.

According to the parameters given in [15], [16] we will consider atomic beams with a radius of $r = 0.2\text{cm}$ and angular divergence of about $1/100$ rad. Space separation in Ramsey scheme L is 30cm . Average speed of atomic beam is $v = 3\text{m/s}$. Velocity dispersion is $\delta v = 1\text{m/s}$. The atomic velocity distribution is numerically simulated according to the dates presented in [16].

We begin investigation of the CPT resonance with analysis of its dependence on external static magnetic field. Due to the Zeeman effect magnetic field causes shift of transition line. However practically in all schemes utilizing the coherent population trapping effect the magnetic field is still used. There are two main reasons for this. First, utilization of magnetic field allows one to select working transition which is less affected by external magnetic field and consequently less comes under influence of its fluctuations. Usually it is so called 0-0 transition. In our specific case it is $F_g = 1, M = 0 \leftrightarrow F_g = 2, M = 0$ transition. Its shift is proportional to second degree of magnetic field strength and scaling factor is 575.15 Hz/Gs^2 . Second, for zero magnetic field several transitions influence on observed CPT signal. Mutual influence of different coherent processes may be negative and increasing in magnetic field can increase the figure of merit of the CPT resonance. The Fig. 1 shows that for geometry considered here such is the case. Fig. 1 is calculated for the following parameters of the laser beam: intensities of the both spectral components are equal to $I = 20\mu\text{W/cm}^2$ at the axes, and thiers Gaussian radii are $w = 0.25\text{cm}$.

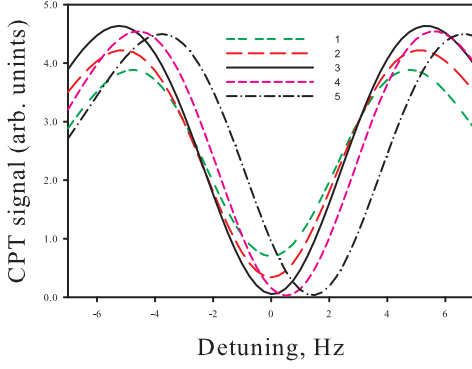


Fig. 1. Dependence of the CPT signal on magnetic field intensity. $I = 20\mu\text{W}/\text{cm}^2$, $w = 0.25\text{cm}$; 1 - $B = 1\text{mGs}$; 2 - $B = 2\text{mGs}$, 3 - $B = 10\text{mGs}$; 4 - $B = 30\text{mGs}$; 5 - $B = 50\text{mGs}$

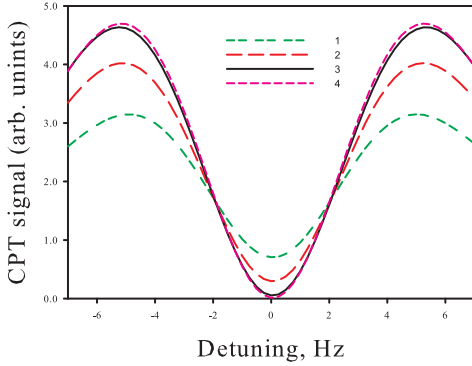


Fig. 2. Dependence of the CPT signal on intensity of light radiation. $B = 10\text{mGs}$, $w = 0.25\text{cm}$; 1 - $I = 5\mu\text{W}/\text{cm}^2$; 2 - $I = 10\mu\text{W}/\text{cm}^2$, 3 - $I = 20\mu\text{W}/\text{cm}^2$; 4 - $I = 30\mu\text{W}/\text{cm}^2$

In Fig. 1 one can clearly see that there is optimal value of the magnetic field. Increase in B increases initially the slope of the resonance. Starting from about $B = 10\text{mGs}$ further increase in magnetic field induction does not increase the slope but causes noticeable level shift. So our calculation shows that optimal value of magnetic field induction is about $B = 10\text{mGs}$. All further calculations are performed for such magnetic field, for which the Zeeman shift is approximately equal to 0.06Hz .

One of the most important parameters which influences on CPT resonance is intensity of electromagnetic field used for resonance excitation. Dependence of the profile of the resonance on this parameter for considered Ramsey registration scheme is shown in Fig. 2. The slope of the resonance increases with intensity. But this dependence is characterized by saturation behavior. For intensities equal approximately to $I \sim 20\mu\text{W}/\text{cm}^2$ the slope reaches practically its maximal value. The similar effect was observed for the case of single-velocity beam [17], [18], though for noticeably smaller intensities. Note also that in considered case the light shift is negligible.

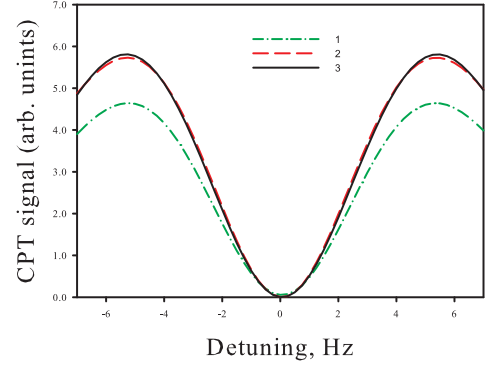


Fig. 3. Dependence of the CPT signal on the width of light beams. $B = 10\text{mGs}$, $I = 20\mu\text{W}/\text{cm}^2$; 1 - $w = 0.25\text{cm}$; 2 - $w = 0.5\text{cm}$, 3 - $w = 0.75\text{cm}$

For the given light intensity the slope of the CPR-Ramsey resonance can be increased by increasing in the width of the light beams. Corresponding dependence is shown in Fig. 3. Here we also observe saturation effect. Coherent population trapping signal practically stops increasing with the width of the optical beams when their dimensions becomes greater than a fixed value. For considered parameters this value is approximately $w = 0.5\text{cm}$.

The qualitative behavior of CPT-Ramsey signal shown in Figs 1-3 coincides with that in the case of monovelocity and narrow beam considered in detail in [17], [18]. However the quantitative differences are essential. Fig. 4 illustrates the influence of finite width of atomic beam and velocity straggling in it. We compare results of several calculations. First, it is coherent population trapping resonance for ideal case when all atoms have the same speed and cross the light beams with zero impact parameter. The other curves show the influence of one or another factor of deviation from the ideal case. The second and the third curves correspond to the case of single-velocity but wide atomic beam. The widths of the beams r_0 are 0.2cm and 0.5cm correspondingly. The fourth line depicts the resonance for narrow and multi-velocity beam. The last curve is calculated for wide beam with velocity spread.

The comparison shows that for light beams with Gaussian radius more or equal to 0.25cm the widening of atomic beam up to 0.2cm plays no role for monovelocity beam. The curves 1 and 2 in Fig. 4 cannot be distinguished as well as the curves 4 and 5. Some influence of the widening is seen when diameter of the beam becomes compare or greater than the light beams. For considered area of parameters the main influence on decreasing of the slope of the CPT-Ramsey resonance comes from atomic velocity spread. In the beam there are both slow and fast atoms. However the velocity distribution in considered specific Zeeman slower is characterized by some asymmetry (see [16]) and negative role of high-speed atoms dominates.

IV. CONCLUSION

In the present work, we have calculated the signal of coherent population trapping in a slow beam of rubidium 87

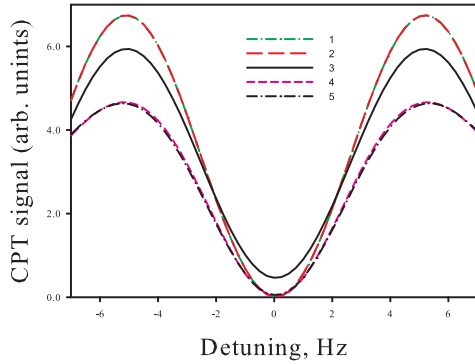


Fig. 4. Comparison of CPT signals for different parameters of the atomic beam. 1 - $r_0 = 0$, $\delta v = 0$; 2 - $r_0 = 0.2\text{cm}$, $\delta v = 0$; 3 - $r_0 = 0.5\text{cm}$, $\delta v = 0$; 4 - $r_0 = 0$, $\delta v = 1\text{m/s}$; 5 - $r_0 = 0.2\text{cm}$, $\delta v = 1\text{m/s}$. For all curves $B = 10\text{mGs}$, $w = 0.25\text{cm}$; $I = 20\mu\text{W/cm}^2$. Two pairs of the curves - 1 and 2, 4 and 5 are practically indistinguishable in chosen scale.

atoms, which is excited and detected by the Ramsey method. We have analyzed the influence of finite velocity spread in the beam, its final width and its angular divergence. Taking into account these factors we determine the value of magneto-static field which is optimal for observation CPT resonance and analyze dependence of the slope of this resonance on intensity of resonant light beams and on their width. We show that the amplitude of CPT resonance reaches a maximal values at relatively low intensities of electromagnetic fields ($I = 20 \div 30\mu\text{W/cm}^2$ depending on the beam aperture) and at accessible dimensions of light beams. For such an intensity the light shift is practically negligible. We observed also saturation behavior of the shape of the resonance depending on the aperture of the light beams. This effect can be observed already at the beam radii of about 0.5cm (depending on the intensity). A further increase in these parameter does not result in a higher resonance amplitude and weakly affects the resonance width.

We show that for this, the most appropriate area of parameters the spread of velocities and impact parameters of different atoms in the beam cause notable reduction of the signal amplitude. The main negative role belongs to residual spread in atomic velocities.

ACKNOWLEDGMENT

This work was supported by the Ministry of Education and Science of the Russian Federation (State Order No. 3.1446.2014/K).

REFERENCES

- [1] B. D. Agap'ev, M. B. Gornyj, B. G. Matisov, and Yu. V. Rozhdestvenskii, "Coherent population trapping in quantum systems," *Physics-Usp.* vol 36, pp. 763- 798, 1993.
- [2] E. Arimondo, "Coherent population trapping in laser spectroscopy," in *Progress in Optics*, ed. E. Wolf (Elsevier, North-Holland, 1996), Vol. XXXV, pp. 257-354, 1996.
- [3] J. Kitching, S. Knappe, and L. Hollberg, "Miniature vapor-cell atomic-frequency references," *Appl. Phys. Lett.* vol. 81, pp. 553-555, 2002.
- [4] S. Knappe, V. Shah, D. Peter, D. Schwindt, L. Hollberg, J. Kitching, L. Liew, and J. Moreland, "A microfabricated atomic clock," *Appl. Phys. Lett.* vol. 85, pp. 1460-1462, 2004.
- [5] J. Vanier, "Atomic clocks based on coherent population trapping: a review," *Appl. Phys. B* vol. 81, pp. 421-442, 2005.
- [6] N. F. Ramsey, "A Molecular Beam Resonance Method with Separated Oscillating Fields," *Phys. Rev.* vol. 78, pp. 695-699, 1950.
- [7] J.E. Thomas, P.R. Hemmer, S. Ezekiel, C.C. Leiby Jr., R.H. Picard, and C.R. Willis. Observation of Ramsey Fringes Using a Stimulated, Resonance Raman Transition in a Sodium Atomic Beam, *Phys. Rev. Lett.* vol. 48, pp. 867-870, 1982.
- [8] T. Zanon, S. Guerandel, E. de Clercq, D. Holleville, N. Dimarcq, and A. Clairon, High Contrast Ramsey Fringes with Coherent-Population-Trapping Pulses in a Double Lambda Atomic System, *Phys. Rev. Lett.* vol. 94, p. 193002, 2005.
- [9] G. Pati, K. Salit, R. Tripathi, and M. Shahriar, "Demonstration of Raman Ramsey fringes using time delayed optical pulses in rubidium vapor," *Opt. Commun.* vol. 281, 4676-4680, 2008.
- [10] C. Xi, Y. Guo-Qing, W. Jin, and Z. Ming-Sheng. Coherent Population Trapping-Ramsey Interference in Cold Atoms, *Chin. Phys. Lett.* vol.27, 113201, 2010.
- [11] F. X. Esnault, E. Blanshan, E. N. Ivanov, R. E. Scholten, J. Kitching and E.A. Donley, "Cold-atom double- Λ coherent population trapping clock," *Phys. Rev. A* vol. 88, pp. 042120, 1- ,(2013).
- [12] Y. Xiao, I. Novikova, D. F. Phillips, and R. L. Walsworth, "Repeated interaction model for diffusion-induced Ramsey narrowing," *Opt. Express* vol. 16, pp. 14128-14141, 2008.
- [13] E. Breschi, G. Kazakov, C. Schori et al., "Light effects in the atomic-motion-induced Ramsey narrowing of dark resonances in wall-coated cells," *Phys. Rev. A*, vol. 82, pp. 063810, 1-7, 2010.
- [14] G. Kazakov, A. Litvinov, and B. Matisov, "Narrowing of the coherent population trapping resonance under zone pumping in cells with different characteristics of the wall coating," *Quantum electronics*, vol. 42, pp. 185-188, 2012.
- [15] V. S. Zholnerov, A. K. Vershovskiy, and Yu. V. Rozhdestvenskiy, "Project of a Satellite Slow Beam Atomic Clock with CPT-Ramsey Registration," *Proc. EFTF*, pp. 320-322, 2014.
- [16] A.K. Vershovskiy, V.S. Zholnerov, Yu.V. Rozhdestvenskiy, O.P. Kharchev Patent RU 2490836 C1, dated 20.08.2013.
- [17] I.M. Sokolov, "Detection of a coherent population trapping resonance in a beam of 87Rb atoms by the Ramsey method," *Quantum Electronics*, vol. 45, pp. 947- 952, 2015.
- [18] I.M. Sokolov, "Ramsey resonance of coherent population trapping in slow rubidium bead," *Int. J. Mod. Phys. Conf. Ser.*, vol. 41, 1660145, 2016 [Online]. Available: <http://dx.doi.org/10.1142/S2010194516601459>
- [19] I. M. Sokolov, D. V. Kupriyanov, R. G. Olave, and M. D. Havey, "Light trapping in high-density ultracold atomic gases for quantum memory applications," *J. Mod. Opt.* vol. 57, pp. 1833-1841, 2010.
- [20] Ya. A. Fofanov, A. S.Kuraptsev, I. M. Sokolov, and M. D. Havey, "Dispersion of the dielectric permittivity of dense and cold atomic gases," *Phys. Rev. A*, vol. 84, pp. 053811, 1-9, 2011.
- [21] A. S. Kuraptsev and I. M. Sokolov, "Spontaneous decay of an atom excited in a dense and disordered atomic ensemble: Quantum microscopic approach," *Phys. Rev. A*, vol. 90, pp. 012511, 2014.
- [22] Y.-Y. Jau, E. Miron, A. B. Post, N. N. Kuzma, and W. Happer, "Push-Pull Optical Pumping of Pure Superposition States," *Phys. Rev. Lett.* vol. 93, p. 160802, 2004.
- [23] A. V. Taichenachev, V. I. Yudin, V. L. Velichansky, and S. A. Zibrov, "On the unique possibility of significantly increasing the contrast of dark resonances on the D1 line of 87Rb," *JETP Letters* vol. 82, pp. 398-403, 2005.
- [24] G. A. Kazakov, B. G. Matisov, I. E. Mazets, G. Mileti, and J. Delporte, "Pseudoresonance mechanism of all-optical frequency-standard operation," *Phys. Rev. A*. 72, 063408, 2005.

Stability and Durability of Resonant SAW Strain Sensors

Victor Kalinin, Arthur Leigh and Alexander Stopps

Transense Technologies plc
Bicester, OX25 3SX, UK
Email: victor.kalinin@transense.co.uk

Abstract— Resonant SAW strain sensing elements used in non-contact torque, force and vibration sensors are investigated from the point of view of their stability and durability. Results of fatigue testing of the SAW sensing elements bonded to metal shafts with a stiff adhesive are presented. They demonstrate the sensor durability and stability of the strain sensitivity up to 13 million strain cycles. Stability of the frequency of the SAW differential resonant sensing elements is also investigated demonstrating an estimated sensor zero drift of 0.8-0.15 microstrain per year.

Keywords—SAW resonator, SAW sensor, strain, durability, reliability

I. INTRODUCTION

SAW strain sensors have been developed and manufactured in low volumes for a number of applications, in particular for passive wireless sensing of torque, force, strain in automotive and power generation industries [1-3]. Acceptance of wireless SAW strain sensors for high volume applications depends on their proven stability and durability. A lot of research was done on this subject in the 70-80s with regard to SAW devices as frequency stabilizing elements in oscillators [4, 5]. However, there were no stability and durability data published for SAW strain sensors.

Resonant SAW strain sensors are subject to the same factors influencing their stability as the SAW resonators in oscillators: stress relaxation in the substrate and the Al film, Al film oxidation and adsorption/desorption of water molecules and other contaminants, etc. However, there is an extra factor that is specific to strain sensors, namely the state of the interface between the sensor's substrate and the part where the strain is measured. Very often this interface is formed by a thin layer of a stiff adhesive that can have a residual stress after curing. This stress relaxes with time causing the frequency shift. Besides, mechanical properties of the bond layer can change with time causing variation of the strain sensitivity. Finally, the bond layer can experience fatigue causing gradual or sudden delamination of the SAW substrate and failure of the sensor. The SAW substrate itself, being made of a brittle material, can also crack under a high strain.

The aim of this paper is to report some results of fatigue and accelerated aging tests for packaged and unpackaged resonant SAW strain sensors working at 428-437 MHz. The SAW sensing elements are described in Section II, results of the fatigue tests for unpackaged devices are presented in Section III

and Section IV is devoted to accelerated aging test for packaged devices.

II. SAW STRAIN SENSING ELEMENTS

The sensing elements are based on two or three one-port SAW resonators connected in parallel and fabricated on a Y+34° rotated cut quartz. Their layout is described in Section IIA in [2]. The unpackaged sensing elements are shown in Fig. 1. Both of them have two resonators positioned at $\approx 90^\circ$ to each other. The resonant frequencies of HFSAW are approximately $f_1 = 437$ MHz for M1 resonator and $f_2 = 435$ MHz for M2 resonator; for LFSAW they are $f_4 = 431$ MHz for M3 resonator and $f_5 = 429$ MHz for M4 resonator. They have been designed to measure shear strain generated on the shaft surface when torque is applied to the shaft. In this case, the sensing elements are bonded to the flat spot on the shaft so that the M1-M4 resonators are at $\pm 45^\circ$ to the shaft axis. The same sensing element can also be used to measure uniaxial strain. In this case, one of the resonators of each die should be positioned along the direction of the strain. The dimensions of the die are $4 \times 6 \times 0.35$ mm³.

The strain measurement is performed by measuring the difference frequencies $F_{m1} = f_1 - f_2$ and $F_{m2} = f_4 - f_5$ that depend linearly on strain with the sensitivity $S_m = 2.2-2.8$ kHz/ $\mu\epsilon$ to the principal component of shear strain. For this reason, we are mainly interested in stability of these difference frequencies and their strain sensitivities.

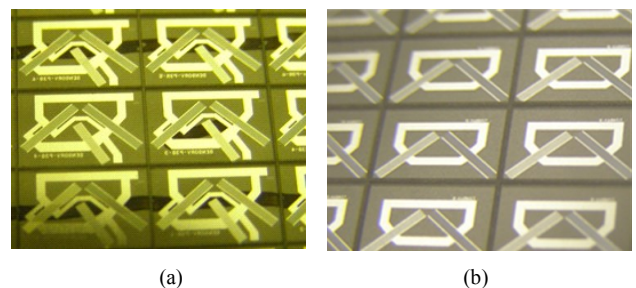


Fig. 1. Unpackaged HFSAW (a) and LFSAW (b) sensing elements.

Stability of the sensitivity and reliability of the bond between the SAW sensing element and the strained part can be evaluated in the course of the fatigue test that is done for the unpackaged sensing elements. However, a long term frequency stability or an accelerated aging test requires packaged sensing elements to minimize contamination of the die surface. They are shown in

Fig. 2c, d in [2]. The SAW die is bonded to the bottom of a steel can with glass fritted pins and hermetically sealed by a laser welded lid in an inert gas atmosphere.

III. FATIGUE TEST RESULTS

Initially, the test was performed for the unpackaged sensing elements bonded to a steel test bar (Fig. 2) and subjected to a sinusoidally varying shear strain at room temperature. The principal strain amplitude of $\pm 453\mu\epsilon$ significantly exceeded strain levels of 50-300 $\mu\epsilon$ typical for the majority of applications. Variation of the resonant frequencies with time was measured by means of a SAW reader [2] connected to pairs of HFSAW and LFSAW by wires.

Two pairs of HFSAW and LFSAW devices (#1 and #2) were bonded to the test bar using a cyanate ester adhesive with a bond line thickness of about 10 μm . They were subject to over 18 million strain cycles with a frequency of 3-5 Hz and the peak-to-peak resonant frequency amplitude was measured for M1 and M3 resonators after a number of cycles. Its variation with the number of cycles is presented in Fig. 3 that shows a stable sensitivity $S_m = 2.19\text{-}2.46 \text{ kHz}/\mu\epsilon$ at least up to 13400000 cycles far exceeding a typical number of test cycles in automotive industry. Some amplitude variation seen in the graph is due to inaccuracy of the peak measurement because of insufficient number of measurement points per period of strain. Later, the number of measurement points was increased that gave more consistent results.

The next test was performed for six pairs of the sensing elements (#1-6) bonded to the test bar with the Delomonopox® stiff epoxy based adhesive. The bond line thickness was 10-20 μm . For comparison purposes, the seventh pair was bonded with an ordinary epoxy adhesive. The bar completed 2.94 million cycles of strain at $\pm 453\mu\epsilon$. The results for the peak-to-peak frequency variation amplitude versus cycle number are shown in Fig. 4.

Practically all samples bonded with the stiff adhesive demonstrated a very stable strain sensitivity $S_m = 2.35\text{-}2.72 \text{ kHz}/\mu\epsilon$ at least up to 2.9 million cycles. An exclusion was LFSAW #2 that showed the drop of sensitivity by 4% that might be due to contamination of the bondline with a particle. At the same time, samples #7 bonded with the standard epoxy experienced a significant gradual reduction of the sensitivity



Fig. 2. Fatigue test rig.

starting from 300000 cycles. The strain sensitivity for them was also noticeably lower (1.9-2 $\text{kHz}/\mu\epsilon$) because of a lower stiffness and possibly thicker bondline of the standard epoxy. None of the samples #1-6 showed any signs of failure at this stage.

A number of safety critical applications require the sensor to survive a significant overload. From this point of view, it is important to know the maximum strain level that the bonded SAW sensing elements can withstand without delamination and cracking. The following overload test described in the Table 1 was performed for the same six pairs of HFSAW and LFSAW devices bonded with the Delomonopox® adhesive. Prior to the overload, the strain sensitivity was determined by applying sinusoidal strain of $\pm 292\mu\epsilon$. Then the sensors were subjected to the overload strain cycles in five stages and the sensitivity measurement was repeated after each stage.

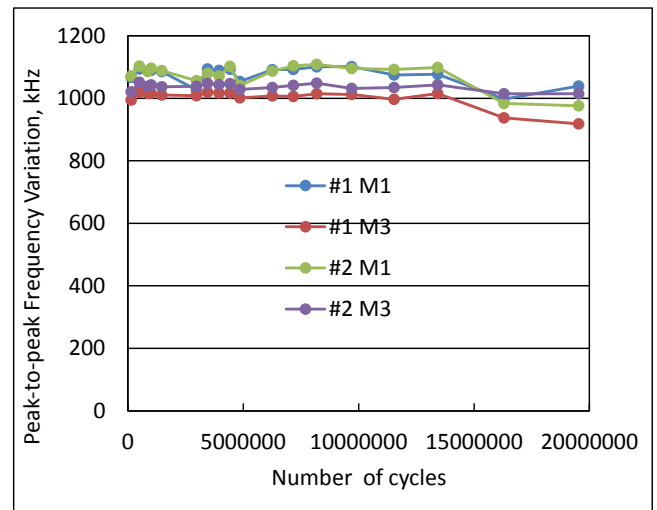


Fig. 3. Peak-to-peak amplitude of the resonant frequency variation with strain cycles for the samples bonded with the cyanate ester adhesive.

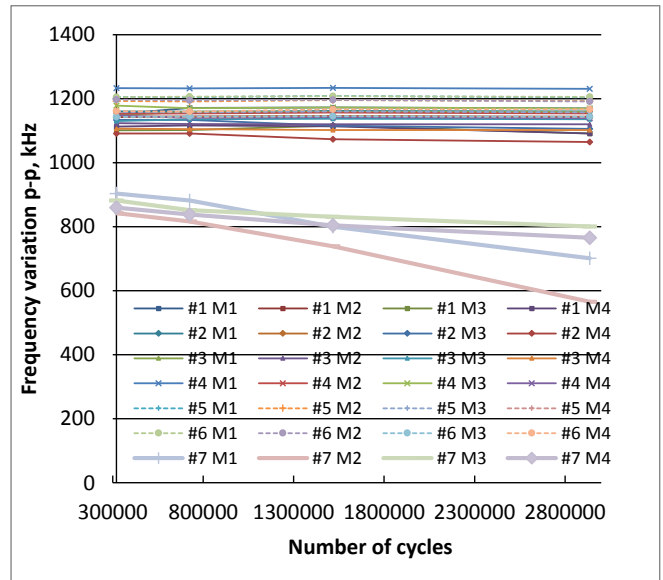


Fig. 4. Peak-to-peak amplitude of the resonant frequency variation with strain cycles for the samples bonded with the Delomonopox® and epoxy adhesives.

TABLE I. TABLE I. OVERLOAD TEST REGIME

Stage	1	2	3	4	5
Number of cycles	60	50	40	40	40
Peak strain, $\mu\epsilon$	875	1000	1163	1300	1450

Fig. 5 presents the variation of the strain sensitivity from stage to stage of the overload test (shown in red). Apart from the LFSAW #2 that demonstrated an abnormal behavior between 0.8 and 1.3 million cycles in the previous test, all the sensing elements started showing signs of bond failure within the stage 4 of the test corresponding to 1300 $\mu\epsilon$ overload. None of the sensing elements were cracked during the test. The common failure mode was delamination of the adhesive from the edges of the quartz substrates that can be seen in the photograph in Fig. 6. The results of the test show that the mechanical design of the sensor should avoid straining the SAW sensing elements above approximately 1200 $\mu\epsilon$ for the adhesive under consideration. For the 20-fold overload protection it would give approximately 54 dB dynamic range of the sensor provided the resolution of the reader is 300 Hz.

IV. ACCELERATED AGING TEST RESULTS

The aim of the test was to establish a long-term stability of the SAW strain sensor zero reading associated with the stability of the difference frequencies $F_{m1,2}$. As mentioned in the introduction, apart from a number of common causes of the SAW device aging, it depends on a gradual relaxation of the residual strain built into the bondline as a result of the SAW die bonding process. To investigate it, five SAW sensing elements were packaged into steel cans as described in Section II with the die bonded to the metal base of the package by the cyanate ester adhesive. Packages of the sensing elements #1 and #2 were attached to the steel test bar with the same adhesive while the other three packages remained unattached. Prior to the aging test, all sensing elements were subject to 10 thermal cycles from -40° to $+125^\circ\text{C}$ to stabilize the bondline properties [2]. The test was performed in the oven (Fig. 7) at the temperature $T = 125^\circ\text{C}$ for 1800 hours. Each resonant frequency was measured every 50

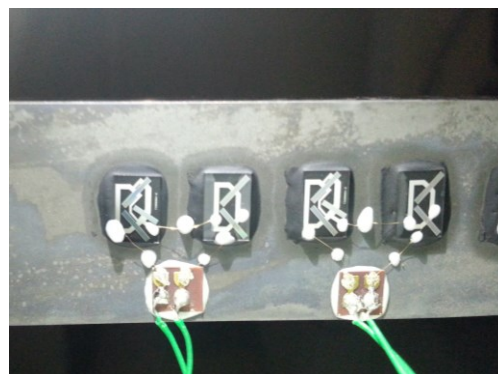


Fig. 6. Test samples after the stage 5 of the overload test. Lighter areas under the quartz substrates indicate areas of adhesion failure.

min by a SAW reader kept at a constant temperature of 39°C . To check stability of the reader, a periodic measurement of a reference frequency generated by a stable synthesizer was performed. The drift of these readings did not exceed 350 Hz. The measured resonant frequencies were adjusted in accordance with this drift.

Fig. 10 shows variation the resonant frequencies of M1 and M2 as well as their difference F_{m1} measured during the test after 20 hours of preliminary aging. The f_1 and f_2 curves have a number of abrupt jumps. One of them, at approximately 720 hours, happened because of the temperature instability of the oven due to an unexpected power cut. Most of other jumps happened simultaneously for a number of sensors so it is unlikely that they were caused by a sudden relaxation of the strain in the bondline. The most likely cause for these jumps is an instability of the oven temperature. The magnitude of the jumps is different for different sensor because the measurements for them were performed at different moments of time with an interval of 10 min.

Most of the time, the resonant frequencies of M1 and M2 resonators drift up and there is no significant difference between the character of the drift between the packages #1 and #2 bonded to the steel bar and the unbonded packages. The amount of drift from 7 ppm to 29 ppm is of the same order as the one reported in [6] for SAW delay lines mounted by epoxy within gold plated Kovar packages. Disregarding the abrupt jumps, the character of the drift is close to the one that is approximately described by a

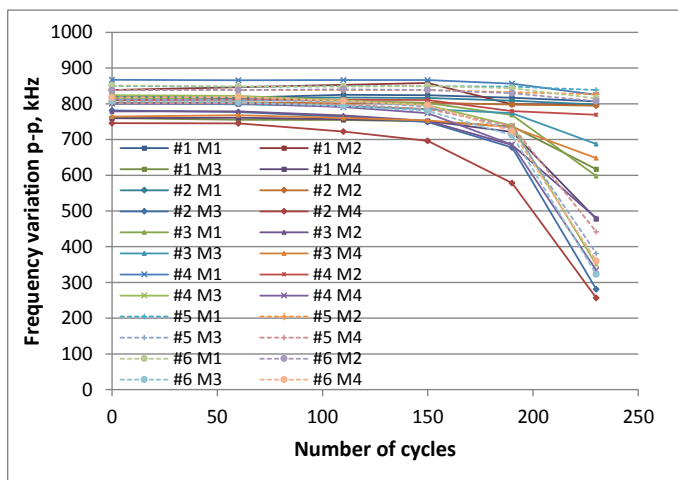


Fig. 5. Peak-to-peak amplitude of the resonant frequency variation with a $\pm 292\mu\epsilon$ strain cycle for the samples bonded with the Delomonopox® adhesives versus the number of the overload cycles.

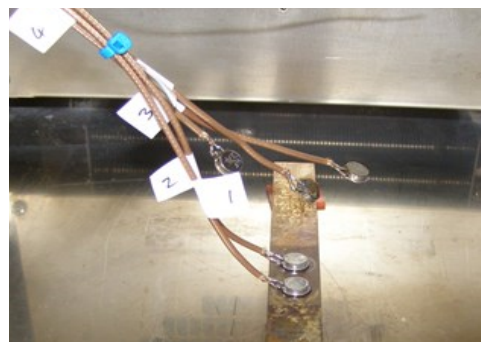


Fig. 7. Packaged sensing elements placed into the oven for the accelerated aging test.

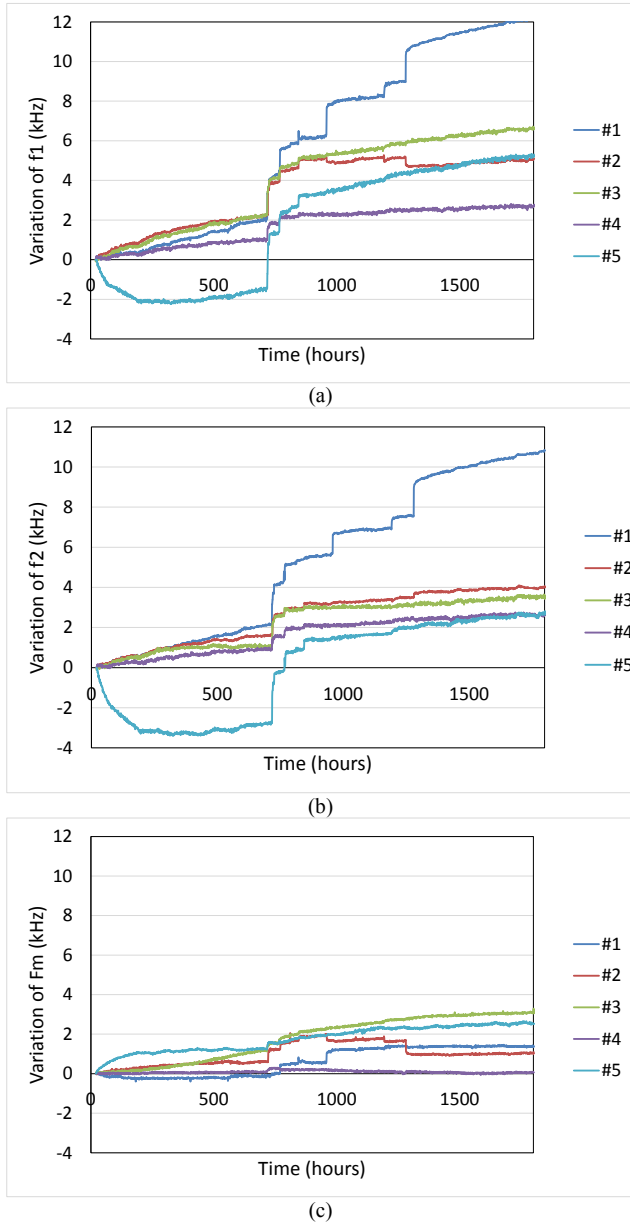


Fig. 10. Variation of the resonant frequencies of M1SAW (a), M2SAW (b) and their difference F_{m1} (c).

composite aging model [6]:

$$\Delta f/f = C \exp[-E/k(273+T)] \ln(1 + At) \quad (1)$$

where C is the aging constant, E is the activation energy, k is Boltzmann's constant, A is the relaxation constant and t is aging time. This model predicts the room temperature drift up to 4.1 ppm per year depending on what set of constants found in [6] is used. The drift of 0.1-0.5 ppm/year was reported for the all quartz packaged SAW resonator in [7], so the presence of the bond layer does affect the stability but the results obtained for the SAW strain sensing elements with the cyanate ester adhesive are quite acceptable.

The amount of the frequency drift and its character shown in Fig. 10a, b are similar for M1 and M2 resonators. As a result the drift for the difference frequency F_{m1} is significantly smaller, from 30 Hz to 3.1 kHz. If we take the worst case of 3.1 kHz drift and assume that the rate of the drift of 0.48 Hz/hour observed after 1800 hours remains constant for the rest of the year (in reality it will most likely be smaller) then the total drift of F_{m1} at 125°C will be around 6.4 kHz after the first year. Then, using (1), taking the lowest figure for the activation energy $E = 0.229$ eV from [6] and assuming that the temperature profile for an automotive application is 8 hours at 90°C and 12 hours at 40°C, the worst expected difference frequency drift is approximately 1.9 kHz after the first year. This corresponds to the sensor zero drift of about 0.76 $\mu\epsilon$ which is 0.25% FS if the full scale of the sensor is 300 $\mu\epsilon$. For a number of SAW devices, the measured activation energy is higher, up to $E = 0.541$ -0.655 eV [6]. In this case, the expected strain sensor zero drift after the first year is only about 0.21-0.14 microstrain.

V. CONCLUSIONS

Fatigue testing was performed at room temperature for unpackaged differential resonant SAW strain sensors bonded to a test bar by cyanate ester and stiff Delomonopox® adhesives by means of applying a periodic strain of $\pm 453 \mu\epsilon$. The strain sensitivity of the resonant frequency did not change after 13.4 million cycles for the cyanate ester and after 2.94 million cycles for the Delomonopox® adhesive. In the last case, it was shown that the SAW sensors and the bondline can withstand overload strain up to 1200 $\mu\epsilon$.

Accelerated aging of the packaged SAW strain sensors was performed for 1800 hours at +125°C. The maximum difference frequency drift for the sensors was 3.1 kHz. Using a composite aging model with the activation energy of 0.229-0.655 eV known from literature, the estimated zero drift of the strain sensor after the first year for a typical automotive application was 0.76-0.14 $\mu\epsilon$.

REFERENCES

- [1] U. Wolff, F. Schmidt, G. Scholl, V. Magory, "Radio Accessible SAW sensors for non-contact measurement of torque and temperature", Proc. 1996 IEEE Ultrason. Symp., pp. 359-362, 3-6 November 1996.
- [2] V. Kalinin, "Wireless physical SAW sensors for automotive applications", Proc. 2011 IEEE Int. Ultrason. Symp., pp. 212 - 221, 18-21 October 2011.
- [3] V. Kalinin, A. Leigh, A. Stopps, E. Artigao, "Resonant SAW torque sensor for wind turbines", Joint 2013 Int. Frequency Control Symp. and European Frequency and Time Forum, Prague, Check Republic, pp. 462-465, 21-25 July 2013.
- [4] D. T. Bell, "Aging process in SAW resonators", Proc. 1977 IEEE Int. Ultrason. Symp., Phoenix, Arizona, pp. 851-861, 26-28 October 1977.
- [5] R. B. Stokes, M. J. Delaney, "Aging mechanisms in SAW oscillators", Proc. 1983 IEEE Int. Ultrason. Symp., Atlanta, Georgia, pp. 247-256, October 31-November 2, 1983.
- [6] P. L. Scraff, M. B. Carey, J. E. Huff, "An aging model for surface acoustic wave devices", IEEE Trans. Ultrason., Ferroelectrics, and Freq. Control, vol. 40, No. 6, pp. 630-641, 1993.
- [7] T.E Parker, J. Callera, G. K. Montress, "A new all quartz package for SAW devices", Proc. 39th Annual Freq. Control Symp., pp. 519-525, 29-31 May 1985.

Extended Source Interferometry in the Compact Regime

Bruno Pelle, Gregory W. Hoth, Stefan Riedl, John Kitching, and Elizabeth A. Donley
 Time and Frequency Division
 National Institute of Standards and Technology
 Boulder, CO, USA
 bruno.pelle@nist.gov

Abstract—We present an atom interferometer based on an expanding cloud of laser-cooled atoms sensitive to rotations along two axes and acceleration along one axis in an effective volume of 1 cm^3 . We observed spatially resolved fringes created by the apparatus' rotation by imaging the expanding cloud after short free-fall durations. If the atom cloud does not start as a point source, a bias is introduced in the scale factor that differs from the simple point-source limit. We explored the scale factor deviation experimentally with different initial cloud sizes and present our understanding of this important systematic.

Keywords—Atomic gravimeter; atomic gyroscope; compact inertial sensor; Point Source Interferometry; scale factor bias.

I. INTRODUCTION

Atom interferometers driven by laser pulses [1, 2] have demonstrated their ability to realize absolute measurements of rotation and acceleration with state-of-the-art sensitivity [3], accuracy [4] and bias drift [5] compared to other technologies. So far these results have largely been implemented in laboratory-size experiments, but current efforts are underway to develop more compact instruments for in-field inertial navigation and geodesy [6-8]. Usually, counter-propagating atomic sources are required to decouple phase shifts induced by rotation and acceleration [3], and atom motion along at least two axes is required to determine all six acceleration and rotation components. These requirements imply complex, multi-axis geometries with multiple atom sources. To accomplish the decoupling of acceleration and rotation and provide a path to a complete six-axis inertial sensor with a single atomic source, we extend the Point Source Interferometry (PSI) technique, so far demonstrated in a 10-meter tower [9], to the compact regime.

II. POINT SOURCE INTERFEROMETRY

In our experiment, we use the usual Mach-Zehnder atom interferometer scheme where we first apply a Raman $\pi/2$ -pulse to induce a spatial separation of the atomic wavepackets *via* a momentum transfer on one arm of the interferometer. Next, a Raman π -pulse is applied, simultaneously reversing both the internal and external states of the wavepackets. Finally, the wavepackets recombine *via* a second Raman $\pi/2$ -pulse, and interfere when their final positions overlap. The laser phase of each pulse is imprinted on the atom phase, leading to a phase difference at the interferometer output [2, 3]

$$\Delta\Phi = \Delta\Phi_{\text{acc}} + \Delta\Phi_{\text{rot}} = \vec{k}_{\text{eff}} \cdot \vec{a}T^2 + 2\vec{\Omega} \cdot (\vec{k}_{\text{eff}} \times \vec{v})T^2, \quad (1)$$

which is reflected in the final atomic level populations. Here $\hbar\vec{k}_{\text{eff}}$ is the effective momentum transferred to the atom ($\sim 2\hbar\vec{k}_{\text{opt}}$, where \vec{k}_{opt} is the wavevector of the light), \vec{v} is the atom velocity, T is the interrogation time between two consecutive Raman pulses, and \vec{a} and $\vec{\Omega}$ are the apparatus acceleration and rotation. In PSI, we use the point-source approximation to describe the transverse atomic velocity $\vec{v}_{\text{trans}} = \vec{r}/2T$, with \vec{r} the final transverse atom position, and re-write the now spatially-dependent phase as:

$$\Delta\Phi(\vec{r}) = \vec{k}_{\text{eff}} \cdot \vec{a}T^2 + \vec{\Omega} \cdot (\vec{k}_{\text{eff}} \times \vec{r})T. \quad (2)$$

Since the cloud contains a range of initial velocities, a rotation of the apparatus will induce a phase gradient in the cloud; while an acceleration will change the overall phase. It

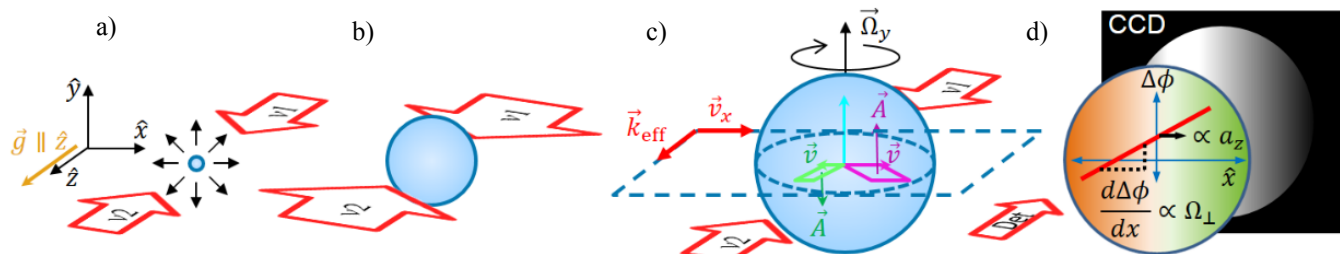


Fig. 1. The first three panels illustrate the Point Source Interferometry scheme with the expanding atomic cloud during a Mach-Zehnder sequence of Raman light pulses. The last panel represents the absorption detection and the extraction of the phase offset for acceleration and phase gradient for rotation.

follows that a spatially resolved measurement of the interferometer phase can determine both rotation and acceleration. The signal appears in the spatial distributions of the final populations of the hyperfine states $|F = 1\rangle$ and $|F = 2\rangle$ due to the perfect match introduced between the internal and external states during a stimulated Raman transition [1].

III. EXPERIMENTAL SET-UP

We realize a 3D magneto-optical trap (MOT) from a ^{87}Rb vapor inside a glass vacuum cell. With MOT beams having a radius at $1/e^2$ of 3.5 mm, we obtain 9×10^6 atoms at 5 μK with approximate Gaussian widths of $\sigma_x = 350 \mu\text{m}$ and $\sigma_y = 220 \mu\text{m}$ [10]. We then release the atoms from the trap and pump all the atoms in the $|F = 1, m_F = 0\rangle$ state to avoid sensitivity to stray magnetic fields to first order.

During the free fall, we apply the Mach-Zehnder sequence of light pulses. To split and recombine the interferometer arms, we use stimulated Raman transitions, in which two photon momenta are transferred to an atom while simultaneously changing its internal hyperfine state. The geometry of each Raman frequency component is described in Fig. 1 by the two red arrows in a counter-propagating configuration. To simulate the apparatus rotation, we tilt the retro-reflecting mirror of one of the Raman beams during the interferometer sequence [11].

We sketch the interferometric sequence in Fig. 1 with the first Raman $\pi/2$ -pulse (a), the Raman π -pulse (b), and the second Raman $\pi/2$ -pulse (c). Then the last panel (d) represents the absorption detection. The gravity \vec{g} is along \vec{z} but for simplicity the cloud's fall is not shown. The thermal expansion of the cloud leads to multiple interferometer trajectories in all the directions. Due to the scalar product in the rotation phase shift, the relevant trajectories are in the plane perpendicular to the rotation axis, *i.e.* (x,z) or (y,z) for a rotation axis $\vec{\Omega}_y$ or $\vec{\Omega}_x$ respectively. Those planes are determined by the effective momentum transferred to the atoms and the atom velocity perpendicular to both the rotation axis and the Raman axis. For each interfering atom, the area $\vec{A} = \hbar/m (\vec{k}_{\text{eff}} \times \vec{v})T^2$ enclosed by the two interferometer arms and therefore the rotation phase shift depend on the atom's initial velocity, as shown in Fig. 1 c). Then, in the point-source limit, the correlation between the atom's initial velocity and final position induces a phase gradient across the atomic cloud. We detect this phase gradient by imaging the populations in $|F = 2\rangle$ and in $|F = 1\rangle + |F = 2\rangle$ on a CCD. The CCD is located at the bottom of the glass cell, imaging the plane (x,y) , while the Raman beams are vertically aligned along \vec{z} .

Thus, with only one cold atom source, we measure two rotation axes perpendicular to the Raman beams' axis (\vec{x} and \vec{y}) through the phase gradient and one acceleration axis along the Raman axis (\vec{z}) through the phase offset. For an inertial sensor, if the apparatus rotations are not perpendicular to or if the apparatus acceleration is not collinear with the Raman beams' axis, the instrument will measure only the projection of the rotation or acceleration onto the principal axis defined by the Raman beams while we expect no blurring or any change in the fringe contrast.

An important feature in our compact device is the short free-fall duration during which we apply the interferometer sequence.

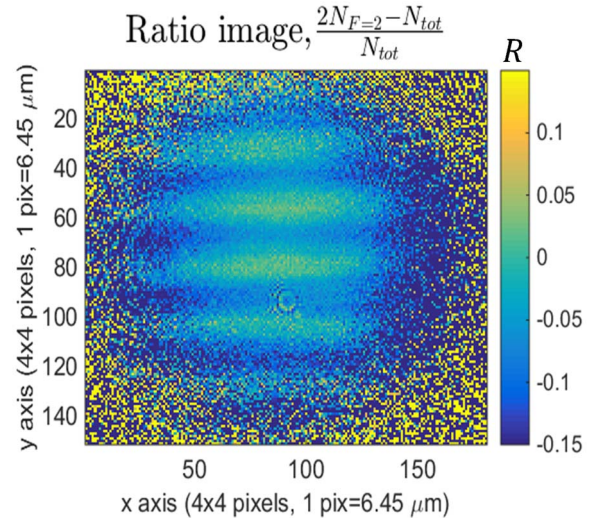


Fig. 2. Spatially resolved interference fringes induced by a rotation $\Omega = 136 \text{ mrad/s}$ around x for a total interrogation time $2T = 16 \text{ ms}$. The ratio image presented here is an average of 30 images and the contrast is 10%.

This constrains the maximum expansion factor, which is defined by the ratio of the initial cloud size to the final cloud size $\sigma_{\text{final}}/\sigma_{\text{initial}}$. In our experiment, the expansion factor is limited to about five at maximum. This expansion factor expresses the importance of the initial cloud size compared to the cloud temperature and the free-fall duration. When the expansion factor is small, the correlation between each atom's initial velocity and final position that leads to the spatial fringe pattern is blurred by the initial atomic cloud extension. We intuitively expect this blurring to cause a loss of contrast. Nonetheless, we also find an interferometer phase gradient \vec{k} that depends on the initial cloud's size, as described in the following.

IV. SPATIALLY RESOLVED FRINGES

Now, we describe the phase gradient extraction from state population images and the scale factor measurement to show that the phase gradient depends on the initial cloud's size.

A. Normalized images

The spatial distribution of atoms in each hyperfine state, $N_{F=1}$ and $N_{F=2}$, is determined from two absorption images: a first shadow image of the $|F = 2\rangle$ population and a second shadow image of the full population in both $|F = 1\rangle$ and $|F = 2\rangle$ states acquired after repumping the atoms in $|F = 1\rangle$ into the $|F = 2\rangle$ state. We plot in Fig. 2 the ratio image, defined by $R = (N_{F=2} - N_{F=1}) / (N_{F=1} + N_{F=2})$, which allows us to suppress the cloud shape, while keeping the rotation induced fringes visible. The contrast in Fig. 2 is twice the contrast in transition probability.

Although the fringes are clearly visible, a residual cloud shape is still present on the ratio images. It comes mainly from an unavoidable short delay between the images of the populations in $|F = 2\rangle$ and $|F = 1\rangle + |F = 2\rangle$, leading to different cloud sizes between these two images. The residual cloud shape prevents us from performing a simple sinusoidal fit to the fringe that would be independent of the cloud shape. This

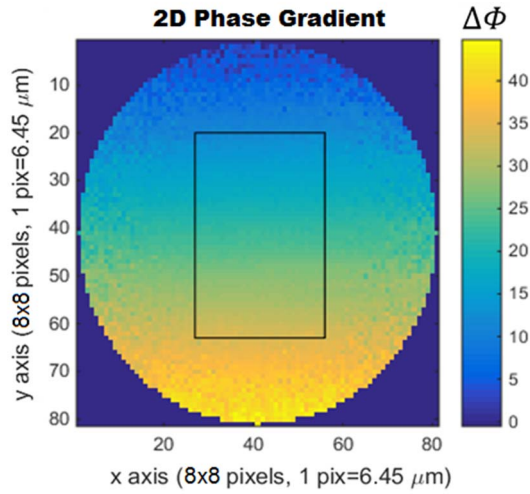


Fig. 3. Extracted phase gradient $k = 10.08 \pm 0.1$ rad/mm along y induced by a rotation of $\Omega = 171$ mrad/s around x for $2T = 16$ ms.

independence is important to avoid introducing a systematic error on the fringe period, which would result in a bias in the phase gradient extraction.

B. Phase gradient extraction

To extract the phase gradient in a model independent way, we take several ratio images with a different phase offset. We record a collection of images while the overall phase is scanned over several interferometer fringes. This is experimentally done by scanning the frequency ramp α applied between the two frequencies of the Raman transitions to compensate for gravity. The collection of ratio images allows us to plot for each pixel the measured transition probability as a function of the applied phase offset ($\vec{k}_{\text{eff}} \cdot \vec{a} - 2\pi\alpha$) and fit a sinusoid to it. From the fit parameters, we reconstruct a map of the interferometer phase as a function of position, as shown in Fig. 3. Finally, we fit a 2D plane to the central region indicated by the black rectangle in Fig. 3 to extract the measured phase gradients along x and y , which is dependent on the applied rotation's direction and amplitude.

C. Scale factor measurement

For the spatially-resolved measurement of the rotation, the scale factor is the proportionality constant linking the applied rotation and the measured fringe period, or phase gradient, and expressed as $F = k/\Omega$. In order to determine the scale factor, defined by the slope of k vs Ω , we measure the phase gradients k_x for different rotations Ω_y . By measuring the phase gradients for two different initial cloud sizes, $\sigma_x = 350$ μm and $\sigma_x = 720$ μm , we observe a strong effect of the finite cloud size on the scale factor for cases where the cloud size has only increased by an expansion factor of $\sigma_{\text{final}}/\sigma_{\text{initial}} \approx 3$ or 1.5 . As can be seen in Fig. 4, the scale factor changes by a factor of two between these two initial cloud sizes.

We have developed a model that takes into account the finite cloud size and predicts the scale factors with an extended

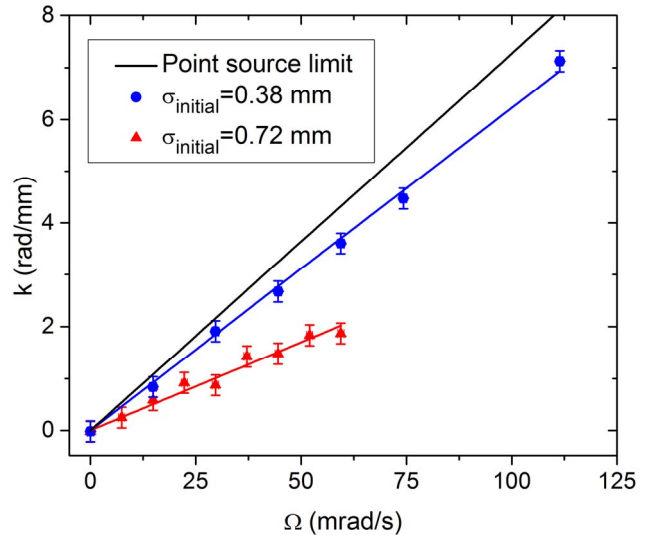


Fig. 4. Scale factor measurement k vs Ω for two different initial cloud sizes, and the theoretical point-source limit, for $2T = 16$ ms. k is measured along x , while Ω is rotated around y . Dotted lines are linear fits to data.

atomic source [12]. If the initial cloud is modeled with a spatial Gaussian distribution and a thermal distribution having a uniform temperature, the scale factor is described by

$$F = \frac{2T^2}{T_{\text{tot}}} k_{\text{eff}} \left(1 - \frac{\sigma_{\text{initial}}^2}{\sigma_{\text{final}}^2} \right), \quad (3)$$

where T_{tot} is the total free fall duration, and the final cloud's size depends on the initial cloud's size and temperature.

From this model, we see that in this short free-fall regime the extended source causes a large deviation on the scale factor from the point-source limit. Accurate determination of the scale factor and hence the rotation rate would therefore require the source phase-space density to be considered. More importantly, these observations imply that size and temperature fluctuations of the initial atom cloud also add to the gyroscope scale factor instability. In an inertial navigation system, the scale factor stability is a critical factor of the gyroscope performance.

V. CONCLUSION

In this paper, we have shown that spatially resolved fringes can be obtained in a compact regime, even if the expansion factor is lower than two. We measured rotations along two axes and acceleration along one axis with only one cold atom source. To measure all six inertial components, three pairs of Raman beams would be needed, one along each axis, leading to six measured phase gradients and three measured shifts, obtained sequentially. There is hence a redundancy in the rotation measurements, useful to compare absolute rotations or implement corrections on an axis-by-axis basis. We also showed that the scale factor is modified by the extension of the initial cloud for a low expansion factor, introducing a deviation from the point-source model initially developed to describe this interferometric scheme.

As a mid-term objective, we intend to address the performance limits of this interferometer with respect to sensitivity, dynamical range and scale-factor stability. We expect the upper limit of the rotation dynamic range to be determined by the atomic cloud’s initial size and the lower limit to be set by atomic shot noise. With a better signal-to-noise ratio, we should be able to measure the Earth’s rotation to characterize the gyroscope instability. This would allow us to also characterize the scale factor instability introduced by the finite-size effect with a cold-atom source provided by a MOT.

We hope ultimately to develop a compact inertial sensor that would complement other sensing technologies with the potential stability provided by atoms.

ACKNOWLEDGMENT

This work is funded by NIST, which is a U.S. government agency. The manuscript is not subject to copyright.

REFERENCES

- [1] C. J. Bordé, “Atomic interferometry with internal state labelling,” *Physics Letters A*, vol. 140, no. 1, pp. 10 – 12 (1989).
- [2] M. A. Kasevich and S. Chu, “Atomic interferometry using stimulated Raman transitions,” *Phys. Rev. Lett.*, vol. 67, no. 2, pp. 181 – 184 (1991).
- [3] T. L. Gustavson, P. Bouyer, and M. A. Kasevich, “Precision rotation measurements with an atom interferometer gyroscope,” *Phys. Rev. Lett.*, vol. 78, no. 11, pp. 2046 – 2049 (1997).
- [4] A. Peters, K. Chung, and S. Chu, “High-precision gravity measurements using atom interferometry,” *Metrologia*, no. 1, vol. 38, pp. 25 – 61 (2001).
- [5] D. S. Durfee, Y. K. Shaham, and M. A. Kasevich, “Long-Term Stability of an Area-Reversible Atom-Interferometer Sagnac Gyroscope,” *Phys. Rev. Lett.*, vol. 97, no. 24, pp. 240801 (2006).
- [6] R. Geiger, V. Ménotet, G. Stern, N. Zahzam, P. Cheinet, B. Battelier, A. Villing, F. Moron, M. Lours, Y. Bidel, A. Bresson, A. Landragin, and Ph. Bouyer, “Detecting inertial effects with airborne matter-wave interferometry,” *Nature Commun.*, no. 2, pp. 474 (2011).
- [7] M. Hauth, C. Freier, V. Schkolnik, A. Senger, M. Schmidt, and A. Peters, “First gravity measurements using the mobile atom interferometer GAIN,” *Applied Physics B*, vol. 113, no. 1, pp. 49 – 55 (2013).
- [8] T. Farah, C. Guerlin, A. Landragin, Ph. Bouyer, S. Gaffet, F. Pereira Dos Santos, S. Merlet, “Underground operation at best sensitivity of the mobile LNE-SYRTE cold atom gravimeter,” *GyroscoPy and Navigation*, vol. 5, no. 4, pp. 266 – 274 (2014).
- [9] S. M. Dickerson, J. M. Hogan, A. Sugarbaker, D. M. S. Johnson, and M. A. Kasevich, “Multiaxis Inertial Sensing with Long-Time Point Source Atom Interferometry,” *Phys. Rev. Lett.*, vol. 111, no. 8, pp. 083001 (2013).
- [10] G. W. Hoth, E. A. Donley, and J. Kitching, “Atom number in magneto-optic traps with millimeter scale laser beams,” *Optics Letters*, vol. 38, no. 5, pp. 661 – 663 (2013).
- [11] S.-Y. Lan, P.-C. Kuan, B. Estey, P. Haslinger, and H. Müller, “Influence of the coriolis force in atom interferometry,” *Phys. Rev. Lett.*, vol. 108 pp. 090402 (2012).
- [12] G. Hoth, B. Pelle, S. Riedl, J. Kitching, and E. A. Donley, in preparation.

The NAC – A Miniature CPT Rubidium Clock

Avinoam Stern, Benny Levy, Chagai Levy, Uriel Arad, Yefim Barash, Rony Mann, Alex Gorelik

AccuBeat Ltd, Jerusalem, 91450 Israel

Email: stern@accubeat.co.il

Abstract— Here we report of the design and characterization of a miniaturized Rubidium Frequency Standard named NAC1 (Nano Atomic Clock 1), now commercially available. Recently, the introduction of the effect of coherent population trapping (CPT) has led to a substantial reduction in power and size of commercial atomic frequency standards. Here, utilizing this effect in a traditional glass technology, we are able to introduce a compact and low power frequency standard.

I. INTRODUCTION

This paper reports of the design and characterization of a miniaturized Rubidium Frequency Standard named NAC1 (Nano Atomic Clock 1), based on the effect of coherent population trapping (CPT).

Recently, the introduction of the effect of coherent population trapping (CPT) has led to a substantial reduction in power and size of commercial atomic frequency standards. The CPT effect renders a narrow transparency window in the transmission spectrum of an atomic vapor cell which can be used as the clock signal of an atomic standard. The CPT is accomplished by means of two laser radiation fields applied in a so-called Λ scheme shown in Fig. 1. In the case of alkali atoms, the fields are applied to atoms in resonance with the transitions between the two hyperfine levels of the $S_{1/2}$ ground state (levels μ, μ') and one of the P-state hyperfine levels (level m). Due to inherent physical quantum properties, interference appears in the excitation process, coherence is created in the ground state, and the atoms are placed in a non-absorbing state called a ‘dark state’. This phenomenon was first reported 1976 by Alzetta et al. [1]. Later in 2004 a pioneer work at NIST introduced for the first time the so called

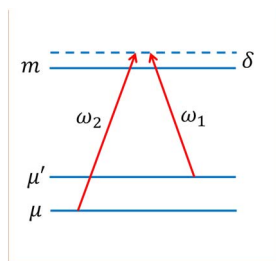


Fig. 1: Λ type system with two ground levels, μ, μ' and an excited level m , in the presence of two coherent radiation fields at angular frequencies ω_1, ω_2 . δ is the detuning.



Fig. 2: Photograph of NAC1 with the dimensions of $41 \times 35 \times 22 \text{mm}^3$ and power consumption of 1.2W.

“Chip-Scale-Atomic-Clock” (CSAC) with a 10mm^3 Physics-Package using MEMS technology [2]. A comprehensive review of CPT atomic clocks is given in [3].

Our design which is reported here utilizes a traditional glass technology instead of MEMS for reasons detailed below, nevertheless able to introduce a compact and low power atomic frequency standard.

II. NAC1 KEY CHARACTERISTICS

The key characteristics of NAC1 are summarized in Table 1. The unit has dimensions of $41 \times 35 \times 22 \text{mm}^3$ and its power consumption is 1.2W. It outputs 10MHz and 1PPS. It can be disciplined to a 1PPS reference as explained below. In the free-running mode it demonstrates a frequency stability (ADEV) of $8 \cdot 10^{-12}$ at 1000s averaging time, and an aging (drift) of $3 \cdot 10^{-10}$ per month.

Table 1

NAC1 Key Characteristics	
Parameter	Characteristic
Output Frequency	10MHz
Dimensions	$41 \times 35 \times 22 \text{mm}^3$
Power Consumption	1.2W
ADEV	$2\text{E-}10$ @ 1 s $8\text{E-}12$ @ 1000s
Phase Noise	-150dBc Floor
Temp. Coefficient and Temp Range	$\pm 1\text{E-}9$ over -20°C to 65°C
Aging	$3\text{E-}10/\text{month}$
Warmup	100s to lock
1 PPS Disciplining	$\pm 100\text{ns}$

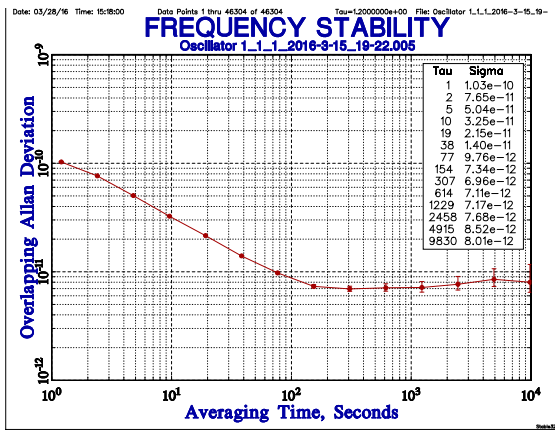


Fig. 3: Measured ADEV (example).

An ADEV characterization of a typical unit at a stable room temperature is shown in Fig. 3. A flicker floor starts at about 200s up to 10,000s.

III. DESIGN

A. The Control Loops

NAC1 uses 5 interrelated loops for controlling: (a) the clock frequency (the Main Loop), (b) the laser wavelength, (c) the RF power, (d) the laser temperature and (e) the cell temperature. We eliminate the use of temperature sensors, by inferring the temperature directly from the atomic vapor density. A 6th loop (f) is used for disciplining the clock to an external 1PPS. The loops operate in a time division multiplexing scheme with three states allocated for each loop thereby achieving a noise reduction.

The Main loop operates as follows. First, a fractional PLL Synthesizer is used to lock a 10MHz TCXO to a 3.4GHz VCO. Next, the VCO modulates the current of a VCSEL laser diode which operates at D1 line (~795nm), thereby producing several sidebands separated by the VCO output frequency as shown in Fig. 7a below. The first two of coherent sidebands excite the Λ transitions. When the two sidebands separation equals the Rubidium “clock frequency” a peak occurs in the vapor transmission. The transmission peak is then used to lock the

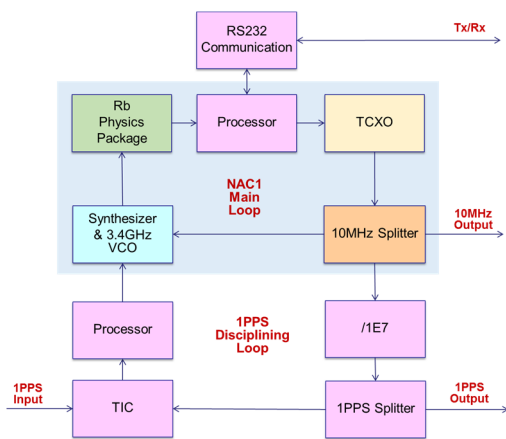


Fig. 4: Block diagram of NAC1 depicting the Main Loop and the 1PPS disciplining loop

TCXO to the CPT resonance line (the “clock transition”).

The 1PPS disciplining loop is a digital PLL loop that compares the 1PPS input to an internal 1PPS, that is derived from the 10MHz output of the TCXO. The timing error between the 1PPS signals is measured by a high resolution Time Interval Counter (TIC) and is sent to the processor. The processor then calculates and sends a correction message to the synthesizer thereby closing the disciplining loop. A block diagram of the main loop (1st) and the 1PPS disciplining loop (6th) is provided in Fig. 4. The main loop operates with short time constant (below 1s), while the disciplining loop works with long time constant (hundreds seconds). The main loop and the disciplining loop combine the short-term-stability of the TCXO with the medium-term-stability provided by the atoms, and the long-term-stability of the 1PPS reference (e.g., from GPS). The disciplining loop synchronizes the clock frequency (10MHz) and synchronized the clock timing (1PPS) to the reference 1PPS input. When the reference is disconnected or lost, NAC1 goes to a Holdover, free-run, mode maintaining accurate frequency and timing as dictated by its own stability.

B. The Physics Package

The Physics Package design comprises a VCSEL diode laser, a quarter wave-plate, a Rubidium vapor cell, a photo diode, C-field coil and a magnetic shield. The VCSEL is housed in a PLCC package.

The Rubidium vapor cell is made of a miniature glass ball coated with a transparent resistive layer which allows for direct heating. We have chosen to use a traditional glass cell technology which has been proven in Rubidium clocks for years to ensure high reliability and to minimize risks. For the similar reason we use Rubidium rather than Cesium due to the long Rubidium heritage in vapor cell atomic clocks.

IV. STABILITY FACTORS

A. Short, Medium and Long Term Stability

The key factors that determine the stability of a vapor cell atomic clock can be summarized as follows:

- **Short Term Stability:**
Factors that determine the short-term-stability are: the atomic transition linewidth, the detection S/N, the light (laser) noise, the vapor pressure and the gas pressure
- **Medium Term Stability:**
Factors that determine the medium-term-stability are: the thermal stability of the cell, the thermal stability of the light source, the cell gas mixture, light-shift effects, and magnetic effects from heating currents and residuals
- **Long Term Stability (Aging):**
Factors that determine the short term stability are: the Rubidium interactions with residual impurities, the Rubidium metal diffusion and migration and the stability of buffer gas mixture in the cell

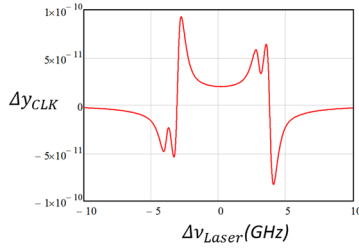


Fig. 5: Calculated Light-Shift, Δy_{CLK} , for a monochromatic laser beam of $1\mu\text{W}/\text{cm}^2$ detuned from D1 by $\Delta\nu_{Laser}$

A careful analysis was performed for all these factors, and was implemented in the design and in the adjustments of the relevant parameters. Here we focus on the light-shift only which is one of the key parameters that determine the stability.

B. Light Shift Analysis

The so called ‘‘light-shift’’ is the shift that occurs in the atomic energy levels due to the presence of the interrogating laser light and as a result shifts clock frequency. The effect of the light shift was studied in several publications, e.g., [4]. However, we found that the analysis in these publications is insufficient to deal with some actual issues and redone the following analysis aiming to deal with the issues we found.

A schematic diagram of the ^{87}Rb D1 line levels is shown in Fig. 5. We have four transitions between the two low hyperfine ground levels μ and μ' and the upper excited levels at m and m' . The Λ -type system occurs between each of the upper levels to the two ground levels μ and μ' . Suppose we have a monochromatic laser light with angular frequency ω_L , then each of the four transitions $a \leftrightarrow b$ with $a = \mu, \mu'$ and $b = m, m'$ shall contribute to the light-shift even if not on resonance with ω_L .

The light shift due to a monochromatic radiation with angular frequency ω_L is given by the following formula [5]

$$\Delta\omega_a(ba) = \frac{|\Omega_R(ba)|^2}{4} \int_{-\infty}^{\infty} \frac{\omega_L - \mathbf{k} \cdot \mathbf{v} - \omega_{ba}}{(\omega_L - \mathbf{k} \cdot \mathbf{v} - \omega_{ba})^2 + \left(\frac{\Gamma_{ba}}{2}\right)^2} p(v) dv \quad (1)$$

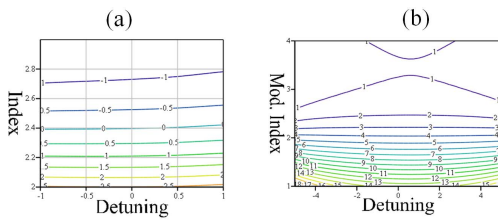


Fig. 6: Light shift maps ($\delta\nu$, θ) in units $[1\text{E-}12/(1\mu\text{W}/\text{cm}^2)]$, illustrating the effect of pure and mixed modulation. Detuning scale is in units $[325\text{MHz}]$. (a) Pure FM. (b) Mixed FM-IM. LS is calculated as a sum of contributions from the 4 optical D1 transitions, and a sum over the central line and 8 sidebands.

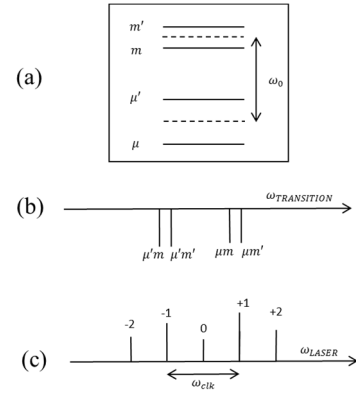


Fig. 7: a) Schematic levels diagram for the ^{87}Rb D1 transition with two ground states and two excited states. (b1) Spectrum of current modulated laser showing the first two sidebands. Asymmetry and non-nulling of the central line occurs with mixed FM-IM. (b2) Absorption spectrum of the D1 lines. (c) Calculated Light shift for a monochromatic laser light, summing up contributions from the four Doppler broadened D1 transitions,

In (1) $\Omega_R(ba)$ is the Rabi frequency related to the transition ab where $a = \mu, \mu'$ and m, m' . $\mathbf{k} \cdot \mathbf{v}$ is the Doppler shift, Γ_{ba} is the decay rate due to collisions and $p(v)$ is the velocities distribution. As mentioned in [4] the Doppler broadening is around 500MHz while collisions with the buffer gas broadened the optical linewidth by several hundred MHz, therefore [4] uses an effective Γ^* with no integral. Here however we have performed the integral using numerical methods and approximations and the result is presented in Fig. 5. Now, the modulated laser light contains the central line and sidebands as shown schematically in Fig. 7. The sidebands are separated by half the ‘‘clock transition’’ frequency at $\sim 3.4\text{GHz}$. The first two sidebands side bands, +1 and -1, are those that interact with the atoms to produce the CPT signals. As can be seen from the plot in Fig. 5, if the central line (0) does not diminish it can produce a substantial light-shift, whereas the two sidebands, (+1 and -1) opposite each other and canceled out, provided they are equal in magnitude. In practice, both conditions are not fully met due the fact that modulating the laser light produces both frequency modulation (FM) and intensity modulation (IM). As a result even if first Bessel $J(0)$ goes to zero (at modulation index of 2.4) the central line does not vanish and produces light shift. Furthermore, intensity modulation causes asymmetrical modulation with light-shift contributions from the first two sidebands as well.

We have performed an analysis for the case of pure FM and mixed FM and IM, summing over the central line and up to 8 sidebands. Results are shown in **Error! Reference source not found.** which compares between the case of pure FM modulation and the case of mixed FM-IM modulation. As expected for the case of pure FM modulation, the light shift diminishes at modulation index of 2.4 and the dependency on the detuning is very small.

The analysis shows that the light-shift effect is manifested through three parameters – the modulation index, the light

intensity and the wavelength detuning. The light shift analysis was used to aid the design in order to minimize the clock sensitivities to the various parameters.

V. CONCLUSION

We presented a brief description and analysis of a miniature atomic clock named NAC1 which is based on the CPT phenomenon in Rubidium. The key characteristics were reported in Table 1. NAC1 is now commercially available and we are working on a next generation, NAC2 aiming to reduce the power consumption to around 0.5W.

REFERENCES

- [1] G. Alzetta, A. Gozzini, M. Moi, G. Orriols, *Nuovo Cimento B* 36, 5 (1976)
- [2] Knappe, S. et al., A microfabricated atomic clock, *Applied Physics Letters*, vol. 85, No. 9, pp. 1460-1462 Aug. 30, 2004
- [3] J. Vanier, Atomic clocks based on coherent population trapping: a review, *Appl. Phys. B* 81, 421–442 (2005)
- [4] Filippo Levi et al., The Light Shift Effect in the Coherent Population Trapping Cesium Maser, *IEEE Transactions on Ultrasonics, Ferroelectrics, and Frequency control*, vol. 47, no. 2, march 2000
- [5] J. Vanier, C. Audoin, *The Quantum Physics of Atomic Frequency Standards*, pp 550, A. Hilgar, 1989

An Ultra Stable Oscillator for the 3GM Experiment of the JUICE Mission

Aviv Shapira, Avinoam Stern, Shemi Prazot, Rony Mann, Yefim Barash,
Edoardo Detoma¹ and Benny Levy

AccuBeat Ltd, Jerusalem, 91450 Israel

Email: stern@accubeat.co.il

Abstract—An Ultra Stable Oscillator is being developed by AccuBeat (named USO) for the Gravity and Geophysics of Jupiter and the Galilean Moons (3GM) radio occultation experiment of the ESA JUICE mission. This paper reviews the oscillator design and the critical issues to be tackled. The USO is a compact 15x13x10cm³ oscillator, based on a quartz crystal resonator and highly stable double oven. A Partial Engineering Model of (PEM) was built and tested in thermal vacuum. The PEM with 5MHz output has demonstrated a frequency stability below 2E-13 for a at averaging times of 1s to 1000s, thus meeting the requirements for technology readiness level 5 (TRL 5), according to the ECSS.

Keywords—Ultra-Stable-Oscillator, USO, USO, JUICE, 3GM

I. INTRODUCTION

An Ultra Stable Oscillator is being developed by AccuBeat (named USO) for the Gravity and Geophysics of Jupiter and the Galilean Moons (3GM) radio occultation experiment [1] of the ESA's Jupiter-Icy-moons-Explorer (JUICE) mission [2]. The JUICE is ESA's prestigious and largest mission aiming to explore the gas giant Jupiter, its icy moons Ganymede, Europa and Calisto, the Jovian rings and Io and other satellites. Launch is planned for 2022, followed by 8 years cruise phase and 3 years of observations in the Jovian system (2030 to 2033). The spacecraft payload includes 11 instruments with total mass of above 100kg. The instruments for the 3GM experiment include

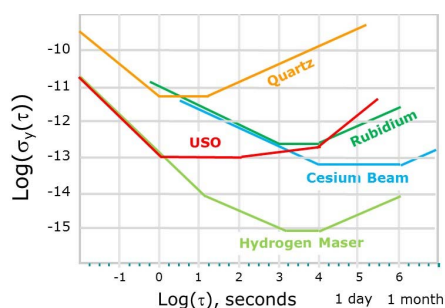


Fig. 2. Short-Term-Stability of a USO vs. some commercial quartz resonators and some commercial atomic clocks. $\sigma_y(\tau)$ is the Allan-Deviation which characterizes the stability of the fractional frequency, y , as a function of the averaging time, τ .



Fig. 1. Picture of USO, an Ultra-Stable-Oscillator for JUICE, measures 15x13x10 cm³

the USO provided by AccuBeat and a Ka band transponder provided by Thales-Alenia. The USO shall provide a highly stable reference signal for the one way (space to ground) radio link in X and Ka band to investigate the structure of the neutral atmospheres and ionospheres of Jupiter and its moons. The 3GM also aims to use radio tracking from ground to map the gravity fields of Jupiter's icy moons, and to reveal internal oceans on two of them.

The USO is a high-precision ultra-stable oscillator, which is based on quartz resonator with double oven technology. The USO exhibits an outstanding stability in the short-term which puts him in a competing position with reference to conventional quartz crystal resonator and some commercial atomic clocks (see Fig. 2), and makes it attractive solution for space applications considering its size and weight. Ultra-Stable-Oscillators (USO's) were used in several space missions since 1975; these include Voyager and Galileo (1975), Mars Observer (1987), Cassini (1993) and Pluto (1994) [3].

In the following sections we review the USO general design and discuss critical issues. We analyze the oscillator design using the Leeson model which provides the transfer function of the sustaining amplifier noise to the oscillator output noise. A key issue is the temperature stabilization of the crystal resonator and its sustaining electronics. We describe the use a double oven design to achieve a very high temperature stability at the relevant time constants of 1 to 1000s. We review the key environmental space requirements which are operation under thermal vacuum, irradiation at the level of 50krad, and hardened structure to

¹ Consultant

withstand vibrations and shock during launch. Analysis and simulations that were performed to verify meeting these requirements are also reviewed.

II. REQUIREMENTS

The key requirements which are dictated by the 3GM experiment and other JUICE instruments are summarized in Table 1. The requirement for short-term-stability is derived from the occultation experiment where the spacecraft transmits radio waves toward a tracking station on the earth while going behind the planet’s ionosphere and neutral atmosphere. This causes bending, attenuation and scintillation of the radio waves and yielding vertical profiles of the refractive index and absorption coefficient, temperature, pressure, neutral density and electrons density profiles. During the occultation a very high frequency stability is needed which defines the ADEV requirements and requires the use of an Ultra-Stable-Oscillator.

The magnetic field sensitivity requirement was determined with reference to the variation of the Jupiter magnetic field during a radio occultation. The later was evaluated and its effects on the oscillator stability have been assessed [4].

TABLE I.

USO for JUICE 3GM - Key Requirements/Challenges	
Parameter	Requirement
Output Frequency	57.5185MHz
Short-Term-Stability (Allan Deviation)	5E-13 @ averaging time 1s 5E-13 @ averaging time 10s 5E-13 @ averaging time 100s 6E-13 @ averaging time 1000s
Integrated Phase Noise	< -73dBc over 10Hz to 100kHz carrier offset
Operating Temperature	-20°C to +50°C
Sensitivity to Temperature	2E-12/°C
Aging	7e-11/day
Sensitivity to Magnetic Field	1E-10/gauss
Radiation	50kRad
Vacuum	<1E-5 torr
Structural	Survives launch phase (harsh shock & vibrations) without degradation
Size	15x13x10 cm ³
Weight	1700 gm
Power Consumption	3.84W

III. DESIGN

The USO design is briefly described in the following paragraphs.

A. General Block Diagram

A general block diagram is shown in Fig. 3. The USO is based on a 4.793MHz quartz crystal oscillator which is multiplied by 12 to obtain the required output at 57.5185MHz. The system comprises a quartz crystal resonator, a sustaining

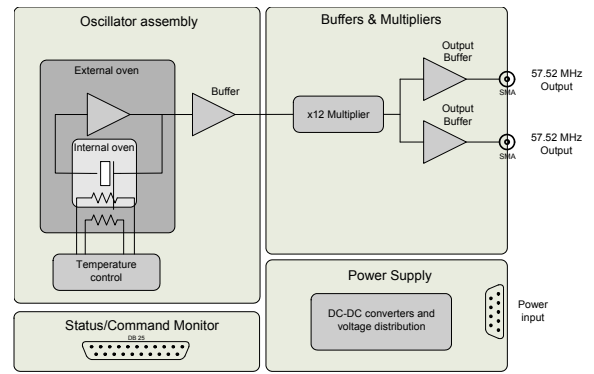


Fig. 3. USO General Block Diagram. It comprises a quartz crystal resonator, a sustaining oscillator circuitry, frequency multiplier, buffers double oven, temperature control circuits and power supply

oscillator circuitry, a frequency multiplier, buffers double oven, temperature control circuits and power supply.

B. Mechanical and Structural Design

The USO mechanical design is described briefly in this section. As shown in Fig. 4 the main construction is made of a single machined aluminum skeleton with machined compartments (cavities) that house the various subassemblies and boards. Each compartment has a screwed cover plate that when opened allows easy access to the housed board or subassembly within. Electrical connections between the compartments are made using feedthrough pins and flex-board wiring. The compartment are designed for EMI isolation. Small holes are made to enable the evacuation the inner spaces during the launch phase and during the tests which are performed under vacuum.

There are 5 compartments:

- Main central compartment. It houses the external and the internal ovens, the resonator, the sustaining oscillator circuitry and part of the temperature control circuitry

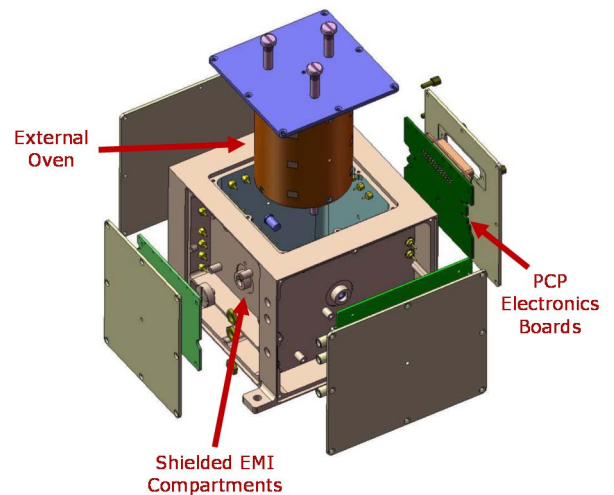


Fig. 4. USO General View of the Mechanical Design. The Internal Oven assembly (not visible) is housed inside the External Oven

- Temperature Control. Houses the temperature control board
- Multiplier: houses the multiplier and buffers
- Power Supply: houses the power supply
- Connections: used for connections wiring

Mechanical supports to the various parts are provided by solid rods made of aluminum, plastic materials and rubbers.

A structural analysis to verify meeting the shock and vibrations requirements was performed using a finite elements simulator.

C. Oscillator Design

The oscillator circuit design is using a topology allowing the crystal resonator to maintain a high loaded-Q. It includes a low flicker noise sustaining amplifier and a low noise limiting and gain control circuitry. For the analysis of the oscillator design refer to section 4 (MODELS AND ANALYSIS).

D. The Resonator

The resonator is an SC-Cut 3rd overtone quartz crystal resonator. For the PEM we have used a 5MHz resonator, however in the next EM phase a 4.793MHz shall be used. Resonators were purchased from 3 suppliers, tested and characterized for internal noise at the FEMTO-ST Institute, Besancon. The phase-noise system uses the carrier suppression technique [7]. Tests results are presented in table 2. In the majority of cases the resonator Allan Deviation (ADEV) flicker floor is in E-14 range, thus presents no issue with meeting the ADEV requirements which are in the E-13 range. This is indeed confirmed with the PEM results reported below using a resonator of manufacturer A.

TABLE II.

Resonator Noise Characterization		
Manufacturer	Resonator #	Flicker floor ADEV
A	3	4.8E-14
A	4	1.3E-13
A	5	6.0E-14
B	1	8.1E-14
B	2	2.1E-13
B	1	6.5E-14

E. Double Oven

The USO uses a double oven design to stabilize the temperature of the crystal resonator and the critical electronics circuitry. Traditional designs of USO's use an evacuated glass Dewar for the thermal isolation of the ovens. Since, of course, vacuum at the spacecraft is available at acceptable level for thermal isolation, we have taken an alternative approach without a glass Dewar. Instead the double oven design uses aluminum envelopes for the ovens (internal and external) and evacuated space surrounding and in between the oven serves for the thermal isolation. Surfaces are polished for low thermal emissivity. Structural supports are provided by plastic spacers and rubbers for absorbing tolerances and shocks.

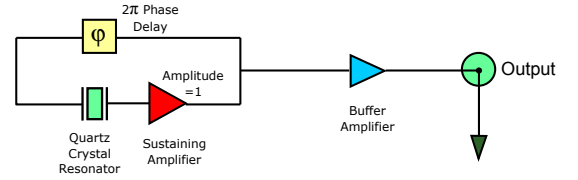


Fig. 5. A closed loop feedback oscillator model used for the Leeson model

F. Design for Radiation Requirements

Radiation analysis for the shielding factor of the USO was performed by 3GM group at the University of Rome using reverse Monte Carlo simulation. All components for the USO are selected from ESA qualified parts list [5] and are screened and hardened to a minimum radiation level of 50kRad. Special care of course is given to quartz swept crystal resonator.

IV. MODELS AND ANALYSIS

This section describes in short analysis, models and simulations that were developed to assist and to verify the design.

A. Analysing the Design using the Leeson Model

The Leeson model is used as a design guide for the low flicker noise circuitry and system design [6]. The Leeson model deals with a closed-loop feedback oscillator, as shown schematically in Fig. 5. Leeson provides the transfer function of the sustaining amplifier noise to the oscillator output noise

$$S_{\phi} = \left(1 + \frac{1}{f^2} \left(\frac{\nu_0}{2Q} \right)^2 \right) S_{\psi} \quad (1)$$

In (1) $S_{\phi}(f)$ is the power-spectral-density (PSD) of the oscillator phase, $S_{\psi}(f)$ is the PSD of sustaining amplifier phase, f is the Fourier frequency, ν_0 is the oscillator frequency and Q is the loaded quality factor of the resonator. A flicker $1/f$ noise of the amplifier is translated by the Leeson formula to $1/f^3$ noise at the oscillator output. The PSD of phase is then translated to an ADEV flicker floor by the relation $\sigma_y^2(\tau) = 2 \ln 2 b_{-3} / \nu_0^2$. For notations and details see [6]. Our region of interest is the ADEV flicker floor between 1s to 1000s. Therefore a great care and attention in the design were given to the flicker noise of the sustaining amplifier circuitry.

B. Proportional Integral Temperature Control Model

Temperature control for the internal and the external ovens is materialized using a Proportional Integral (PI) method. We have developed analytical model as well as simulation for the PI control loop. The analytical model was developed for both a single oven and a double oven scheme. Equation which governs the a PI loop is equivalent to an equation a forced and damped oscillator and like in control theory is characterized by a natural frequency ω_n and damping factor ζ . These are related to the proportional factor, and the integral factor, the oven thermal time constant and thermal isolation. The equivalent force is the ambient temperature fluctuations. The attenuation A of ambient temperature fluctuations, i.e., the response of the "plant" (the object whose temperature is to be stabilized) at low frequencies

(below ω_n) is shown to be proportional to the thermal conductance σ divided by the proportional factor k_I response of loop.

$$A \approx i\omega \frac{\sigma}{k_I} \quad (2)$$

It is interest to see that the attenuation (response) at low frequencies depends only on the thermal conductance to the surrounding (or in opposite term, the thermal isolation) and not on heat capacitance. We have further analyzed the case of double oven with an internal oven housed inside an external oven. The attenuation of the ambient temperature fluctuations at frequencies lower than the natural frequencies of both ovens is given by

$$A \approx A_1 A_2 = -\omega^2 \frac{\sigma_1 \sigma_2}{k_{I1} k_{I2}} \quad (3)$$

Here, σ_1 is the thermal conductance between the internal and the external oven and σ_2 is the thermal conductance between the external oven and the surrounding ambient. This is somewhat obvious result however it shows again the sole dependence on thermal conductance's (isolations) and the equal importance of the isolations of both ovens.

In addition to the analytical model we have developed and performed simulation for the PI control loop composed of two sections. The thermal section is modeled by an equivalent electronic circuit which is combined with the actual electronics circuitry. Simulation results matched the analytical model results and were used to optimize the design.

To verify the proper stabilization of the temperature, the thermistor readings were analyzed in terms of ADEV at time constants between 1s to 1000s. Results for a single oven gave stabilities in the 100 μ K range. Taking into account a resonator sensitivity of 1E-9/K, the contribution of temperature instability to the oscillator ADEV is estimated at 1E-13 for the relevant time constants.

V. TESTS AND RESULTS

A. Thermal Vacuum Test System

To be able to test the unit under thermal vacuum we have designed and built. It is shown schematically in Fig. 6. It includes a UHV vacuum chamber ("bell jar") and inner and outer thermoelectric coolers that enable controlling the temperatures over the required rang of -20 $^{\circ}$ C to +50 $^{\circ}$ C.

B. Frequency Stability Test System

For the characterization the frequency stability we have used the following instruments and software: a high resolution counter, a digital double-heterodyne phase-noise meter (Symmetricom model 5125), Rubidium Frequency Standard (AccuBeat model AR133A), an ultra-stable oscillator (Rakon model HSO14) and a software for frequency stability analysis (Stable32, Hamilton Technical Services).

C. PEM Built and Tests Results

A partial engineering model (PEM) of the USO was built and tested using the thermal vacuum test system described above. As implied by the name the PEM is a partial model with respect to the full Engineering Model (EM), lacking the power supply board and the multiplier board. In addition the PEM

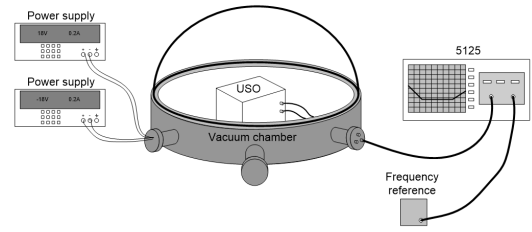


Fig. 6. Schematic drawing of the thermal vacuum System that was built to test the USO under thermal vacuum. Thermoelectric coolers/heater (not shown) are used to control the temperature

provides an output at 5MHz origins from the oscillator without the $\times 12$ multiplier. In the final EM the output frequency is shall be provided at 57.52MHz from the multiplier board, and the oscillator shall be designed to provide an output at a frequency of $57.52\text{MHz}/12 = 4.793\text{MHz}$.

We have used the thermal vacuum test system to test the PEM in order to demonstrate and test for a Technology Readiness Level 5 (TRL5) according to the ECSS standards. Key tested parameters were: ADEV at stable temperatures of -20 $^{\circ}$ C, +20 $^{\circ}$ C, +25 $^{\circ}$ C and +50 $^{\circ}$ C, frequency vs. temperature sensitivity and aging. At all temperatures the PEM exhibited an ADEV around and below 2E-13, at averaging times between 1 to 100s, and around and below 4E-13, at an averaging time of 1000s, thus meeting the requirements. ADEV results for +20 $^{\circ}$ C are shown in Fig. 7.

Frequency to temperature sensitivity was measured at less than 1.5E-12/ $^{\circ}$ C again meeting the requirements. The measured aging (frequency drift as a function of time) was somewhat above the requirement which is attributed to the fact that both the crystal resonator and the complete circuit has not gone through a long enough aging process.

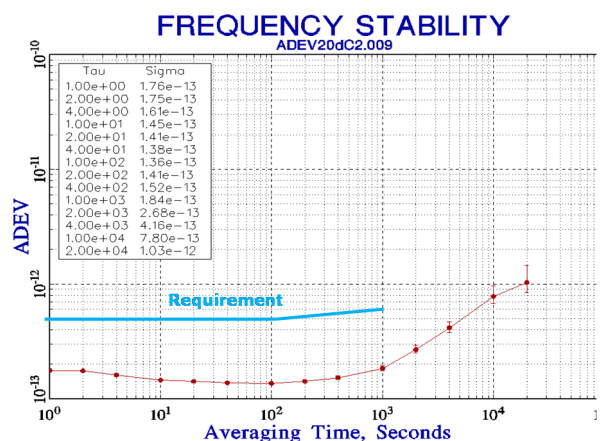


Fig. 7. PEM ADEV (drift removed) results at 20 $^{\circ}$ C. The red dots and figures in the inset block are calculated from the frequency measurements and the blue line represents the requirement.

VI. CONCLUSION

We have designed, modeled and analyzed an Ultra-Stable Oscillator for space environment targeting frequency stability in the low E-13 range for averaging time constants of 1s to 1000s.. A Partial Engineering Model was built and tested under thermal vacuum and has proved meeting the requirements in the low E-13 range for averaging time of 1s to 100s.

The full Engineering Model (EM) which will include the multiplier board and the power supply shall be completed and tested by March 2018.

ACKNOWLEDGMENT

We thanks Yohai Kaspi from the Weitzman Institute, Israel, Luciano Iess from the Sapienza University of Rome, Italy, for their support, and Enrico Rubiola from FEMTO-ST Institute, Besancon, France, for advice and for the characterization of resonators noise.

REFERENCES

- [1] The JUICE ESA mission – see <http://sci.esa.int/juice/>
- [2] “3GM: Gravity and Geophysics of Jupiter and the Galilean Moons”, L. Iess and the 3GM Team, EPSC Abstracts, Vol. 8, EPSC2013-491, 2013, European Planetary Science Congress 2013
- [3] “Science-Quality Oscillators for Deep Space Probes”, S.W. Asmar, D.H. Atkinson, G. Weaver, N. Yu
“Ultra-Stable Oscillators For Probe Radio Science Investigations”, Sami Asmar, Jet Propulsion Laboratory California Institute of Technology, Pasadena CA, USA, 16 June 2012
- [4] Magnetic Field Evaluation During 3GM Occultation Experiment. Eli Galanti & Yohai Caspi, Weizmann Ins., not published
- [5] ESCIES: European Space Components Information Exchange System - <https://escies.org/>
- [6] “Phase-Noise and Frequency Stability in Oscillators”, Author: Enrico Rubiola, The Cambridge RF and Microwave Engineering Series, Jun 10, 2010
- [7] “About Quartz Crystal Resonator Noise: Recent Study” F. Sthal et al, Proc. 20th International Conference on Noise and Fluctuations, Pisa, Italy, June 2007, pp. 607–610

TWSTFT Results by using Software-Defined Receiver Data

Yi-Jiun Huang, Wen-Hung Tseng,
and Shinn-Yan Lin
Telecommunication Laboratories,
Chunghwa Telecom,
Taoyuan, TAIWAN

Sung-hoon Yang
Korea Research Institute of
Standards and Science,
Daejeon, SOUTH KOREA

Miho Fujieda
National Institute of Information and
Communications Technology,
Tokyo, JAPAN

Abstract—The precision of two-way satellite time and frequency transfer (TWSTFT) is currently limited due to instabilities of signal arrival time. We use a software-defined receiver to measure the arrival time of code signal transmitted by SATRE modem. The SDR systems have been successfully installed and performed at TL, NICT and KRISS. The SDR results show excellent suppression on the diurnals. For data of the KRISS-TL link, the TDEV of the SATRE modem shows a peak of 135 ps at 8 hours; where the TDEV of SDR is only 38 ps.

Keywords—software-defined receiver; TWSTFT; diurnal

I. INTRODUCTION

The new development of two-way satellite time and frequency transfer (TWSTFT) focuses on enhancing its short-term stabilities, e.g., employing dual pseudo-random noise (DPN) codes, and carrier-phase (CP) based TWSTFT [1-3]. However, the precision of conventional TWSTFT is still limited due to instabilities of signal arrival time and often suffers the problem of diurnal variations of up to a few nanoseconds. Although the sources of diurnals have been generally investigated [4-6], it is still difficult to explain the ns-level variations clearly. Many studies indicate the sources of diurnals may be not only the non-reciprocity of physical two-way propagation delays, but also a combination including variations of temperature [7], range delays [8], interferences [9] and imperfection of the TWSTFT receiver [10]. To further improve the performance of TWSTFT results, it is effective to prepare another receiver to accurately determine the time of arrival (TOA) and the carrier phase.

A software-defined receiver (SDR) was originally designed for implementing the DPN-based or CP-based TWSTFT measurements [1-3]. We used the SDR to measure the arrival time of code signal transmitted by SATRE modem, and we found the capacity to reduce diurnal variations. Then, for reducing the reciprocities contributed by the receivers, a TWSTFT receiver based on the open-loop method was proposed and implemented on the SDR [11]. Since September 2014, TL and NICT have started the observation with the SDR [12], which consists of a high-resolution correlator (HRC) and successive interference cancellation (SIC) associated with open-loop configuration. In October 2015, KRISS also joined

the observation. Now, three laboratories in Asia-Pacific region have employed the SDR in their TWSTFT systems.

In this paper, we introduce the experimental setup of the software-defined receivers and analyze the recent results in Asia-Pacific TWSTFT links.

II. EXPERIMENTAL SETUP

Fig. 1 illustrates the experimental configuration of the software-defined receiver in a TWSTFT system. There is no change for the conventional TWSTFT system. The only necessary thing is to split the reception signal for both SDR and SATRE modem. To do so, TL adds a power splitter, and NICT and KRISS use the intermediate frequency (IF) monitor port of the SATRE modems for the input of the SDR. A SDR consists of an attenuator and an amplifier for optimizing the power level of the IF signal, an analog-to-digital (A/D) converter for sampling the reception signal (e.g. K5/VSSP32 or NI USRP N210), and a personal computer (PC) for collecting the samples and performing the measurement by developed software. The PC is equipped with the Nvidia's graphics processor units (GPU) for efficiently computing cross-correlation. And, the Linux Ubuntu operating system is used.

The software is now developed and maintained by TL cooperated with NICT and KRISS. The GNU C++ and CUDA library are included in the software. Some digital signal processing (DSP) algorithms are applied to implement HRC, SIC and open-loop configuration to measure the time of arrival (TOA). Thanks to DSP, the multiple channels can be easily measured more than one TOA at the same time. Since the setup enables completely independent operations for SATRE modem and SDR, two parallel TWSTFT measurements can be performed simultaneously.

In current Asia-Pacific TWSTFT network, one Ku-band transponder of the Eutelsat 172A satellite is employed. The chip rate of the pseudo-random noise (PRN) coded signals generated from SATRE modems is 2.5 Mcps. The actual bandwidth is restricted to 2 MHz, and the transmission power is also adjusted to keep reception C/N_0 around 55 dBHz.

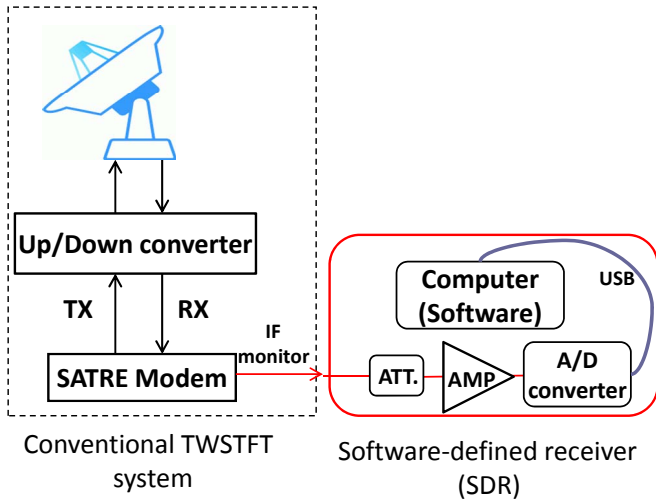


Fig. 1. Experimental setup of a SDR in a TWSTFT system. A/D converter: analog-to-digital converter; ATT: attenuator; AMP: amplifier for optimizing the power level of the intermediate frequency (IF) signal.

III. EXPERIMENTAL RESULTS

First, the comparisons between SATRE data and SDR data from parallel TWSTFT measurements are presented. Then, the SDR measurements are compared with the GPS PPP data.

A. Comparison between SATRE and SDR Data

From October 2015, there are three TWSTFT links in the Asia-Pacific network. For good presentation in plots, we use the 20-day data from MJD 57400 (13 January 2015) to MJD 57419 (1 February 2015). Fig. 2 shows hourly TWSTFT results for the KRISS-TL link by using SDR and SATRE modem. The diurnal variations of about 0.5 ns are clearly seen for SATRE data, but unobvious for SDR data.

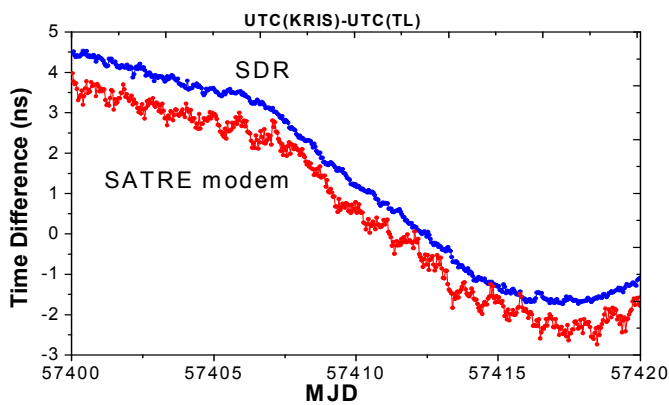


Fig. 2. TWSTFT results for the KRISS-TL link. The plot shows time differences using SDR and SATRE modem. Offsets are inserted into both results for better visibility.

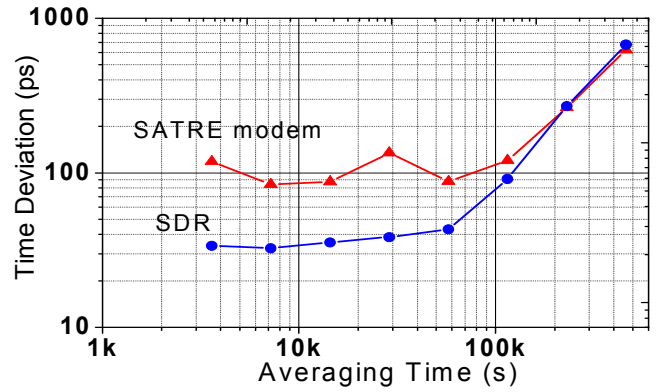


Fig. 3. Time deviations for the KRISS-TL TWSTFT data. Both data for SDR and SATRE modem are presented.

Fig. 3 shows the plot of time deviations (TDEV) for the KRISS-TL TWSTFT results by using SDR and SATRE modem. The TDEVs at the averaging time of one hour are 34 ps and 118 ps for SDR and SATRE data, respectively. Comparing with the SDR results, the TDEV plot of SATRE modem shows much noise in short-term, and it has a bump at the averaging time of 2.88×10^4 s (i.e., 8 h) due to the diurnal variations. The TDEV of the SATRE modem shows a peak of 135 ps at 8 hours; where the TDEV of SDR is only 38 ps. Both TDEV curves eventually meet for the averaging times larger than 2.6 days.

Fig. 4 shows hourly TWSTFT results for the NICT-TL link by using SDR and SATRE modem. The diurnal variations are larger than 0.5 ns for SATRE data, but very small or unobvious for SDR data. Fig. 5 shows the plot of TDEV for the TWSTFT results by using SDR and SATRE modem. The TDEV at the averaging time of one hour are 46 ps and 121 ps for SDR and SATRE data, respectively. The TDEV plot of SATRE modem shows much noise in short-term, and it also has a bump at the averaging time of 2.88×10^4 s (i.e., 8 h) due to the diurnal variations. The TDEV plot of the SDR has a slight bump at 4-h averaging time. For the averaging times larger than 2.6 days, the TDEVs of SDR are a little lower than those of SATRE.

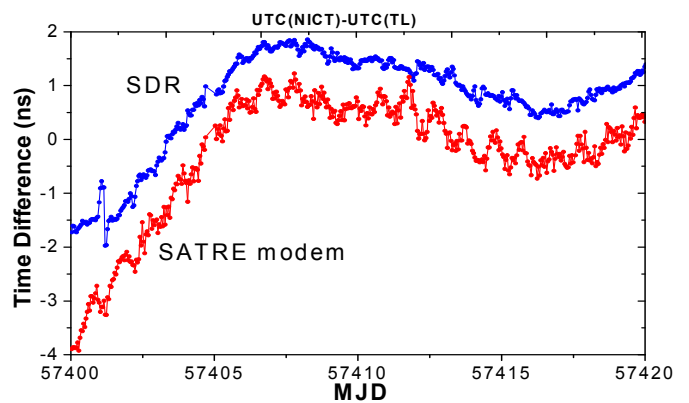


Fig. 4. TWSTFT results for the NICT-TL link. The plot shows time differences using SDR and SATRE modem. Offsets are inserted into both results for better visibility.

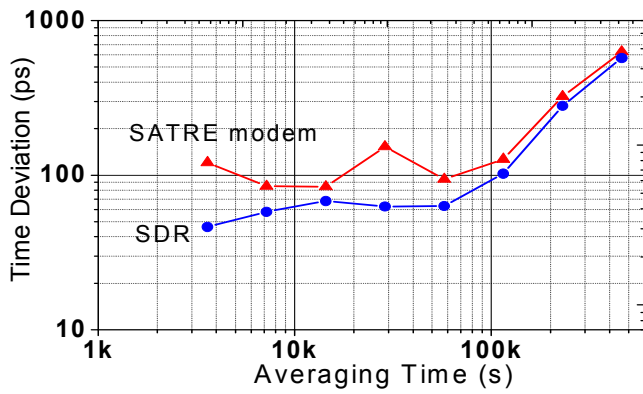


Fig. 5. Time deviations for the NICT-TL TWSTFT data.

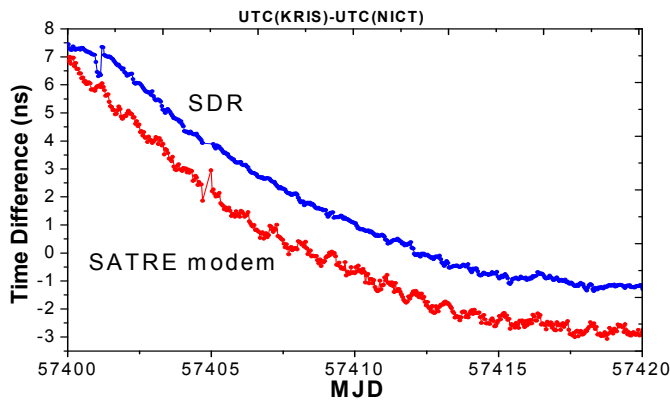


Fig. 6. TWSTFT results for the KRIS-NICT link. The plot shows time differences using SDR and SATRE modem. Offsets are inserted into both results for better visibility.

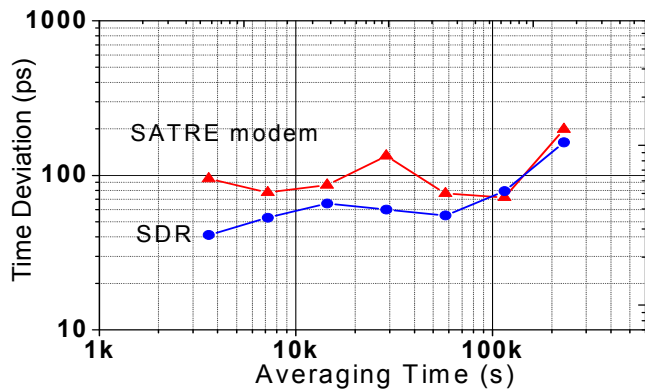


Fig. 7. Time deviations for the KRIS-NICT TWSTFT data.

Fig. 6 shows hourly TWSTFT results for the KRIS-NICT link by using SDR and SATRE modem. The SATRE data are much noisy and have more clear diurnal variations. Fig. 7 shows the plot of TDEV for the SDR and SATRE results. The TDEV at the averaging time of one hour are 41 ps and 95 ps for SDR and SATRE, respectively. The TDEV plot of SATRE modem shows much noise in short-term and eventually meets the curve of the SDR for the averaging times larger than 1.3 days.

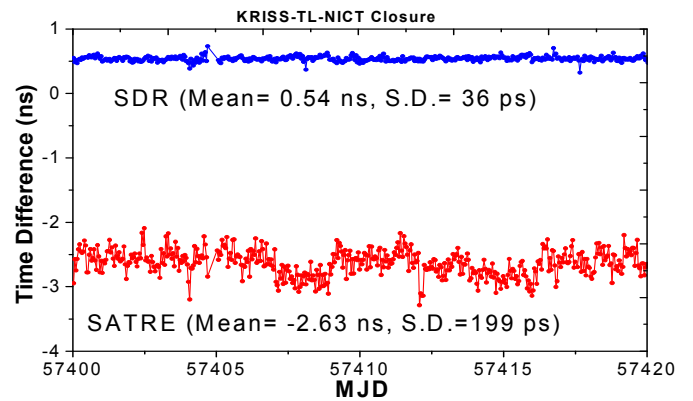


Fig. 8. Closure sums of KRIS-TL, TL-NICT and NICT-KRIS links.

The closure sum is defined as the signed sum of the time differences between stations A, B, and C: $(A-B) + (B-C) + (C-A)$ [13]. Fig. 8 shows the closure sums of KRIS-TL-NICT links. The closure values are not zero because the time transfer links among KRIS, TL and NICT are not calibrated. The standard deviation for the SATRE closure sums is 199 ps, and that of the SDR data is only 36 ps.

B. Compared with the GPS PPP

The TWSTFT data for the KRIS-TL link are used in the comparison with Global Positioning System (GPS) precise point positioning (PPP) (i.e., the TAI-PPP [14] downloaded from BIPM). Fig. 9 shows the double differences of TWSTFT and GPS PPP. Since the curves for SDR and SATRE look similar, the slight long-term variation may be caused by an inconsistency between TWSTFT and GPS PPP. Thanks to the suppressed diurnals, the peak-to-peak difference between the SDR and PPP is 0.9 ns. While, that of the SATRE and PPP is 1.68 ns during the 20 days. Fig. 10 shows the Modified Allan deviations of the double differences. The data for PPP-SDR reach the level of 10^{-16} after the averaging times larger than 16.6 h (6×10^4 s). In the short-term, the PPP-SDR results also have better performance than PPP-SATRE results.

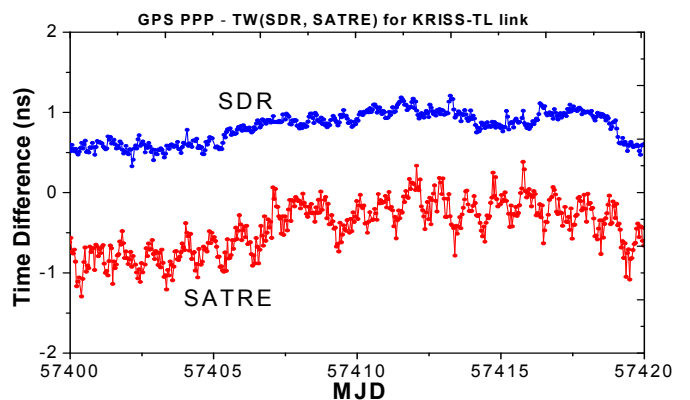


Fig. 9. Double differences of Global Positioning System (GPS) precise point positioning (PPP) and TWSTFT {SDR, SATRE} for the KRIS-TL link. The mean value was subtracted from the data.

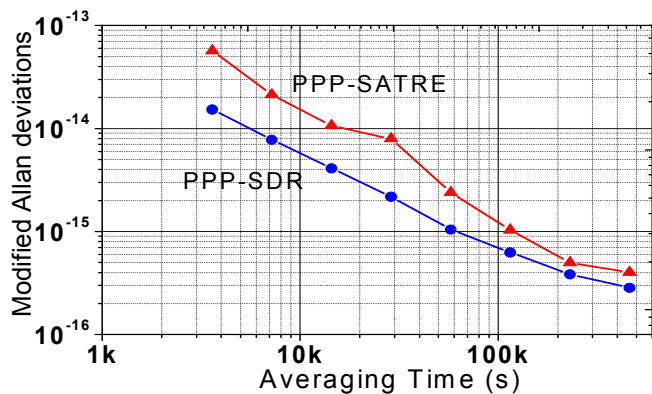


Fig. 10. Modified Allan deviations for the double differences of GPS PPP and TWSTFT for KRISS-TL time transfer data. Both data for SDR and SATRE modem are presented.

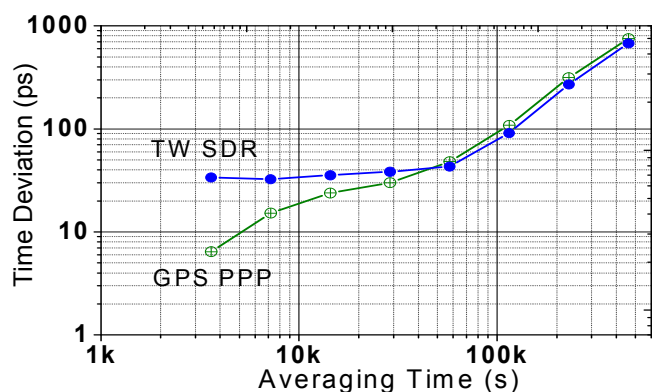


Fig. 11. Time deviations for TWSTFT SDR and GPS PPP data of the KRISS-TL link.

Fig. 11 shows the TDEVs for the TWSTFT SDR and GPS PPP data. In the short-term, the GPS PPP results have better performance than the SDR. This is because the PPP uses not only the code but also the carrier phase observations. After the averaging times larger than 16 h (5.76×10^4 s), the TDEVs of SDR are a little lower than those of the GPS PPP.

IV. CONCLUSION

In this paper, we have presented the TWSTFT results by using SDR. Through the analysis of the three TWSTFT links in the Asia-Pacific network, we confirm that the short-term stabilities of the SDR are better than those of the SATRE modem. The SDR results also show excellent suppression on the diurnals. Since the SDR and SATRE modem can be

operated independently, the SDR is effective to analyze the instability of conventional TWSTFT results. In the future, we will evaluate the SDR in other TWSTFT networks, such as Eu-Eu and Eu-Asia networks.

REFERENCES

- [1] T. Gotoh et al., "Development of a GPU-based two-way time transfer modem," *IEEE Trans. IM*, vol. 60, no. 7, pp. 2495–2499, Jul. 2011.
- [2] W.-H. Tseng et al., "First international two-way satellite time and frequency transfer experiment employing dual pseudo-random noise codes," *IEEE Trans. UFFC*, vol. 59, no. 3, pp. 531–538, Mar. 2012.
- [3] M. Fujieda et al., "Carrier-phase two-way satellite frequency transfer over a very long baseline," *Metrologia*, vol. 51, pp. 253–262, 2014.
- [4] T. E. Parker and V. Zhang, "Source of instabilities in two-way satellite time transfer," in Proc. Joint IEEE IFCS, in Proc. 37th PTTI Syst. Appl. Meeting, 2005, pp. 745–751.
- [5] D. Piester, A. Bauch, M. Fujieda, T. Gotoh, M. Aida, H. Maeno, M. Hosokawa, and S. H. Yang, "Studies on instabilities in long-baseline two-way satellite time and frequency transfer (TWSTFT) including a troposphere delay model," in Proc. 39th PTTI Syst. Appl. Meeting, 2007, pp. 211–222.
- [6] H.-T. Lin, Y.-J. Huang, W.-H. Tseng, C.-S. Liao and F.-D. Chu, "Recent development and utilization of two-way satellite time and frequency transfer," *MAPAN-Journal of Metrology Society of India*, vol. 27, no. 1, pp. 13–22, 2012.
- [7] H.-T. Lin, W.-H. Tseng, S.-Y. Lin, and C.-S. Liao, "The Calibration device for TWSTFT station at TL," in Proc. of 2005 Joint IEEE International Frequency Control Symposium (IFCS) and Precise Time and Time Interval (PTTI) Meeting, Vancouver, Canada, pp. 712–715, Aug. 2005.
- [8] W.-H. Tseng, Y.-J. Huang and S.-Y. Lin, "Recent TWSTFT activities at TL," in Proc. the 2013 Precise Time and Time Interval Systems and Applications Meeting, pp.198-207, ION PTTI 2013, Bellevue, Washington, USA, Dec. 2-5, 2013.
- [9] F. G. Ascarrunz, T. E. Parker, and S. R. Jefferts, "Group-delay error due to coherent interference," in Proc. Joint IEEE Int. Frequency Control Symp.–European Frequency and Time Forum, 1999, pp. 198–202.
- [10] G. Hejc and W. Schaefer, "Tracking biases caused by imperfections in DLL receivers," in Proc. 41st Precise Time and Time Interval Syst. Appl. Meeting, 2009, pp. 551–558.
- [11] Y.-J. Huang and H.-W. Tsao, "Design and Evaluation of an Open-Loop Receiver for TWSTFT Applications," *IEEE Trans. IM*, vol. 64, no. 5, pp. 1553–1558, 2015.
- [12] Y.-J. Huang, M. Fujieda, H. Takiguchi, W.-H. Tseng, and H.-W. Tsao, "Stability improvement of an operational two-way satellite time and frequency transfer system," *Metrologia*, vol. 53, no. 2, pp. 881–890, Mar. 2016.
- [13] D. Matsakis, L. Breakiron, A. Bauch, D. Piester, and Z. Jiang, "Two-way satellite time and frequency transfer (TWSTFT) calibration constancy from closure sums," in Proc. 40th Precise Time and Time Interval (PTTI) Meeting, 2008, pp. 587–604.
- [14] G. Petit, and Z. Jiang, "Precise Point Positioning for TAI computation," *Int. J. Nav. Obs.*, 562878, 2008.

The Raman Laser system for Mach-Zehnder Atom Interferometry

Nan Li¹, Kaikai Huang¹, Xuanhui Lu^{1*}

¹ Institute of Optics, Department of Physics, Zhejiang University
Hangzhou 310027, China

*Email: xhlu@zju.edu.cn

Abstract—We produced two Raman-laser beams with a frequency offset of 6.834GHz by injection-locking of a master diode-laser to a slave diode-laser. The master laser was phase-modulated at 6.834 GHz with an Electro-Optic Modulator and then injected into the slave laser that was oscillating around one of the side-bands. The relative linewidth of the two lasers was less than 1 Hz. Utilizing these laser beams, we realized the coherent manipulation of atomic wave packets in a Mach-Zehnder type atom interferometry.

Keywords—Raman laser, injection locking, atom interferometry

I. INTRODUCTION

Atom interferometry has developed rapidly over the past two decades and it is currently one of the most intriguing and promising frontiers of precision metrology, opening up unprecedented prospects. In particular, gravimeters, gradiometers, and gyroscopes based on atom interferometry have all demonstrated extremely high accuracies [1~3]. Among these, gravimeters attract great interests for a wide range of essential applications, from fundamental physics [4-5] to geophysics and navigation. An identical type of atom-interferometer is based upon the interaction of Raman laser pulses with an atom at three distinct times. In this article we demonstrate the Raman laser system, one of the most important part in atom interferometry and the experimental results in our lab.

II. THEORY

Raman pulses are very suitable to drive transitions between two long living states and to transfer a big momentum to the atoms. First we assume an atom with two ground level states $|g\rangle$ and $|e\rangle$ and an intermediate excited level $|i\rangle$, interacting with two lasers

$$\begin{aligned} \mathbf{E}_1(\mathbf{r}, t) &= \mathbf{E}_{1,0} \cos(\omega_1 t - \mathbf{k}_1 \mathbf{r} + \phi_{1,0}) \text{ and} \\ \mathbf{E}_2(\mathbf{r}, t) &= \mathbf{E}_{2,0} \cos(\omega_2 t - \mathbf{k}_2 \mathbf{r} + \phi_{2,0}) \end{aligned} \quad (1)$$

with frequency ω_1 and ω_2 is detuned transition frequency as shown in Fig.1.

The external degrees of freedom are closely coupled to the internal ones because the atom can only change its state by absorption or stimulated emission of the laser photons.

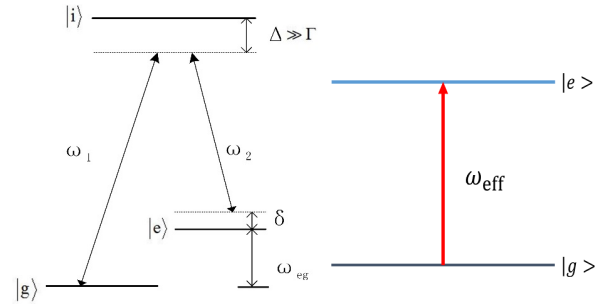


Fig.1. The structure of three level system and two Raman lasers.

In the case of big detuning, the intermediate state can be eliminated and the system treated as a two-level system with resonance frequency ω_{eff} and a momentum difference of $\hbar \mathbf{k}_{eff}$ with the correspondence as following,

$$\begin{aligned} \omega_{eff} &= \omega_1 - \omega_2 \\ \mathbf{k}_{eff} &= \mathbf{k}_1 - \mathbf{k}_2 \\ \Omega_{eff} &= \Omega_1 \Omega_2 / \Delta \\ \phi_{eff} &= \phi_1 - \phi_2 \end{aligned} \quad (2)$$

III. EXPERIMENTAL SETUP

The experimental setup for the injection-locking is shown in Fig.2.

We utilize two external cavity diode lasers(ECDL), a master laser and a slave laser, each comprising a tapered amplifier laser diode (TA) as the source of Raman system. About 50mW power is split to be diffracted by an AOM (Brimrose, GPF-1000-200-.780), with the centre frequency of 1GHz. After the +1 order laser being frequency-stabilized on the saturated absorption spectroscopy of Rubidium atoms with DAVLL method, the part which does not pass through the AOM has a frequency -1GHz detuned from the transition frequency ($F=1 \rightarrow F'=2$), which is one of the Raman beams. To obtain another Raman beam, several mW of the master laser is coupled into the EOM (Photline NIR-MPX800-LN-10) which operates at 6.8GHz producing the sidebands. The three different frequency components are: the carrier(f_0) and two first-order sidebands ($f_0 \pm 6.8$ GHz). In order to selecting the sideband of $f_0 - 6.8$ GHz, the output of EOM is injected into an ECDL as a seed laser. After careful adjustment, with the

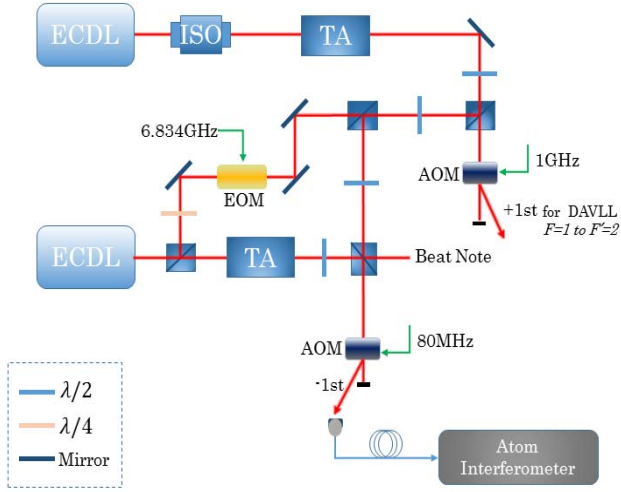


Fig.2. Experimental setup for producing phase-coherent Raman laser beams by injection-locking method

frequency selective property of grating in ECDL, the -1 order diffraction frequency could be selected as the output of slave laser. After amplification, the slave laser is combined with master laser with proper power ratio. To realize precise control of Raman length, we make use of an AOM with 80MHz centre frequency and couple the -1st order into a polarization-maintaining fiber. Then the Raman lasers are guided to interference tube to coherently manipulate atomic packet.

IV. EXPERIMENTAL RESULTS

Fig.3 is the beat note signal of two Raman lasers. The relative bandwidth is about 1Hz when the spectrum analyser is configured for the 1Hz resolution bandwidth (RBW). It has fully satisfied the requirement of atom interferometry because the bandwidth is much smaller than the width of stimulated Raman transitions

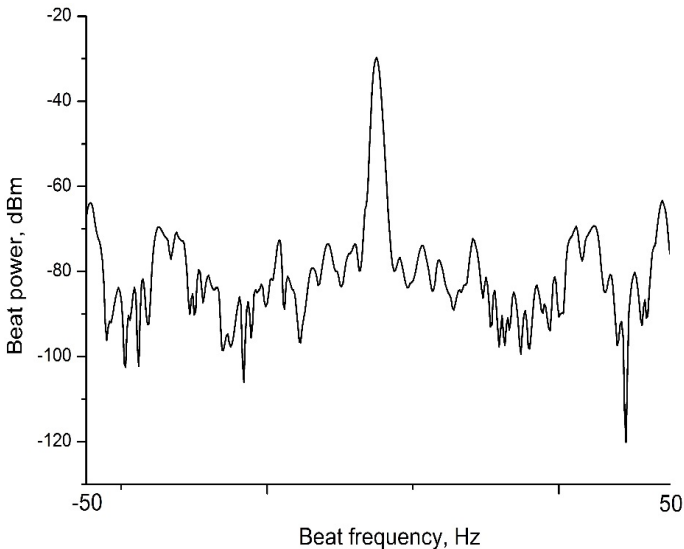


Fig.3. Beat-note spectrum of the two sideband injection-locked laser diodes

In our experiment, each of the six molasses laser beams (diameter 20 mm, $e^{-1/2}$ level) is delivered by its own polarization-maintaining optical fiber and expanded by a collimator mounted directly on the fountain structure. After launching stage, laser beam intensities are ramped down, and their detuning are ramped from the original ~ 10 MHz to ~ 50 MHz by modulating the laser current. Less than 10 μ K temperature is achieved after this polarization gradient cooling process. After obtaining the temperature of 8.5 μ K and the number of 3×10^8 for cold atom, we get the source for atom interferometry.

The interferometry sequence is composed of three pulses ($\pi/2-\pi-\pi/2$) spaced by a time T. In Doppler-sensitive scheme as shown in Fig.4, the Raman beams have a configuration of counter-propagation and the effective wave vector is $1.6 \times 10^7/\text{m}$, which means the Doppler shift can not be ignored. The acceleration induced Doppler shift causes a continuous change of the atomic transition frequency. To compensate it, the Raman frequency difference is adjusted/chirped in discrete steps.

In order to obtain the interference fringe, the chirp rate α of each point is changed and 40 points for each cycle is recorded. Population vs chirp rate shows an interference fringe in Fig.5. The expression of gravity induced phase shift indicates that increasing the time T will improve the measurement resolution. However, if the time T is too long, the contrast of interference fringe will become poor due to Raman phase noise, vibrational noise and other system effects. So it is crucial to choose a proper T in each system. From our preliminary results, within an integration time of 360s, the resolution is $7.4 \times 10^{-8}g$.

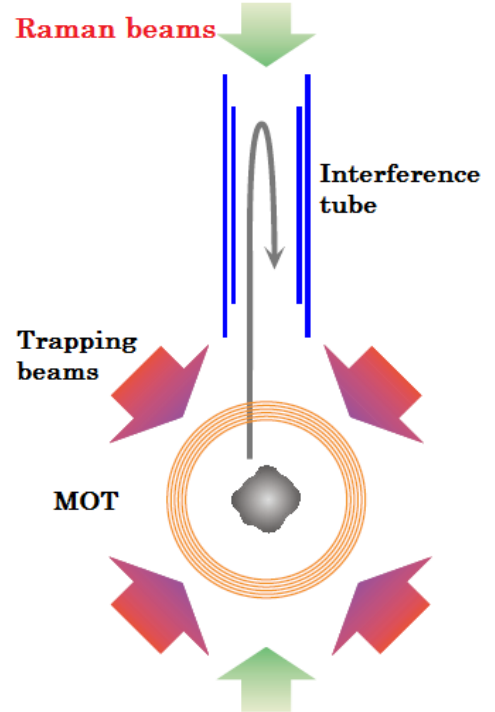


Fig.4. Schematic of atom interferometry

REFERENCES

- [1] A Peters, K Y Chung and S Chu, High-precision gravity measurements using atom interferometry, *Metrologia* 38 25 2001
- [2] J. M. McGuirk, G. T. Foster, J. B. Fixler, M. J. Snadden, and M. A. Kasevich, Sensitive absolute-gravity gradiometry using atom interferometry, *Phys. Rev. A* 65, 033608
- [3] T. L. Gustavson, P. Bouyer, and M. A. Kasevich, Precision Rotation Measurements with an Atom Interferometer Gyroscope, *Phys. Rev. Lett.* 78, 2046
- [4] G. Lamporesi, A. Bertoldi, L. Cacciapuoti, M. Prevedelli, and G. M. Tino, *Phys. Rev. Lett.* 100, 050801 (2008).
- [5] H. Müller, S. Chiow, S. Herrmann, S. Chu, K. Y. Chung, *Phys. Rev. Lett.* 100, 180405 (2008).

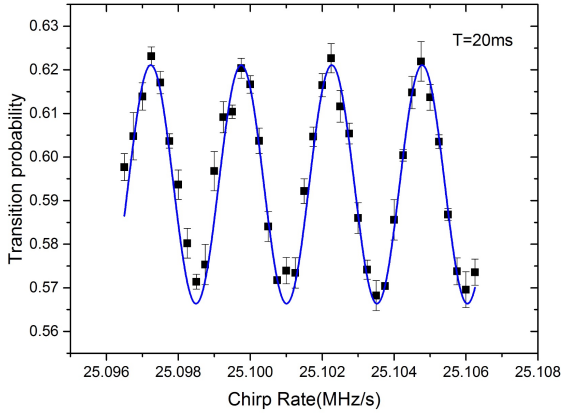


Fig.5. Interference fringe. The resolution of gravity measurement is measured as $7.4 \times 10^{-8}g$

When the chirp rate of the Raman laser equals to the Doppler shift due to the gravity, the phase shift of Raman beams will exactly compensate for the gravitational phase shift. We obtained the interference fringes with different T . The chirp rate corresponding to the center point of the interference fringes does not depend on T , and we can deduce the absolute g value from the equation

$$\begin{aligned} \Delta\phi &= (k_{eff}g - \alpha)T^2 \\ \alpha &= k_{eff}g \end{aligned} \quad (3)$$

In our experiment, we obtain interference fringes with different T , as shown in Fig.6. So we can then deduce the absolute g value from the equation (3). All fringes reach a minimum value at $\alpha = 25.102932 \text{ MHz/s}$, which could be inferred that the local gravity $g = 9.7931812 \text{ m/s}^2$.

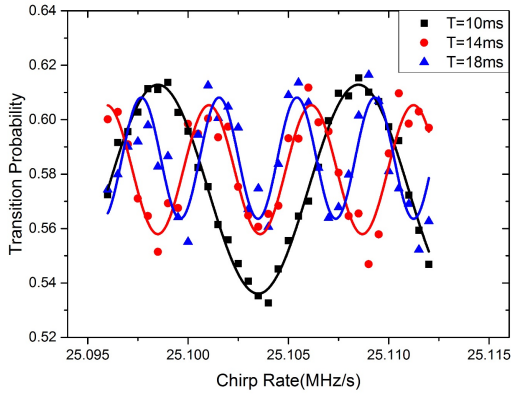


Fig.6. Absolute value of local gravity acceleration

Performance of the NeQuick G Iono Model for Single-Frequency GNSS Timing Applications

R. Píriz, P. Roldán, R. Golez, C. Moriana
GMV
Tres Cantos, Madrid, Spain
rpíriz@gmv.com

J. Leute
Physikalisch-Technische Bundesanstalt (PTB)
38116 Braunschweig, Germany

Abstract - GNSS timing is currently used worldwide in critical real-time systems that require precise synchronisation or time-stamping at geographically dispersed sites, such as wireless telephone stations, electrical power grids and financial services. For applications where multiple timing equipment needs to be deployed, it is desirable to use low-cost, single-frequency receivers. Together with calibration issues, the ionospheric delay is the major limiting factor for accurate timing in single-frequency setups. Increasing demands in cost-saving and accuracy will make the availability of precise single-frequency solutions more and more interesting.

In this paper we analyse single-frequency timing accuracy using the Galileo NeQuick G model, as compared with the standard GPS Klobuchar model, and taking the dual-frequency iono-free solution as reference. The analysis is done by post-processing RINEX files from two calibrated GNSS receivers, one located at mid-latitude and the other one close to the equator.

Unlike Klobuchar, NeQuick G is based on a rather complex mathematical algorithm. For offline applications in post-processing this is not an issue, but for a real-time implementation it might be necessary to evaluate the model not too frequently, in order to improve execution speed. NeQuick G efficiency is analysed from this point of view also.

Keywords - Galileo, GNSS time and frequency transfer, ionosphere, delay calibration.

I. INTRODUCTION

For single-frequency applications, the GPS navigation message provides parameters for the well-known Klobuchar ionospheric model, and thus this is implemented in virtually all GNSS receivers nowadays. For Galileo, the European Union has recently published a detailed description and implementation guidelines for the NeQuick G user model [1]. NeQuick is designed to reach a correction capability of at least 70% of the ionospheric code delay (RMS). GMV has implemented (in the C programming language) and validated the NeQuick model according to [1].

This paper analyses NeQuick's performance based on post-processing of pseudorange measurements and navigation messages in RINEX format from two GNSS receivers. One receiver is called GPTB and is located at PTB in Germany, connected to the UTC(PTB) timescale. GPTB tracks both GPS

and Galileo. The other receiver is called SGBK and is located in Singapore, connected to the UTC(SG) timescale [2]. SGBK tracks GPS only.

GPTB and SGBK pseudorange calibrations are available for GPS P1 and P2. In addition, GPTB calibrations are available for Galileo E1 and E5a. Calibration is important in iono model characterization for timing, since the uncorrected iono delay might introduce not only a higher timing noise but also an additional non-zero net delay.

In this study we consider two scenarios: GPS-only, and Galileo-only. Although the NeQuick parameters are broadcast by Galileo, the model can be applied to GPS measurements as well. The basic measurand from the processing is the [UTC(k)-GNSStime] difference, where UTC(k) is UTC(PTB) or UTC(SG). GNSStime is GPS Time (GPSt) or Galileo System Time (GST), for GPS-only processing and Galileo-only processing, respectively. The GNSS antenna position is fixed in the processing. The [UTC(k)-GNSStime] solution from dual-frequency iono-free processing is taken as "true" reference for the evaluation of single-frequency solutions.

II. RECEIVER COORDINATES AND CALIBRATION

Receiver antenna coordinates have been calculated using Precise Point Positioning (PPP) following the guidelines provided in [3]. The antenna marker coordinates from PPP have been translated to Antenna Phase Center (APC) coordinates using antenna eccentricity vectors as contained in the IGS ANTEX file for each antenna type. Although the single-frequency APC position is not exactly the same as the dual-frequency APC position, the difference is only of up to a couple of cm for the antenna types involved (equivalent to less than 0.1 ns in time). Therefore the same set of dual-frequency APC coordinates from PPP has been used for dual-frequency and for single-frequency solutions. Also, since no information is available about antenna eccentricity vectors for Galileo signals, it is assumed that the APC position is the same for GPS and for Galileo.

Regarding receiver pseudorange calibration, for SGBK we have used the GPS P1 and P2 delays contained in the CGGTTS files from that receiver submitted to the BIPM. For GPTB, the GPS P1 and P2 delays have been calibrated in "common-clock" with the PTBB receiver contributing to the

BIPM. GPTB Galileo delays have been calculated relative to GPS using the method developed by the Royal Observatory of Belgium (ORB) [4]. More information about Galileo calibration for GPTB can be found in [5].

III. DESCRIPTION OF THE PROCESSING

Satellite pseudoranges and position/clock information are processed according to (1) for a given frequency.

$$P_i = r_i + c[(t_{rx} - t_{sat}) - d_{rel} + d_{tropo} + d_{iono} + TGD_i - INTDLY_i + CABDLY - REFDLY] \quad (1)$$

For the dual-frequency solution, equations in two different frequencies are combined, so that the ionospheric delay is removed. In this study, the L1 and L2 frequencies have been used for GPS, while E1 and E5a frequencies have been used for Galileo. Equation (2) shows the result of combining two different frequencies.

$$P_{2F} = \frac{f_1^2 P_1 - f_2^2 P_2}{f_1^2 - f_2^2} = r_i + c \left[(t_{rx} - t_{sat}) - d_{rel} + d_{tropo} - \frac{f_1^2 INTDLY_1 - f_2^2 INTDLY_2}{f_1^2 - f_2^2} + CABDLY - REFDLY \right] \quad (2)$$

The Klobuchar model [6] provides the ionospheric delay as a cosine function of time, with a maximum at 14:00 local time. The amplitude and the period of this function are obtained from the latitude and the alpha and beta coefficients broadcast in the GPS navigation message, according to (3). Equations (4) and (5) give the slant factor F as a function of the elevation angle E , and the phase of the ionospheric delay X , respectively.

$$d_{iono} = \left[5 \cdot 10^{-9} + \sum_{n=0}^3 \alpha_n \varphi_m^n \left(1 - \frac{X^2}{2} + \frac{X^4}{24} \right) \right] \cdot F \quad \text{if } |X| \leq 1.57 \quad (3)$$

$$d_{iono} = 5 \cdot 10^{-9} \cdot F \quad \text{if } |X| > 1.57$$

$$F = 1.0 + 16.0(0.53 - E)^3 \quad (4)$$

$$X = \frac{2\pi(t - 50400)}{\sum_{n=0}^3 \beta_n \varphi_m^n} \quad (5)$$

The NeQuick model is the ionosphere model recommended for the processing of Galileo satellite signals. It models the Slant Total Electron Content (STEC), which is the total number of electrons in the path followed by the signal. From this value it is possible to compute the ionospheric delay according to (6).

$$d_{iono} = \frac{40.3 \cdot 10^{16}}{f^2} STEC \quad (6)$$

A full description of NeQuick is can be found in [1]. To estimate the STEC, NeQuick uses as input three Effective

Ionization Level Az coefficients currently broadcast in the Galileo navigation message.

In the single-frequency processing it is necessary to apply the Total Group Delays (TGDs). In the case of Galileo, broadcast TGDs are un-calibrated: they are estimated by the system using a zero-mean condition. The effect of this miscalibration on the single-frequency solution is a bias of around 5 ns. To improve the results, we have aligned all Galileo broadcast TGDs to the calibrated values available for the four In-Orbit Validation (IOV) satellites [5].

The relativistic correction and the tropospheric delay need also to be applied in both single- and dual-frequency. For the tropospheric delay, the NATO hydrostatic model [7] has been used, as recommended in [3]. The receiver internal delay (INTDLY), the antenna cable delay (CABDLY), and the receiver clock delay (REFDLY) must be also applied. In general, the processing follows the guidelines provided in [3].

IV. EVALUATION PERIOD AND SAMPLING RATE

The processing period comprises 3 months: January to March, 2016. In this period, the solar activity is medium, ionospheric conditions are nominal, and no remarkable ionospheric event has been observed.

Solutions in the form of [UTC(k)-GNSStime] differences every 5 minutes have been obtained averaging observations over the 3 months. The original sampling rate in the RINEX observation files is 30 seconds. Daily averages have been also calculated in order to reduce the short-term noise and better evaluate the long-term performance.

V. GPS-ONLY RESULTS

Fig. 1 shows UTC(PTB)-GPS_t differences for the 3-month period (daily averages), from GPTB processing. As can be seen the NeQuick model shows in general a better performance than Klobuchar. In particular, notice the nearly-zero mean difference between NeQuick and the dual-frequency solution.

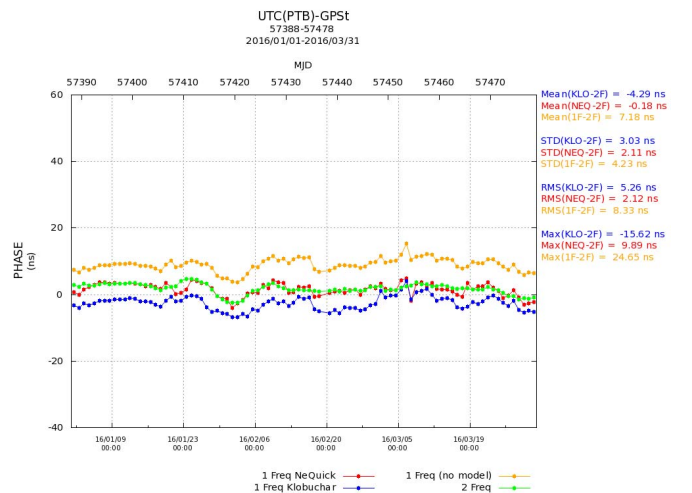


Fig. 1. [UTC(PTB)-GPS_t] time differences over 3 months (daily values, GPS-only processing). Statistics refer to 5-min values.

Fig. 2 shows solutions every 5 min from GPTB processing over a shorter time period (3 days). Again, NeQuick's performance is better than the behaviour of Klobuchar, as observed in the long-term evolution.

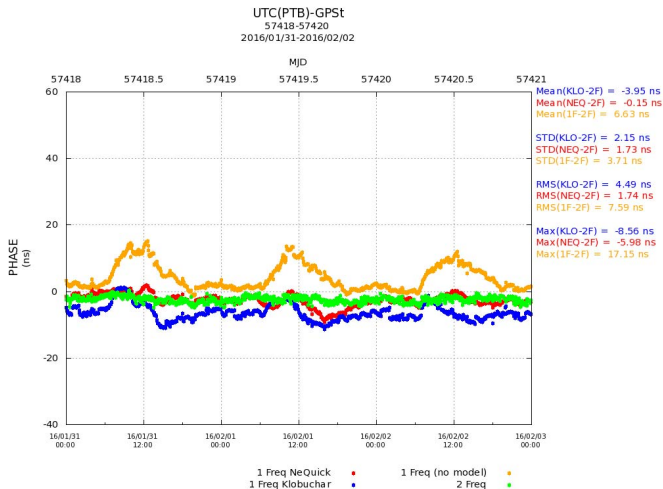


Fig. 2. [UTC(PTB)-GPSt] time differences over 3 days (5-min values, GPS-only processing).

In general, the ionospheric delay observed at PTB during the evaluation period is not especially large. To analyse the performance of ionospheric models in case of larger ionospheric delays, the same analysis has been performed for SGBK, which is located near the equator and is therefore affected by higher ionospheric activity. Fig. 3 shows the UTC(SG)-GPS time differences for the 3-month period (daily averages), from SGBK processing. It can be observed that in the case of SGBK the difference between single-frequency without any ionospheric model and dual-frequency is larger than in the case of GPTB. Despite this fact, the ionospheric models are able to remove this delay with an accuracy of around 5 ns.

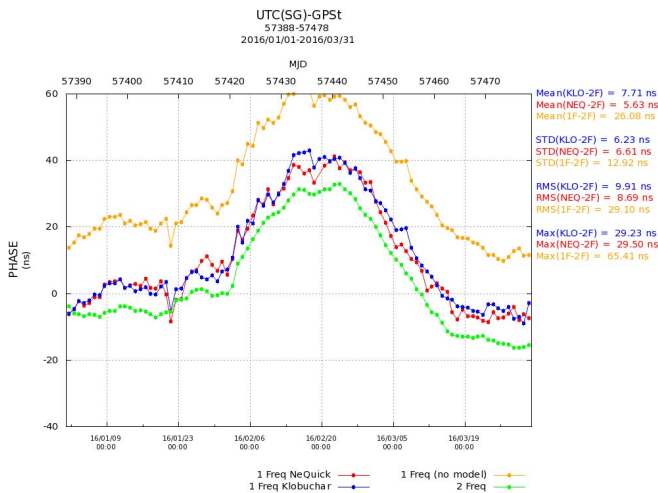


Fig. 3. [UTC(SG)-GPSt] time differences over 3 months (daily values, GPS-only processing). Statistics refer to 5-min values.

Fig. 4 shows solutions every 5 min from SGBK processing over 3 days. It can be observed that the maxima in the hours of maximum solar activity are larger than at GPTB, and that ionospheric models are not able to model these peaks so well.

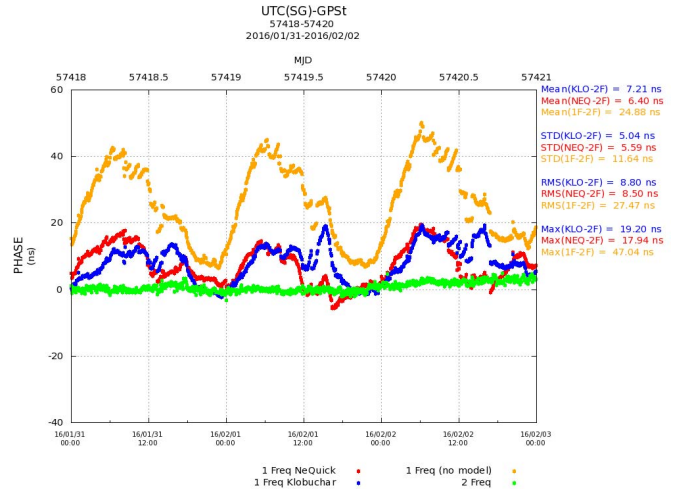


Fig. 4. [UTC(SG)-GPSt] time differences over 3 days (5-min values, GPS-only processing).

VI. GALILEO-ONLY RESULTS

Even if GNSS timing applications have traditionally used GPS satellites, with the launch of the latest Galileo satellites it is also possible to use Galileo for timing. Fig. 5 and Fig. 6 show results from GPTB processing equivalent to the ones presented in the previous section, but based on Galileo-only processing instead of on GPS-only. The number of Galileo satellites available in the reported period is between 7 and 9. It can be seen that a continuous timing solution is possible despite the reduced number of satellites in view (sometimes one or even zero). The NeQuick performance is similar to the GPS-only case.

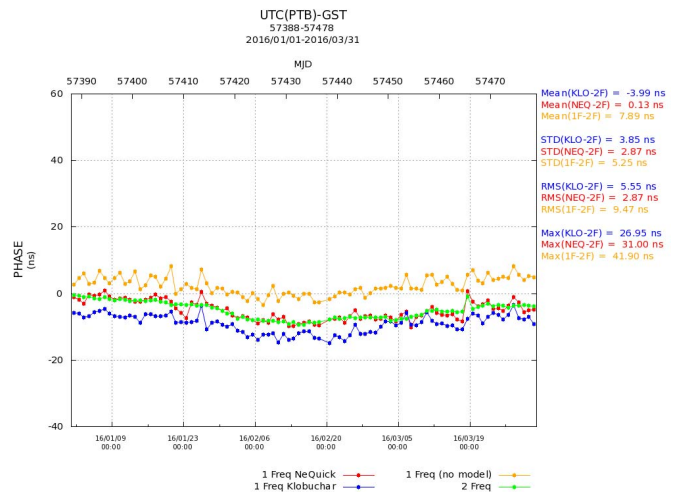


Fig. 5. [UTC(PTB)-GST] time differences over 3 months (daily values, Galileo-only processing). Statistics refer to 5-min values.

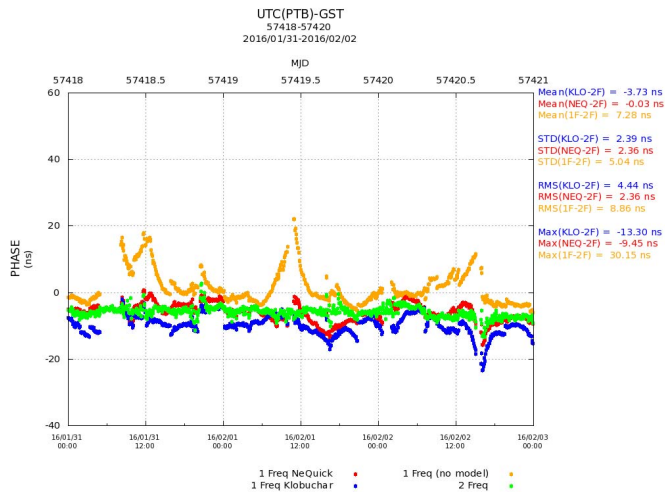


Fig. 6. [UTC(PTB)-GST] time differences over 3 days (5-min values, Galileo-only processing).

VII. COMPUTER OPTIMIZATION

NeQuick is based on a more complex algorithm than Klobuchar, and therefore its computer execution time is larger. To overcome this drawback, it is possible to evaluate the model at a rate larger than the sampling rate of observations. In the interval between executions, the ionospheric delay is assumed to be constant.

This method has been tested with execution rates for NeQuick of 30, 60, 120, 300, 600, 1200, and 1800 seconds. In the last case (half-hour rate), the execution time of NeQuick is similar to Klobuchar. Fig. 7 shows results for a 3-day period.

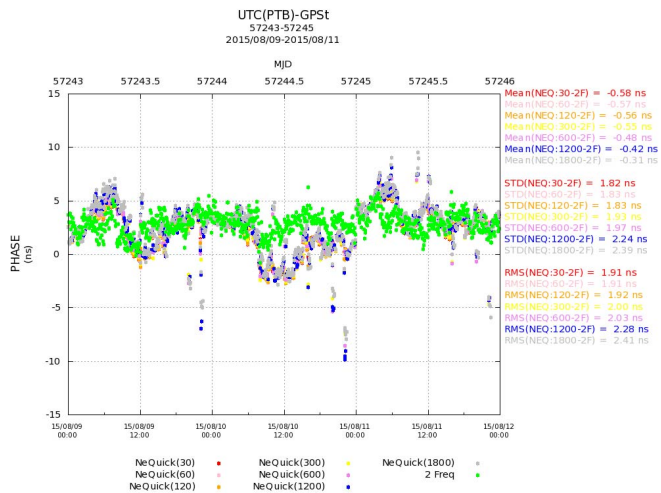


Fig. 7. [UTC(PTB)-GPSt] time differences over 3 days (5-min values, GPS-only processing). NeQuick execution rates of 30, 60, 120, 300, 600, 1200, and 1800 seconds are shown.

It can be observed that the impact of increasing the NeQuick execution rate is not too important. An execution

rate of half an hour leads to an increase in RMS error of less than 1 ns. However some outliers can be observed in this case. Using an execution rate of 5 or 10 min seems to be a good compromise between accuracy and computer efficiency.

VIII. CONCLUSIONS

The first 3 months of 2016 have been processed for two stations, one located at mid-latitude in Germany (GPTB), and the other one near the equator in Singapore (SGBK).

Over the 3 months, for GPTB, in the GPS-only solution, NeQuick shows a RMS error of 2.1 ns (5.3 ns for Klobuchar), and a bias of 0.2 ns (4.3 ns for Klobuchar). The Galileo-only solution provides similar figures. Thus at mid-latitudes NeQuick's improvement in timing accuracy seems to be quite noticeable, at least for the current mild ionospheric activity.

At low latitudes (SGBK) NeQuick's performance seems to be only marginally better than Klobuchar, with a RMS error of 8.5 ns (8.8 ns for Klobuchar), and a bias of 6.4 ns (7.2 ns for Klobuchar).

NeQuick's computer execution time is around 60 times slower than Klobuchar's. However this disadvantage can be mitigated by increasing NeQuick's execution rate (for example to every 5 or 10 minutes), with negligible loss of accuracy.

ACKNOWLEDGMENT

Dr. Liu Yan Ying, from the Time and Frequency Laboratory, National Metrology Centre, A*STAR, Singapore, kindly provided permission to use SGBK data [2].

The European Space Agency (ESA) kindly provided permission to use GPTB data [5].

REFERENCES

- [1] European Union, "Ionospheric Correction Algorithm for Galileo Single Frequency Users", Issue 1.1, June 2015. ISBN: 978-92-79-44700-6.
- [2] Liu Y.Y. & Z. Jiang, "Improvement of Time Transfer in Singapore", 2010 Asia-Pacific Radio Science Conference (AP-RASC'10), Toyama, Japan.
- [3] P. Defraigne and G. Petit, "CGGTTS-Version 2E : an extended standard for GNSS Time Transfer", Metrologia 2015 52 G1.
- [4] P. Defraigne et al., "Calibration of Galileo signals for time metrology", IEEE transactions on Ultrasonics, Ferroelectrics, and Frequency control 12/2014 61(12):1967-75.
- [5] R. Piriz et al., "Relative Calibration of Galileo Receivers within the Time Validation Facility (TVF)", Proc. of the Joint Meeting of the 2015 IFCS and of the 29th EFTF, Denver, Colorado, April 2015.
- [6] GPS Interface Specification, IS-GPS-200, Revision H, 24 Sep 2013.
- [7] North Atlantic Treaty Organization (NATO), Navstar Global Positioning System (GPS) System Characteristics, NATO Standardization Agreement (STANAG) 4294, 1993.

Cold-atom Inertial Sensor without Deadtime

B. Fang, I. Dutta, D. Savoie, B. Venon, C. L. Garrido Alzar, R. Geiger and A. Landragin
 LNE-SYRTE, Observatoire de Paris, PSL Research University, CNRS, Sorbonne Universités
 UPMC Univ. Paris 06, 61 avenue de l'Observatoire, 75014 Paris, France
 Email: bess.fang@obspm.fr

Abstract—We report the operation of a cold-atom inertial sensor in a joint interrogation scheme, where we simultaneously prepare a cold-atom source and operate an atom interferometer in order to eliminate dead times. Noise aliasing and dead times are consequences of the sequential operation which is intrinsic to cold-atom atom interferometers. Both phenomena have deleterious effects on the performance of these sensors. We show that our continuous operation improves the short-term sensitivity of atom interferometers, by demonstrating a record rotation sensitivity of $100 \text{ nrad}\cdot\text{s}^{-1}/\sqrt{\text{Hz}}$ in a cold-atom gyroscope of 11 cm^2 Sagnac area. We also demonstrate a rotation stability of $1 \text{ nrad}\cdot\text{s}^{-1}$ after 10^4 s of integration, improving previous results by an order of magnitude. We expect that the continuous operation will allow cold-atom inertial sensors with long interrogation time to reach their full sensitivity, determined by the quantum noise limit.

I. INTRODUCTION

Over the last twenty years, inertial sensors based on atom interferometry have evolved significantly in terms of performance and transportability. Such progress ensures the relevance of atom interferometer (AI) based inertial sensors in various field applications, ranging from inertial navigation [1], [2], [3] to geophysics and geodesy [4], [5], [6], [7], as well as in fundamental physics [8], [9], [10]. Although new techniques are currently explored to further improve the sensitivity of these sensors [11], [12], [13], [14], [15], the issues associated with measurement dead time remain a strong obstacle to their ultimate performance [16].

Dead times in AIs correspond to the time needed to prepare and to detect the atoms before and after the interferometric sequence. They result in loss of inertial information, leaving AIs unsuitable for inertial measurement units (IMUs) in navigation [17] or for recording fast varying signals in seismology [18] for the time being. Noise aliasing coming from the sequential operation also degrades the AI sensitivity in the presence of dead times, similar to the Dick effect in cold atomic clocks [19].

In this paper, we report the first continuous operation of a cold-atom inertial sensor. This is demonstrated in a gyroscope configuration featuring a macroscopic Sagnac area of 11 cm^2 . We achieve a short-term rotation stability of $100 \text{ nrad}\cdot\text{s}^{-1}/\sqrt{\text{Hz}}$, and a long-term stability as low as $1 \text{ nrad}\cdot\text{s}^{-1}$ after 10^4 s of integration, setting the record of all atom gyroscopes.

II. EXPERIMENTAL SETUP

We realize a light-pulse gyroscope in a cesium fountain, see Fig. 1. Counter-propagating Raman beams coupling the $|F = 4, m_F = 0\rangle$ and $|F = 3, m_F = 0\rangle$ clock states are used

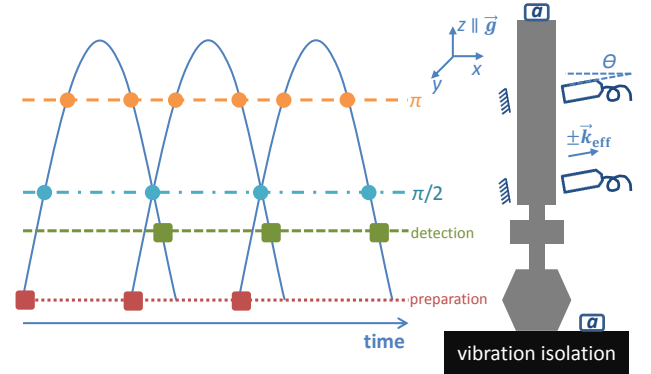


Fig. 1. Operation principle and setup of the continuous cold-atom gyroscope.

to split, deflect and recombine the free-falling cold atoms¹. With four light pulses ($\pi/2$ - π - π - $\pi/2$), the two arms of the interferometer enclose a physical area up to 11 cm^2 , representing a 27-fold increase with respect to previous experiments [21]. This gives rise to a rotation phase shift Φ_Ω according to the Sagnac effect [22], given by

$$\Phi_\Omega = \frac{1}{2} \vec{k}_{\text{eff}} \cdot (\vec{g} \times \vec{\Omega}) T^3, \quad (1)$$

where \vec{k}_{eff} is the two-photon momentum transfer, \vec{g} is the gravitational acceleration, $\vec{\Omega}$ is the rotation rate, and T is half the interferometric time. Following the atom juggling methods initially introduced to measure collisional shifts in fountain clocks [23], we implement a sequence of joint interrogation of successive atom clouds as described in [24]. In other words, each $\pi/2$ Raman pulse is common to the two adjacent interferometer sequences, setting the cycle time T_c equal to the total interrogation time $2T$.

The interrogation light contains two frequencies, each addressing one of the two clock states. The counter-propagating configuration is achieved by means of retroreflecting the incoming beam (see Fig. 1), so that two configurations are possible, transferring opposite momenta (denoted as $\pm \vec{k}_{\text{eff}}$) to the atoms. The degeneracy of these two configurations is lifted by tilting the Raman beams by an angle of inclination $\theta \simeq 4^\circ$, as the Doppler effect associated with the vertical velocity of the atoms shifts the resonance frequency of the stimulated Raman transition in the opposite directions. The joint interrogation simultaneously addresses two atom clouds with opposite vertical velocity, thus alternating between the $\pm \vec{k}_{\text{eff}}$ configurations.

¹We focus on the inertial measurement and analysis in this paper. Details of the atom preparation and detection can be found in [20].

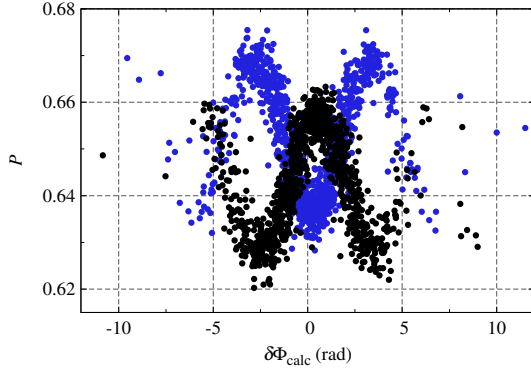


Fig. 2. Measured probability P versus calculated vibration phase $\delta\Phi_{\text{calc}}$ for the $\pm\vec{k}_{\text{eff}}$ configurations.

Increasing the sensitivity of such AI-based inertial sensors necessarily comes at the cost of an increased sensitivity to the vibration noise, as a consequence of the Equivalence Principle. Noninertial effects such as the Raman laser phase noise and light shift also contribute to the interferometer output. We can thus breakdown the interferometric phase into rotation phase, vibration phase and noninertial phase, i.e. $\Delta\Phi = \Phi_{\Omega} + \delta\Phi_{\text{vib}} + \delta\Phi_0$. Vibration noise has a strong impact on our setup. A vibration isolation platform reduces the effect of the ground vibration $\gtrsim 1$ Hz to an rms AI phase noise of about 2.5 rad for $2T = 800$ ms. Since the vibration noise spans several interferometer fringes, auxiliary inertial sensors are necessary to recover the signal.

We use two commercial accelerometers (marked ‘ a ’ in Fig. 1) to record and correct the vibration noise. The acquired acceleration signal is weighted using the transfer function [25] in order to compute the vibration phase. Fig. 2 shows the measured probability of transition P versus the calculated vibration phase $\delta\Phi_{\text{calc}}$ for the $\pm\vec{k}_{\text{eff}}$ configurations. Despite the overwhelmingly large vibration noise, the inertial stability of our gyroscope is given by the horizontal scatter of the fringes. This will be evaluated in the following section.

III. STABILITY OF ROTATION MEASUREMENT

We divide a data set into packets of 40 points. As the data alternates between the the $\pm\vec{k}_{\text{eff}}$ configurations, 20 points of each configuration are used to fit a sinusoidal model,

$$P = P_0 + A \cos(\delta\Phi_{\text{calc}} + \Phi^{(\pm)}), \quad (2)$$

where P_0 is the offset of the interferometric signal, A is the fringe amplitude, and the phase offset is given by $\Phi^{(\pm)} = \pm\Phi_{\Omega} + \delta\Phi_0$. This yields a rotation phase $\Phi_{\Omega} \equiv (\Phi^{(+)} - \Phi^{(-)})/2 \pmod{\pi}$. All fitting parameters P_0 , A and $\Phi^{(\pm)}$ were constrained loosely in order to avoid cross talk between phase noise and probability or amplitude noise. The convergence of the fit routine is ensured by the large span of the vibration phase.

Figure 3 (top) shows an uninterrupted measurement over about 6 hours. The Allan standard deviation (ADEV) of the rotation rate sensitivity is shown in Fig. 3 (bottom). As the ADEV follows the $\tau^{-1/2}$ scaling, where τ is the integration time, we obtain a short-term rotation sensitivity

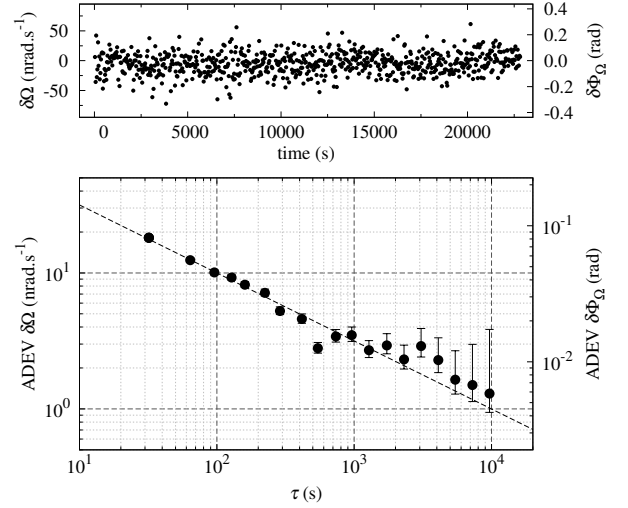


Fig. 3. Top: The time sequence of rotation rate measurement around its mean value. The equivalent fluctuation of rotation phase is shown on the right axis. Bottom: ADEV of the measurement. The error bars indicate the 68% confidence interval, and the dashed line follows a $\tau^{-1/2}$ scaling.

of $100 \text{ nrad}\cdot\text{s}^{-1}/\sqrt{\text{Hz}}$. This establishes the best performance among all cold-atom gyroscopes to date [21], and represents a 30-fold improvement compared to previous four-pulse gyroscopes [1], [3]. Comparing the normal and the continuous mode, the performance of our gyroscope improves by about a factor 1.4. This is consistent with the speedup of the cycling frequency².

Such a sensitivity is currently limited by the detection noise (about $400 \text{ mrad}/\sqrt{\text{Hz}}$ for $A \simeq 2\%$). This also bounds the efficiency of the vibration correction protocol to about a factor 5 in the present case. The technical difficulties associated with the joint operation (primarily light shift and contrast reduction due to scattered light by the MOT) are assessed in [24], together with strategies for improvement.

Nevertheless, the long-term stability of our rotation rate measurement reaches $1 \text{ nrad}\cdot\text{s}^{-1}$ after 10^4 s of integration time. This represents the state of the art of all atom gyroscopes [26] (see [27] for a recent review), and a 20-fold improvement from previous cold-atom gyroscopes [21], [28]. Such a stability is a direct consequence of the macroscopic Sagnac area and the folded four-pulse geometry, giving a T^3 dependence of the scale factor. With a long interrogation time, fluctuations of the atom cloud trajectories, a known limit in previous experiments [21], [28], are scaled down for its linear dependence in T . One-photon light shift, a source of slow drift in stability due to the drift of the power ratio of the Raman lasers, is removed by combining the measurement from the $\pm\vec{k}_{\text{eff}}$ configurations.

A symmetric four-pulse interferometer offers zero sensitivity to a DC acceleration parallel to \vec{k}_{eff} . This however comes at the expense of an enhanced probability noise in practice, as imperfect π pulses give rise to parasitic interferometers [3]. We introduce a timing asymmetry of $\Delta T = 300 \mu\text{s}$, see Fig. 4 (top), in order to prevent the closure of the parasitic

²The dead time in normal mode $T_D = 0.8$ s by coincidence, so that the cycling frequency doubles when we operate our gyroscope in the continuous mode.

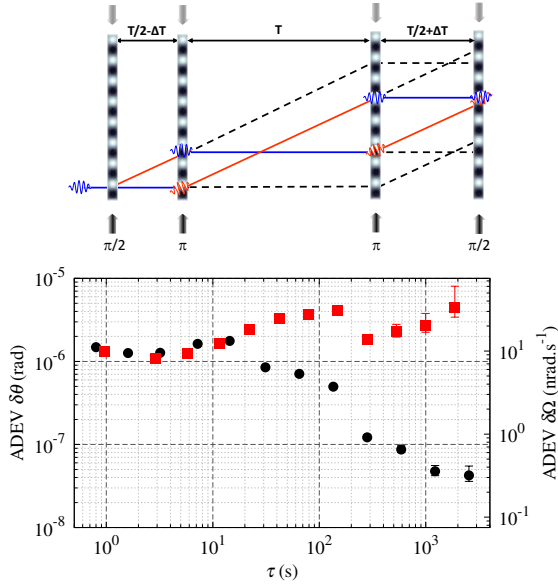


Fig. 4. Top: The space-time diagram of the asymmetric four-pulse interferometer. Bottom: ADEV of the tilt measurement before (squares) and after (circles) active stabilization.

interferometers. This gives rise to a sensitivity to DC accelerations, $\Phi_{\text{DC}} = 2k_{\text{eff}}T\Delta Tg \sin \theta$. In other words, a 1 mrad fluctuation of θ translates into a ~ 70 rad fluctuation of Φ_{DC} . We therefore stabilize the tilt of the experiment to reduce these fluctuations. A commercial tiltmeter is used to reduce the tilt signal, the variations of which are compensated by a current controlled magnetic actuator acting on the vibration platform. Figure 4 (bottom) shows the ADEV of $\delta\theta$ with and without the tilt lock. We stabilize $\delta\theta$ down to $\sim 4 \times 10^{-8}$ rad, corresponding to a long-term stabilization of Φ_{DC} below $0.3 \text{ nrad}\cdot\text{s}^{-1}$ level after 2000 s of integration. Alternating measurements between $\Delta T = \pm 300 \mu\text{s}$ allowed us to verify that Φ_{DC} does not impact the stability of the rotation rate measurement. We also monitor the cross-axis tilt and observe a negligible phase drift due to the change of the projection of the rotation vector on the interferometer area.

IV. TOWARDS QUANTUM NOISE LIMITED ATOM INTERFEROMETERS

The continuous operation introduces phase correlations between successive measurements. This in principle allows faster noise averaging following a τ^{-1} scaling in ADEV. It has been demonstrated on our setup in the clock mode [24] where the Dick effect from a degraded local oscillator is quickly reduced with integration.

In order to demonstrate the same τ^{-1} scaling in our inertial measurements, we need to reduce the uncorrelated detection noise, and to operate our AI at mid-fringe in order to preserve the maximal sensitivity, i.e. $|dP/d\Delta\Phi| = A$. This is confirmed by a simulation of the ADEV for different levels of vibration noise, which is corrected by auxiliary sensors. The residual phase noise $\delta\Phi_{\text{res}}$ (including the inertial noise not corrected by the auxiliary sensors and some noninertial noise) is correlated between successive shots. Its rms $\sigma_{\text{res}} = 120$ mrad is kept constant in all three cases. The vibration noise calculated from

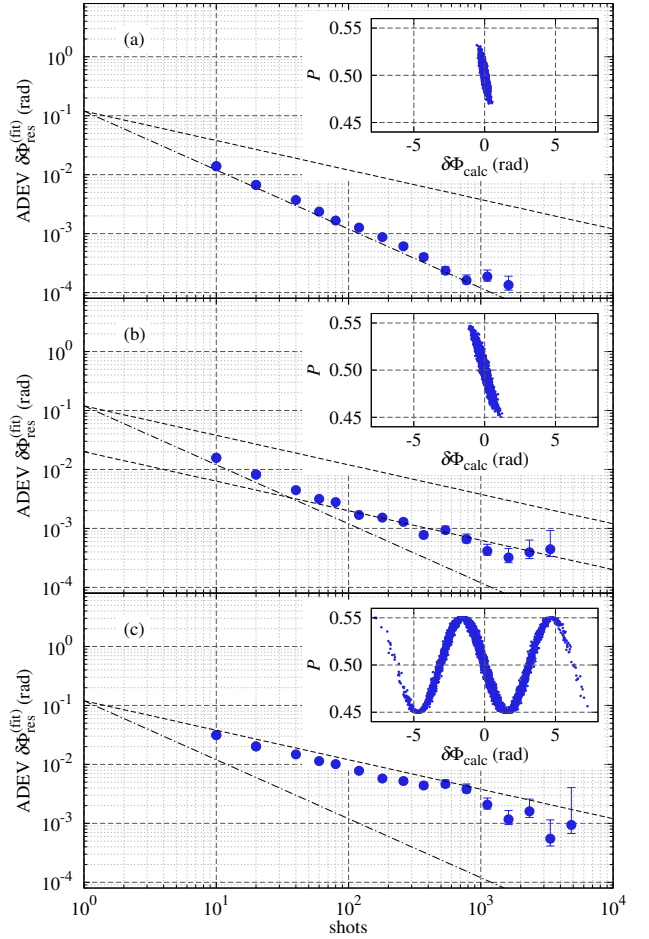


Fig. 5. Simulation of the gyroscope phase stability with increasing vibration noise. (a) - (c) correspond to $\sigma_{\text{vib}} = 0.13$ rad, 0.32 rad, and 2.1 rad added to a constant level of residual correlated noise $\sigma_{\text{res}} = 120$ mrad. The fast noise averaging following τ^{-1} scaling (dash-dotted lines) is gradually lost for AIs that operate away from mid-fringe, recovering the $\tau^{-1/2}$ scaling (dashed lines). The insets show the simulated P versus $\delta\Phi_{\text{calc}}$.

the auxiliary sensor signals is generated randomly, with an rms of $\sigma_{\text{calc}} = 0.13$ rad, 0.32 rad, and 2.1 rad. For $P_0 = 0.5$ and $A = 5\%$, we compute $P = P_0 - A \sin(\delta\Phi_{\text{calc}} + \delta\Phi_{\text{res}})$ to simulate the AI operation. Fitting P versus $\delta\Phi_{\text{calc}}$ using 10-point packets yields $\delta\Phi_{\text{res}}^{(\text{fit})}$, similar to our data analysis procedure. The ADEV of $\delta\Phi_{\text{res}}^{(\text{fit})}$ is shown in Fig. 5, indicating a loss of the τ^{-1} scaling when the vibration noise brings the AI out of the linear regime. Note that fringe fitting is equivalent to linear regression as long as the AI remains at mid-fringe, see Fig. 5 (a).

We can retain a mid-fringe operation using a real-time compensation of the vibration noise, first demonstrated on an atom gravimeter [29]. A phase jump of the interrogation laser right before the end of the interferometer sequence can cancel the vibration phase and reduce the span of the interferometric phase. Alternatively, we can implement a more elaborated protocol using quantum weak measurement, as shown in the clock mode in [30]. Assuming a quantum projection noise limited detection with 10^6 atoms and $A = 10\%$, a rotation sensitivity below $1 \times 10^{-10} \text{ rad}\cdot\text{s}^{-1}$ in a few 100 s is accessible with our setup.

V. CONCLUSION

The continuous operation of our atom gyroscope allows us to improve the stability of the rotation rate measurement without loss of inertial information. We report $100 \text{ nrad.s}^{-1}/\sqrt{\text{Hz}}$ rotation sensitivity, and a stability of 1 nrad.s^{-1} after 10^4 s of integration. This is well within the specifications of a strategic grade gyroscope ($< 4 \text{ nrad.s}^{-1}$ stability [31]), making AI more attractive for inertial navigation. We also foresee applications in geodesy and geophysics, where seismic signals in the a few mHz to 10s of Hz frequency band could be accessible with such inertial sensors. AI operating in continuous mode are also useful in the search of time-dependent signals such as gravitational waves [9], [10].

REFERENCES

- [1] B. Canuel, F. Leduc, D. Holleville, A. Gauguet, J. Fils, A. Virdis, A. Clairon, N. Dimarcq, C. J. Bordé, A. Landragin, and P. Bouyer, "Six-axis inertial sensor using cold-atom interferometry," *Phys. Rev. Lett.*, vol. 97, p. 010402, Jul 2006.
- [2] R. Geiger, V. Menoret, G. Stern, N. Zahzam, P. Cheinet, B. Battelier, A. Villing, F. Moron, M. Lours, Y. Bidel, A. Bresson, A. Landragin, and P. Bouyer, "Detecting inertial effects with airborne matter-wave interferometry," *Nat Commun*, vol. 2, p. 474, Sep. 2011.
- [3] J. K. Stockton, K. Takase, and M. A. Kasevich, "Absolute Geodetic Rotation Measurement Using Atom Interferometry," *Phys. Rev. Lett.*, vol. 107, no. 13, p. 133001, Sep. 2011.
- [4] P. Gillot, O. Francis, A. Landragin, F. P. D. Santos, and S. Merlet, "Stability comparison of two absolute gravimeters: optical versus atomic interferometers," *Metrologia*, vol. 51, no. 5, p. L15, 2014.
- [5] R. Geiger et al, "Matter-wave laser interferometric gravitation antenna (miga): New perspectives for fundamental physics and geosciences," in *Proceedings of the 50th Rencontres de Moriond*, 2015.
- [6] C. Freier, M. Hauth, V. Schkolnik, B. Leykauf, M. Schilling, H. Wziontek, H.-G. Scherneck, J. Müller, and A. Peters, "Mobile quantum gravity sensor with unprecedented stability," in *Proceedings for the 8th Symposium on Frequency Standards and Metrology*, 2015.
- [7] G. Rosi, L. Cacciapuoti, F. Sorrentino, M. Menchetti, M. Prevedelli, and G. M. Tino, "Measurement of the gravity-field curvature by atom interferometry," *Phys. Rev. Lett.*, vol. 114, p. 013001, Jan 2015.
- [8] B. Altschul, Q. G. Bailey, L. Blanchet, K. Bongs, P. Bouyer, L. Cacciapuoti, S. Capozziello, N. Gaaloul, D. Giulini, J. Hartwig, L. Iessm, P. Jetzer, A. Landragin, E. Rasel, S. Reynaud, S. Schiller, C. Schubert, F. Sorrentino, U. Sterr, J. D. Tasson, G. M. Tino, P. Tuckey, and P. Wolf, "Quantum tests of the einstein equivalence principle with the ste?quest space mission," *Advances in Space Research*, vol. 50, p. 501, 2015.
- [9] S. Dimopoulos, P. W. Graham, J. M. Hogan, M. A. Kasevich, and S. Rajendran, "Atomic gravitational wave interferometric sensor," *Phys. Rev. D*, vol. 78, p. 122002, Dec 2008.
- [10] W. Chaibi, R. Geiger, B. Canuel, A. Bertoldi, A. Landragin, and P. Bouyer, "Low frequency gravitational wave detection with ground-based atom interferometer arrays," *Phys. Rev. D*, vol. 93, p. 021101, Jan 2016.
- [11] P. Cladé, S. Guellati-Khélifa, F. Nez, and F. Biraben, "Large momentum beam splitter using bloch oscillations," *Phys. Rev. Lett.*, vol. 102, p. 240402, Jun 2009.
- [12] S.-w. Chiow, T. Kovachy, H.-C. Chien, and M. A. Kasevich, "102h?k large area atom interferometers," *Phys. Rev. Lett.*, vol. 107, p. 130403, Sep 2011.
- [13] J. E. Debs, P. A. Altin, T. H. Barter, D. Döring, G. R. Dennis, G. McDonald, R. P. Anderson, J. D. Close, and N. P. Robins, "Cold-atom gravimetry with a bose-einstein condensate," *Phys. Rev. A*, vol. 84, p. 033610, Sep 2011.
- [14] I. D. Leroux, M. H. Schleier-Smith, and V. Vuletić, "Implementation of cavity squeezing of a collective atomic spin," *Phys. Rev. Lett.*, vol. 104, p. 073602, Feb 2010.
- [15] O. Hosten, N. J. Engelsen, R. Krishnakumar, and M. A. Kasevich, "Measurement noise 100 times lower than the quantum-projection limit using entangled atoms," *Nature*, vol. 529, no. 7587, pp. 505–508, Jan. 2016.
- [16] B. Fang, I. Dutta, P. Gillot, D. Savoie, J. Lautier, B. Cheng, C. L. Garrido Alzar, R. Geiger, S. Merlet, F. Pereira Dos Santos, and A. Landragin, "Metrology with atom interferometry: Inertial sensors from laboratory to field applications," in *Proceedings for the 8th Symposium on Frequency Standards and Metrology*, 2016.
- [17] C. Jekeli, "Navigation Error Analysis of Atom Interferometer Inertial Sensor," *Navigation*, vol. 52, no. 1, pp. 1–14, Mar. 2005.
- [18] K. U. Schreiber and J.-P. R. Wells, "Invited review article: Large ring lasers for rotation sensing," *Rev. Sci. Instrum.*, vol. 84, no. 4, 2013.
- [19] G. Santarelli, A. Audoin, C. and Makdissi, P. Laurent, G. J. Dick, and A. Clairon, "Frequency stability degradation of an oscillator slaved to a periodically interrogated atomic resonator," *IEEE Trans. Ultrason. Ferroelectr. Freq. Control*, vol. 45, pp. 887–894, 1998.
- [20] I. Dutta, D. Savoie, B. Fang, B. Venon, C. L. Garrido Alzar, R. Geiger, and A. Landragin, "Continuous cold-atom inertial sensor with 1 nrad.s^{-1} rotation stability," *Physical Review Letters*, in press.
- [21] P. Berg, S. Abend, G. Tackmann, C. Schubert, E. Giese, W. P. Schleich, F. A. Narducci, W. Ertmer, and E. M. Rasel, "Composite-Light-Pulse Technique for High-Precision Atom Interferometry," *Phys. Rev. Lett.*, vol. 114, no. 6, p. 063002, Feb. 2015.
- [22] G. Sagnac, "L'éther lumineux démontré par l'effet du vent relatif d'éther dans un interféromètre en rotation uniforme," *C. R. Acad. Sci. (Paris)*, vol. 157, p. 708, 1913.
- [23] R. Legere and K. Gibble, "Quantum scattering in a juggling atomic fountain," *Phys. Rev. Lett.*, vol. 81, pp. 5780–5783, Dec 1998.
- [24] M. Meunier, I. Dutta, R. Geiger, C. Guerlin, C. L. Garrido Alzar, and A. Landragin, "Stability enhancement by joint phase measurements in a single cold atomic fountain," *Phys. Rev. A*, vol. 90, p. 063633, Dec 2014.
- [25] P. Cheinet, B. Canuel, F. Pereira Dos Santos, A. Gauguet, F. Leduc, and A. Landragin, "Measurement of the sensitivity function in time-domain atomic interferometer," *IEEE Trans. on Instrum. Meas.*, vol. 57, p. 1141, 2008.
- [26] D. S. Durfee, Y. K. Shaham, and M. A. Kasevich, "Long-term stability of an area-reversible atom-interferometer sagnac gyroscope," *Phys. Rev. Lett.*, vol. 97, p. 240801, Dec 2006.
- [27] B. Barrett, R. Geiger, I. Dutta, M. Meunier, B. Canuel, A. Gauguet, P. Bouyer, and A. Landragin, "The Sagnac effect: 20 years of development in matter-wave interferometry," *Comptes Rendus Physique*, vol. 15, no. 10, pp. 875–883, Dec. 2014.
- [28] A. Gauguet, B. Canuel, T. Lvque, W. Chaibi, and A. Landragin, "Characterization and limits of a cold-atom Sagnac interferometer," *Phys. Rev. A*, vol. 80, no. 6, p. 063604, Dec. 2009.
- [29] J. Lautier, L. Volodimer, T. Hardin, S. Merlet, M. Lours, F. Pereira Dos Santos, and A. Landragin, "Hybridizing matter-wave and classical accelerometers," *Appl. Phys. Lett.*, vol. 105, no. 14, p. 144102, Oct. 2014.
- [30] R. Kohlhaas, A. Bertoldi, E. Cantin, A. Aspect, A. Landragin, and P. Bouyer, "Phase locking a clock oscillator to a coherent atomic ensemble," *Phys. Rev. X*, vol. 5, p. 021011, Apr 2015.
- [31] H. C. Lefèvre, "The fiber-optic gyroscope, a century after Sagnac's experiment: The ultimate rotation-sensing technology?" *Comptes Rendus Physique*, vol. 15, no. 10, pp. 851–858, Dec. 2014.

A Paper Clock Prediction Model for UTC(TL)

Shinn-Yan Lin

Telecommunication Laboratories
Chunghwa Telecom Co., Ltd.

Taoyuan Taiwan
sylin@cht.com.tw

Abstract—A modified paper clock timescale weighted after removing the linearized frequency drift of each cesium clock in TL’s 12-cesium-clock ensemble is used to be the mid-term prediction reference before the next coming BIPM Circular T announcement. After removing the frequency drift pattern according to Circular T announcements, the noise type of each cesium clock in ensemble is dominated by white noise when the average time was less than about 100 days. To achieve approximately equal weighting and rational upper limit, an inversely exponential weighting procedure is also used to weight each cesium clock according to the inversely exponential function of their Allan variance; for our 12-cesium-clock ensemble, a 4 years test shows the phase error of the paper clock time scale is less than 10 ns in 45 days prediction.

Keywords—UTC; time scale;

I. INTRODUCTION

The National Time and Frequency Standard Laboratory of Chunghwa Telecomm Laboratories, TL, is entrusted by central government of Taiwan to maintain, trace, and improve the national standard time and frequency of Taiwan, UTC(TL), according to the Coordinated Universal Time (UTC) which monthly announced by Bureau international des poids et mesures (BIPM). As BIPM typically announces the time difference between UTC and the local realizations UTC(k) in Circular T monthly report [1] at the mid of each month, there may have about 40~45 days windows period from the last known UTC – UTC(TL) to next coming announcement. The aim of this study is to generate a stable paper clock time scale reference of UTC(TL) in the as long as 45 days Circular T monthly announcement windows period.

TL developed and announced its atomic time scale, TA(TL), since 2003[2-4]. TA(TL) is a free running time scale and computed with data from about 10-13 industrial cesium standards (Microsemi 5071a with high performance tube, abbreviate to 5071a hereafter). The stability of TA(TL) is limited by the intrinsic characters of 5071a clocks. Figure 1 shows the Allan deviations of each atomic clocks of TL with respect to UTC. We find, for most of 5071a clocks, their noise types are dominated by random walk FM noise or clock drift while average time is larger than 30 days [5]. That the mid-term (average time 30~60 days) behavior of the free running time scale TA(TL) is also dominated by random walk or clock drift because the weighting algorithm of TA(TL) can’t filter out

the random walk FM and clock drift noise (Figure 1. red dot-line).

To generate a paper clock time scale which is more approaching UTC than TA(TL) and used it to be the only reference of UTC(TL) in Circular T announcement windows period, we try to find and reduce the mid-term noise pattern of 5071a clocks, and weight each 5071a clock to get the paper clock more stable and predictable than TA(TL) in the mid-term especially from 30 to 45 days.

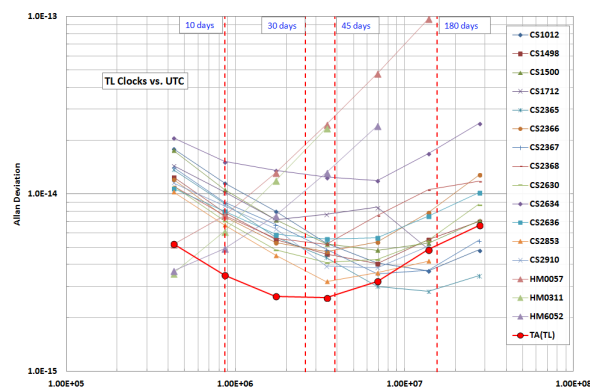


Fig. 1. The Allan Deviations of TL clocks and TA(TL) with respect to UTC

In this paper, we re-examine the time difference of 5071a clocks in TL atomic clock ensemble with respect to UTC and look for a linear function to describe them in section II. The weighting procedure and the simulation result of the paper clock used for UTC(TL) steering are described in section III and IV.

II. CHARACTERS OF TL ATOMIC CLOCKS

TA(TL) is a free running time scale and the weighting averaged of all 5071a clocks in ensemble. It's reasonable to expect the TA(TL) would be always stable and linearly predictable only if the frequency offset of all 5071a clocks are stationary or dominated by white noise all the time. Unfortunately, from Figure 1, the behavior of 5071a clocks are dominated by random walk FM noise and clock drift when the average time more than about 40 days and, in consequence, the long-term stability of TA(TL) which averaged from 5071a clock ensemble is also dominated by random walk FM noise and clock drift.

Figure 2 shows the frequency offsets of 4 5071a clocks with respect to UTC (leap second compensated), we find the slopes of their frequency offsets are generally stationary. The distribution of their frequency offsets will be roughly normal when remove their frequency drift. In the other words, relative to the frequency offset, the frequency drift is the better linear index for sketching the behavior 5071a clocks and may be used for reducing the random walk FM noise of 5071a clocks.

For test, we remove the 900 days frequency drift of one 5071a clock (series number 2910, CS2910) in our clock ensemble and compare its phase offset (right graph of Figure 3) with the result of removing the frequency offset only (left graph of Figure 3). To optimize the random walk FM noise, here the frequency drift of CS2910 is calculated by averaging

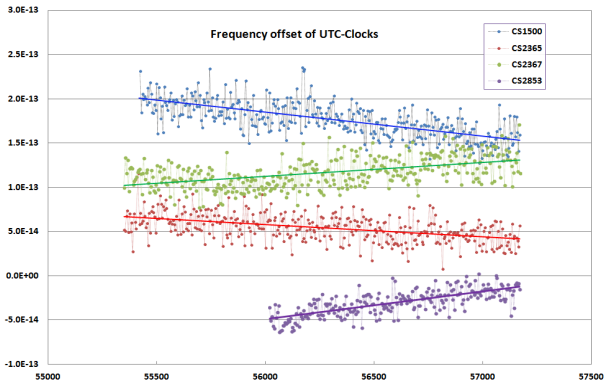


Fig. 2. Frequency offsets of 4 5071a cesium standard.

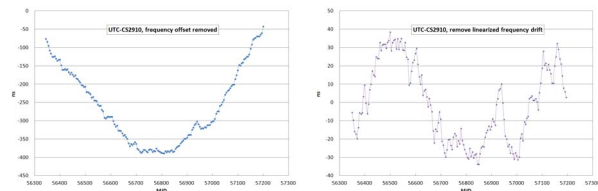


Fig. 3. The phase difference of CS2910 5071a clock with respect to UTC, remove frequency offset (left) and linearized linearized frequency drift (right).

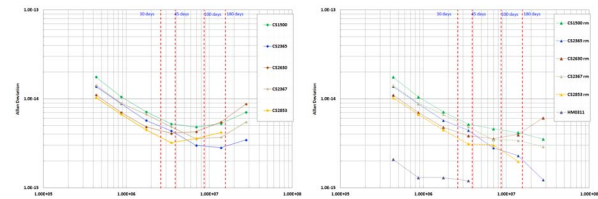


Fig. 4. The Allan Deviation of 4 5071a clocks, left: original data, right: remove linearized frequency drift.

its 2nd order phase differential with respect to UTC [6]. Figure 3 shows the peak to peak phase difference with respect to UTC is about 450 ns if we remove its frequency offset and about 80 ns if we remove the linearized frequency drift.

We also examine the frequency domain characters of 5071a clocks after removing their frequency drifts. Figure 4 shows the Allan deviations of 4 5071a clocks (series number 1500, 2360, 2365, and 2853) before and after removing frequency drift. The right graph of Figure 4 shows the random walk FM

noises of most of the 5071a clocks are reduced and their mid-term stabilities of 5071a clocks are also improved.

III. THE WEIGHTING PROCEDURE

In section II, we demonstrated the frequency drift of 5071a clocks are approximately invariant during at least hundreds days and can be used to sketch and predict the phase offset of 5071a clocks. From section II, we know the short-term noise of each 5071a clock are dominated by white noise and their random walk FM noise of can be reduced after removing their frequency drift, therefore, if we remove the pattern of frequency drift, the mid-term noise type of 5071a clocks is generally white noise (Figure 4), and we can generate an accurate paper clock just simply averaging all clock in ensemble after removing each clock's frequency drift with respect to UTC.

Typical time scale algorithms are designed to optimize frequency stability, the weight attributed to each clock is chosen to be inversely proportional to the clock's frequency variance [7]. The result ensemble time scale may be dominated by few very stable clocks or we have to set a cutting head weight upper limit for scaling algorithm.

To optimize the best long term accuracy, the actual weighting algorithm used for our UTC(TL) reference paper clock, we name it as TA₁(TL) hereafter, is similar to the algorithm we use for TA(TL) [2], the weight of each 5071a clock is proportional to the inversely exponential with the index of each clock's frequency variance:

$$TA_1(TL)(t) = \sum_{i=1}^N w_i(t) \cdot [x_i(t) - (t - \Delta t) \cdot d_i(t - \Delta t)] \quad (1)$$

$$w_i(t) = \frac{e^{-b\sigma_i^2(t-\Delta t)}}{\sum_{i=1}^N e^{-b\sigma_i^2(t-\Delta t)}}$$

deviation between hydrogen and 5071a clock_i during the period (t- Δt) to t.

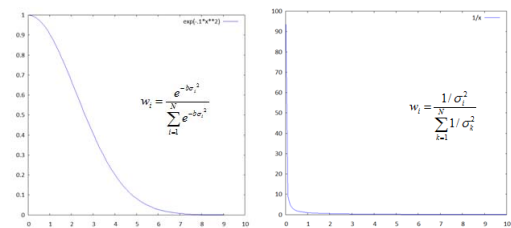


Fig. 5. The comparison between inversely exponential function (left graph) and inversely function (right graph).

Figure 5 shows the comparison between the inversely exponential proportional function and the inversely proportional function which used for typical weighting procedures. Compared with the inversely proportional function, the outputs of inversely exponential proportional function are approximately the same even their input frequency variance values are slightly different. Therefore the result of TA₁(TL) is

approximately the same as the results of equal weighting procedure. But relative to equal weighting procedure, the advantage of $TA_1(TL)$ is it can filter out the bad clock data automatically in an abnormal frequency variance input. Meanwhile, the inversely exponential proportional function has a rational upper limit itself, that guarantee the $TA_1(TL)$ will not be dominated by few clocks in ensemble, the $TA_1(TL)$ will keep stable even if one very stable clock is out of order unpredictably.

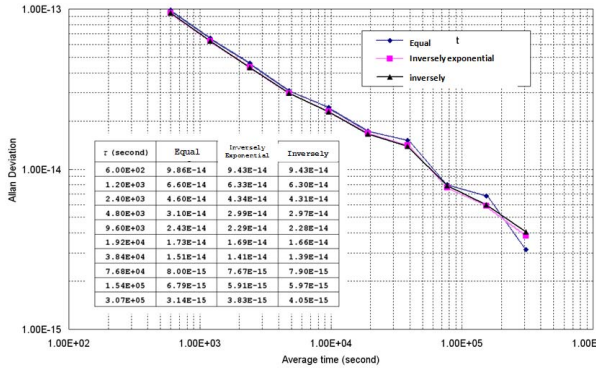


Fig. 8. The short term stabilities of the results of equal weight, inversely exponential weight, and inverse weight procedures. There is no significant difference between 3 weighting processes.

To compute $TA_1(TL)$, we first calculate and remove the 60 days linearized frequency drift of each 5071a clock in ensemble by averaging its 2nd order phase differential with respect to UTC whenever BIPM announces the time difference value of UTC-UTC(TL) every month, after removing the frequency drift patterns of each 5071a clock, the $TA_1(TL)$ is the weighting result of equation (1).

Even $TA_1(TL)$ is optimized for best mid-term accuracy, we expect its short term stability will roughly be the same as inversely proportional weighting procedure because of the short term characters of each 5071a clock are generally the same. Figure 6 shows the comparison between 3 kinds of weighting procedures. We calculated the weighting result of TL 5071a clock ensemble using $TA_1(TL)$, equal, and inversely proportional weighting procedure, then compare their stability with an active hydrogen maser (Kvarz CH1-75, series number 76052). The short term stabilities of the weighting results of 3 kinds of procedures have no significant difference when average time less than 3 days.

IV. PREDICTION ERRORS VS. UTC

To verify the prediction ability of $TA_1(TL)$, a prediction simulation over 4 years is performed. We simulate and examine the time difference between UTC(TL) and $TA_1(TL)$ after 30 and 45 days prediction, then compare the time difference with UTC – UTC(TL) from MJD 55500 to 57100. For UTC is the ultimate reference of UTC(TL), we treat the time difference between $TA_1(TL)$ and UTC to be its prediction error. More than 4 years simulation demonstrates the 30 days prediction error is about ± 5 ns (Figure 7) and about ± 10 ns for 45 days prediction simulation (Figure 8).

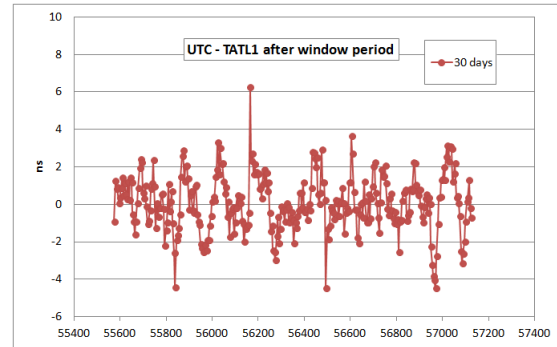


Fig. 6. The 30 days prediction result of $TA_1(TL)$ vs. UTC

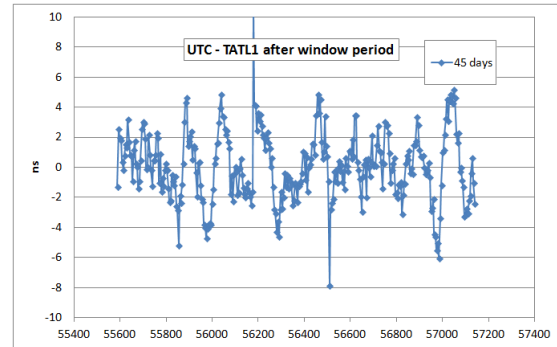


Fig. 7. The 45 days prediction result of $TA_1(TL)$ vs. UTC

V. SUMMARY AND FUTURE WORK

We investigate the characteristics of atomic clocks in TL atomic clock ensemble, and use the linearized frequency drift to sketch and predict their behavior. The discussion of session II shows the frequency drifts of 5071a clocks in TL ensemble are approximately stationary within 100 days, model and remove the frequency drift pattern of each clock can get a relative accurate, UTC approaching time scale.

After removing the frequency drift pattern with respect to UTC, A paper clock time scale, $TA_1(TL)$, is computed from the weighting average of 5071a clocks. We simulate the prediction ability of $TA_1(TL)$ and demonstrate its 45 days holdover error with respect to UTC is less than ± 10 ns. The $TA_1(TL)$ is used for UTC(TL) steering during UTC announcement windows periods, that help TL to keep the time difference between UTC and UTC(TL) within ± 10 ns.

Since the frequency drift of a typical active hydrogen maser is more stable than commercial cesium clocks, a paper clock algorithm combined hydrogen masers with 5071a clocks in TL atomic clock ensemble is under studying, we expect the prediction ability of new paper clock time scale will be better than our current model and can improve the accuracy of UTC(TL).

REFERENCES

- [1] <ftp://ftp2.bipm.org/pub/tai/publication>
- [2] S. Lin and H. Peng H, "A paper clock model for cesium clock ensemble of TL". 35th Annual Precise Time and Time Interval Meeting, 2003.

- [3] S. Lin, H. Peng, W. Tseng, H. Lin, and C. Liao, "The Future Model of TA(TL)", 36th Annual Precise Time and Time Interval Meeting, 2004
- [4] S. Lin, H. Peng, W. Tseng, H. Lin, and C. Liao, "An Improvement of TA(TL): Using the Combination of a Hydrogen Maser And a Cesium-Clock Ensemble", Joint Meeting of IEEE International Frequency Control Symposium and European Frequency and Time Forum, 2007
- [5] D. W. Allan, "Time and Frequency (time domain) characterization, estimation, and prediction of precision clocks and oscillators". IEEE trans. Ultrasonics, Ferroelectrics and Frequency Control, UFFC-34, 647-654, 1987.
- [6] J.A. Barnes, "The Measurement of Linear Frequency Drift in Oscillators," Proc. 15th Annu. PTI Meeting, pp. 551-582, Dec. 1983
- [7] ITU Handbook selection and use of precise frequency and time system, Chapter 6, 1997.
- [8] J. Azoubib, M. Granveaud, and B. Guinot B, "Estimation of the scale unit duration of time scales", Metrologia, Vol. 13, 87-93, 1977.
- [9] Symmetricon Co. Ltd. "5071A Primary Frequency Standard Operating and Programming Manual", Rev. H, August 14, 2009
- [10] P. Tavella and C. Thomas C. "Comparative study of time scale algorithms. Metrologia", Vol. 28, 57-63, 1991.
- [11] S. Lin, "A Phase Locked Mechanism for Time Scaling Frequency Control System" IEEE International Ultrasonics, Ferroelectrics, and Frequency Control Joint 50th Anniversary Conference, 2004.
- [12] S. Lin, H. Peng, W. Tseng, H. Lin, and C. Liao, "An Improvement of the Controlling Algorithm for Taiwan's Time Scaling System", Joint IEEE International Frequency Control Symposium and Precise Time and Time Interval Systems and Applications Meeting, 2005.

Towards sub-nanosecond synchronization of a telecom network by fiber optic distribution of UTC(k)

Śliwczynski Ł., Krehlik P.
 AGH University of Science and Technology
 Department of Electronics
 Krakow, Poland
 sliwczyn@agh.edu.pl

Imlau H., Ender H.
 Deutsche Telekom Technik GmbH
 Bremen, Germany
 Helmut.Imlau@telekom.de

Schnatz H., Piester D., Bauch A.
 Physikalisch-Technische Bundesanstalt (PTB),
 Braunschweig, Germany
 Harald.Schnatz@ptb.de

Abstract— The operation of a mobile telecom network relies directly on the synchronization of thousands of base stations that must be robust and operate reliably 24 hours a day. Nowadays networks using advanced Long Time Evolution (LTE) standard need not only frequency syntonization, but also time synchronization that should ideally be traceable to UTC. In this work we present first results of providing UTC(PTB) (1 PPS and 10 MHz) by optical fiber to a test center of Deutsche Telekom in Bremen. The work aimed at a proof-of-concept in real telecommunication environment and the demonstration of the long-term operation capability and scalability of the approach. A potential future application is the comparison of UTC(PTB) and UTC(DTAG).

Keywords— UTC(k) dissemination, delay stabilization; fiber network; telecom network

I. INTRODUCTION

Many telecom network applications require synchronization to allow its standard operation (i.e. voice and data transmission). The synchronization chain is constructed in a hierarchical and layered way, in which each piece of network equipment draws its synchronization signal from a superior hierarchy element located closer to the primary synchronization source.

A generic block diagram that is considered by the International Telecommunication Union (ITU) for synchronization of a mobile telecom network is shown in Fig. 1 [1]. In this diagram the highest block in the hierarchy is a Primary Time Reference Clock (PRTC) that is used to

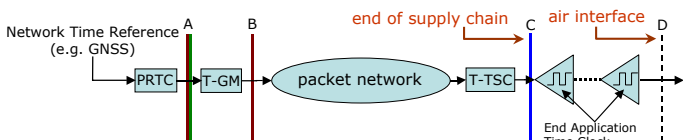


Fig. 1. Block diagram of synchronization supply chain used in mobile telecom, adapted from [1].

This work was supported in parts by Faculty of Computer Science, Electronics and Telecommunications, AGH University of Science and Technology.

synchronize the Telecom Grand Master (T-GM). The Telecom Time Slave Time Clock (T-TSC) is synchronized using signals drawn from a packet data transmission network. The PRTC provides a reference time signal that should be traceable to a recognized time standard [e.g., coordinated universal time (UTC)]. UTC can be obtained from a UTC time laboratory collaborating with the Bureau International des Poids et Mesures (BIPM) or from a global navigation satellite system (GNSS) [2]. In fact, Deutsche Telekom operates its timing centre in Frankfurt/Main (DE) and obtains traceability of UTC(DTAG) to UTC through the BIPM Circular T as many National Metrology Institutes and research institutes. In the telecom world it is, however, quite common to seek traceability to international standards by receiving signals from a global navigation satellite system (GNSS), typically today GPS.

Recommendations concerning the telecommunication time reference clocks at some near future will be developed towards enhanced PRTC (ePRTC) and coherent network PRTC (cnPRTC) [3].

In an approach as sketched in Fig. 1 the quality of the synchronizing signals degrades progressively, being the highest at the very start of the synchronization chain. However, the end application clock must still fulfill some requirements to allow operation of the entire network [4]. In particular, for the

TABLE I. MAXIMUM TIME ERROR SPECIFICATIONS FOR VARIOUS REQUIREMENT CLASSES (adopted from [1])

Class	Time Error (TE)	Application
1	500 ms	billings, alarms
2	100 μ s	IP delay monitoring
3	5 μ s	LTE-TDD (large cell)
4	1.5 μ s	UTRA-TDD LTE-TDD (small cell)
5	1 μ s	Wimax-TDD
6	< x ns (under study)	a few LTE-A features and location based services

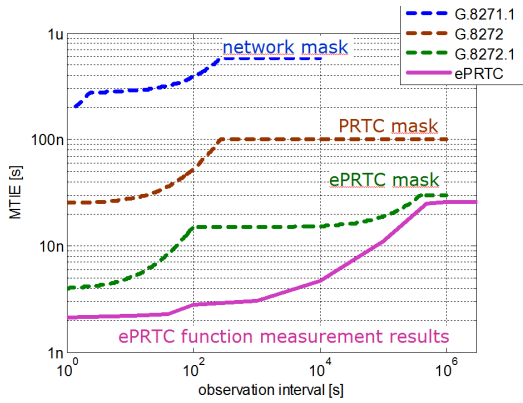


Fig. 2. MTIE masks accordingly to ITU-T G.827x recommendations.

operation of the mobile communication based on LTE standard (class 4 in Tab. 1) the inaccuracy of the time synchronization specified as maximum Time Error (maxTE) must not exceed $1.5 \mu\text{s}$ at the air interface (reference point D in Fig. 1). This value is related to mobile Time Division Duplex (TDD) operation requirements and features like enhanced Inter-Cell Interference Cancellation (eICIC), or Coordinated Multi Point (CoMP) Joint Processing. A few LTE-A (advanced) features and location-based services) will require even more accurate synchronization - exact values are still subject of studies by ITU telecom experts [4]. The values of maxTE are based on the analysis of the time error budget, taking into account the PRTC/T-GM inherent inaccuracy, the constant time error (cTE) resulting from nodes and network asymmetry and the dynamic time error (dTE) caused by random effect in the network equipment and network links. The dTE in various points inside the network has its own limiting specifications given as Maximum Time Interval Error (MTIE) and Time Deviation (TDEV) - see the relevant masks shown in Fig. 2.

In a mobile network the required level of accuracy may be obtained using a combination of methods offered by synchronous Ethernet (SyncE) and Precision Time Protocol (PTP) with Full Timing Support from the network (PTP-FTS) according to the ITU-T recommendation series G.827x.

However, to assure the robust operation of the network one additional level of synchronization hierarchy would be desirable, allowing monitoring and supervising the real performance of the highest-level equipment, like e.g. the PRTC. To do this, an access to a UTC signal of much higher accuracy than available through GNSS is an attractive option to

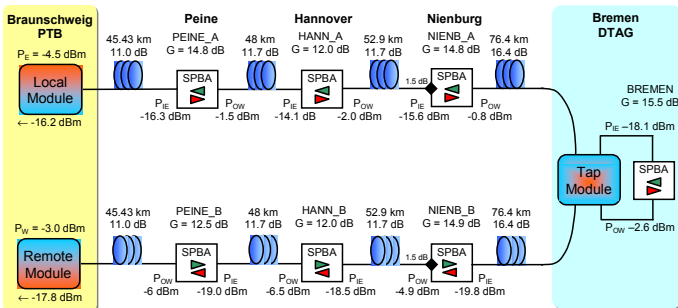


Fig. 3. The block diagram of the PoC time and frequency fiber optic transfer link installed on the route Braunschweig- -Bremen - Braunschweig.

follow.

In addition, when UTC traceability of PRTCs is based on local GNSS receivers only, a strategic risk arises for network operators, as they have no control and influence on satellite systems. Moreover, signals from the GNSS systems may be relatively easily jammed or spoofed [5]; potential risks of satellites' crashes/malfunction are also discussed [6].

Many of such problems may be circumvented by accommodating fiber optic time and frequency dissemination techniques that recently have been developed. Until now, only a few installations of this type were set up, oriented either for experimental or scientific purposes [7]-[10]. In this work we present a proof of concept (PoC) experiment, delivering UTC(PTB) (1 PPS and 10 MHz) by optical fiber to the test center of Deutsche Telekom in Bremen. The experiment started in July 2015, and is a joint initiative of Physikalisch-Technische Bundesanstalt, Germany's National Metrology Institute, and by law entrusted to disseminate legal time for the country, Deutsche Telekom, user of the synchronization signals and AGH, developer of the fiber optic time and frequency transfer technology - ELSTAB [11]. Its results prove that such a solution may satisfy the telecom operator needs related to both accuracy/stability requirements and the long-term reliability. The proof of concept experiment was designed to allow transfer of UTC(PTB) to Bremen and should be seen as precursor to an installation linking PTB with the Frankfurt site where UTC(DTAG) is realized. In the final version UTC(PTB) and UTC(DTAG) could be compared to each other avoiding the use of GNSS signals.

II. PROOF OF CONCEPT EXPERIMENT

The plan of the PoC required installing a fiber optic link that would be able to deliver continuously 1 PPS and 10 MHz signals, traceable to UTC(PTB) with an inaccuracy much lower than 1 ns between the PTB in Braunschweig and the test center of Deutsche Telekom in Bremen. To be able to monitor and

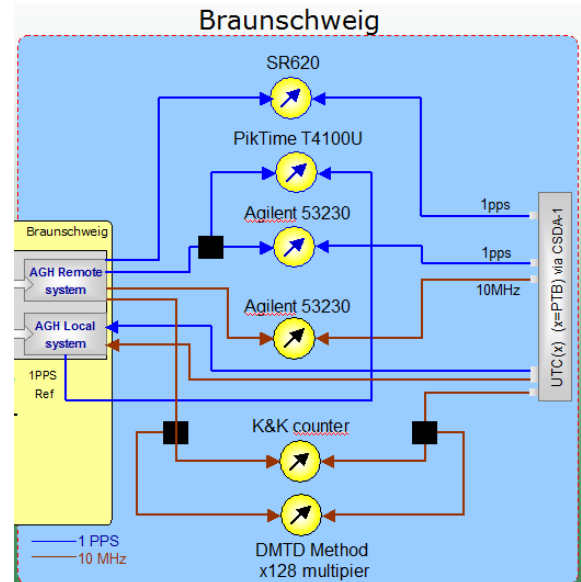


Fig. 4. Measurement setup used in Braunschweig to evaluate the round-trip performance of the optical time and frequency transfer link.

evaluate the performance of the signals we decided to arrange a loop configuration with the local and remote modules located in Braunschweig and to additionally install a so-called Tapping Module [12] in Bremen - see Fig. 3. In addition seven single-path bidirectional fiber optic amplifiers (SPBA) needed to be installed along the fiber route to compensate for its loss (two in each location in Peine, Hannover and Nienburg, respectively, plus one more in Bremen). Each piece of such equipment included an Ethernet interface for remote monitoring and management. The total length of the fiber link is 448 km roundtrip (Braunschweig-Braunschweig) and half of this length from Braunschweig to Bremen. The fibers used are standard single mode fibers (G.652) supplied by Deutsche Telekom which have been installed between 2000 and 2015.

The experiment was divided into two parts. The first one, lasting from July 2015 to December 2015, was dedicated to observe and solve some potential problems arising from field deployment, to check the operation of remote control of installed equipment and to develop efficient procedures for logging various types of events. This phase appeared to be very important and effective because it allowed discovering and eliminating problems such as electromagnetic pickup from mobile phones at PTB and issues with interruptions of power supply at SPBA locations. The second part of the experiment was aimed on the regular operation of the link and long-term evaluation of the parameters of transferred signals.

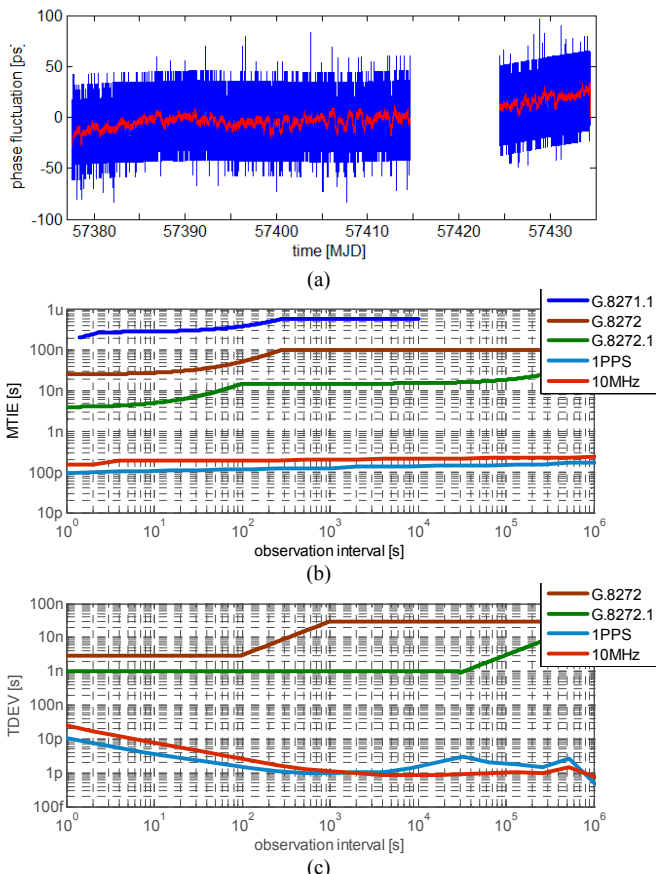


Fig. 5. Comparison of UTC(PTB) with 1 PPS signal after 448 km of fiber optic link using ELSTAB technology (a) and resulting MTIE (b) and TDEV (c) compared with relevant ITU-T masks.

III. EXPERIMENTAL RESULTS

In Fig. 4 we show the measurement setup used to evaluate the performance of the fiber optic time and frequency transfer link at Braunschweig. We used various instruments and techniques to in-depth characterize the system and to get enough redundancy in case of a possible failure of one of the instruments. Aside from usual time interval counters for 1 PPS and 10 MHz signals we exploited a dual-mixer time difference (DMTD) method for stability assessment of 10 MHz signal.

The results presented herein are related mainly to the telecom-type measurements, oriented on the relation to the reference masks (as presented e.g. in Fig. 2) and showing the potential of the fiber optic time and frequency transfer. The measurements of the time/phase differences for both 1 PPS and 10 MHz signals were performed in the loop configuration, with a UTC(PTB) signal used as one input to the measurement instrument and the output of the Remote Module as a second one. We used Agilent 53230 counters for this purpose, as this is a kind of equipment routinely used by Deutsche Telekom. The original record registered by one of the counters for 1 PPS signal is shown in Fig. 5a (a red line shows a 10-minutes average), whereas calculated values of MTIE and TDEV shown in Figs. 5b and 5c, respectively.

The most important result of the evaluation of the collected data is that both MTIE and TDEV values are substantially below the even most restrictive masks, proposed for enhanced PRTC functions (ePRTC) accordingly to ITU-T G.8272.1. It should also be noted that the counters used for measuring the time differences have relatively low resolution (20 ps according to the datasheet) which influences the results substantially. Evaluations performed using different counters, namely Stanford Research SR-620 and PikTime T4100U, show TDEV at 1 s around 6 ps. In each case the noise of the counter seems to be a noticeable factor influencing the results.

The evaluation of the quality of 1 PPS signal delivered to the Deutsche Telekom laboratory in Bremen via the fiber link was performed using GPS dual-frequency code- and carrier-phase comparison with L3P data acquired using a GPS timing

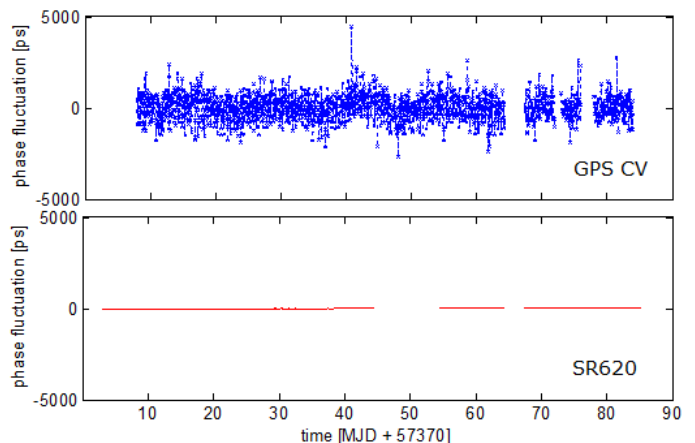


Fig. 6. Upper plot: one-hour averages of comparison of UTC(PTB) with UTC(PTB) at the output of the Tapping Module located in Bremen using GPS CV. Lower plot: phase fluctuations measured after the round-trip transfer Braunschweig-Braunschweig. Both data sets were normalized to zero mean independently. See description in the text.

receiver (DICOM GTR-51). The results of comparison averaged for one hour are presented in the upper part of Fig. 6. In the lower part of this figure the one-hour average for a similar period of the time is shown for the round-trip transfer (Braunschweig - Braunschweig) and measured with a SR-620 counter. The comparison of booth curves clearly shows the potential and advantages of the optical time and frequency transfer. This can be considered in fact as a continuous service, offering much better long and short-term instability and requiring no data processing.

IV. CONCLUSION

After a few months of continuous operation of the link Braunschweig-Bremen-Braunschweig it may be stated that the synchronizing signals transferred using optical fiber satisfy the needs of a telecom operator concerning stability requirements, even considering future demanding applications. An optical fiber link may be considered as a solution to the problem of supervising and monitoring the operation of telecom primary reference time clocks or could even constitute a source to synchronize a mobile network. It is independent from GNSS signals and thus introduces a redundancy element into the network architecture.

At low averaging times (1-100 s), the verification of the true performance of the time transfer link appears to be a metrological problem as the results depend on the equipment used for the measurements and are probably limited by the noise of the counters used. For longer averaging times we are also limited by the long-term instability of the measurement equipment, and it is difficult to clearly distinguish this from instability caused by the link. Nevertheless we still have a good safety margin, at least an order of magnitude, when comparing with the PRTC and ePRTC masks.

In the next period of collaboration we will leave the link running for an extended period of time and observe its performance. From the telecom operator point of view some work is still to be done to make the system as maintenance-free as possible. This especially includes the problems with squelching the output signals in case of loss of optical signal (e.g. because of a fiber break).

During the operation of the link we encountered occasional problems with the internal laser wavelength stabilization system and with the loss of power in one of SPBA stations.

However, all these problems were successfully managed (or at least detected, as it was for the loss of the power supply) using Ethernet network interfaces that are installed in all the modules of the link.

ACKNOWLEDGMENT

We would like to thank Marvin Barasi, Uwe Habighorst and René Baas from Deutsche Telekom and Holger Seifert and Hermann Brandt from PTB for their help in organizing and enabling the fiber and Ethernet connections with all remote parts of the link.

REFERENCES

- [1] ITU-T Recommendation ITU-T G.8271.1/Y.1366.1: "Network limits for time synchronization", ITU, 2013.
- [2] ITU-T Recommendation ITU-T G.8272/Y.1367: "Timing characteristics of primary reference time clocks", ITU, 2015.
- [3] H. Imlau, "Primary Reference Clocks in Telecommunication Networks: PR(T)C, ePRTC and cnPRTC," WSTS 2015, San Jose, 11.3.2015
- [4] ITU-T Recommendation ITU-T G.8271/Y.1366 "Time and phase synchronization aspects of packet networks in packet networks", ITU, 2012
- [5] D. Last, "GNSS: the present imperfect", InsideGNSS, vol. 5, pp. 60-64, 2010.
- [6] J. Saarinen, "Satellite failure caused global GPS timing anomaly," <http://www.itnews.com.au/news/satellite-failure-caused-global-gps-timing-anomaly-414237> - maybe something better?
- [7] Ł. Śliwczyński, P. Krehlik, A. Czubla, Ł. Buczek and M. Lipiński, "Dissemination of time and RF frequency via a stabilized fibre optic link over a distance of 420 km," *Metrologia*, vol. 50, pp. 133–145, 2013.
- [8] D. Piester, M. Rost, M. Fujieda, T. Feldmann, A. Bauch, "Remote atomic clock synchronization via satellites and optical fibers," *Adv. Radio Sci.*, 9, 1–7, 2011.
- [9] O. Lopez, A. Kanj, P-E. Pottie, D. Rovera, J. Achkar, Ch. Chardonnet, A. Amy-Klein, G. Santarelli, " Simultaneous remote transfer of accurate timing and optical frequency over a public fiber network," *Applied Physics B*, vol 110, pp 3-6, 2013.
- [10] S. Raupach, G. Grosche, "Chirped frequency transfer: a tool for synchronization and time transfer," *IEEE Trans. Ultrason., Ferroelectr., Freq. Control*, vol. 61, pp. 920-929, 2014.
- [11] P. Krehlik, Ł. Śliwczyński, Ł. Buczek, J. Kołodziej and M. Lipiński, "ELSTAB - fiber optic time and frequency distribution technology - a general characterization and fundamental limits," *IEEE Trans. Ultrason., Ferroelectr., Freq. Control*, DOI 10.1109/TUFFC.2015.2502547, 2015.
- [12] Ł. Śliwczyński and P. Krehlik, "Multipoint joint time and frequency dissemination in delay-stabilized fiber optic links," *IEEE Trans. Ultrason., Ferroelectr., Freq. Control*, vol. 62, pp. 412-420, 2015.

Frequency Synthesis from Cryogenic Sapphire Oscillator

Etienne Vaillant, Fabrice Sthal, Joel Imbaud,
Yannick Gruson, Christophe Fluhr, Serge Grop,
Vincent Giordano, Enrico Rubiola.
FEMTO-ST Institute UFC, CNRS, ENSMM, UTBM,
UBFC Besançon, France
Email: fsthal@ens2m.fr

François-Xavier Esnault, Gilles Cibiel
Microwave and Time-Frequency Department, CNES,
Toulouse, France
Email: francois-xavier.esnault@cnes.fr

Abstract—In this paper we present several configurations enabling to obtain a low-noise 5 MHz signal from the 100 MHz delivered by the frequency synthesis of a Cryogenic Sapphire Oscillator. The residual single-sideband phase noise of several dividers is reported. Especially the noise of a custom built regenerative divider has been measured to be around $\mathcal{L}_{5\text{MHz}}(1\text{ Hz}) = -145\text{ dBc/Hz}$. This performance is sufficient to measure the residual phase noise of an ultra-stable quartz crystal resonator using a carrier suppression system.

I. INTRODUCTION

The FEMTO-ST Institute, Besançon, France and the French space agency (CNES), Toulouse, France investigate the origins of noise in bulk acoustic wave resonators for several years [1]. To characterize ultra-stable resonators, the carrier suppression technique is used to measure the inherent phase noise of the DUT. The traditional method is based on a setup made with two arms in which two nearly identical resonators are inserted. When the two arms are equilibrated the noise of the driving source is rejected [2], [3]. Eventually 3 dB are subtracted from the measured noise assuming the two resonators are identical. This assumption may not be true especially when dealing with state-of-the-art resonators. In this way it is interesting to search to develop a new tool able to characterize only one resonator. In this case, the key point is the phase noise of driving source, which should be very low. At 5 MHz, the power spectral density (PSD) of phase fluctuations of the best quartz crystal resonators is expected to approach -140 dBc/Hz at 1 Hz from the carrier.

The development of Cryogenic Sapphire Oscillators based on whispering gallery mode sapphire resonator has allowed an improvement of 1 to 2 orders of magnitude in terms of frequency stability, between one and several thousand seconds of integration time, compared to the hydrogen maser [4], [5]. The state-of-the-art of such a source in terms of frequency stability is around 6.10^{-16} at 1s of integration time [5]-[9]. Other technologies are able to produce ultra-low-noise microwave signals, like optical-comb-based frequency division of a cavity-stabilized laser [11]-[13].

In this paper, we present the preliminary results on a new frequency division chain delivering a 5 MHz signal from the 100 MHz coming from the frequency synthesis of a CSO [4].

The limit imposed by commercial dividers is shown. A better result has been obtained by using a custom regenerative divider (RD) in the last division stage. Further investigations are proposed in order to improve these results.

II. FREQUENCY SYNTHESIS

A. Cryogenic Sapphire Oscillator source

The CSO has been described in [14]. It generates an ultra-stable signal near 10 GHz achieving in the best configuration a fractional frequency stability of 4.5×10^{-16} at 1 s. Three almost identical CSOs have been recently implemented in the lab in the frame of the Oscillator IMP project. Each of them is complemented with a low noise frequency synthesis delivering a 100 MHz signal [15]. The phase noise measured by beating two synthesized 100 MHz signals is presented in Fig. 1.

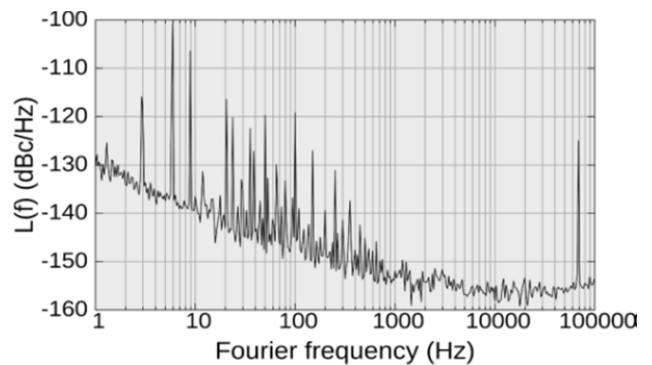


Fig. 1. Absolute phase noise of the 100 MHz signal delivered by the CSO synthesis chain. This result has been obtained by beating two nearly identical sources. The phase noise of one unit is assumed to be 3 dB lower.

At 100 MHz the phase noise of one unit is -133 dBc/Hz at 1 Hz offset from the carrier. It should be mentioned that this performance is limited by the noise of the frequency dividers implemented in the frequency synthesis chain, initially designed to get a fractional frequency stability of 3×10^{-15} , thus practically one order of magnitude higher than the current CSO performance. The phase noise of the CSO 10 GHz signal has been measured: $\mathcal{L}_{10\text{GHz}}(1\text{ Hz}) = -100\text{ dBc/Hz}$ [7]. For an ideal 100 MHz frequency synthesis the expected phase noise is

-140 dBc/Hz. These numbers demonstrate that there is some margin (7 dB) to improve the current system.

The simplest way to get a 5 MHz signal from a 100 MHz source is to use a chain of several dividers reaching the appropriate ratio, i.e. 20. This simple design is shown in Fig. 2.

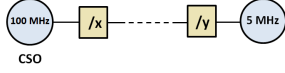


Fig. 2. Simple cascade of several frequency dividers in order to get 5 MHz.

For an ideal division by ratio N , the phase noise is expected to be divided by N^2 . The single sideband PSD of the input and output signals are thus related by:

$$\mathcal{L}_{5\text{MHz}}(f) = \mathcal{L}_{100\text{MHz}}(f) - 20 \cdot \log\left(\frac{100}{5}\right)$$

Assuming the input signal with $\mathcal{L}_{100\text{MHz}}(1 \text{ Hz}) = -133 \text{ dBc/Hz}$, a noise-free synthesis is expected to deliver a 5 MHz output signal such as $\mathcal{L}_{100\text{MHz}}(1 \text{ Hz}) = -159 \text{ dBc/Hz}$. Unfortunately such theoretical limit cannot be practically reached due to the phase noise of the RF components (dividers, amplifiers) entering in the design of the frequency synthesis. The aim of this work is to evaluate the limit achievable with a simple solution based as much as possible on commercially available frequency dividers.

B. Commercial frequency dividers

We tested several commercial frequency dividers that could be implemented in the first stage of our frequency division chain. The measurement principle we implemented is represented in Fig.3.

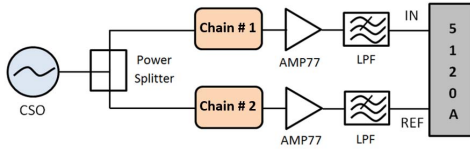


Fig. 3. Measurement system configuration for commercial dividers.

The setup is based on a digital cross-correlation PM-noise measurement system (Symmetricom-5120A Microsemi Corporation). The power of the CSO 100 MHz signal is divided in two arms consisting in two identical divider chains.

Different combinations have been tested. The measurement results are presented in section III (see Fig. 8). One of the most convenient divider is the HMC705 (Hittite Microwave, Analog Devices). The division ratio of the HMC705 can be set between 1 to 17, and thus can constitute the first stage of the frequency division chain.

C. Regenerative Frequency Divider

The regenerative frequency divider (RD) is known for its very low phase noise. The RD principle presented in Fig. 4 can be extended in a wide frequency range [17]-[20].

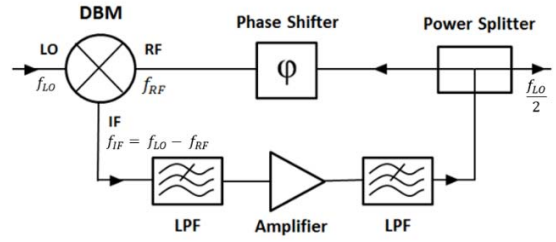


Fig. 4. Block diagram of a frequency regenerative divider by 2.

This divider uses a mixer, an amplifier, some low-pass filters and a phase shifter in a closed loop configuration. The input signal of the divider f_{LO} is mixed with the RF signal f_{RF} . The IF signal contains two frequencies:

$$f_{IF} = f_{LO} \pm f_{RF} \quad (1)$$

The sum frequency is suppressed by a first low-pass filter (LPF). The closed loop condition imposes:

$$f_{IF} = f_{RF} \quad (2)$$

Combining equations 1 and 2 leads to an output signal frequency equals to $\frac{f_{LO}}{2}$. The second low pass filter is used to remove the broadband noise due to the thermal noise of the amplifier [18]-[20]. The built mixer is a well-proven double balanced mixer with a diode ring composed of four 2N2222A [21]. The transistors behave as diodes since the base is shorted to the collector. The principle of such a mixer is given in Fig. 5.

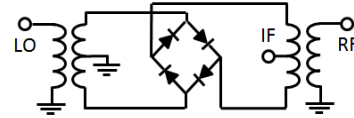


Fig. 5. Principle of a double balanced mixer with a diode ring. Our mixer is composed of four 2N2222A transistors acting as diodes.

The amplifier is used to ensure an open loop gain superior to 1. The phase condition, which is close to 2π like in an oscillator, is set by a phase shifter. The regeneration starts due to the thermal noise inside the loop [17], [18]. The amplifier is a low-noise AMP77 (Mini-Circuits). Its low level gain is 15 dB and its output power at the 1 dB compression point is around 18 dBm at 5 MHz. In the RD loop the amplifier saturates [18], [22]. The output signal power is +12 dBm.

In order to measure the phase noise of the RD, we modified the previous set-up as shown in Fig. 6. The 100 MHz signal from the CSO is frequency divided by 10 with a HMC705 before the power splitter. The noise of this divider is subtracted out in the test system leaving the phase noise of the regenerative dividers.

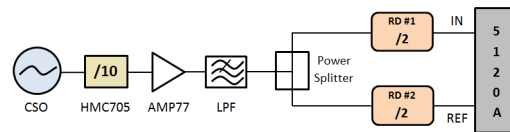


Fig. 6. Block diagram of the measurement system for regenerative dividers.

The residual PM noise of a pair of RD is shown in Fig. 7. In this configuration, the divider pair reached -142 dBc/Hz at 1 Hz offset from the carrier. Both dividers have the same scheme and same components; therefore it is possible to subtract 3 dB from the measured phase noise to determine the contribution of each divider. Thus, each of our dividers shows an estimated residual phase noise of

$$\mathcal{L}_{5\text{MHz}}(1 \text{ Hz}) = -145 \text{ dBc/Hz}$$

$$\text{and } \mathcal{L}_{5\text{MHz}}(10 \text{ kHz}) = -175 \text{ dBc/Hz.}$$

The phase optimization in the loop of the divider and the tuning of the maximum output amplitude will decrease this phase noise [18].

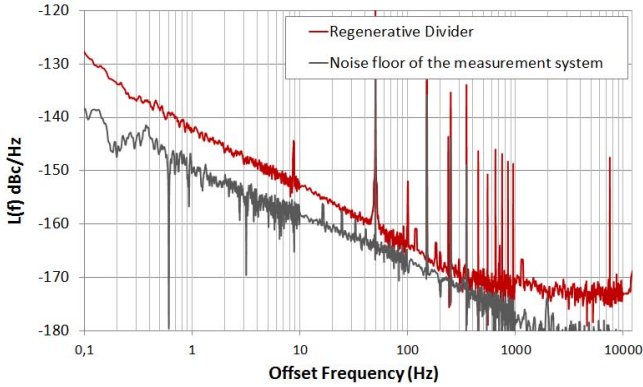


Fig. 7. Residual single-sideband phase noise of two frequency regenerative dividers at 5 MHz output for a 10 MHz input.

A phase noise of $\mathcal{L}_{5\text{MHz}}(1 \text{ Hz}) = -145 \text{ dBc/Hz}$ allows to measure quartz resonators whose frequency stability in the Allan deviation is $\sigma_y(\tau) = 4.7 \times 10^{-14}$.

III. PRELIMINARY RESULTS OF FREQUENCY SYNTHESIS

The phase noise of the tested configurations is shown in Fig. 8. The noise floor of the measurement system is at least 15 dB lower than those of the measured devices. Supplementary RF amplifiers are required to inject the signals in the 5120A with the appropriate power level.

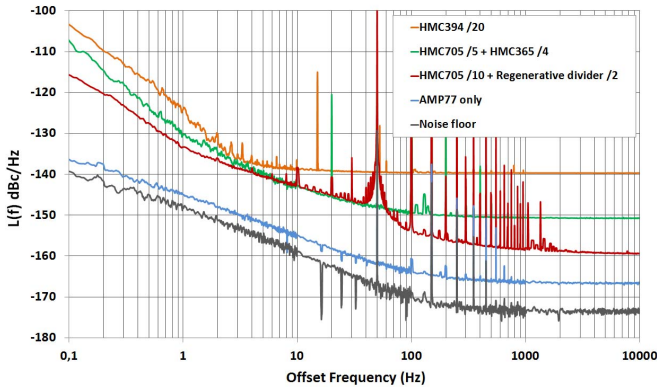


Fig. 8. Residual single-sideband phase noise of several frequency dividers configurations at 5 MHz output for a 100 MHz input.

The noise of a pair of AMP77 amplifiers has been thus also measured. It appears close to the noise floor of the measurement system and at least 10 dB below the divider noise. Although they are easy to use and offer many division combinations, the commercial dividers are clearly too noisy. The best result is a HMC705 with a division ratio of 10 followed by a RD. In this case HMC705 noise limits the general performance. The residual and the estimated absolute phase noises are summarized in Table I.

TABLE I. NOISE RESULTS OF SEVERAL CONFIGURATIONS OF CASCADED COMMERCIAL DIVIDERS

Cascaded dividers	Input frequency	100 MHz		
		Division ratios	Estimated absolute phase noise ; $\mathcal{L}(1 \text{ Hz})$ dBc/Hz	Equivalent flicker noise (ADEV, $\sigma_y(\tau)$)
HMC394	20		-128	2.3×10^{-13}
HMC705 ; HMC365	5 ; 4		-133	1.3×10^{-13}
HMC705 ; RD	10 ; 2		-137	1.2×10^{-13}

The best noise value at 1 Hz is -137 dBc/Hz. In term of fractional frequency stability, this is equivalent to a flicker noise floor in the Allan deviation: $\sigma_y(\tau) = 1.2 \times 10^{-13}$. This preliminary result has been obtained with a very simple configuration and can be improved. Indeed it has already been proven that a succession of several regenerative dividers is a suitable way to provide an ultra-low-noise frequency synthesizer [23]. With a chain of dividers-by-2, it is not possible to get 5 MHz from a 100 MHz signal. The input signal has to start from a divisible by 5×2^n frequency, e.g. 80 MHz. In order to use such frequencies the initial frequency synthesis (from 10 GHz to 100 MHz) will be adapted by modifying the frequency of the Dielectric Resonator Oscillator [15].

IV. CONCLUSION

In this paper, different dividers are reported to get 5 MHz from the 100 MHz signal of a Cryogenic Sapphire Oscillator. The residual phase noise has been measured for different configurations of cascaded commercial dividers. The lowest estimated phase noise has been shown at $\mathcal{L}(1 \text{ Hz}) = -137 \text{ dBc/Hz}$. This is why only regenerative dividers are going to be used. Indeed such dividers (with a ratio of 2) shown an absolute phase noise of $\mathcal{L}(1 \text{ Hz}) = -145 \text{ dBc/Hz}$, which is still perfectible but very likely the best choice in term of dividers.

The necessity to start from 100 MHz was the main reason of using commercially available dividers. Some of them present interesting low phase noise performances [6], but they are still not enough to get a state-of-art synthesized signal at 5 MHz.

Further work will involve the improvement of the general frequency synthesizer absolute phase noise. The optimization of the noise of frequency regenerative dividers is the first objective. Moreover the global performance of the frequency synthesizer is still improvable because some digital dividers are present in the first stage of the division, from 10 GHz to 100 MHz. The possibility to replace them by regenerative dividers could significantly reduce the phase noise.

ACKNOWLEDGMENT

Authors thank the “Région Franche-Comté”, the Oscillator-IMP project (PIA ANR) and the French Space Agency (CNES) for the founding support.

REFERENCES

- [1] F. Sthal, M. Devel, J. Imbaud, R. Bourquin, G. Cibiel, “Fluctuation-dissipation theorem and 1/f noise of bulk acoustic wave cavities”, *Appl. Phys. Lett.*, vol. 107, 103502, pp. 1-4, 2015.
- [2] Rubiola, E., Gros Lambert, J., Brunet, M., V. Giordano, “Flicker noise measurement of HF quartz resonators”, *IEEE Transactions on Ultrasonics Ferroelectrics and Frequency Control*, 47(2), 361-368, 2000.
- [3] F. Sthal, J. Imbaud, X. Vacheret, P. Salzenstein, G. Cibiel, S. Galliou, “Computation method for the short-term stability of quartz crystal resonators obtained from passive phase noise measures”, *IEEE Trans. on Ultrasonics, Ferroelectrics and Frequency Control*, vol. 60, no. 7, pp. 1530-1532, July 2013.
- [4] A. Solana, W. Schäfer, T. Schwall, S. Froidevaux, M. A. Ramos, J. de Vicente, V. Giordano, S. Grop, B. Dubois, “Design of the F&T Subsystem for ESA’s Deep Space Antenna 3”, *Proc. Joint UFFC, EFTF and PFM Symposium, Prague (Czech Republic)*, 21-25 July, pp. 636-640, 2013.
- [5] N. R. Nand, J. G. Hartnett, E. N. Ivanov and G. Santarelli, “Ultra-stable very-low-phase-noise signal source for very long baseline interferometry using a cryocooled sapphire oscillator”, *IEEE Trans. Microw. Theory Tech.*, vol. 59, no. 11, pp. 2978-2986, 2011.
- [6] J.G. Hartnett, N. R. Nand, C. Lu, “Ultra-low-phase-noise cryocooled microwave dielectric-sapphire-resonator oscillators with 1×10^{-16} frequency instability”, *arXiv*, March 6th, 2012.
- [7] V. Giordano, S. Grop, C. Fluhr, B. Dubois, Y. Kersalé, E. Rubiola, “The autonomous Cryocooled Sapphire Oscillator : A Reference for Frequency Stability and Phase Noise Measurements,” 8th Symposium on Frequency Standards and Metrology (FSM 2015). 12-16 October 2015, Potsdam, Germany. To be published in *Journal of Physics: Conference Series (JPCS)*, 2016.
- [8] C. Fluhr, S. Grop, T. Accadia, A. Bakir, Y. Kersalé, B. Dubois, E. Rubiola, and V. Giordano, “Characterization of a set of Cryocooled Sapphire Oscillators at the 10–16 level with the three-cornered hat method”, *Proc. IEEE Joint UFFC, EFTF and PFM Symp.*, Denver, Colorado, 12-16 April, pp. 347-350, 2015.
- [9] V. Giordano_ and C. Fluhr, S. Grop, B. Dubois, “Tests of Sapphire Crystals Manufactured with Different Growth Processes for Ultra-stable Microwave Oscillators”, *IEEE Trans. Microwave and Techniques Society*, vol. 64, no. 1, pp. 78-85, Jan. 2016.
- [10] J.G. Hartnett, S.R. Parker, E.N. Ivanov, T. Povey, N.R. Nand and J.-M. le Floch, “Radio frequency signals synthesised from independent cryogenic sapphire oscillators”, *Electron. Lett.*, Vol. 50, no. 4, pp 294-295, Feb. 2014.
- [11] T. M. Fortier, M. S. Kirchner, F. Quinlan, J. Taylor, J. C. Bergquist, T. Rosenband, N. Lemke, A. Ludlow, Y. Jiang, C. W. Oates, and S. A. Diddams, “Generation of ultrastable microwaves via optical frequency division”, *Nature Photonics*, vol. 5, pp. 425–429, July 2011.
- [12] F. Quinlan, T. M. Fortier, M. S. Kirchner, J. A. Taylor, M. J. Thorpe, N. Lemke, A. D. Ludlow, Y. Y. Jiang, and S. A. Diddams, “Ultralow phase noise microwave generation with an Er: fiber-based optical frequency divider”, *Optical Letter*, vol. 36, pp. 3260–3262, Aug. 2011.
- [13] W. C. Swann, E. Baumann, F. R. Giorgetta, and N. R. Newbury, “Microwave generation with low residual phase noise from a femtosecond fiber laser with an intracavity electro-optic modulator,” *Optical Express*, vol. 19, pp. 24387-24395, Nov. 2011.
- [14] S. Grop, P.Y. Bourgeois, N. Bazin, Y. Kersalé, E. Rubiola, C. Langham, M. Oxborrow, D. Clapton, S. Walker, J. De Vicente and V. Giordano, “ELISA : a cryocooled 10 GHz oscillator with 10–15 frequency stability” . *Review of Scientific Instruments* , 81, 025102 (2010).
- [15] S. Grop, P.-Y. Bourgeois, E. Rubiola, W. Schafer, J. De Vicente, Y. Kersale and V. Giordano, “Frequency synthesis chain for ESA deep space network”, *Electron. Lett.*, vol.47, no. 6, March 2011.
- [16] S. Grop, P.-Y. Bourgeois, R. Boudot, Y. Kersale, E. Rubiola, and V. Giordano, “10 GHz cryocooled sapphire oscillator with extremely low phase noise”, *Electron. Lett.*, vol. 46, no. 6, pp. 420–422, March 2010.
- [17] R.G Harrison, “Theory of Regenerative Frequency Dividers using double-balanced mixers”, *IEEE MTT-Symp. Digest*, 13-15 June, pp. 459-462, 1989.
- [18] E. Rubiola, M. Olivier, J. Gros Lambert, “Phase noise in Regenerative Frequency Dividers”. *IEEE Trans. on Instrumentation and Measurement*, vol 41, no. 3, pp. 353-360, June 1992.
- [19] E. S. Ferre-Pikal, F. L. Walls, “Microwave Regenerative Frequency Dividers with Low Phase Noise”, *IEEE Trans. on Ultrasonics, Ferroelectrics and Frequency Control*, vol. 46, no. 1, pp. 216-219, Jan. 1999.
- [20] E. S. Ferre-Pikal and F. L. Walls , “Low PM noise regenerative dividers”, *Proc. IEEE Int. Freq. Contr. Symp*, pp 478-484, 1997.
- [21] C.A. Barnes, A. Hati, C.W. Nelson, D.A. Howe, “5 MHz phase detector with low residual flicker”. *Electron. Lett.*, vol. 47, no. 19, pp. 1066-1067, Sept. 2011.
- [22] A. Hati, C. W. Nelson, C. Barnes, D. Lirette, J. A. DeSalvo, T. Fortier, F. Quinlan, A. Ludlow, T. Rosenband, S. A. Diddams and D. A. Howe, “Ultra-low-noise Regenerative Frequency Divider for High-Spectral-Purity RF Signal Generation”, in *Proc. IEEE Int. Freq. Contr. Symp.*, 21-24 May, pp 625-628, 2012.
- [23] Archita Hati, Craig W. Nelson, Corey Barnes, Danielle Lirette, Tara Fortier, Franklyn Quinlan, Jason A. DeSalvo, Andrew Ludlow, Scott A. Diddams, and David A. Howe, “State-of-the-Art RF Signal Generation From Optical Frequency Division”, *IEEE Trans. on Ultrasonics, Ferroelectrics and Frequency Control*, vol. 60, no. 9, pp. 1796-1803, Sept. 2013.

Gold Thin Film Viscoelastic Losses of a Length Extension Mode Resonator

Béatrice Bourgeteau-Verlhac, Raphaël Lévy, Thomas Perrier, Pierre Lavenus, Jean Guérard, Olivier Le Traon
 dept. DMPH/CMT
 ONERA, The French Aerospace Lab
 Châtillon, FRANCE

Abstract—In [1] we presented a new length extension mode (LEM) piezoelectric micro-resonator. Thanks to a specific design, anchor losses were lowered to maximize the $Q \cdot f$ product and the resonator. Viscous fluid damping is neglected since the resonator is under vacuum and so is the thermoelastic damping for a length extension mode. With a Q predicted over one million the resonator is well suited for MEMS oscillator devices. Nevertheless it appears that one remaining loss source was not evaluated through our previous work: the viscoelastic damping arising from the presence of gold electrodes on the resonator surface. To investigate the influence of the gold thin film on this new resonator, we studied several papers on the quality factor of gold coated resonators and deduced a frequency dependence of the viscoelastic behavior of the gold thin film. This dependence shows that the damping for the LEM resonator won't be as important as firstly predicted and is compliant for time and frequency applications. Furthermore, the damping can be reduced to improve the quality factor with new electrode designs. These designs shall also provide low motional resistances in order not to deteriorate the phase noise far from the carrier. Two different approaches are compared to reduce electrode damping for the LEM resonator: contactless electrodes and partial electrode coating on the resonator surface. It appears that both approaches are interesting regarding the available processing technologies and give promising phase noise predictions.

Keywords—Time & Frequency; MEMS oscillator; Quality factor; gold thin film; Quartz resonator; Viscoelastic damping; Motional resistance; Phase noise; Electrode design; Contactless electrodes.

I. INTRODUCTION

In order to guarantee high stability of time and frequency resonators each new design must be thoroughly optimized to reduce losses and maximize the quality factor per frequency product $Q \cdot f$. The quality factor can be described as the sum of intrinsic and external losses:

$$\frac{1}{Q_{tot}} = \frac{1}{Q_{anchor}} + \frac{1}{Q_{air}} + \frac{1}{Q_{TED}} + \frac{1}{Q_{AKE}} + \frac{1}{Q_{visc}} \quad (1)$$

We presented in a previous paper [1] a new length extension mode (LEM) piezoelectric micro-resonator, consisting in two beams vibrating in length extension out of phase from the main central pillar. Figure 1 illustrates the geometry and the deformed mode of the LEM. In [1] we focused our work on anchor losses and temperature sensitivity regarding quartz cuts to evidence its potential for time and frequency applications. We demonstrated with finite element analysis that the specific

design of the LEM resonator family allows $Q_{anchor} > 10^8$. The $Q \cdot f$ product for quartz is limited by Akhiezer losses this maximum value for MHz range frequencies is given in [2]: $Q \cdot f = 3.2 \times 10^{13}$. Assuming viscous fluid damping ($1/Q_{air}$) is negligible since the resonator is held under vacuum and so is the thermoelastic damping ($1/Q_{TED}$) since the resonator is in a length extension mode it appears that the maximum value Q_{tot} for a 1.3 MHz LEM resonator is well above one million allowing applications in devices such as MEMS oscillators.

However one last dissipation source has not been investigated theoretically yet: the viscoelastic damping $1/Q_{visc}$ arising from the gold electrode which in our case is an evaporated thin film. Two main configurations of electrodes were considered in [1] for Z and X quartz cuts. For Z configuration electrodes can be deposited on either or both faces of the resonator, for the X cut, electrodes are compulsory on both faces (see Figure 2).

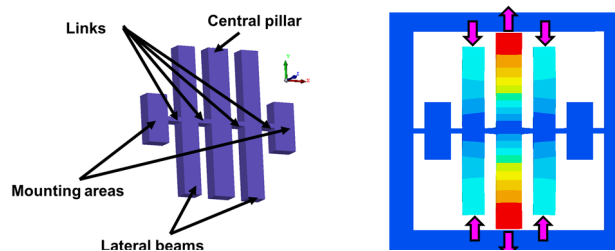


Fig. 1. LEM resonator geometry on the left and its deformation mode in length extension with an anchoring frame on the right.

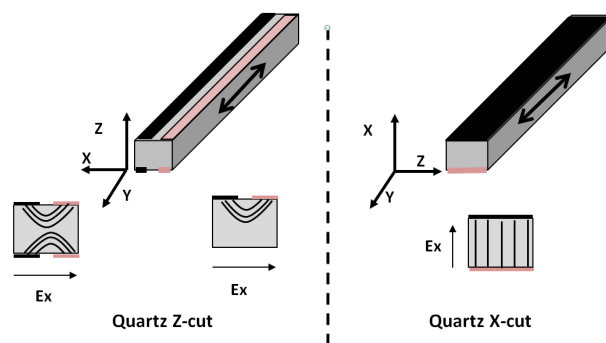


Fig. 2. Electrode system for a Quartz Z-cut on the left and for a X-cut on the right.

The LEM due to its symmetry can be assimilated to a clamped free length extension beam of half the length of the central

pillar. This approximation will help us investigate analytically the viscoelastic damping of the gold electrode on the beam.

II. VISCOELASTIC DAMPING

A. Linear Kelvin Voigt model at low frequencies

In first place we assume a linear viscoelastic behavior of the gold thin film layer and an elastic behavior of the quartz beam. We use a Kelvin Voigt model constituted with a dashpot with a loss coefficient η_{Au} in parallel with a spring standing for the elastic stiffness with an equivalent Young modulus E_{Au} . The stress σ in the gold layer can be written as:

$$\sigma = E_{Au}\epsilon + \eta_{Au}\dot{\epsilon} \quad (2)$$

The quality factor associated with electrodes Q_{visc} can be expressed as follows according to [3].

$$Q_{visc} = \frac{2\pi W_{stored}}{W_{periodtot}} = \frac{2\pi \int_{V_{quartz}} E_{quartz} \epsilon_0^2 dV}{\int_{V_{Au}} \eta_{Au} \epsilon_0^2 \pi \omega dV} \quad (3)$$

Since damping in quartz material is low enough to be negligible the stored energy is mainly due to the elastic part of the quartz beam behavior E_{quartz} . The dissipated part of the energy is mainly due to the viscosity of the thin film. For a length extension mode along the y axis: $\epsilon_0(y) = \frac{\partial u_x(y)}{\partial y}$.

The two different quartz cut (X and Z) and electrode systems described in Figure 2 are studied. Dimensions of the beam are noted h_q for the thickness (200 μm for a 1.3 MHz resonator) and w_q for the width. The width of each electrode is noted w_e and the evaporated gold layer thickness is h_e (0.2 μm). Considering from [3] that $\eta_{Au} \approx 2000$ Pa.s (experimental value obtained for a flexural resonator at 8800 Hz), the values of Q_{visc} deduced are described in the following table. The value for a one faced X-cut is calculated for information purpose only, since this configuration won't allow a proper actuation of the device.

TABLE I. ESTIMATED VALUES OF Q_{visc} FOR THE LEM RESONATOR ACCORDING EXPERIMENTAL VISCOSITY OF COGLD MEASURED IN [3]

Q_{visc} For two faces Z cut	Q_{visc} For two faces X cut
$Q_{visc} = \frac{E_{quartz} h_q w_q}{\eta \pi f h_e 4 w_e}$	$Q_{visc} = \frac{E_{quartz} h_q}{\eta \pi f 2 h_e}$
$Q_{visc} \approx 7160$	$Q_{visc} \approx 4770$
Q_{visc} For one face Z cut	Q_{visc} For one face X cut (not functional)
$Q_{visc} = \frac{E_{quartz} h_q w_q}{\eta \pi f h_e 2 w_e}$	$Q_{visc} = \frac{E_{quartz} h_q}{\eta \pi f h_e}$
$Q_{visc} \approx 14320$	$Q_{visc} \approx 9550$

Using the viscosity measured in [3] predicts a very poor quality factor for the LEM. Such values would be prohibitive for time and frequency applications. Despite those first calculations other coated length extension mode resonators demonstrate much higher quality factors [7, 11]. This raises the question of the relevance of the linear viscoelastic behavior model used for the gold thin film layer in this first analysis deduced from [3].

B. Frequency dependence

To go further, we investigated the frequency dependence of gold viscoelasticity. To do so, articles describing the evolution

of the quality factor of coated resonators at different frequencies were studied: [5] for low range frequencies (200 Hz up to 20 kHz), [6] for middle range frequencies (200 kHz to 490 kHz) and [7] for upper frequencies (500 kHz to 1.5 MHz). Gold damping is strongly dependent on the microstructure and the deposition process. Since the gold used in our laboratory is deposited by evaporation we can expect a good agreement between [5] where the gold layer is evaporated and our results.

In [5] gold thin film damping is investigated for several flexural silicon cantilevers with several thicknesses of thin film deposited by evaporation. Damping in silicon as well as in quartz is expected to be low ($Q.f=2.3 \times 10^{13}$ [2]). The behavior is still considered to be a Kelvin-Voigt model, but the coefficient $\eta_{Au}(f)$ was calculated for each frequency and (3) was evaluated with $\epsilon_0(x) = -z \frac{\partial^2 u_x(y)}{\partial y^2}$. The results are presented in Figure 4 for 200 nm and 100 nm gold layers.

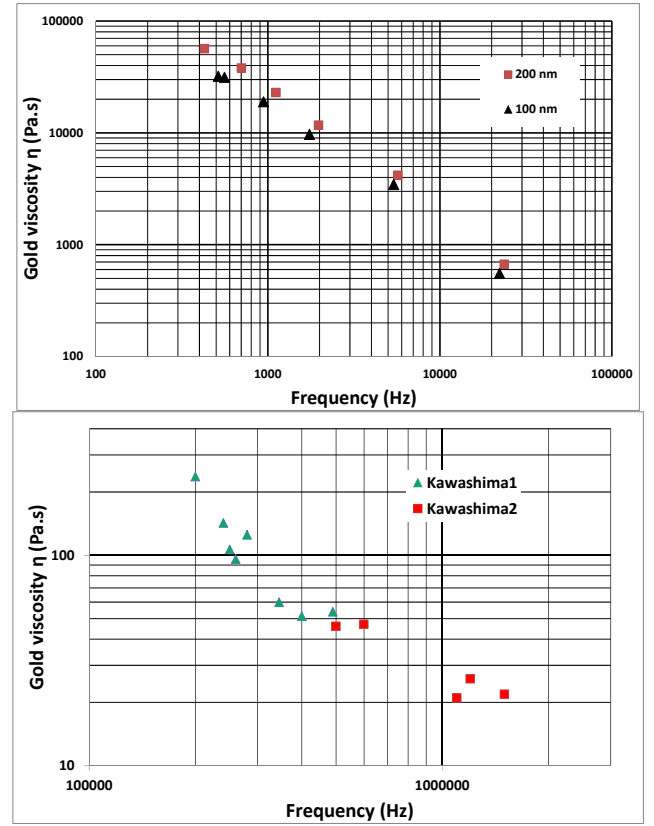


Fig. 3. Frequency dependence of gold viscosity $\eta_{Au}(f)$ deduced from [5] (upper curves) and from [6] and [7] (lower curves).

The two other articles [6, 7] deal with length extension quartz resonators which behavior is quite similar to the LEM resonator. For this reason, the damping of electrodes shall prevail (no thermoelastic loss, low anchor losses). The value of $\eta_{Au}(f)$ was also calculated from (3). Figure 4 shows the values of $\eta_{Au}(f)$ deduced from [5], [6], and [7] evidencing that the damping dramatically decreases according to a fractional power law of the frequency. The values obtained in the three articles are consistent and give a continuous evolution of the

frequency over 200 Hz to 1.5 MHz. The value of around 2000 Pa.s measured in [3] around 9 kHz is confirmed.

Although we have no information on the deposition made in [6] and [7], the results seem consistent with the values obtained for an evaporated thin film.

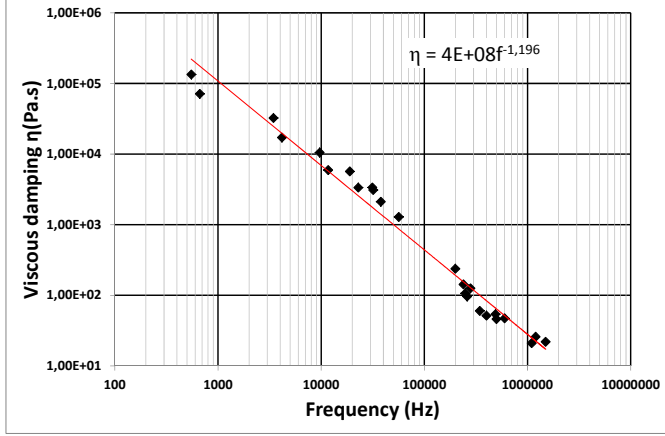


Fig. 4. Frequency dependence of gold viscosity deduced from [6] and [7].

C. Modelling and prediction for the LEM resonator

The fractional power law frequency dependence can be compared with constitutive models usually applied to polymer viscoelastic coatings [8]. Writing the behavior of the viscoelastic thin film thanks to a complex modulus:

$$\sigma(t) = E^*(\omega)\varepsilon(t) \quad (4)$$

This complex modulus can be written as:

$$E^*(\omega) = E' + jA(\omega)^\alpha \quad (5)$$

We can identify on the above data the following coefficients: $\alpha = -0.196$ and $A \approx 4e8/(2\pi)^\alpha$, with $E' = E_{Au}$ the Young modulus of gold. We can expect a $\eta_{Au} = 25$ Pa.s at 1.3 MHz, table II gives the new values of Q_{visc} and the motional resistance (R_m) for the four upper configurations.

TABLE II. ESTIMATED VALUES OF Q_{visc} FOR THE 2D-LEM RESONATOR WITH THE REEVALUATED VISCOELASTICITY 25 PA.S.

Q_{visc} For two faces Z cut	Q_{visc} For two faces X cut
$Q_{visc} \approx 572\ 000$	$Q_{visc} \approx 381\ 000$
$R_m = 648\ \Omega$	$R_m = 311\ \Omega$
Q_{visc} For one face Z cut	Q_{visc} For one face X cut (not functional)
$Q_{visc} \approx 1\ 145\ 000$	$Q_{visc} \approx 763\ 000$
$R_m = 926\ \Omega$	N. A.

Although Q_{visc} is much higher than earlier predicted and can provide acceptable performances for time and frequency applications, it appears that viscoelastic losses are limiting the Q_{tot} in most cases.

III. OPTIMISATION OF ELECTRODES FOR THE LEM

In this paragraph two major leads are exposed to increase Q_{tot} i.e. Q_{visc} and keep an optimized motional resistance at the same time:

- Optimized designs of electrodes;
- Contactless electrodes.

Nevertheless both solutions deteriorate the motional resistance thus increasing the phase noise far from the carrier. Indeed the phase noise for from the carrier depends on the power P_0 and thus on the motional resistance R_m . The lower the motional resistance is, the lower is the noise. Samewise the phase noise near from the carrier depends on Q_{tot} since the Leeson frequency diminishes with a higher Q and so is the phase noise near from carrier. In this part we seek a compromise between a high Q_{visc} and a low R_m .

A. Influence of the location of electrodes on the beam surface

In this paragraph we draw the reader's attention on the electrode location. In [9], the influence of a full or partial coating of a flexural cantilever is studied in order to optimize the surface coating location.

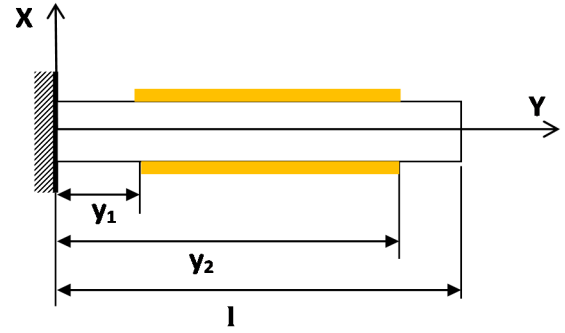


Fig. 5. A partial coating of a length extension beam and its dimensions.

Considering for a length extension an axial strength along the Y axis, the equation (3) becomes for a partial coating:

$$Q_{visc} = \frac{E_{quartz} h_q}{\eta \pi f 2 h_e} \frac{\int_0^l (\varepsilon_{max}(y))^2 dy}{\int_{y_1}^{y_2} (\varepsilon_{max}(y))^2 dy} \quad (6) \text{ with}$$

$$\alpha = \frac{\int_0^l (\varepsilon_{max}(y))^2 dy}{\int_{y_1}^{y_2} (\varepsilon_{max}(y))^2 dy} \quad (7)$$

For a beam in length extension the mode shape is given by at the first order:

$$\phi_1(y) = \sin(\sigma_1 y) = \sin\left(\frac{\pi y}{2l}\right) \quad (8)$$

$$\varepsilon_{max}(y) = \frac{d\phi_1(y)}{dy} \quad (9)$$

It is obvious from the results presented in [9] that the electrodes placed on the tip of a flexural beam will induce less damping than electrodes located near the clamped surface. This tendency is the same for a length extension beam.

We also calculated thanks to finite element analysis the motional resistance R_m as a functions of the y_1/l ratio considering $y_2=l$. For example when $y_1/l=0.3$ $Q_{visc}=572\ 000$ and $R_m=581\ \Omega$. The best compromise is obtained with a Q_{visc} of one million and $R_m \approx 2100\ \text{ohm}$ and $y_1/l=0.6$. It is although interesting to note that a higher Q is achievable if $y_1/l > 0.6$ but the R_m will increase and so will the phase noise far from the carrier.

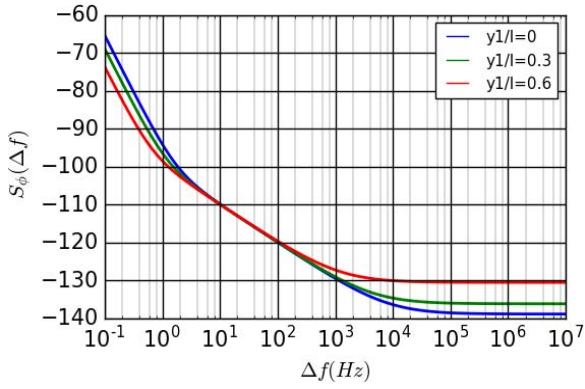


Fig. 6. Phase noise curves for partial coatings of the LEM with $y1/l$ ranging from 0 to 0.6 and $y2=l$.

B. Contactless electrodes

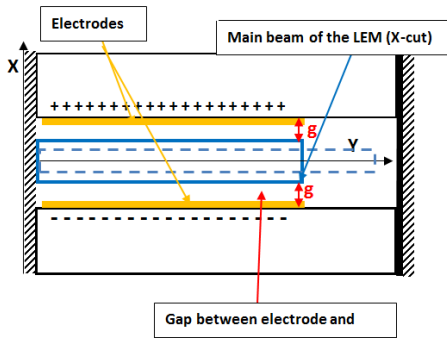


Fig. 7. Contactless electrodes, lateral view for an X-Cut of the LEM.

Another lead is contactless electrode devices that can be considered thanks to new technological approaches such as wafer level bonding and DRIE [12] (Figure 7). Assuming no damping is induced by such systems as BVAs [10], the quality factor is assumed to be $Q \geq 1\,000\,000$ and we studied by finite element analysis the evolution of R_m regarding the gap.

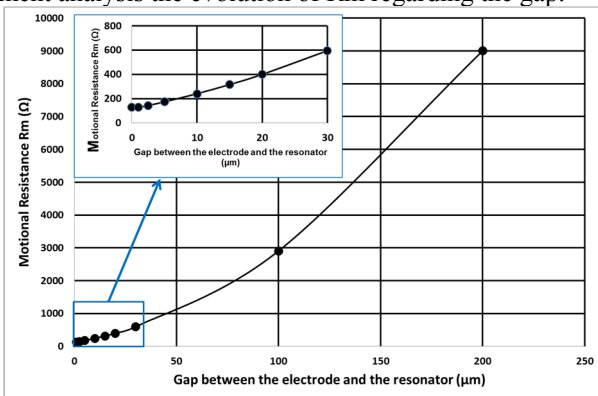


Fig. 8. Evolution of R_m with the gap between electrodes and resonator.

By comparison with the first approach of electrode design optimization, to be competitive (i.e. $R_m=2000\Omega$), the maximum acceptable gap is around $75\ \mu\text{m}$. This means that both option of electrodeless and optimized electrode design are relevant for the LEM resonator, since

comparable values for Q and R_m are achievable. The choice of one or other solution relies on the available technologies, especially for electrodeless resonators [12].

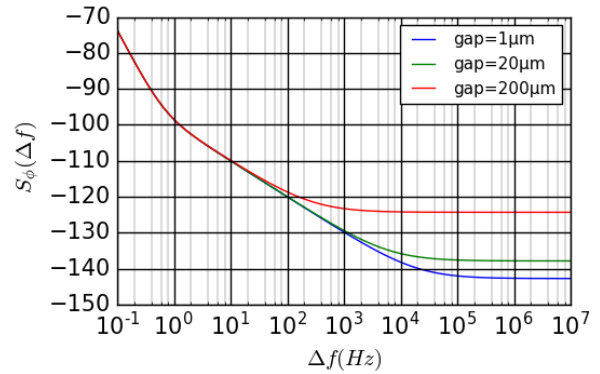


Fig. 9. Phase noise regarding the gap between resonator and electrodes.

IV. CONCLUSION

In this paper we demonstrated that viscoelastic behavior of gold evaporated thin films follows a fractional power law of the frequency. At 1.3 MHz for Z-cut and one face of electrodes the quality factor of the LEM can reach one million with a R_m of $930\ \Omega$ which is compliant for time and frequency applications. For other configurations (i.e. X-cut) Q can be improved through electrode design, either by partial coating or contactless electrodes. In both cases, a $Q=1\,000\,000$ and $R_m=2000\Omega$ are achievable with an X-Cut, depending on the technologies available [12].

- [1] B. Bourgeteau et Al., "Quartz Resonator for MEMS Oscillator", EFTF, 2014.
- [2] S. Ghaffari et Al., "Quantum Limit of Quality Factor in Silicon Micro and Nano Mechanical Resonators", Scientific reports, 2013.
- [3] O. Le Traon et Al., "LGS and GaPO4 piezoelectric crystals: New results," Solid Stat Sciences, vol.12 pp 318-324, 2010.
- [4] L.-W. Hung et Al., "Capacitive-Piezoelectric Transducers for High-Q Micromechanical AlN Resonators", Journal of Microelectromechanical Systems, vol. 24, no. 2, april 2015.
- [5] R Sandberg et Al., "Effect of gold coating on the Q-factor of a resonant cantilever", J. Micromech. Microeng. 15 (2005) 2249-2253.
- [6] H. Kawashima et Al., "Vibration Analysis of New Shape Length Extensional Mode Quartz Crystal Resonator with Barbell-Type Vibration Bar", 1991, Ultrasonics Symposium, pp. 511-515.
- [7] H. Kawashima et Al., "Variational Analysis of New Shape Length Extensional Mode Quartz Crystal Resonator Taking Account of Lateral Motion", IEEE Conference Publications, pp 378-386.
- [8] P. Paolino et Al., "Frequency dependence of viscous and viscoelastic dissipation in coated micro-cantilevers from noise measurement", Nanotechnology 20, 405705 (2009).
- [9] P. Lu et Al., "Analysis of surface effects on mechanical properties of microcantilevers", Mater.Phys.Mech. 4 (2001) 51-55.
- [10] R. J. Besson et Al., BVA resonators and oscillators : a review. Relation with space requirements and quartz material characterization., 1995 IEEE International Frequency Control Symposium.
- [11] R. Tabrizian et Al., "a 27 mhz temperature compensated mems oscillator with sub-ppm instability", MEMS 2012.
- [12] S. Grousset et Al., "Quartz-based vibrating MEMS fabricated using a wafer-bonding process with sealed cavities." Frequency Control Symposium (FCS), 2014 IEEE International.

The 2015 TWSTFT calibration for UTC and related time links

Z. Jiang¹, D. Piester², C. Schlunegger³, E. Dierikx⁴, V. Zhang⁵, J. Galindo⁶, D. Matsakis⁷

¹ BIPM, Bureau International des Poids et Mesures, zjiang@bipm.org.

² PTB, Physikalisch-Technische Bundesanstalt, Bundesallee 100, 38116 Braunschweig, Germany

³ METAS, Federal Institute of Metrology METAS, Lindenweg 50, 3003 Bern-Wabern, Switzerland

⁴ VSL, Dutch Metrology Institute, Thijssseweg 11, 2629 JA Delft, Netherlands

⁵ NIST, National Institute of Standards and Technology, 325 Broadway, Boulder, CO80305, US

⁶ ROA, Real Instituto y Observatorio de la Armada en San Fernando, Plaza de las Tres Marinas s/n, 11100 San Fernando, Spain

⁷ USNO, United States Naval Observatory, 3450 Massachusetts Ave, NW, Washington DC 20392, US

Abstract

Two-Way Satellite Time and Frequency Transfer (TWSTFT or TW) is one of the primary time transfer techniques for UTC generation. In this framework the Triangle Closure Calibration (TCC) method has been used to calibrate links between certain laboratories whose links to the pivot lab are directly calibrated. TCC is based upon requiring the closure of three co-joined links to be zero. In this paper, the results of the 2015 calibration computation are presented. The uncertainties are usually below 2 ns.

Key words: TWSTFT or TW, TCC, Calibration, Uncertainty, TW Network, CALR, ESDVAR.

1. Introduction

The use of triangle closure calibration (TCC) was first proposed in 2005 [1], and the first TCC was performed in 2008 [2]. In 2014, it was highlighted by Dr. Klepczynski as one of the four most significant developments in TWSTFT history [3]. TCC was approved as a standard method for TW calibrations at the 23rd meeting of the Consultative Committee for Time and Frequency (CCTF) Working Group on TWSTFT in September, 2015, and according to the TW calibration guidelines [4] the BIPM is approved to apply TCC when necessary.

The practical need for TCC stems from the fact that a network with N labs consists of $N(N-1)/2$ links, of which $N-1$ are direct links to the pivot. Of all $N(N-1)(N-2)/6$ closures, $(N^2-3N+2)/2$ are independent. For example, if $N=13$, there are 12 pivoted links and 78 links in total. It would be difficult to calibrate all the 78 links directly with a mobile station (MS), but TCC makes it possible to do this analytically.

The principle of the TCC is quite simple:

- The closure of the three links in a triangle should be zero within the measurement noise;
- If two links are calibrated, the non-zero closure is the calibration correction for the third link.

The calibration value is specified in TW ITU-format files by the CALR and ESDVAR values of each site; typically the CALR value is changed.

As shown in Figure 1, if we have the two calibrated links (LAB_i -PTB and LAB_j -PTB), we can calibrate the link (LAB_i - LAB_j) through the closure condition:

$$\text{Closure} = [\text{UTC}(LAB_i) - \text{UTC}(PTB)] - [\text{UTC}(LAB_j) - \text{UTC}(PTB)] + [\text{UTC}(LAB_j) - \text{UTC}(LAB_i)] \equiv 0. \quad (1)$$

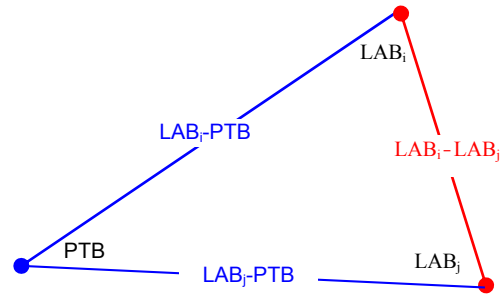


Fig. 1 The non-UTC TW link calibration via triangle closure condition (TCC)

The initially non-zero closure, using one uncalibrated link, is numerically equal to the calibration correction for that link:

$$\text{CALR}_i = -\text{CALR}_j = \text{Closure} + (\text{ESDVAR}_j - \text{ESDVAR}_i)/2. \quad (2)$$

The final calibration value is typically obtained by averaging over a month. Assuming 12 measurements per day, there are about 360 measurements. Since the observation times between links in a closure can differ by up to an hour, measured TW time differences are interpolated to the nearest common scheduled epoch, and then the closures are calculated for each epoch. The mean value and its standard deviation are computed from the individual closures. The uncertainty of the calibration can be estimated by the following equation:

$$U_{\text{CALR(TCC)}} = \sqrt{\{u_i^2 + u_j^2 + S^2\}}. \quad (3)$$

Here:

$$\begin{aligned} u_i &= u_B [\text{UTC}(LAB_i) - \text{UTC}(PTB)] \\ u_j &= u_B [\text{UTC}(LAB_j) - \text{UTC}(PTB)] \\ S &= \text{Std} / \sqrt{N} \end{aligned}$$

where Std is the Standard Deviation of the triangle closures, N is the number of triangle closures, and u_B are the calibration uncertainties of the calibrated links.

Values of S are listed in Table 5. They are of order of u_A/\sqrt{N} where u_A , the RSS (square root of the summed squares) of the links' statistical uncertainties, is set to 0.5 ns. Since N is about 360 over a month, $S \sim 0.03$ ns. Inserting these very small values and the $u_B \leq 1$ ns TW calibration uncertainty via MS [5-7,9,14-16], into equation 3, the link uncertainty estimate is ≤ 1.4 ns. For a TW link calibrated via GPS, we have $u_B \leq 1.5$ ns [10,11], and the TCC uncertainty is ≤ 1.8 ns. The BIPM currently assigns a nominal uncertainty of 2 ns to all TCC calibrations.

2. The Data Set October, 2015 (1510)

The 1510 UTC dataset includes European and North American TW data from MJD 57292-57329. There are nine TW laboratories involved (PTB, NIST, USNO, OP, IT, ROA, VSL, CH and SP), cf. Figure 2 and Tables 1-2.

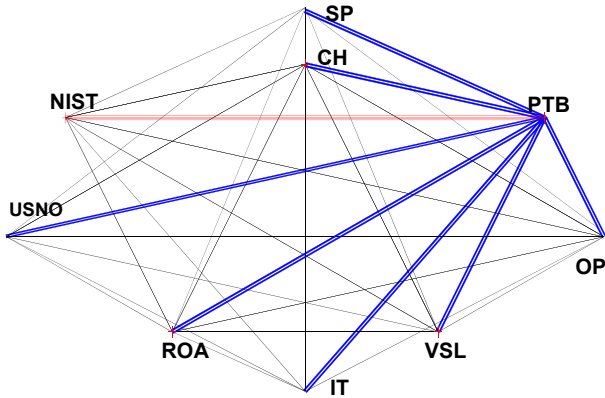


Fig. 2 The UTC time links (blue or red lines) and the redundant/non-UTC links (black lines) The blue links are calibrated with the TW mobile station ($u_B \leq 1$ ns) and the red links with the GPS calibrator ($u_B \leq 1.5$ ns)

Table 1 All available TW links in October, 2015

No	Lab2-Lab1	No	Lab2-Lab1
1.	CH IT	19.	IT OP
2.	PTB CH	20.	VSL IT
3.	IT PTB	21.	SP IT
4.	CH NIST	22.	IT ROA
5.	NIST IT	23.	PTB NIST
6.	USNO CH	24.	NIST OP
7.	NIST USNO*	25.	SP NIST
8.	CH OP	26.	NIST ROA
9.	VSL CH	27.	PTB OP
10.	OP VSL	28.	USNO OP
11.	SP CH	29.	SP OP
12.	PTB SP	30.	USNO PTB
13.	CH ROA	31.	VSL PTB
14.	ROA OP	32.	PTB ROA
15.	SP USNO	33.	VSL ROA
16.	USNO ROA	34.	SP ROA
17.	VSL NIST	35.	VSL SP
18.	USNO IT	36.	VSL USNO

* Measurements were not available in this calculation

Table 2 Set of independent triplets (all other triplets are linear combinations of these)

Lab1-Lab2-Lab3	Lab1-Lab2-Lab3
PTB IT USNO	PTB SP USNO
PTB IT VSL	PTB SP VSL
PTB NIST OP	PTB USNO VSL
PTB NIST ROA	PTB CH IT
PTB NIST SP	PTB CH NIST
PTB NIST USNO*	PTB CH OP
PTB NIST VSL	PTB CH ROA
PTB OP ROA	PTB CH SP
PTB OP SP	PTB CH USNO
PTB OP USNO	PTB CH VSL
PTB OP VSL	PTB IT NIST
PTB ROA SP	PTB IT OP
PTB ROA USNO	PTB IT ROA
PTB ROA VSL	PTB IT SP

* Measurements were not available in this calculation

3. The computation of the TCC calibration

Table 3 gives the changes in the closures of the 27 independent triangles composed by the 9 TW labs using the original 1510 dataset with earlier calibrations from 2011 [12] and 2014 [5].

Table 3 Deviations of some of the TCC values from their 2011 and 2014 determinations (unit in ns)

Triangle	Min	Max	Closure	StdD
PTB CH IT	-1.70	-0.90	-1.32	0.24
PTB CH NIST	0.10	0.70	0.33	0.20
PTB CH OP	0.30	0.80	0.62	0.17
PTB CH ROA	-5.40	-4.80	-5.10	0.25
PTB CH SP	-5.40	-4.80	-5.12	0.19
PTB CH VSL	-0.50	0.10	-0.10	0.22
PTB IT NIST	1.60	2.40	2.10	0.31
PTB IT OP	-0.30	0.70	0.15	0.36
PTB IT ROA	-0.60	0.10	-0.35	0.26
PTB IT SP	0.20	1.00	0.50	0.26
PTB IT USNO	-0.60	0.10	-0.25	0.30
PTB IT VSL	1.80	2.80	2.13	0.36
PTB NIST OP	0.30	0.90	0.68	0.21
PTB NIST ROA	-6.00	-5.40	-5.73	0.20
PTB NIST SP	-4.40	-4.20	-4.33	0.07
PTB NIST VSL	-0.50	0.40	0.07	0.34
PTB OP ROA	-0.90	-0.30	-0.45	0.21
PTB OP SP	-0.20	0.10	-0.05	0.11
PTB OP USNO	-0.50	-0.10	-0.40	0.14
PTB OP VSL	-1.00	-0.60	-0.77	0.14
PTB ROA SP	0.00	0.60	0.28	0.19
PTB ROA USNO	-1.10	-0.60	-0.77	0.16
PTB ROA VSL	3.90	4.50	4.25	0.18
PTB SP USNO	-0.80	-0.30	-0.53	0.21
PTB SP VSL	4.20	5.10	4.60	0.34

The closure mean values in column 4 of Table 3 fall into two categories. Those among mainly PTB, IT, OP, ROA, SP, and USNO [5] (cf. the blue lines in the table) are smaller than 0.86 ns ($\sqrt{3}$ times the Type A uncertainty 0.5 ns of an individual link) and those likely impacted by long-term variations in the closures that are discussed in Section 5. The triplets with larger changes would be due to changes in equipment, the laboratory setups, or the applied calibration values [5,12].

Figure 3 is a histogram of the closure of the PTB-OP-SP triplet. There are 291 measurements; whose quasi-normal distribution has an RMS of 119 ps and mean value close to zero. This suggests a high stability for the three links since their calibration one and a half year before, although Figure 4 (in Section 5) may indicate that the agreement is fortuitous.

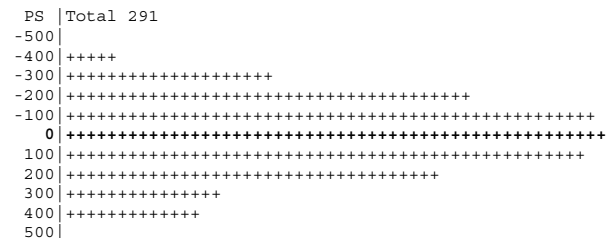


Figure 3 Histogram of the closure of the triangle Δ PTB-OP-SP, after TCC calibration by the 2014 Europe campaign (unit in ps)

4. The Results of the TW Calibration: CALR and ESDVAR

In the following sections, the final calibration results are given: CALR, ESDVAR, CI, TYPE and the uncertainties. Most have been implemented in the ITU TWSTFT data files. Results involving NIST are not presented because NIST has not yet implemented the calibration.

4.1 The CALR/ESDVAR for the UTC links

Table 4 Revised CALR/ESDVAR values for implementation (unit in ns)

Lab _i	Lab _j	CALR	ESDVAR	CI	Type	u _B
PTB01	CH01	+713.4	0.000	284	LC(TWSTFT)	1.0
PTB01	VSL01	+986.3	0.000	295	LC(TWSTFT)	1.0
PTB01	USNO01	+501.7	0.000	392	LC(TWSTFT)	1.0

Based on the TW calibrations via MS [6,7,9], we first revised the calibrations and uncertainties of the links

Table 5 The CALR Values for the non UTC links to be implemented in the 1512 TW ITU data files (unit in ns)

CI	Type	u _B	Lab _i	Lab _j	S	CALR	ESDVAR	StDev	N	S	No.	CALR'	Dif.
2.0	IT02		OP01		1	6837.706	00000.000	±0.192	304	0.011	9	6837.3	0.4
2.0	IT02		ROA01		1	-307.736	00000.000	±0.286	304	0.016	10	-307.7	0.0
2.0	IT02		SP01		1	-274.671	00000.000	±0.232	304	0.013	11	-275.7	0.9
2.0	OP01		ROA01		1	-7145.375	00000.000	±0.256	312	0.015	18	-7145.0	-0.3
2.0	OP01		SP01		1	-7112.887	00000.000	±0.177	303	0.010	19	7112.9	0.0
2.0	ROA01		SP01		1	32.431	00000.000	±0.278	312	0.016	22	32.1	0.3
396	TCC	2.0	CH01	IT02	1	268.748	00000.000	±0.274	295	0.016	1		
398	TCC	2.0	CH01	OP01	1	7106.790	00000.000	±0.174	303	0.010	3		
399	TCC	2.0	CH01	ROA01	1	-38.238	00000.000	±0.271	303	0.016	4		
400	TCC	2.0	CH01	SP01	1	-6.244	00000.000	±0.231	303	0.013	5		
401	TCC	2.0	CH01	USNO01	1	-212.499	00000.000	±0.156	303	0.009	6		
402	TCC	2.0	CH01	VSL01	1	271.878	00000.000	±0.437	302	0.025	7		
404	TCC	2.0	IT02	USNO01	1	-481.546	00000.000	±0.287	303	0.016	12		
405	TCC	2.0	IT02	VSL01	1	3.620	00000.000	±0.366	304	0.021	13		
410	TCC	2.0	OP01	USNO01	1	-7318.351	00000.000	±0.170	312	0.010	20		
411	TCC	2.0	OP01	VSL01	1	-6834.323	00000.000	±0.331	312	0.019	21		
412	TCC	2.0	ROA01	USNO01	1	-173.652	00000.000	±0.192	312	0.011	23		
413	TCC	2.0	ROA01	VSL01	1	310.189	00000.000	±0.298	312	0.017	24		
414	TCC	2.0	SP01	USNO01	1	-206.167	00000.000	±0.116	312	0.007	25		
415	TCC	2.0	SP01	VSL01	1	277.904	00000.000	±0.397	311	0.022	26		
416	TCC	2.0	USNO01	VSL01	1	484.234	00000.000	±0.604	287	0.036	27		

Table 6 Closures using the calibrated CALR and ESDVAR values for the non-UTC links

Triangle	Min	Max	Clos.	StdD
PTB CH IT	-0.50	0.30	0.00	0.25
PTB CH OP	-0.20	0.10	-0.03	0.11
PTB CH ROA	0.30	0.50	0.37	0.07
PTB CH SP	-0.50	0.10	-0.13	0.19
PTB CH USNO	-0.10	0.20	0.07	0.12
PTB CH VSL	-0.50	0.00	-0.33	0.16
PTB IT OP	-0.20	0.20	-0.02	0.13
PTB IT ROA	-0.40	0.80	0.00	0.39
PTB IT SP	-0.20	0.30	0.03	0.16
PTB IT USNO	-0.40	0.40	-0.05	0.26
PTB IT VSL	-0.40	-0.30	-0.33	0.05
PTB OP ROA	0.00	0.40	0.17	0.15
PTB OP SP	-0.20	0.10	-0.03	0.09
PTB OP USNO	-0.20	0.10	-0.03	0.09
PTB OP VSL	-0.60	-0.30	-0.47	0.11
PTB ROA SP	-0.40	0.00	-0.23	0.14
PTB ROA USNO	-0.30	0.20	-0.07	0.16
PTB ROA VSL	-0.30	0.20	-0.03	0.17
PTB SP USNO	-0.20	0.10	-0.02	0.11
PTB SP VSL	-0.60	-0.20	-0.37	0.14
PTB USNO VSL	-1.00	0.10	-0.57	0.42

Table 6 lists the statistical results of the 21 closures

to the pivot with the ESDVAR set to zero (Table 4). The USNO-PTB link calibration in July 2015 varied by only 0.4 ns from that of 2014 [5,9], less than its uncertainty.

4.2 The CALR/ESDVAR for the Non-UTC links

Table 5 lists the CALR/ESDVAR TCC calibration results for the non-UTC European-USA links.

Only the new calibrations (the red lines) concerning CH, VSL, and USNO etc. are to be implemented at this time. For those calibrations already given in [5], the same values are kept in the ITU data, as listed in the CALR' column. N and S are defined in equation 3. In the Table 5, the column *Dif.*, which is the difference CALR-CALR', compares our 2015 computation with that given in the ITU data files of 1510 (Oct. 2015), which was derived from the 2014 European calibration report [5]. The differences are small compared to the 2 ns nominal uncertainty.

using only the averages over the six standard MJDs of the 1510 data set. From the table, the mean values are approximately zero, as expected. The 0.4 ns maximum standard deviation is consistent with $\sqrt{3}$ times the Type A uncertainty of $u_A=0.5$ ns. The implementation for these labs was made on 57357 (1 Dec. 2015) at 0h UTC [13].

5. Long-term variation of the closures

The calibrations herein are strictly applicable only at the times of calibration. Calibration variations are often assumed to be mostly due to hardware delay changes that affect all observations at a given station. We note that it is possible to obtain a lower limit of about 0.5 ns to the long-term stability of all TW links by observing the closures' variations. Figures 4-6 are plots of the 5-day averages of closures between some European lab triplets. To make this plot the CALR and ESDVAR values were ignored; if they had been consistently included, the only difference would be to make the mean zero. Where the curve is not

continuous between equipment or satellite changes, the triplet's variation captures those components of delay variations that are not common to all three sites and baselines. Therefore they truly provide a lower limit to the variations. A continually updated set of closures for all European and North American triplets is made available on-line by SP [8]. The closures are the *true* errors indicating important information on the *true* Type A and Type B uncertainties and their variation. Further investigations, by different authors, are ongoing.

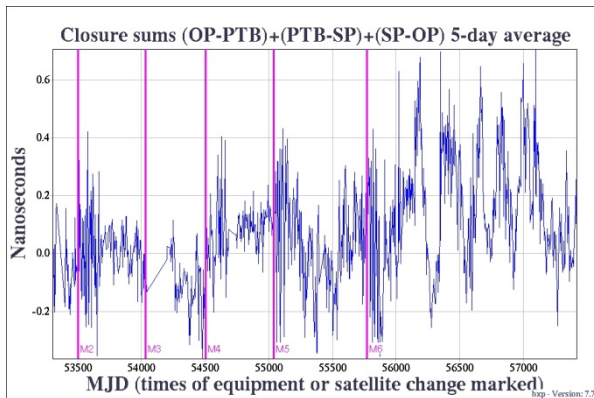


Figure 4 Closure variations between OP, PTB, and SP. Markers indicate satellite or equipment changes.

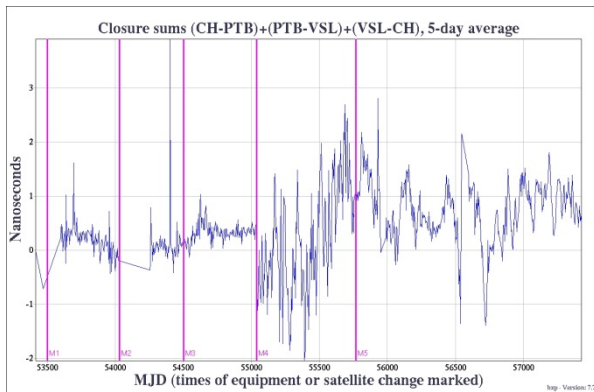


Figure 5 Closure variations between CH, PTB, and VSL. Markers indicate satellite or equipment changes.

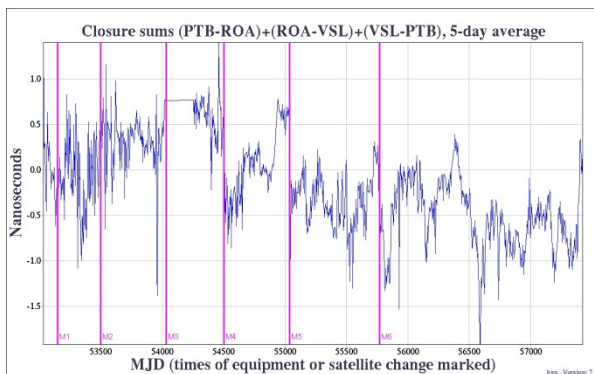


Figure 6 Closure variations between PTB, ROA, and VSL. Markers indicate satellite or equipment changes.

6. Conclusion

TCC is now an operational technique that enables any TW link to be analytically calibrated provided its two adjacent laboratories have calibrated their links to a third lab, with a slight degradation in accuracy. When measurement data are available, it will be a simple matter to carry out the similar calibrations for all European, USA and Asian laboratories in the network.

References

- [1] Z. Jiang, D. Matsakis, and W. Lewandowski (2005) "TW network time transfer and baseline dependent uncertainties analysis," BIPM TM 138, 5 May 2005.
- [2] Z. Jiang, W. Lewandowski, D. Piester (2008) "Calibration of TWSTFT Links Through the Triangle Closure Condition," Proc. 40th PTI, Reston Virginia, USA, 1-4 Dec 2008, pp.467-483.
- [3] W. Klepczynski (2014) "TWSTFT: It's History, Evolution and People", Proc. PTI 2014.
- [4] TWSTFT Calibration Guidelines for UTC Time Links V1.0 <http://tai.bipm.org/TFG/TWSTFT-Calibration/Guidelines>
- [5] F.J. Galindo, H. Esteban, A. Bauch, D. Piester, I. Sesia, P. Uhrich, K. Jaldehag, C. Rieck, R. Piriz (2016) "European TWSTFT Calibration Campaign 2014 of UTC(k) laboratories in the Frame of Galileo FOC TGVF," Proc. PTI 2016.
- [6] C. Schlunegger (2015) Application of CALR values from calibration report CAL-TIM-RP-001
- [7] E. Dierix (2015) Linking document for the TWSTFT calibration campaigns of October/November 2012 and April/May 2013.
- [8] TWSTFT quasi-real-time service maintained by SP: <http://igsrt.sp.se/twstft/>
- [9] D. Piester, R. Bumgarner, J. Wright, A. McKinley, A. Bauch (2015) "Report of The July 2015 calibration of the link UTC(USNO) – UTC(PTB) by means of the USNO portable X-band TWSTFT station."
- [10] H. Esteban, J. Galindo, A. Bauch, T. Polewka, G. Cerretto, R. Costa, P. Whibberley, P. Uhrich, B. Chupin, Z. Jiang (2015) "GPS Time Link Calibrations in the Frame of EURAMET Project 1156," Proc. EFTF/IFCS2015.
- [11] Z. Jiang (2015) "Link calibration or receiver calibration for accurate time transfer?" Proc. EFTF/IFCS2015.
- [12] Z. Jiang, W. Lewandowski, A. Harmegnies, D. Piester, and V. Zhang (2011) "Restoration the TWSTFT link calibration using GPSPPP bridging after the satellite change on MJD 55769/27 July 2011," BIPM TM198bis.
- [13] Z. Jiang, D. Piester, C. Schlunegger, E. Dierix, V. Zhang, J. Galindo, J. Hirschauer (2015) "BIPM 2015 TWSTFT calibrations for UTC links and Triangle Closure Calibrations for Non-UTC links," BIPM TM256.
- [14] D. Piester, A. Bauch, L. Breakiron, D. Matsakis, B. Blanzano, O. Koudelka, "Time transfer with nanosecond accuracy for the realization of International Atomic Time," Metrologia, vol. 45, no. 2, pp. 185-198, 2008.
- [15] D. Piester, M. Rost, M. Fujieda, T. Feldmann, A. Bauch, "Remote atomic clock synchronization via satellites and optical fibers," Advances in Radio Science, vol. 9, pp. 1-7, 2011.
- [16] T. Feldmann, A. Balu, S. Liu, W. Schäfer, A. Bauch, J. Becker, D. Piester, J. Achkar, A. Kanj, C. Schlunegger, J. Morel, "TWSTFT Calibration Involving Four Sites Using a Mobile Station on a Trailer," Proc. 2013 Joint UFFC, EFTF and PFM Symposium, 21-25 Jul 2013, Prague, Czech Republic, pp. 485-491, 2013.

Cross-spectral Collapse from Anti-correlated Thermal Noise in Power Splitters

Craig W. Nelson, Archita Hati and David. A. Howe

Time and Frequency Division
National Institute of Standards and Technology
Boulder, CO/USA
nelson@nist.gov

Abstract—We discuss the cross-spectral collapse due to anti-correlated thermal noise that originates from the common-mode power divider (splitter) in a cross-spectrum noise measurement system. We studied this effect for different power splitters and discuss its influence on the measurement of thermal-noise limited oscillators.

Keywords—anti-correlation; cross-spectrum; oscillator; phase inversion; phase noise; power spectral density; thermal noise

I. INTRODUCTION

The cross-spectrum technique is a standard procedure used for the measurement of phase modulation (PM) and amplitude modulation (AM) noise of oscillators [1]–[4]. Despite being commonly used, this technique is susceptible to experimental errors [5], [6]. One among many of these errors is caused either by positive or negative correlations resulting in over-estimation or under-estimation respectively of the oscillator noise [7], [8].

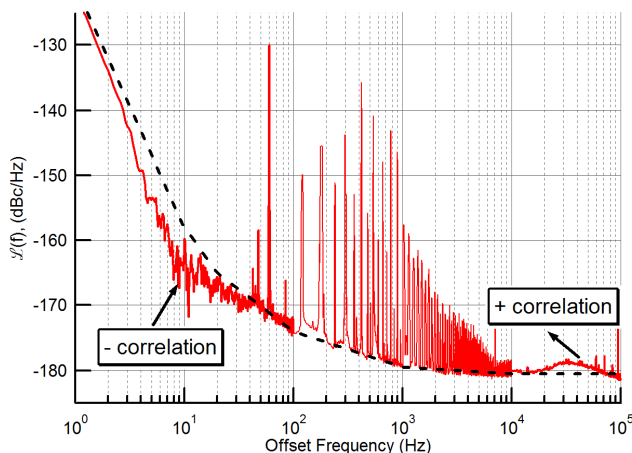


Fig. 1. Phase noise of a 5 MHz oscillator. The red curve shows the effect of positive and negative correlation on the phase noise. The curve in black is the actual noise of oscillator.

An example of such effect on the phase noise is illustrated in Fig. 1. Here, the red curve is the measured phase noise of a

¹ Contribution of the U.S. government, not subject to copyright. Commercial products are mentioned in this document for completeness. No endorsement is implied.

5 MHz quartz-crystal oscillator; it displays simultaneously the effect of both positive correlation above 10 kHz offset and negative correlation around 10 Hz offset. One cause of the noise under-estimation as explained in [8] can occur due to the anti-correlation (phase-inversion) collapse mainly from AM noise leakage. More recently, a different source of anti-correlation in a cross-spectrum measurement has been identified; its origin is from the common-mode power splitter [9]–[11]. Correlated thermal noise of the power splitter appears equally but in opposite phase in two channels of the cross-spectrum system. In this paper, we will discuss the effect of thermal noise of various reactive and resistive power splitters on the noise measurement of thermally-limited oscillators.

II. CROSS-SPECTRAL COLLAPSE DUE TO POWER SPLITTERS

In recent years, several commercial ultra-low phase noise (ULPN) oscillators have been introduced whose phase noise is near the thermal limit. In this new class of oscillators, a bias (either positive or negative) from the power splitter thermal noise can dominate the cross-spectrum result. In order to study the effect of thermal noise of the common mode power splitter on absolute noise measurements, a selection of reactive and resistive power splitters as shown in Fig. 2 were tested with an ULPN oscillator at 100 MHz [Golden Citrine from Wenzel Associates, Inc.].

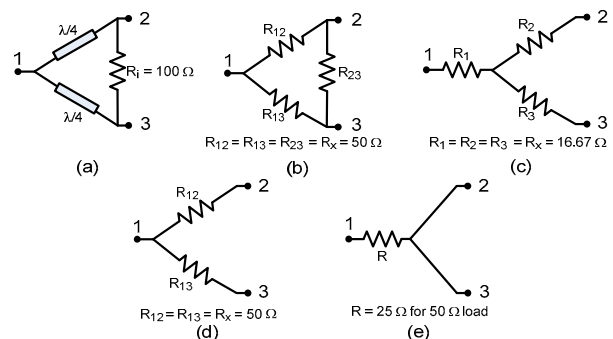


Fig. 2. Schematic of different power splitters: (a) Wilkinson power splitter, (b) Resistive 3-R (Delta configuration), (c) Resistive 3-R (Wye configuration), (d) Resistive 2-R and (e) Resistive 1-R.

The measurement set-up as shown Fig. 3 is used for the phase noise measurement of this oscillator. A variable dc offset

voltage was added at the input of the phase locked loop (PLL) integrator to reduce the device under test (DUT) AM noise thus minimizing the effect of anti-correlation collapse due to the AM noise leakage [8]. At first a Wilkinson power splitter (WPS) was chosen and the phase noise of the oscillator was measured with attenuator ‘A’ equal to 3 dB at the output of the oscillator. Assuming a 50 Ω system and taking into account the loss of DUT signal strength in the impedance matching and harmonic filtering (IMHF) circuit, the theoretical noise of a thermally-limited oscillator should be -188.5 dBc/Hz i.e., $-177 - P_{Ps}$. As shown in Fig. 4, a complete collapse (limited by the number of FFT averages) of the thermal noise spectrum was observed due to the anti-correlated noise of the WPS. Next, the measurement was repeated with approximately 9 dB attenuation of the test signal; instead of the theoretical noise level of -182.5 dBc/Hz we again achieved a cross-spectrum collapse. The power levels at the LO and RF ports of the phase detector in each channels were kept constant for both 3 dB and 9 dB measurements.

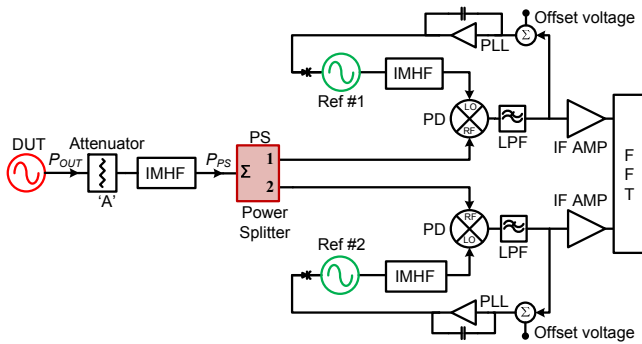


Fig. 3. Block diagram of a cross-spectrum phase noise measurement system. DUT – Device under test, IMHF – Impedance matching and harmonic filtering, LPF – Low pass filter, PD – Phase Detector, FFT – Fast Fourier Transform, PLL – Phase Locked Loop.

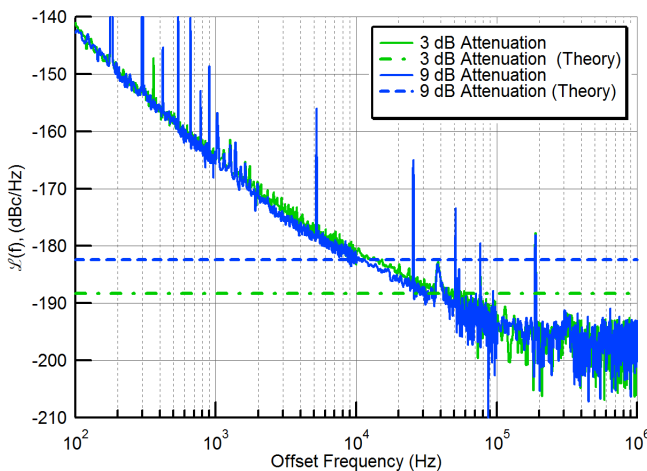


Fig. 4. Phase noise of a 100 MHz oscillator measured with a Wilkinson power splitter. Theoretical noise of this oscillator referenced to the input power of common-mode power splitter (P_{Ps}) is respectively -188.5 dBc/Hz and -182.5 dBc/Hz for attenuator ‘A’ equal to 3 dB and 9 dB. These values are calculated from $(-177 - P_{Ps})$ assuming a 50 Ω system. The far-from-the-carrier noise in both cases are limited by the number of FFT averages ($N = 100,000$) but there is clear indication of a spectrum collapse.

It is especially worth noting that for 9 dB attenuation in Fig. 4, one can actually extract underlying multiplicative sloped noise of the oscillator between 10 kHz and 50 kHz offset frequencies even though it is normally masked by the thermal noise. This observation validates the power-law noise model [12], [13].

The PM noise of the same oscillator was also measured with 3-R, 2-R and 1-R resistive power splitters (Fig. 2(b)-(e)) and the results are shown in Fig. 5. The measured thermal noise is almost 3 dB lower than the simulated noise levels (Table 1) in each case. This discrepancy is due to the fact that the simulations are performed with an ideal 50 Ω load impedance; however, in actual experiment the power splitter is connected to the reactive load of the double balanced mixer used as a phase detector. In spite of the discrepancy between the measurements and simulation, the relative differences in the measured thermal noise levels between 1-R and 3-R as well as between 3-R and 2-R power splitters are nearly the same as the simulated results. In [11], we demonstrated that if the power splitter is connected to a real 50 Ω load impedance, the simulation and experimental results agree well; we verified this for the AM noise measurements.

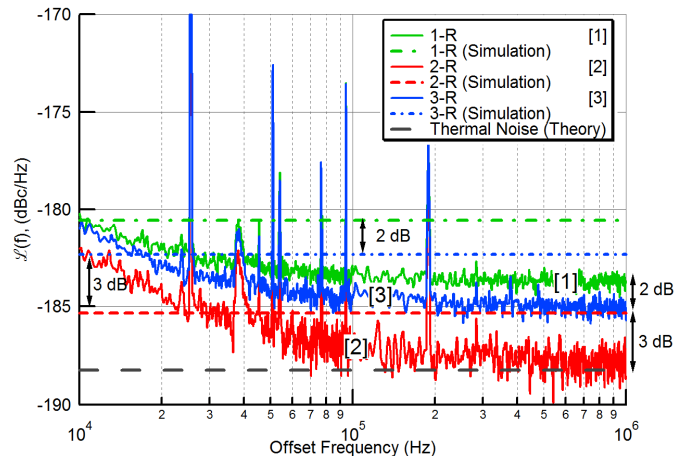


Fig. 5. Phase noise of a 100 MHz oscillator measured with resistive 1-R, 2-R and 3-R power splitters. The simulated noise for three different power splitters is obtained from Table 1, column 8.

The simulation results given in Table 1 for different types of power splitters were performed in the Advanced Design System (ADS) software. The block diagram for the simulation is shown in Fig. 6. For this simulation, the thermal noise contribution of the source, the power splitter and the load resistors are considered. A detailed description of the simulation can be found in [11]. Table 1 tabulates the results of thermal noise contribution of the individual component to the output cross-spectrum as a fraction of the noise from R_s . The simulation is performed for load and source impedances equal to 50 Ω and at 300 K temperature. The values reported in the table are from the expected value of the cross-spectrum. All uncorrelated cross-terms, which reside in the imaginary component of the cross-spectrum, are zero and the result is an entirely real number. For an exact measurement of the thermal noise of an oscillator, columns 3 and 8 should be equal.

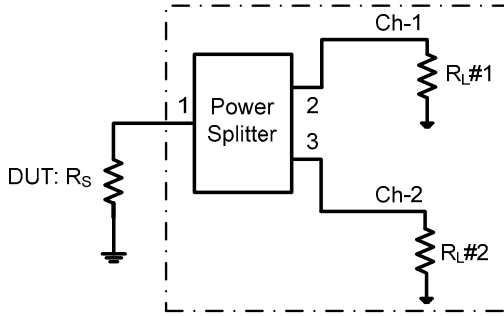


Fig. 6. The main sources of thermal noise used for ADS simulation. R_s represents the thermal noise of the source or the device under test (DUT). Total number of resistors in the power splitter varies from 0 to 3 depending on the configuration (see Fig. 2). The load resistors $R_{L\#1}$ and $R_{L\#2}$ represent the thermal noise of the measurement system.

Table 1: 2-way Power Splitter (PS): Source impedance (Z_S) = Load Impedance (Z_L) = 50Ω , $T = 300 \text{ K}$, Isolator: Insertion Loss = 0 dB , Isolation = ∞

Case #	Type of Power splitter (PS)	Relative cross-spectrum of individual component						Total Noise	
		$S_{Ch2-Ch1}(f)/S_{R_s}(f)$							
		R_s	Power Splitter			$R_{L\#1}$	$R_{L\#2}$	w/o R_s	All Components
		R_1	R_2	R_3					
1	Wilkinson $R_i = 100 \Omega$	1	-1			0	0	-1	0
2	3-R Wye $R_x = \sim 17 \Omega$	1	1/3	-2/3	-2/3	2	2	3	4
3	3-R Delta $R_x = 50 \Omega$	1	0	-1	0	2	2	3	4
4	2-R $R_x = 50 \Omega$	1	0	-3/4	-3/4	5/4	5/4	1	2
5	1-R, $R = 25 \Omega$	1	1/2	-	-	9/5	9/5	5	6

Here, R_i and R_x respectively correspond to the isolation resistor and the resistors for 2-R and 3-R power splitters.

The simulation results in Table 1 indicate that the 3-R (Delta or Wye) and 2-R splitters produce anti-correlated thermal noise between the outputs. Also, the resistive power splitters do not have sufficient isolation to allow a cross-spectrum measurement to overcome the loss of signal-to-noise ratio in each individual channel. They cannot be used to accurately measure a thermally limited source because the dominating noise of the load to the power splitter appears correlated in both channels and cannot be rejected.

We also observed large variations in the measured thermal noise as shown in Fig. 7 when different phase detectors were used. The dissimilar reactive load presented by different phase detectors to the power splitter affects the degree of anti-correlation.

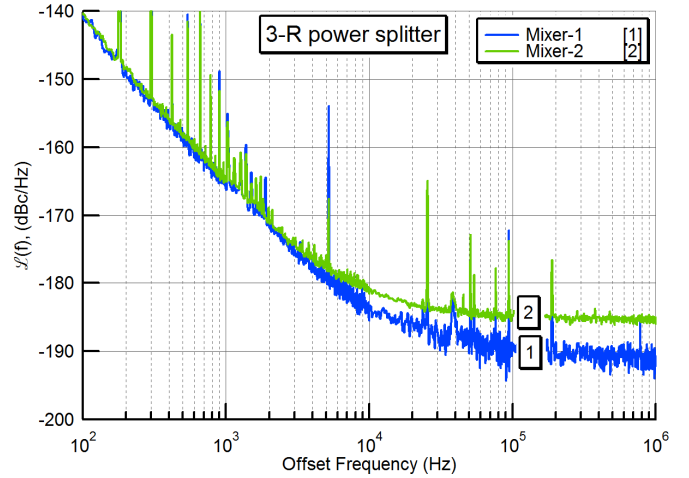


Fig. 7. Phase noise of a 100 MHz oscillator measured with a resistive 3-R power splitter but different mixers (phase detectors) with different input impedances.

III. CONCLUSION

We discussed cross-spectral collapse due to anti-correlated thermal noise of the common-mode power divider (splitter) in a cross-spectrum noise measurement system. The simulation and experimental results indicate that the reactive and resistive power splitters cannot accurately measure a thermal-noise limited oscillator using the scheme in Fig. 3, if the oscillator and power splitter are at the same temperature.

REFERENCES

- [1] W. F. Walls, "Cross-correlation phase noise measurements," in *Frequency Control Symposium, 1992. 46th., Proceedings of the 1992 IEEE*, 1992, pp. 257–261.
- [2] D. Fest, J. Gros Lambert, and J.-J. Gagnepain, "Individual Characterization of an Oscillator by Means of Cross-Correlation or Cross-Variance Method," *IEEE Trans. Instrum. Meas.*, vol. 32, no. 3, pp. 447–450, 1983.
- [3] E. Rubiola and V. Giordano, "Correlation-based phase noise measurements," *Rev. Sci. Instrum.*, vol. 71, no. 8, pp. 3085–3091, 2000.
- [4] F. L. Walls and E. Ferre-Pikal, "Measurement of Frequency, Phase noise and Amplitude noise," in *Wiley Encyclopedia of Electrical and Electronics Engineering*, 1st ed., vol. 12, 24 vols., Wiley-Interscience, 1999, pp. 459–473.
- [5] A. K. Poddar, U. L. Rohde, and A. M. Apte, "How Low Can They Go?: Oscillator Phase Noise Model, Theoretical, Experimental Validation, and Phase Noise Measurements," *IEEE Microw. Mag.*, vol. 14, no. 6, pp. 50–72, Sep. 2013.
- [6] U. L. Rohde and A. K. Poddar, "Phase noise measurement techniques, associated uncertainty, and limitations," in *European Frequency and Time Forum International Frequency Control Symposium (EFTF/IFC), 2013 Joint*, 2013, pp. 438–441.
- [7] C. W. Nelson, A. Hati, and D. A. Howe, "Phase inversion and collapse of cross-spectral function," *Electron. Lett.*, vol. 49, no. 25, pp. 1640–1641, Dec. 2013.
- [8] C. W. Nelson, A. Hati, and D. A. Howe, "A collapse of the cross-spectral function in phase noise metrology," *Rev. Sci. Instrum.*, vol. 85, no. 2, p. 024705, Feb. 2014.

- [9] J. Gorin, "Power splitter anti correlation, Cross-spectrum L(f) workshop," Denver, CO, USA, 12-Apr-2015.
- [10] A. Hati, C. W. Nelson, and D. A. Howe, "Effect of anti-correlation on cross-spectrum measurements of thermally limited oscillators," presented at the The 8th Symposium on Frequency Standards and Metrology 2015, Potsdam, Germany, 12-Oct-2015.
- [11] A. Hati, C. W. Nelson, and D. A. Howe, "Cross-spectrum Measurement of Thermal-noise Limited Oscillators," *Rev. Sci. Instrum.*, vol. 87, no. 3, p. 034708, 2016. DOI: 10.1063/1.4944808
- [12] D. A. Howe, D. U. Allan, and J. A. Barnes, "Properties of Signal Sources and Measurement Methods," in *Thirty Fifth Annual Frequency Control Symposium. 1981*, 1981, pp. 669–716.
- [13] D. B. Sullivan, D. W. Allan, D. A. Howe, and F. L. Walls, "Characterization of Clocks and Oscillators," in *Technical Note 1337*, 1990.

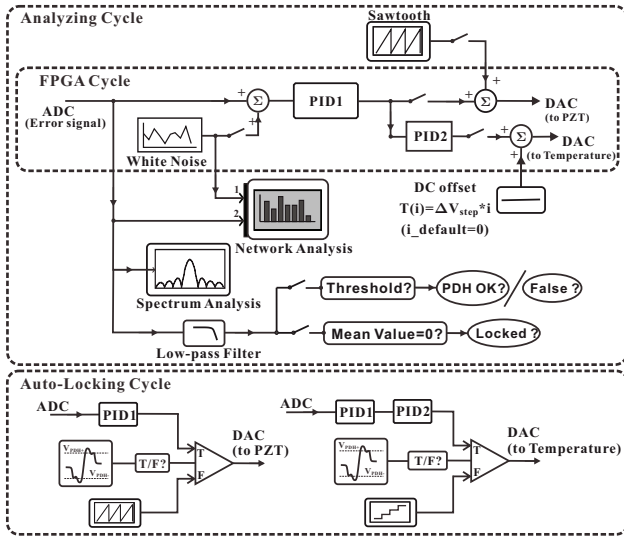


Fig. 2. Block-diagram of the digital controller which includes self-analyzing functions of the loop status and additional auto-locking capabilities.

been programmed in a LabVIEW environment. This controller yields sufficient control bandwidth, excellent noise suppression abilities and effective self-analyzing algorithms. The simplified block-diagram of the digital controller is shown in Fig. 2, in which the FPGA cycle operates the high speed laser feedback commands with the loop speed of higher than 340 kHz. The analyzing cycle includes spectrum and network analyzers for closed-loop diagnosis and real-time adjustment. In the same cycle the demodulated error signal is continuously interrogated to determine the loop status. The additional auto-locking cycle is in charge of various control commands that are triggered by the loop status, and performs the initial auto-locking of the free-running laser to one of the cavity resonances. Auto-locking is essential for automatic in-orbit operations of the laser source.

III. EXPERIMENTAL RESULTS

The preliminary experimental results include the results of the auto-locking performance and the results of the actual laser stability measured by the beat note analysis of another independently stabilized laser source. Fig. 3(a) shows the error signal detected during a complete initial auto-locking procedure of the laser source. In the sub-figures 3(b) and 3(c) the error signal profile is enlarged in correspondence of the scanning process in search of a cavity resonance (Fig. 3(b)) and in correspondence of the lock-in process following the PDH signal detection (Fig. 3(c)). The corresponding error signal spectra are measured and monitored by the built-in spectrum analyzer in real time, and are shown in Fig. 3(d)-(f) respectively. The spectrum of Fig. 3(f) obtained when the laser is in-locked exhibits a control bandwidth of about 30 kHz, which is sufficient to cover the whole laser frequency noise band in Fig. 3(e) measured during the PDH signal detection. A good noise suppression capability is confirmed by observing that the in-locked residual noise level is below the measurement noise floor of the system in Fig. 3(d). Once the system is in closed loop, the auto-locking cycle ends and the locked status of laser is continuously monitored until an unlock condition is detected, which automatically triggers the

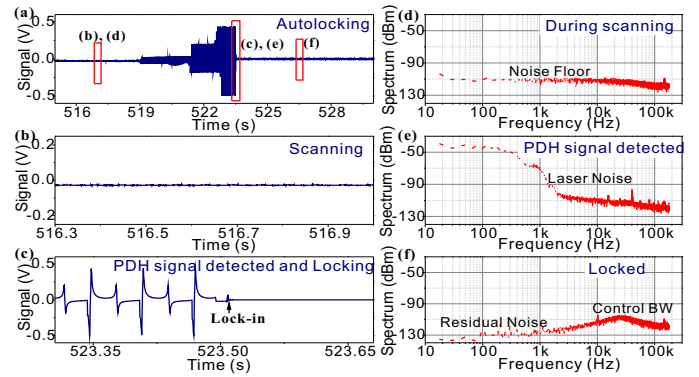


Fig. 3. (a) Error signal during auto-locking process to the cavity. (b) Enlargement of (a) during laser frequency scanning. (c) Enlargement of (a) during lock-in process. (d) Error signal spectra (d) during scanning, (e) of the PDH signal detected and (f) during locked status.

auto-locking process to recommence. The experimental results have shown proven reliability of the auto-locking algorithm.

The actual frequency stability of laser source has been measured by the beat note analysis with an ultra-stable clock laser of sub-Hz level. Since the stability of the clock laser is more than 1 order of magnitude higher than the prototype, the frequency noise of the beat note can be ascribed to the prototype laser of this paper. The beat note has been measured by sending the prototype laser signal to the ultra-stable clock laser via a 25 m long polarization-maintaining (PM) fiber, as shown in the simplified layout of Fig. 4. The fiber-induced linewidth broadening and additional frequency noise are actively cancelled by the frequency modulation of a double-pass acoustic-optic modulator (AOM) [9], with the residual fiber noise suppressed to a negligible level not to affect the beat note measurement.

Fig. 5(a) shows the 50 Hz linewidth of the beat note frequency along with Lorentz fitting, obtained by short-term spectrum analysis with a resolution bandwidth of 20 Hz. The dithering noise observed in the measurement is such to limit the achievable linewidth in longer term, since it may be affected by the flicker noise from the air environment to the fiber optical system. The frequency noise spectral density has been also measured and analyzed as shown in Fig. 5(b), where a frequency noise of less than $30 \text{ Hz/Hz}^{1/2}$ from 0.7 Hz to 10 Hz is obtained. Unfortunately the noise level in the lower frequency range is still too high compared with the mission requirement. Preliminary analysis suggested that this low frequency noise is mainly caused by fluctuations of PDH error signal offset shown as a pink curve in Fig. 5(b). The cause may be ascribed to the residual amplitude modulation (RAM) of the optical system, to be actively cancelled in the on-going developments. In Fig. 5(b), the electronic noise (green curve) has been assessed by measuring the locked error signal through an independent analog-to-digital-converter (ADC) route. The locking performance of the controller has been evaluated by the in-loop residual noise that is estimated to be less than $0.07 \text{ Hz/Hz}^{1/2}$ with a PDH discrimination factor of 0.29 MHz/V.

IV. APPLICATION ON LASER INTERFEROMETER

The laser of the prototype has been applied, as a master laser, to the ground test bed of a spaceborne laser interferome-

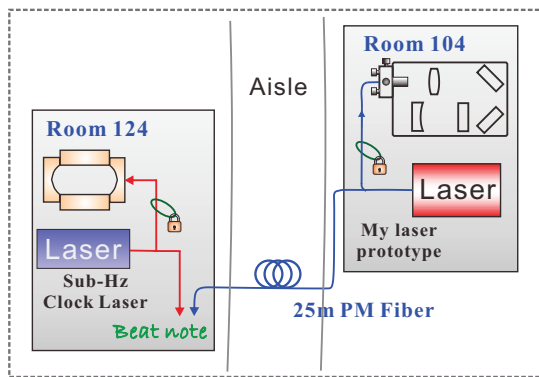


Fig. 4. Beat note experimental setup of the laser signal transmission from the prototype to an ultra-stable laser via a 25 m fiber.

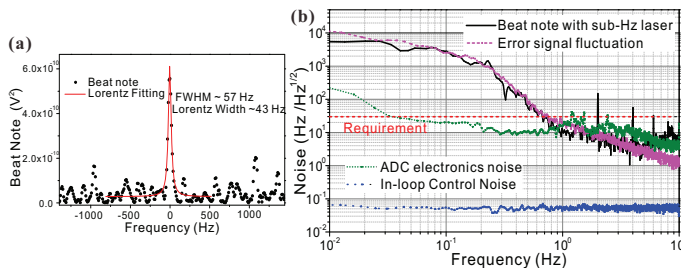


Fig. 5. (a) Linewidth of the laser beat note frequency. (b) Frequency noise spectral density and noise analysis of the laser beat note.

try ranging prototype. The overall experimental setup is illustrated in Fig. 6. During the test, the frequency-stabilized master laser signal is sent to the interferometer system via a 25 m long PM fiber and the fiber-induced frequency noise has been actively compensated to a negligible level. The interferometer consists of two identical optical benches (master and slave bench) which are fabricated by hydroxide-catalysis bonding with precisely positioned optical layouts, and are placed 1.5 m apart from each other to simulate the interferometer ranging arm. As shown in Fig. 6, in order to emulate the long-distance inter-satellite laser communication, the slave laser source is phase heterodyne locked to the received master laser at 2 nW level of incoming power, and then sent back to the master bench for the relative displacement measurement along the arm. The alignment between the interfering master and slave laser sources is measured by a quadrant photo detector (QPD) and a digital 4-channel phasemeter [10]. Laser source pointing is optimized and stabilized by the closed-loop control of a fast steering mirror. Finally, the relative displacement is measured from the interfering phase variation obtained by the averaged read out of QPD and phasemeter.

Fig. 7 shows a typical noise floor of the displacement measurement of the laser interferometer: a noise level of 1 nm/Hz^{1/2} around 0.1 Hz and of about 30 nm/Hz^{1/2} around 0.01 Hz has been obtained. The measurement resolution has been tested by actively driving a 6-axis positioner which step by step moves the optical bench along the interferometer ranging arm and by recording at the same time the phase variation. The resolution of 10 nm displacement steps at 0.1 Hz has been measured and the recorded phase variation is shown in Fig. 8.

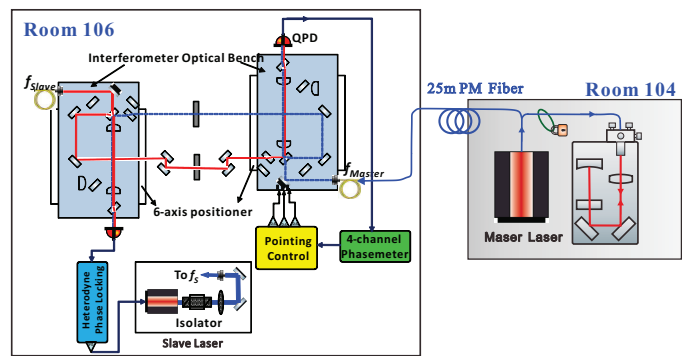


Fig. 6. Experimental setup of ground demonstration of the laser interferometry ranging prototype.

V. CONCLUSION AND OUTLOOK

A preliminary laser frequency stabilization prototype for spaceborne laser interferometry missions has been developed based on hydroxide-catalysis bonding, fiber optics and multi-functional automatic digital control. Frequency stability has been estimated from the beat note with an independent ultra-stable laser. The prototype laser source applied as a master laser on the ground test bed of a spaceborne interferometry prototype. Preliminary experimental results have been presented and discussed. Further improvements of the prototype include suppression of the fluctuations of PDH error signal offset, thermal stabilization at the zero-crossing temperature of the optical bench coefficient of thermal expansion (CTE), further upgrading of the automatic functions of the digital controller, integration of the system into a space-qualified FPGA chip. In the next generation of the prototype, the fiber injector will be implemented by precise bonding technique instead of a mechanical collimator. Finally the optical bench should be mounted rigidly and robustly with squeeze-immune and vibration insensitive designs.

ACKNOWLEDGMENT

The authors are grateful to Professor Enrico Canuto of Politecnico di Torino Italy, for kind and valuable advices, and to Professor Gerhard Heinzel of Albert Einstein Institute Germany, for helpful discussions and technical suggestions. This work was supported by the National Science Foundation of China (Grant No. 91336109).

REFERENCES

- [1] O. Jennrich, "LISA technology and instrumentation," *Class. Quantum Grav.*, vol. 26, pp. 3001–3033, 2009.
- [2] B. S. Sheard, G. Heinzel, K. Danzmann, D. A. Shaddock, W. M. Klipstein, and W. M. Folkner, "Intersatellite laser ranging instrument for the GRACE follow-on mission," *Journal of Geodesy*, vol. 86, pp. 1083–1095, 2012.
- [3] P. L. Bender, J. L. Hall, J. Ye, and W. M. Klipstein, "Satellite-satellite laser links for future gravity missions," *Space Science Reviews*, vol. 108, pp. 377–384, 2003.
- [4] R. W. P. Drever, J. L. Hall, F. V. Kowalski, J. Hough, G. M. Ford, A. J. Munley, and H. Ward, "Laser phase and frequency stabilization using an optical resonator," *Appl. Phys. B*, vol. 31, pp. 97–105, 1983.
- [5] E. J. Elliffe, J. Bogenstahl, A. Deshpande, J. Hough, C. Killow, S. Reid, D. Robertson, S. Rowan, H. Ward, and G. Cagnoli, "Hydroxide-catalysis bonding for stable optical systems for space," *Class. Quantum Grav.*, vol. 22, pp. S257–S267, 2005.

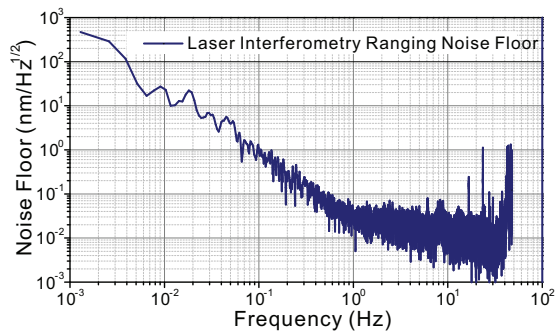


Fig. 7. Displacement noise floor of the laser interferometer measurement.

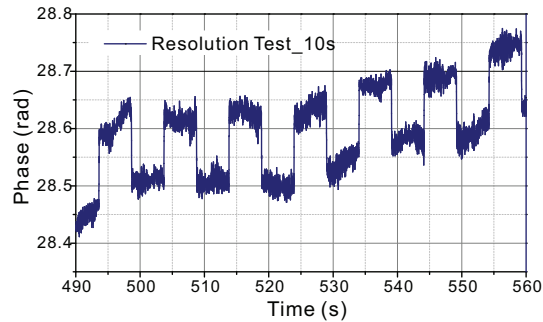


Fig. 8. Displacement measurement resolution test of 10 nm step at 0.1 Hz by the laser interferometer.

- [6] Y. Luo, H. Li, H. C. Yeh and J. Luo, "A self-analyzing double-loop digital controller in laser frequency stabilization for inter-satellite laser ranging," *Rev. Sci. Instrum.*, vol. 86, pp. 044501, 2015.
- [7] C. W. Everitt, D. B. DeBra, B. W. Parkinson, J. P. Turneure, J. W. Conklin, M. I. Heifetz, G. M. Keiser, A. S. Silbergleit, T. Holmes, J. Kolodziejczak, M. Al-Meshari, J. C. Mester, B. Muhifelder, V. G. Solomonik, K. Stahl, P. W. Jr. Worden, W. Bencze, S. Buchman, B. Clarke, A. Al-Jadaan, H. Al-Jibreen, J. Li, J. A. Lipa, J. M. Lockhart, and B. Al-Suwaidan, "Gravity Probe-B: final results of a space experiment to test general relativity," *Phys. Rev. Lett.*, vol. 106, pp. 221101, 2011.
- [8] S. A. Webster, M. Oxborrow, and P. Gill, "Vibration insensitive optical cavity," *Phys. Rev. A*, vol. 75, pp. 011801, 2007.
- [9] L. S. Ma, P. Jungner, J. Ye and J. L. Hall, "Delivering the same optical frequency at two places: accurate cancellation of phase noise introduced by an optical fiber or other time-varying path," *Opt. Lett.*, vol. 19, pp. 1777, 1994.
- [10] Y. Liang, H. Duan, H. C. Yeh and J. Luo, "Fundamental limits on the digital phase measurement method based on cross-correlation analysis," *Rev. Sci. Instrum.*, vol. 83, pp. 095110, 2012.

Design of a new calibration device for Two-Way Satellite Time and Frequency Transfer Station

Xueyun Wang, Hang Yu, Shengkang Zhang, Liang Wang, Haifeng Wang,

Hongbo Wang, Chao Wang, Peng Wang, Hang Yi, Fan Shi, Dongliang Yan

Beijing Institute of Metrology & Measurement, Beijing, china, 100854

Email: wxy203_3@126.com

Abstract: The Calibration Device is used to measure the time delay difference between the transmission and receiving paths inside Two-Way Satellite Time and Frequency Transfer (TWSTFT) earth station, it can improve the time comparison precision. A new calibration device for TWSTFT has been developed recently at Beijing Institute of Radio Metrology and Measurement (BIRMM). The signal paths inside calibration device is bidirectional which allow both the transmission and receiving signal passed, so the delay difference of the transmission and receiving inside calibration device almost be zero. The calibration device works on Ku-band. To evaluate the performance of the BIRMM calibration device, a local TWSTFT experiments was done with SATRE modem. The measurement results show that the time delay difference was quite small instability with standard deviation (1σ) equal to 0.17ns.

Key words: two-way satellite time and frequency transfer (TWSTFT); calibration device; time delay measure

□. INTRODUCTION

Two-Way Satellite Time and Frequency Transfer (TWSTFT) is a precise time and frequency comparison technique, which is widely used in time metrology [1-2], time synchronization in the applications of satellite navigation, radio ranging and measurement [3], etc. Its performance is based on the reciprocity of the TWSTFT signals' bidirectional paths, so the time delay difference between the transmission and receiving paths must be precisely measured and calibrated. There are two ways to accomplish the calibration, one way is using a transportable TWSTFT station collocated with both stations to perform the common-clock measurements, and then the relative delay differ-

ence can be calculated. The other way is using the separate calibration technique to measure the absolute Tx/Rx delays at each station. This paper was focus on the second method.

Recently, a new calibration device for TWSTFT has been developed at Beijing Institute of Radio Metrology and Measurement (BIRMM), which works on Ku-band. The signal path is bidirectional which allows both the transmission and receiving signal passed, the delay difference between the transmission and receiving signal inside calibration device almost was zero. So it can precisely calibrate the time delay of TWSTFT earth station.

To evaluate the performance of the calibration device, a local experiment was done. A TWSTFT earth station with calibration function was established by one 1.2 m dish, anacom transceiver, timetech SATRE modem and BIRMM calibration device. The measurements for obtaining the delay values of some internal loops in earth station were performed, and the time delay difference of the transmission and receiving path inside the TWSTFT earth station were calculated and shown that the delay difference was quite small instability with standard deviation (1σ) equal to 0.17 ns.

II. DESIGN OF THE CALIBRATION DEVICE

A. The calibration principle

The time difference between site A and site B in TWSTFT link can be show by following equation [4]:

$$\tau_{CAL} = 0.5(\tau_A^{TX} - \tau_A^{RX}) \quad (4)$$

The time delay was measured by TWSTFT modem not only contains the τ_A^{RX} and τ_A^{TX} but also contains the delay of two cables which connect indoor unit and TWSTFT modem(T_1 , T_4), the delay of the cable which connect indoor unit and outdoor unit(T_7) and the delay of BIRMM calibration device self(T_{TR}), So the delay of all transmission(T_{TX}) and receiving(T_{RX}) path by modem measured can be expressed by the following equations:

$$T_{TX} = T_2 + T_{ODUTX} + T_3 + T_1 + T_4 + T_{TR} \quad (5)$$

$$T_{RX} = T_5 + T_{ODURX} + T_6 + T_1 + T_4 + T_{TR} \quad (6)$$

Then the delay difference τ_{CAL} can be obtained by subtracting the above two equations.

B. DESIGN OF INDOOR UNIT

Indoor unit includes a switch matrix, bidirectional filters and amplifiers, interface control circuit. It was used to control outdoor unit and switch operating modes. Fig.2 shows the principle of indoor unit.

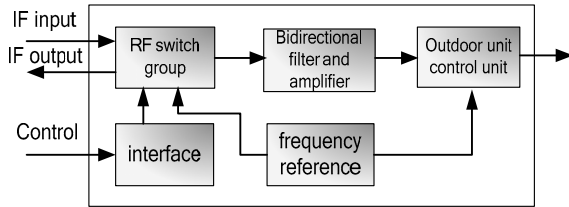


Figure2. The principle of indoor unit



Fig.3: Indoor unit of the BIRMM calibration device.

C. DESIGN OF OUTDOOR UNIT

In BIRMM calibration device, the transmission and receiving signals are on one path through. because of the transmitter and receiver using different frequencies, the calibration device requires twice frequency conversion.

Assuming the transmission frequency is f_{TX} , the receiving frequency is f_{RX} . The first local oscillator frequency is f_1 , The second

local oscillator frequency is f_2 . Fig.4 shows the principle of outdoor unit.

In order to ensure that the calibration device does not need to change the parameter setting when switching between TX calibration mode and RX calibration mode, the frequency of local oscillators must be designed very carefully. In this device, the f_1 and f_2 can be calculated by following equations:

$$f_1 = |f_{TX} - f_{RX}|/2 + f_0 \quad (7)$$

$$f_2 = (f_{TX} + f_{RX})/2 \quad (8)$$

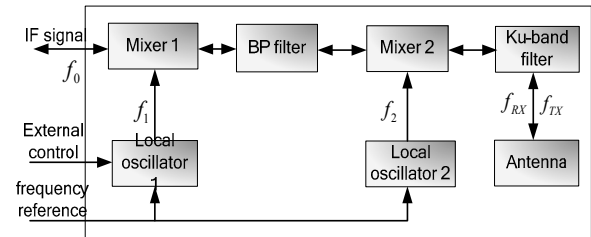


Figure4. The principle of outdoor unit



Fig.5: Outdoor unit of the BIRMM calibration device.

III. EXPERIMENTS AND DISCUSSIONS

In order to evaluate the performance of the BIRMM calibration device, a local experiment was done. The devices and the cable connections of the experimental system are illustrated as shown in Fig. 1. The code rate of SATRE Modem is 2.5Mchip/s, and the output power is -25dBm. Then select the measure mode of BIRMM calibration device and start measure. The measure time is one hour in each mode.

Fig.6 shows the outdoor experimental system on a building roof.



Figure6. The outdoor experiment system

Fig. 7 shows the measurement results of the transmission path. There are some discrete gross error values which can be processed by some filtering algorithm. Fig.8 shows the measurement results of the receiving path. Fig.9 is the calculated results of [Tx-Rx] values. The calibration results have an average value of 17.95 ns, and have instability with standard deviation (1σ) equal to 0.17ns.

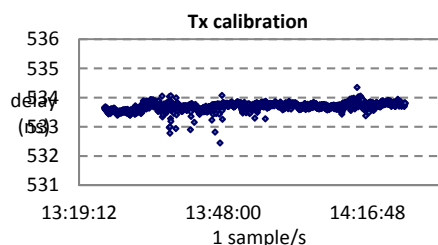


Figure7. The time delay calibration results of transmission path

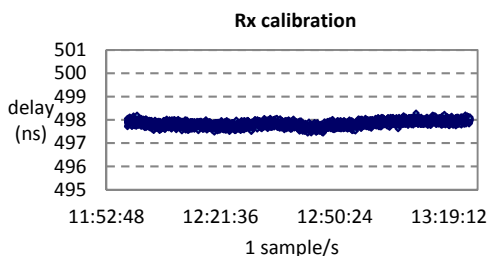


Figure8. The time delay calibration results of receiving path

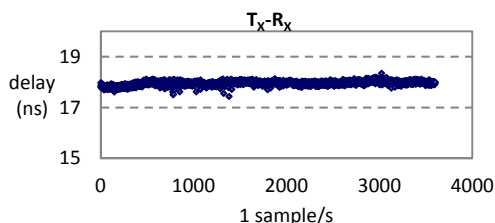


Figure9. The time delays difference calibration results of the transmission and receiving paths

IV. CONCLUSION

From the experimental results, it can be known that the performance of the calibration device is completely satisfied with the requirement of the two-way satellite time transfer system for the time delay measurement of the earth station. In practical application, because of the influence by temperature change and other factors, we need to complete the time delay measurement of

transmission and receiving path in a relatively short time. Finally, calculate the time delay difference which was used to compensate the time comparison results.

References

- [1] V. Zhang and M. A. Lombardi, "Time and Frequency Transfer Activities at NIST," Proc. 40th Precise Time and Time Interval (PTTI) Meeting, pp. 623-639, 2008.
- [2] M. Imae, M. Hosokawa, K. Imamura, et al. Two-way satellite time and frequency transfer networks in Pacific Rim region, IEEE Trans. on Instrumentation and Measurement, 2001,50(2),pp.559-562.
- [3] S. Zhang, L. Zhang and Y. Yang, "Ultra-Short Term Clock Offset Prediction for Two-Way Satellite Time Synchronization," 2013 Joint UFFC, EFTF and PFM Symposium, pp. 335-338, 2013.
- [4] D. Kirchner, "Two-Way Time Transfer via Communication Satellites," in Proc. of the IEEE, 79, pp.983-990, 1991.

Remote atomic clock delivery to the VLBI station in Toruń

Krehlik Przemysław¹, Adamowicz Waldemar², Binczewski Artur³, Bogacki Wojbor³, Buczek Łukasz¹, Campbell Bob⁴, Ciuryło Roman⁵, Dunst Piotr⁶, Kołodziej Jacek¹, Lemański Dariusz⁶, Lipiński Marcin¹, Marecki Andrzej⁵, Nawrocki Jerzy⁶, Nogaś Paweł⁶, Pawszak Tadeusz², Pazderski Eugeniusz⁵, Pieczerak Janusz², Stroński Maciej³, Śliwczyński Łukasz¹, Turza Krzysztof³, Zawada Michał⁵

¹Dep. of Electronics, AGH University of Science and Technology, Kraków, Poland

²Orange Polska S.A., Warsaw, Poland

³Poznań Supercomputing and Networking Center, Poznań, Poland

⁴Joint Institute for VLBI ERIC, Dwingeloo, The Netherlands

⁵Faculty of Physics, Astronomy, and Informatics, N. Copernicus University, Toruń, Poland

⁶Astrogeodynamic Observatory (AOS), Borowiec, Poland

Email: krehlik@agh.edu.pl

Abstract—The remote synchronization of a Very Long Baseline Interferometry (VLBI) station with a “virtual” atomic clock delivered via an optical fiber is described. The time and frequency signals are provided from UTC(AOS) laboratory located at a distance of 345 kilometers from the VLBI station. Evaluation of the remote synchronization carried out by Joint Institute for VLBI ERIC is presented. To our best knowledge, this is the first operational fiber-optic link synchronizing VLBI observations.

Keywords—VLBI; synchronization; fiber-optic networking; virtual atomic clock

I. INTRODUCTION

In 2015, Polish fiber-optic network for time and frequency (T&F) distribution (OPTIME) reached Toruń University [1]. This created an opportunity to synchronize the VLBI station in Piwnice near Toruń (hereafter: “Toruń”) to both Polish UTC laboratories: UTC(AOS) and UTC(PL). The motivation of presented work was to demonstrate a possibility of remote synchronization of VLBI system and to investigate the impact of UTC-traceable synchronization on VLBI observations. Up to our knowledge, other VLBI stations across Europe will also be remotely synchronized to UTC-traceable frequency references. This would open an opportunity for further experiments and possibly an improvement of the quality of VLBI observations in general.

II. REMOTE SYNCHRONIZATION

The backbone segment of OPTIME connects two UTC laboratories [UTC(PL) in Warsaw and UTC(AOS) in Borowiec near Poznań] and National Laboratory for Atomic, Molecular, and Optical Physics (KL FAMO) located at Toruń University. In November 2015, Toruń Radio Astronomy Observatory based in Piwnice near Toruń was connected to the backbone

(Fig. 1) and started to receive the T&F signals from UTC(AOS). The length of UTC(AOS)–Toruń link is 330 km and the slave link to Piwnice is 15-km long. Stabilized T&F distribution in the OPTIME network is realized by means of ELSTAB technology developed at AGH University [2]. The expected frequency transfer stability of the installed ELSTAB system was estimated as $5 \cdot 10^{-13}$ for 1 s averaging and $8 \cdot 10^{-16}$ for 10^3 s averaging – see Fig. 2.

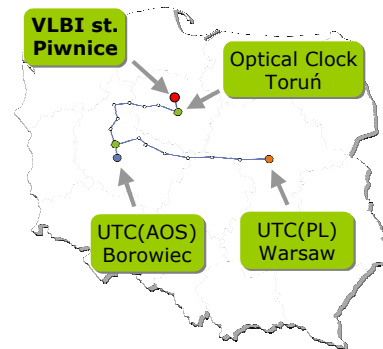


Fig. 1. Centre for Astronomy in Piwnice connected to the fiber optic T&F distribution network developed under OPTIME project.

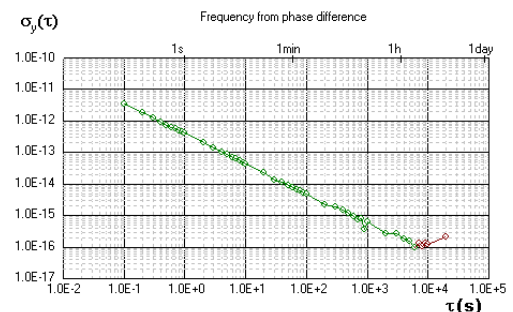


Fig. 2. Typical stability of long-haul T&F dissemination by ELSTAB.

This work was supported by Polish National Science Center (NCN) under project no. 2015/17/B/ST7/03628.

III. PROOF-OF-CONCEPT EXPERIMENT

On 18th Dec. 2015, a dedicated VLBI session was arranged with Westerbork (NL), Medicina (IT), Yebes (ES), and Onsala (SE) VLBI stations invited to participate. The well known “fringe finder” radio source 2007+777 was observed. The raw data from all participants were transferred to the Joint Institute for VLBI ERIC (JIVE) and the correlation proceeded in real-time (the e-VLBI technique). Additionally, the raw data from the stations were recorded at JIVE for further processing.

During the session, remote synchronization was evaluated by swapping the local H-maser for a “virtual” one, provided via the fiber. The analysis carried out at JIVE showed that the fringe visibility phase noise was very similar for both synchronization schemes for all four baselines to Toruń, over time-scales ranging from two seconds to 45 minutes. An example of interferometer phase residual in respect to the correlator model in sub-band 2 is plotted in Fig. 3, and Table 1 summarizes phase noise for all sub-bands and baselines. The important difference was observed in terms of phase drift when the local H-maser was exchanged to the remote, UTC-traceable one. In the first part of the experiment, the correlator had to assess and remove the phase drift (modeled as linear trend with the slope of -19.9 ps/s), whereas in the second part (remote synchronization) there was no measurable drift.

IV. CURRENT STATUS AND FURTHER PLANS

After the successful experiment in December 2015, Toruń station has ceased to use its local H-maser and has been synchronizing all VLBI sessions with the remote signals provided by the fiber from UTC(AOS) laboratory. Till now (March 2016), three sessions were performed: 12th/13th

TABLE I. PHASE NOISE (STANDARD DEVIATION) FOR DIFFERENT BASELINES AND SUB-BANDS.

Westerbork - Toruń			Medicina - Toruń		
s-b	local	remote	s-b	local	remote
0	24.59	26.10	0	14.31	14.16
1	24.46	27.38	1	14.32	14.13
2	25.36	27.31	2	15.44	15.08
3	25.55	27.22	3	15.72	16.33

Onsala - Toruń			Toruń - Yebes		
s-b	local	remote	s-b	local	remote
0	19.31	19.76	0	13.34	13.51
1	20.21	20.86	1	12.87	13.61
2	19.88	19.57	2	13.97	13.37
3	19.93	20.07	3	13.70	13.52

January, 2nd/3rd February, and the longest one lasting from 18th February till 10th March. No problems were observed.

In the next stage, we plan to arrange the synchronization scheme taking advantage of both the local H-maser and the remote signals. The idea is to use the local H-maser as a “flywheel” disciplined by the UTC-traceable remote signal. This way we would benefit both from the excellent short-term stability of the (local) H-maser, and long-term stability and UTC-traceability of the fiber-delivered reference.

The other option we are going to evaluate is to use frequency reference derived from strontium optical-lattice clock operated at National Laboratory for Atomic, Molecular, and Optical Physics in Toruń [3].

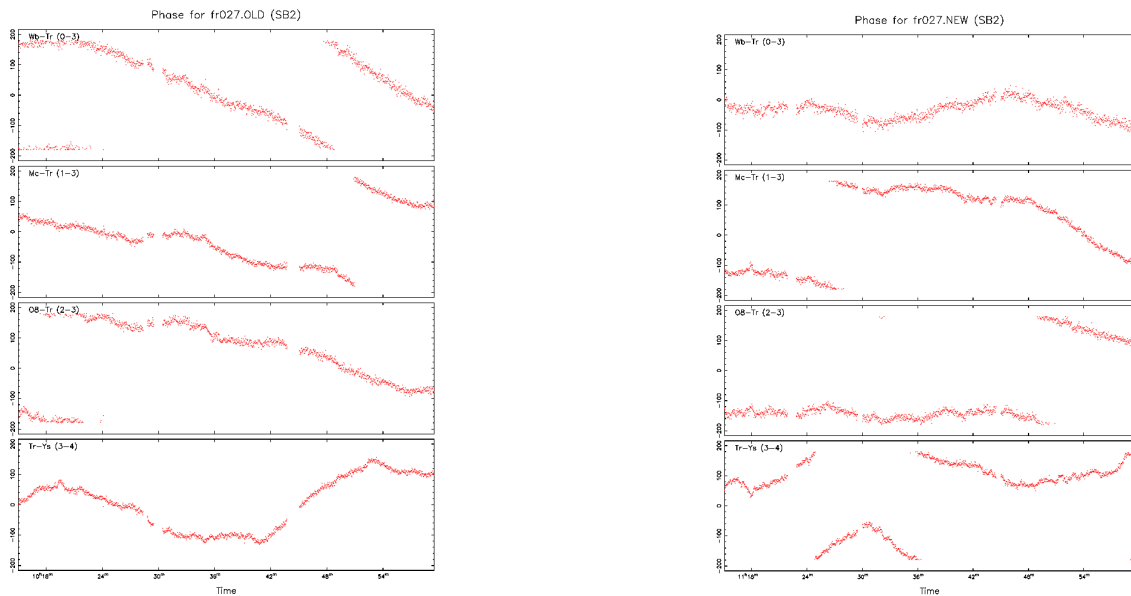


Fig. 3. Interferometer phase residual in respect to the correlator model (sub-band 2). The x-axis is time of observation, and the y-axis is phase (in degrees) vector-averaged over the middle 80% of the band, with separate points for each individual two-second integration. Left column shows the period when synchronization was based on local H-maser, right is for remote synchronization.

V. CONCLUSION

We demonstrated, probably for the first time, the operational solution for remote synchronization of VLBI observations by means of delivery of signals provided by the dedicated UTC(k) laboratory via stabilized fiber-optic link. This paves the way for investigation of new methods of T&F synchronization in radio astronomy.

REFERENCES

- [1] A. Binczewski et al. "OPTIME - the system grows - a new 330 km line", Proceedings of 2015 joint conference of the IEEE international Frequency Control Symposium & the European frequency and time forum, 2015.
- [2] P. Krehlik et al., "Ultrastable long-distance fibre-optic time transfer: active compensation over a wide range of delays," Metrologia, 2015.
- [3] P. Morzyński et al. "Absolute measurement of the $1S_0 - 3P_0$ clock transition in neutral ^{88}Sr over the 330 km-long stabilized fibre opticlink", Scientific Reports, 2015.

The optical ^{88}Sr lattice clocks and stabilized fibre links: a frequency reference for the VLBI system over a 15.5-km link and an absolute measurement of the clock transition over a 330-km link

P. Morzyński*, M. Bober*, P. Krehlik[†], Ł. Śliwczyński[†], M. Lipiński[†], E. Pazderski[‡], A. Marecki[‡], J. Nawrocki[§], P. Ablewski*, B. Campbell[¶], P. Masłowski*, A. Cygan*, P. Nogaś[§], D. Lisak*, R. Ciuryło* and M. Zawada*

Email: zawada@fizyka.umk.pl

* Institute of Physics, Faculty of Physics, Astronomy and Informatics, Nicolaus Copernicus University, Grudziądzka 5, PL-87-100 Toruń, Poland

[†] Department of Electronics, AGH University of Science and Technology, al. Mickiewicza 30, PL-30-059, Kraków, Poland

[‡] Centre for Astronomy, Faculty of Physics, Astronomy and Informatics, Nicolaus Copernicus University, Grudziądzka 5, PL-87-100 Toruń, Poland

[§] Time and Frequency Department, Astrogeodynamic Observatory of Space Research Center, Borowiec, Drapałka 4, PL-62-035 Kórnik, Poland

[¶] Joint Institute for VLBI ERIC, Oude Hoogeveensedijk 4, 7991 PD Dwingeloo, The Netherlands

Abstract—We report a system of two independent strontium optical lattice standards with ^{88}Sr probed with a single shared ultra-narrow laser. We achieved frequency stability (frequency between two standards) of 7×10^{-17} . The absolute frequency of the clock transition can be measured by the use of an optical frequency comb referenced to the UTC(AOS) and UTC(PL) via the 330-km stabilized fibre optic link of the OPTIME network. The 15.5-km stabilized fibre optic link between National Laboratory for Atomic, Molecular, and Optical Physics (KL FAMO) and Toruń Centre for Astronomy made it possible to use the optical clocks as a frequency reference for the 32-metre precise parabolic antenna of the radio telescope in the Toruń Centre for Astronomy participating in the VLBI networks. We report the world's first astronomical VLBI measurements referenced to an optical atomic clock.

Keywords—optical lattice atomic clocks, VLBI, fibre-optic networking

I. INTRODUCTION

Most of the present realizations of the optical lattice clocks are made with fermionic strontium isotope ^{87}Sr [1]–[5]. The bosonic isotopes are expected to have larger collisional effects on the clock transition. Additionally, the bosonic isotopes require at least one extra field to induce the clock transition, which implies careful control of this field and its respective field shift. On the other hand, the bosonic lattice clocks have some advantages over their fermionic counterpart: no first order Zeeman shift, no vector or tensor lattice Stark shifts and much higher isotopic abundance. Lack of hyperfine structures in both 1S_0 and 3P_0 states and higher abundance reduce the time required for one lock cycle. Furthermore, the set-up of cooling and trapping the bosonic isotope is simpler, which is important for transportable systems.

We report a system of two independent bosonic strontium optical lattice standards with ^{88}Sr probed with a single shared ultra-narrow laser [6]. The absolute frequency of the clock transition [7] is measured by the use of a frequency-doubled Er:fibre polarization-mode-locked optical frequency comb referenced to the UTC(AOS) and UTC(PL) [8], [9] via the 330-km-long stabilized fibre optic link of the OPTIME network [10], [11]. The 15.5-km stabilized fibre optic link between the KL FAMO and Toruń Centre for Astronomy enabled us to perform the world's first astronomical VLBI measurements referenced to an optical atomic clock.

II. OPTICAL LATTICE STANDARDS

Two optical frequency standards (Sr1 and Sr2) are based on the $^1S_0 - ^3P_0$ transition in neutral ^{88}Sr atoms. Two clouds of cold atoms in Sr1 and Sr2, trapped in the vertical optical lattices, are independently probed by an ultra-stable laser with spectral width below 1 Hz. The laser beam is split into two optical paths. The frequencies of both beams are independently digitally locked to the narrow atomic resonances in each standard by feedback to the acousto-optic frequency shifters.

The frequencies of the clock transitions can be compared by the use of an optical frequency comb with the UTC(AOS). The 330-km-long time and frequency dissemination line between the Space Research Centre at Borowiec Astrogeodynamic Observatory (AOS) and KL FAMO in Toruń is electronically stabilized with the ELSTAB technology [12]. The underlying idea of the ELSTAB solution is to implement the compensation of the fibre delay fluctuations in the electronic domain, by using a pair of precisely matched variable delay lines. The delay lines are both placed in the forward and backward paths of the delay-locked-loop (DLL) structure.

The local module is installed at the AOS in Borowiec and the remote module is installed at the KL FAMO in Toruń. Additionally, the line contains seven specialized optical bidirectional amplifiers based on erbium-doped fibres. Thanks to bidirectional operation over the same optical path for the forward and backward directions, the propagation delay is constant for both directions. Consequently, the possible phase fluctuations compensate and the insertion of the amplifier does not destroy the symmetry of the optical path.

To estimate the quality of the link, the pre-installation tests with a 300-km fibre on spools and bidirectional optical amplifiers were performed. The stability of the remote 10 MHz signal was measured with respect to the local input, using the A7-MX Signal Stability Analyser. The overlapping Allan deviation is equal to 4×10^{-13} for 1 s integration period, and drops down to 3×10^{-16} within 1 h (Fig. 1).

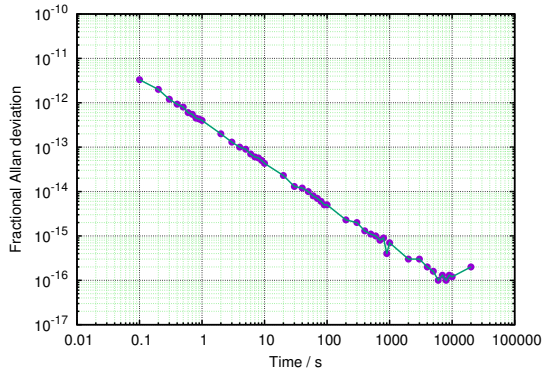


Fig. 1. The quality of the fibre link. Frequency transfer stability obtained during the pre-installation test of the ELSTAB system in fractional units represented by the Allan standard deviation.

The local representation of the Coordinated Universal Time at AOS in Borowiec, UTC(AOS), is realized directly in the form of a 1 PPS by a system of an active H-maser and an offset generator (AOG). The AOG compensates the linear frequency drift of the maser on a daily basis and adds corrections in respect to the UTC, extrapolated from differences UTC- UTC(AOS) and UTCr-UTC(AOS) published monthly and weekly, respectively, in Circular-T [13].

The difference between the corrections of the digital locks in the Sr1 and Sr2 standards yields the momentary frequency difference between the two clocks. The measured frequency stability in fractional units represented by the Allan standard deviation is presented in Fig. 2 which two standards operating synchronously and asynchronously (red and green lines, respectively). The short-time stability of the standards, up to 100 s of averaging, is limited by the quality of the ultrastable laser. The synchronous operation is mostly free from ultrastable laser fluctuations, except of small residual caused by independent setting of digital locks in the two standards. The measured stability of the synchronously operated clocks, with a clock cycle time of 1.32 s and interrogation time of 40 ms, reached 7×10^{-17} after 10000 s of averaging. The two fundamental limitations of the optical clock stability, i.e. the quantum projection noise (QPN) limit [14] for $N = 32000$ atoms of an individual clock and the Dick effect limit [15], [16], derived from the power spectral density of the ultrastable

clock laser and the clock cycle time, are also depicted in Fig. 2.

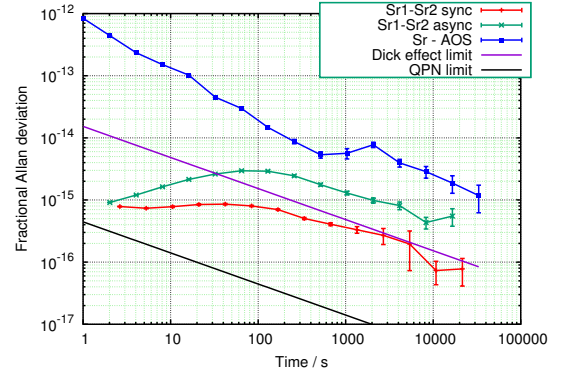


Fig. 2. The measured frequency stability. The frequency difference of the two synchronously and asynchronously operated two optical lattice standards (red and green lines, respectively) and between Sr1 system and the UTC(AOS) (blue line) in fractional units represented by the Allan standard deviation. The comparison between Sr1 and UTC(AOS) was made over the dedicated 330-km stabilized fibre optic link. The two fundamental limitations of the optical clock stability, i.e. the quantum projection noise (QPN) limit, which is $\sqrt{2}$ times the QPN limit for $N = 32000$ atoms of an individual clock, and the Dick effect limit, derived from the power spectral density of the ultrastable clock laser for a clock cycle time of 1.32 s, are depicted by black and violet lines, respectively.

We have evaluated the main contributions to the frequency shifts in both Sr1 and Sr2 standards. The accuracy budgets are compared in Table I for typical experimental conditions: applied B-fields inducing clock transition equal to 2.725 and 2.383 mT, clock laser intensities equal to 207 and 488 mW/cm² and resultant Rabi frequencies [17] equal to 7.4 and 9.7 Hz for Sr1 and Sr2, respectively. Most of the systematic contributions presented there were evaluated by making a series of several simultaneous (interlaced) locks to the atomic line with different values of particular physical parameter in one of the standard, with the other standard serving as a stable reference. Examples of such evaluations are presented in Fig. 3. The notable exceptions were the blackbody radiation (BBR) shift, gravitational red shift and post-processed corrections between UTC(AOS), UTC and TT (the SI second on the geoid).

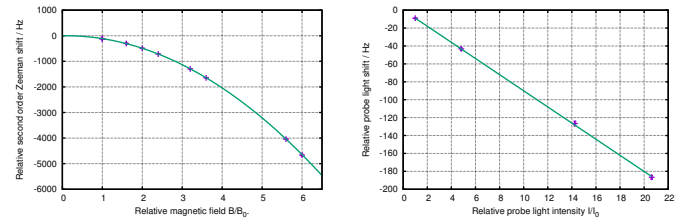


Fig. 3. Examples of evaluations of systematic shifts. Left panel: evaluation of the quadratic Zeeman shift in Sr2. The second order Zeeman correction depends on the absolute value of the magnetic field, therefore similar measurements are made in all three directions. $B_0 = 2.383$ mT corresponds to the applied B-field inducing clock transition at standard operating conditions. Right panel: evaluation of the probe light shift in Sr2. $I_0 = 488$ mW/cm² corresponds to the clock laser intensity at standard operating conditions.

The described procedure yielded the absolute frequency of the $^1S_0 - ^3P_0$ clock transition in bosonic ^{88}Sr equal to $429\,228\,066\,418\,008.3(1.9)_{\text{sys}}(0.9)_{\text{stat}}$ Hz for Sr1 and

TABLE I. ACCURACY BUDGET FOR TYPICAL EXPERIMENTAL CONDITIONS USED IN THE MEASUREMENT OF THE ABSOLUTE FREQUENCY. ALL NUMBERS ARE IN HERTZ.

Effects	Shift(Uncert.)	
	Sr1	Sr2
Quadratic Zeeman	-151.9(1.7)	-115.42(2.7)
Probe light	-3.82(0.35)	-9.02(0.37)
Lattice light	-0.34(0.47)	-1.55(0.48)
Collisions	0.35(0.52)	0.33(0.46)
Blackbody radiation	-2.210(0.075)	-2.405(0.075)
Grav. red shift	2.34(0.10)	2.34(0.10)
UTC(AOS) – UTC	-0.40(0.43)	-0.40(0.43)
UTC – TT	0.10(0.11)	0.10(0.11)
DDS & electronics	0.00(0.16)	0.00(0.12)
Total:	-155.9(1.9)	-126.0(2.8)

429 228 066 418 007.3(2.8)_{syst}(0.9)_{stat} Hz for Sr2. Fig 4 documents the measurement record of both Sr1 and Sr2 standards, binned at 100 s and histograms of the frequency measurements, plotted with an offset frequency $\nu_{BIPM}=429\,228\,066\,418\,012$ Hz, i.e the BIPM recommended value [18].

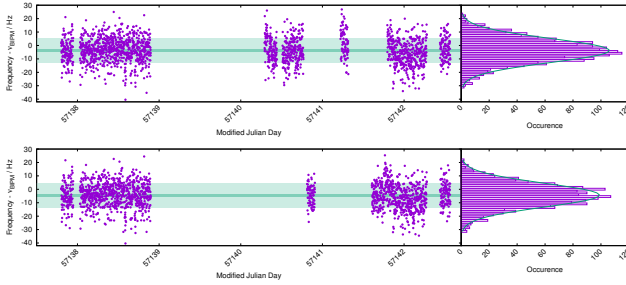


Fig. 4. Frequencies of the $^1S_0 - ^3P_0$ clock transition in bosonic ^{88}Sr recorded in Sr1 and Sr2 at the indicated MJD (top and bottom panels, respectively). In the left panels each solid circle represent 100 s of averaged data, the light and dark-green regions represent 1σ standard deviation and standard deviation of the mean, respectively. The offset frequency ν_{BIPM} is the BIPM recommended frequency value [18]. The right panels show a histogram of the frequency measurements with fitted Gaussian function.

III. VLBI TEST MEASUREMENT

The bright, compact radio calibrator source 0234+285 was observed at a frequency of 5 GHz in the test period preceding the European VLBI Network real-time e-VLBI session on 15 March 2016. Ten VLBI stations participated in the observation (Effelsberg (DE), Jodrell Bank (UK), Medicina (IT), Noto (IT), Onsala (SE), Toruń (PL), Yebes (ES), Westerbork (NL), Hartebeesthoek (ZA), Tianma (CN)).

The station at Toruń was referenced to the Sr1 optical clock over the system of optical frequency clock and 15.5-km-long ELSTAB fibre link. The optical frequency comb was locked to the 689 nm light from the Sr1. Repetition frequency of the comb was used to produce the 10 MHz signal by a Direct Digital Synthesizer (DDS) (see Fig. 5). The 10 MHz signal was subsequently transmitted to Toruń Centre of Astronomy over the fibre link.

Fig. 6 presents residual interferometer phase on baselines formed among the telescopes Effelsberg, Medicina, Toruń, and Yebes. The correlator model includes standard geometric, geophysical, and relativistic terms, plus a linear a priori clock model per telescope. Three 15-min scans were made with Toruń station referenced to the Sr1 optical lattice clock and, for

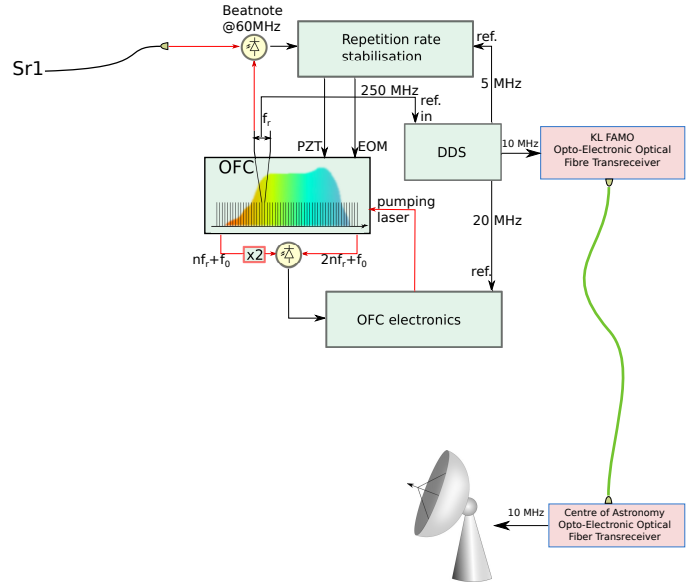


Fig. 5. The optical frequency comb locked to the 689 nm light from the Sr1 optical lattice clock. The 10 MHz signal is produced by a Direct Digital Synthesizer (DDS) referenced to the repetition frequency of the comb. The 10 MHz signal is subsequently transmitted to Toruń Centre of Astronomy over the fibre link.

comparison, two 15-min scans were made with Toruń station referenced to the hydrogen maser.

The phase noise in baselines to Toruń is comparable in both time-ranges, suggesting that the optical lattice clock can serve as the operational time/frequency reference for VLBI stations. The phase noise present in these preliminary results is likely dominated by propagation effects through the troposphere and by the electrical paths through the telescopes' receiver + IF + back-end chains.

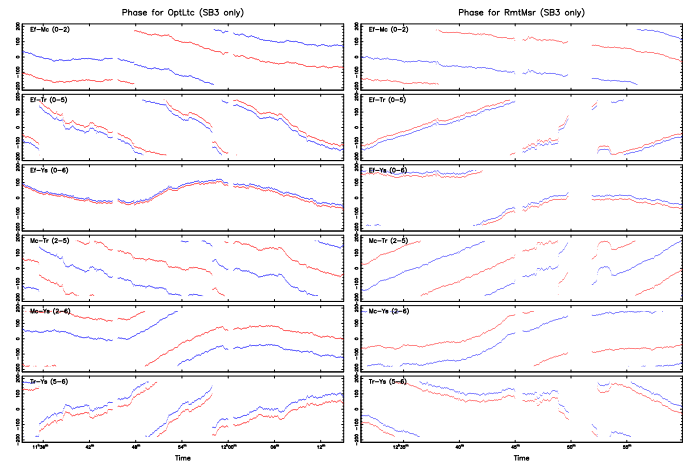


Fig. 6. Plots of phase(t): in the left panel Toruń (Tr) station is referenced to the Sr1 optical lattice clock, while in right panel Tr station is referenced to a hydrogen maser. Ef, Mc, Ye denote Effelsberg, Medicina and Yebes stations, respectively. Only one of the eight 16-MHz subbands is shown, for clarity in being able to follow the phase fluctuations. The two hands of circular polarization are color-coded: red and blue correspond to RCP and LCP, respectively.

IV. CONCLUSION

We have performed a series of measurements of the absolute frequency of the $^1S_0 - ^3P_0$ transition in neutral ^{88}Sr . The measurements have been made in two independent optical lattice clocks with an optical frequency comb referenced to the UTC(AOS) by a long-distance stabilized fibre optic link. Presented results agree with the recommendation of BIPM and should improve the accuracy of future recommendation.

We also performed the world's first astronomical VLBI observations referenced to an optical atomic clock. Preliminary results give every confidence that such time/frequency control in an operational VLBI setting would be successful, and in turn would enable applications that would benefit from the reduced Allan variance.

ACKNOWLEDGMENT

Part of work focused on optical atomic clocks has been performed in the National Laboratory FAMO in Toruń and supported by the subsidy of the Ministry of Science and Higher Education. The European VLBI Network is a joint facility of independent European, African, Asian, and North American radio astronomy institutes. Individual contributors were partially supported by the Polish National Science Centre Projects No. 2012/07/B/ST2/00235 and DEC-2012/05/D/ST2/01914. The fibre optic link development and installation was supported by the Polish National Centre for Research and Development under the decision PBS1/A3/13/2012.

REFERENCES

- [1] B.J. Bloom *et al.* An optical lattice clock with accuracy and stability at the 10^{-18} level *Nature* **506** 71-75 (2014)
- [2] R. Le Targat *et al.* Experimental realization of an optical second with strontium lattice clocks *Nature Commun.* **4** 2109 (2013)
- [3] N. Hinkley *et al.* An atomic clock with 10^{-18} instability *Science* **341** 1215-8 (2013)
- [4] S. Falke *et al.* A strontium lattice clock with 3×10^{-17} inaccuracy and its frequency *New J. Phys.* **16** 073023 (2014)
- [5] I. Ushijima, M. Takamoto, M. Das, T. Ohkubo & H. Katori, Cryogenic optical lattice clocks *Nature Photon.* **9** 185-189 (2015)
- [6] M. Bober *et al.* Strontium optical lattice clocks for practical realization of the metre and secondary representation of the second *Meas. Sci. Technol.* **26** 075201 (2015)
- [7] P. Morzyński *et al.* Absolute measurement of the $^1S_0 - ^3P_0$ clock transition in neutral ^{88}Sr over the 330-km-long stabilized fibre optic link *Sci. Rep.* **5** 17495 (2015)
- [8] J. Azoubib, J. Nawrocki & W. Lewandowski, Independent atomic timescale in Poland - organization and results *Metrologia* **40** S245 (2003)
- [9] Z. Jiang, A. Czubla, J. Nawrocki, W. Lewandowski & E.F. Arias, Comparing a GPS time link calibration with an optical fibre self-calibration with 200 ps accuracy *Metrologia* **52** 384 (2015)
- [10] Ł. Śliwczynski, P. Krehlik, A. Czubla, Ł. Buczek & M. Lipiński, Dissemination of time and RF frequency via a stabilized fibre optic link over a distance of 420 km *Metrologia* **50** 133-145 (2013)
- [11] P. Krehlik, Ł. Śliwczynski, Ł. Buczek, J. Kołodziej & M. Lipiński, Ultrastable long-distance fibre-optic time transfer: active compensation over a wide range of delays *Metrologia* **52** 82 (2015)
- [12] Ł. Śliwczynski, P. Krehlik, Ł. Buczek & M. Lipiński, Active propagation delay stabilization for fiber optic frequency distribution using controlled electronic delay lines *IEEE Trans. Instrum. Meas.* **60** 1480 (2011)
- [13] BIPM Circular T, Available at <http://www.bipm.org/jsp/en/TimeFtp.jsp>
- [14] G. Santarelli *et al.* Quantum Projection Noise in an Atomic Fountain: A High Stability Cesium Frequency Standard *Phys. Rev. Lett.* **82** 4619 (1999)
- [15] G. Dick, Local oscillator induced instabilities in trapped ion frequency standards *Proc. Precise Time and Time Interval, Redondo Beach, CA*, 133 (1987)
- [16] G. Santarelli *et al.* Frequency stability degradation of an oscillator slaved to a periodically interrogated atomic resonator *IEEE Trans. Ultrason. Ferroelectr. Freq. Control* **45** 887 (1998)
- [17] A. V. Taichenachev *et al.* Magnetic field-induced spectroscopy of forbidden optical transitions with application to lattice-based optical atomic clocks *Phys. Rev. Lett.* **96** 083001 (2006).
- [18] Bureau International des Poids et Mesures (BIPM) *Recommended Values Of Standard Frequencies For Applications Including The Practical Realization Of The Metre And Secondary Representations Of The Definition Of The Second, Strontium 88 Atom ($f \approx 429 \text{ THz}$)*, (BIPM, Sèvres, France, 2009)

Elimination of Spurious Modes in Zinc Oxide Micro-Resonators by Optimizing Structure Parameters

Mortada Ossama, Chatras Matthieu, Zahr Abdel Halim, Blondy Pierre, Crunteanu Aurelian, Micro and Nanotechnologies for optoelectronic and microwave components (MINACOM) department XLIM UMR 7252, University of Limoges/ CNRS 87060 Limoges Cedex, FRANCE
ossama.mortada@xlim.fr

Jean-Christophe Orlianges
SPCTS UMR 7513, University of Limoges/CNRS
87068 Limoges Cedex, FRANCE
jean-christophe.orlianges@unilim.fr

Abstract— The design, simulation, fabrication and test results of micro-resonators integrating piezoelectric zinc oxide (ZnO) layers are reported in this paper. Interdigitated electrodes are used to excite the thin piezoelectric layer. These micro-resonators are built on top of 2 μm silicon membranes of SOI wafers. To improve the quality factor Q and the electromechanical coupling coefficient k_t^2 of the proposed devices different numbers and different lengths of inter-digitated (IDTs) electrodes have been tested.

Keywords— Piezoelectric micro-resonators, ZnO, quality factor, electromechanical coupling coefficient, IDTs electrodes.

I. INTRODUCTION

Microelectromechanical system (MEMS) resonators have emerged as a promising alternative to quartz-crystal [1], SAW [2] and BAW [3][4] resonators or sensors [5]. They are more compact, can be co-integrated with CMOS circuits, can be used for RF communication system so they are the best candidate for the implementation into multi-frequency banks of high-quality-factor. They are attended for the fabrication of next-generation reconfigurable local oscillators and filters for RF transceivers.

Here, a novel piezo-acoustic device based on suspended piezoelectric micro-resonators is presented. The optimization of such devices allows reaching high quality factor Q [6][7] and high electromechanical coupling coefficient k_t^2 [8]. These two parameters are very important because the adoption of piezoelectric micro-resonators for oscillators or filters depends mainly on their ability to achieve a high figure of merit (FoM) which is directly associated with its quality factor (Q) and electromechanical coupling (k_t^2) [9].

In this paper, a detailed study has been realized on micro-resonators topology, in order to identify the optimum geometrical parameters (especially the length, the number of IDTs electrodes) affecting the micro-resonators performances.

II. MICRO-RESONATORS FABRICATION

Fig. 1 shows a cross-section of the proposed micro-resonator. It is made with metal IDTs electrodes acoustically coupled to a suspended composite ZnO/Si structure.

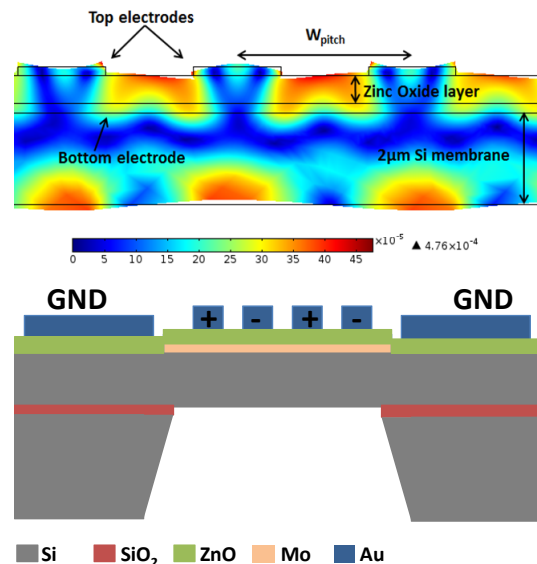


Fig. 1. Cross section representation of the displacement of an acoustic wave in ZnO and Si membrane layers. The figure shows only few of the IDTs finger electrodes as representatives of the overall device behavior.

Different IDTs lengths, as well as different numbers of IDTs electrodes We intend to investigate the influence of changing the length and electrode number of IDTs on the quality factor Q and the electromechanical coupling coefficient k_t^2 while comparing the measured responses of micro-resonators to the electric model MBVD (Modified Butterworth Van Dyke) of the devices

The proposed resonators are fabricated using a simple 3-masks process, as illustrated in Fig. 2, with 6 steps.

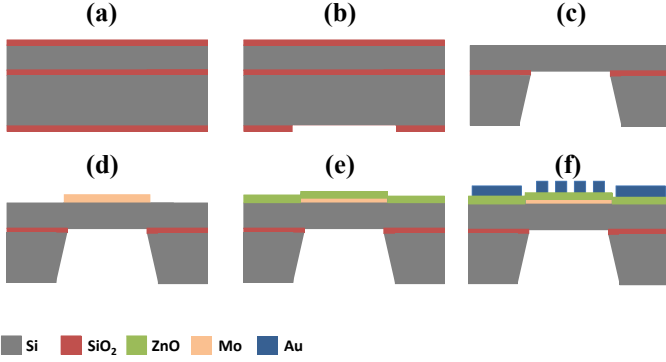


Fig. 2. Flow chart of the fabrication process: (a) used SOI wafers; (b) Back-side etching. A photolithography is carried to expose silicon areas on the back-side and SiO_2 is etched using buffered hydrofluoric acid (BHF); (c) 450- μm deep etching of silicon using Tetra Methylamine Hydroxide at 85°C. Etching is completed when the 2- μm thick Si membrane is released and suspended on the silicon substrate; (d) 200-nm thick molybdenum (Mo) layer is DC sputtered on the wafer at 300°C. The bottom Mo electrode is then patterned; (e) Deposition of ZnO film layer by Pulsed Laser Deposition; (f) Inter-digitated electrodes (200-nm thick Au/Ti) are deposited and lifted off.

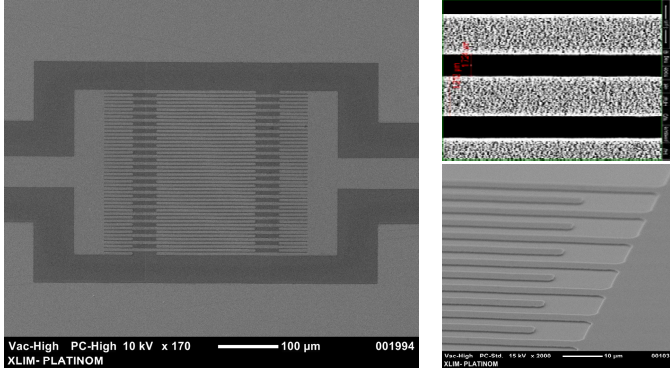


Fig. 3. SEM pictures of the fabricated micro-resonators. The overall dimensions of the fabricated device are approximately 250 μm x 300 μm .

III. DEVICE MEASUREMENTS

The fabricated prototypes have been tested using a Vector Network Analyzer and a Cascade probe station.

A theoretical study of [S] parameters was performed using the equivalent electrical model MBVD to extract the values of the electrical model components describing these micro-resonators and calculate the quality factor Q of each micro-resonator dimensions. Fig.4 shows one comparison between the measured S_{21} parameters and the corresponding MBVD model. We can notice a very good agreement.

First, by comparing micro-resonators having the same IDTs number ($n = 25$ IDTs for example), we have noticed that decreasing IDTs length increases the quality factor, from 416 (for the 50λ IDTs length) to 730 (for the 25λ IDTs length).

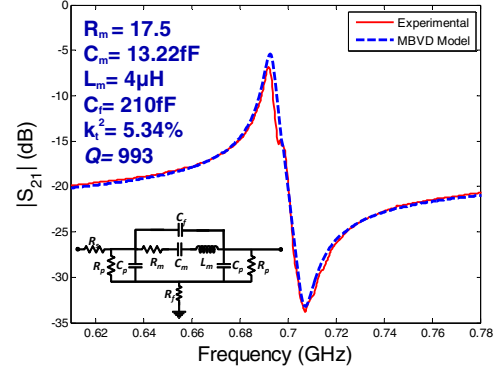


Fig. 4. Comparison between the measured S_{21} parameters and the corresponding MBVD model with parameters extraction for a fabricated micro-resonator ($n=40$ & $L=50\lambda$).

Second, for a fixed IDTs length $L=25\lambda$, the quality factor increases from 730 (for $n = 25$ IDTs) up to 1180 (for $n=40$ IDTs) then down to 612 and to 590 for $n=50$ and $n=80$ respectively. We can notice a high peak quality factor when $n=40$ IDTs. This behavior is repeated for the other three lengths $L = 35\lambda$, 42λ and 50λ . So, experimental results show that Q improves drastically when $n=40$ and the length $L=25\lambda$.

Looking at [S] parameters of the measured circuit in fig.5, we noted the presence of spurious modes in close proximity of the main mechanical resonance of certain micro-resonators: micro-resonators having a large number of IDTs electrodes have a plurality of resonance modes which are mixed together at the main mechanical resonance so that the resonance peak becomes less selective and less "clean" which corresponds to a low Q . So, spurious modes appear and multiple when the number of IDTs is increasing. It is due to reflected acoustic waves in the system, especially when the membrane is so large and comport a high number of IDTs.

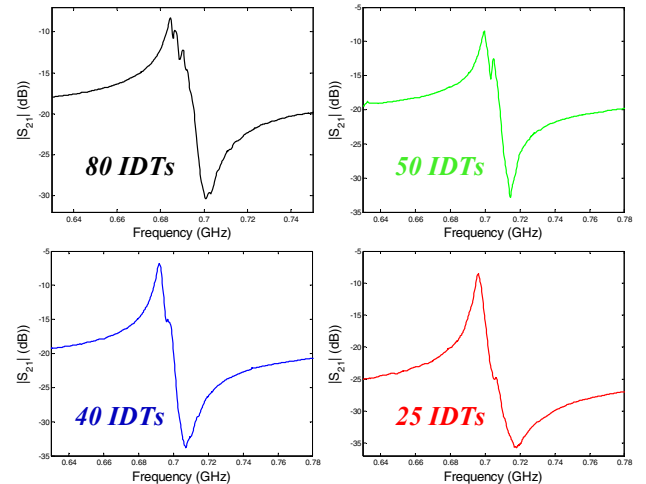


Fig. 5. Measured transmission response of fabricated ZnO micro-resonators operating at 700MHz with four different IDTs number.

IV. CONCLUSION

Design, fabrication and testing of piezoelectric ZnO micro-resonator operating around 700MHz have been demonstrated. A study on the effect of the number and length of IDTs electrodes has been proposed in order to efficiently suppress the spurious modes associated with the large number of IDTs electrodes which are in close proximity of the main mechanical resonance, in order to increase quality factor of the devices.

Future work will focus on increasing the frequency of operation of the micro-resonators towards GHz frequencies domain.

REFERENCES

- [1] A. Asakura, T. Fukuda and F. Arai, "Design, fabrication and characterization of compact force sensor using AT-cut quartz crystal resonators," *Intelligent Robots and Systems, 2008. IROS 2008. IEEE/RSJ International Conference on*, Nice, 2008, pp. 506-511.
- [2] X. Lu, K. Mouthaan and Y. T. Soon, "Wideband Bandpass Filters With SAW-Filter-Like Selectivity Using Chip SAW Resonators," in *IEEE Transactions on Microwave Theory and Techniques*, vol. 62, no. 1, pp. 28-36, Jan. 2014.
- [3] Catherinot, L., Giraud, S., Chatras, M., Bila, S., Cros, D., Baron, T., Ballandras, S., Estagerie, L. and Monfraix, P. (2011), A general procedure for the design of bulk acoustic wave filters. *Int J RF and Microwave Comp Aid Eng*, 21: 458–465.
- [4] S. Giraud, S. Bila, M. Chatras, D. Cros and M. Aubourg, "Bulk acoustic wave filters synthesis and optimization for multi-standard communication terminals," in *IEEE Transactions on Ultrasonics, Ferroelectrics, and Frequency Control*, vol. 57, no. 1, pp. 52-58, Jan. 2010.
- [5] T. Baron *et al.*, "A pressure sensor based on a HBAR micromachined structure," *Frequency Control Symposium (FCS), 2010 IEEE International*, Newport Beach, CA, 2010, pp. 361-364.
- [6] O. Mortada, P. Blondy, J. C. Orlianges, M. Chatras and A. Crunteanu, "Quality factor optimization of composite piezoelectric single-crystal silicon MEMS resonators," *Microwave Symposium (IMS), 2015 IEEE MTT-S International*, Phoenix, AZ, 2015, pp. 1-3.
- [7] M. Ossama, B. Pierre, C. Aurelian, C. Matthieu and J. C. Orlianges, "A zinc dioxide-on-silicon MEMS resonator for narrowband filtering," *Electronics, Circuits and Systems (ICECS), 2014 21st IEEE International Conference on*, Marseille, 2014, pp. 586-589.
- [8] L. Khine, J. B. W. Soon and J. M. Tsai, "Piezoelectric ALN MEMS resonators with high coupling coefficient," *Solid-State Sensors, Actuators and Microsystems Conference (TRANSDUCERS), 2011 16th International*, Beijing, 2011, pp. 526-529.
- [9] W. P. Mason, *Piezoelectric Crystals and Their Application to Ultrasonics*. New York, NY, USA: Van Nostrand, 1950.

Searching for Dark Matter with Atomic Clocks and Laser Interferometry

Yevgeny Stadnik and Victor Flambaum

School of Physics, University of New South Wales, Sydney 2052, Australia

Abstract—We propose new schemes for the direct detection of low-mass dark matter with atomic clock and laser interferometry experiments. Dark matter, which consists of low-mass bosons, can readily form an oscillating classical field that survives to reside in the observed galactic dark matter haloes if these particles have sufficiently low mass and are sufficiently feebly interacting. We have recently shown that the interaction of an oscillating classical dark matter field ϕ with Standard Model fields via quadratic-in- ϕ couplings produces both a ‘slow’ cosmological evolution and oscillating variations in the fundamental constants. Oscillating variations in the fundamental constants produce oscillating shifts in the transition frequencies of atomic clocks and other related systems, which can be used as high-precision probes to search for dark matter. Using recent atomic dysprosium spectroscopy data, we have derived limits on the quadratic interaction of ϕ with the photon that improve on existing constraints by up to 15 orders of magnitude. We have also proposed the use of laser and maser interferometry, in which a photon wavelength is compared with the interferometer arm length, as a novel high-precision platform to search for dark matter, with effects due to the variation of the electromagnetic fine-structure constant on alterations in the accumulated phase enhanced by up to 13 orders of magnitude.

I. INTRODUCTION

There is strong astrophysical evidence for the existence of dark matter (DM) through its attractive gravitational effects on Standard Model (SM) matter, see, e.g., Ref. [1] and the references therein. Indeed, astrophysical observations indicate that there is ~ 5 times more DM in the Universe than SM matter. Extensive laboratory searches for weakly interacting massive particle (WIMP) DM through scattering-off-nuclei experiments have failed to produce a strong positive result to date, which motivates searches for alternative forms of DM.

New low-mass spin-0 particles are a well-motivated candidate for the observed DM. Such particles can be produced efficiently via non-thermal production mechanisms in the early Universe (e.g., through vacuum decay [2], [3], [4]), and form a coherently oscillating classical field:

$$\phi = \phi_0 \cos(\omega t), \quad (1)$$

which oscillates with angular frequency $\omega \simeq m_\phi c^2/\hbar$, where m_ϕ is the mass of the DM particle, c is the speed of light and \hbar is the reduced Planck constant. Hereafter, we will use the units $\hbar = c = 1$, with $1 \text{ eV} = 2.4 \times 10^{14} \text{ Hz}$. The energy density carried by the field (1) is given by:

$$\rho_\phi \simeq \frac{m_\phi^2 \phi_0^2}{2}. \quad (2)$$

Although low-mass bosonic DM particles are typically produced with negligible kinetic energy, the gravitational

interactions between DM and SM particles during galactic structure formation subsequently virialise these DM particles ($v_{\text{vir}}^{\text{local}} \sim 10^{-3}c$), which gives an oscillating galactic DM field the finite coherence time:

$$\tau_{\text{coh}} \sim \frac{2\pi}{m_\phi v_{\text{vir}}^2} \sim 10^6 \left(\frac{2\pi}{m_\phi} \right), \quad (3)$$

which can be equivalently expressed in terms of the relative spread in the angular frequency of oscillation: $\Delta\omega/\omega \sim 10^{-6}$.

An upper limit on the mass of generic spin-0 particles, which saturate the observed cold DM content and form an oscillating classical field, is set by the requirement that there are a large number of such particles within the reduced de Broglie volume (i.e., $n_\phi (\lambda_{\text{dB}}/2\pi)^3 \gg 1$): $m_\phi \lesssim 0.1 \text{ eV}$. A lower limit on the mass of generic spin-0 particles, which saturate the observed cold DM content, comes from the requirement that the de Broglie wavelength of these particles not exceed the halo size of the smallest dwarf galaxies ($R \sim 1 \text{ kpc}$): $m_\phi \gtrsim 10^{-22} \text{ eV}$. Due to its effects on structure formation, ultra-low-mass spin-0 DM in the mass range $10^{-24} \text{ eV} \lesssim m_\phi \lesssim 10^{-20} \text{ eV}$ has been proposed to resolve several long-standing astrophysical puzzles, such as the cusp-core, missing satellite, and too-big-to-fail problems.

Spurred on by the tremendous recent advances in atomic clock technology [5], [6], there has been significant recent interest in using atomic clocks and related devices to search for the oscillating signatures produced by ultra-low-mass scalar DM fields [7], [8], [9], [10], [11]. The attractive features of searching for DM with such devices is their extremely high precision and their complementarity to traditional scattering-off-nuclei and collider-based searches for DM, which by contrast are insensitive to ultra-low-mass DM. Indeed, large regions of the mass range $10^{-24} \text{ eV} \lesssim m_\phi \lesssim 0.1 \text{ eV}$ (corresponding to the frequency range $10^{-10} \text{ Hz} \lesssim f \lesssim 10^{13} \text{ Hz}$) are already accessible with existing atomic clock and laser interferometry technologies.

II. THEORY

The relevant quadratic couplings of a scalar field ϕ to the SM fields are the following:

$$\begin{aligned} \mathcal{L}_{\text{int}} = & + \frac{\phi^2}{(\Lambda'_\gamma)^2} \frac{F_{\mu\nu} F^{\mu\nu}}{4} - \sum_f \frac{\phi^2}{(\Lambda'_f)^2} m_f \bar{f} f \\ & + \sum_V \frac{\phi^2}{(\Lambda'_V)^2} \frac{M_V^2}{2} V_\nu V^\nu. \end{aligned} \quad (4)$$

The first term represents the coupling of the scalar field to the SM fermion fields f , with m_f being the standard mass of the fermion and $\bar{f} = f^\dagger \gamma^0$. The second term represents the coupling of the scalar field to the electromagnetic field tensor F . The third term represents the coupling of the scalar field to the SM massive vector bosons V , with M_V being the standard mass of the boson.

Supernova energy-loss bound arguments applied to the photon pair-annihilation channel $\gamma + \gamma \rightarrow \phi + \phi$ and nucleon bremsstrahlung channel $N + N \rightarrow N + N + \phi + \phi$ constrain the interaction parameters that appear in Eq. (4) to be [12]: $\Lambda'_\gamma \gtrsim 3 \times 10^3$ GeV and $\Lambda'_p \gtrsim 1.5 \times 10^4$ GeV, respectively, for $m_\phi \lesssim 30$ MeV. There also weaker limits from fifth-force experimental searches [12].

Comparing the terms in Eq. (4) with the relevant terms in the SM Lagrangian:

$$\mathcal{L}_{\text{SM}} = -\frac{F_{\mu\nu}F^{\mu\nu}}{4} - \sum_f m_f \bar{f}f + \sum_V \frac{M_V^2}{2} V_\nu V^\nu, \quad (5)$$

we see that the SM particle masses are altered as follows:

$$m_f \rightarrow m_f \left[1 + \frac{\phi^2}{(\Lambda'_f)^2} \right], \quad M_V^2 \rightarrow M_V^2 \left[1 + \frac{\phi^2}{(\Lambda'_V)^2} \right]. \quad (6)$$

In order to see the effect of the quadratic coupling of ϕ to the electromagnetic field tensor, it is convenient to write the relevant terms in a different system of units:

$$\mathcal{L} = -\frac{F_{\mu\nu}F^{\mu\nu}}{4e^2} + \frac{\phi^2}{(\Lambda'_\gamma)^2} \frac{F_{\mu\nu}F^{\mu\nu}}{4e^2}, \quad (7)$$

from which we deduce that the electromagnetic fine-structure constant α is altered as follows:

$$\alpha \rightarrow \frac{\alpha}{1 - \phi^2/(\Lambda'_\gamma)^2} \simeq \alpha \left[1 + \frac{\phi^2}{(\Lambda'_\gamma)^2} \right], \quad (8)$$

provided that changes in ϕ are adiabatic.

For a coherently oscillating classical field of the form (1), the variations in the electromagnetic fine-structure constant and particle masses in Eqs. (6) and (8) can be written as:

$$\frac{\delta X}{X} = \frac{\phi_0^2}{2(\Lambda'_X)^2} + \frac{\phi_0^2}{2(\Lambda'_X)^2} \cos(2m_\phi t), \quad (9)$$

which consist of a non-oscillating part (that changes in magnitude if the DM energy density changes) and an oscillating part. The ‘slow’ drifts in the fundamental constants are constrained most stringently from astrophysical phenomena, most notably Big Bang nucleosynthesis (BBN) and cosmic microwave background (CMB) measurements, while the oscillating variations in the fundamental constants can be sought for with high-precision laboratory measurements, including atomic clock and laser interferometry experiments.

III. ASTROPHYSICAL CONSTRAINTS

Comparison of measurements and SM calculations of the primordial ^4He abundance produced during the BBN epoch

in the early Universe constrain the interaction parameters that appear in Eq. (4) for scalar DM as follows [10]:

$$\Lambda'_\gamma \gtrsim \frac{2 \times 10^9 \text{ eV}^2}{m_\phi}, \quad \text{for } m_\phi \gg 10^{-16} \text{ eV}, \quad (10)$$

$$\Lambda'_\gamma \gtrsim \frac{2 \times 10^{21} \text{ eV}^{5/4}}{m_\phi^{1/4}}, \quad \text{for } m_\phi \ll 10^{-16} \text{ eV}, \quad (11)$$

$$\Lambda'_e \gtrsim \frac{3 \times 10^8 \text{ eV}^2}{m_\phi}, \quad \text{for } m_\phi \gg 10^{-16} \text{ eV}, \quad (12)$$

$$\Lambda'_e \gtrsim \frac{2 \times 10^{21} \text{ eV}^{5/4}}{m_\phi^{1/4}}, \quad \text{for } m_\phi \ll 10^{-16} \text{ eV}, \quad (13)$$

$$\tilde{\Lambda}'_q \gtrsim \frac{9 \times 10^9 \text{ eV}^2}{m_\phi}, \quad \text{for } m_\phi \gg 10^{-16} \text{ eV}, \quad (14)$$

$$\tilde{\Lambda}'_q \gtrsim \frac{7 \times 10^{21} \text{ eV}^{5/4}}{m_\phi^{1/4}}, \quad \text{for } m_\phi \ll 10^{-16} \text{ eV}, \quad (15)$$

$$\tilde{\Lambda}'_V \gtrsim \frac{9 \times 10^9 \text{ eV}^2}{m_\phi}, \quad \text{for } m_\phi \gg 10^{-16} \text{ eV}, \quad (16)$$

$$\tilde{\Lambda}'_V \gtrsim \frac{6 \times 10^{21} \text{ eV}^{5/4}}{m_\phi^{1/4}}, \quad \text{for } m_\phi \ll 10^{-16} \text{ eV}, \quad (17)$$

assuming that scalar DM saturates the present-day DM content ($\bar{\rho}_{\text{DM}} = 1.3 \times 10^{-6}$ GeV/cm³ [13]). The light quark and massive vector boson interaction parameters are defined as $(\tilde{\Lambda}'_q)^2 = |(\Lambda'_u)^2(\Lambda'_d)^2(m_d - m_u)/[(\Lambda'_u)^2 m_d - (\Lambda'_d)^2 m_u]|$ and $(\tilde{\Lambda}'_V)^2 = |(\Lambda'_W)^2(\Lambda'_Z)^2/[(\Lambda'_Z)^2 - 1.4(\Lambda'_W)^2]|$. For the interactions of scalar DM with the photon and electron in Eq. (4), there are also weaker limits from CMB measurements [10]. The astrophysical constraints from BBN and CMB measurements are presented in Fig. 1.

IV. ATOMIC CLOCK AND SPECTROSCOPY SEARCHES

Oscillating variations in the fundamental constants produce oscillating shifts in the ratio of two atomic clock transition frequencies. The recent atomic dysprosium spectroscopy measurements of Ref. [9] can be used to constrain the quadratic interaction of scalar DM with the photon in Eq. (4), as shown in Fig. 1, with a peak sensitivity of $\Lambda'_\gamma \gtrsim 3 \times 10^{18}$ GeV for $m_\phi \lesssim 3 \times 10^{-23}$ eV [10], assuming that scalar DM saturates the local cold DM content ($\rho_{\text{CDM}}^{\text{local}} \approx 0.4$ GeV/cm³ [13]). A variety of other spectroscopic systems, including atomic clocks [14], [15], [16], [17], [18], [19], [20], [21], [22], highly-charged ions [23], [24], [25], molecules [26], [27], [28], [29], [30], [31] and nuclear clocks [32] may also be used to search for such oscillating variations in the fundamental constants.

V. LASER INTERFEROMETRY SEARCHES

Instead of comparing two clock transition frequencies, one may instead compare a photon wavelength with an interferometer arm length [8], [11]. In the simplest case, when the frequency of light inside an interferometer is determined by an optical atomic transition frequency and the interferometer

arm length is allowed to vary freely, the accumulated phase in the arm is:

$$\Phi = \frac{\omega L}{c} \propto \left(\frac{e^2}{a_B \hbar} \right) \left(\frac{N a_B}{c} \right) = N \alpha, \quad (18)$$

where the optical atomic transition frequency ω is proportional to the atomic unit of frequency $e^2/a_B \hbar$. In this case, variation of α gives rise to the following phase shift:

$$\delta\Phi \simeq \Phi \frac{\delta\alpha}{\alpha}. \quad (19)$$

The accumulated phase in a single to-and-back passage of the light beam varies from $\Phi \sim 10^7$ in a small-scale tabletop interferometer ($L \sim 0.5$ m) to $\Phi \sim 10^{11}$ in a large-scale gravitational-wave detector ($L \sim 4$ km). Multiple reflections of the light beam inside an interferometer enhance the observable effects due to variation of the fundamental constants by the effective mean number of passages N_{eff} , which varies from $N_{\text{eff}} \sim 10^2$ in a large-scale gravitational-wave detector to $N_{\text{eff}} \sim 10^5$ in a silicon-cavity-based interferometer. Thus, effects due to the variation of the electromagnetic fine-structure constant on alterations in the accumulated phase can be enhanced by up to 13 orders of magnitude.

VI. CONCLUSION

Atomic clocks and laser interferometers offer extremely powerful new platforms to directly search for scalar DM in the laboratory via its induction of oscillating variations in the electromagnetic fine-structure constant and particle masses. Using recent atomic dysprosium spectroscopy data, we have derived limits on the quadratic interaction of scalar DM with the photon that improve on existing constraints by up to 15 orders of magnitude. In laser and maser interferometry searches, in which a photon wavelength is compared with the interferometer arm length, the effects due to the variation of the electromagnetic fine-structure constant (e.g., due to scalar DM) on alterations in the accumulated phase can be enhanced by up to 13 orders of magnitude. Finally, we mention that, apart from clock-based searches for scalar DM, one may also use atomic and related systems to search for pseudoscalar DM via its generation of coherently oscillating spin-dependent effects, such as anomalous spin-precession effects and oscillating electric dipole moments [33], [34], [35], [36], [37], [38], [39].

ACKNOWLEDGEMENT

This work was supported by the Australian Research Council.

REFERENCES

[1] *Particle Dark Matter: Observations, Models and Searches*, edited by G. Bertone, (Cambridge University Press, Cambridge, England, 2010).
[2] J. Preskill, M. B. Wise, F. Wilczek, Phys. Lett. B **120**, 127 (1983).
[3] L. F. Abbott, P. Sikivie, Phys. Lett. B **120**, 133 (1983).
[4] M. Dine, W. Fischler, Phys. Lett. B **120**, 137 (1983).
[5] A. Derevianko, H. Katori, Rev. Mod. Phys. **83**, 331 (2011).
[6] A. D. Ludlow, M. M. Boyd, J. Ye, E. Peik, P. O. Schmidt, Rev. Mod. Phys. **87**, 637 (2015).

[7] A. Arvanitaki, J. Huang, K. Van Tilburg, Phys. Rev. D **91**, 015015 (2015).
[8] Y. V. Stadnik, V. V. Flambaum, Phys. Rev. Lett. **114**, 161301 (2015).
[9] K. Van Tilburg, N. Leefer, L. Bougas, D. Budker, Phys. Rev. Lett. **115**, 011802 (2015).
[10] Y. V. Stadnik, V. V. Flambaum, Phys. Rev. Lett. **115**, 201301 (2015).
[11] Y. V. Stadnik, V. V. Flambaum, arXiv:1511.00447.
[12] K. A. Olive, M. Pospelov, Phys. Rev. D **77**, 043524 (2008).
[13] K. A. Olive *et al.* (Particle Data Group), Chin. Phys. C **38**, 090001 (2014).
[14] V. A. Dzuba, V. V. Flambaum, J. K. Webb, Phys. Rev. Lett. **82**, 888 (1999).
[15] E. J. Angstrom, V. A. Dzuba, V. V. Flambaum, Phys. Rev. A **70**, 014102 (2004).
[16] M. Fischer *et al.*, Phys. Rev. Lett. **92**, 230802 (2004).
[17] V. V. Flambaum, A. F. Tedesco, Phys. Rev. C **73**, 055501 (2006).
[18] T. Rosenband *et al.*, Science **319**, 1808 (2008).
[19] N. Leefer, C. T. M. Weber, A. Cingoz, J. R. Torgerson, D. Budker, Phys. Rev. Lett. **111**, 060801 (2013).
[20] R. M. Godun *et al.*, Phys. Rev. Lett. **113**, 210801 (2014).
[21] N. Huntemann, B. Lipphardt, C. Tamm, V. Gerginov, S. Weyers, E. Peik, Phys. Rev. Lett. **113**, 210802 (2014).
[22] M. Takamoto *et al.*, Comptes Rendus Physique **16**, 489 (2015).
[23] O. Yu. Andreev, L. N. Labzowsky, G. Plunien, G. Soff, Phys. Rev. Lett. **94**, 243002 (2005).
[24] J. C. Berengut, V. A. Dzuba, V. V. Flambaum, Phys. Rev. Lett. **105**, 120801 (2010).
[25] J. C. Berengut, V. A. Dzuba, V. V. Flambaum, A. Ong, Phys. Rev. Lett. **106**, 210802 (2011).
[26] S. Schiller, V. Korobov, Phys. Rev. A **71**, 032505 (2005).
[27] V. V. Flambaum, Phys. Rev. A **73**, 034101 (2006).
[28] E. R. Hudson, H. J. Lewandowski, B. C. Sawyer, J. Ye, Phys. Rev. Lett. **96**, 143004 (2006).
[29] V. V. Flambaum, M. G. Kozlov, Phys. Rev. Lett. **99**, 150801 (2007).
[30] T. Zelevinsky, S. Kotochigova, J. Ye, Phys. Rev. Lett. **100**, 043201 (2008).
[31] D. DeMille, S. Sainis, J. Sage, T. Bergeman, S. Kotochigova, E. Tiesinga, Phys. Rev. Lett. **100**, 043202 (2008).
[32] V. V. Flambaum, Phys. Rev. Lett. **97**, 092502 (2006).
[33] P. W. Graham, S. Rajendran, Phys. Rev. D **84**, 055013 (2011).
[34] V. V. Flambaum, talk presented at the *9th Patras Workshop on Axions, WIMPs and WISPs*, Schloss Waldthausen, Mainz, Germany, 24th June 2013, <http://axion-wimp2013.desy.de/e201031>
[35] P. W. Graham, S. Rajendran, Phys. Rev. D **88**, 035023 (2013).
[36] Y. V. Stadnik, V. V. Flambaum, Phys. Rev. D **89**, 043522 (2014).
[37] D. Budker, P. W. Graham, M. Ledbetter, S. Rajendran, A. O. Sushkov, Phys. Rev. X **4**, 021030 (2014).
[38] B. M. Roberts, Y. V. Stadnik, V. A. Dzuba, V. V. Flambaum, N. Leefer, D. Budker, Phys. Rev. Lett. **113**, 081601 (2014).
[39] B. M. Roberts, Y. V. Stadnik, V. A. Dzuba, V. V. Flambaum, N. Leefer, D. Budker, Phys. Rev. D **90**, 096005 (2014).

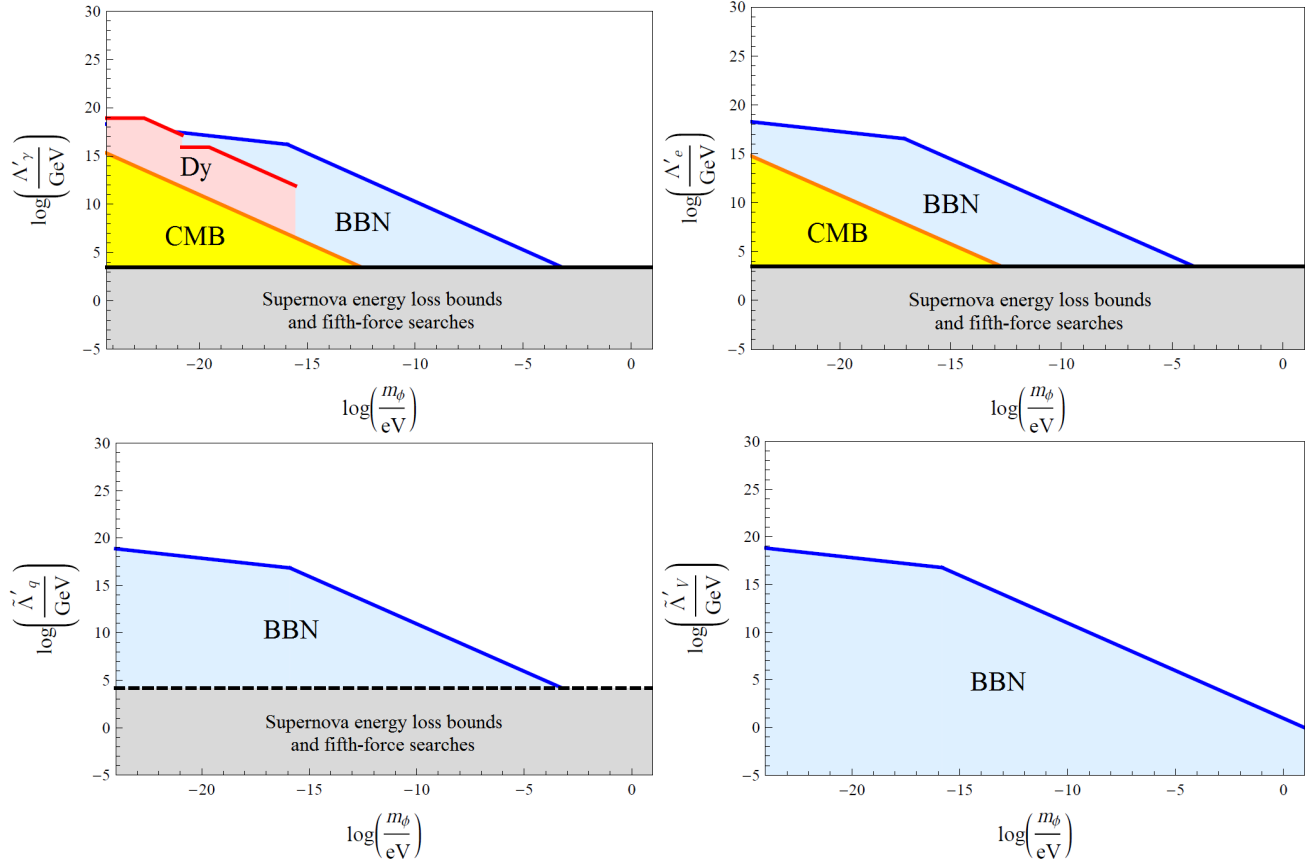


Fig. 1. From top left to right: Limits on the quadratic interactions of ϕ with the photon, electron, light quarks and massive vector bosons, as functions of the scalar particle mass m_ϕ . Region below blue line corresponds to constraints from consideration of the primordial ${}^4\text{He}$ abundance produced during BBN [10]. Region below yellow line corresponds to constraints from consideration of CMB angular power spectrum measurements [10]. Region below red line corresponds to constraints from atomic dysprosium spectroscopy measurements [10]. Region below black line corresponds to constraints from consideration of supernova energy-loss bounds and fifth-force experimental searches [12]. The light quark and massive vector boson interaction parameters are defined as $(\tilde{\Lambda}'_q)^2 = |(\Lambda'_u)^2(\Lambda'_d)^2(m_d - m_u)/[(\Lambda'_u)^2 m_d - (\Lambda'_d)^2 m_u]|$ and $(\tilde{\Lambda}'_V)^2 = |(\Lambda'_{W'})^2(\Lambda'_{Z'})^2/[(\Lambda'_{Z'})^2 - 1.4(\Lambda'_{W'})^2]|$.

Application of New Time Receivers in GLONASS

A.S. Bandura, P.P. Bogdanov, M.G. German
 Russian Institute of Radionavigation and Time
 Saint-Petersburg, Russia

Abstract—One of the ways to improve GLONASS performance is to increase the accuracy of GLONASS Time generation and its synchronization to Russian national time scale UTC(SU). This approach is planned to be realized by, first of all, increasing the accuracy of time scale comparisons between the Main and Reserved Central Synchronizers (CS) which are the basis for GLONASS Time generation and State Time and Frequency Reference (STFR) which is the basis for UTC(SU) generation as well as by increasing the accuracy of mutual comparisons between the Main and Reserved CSs. The paper presents the preliminary results of estimating the accuracy of CS–STFR time scale comparisons with using a new dual-frequency Time Transfer Unit TTU-1 developed at Russian Institute of Radionavigation and Time (RIRT) installed at both CSs and STFR and a new time receiver GTR-51 installed at STFR.

Keywords—Global Navigation Satellite System; time scale; time and frequency reference; time transfer unit; time receiver

I. INTRODUCTION

Using GLONASS and GPS signals is still one of the basic approaches to accurate comparisons of remote clocks [1]. In GLONASS this method is used for time scale comparisons between the Main and Reserved CSs and STFR as well as for mutual comparisons between the Main and Reserved CSs. Till recently, time scale comparisons between CSs and STFR have been performed with using Time Transfer Unit (TTU) at CSs and TTS-3/TTS-4 receivers at STFR. TTU is based on 16-channel single-frequency receiver of Standard Precision (SP) GLONASS/GPS signals in L1 frequency band. TTS-3 receiver performs SP measurements in L1 frequency band and Precise (P) measurements in L1/L2 frequency bands. TTS-4 receiver performs SP and P measurements in L1/L2 frequency bands. At the end of 2014 new equipment for time scale comparisons was additionally installed at CSs and STFR: Time Transfer Unit TTU-1 developed at RIRT on the basis of 36-channel GLONASS/GPS receiver for SP signals in L1/L2 frequency bands – at CSs and STFR and the new GTR-51 time receiver of SP and P signals in L1/L2 frequency bands – at STFR. The paper presents the preliminary results of estimating the accuracy of CS–STFR time scale comparisons accuracy as well as the results of Main – Reserved CS mutual comparisons with using the new equipment.

II. GLONASS TIME – UTC(SU) SYNCHRONIZATION

GLONASS Time is generated as a continuous “paper” time scale on the basis of the Main or Reserved CS time scale in accordance with the following equation:

$$\begin{aligned} \Delta T_{GL}(t) &= \Delta T_M(t) + \Delta T_M^{ph}(t_i) + \Delta T_M^{fr}(t_j) - \Delta T^c(t) = \\ &= \Delta T_R(t) + \Delta T_R^{ph}(t_k) + \Delta T_R^{fr}(t_l) - \Delta T^c(t) - \Delta T_{M-R}(t) \end{aligned} \quad (1)$$

where $\Delta T_{GL}(t)$ – GLONASS Time offset relative to STFR time scale; $\Delta T_M(t)$, $\Delta T_R(t)$ – Main/Reserved CS time offset relative to STFR time scale; $\Delta T_M^{ph}(t_i)$, $\Delta T_R^{ph}(t_k)$ – corrections for Main/Reserved CS phase steering; $\Delta T_M^{fr}(t_j)$, $\Delta T_R^{fr}(t_l)$ – corrections for Main/Reserved CS frequency steering; $\Delta T^c(t)$ – correction for controlling GLONASS Time – Reference Time offset; $\Delta T_{M-R}(t)$ – the offset between the Main and Reserved CSs time scales.

The offset of CS time scale relative to STFR time scale is calculated on the basis of their mutual comparisons by the signals from SVs of GLONASS and GPS in differential mode with using “all-in-view” method according to the following formula:

$$\Delta T_{STFR-CS}(t_i) = \Delta T_{GL(GPS)-CS}(t_i) - \Delta T_{GL(GPS)-STFR}(t_i) \quad (2)$$

where $\Delta T_{STFR-CS}$ – CS time scale offset relative to STFR time scale; $\Delta T_{GL(GPS)-CS}$ – CS time scale offset relative to GLONASS/GPS Time; $\Delta T_{GL(GPS)-STFR}$ – STFR time scale offset relative to GLONASS/GPS Time.

Data on the results of CS – STFR time comparisons by GLONASS/GPS signals are daily transferred to the GLONASS System Control Center where they are used for generating GLONASS Time and calculating corrections to GLONASS Time relative to UTC(SU) which are further uploaded and broadcast to users in navigational signals.

Besides, the results of STFR time scale comparisons are transferred to the Main and Reserved CSs where they are used for controlling CS time generating and estimating the relative frequency error.

Now the error of calculating Main CS – STFR time offset is about 8 ns (rms), Reserved CS – STFR time offset – 13 ns (rms).

III. FUNCTIONALITY, MAIN CHARACTERISTICS AND COMPOSITION OF TTU-1

TTU-1 is used for determining the offset between local clocks and GLONASS/GPS Time with further calculating

remote clocks mutual time offset, as well as for generating time scale signals synchronized to UTC(SU) [2].

A. Main Technical Characteristics of TTU-1

- receiving and processing SP navigation signals from up to 36 GLONASS/GPS space vehicles (SV) in L1/L2 frequency bands;
- calculating the offset between a local clock and GLONASS/GPS Time with the error below 35 ns (rms) by GLONASS signals and below 20 ns (rms) by GPS signals over 13-min measurement interval;
- calculating the mutual time scale offset between two remote clocks using GLONASS/GPS signals with the error below 5 ns (rms) for the distances between clocks up to 100 km and below 10 ns (rms) for the distances up to 8000 km over 13-min measurement interval;
- synchronizing the output signals 1 Hz, 1/60 Hz and 1/300 Hz to UTC(SU) with the error below 50 ns (rms).

B. Components of TTU-1

- an antenna with built-in amplifier;
- a comparison unit including a receiver, a synchronizing device, an indication device and a power supply unit;
- a personal computer with special software for TTU-1 operation;
- a mounting kit.

The antenna and receiver are calibrated during their manufacturing process and the signal delays for GLONASS and GPS are calculated for each frequency to be accounted for in measurement processing. Now the total error of calculating absolute GLONASS/GPS signal delays is below 5 ns. The delay corrections for each GLONASS frequency are measured with the error below 1 ns.

C. Output Data Provided by TTU-1

- time comparison results in the standard international format “cggtts_format_v2” for the following types of measurements: L1C – SP code measurements in L1 frequency band, L2C – SP code measurements in L2 frequency band, L3C - ionosphere-free combination of dual-frequency SP code measurements, CL3 - ionosphere-free combination of dual-frequency code and carrier phase measurements;
- radionavigation parameters and digital information from SV in the standard international format RINEX.

Time receiver GTR-51 provides time comparison results for the following measurements: L1C – SP code measurements in L1 frequency band, L2C – SP code measurements in L2 frequency band, L1P – P code measurements in L1 frequency band, L2P – P code measurements in L2 frequency band, L3P - ionosphere-free combination of dual-frequency P code measurements, L5C –code measurements by GPS signals in L5 frequency band.

IV. PRELIMINARY RESULTS OF ESTIMATING THE ACCURACY OF TIME SCALE SYNCHRONIZATION

The results of estimating the accuracy of time scale comparisons between CS and STFR with using TTU at CSs and TTS-3/TTS-4 receivers at STFR are presented in Table 1 and the results with using TTU-1 at CSs and TTU1/GTR-51 at STFR are presented in Table 2. The results of estimating mutual comparisons between the Main and Reserved CSs and STFR with using TTU at CSs and TTS-3/TTS-4 receivers at STFR are presented in Table 3 and the results with using TTU-1 at CSs and TTU-1/GTR-51 receiver at STFR are presented in Table 4.

The value of the square root of least squares remaining variance for 1-day measurements over all sessions with using a linear model for time scales offset was used as an accuracy estimate. STFR(GTR-51) results are based on L3P measurements.

TABLE I. TIME SCALES ACCURACY ESTIMATES WITH USING TTU AND TTS-3/TTS-4

Set	Error, ns					
	GLONASS			GPS		
	L1C	L2C	L3P	L1C	L2C	L3P
CS _M (TTU)	3.6-6.8	-	-	2.8-5.5	-	-
CS _R (TTU)	4.3-7.5	-	-	3.3-5.4	-	-
STFR(TTS-3)	2.7-7.1	-	5.4-12.0	2.2-5.9	-	0.8-1.2
STFR(TTS-4)	2.7-5.0	2.3-4.5	2.4-4.0	1.3-4.1	1.0-2.4	0.6-1.2

TABLE II. TIME SCALES ACCURACY ESTIMATES WITH USING TTU-1 AND GTR-51

Sets	Error, ns					
	GLONASS			GPS		
	L1C	L2C	L3P	L1C	L2C	L3P
CS _M (TTU-1)	2.4-6.6	1.9-3.4	-	2.5-5.9	2.4-3.6	-
CS _R (TTU-1)	2.4-5.6	2.1-4.0	-	2.9-4.6	1.5-2.3	-
STFR(TTU-1)	2.3-6.5	1.9-3.1	-	2.1-5.8	1.2-1.7	-
STFR(GTR-51)	2.5-6.2	-	2.2-3.7	2.0-4.5	-	0.8-1.4

TABLE III. MUSUAL TIME SCALES ACCURACY ESTIMATES WITH USING TTU AND TTS-3/TTS-4

Set	Comparison error (rms), ns		
	GLONASS	GPS	GLONASS+GPS
	L1C	L1C	L1C
STFR(TTS-3) – CS _M (TTU)	6.6-9.9	1.0-2.5	7.3-8.6
STFR(TTS-3) – CS _R (TTU)	7.9-12.8	4.3-9.3	7.8-11.3
STFR(TTS-4) – CS _M (TTU)	6.2-8.9	1.1-2.4	7.3-8.5
STFR(TTS-4) – CS _R (TTU)	8.0-13.0	4.3-7.0	8.1-10.8
CS _M (TTU) – CS _R (TTU)	6.4-9.5	5.3-9.5	6.3-9.5

TABLE IV. MUSUAL TIME SCALES ACCURACY ESTIMATES WITH USING TTU-1 AND GTR-51

Set	Comparison error (rms), ns		
	<i>GLONASS</i>	<i>GPS</i>	<i>GLONASS+GPS</i>
	<i>LIC</i>	<i>LIC</i>	<i>LIC</i>
STFR(TTU-1) – CS _M (TTU-1)	0.7-0.9	2.4-2.9	0.3-0.7
STFR(TTU-1) – CS _R (TTU-1)	4.3-8.7	3.6-4.7	5.1-9.6
STFR(GTR-51) – CS _M (TTU-1)	0.9-1.8	1.5-2.0	0.5-0.8
STFR(GTR-51) – CS _R (TTU-1)	4.5-9.5	2.9-4.2	4.9-9.4
CS _M (TTU-1) – CS _R (TTU-1)	3.8-8.1	1.8-2.5	5.2-8.7

The results presented in Tables 1–4 show that using TTU-1 and GTR-51 time receiver improves the accuracy of Main CS – STFR, Reserved CS – STFR and Main CS – Reserved CS mutual time comparisons mainly when operating by GLONASS signals. At the same time, it is reasonable to use single-frequency measurements for Main CS – STFR time comparisons and dual-frequency measurements for Reserved CS – STFR and Main CS – Reserved CS time comparisons.

To increase the accuracy of time scale comparisons when operating by simultaneous GLONASS/GPS measurements it is necessary to increase the accuracy of calibrating delays in the components of the receiving equipment.

V. CONCLUSION

New TTU-1 at the Main and Reserved CS and STFR and GTR-51 time receiver at STFR provide significant increase of time scale comparisons in GLONASS. The error of Main CS – STFR time scales comparisons with using single-frequency measurements in L1 band has become about 1.0 ns (rms) by GLONASS signals and 0.5 ns (rms) by GPS signals. The error of Reserved CS – STFR and Main CS–Reserved CS mutual time scale comparisons with using dual-frequency measurements has become about 3.5 ns (rms) by GLONASS signals and 2.5 ns (rms) by GPS signals.

ACKNOWLEDGMENT

Authors thank the colleagues from RIRT for their assistance in testing the equipment and processing and analyzing the results obtained.

REFERENCES

- [1] BIPM Annual Report on Time Activities. Volume 9. 2014.
- [2] Бандура А.С., Богданов П.П., Герман М.Г. Аппаратура высокоточного сличения шкал времени по сигналам ГНСС ГЛОНАСС и GPS//Метрология времени и пространства. Доклады 6-го Международного симпозиума.- 17-19 сентября 2012, Менделеево.- Менделеево: ФГУП ВНИИФТРИ».- 2013. С. 422-425.

OPTIME - final release

L. Buczek, J. Kołodziej, P. Krehlik,
M. Lipiński, Ł. Śliwczyński
AGH University of Science and Technology
Krakow, Poland
mlipinsk@agh.edu.pl

A. Binczewski, W. Bogacki, P. Ostapowicz,
M. Stroński, K. Turza
Poznan Supercomputing and Networking Center, PSNC
Poznan, Poland
wojbor@man.poznan.pl

P. Dunst, D. Lemański, J. Nawrocki, P. Nogaś
Astrogeodynamic Observatory
Space Research Centre PAS, AOS
Borowiec, Poland
nawrocki@cbk.poznan.pl

W. Adamowicz, J. Igalson, T. Pawszak, J. Pieczerak
Orange Polska, TPSA
Warsaw, Poland
Janusz.Pieczerak@orange.com

A. Czubla
Central Office of Measures, GUM
Warsaw, Poland
a.czubla@gum.gov.pl

M. Zawada
Institute of Physics, Faculty of Physics, Astronomy and
Informatics, Nicolaus Copernicus University, Torun, Poland
zawada@fizyka.umk.pl

Abstract— The OPTIME project creates an ultra-precise time and frequency signals dissemination system based on telecommunication networks. End users obtain access to these signals without incurring huge costs for the purchase of their own atomic clocks, and receive the service related to laboratories generating international atomic time scales, to which any precise time must be referred. This document describes the final stage of OPTIME project – which developed a self-calibrating, high precision dissemination system for time and frequency reference signals based on optical fiber links and ELSTAB devices developed at AGH University.

Keywords— Atomic clock, fiber optical network, high precision dissemination of time and frequency reference signals, time and frequency transfer, local repositories.

I. FIRST STAGE – 2012/2013

The OPTIME project started in December 2012. The consortium of 4 Polish partners: University of Science and Technology in Krakow (AGH), Space Research Centre, Borowiec Astrogeodynamic Observatory (AOS), Poznan Supercomputing and Networking Center (PSNC) – as a project leader, Orange Polska S.A. (OPL), received founding by the National Center for Research and Development from Poland in the Applied Research Programme to build an ultra-precise time and frequency (T&F) signals dissemination system based on telecommunication networks, especially on fiber optic links.

First part of the project was focusing on design of the system architecture. Project partners have created architecture that is distributed – may cover the whole country, easy to extend – new devices (as atomic clocks) are easy to implemented on our architecture, reliable - provides seamless

The OPTIME project (no. PBS1/A3/13/2012) is co-funded by the *National Center for Research and Development from Poland in the Applied Research Programme*.

access to time and frequency signals, prefers Polish solution.

The OPTIME architecture based on the three main elements:

- reference time and frequency laboratories – which provides time and frequency signals to the dissemination network,
- local time and frequency repositories – which are responsible for providing time and frequency signals during connection failure to reference time and frequency laboratories,
- fiber optical disseminating network – which is equipped in specialized transmission devices to transfers signals between reference laboratories, local repositories and end users' systems.

A backbone of the OPTIME system was an experimental 421,4 km-long fiber-optic connections between Central Office of Measures (GUM) in Warsaw and the Astrogeodynamic Observatory (AOS) in Borowiec near Poznan being a practical realization of the idea of the active propagation delay stabilization provided by project partners AGH. The link was launched on the 27th January 2012.

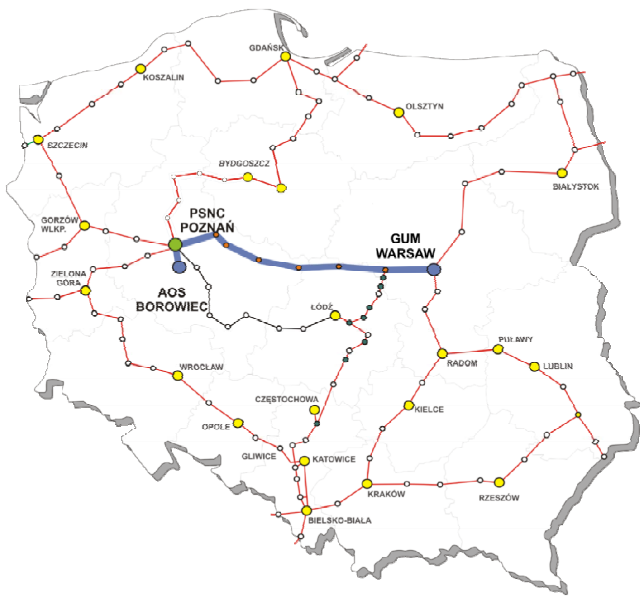


Fig. 1. OPTIME system in 2013

The topology of OPTIME system in the end of the 2013 is shown on Fig. 1.

II. SECODN STAGE – 2014

During the 2014 the OPTIME project was focusing to create another long distance time and frequency optical line from the Astrogeodynamic Observatory (AOS) in Borowiec to the National Laboratory of Atomic, Molecular and Optical Torun.

The choice of KL FAMO laboratory was dictated by work in the field of metrology, which are carried out there. The KL FAMO offers a system of two independent strontium optical lattice standards probed with a single shared ultra-narrow laser.

The new 330 km time and frequency dissemination line became operational in December 2014. The line contains 7 specialized optical Bidirectional Amplifiers, one Local Module was installed at the AOS in Borowiec and one Remote Module was installed at the KL FAMO in Torun. All these devices were designed and built by project partner AGH University of Science and Technology. In this link an improved T&F distribution system with the range of delay fluctuations compensation extended to $1\mu\text{s}$ [1] was implemented for the first time. All active devices along this link were connected to integrated remote control and supervision system.

Moreover, in the same year project partners prepared the final scheme of Local T&F repository, which was built in Poznan Supercomputing and Networking Center (PSNC) in Poznan.

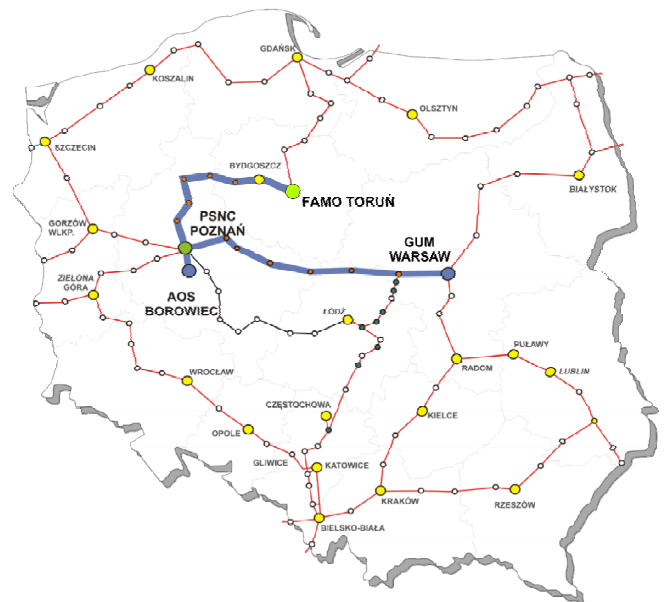


Fig. 2. OPTIME system in 2014

In the end of 2014 the OPTIME system reaches about 750 km long – see Fig. 2.

III. FINAL STAGE – 2015

2015 was the final year of OPTIME project. During this year the OPTIME project crated two more time and frequency transfer lines, and finished Local Time and Frequency Repository in Poznan. The Fig. 3 shown the final stage of OPTIME system in 2015.

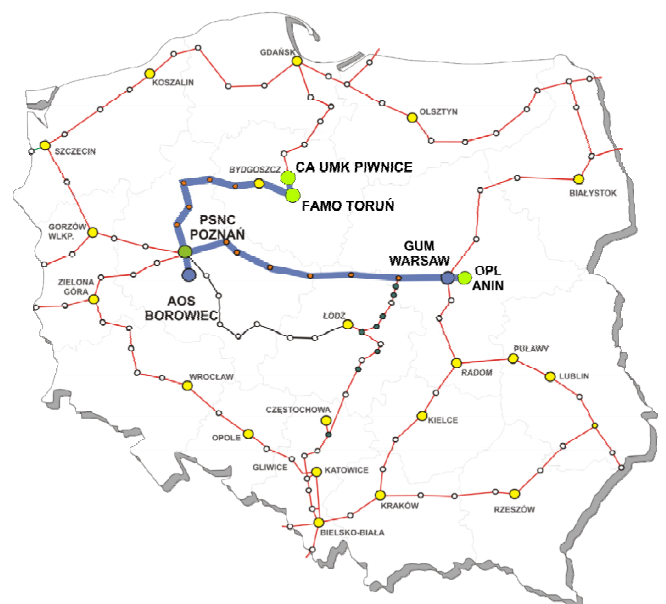


Fig. 3. OPTIME system in 2015

The first one connected Central Office of Measures (GUM) with a Centrum of Network Synchronization Orange Polska (OPL) in Anin near Warsaw. This line is about 40 km long.

The second line connected KL FAMO Laboratory in Torun with Torun Center for Astronomy Nicolaus Copernicus University located in Piwnice, where there is one of the biggest polish radio telescope. This is a short link – 15,5 km long.

The link connecting GUM and AOS was updated by changing the devices for a novel design with extended delay compensation range.

At the T&F repository in Poznan a Tapping Module was installed, which provides a stabilized T&F signals from GUM as a primary reference for the repository.

The OPTIME system created also a new Local Time and Frequency Repository located in Poznan. The local repository is equipped with several specialized devices which are responsible for provision of time and frequency signals to the dissemination network when failure of connection to the reference time laboratories occurs. The local repository contains: atomic clock – model Vremya-CH VCH-1008, multichannel counter, FemtoStepper, Time Transfer System TTS-4, and multiplexer - which is was constructed by project partners PSNC.

Right now the OPTIME system reaches more than 800 km optical fibres for time and frequency dissemination signals. Connects two UTC laboratories GUM – UTC(PL), AOS – UTC(AOS), local repository in Poznan, Center of Network Synchronization our business partner Orange Polska. OPTIME system also provides time to KL FAMO laboratory and Torun Center for Astronomy.

The OPTIME system connects AOS T&F Laboratory to the National Laboratory for Atomic, Molecular and Optical Physics - KL FAMO (330 km long link). UTC(AOS) is realized using active H-maser CH1-75A. Short term stability of CH1-75A is in the range of 2×10^{-13} for averaging time of 1 s, and goes down to 7.1×10^{-16} for one day. To compensate for the frequency drift of the H-maser a correction equal to -3×10^{-16} is applied once a day. Additional corrections, steering the UTC(AOS) reference frequency to UTC, are applied irregularly, and do not exceed 2×10^{-15} . The reference for the realized UTC(AOS) are differences UTC - UTC(AOS) and UTCr - UTC(AOS) published respectively monthly and weekly by the BIPM [2]. Generated by the AOG 5 MHz and 1pps signals are fed to frequency and pulse distribution & amplifier units. The reference point of UTC(AOS) is defined as no 1 output of the Pulse Distribution Unit. The frequency distributor doubles the reference frequency to 10 MHz standard signal which then is directly fed to local module of the Opto-Electronic Optical Fiber Transceiver (Fig 4).

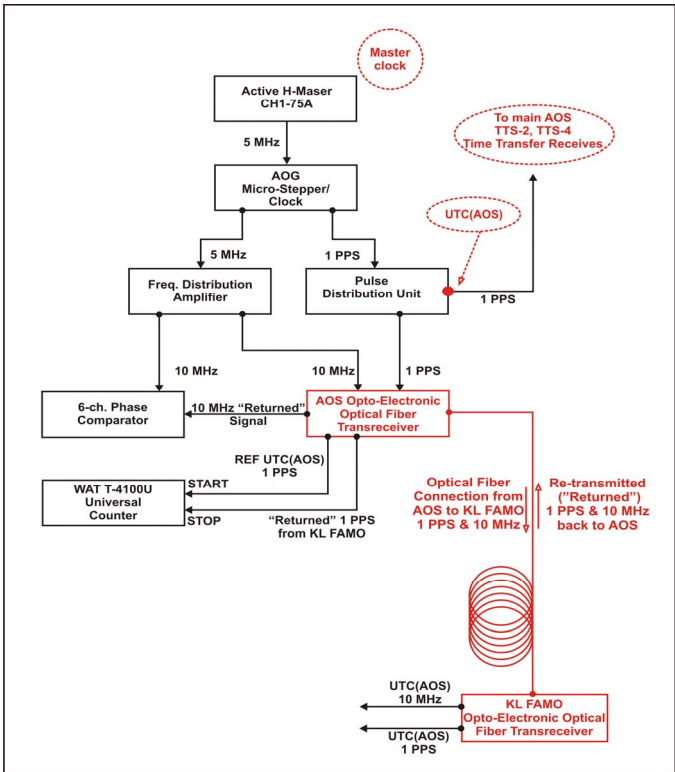


Fig. 4. Diagram of connections in AOS

IV. OPTIME RESULTS

The OPTIME system was used to synchronize VLBI station in Toruń Centre for Astronomy (CA UMK) located in Piwnice. The link between Toruń and Piwnice is 15 km long. VLBI observation using remote synchronization via optical fiber link was carried out on 18th Dec. 2015. The participating stations were Toruń(PL), Westerbork(NL), Medicina(IT), Yebes(ES), and Onsala(SE). The correlation was performed online (e-VLBI) at the Joint Institute for VLBI (JIVE ERIC), and additionally the raw data from the stations were recorded for further processing. The T&F signals, i.e. 1 PPS and 10 MHz, were delivered from UTC(AOS) via cascaded link Borowiec-Toruń (330 km) and Toruń-Piwnice (15 km). (KLFAMO).

Absolute molecular transitions frequencies measured by three cavity-enhanced spectroscopy techniques $^{12}\text{C}^{16}\text{O}$ (KL FAMO).

The AOS – KL FAMO link, then extended to Toruń Centre for Astronomy, allowed to obtain several interesting scientific results. The most important one was absolute measurement of the $^1\text{S}_0 - ^3\text{P}_0$ clock transition in neutral ^{88}Sr , the result is equal to 429 228 066 418 008.3 Hz measured with systematic error of 1.9 Hz and statistical error of 0.9 Hz [3]

The results of the optical fibre comparisons of UTC(AOS) and UTC(PL) are presented in Fig. 5. The measurements cover the period from January 1st - December 31st 2015.

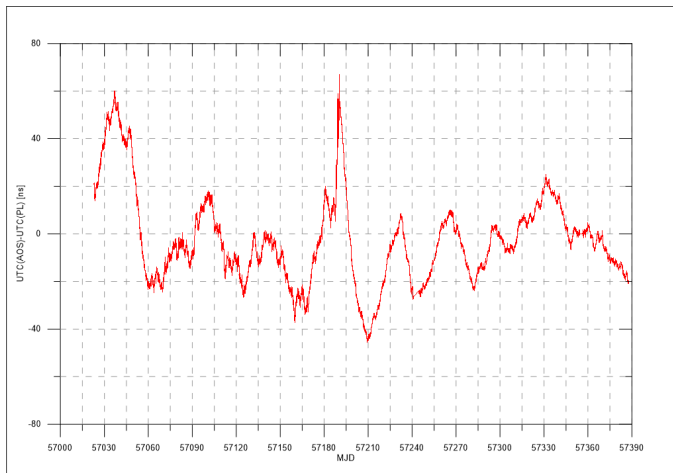


Fig. 5. Results of optical fibre comparisons, UTC(AOS) - UTC(PL), January-December 2015

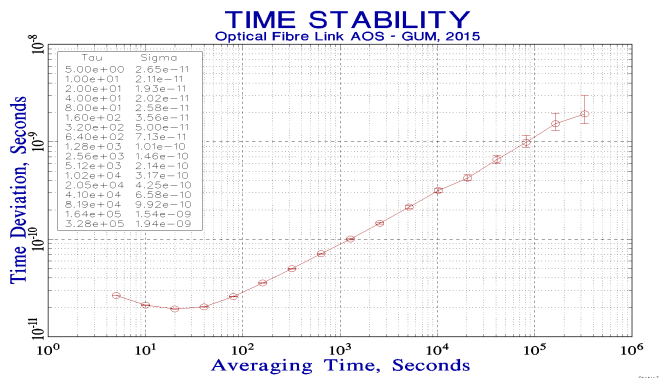


Fig. 6. Time deviation measured with the AOS-GUM link.

Fig. 6 shows the time deviation of the UTC(AOS)-UTC(PL) link. For averaging times of 20 s time deviation of the link equals approximatively 20 ps. The estimation of the precision is limited by:

- stability of the clocks used for the realization of the UTC, commercial HP 5071A Cs clock at GUM and active H-maser at AOS.

- precision of the Stanford SR-620 counter used in the comparisons, with uncertainty of 20 ps single shot.

The total uncertainty of the link is 150 ps and includes uncertainties of the connections between UTC(AOS) and UTC(PL) reference points and the opto-electronic transceivers. [4] [5]

V. BEYOND OPTIME PROJECT

Project OPTIME is a realization of idea ultra-precise time and frequency dissemination system on long range distance. Project has created the stable system which is available for end users by 24 hours/year.

The next step will be extending of the system on new location in Poland, and also cooperation with other European partners to create European Time and Frequency Dissemination System.

REFERENCES

- [1] P. Krehlik, L. Śliwczynski, L. Buczek, J. Kołodziej and M. Lipiński, "Ultrastable long-distance fibre-optic time transfer: active compensation over a wide range of delays," Metrologia, vol. 52, pp. 82–88, 2015.
- [2] BIPM Circular T, <http://www.bipm.org/jsp/en/TimeFtp.jsp?TypePub=publication>
- [3] Absolute measurement of the $^1S_0 - ^3P_0$ clocktransition in neutral ^{88}Sr over the 330 km long distance stabilized fibre optic link. P. Morzynski, M. Bober, D. Bartoszek-Bober1, J. Nawrocki, P. Krehlik, L. Śliwczynski, M. Lipinski, P. Maslowski, A. Cygan, P. Dunst, M. Garus, D Lisak, J Zachorowski, W. Gawlik, C. Radzewicz, R. Ciurylo, M. Zawada, Nature Scientific Reports, December 2015
- [4] Z. Jiang, A. Czubla, J. Nawrocki, W. Lewandowski & E.F. Arias, Comparing a GPS time link calibration with an optical fibre selfcalibration with 200 ps accuracy Metrologia 52 384 (2015).
- [5] BIPM Annual Report on Time Activities Volume 9/2014, BUREAU INTERNATIONAL DES POIDS ET MESURES Pavillon de Breteuil, F-92312 SÈVRES Cedex, France

Rb-stabilized optical frequency reference at 1572 nm

William Moreno, Renaud Matthey, Florian Gruet, Pierre Brochard, Stéphane Schilt, Gaetano Mileti

Laboratoire Temps-Fréquence, Université de Neuchâtel, Neuchâtel, Switzerland

Email: william.moreno@unine.ch

Abstract—In the framework of an on-board optical reference system, a 1560-nm DFB laser frequency-doubled and locked onto the D₂ line of ⁸⁷Rb using a 2-cm long vapour glass cell is used to generate an optical frequency comb. A second DFB laser operating at 1572 nm, a wavelength corresponding to a CO₂ transition is offset-locked to one mode of the comb. At 1572 nm, a relative frequency stability of $1 \cdot 10^{-11}$ at 1 s was obtained, reaching less than $4 \cdot 10^{-12}$ from 3,000 s up to at least 3 days. Limitations arising from the 1560-nm stabilized laser are discussed.

Keywords—Rubidium, Frequency stabilization, Frequency doubling, Optical frequency comb, Lidar

I. INTRODUCTION

The integrated-path differential-absorption lidar (IPDA) technique allows high-precision remote sensing of the atmospheric CO₂ concentration [1]. Such a lidar instrument is based on a laser source emitting pulsed radiation at a precise wavelength corresponding to an appropriate CO₂ absorption line in the near-infrared. To provide a global and denser distributed set of measurements allowing the identification of sources and sinks of CO₂, a satellite mission is envisaged.

For this purpose, a compact fiber-coupled rubidium-stabilized multi-frequency optical reference was previously reported [2]. A distributed-feedback (DFB) laser, used as a master laser, is frequency-doubled and stabilized onto a sub-Doppler feature of the D₂ line of ⁸⁷Rb using a 2-cm-long vapor cell. The frequency-stabilized light is injected into an optical frequency comb generator (OFCG). An optical frequency comb (OFC) centered at 1560 nm covering a span of 40 nm is obtained. The rubidium-stabilized comb is used to transfer the frequency stability of the 1560-nm master laser to a 1572-nm DFB slave laser offset-locked to one comb mode [3].

The present work is dedicated to explore the frequency limitations of the frequency-stabilized 1572-nm laser induced by the master laser. First, the frequency stability of the 1560-nm and 1572-nm lasers is compared. Bias and reproducibility of the optical frequency of the 1560-nm laser are investigated and compared to those of other 780-nm rubidium-stabilized laser heads with a similar design [4]. A characterization of the spectral properties of the frequency-doubling unit is presented and its implication as source of noises is examined.

II. EXPERIMENTAL SETUP

A. Master Laser Stabilization

The master laser is a fiber-pigtailed DFB laser (Emcore) with 38 mW of optical power at 1560.5 nm. A fraction of the

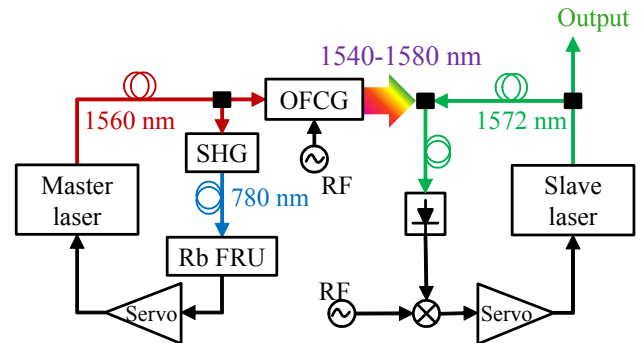


Fig. 1. Schematics of the laser system. Colored arrows: optical fiber. Dark arrows: electrical links. PPLN: periodic-poled lithium niobate waveguide for second harmonic generation. Rb FRU: rubidium frequency reference unit. OFCG: optical frequency comb generator. RF: radio frequency oscillator.

output power is injected into a fiber-coupled second harmonic generation (SHG) module that consists of a 34-mm long periodic-poled lithium niobate (PPLN) waveguide (Fig. 1). The temperature of the PPLN, as well as the frequency and power of the input light are decisive to achieve a high output power at 780 nm. An efficiency of $\sim 300\%/W$ was measured at 50°C temperature and 1560.48-nm input wavelength [2].

The frequency-doubled light is injected into a home-made frequency reference unit (FRU) which is a compact metallic package (160x80x60 mm³) enclosing an evacuated cylindrical Rb-vapor cell (10-mm diameter by 19-mm length). The cell is thermalized and magnetically shielded. The 780-nm beam is retro-reflected in order to probe the D₂ transition of ⁸⁷Rb in a sub-Doppler absorption scheme resulting in narrow resonances (~ 15 MHz full width at half maximum - FWHM). The master laser is frequency-locked by wavelength modulation spectroscopy applied by dithering its injection current at 50-kHz combined with synchronous demodulation at the first harmonic.

B. Optical Frequency Comb Generation

The frequency-stabilized master laser is used to seed an OFCG (OptoComb). Sidebands are generated on the master laser frequency by an electro-optical modulator (EOM) enclosed in a waveguide Fabry-Perot cavity. The EOM is modulated by a radio-frequency (RF) signal at 10 GHz in resonance with the cavity. Centered at the master laser frequency, an OFC covering a span of 40 nm is generated. The RF modulation frequency is obtained from a local oscillator referenced to an H-maser. By denoting f_m and ν_M the RF modulation and master laser frequency, respectively, the

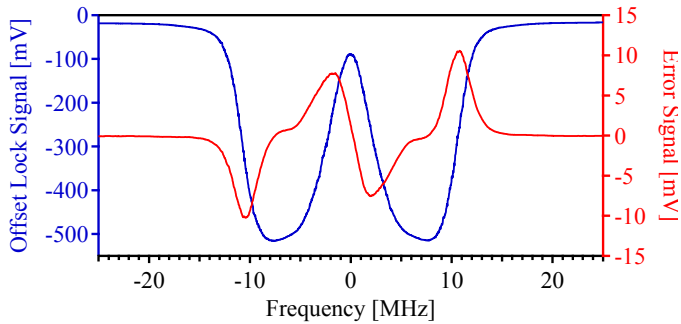


Fig. 2. Blue line: offset-lock absorption-like signal. Red curve: $1f$ error signal.

frequency ν_n of the n th optical comb mode, is given by $\nu_n = \nu_M + n \cdot f_m$, where n can take a positive or negative integer value. The frequency modulation applied to lock the master laser is imprinted on each mode of the comb.

C. Slave Laser Stabilization

The slave laser is a fiber-pigtailed DFB laser (Fitel) emitting at 1572 nm. The laser is frequency-stabilized using a similar offset-lock technique as proposed by Schilt *et al.* [5]. For this purpose, the offset frequency between the slave laser and the nearest comb mode is detected from the beat note on a fast photo-detector. The beat signal is amplified and frequency down-converted by mixing it with a local oscillator frequency f_{LO} referenced to the same H-maser. A combination of high-pass and low-pass filters followed by an envelope detector is used as a frequency discriminator in order to produce an absorption-like feature (see Fig. 2). A voltage error signal is obtained by demodulating this signal at the master laser modulation frequency. The error signal is amplified in a servo controller and is fed back to the injection current of the slave laser in order to keep the down-converted offset frequency at the center of the absorption-like feature. The slave laser frequency is given by: $\nu_S = \nu_M + n \cdot f_m + f_{LO}$.

III. FREQUENCY STABILITY

The frequency stability of the master and slave lasers was evaluated by heterodyne measurements with external optical frequency references [3].

A. Frequency Measurements

The master laser frequency stability was simultaneously evaluated at 780 nm and at 1560 nm. At 780 nm, the frequency stability was obtained from a beat note between the frequency-doubled master laser and an external Rb-stabilized reference laser head locked onto the cross-over CO22/23. This reference laser demonstrates a frequency stability at the level of or below $1 \cdot 10^{-11}$ for all time scales from 1 s up to 1 day [4]. At 1560 nm and 1572 nm, the frequency stability was obtained by heterodyning the lasers with a commercial Er-fiber comb fully-stabilized to the H-maser. The master laser was locked onto the direct F23 transition.

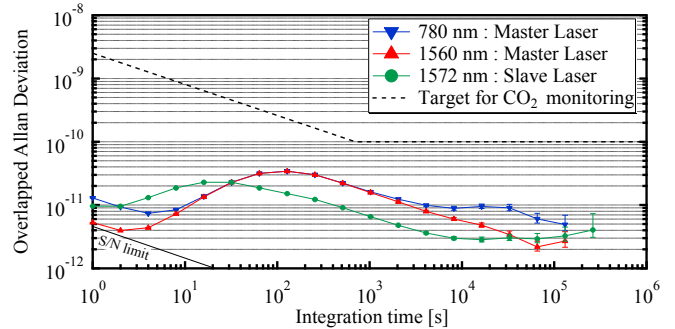


Fig. 3. Relative frequency stability of the main components of the laser system. 780 nm (blue): frequency-doubled master laser heterodyned with a reference laser head; 1560 nm (red): master laser heterodyned with a self-referenced optical frequency comb stabilized to a hydrogen maser. 1572 nm (green): slave laser heterodyned with the self-referenced comb. Dashed line: required frequency stability for the CO₂ IPDA instrument [6,7].

B. Results and Discussion

Figure 3 show the frequency stabilities of the master laser and the slave laser. At 1560 nm, a fractional frequency stability of $5.2 \cdot 10^{-12}$ was obtained at 1-s averaging time, in good agreement with the estimated signal-to-noise limit. This corresponds to absolute frequency variations of less than 1 kHz. From $4 \cdot 10^3$ s up to $1.3 \cdot 10^5$ s, the relative stability is always better than $1 \cdot 10^{-11}$. Between 200 s and 3,000 s, the frequency stabilities measured at 780 nm and 1560 nm are identical. At 1572 nm, a relative frequency stability of $1 \cdot 10^{-11}$ was obtained at 1 s, reaching less than $4 \cdot 10^{-12}$ from 3,000 s up to at least 3 days.

The main limitation in the stability of the lasers results from the bump present at $\approx 10^2$ s in the Allan deviation of the master laser and at ≈ 20 s for the slave laser. They are due to the presence of a defect in the output fiber of the frequency-doubling module that induces etalon fringes. As this effect is particularly temperature-sensitive, the measurements were affected differently. For the measurement at 1572 nm, the setup was less protected against rapid temperature changes which increased the amount of the frequency fluctuations associated to the etalon fringes. This resulted in a shift of the instability bump to lower integration time for the 1572-nm measurement.

At 780 nm, the stability is limited by the reference laser head for integration times longer than 2000 s and by the resolution of the frequency counter at short term. The instrument was different from the one used for the 1560-nm measurement, what explains the variation in the short term stability although the two measurements were done simultaneously.

IV. FREQUENCY REFERENCE UNIT : BIAS AND REPRODUCIBILITY

In this section, the bias and reproducibility of the optical frequency of the master laser and of three Rb-stabilized 780-nm laser heads with a similar design [4] are investigated. The direct F23 transition was used to lock all lasers.

A. Optical Frequency Measurement

Optical frequency determination at 1560 nm and 780 nm was performed with the fundamental and second harmonic component, respectively, of the self-referenced Er-fiber comb. The Er-fiber comb repetition rate f_{rep} and carrier-envelope offset frequency f_{CEO} , as well as the beat frequency f_{beat} , were simultaneously measured on a multi-channel counter and the optical frequency was retrieved as follows:

$$\nu_{\text{laser}} = m \cdot f_{\text{rep}} \pm f_{\text{CEO}} \pm f_{\text{beat}}, \quad (1)$$

where m is the index of the comb mode that is heterodyned with the laser. The signs of f_{CEO} and f_{beat} were assessed before each measurement and the comb mode number m was determined from the reference frequency of the direct F23 transition reported by Ye *et al.* [8].

Six measurements of the absolute frequency of the 1560-nm master laser were performed over a period of one year in various environmental and locking parameters conditions. The frequency repeatability of the master laser and of the laser heads was assessed from measurements of 15 minutes where the operating parameters (cell temperature, temperature and current of the laser, locking parameters) of the lasers were unchanged. The lasers were switched off 15 minutes between each measurement.

B. Results and Discussion

The beat frequencies averaged over the measurement duration are shown in Fig. 4. The nine 15-min long measurements of the master laser gave an average frequency bias of +69 kHz from the reference value with a repeatability of 2 kHz (standard deviation). This corresponds to a bias of +138 kHz and a repeatability of 4 kHz for the frequency-doubled component at 780 nm. For the Rb-stabilized 780-nm laser heads, a bias of +99 kHz (average of the three 780-nm lasers' biases) with a repeatability of 6 kHz (average of the three 780-nm lasers repeatabilities) were obtained.

In the case of four reproductions of the same laser system described in [4] (the master laser and the three 780-nm laser heads) operated in different conditions, the reproducibility system can be estimated from the data of Fig. 4. At 780 nm, a bias of +97 kHz with a reproducibility of 60 kHz is obtained.

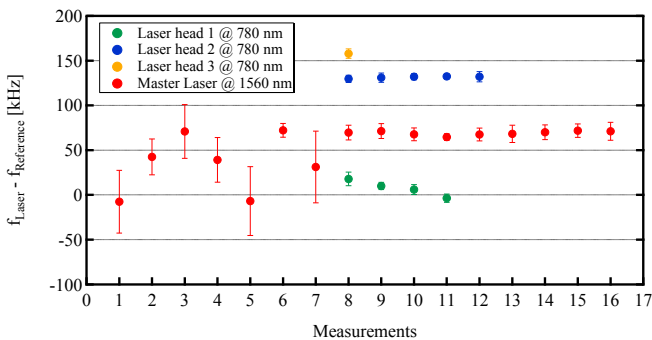


Fig. 4. Frequency difference between the master laser optical frequency at 1560 nm (red dots) and for three Rb-stabilized 780-nm laser heads (green, blue and yellow dots) with respect to the reference value reported by Ye *et al.* [7]. Measurements 1-6: master laser operated with different parameters. Measurement 7 and above: unchanged operating parameters for each laser. The error bars represent the standard deviation of the measured data.

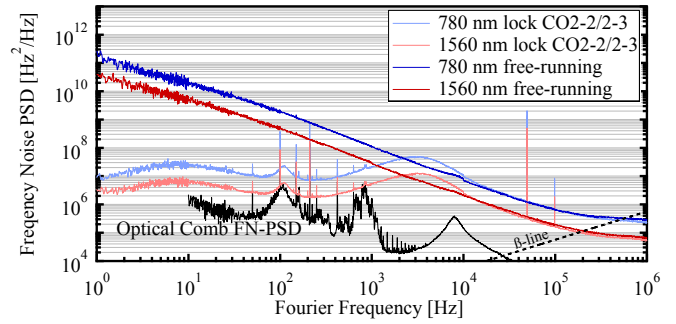


Fig. 5. Frequency noise power spectral density (FN-PSD) of the master laser in free-running regime and locked on the cross-over CO22/23 transition. The contribution of the comb noise at 1560 nm is also shown for comparison (black curve).

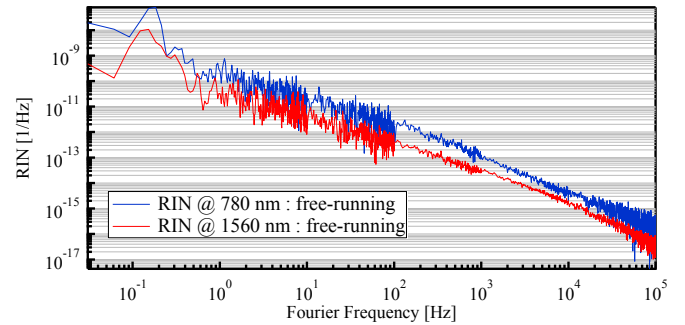


Fig. 6. Relative intensity noise of the free running master laser before (at 1560 nm) and after (at 780 nm) the frequency-doubling process.

The bias measured for the master laser and the 780-nm laser heads are comparable with the uncertainty of 100 kHz reported by Masuda *et al.* [9]. In this case, a DFB laser diode was frequency-locked using demodulation at the third harmonic of the sub-Doppler absorption spectrum, which strongly reduces the offset in the error signal induced by the Doppler background as discussed by Affolderbach *et al.* [10].

V. FREQUENCY-DOUBLING MODULE : SPECTRAL CHARACTERIZATION

A. Frequency Noise

The frequency noise of the fundamental (1560 nm) and frequency-doubled (780 nm) components of the master was measured by analyzing the noise of the respective beat notes with the fundamental or second harmonic component of the self-referenced comb using a signal source analyzer. Measurements were performed both in free-running regime and with stabilization to the crossover CO22/23 transition. In order to reduce the frequency drift of the beat-note signal during the measurements of the free-running lasers, the beat-note signals were first frequency up-converted to 15 GHz and then frequency-divided by a factor of nine.

Figure 5 displays the corresponding frequency noise power spectral density (FN-PSD). The frequency noise spectra of the locked laser at both wavelengths present a bump at 3 kHz corresponding to the bandwidth of the stabilization loop. Another bump in the spectra at ~100 Hz results from the servo bump of the repetition rate stabilization in the Er: fiber comb.

The FN-PSD at 780 nm is four times higher than at 1560 nm both in the free-running and locked cases, which is in good agreement with the doubled frequency and indicates that no significant noise is added by the frequency-doubling module.

The FWHM of the free-running master laser was retrieved from its measured FN-PSD using the concept of the β -separation line [11]. A laser linewidth of 1.3 ± 0.1 MHz at 1560 nm and 2.7 ± 0.3 MHz at 780 nm is obtained for a low cut-off frequency of 10 Hz (100-ms observation time), corresponding approximately to a 2-fold increase through the SHG process.

B. Relative Intensity Noise

The relative intensity noise (RIN) of the free-running master laser was measured before and after the frequency-doubling module using a fast Fourier transform (FFT) spectrum analyzer. Results are shown in Fig. 6. An increase of the RIN by a factor of four through the SHG module is observed, which results from the quadratic dependence of the SHG process on the incident intensity.

C. Side-Mode Suppression Ratio

The evolution of the side-mode suppression ratio (SMSR) through the frequency-doubling unit was also evaluated. At both wavelengths the spectrum of the master laser was measured using an optical spectrum analyzer. Before the PPLN waveguide, it shows an SMSR of 44 dB. After frequency-doubling, all side-modes are attenuated under the noise floor of the spectrum analyzer corresponding to an SMSR >60 dB. This is a result of the non-linear intensity-dependence of the frequency-doubling process. The low power in the side-modes (< -30 dBm) results in a completely inefficient SHG.

VI. CONCLUSION

A fiber-coupled DFB laser emitting at 1560 nm was frequency-doubled and locked to the D_2 line of ^{87}Rb , achieving a relative frequency stability of $5.2 \cdot 10^{-12}$ at 1 s integration time. This laser fed an optical frequency comb generator producing a 40-nm wide spectrum centered at 1560 nm. This comb was used to offset-lock a second DFB laser emitting at 1572 nm, which achieved a relative frequency stability of $1 \cdot 10^{-11}$ at 1 s integration time and $4 \cdot 10^{-12}$ above 3,000 s.

Possible limitations arising from the master laser stabilization process were investigated. A frequency bias of +138 kHz with a repeatability of 4 kHz was measured for the frequency-doubled master laser locked onto the direct F23 transition. The mean bias of three other laser heads based on the same sub-Doppler stabilization scheme was measured to

be +99 kHz with a repeatability of 6 kHz in concordance with the bias of the frequency-doubled master laser.

A spectral characterization of the PPLN wave-guide was presented. The frequency noise and linewidth of the master laser are not affected by additional technical noise arising from the frequency-doubling unit. Both frequency noise and RIN are increased by a factor of four (in terms of PSD) as a result of the doubled optical frequency and quadratic power dependence, respectively, of the SHG process.

ACKNOWLEDGMENT

This work was supported by the European Space Agency and the Swiss National Science Foundation (project number 156621). We thank our colleague Dr. Christoph Affolderbach and Dr. Andreas Fix (DLR, Germany) for helpful discussions.

REFERENCES

- [1] G. Ehret, C. Kiemle, M. Wirth, A. Amediek, A. Fix and S. Houweling, "Space-borne remote sensing of CO_2 , CH_4 , and N_2O by integrated path differential absorption lidar: a sensitivity analysis," *Appl. Phys. B* **90**, 593 (2008)
- [2] R. Matthey, F. Gruet, S. Schilt and G. Mileti, "Compact rubidium-stabilized multi-frequency reference source in the 1.55- μm region," *Opt. Lett.* **40**, 2576 (2015)
- [3] R. Matthey, W. Moreno, F. Gruet, P. Brochard, S. Schilt and G. Mileti, "Rb-stabilized laser at 1572 nm for CO_2 monitoring," *Journal of Physics: Conference Series*, in press (2016)
- [4] F. Gruet, C. Affolderbach, M. Pellaton, T. Bandi, R. Matthey and G. Mileti, "Compact and frequency stabilized laser heads for rubidium atomic clocks," in *Proceedings of the International Conference on Space Optics (ICSO)*, Ajaccio (2012), paper 048
- [5] S. Schilt, R. Matthey, D. Kauffmann, C. Affolderbach, G. Mileti and L. Thévenaz, "Laser offset-frequency locking up to 20 GHz using a low-frequency electrical filter technique," *Appl. Opt.* **47**, 4336 (2008)
- [6] F.M. Bréon and P. Ciais, "Spaceborne remote sensing of greenhouse gas concentrations," *Comptes Rendus Geoscience* **342**, 412-424 (2010)
- [7] J. Caron, Y. Durand, J-L. Bezy and Roland Meynart, "Performance modeling for A-SCOPE: a space-borne lidar measuring atmospheric CO_2 ," in *Proceedings Lidar Technologies Techniques and Measurements for Atmospheric Remote Sensing V*, (2009), SPIE paper 74790E
- [8] J. Ye, S. Swartz, P. Jungner and J. Hall, "Hyperfine structure and absolute frequency of the ^{87}Rb $5P_{3/2}$ state," *Opt. Lett.* **21**, 1280 (1996)
- [9] S. Masuda, A. Seki and S. Niki, "Optical frequency standard by using a 1560 nm diode laser locked to saturated absorption lines of rubidium vapor," *Appl. Opt.* **46**, 4780 (2007)
- [10] C. Affolderbach and G. Mileti, "A compact laser head with high-frequency stability for Rb atomic clocks and optical instrumentation," *Review of Scientific Instruments* **76**, 073108 (2005)
- [11] G. Di Domenico, S. Schilt and P. Thomann, "Simple approach to the relation between laser frequency noise and laser line shape," *Appl. Opt.* **49**, 4801 (2010)

Network Time Security Specification

Protecting Network-based Time Synchronization

Dieter Sibold, Kristof Teichel

Physikalisch-Technische Bundesanstalt (PTB)

Braunschweig, Germany

dieter.sibold@ptb.de

Abstract—The Network Time Security specification provides measures which are designed to add security to time synchronization protocols, while considering their specific timing-related requirements. The development of the specification is accompanied by formal analysis of its security model. Special attention is paid to the Network Time Protocol, for which an implementation of those measures is in progress.

Keywords—time dissemination; security; computer security; authentication; message authentication; standardization

I. INTRODUCTION

Time synchronization protocols play an increasingly important role in packet switched networks. Areas of application include distributed and internet-connected production chains, and the finance industry, especially high-frequency trading. Many national metrology institutes apply the Network Time Protocol (NTP) [1] – one of the predominant time synchronization protocols – for the dissemination of UTC [2]. In many use cases, the protection of time synchronization protocols is indispensable, either because of existing threats or because of compliance or legal reasons. Currently, neither NTP nor the Precision Time Protocol (PTP) [3] are able to protect time synchronization packets in modern and complex networks adequately. In this paper, we present the Network Time Security specification (NTS). It comprises security measures that are designed to protect time synchronization messages.

II. THREAT ANALYSIS AND SECURITY REQUIREMENTS

The security goals aspired to by the NTS specification are based on a profound threat analysis for time synchronization protocols performed by the Internet Engineering Task Force (IETF) in RFC 7384 [4].

A. Threats

Time synchronization packets are exposed to numerous threats if they are exchanged over unprotected networks, especially over the internet. An adversary may, depending on its capabilities, intercept, remove, replay or alter time synchronization packets or it may spoof the identity of a time server and inject false packets, causing degradation of time synchronization performance, or the transmission of false time.

Additionally, time synchronization protocols are also exposed to specific attacks such as packet delay and rogue master attacks. In a packet delay attack an adversary adds an asymmetric delay in the transmission time of the packets exchanged between client and server. This delay acts like an unknown asymmetry and adds to the uncertainty of the calculation of the time offset [5]. This attack is exceptionally effective since the adversary does not need to alter the packets. In a rogue master attack, an adversary causes the client to believe it is a valid time server, merely by using the time protocol's election mechanisms.

B. Security Requirements

Based on the threat analysis, [4] compiles a list of requirements for securing a time synchronization protocol.

1) Common Security Requirements

Security measures have to enable a client to verify the identity and authorization of a time server. Additionally, the security measures must protect the integrity of the exchanged packets. The content of time synchronization packets is not considered confidential and its protection is not required.

2) Time Protocol Specific Security Requirements

Apart from common security requirements, [4] also requires protection against delay attacks and that the applied measures not impede the performance of the time synchronization. In recent years, NTP servers have fallen victim to massive Denial-of-Service (DoS) attacks or have been abused to amplify such attacks [6]; thus, security measures should protect against such attacks [4].

III. EXISTING SECURITY PROTOCOLS

In the following, we present an overview regarding the state of the currently defined security measures of NTP and PTP.

A. Network Time Protocol

NTP provides two security procedures for the protection of integrity and authenticity: the pre-shared key scheme and the Autokey protocol [7]; however, neither of them fulfills state-of-the-art security requirements. The disadvantage of the shared key scheme is that it does not provide sufficient scalability, which prohibits its use in large environments. While Autokey does provide the required scalability, its applied cryptographic primitives are too weak to withstand modern attacks.

Furthermore, its key exchange mechanism suffers from a severe vulnerability that allows an adversary to obtain the shared secret between a client and a server and to use this in order to masquerade as a legitimate server towards the client, even if stronger cryptographic primitives are employed [8, 9].

B. Precision Time Protocol

The situation concerning PTP is similar: although the standard specifies a security procedure within Annex K, this experimental annex is typically not implemented.

IV. NTS SPECIFICATION

The NTS specification is a newly engineered protocol security model for NTP – and potentially other time synchronization protocols, especially PTP. It is designed to meet the security requirements listed in II.B. The specification is separated into a set of documents: Firstly, the NTS document [10] which describes all NTS messages and outlines the exchange procedures; secondly, a document that specifies detail for the application of NTS to NTP [11]; and thirdly, a document that describes the syntax used for the encoding of the NTS messages [12].

To fulfill its requirements, NTS differentiates between two phases: the first phase, in which a client authenticates its server and both of them exchange keys, and the second phase, in which the actual time synchronization exchanges occur.

A. First Phase: Authentication and Key Exchange

NTS specifies the preconditions which have to be fulfilled during this phase. It also proposes a certificate-based authentication scheme with an associated key exchange mechanism, secured by asymmetric cryptography which meets those preconditions. Note that the use of this scheme is optional, but it is mandated if NTS is applied to NTP.

1) Normative Preconditions

At the end of the first phase, the client and the server have established an association and have exchanged a key input value (KIV) and a cookie. The KIV serves as state information for this association and may be opaque to the client. The cookie is the mutual secret key for the association and is given by

$$\text{cookie} = f(\text{server seed}, \text{KIV}), \quad (1)$$

in which f is a one-way function and the server seed is a secret known to the server only. Note that the cookie has to be exchanged confidentially, whereas the KIV may be public.

2) Optional Authentication and Key Exchange Scheme

This scheme fulfills the preconditions of IV.A.1). It consists of three message exchanges as shown in Fig. 1. The access messages exchange an access key which works similarly to the initially exchanged cookie in the Photuris protocol [8], protecting the server from DoS attacks. During the association exchange the client verifies the server's authenticity based upon its provided certification chain, and the participants negotiate the cryptographic functions that are to be used. During the third exchange the client provides the KIV as a hash

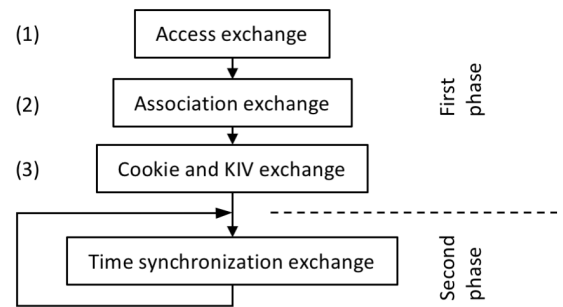


Fig. 1. First phase: Sequence of exchanged messages for the optional authentication and cookie exchange. Second phase: After successful exchange of cookie and KIV, time synchronization packets are exchanged.

of its own certificate. The server calculates the cookie according to (1) and passes it to the client, encrypted with the public key from the client's certificate and signed with its own private key. The client verifies the integrity and authenticity of the received message based upon the appended signature and then decrypts the encrypted cookie with its own private key.

B. Second Phase: Protection of the Time Synchronization

Latencies introduced due to cryptographic operations on time synchronization packets may impede the performance of the synchronization protocol. Hence, employed cryptographic primitives must be fast to calculate. NTS acknowledges this by protecting the time synchronization packets via a Message Authentication Code (MAC) [13]. The MAC, appended by a server and a client to each time synchronization packet, is calculated as:

$$\text{MAC} = f(c, p), \quad (2)$$

where f is the MAC-generating function, which is identical to the one-way function f used to calculate the exchanged cookie c , and p is the payload of the time synchronization packet as displayed in Fig. 2. The receiver of the packet recalculates the MAC based on the obtained payload and compares the result with the received MAC. If identical, the integrity and authenticity of the received packet is proved. Otherwise, the packet has to be discarded, since it was either altered during transmission or it is not authentic.

1) Unicast Associations

A unicast association is a one-to-one relationship between a client and a server. In the case of NTP, a client in unicast mode polls the server for time information periodically. The time synchronization exchange consists of a time request and a time response message. Both of these messages append two extension fields to the NTP header (see Fig. 2). The first provides NTS-related information: a nonce for replay protection and, in the case of a time request, the KIV and the negotiated MAC algorithm. The second extension field contains the MAC itself. This secured time exchange can be repeated until the server decides to renew its server seed, after which all of its clients need to acquire a new cookie, according to (1).

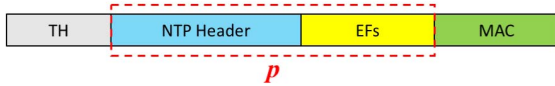


Fig. 2. NTP packet composed of the transport header (TH), the NTP header itself, one or more NTP extension fields (EF) [1], and the MAC. The red framed part of the packet p is used to calculate the MAC according to (2). Note that the MAC itself is included in an extension field.

2) Broadcast / Multicast

A broadcast association is a one-to-many relationship in which a time server disseminates time to a group of clients. Such scenarios are of particular interest in sensor networks [14, 15]. As in the unicast mode, NTS uses a MAC to protect the transmitted packets. However, the usage of a unique cookie would require that all members of the group know the cookie, which would allow any member of the group to masquerade as a legitimate server and to transmit false time. To avoid this situation, NTS applies the TESLA [16] protocol to verify the broadcast-type packets' authenticity. TESLA uses a one-way chain of keys, where each key is the output of a one-way function applied to the previous key in the chain. The server securely exchanges the last key of the chain – the trust anchor – with the clients, splits time into uniform intervals and assigns each key to an interval in reverse order. The server appends a MAC to each transmitted packet where the MAC is calculated with the key that corresponds to the current time interval. Furthermore, the transmitted packets also contain the disclosed key from a previous time interval. The clients have to buffer a received packet until the key associated with its time interval is disclosed, after which the clients are able to verify the MAC of the received packet a posteriori. Packets may only be buffered for later verification if they arrive in their intended time interval. To be able to verify this, clients have to be loosely time synchronized with their server prior to the initiation of a broadcast association. The NTS specification does not mandate an explicit approach to the initial time synchronization. However, in the case of NTP, [11] specifies that a client use a unicast association for the initial time synchronization and for the exchange of TESLA's disclosure schedule and trust anchor.

V. RESULTS

A. Achieved Security Goals

NTS completely meets most of the requirements of [4], as listed in Tab. 1. However, there are two points for discussion. NTS does not mandate procedures to authenticate and authorize a client to the server. However, it provides the necessary infrastructure – in the form of certificates with appropriate extensions – to supply this feature to an implementation. Furthermore, in a delay attack, an adversary does not have to alter a packet, therefore the attack cannot be detected by a cryptographic approach such as NTS. However, the time synchronization protocol itself can detect it by using multiple servers together with appropriate sanity checks [5].

TABLE I. COMPARISON OF NTS SPECIFICATION AGAINST SECURITY REQUIREMENTS IN RFC 7384 [4]

Requirement of RFC7384	Requirement level ^a	NTS
Authentication and authorization of server	MUST	OK
Authentication and authorization of client	MAY	Optional
Integrity protection	MUST	OK
Spoofing protection	MUST	OK
Protection from DoS attacks against the time protocol	SHOULD	OK
Replay protection	MUST	OK
Key freshness	MUST	OK
Security association	MUST	OK
Unicast and multicast associations	SHOULD	OK
Performance. No degradation in quality of time transfer	MUST	OK
Performance: lightweight computation, storage, bandwidth	SHOULD	OK
Protection against interception and delay attacks	MUST	Limited
Secure mode	MUST	OK

^a The interpretation of the requirement level is described in [17].

B. Formal Analysis

The development of the NTS specification is assisted by formal security analysis of the modeled protocol. This analysis is performed by means of model checking and theorem proving. Formal analysis has proven to be very useful for finding security vulnerabilities during the process of protocol specification [18].

For the analysis of an early version of the NTS specification, we employed a technique that separated the timing aspects from the protocol security aspects of the specification. We then utilized the model checker ProVerif to examine the security protocol aspects of the first NTS phase (authentication and key exchange) for unicast associations. With the help of ProVerif, we were able to discover two possible attacks on the protocol as specified in the third version of the draft's specification. Additionally, ProVerif enabled us to isolate the underlying weaknesses allowing those attacks and to derive countermeasures; for detail see [18]. We considered all of those discoveries in the further development of NTS. The draft's fifth version introduces the usage of the Cryptographic Message Syntax (CMS) [19]. The usage of the CMS represents a strong countermeasure to the second of the discovered attacks. Moreover, the specification has since then adapted changes in the cookie exchange that match countermeasures against the first of the attacks. In addition, the automated analysis provides formal security verification about the current, updated specification version.

The analysis with ProVerif left some questions about timing aspects open, and it only treated unicast associations. One currently still open problem is related to a scenario where, in authenticated broadcast, an attacker employs packet delay attacks to perform a small-step-big-step attack which, if left untreated, could break the security provided by TESLA. NTS therefore uses another, more rigorous check in addition to the clock lookup used in the TESLA protocol as a countermeasure against such attacks [20]. An automated verification of the security of this procedure is in progress.

VI. REALIZATION OF NTS

A. Network Time Protocol

NTS is specially designed to enable NTP to guarantee authenticity and integrity of its time synchronization packets.

1) Specification

NTS is currently in the process of being standardized within the IETF, the standardization body that also specified NTP. At the time of this writing, the specification still has to pass evaluation by the working group and the Internet Engineering Steering Group, although its state is quite mature.

2) Implementation

An implementation of NTS for NTP is currently being developed by the Network Time Foundation, the organization which is responsible for NTP's reference implementation. The first results of the implementation demonstrate that NTS-secured NTP does fulfill the security requirements of [4]. Including this code in NTF's reference implementation of NTP will significantly enhance the availability of secure time synchronization.

B. Precision Time Protocol

Currently, IEEE's P1588 working group is revising the 2008 specification of PTP. The working group aims to enhance PTP by an inherent security protocol that protects integrity and authenticity of the packets by means of a MAC. The security requirements are based on [4]. Two key management schemes are under consideration: a group key approach based on GDOI [21] and the TESLA approach, as used by NTS. The former aims to provide instant verification; the latter is to provide delayed verification of received packets.

VII. CONCLUSION

We present the Network Time Security specification, which is designed to protect time synchronization protocols. Apart from common security requirements, such as protection of packet integrity and authenticity, NTS also meets specific security requirements formulated for time synchronization protocols by the Internet Engineering Task Force in [4]. There is ongoing specification work with the aim of applying NTS to both the Network Time Protocol and the Precision Time Protocol. The work for the former specification is done within the IETF, whereas the aspects of the latter specification are considered by IEEE's P1588 working group. The specification of NTS was accompanied by a formal analysis of the underlying model of the protocol. This approach has proven to be useful as it revealed several security vulnerabilities in early specifications which have been mitigated in its subsequent editions. The work to include timing aspects in the formal analysis still has to be completed, but it is already well advanced.

REFERENCES

- [1] J. Burbank, W. Kasch, and D. L. Mills, "Network time protocol version 4: Protocol and algorithms specification," Request for Comments 5905, IETF RFC 5905, 2010.
- [2] R. Lapuh, Euramet countries' legal time regulations and practices: European Association of National Metrology Institutes (EURAMET), 2011.
- [3] IEEE, "Precision clock synchronization protocol for networked measurement and control systems," *IEEE Std 1588-2008 (Revision of IEEE Std 1588-2002)*, The Institute of Electrical and Electronics Engineers, Inc, 2008, p. 271.
- [4] T. Mizrahi, "Security requirements of time protocols in packet switched networks," Request for Comments 7384, IETF RFC 7384, 2014.
- [5] T. Mizrahi, "A game theoretic analysis of delay attacks against time synchronization protocols," in International IEEE Symposium on Precision Clock Synchronization for Measurement Control and Communication (ISPCS), 2012, San Francisco, CA, 2012, pp. 1-6.
- [6] J. Czyz, M. Kallitsis, M. Gharaibeh, C. Papadopoulos, M. Bailey, and M. Karir, "Taming the 800 pound gorilla: The rise and decline of NTP DDoS attacks," in Proceedings of the 2014 Conference on Internet Measurement Conference, Vancouver, BC, Canada, 2014, pp. 435-448.
- [7] D. L. Mills, and B. Haberman, "Network time protocol version 4: Autokey specification," Request for Comments 5906, IETF RFC 5906, 2010.
- [8] D. L. Mills. "NTP security analysis," May, 2012, [Online]. Available: <https://www.eecis.udel.edu/~mills/security.html>.
- [9] S. Röttger, "Analysis of the NTP autokey procedures," unpublished.
- [10] K. Teichel, D. Sibold, and S. Roettger, "Network time security," Internet-Draft, Internet Engineering Task Force, 2016.
- [11] D. Sibold, S. Roettger, and K. Teichel, "Using the network time security specification to secure the network time protocol," Internet-Draft, Internet Engineering Task Force, 2016.
- [12] D. Sibold, S. Roettger, K. Teichel, and R. Housley, "Protecting network time security messages with the cryptographic message syntax (CMS)," Internet-Draft, Internet Engineering Task Force, 2016.
- [13] A. J. Menezes, P. C. Van Oorschot, and S. A. Vanstone, *Handbook of applied cryptography*, Boca Raton: CRC Press, 1997.
- [14] K. Sun, P. Ning, and C. Wang, "TinySeRSync: Secure and resilient time synchronization in wireless sensor networks," in Proceedings of the 13th ACM conference on Computer and communications security, Alexandria, Virginia, USA, 2006, pp. 264-277.
- [15] X. L. Yin, W. D. Qi, and F. Fu, "ASTS: An agile secure time synchronization protocol for wireless sensor networks," 2007 International Conference on Wireless Communications, Networking and Mobile Computing, Vols 1-15, pp. 2808-2811, 2007.
- [16] A. Perrig, R. Canetti, D. Song, D. Tygar, and B. J. Briscoe, "Timed efficient stream loss-tolerant authentication (TESLA): Multicast source authentication transform introduction," Request for Comments 4082, IETF RFC 4082, 2005.
- [17] S. O. Bradner, "Key words for use in RFCs to indicate requirement levels," Request for Comments 2119, IETF RFC 2119, 1997.
- [18] K. Teichel, D. Sibold, and S. Milius, "First results of a formal analysis of the network time security specification," in Security Standardisation Research: Second International Conference, SSR 2015, Tokyo, Japan, 2015, pp. 218-245.
- [19] R. Housley, "Cryptographic message syntax (CMS)," Request for Comments 5652, IETF RFC 5652, 2009.
- [20] K. Teichel, D. Sibold, and S. Milius, "An attack possibility on time synchronization protocols secured with TESLA-like mechanisms," unpublished.
- [21] T. Hardjono, S. Rowles, and B. Weis, "The group domain of interpretation," Request for Comments 6407, IETF RFC 6407, 2011.

New Approaches in Deep Laser Cooling of Magnesium Atoms for Quantum Metrology

Oleg N. Prudnikov,
Valeriy I. Yudin
Novosibirsk State University (NSU)
Novosibirsk, Russia
Email: oleg.nsu@gmail.com

Anatoly E. Bonert,
Denis V. Brazhnikov,
Andrey N. Goncharov,
Alexey V. Taichenachev
Institute of Laser Physics SB RAS
Novosibirsk, Russia
Email: brazhnikov@laser.nsc.ru

Abstract—We theoretically describe two approaches aimed at solving the existing problem of deep laser cooling of neutral magnesium atoms. The first approach based on using optical molasses with orthogonal linear polarizations of light waves, while the second one implies exploiting “nonstandard” magneto-optical trap composed of elliptically polarized (in general) light waves. The widely used semiclassical approximation based on the Fokker-Planck equation as well as the full quantum treatment (with full account of the recoil effect) are applied for theoretical analysis. The results are crucial for metrological and some other applications of cold atoms.

Keywords—laser cooling; magneto-optical trap; magnesium; optical molasses; recoil effect; quantum metrology

I. INTRODUCTION

Laser cooling and trapping of atoms play an important role in modern quantum metrology of time, which has been rapidly developing in recent years [1]. Modern time standards are based on the frequency standards, which determine their stability and accuracy to a considerable degree. Alkaline-earth and alkaline-earth-like atoms such as Yb, Ca, Sr, Hg, and Mg are among the main candidates for creating the new-generation of frequency standards, based on so-called "optical lattices". This relatively young direction of designing the frequency standards has already demonstrated the values of fractional instability and inaccuracy on extremely low levels down to 10^{-18} [2]. Magnesium atom has some advantages over the other candidates [3]. Unfortunately, deep laser cooling of magnesium atoms close to the recoil energy limit (several microkelvins) is the intricate problem in contrast to the other elements. The minimum temperature of a magnesium cloud that has been obtained by laser cooling is about 500 μ K [4] that is too far from the desirable value.

In the recent experiments [5,6] researchers managed to obtain magnesium atoms owing temperature about several microkelvins and confined them in the lattice. However, velocity-selecting cooling technique in a shallow dipole trap was applied immediately after the magneto-optical trap stage (MOT), which led to great loss in number of atoms ($\sim 0.01\%$

from the initial number in the MOT). At the same time, temperature of a cloud in the MOT was not lower than 1 mK. Therefore, we can state that the problem of deep cooling of magnesium atoms by means of laser radiation is still unsolved. Moreover, increasing ultracold atomic number has principal importance for many applications of cold atoms.

Here we propose two approaches for solving the problem of deep laser cooling of magnesium atoms. Our theory analyzes the dipole transition $3^3P_2 \rightarrow 3^3D_3$ ($\lambda \approx 383.3$ nm), which was also used in the experiments by our colleagues from Hanover [5,6]. Basing on the numerical calculations we try to understand the origins of the existing difficulties.

II. PROBLEM STATEMENT

For short, we do not provide here the detailed formalism of our theory, which can be found in [3,7]. Let us just note that the standard quantum-mechanical approach for studying kinetics of atoms under electromagnetic fields based on the density matrix $\hat{\rho}$ is exploited. In the coordinate two-point representation we have [7,8]

$$\frac{\partial}{\partial t} \hat{\rho}(z_1, z_2, t) = -\frac{i}{\hbar} \left[\hat{H}(z_1, t) \hat{\rho} - \hat{\rho} \hat{H}(z_2, t) \right] + \hat{\Gamma} \{ \hat{\rho} \} \quad (1)$$

with the Hamiltonian $\hat{H}(z, t) = \left(\hat{p}^2 / 2M \right) + \hat{H}_0 + \hat{V}(z, t)$, where the first term is the operator of kinetic energy of an atom of mass M , \hat{H}_0 describes intratomic degrees of freedom and \hat{V} corresponds to the atom-field dipole interaction. Light component of the field is composed of counterpropagating waves with equal amplitudes E_0 and frequencies ω (Fig. 1). The magnetic component is a static field that in case of MOT can be approximated by the linear dependence in the trap's center with $b_0 = dB/dz$ the gradient. The linear operator functional $\hat{\Gamma} \{ \hat{\rho} \}$ in (1) describes relaxation processes in an atom.

This work has been financially supported by the Russian Foundation for Basic Research (grants nos. 15-02-06087, 15-32-20330, 14-02-00806, 14-02-00712) and by Presidium of the Siberian Branch of RAS.

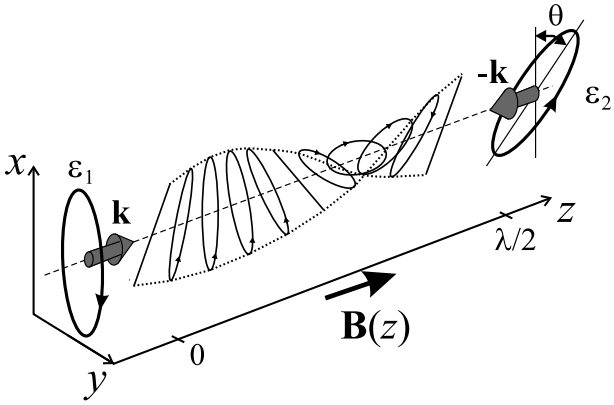


Fig. 1. Configuration of the electromagnetic field composed of the counterpropagating light waves with elliptical (in general) polarizations and a static magnetic field. Here $\varepsilon_{1,2}$ are the ellipticities ($|\varepsilon| \leq \pi/4$), θ is the angle between main axes of the polarization ellipses.

We are interested in calculating the steady-state average kinetic energy of an atom, which can be evaluated with the help of the formula:

$$E_{kin} = \int_{-\infty}^{+\infty} p^2 f(p) dp, \quad (2)$$

where the linear momentum of an atom p is taken in units of the recoil momentum $\hbar k$, while the energy in terms of the recoil energy $E_{rec} = \hbar^2 k^2 / 2M = \hbar \omega_{rec}$ with ω_{rec} the recoil frequency. Function $f(p)$ in (2) is the space-averaged atomic momentum distribution in steady state that can be found from solving the main equation (1).

The quantum treatment with full account of the recoil effect can be very sophisticated task in many cases of kinetics of atom under a light field. Besides, in many cases this accurate approach does not allow finding the qualitative physical understanding of processes occurring with atoms under a light field, because it does not include such classical concepts as the light force, the atomic diffusion or the optical potential. All these terms appear in so-called semiclassical approach that often simplifies the quantum treatment to a considerable degree.

Basic equation in the semiclassical approach can be derived by reducing the exact quantum kinetic equation for the density matrix (1) by decomposition technique on small parameter $\hbar k / \Delta p \ll 1$ to the second-order terms (with Δp the typical width of stationary linear momentum distribution). This procedure is well known (e.g., see [9]). Then one can come directly to the equation for the center-of-mass Wigner function $f(p, z, t)$ of an atom – the Fokker-Planck equation, which in steady state takes the form:

$$\frac{p}{M} \frac{\partial}{\partial z} f(z, p) = \left[-\frac{\partial}{\partial p} F(z, p) + \frac{\partial^2}{\partial p^2} D(z, p) \right] f(z, p). \quad (3)$$

Here, $F(z, p)$ is the laser-field force on the atom, $D(z, p)$ is the atom diffusion in the light field. In many studies the localization effects are often neglected, i.e. one can assume $F(p) = \langle F(z, p) \rangle_z$ and $D(p) = \langle D(z, p) \rangle_z$, where $\langle \dots \rangle_z$ is space averaging. Moreover, the slow atoms approximation is also widely used (for instance, see [9,10]), which also allows one using the final linearizing assumptions $F(p) \approx -\alpha p / M$ and $D(p) \approx D_0$ with α the friction coefficient. After all the approximations have been done, one can come to the simple Maxwellian-like momentum distribution $f(p) \propto \text{Exp}[-p^2 / 2M k_B T]$ with k_B the Boltzmann constant. In this simple case the atomic cloud can be characterized by the effective temperature $T = D_0 / k_B \alpha$.

III. OPTICAL MOLASSES

First of all, we focus on the electromagnetic field composed of two counterpropagating laser waves with opposite circular polarizations ($\sigma^+ \sigma^-$ configuration). Probably, since it was proposed in [11] as the effective configuration for laser cooling, it is used everywhere in a MOT (in 3D case, of course, one have three pairs of σ^+ and σ^- waves). In this section we neglect the influence of a static magnetic field on the kinetics of atoms assuming the field to be sufficiently small at the scale of a cloud in the trap. This influence will be considered in the next section. Also, we do not limit our analysis by the approximations mentioned above to understand the kinetics of magnesium atoms in wide range of light field intensities and frequency detunings. Indeed, in some regimes it is not correct to exploit the linear approximations for $F(p)$ and $D(p)$. According to that the momentum distribution may be very far from just Maxwellian-like (e.g., see [12]). Therefore, in general we must use the energy characteristic of cold atoms defined by (2), instead of the term "temperature". However, sometimes we still use the term "temperature" that can be defined just via relation $E_{kin} = (1/2) k_B T$.

Now let us compare the results of quantum and semiclassical treatments obtained by numerical solutions of (1) and (3), respectively. Fig. 2 shows the average kinetic energy of an atom as the function of light field intensity (at the figure $\delta = \omega - \omega_0$ is the detuning of the laser radiation frequency ω from the atomic transition frequency ω_0 and $\gamma \approx 2\pi \times 26.7$ MHz is the spontaneous relaxation rate of the excited state 3^3D_3). The semiclassical approach (dashed line) gives the minimum kinetic energy of an atom at the level of $E_{min} \approx 30 \times E_{rec}$, that is several times smaller than the estimated Doppler limit for this transition $E_D \approx 87.5 \times E_{rec}$. The corresponding effective temperature is about 150 μ K. This is rather far from the desirable range of values ($\approx 1-10$ μ K). However, strictly speaking, the semiclassical approximation is not valid in our case. Indeed, some of the basic requirements of the semiclassical approach can be violated even under the regular experimental conditions of laser cooling (e.g., see [3]). In particular, a typical width Δp of the momentum distribution $f(p)$ can be of the order $\hbar k$. Therefore, we have to treat the problem with full account of the recoil effect to find out the optimal conditions of laser cooling of magnesium atoms.

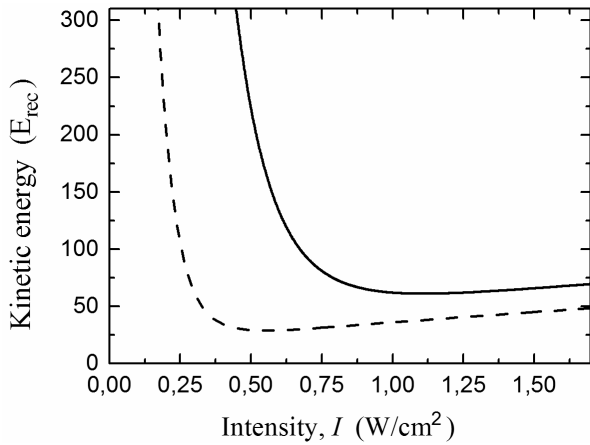


Fig. 2. Average kinetic energy of an atom as the function of light-field intensity: Comparison of the results of semiclassical (dashed line) and quantum (solid line) treatments at $\delta = -5\gamma \approx -2\pi \times 130$ MHz.

Solid line on the Fig. 2 corresponds to the quantum treatment. It shows the result for atomic energy just a little bit smaller than the Doppler limit: $E_{min} \approx 62 \times E_{rec}$ and $T \approx 310$ μ K. So, we can state, that the quantum treatment gives the minimum kinetic energy of an atom noticeably higher than the semiclassical one. Fig. 3 helps us to understand the physical origins of this difference. In particular, the figure shows that in some regimes the semiclassical and quantum treatments give very different results for momentum distribution of cold atoms: the quantum calculations demonstrate very small ultracold atomic fraction (the atoms with $p \sim \hbar k$) in comparison with the semiclassical one. Fortunately, there are two ways at least that can be chosen for overcoming this problem.

The first way consists in using optical molasses with orthogonal linear polarizations of the laser waves (*lin* \perp *lin* configuration), instead of the conventional $\sigma^+\sigma^-$ configuration. We have calculated the average kinetic energy of an atom using the quantum treatment and the results are show on Fig. 4. It demonstrates much lower minimum kinetic energy than in case of $\sigma^+\sigma^-$ configuration as in a conventional MOT.

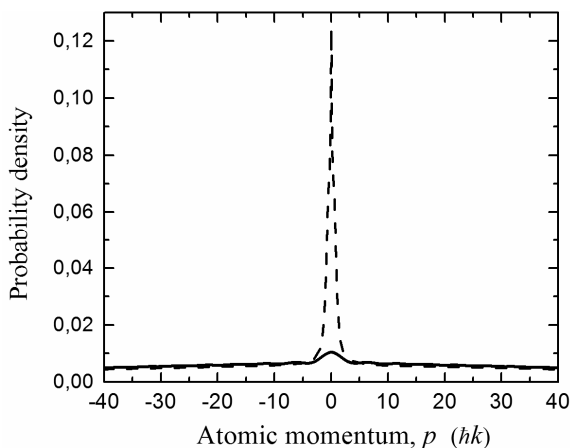


Fig. 3. Momentum distributions of magnesium atoms: comparison of semiclassical (dashed line) and quantum (solid line) treatments at $\delta = -5\gamma$ and $I \approx 20$ mW/cm².

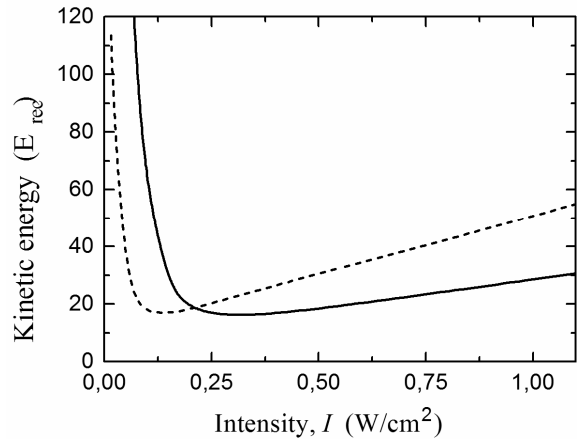


Fig. 4. Quantum calculations of average kinetic energy of a magnesium atom under the *lin* \perp *lin* light-field configuration calculated on the basis of quantum treatment at $\delta = -5\gamma$ (solid) and $\delta = -2\gamma$ (dashed).

The minimum kinetic energy of atoms as low as $16 \times E_{rec}$ can be obtained, which is corresponds to the effective temperature of about 80 μ K. This value is several times smaller than in the case of Fig. 2 (solid). At the same time, it is necessary to cool atoms down to several microkelvins. This problem can be solved by the velocity-selective cooling as in [5,6]. At that, the special conditions must be satisfied before the velocity-selective cooling stage to save the most of ultracold atoms in a cloud. For instance, the calculations demonstrate that about 60% of atoms can be collected in the ultracold fraction ($p \sim \hbar k$) under the light intensity per beam in the range 70–200 mW/cm² depending on the frequency detuning.

To generalize the obtained results we have also calculated the kinetic energy of atoms for various light waves ellipticities and angles θ . Here, for short, the results are not shown, but we would like to note that the low temperatures (< 100 μ K) can be also obtained in *lin* $-\theta$ *lin* configuration with $\theta \neq \pm\pi/2$. This fact is crucial for the next section where we are analyzing a nonstandard MOT, because a magneto-optical potential is absent under $\theta = \pm\pi/2$.

IV. NONSTANDARD MAGNETO-OPTICAL TRAP

As it has been shown in the previous section, the laser field configuration *lin* \perp *lin* accompanied by the velocity-selective-cooling technique can be used for effective 1D cooling of magnesium atoms down to $T \sim 1$ μ K. However, that configuration does not provide any deep potential for accumulating and keeping the cold magnesium atoms for a long time (hundreds of milliseconds and more). If one need to collect and cool atoms during the seconds, a deep trapping potential is required. Fortunately, the *lin* $-\theta$ *lin* ($\theta \neq \pm\pi/2$) configuration provides low temperatures as well. In particular, we take $\theta = -\pi/4$. Besides, this configuration allows us using the static magnetic field as in a conventional magneto-optical trap. Here we call such the trap as "nonstandard" magneto-optical trap (NMOT) to distinguish it from that used everywhere (with $\sigma^+\sigma^-$ configuration). The angle θ has a negative sign to make the magneto-optical force negative, which is necessary to trap the atoms in a MOT.

In this section we are working with the semiclassical approach for studying the kinetics of magnesium in the NMOT in terms of magneto-optical force F_B and potential U . These quantities assumed to be averaged over fast space oscillations ($\sim \lambda$) that leads only to slow z -variations due to the gradient of a magnetic field. In other words, we analyze F_B and U as the functions of the Larmor frequency Ω_g , which is linearly proportional to the magnetic field. The radius r of the laser beams defines the acting area of the magneto-optical potential. So, the z -coordinate takes the values $|z| \leq r$. The optical potential depth can be calculated as follows:

$$U_0 \approx -\frac{r}{\Omega_g(r)} \int_0^{\Omega_g(r)} F_B^{(0)}(\Omega_g) d\Omega_g. \quad (4)$$

Here $F_B^{(0)}$ is the magneto-optical force acting on an atom at the rest. For numerical calculations in this section we take $r = 0.5$ cm. As the radius fixed and the g -factor of the state 3P_2 equals to $3/2$, the boundary value $\Omega_g(r) = \gamma$ corresponds to the magnetic field gradient $b_0 \approx 24.1$ G/cm.

As one can see from Fig. 5a, the magneto-optical force is strongly nonlinear on the B -field and even can be repulsive in some regions. It is also seen from the figure that the force demonstrates significant sensitivity to the ellipticities of the waves. Corresponding magneto-optical potential depth at the edge of the trap is shown on Fig. 5b. Even at the low magnetic-field gradients ($\Omega_g \sim 0.1\gamma$ at the trap's edge) the depth is quite enough for confining the magnesium atoms right after the first-stage laser cooling with the help of conventional MOT operating on $^1S_0 \rightarrow ^1P_1$ dipole transition with $\lambda = 285$ nm. In particular, after the first stage $T \approx 2-3$ mK, and $E_{kin} \approx T/T_{rec} \approx (400-600) \times E_{rec}$, while the potential depth $\sim (10^5-10^6) \times E_{rec}$.

We should note that the large magnetic-field gradients are not only unnecessary for the second-cooling stage (NMOT), but they must be avoided, because there is a critical field, when the force changes its sign. The calculations demonstrates that the gradients must not exceed several tens of G/cm².

REFERENCES

- [1] F.Riehle, Frequency Standards: Basics and Applications. Weinheim: Wiley, 2004.
- [2] B.J. Bloom, T.L. Nicholson, J.R. Williams, S.L. Campbell, M. Bishof, X. Zhang, W. Zhang, S.L. Bromley, and J.Ye, "An optical lattice clock with accuracy and stability at the 10^{-18} level", Nature, vol. 506, p. 71, 2014.
- [3] O.N. Prudnikov, D.V. Brazhnikov, A.V. Taichenachev, V.I. Yudin, A.E. Bonert, R.Ya. Il'enkov, and A.N. Goncharov, "Quantum treatment of two-stage sub-Doppler laser cooling of magnesium atoms", Phys. Rev. A, vol. 92, p. 063413, 2015.
- [4] T.E. Mehlstäubler, K. Moldenhauer, M. Riedmann, N. Rehbein, J. Friebe, E.M. Rasel, and W. Ertmer, "Observation of sub-Doppler temperatures in bosonic magnesium", Phys. Rev. A, vol. 77, p. 021402(R), 2008.
- [5] M. Riedmann, H. Kelkar, T. Wübena, A. Pape, A. Kulosa, K. Zipfel, D. Fim, S. Rühmann, J. Friebe, W. Ertmer, and E. Rasel, "Beating the density limit by continuously loading a dipole trap from millikelvin-hot magnesium atoms", Phys. Rev. A, vol. 86, p. 043416, 2012.

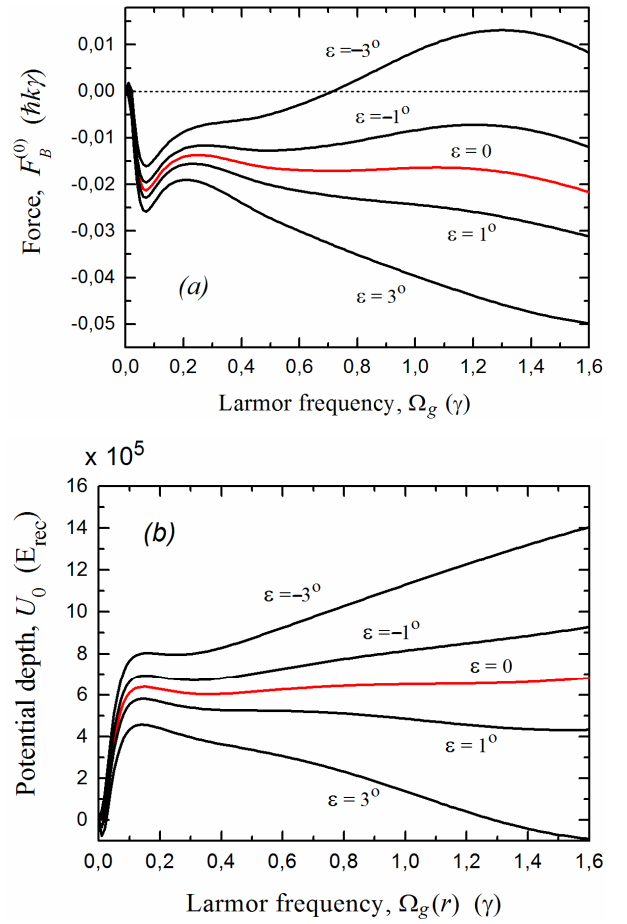


Fig. 5. (a) Magneto-optical force (in $\hbar k \gamma$ units) and (b) potential depth in the NMOT composed of laser waves with $\epsilon_1 = -\epsilon_2 = \epsilon$ and $\theta = -\pi/4$ as the function of magnetic field (the Larmor frequency of the ground atomic state in γ units). Red line corresponds to the linear polarizations of counterpropagating laser beams. Other parameters: $\delta = -\gamma$, $I = 100$ mW/cm².

- [6] A.P. Kulosa, D. Fim, K.H. Zipfel, S. Rühmann, S. Sauer, N. Jha, K. Gibble, W. Ertmer, E.M. Rasel, M.S. Safronova, U.I. Safronova, and S.G. Porsev, "Towards a Mg lattice clock: Observation of the $^1S_0 \rightarrow ^3P_0$ transition and determination of the magic wavelength", Phys. Rev. Lett., vol. 115, p. 240801, 2015.
- [7] O.N. Prudnikov, R.Ya. Il'enkov, A.V. Taichenachev, A.M. Tumaikin, V.I. Yudin, "Steady state of a low-density ensemble of atoms in a monochromatic field taking into account recoil effects", J. Exp. Theor. Phys., vol. 112, p. 939, 2011.
- [8] A.P. Kazantsev, G.I. Surdutovich, and V.P. Yakovlev, Mechanical action of light on atoms. London, Singapore: World Scientific, 1990.
- [9] V.G. Minogin, "Kinetic equation for atoms interacting with laser radiation", J. Exp. Theor. Phys., vol. 52, p. 1032, 1980.
- [10] J. Dalibard and C. Cohen-Tannoudji, "Laser cooling below the Doppler limit by polarization gradients: simple theoretical models", J. Opt. Soc. Am. B, vol. 6, no. 11, p. 2023, 1989.
- [11] J. Dalibard, S. Reynaud, and C. Cohen-Tannoudji, "Potentialities of a new $\sigma_+ \sigma_-$ laser configuration for radiative cooling and trapping", J. Phys. B: At. Mol. Opt. Phys., vol. 17, p. 4577, 1984.
- [12] D.V. Brazhnikov, A.E. Bonert, A.N. Goncharov, A.V. Taichenachev, and V.I. Yudin, "Deep laser cooling of magnesium atoms using $^3P_2 \rightarrow ^3D_3$ dipole transition", Laser Phys., vol. 24, p. 074011, 2014.

Optical Two-Way Timing System for Space Geodesy Applications

Jan Kodet^{1,3}, Ulrich Schreiber¹

¹Technische Universität München, Wettzell Observatory
93444 Bad Kötzing, Germany
kodet@fs.wettzell.de

Petr Panek²

²Institute of Photonics and Electronics
Academy of Sciences of the Czech Republic,
Prague, Czech Republic

Ivan Prochazka³

³Czech Technical University in Prague, Prague, Czech
Republic

Benjamin Männel⁴

⁴Institute of Geodesy and Photogrammetry ETH Zurich,
Switzerland

Torben Schüler⁵

⁵Federal Agency for Cartography and Geodesy,
Germany

Abstract—Until now, time itself is not an observable in space geodesy. The major reason for this fact is the considerable difficulty to keep track of the phase of the clock oscillation between the point of origin and the point of the measurement. However, if geodesy will attempt to provide a reference frame fully based on general relativity, a proper treatment of time is mandatory. The Geodetic Observatory Wettzell is currently in the process to modernize the timing system such that the phase of the master clock can be established at all times. The ultra-short pulses of an optical frequency comb are transporting both time and frequency from the master clock of the observatory to the individual space geodetic techniques, namely Very Long Baseline Interferometry (VLBI), Satellite Laser Ranging (SLR) and Global Navigation Satellite System (GNSS), using a two-way approach. In order to verify the functionality of this system not only in sense of delay stability but also accuracy, we have developed a new TWTT system based on the exchange of timing signal via standard optical telecommunications Small Form-factor Pluggable (SFP) transceivers to transfer timing information between two or more terminals with the accuracy below 1 ps via optical fibers of a length of up to several tens of kilometers. The heart of the measurement device is an event timing module using surface acoustic wave filters as a time interpolator, which allows the registration of the times-of-arrival of electrical pulses with sub-picosecond timing resolution, linearity and stability. These pulses are derived from the optical signal, which is used for the communication between the terminals. Great care was taken in order to minimize terminal internal delays instability, which can be the result of temperature changes inside terminals. The design, applications and the first experiments at GO Wettzell will be discussed.

Keywords—Two Way Optical Time Transfer; time distribution; GNSS; GPS; VLBI

I. INTRODUCTION

The objective of this work is an improvement and establishment of new ties between the space geodetic techniques. We are taking the variety of co-located instruments at the Geodetic Observatory Wettzell (GO Wettzell), which operates three radio-telescopes used for geodetic Very Long Baseline Interferometry (VLBI), two Satellite Laser Ranging (SLR) telescopes and number of Global Navigation Satellite Systems (GNSS) receivers.

A lot of work is currently focused on combining different observation techniques. The significant improvement of the measurement can be achieved if the clocks at different space geodetic techniques are synchronized and the internal instrumental delays are held constant. This was studied for example in case of GNSS, where the receiver clocks are typically estimated epoch-wise. However, if the receivers clocks would be synchronized or at least high coherent one can apply an appropriate clock model for high-stability receivers and in view of the strong correlation between the station height and clock parameters, significant improvement of positioning results can be achieved. For such a clock, the kinematic solution can be significantly improved in the less accurate vertical direction. Namely, by a factor of 2 to 3 [1].

Even greater improvement would be achieved if the GNSS solution is combined with VLBI, because the current VLBI technology provides only few observations per hour in contrast to GNSS. The previous work [2] focuses on development of a software package combining VLBI and GNSS solution. This software was further used in the study of GNSS and VLBI combination for inter-continental frequency transfer based on CONT11 observation campaign, which proved VLBI improvement using real observation data [3]. They are

requiring that further calibration and monitoring of internal delays would help to improve the solution.

Therefore as a part of the current research and development program of the GO Wettzell, we are in the transition from a purely electrical to an actively stabilized two-way optical time and frequency distribution system. In the literature a lower limit of $\Delta f/f$ of 10^{-17} and below for the frequency transfer has already been demonstrated [4], making this a viable goal. The concept of the timing signals distribution at GO Wettzell is as follows, see Fig. 1. The Maser reference frequency will be used as our main frequency source, which will be connected to an optical frequency comb, whose repetition rate is stabilized by the maser frequency. The optical pulses are distributed at the observatory campus in a star topology through optical fibers. The propagation delay between end terminals is held constant in such a way, that part of the signal is reflected by the terminal back and using optical correlation and optical delay line the delay is kept constant. A combination of an ordinary fiber and a conjugate fiber ensures that the pulse width of the comb pulses are not degraded by dispersion. The pulse train of optical comb of 100 MHz transfers the frequency and time between different buildings and elevation cabins of the radio-telescopes. The output signal of the photo-detector synchronizes a set of low noise electronics to generate a set of three frequencies 5, 10 and 100 MHz. The time is extracted from the optical pulse train by gating out every millionth pulse. The gating signal is transferred to the back terminal using different wavelength and using the same optical fiber. To ensure that the distributed 1 PPS signal will be always the same in relation to the master clock 1 PPS signal, the selected pulse from optical comb will be synchronized with the master clock 1 PPS. At the time of writing this paper the timing system is in development by Menlo Systems, GmbH.

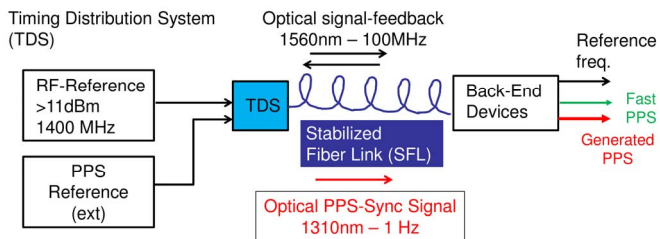


Fig. 1. The schematic diagram of new timing system at Geodetic Observatory Wettzell, explanation in the text. The diagram is reprinted with permission of Menlo Systems, GmbH.

The new timing system allows to treat time as a new and independent tie between the different space geodetic techniques. Closure measurements over several measurement systems using a clock as the origin and endpoint reveal even small time delays thus going beyond the currently applied calibration schemes. Fig. 2 outlines the principle of closure measurements in the techniques of space geodesy by using a common clock between two SLR stations and two radio-telescopes. The sum of all delays between the clock and the target must be the same at both observation paths after considering all the delays along the path of signal propagation.

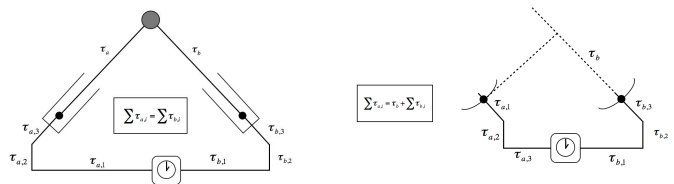


Fig. 2. Using two or more measurement systems of the same technique with a common clock provides equal delays in the time regime if all systematic biases are correctly established. The illustration shows the case for SLR on the left and VLBI on the right side.

II. TWO WAY OPTICAL TIME TRANSFER

A. System Design Description

In the past, a lot of effort went into the development of a very precise two-way time transfer (TWTT) using a coaxial cable as the transmission link [5] with the aim to identify unaccounted system delays at the Geodetic Observatory Wettzell. The main disadvantage of this approach is a rather steep increase in the time transfer error with the length of the link due to the propagation loss at high frequencies. It provides good results for links of the length up to several hundred meters, but for distances of several kilometers accuracy better than 100 ps cannot be expected even though high performance cable is used.

Besides improving of the stability of timing signals distribution at Geodetic Observatory Wettzell, the new timing system must exceed the possibility to be able to measure absolute time delays between the distribution points and verify the long term stability of the delays. Therefore, we have redesigned the TWTT resolving the limitations by using optical telecommunications technology. With the aim to enlarge the area where the time transfer with picosecond accuracy can be ensured, we started to work on a new Two-Way Optical Time Transfer (TWOTT) system implementing standard small form-factor pluggable (SFP) optical transceivers to transfer timing information between two or more terminals. This system will be besides used for verification of implemented timing distribution at the observatory. During the design we focused on the potential application where comparisons of two or more clocks deployed in a relatively small area are required. These cases are typically observatories and large laboratory campuses where the typical length of the optical links is no longer than several kilometers. Thanks to this limitation, we do not need to consider effects like the fiber chromatic dispersion, large link attenuation, and relativistic effects [6].

On the other hand, when relatively short fibers are considered and the above-mentioned effects can be neglected, the dominant source of systematic measurement errors will be the temperature dependence of internal delays within the TWOTT terminal units. The TWOTT technique perfectly eliminates the influence of the large link delay including its variations, but it does not suppress the impact of some partial internal delays within the terminal units.

B. Achieved Results

The developed system was tested in series of common clock experiments [7]. The reference frequency and 1 PPS signals were passively split and connected into two terminals. A 20 m single mode optical fiber was used as a transmission link between the terminals. At the first experiments the temperate calibration of the terminals was evaluated during dedicated measurements. The temperatures inside the terminals were measured using built in temperature sensors situated inside the SFPs.

The resulting temperature dependency of time the difference was established in another experiment when the temperature of both terminals was first stabilized and then slow temperature change was introduced in one of the terminals. The resulting temperature dependency before and after temperature compensation is in Fig. 3.

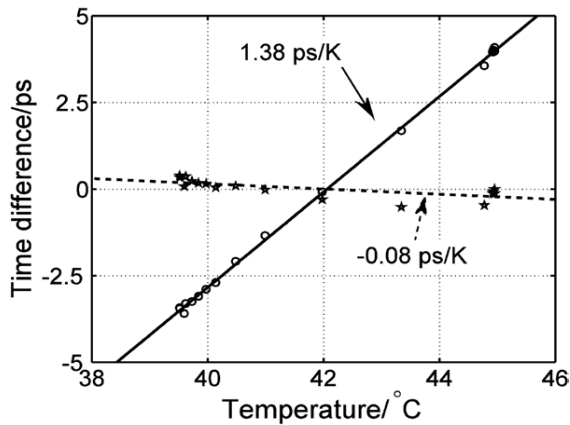


Fig. 3. Resulting temperature dependence coefficients without temperature correction (solid line) and with temperature correction (dashed line) are 1.38 ps K^{-1} and -0.08 ps K^{-1} , respectively.

The time transfer stability characterized by TDEV computed from the results of the 1 s comparisons is plotted in Fig 3. The TDEV curve is composed of three regions. In the first region, the TDEV follows the white phase noise slope up to averaging intervals of several tens of seconds. In this region the influence of the 1PPS time mark jitter is suppressed by filtering and the TDEV represents the optical time transfer noise only. On the other hand, in the third region, which starts around 1 h, the 1PPS jitter filtering is no longer effective and the TDEV represents mainly the 1PPS jitter, which is dominant with respect to the time transfer noise. In the transition region the TDEV is leveling around 50 fs.

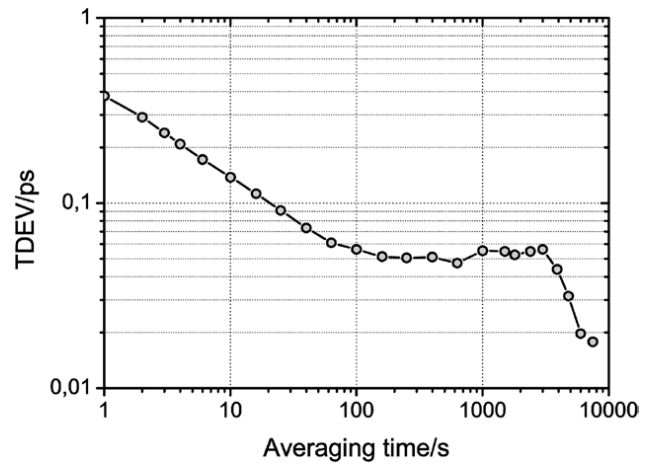


Fig. 4. Time transfer stability characterized by TDEV computed from the results of 1 s comparisons.

Since for a lot of applications it is not necessary to know timing stability evaluated using TDEV, we have analyzed the same data set also with Allan Deviation (ADEV) which is usually used for evaluation of frequency stability. The resulting frequency transfer stability characterized by ADEV computed from the same data set as used for TDEV evaluation is in Fig 4. The ADEV plot follows the white/flicker phase noise slope in the entire considered range of averaging intervals up to 10 000 s where the ADEV falls under 10^{-16} . We have compared the TWOTT ADEV with ADEV computed from results of comparison of two H-masers [8], and ADEV of comparison based on VLBI measurements.

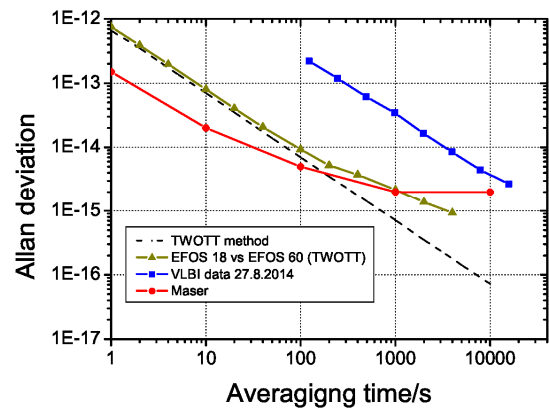


Fig. 5. Frequency transfer stability characterized by Allan deviation (ADEV) computed from results of 1 s comparisons compared with ADEV of commercially available H-Maser, real comparison of two masers and VLBI solution comparing two H-masers at GO Wettzell.

One can see that the TWOTT ADEV is worse than the stability of the H-Maser at time scale 1 s to 200 s. That means that the measurement method is adding some noise into the

frequency instability evaluation. However for averaging times from 200 s up to 10000 s the H-Maser stability is starting to bend and TWOTT method is better and therefore suitable for comparing H-Masers, which was experimentally proved. In the next we will focus on one of the possible application and it is comparing two H-Masers using TWOTT method and VLBI measurement. The goal of this work is to investigate unaccounted system delays between radio-telescopes. From Fig. 4 it is evident that TWOTT method has better ADEV then VLBI, therefore investigating clock behavior between two radio-telescopes using TWOTT is legitimate.

III. COMPARING H-MASERS WITH TWOTT AND VLBI

The two terminals running TWOTT are currently installed at 20 m radio-telescope Wettzell (RTW) and at the new TWIN VLBI at GO Wettzell since September 2015. Each of the radio-telescopes is connected to a different H-maser located in the radio-telescope basement. The baseline between the radio-telescopes is 123 m. Up to now we have collected more than 100 days of TWOTT measurement data covering 18 VLBI sessions.

We did two VLBI data evaluations using two different software packages. The first VLBI analysis was performed using the Levika software [9] and was focused on the local VLBI baseline at GO Wettzell. We put some effort to overcome the problem that VLBI provides only few observations per hour. Therefore, we used local tie measurement and fixed the coordinate positions of both two telescopes. Putting constrains on the ionosphere and the troposphere one can conclude that these delays are the same for both telescopes, which is our case. Under these assumptions, we were able to estimate the VLBI clock difference from each single quasar observation. This gave us the unique chance to analyze VLBI clocks during 24 hour sections with the highest possible resolution.

The second VLBI processing was done using a project version of the Bernese GNSS Software [10] capable to process VLBI observations. In the processing we estimate station coordinates (24 h), tropospheric wet zenith delays (piecewise-linear, 2 h), tropospheric gradients (24 h), receiver clock offsets (piece-wise linear, 2 h), and Earth Rotation Parameters (24 h). The datum definition was realized by a no-net-translation and no-net-rotation constraint applied over a sub-network of the VLBI stations. Clock jumps were considered as they were noticed in the session's Analyst Comments. The processing is currently done session-wise and automatized with the Bernese Processing Engine. However, compared to the local processing with Levika the global solutions are derived from different networks with changing data amount and noise levels. Therefore, a larger scatter between individual sessions can be expected.

The clock difference measured using TWOTT and VLBI parameter estimation is shown in Fig. 6.

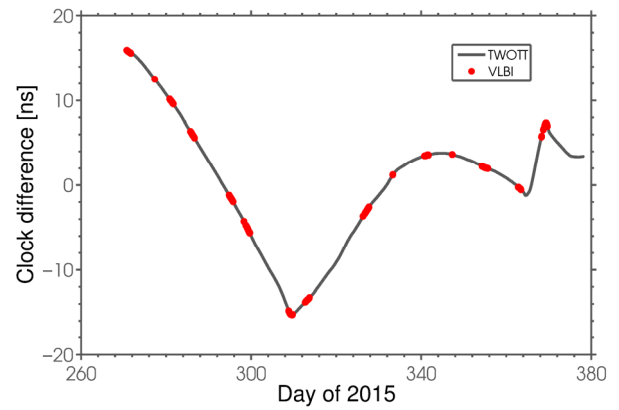


Fig. 6. The clock difference between 20 m RTW and new TWIN radio-telescope at GO Wettzell, the common linear trend was removed.

The problem which occurred during VLBI data evaluation is that the VLBI solution is not smooth in the entire plotted time span. For each VLBI section different uncalibrated instrumental delays can be found. These station and session-dependent delays are absorbed by the clock estimates. Therefore, the clock estimates differs from the real clock behavior and jumps between the sessions in order of tens of nanoseconds can be found. We removed these delays manually. At the first sight the data are close to each other, however when we distract both solution one can see discrepancies between the measurement technique reaching ± 50 ps and 20 ps rms, see Fig. 7.

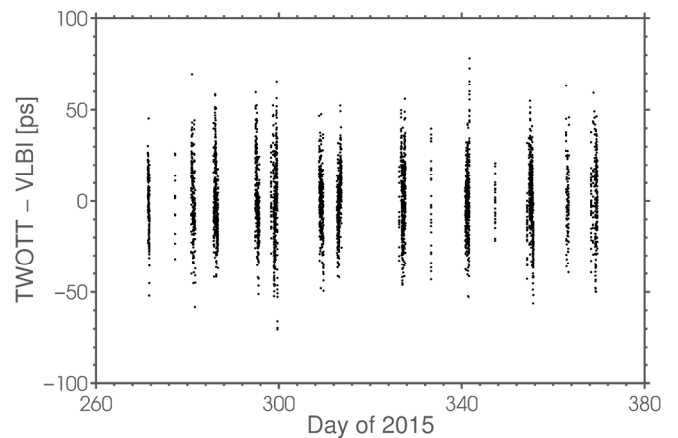


Fig. 7. Difference between TWOTT and local VLBI network.

During measurement there is visible trend deviation between both clock comparisons, which is common for all measurement session. As an example see data set from October 2015 in Fig. 8 and Fig. 9.

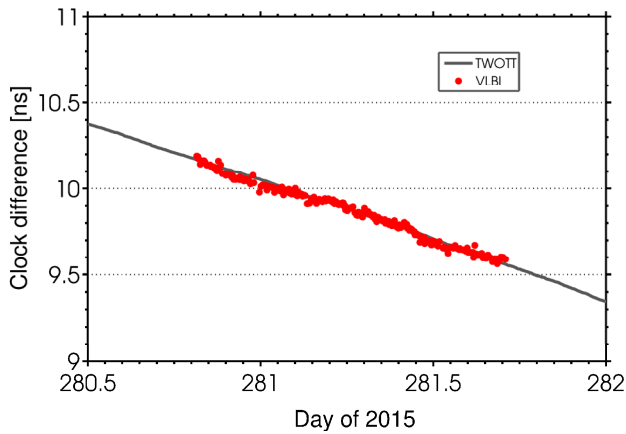


Fig. 8. The clock comparison between 20 m RTW and new TWIN radio-telescope at GO Wettzell, the common linear trend removed during October 2015 sections.

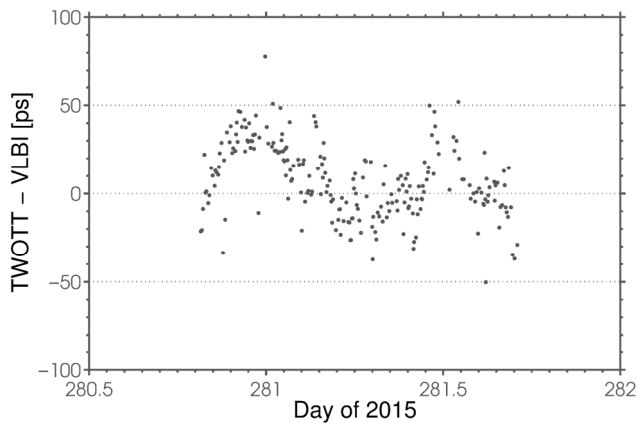


Fig. 9. Difference between TWOTT and VLBI solution, linear trend removed during January 2015 sections.

The delay variation between TWOTT and VLBI is probably caused by incorrect delay compensation in VLBI instrument. The observation data were collected short time after the telescope was put into a regular a measurement. At that time there was no pCal generator and a cable delay system measuring link delay of the reference frequency cable going from VLBI control room up to the VLBI antenna. Those two systems are crucial for compensating VLBI variable instrumental delay. It cannot be also excluded that this systematic bias can be caused by improper atmospheric delay estimation. Both delay sources will be investigated in future.

The same way as we compared the clock estimates from the local VLBI network with TWOTT we have also compared the results from the global VLBI network. In this solution, coordinates and troposphere have to be estimated, therefore, the clock estimates have a significantly lower resolution in time. The results are shown in Fig. 10. The data are spread more than 200 ps peak to peak.

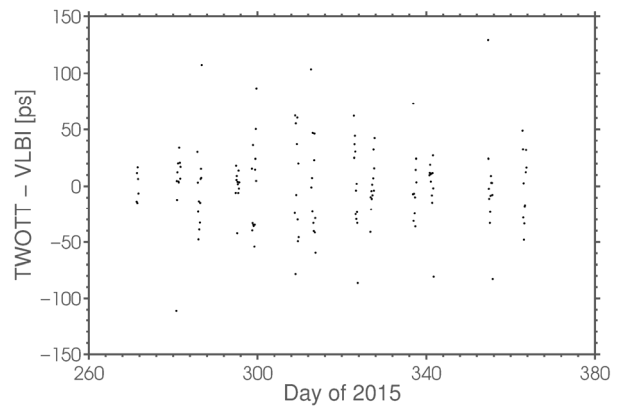


Fig. 10. Difference between TWOTT and global VLBI network.

IV. CONCLUSION

As a part of the current research and development program of the GO Wettzell, we are in the transition from a purely electrical to an actively stabilized two-way optical time and frequency distribution system. In order to verify the functionality in terms of the long term stability and correct functionality of the delay management, we have develop a tow-way optical time transfer system, which enables independent testing of the new timing system.

The properties of this system have been evaluated in a series of common clock experiments. The resulting standard deviation of the time transfer is 415 fs for 1 s comparisons, the standard deviation of 5 min linear fits is 82 fs, and the time transfer stability characterized by TDEV is better than 60 fs for the range of averaging intervals from 100 s to 10 000 s.

We also assessed the performance of the TWOTT system in the regime when it is used just for the frequency comparison of the external reference frequency sources. The resulting frequency transfer stability characterized by ADEV follows the white/flicker phase noise slope in the entire considered range of averaging intervals up to 10 000 s where the ADEV falls under 10^{-16} .

The system is currently used for comparing of two time scales generated by two H-masers, which are used as a reference frequency sources for two radio-telescopes. The goal of this measurement is investigation of VLBI clock parameter solution and its dependency on the system delay.

ACKNOWLEDGMENT

This work was partially supported by DFG project FOR1503 and RVO 68407700.

REFERENCES

- [1] K. Wang and M. Rothacher, "Stochastic modeling of high-stability ground clocks in GPS analysis," *Journal of Geodesy*, vol. 87, pp. 427-437, 2013.
- [2] T. Hobiger, T. Otsubo, M. Sekido, T. Gotoh, T. Kubooka, H. Takiguchi, Hiroshi, "Fully automated VLBI analysis with c5++ for ultra-rapid determination of UT1," *Earth, Planets and Space*, vol. 62, pp. 933-937, 2011.

- [3] T. Hobiger, C. Rieck, R. Haas, Y. Koyama, "Combining GPS and VLBI for inter-continental frequency transfer," *Metrologia*, vol. 52, pp. 251, 2015.
- [4] O. Lopez and C. Daussy and A. Amy-Klein and C. Chardonnet and F. Narbonneau and M. Lours and G. Santarelli, "Fiber frequency dissemination with resolution in the 10^{-18} range," *International Frequency Control Symposium and Exposition*, pp. 80-82, June 2006.
- [5] P. Pánek, J. Kodet, I. Procházka, "Accuracy of two-way time transfer via a single coaxial cable," *Metrologia*, vol. 50, pp. 60, 2013.
- [6] J. Geršl, P. Delva, P. Wolf, "Relativistic corrections for time and frequency transfer in optical fibers," *Metrologia*, vol. 52, pp. 552, 2015.
- [7] J. Kodet, P. Pánek, I. Procházka, "Two-way time transfer via optical fiber providing subpicosecond precision and high temperature stability," *Metrologia*, vol. 53 (2016), no. 5, p. 18-26.
- [8] <http://www.t4science.com/>
- [9] T. Schüller, G. Kronschnabl, C. Plötz, A. Neidhardt, A. Bertarini, S. Bernhart, L. Porta, S. Halsig, A. Nothnagel, "Initial Results Obtained with the First TWIN VLBI Radio Telescope at the Geodetic Observatory Wettzell," *Sensors*, vol. 15, pp. 18767, 2015.
- [10] R. Dach, U. Hugentobler, P. Fridez, M. Meindl, "Bernese GPS Software Version 5.0," 2007.

Verification of Time Signals

Matthias Schneider and Christoph Ruland
 Chair for Data Communication Systems
 University of Siegen
 57068 Siegen, Germany
 {matthias.schneider, christoph.ruland}@uni-siegen.de

Abstract—A continuous broadcast transmission of time information is actually common. In every data network the accurate system time has to be available in any devices. This paper describes a method to verify received time signals over different existing time transmission systems. By this approach, the time between two received time signals is continuously measured and compared with the time difference calculated by the time information contained in the time signals. In other words, physical and logical information is compared. The physical time difference is directly calculated using the recovered or reconstructed carrier frequency of the transmission system (for example: the DCF77 time distribution system in Germany uses a carrier frequency of 77.5 kHz with ASK/PSK modulation). A time counter is clocked by the recovered or reconstructed carrier frequency of the system. The physical time difference between the transmission of two time signals can be derived from the number of oscillations. The logical time difference is given by the time information contained in the received time signals. The time counter value of the time counter is stored, evaluated, restarted and compared to the logical time difference after any correct received time signal in the receiver. The comparison of physical and logical time differences is continuously verified to detect time leaps, which may appear during the transmission of time signals. Manipulated or delayed time signals can be identified accurately. This method can be applied without changing the time distribution protocol and can be applied to other time distribution services. The verification process takes place exclusively in the receiver and does not disturb the reception of the present recipients in the reception area of the transmitter station.

Verification, Authenticity, DCF77, WWV, WWVB, WWVH, MSF, JJY40/60,

I. INTRODUCTION

In every device in a computer network, industrial network, Smart Grid, Internet of Things (IoT), etc., the exact system time is a crucial system parameter. This implies that the actual system time has to be distributed in the whole communication network. Without a synchronized system time in all devices no time controlled process can be started in a communication network. The distribution of time signals is used to synchronize the system clocks, for example the internal real time clocks (RTC). Many computer systems and networks use public broadcast time signal services without a backchannel which are available all over the world to synchronize their central network time. Fig. 1 shows the general system architecture of a broadcast time distribution systems which includes the

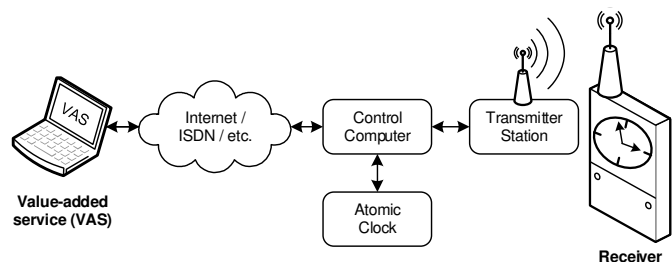


Fig. 1. System architecture of broadcast time distribution systems

different instances (Value Added Services (VAS), Control Computer, Transmitter Station and Receiver).

II. TIME CODE TRANSMITTER

Time code transmitters transmits time signals in different frequency bands. Fig. 1 shows the different instances of a broadcast time distribution system. Normally a time distribution system has only one common carrier, but in some time distribution systems additional information can be transmitted, e.g. weather information, warning messages or other user data. Examples for time distribution system with Value Added Services (VAS) are the DCF77 time distribution system in Germany and the wireless ripple control system [1][2].

Every time code service uses an individual type of modulation like ASK, PSK, FSK or a combination of them. Table I shows a small range of international time code transmitters with calling sign, location, carrier frequency f_c and modulation type.

TABLE I. TIME CODE TRANSMITTER

Call Sign	Location	Carrier Frequency	Modulation
DCF77	GER	77.5 kHz	ASK / PSK
MSF	GB	60 kHz	ASK
WWV	USA	2.5/5/10/15/20 MHz	ASK
WWVB	USA	60 kHz	ASK / BPSK
WWVH	USA	2.5/5/10/15 MHz	ASK
JJY	JP	40/60 kHz	ASK

All these transmitters broadcast a continuous time code 24 hours a day. Detailed information about this time code

transmitters and the technical implementation of the various protocols are published in [1][3][4][5][6].

The beginning of every second is marked by reducing the carrier power for an interval and the duration of the reduction depends on the transmitted logical information. In all time services presented in Table I the integration of security mechanism is difficult, because of the restricted bandwidth and the slow data rate.

III. RISKS

In all transmission protocols of the time services shown in Section II there are no security features integrated. Only parity checks and sometimes checksums are used in the presented time signal transmission protocols.

Passive attacks like data monitoring represent no danger for this time signal distribution systems, because all the presented time code transmitters transmit their time signals as plaintext. For this reason all receivers in the reception area of the transmitter station are able to receive the transmitted time signals.

The transmission of time signals is not protected against active cyber-attacks like denial of service attacks (DoS), man in the middle attacks (MITM) or replay attacks. It is difficult to protect a receiver without an internal backchannel against DoS-attacks, because the receiver cannot distinguish between a disturbance of the transmit channel and a DoS-attack. Possible attacks on time signal distribution systems are published in [7] using the example of long wave ripple control technology.

IV. VERIFICATION OF TIME SIGNALS

All presented time code transmitters currently work for many years and in some transmission systems there are over a million receivers installed. Because of this reason it is important that a verification protocol does not disturb the reception of the already installed receivers in the reception area of the transmitter station. This implies that the existing time code protocols are not be changed by a verification protocol. To check the authenticity of general information, data is signed digitally by the author of the information. This signifies that the sender signs data with its secret key and the receiver verifies the received signed data by using the public key of the sender as described in [2][8]. In this case the transmitted data consists of the actual data and additional the digital signature bits of the data. Depending on the signature algorithm the data length of the resulting digital signature is always longer than 192 bit [9][10]. This corresponds to the data length of more than 3 DCF77 time signals. In all off the presented time code protocols there is no bandwidth to transmit such a long additional digital signature. Also there is no guarantee that a backchannel is integrated in a receiver to verify the received time signal by the use of a duplex transmission protocol. Further there must be a PKI (Public Key Infrastructure) in the communication network, to manage the signature keys. By the way, digital signatures does not protect against suppressed and delayed times information.

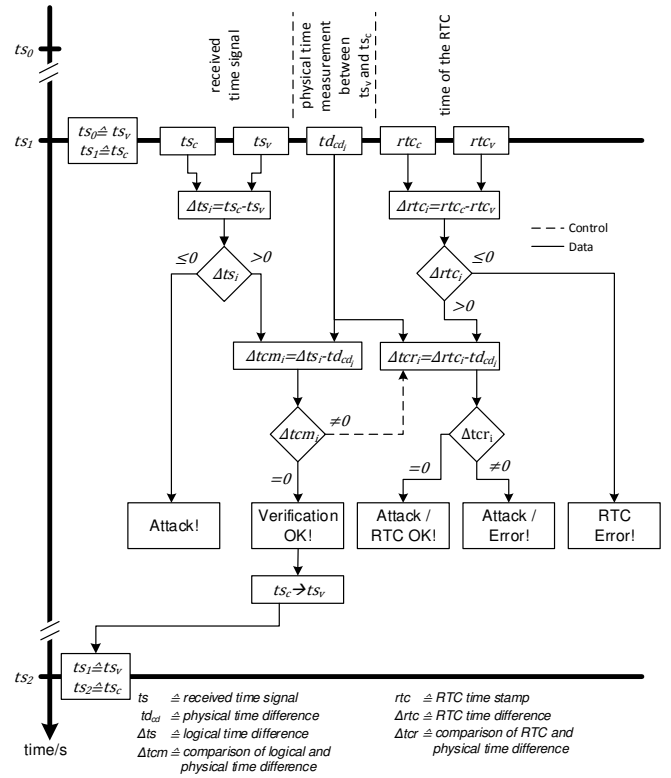


Fig. 2. Flow chart of the verification process

The verification process for time signals described in this paper is based on a plausibility check without the use of digital signatures. All information needed for the verification of the received time data will be extracted from the received modulated signal in the receiver. For the verification process, it is not important who sends the time signal. Only the correctness of the received time information is significant for the user. To reach this goal the receiver must extract additional information from the received modulated signal in the receiver. In addition to the time information, the field strength and the recovered carrier frequency of the received signal can be evaluated in the receiver.

The field strength of the received signal depends on the channel characteristic and can be changed by environmental influences. Because of this reason, the field strength of the received signal is not an optimal parameter when used by a verification process. The field strength can only be used as additional information to indicate the actual quality of the transmission channel.

The carrier frequency in most of the time signal distribution systems is very precise and can also be used as a standard frequency for further use. Therefore, it is proposed to use the carrier frequency as an additional parameter in the verification process in order to enhance security. With the help of the recovered or reconstructed carrier frequency f_c , a time measurement can be implemented. The difference time td_{cd} between two consecutive correctly received time signals can be measured for example by counting the periods of the recovered carrier frequency with a digital counter. The type of counting

depends on the modulation used in the time distribution system and will be described in Section V.

There is one essential procedure within the verification process:

The time between two consecutive correctly received time signals is measured physically and compared with the logical time difference calculated from the time information contained in the received time signals. If the difference of both time intervals is smaller than a predefined threshold, the time information is accepted and the verification process is finished successfully. Otherwise an attack or an internal error is detected by the verification process.

Fig. 2 shows the complete flow chart of the verification process. A detailed description of the verification process is given in [2].

The physical time difference td_{cd} between the last verified time signal ts_v and the currently received time signal ts_c is measured from the last received data bit of ts_v to the last received data bit of ts_c . To verify the first time signal after start or restart of the verification process, the receiver must load an initial time information from a trustworthy source. The initial time information marks the trustworthy reference point for the verification of the first received time signal.

If a corrupted time signal is received, but the carrier frequency can be recovered or reconstructed correctly, the verification process is not influenced in any way. The physical timekeeping of td_{cd} will be stored and restarted only if a correct and error-free time signal is detected. During the verification process, td_{cd} is compared with the logical time difference (Δts) of the time information included in the time signals ts_v and ts_c . If the result of this comparison (Δtcm_i) is ZERO or smaller than a predefined threshold, the verification of the current received time signal ts_c is OK. If the value is larger than the threshold, an active attack or an error is detected and an error signal is generated to indicate the error. With the further evaluation of td_{cd} and the output of the internal system clock (e.g. RTC), the error of the verification process can be defined more precisely (Fig. 2).

V. PHYSICAL TIME MEASUREMENT

The physical time measurement of td_{cd} is based on counting the periods of the received signal resp. counting the periods of reconstructed carrier (f_c). First the received signal resp. the reconstructed carrier, will be amplified and transformed into a digital clock. For this purpose, a comparator with a fixed threshold is used. The threshold value of the comparator depends on the used hardware technology. The output of the comparator is a square signal which is used as clock signal for the period counter cd . Depending on the modulation scheme, one or more counters are needed.

A. ASK modulation

If ASK modulation is used in the transmission system, only one period counter (cd) is needed, because there are no phase shifts in the reconstructed carrier frequency. The counter value of cd is stored with the reception of the last bit of the actual

time signal ts_c and then the counter cd is restarted immediately. Now the counter starts counting the periods of the carrier frequency to determine the difference time td_{cd} for the next verification process of the following time signal. The resulting time td_{cd} will be calculated by multiplying the counter value with the time period of the carrier frequency. An important fact for the implementation of the verification process is that the verification of received data can only work, if a reconstructed or recovered carrier frequency is available during the whole verification process. This implies that no on-off carrier modulation can be used in the time code distribution system like in the NPL Time Service MSF [3].

There are no problems with the integration of the verification process, if the carrier Frequency of the time service can also be used as a normal frequency.

B. PSK modulation

If PSK modulation scheme is used, two period counters must be implemented in the receiver, since this modulation scheme works with a phase shift of the carrier. Depending on the transmitted data (logical "1" or "0") the modulation phase of the carrier frequency is changed in the modulator. In the case of BPSK-modulation, the phase shift φ of the carrier frequency is $\varphi=180^\circ$ (e.g. logical "0" $\rightarrow \varphi=0^\circ$, "1" $\rightarrow \varphi=180^\circ$). The periods of each phasing are counted by a separate period counter. To get the difference time td_{cd} , the counter values of the two counters will be added and multiplied with the time period of the carrier frequency. For higher modulation schemes more counter are needed.

C. BPSK modulation

In the special case of BPSK modulation, a single counter can be used instead of the two used in general PSK, if the phase shift occurs at the zero crossing points of the received signal. The received signal must be amplified and rectified by a full-wave rectification. The result of the full-wave rectification is the clock signal for the digital counter cd . The stored counter values of cd multiplied by the time period of the carrier frequency and divided by two results in the difference time td_{cd} .

D. FSK modulation

If the modulation scheme FSK is used in the transmitter, the logical data is modulated through discrete frequency changes of the carrier frequency. A logical "1" is modulated by the mark frequency (e.g. $f_m=f_c-\Delta f$) and a logical "0" by the space frequency ($f_s=f_c+\Delta f$).

For example, this modulation scheme is used by the wireless ripple control technology in Germany (DCF49: $f_c=129,1\text{ kHz} \pm 170\text{ Hz}$) and implies for the difference time measurement of td_{cd} that the periods of the received signal must be counted with two independent period counters. If a logical "0" is received, the respective periods of the received signal are counted by cd_s and then multiplied with the time period corresponds to the frequency f_s . Likewise, if a logical "1" is received, the respective periods of the received signal is counted by cd_m and then multiplied with the time period that corresponds to the frequency f_m .

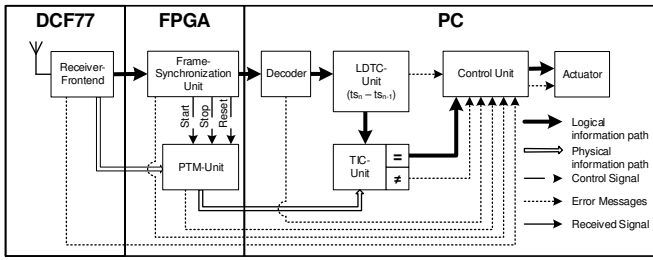


Fig. 3. Block diagram of the DCF77 prototype

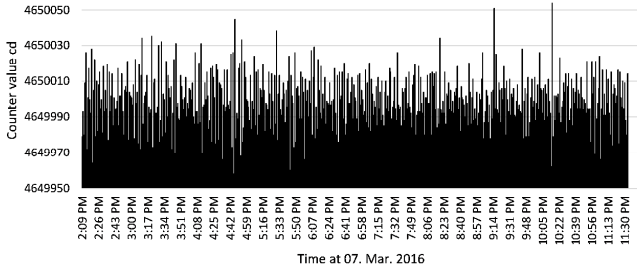


Fig. 4. Counter value of the period counter

VI. IMPLEMENTATION AND TEST ENVIRONMENT

The verification process was tested in the DCF77 long wave time distribution system and the test environment consists of the Meinberg DCF77 receiver UA24V [11], a FPGA measurement logic and a PC software.

In Fig. 3, the block diagram of the test environment is shown which consists of three components:

The first component is the DCF77 HF-Receiver Frontend. In the Receiver Frontend, the received data are demodulated (logical data path) and output to the Frame-Synchronization Unit. Further the clock signal for the Physical-Time-Measurement-Unit (PTM-Unit) will be recovered resp. reconstructed in the Receiver Frontend (physical information path). These both signals are tapped at the Meinberg DCF77 receiver. The Frame-Synchronization Unit and the Physical-Time-Measurement-Unit are realized on a FPGA. These logical units are realized on a FPGA, because all counters can be triggered exactly by the rising or falling edge of control signals using the programming language VHDL. All other logical units, like the Decoder of the logical time information, the Logical-Difference-Time-Calculating-Unit (LDTC-Unit), the Time-Interval-Comparison-Unit (TIC-Unit) and the Control-Unit will be realized in a PC C-Program.

The complete test environment for the presented verification process will be operate in the real DCF77 reception area. For all measurements real DCF77 time signals received in Siegen (Germany 50°54'20.2"N 8°01'47.0"E) will be used. The carrier frequency f_c in the DCF77 distribution system is $f_c = 77.5 \text{ kHz}$. With the help of the frequency f_c , the real number of oscillation of one complete DCF77 time signal frame (60 seconds) can be calculated. The calculated counter value of the counter cd is $cd_{calc} = 60 \text{ s} \cdot 77.5 \text{ kHz} = 4650000$ oscillations.

Fig. 4 shows the accuracy of the counting of the period counter cd . In the measurement interval from the 07. Mar. 2016, 02:09 PM up to the 07. Mar. 2016, 11:33 PM the difference time td_{cd} of 565 received DCF77 time signals was measured. The corresponding counter values are in the range of $cd_{min} = 4649958$ up to $cd_{max} = 4650054$ with an arithmetic mean value of $cd_{arth} = 4649999,9$ oscillations.

So the difference (Δcd) between the calculated difference value cd_{calc} and the measured counter value of cd is smaller than $\Delta cd < \pm 55$ oscillations. Considering the accuracy of the counter value cd that implies a measuring error time smaller than $t_{error} < 709.7 \mu\text{s}$.

VII. FUTURE WORK

This paper presents a verification process for time signals, transmitted in continuous broadcast distribution systems like DCF77, WWVB, etc. Next, we want to enhance this process in order to make it useable in satellite communication system like GPS and Galileo. In this environment, a group of verification logics is needed. One for each satellite in LOS (Line of Sight). Furthermore the CDMA technique must be integrated in the HF-Receiver Frontend.

REFERENCES

- [1] Piester, D.; Bauch, A.; Becker, J.; Hoppmann, A.: Time and Frequency Broadcast with DCF77. In: Proc. 43rd Annual Time and Time Interval (PTTI) Systems and Applications Meetings, S. 185–196. J. Clerk Maxwell, A Treatise on Electricity and Magnetism, 3rd ed., vol. 2. Oxford: Clarendon, 1892, pp.68–73.
- [2] Matthias, Schneider; Christoph, Ruland (2015): Verification of time telegrams in Long Wave Radio systems. In: Frequency Control Symposium & the European Frequency and Time Forum (FCS), 2015 Joint Conference of the IEEE International. IEEE, S. 270–275.
- [3] National Physical Laboratory (2007): NPL Time & Frequency Services. MSF 60 kHz Time and Date Code. Teddington (TAF001v06).
- [4] Nelson, G. K.; Lombardi, M. A.; Okayama, D. T. (2005): Nist time and frequency radio stations: WWV, WWVH, and WWVB. In: NIST Special Publication 250 (67).
- [5] Lowe, John (2013): Enhanced WWVB Broadcast Format. NIST.
- [6] National Institute of Information and Communications Technology (2008): Japan Standard Time Project-the Generation, Comparison, and Dissemination of Japan Standard Time and Frequency Standard.
- [7] Schneider, M.; Ruland, Ch. (2013): Sicherheit von Broadcast-Datendiensten im Smart Grid am Beispiel der Rundsteuertechnik. In: Michael Hange (Hg.): Informationssicherheit stärken - Vertrauen in die Zukunft schaffen. Tagungsband des 13. BSI-Kongresses. Unter Mitarbeit von Michael Hange. Gau-Algesheim: SecuMedia, S. 483–496.
- [8] Paar, Christof; Pelzl, Jan (2010): Understanding cryptography. A textbook for students and practitioners. 2. corrected printing. Berlin: Springer.
- [9] Barker, Elaine (2016): Recommendation for Key Management Part 1 Revision 4: General: National Institute of Standards and Technology.
- [10] Bundesamt für Sicherheit in der Informationstechnik (BSI) (2016): Kryptographische Verfahren: Empfehlungen und Schlüssellaengen. BSI TR-02102-1.
- [11] Meinberg Funkuhren (Hg.) (1997): Technische Daten; Inbetriebnahme; DCF77 UA24V; ABB.

WR-ZEN: Ultra-accurate synchronization SoC based on Zynq Technology

Miguel Jiménez-López,
José Luis Gutiérrez-Rivas
and Javier Díaz
University of Granada
Granada, Spain
Email: klyone@ugr.es
Email: jlgutierrez@ugr.es
Email: jda@ugr.es

Emilio López-Marín
and Rafael Rodríguez
Seven Solutions
Granada, Spain
Email: emilio@sevensols.com
Email: rrodriguez@sevensols.com

Abstract—Nowadays, many industrial synchronization systems rely on the Precise Time Protocol (PTP or IEEE1588) that provides sub-microsecond precision time transfer. However, there are some applications such as next generation of telecommunication systems (LTE-A & 5G) or scientific infrastructures that have stricter timing requirements that must guarantee the timing service regardless of traffic load conditions. Recently, the White-Rabbit (WR) technology has been proposed as alternative to provide deterministic sub-nanosecond synchronization using Gigabit Ethernet standard. Currently, most WR nodes are implemented using only FPGAs and they can be plugged in a conventional computer or can be used as standalone node. Nevertheless, this approach presents some limitations because all the functionality must be implemented in the FPGA due to the lack of a hard microprocessor on the board. The White-Rabbit Zynq Embedded Node (WR-ZEN) is a platform based on the Xilinx Zynq SoC technology that solves these issues. It has a Processing System (PS) based on a dual core ARM hard processor that can run any conventional OS like Linux and simultaneously use the Programmable Logic (PL) inside the same chip. The flexibility of the platform has motivated that WR-ZEN is under study to be used in important scientific infrastructures such as Square Kilometer Array (SKA) and Cherenkov Telescope Array (CTA) among others. In this contribution, we address the new platform design including hardware, gateway and firmware architecture. We describe the new clocking scheme, aspects of the Linux customization, kernel modules, user-space tools and the Fine Delay FMC support, clearly stating the benefits of the presented approach compared with previous WR platforms. Finally, we present experimental results and validation of the timing features compared with other solutions and we demonstrate that the WR-ZEN is fully compatible with other WR devices and it achieves a subnanosecond precision.

I. INTRODUCTION

Nowadays, many industrial systems rely on a timing synchronization mechanism to work properly and safety. The synchronization systems are responsible to provide an uniform time scale for all the devices of a network. However, each node presents a different local oscillator that is running free in relation to the other oscillators in the network. A communication protocol is needed to adjust the oscillators in order to set the same time in all of them. This protocol defines master devices that are encouraged to share its time to the rest of the network and slave devices that must adjust its oscillator to follow

this reference. The most popular packet-based synchronization algorithms are the Network Time Protocol (NTP) and the Precise Time Protocol (PTP).

The NTP protocol is designed to work in IP networks and uses UDP packets to transmit the time information. The NTP presents a hierarchical structure divided into stratum [1]. The first stratum is usually connected to a primary reference from a GPS or an Atomic clock. The second stratum is synchronized with the stratum 1 and so on. The NTP uses UTC format for the timestamps and is fault tolerant because there is a mechanism to decide which is the best time source to follow [2].

The PTP also known as IEEE 1588 is a packet-based algorithm with master and slaves devices similar to NTP. It achieves a more accurate synchronization than NTP [3] thanks to the hardware implementation of the timestamps [4]. However, the PTP uses TAI format instead of UTC so a conversion is needed if the UTC time is required. The PTP defines several types of clocks [5] Ordinary clock (OC), Transparent clock (TC) and Boundary clock (BC). The OC are devices that have only a interface and acts as slaves or grandmasters in the network. The slave nodes must follow the received master reference and the grandmasters are responsible for obtaining a primary reference source and transmitting it to the network. The intermediate switches/routers can behave as TC or BC depending on if they should be synchronized or not. The TC has hardware timestamp support but it does not have to be synchronized. On the other hand, the BC has a slave port and must keep the synchronization on its interface.

Many applications can work properly with NTP or PTP but there are others such as next generation of telecommunication systems (LTE-A & 5G) or scientific infrastructures that have stricter timing requirements and must guarantee the timing service regardless of traffic load conditions. Recently, the White-Rabbit (WR) technology has been proposed as alternative to face these new demands and now it is under study to be included in the a new high accuracy profile of the PTPv3. In the following section, we describe in more detail the WR protocol and all its features.

II. WHITE RABBIT

The White-Rabbit [6] (WR) is a fully-open hardware/software and vendor independent technology that extends the Gigabit Ethernet and PTP protocol for optical fiber links to provide a timing synchronization with an accuracy better than a nanosecond and a precision of few picoseconds. WR offers a deterministic and reliable data transfer over networks that contains thousand of nodes and links between them up to 10 km.

The WR network topology [7] is a hierarchical tree where the root node is the grandmaster device responsible for sharing the primary time reference to the rest of the network. The WR switches are multi-port devices that acts as PTP BC. They have a slave interface for the uplink and several master ports for the downlinks that propagate the synchronization to the next level of the hierarchy. The leaf nodes are slave devices that are synchronized with the upper level of the network and perform some specific task.

The main technologies of the WR are:

- **SYNCHRONOUS ETHERNET (SYNCE):** It uses the physical layer to transmit the master clock inside the data stream to the network. The slave nodes recover the master clock and uses it to lock an internal PLL with its local oscillator. It allows to syntonize the slave clock with the master one.
- **WR-PTP:** The WR includes an enhanced version of the PTPv2. Currently, there is a workgroup, the High Accuracy sub-committee, encharged to include it as a profile in the new PTP release, the PTPv3.
- **PHASE ALIGNMENT TECHNIQUES:** The current implementation of WR uses a Digital Dual Mixed Time Difference (DDMTD) that is a new module that measures the phase between two clocks in a more convenient way than a fast digital counter.

The WR technology is thought to be programmed in a FPGA device and the reference designs are done in HDL (mainly VHDL) code. The most important Intellectual Property (IP) core is the WR PTP core (WRPC) that incorporates all the logic needed by the WR protocol implementation in the nodes. The WR nodes are implemented in boards with a FPGA device such as SPEC [8] or SVEC [9]. These platforms do not have a hard microprocessor and it forces to use these cards plugged in a socket of a conventional PC.

Other alternative is to implement a microprocessor inside the FPGA wasting logic gates. The soft microprocessor presents less performance and usually has a slower clock frequency. Moreover, there are some microprocessors that consume many logic gates and can not be synthesized in several FPGA devices due to the lack of resources. This is an important limiting factor to be in consideration. For all the above mentioned, it is very interesting to get a design where a FPGA device and a hard microprocessor are available for WR nodes. This is the WR Zynq Embedded Node (WR-ZEN) by Seven Solutions company [10]. In the next section, we talk about it and describe the reference architecture.

III. WR-ZEN

The WR-ZEN is a new kind of WR node that incorporates a FPGA device and a hard ARM dual core microprocessor inside the same chip. The ARM is able to run a Linux kernel and this eliminates the need to use a conventional PC with an operating system. The flexibility of the platform has motivated that WR-ZEN is under study to be used in important scientific infrastructures such as Square Kilometer Array [11] (SKA) and Cherenkov Telescope Array [12] (CTA) among others.



Fig. 1. The WR-ZEN board. This new platform has a Zynq device, two optical fiber ports, two copper Ethernet ports, a new and improved clock circuitry, a FMC socket, an SAMTEC expansion connector and some memory chips.

A. Hardware

The WR-ZEN is a small stand-alone board that integrates the latest Xilinx Zynq Z-7015 device with a Dual ARM Cortex-A9 MPCore with CoreSight and containing an Artix FPGA-logic with 74K logic cells, 380KB of embedded memory and 160 DSP blocks. It has two optical SFP Ethernet interfaces, two copper Ethernet ports and the FMC expansion connector. On addition to FMC, a SAMTEC connector is available for developing of simple expansion boards and some USB sockets for monitoring. The WR-ZEN node is provided with improved oscillators, PLLs and a clocking scheme that provides significant better short term stability than previous WR node designs. It also includes several SMA outputs that can be configured to generate signals from the FPGA and an input that allows the WR-ZEN to behave as grandmaster. The WR-ZEN can be used with several FMC cards depending on the application: ADC, DAC, TDC, DDS, Fine delay, Digital I/O, etc.

B. Gateware

The gateware refers to the design that must be programmed in the Programmable Logic (PL) and the Processing system (PS) configuration to be applied. The PL is based on the Wishbone (WB) bus [13] and has a main crossbar that interconnects the different IP cores.

In the Fig. 2, the PL architecture is represented in more detail.

- **GIGABIT TRANSCEIVER PORTS (GTP):** These blocks contain primitives to transfer data through a high performance dedicated interfaces. The GTPs are connected to the SFP sockets and allow to send/receive packets to/from the Gigabit Ethernet network.
- **WR PTP DUAL PORT CORE (WRPC-2P):** It is the key core for WR nodes and contains all the elements

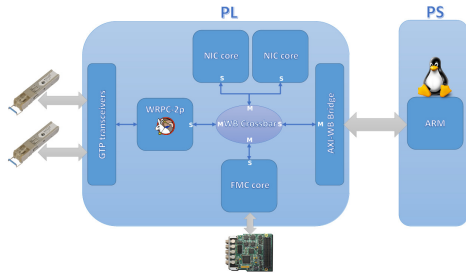


Fig. 2. WR-ZEN Reference Design. It contains some components as WRPC-2p that is responsible to implement the WR protocol, an AXI-WB bridge that allows the communication between the FPGA logic and the ARM microprocessor and other additional modules such as NICs or a FMC core.

needed to implement the WR protocol for two optical fiber ports.

- AXI TO WB BRIDGE (AXI-WB BRIDGE): The PS must be able to talk to the PL. However, the PS uses the AMBA/AXI bus specification instead of the WB one of the PL. The AXI-WB bridge is able to convert from WB transactions to AXI transactions and viceversa.
- FMC CORE: This IP core gives the specific functionalities for a certain kind of FMC card. In the reference design, the Fine Delay FMC core is included.
- NETWORK INTERFACE CORE (NIC): It provides a network controller that is directly accesible from the Linux kernel. The NIC module can be managed like a standard network interface thanks to a specific driver.

The gateway design carries out a WR compliant node with network capabilities and support for several FMC cards. However, the reference design only uses the Fine Delay FMC card, it can be extended easily to work with other cards such as DIO, TDC, ADC, etc.

C. Software

In this section, the software components needed to run a Linux kernel/Baremetal application on the WR-ZEN board are described. The Zynq devices needs a binary file (BOOT.bin) that is composed of a specific Xilinx bootloader known as First Stage Bootloader (FSBL), a gateway bitstream to program the FPGA and a baremetal application or a Second Stage Bootloader (SSBL) if Linux kernel must be loaded. The FSBL is encharged to initialize different peripherals, configure the FPGA with a bitstream and run the baremetal application or the SSBL. The baremetal application is encouraged to be coded with the Xilinx SDK because all the gateway details are imported to the software project and we can use all the functionalities of the Xilinx Board Package Support (BSP). On the other hand, the SSBL is a independent project and must be downloaded and compiled separately. The most common SSBL are U-boot [14] and Barebox [15]. The chosen bootloader is U-boot instead of Barebox because there is a Xilinx repository [16] that includes custom code for the Zynq devices. When everything is generated, the Xilinx SDK or bootgen tool must be used to pack all the binaries in a single file, the BOOT.bin.

The following step is to compile the Linux kernel, kernel modules, libraries and userspace tools. To face this task, there

are two ways. The first one is to compile every component separately and manually. It is very slow, tedious and error prone but it is the best way to control the different steps and customize them if necessary. On the other hand, there are some tools that automate the process such as Yocto [17] or Buildroot [18]. However, they present a disadvantage: the user loses the control and it is more difficult to add some modifications because the tool does everything automatically. For the reference design, the Buildroot is used to ease and speed up the compilation of the Linux kernel, U-boot bootloader, the kernel modules and userspace tools. The Buildroot package is retrieved from the official project website. It is very configurable and includes the Kconfig support to enable/disable the different features similar to the Linux kernel. Although the Buildroot eases very much the compilation process, it has many options and may be confusing for a non-expert user. To solve this issue, a set of scripts have been implemented to perform all the actions needed and configuration files for the Busybox, Linux kernel and the Buildroot are provided. This scripts are based on others from the WR Switch Software project [19] of the OHWR repository.

In addition of the Linux kernel and the bootloader, some kernel modules and userspace tools for the WR-ZEN board have been written. The main kernel driver is the WR-ZEN carrier, known as zen, and is responsible for reprogramming the FPGA device and reading the EEPROM information of the WR-ZEN board. This driver is based on the fmc-bus [20] (OHWR) and it also gives NIC capabilities to manage the optical fiber ports as standard network interfaces from the Linux kernel. Some userspace tools to read/write the FPGA register (zenmem), reprogram the FPGA bitstream (zen-fwloader.sh), reprogram the soft-microprocessor program (zen-cl) and send commands to the soft-microprocessor (zen-uart) are included too. The driver and all these tools are inspired by the SPEC Software project [21] of the OHWR repository. As we saw in the previous section, the reference design has also a Fine Delay core that must be controlled by a specific kernel driver. Actually, there are two drivers (zio [22] and fmc-fine-delay [23]) and some userspace tools in the OHWR for the Fine Delay FMC card in a SPEC card. Using these ones as starting point, some minor modifications have been made to incorporated them to the WR-ZEN reference design.

IV. TEST

The WR-ZEN board must be tested to ensure that the WR protocol is working properly. We have defined a test scenario with a WR master (WR-ZEN) and a WR slave (WR-ZEN) connected by a fiber link and we use a Tektronix DPO 7354 oscilloscope and two 1.5m BNC-SMA cables for PPS signals. Then, the devices must be configured in the different modes and the WR-PTP must be started. When the synchronization slave process reaches the TRACK_PHASE state (see the monitoring tools for the WR-ZEN), the PPS signals must be measured in order to know if the devices are synchronized properly. The PPS offset of this scenario is about 17 ps so the subnanosecond precision is achieved. Note it is very convenient that the calibration procedure [24] is applied to the WR-ZEN before testing to guarantee subnanosecond synchronization.

Finally, we have performed some additional tests with WR-

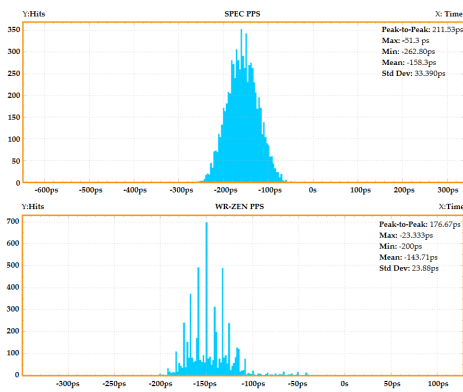


Fig. 3. PPS stability for the WR-ZEN and SPEC boards. We have defined two different tests. The former is between two WR-ZEN (one as master and the other as slave) connecting with a fiber link and with the oscilloscope to measure the PPS signals. The latter is the same setup but using SPEC+DIO FMC boards using two 1.5 BNC-LEMO cables.

ZEN and SPEC boards to obtain the timing improvements of the new WR node platform. The Fig. 3 shows the WR-ZEN presents a better timing behaviour, thanks to the new clocking circuitry, with a peak-to-peak offset of 176.67ps and a standard deviation of 23.88ps.

V. CONCLUSION

We have presented a new platform that implement the WR protocol, the WR-ZEN. The main conclusions are:

- The WR-ZEN has a new clocking circuitry that improves the timing performance in relation to the previous WR nodes.
- The WR-ZEN has a Zynq device (ARM+FPGA logic) that allows a higher flexibility and the application of codesign techniques. Moreover, it is easy to use for non-hw experts.
- The WR-ZEN is a fully standalone node that does not need a conventional PC anymore. In addition, other advanced features are also included such as Fine Delay FMC and NIC support.

For fist time, we have demonstrated that the WR technology can be used in Zynq devices and the Zynq PL GTPs are deterministic.

VI. FUTURE WORK

Most promising future work lines we have identified are the following:

- Increase the bandwidth for the optical fiber ports for both data and timing information including a DMA module in the gateway.
- Extend the FMC support for new cards such as DIO, TDC, ADC, etc.
- Optimize the system parameters to reduce the jitter. It must take into account the FPGA MMCMs, WR PLL control algorithm and Hardware PLL.

ACKNOWLEDGMENT

The authors would like to thank to the CERN BE-CO-HT group, the WR community, the Seven Solutions staff and other institutions such as JIVE for its collaboration testing the WR-ZEN board. This work has been partially funded by the Horizon 2020 (H2020) ASTERICS (grant number 653477) and VITVIR (TIC-8120, Junta de Andalucia) projects.

REFERENCES

- [1] W. Kelly. The network time protocol (ntp) distribution. Last checked: 28/03/2016. [Online]. Available: <https://www.eecis.udel.edu/~mills/ntp/html/index.html>
- [2] U. Windl and D. Dalton. Understanding and using the network time protocol. Last checked: 28/03/2016. [Online]. Available: <http://www.ntp.org/ntpfaq/NTP-a-faq.htm>
- [3] D. Arnold. Ntp vs ptp: Network timing smackdown! Last checked: 28/03/2016. [Online]. Available: <http://blog.meinbergglobal.com/2013/11/22/ntp-vs-ptp-network-timing-smackdown/>
- [4] ——. Why is ieee 1588 so accurate? Last checked: 28/03/2016. [Online]. Available: <http://blog.meinbergglobal.com/2013/09/14/ieee-1588-accurate/>
- [5] ——. What are all of these ieee 1588 clock types? Last checked: 28/03/2016. [Online]. Available: <http://blog.meinbergglobal.com/2013/10/21/ieee-1588-clock-types/>
- [6] OHWR. White rabbit. Last checked: 28/03/2016. [Online]. Available: <http://www.ohwr.org/projects/white-rabbit/wiki>
- [7] G. Daniluk, “White rabbit ptp core the sub-nanosecond time synchronization over ethernet,” Master’s thesis, Warsaw University of Technology, 2012, last checked: 28/03/2016. [Online]. Available: <http://www.ohwr.org/documents/174>
- [8] OHWR. Spec board project. Last checked: 28/03/2016. [Online]. Available: <https://www.ohwr.org/projects/spec-sw>
- [9] ——. Svec board project. Last checked: 28/03/2016. [Online]. Available: <https://www.ohwr.org/projects/zio>
- [10] Seven-Solutions. Wr-zen (zynq embedded node). Last checked: 28/03/2016. [Online]. Available: <http://www.sevensols.com/es/productos/wr-zen.html>
- [11] SKA. Square kilometer array website. Last checked: 28/03/2016. [Online]. Available: <https://www.skatelescope.org>
- [12] CTA. Cherenkov telescope array website. Last checked: 28/03/2016. [Online]. Available: <https://www.cta-observatory.org>
- [13] OpenCores. Wishbone bus v4 specification. Last checked: 28/03/2016. [Online]. Available: http://cdn.opencores.org/downloads/wbspec_b4.pdf
- [14] Denx. Das u-boot, the universal boot loader. Last checked: 28/03/2016. [Online]. Available: <http://www.denx.de/wiki/U-Boot>
- [15] Barebox. Barebox website. Last checked: 28/03/2016. [Online]. Available: <http://www.barebox.org/>
- [16] Xilinx. Xilinx u-boot repository. Last checked: 28/03/2016. [Online]. Available: <https://github.com/Xilinx/u-boot-mlx>
- [17] Yocto. Yocto project website. Last checked: 28/03/2016. [Online]. Available: <https://www.yoctoproject.org/>
- [18] Buildroot. Buildroot website. Last checked: 28/03/2016. [Online]. Available: <https://buildroot.org/>
- [19] OHWR. Wr switch software. Last checked: 28/03/2016. [Online]. Available: <http://www.ohwr.org/projects/wr-switch-sw/wiki>
- [20] ——. Fmc bus driver project. Last checked: 28/03/2016. [Online]. Available: <https://www.ohwr.org/projects/fmc-bus>
- [21] ——. Spec driver project. Last checked: 28/03/2016. [Online]. Available: <https://www.ohwr.org/projects/spec-sw>
- [22] ——. Zio driver project. Last checked: 28/03/2016. [Online]. Available: <https://www.ohwr.org/projects/zio>
- [23] ——. Fine delay driver project. Last checked: 28/03/2016. [Online]. Available: <https://www.ohwr.org/projects/fine-delay-sw>
- [24] ——. White rabbit devices calibration. Last checked: 28/03/2016. [Online]. Available: <https://www.ohwr.org/projects/white-rabbit/wiki/Calibration>

An Electro-Optic Modulator with ultra-low residual amplitude modulation

Zhaoyang Tai^{1,2}, Lulu Yan¹, Yanyan Zhang¹, Long Zhang¹, Haifeng Jiang^{1,*} and Shougang Zhang¹

¹ Key laboratory of Time and Frequency Standards, National Time Service Center, Xi'an/China

² Graduate University of Chinese Academy of Sciences, Beijing/China

Email: haifeng.jiang@ntsc.ac.cn

Abstract—Reduction of residual amplitude modulation (RAM) level induced by electro-optic modulation is important for frequency modulation (FM) technique to reach higher sensitivity. Here, we present a passive approach to make a well-designed electro-optic modulator (EOM) with ultra-low RAM. Although low RAM could be achieved by critical active controls of temperature and voltage of a common EOM. This passive approach is more simple, reliable and easier to be realized. We evaluate performance of such an EOM by comparing system noise level of a standard PDH frequency-stabilization system using this EOM with a commercial one with the addition of a good quality polarizer. RAM depth (versus phase modulation (PM) depth) of this EOM is at 10^{-6} level. Frequency instability induced by this EOM is below 1×10^{-16} @ 1s, which is more than one order lower than the other.

Keywords—electro-optic modulator (EOM); residual amplitude modulation (RAM); passive; PDH; ultra-stable laser

I. INTRODUCTION

Frequency modulation (FM) spectroscopy technique has been applied in many advanced scientific fields such as the recently successful gravitational wave detection [1], trace gas sensing in medicine and atmospheric sciences [2] and frequency standards [3]. Electro-optic modulators (EOM) are components to modulate the phase/frequency of lasers. However, these modulations always accompany with residual amplitude modulations (RAM). RAM is at the same frequency of phase/frequency modulation, as an unwanted background noise destroying the accuracy of FM spectroscopy technique.

II. ANALYSIS OF RESIDUAL AMPLITUDE MODULATION

RAM is caused by a variety of effects, particularly the parasitic etalon effect [4] and polarization rotation effect [5] inside the EOM. Parasitic effect is caused by the parallel surfaces' reflection in the EOM, and it would convert part of the phase modulation to RAM. The RAM caused by etalon effect depends on the equivalent length and the reflectivity of the anti-reflective coatings of the EOM, so the refractive index of the EO crystal, the optic path through the EOM, temperature and mechanical vibration of the EOM would influence the magnitude of RAM. Another very important effect lead to RAM is polarization rotation effect in the EOM which is induced by birefringence of the EO crystal. When the polarization of the incident light is not strictly match the

principal axe of the EOM, the RF-voltage-induced birefringence combined with natural birefringence make polarization rotate with modulation frequency in the crystal, and when the polarization-rotated light pass through polarizing optical components downstream such as polarizers or polarization beam splitters, polarization rotation fluctuation would converted to RAM with the modulation frequency. The polarization rotation effect is temperature and RF voltage dependent. The total influence of RAM can also be described as the two sidebands created in phase/frequency modulation are not equal in magnitude and opposite in phase as pure phase/frequency modulation do, so they cannot be canceled to zero at the detection of photocurrent at the modulation frequency.

III. METHODS TO REDUCE RAM

A. Common Passive Methods

To reduce the level of RAM, passive methods are first choices for simplicity and easy realization. The widely used way is to make the optical surfaces in the optical path slightly tilted including tilting the EOM, to avoid etalon effect. But in this way the RF field inside the EOM would also be tilted off the incident light, it would cause a more serious polarization rotation effect. The other passive method is to add a polarizer with high extinction in front of the EOM to optimally match the polarization of the incident light, in order to reduce the RAM caused by polarization rotation. But even with best quality polarizers, the RAM can not be eliminated to the level could be ignored.

B. Common Active Methods

For RAM is complicated and it is fluctuating with environmental factors, the passive methods seem not able to reduce RAM to lower levels, thus many active methods have been applied [5-8]. Initial method is proposed by Wong and Hall [5], they implement a bias tee to add attached DC voltage to the EOM to compensate the natural birefringence of EO crystal to avoid RAM. After that, lots of similar methods has been invented to reduce RAM [6-8], using actively feedback systems to cancel the instant RAM by controlling the electric field and temperature of the EOM as well [6], or the drive current of the laser source [7], or the other components like AOM [8]. But the active methods are complicated and hard to realize. For reducing the RAM level fundamentally and easily,

we present a simpler and passive method aiming at the two dominating effects mentioned above which cause RAM, and using this method we could reach the same RAM stability level as they did in the resent reports using active methods [6].

C. Our Method

A new passive method using a well-designed EOM is proposed. Fig. 1 shows the design of the EOM, $\angle \Theta$ is Brewster's angle. Generally, this Brewster's angle cut EOM has two advantages which traditional EOMs do not have for avoiding RAM. First, the incidence and emergence surfaces are not vertical to the laser beam as traditional EOMs are, so this EOM avoids parasitic etalon effect, which is the first significant effect lead to RAM. Second, if the incident light do not match the principal axis of the EOM perfectly, incident light with perpendicular polarizations are spatially separated for the reason of natural birefringence, further, the two surfaces with Brewster's angle reflect part of the light with unwanted polarization, therefore, the polarization rotation effect inside the EOM is avoided, no more polarizer with high extinction ratio in front of the EOM is needed which may lead to RAM caused by vibration and temperature change of this polarizer. In addition, as Fig.1 shows, the incident and outgoing angles are Brewster's angles, the light with matched polarization would totally reflect into the crystal, thus no more anti-reflective coatings are needed which cost more money and time, and may cause some other troubles.

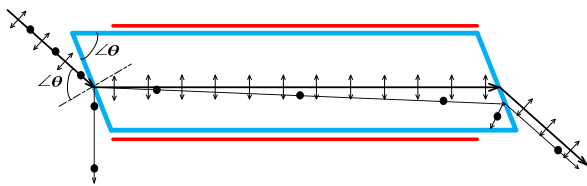
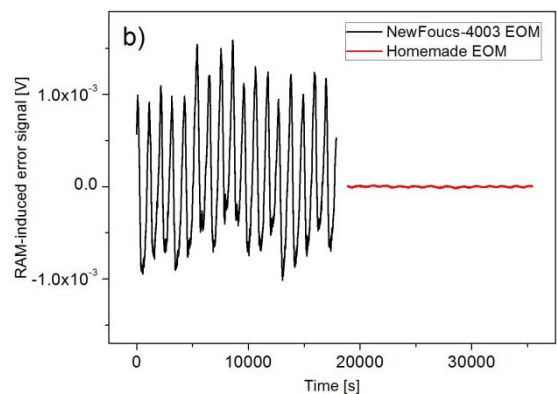
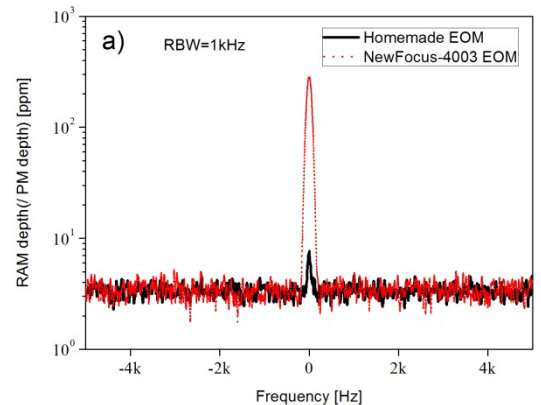


Fig. 1. Design of the EOM. This is a plan form of the EOM. The two acute angles $\angle \Theta$ in the crystal are cut to be Brewster's angles, the incidence angle and the emergence angle are $\angle \Theta$ too. The dots and the double headed arrows represent ordinary and extraordinary lights respectively, the black solid lines and dashed lines represent their optical paths respectively. Red lines are electrodes. The electrodes are designed upright against each other in the horizontal direction and the parts which do not face right against each other are cut off. this ensures that the RF electric fields in the direction of the polarization of extraordinary light, for generating the max and pure phase modulation depth. Our original idea is to cut the LiNbO3 crystal into a diamond shape for symmetry; and we find it is feasible to cut other kinds of EO crystals into other kinds of shapes like ladder shape or other shapes

IV. EXPERIMENTS AND RESULTS

We want to use such an EOM to reduce the RAM in ultra-stable laser. For cavity-based lasers [9-10, 12-15] using Pound-Drever-Hall (PDH) [16] technique to lock the lasers' frequencies to optical cavities, RAM would raise a DC offset to the PDH error signal, and this DC offset would convert to frequency offset when the error signal is used for lock the laser's frequency.

To evaluate the performance of such an EOM. We set it into a standard PDH frequency-stabilization system, the PDH error signal we get here equals to the cavity off-resonance error signal, and this PDH error signal represents the out-of-loop RAM level. We use our homemade EOM in the setup, and compare with that of a commercial EOM (New Focus-4003) with a high extinction ratio ($>10^4$) polarizer before to minimize RAM. The laser from a single-mode polarization-maintaining fiber laser pass across the EOM and get phase-modulated, the modulated laser go through a polarizer behind the EOM and then focuses into a photo detector (PD), the photocurrent is separated into two ports, one port is fed into spectrum analyzer (SA) to monitor the magnitude of the RAM, the other into a double balanced mixer (DBM), mixed with the LO to generate the PDH error signal. The phases of RF signals have been adjusted to give a maximum output of error signal. The RAM-induced PDH error signal is analyzed by both a fast Fourier transform (FFT) analyzer and a digital voltage meter (DVM).



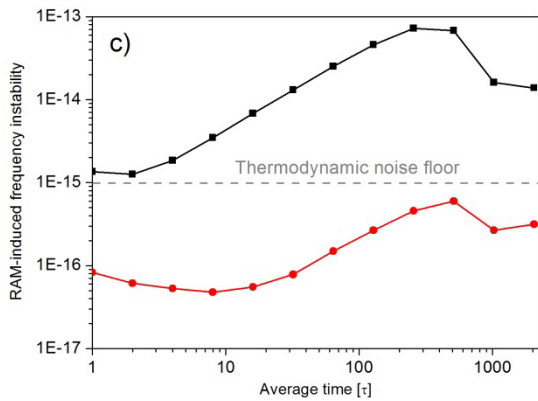


Fig. 2. RAM stability of a New Focus-4003 EOM (black line) and the homemade EOM (red line). (a) RAM depth (b) RAM-induced Error signal (c) RAM-induced frequency instability calculated from (b) using a measured PDH error signal discrimination slope, the grey dashed line is the calculated thermodynamic noise of the cavity mirrors.

Fig 2a is the maximum RAM level, and this date has been normalized versus the PM depth, the RAM level of the homemade EOM is 7ppm, 32dB lower than that of the commercial one. Fig. 2b is the measured RAM-induced error signals of the two EOMs, it is clear that the setup using the home-made EOM is more stable than the other, the fluctuation is supposed to be introduced by temperature fluctuation. For cavity-based ultra-stable lasers using PDH technique, and we calculate the data in Fig. 2b into relative frequency shifts of a high cavity stabilized 1.55 μ m ultra-stable laser, according to a measured relation between laser frequency and error signal, as shown in Fig. 2c, the RAM-induced frequency instability of the home-made EOM is one order in magnitude lower at 1s average time, 100 times lower at 10s, and 200 times lower at 100s.

DISCUSS

We also measure the RAM-induced frequency noise level as a function of laser amplitude noise. For both setups of the homemade EOM and the commercial EOM, the lasers before the EOMs are amplitude-modulated at different frequency points (0.5Hz, 1Hz, 5Hz, 10Hz, 100Hz, 1kHz, 10kHz). We record the RAM-induced error signal and analyze these data with the FFT analyzer, thus we got 7 groups of the RAM-induced frequency noise spectrum, then the 7 frequency points of each EOM are picked up, and last, the data of voltage noise spectrum is converted to frequency noise by the PDH error signal discrimination. At corresponding frequency points, the frequency noises of home-made EOM are about 15 dB lower than that of the commercial one, this date fits well with the short-term RAM-induced frequency instability. And for long-term instability, the temperature fluctuation is supposed to contribute the most. For the first time, we expose that short-

term fluctuation of RAM is mainly determined by the amplitude noise of the laser source, not caused by other factors such as mechanical vibration or disturbance of airflow.

CONCLUSION

We analyze the two dominant effects lead to RAM and present a passive method using a well-designed EOM to avoid the effects. The RAM level is suppressed to 10^{-6} level, and The RAM-induced frequency instability for our cavity-based ultra-stable laser has been reduced less than 1×10^{-16} using the homemade EOM. At last we expose that the short-term fluctuation of RAM is mainly determined by the amplitude noise of the laser.

ACKNOWLEDGMENT (Heading 5)

The preferred spelling of the word “acknowledgment” in America is without an “e” after the “g.” Avoid the stilted expression “one of us (R. B. G.) thanks ...”. Instead, try “R. B. G. thanks...”. Put sponsor acknowledgments in the unnumbered footnote on the first page.

REFERENCES

- [1] B. P. Abbott et al, “Observation of Gravitational Waves from a Binary Black Hole Merger,” *Phys. Rev. Lett.*, vol. 116, pp. 061102, 2016.
- [2] A. Elia, P. M. Lugarà, C. D. Franco and V. Spagnolo, “Photoacoustic Techniques for Trace Gas Sensing Based on Semiconductor Laser Sources,” *Sensors*, Vol. 9, pp. 9616, 2009.
- [3] Y. Y. Jiang, A. D. Ludlow, N. D. Lemke, R. W. Fox, J. A. Sherman, L.-S. Ma and C. W. Oates, “Making optical atomic clocks more stable with 10^{-16} -level laser stabilization,” *Nat. Photonics.*, Vol. 5, pp. 158, 2011.
- [4] E. A. Whittaker, M. Gehrtz, and G. C. Bjorklund, “Residual amplitude modulation in laser electro-optic phase modulation,” *J. Opt. Soc. Am. B.*, vol. 2, pp. 1320, 1985.
- [5] N. C. Wong and J. L. Hall, “Servo control of amplitude modulation in frequency-modulation spectroscopy: demonstration of shot-noise-limited detection,” *J. Opt. Soc. Am. B.*, vol. 2, 1527 1985.
- [6] W. Zhang, M. J. Martin, C. Benko, J. L. Hall, J. Ye, C. Hagemann, T. Legero, U. Sterr, F. Riehle, G. D. Cole, and M. Aspelmeyer, “Servo control of amplitude modulation in frequency-modulation spectroscopy: demonstration of shot-noise-limited detection,” *Opt. Lett.*, vol. 39, pp. 1980, 2014.
- [7] F. Du Burck, O. Lopez, and A. El Basri, “Narrow-Band Correction of the Residual Amplitude Modulation in Frequency-Modulation Spectroscopy,” *IEEE Trans. Instrum. Meas.*, vol. 52, pp. 288, 2003.
- [8] H. Müller, S. Herrmann, T. Scholdt, M. Scholz, E. Kovalchuk, and A. Peters, “Offset compensation by use of amplitude-modulated sidebands in optical frequency standards,” *Opt. Lett.*, vol. 28, pp.2186, 2003.
- [9] R. W. P. Drever, J. L. Hall, F. V. Kowalski, J. Hough, G. M. Ford, A. J. Munley, and H. Ward, “Laser Phase and Frequency Stabilization Using an Optical Resonator,” *Appl. Phys. B.*, vol. 31, pp. 97, 1983.
- [10]

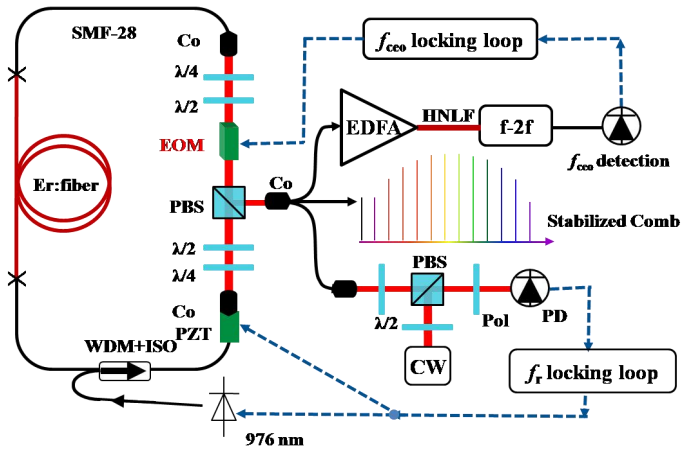


Fig. 1. The setup of the Erbium fiber laser frequency comb. $\lambda/2$: Half-wave plate; $\lambda/4$: Quarter-wave plate; WDM: Wavelength division multiplexer; ISO: Isolator; PBS: Polarization beam splitter; CO: Collimator; PD: Photodetector; PZT: Piezoelectric transducer; EOM: Electro-Optic Modulator; EDFA: Erbium-Doped fiber amplifier; HNLF: Highly nonlinear fiber; CW: Continuous laser.

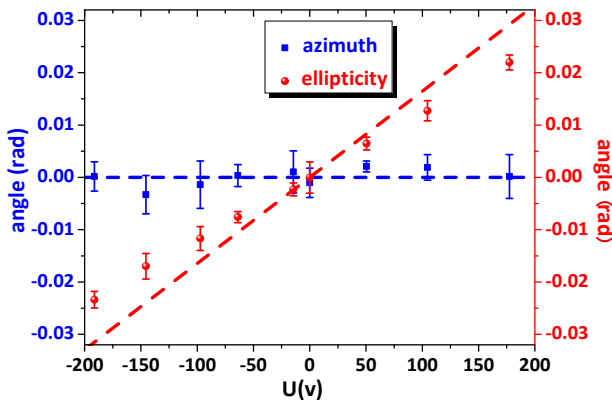


Fig. 2. The relation between the polarization state tuning and the voltage on the EOM (theoretical data: dashed line, experimental data: points)

The output of the laser is separated into three branches as shown in the right half of Fig. 1. One branch is the optical frequency comb output for utilization; the other two are used for produce an f_{cco} signal and a beat note with a 1550 nm continuous wave (CW) laser, respectively. The f_{cco} signal detected by an inline $f-2f$ interferometer at ~ 1000 nm after amplifying ~ 30 mW output power from the laser. The signal-to-noise ratio (SNR) of the detected f_{cco} signal is about 40 dB under 300 kHz resolutions.

We record the variation of the f_{cco} to the voltage on the EOM using a counter when the laser operates in a certain state. The frequency control dynamic range of f_{cco} is about 400 MHz, as shown in Fig. 3. Comparing to the traditional intro-cavity EOM with the same size, the frequency sensitivity of f_{cco} to voltage is ~ 50 times larger. We propose that the corresponding large frequency control dynamic range because it benefits from birefringence of the whole cavity fiber instead of only index change of an EOM crystal driven by tunable electric-field. Polarization state tuning of the laser can lead to a group-velocity shift while the phase velocity keeps relatively stable in

the mode-locked laser. Hence, f_{cco} , representing difference between group velocity and phase velocity, is sensitive to polarization state of the fiber laser. Note that the EOM in our system, only tuning the polarization state in ellipticity, may not represent the maximum frequency dynamic range. However, we can conclude that a relatively large dynamic frequency steering (at least a few of 10^{-7}) can be achieved by tuning lasers polarization state. And we also note that no side effect is observed during experiment by monitoring the optical spectrum and the relative intensity noise of the laser.

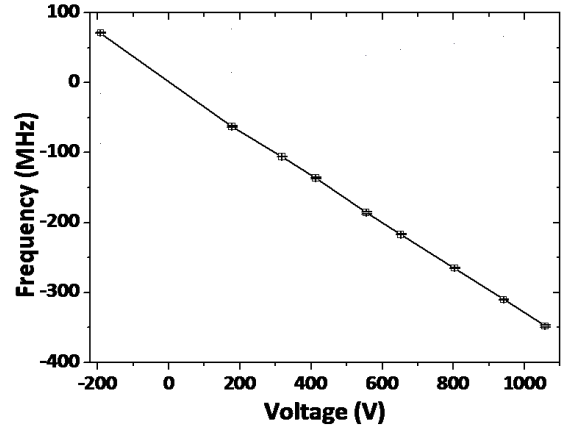


Fig. 3. Frequency variation of f_{cco} as a function of voltage for certain operation state.

To investigate the ability of the special home-made EOM, we used it to stabilize f_{cco} onto a RF reference signal. The signal at 245.5 MHz is flitted and enters a double-balance mixer to produce an error signal by comparing with the RF reference signal. The error signal is then fed back to the EOM with a home-made loop filter. On the other hand, we stabilize a comb tooth onto a CW laser at 1550 nm by controlling both pumping power and the PZT.

Fig. 4(a) shows frequency spectra of the phase stabilized the f_{cco} . We observe servo gain bumps at ~ 650 kHz and ~ 1.8 MHz by optimizing loop filter parameters, indicating that f_{cco} control loop has a broad servo bandwidth. In this state of the system, we measured that the phase noise of f_{cco} is generally in the range of -75 dB rad^2/Hz \sim -85 dB rad^2/Hz expect some noise bumps from 1 Hz to 100 kHz, and the corresponding phase jitter is about 0.16 rad, as shown in fig. 4(b). Down-converted frequency of f_{cco} at 30 MHz is recorded with a Π -type counter (made by K&K company). Fig. 4(c) shows the relative in-loop frequency stability of f_{cco} (normalized with the optical frequency of ~ 192 THz) is about 2×10^{-17} at 1 s and scales down with a slope of $1/\tau$ for short term. The peak-to-peak fluctuation is about 20 mHz. Note that the in-loop frequency stability of a comb tooth is about 10 times higher due to the limitation of the pumping power. We also note that the power fluctuation caused by f_{cco} control with our home-made EOM is only $1/270^{\text{th}}$ of the pumping power control method [12].

III. CONCLUSION

In summary, we demonstrate a servo control method for f_{ceo} stabilization of an Er: fiber optical frequency comb system with a home-made EOM by tuning polarization state of the laser. This approach can be used to control f_{ceo} in broad bandwidth and a large dynamic range by taking the birefringence of the laser cavity fiber. We obtain the phase noise of the stabilized f_{ceo} is 0.16 rad from 1 Hz to 100 kHz. And the in-loop frequency stability of f_{ceo} is about 2×10^{-17} at 1 s and roll down to 10^{-19} at 10^3 s. The EOM in our system tunes polarization state only in ellipticity. We plan to design a new EOM to rotate the laser's polarization state in azimuth or/and in ellipticity, which may obtain a larger frequency controlling dynamic.

References

- [1] S. A. Diddams, L. Hollberg, and V. Mbele. "Molecular Fingerprinting with the Resolved Modes of a Femtosecond Laser Frequency Comb." *Nature* 445, 7128 (2007): 627-30.
- [2] B. J. Bloom, T. L. Nicholson, J. R. Williams, S. L. Campbell, M. Bishof, X. Zhang, W. Zhang, S. L. Bromley, and J. Ye. "An Optical Lattice Clock with Accuracy and Stability at the 10⁻¹⁸ Level." *Nature* 506, 7486 (2014): 71-75.
- [3] A. Wirth, M. T. Hassan, I. Grguras, J. Gagnon, A. Moulet, T. T. Luu, S. Pabst, *et al.* "Synthesized Light Transients." *Science* 334, 6053 (2011): 195-200.
- [4] J. J. McFerran, E. N. Ivanov, A. Bartels, G. Wilpers, C. W. Oates, S. A. Diddams, and L. Hollberg. "Low-Noise Synthesis of Microwave Signals from an Optical Source." *Electronics Letters* 41, 11 (2005): 650-51.
- [5] I. Coddington, W. C. Swann, L. Nenadovic, and N. R. Newbury. "Rapid and Precise Absolute Distance Measurements at Long Range." *Nature Photonics* 3, 6 (2009): 351-56.
- [6] J. Rauschenberger, T. M. Fortier, D. J. Jones, J. Ye and S. T. Cundiff, "Control of the frequency comb from a mode-locked Erbium-doped fiber laser." *Optics Express* 10, 24 (2002):1404-10.
- [7] D. D. Hudson, K. W. Holman, R. J. Jones, S. T. Cundiff, J. Ye, and D. J. Jones. "Mode-Locked Fiber Laser Frequency-Controlled with an Intracavity Electro-Optic Modulator." *Optics Letters* 30, 21 (2005): 2948-50.
- [8] B. R. Washburn, R. W. Fox, N. R. Newbury *et al.* "Fiber-laser-based frequency comb with a tunable repetition rate." *Optics Express* 12, 20 (2004):4999-5004.
- [9] C. C. Lee, C. Mohr, J. Bethge, S. Suzuki, M. E. Fermann, I. Hartl, and T. R. Schibli. "Frequency Comb Stabilization with Bandwidth beyond the Limit of Gain Lifetime by an Intracavity Graphene Electro-Optic Modulator." *Optics Letters* 37, 15 (2012): 3084-86.
- [10] S. Koke, C. Grebing, H. Frei, A. Anderson, A. Assion, and G. Steinmeyer. "Direct frequency comb synthesis with arbitrary offset and shot-noise-limited phase noise." *Nature Photonics* 4, (2010): 462-465.
- [11] M. Nakazawa, K. Kikuchi and T. Miyazaki. "High spectral density optical communication technologies." Ch 2 (Springer, New York, 2010).
- [12] Y. Y. Zhang, L. L. Yan, W. Y. Zhao, *et al.* "A Long-Term Frequency-Stabilized Erbium-Fiber-Laser-Based Optical Frequency Comb with an Intra-Cavity Electro-Optic Modulator." *Chin. Phys. B* 24, 6 (2015): 64209-064209.

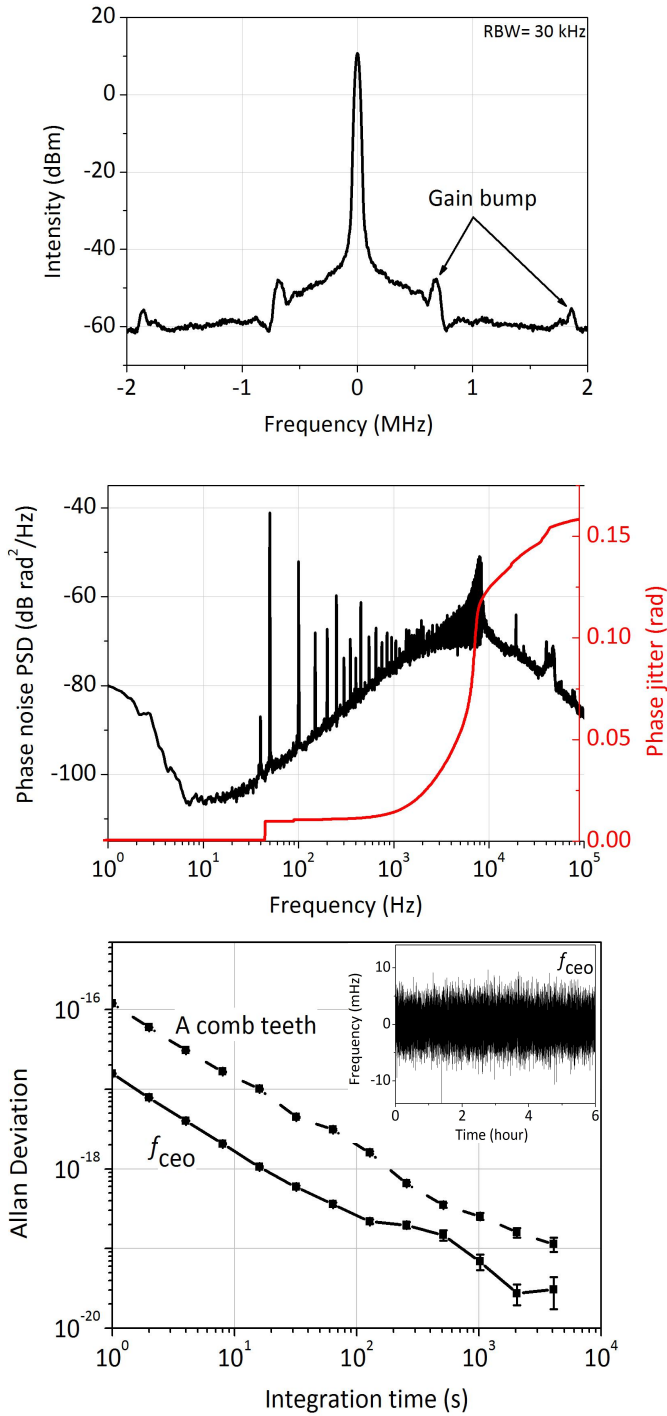


Fig. 4. (a) frequency spectrum of in-loop f_{ceo} ; (b) phase noise and phase jitter of in-loop f_{ceo} ; (c) In-loop frequency stability of f_{ceo} (solid black square) and a comb tooth @ 1550 nm (solid black square).

Time transfer over a White Rabbit network

Namneet Kaur, Philip Tuckey, and Paul Eric Pottie

LNE-SYRTE, Observatoire de Paris, PSL Research University, CNRS, Sorbonne Universités,
UPMC Univ. Paris 06, 61 avenue de l'Observatoire,
75014 Paris, France
namneet.kaur@obspm.fr

Abstract—We started experiments with White Rabbit at LNE-SYRTE for time and frequency dissemination to a large number of users over long haul telecommunication networks. We consider in this paper preliminary work performed on fiber spools, and comparing two situations, one link with one optical fiber and two colors, and a second link with two fibers and a single wavelength. We present preliminary results showing time deviation down to 1 ps at 1000 seconds and Allan deviation as low as 10^{-15} for about 10000 seconds, for both configurations. We discuss the effect of chromatic dispersion on long haul time transfer regarding stability and accuracy. Finally, we outline our plan for future work.

Keywords—White Rabbit, Long haul time and frequency dissemination, Chromatic dispersion

I. INTRODUCTION

Over the last fifteen years, optical fiber links have been intensively studied for frequency dissemination. They have demonstrated frequency transfer with uncertainties below 10^{-17} over several hundred km [1 and references therein]. Today optical fiber links are the most accurate way for comparing remotely located atomic clocks [2]. Time transfer was by comparison less intensively studied. After seminal work by Jefferts *et al.* [3], using SONET or SDH frames, relatively few experiments were carried out over the following decade as Global Navigation Satellite System (GNSS) solutions fulfilled most needs. However weaknesses of GNSS solutions, such as their vulnerability to jamming or spoofing, but also the increasing need for accurate and secure time dissemination for critical applications, have led to renewed interest for this research [4]. There has been an increasing demand for access to precise time and frequency standards in areas such as telecommunication, navigation, internet, metrology for industry and for scientific applications.

Time and frequency transfer over optical fiber links has emerged as an excellent alternative to GNSS based methods. Several studies are being undertaken all over the world for large scale time dissemination [6-10]. The main objective of our study is to disseminate time (and frequency) to multiple users (typically hundreds of users) over long haul telecom fiber links with time accuracy in the range of one microsecond at worst to about one nanosecond. We initiated for that purpose an experiment with White Rabbit technology.

II. WHITE RABBIT

A. Introduction

White Rabbit (WR) is a multi-laboratory, multi-company collaboration for the development of an Ethernet based network ensuring sub-nanosecond synchronization and

deterministic data transfer [5]. It was initiated at CERN in 2008 as a potential successor for the General Machine timing system. It was developed for providing accurate time synchronization for CERN's accelerator complex consisting of particle detectors such as ATLAS, ALICE and others. White Rabbit technology is based on PTP (Precision time protocol) using Synchronous Ethernet and Digital Dual-Mixer Time Difference (DDMTD) phase detection. It demonstrates sub-nanosecond time stability and synchronization of arrays of instruments over 10 km scale networks [6].

B. White Rabbit for precise time transfer on long haul fiber links

In view of the timing capabilities of WR, several studies have focused on precise time and frequency transfer using White Rabbit in the last two years. Two experiments were built. The first one is a time transfer experiment between Espoo and Kajaani, where WR is carried on a dark C-band channel over an active Dense Wavelength Division Multiplexing network of the Finnish University Research Network (FUNET). The link length is 950 km. Including a large number of compensation dispersion spools and unidirectional EDFAs, the VTT group demonstrated standard deviation in time as low as 20 ps at 1000 seconds integration time, probably limited by the local GPS receiver in Kajaani for long integration time [7]. The second experiment connects VSL to VuA and NiKhef with a bi-directional link of 2 x 137 km. WR is carried by SURFNet on their active telecommunication network on the Coarse Wavelength Division Multiplexing band. This experiment achieved a time stability of 10 ps at 1000 seconds integration time [7]. Finally these two experiments recently presented an accuracy budget below 8 ns using two quite different approaches [7].

III. WHITE RABBIT AT SYRTE

We are following the approach of VTT, and our work focuses on using WR for accurate long haul time dissemination compatible with active telecommunication networks, using unidirectional configurations, long range small form factor pluggable (SFP) optical transceivers and dense wavelength division multiplexing (DWDM) technology.

We present here the preliminary work we have performed in the laboratory, with two white rabbit switches and two end-node receiver (SPEC-boards). To study the role of chromatic dispersion we use fiber spools and several sets of SFP emitters. We describe in the next section our experimental White Rabbit network setup, expectations on the role of chromatic dispersion, and the experimental results.

A. Experimental Setup

The experimental setup is illustrated in Figure 1. We have two White Rabbit Switches (WRS) and two White Rabbit nodes of type SPEC-DIO [5]. The Grandmaster White Rabbit Switch (GM) is frequency and phase locked to a local 10 MHz reference (from a SYRTE H-Maser signal) and a one pulse per second reference (PPS REF) of the laboratory. This switch provides the timing reference for the entire White Rabbit network. The second switch, called the Master, is synchronized to the GM by a short unidirectional link of length comprised between 14 m and 25 km. This realizes an architecture close to the one that could be implemented in the future on an active network.

We then installed two links from the Master to the slave SPEC boards #1 and #2. First the unidirectional link utilizes two fiber spools with approximately equal lengths. We work with a single wavelength of about 1541 nm. The SFPs are from the same manufacturer. They are long range SFPs with a specified range of 120 km. In order to avoid saturation of the receiver, we insert in both arms a 15 dB attenuator. This link is referred to as “bi-fiber”.

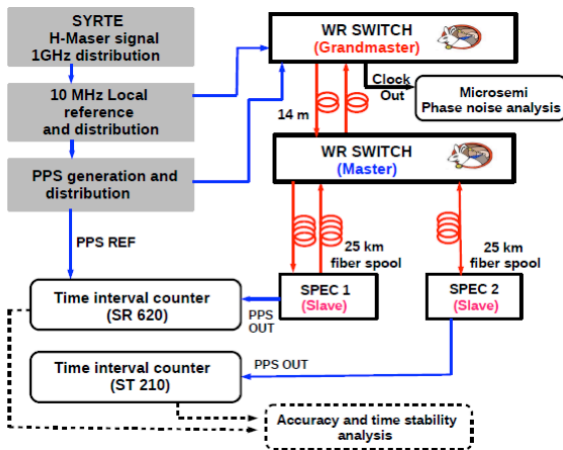


Figure 1. Experimental setup

The second slave node, SPEC2, is synchronized to the Master switch over a bidirectional link using one 25 km fiber spool. We work with bi-color SFPs, at 1310 and 1490 nm. The uplink was at 1490 nm and the down link at 1310 nm. This setup is referred to as “bi-color”.

Time is transferred from the Grandmaster to the Master and then to the slaves in a hierarchical manner using a cascaded topology network. Each of the switches and nodes outputs a PPS signal that may be compared with the PPS time reference signal. A time interval counter (TIC) measures the delay between the PPS REF signal from the Pulse Distribution Unit (PDU) and the PPS out of the slave boards. We use an SR620 for the bi-fiber configuration (SPEC1), and a high performance time interval counter Phusipus ST201 [13-14] for the bi-color configuration (SPEC2). The experiment is performed under well controlled environmental conditions. The two links to the end-nodes are used and recorded simultaneously. Thus any

variation of the reference signal and the first link from GM to Master is in common mode.

B. Effect of Chromatic Dispersion

Chromatic Dispersion is caused by the variation of the refractive index with wavelength. This generates delays between the wavelengths and broadens the transmission pulse as it propagates along the fiber. The propagation delay t for a fiber of length L is given by the equation

$$t = \frac{n(\lambda)L}{c} \quad (1)$$

where $n(\lambda)$ is the refractive index as a function of wavelength λ , given by the Sellmeier equation

$$n^2(\lambda) = 1 + \frac{B_1\lambda^2}{\lambda^2 - C_1} + \frac{B_2\lambda^2}{\lambda^2 - C_2} + \frac{B_3\lambda^2}{\lambda^2 - C_3} \quad (2)$$

where $B_{1,2,3}$ and $C_{1,2,3}$ are experimentally determined Sellmeier coefficients (note that these are not accurately known). The chromatic dispersion coefficient D is defined as:

$$D(\lambda) = \frac{1}{L} \frac{dt}{d\lambda} \quad (3)$$

$D(\lambda)$ represents the variation of the delay with the wavelength. For SMF28 fiber the dispersion is equal to 17 ps/nm/km at 1550 nm and 13 ps/nm/km at 1490 nm [18].

25 km spools	1310/1490	1541
Wavelength difference (nm)	180	<.5
Time shift (ns)	30.8	<.1
Linewidth (nm, as specified)	3	0.08
Instability associated to specification (ps)	515	25
Linewidth (nm, measured 4s measurement time)	0.032	0.024
Instability @4s (ps)	5.5	7.3

Table 1. Comparison of the effect of chromatic dispersion on stability and time offset for a link using commercial SFPs in two situations: a bi-color link using 1310/1490nm emitters and a single fiber, and a bi-fiber link using DWDM long range emitters @ 1541 nm and two fibers.

Chromatic dispersion affects both the accuracy and the stability of the time transfer. We evaluate the order of magnitude of the effect on our 25 km spools. To do so, we perform optical spectrum analysis of our emitters with a spectrum analyzer Yokogawa AQ6370C, using a resolution bandwidth of 2pm. We observe that the spectrum of emission of 1310 emitters are extremely poor, with many peaks over tens of nm. Using a gaussian fit to the recorded spectra of the SFPs at 1490 nm and 1541 nm we measured linewidths of 32.1

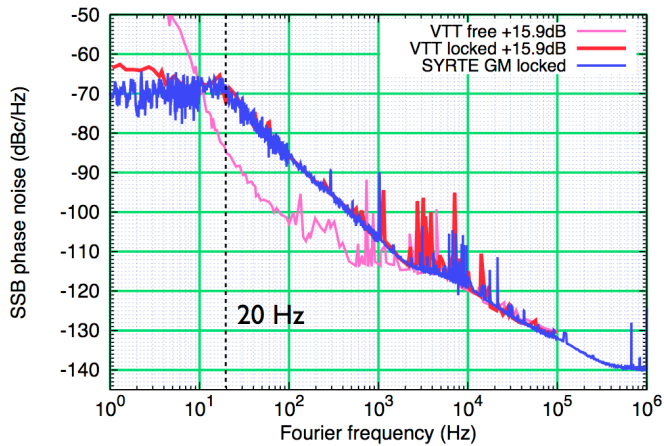


Figure 2. Power spectral density of the White Rabbit switch clock output in locked and free running modes, showing the results of this work and the previous measurements by A. Wallin of VTT [17].

pm and 23.6 pm respectively over 4 s measurement time. The spectrum of the CWDM SFPs is clearly wider than that of the DWDM SFPs. A better measurement campaign should still be carried out with a better resolution and better control of the bandwidth of measurement. We summarize in the table 1 the results of the evaluation of the effect of chromatic dispersion for a WR link, in both the uni-directional and bi-directional configurations, using the linewidth specifications of the SFPs and our measured linewidths. It is important to keep in mind that the chromatic dispersion scales linearly with the length of the link. From the values reported here, it is clear that chromatic dispersion plays an important and limiting role for long haul fiber links with SFPs, and that care must be taken on the frequency stability of the emitters for links longer than 100 km.

C. Results

The Power Spectral Density (PSD) of the phase noise of the Grandmaster for free-running and locked modes is evaluated using a Microsemi Phase test set 5120A. The result is presented in Figure 2. The PSD measured for the 62.5 MHz clock output is approximately -70 dBc/Hz below the locking frequency of about 20 Hz. Much lower phase noise could be achieved by improving the local oscillator of the master switch and by improving the PLL bandwidth [16]. We plot for comparison the result of a similar measurement performed by A. Wallin of VTT [17]. The two data sets are in perfect agreement, when taking into account the frequency ratio between the two outputs of our respective white rabbit switches (10 MHz at VTT and 62.5 MHz at SYRTE).

The time transfer performance to the slave outputs is obtained from the TIC measurements. Figure 3 displays a few days of phase data for the bi-fiber and bi-color data set, showing peak-peak fluctuations of about 150 ps. We observe very stable long data sets with almost no phase drift (typically a few $10^{-17}/s$). We also observe occasional phase glitches, such as the one shown in Figure 3, for which the reasons remain unknown. The time deviation plot is presented in Figure 4. We observe that the TDEV reach a minimum of about 1-2 ps at 1000 s, after which the TDEV follows a rebound. This TDEV

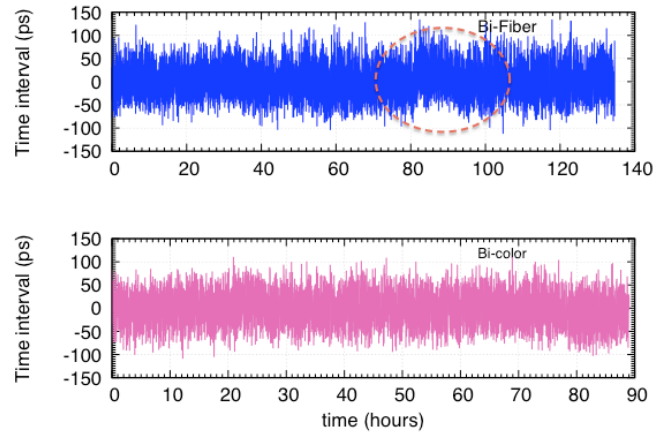


Figure 3. Time intervals raw data using the bi-fiber and the bi-color end-node modules. The time offset were removed.

minimum is 5 times lower than the previously reported value.. WR technology is improving fast, and we now have off the shelf devices whose performance approaches the resolution limit of time interval counters such as the SR620.

The Allan deviation is presented in Figure 5. It scales down as τ^{-1} , and becomes smaller than 10^{-15} at 65000 s of integration time. We also perform a measurement with 50 km of fiber spools between the master and the slave, with the uni-directional setup and with the SR620 TIC. We observe a similar TDEV, even slightly better. Figures 4 and 5 summarize all of the measurements done.

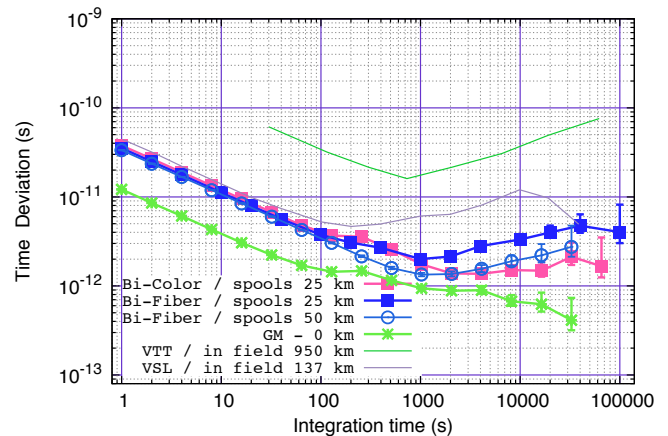


Figure 4. Time deviation for the unidirectional and bidirectional links.

With 25-km fiber spools we expect a contribution of the chromatic dispersion to the instability of about 5-7 ps @ 4 s. At the present level of performance of White Rabbit, this effect is not detectable in the our short-distance experiment in the laboratory, and we observe similar behaviors for the two configurations.

IV. CONCLUSION

We tested a White Rabbit solution to disseminate time to many users. We performed preliminary tests in the laboratory using a complete WR architecture comprising two white rabbit switches and two end nodes. We measured the time deviation of the end nodes compared to the laboratory reference using the

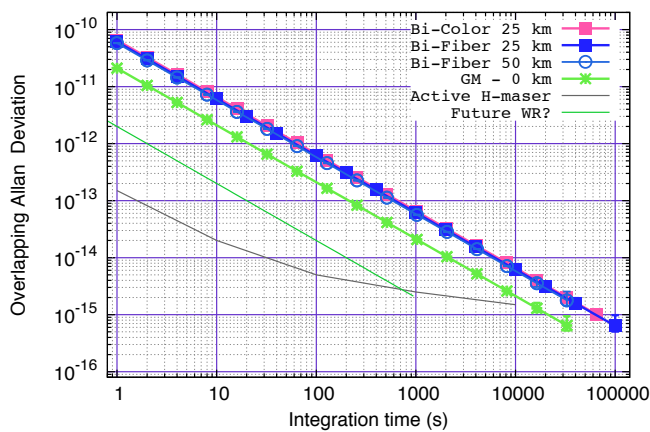


Figure 5. Overlapping Allan deviation for unidirectional and bidirectional link setup.

two popular link configurations: a unidirectional link using one wavelength and two fibers, and a bidirectional link using two colors and one fiber. The links were built using 25 km fiber spools. We obtained very similar performances for these two links over this short distance. We obtained a time deviation of about a picosecond at 1000 seconds of integration time, which is about 5 times better than the previously reported value. We also obtained an overlapping Allan deviation of 10^{-15} at 65000 seconds under well controlled laboratory conditions. For long haul links of length greater than 100 km, the unidirectional configuration must be utilized to ensure compatibility with telecom networks and benefit from the installed backbone equipment. The first challenge to overcome, in order to limit the time deviation to the level of a few tens of ps at short integration times, is to control and reduce the effect of chromatic dispersion. The second drawback of the DWDM approach is that the fiber path length imbalance can lead to a dramatic time offset and hence inaccuracy if the lengths are not accurately measured. The challenge here is to measure accurately the one-way propagation delay. Pseudo-ranging methods as employed in GNSS, based on the autocorrelation of pseudo-random codes, seem to be a promising technique [8,15]. The practical implementation of such techniques in White Rabbit is still an open question that needs to be addressed in order to reach high timing accuracy.

REFERENCES

[1] O. Lopez, F. K  f  lian, H. Jiang, A. Haboucha, A. Bercy, F. Stefani, B. Chanteau, A. Kanj, D. Rovera, J. Achkar, C. Chardonnet, P.-E. Pottie, A. Amy-Klein, G. Santarelli, "Frequency and time transfer for metrology and beyond using telecommunication network fibres", *Comptes Rendus Physique*, 16 (5), pp. 459-586 (2015)

[2] C. Lisdat, G. Grosche, N. Quintin, C. Shi, S.M.F. Raupach, C. Grebing, D. Nicolodi, F. Stefani, A. Al-Masoudi, S. D  rscher, S. H  fner, J.-L. Robyr, N. Chiodo, S. Bilicki, E. Bookjans, A. Koczwarra, S. Koke, A. Kuhl, F. Wiotte, F. Meynadier, E. Camisard, M. Abgrall, M. Lours, T. Legero, H. Schnatz, U. Sterr, H. Denker, C. Chardonnet, Y. Le Coq, G. Santarelli, A. Amy-Klein, R. Le Targat, J. Lodewyck, O. Lopez, P.-E. Pottie, "A clock network for geodesy and fundamental science," <http://arxiv.org/ftp/arxiv/papers/1511/1511.07735.pdf>

[3] S. R. Jefferts, M. A. Weiss, J. Levine, S. Dilla and T. E. Parker, "Two-way time transfer through SDH and SONET systems," *European Frequency and Time Forum* (1996), pp. 461-464. DOI: 10.1049/cp:19960095

[4] M. Weiss, J. Eidson, C. Barry, D. Broman, L. Goldin, B. Iannucci, E.A. Lee and K. Stanton. *Time-Aware Applications, Computers, and Communication Systems (TAACCS)*. NIST Tech Note 1867, (2015).

[5] P. Krehlik, L. Sliwczynski, L. Buczek, M. Lipinski, "Fiber-Optic Joint Time and Frequency Transfer With Active Stabilization of the Propagation Delay", *IEEE Trans. Instrum. Meas.*, vol. 61, no. 10, pp. 2844-2851, (2012).

[6] G Wu, L. , H. Zhang, J. Chen., "High-precision two-way optic-fiber time transfer using an improved time code", *Rev. Sci. Instruments* 85(11):114701 (2014); G. Wu, J.g Hu, H. Zhang, and J. Chen, "Distributed high-precision time transfer through passive optical networks " *Optical Engineering* 53(9), 096113 (2014)

[7] E.F. Dierikx, A.E. Wallin, T. Fordell, J. Myyry, P. Koponen, M. Merimaa, T.J. Pinkert, J.C.J. Koelemeij, H.Z. Peek and R. Smets, "White Rabbit Precision Time Protocol on Long Distance Fiber Links ", *IEEE Transactions on Ultrasonics, Ferroelectrics, and Frequency Control* In press, TUFFC, DOI: 10.1109/TUFFC.2016.2518122

[8] N. Sotiropoulos, C. M. Okonkwo, R. Nuijts, H. de Waardt, and J. C. J. Koelemeij Delivering 10 Gb/s optical data with picosecond timing uncertainty over 75 km distance *Optics Express* 21(26), pp. 32643-32654 (2013) doi: 10.1364/OE.21.032643

[9] V. Smotlacha, A. Kuna and W. Mache, "Time transfer using fiber links," *EFTF-2010 24th European Frequency and Time Forum*, Noordwijk, 2010, pp. 1-8. DOI: 10.1109/EFTF.2010.6533650

[10] S.-C Ebenhag, P. O. Hedekvist, K. Jaldehag, C. Rieck, Time transfer between UTC(SP) and UTC(MIKE) using frame detection in fiber-optical communication networks, *Precise Time and Time Interval Meeting (PTTI'11)*, Long Beach, Ca, 2011-11-14

[11] White Rabbit. <http://www.ohwr.org/projects/white-rabbit>.

[12] M. Lipinski, T. Wlostowski, J. Serrano, and P. Alvarez, "White rabbit: a PTP application for robust sub-nanosecond synchronization," *Proc. of the International IEEE Symposium on Precision Clock Synchronization for Measurement Control and Communication (ISPCS)*, 2011. <http://ieeexplore.ieee.org/stamp/stamp.jsp?tp=&arnumber=6070148>

[13] E. Samain et al., "Time Transfer by Laser Link - T2L2: Current status and future experiments", *IFCS proceeding 2011*, DOI: 10.1109/IFCS.2011.5977854.

[14] ST201,PHUSIPUS integration,8 ALLEE BELLEVUE, 06460 SAINT VALLIER DE THIEY, FRANCE

[15] L. Sliwczynski, P. Krehlik, A. Czubla, L. Buczek, and M. Lipinski, "Dissemination of time and RF frequency via a stabilized fibre optic link over a distance of 420 km," *Metrologia* 50, 133 (2013).

[16] M. Rizzi, 9th WR Workshop, talks available at <http://www.ohwr.org/projects/white-rabbit/wiki/Mar2016Meeting>

[17] <http://www.ohwr.org/projects/white-rabbit/wiki/Mikes>; see also http://www.anderswallin.net/2014/11/white-rabbit-switch-pps-output-test/wrs_tdev_2014-11-26/ TDEV data from the 20th November 2014

[18] *ITU-T Rec. G.652* <https://www.itu.int/rec/>

Sub-Nanosecond Synchronization Accuracy for Time-Sensitive Applications on Industrial Networks

José Luis Gutiérrez-Rivas
Department of Computer
Architecture and Technology
University of Granada
Granada, Spain
Email: jlgutierrez@ugr.es

César Prados
GSI Helmholtz Centre for Heavy Ion Research
Darmstadt, Germany
Email: c.prados@gsi.de

Javier Díaz
Department of Computer
Architecture and Technology
University of Granada
Granada, Spain
Email: jda@ugr.es

Abstract—White Rabbit (WR) is a technology born at CERN able to provide sub-nanosecond accuracy for time and frequency transfer using standard PTP and Synchronous Ethernet (SyncE). WR was designed to be the main time provider system for scientific infrastructures such as particle accelerators and colliders. This contribution proposes a change of approach for the WR PTP distribution to become a timing solution with strong focus on engineering frameworks, such as Smart Grid. This approach includes a new design following IEC 61850, where new developments make possible for WR devices to work as Transparent Clocks (TCs) instead of Boundary clocks (BCs) as in the case today. This maximizes the interoperability with other industrial devices and, at the same time, the utilization of TCs offers better synchronization results since PTP messages include the entire network delay considering all TCs as a unique fiber. Using TCs for time and data propagation also opens the doors to high-availability and fault tolerance features for mission-critical and time-sensitive applications. It supports the development of redundancy protocols, such as HSR or PRP to guarantee the delivery and reception of critical services such as timing and substation events (GOOSE, GSSE, SMV). Finally, P2P approach offers a better synchronization mechanism to avoid synchronization loss of middle nodes and also supports the development of redundancy protocols to make possible the migration of WR to industrial networks.

I. INTRODUCTION

Smart Grid combines electricity and IT infrastructures combining and interconnecting all users (producers, operators, marketers, consumers etc) in order to continue working on balancing supply and demand over an increasingly complex network.

The evolution of Smart Grid imposes the utilization of dependable communication networks, where availability, safety, security and reliability are therefore key elements. At the same time, the utilization of widespread infrastructures like Ethernet networks is desirable. For this end, single point of failure should be avoided and low latency mechanisms are very desirable, so that control actions can be executed with fast responses.

On the other hand, timing information is considered critical in these kind of environments since a proper synchronized communication must be guaranteed between the different elements that conform the grid. For this reason, high accurate, reliable and scalable technologies are required to distribute time for next generation SmartGrid networks. Typically, the

highest accuracy requirement for time synchronization comes from Phasor Measurement Units (PMUs) [7]. These are fundamental components in grids and are significantly affected by the reliability of synchronization sources like Global Navigation Satellite Systems (GNSS). In fact, using a distributed implementation of PMUs in the power grid, its usage can be further optimized, however vulnerable to a loss or disturbance of synchronization. The IEEE recommends to pursue an alternative method using terrestrial systems as stated in [5]. This is the fact that motivates the utilization/combination of solutions based on GNSS systems with wired time transfer solutions as IRIG-B and most recently, Precision Time Protocol (PTP) IEEE 1588 based on Ethernet networks [1].

Due to the strict requirements of SmartGrid regarding availability and fault tolerance, IEC 61850 [2] suggests the implementation of redundancy protocols within the services offered in the network focusing in substation automation. There are several protocol suggested but SmartGrid and engineering networks mainly use two: the Parallel Redundancy Protocol (PRP) and the High-availability Seamless Redundancy (HSR) protocol. Both PRP and HSR were standardized by the International Electrotechnical Commission in Geneva, as IEC 62439-3 Clause 3 and 5 respectively [3]. Widely used in Power grid, PRP and HSR are redundancy protocol for Ethernet (standardized as IEEE 802.3) networks. The former is used in tree topologies with separate LANs, and the latter in ring topologies and expandable to mesh topologies. Both of them provide zero-time recovery in case of failure of one component. It is suited for applications that demand high-availability and very short switch over time, for example, protection for electrical substation automation. On Smart Grid the recovery time of commonly used protocols like the Rapid Spanning Tree Protocol (RSTP) is not acceptable and therefore solutions implemented at the physical network level like PRP and HSR are necessary. Both of them presents a profile for time distribution in [3] that specifies how time should be distributed using these protocols.

Authors proposed approach is based on a modified PTPv2 protocol technology based on Ethernet optical fibers. The robustness of optic fiber solutions is paramount for a robust and efficient power distribution grid. Furthermore, the utilization of a precise and reliable timing solution that offers synchronization with an accuracy of nanoseconds, is of great importance when implementing areas with demand-side-management, as

planned in the SmartGrid framework where most of the European Countries aim at. For these reasons, the timing technology used in this approach is called White Rabbit (WR), a timing distributor system able to provide time with sub-nanosecond accuracy [6]. The current WR implementation is not compatible with SmartGrid networks reliable requirements since WR was conceptualized to be used in scientific but not engineering infrastructures. For this reason, several developments must be carried out to meet SmartGrid requirements, focusing on PTP dissemination compatibilities, redundancy configurations and scalability for the timing system. These requirements and developments will be presented in this paper in Section II.

II. WHITE RABBIT ADAPTATION TO SMARTGRID NETWORKS

A. White Rabbit Technology

White Rabbit was born at CERN as an Ethernet technology to synchronize devices with a accuracy of less than one nano-second in scientific facilities such as accelerators and colliders. It is based on three elements: an extension of IEC 1588 PTPv2, the distribution of frequency using Synchronous Ethernet (SyncE), and the recovery of the signal phase using Dual Digital Mixer Time Difference (DDMTD) components. WR PTP, called Ported to Silicon PTP (PPSi), implements a hierarchical master-slave architecture where the master uses a two-step synchronization mechanism to send its time to the slave. WR is distributed under an open hardware license and it is available at the Open Hardware Repository. WR main features are:

- Sub-nanosecond synchronization
- Connecting thousands of nodes
- Typical distances of 10 km between nodes but extensible beyond 100Km
- Ethernet-based Gigabit rate reliable data transfer
- Fully open hardware, firmware and software

WR devices are nowadays implemented as Boundary Clocks (BC), which performs the estimation of the link delay and the synchronization hop by hop using a two-step end-to-end (E2E) mechanism to propagate the clock, and *Delay-Request* messages to estimate the delay between them. Each device recovers the clock from its immediately before master frequency reference using SyncE, and after estimating the delay to the master, it computes the offset to the master using PTP frames. E2E is meant to be the best solution in scientific infrastructures, where there is not a complete knowledge of the network topology and PTP-like and non-PTP-like devices may share the network. Regarding scalability, E2E studies have stated that this mechanism increases both jitter and skew of Pulse per Second (PPS) signals as soon as we increment the number of hops in the network. In addition, although E2E can be used in redundant protocols implementation like PRP/HSR, [3] suggests the utilization of P2P instead of E2E for engineering networks.

For this reason, the development of a P2P mechanism becomes almost mandatory to use WR in SmartGrid networks as the main time provider, leading to the utilization of Transparent Clocks (TCs) instead of BCs for the middle nodes

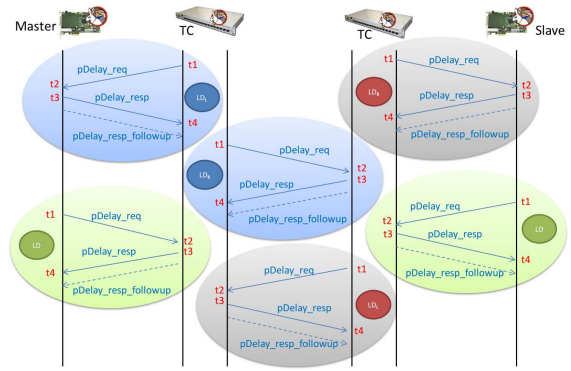


Fig. 1. White-Rabbit delay measurement using Peer-Delay. In contrast to Delay-Request, Peer-delay uses three type of messages (*PDelay_Request*, *PDelay_Response* and *PDelay_resp_followup*) and generates four timestamps to estimate the delay between two adjacent nodes (t_1 , t_2 , t_3 and t_4). The delay is computed as (1).

that compounds the network. Next section II-B describes the implementation of WR TCs using P2P as the main mechanism to distribute time.

B. White Rabbit Transparent Clocks

The development of WR TCs involves the implementation of mainly two mechanisms: a P2P mechanism to send *announce*, *sync* and *follow_up* messages from the master to the slave, and a *Peer-Delay* mechanism to estimate the delay between neighbor devices. P2P is used in engineering networks where all nodes are known to be IEC 1588 compatible and able to distribute time frames. In this type of networks PTP frames and sent from the master to the slave node and forwarded by middle nodes like switches and routers, considering the entire network as a simple fiber link.

Peer-Delay measures the delay of the link between two adjacent nodes using four timestamps (t_1 , t_2 , t_3 and t_4) as Figure 1 shows using three type of messages: *PDelay_Request*, *PDelay_Response* and *PDelay_resp_followup*. First, t_1 corresponds to the moment a node sends a *PDelay_Request* to its adjacent node, t_2 is generated in the other node as soon as *PDelay_Request* is received. This second node responds with a *PDelay_Response* message and generated t_3 , which is received in the requester as t_4 . Previous t_3 is received immediately after in a *PDelay_resp_followup* message. The receiver uses the timestamps to calculate the delay as it follows:

$$delay_{node,node} = (t_2 - t_1 + t_4 - t_3)/2 \quad (1)$$

In P2P, in order to measure the clock offset, *announce*, *sync* and *follow_up* messages are sent from the master to the slave, considering all middle nodes of the network as TCs, where these messages are just forwarded as Figure 2 shows. A Slave node is not aware of the delay from the master since its delay is estimated with the current neighbor nodes using *Peer-Delay*, for this reason it is necessary to keep the track of the delay accumulated by all the links/nodes of the network path. This is performed using the *Correction_Field* (cField) of *follow_up* messages.

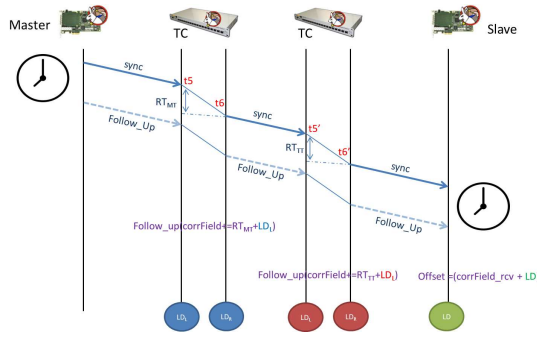


Fig. 2. Clock offset measurement using White Rabbit Transparent Clocks. Master sends *announce*, *sync*, and *follow_up* messages to the slave through TCs. Each time a *sync* goes through a TC, its residence time in the divided is measures and, together with the link delay of the incoming port, it is added to the Correction Field of the next *follow_up*.

Right after the Master sends a *sync* message, t_5 is generated and sent in the next *follow_up*. When a *sync* message is received in a TC, a timestamp $t_{sync_ingress}$ is generated and the message is immediately forwarded to the other active ports generating a t_{sync_egress} timestamp. These two timestamps are used to calculate the *Residence Time* (RT) of each *sync* message on each of the outgoing ports (2). In addition, cField might also add the link delay computed in the incoming port (3).

$$RT = sync_egress - sync_ingress \quad (2)$$

$$cField = RT + link_delay \quad (3)$$

When the end-node receives a *sync* message, it generates t_6 and waits for the *follow_up*, which contains t_5 and the total link delay in the cField. By using (4), the slave adjust its local clock to the Master reference.

$$offset_{ms} = (t_6 - t_5 + cField + link_delay) / 2 \quad (4)$$

Regarding precision problems caused by timestamps generation, note that WR uses hardware timestamps that are generated immediately before/after a PTP frame is sent/received so that the uncertainty that could be introduced by the utilization of these timestamps at higher levels of the OSI model can be reduced to despicable values.

The utilization of P2P is the first key step to adequate WR to SmartGrid, enhancing jitter and skew results and also opening doors to the development of redundancy protocols such as PRP and HSR as [2] suggests for communication networks for power utility automation. Next section II-C presents the implementation of redundancy protocols taking as a reference point the utilization of P2P in engineering networks and thus, SmartGrid.

C. White Rabbit Redundancy Protocols Implementation

PRP and HSR are suggested for time-critical applications in SmartGrid because of two features: reliability and high-availability. Both protocols are based on the duplication of frames in the network. The former is normally used in very

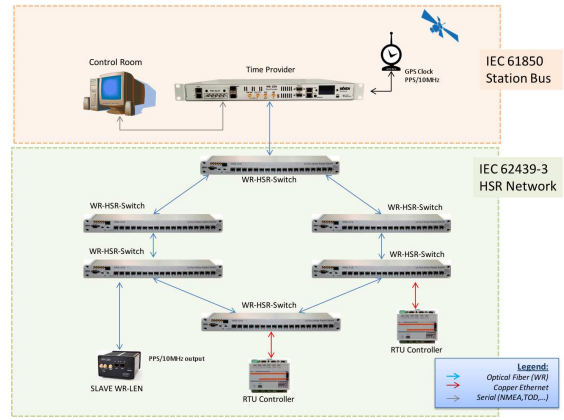


Fig. 3. White Rabbit HSR network for IEC 61850 control substations. The HSR ring is composed by six WR-Switches configured as P2P TCs. The synchronization is propagated from the time provider to the slave nodes following the suggestions of IEC 62439-3. In case of single point of failure in the ring, slave nodes maintains the synchronization with no loss.

big networks composed by more than one LAN. PRP demands to duplicate all network paths, links and devices. The latter is used in ring topologies and requires of a especial hardware to forward the frames through the ring. Due to the few resources needed by HSR, this is the developed protocol chosen for WR devices. In addition, the utilization of redundancy protocols increases fault tolerance and thus, the possibility to recover from a system failure in any of the network paths or devices in approximately zero-time recovery.

All services offered in any industrial network including timing must be reliable. Since all services rely on synchronization, timing dissemination must be done in a very reliable and precise way where the services that depends on time must be available as soon as possible. Hence, a HSR-WR solution using TCs and P2P offers a very precise and reliable technology for SmartGrid.

The implementation of HSR for WR is divided into two phases, the development of the HSR protocol at software level for the WR-PTP, and the hardware required to duplicate and forward frames from one port to others.

III. RESULTS

For the results of this experiment our setup is composed of six WR switches in a daisy chain configuration as figure 4 describes. This paper presents three experiments depending of the middle nodes implementation: E2E Boundary Clocks, P2P Synchronized TCs and P2P Sintonized TCs. Measures have been done in terms of jitter and skew of the 1-PPS signal, comparing the 1-PPS output of the first free-running Master switch to the last one using a Tektronix FCA3000/3100 Counter analyzer [8].

For the first one, all nodes are using the E2E implementation of WR to disseminate the clock information. Middle nodes are configured as a daisy-chain where one port is a slave of the previous one, and the second port is master of the next one. Comparing the first and the last PPS outputs, the insertion of one hops increases skew between these two signals, obtaining as averaged results: 74ns per one hop, 93ns for two hps, 222ns for three hops, 340ns for four hops and 450ns for five hops.

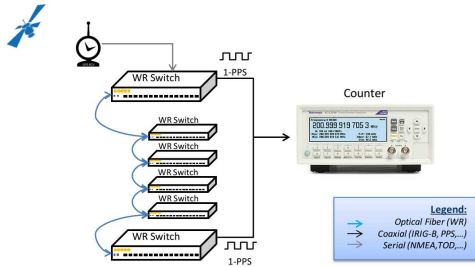


Fig. 4. Experiment Setup. The setup is composed of six WR switches in a daisy-chain configuration, where the first one is the GrandMaster, the last node is the slave, and the middle nodes are configured as 3 different setups: Boundary Clocks, Synchronized-TCs and Sintonized-TCs. The skew of the PPS signals of both the GrandMaster and Slave nodes are compared using a Tektronix FCA3000/3100 counter analyzer.

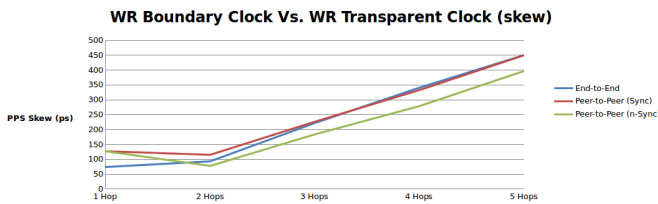


Fig. 5. White Rabbit End-to-End Vs Peer-to-Peer results for PPS skew. E2E and synchronized-TCs present similar results for the skew between the first and the last node PPS output. Using a non-synchronized version of the TC, the skew between the first and the last PPS presents an improvement of 50ps on each hope.

For the second one, all nodes implements a P2P mechanism to estimate the delay and the clock offset. In this experiment, all nodes distribute SyncE and also computes the PTP after forwarding the frames. In other words, middle nodes are sintonized to the main distributed frequency and also synchronized. For this experiment the results are quite similar to the previous one as Table I shows since PTP is still performed in middle nodes.

For the last experiment we have used TCs and P2P with a slightly difference, the do not apply PTP frames to its local clock. In other words, middle nodes are sintonized to the distributed frequency but not synchronized. The results shows that not synchronizing middle nodes, the skew between the PPS outputs is less because less jitter is accumulated per hop, presenting differences of more than 50ps for larger chains (Table I).

Figure 5 shows how P2P offers better synchronization results and more accuracy than the WR implementation using E2E. In terms of jitter and skew, E2E presents an increase as long as the number of hops increases. For the P2P version using sintonized and synchronized TCs, those results are quite similar than the E2E one since the correction of the offset is done by the middle nodes. This correction affects jitter locally and it is accumulated towards the last node.

In concontrast, using TCs which only sintonize to the distributed frequency but not computing the PTP offset, jitter is reduced in every middle node and thus, not accumulated towards the end node as we have been in Figure 5. The worst and the best results using sintonized-TCs presents an improvement of more than 50ns in comparison to the E2E

TABLE I. SKEW RESULTS (PS) FOR E2E, SYNC-P2P AND NON-SYNC-P2P

Skew (ps)	1 Hop	2 Hops	3 Hops	4 Hops	5 Hops
End-to-End	74,1	93,2	222	340,9	450,3
Sync-Peer-to-Peer	127,2	115,2	226,4	332,8	449,8
Non-Sync-Peer-to-Peer	127,2	77,8	183,8	278,7	396,7

Boundary Clocks implementation of WR.

IV. CONCLUSION & FUTURE WORK

Authors are in the way to provide the industrial domain a very accurate solution with redundancy features able to recover from a system failure for both data and time using the most accurate PTP solution nowadays. The implementation of WR TCs using a P2P mechanism to distribute and measure the delay using peerDelay messages in the network, increases the scalability of the timing network offering better results in terms of jitter and skew although this factor is still dependent of the frequency distribution (SyncE). The implementation of non-synchronized TCs improves skew results per hop in more than 50ps compared to the current E2E implementation for WR devices.

Using P2P also offers the possibility to make WR compatible to redundant configurations [3] able to increase service availability and thus, reliability in industrial networks in terms of timing. Future software and hardware (gateway) developments will make possible to recover from a system failure with approximately zero-time recovery for both data and timing frames, which is essential for SmartGrid [2].

ACKNOWLEDGMENT

These results have been partially funded by the Andalusian excellence project VITVIR (TIC-8120) and H2020 Asterics project, grant number 653477. The authors of this paper would like to thank CERN BE-CO-HT unit for all the support provided and especially to Maciej Lipiński for the discussion sessions.

REFERENCES

- [1] IEEE Instrumentation and Measurement Society. *IEEE 1588 Standard for a Precision Clock Synchronization Protocol for Networked Measurement and Control Systems*.
- [2] International Electrotechnical Commission. *IEC 61850 Communication networks and systems for power utility automation*.
- [3] International Electrotechnical Commission. *IEC 62439-3 Industrial communication networks. High Availability Automation Networks*.
- [4] CERN, Open Hardware Repository. <http://www.ohwr.org/>.
- [5] IEEE Std C37.242-2013 *IEEE Guide for synchronization, calibration, testing and installation of PMUs for power system protection and control*.
- [6] Moreira P., Serrano J, Wlostowski T., Loschmidt P. and Gaderer G. *White rabbit: Sub-nanosecond timing distribution over ethernet*. ISBN 978-1-4244-4391-8. International Symposium on Precision Clock Synchronization for Measurement, Control and Communication, 2009. ISPCS 2009.
- [7] C. H. Hauser, D. E. Bakken, and A. Bose, A failure to communicate Next-generation communication requirements, technologies, and architecture for the electric power grid, *IEEE Power Energy Mag.*, vol. 3, no. 2, pp. 4755, Mar./Apr. 2005.
- [8] Tektronix FCA3000/3100 Timer/Counter/Analyzer. <http://www.tek.com/datasheet/fca3000-and-fca3100-series>.

Synchronous Mode-locked Laser Network with Sub-fs Drift and Multi-km Distance

Kemal Şafak^{1,2,*}, Ming Xin^{1,3}, Michael Y. Peng³ and Franz X. Kärtner^{1,2,3}

¹Center for Free-Electron Laser Science, Deutsches Elektronen-Synchrotron, Notkestrasse 85, Hamburg 22607, Germany

²Physics Department, University of Hamburg, Luruper Chaussee 149, 22761 Hamburg, Germany

³Research Laboratory of Electronics, Massachusetts Institute of Technology, Cambridge, Massachusetts 02139, USA

*Email: kemal.shafak@cfel.de

Abstract— We report recent progress made in a synchronous multi-color mode-locked laser network over 4.7-km distance. Output of two remotely synchronized lasers shows only 0.6-fs RMS drift over 40 hours reaching 20th decimal uncertainty in less than 10000-s averaging time. This work will enable sub-fs synchronization of new generation photon science facilities and allow km-scale optical clock comparison with unprecedented precision.

Keywords—Mode-locked lasers; all-optical networks; synchronization; timing jitter; phase noise

I. INTRODUCTION

Mode-locked lasers continue to revolutionize the fields of frequency metrology and laser spectroscopy due to their ultra-low noise properties [1, 2]. To realize the long standing scientific dream of capturing ultrafast structural dynamics with atomic resolution, new generation scientific facilities such as X-ray free-electron lasers [3] and intense laser beamline centers [4] aim to synchronize numerous mode-locked lasers with sub-fs precision across km-distances [5, 6]. Once equipped with such precision, these facilities will initiate radically new science by revealing molecular and atomic processes happening on attosecond timescale. Similarly, comparison of remote optical clocks requires stabilized mode-locked lasers at each clock location to transfer the ultra-stable optical frequency to radio frequency (RF) domain as well as to the slave laser frequency responsible for the fiber-optic transmission [7, 8]. Here we demonstrate a multi-color long-term stable synchronous mode-locked laser network with sub-fs precision and 4.7-km distance using balanced optical cross-correlators (BOC) [9]. Out-of-loop timing drift between two remote lasers is only 0.6 fs RMS over 40 hours corresponding to a timing instability of 1.2×10^{-20} at 70000-s averaging time.

II. SYNCHRONOUS MODE-LOCKED LASER NETWORK

Fig. 1(a) and (b) describe the experimental setup of the synchronous mode-locked laser network incorporating 3 lasers in a star network topology. Our master laser (ML) is a mode-locked laser operating at 1554-nm center wavelength with 216.67-MHz repetition rate locked to a RF reference. The output of the ML is split into two independent timing links with a total length of 4.7 km. Each link consists of a polarization-maintaining (PM) dispersion-compensated fiber spool (1.2 km and 3.5 km long), a PM fiber stretcher, a

motorized delay stage (MD) and a bi-directional PM fiber amplifier (Bi-EDFA). A partially reflecting mirror at the end of each link reflects 10% of the optical power back to the link input.

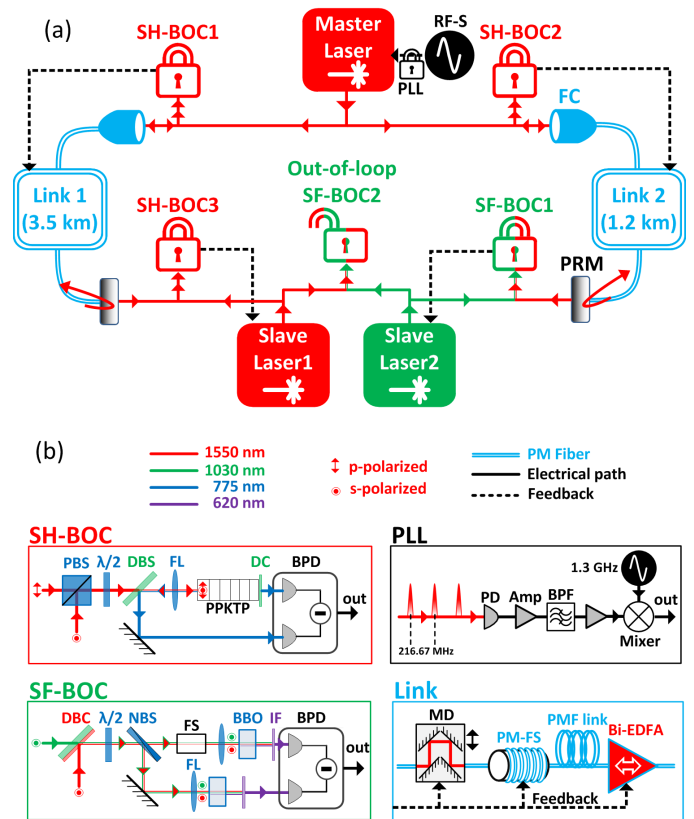


Fig. 1: (a) Experimental setup of the synchronous mode-locked laser network employing 3 lasers. (b) Detailed schematic of the individual components of the experiment. Abbreviations: SH-BOC: second-harmonic BOC; SF-BOC: sum-frequency BOC; PLL: phase-locked loop; RF-S: RF synthesizer; FC: fiber collimator; PRM: partially reflecting mirror; PBS: polarization beam splitter; $\lambda/2$: half-wave plate; DBS: dichroic beam splitter; PPKTP: periodically poled potassium titanyl phosphate crystal; DC: dichroic coating; BPD: balanced photodetector; PD: photodetector; AMP: voltage amplifier; BPF: 1.3-GHz electronic bandpass filter; DBC: dichroic beam combiner; NBS: neutral 50:50 beam splitter; FS: fused-silica plate; BBO: barium borate crystal; IF: interference filter; MD: motorized delay; PM-FS: polarization maintaining fiber stretcher; PMF: PM fiber; Bi-EDFA: PM bi-directional erbium doped fiber amplifier.

The reflected pulses are then combined with fresh pulses from the ML in the type-II second-harmonic (SH) BOCs. SH-BOCs operate at 1554-nm wavelength and realize the cross-correlation with the birefringence between two orthogonally polarized input pulses. SH-BOC1 and SH-BOC2 measure the propagation delay fluctuations in the links and generate error voltages, which are then applied to the fiber stretchers and the motorized delays to compensate for fast jitter and long-term drift, respectively. Furthermore, a third feedback is sent to the pump current of the Bi-EDFAs to eliminate the link power fluctuations caused by the beam misalignments upon the movement of the motorized delays. As detailed in [10], this feedback mechanism ensures drift-free, attosecond precision timing link stabilization by minimizing the jitter induced by the link nonlinearities on the propagating pulses.

Finally, the outputs of the timing-stabilized links are used for remote synchronization of two slave mode-locked lasers. Slave laser 1 (SL1) has the same center wavelength and repetition rate as the ML. Therefore, SH-BOC3 is built to synchronize SL1 to Link 1 output by tuning the repetition rate via its intracavity piezoelectric-actuated (PZT) mirror. Slave laser 2 (SL2), on the other hand, operates at 54.17-MHz repetition rate with an output optical spectrum centered at 1030 nm. To synchronize SL2 to Link 2 output, we build a type-I sum-frequency BOC (SF-BOC1) between 1030 nm and 1554 nm using two BBO crystals (refer to SF-BOC in Fig. 1(b)). Time delay difference between the two arms is adjusted with a glass plate to maximize the timing sensitivity of the balanced detection. Finally, the outputs of SL1 and SL2 are combined in the free-running SF-BOC2 to evaluate the timing precision of the synchronous laser network.

III. EXPERIMENTAL RESULTS AND DISCUSSION

A. Drift Results

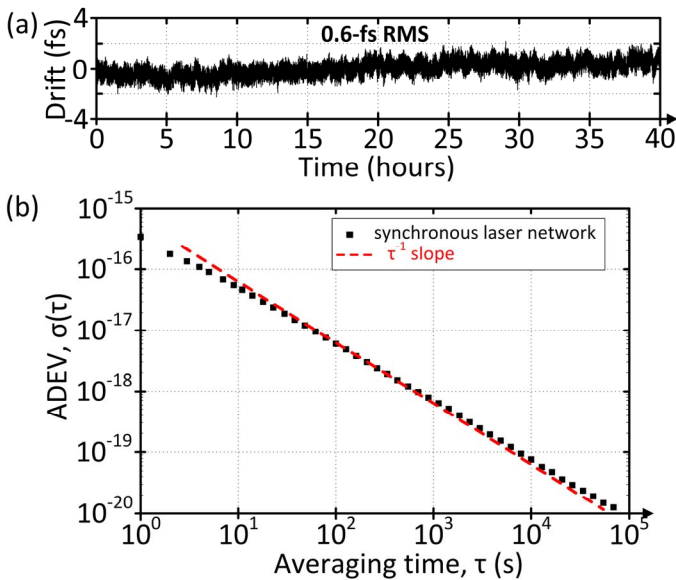


Fig. 2: (a) Out-of-loop timing drift below 1 Hz as measured by SF-BOC2 for 40 hours of continuous operation. (b) Overlapping Allan deviation (ADEV) between SL1 and SL2 calculated from the timing drift data.

Relative timing stability of the synchronous laser network is monitored continuously for 40 hours. As can be seen from Fig. 2(a), out-of-loop timing drift below 1 Hz is only 0.6 fs RMS. Fig. 2(b) shows the overlapping Allan deviation calculated from the drift data. The timing instability between the two slave lasers is only 5×10^{-17} in 10-s averaging time (τ) and reaches 1.2×10^{-20} in 70000 s by following a deterministic τ^{-1} slope.

B. Timing Jitter Spectral Density

The jitter spectral density between SL1 and SL2 is measured with a baseband analyzer which Fourier-transforms the BOC output above 1 Hz. The black curve on Fig. 3 shows the out-of-loop jitter measured by SF-BOC2 when all the five locks in Fig. 1(a) are employed. The integrated jitter is only 1.3-fs RMS corresponding to a total phase error of 83 μ rad for a 10 GHz carrier frequency.

To investigate the high frequency jitter limitations of the network, SL1 and SL2 are disengaged from the links and locally synchronized to each other using SF-BOC2. The red curve on Fig. 3 shows the corresponding in-loop jitter spectral density which closely follows the network results for frequencies between 10 kHz and 1 MHz (less than 7 dB difference). As the in-loop detector suppresses the noise between SL1 and SL2 for frequencies lower than the locking bandwidth (~ 10 kHz, limited by laser's PZT resonance), the local jitter spectral density shows larger deviation from the network results in this region (see the red dotted-curve on Fig. 3 for frequencies below 10 kHz). Nevertheless, the integrated jitter of the local synchronization is as high as 0.9 fs RMS pointing out the unsuppressed jitter of SL1 and SL2 beyond the locking bandwidth as the prominent noise contribution. Thus, the high frequency performance of the synchronous laser network could be improved even further to the attosecond regime by developing lower noise mode-locked lasers with larger PZT bandwidths.

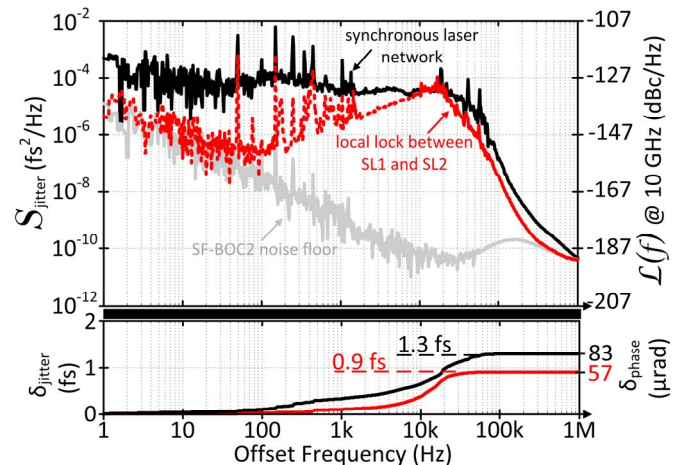


Fig. 3: Left axes: Timing jitter spectral density S_{jitter} and its integrated jitter δ_{jitter} ; right axes: equivalent single-sideband phase noise $L(f)$ and its integrated phase δ_{phase} scaled at 10-GHz carrier frequency. The grey curve shows the noise floor of the timing detector SF-BOC2.

IV. CONCLUSION

We believe that such a synchronous laser network will provide the new photon science facilities with high-temporal resolution and enable radically new spectroscopy experiments by shedding light on ultrafast molecular dynamics. This synchronization scheme can also be employed to compare optical clocks in relatively short distances (<10 km) and for laboratory applications [8] with extremely low uncertainty.

ACKNOWLEDGMENT

The authors thank Dr. Laurens Wissmann, Dr. Jinxiong Wang and Dr. Maximilian Lederer for allowing the use of the laser Origami10 in the experiment. This work was supported by the Center for Free-Electron Laser Science at Deutsches Elektronen-Synchrotron, a research center of the Helmholtz Association in Germany.

REFERENCES

- [1] A. J. Benedick, J. G. Fujimoto, and F. X. Kärtner. "Optical flywheels with attosecond jitter." *Nature Photonics* **6**, 2012, pp. 97-100.
- [2] Y. Song, C. Kim, K. Jung, H. Kim, and J. Kim, "Timing jitter optimization of mode-locked Yb-fiber lasers toward the attosecond regime," *Opt. Express* **19**, 2011, pp. 14518-14525.
- [3] P. Emma et al., "First lasing and operation of an angstrom-wavelength free-electron laser," *Nat. Photonics* **4**, 2010, pp. 641-647.
- [4] G. Mourou and T. Tajima, "The Extreme Light Infrastructure: Optics' Next Horizon," *Optics & Photonics News* **22**, 2011, pp. 47-51.
- [5] M. Xin, K. Şafak, M. Y. Peng, P. T. Callahan, and F. X. Kärtner, "One-femtosecond, long-term stable remote laser synchronization over a 3.5-km fiber link," *Opt. Express* **22**, 2014, pp. 14904-14912.
- [6] K. Şafak, M. Xin, P. T. Callahan, M. Y. Peng, and F. X. Kärtner, "All fiber-coupled, long-term stable timing distribution for free electron lasers with few-femtosecond jitter," *Structural Dynamics* **2**, 2015, p. 041715.
- [7] K. Predehl, G. Grosche, S. M. F. Raupach, S. Droste, O. Terra, J. Alnis, T. Legero, T. W. Hänsch, T. Udem, R. Holzwarth, H. Schnatz, "A 920-Kilometer Optical Fiber Link for Frequency Metrology at the 19th Decimal Place," *Science* **336**, 2012, pp. 441-444.
- [8] C. W. Chou, D. B. Hume, T. Rosenband, and D. J. Wineland, "Optical clocks and relativity." *Science* **329**, 2010, pp. 1630-1633.
- [9] P. T. Callahan, K. Şafak, P. Battle, T. Roberts, and F. X. Kärtner, "Fiber-coupled balanced optical cross-correlator using PPKTP waveguides," *Opt. Express* **22**, 2014, pp. 9749-9758.
- [10] M. Xin, K. Şafak, M. Y. Peng, A. Kalaydzhyan, W. Wang, O. D. Mücke, and F. X. Kärtner, "Attosecond Precision Multi-km Laser-Microwave Network" unpublished.

A Study on Reducing the Diurnal in the Europe-to-Europe TWSTFT Links

V. Zhang¹, T. Parker¹, S. Zhang^{1,2}

¹ Time and Frequency Division, National Institute of Standards and Technology (NIST), Boulder, Colorado, U.S.A

² Science and Technology on Metrology and Calibration Laboratory, Beijing Institute of Radio Metrology and Measurement (BIRMM), Beijing, China

Abstract—Most of the Two-Way Satellite Time and Frequency Transfer (TWSTFT or TW) links exhibit a daily variation (diurnal) on the order of 1 ns in the differences. The stability of TW is degraded by the diurnal. Many studies on the sources of diurnal have been carried out, but no dominating cause of the diurnal has been found.

In this study, we examine the diurnal in several Europe-to-Europe TW links and report that the diurnal and the short-term transfer noise can be reduced by using the triangle difference of the transatlantic TW. We will also analyze where the improvement comes from.

Keywords—Two-Way Satellite Time and Frequency Transfer (TWSTFT or TW), time and frequency transfer stability, TW diurnal, triangle TW difference, Triangle Closure Calibration

I. INTRODUCTION

Two-Way Satellite Time and Frequency Transfer (TWSTFT or TW) is used by many international timing laboratories to compare their clocks and to contribute their timescale data to the generation of International Atomic Time (TAI) and Coordinated Universal Time (UTC). Currently, 15 European timing laboratories participate in the Europe-to-Europe Two-Way Satellite Time and Frequency Transfer (TW hereafter) network. These European timing laboratories also participate in the transatlantic TW network with two timing laboratories in the U.S. The Europe-to-Europe and transatlantic TW networks use three Ku-band transponders on a geostationary satellite. One transponder with 1.7 MHz bandwidth is used by the Europe-to-Europe TW. The other two transponders, each with 1.6 MHz bandwidth, are used for the transatlantic TW. The TW measurements between each pair of timing laboratories are made during a two-minute interval of a scheduled time slot in every even UTC hour. The timing information is carried by the 1 MChip/s pseudo-random noise (PRN) codes. Among all of the TW links, the TW links to the Physikalisch-Technische Bundesanstalt (PTB) in Germany are referred to as UTC links because these TW data are used by the International Bureau of Weights and Measures (BIPM) in the generation of TAI and UTC.

In recent years, various successful TW link calibrations using a TW mobile station reported a calibration uncertainty of 1 ns. However, most of the TW links exhibit a daily variation (diurnal) on the order of 1 ns in the TW differences. The diurnal degrades the stability of TW links and therefore increases the combined uncertainty of TW links. It can also increase the TW link calibration uncertainty when a TW mobile station is used to calibrate a TW link and when the calibration measurements are made in less than one day.

There have been several studies searching for the origin or origins of the diurnal in the TW differences. These studies have investigated environmental effects in the TW indoor and outdoor equipment, the daily propagation delay variation due to the ionospheric delay change, the impact of satellite motion on the signal time of arrival, the Sagnac and the Doppler effects on the TW measurements [1-3]. Nevertheless, none of these studies found the dominant cause of the diurnal. A recent study [4] showed the diurnal in the Asian-Pacific region TW links was minimized by using a software defined receiver (SDR) technique. A pilot study on using the SDR technique will be launched this year to verify if the technique can also minimize the diurnal for the Asia-to-Europe, Europe-to-Europe, and transatlantic TW links.

In this paper, we present our analysis on reducing the diurnal in the Europe-to-Europe TW links with the transatlantic triangle TW differences. In Section II, we examine the diurnal in TW difference for five Europe-to-Europe links and report that the diurnal and the short-term transfer noise can be reduced by using the triangle difference of the transatlantic TW differences. We will analyze where the improvement comes from in Section III and conclude the study in Section IV.

II. USING TRANSATLANTIC TRIANGLE TW DIFFERENCES FOR THE EUROPE-TO EUROPE TW

In our study, we examine the diurnal in five Europe-to-Europe TW UTC links for the data period from January 1, 2013 to December 31, 2015 (MJDs 56293 to 57387). The five UTC links are listed in Table I. The magnitude of the diurnal in these links varies from link to link and from time to time. Fig. 1 shows an example of the five links' direct TW difference over a 5-day period. On average, the peak-to-peak diurnal of the Europe-to-Europe direct TW links is about 1 ns.

TABLE I. FIVE EUROPE-TO-EUROPE TW UTC LINKS

Pivot station	Remote station
PTB	Federal Institute of Metrology (METAS), Bern-Wabern, Switzerland (CH)
PTB	Istituto Nazionale di Ricerca Metrologica (INRIM), Torino, Italy (IT)
PTB	Laboratoire national de métrologie et d'essais – Systèmes de références space-temps, Observatoire de Paris (LNE-SYRTE), Paris, France (OP)
PTB	Real Instituto y Observatorio de la Armada, San Fernando, Spain (ROA)
PTB	Sveriges Provnings-och Forskningsinstitut (Swedish National Testing and Research Institute), Borås, Sweden (SP)

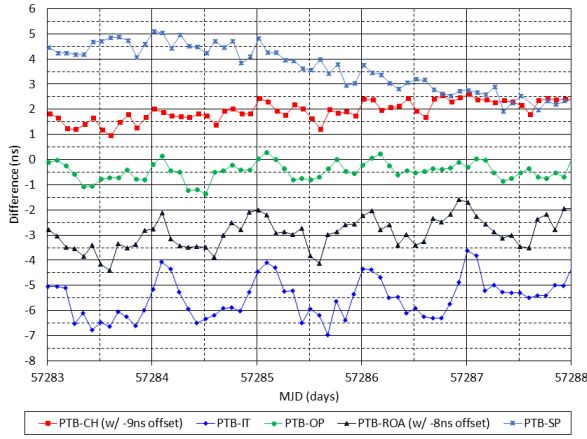


Fig. 1. Example of the direct Europe-to-Europe TW differences. The differences are offset for illustration purpose.

The transatlantic TW differences between the six European stations and the National Institute of Standards and Technology (NIST) are used to compute the triangle differences for the Europe-to-Europe TW links. For example, the triangle difference for the (PTB – OP) link is computed with the transatlantic TW differences of (NIST – OP) – (NIST – PTB). Because the two transatlantic TW measurements are made at different times during the even UTC hours, we use the Time Deviation (TDev) to verify if the triangle difference with a matching approach introduces error or noise compared to that of an interpolation approach. In the matching approach, we treat the two transatlantic TW differences of the same hour as if they were made at the same epoch. In the interpolation approach, the two transatlantic TW differences are interpolated to the beginning of the hour. Fig. 2 shows the comparison for the (PTB – OP) link via the transatlantic TW with NIST. For averaging times less than eight hours, the TDevs for the matching approach are a little higher than that of the interpolation approach. The improvement of the interpolation approach is due to the average between the two adjacent data points. With this result, we will use the matching approach for computing the transatlantic triangle TW differences, because it is simpler.

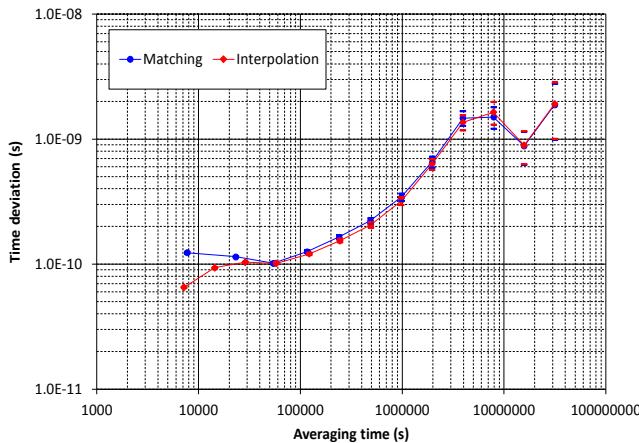


Fig. 2. Time deviations of triangle differences of the (PTB – OP) link using the transatlantic TW with NIST.

The spectral analysis of the diurnal (day component) and other components in the direct and triangle TW differences for the (PTB – OP) link are shown in Fig. 3. The results are obtained from the Fast Fourier Transform (FFT). The diurnal in the triangle difference is noticeably reduced. The other components are also reduced, except for the half-day component (pattern occurs twice a day) which is slightly increased. We use the diurnal component of the direct TW differences as the reference and divide it by the diurnal component of the triangle difference to obtain the diurnal reduction factor. Table II shows the results for the five Europe-to-Europe UTC TW links. The results show that the transatlantic triangle TW difference indeed reduces diurnals in the Europe-to-Europe direct TW difference for all of the five links studied. The diurnal in the triangle difference is at least 2.7 times smaller than that in the direct difference. To check if the diurnal reduction is transatlantic link dependent, we computed the transatlantic TW differences among the U.S. Naval Observatory (USNO), PTB and CH. The FFT result of triangle difference of (USNO – CH) – (USNO – PTB) also shows the diurnal of the triangle difference is 7.1 times smaller than that of the direct (PTB – CH) difference. A 5-day TW difference plot for the (PTB – CH) link is shown in Fig. 4, which shows that both of the transatlantic links with NIST and USNO reduce the diurnal.

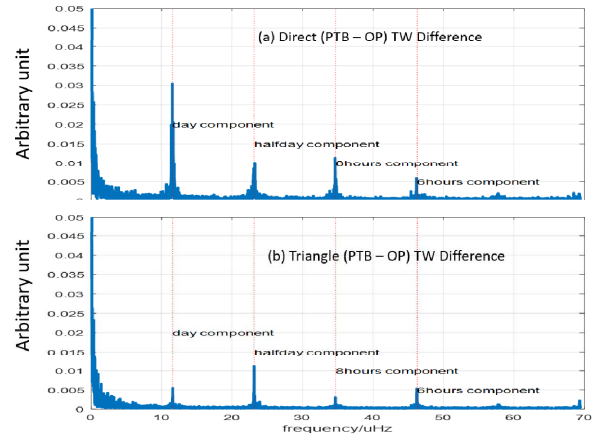


Fig. 3. Spectral analysis of diurnal and other components in (PTB – OP) TW difference. The components of the TW differences are presented with an arbitrary unit because we are only interested in the comparison of the diurnal reduction of the triangle difference relative to the direct difference.

TABLE II. DIURNAL REDUCTION USING THE TRANSATLANTIC TRIANGLE DIFFERENCES.

Link	PTB-CH	PTB-IT	PTB-OP	PTB-ROA	PTB-SP
Diurnal Reduction	11.0	2.7	5.5	3.4	3.0

Figures 5 to 9 show the TDev of the direct and triangle differences for the five links. The diurnal in each of the five links is reduced by using the triangle difference approach. As shown in Fig. 5, both of the (USNO – CH) – (USNO – PTB) and the (NIST – CH) – (NIST – PTB) triangle differences reduce the diurnal and the TW transfer noise for averaging

times less than eight hours, but the transatlantic TW differences via USNO contain higher TW transfer noise. The TDevs at averaging times around 12 hours are shown in Table III for a quick overview.

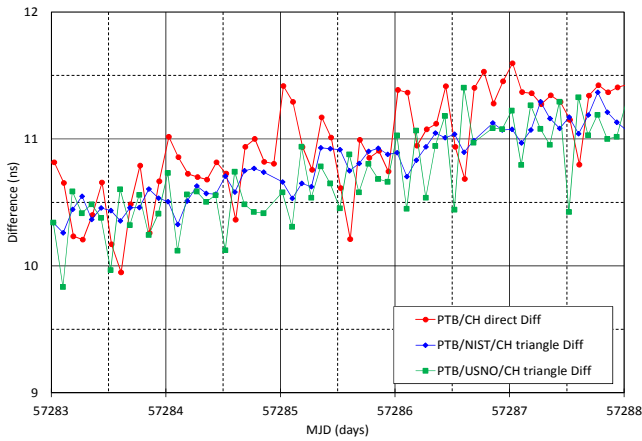


Fig. 4. (PTB – CH) direct and triangle TW differences.

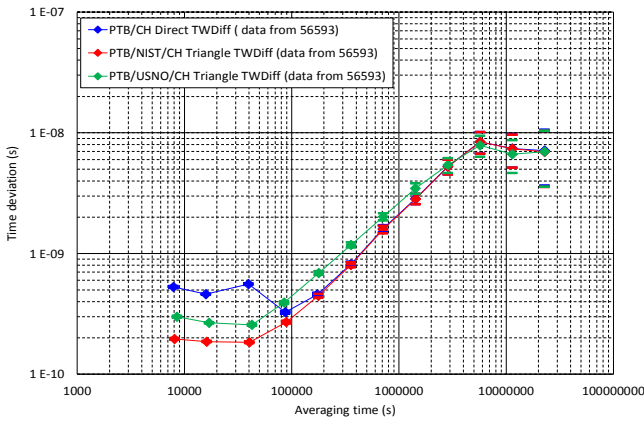


Fig. 5. Time deviations of the (PTB – CH) TW differences.

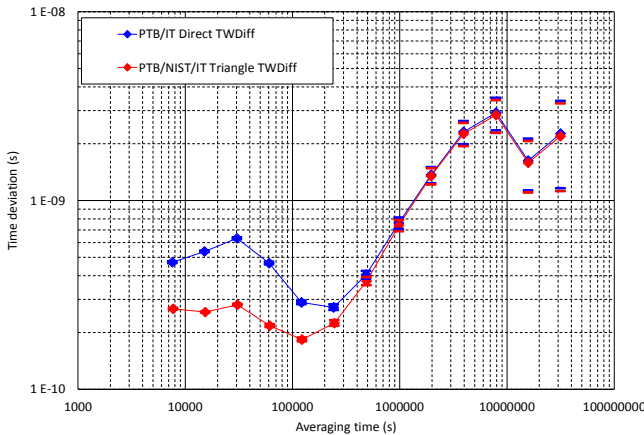


Fig. 6. Time deviations of the (PTB – IT) TW differences.

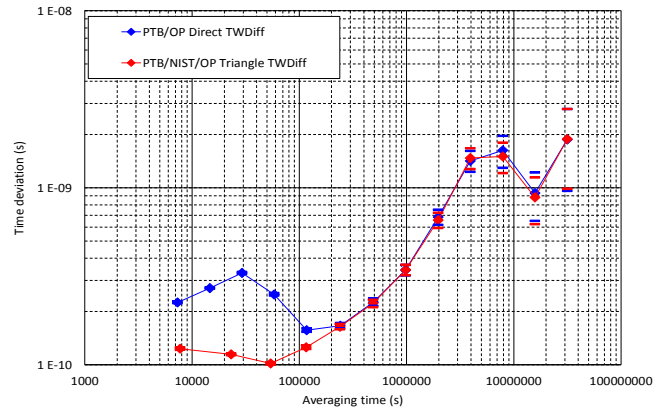


Fig. 7. Time deviations of the (PTB – OP) TW differences.

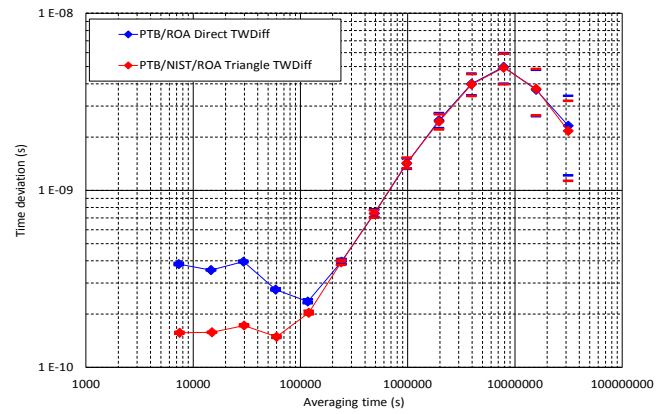


Fig. 8. Time deviations of the (PTB – ROA) TW differences.

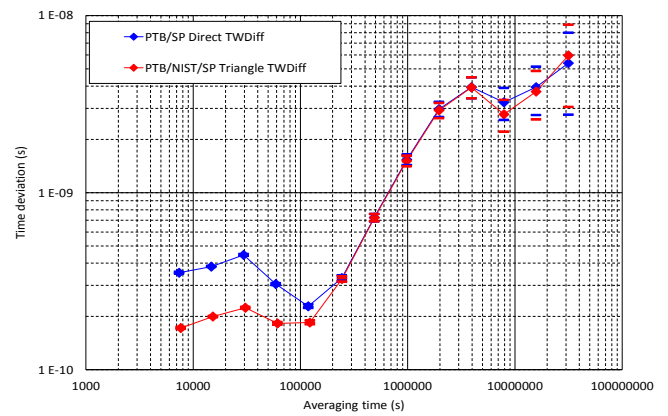


Fig. 9. Time deviations of the (PTB – SP) TW differences.

TABLE III. TIME DEVIATIONS FOR AVERAGING TIME AROUND 12 HOURS.

Link	PTB-CH	PTB-IT	PTB-OP	PTB-ROA	PTB-SP
TDev of Direct difference (ns)	0.557	0.631	0.331	0.395	0.445
TDev of Triangle difference (ns)	0.184	0.281	0.102	0.172	0.224

III. SOURCES OF DIURNAL IN THE EUROPE-TO-EUROPE TW LINKS

Section II shows that the diurnal in the Europe-to-Europe TW links is reduced by using the transatlantic triangle TW differences. Although the triangle difference results do not directly show the source of the diurnals in the Europe-to-Europe TW links, they do strongly suggest some possible causes and also some things that are not causes.

One can visualize the situation by dividing the link geometry into two parts. One is the part east of the satellite (i.e. Europe) and the other part is west of the satellite (i.e. North America) as shown in Fig. 10. In the direct Europe-to-Europe links only the area east of the satellite is relevant. In the triangle links the geometry in the east is identical to that of the Europe-to-Europe links, but now the western area is added. However, the geometry of the western area will be essentially identical for the two European stations in the triangle links. The only reason the two parts are not identical for the direct and triangle links is that the up and down link frequencies are not exactly the same and the times at which the TW sessions take place are not identical. The uplink carrier frequencies differ by only 1.7 % at most, while the downlink carrier frequencies differ by a maximum of 7.1 %. The average times between direct and triangle links range from about 3 to 38 minutes. The times between the sessions of the two relevant station pairs at the NIST end range from 3 to 21 minutes. None of these factors should make a significant contribution to the diurnals.

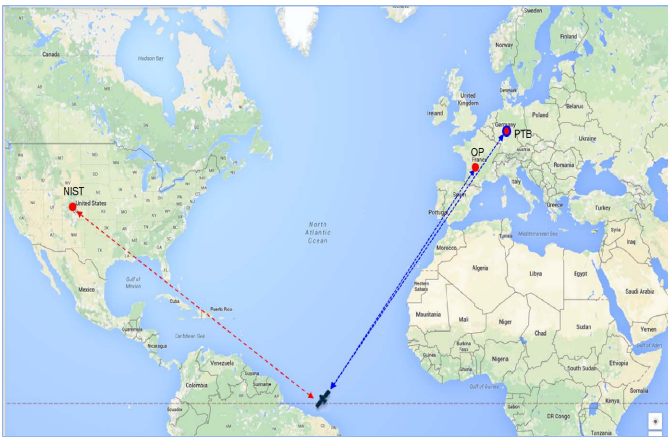


Fig. 10. The geometry example of the Europe-to-Europe and transatlantic TW links among NIST, OP and PTB.

Because the eastern geometry and station equipment are virtually identical for the direct and triangle links, the sources of the diurnal due to environment (temperature and humidity), modems, ionosphere, and satellite motion (Sagnac, Doppler and time of arrival) must also be nearly identical and therefore small. Of course, in the triangle links there is the addition of the western part where all the same issues come into play. However, these contributors will nearly cancel because both European stations will see virtually the same contributors. Taking these conditions into account, the only major differences between the direct and triangle links are the transponders (hardware and traffic) on the satellite. The only

caveats are the small differences in carrier frequencies and session times. For the direct Europe-to-Europe links, the same transponder is used for both directions. For the transatlantic links, two transponders are used, one for the east to west direction and one for the west to east direction. Thus it appears that something related to the transponder for Europe is a dominant source of the diurnal in the direct Europe-to-Europe links. Since the two station to station signals pass through the same transponder at virtually the same time it is unlikely that a transponder hardware issue such as a temperature coefficient could cause the diurnal. About the only possibility remaining is some code dependent in-band or out-of-band interference issue.

The Europe-to-Europe links are crowded. Up to five links are making TW measurements at the same time. In addition, there are strong signals on both sides of the TW frequency band. On the other hand, there are only up to two transatlantic TW measurements at the same time and there is only one neighboring signal next to the Europe-to-US TW signal. In general, the diurnal in the transatlantic links is smaller than that of the Europe-to-Europe links. Thus, we suspect that in-band and/or out-of-band interference are major contributors to the diurnal in the Europe-to-Europe TW.

IV. CONCLUSIONS

Our study has shown that the diurnal in the Europe-to-Europe TW can be reduced analytically with the transatlantic triangle differences. The triangle difference approach cuts down the diurnal component in the direct Europe-to-Europe TW differences by a minimum of 2.7 times. Compared to that of the direct TW difference, the TDev of the triangle differences is decreased by more than 200 ps for averaging times less than 12 hours. It is not clear what the rationale is behind the diurnal reduction using the triangle difference, although we think the in-band and out-of-band interferences are major contributors of the diurnal in the Europe-to-Europe TW.

If the non-UTC transatlantic TW links are calibrated with the Triangle Closure Calibration described in the newly approved TW calibration guidelines [5], the transatlantic triangle TW links can be used as the Europe-to-Europe TW UTC links with improved link uncertainty in the TAI and UTC computation.

REFERENCES

- [1] T. Parker and V. Zhang, "Sources of Instabilities in Two-Way Satellite Time Transfer," Proc. 2005 Joint IEEE IFCS and PTTI Meeting, pp. 745-751, August 2005.
- [2] W. Tseng, K. Feng, S. Lin, H. Lin, Y. Huang and C. Liao, "Sagnac Effect and Diurnal Correction on Two-Way Satellite Time Transfer," IEEE Transactions on Instrumentation and Measurement, Vol. 60, Issue 7, pp. 2298-2302, July 2011.
- [3] V. Zhang and T. Parker, "A study of the Diurnal in the Transatlantic TWSTFT Differences," Proc. 2013 Asia-Pacific Time and Frequency (ATF) Workshop, September 2013.
- [4] Y. Huang, H. Tsao, "Design and Evaluation of an Open-Loop Receiver for TWSTFT Applications," IEEE Transactions on Instrumentation and Measurement, vol. 64, no. 6, pp. 1553-1558, June 2015.
- [5] Task Group of CCTF Working Group on TWSTFT (2015) TWSTFT Calibration Guidelines for UTC Time Links V3.0.

Progress Towards a Strontium Single-Ion Optical Clock with mHz Uncertainty

Pierre Dubé*, Bin Jian*[†] and Alan A. Madej*[†]

* National Research Council Canada, Ottawa, Ontario, Canada

[†] Department of Physics and Astronomy, York University, Toronto, Ontario, Canada

Email: pierre.dube@nrc-cnrc.gc.ca

Abstract—The strontium ion clock developed at the National Research Council of Canada has reached an uncertainty level of 5 mHz in recent years. This low level of uncertainty was achieved in great part by using methods that harness specific properties of the clock transition that allow either a very high level of cancellation or a strong suppression of frequency shifts that would otherwise dominate the uncertainty budget. The shifts controlled by these methods are the electric quadrupole shift, the tensor Stark shifts, and the micromotion shifts. With these methods in place, the main limitation to the accuracy of the clock transition frequency is the uncertainty in the evaluation of blackbody radiation (BBR) field. In this paper, we review the methods used to control the shifts to the 5 mHz level and present our plans for the evaluation of the BBR field that is expected to reduce the total uncertainty to the mHz level.

I. INTRODUCTION

In recent years, the best optical clocks based on either single ions or neutral atoms in optical lattices have reached or surpassed the 10^{-17} fractional uncertainty level, outperforming by more than one order of magnitude the evaluated uncertainties of state-of-the-art cesium fountain clocks that realize the SI second [1]–[11]. Each of these systems has specific strengths and weaknesses regarding sensitivity of the clock transition to external perturbations. Rapid progress is observed to address the limitations and push the uncertainty evaluations towards the 10^{-18} level and lower, with exciting new perspectives for tests of fundamental physics and more accurate time keeping.

The optical frequency standard developed at the National Research Council of Canada is based on the $5s^2S_{1/2}-4d^2D_{5/2}$ transition of a trapped and laser-cooled single ion of $^{88}\text{Sr}^+$. The 445 THz electric quadrupole $S-D$ transition has a linewidth of 0.4 Hz and a line Q of 10^{15} , suitable for a highly accurate optical clock.

There are a number of external perturbations that can shift the frequency of the $S-D$ transition of $^{88}\text{Sr}^+$. The most important are caused by excess micromotion, by electric field gradients interacting with the quadrupole moment of the upper state of the clock transition, and by the blackbody radiation (BBR) field. The total shift has an evaluated fractional frequency uncertainty of 1.2×10^{-17} (5 mHz). The single most important contribution to the uncertainty is currently the evaluation of the BBR field that causes an uncertainty of 1.1×10^{-17} . By comparison, the next largest shift is evaluated at 2×10^{-18} .

We present in this paper a brief review of the most important frequency shifts of the $^{88}\text{Sr}^+$ ion and the methods

used to eliminate, reduce or evaluate with improved accuracy their contributions to the uncertainty budget. We also outline our plans for the evaluation of the thermal field and its expected impact on the total uncertainty of the $^{88}\text{Sr}^+$ clock transition frequency.

II. STRONTIUM ION OPTICAL CLOCK

The optical clock is realized with a single ion of $^{88}\text{Sr}^+$ held at the center of an rf quadrupole trap of the endcap design. It is Doppler-cooled to 2 mK using a frequency-stabilized 422 nm laser source that is red-detuned from the strongly-allowed $5s^2S_{1/2}-5p^2P_{1/2}$ transition. The upper state of the cooling transition has a 5.6% probability of decaying to the metastable $^2D_{3/2}$ state [12]. This decay is prevented by a 1092 nm repumper laser in resonance with the $4d^2D_{3/2}-5p^2P_{1/2}$ transition.

The $5s^2S_{1/2}-4d^2D_{5/2}$ clock transition is probed with a 674 nm ultra-stable laser source that has a spectroscopic resolution of 4 Hz [13]. The $S-D$ transition is detected by the electron shelving method whereby the presence in the upper D state is determined by the interruption of the 422 nm fluorescence with near unity efficiency. The transition probability for a given detuning is easily determined from the number of transitions observed divided by the number of interrogation pulses. Transition probabilities on each side of the resonance are used to find the frequency offset from line center and steer the laser accordingly for locking to the resonance line center.

The clock transition spectrum is split into ten Zeeman components using a small magnetic field of a few μT . $^{88}\text{Sr}^+$ has no magnetic insensitive resonance. The virtual line center is obtained by averaging the frequencies of a symmetric pair of components to cancel the linear Zeeman shift. As discussed in Sec. III-B, other important frequency shifts can be canceled by probing three symmetric pairs of components chosen to include all of the $^2D_{5/2}$ magnetic sublevels.

A significant improvement in the signal from the single ion is obtained with ground-state preparation prior to each probe pulse. In our implementation, state detection and state preparation are performed at each cycle during the cooling pulse. The first half of the pulse is reserved for state detection and the second half for state preparation. State preparation begins by sending the ion back to the ground state with a clear out laser at 1033 nm. Then, near the end of the cooling pulse, a Pockels cell switches the 422 nm laser polarization from linear to circular for a few milliseconds for optical

pumping into the desired ground-state magnetic sublevel. The bias magnetic field is carefully aligned along the cooling laser beam propagation direction for optimum optical pumping. In our setup, the ion is prepared in the correct ground state 99% of the time [14]. The stability of the single-ion clock is estimated at $3 \times 10^{-15}/\sqrt{\tau}$ for a probe pulse length of 100 ms. τ is the averaging time in seconds. The reader is referred to published work for more details about the experimental setup [13] and the state-preparation [14].

III. FREQUENCY SHIFTS

A. Micromotion Shifts

The clock transition of the $^{88}\text{Sr}^+$ ion is sensitive to external perturbations that create electric or magnetic fields, and to the second-order Doppler effect. The most important shift is potentially caused by the rf fields of the trap itself, when the ion is not properly centered in the quadrupole trapping potential. Ion displacement caused by stray electric fields results in two correlated effects: Stark shifts from the non-vanishing trapping electric field and a second-order Doppler shift from the driven motion. These shifts are often called (excess) micromotion shifts [15], [16].

The micromotion shifts from displacement can be very large. For example, we have observed $\sim 10^{-13}$ fractional frequency shifts in an earlier $^{88}\text{Sr}^+$ ion trap system that wasn't designed to minimize micromotion in three dimensions [5]. In our most recent ion trap of the endcap design, micromotion can be minimized in three dimensions with trim electrodes. The micromotion shifts in this system can be reduced to the 10^{-17} level [13]. Although a very significant improvement over the previous system, this level of frequency shift remains unsuitable for an optical clock at the 10^{-18} level.

A further reduction of the micromotion shifts can be obtained for the $^{88}\text{Sr}^+$ ion clock by tuning the rf trap drive frequency such that the second-order Doppler shift and the scalar Stark shift cancel each other. The frequency of cancellation is given to first-order approximation by the following formula [5]:

$$\Omega_0^2 \simeq -\frac{h\nu_0}{\Delta\alpha_0} \left(\frac{e}{mc}\right)^2, \quad (1)$$

where Ω_0 is the trap drive frequency in rad/s, h is Planck's constant, ν_0 is the clock transition frequency in Hz, e is the elementary charge, m is the mass of $^{88}\text{Sr}^+$, and c is the speed of light. $\Delta\alpha_0 = \alpha_0(^2D_{5/2}) - \alpha_0(^2S_{1/2})$ is the differential static scalar polarizability of the clock transition. A more accurate formula that takes into account harmonics of ion motion can be found in Ref. [5].

Such a magic drive frequency only exists for ion optical clocks that have a positive scalar Stark shift since the second-order Doppler shift is always negative. Ion clock transitions with this property can be identified by their positive BBR shift.

Ω_0 depends on well-known physical constants and on $\Delta\alpha_0$. We have determined Ω_0 to high accuracy by comparing the trap that has micromotion shifts at the 10^{-13} level with the endcap trap reference system that has a total frequency uncertainty of 1.2×10^{-17} . The results are shown in Fig. 1. We found $\Omega_0/2\pi = 14.404(10)$ MHz for the $^{88}\text{Sr}^+$ ion [5]. This measurement has another important benefit for the uncertainty

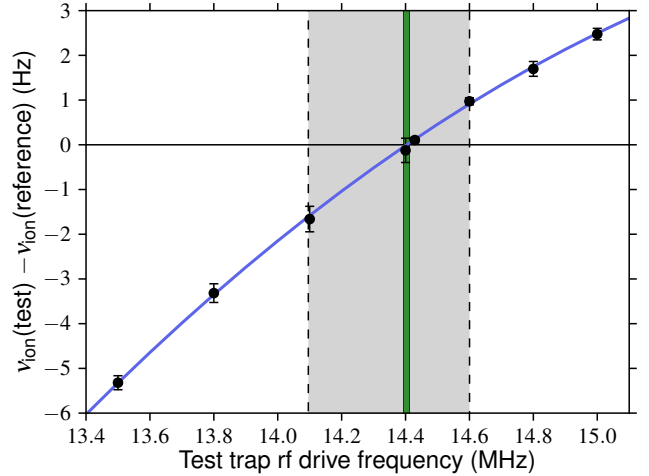


Fig. 1. Comparison of the clock transition frequencies of two $^{88}\text{Sr}^+$ ions in different traps as a function of the rf drive frequency of the test trap [5]. The ion in the test trap has high micromotion shifts. The magnitude of its second-order Doppler shift decreases with increasing rf trap drive frequency. The narrow vertical band shows the value and uncertainty of the experimental determination of the drive frequency $\Omega_0/2\pi$ where the scalar Stark and second-order Doppler shifts cancel each other. The gray area is the predicted zone for the cancellation based on state-of-the-art theoretical calculations [12]. The experimental measurement has reduced the uncertainty of $\Delta\alpha_0$ by a factor of 24.

evaluation of the $^{88}\text{Sr}^+$ ion as knowledge of Ω_0 also provides an accurate determination of $\Delta\alpha_0$ which plays an important role in the evaluation of the BBR shift as discussed in Section III-C.

By driving the trap at a frequency of Ω_0 , we estimate that the micromotion shifts are reduced by additional factor of 200 or more, for a net uncertainty contribution of $\lesssim 10^{-19}$. Note that only the scalar part of the Stark shift is suppressed by this method. The tensor part remains at the 10^{-17} level [13]. Further reduction of the tensor Stark shift is obtained by the method described in the next section.

B. Electric Quadrupole Shift

Another important systematic shift of the $^{88}\text{Sr}^+$ ion system is the electric quadrupole shift (EQS). It is caused by the interaction of the $^2D_{5/2}$ state with an electric field gradient. It has been investigated in the endcap trap system and its magnitude, when the quantization axis is aligned to maximize the frequency shift, was found to be on the order of 8 Hz for the most sensitive Zeeman component pair [13]. If not properly evaluated, the EQS can produce fractional frequency shifts at the 10^{-14} level and seriously limit the performance of the optical clock.

There are two commonly used methods to cancel this shift in ion optical clocks. The first uses the property that the EQS can be canceled by averaging the center frequencies measured for three mutually orthogonal directions of the magnetic field [17]. This method has the advantage that a single magnetic insensitive resonance can be used for the evaluation. The level of cancellation depends on how accurately the three magnetic field directions can be made orthogonal to each other.

Another method uses averaging of the magnetic sublevel energies of the upper state of the clock transition. For the

$^{88}\text{Sr}^+$ ion, this is realized simply by measuring three pairs of Zeeman components with upper state magnetic sublevels $m_J = \pm 1/2, \pm 3/2$, and $\pm 5/2$ [13], [18]. The method is exact since the electric quadrupole interaction Hamiltonian is traceless. We have identified time variations in the electric field gradient and the quantization axis direction during the measurements as possible sources of uncertainty. From experimental investigations, these effects are found to be extremely small, estimated at $\lesssim 3 \times 10^{-19}$ when state preparation was not implemented [13]. In the present system state preparation has allowed a reduction of the cycling time through the six Zeeman components by a factor of about 5. We expect that the EQS uncertainty or bias in our system should be below the 10^{-19} level.

The Zeeman averaging method also cancels all tensor Stark shifts as the functional dependence on the magnetic sublevels is the same as that of the EQS. The 10^{-17} micromotion tensor Stark shifts discussed in the previous section are canceled to a level estimated at 10^{-21} with Zeeman averaging.

In our algorithm for locking to the ion, the Zeeman averaging is an integral part of the measurement. The laser frequency cycles continuously through six Zeeman components to determine their line centers. This can be viewed as three independent locks to three pairs of Zeeman components. The average of those frequencies realizes a new virtual line center, one that, in addition of removing the linear Zeeman shift, removes the EQS and the tensor Stark shifts. When combined with suppression of the micromotion shifts obtained by tuning the trap drive frequency to a special value as discussed in Section III-A, one obtains a virtual line center frequency that has very low sensitivity to several important external perturbations.

C. Blackbody Radiation Shift

The blackbody radiation shift is given by [19], [20]:

$$\Delta\nu_{\text{BBR}} = -\frac{1}{2h}\langle E^2 \rangle_T \Delta\alpha_0 (1 + \eta), \quad (2)$$

where $\Delta\nu_{\text{BBR}}$ is expressed in Hz. $\langle E^2 \rangle_T$ is the thermal (BBR) mean squared electric field at the ion and η is a dynamic correction that accounts for the response of the atomic energy levels to the BBR spectrum.

Evaluation of $\Delta\nu_{\text{BBR}}$ involves three parameters that determine its uncertainty: $\langle E^2 \rangle_T$, $\Delta\alpha_0$, and η . $\langle E^2 \rangle_T$ must be evaluated experimentally. $\Delta\alpha_0$ and η can be obtained either experimentally or by using atomic structure calculations. A state-of-the-art calculation of the $^{88}\text{Sr}^+$ atomic parameters [12] gives a value of $\Delta\alpha_0$ that contributes a fractional uncertainty of 2×10^{-17} to the ion frequency and a value of η that contributes 8.4×10^{-20} [5]. The contribution of η is well below the 10^{-18} level and does not require further investigation. The uncertainty of $\Delta\alpha_0$, on the other hand, is quite significant and was the largest contributor to the uncertainty budget of our $^{88}\text{Sr}^+$ ion clock in 2013 [13]. We have since made a measurement of $\Delta\alpha_0$ with high accuracy as mentioned in Section III-A. Its value of $-4.7938(71) \times 10^{-40} \text{ J m}^2/\text{V}^2$ with an uncertainty of 0.15% is to our knowledge the most accurate determination of $\Delta\alpha_0$ for an ion clock [5], [11]. The contribution of $\Delta\alpha_0$ to the ion frequency uncertainty has been reduced to 8.3×10^{-19}

TABLE I. SIMPLIFIED UNCERTAINTY BUDGET OF THE NRC $^{88}\text{Sr}^+$ ION OPTICAL CLOCK

Source	mHz	Fractional
BBR field evaluation, $\langle E^2 \rangle_T$	4.9	1.1×10^{-17}
Collisional shift	1	2×10^{-18}
1092 nm ac Stark shift	1	2×10^{-18}
Second-order Doppler (thermal)	0.5	1×10^{-18}
BBR coefficient, $\Delta\alpha_0$	0.37	8.3×10^{-19}
Excess micromotion	0.05	1×10^{-19}
Electric quadrupole shift	$\lesssim 0.05$	$\lesssim 1 \times 10^{-19}$
Total uncertainty	5.1	1.2×10^{-17}

and is no longer a significant contributor to the uncertainty budget [5].

The last parameter required to determine the BBR shift is the thermal field $\langle E^2 \rangle_T$. It was evaluated a few years ago for our endcap trap system, and found to contribute a fractional uncertainty of 1.1×10^{-17} [13]. This is at present the largest source of uncertainty for our $^{88}\text{Sr}^+$ ion optical clock, five times larger than the next leading source.

We are preparing to improve on the evaluation of $\langle E^2 \rangle_T$ by measuring the trap component temperatures using a dummy trap and a thermographic camera [21]. The dummy trap will be a close copy of the frequency standard endcap trap for accurate temperature estimates. The emissivities of the materials will also be investigated experimentally to reduce the total uncertainty of the BBR field evaluation. Based on measurements made on other ion traps of the endcap design, we anticipate a reduction of the BBR field uncertainty contribution from 1.1×10^{-17} to $\approx 2.8 \times 10^{-18}$ [21].

D. Uncertainty Budget

Table I is a summary of the present uncertainty budget for the $^{88}\text{Sr}^+$ ion at the National Research Council of Canada (NRC). The BBR field evaluation is the main source of uncertainty as discussed in the previous section. The next leading source is the collisional shift with a fractional uncertainty contribution of 2×10^{-18} . This shift was calculated using a simple model that gives an upper limit estimate of the frequency shift [1], [13]. The actual shift could be significantly smaller [13], [22]. Further investigation will become important when the BBR field uncertainty is decreased to the low 10^{-18} level.

The 1092 nm ac Stark shift also contributes a fractional frequency uncertainty of 2×10^{-18} . Its origin is light leakage in the shuttering system that relies on an acousto-optic modulator (AOM). This technical limitation is easily solved with an improved shutter, for example with an additional AOM shutter or with a mechanical shutter.

Using the data of Table I, we anticipate a total uncertainty of approximately 1.7 mHz or 3.8×10^{-18} in fractional frequency units for the $^{88}\text{Sr}^+$ ion clock once the BBR field has been re-evaluated as described in Section III-C. It is assumed here that the 1092 nm light shift has been reduced to insignificant levels.

IV. CONCLUSIONS

The uncertainty of the $^{88}\text{Sr}^+$ ion clock transition has been reduced by several orders of magnitude in recent years to reach a fractional frequency uncertainty of 1.2×10^{-17} . Experimental methods were developed and implemented in our system to control several important systematic shifts. Specifically, the electric quadrupole shift and tensor Stark shifts are canceled by the Zeeman averaging method, and the micromotion shifts are suppressed by an extra factor of 200, to the 10^{-19} level, by tuning the trap drive frequency such that the second-order Doppler shift and the scalar Stark shift cancel each other. These methods make the virtual clock transition line center especially immune to the electric quadrupole and micromotion shifts.

The main source of uncertainty in the present system is the evaluation of the BBR field that contributes a fractional uncertainty of 1.1×10^{-17} . Experiments are planned to evaluate the BBR field more accurately using a thermal imaging camera on a dummy trap built to be identical within fabrication tolerances with the operational trap. We estimate that a new evaluation of $\langle E^2 \rangle_T$ should bring the total uncertainty of the $^{88}\text{Sr}^+$ ion developed at the NRC to $\approx 3.8 \times 10^{-18}$.

Reaching fractional uncertainties of 2×10^{-18} and lower is feasible for the $^{88}\text{Sr}^+$ ion but would require a new ion trap designed for a lower uncertainty of the thermal field at the ion [21], [23].

ACKNOWLEDGMENT

The authors would like to thank B. Hoger, W. Pakulski and R. Pelletier for their help with the electronic systems used in the single-ion clock system.

REFERENCES

- [1] T. Rosenband, D. B. Hume, P. O. Schmidt, C. W. Chou, A. Brusch, L. Lorini, W. H. Oskay, R. E. Drullinger, T. M. Fortier, J. E. Stalnaker, S. A. Diddams, W. C. Swann, N. R. Newbury, W. M. Itano, D. J. Wineland, and J. C. Bergquist, "Frequency ratio of Al^+ and Hg^+ single-ion optical clocks; metrology at the 17th decimal place," *Science*, vol. 319, no. 5871, pp. 1808–1812, Mar. 2008.
- [2] C. W. Chou, D. B. Hume, J. C. J. Koelemeij, D. J. Wineland, and T. Rosenband, "Frequency comparison of two high-accuracy Al^+ optical clocks," *Phys. Rev. Lett.*, vol. 104, p. 070802, Feb. 2010.
- [3] S. A. King, R. M. Godun, S. A. Webster, H. S. Margolis, L. A. M. Johnson, K. Szymaniec, P. E. G. Baird, and P. Gill, "Absolute frequency measurement of the $^2S_{1/2}$ - $^2F_{7/2}$ electric octupole transition in a single ion of $^{171}\text{Yb}^+$ with 10^{-15} fractional uncertainty," *New J. Phys.*, vol. 14, no. 1, p. 013045, Jan. 2012.
- [4] A. A. Madej, P. Dubé, Z. Zhou, J. E. Bernard, and M. Gertsvolf, " $^{88}\text{Sr}^+$ 445-THz single-ion reference at the 10^{-17} level via control and cancellation of systematic uncertainties and its measurement against the SI second," *Phys. Rev. Lett.*, vol. 109, p. 203002, Nov. 2012.
- [5] P. Dubé, A. A. Madej, M. Tibbo, and J. E. Bernard, "High-accuracy measurement of the differential scalar polarizability of a $^{88}\text{Sr}^+$ clock using the time-dilation effect," *Phys. Rev. Lett.*, vol. 112, p. 173002, Apr. 2014.
- [6] G. P. Barwood, G. Huang, H. A. Klein, L. A. M. Johnson, S. A. King, H. S. Margolis, K. Szymaniec, and P. Gill, "Agreement between two $^{88}\text{Sr}^+$ optical clocks to 4 parts in 10^{17} ," *Phys. Rev. A*, vol. 89, p. 050501, May 2014.
- [7] B. J. Bloom, T. L. Nicholson, J. R. Williams, S. L. Campbell, M. Bishop, X. Zhang, W. Zhang, S. L. Bromley, and J. Ye, "An optical lattice clock with accuracy and stability at the 10^{-18} level," *Nature*, vol. 506, no. 7486, pp. 71–75, Feb. 2014.
- [8] I. Ushijima, M. Takamoto, M. Das, T. Ohkubo, and H. Katori, "Cryogenic optical lattice clocks," *Nat. Photon.*, vol. 9, no. 3, pp. 185–189, Mar. 2015.
- [9] T. L. Nicholson, S. L. Campbell, R. B. Hutson, G. E. Marti, B. J. Bloom, R. L. McNally, W. Zhang, M. D. Barrett, M. S. Safronova, G. F. Strouse, W. L. Tew, and J. Ye, "Systematic evaluation of an atomic clock at 2×10^{-18} total uncertainty," *Nat. Commun.*, vol. 6, p. 6896, Apr. 2015.
- [10] N. Huntemann, C. Sanner, B. Lipphardt, C. Tamm, and E. Peik, "Single-ion atomic clock with 3×10^{-18} systematic uncertainty," *Phys. Rev. Lett.*, vol. 116, p. 063001, Feb. 2016.
- [11] A. D. Ludlow, M. M. Boyd, J. Ye, E. Peik, and P. O. Schmidt, "Optical atomic clocks," *Rev. Mod. Phys.*, vol. 87, pp. 637–701, Jun. 2015, and references therein.
- [12] D. Jiang, B. Arora, M. S. Safronova, and C. W. Clark, "Blackbody-radiation shift in a $^{88}\text{Sr}^+$ ion optical frequency standard," *J. Phys. B: At. Mol. Opt. Phys.*, vol. 42, no. 15, p. 154020, Jul. 2009.
- [13] P. Dubé, A. A. Madej, Z. Zhou, and J. E. Bernard, "Evaluation of systematic shifts of the $^{88}\text{Sr}^+$ single-ion optical frequency standard at the 10^{-17} level," *Phys. Rev. A*, vol. 87, p. 023806, Feb. 2013.
- [14] P. Dubé, A. A. Madej, A. Shiner, and B. Jian, " $^{88}\text{Sr}^+$ single-ion optical clock with a stability approaching the quantum projection noise limit," *Phys. Rev. A*, vol. 92, p. 042119, Oct. 2015.
- [15] D. J. Berkeley, J. D. Miller, J. C. Bergquist, W. M. Itano, and D. J. Wineland, "Minimization of ion micromotion in a Paul trap," *J. Appl. Phys.*, vol. 83, no. 10, pp. 5025–5033, May 1998.
- [16] J. Keller, H. L. Partner, T. Burgermeister, and T. E. Mehlstäubler, "Precise determination of micromotion for trapped-ion optical clocks," *J. Appl. Phys.*, vol. 118, p. 104501, Sep. 2015.
- [17] W. M. Itano, "External-field shifts of the $^{199}\text{Hg}^+$ optical frequency standard," *J. Res. Natl. Inst. Stand. Technol.*, vol. 105, no. 6, pp. 829–837, Nov. 2000.
- [18] P. Dubé, A. A. Madej, J. E. Bernard, L. Marmet, J.-S. Boulanger, and S. Cundy, "Electric quadrupole shift cancellation in single-ion optical frequency standards," *Phys. Rev. Lett.*, vol. 95, p. 033001, Jul. 2005.
- [19] W. M. Itano, L. L. Lewis, and D. J. Wineland, "Shift of $^2S_{1/2}$ hyperfine splittings due to blackbody radiation," *Phys. Rev. A*, vol. 25, pp. 1233–1235, Feb. 1982.
- [20] S. G. Porsev and A. Derevianko, "Multipolar theory of blackbody radiation shift of atomic energy levels and its implications for optical lattice clocks," *Phys. Rev. A*, vol. 74, p. 020502, Aug. 2006.
- [21] M. Doležal *et al.*, "Analysis of thermal radiation in ion traps for optical frequency standards," *Metrologia*, vol. 52, no. 6, p. 842, Nov. 2015.
- [22] K. Gibble, "Scattering of cold-atom coherences by hot atoms: Frequency shifts from background-gas collisions," *Phys. Rev. Lett.*, vol. 110, p. 180802, May 2013.
- [23] P. B. R. Nisbet-Jones, S. A. King, J. M. Jones, R. M. Godun, C. F. A. Baynham, K. Bongs, M. Doležal, P. Balling, and P. Gill, "A single-ion trap with minimized ion–environment interactions," *Appl. Phys. B*, vol. 122:57, no. 3, pp. 1–8, Mar. 2016.

Carrier-Phase Two-Way Satellite Frequency Transfer between LNE-SYRTE and PTB

Miho Fujieda, Hiroshi Takiguchi
National Institute of Information and
Communications Technology
Tokyo, JAPAN

Joseph Achkar, Michel Abgrall,
and Jocelyne Guéna
LNE-SYRTE, Observatoire de Paris,
PSL Research University, CNRS, Sorbonne
Universités, UPMC Univ. Paris 06
Paris, FRANCE

Franziska Riedel, Erik Benkler,
Stefan Weyers, and Dirk Piester
Physikalisch-Technische
Bundesanstalt
Braunschweig, GERMANY

Abstract—We performed a carrier-phase two-way satellite frequency transfer (TWCP) experiment between LNE-SYRTE and PTB for several days in September 2015. Different hardware configurations were analyzed at the LNE-SYRTE earth station and a suitable configuration was identified by placing up- and down-converters indoors. Additionally atomic fountain frequency standards were operated simultaneously at both institutes. This offered a comparison of two reference clocks at LNE-SYRTE and PTB independently by means of TWCP and via the fountain clocks. Even with a very limited and not continuous measurement time of about 8 hours for TWCP measurements, a frequency transfer uncertainty below 2×10^{-15} was achieved and the results by the fountain clocks and TWCP agreed well within this uncertainty.

Keywords—carrier-phase, TWSTFT, atomic fountain frequency standard

I. INTRODUCTION

Carrier-phase two-way satellite frequency transfer (TWCP) is a promising method to provide a stable frequency transfer over a long baseline. A dedicated setup was developed at the National Institute of Information and Communications Technology (NICT) [1] and was operated on the intercontinental baseline between NICT and Physikalisch-Technische Bundesanstalt (PTB) [2]. Here, we report on the application of the TWCP technique for a frequency transfer measurement between LNE-SYRTE and PTB. To employ this technique, an arbitrary waveform generator (AWG) and an analog-to-digital (A/D) sampler developed by NICT were installed into earth stations at LNE-SYRTE and PTB. The measurement was done once every 2 hours using a 200-kHz-bandwidth signal on a satellite link where TWSTFT measurements are regularly performed among metrology institutes in Europe and USA. A short-term instability of 2×10^{-13} at 1 s averaging time was obtained successfully.

In the TWCP technique, the phases of the transmitted and received signals should be kept coherent to those of the reference clocks' signals of the station. Thus, it is necessary that frequency up/down converters (U/C, D/C) lock to the reference signal. They are key devices whose phase noise in frequency conversion has a significant impact on the TWCP resolution [1]. The setup of the station at LNE-SYRTE

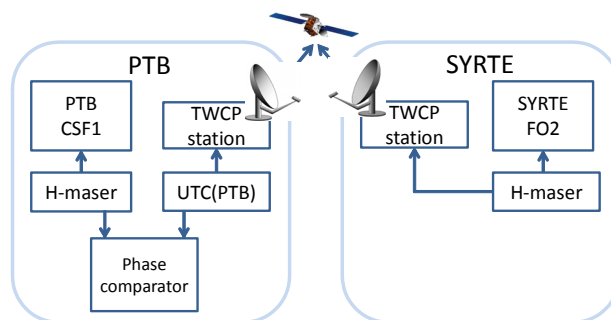


Fig. 1: Carrier-phase two-way satellite frequency transfer (TWCP) setup between PTB and LNE-SYRTE.

allowed us to examine different configurations and to identify the best suited one for TWCP. The reference clocks at both institutes were compared by TWCP and with the help of atomic fountain frequency standards which were operated simultaneously. The results are discussed in this paper.

II. MEASUREMENT SETUP

The configuration of the frequency transfer measurement is shown in Fig. 1. The TWCP station at PTB was connected to UTC(PTB). The frequency of a H-maser was measured by the atomic fountain frequency standard PTB-CSF1 [3]. The phase between UTC(PTB) and the H-maser was measured by a phase comparator.

The TWCP station at LNE-SYRTE was connected to a H-maser, whose frequency was measured by the atomic fountain frequency standard SYRTE-FO2 [4]. The frequency difference between UTC(PTB) and the H-maser at LNE-SYRTE (called HM(SYRTE) hereafter) was measured by TWCP and independently deduced from the two atomic fountain measurements from MJD 57266 to MJD 57271. Please note that the frequency difference between UTC(PTB) and the H-maser was bridged using the measurement result by the phase comparator at PTB. During the period, the measurements of PTB-CSF1 and SYRTE-FO2 were performed continuously. Meanwhile, the TWCP measurement was performed for about 3 000 s every two hours via the geostationary satellite T-11N. Only every second hour was available for this experiment because of the regular TWSTFT measurements performed in the same frequency band during the even hours. The TWCP

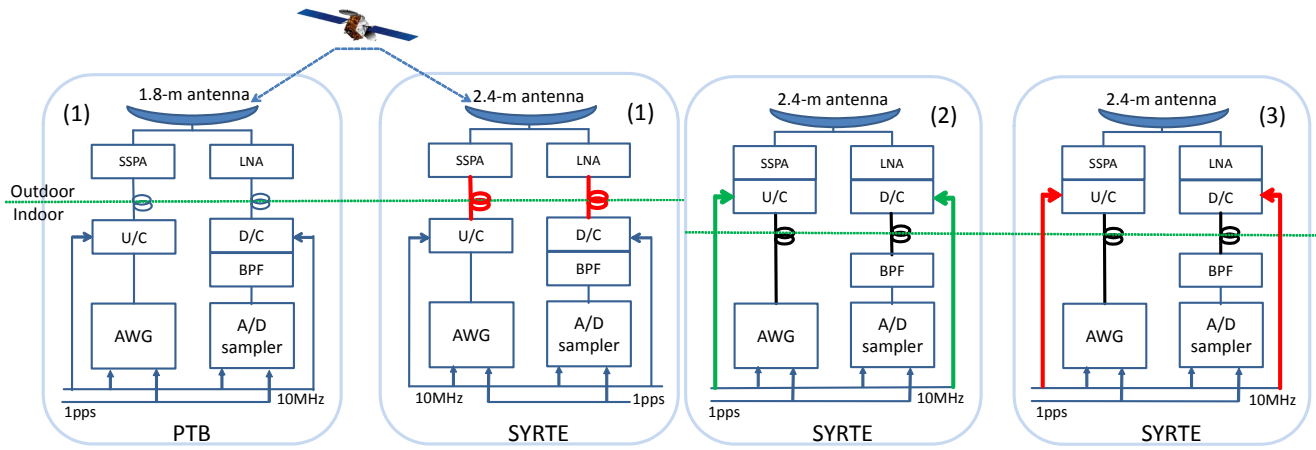


Fig. 2: TWCP station setups at PTB and LNE-SYRTE. Three different configurations were used at LNE-SYRTE. Indoor U/C and D/C were used in setup (1). Outdoor U/C and D/C were used in setups (2) and (3). Between setups (2) and (3) different coaxial cables were used for the 10-MHz reference signal transfer from indoor to outdoor. U/C: frequency up converter, D/C: frequency down converter, BPF: bandpass filter, AWG: arbitrary waveform generator, A/D: analog-to-digital, SSPA: solid-state power amplifier, LNA: low noise amplifier.

measurement data were recorded every second in the available measurement slots. The measurement start and stop processes ran automatically. Since they took some minutes, the measurement time was limited to about 3 000 s in each 3 600s slot.

The setup of the TWCP station at LNE-SYRTE was changed two times over the measurement period to identify a suitable configuration for TWCP, while that at PTB was fixed.

A. Setup 1 for PTB and LNE-SYRTE stations

Fig. 2 (1) depicts the schematic of the station setups at PTB and LNE-SYRTE, called setup 1 hereafter. Both stations employed identical configurations, where the equipment other than the AWG and A/D sampler was standard equipment as used in conventional TWSTFT stations. The same models of the U/C and D/C were used at both PTB and LNE-SYRTE stations and they were installed indoors. The transmission and reception signals in the Ku-band were transferred between indoor and outdoor by coaxial cables, with cable lengths of 25 m at PTB and 45 m at LNE-SYRTE, respectively. The reference frequency signals were provided to the U/C and D/C by short cables at LNE-SYRTE and at PTB additionally by a fiber transfer of UTC(PTB) from the time laboratory to the location of the TWCP setup.

B. Setup 2 with change in LNE-SYRTE station

In setup 2, the station configuration at LNE-SYRTE was changed to Fig. 2 (2). Different U/C and D/C made for outdoor use were installed close to the antenna. The reference frequency signals were sent from indoor to outdoor by coaxial cables, called green cables hereafter. They were usually used in the LNE-SYRTE station to provide the reference frequency signals to the U/C and D/C for TWSTFT.

C. Setup 3 with further change in LNE-SYRTE station

In setup 3, the station configuration at LNE-SYRTE was changed to Fig. 2 (3), where the same outdoor U/C and D/C as in setup 2 were employed but different coaxial cables, called

red cables hereafter, were used for the transfer of the reference frequency signal. Actually the red cables were installed for the TWCP measurement and employed to transfer the TWCP signals between indoor and outdoor in setup 1. Their cable types are given in Table 1. As a summary, the main points of the three setups are:

- Setup 1: indoor U/C and D/C at PTB and LNE-SYRTE
- Setup 2: outdoor U/C and D/C, reference frequency signals sent by original (green) cables in LNE-SYRTE station.
- Setup 3: outdoor U/C and D/C, reference frequency signals sent by red cables in LNE-SYRTE station.

Table 1: Cable types.

Identification	Model	Length [m]
Red	Junkosya MWX322	45
Green	Atem M400-2121 N-type	45
Dark-green	RG213 N-type	45

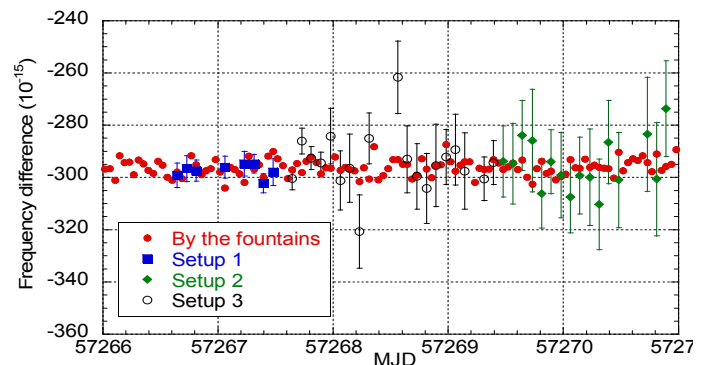


Fig. 4: Frequency differences of UTC(PTB)-HM(SYRTE) measured by the fountains and by TWCP setups 1, 2 and 3.

III. RESULTS

A. SYRTE-FO2 and PTB-CSF1

We check the frequency agreement between SYRTE-FO2 and PTB-CSF1 roughly by simply comparing their estimations of the TAI scale interval as published in BIPM Circular T 333 (September 2015) [5] and reported in Table 2. The fountain frequency difference of only -0.9×10^{-16} is well within the quadratic sum of the stated total uncertainties 0.8×10^{-15} .

Table 2: Frequency difference between SYRTE-FO2, PTB-CSF1 and TAI.

Data extracted from Circular T 333 [5].

Name	Period	Difference (10^{-15})	Systematic uncertainty (10^{-15})	Total uncertainty (10^{-15})
SYRTE-FO2	MJD 57264- 57289	0.39	0.28	0.43
PTB-CSF1	MJD 57264- 57294	0.48	0.69	0.70
(SYRTE-FO2)- (PTB-CSF1)		-0.09	0.74	0.82

B. Impact of location (indoor/outdoor) for U/C and D/C

The frequency measurement data by TWCP, by the phase comparator and by the two fountains were averaged for 1 hour and the midpoints were chosen on the full hour for further computation. Fig. 4 shows the frequency differences UTC(PTB)-HM(SYRTE) measured by the fountains and by TWCP. Each point represents a 1-h mean, where the outliers were eliminated before averaging. The error bars for TWCP points represent the standard error, that is, the standard deviation divided by the root of the number of data points in the 1-h measurement slot. This is because the TWCP instability is mainly limited by white frequency noise after an averaging time longer than 100 s. The frequency differences UTC(PTB)-HM(SYRTE) measured by setup 1 clearly agrees with the results of the comparison by the fountains. In comparison to these, large dispersion and excursion are clearly seen in the data of setup 2 and 3. The setup with indoor U/C and D/C are clearly superior to the outdoor configuration.

C. Impact of cable type for transfer of reference frequency signal

Different types of cables were used for the transfer of the reference frequency signal to the outdoor U/C and D/C between setups 2 and 3. There is no clear difference in the results obtained by these setups (see Fig. 4). Nevertheless, the number of removed outliers was larger in setup 2 than in setup 3. Additionally, the means of the standard errors of the 1-h slots were 8.4 and 5.4 in 10^{-13} for setup 2 and setup 3, respectively. It is likely that setup 2 exhibits a slightly higher instability. The green cables used in setup 2 are normally used in TWSTFT measurement at LNE-SYRTE, while the red cables were specially installed to transfer Ku-band signals for TWCP measurements. The insertion losses of the red cables are -44 dB at 14 GHz. We also checked the cable

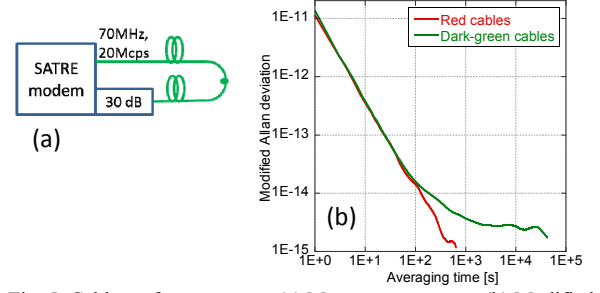


Fig. 5: Cable performance test. (a) Measurement setup, (b) Modified Allan deviation.

performances by the phase stability of a 70-MHz signal transfer, where the measurement was done using a SATRE modem with 20-Mcps modulation (see Fig. 5). We joined the two cables outdoors and established a loop between indoor and outdoor. As the green cables could not be used in the same manner, similar (dark-green) cables were used instead. Then we compared the signal phases of both configurations. Fig. 5 (b) shows the modified Allan deviation of the measured phase variations. It is likely that the dark-green cables degrade the stability of the reference signal as the instability of the dark-green cable is significantly higher compared with the instability of the red cable at averaging times above 100 s. The instability of the reference frequency signals could limit the stability in frequency transfer because it is impossible to obtain a better stability in frequency transfer than that of the reference signal. When we place U/C and D/C outdoors, we have to take care of the reference signal quality provided to them. In setup 2, unstable reference frequency signals might have affected the performance of the outdoor U/C and D/C.

D. Uncertainty for TWCP setup 1

It is clear that setup 1 offers the best result in this experiment. We compared the frequency differences measured by setup 1 and by the fountains. The measurement was executed 11 times using setup 1. However, the measurements failed three times due to a wrong tuning of the automatic running process. As a result, 8 points as depicted in Fig. 4 became available. The frequency differences by the fountains which had the same time label as the setup 1 measurements were selected for comparison. The frequency differences UTC(PTB)-HM(SYRTE) calculated from the 8 points are:

- By the fountains: $(-297.8 \pm 1.2) \times 10^{-15}$

- By setup 1: $(-297.3 \pm 1.4) \times 10^{-15}$

The uncertainty by the fountains represents the root sum square of the total uncertainties of 0.80×10^{-15} and 0.96×10^{-15} for SYRTE-FO2 and PTB-CSF1, respectively. The uncertainty for setup 1 is the root sum square of u_A , u_B and u_{dt} , where u_{dt} is the uncertainty caused by dead time. The type A uncertainty u_A is determined from the standard error of the 8 points: 0.9×10^{-15} . The type B uncertainty u_B is conservatively estimated to 1.0×10^{-15} . This value is same as the one calculated from the double-difference instability of GPSCP-TWCP at 8 hours in the NICT-PTB link [2]. The uncertainty u_{dt} is

0.3×10^{-15} which was calculated from the below equation in the case of white frequency noise [6].

$$u_{dt} = \frac{\sqrt{3}}{T} \sqrt{\sum_{i=1}^N [\sigma(\tau_{g,i})]^2}$$

τ_g is the dead time and σ is the time deviation. For example, in the 1-h measurement slots, the mean dead time was 614 s and $\sigma(614 \text{ s})$ was about 1.7×10^{-12} s. T is 28 800 s and N is 8. We estimate a total uncertainty of 1.4×10^{-15} for 8 data points of 1-h averaging and therefore conclude that the result agrees well with the value obtained from the fountain measurements.

E. Frequency stability

Fig. 6 (a) shows the modified Allan deviation of the results obtained by setups 1, 2 and 3, which were calculated by using the frequency difference data. The measurement gaps which intervals were not equal were distributed and simply filled by Stable32 software. In Fig. 6 (b), the frequency instabilities of setup 1 with two different gap handlings are presented: modified Allan deviation with distributed and filled gaps by Stable32 and modified Allan deviation with lumped data without gaps. Unfortunately, the measurement period for setup 1 was rather short and there were some missing data. A frequency instability in the 10^{-16} range was computed, however.

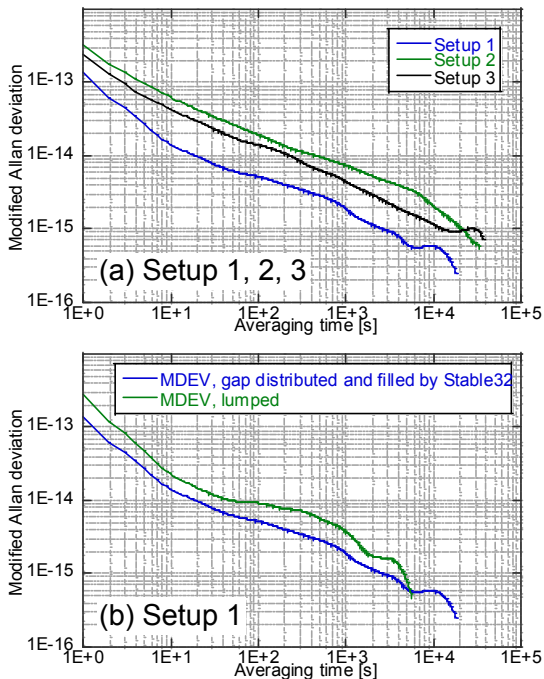


Fig. 6 (a) Modified Allan deviation by setups 1, 2 and 3. (b) Modified Allan deviation by setup 1 with different gap handlings.

IV. CONCLUSION

We performed carrier-phase two-way satellite frequency transfer (TWCP) experiment in the LNE-SYRTE - PTB link for several days in September 2015. The earth station configuration at PTB was fixed over the period, while the configuration was changed twice at LNE-SYRTE to examine the suitable placement for the frequency up and down converters. As a result, the frequency converters installed indoors realized better stability. It seems that the frequency converters installed outdoors are sensitive to the environment, although they are specified for outdoor use. Additionally the quality of the reference frequency signal provided to the outdoor converters also should be taken into careful consideration.

During the TWCP campaign, the atomic fountain frequency standards, SYRTE-FO2 and PTB-CSF1, were measuring continuously the frequency of the local H-masers at LNE-SYRTE and PTB, respectively. By comparing the results obtained from the fountains and by TWCP, an excellent agreement between the two methods was achieved with low 10^{-15} uncertainty for only 8 data points of 1-h averaging. Besides, the frequency stability by TWCP reached the 10^{-16} range. However, the measurement period was limited and with longer measurement time a comparison of frequency standards with an uncertainty in the low 10^{-16} range should be possible by TWCP.

ACKNOWLEDGMENT

The authors would like to thank D. Rovera from LNE-SYRTE, J. Becker from PTB and T. Gotoh from NICT for their fruitful advices and kind supports. The authors would like to thank members of CCTF WG on TWSTFT for making the satellite frequency band available for this experiment.

REFERENCES

- [1] M. Fujieda et al., "Carrier-Phase-Based Two-Way Satellite Time and Frequency Transfer", IEEE Trans. Ultrason. Ferroelectr. Freq. Control, vol. 59, pp. 2625-2630, 2012.
- [2] M. Fujieda et al., "Carrier-phase two-way satellite frequency transfer over a very long baseline", Metrologia, 51, pp. 253-262, 2014.
- [3] S. Weyers, U. Hübner, R. Schröder, Chr. Tamm, A. Bauch, "Uncertainty evaluation of the atomic caesium fountain CSF1 of PTB", Metrologia **38** (4), p. 343-352 (2001); S. Weyers, A. Bauch, R. Schröder, Chr. Tamm, "The atomic caesium fountain CSF1 of PTB" in: Proceedings of the 6th Symposium on Frequency Standards and Metrology 2001, University of St Andrews, Fife, Scotland, p. 64-71, ISBN 981-02-4911-X (World Scientific)
- [4] J. Guéna et al., "Progress in atomic fountains at LNE-SYRTE", IEEE Trans. Ultrason. Ferroelectr. Freq. Control, vol. 59, p. 391-410, 2012.
- [5] Circular T 333. <http://www.bipm.org/en/bipm-services/timescales/time-ftp/publication.html#nohref>
- [6] National Physical Laboratory, "Evaluation of the frequency of the H-maser 1401701 by the primary frequency standard NPL-CsF1", LIMS ref. E05050210.

The Development of GPS/BDS Time Transfer System

Hongbo Wang*[†] Hang Yi*[†] Shengkang Zhang*[†] Haifeng Wang*[†] Fan Shi*[†] and Xueyun Wang*

*Beijing Institute of Radio Metrology and Measurement, Beijing China 100854

[†]Science and Technology on Metrology and Calibration Laboratory, Beijing China 100854

Abstract — This paper describes a time transfer system that allows timing laboratories, including metrology institutes and other designated institutions, to compare the local realization of Coordinated Universal Time (UTC) with each other. The time transfer system could calculate the difference between the local time and GPS time, and the difference between the local time and BDS time. It stores the measurement results in a format compatible with international standards, which has just extended to include BDS data. The system was designed to be easy to use, allowing recently established timing laboratories to begin tracing to UTC with both GPS and BDS.

Keywords—Beidou; GPS; Coordinated Universal Time(UTC) ; Time transfer

I. INTRODUCTION

The GPS Common-View (CV) time transfer [1] has been used by the Bureau International des Poids et Mesures (BIPM) since 1980s to compare the UTC realizations of timing labs in order to generate the International Atomic Time (TAI). The same approach has then been used widely for synchronization of local time scales with the legal time references available in National Metrological Institutes. At the end of 2014, 73 time laboratories supplied data for the calculation of TAI and UTC. The measurement data were collected with several different time transfer techniques, each of which currently involves satellites [2].

The standard for GNSS time transfer was first defined in 1984. It was updated at a few instances to follow the evolution of GPS, of the receivers, and the inclusion of GLONASS. With the emergence of additional navigation systems like Galileo, BeiDou, QZSS, the standard is extended by the CCTF Working Group on GNSS Time Transfer, named CGGTTS for Common GNSS Generic Time Transfer Standard, and the corresponding Version 2E of the format [3].

With the development of Chinese Beidou System in recent years, BDS becomes an alternative way of GNSS time transfer. The CGGTTS V2E could well support BDS time transfer, and more geodetic GNSS receivers could receive B1&B2 dual frequency signals. Beijing Institute of Radio Metrology and Measurement (BIRMM) has developed a time transfer system which could utilize both GPS and BDS to realize time transfer. This system may generate data in CGGTTS format for time transfer and in RINEX format of the raw GNSS observations.

II. SYSTEM HARDWARE DESIGN

The GPS/BDS time transfer system was designed with commercially-available GNSS geodetic OEM receiver and embedded computer. A block diagram of the time transfer system is provided in Fig. 1.

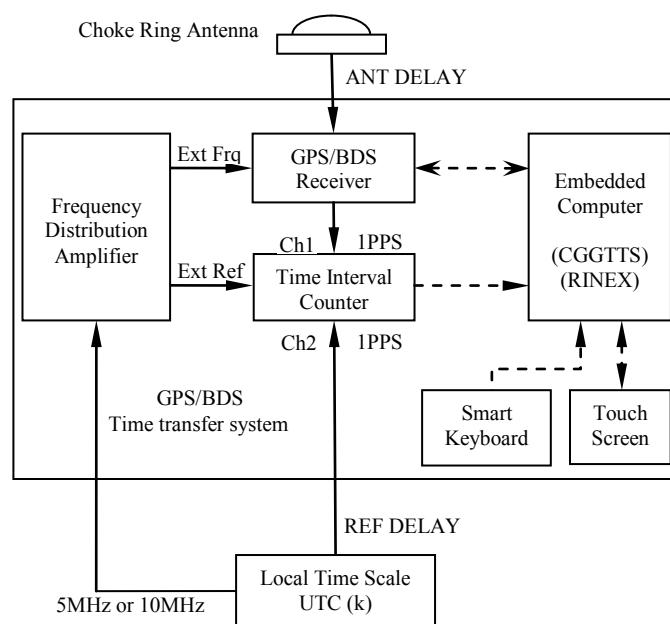


Fig. 1. The diagram of GPS/BDS time transfer system

The system is housed in a 4U-height chassis (Fig. 2) that includes a 257mm diagonal (10.1 inch) touch screen display with a resolution of 1280 × 800 pixels and a smart keyboard.



Fig. 2. The front panel of GPS/BDS time transfer system

Overview		Satellite Info		GPS CCGTTS		BDS CCGTTS		AT Chart		Setting	
Alt	CL	RIS	PRN	PRN	PRN	PRN	PRN	PRN	PRN	PRN	PRN
001	FF	37542	000000	780	2407	20447	-36	975	-0	2	1
002	FF	37542	000000	780	2407	20447	-36	975	-0	2	1
003	FF	37542	000000	780	2407	20447	-36	975	-0	2	1
004	FF	37542	000000	780	2407	20447	-36	975	-0	2	1
005	FF	37542	000000	780	2407	20447	-36	975	-0	2	1
006	FF	37542	000000	780	2407	20447	-36	975	-0	2	1
007	FF	37542	000000	780	2407	20447	-36	975	-0	2	1
008	FF	37542	000000	780	2407	20447	-36	975	-0	2	1
009	FF	37542	000000	780	2407	20447	-36	975	-0	2	1
010	FF	37542	000000	780	2407	20447	-36	975	-0	2	1
011	FF	37542	000000	780	2407	20447	-36	975	-0	2	1
012	FF	37542	000000	780	2407	20447	-36	975	-0	2	1
013	FF	37542	000000	780	2407	20447	-36	975	-0	2	1
014	FF	37542	000000	780	2407	20447	-36	975	-0	2	1
015	FF	37542	000000	780	2407	20447	-36	975	-0	2	1
016	FF	37542	000000	780	2407	20447	-36	975	-0	2	1
017	FF	37542	000000	780	2407	20447	-36	975	-0	2	1
018	FF	37542	000000	780	2407	20447	-36	975	-0	2	1
019	FF	37542	000000	780	2407	20447	-36	975	-0	2	1
020	FF	37542	000000	780	2407	20447	-36	975	-0	2	1
021	FF	37542	000000	780	2407	20447	-36	975	-0	2	1
022	FF	37542	000000	780	2407	20447	-36	975	-0	2	1
023	FF	37542	000000	780	2407	20447	-36	975	-0	2	1
024	FF	37542	000000	780	2407	20447	-36	975	-0	2 </tr	

Fig. 6. The interface of “BDS CCGTTS” Tab of the software

Every common-view period, with all the tracked GPS satellite data and BDS satellite data, the software could synthesize the time difference between the local time scale and GPS, and the time difference between the local time scale and BDS. The “ ΔT Chart” Tab (Fig. 7) would display all these time differences, and show the chart for the recent 24 hours.



Fig. 7. The interface of “ ΔT Chart” Tab of the software

In the “Setting” Tab, many parameters for the system could be set, including the surveyed coordinate for the antenna, the phase center offset of the antenna, the antenna cable delay, the 1PPS cable delay for the first part of REFDFLY, and other parameters for the CCGTTS and RINEX files.

IV. SYSTEM CALIBRATION

For a time transfer system, the calibration is quite important. All the GNSS time transfer system should be calibrated.

According to [2], REFDFLY is the time offset between the receiver internal clock and the local clock at the station, which can be a realization of UTC. In most cases, this time offset contains two components: the cable delay between the local clock and the receiver input connector and the time offset between the input connector and the internal reference. So the time offset between the system input connector and the internal reference is determined first as part of the REFDFLY value.

The hardware delays of the GPS and BDS part of this system are calibrated separately. The GPS receiver calibration

is performed by comparing with a calibrated TTS-4 in NIM as detailed in the BIPM guidelines for Calibration [5].

Since there is not a “golden receiver” for BDS, the BDS calibration could not be implemented by comparison. Instead, a BDS simulator was used for receiver absolute delay calibration. With the method in [6], the delay of BDS receiver is calibrated. And the antenna cable delay is measured for all the navigation signal frequency by a vector network analyzer. These values are predefined in the software.

V. SYSTEM TEST

A. Single Station Timing

When the system is tested for single station timing, the precision of GPS is much better than BDS. By analyzing the CCGTTS data, the time difference between local time and each Beidou satellite clock are derived. Fig.8 shows the timing result calculated by Beidou B1 observations. The ionospheric delay is not removed. The black solid line is the average for all Beidou satellite.

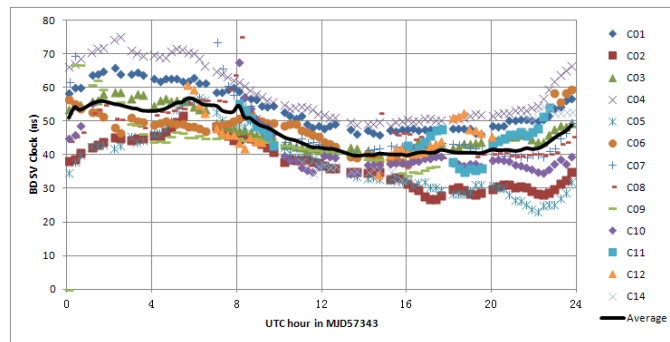


Fig. 8. The timing result by Beidou satellite B1 observation (including ionospheric delay)

After the ionospheric delay is removed, the time difference between local time and each Beidou satellite clock differs obviously, especially for Beidou GEO satellites as Fig. 9 shows. This is caused by the Beidou satellite Differential Code Bias (DCB). The system calibration only measured the ground delay. The obvious Beidou satellite DCB affects the timing result. When a Beidou satellite is added into or removed from the constellation, the time difference will have a fluctuation.

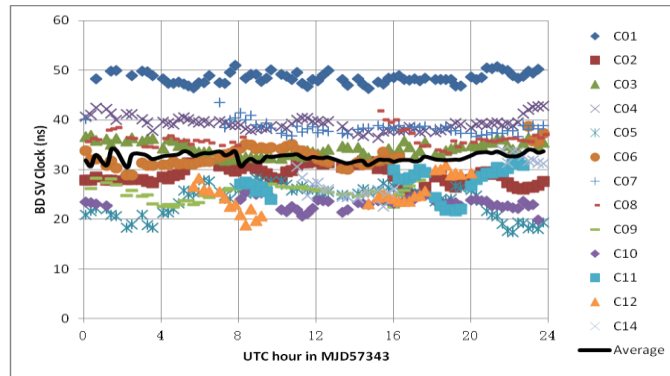


Fig. 9. The timing result by Beidou satellite iono-free observation

In the Multi-GNSS Experiment (MGEX) project launched by IGS, the Differential Code Bias (DCB) for Beidou satellites is monitored [7]. The Beidou DCB product from IGS is consistent with the analysis result. So applying Beidou DCB product to the time transfer system would improve the Beidou timing precision. On the other hand, if the time transfer system is well calibrated, it could be used to monitor the DCB of Beidou satellite system.

B. Zero Baseline Test

The two same time transfer systems were connect to the same antenna distributed signal, reference frequency and 1PPS signal. The zero-baseline time transfer results from GPS and BDS are shown in Fig.10 and Fig.11.

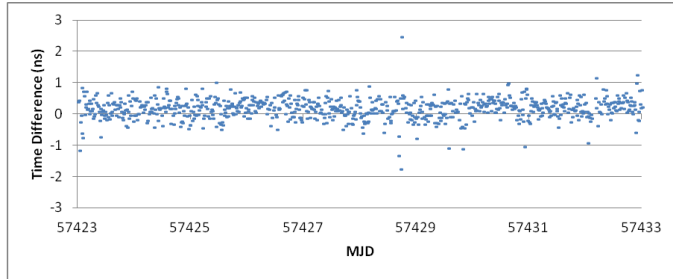


Fig. 10. Zero-baseline common clock time transfer result from GPS P3

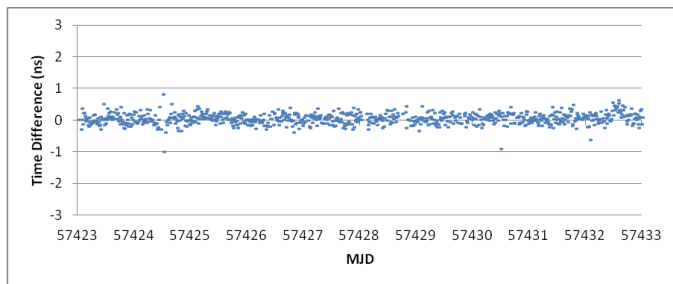


Fig. 11. Zero-baseline common clock time transfer result from BDS P3

The standard deviation for GPS zero-baseline common clock test result is 0.348ns. For BDS, it is 0.174ns.

VI. DISCUSSION

Since the DCB values for Beidou System could be obtained from the IGS product, they are considered to be taken into account for BDS timing. Furthermore, after the delays of local

time to BDS system time from all the Beidou SVs have been calculated, the average method could be improved. Beidou constellation is composed with three different types of satellite, including 5 GEO, 5 IGSO and 4 MEO satellites. Now the time difference calculated from the high orbit GEO satellite is much larger than the others, so when melting all the Beidou satellite clock offsets, the weight for GEO should be decrease.

VII. CONCLUSION AND PERSPECTIVES

BIRMM has developed a time transfer system which could support both GPS and BDS. The system software could display a variety of parameters, save the raw observations in RINEX 3.03 format, calculate the time difference between local time and GPS time or Beidou time, generate files in the newest CGGTTS V2E format. The local timing test result from GPS is better than BDS. At present, we are doing experiments to apply the IGS Beidou DCB products to the system, and adjust the weights for different types of satellites to improve the Beidou timing precision. Furthermore, a communication module is intended to be ensemble in the system so that the systems in different places could exchange their local files near real-time.

REFERENCES

- [1] Allan, D.W., Weiss, M., "Accurate time and frequency transfer during common-view of a GPS satellite", Proc. 1980 IEEE Freq. Contr. Symp., Philadelphia, PA, pp. 334-356, 1980.
- [2] BIPM, Director's Report on the Activity and Management of the International Bureau of Weights and Measures Supplement: Time Department, 3 (2015).
- [3] P. Defraigne, G. Petit, "CGGTTS-Version 2E: an extended standard for GNSS Time Transfer", Metrologia, 52, 2015.
- [4] China Satellite Navigation Office, Beidou Navigation Satellite System Signal In Space Interface Control Document Version 2.0, 2013
- [5] BIPM GNSS equipment calibration guideline (Draft), 2015
- [6] H.Wang, H. Yi, S.Zhang and H. Wang, "The study of Beidou timing receiver delay calibration", Proceedings of Joint Meeting of the IEEE Frequency Control Symposium and European Frequency and Time Forum, 2015, pp. 541-544.
- [7] O. Montenbruck, P. Steigenberger, R. Khachikyan, G. Weber, R. Langley, L. Mervart and U. Hugentobler, "IGS-MGEX: Preparing the Ground for Multi-Constellation GNSS Science", InsideGNSS 9 (1):42-49 (2014).

Determination of differential delays of earth stations in Paris and Torino from the calibrated OP-IT TWSTFT link

Joseph Achkar, Daniele Rovera

LNE-SYRTE

Observatoire de Paris, PSL Research University, CNRS,
Sorbonne Universités, UPMC Univ. Paris 06
Paris, France

Ilaria Sesia, Patrizia Tavella

INRiM

Istituto Nazionale di Ricerca Metrologica
Torino, Italy

Abstract— INRiM (Torino) and LNE-SYRTE (Paris) operate two earth stations from which a calibrated two-way link, at the nanosecond level, is established and regularly works in the context of contributions to ongoing activities (TAI of the BIPM) or specific activities (Galileo). Torino and Paris also use two additional earth stations that can be used for specific scientific applications or for redundancy to regular scientific operations. This paper describes the determination of the relative differential delays of the additional stations, from the reference calibrated link, with a combined uncertainty of 1 ns and highlights a bias around 370 ps on the reference calibrated link that may be caused by interference problems between codes at 1 MChip/s within the TWSTFT network.

Keywords—TWSTFT; calibration; time stability; characterization; uncertainty; interference

I. INTRODUCTION

Two-Way Satellite Time and Frequency Transfer (TWSTFT) technique [1] is used in most of the national metrology institutes (NMIs) or Designated Institutes (DIs) as the primary link method for time-scales comparisons. A major advantage of this technique is direct comparisons of time-scales in almost real time using remote earth stations in microwave links through a geostationary satellite. A best link quality can be achieved in reducing residual non-reciprocal effects, using well-characterized earth stations and improved carrier-to-noise ratio of two-way links during measurement within time-slots period for which the transponder is less busy on a regular basis over an appropriate period of time.

II. LNE-SYRTE AND INRiM TWSTFT EARTH STATIONS

A. LNE-SYRTE earth stations

Two two-way earth stations are operated at LNE-SYRTE: OP01 is regularly used within the Europe and Transatlantic TWSTFT networks; it constitutes our primary station in the international time links organized by the BIPM for our contribution to the realization of TAI/UTC, and also participates in various activities related to Galileo; OP02 is most commonly used for research and development [2]. Both

earth stations are equipped with TimeTech SATRE modems, Miteq separate frequency up-converters and down-converters with external reference frequency, and 2.4 m diameter dual offset antennas. The UTC(OP) based on a hydrogen maser steered by the LNE-SYRTE atomic fountains, is directly connected to both earth stations.

In LNE-SYRTE, the reference time-scale UTC(OP) is defined at the output connector number 16 of the TimeTech PPS distributor unit that distributes the output of the micro-phase stepper.

B. INRiM earth stations

Two TWSTFT earth stations are installed at INRiM, designated IT01 and IT02.

IT02 station is used to officially contribute to TAI/UTC as calculated and published by the BIPM in the Circular T; this station is also used to compare UTC(IT) to the Galileo system Time generated at the two Precise Time Facility (PTF) in the frame of the Galileo project [3].

The second station, IT01, was recently used in the frame of ITOC project [2] for comparisons of optical clocks using improved broadband two-way satellite time and frequency transfer. It is planned to use IT01 as hot-redundant back-up station of the operational IT02 station, hence the need for IT01 calibration.

Both INRiM stations are equipped with TimeTech SATRE modems, Anacom SEKu transceivers and 1.8 m offset antennas. All the equipment is currently connected to an active H-maser, which is UTC(IT) master clock; it is planned to connect IT01 and IT02 stations to UTC(IT) by April 2016.

III. TECHNICAL AND EXPERIMENT SETUP FOR THE DETERMINATION OF DIFFERENTIAL DELAYS

Four Ku-band TWSTFT earth stations equipped with four SATRE modems, implemented in LNE-SYRTE (Paris) and INRiM (Torino) are used: OP01, OP02, IT01 and IT02 (Fig. 1). Different Pseudo-Random Noise (PRN) codes at 1 Chip/s and modulated signals frequencies are applied. Measurements

are performed on time slots of two minutes per each link, and then repeated every two hours. The differential delays of each pair of stations are thus determined from measurements of the various two-way links, relying the measurements taken by the calibrated OP01-IT02 TWSTFT link [4].

In principle, the characterization of signal delays in the laboratory's equipment is essential for performing accurate time transfer. The TWSTFT links have mostly been calibrated by using a portable TWSTFT station [4]. For laboratories who are equipped with more than one earth station can characterize additional TWSTFT links from a reference calibrated two-way link, the topic of this paper. In the computation of the time transfer by TWSTFT, it must be taken into account the delays of the two-way signals measured by the modem, the delays from the local time-scale reference point to the modem signal output, and the calibration result known as CALR. Thus, CALR includes all terms of the two-way equation except the time transfer (two-way) measurements and the reference measurements REFDELAY of the local and remote station, respectively. To do this, we computed the offset between the time transfer performed thru a calibrated TWSTFT and the one performed thru the un-calibrated TWSTFT. CALR is the difference between these two values.

According to the ITU-R recommendation [1], the delay of the reference with respect to the local UTC, known by REFDELAY, includes three terms to be determined:

- The delay 1PPSREF-1PPSTX measured either by internal or external Time-Interval Counter (TIC) depending on the model of the modem used;
- The delay CLOCK-1PPSREF measured by a TIC;
- The delay UTC(k)-CLOCK, when it exists in the time distribution in the laboratory. For the purpose of this characterization, the time difference UTC(k)-CLOCK is not considered in the REFDELAY parameter.

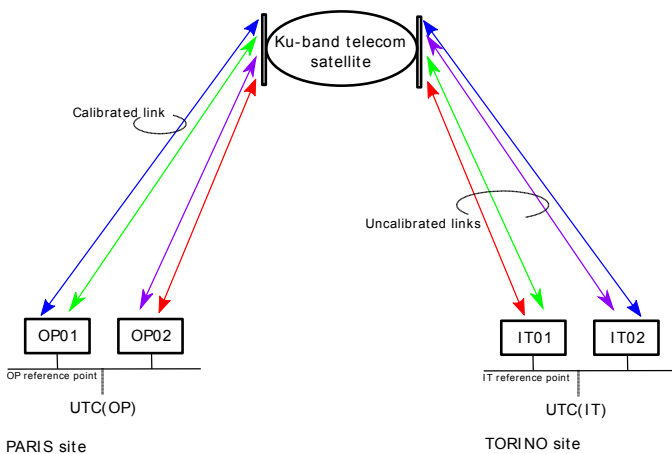


Fig. 1. Configuration diagram of the various combinations of links between four stations which are fed, in pairs, by a common clock reference at each site, in Paris and Torino. The blue link (OP01-IT02) is the calibrated link, the remaining three links, in green (OP01-IT01), in violet (OP02-IT02) and in red (OP02-IT01) are those which are being characterized.

Furthermore, an overall measurement of CLOCK-1PPSTX delay was accurately performed.

On the other hand, the schedule adopted for the experiment was run during the Odd Hours (OH) in UTC for which the European Ku-band transponder on board the T11-N satellite is quiet. It was prepared with the following slots:

- From OH:03:06 to OH:05:59, setting link OP01-IT02 (1-min preparation, 2-min measurement);
- From OH:06:06 to OH:08:59, setting link OP01-IT01;
- From OH:09:06 to OH:11:59, setting link OP02-IT01;
- From OH:12:06 to OH:14:59, setting link OP02-IT02;
- From OH:15:06 to OH:17:59, setting link OP01-IT02 for closure.

For each set of repetitive measurements, closure measures are systematically performed.

IV. RESULTS OF THE TWSTFT LINKS CHARACTERIZATION

A. Characterization of earth stations

The experiment was performed from MJD 57399 to MJD 57457 with the target to determine the differential delays of earth stations OP02 and IT01 with respect to IT02 and OP01; thereby, the CALR was evaluated by averaging the time differences between the reference calibrated two-way link IT02-OP01 (CALR = 6837.300 ns ± 0.8 ns [4]) at even UTC hours (regular sessions) and the two-way links IT02-OP02 (Fig. 2) and IT01-OP01 (Fig. 3) established during the odd UTC hours, we obtained the following values:

- CALR (OP02-IT02) = 275.310 ns
- CALR (IT01-OP01) = 7083.760 ns

At INRiM, IT01 was connected to two different clocks at two different periods (Fig. 3), a Maser and UTC(IT). The slight observed offset is due to the auxiliary delay measurements. A time instability of IT02 around MJD 57410 is noticed.

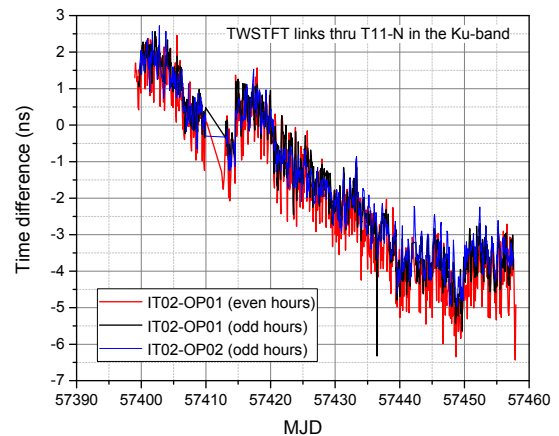


Fig. 2. Time difference between UTC(OP) and UTC(IT) linked by TWSTFT involving two earth stations at LNE-SYRTE, for the characterization of OP02.

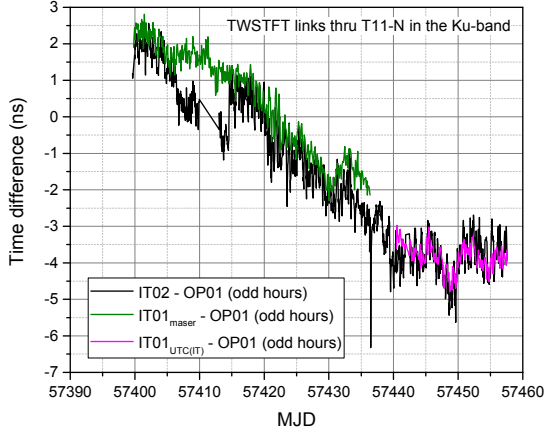


Fig. 3. Time difference between UTC(OP) and UTC(IT) linked by TWSTFT involving two earth stations at INRiM, for the characterization of IT01. Time instability of IT02 is detected around MJD 57410.

B. Time stability of various OP-IT links

The frequency stability of UTC(IT) and UTC(OP) for the links considered in Fig. 2 and Fig. 3 is evaluated by means of the Allan deviations (Fig. 4), properly taking into account outliers and missing data [5].

We note that:

- The link IT02-OP01 involving the nominal earth stations at INRiM and OP, exhibit more noise during even hours (red line) than during odd hours (black line);
- IT01 shows a better stability (green line) than IT02 nominal station (black line)
- The effect of diurnals is slightly more evident on OP02 (resulting in bumps on the ADEV, blue line) than in OP01 (black line).

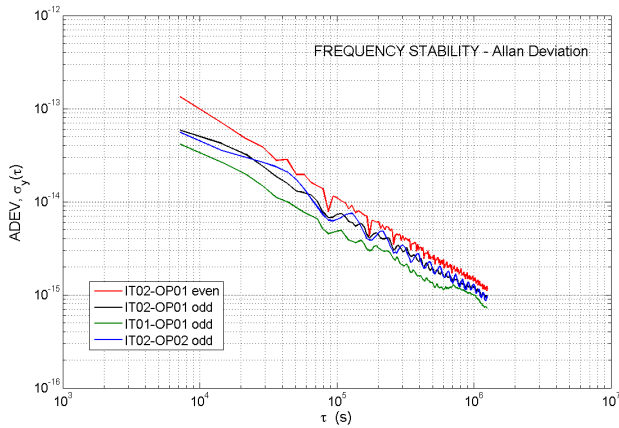


Fig. 4. Frequency stability of the time difference between UTC(OP) and UTC(IT) reported in Fig. 2 and Fig. 3.

C. The uncertainty budget

Due to the nature of the method used to characterize the additional OP-IT links with respect to the reference calibrated link, contributions to the uncertainty budget can be estimated as follows:

- Uncertainty related to the reference calibrated link OP01-IT02 : $U_{link} = 0.8$ ns [2];
- Uncertainty related to local delays measurement in LNE-SYRTE : $U_{tic_op} = 0.2$ ns;
- Uncertainty related to local delays measurements in INRiM : $U_{tic_it} = 0.2$ ns;
- Statistical uncertainty with respect to Time stability of the OP-IT links : $\sigma_{CALR} = 0.4$ ns;

From the above values, one can calculate the combined uncertainty [6] associated to CALR values as:

$$\sqrt{U_{link}^2 + U_{tic_op}^2 + U_{tic_it}^2 + \sigma_{CALR}^2} = 1.0 \text{ ns}$$

D. Possible interferences between PRN codes at 1 Mchip/s

From Fig. 2, we observe a clear offset in the time transfer of the reference link OP01-IT02 between the data recorded during the even UTC hours when most of European stations are transmitting during the regular schedule adopted by the CCTF working group on TWSTFT and data recorded during the odd UTC hours when the same transponder is almost quiet. The difference between the even and odd UTC hours links is given in Fig. 4. By averaging the plotted data, a bias of 364 ps is obtained. This bias found may be caused partly by interferences between pseudo-random noise codes at 1 Mchip/s.

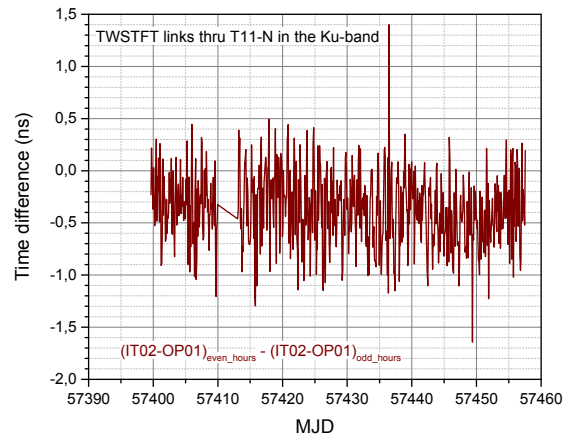


Fig. 5. Time difference between odd and even hours on the link OP-IT. A bias of 364 ps is shown, potentially caused by interferences between codes.

E. Influence of environmental conditions

The influence of environmental conditions should be considered when dealing with accuracy of transfer techniques. The uncertainty of TWSTFT is currently at nanosecond level and a few ns is the one of GPS time transfer methods.

Immediately after this experience for the characterization of stations, a moderate snowfall occurred at INRIM, on 16 March (MJD 57463). The effect on both INRIM GPS receiver and TWSTFT station is reported in Fig. 6, both GPS and TWSTFT measures show a variation of about 5 ns lasting a few hours.

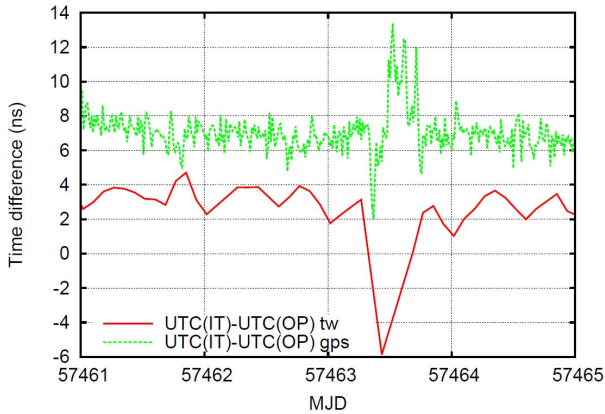


Fig. 6. Time difference between UTC(OP) and UTC(IT) via GPS and TWSTFT.

V. CONCLUSION

We describe an accurate characterization of the earth stations operated in LNE-SYRTE and INRiM for two-way satellite links by determining the differential delays of these links with a combined uncertainty at the nanosecond level. We highlight a time instability (1~2 ns) of the IT02 earth station around MJD 57410 and a bias of about 370 ps on the calibrated two-way link OP01-IT02 whose cause can potentially be due to interference between PRN codes.

ACKNOWLEDGMENT

The authors thank the CCTF Working Group on TWSTFT for its support.

REFERENCES

- [1] "The operational use of two-way satellite time and frequency transfer employing pseu-dorandom noise codes", Recommendation ITU-R TF.1153-4, 2015.
- [2] H. Margolis et al., "International timescales with optical clocks (ITOC)", Proc. of the 2013 Joint European Frequency and Time Forum & International Frequency Control Symposium (EFTF/IFCS), pp 908-911, 2013.
- [3] I. Sesia, G. Signorelli, G. Cerretto, E. Cantoni, P. Tavella, A. Cernigliaro, A. Samperi, "The First Months of the Galileo Timekeeping and Time Dissemination: Role of the Time Validation Facility", in Proceedings of ION-PTTI 2013, 2-5 December 2013, Bellevue, Washington, USA.
- [4] F. J. Galindo, H. Esteban, A. Bauch, D. Piester, I. Sesia, J. Achkar, K. Jaldehag, C. Rieck, R. Piriz, "European TWSTFT Calibration Campaign 2014 of UTC(k) laboratories in the Frame of Galileo FOC TGVF", PTTI 2016, Monterey, California, USA 2016.
- [5] I. Sesia, P. Tavella, "Estimating the Allan variance in the presence of long periods of missing data and outliers", Metrologia, Volume 45, Number 6, December 2008, pp. 134-142.
- [6] "Evaluation of measurement data – The role of measurement uncertainty in conformity assessment", JCGM 106:2012.

Remote Time and Frequency Transfer Experiment Based on BeiDou Common View

Hang Yi*† Hongbo Wang*† Shengkang Zhang*† Haifeng Wang*† Fan Shi*† Xueyun Wang*

*Beijing Institute of Radio Metrology and Measurement, Beijing China 100854

†Science and Technology on Metrology and Calibration Laboratory, Beijing China 100854

Abstract—Last year the zero-baseline common-view test using BeiDou Navigation Satellite system (BDS) is done in BIRMM and the result is better than 5 ns. In this year, we have developed our own GPS/BD common view time and frequency transfer receiver. Using this receiver we carried out two remote common view experiments in BIRM-SIMT link and BIRM-NTSC link, separately. Besides, we took out TWSTFT experiment together when we made the common view experiment to check out our common view result. The experiment and some results are shown in this paper which show that the common view precision using BD is at the same level of GPS but slightly lower than that of GPS.

Keywords—time transfer; BeiDou; common view experiment;

I. INTRODUCTION

BDS is the global navigation satellite system developed by China independently. At present, there are already 5 GEO, 5 IGSO and 4 MEO BD navigation satellites in orbit which can provide stable and continuous navigation services for the Asia-Pacific region. With the development of BDS, BDS can be another choice for remote precise time and frequency transfer.

In order to check the performance of BDS in time and frequency transfer field, we developed our own GPS/BD common view time and frequency transfer receiver (BM1308-52) and made some experiment based on BD common view. Last year, we made the zero-baseline common view test using BDS and the result is better than 5 ns. [1] In this paper, some remote time and frequency transfer experiment was carried out using BM1308-52. Besides, we took out TWSTFT experiment together when we made the common view experiment to check out our common view results. Since we have TTS-4 common view receiver, the performance of our receiver and TTS-4 is compared and the result of GPS common view and BD common view is compared.

This paper is organized as follows: the experiment is introduced in section II. Data collection and analysis is discussed in section III. The results and conclusion is given in section IV. Finally, in section V, it is about our future research.

II. TIME AND FREQUENCY TRANSFER EXPERIMENT

TWSTFT is one of the most accurate means for remote time and frequency transfer and it can be used to check out the common view results. As shown in Fig.1, The TWSTFT system and common view system use the same 10MHz and 1PPS signal. We collect the time comparison results of the two systems at the same time and the results will be identical if the time delay is corrected exactly.

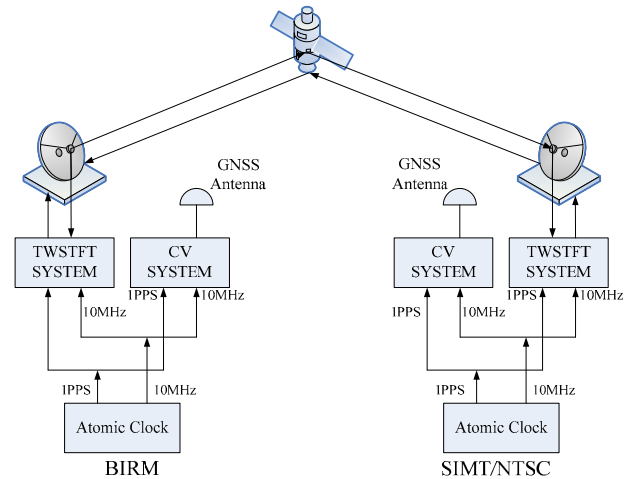


Fig. 1. Remote time and frequency transfer experiment

Our experiment is carried out both in BIRM-SIMT link and BIRM-NTSC link. BIRM, SIMT and NTSC are three time and frequency laboratories in China and they are keeping their own UTC (k). The distance from BIRM to SIMT is 1083km and the distance from BIRM to NTSC is 876km. The conditions of the 3 stations are shown in Table.1.

Table.1 Equipment for two stations

Station	Measurement system	Equipment
BIRM	CV System	BM1308-52 TTS-4
	TWSTFT System	SATRE Modem
SIMT	CV System	BM1308-52 TTS-5

	TWSTFT System	SATRE Modem
NTSC	CV System	BM1308-52
	TWSTFT System	SATRE Modem

According to Table.1, our experiment is arranged as follows: first of all, we carry out the GPS common view experiment through BIRM-SIMT link to compare the performance of BM1308-52 receiver and TTS-4/TTS-5 receiver. Secondly, the performance of GPS common view and BD common view is compared through the results of BM1308-52 receiver. Finally, all the common view results are compared with the TWSTFT result. Then, we do the experiment again through the BIRM-NTSC link to compare the performance of GPS common view and BD common view.

III. DATA COLLECTION AND ANALYSIS

In our experiment, we collect the CGGTTS file from BM-1308-52 and TTS-4/TTS-5, then, we can calculate the clock error between the two remote stations according to the common view schedule. In another hand, we can get the clock error through TWSTFT system second by second.

A. Common view Data of BIRM - SIMT

From Nov.11 2015 to Nov.19 2015, we carried out our experiment in BIRM-SIMT link. Since we have TTS-4 common view receiver in BIRM and TTS-5 common view receiver in SIMT except BM1308-52, the experiment is arranged as in Table.2.

Table.2 Four experiment in BIRM-SIMT link

Station	1		2	3	4
	GPSCV	BDCV	GPSCV	GPSCV	GPSCV
BIRM	BM1308-52		TTS-4	BM1308-52	TTS-4
SIMT	BM1308-52		TTS-5	TTS-5	BM1308-52

The common view results are shown in Fig.2~Fig.6. In our experiment, the coordinate we set to the BM1308-52 has an error about several meters. Owing to this mistake, the peak-to-peak jitter of the clock error shown in Fig.2, Fig. 3 and Fig.5 is very large. Except for this, compare Fig.2 and Fig.3, we can see that the trend of the clock error between BIRM and SIMT is the same; no matter we use GPS common view or BD common view. Also, compare Fig.3 and Fig.5, Fig.4 and Fig.6; we can see that the performance of BM1308-52 is similar with that of TTS-4/TTS-5.

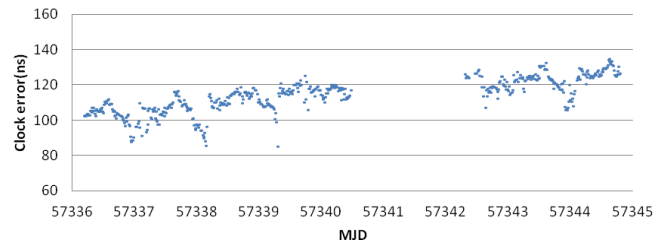


Fig. 2. Result based on BD common view
BIRM(BM1308-52)-SIMT(BM1308-52)

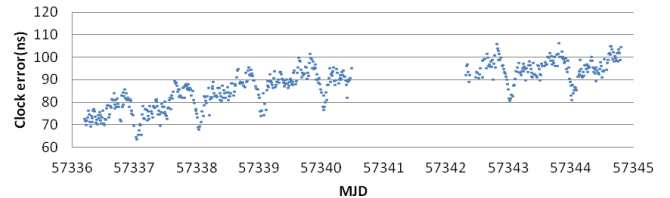


Fig. 3. Result based on GPS common view
BIRM(BM1308-52)-SIMT(BM1308-52)

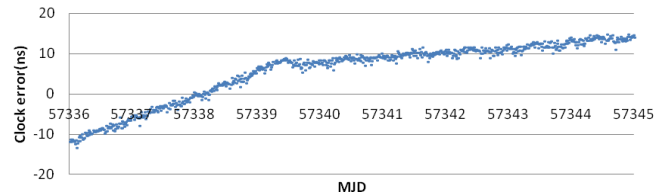


Fig. 4. Result based on GPS common view
BIRM(TTS4)-SIMT(TTS5)

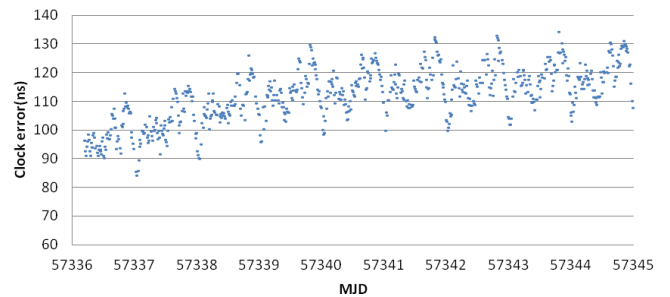


Fig. 5. Result based on GPS common view
BIRM(TTS4)-SIMT(BM1308-52)

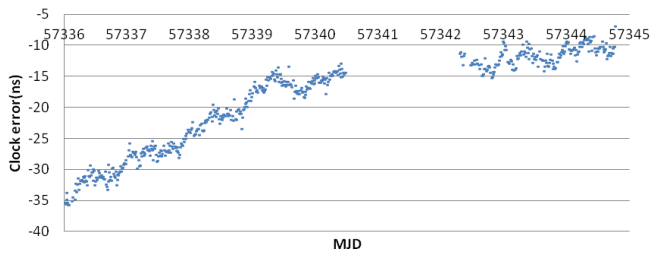


Fig. 6. Result based on GPS common view
BIRM(BM1308-52)-SIMT(TTS5)

B. TWSTFT Data of BIRM - SIMT

Fig. 7 shows the result of TWSTFT system. According to Fig.2~Fig.6, we can see that the trend of the clock error of BIRM and SIMT is the same no matter we use TWSTFT or common view method.

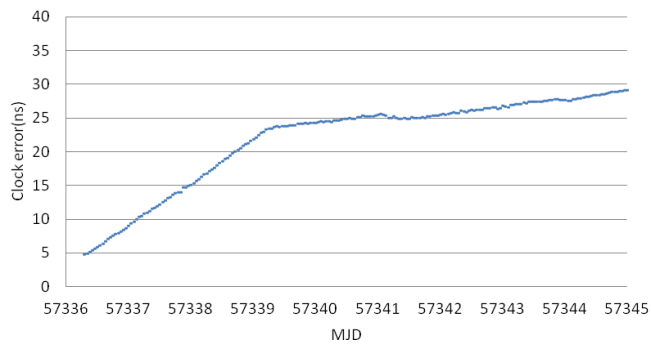


Fig. 7. Result based on TWSTFT(BIRM-SIMT)

C. Common view Data of BIRM - NTSC

From Dec.15 2015 to Dec.28 2015, we carried out our experiment in BIRM-NTSC link. Since we have proved that BM1308-52 has the same performance with TTS-4 and we have only BM1308-52 in NTSC, we use BM1308-52 to carry out the common view experiment. The performance of GPS common view and BD common view is compared in this experiment. From Fig.8 ~ Fig.9, we can see that the peak-to-peak jitter of BD common view result is about 20ns which is a litter larger than that of GPS common view.

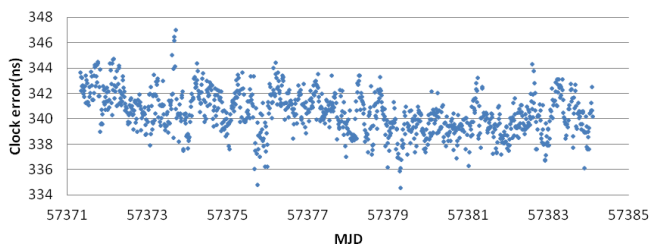


Fig. 8. Result based on GPS common view
BIRM(BM1308-52)-NTSC(BM1308-52)

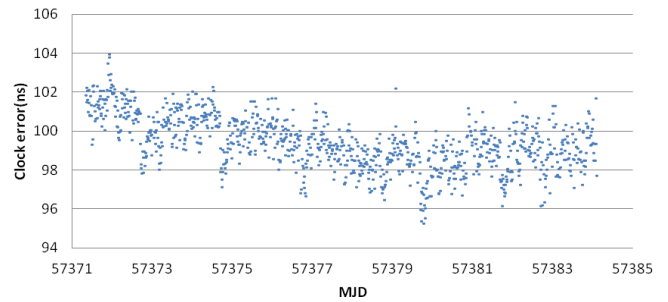


Fig. 9. Result based on GPS common view
BIRM(BM1308-52)-NTSC(BM1308-52)

D. TWSTFT Data of BIRM - NTSC

Since the TWSTFT was used for another program after MJD=57374, we carry out TWSTFT experiment in BIRM-NTSC link only from Dec.15 2015 to Dec.18 2015. The result is shown in Fig.10. According to Fig.8~Fig10, we can see that the trend of the clock error of BIRM and NTSC is the same no matter we use TWSTFT or common view method.

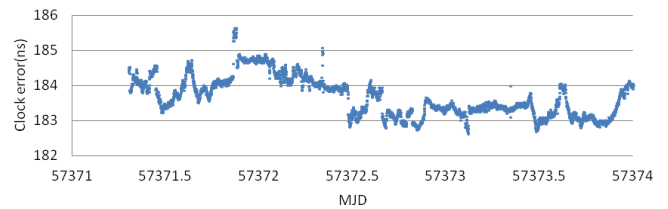


Fig. 10. Result based on TWSTFT(BIRM-NTSC)

IV. CONCLUSIONS

According to section III, we can see that remote time and frequency based on BD common view is verified. BD common view can be used in the time and frequency transfer field in the Asia-Pacific region now and all over the world in the future. The performance of GPS common view by BM1308-52 is similar with TTS-4 and the performance of BD common view by BM1308-52 is also considerable.

V. FURTHER RESEARCH

In this paper the calibration of the common view receiver is not taken into account, and we are going to do some research in the receiver calibration. [4]

ACKNOWLEDGMENT

The authors thank Yuan Haibo and Zhang Jihai of Nation Time Service Center, Dong Lian of Shanghai Institute of Measurement and Testing Technology and Zhou Mingxiang of Shanghai Astronomical Observatory for their help in our experiment.

REFERENCES

- [1] Hang Yi, Hongbo Wang, Shengkang Zhang, Haifeng Wang, Fan Shi, Research on Time and Frequency Transfer based on BeiDou Common View, 2015 IEEE IFCS/EFTF Joint Conference, 2015.
- [2] Tao He, Nan Jiang, Qing Gu, Shaohua Sun, Huijun Zhang, GPS Multi-channel Common-view Based Experimental Research of Time and Frquency traceability and Measurement, 2014 Seventh International Symposium on Computational Intelligence and Design, 2014.
- [3] Yao Kong, Xuhai Yang, Hong Chang, Weijin Qin, Fen Cao, Zhigang Li, Baoqi Sun, Method of Precise Common-View frequency transfer based on BeiDou GEO satellite, Frequency Control Symposium (FCS), 2014 IEEE International.
- [4] Liu Yinhua, LiXiaohui, Ruan Jun, Zhang Huijun, Yang Lin, The Analysis of Differential Code Bias of BeiDou Satellite Navigation System, Frequency Control Symposium (FCS), 2014 IEEE International.

Mapping acoustic field distributions of VHF to SHF SAW transducers using a Scanning Electron Microscope

A. Godet, J.M. Friedt, S. Dembélé, N. Piat, A. Khelif, P. Vairac, J. Agnus, P.Y. Bourgeois, G. Goavec-Mérou
FEMTO-ST Institute UMR 6174, Université de Franche-Comté, CNRS, ENSMM, UTBM
26 rue de l'Épitaphe, 25000 Besançon, France

Abstract—Mapping the energy distribution of Surface Acoustic Wave (SAW) devices operating in the Very High Frequency (VHF) and Super-High Frequency (SHF) range provides a quantitative indicator of energy confinement, a core parameter when addressing low loss filters or high quality factor resonators. We here demonstrate the use of Scanning Electron Microscopy (SEM) for mapping Rayleigh wave acoustic field and shear transverse wave (STW) propagating on quartz. Furthermore, the availability of Focused Ion Beam (FIB) for milling the piezoelectric substrate allows for creating obstacles on the acoustic path and hence tune the acoustic wave propagation direction by reflecting the waves along directions which might otherwise exhibit poor electromechanical coupling.

I. CONTEXT AND MOTIVATION

Acoustic field distribution in surface acoustic wave (SAW) devices relates to acoustic energy confinement and hence acoustic losses (in filters and delay lines) or quality factor (in resonators). Classical mapping techniques are based on optical interferometry [1], [2], [3], in which crystalline lattice motion associated with SAW propagation is detected in an interferometer setup with the SAW surface acting as one of the arm end. Despite the ability to *quantitatively* measure the out-of-plane vibration amplitude, optical interferometric methods are unable to measure in-plane vibration components. One competing approach is the observation of the electric field associated with SAW propagation in piezoelectric substrates [4], [5], [6], [7]: in scanning electron microscopy (SEM) observations, electrons illuminate the surface under investigation and secondary electrons generated closest to the surface are collected to create an image representative of surface characteristics. Electric fields on the surface under investigation modulate the secondary electron path and hence the image observed: SAW propagating is observed using SEM.

In this presentation, we use a SEM for the observation of Rayleigh SAW on lithium niobate and shear transverse waves (STW) propagating on quartz. In all cases, we focus on delay line geometries: despite not exhibiting a standing wave pattern as observed on resonators, the propagating wave is readily observed in both configurations. The reason for selecting these two experimental setups as appropriate to emphasize some advantages of the SEM approach over the optical characterization methods are in the former case the wavelength of the device – operating at 2.45 GHz with an acoustic velocity of 3992 m/s [8] – exhibits a wavelength

of 1.6 μm or only 2 to 5 optical wavelengths, and in the latter case the shear polarization of the wave which does not exhibit out-of-plane displacement component. In all cases, we have also observed that SEM imaging speed – a few seconds at most – is greatly improved over the raster scanning technique of the optical interferometer which always last a few minutes to hours : a 1024×768 pixel SEM image requires an acquisition time of 122 ms, allowing much faster sampling rates than scanning probe techniques lasting at best 20 minutes for 2500×400 pixels for the fastest instruments [9].

II. HISTORICAL BACKGROUND

SEM characterization has periodically reappeared in the history of acoustic device characterization. The oldest record we have identified of dynamic oscillator characterization using SEM dates back to 1969 [10], while the observation of the electric field associated with acoustic wave propagation in piezoelectric media dates back to 1971 [11] for bulk acoustic resonators and 1978 for SAW [12]. Interest has grown in this field until 1980, with afterwards a ten year gap until renewed interest sparked a series of publications in the 1990s. Finally, the SEM has become a standard tool for characterizing even exotic substrates such as langasite [13], yet most investigations focus on standing wave patterns. Despite the bandwidth limitation of the scintillator used to convert the electrons to an optical signal, dynamic phenomena monitoring require some bandwidth increase so that the instrument reaches a larger bandwidth than the time constant of the physical phenomena under investigation. The classical approach to this dilemma is stroboscopy, in which the slow detector is only illuminated while the physical phenomenon is in a known, repeatable state, by a short incoming signal. In the case of SEM, the illuminating electron beam is chopped in order to illuminate the SAW device only when the wave packet is in a known position, yielding such famous images as those found in [14].

One explanation provided for the ability to visualize propagating SAW using SEM, despite the lack of reflectors to create the standing wave pattern found in resonators, is an interference mechanism between the electromagnetic field radiated by the interdigitated transducers – propagating at the speed of light and virtually instantaneously with respect to the acoustic wave speed – and the electric field associated with the acoustic wave propagation on the piezoelectric media. Because

these two fields are synchronous, the interference pattern is stationary as seen by the slow SEM detector.

III. EXPERIMENTAL MEASUREMENTS

All experiments have been performed in a Carl Zeiss Auriga 60 SEM fitted with a focused ion beam (FIB, Ga⁺ ions accelerated at 30 kV) capability. The electron acceleration voltage was reduced to 1 kV to reduce charge accumulation on the piezoelectric insulating surface since at the low magnification we will consider throughout this investigation, higher acceleration voltage would induce excessive static buildup with little improvement in resolution. Working distance was set to about 5.1 mm for the sample to be close to the convergence point of the FIB and SEM column axis. The signal of a secondary electron (SE) detector inside the electron column (in-lens) was used. A Rohde & Schwarz SMC 100A synthesizer was used to drive the SAW devices.

A. Imaging 2450 MHz Rayleigh wave on lithium niobate

2450 MHz acoustic delay lines were imaged using an SEM. In all cases, the radiofrequency power is +15 dBm and the device is continuously powered. In all images, the reference image of the bare surface is shown on the right side of the picture, and the powered device with the acoustic wave propagating on the substrate is shown on the left. Fig. 2 exhibits a zoom on the acoustic path visible in the broad view of Fig. 1, with the interdigitated transducer on the top and the first mirror on the bottom.

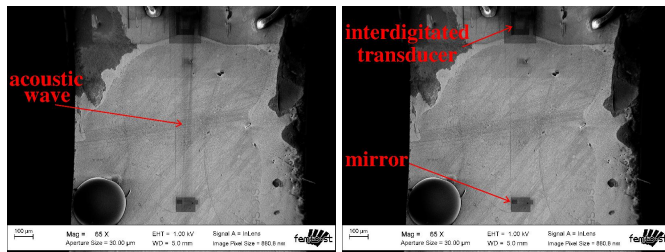


Fig. 1. General view of the acoustic delay line, with the interdigitated transducer on top and the first mirror on the bottom.

The collimation of the acoustic beam is well defined and the divergence is low enough for the acoustic field to be confined to the area over which the mirrors are located, even after a propagation path long enough to allow for a 500 ns delay.

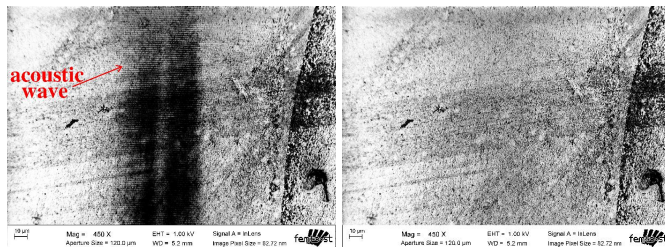


Fig. 2. Zoom on the acoustic path.

B. Obstacles to 2450 MHz Rayleigh waves

In addition to observing the freely propagating Rayleigh SAW, obstacles were patterned using the FIB to either generate point-like source, or bounce the wave off-axis. Adding obstacles was on the one hand attempted to assess whether the milling depth is sufficient to affect a Rayleigh SAW wave, and create structures hardly accessible by patterning interdigitated transducers such as a point-like source (Fig. 3), propagation in any direction independently of the electromechanical coupling coefficient (Fig. 4) or even a half-coral (Figs. 5-7).

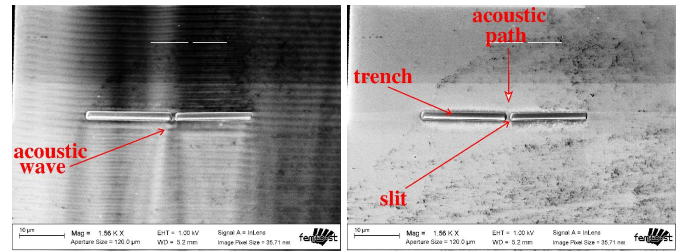


Fig. 3. A point-like source is created by patterning two trenches separated by a slit through which the acoustic field coming from the top scatters.

In the former example, the point like source is created by introducing a slit between two obstacles with a width of the order of the wavelength. The scattered wave is well visible beyond the slit, on the bottom of Fig. 3.

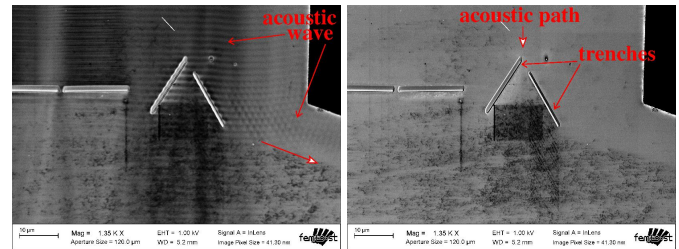


Fig. 4. Oblique trenches are patterned on the acoustic path: the trench deflecting the acoustic field towards the right exhibit strong efficiency and the deflected beam is well visible, while the trench supposed to deflect the beam towards the left has hardly any effect on the incoming wave.

An oblique obstacle is patterned on the acoustic path to reflect the wave in a direction in which no mirror is located and demonstrate that indeed the SEM is able to image a propagating wave. Here no cause of standing wave pattern could be due to obstacles located on the path after reflection. The reflected wave is well visible towards the right of Fig. 4, but not on the left.

Finally, the half coral geometry was introduced to try and create some interference pattern from confined acoustic waves. The interference between the incoming and reflected wave is well visible on Fig. 5, while the broader view from Fig. 6 emphasizes some acoustic field leakage below the wall and through the slits between adjacent walls, and the lowest magnification of Fig. 7 shows some of the diverging beams created by the off-axis reflection in the coral walls and propagation through the interdigitated transducer.

Hence, the combination of SEM and FIB seems ideal for real time observations of obstacles created along the acoustic

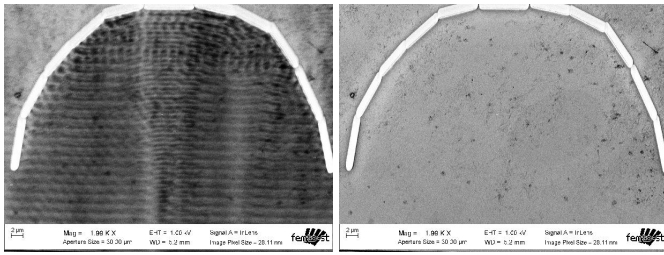


Fig. 5. Zoom on the half coral demonstrating the interference pattern between the incoming wave propagating from bottom to top and most significantly the wave reflected on the left oblique walls propagating towards the right of the image.

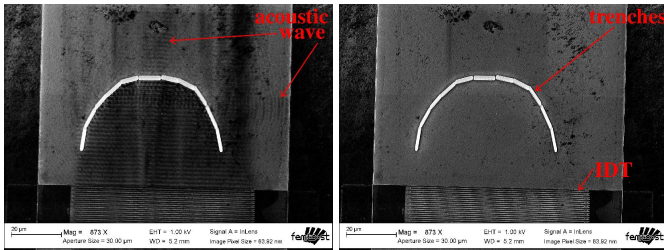


Fig. 6. The half coral lets some of the acoustic field escape under the trenches and through the slits connecting the trenches (top part of the left image), or some of the reflected energy leaks towards the right after propagating under the right-most trenches.

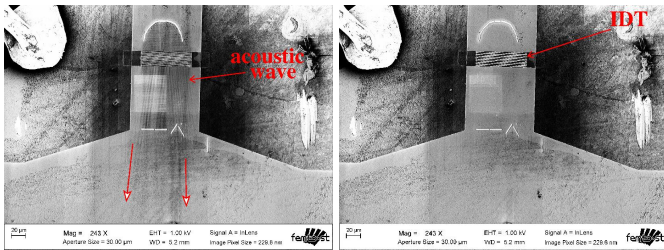


Fig. 7. Broad view of the SAW device with the half coral on the top region above the interdigitated transducers exhibiting the diverging acoustic beams on the acoustic path towards the mirrors on the bottom of the images.

path, and defining new propagation modes reminiscent to the principles used in phononic crystals. The high operating frequency is a mandatory condition for the shallow structures milled by the FIB to significantly affect the SAW propagation, as will be seen in the next section.

C. 125 MHz STW wave on quartz

Observing Rayleigh wave propagation with a SEM on a strongly coupled substrate such as $YXl/128^\circ$ lithium niobate is well known and our contribution so far has been the addition of obstacles during the observation cycle. We are now interested in observing shear waves as the STW propagated on ST cut quartz, a measurement which is not possible using optical means due to the lack of out-of-plane vibration component.

The following pictures (Fig. 8) are taken as the delay line is powered by a continuous wave of +18 dBm. The shear wave propagating beyond the electrodes in the area free of any structure on the left-side of the pictures is well visible. Here again, some obstacles were patterned on the acoustic path, with no effect this time. However, considering the shallow obstacles (the trench depth was measured using a mechanical profiler to

be above 800 nm) with respect to the wavelength, such a lack of reflection is hardly surprising.

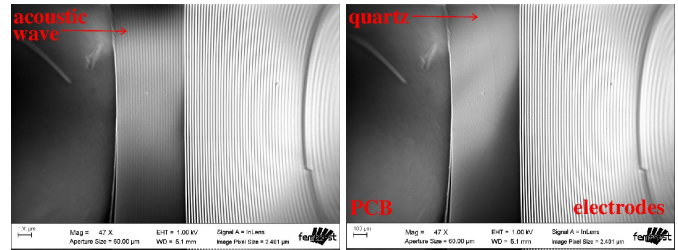


Fig. 8. STW wave propagating on quartz. The electrode pattern on the right of the image connects the ground bus (towards the bottom of the image) to the top electrodes of the interdigitated transducers generating the wave (out of the field of these images). The area on the left of the electrode pattern is bare quartz free of metallic structures. The left-most part of the image is the printed circuit board on which the piezoelectric substrate is glued.

IV. DISCUSSION

The observation of VHF to SHF SAW associated electric field should require a measurement bandwidth of at least twice the operating frequency. Measuring the transfer function of the secondary electron detector (Fig. 9) demonstrates a bandwidth of a few megahertz at most, suitable for micro-electromechanical system characterization but well below the SAW operating frequency. Thus, the observation of a pattern representative of SAW propagation is either associated with a standing wave pattern (as found in resonator architectures), or in an interference between the radiated excitation signal and the electric field associated with SAW propagation on piezoelectric media [5].

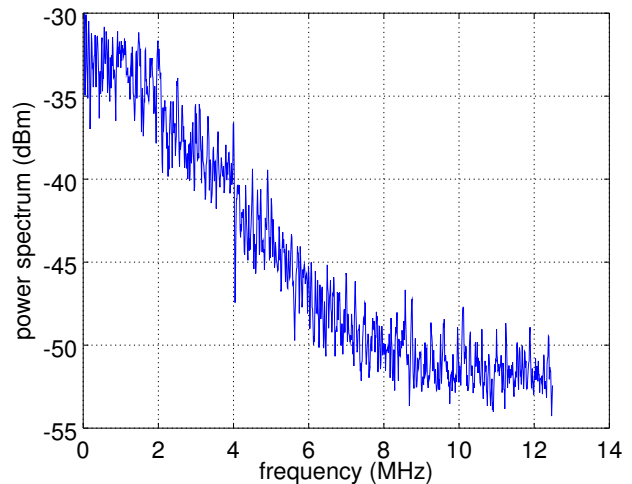


Fig. 9. SE2 secondary electron detector transfer function as observed from the noise power density spectrum.

The failure to observe a Love SAW confined in a 2 μm silicon dioxide layer atop a quartz substrate hints at a strong interaction of the SEM electrons with the electric field at the surface of the piezoelectric material. Indeed, despite the electric field extending about a wavelength in air at the interdigitated electrode level [8, p.18], a thin (5% of the acoustic wavelength) insulating layer prevents the secondary electrons from being affected by the electric field associated with acoustic wave propagation.

Optical mapping of the STW device shown in Fig. 8 with the setup described in [15] indicates a 10 pm vibration amplitude over the interdigitated transducers and negligible amplitude (below measurement resolution) in the bare quartz area, hence emphasizing the added value of SEM acoustic field mapping.

Finally, the operating frequency of the SAW device used for basic acoustic research in the context of interactions with the FIB-generated structure is dictated by the penetration depth of the wave in the substrate with respect to the ability of the trenches to significantly affect the acoustic wave velocity. The penetration depth of a Rayleigh wave in the piezoelectric substrate is of the order of the acoustic wavelength [16], while FIB-milled rectangles $72 \times 16 \mu\text{m}^2$ at a current of 2 nA in ST-cut quartz indicate depths of 18 ± 1 nm, 52 ± 1 nm and 128 ± 2 nm for milling durations of 1.5, 3 and 6 minutes respectively. The resulting milling rate of $0.14 \pm 0.03 \mu\text{m}^3/\text{nC}$ is consistent with the values reported for lithium niobate in [17], [18]. Thus, trenches a few micrometers deep at most can be milled this way, and operating at high frequencies enhances the interactions of the wave with the structures. In our case, even after milling a trench for over 30 minutes at a current of 2 nA, no reflected wave was observed in the case of the 126 MHz STW-wave propagating on quartz, while the effect was significant on the 2450 MHz Rayleigh wave propagating on lithium niobate after milling durations of 60 seconds at a current of 200 pA, or 30 seconds for the half-coral shaped trenches.

V. CONCLUSION

We have repeated well known surface acoustic wave associated electric field mapping using scanning electron microscope, and extended the technique on the one hand to the observation of the influence of focused-ion beam induced structures on the acoustic path, and on the other hand to shear transverse wave propagation in quartz. While lacking the quantitative vibration amplitude characteristics of optical interferometric methods, the scanning electron microscope offers the ability of fast characterization and interaction with the acoustic field when a focused ion beam is available. Our experiments only use the low-bandwidth in-lens secondary electron detector for imaging standing wave patterns, whether resulting from reflections of the acoustic wave on Bragg mirrors or trenches patterned on the acoustic path, or resulting from the interference of the radiated electromagnetic field with the propagating acoustic wave. Further developments will focus on adding a stroboscopic imaging capability for time resolved acoustic wave packet imaging [19], [20], in which the slow detector is only illuminated by the incoming electron beam when the physical setup is in a known state defined by the excitation electric signal powering the interdigitated transducer powering the surface acoustic wave device.

ACKNOWLEDGEMENT

We acknowledge fruitful discussions with L. Reindl (IMTEK, Freiburg, Germany) who provided references on the historical background of SEM characterization of SAW devices. D. Teyssieux (FEMTO-ST, Besançon, France) proofread

the manuscript and performed the optical analysis on the STW-device. Funding for this project is provided by the (ANR-11-LABX-01-01) ACTION Labex grant and supported by the (ANR-10-EQPX-44-01) ROBOTEX equipex as well as a 2015 ENSMM BQR grant.

REFERENCES

- [1] J. V. Knuutila, P. T. Tikka, and M. M. Salomaa, "Scanning michelson interferometer for imaging surface acoustic wave fields," *Optics Letters*, vol. 25, no. 9, pp. 613–615, May 2000.
- [2] K. Kokkone and M. Kaivola, "Scanning heterodyne laser interferometer for phase-sensitive absolute-amplitude measurements of surface vibrations," *Applied Physics Letters*, vol. 92, no. 6, p. 063502, 2008.
- [3] H. Martinussen, A. Aksnes, and H. Engan, "Wide frequency range measurements of absolute phase and amplitude of vibrations in micro- and nanostructures by optical interferometry," *Optics express*, vol. 15, no. 18, pp. 11 370–11 384, 2007.
- [4] G. Eberharter and H. Feuerbaum, "Scanning electron microscope observations of propagating acoustic waves in surface acoustic wave devices," *Applied Physics Letters*, vol. 37, p. 698, 1980.
- [5] D. V. Roshchupkin, T. Fournier, M. Brunel, O. A. Plotitsyna, and N. G. Sorokin, "Scanning electron microscopy observation of excitation of the surface acoustic waves by the regular domain structures in the LiNbO₃ crystals," *Applied Physics Letters*, vol. 60, p. 2330, 1992.
- [6] D. Roshchupkin and M. Brunel, "Scanning electron microscopy observation of surface acoustic wave propagation in the LiNbO₃ crystals with regular domain structures," *IEEE Trans. Ultrasonics, Ferroelectrics & Freq. Control*, vol. 41, no. 4, pp. 512–517, 1994.
- [7] D. Roshchupkin, M. Brunel, and L. Tucoulou, "Visualization of surface acoustic waves by scanning electron microscopy," *Journal de Physique IV*, vol. 04, no. C5, pp. C5–1229–C5–1232, 1994.
- [8] C. Campbell, *Surface Acoustic Wave Devices and their signal processing applications*. San Diego, CA, USA: Academic Press, 1989.
- [9] K. Hashimoto, K. Kashiwa, N. Wu, T. Omori, M. Yamaguchi, O. Takano, S. Meguro, and K. Akahane, "A laser probe based on a Sagnac interferometer with fast mechanical scan for RF surface and bulk acoustic wave devices," *IEEE Trans Ultrason Ferroelectr Freq Control*, vol. 58, no. 1, pp. 187–194, Jan 2011.
- [10] N. C. MacDonald, G. Y. Robinson, and R. M. White, "Time resolved scanning electron microscopy and its application to bulk effect oscillators," *Journal of Applied Physics*, vol. 40, p. 4516, 1969.
- [11] R. J. Gerdes and C. E. Wagner, "Scanning electron microscopy of resonating quartz crystals," *Applied Physics Letters*, vol. 18, no. 39, pp. 39–41, 1971.
- [12] P. Hiesinger, "Scanning electron microscopy of resonating surface acoustic wave devices," in *IEEE Proc. Ultrasonics Symposium*, 1978, p. 611.
- [13] S. Sakharov, O. Buzanov, and D. Roshchupkin, "Investigation of saw and psaw propagation in lgs crystal by scanning electron microscopy method," in *Proc. IEEE International Frequency Control Symposium and PDA Exhibition*, 2003, pp. 698–700.
- [14] E. Mackensen and L. Reindl, "Wireless passive saw identification marks and sensors," in *Proceedings of the NATO Advanced Study Institute on Smart Sensors and MEMS*. Povo de Varzim, Portugal: Springer, September 2003, pp. 155–202.
- [15] D. Teyssieux, T. Baron, J.-M. Friedt, G. Martin, and P. Vairac, "Absolute phase and amplitude mapping of surface acoustic wave fields," in *Proc. IEEE IFCS*, Prague, Czech Rep., 2013.
- [16] E. Ash and E. Paige, Eds., *Rayleigh-Wave Theory and Application*, 1st ed., ser. Springer Series on Wave Phenomena 2. Berlin Heidelberg: Springer-Verlag, July 1985.
- [17] F. Lacour, N. Courjal, M.-P. Bernal, A. Sabac, C. Bainier, and M. Spajer, "Nanostructuring lithium niobate substrates by focused ion beam milling," *Optical materials*, vol. 27, no. 8, pp. 1421–1425, 2005.
- [18] F. Sulser, G. Poberaj, M. Koechlin, and P. Günter, "Photonic crystal structures in ion-sliced lithium niobate thin films," *Optics express*, vol. 17, no. 22, pp. 20 291–20 300, 2009.
- [19] A. Gopinath and M. Hill, "Deflection beam-chopping in the sem," *J. Phys. E: Sci. Instrum.*, vol. 10, p. 229, 1977.
- [20] H. P. Feuerbaum and J. Otto, "Beam chopper for subnanosecond pulses in scanning electron microscopy," *J. Phys. E: Sci. Instrum.*, vol. 11, p. 529, 1978.

Main Features of Space Rubidium Atomic Frequency Standard for BeiDou Satellites

Ganghua Mei, Da Zhong, Shaofeng An, Feng Zhao, Feng Qi, Fang Wang, Gang Ming, Wenbin Li, Pengfei Wang

Key Laboratory of Atomic Frequency Standards,

State Key Laboratory of Magnetic Resonances and Atomic and Molecular Physics,

Wuhan Institute of Physics and Mathematics, Chinese Academy of Sciences, Wuhan 430071, Hubei, China

E-mail: mei@wipm.ac.cn

Abstract—Wuhan Institute of Physics and Mathematics (WIPM) has been developing the space rubidium atomic frequency standard (RAFS) for BeiDou navigation satellite system since the late of 1990's. Design of the RAFS aims to realize high stability, small size, long lifetime, high reliability and space environmental adaptability. The physics package was designed in SFT scheme. A slotted tube cavity with small size and TE_{011} resonant mode was used to construct the cavity-cell assembly, and an argon lamp with long lifetime was used as the pumping source. The microwave chain includes a 10MHz VCXO, a 5.3125MHz synthesizer, a $\times 9$ RF multiplier and a $\times 76$ SRD multiplier. Electronic circuits were designed by using analog circuitry to minimize the risk of element failure in space. The day stability of the space RAFS's developed for BeiDou regional system distributes within $2\text{--}5 \times 10^{-14}$. To meet the needs of BeiDou global system, design of the RAFS has been improved further. A slotted tube cavity with larger size and better resonant mode was used, the argon lamp was substituted with a filtered xenon lamp, and the phase noise of microwave chain was depressed further. A prototype of new generation space RAFS was built recently. Preliminary test showed that the day stability of the prototype has reached 3×10^{-15} .

Keywords—space rubidium atomic frequency standard; BeiDou navigation satellite system; physics package; electronics; performance

I. INTRODUCTION

Rubidium atomic frequency standard is the most widely used space clock for satellite navigation systems. To meet the needs of BeiDou navigation satellite System, Wuhan Institute of Physics and Mathematics (WIPM), Chinese Academy of Sciences has been engaging in research and manufacture of space RAFS since the late 1990's. Earlier work focused on realization of performance and adaptability for space environment. A test model was built in 2005, and the product was space qualified in 2006. During the period from 2007 to 2011, totally 10 space RAFS products developed by WIPM were equipped in the satellites of BeiDou regional system, which has provided service since 2012. To meet the needs of the BeiDou global system, further improvement of the RAFS has been performed at WIPM. A prototype of new generation space RAFS was built recently, and preliminary test showed that the performance of the RAFS has been significantly improved.

In this paper we outline design features of the space RAFS designed by WIPM, including the RAFS developed for BeiDou regional system and the RAFS newly designed for BeiDou global system. Application in satellite navigation requires the space RAFS to be of high stability, small size, long lifetime, high reliability and space environmental adaptability. In the paper we will discuss main aspects of the design to meet these requirements.

II. PHYSICS PACKAGE

The performance of a RAFS depends strongly on the structure of physics package used. To realize high stability, the physics package was designed in the separated filtering technique (SFT) scheme. Compared with mostly used integrated filtering technique (IFT), the SFT scheme is of high optical pumping efficiency and advantage in reducing light shift and temperature coefficient of the RAFS. The structure of the physics package is shown Fig. 1.

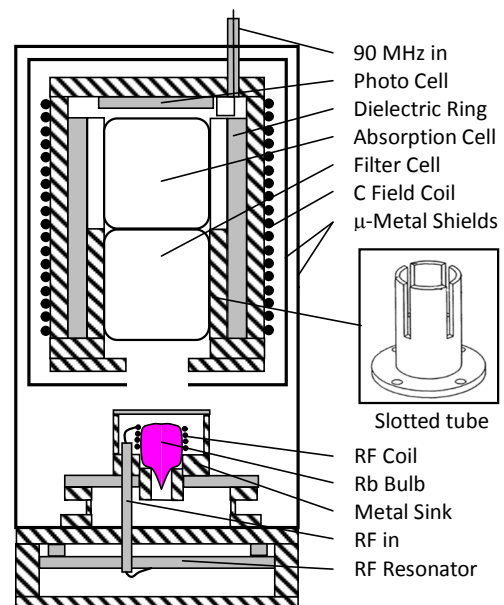


Fig. 1. Structure of the physics package.

As shown in Fig. 1, the physics package consists mainly of a cavity-cell assembly and a rubidium spectral lamp. The most prominent feature of the physics package is use of a new type of slotted tube cavity [1, 2]. As core of the cavity, the slotted tube is a tubular structure with several equally spaced slots on

top (see Fig.1). Simulation showed that a standing microwave field with resonant frequency at rubidium clock transition inside the slotted tube cavity can be stimulated by choosing adequate slot parameters, such as width and length. The microwave mode is similar to TE₀₁₁. As shown in Fig.2, inside the slotted tube, magnetic lines are distributed only in upper region (the region surrounded by slots), and highly parallel to axis; on the other hand no magnetic field exists in lower region. Therefore it's reasonable to put the absorption cell in the upper region and the filter cell in the lower region, constructing a compact structure for the cavity-cell assembly [3].

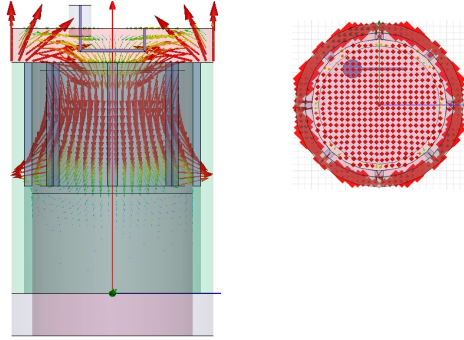


Fig.2. Magnetic lines in the slotted tube cavity

Mainly for use of the slotted tube, partly for use of the dielectric ring, the cavity is of small volume and rigid structure. Both the absorption cell and the filter cell have diameters of 14mm, and lengths of about 15mm, much smaller than cells used for the standard TE₁₁₁ cavity, which is of ~25mm in diameter normally.

As the optical pumping source, a rubidium spectral lamp filled with adequate amount of ⁸⁷Rb metal and argon buffer gas was used. The rubidium lamp seems to be the vulnerable spot of a space RAFS in reliability, lifetime and vacuum environment adaptability. In our design the lamp bulb with diameter of 8mm was amounted in a metal sink with silicon glue. This design has many advantages. Firstly, the accumulated heat in bulb can be conducted to environment to overcome overheat effect in vacuum condition; secondly, the use of soft glue avoids the bulb from breaking when environment temperature is sharply changing; finally, the tail tip will be the cold point of the bulb, the liquid rubidium metal in the bulb will stay there steadily, avoiding the influence of liquid rubidium migration on stability of light intensity.

The lifetime of a RAFS depends on rubidium consumption rate of the bulb. To obtain reliable design lifetime data of the space RAFS, the rubidium consumption of three lamps has been measured continually for seven years in our laboratory. The measured data and fitting curve are shown in Fig.4. The fitting curve validates $M(t)=85.85(1-e^{-0.000282t})+0.064t^{-1/2}$ [4]. Our model is close to Cook's [5], but seems to be more accurate. Main reason might be due to that our measurement took longer time and we improved the method to measure the rubidium amount in lamp [4]. According to the experimental result, a rubidium filling slightly larger than 110 μg can ensure a 20 years lifetime of the RAFS.

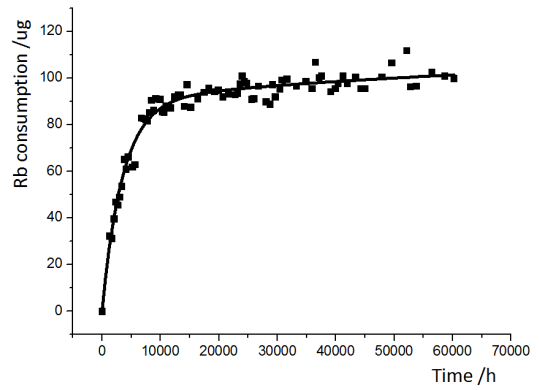


Fig. 3. Rubidium consumption of the spectral lamp as a function of operation time. Measured data (points) were obtained by averaging the results of three lamps, the solid line is the fitting curve

As shown in Fig.1, the physics package has two layers of magnetic shield, one encloses the cavity-cell assembly and the other encloses both the cavity-cell assembly and the rubidium lamp. To obtain better signal to noise ratio of physics package reduce the light shift and thermal sensitivity of the RAFS, operation parameters were optimized. The temperature of the cavity-cell assembly was set at 68°C, and the lamp temperature was set at ~135°C.

III. ELECTRONICS AND RAFS STRUCTURE DESIGNS

Fig. 4 shows schematically electronic structure of the space RAFS. The whole RAFS unit is composed of a frequency locking loop, supporting circuits and a temperature controlled plate.

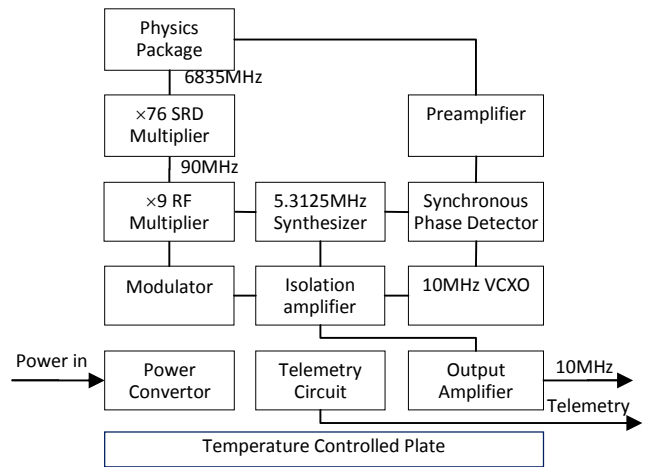


Fig. 4. Schematic structure of the space RAFS.

The locking loop includes the 10MHz VCXO, the isolation amplifier, the 5.3125MHz synthesizer, the modulator, the ×9 RF multiplier, the ×76 SRD multiplier, the physics package, the preamplifier and the synchronous phase detector. The 5.3125MHz synthesizer was designed at fixed frequency, therefore can't be used to adjust the frequency accuracy of the RAFS. To overcome this shortage we developed a technique to precisely control the resonate frequency of the absorption cell. In design of the SRD multiplier, the cavity in the physics

package was used for frequency selection. This scheme simplifies structure of electronics, but makes it difficult to know exactly the microwave power inside the cavity. While no evidence shows the design has significant influence on stability of the RAFS. The isolation amplifier converts 10MHz signal from the VCXO into three mutually isolated signals. The modulator provides a 136 Hz square wave for modulation of the interrogation signal of physics package.

The supporting circuits include the output amplifier, the voltage converter, and the telemetry circuit. The output amplifier amplifies the locked 10MHz signal to about 10dBm for satellite use. The power converter converts voltage signals from a secondary power supplier to values adequate for all individual electronic assemblies. The secondary power supplier is provided by satellite, not enclosed in RAFS. The telemetry signals include frequency locking indication and light intensity of the rubidium spectral lamp.

The temperature controlled plate, containing actually a metal plate, a μ -metal box and a temperature control circuit, was designed to reduce thermal sensitivity of the RAFS. All of the parts in the frequency locking loop are mounted on the thermally controlled plate operated at 35°C. The μ -metal box, mounted surrounding the frequency locking loop, was used to improve the thermal controlling precision, meanwhile provides the third layer of magnetic shield for physics package.

All the electronic circuits were designed with analog circuitry, no digital technique was used. The purpose is to minimize the risk of element failure in space.

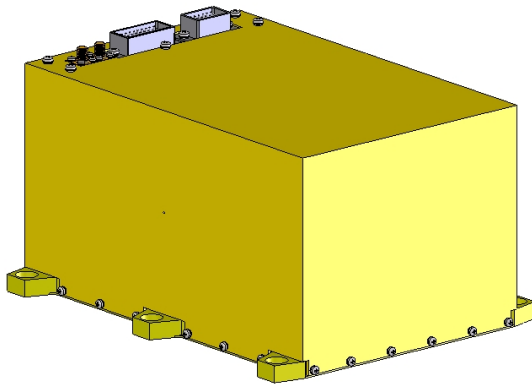


Fig. 5. Profile of the space RAFS

Fig.5 shows the profile of the RAFS for BeiDou regional system. Two SMA outlets are for 10MHz output and locking indication signals respectively, and the two low frequency outlets are for the power supplier and the telemetry/telecontrol signals respectively. The whole unit weights nearly 5kg and is of ~5 liters in volume. In satellite application, the RAFS is mounted in a temperature controlled plate.

IV. PERFORMANCE OF THE RAFS FOR BEIDOU REGIONAL SYSTEM

For a satellite navigation system in operation, the space clock is synchronized to the ground clock periodically. The

period is normally within ten thousands seconds to one day, therefore the frequency stability of the space clock with sampling time within 10^4 seconds to one day plays key role in determining system's precisions. The design timing and positioning precisions of BeiDou regional system are 30nm and 10m respectively, therefore the stability requirement for space RAFS is $1 \times 10^{-11} \tau^{-1/2}$ for short term and 3×10^{-13} for 10^4 seconds or one day. From 2007 to 2011, totally 10 space RAFS products were built by WIPM for BeiDou regional system. The RAFS's were tested in vacuum condition. As shown in Fig.6, the short term stability of the RAFS's is approximately $3 \times 10^{-12} \tau^{-1/2}$; the 10^4 seconds and day stabilities are within $2 \sim 5 \times 10^{-14}$ in Hadamard deviation [6], nearly one order of magnitude better than requirement, comparable with those used in GPS Block IIR [7]. All the RAFS's were equipped in the satellites of BeiDou regional system, which had provided service by the end of 2012.

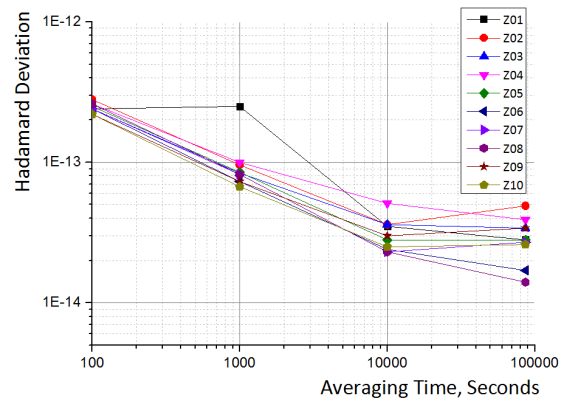


Fig. 6. Frequency stability of the space RAFS's for BeiDou regional system. The data is obtained from ground tests

V. IMPROVEMENT

The BeiDou global navigation system, which will provide service in 2020 according to schedule, aims at 3ns timing and 1m positioning precisions. In order to meet this application, RAFS design has been further improved at WIPM.

To enhance signal to noise ratio of the physics package, two mayor improvements have been carried out.

Firstly, a cavity with larger size and better microwave distribution was used. Not alike the standard cavities such as TE_{011} or TE_{111} ones, the slotted tube cavity can be designed with any size in diameter and length in a reasonable range, and the magnetic field distribution inside the cavity can be improved by optimizing the slot parameters. Owing to this feature, a new type cavity with inner diameter of 20mm and better microwave resonant mode was designed, enabling to use absorption and filter cells with diameter of 20mm [8].

The other improvement is to substitute the Ar lamp with a filtered Xe lamp, which has been used successfully in the space RAFS for GPS IIF [9]. We have tried to use a Ar lamp with light filtered by a coherent filter as the pumping source, but failed to obtain a stability better than $1 \times 10^{-12} \tau^{-1/2}$. To clarify the reason, the rubidium hyperfine spectra of the three traditionally used lamps were investigated [10, 11]. It was found that there is serious self-absorption effect in rubidium

hyperfine spectrum for the Ar lamp. This effect broadens and distorts the spectral profile of pumping light, and thus lowers pumping efficiency as well as the short term stability. It was found also that the self-absorption could move the zero light shift temperature by as far as several centigrade degrees, leading difficulty to reduce the influence of light shift on long-term stability [11]. Experiments showed that the Kr lamp has also self-absorption but not so serious, while the Xe lamp has almost no. Based on these results, we conclude that the Xe lamp seems to be the best choice for pumping source for the RAFS.

Design of the electronics remains nearly unchanged, but phase noise of the microwave chain was depressed by optimizing the layout and adjustment of circuits.

The light shift and temperature coefficient of the RAFS were reduced further. By optimizing operation parameters of physics package, a light shift of 1×10^{-11} over 10% light intensity change and a temperature coefficient smaller than $3 \times 10^{-14}/^\circ\text{C}$ have been achieved.

A prototype of new generation space RAFS has been built recently at WIPM. The prototype has been tested in vacuum environment with a hydrogen maser as the reference. Concerning that the prototype is a fresh one thus the frequency drift is changing, a drift removed Hadamard deviation was used to calculate the frequency stability. In drift removal calculation, the frequency curve was assumed to fit the diffusion model $f = a + b(t+c)^{1/2}$. The result is shown in Fig.7.

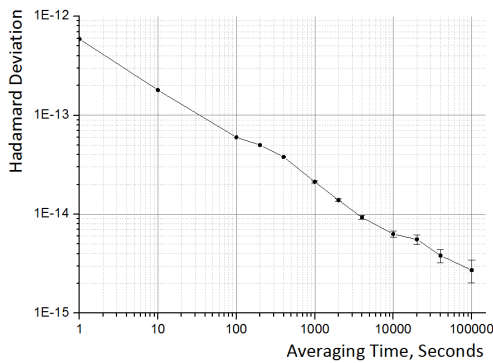


Fig.7. Frequency stability of the improved RAFS

From Fig.7 we can see that the prototype is of a short term frequency better than $7 \times 10^{-13} \tau^{-1/2}$, and a day stability nearly

3×10^{-15} , at the same level as the RAFS's applied in GPS Block IIF satellites [7].

Additionally, we believe the above method to calculate frequency stability is an appropriate way to evaluate the performance of RAFS with stability at 10^{-15} level. We don't think it will affect application in navigation satellites. Actually, modeling is needed to predict the satellite time given by the space clock. One can just use the diffusion model for high performance space RAFS.

REFERENCES

- [1] G.H. Mei, D. Zhong, S.F. An, X.R. Huang, J.T. Liu, "Miniaturized microwave cavity for atomic frequency standard," US Patent: US6225870B1, 2001.
- [2] G.H. Mei, J.T. Liu, "A miniaturized microwave resonator for rubidium frequency standards," Proceedings, 1999 Joint IEEE IFCS-EFTF, Besancon, April 13-16, 1999, pp. 601.
- [3] B.H. Xia, D. Zhong, S.F. An, G.M. Mei, "Characteristics of a novel kind of miniaturized cavity-cell assembly for rubidium frequency standards," IEEE Trans. Instrum. and Meas., vol. 55, no. 3, pp. 1000-1005, June 2006.
- [4] S.G. He, F. Wang, F. Zhao, H.H. Wu, G.H. Mei, "Rubidium mass measurement and lifetime evaluation of the lamp bulb of a rubidium atomic clock," ACTA METROLOGICA SINICA (in Chinese), in press.
- [5] R.A. Cook, R.P. Frueholz, "An improved rubidium consumption for discharge lamps used in rubidium frequency standards," Proceedings of the 42th annual frequency control symposium, pp. 525-531, 1988.
- [6] D. Zhong, G.H. Mei, "Study of a high performance rubidium atomic frequency standard", Proceedings, 2011 IEEE Int. Frequency Control Symp., San Francisco, California, May 1-5, 2011, pp. 215-217.
- [7] F. Vannicola, R. Beard, J. White, K. Senior, "GPS Block IIF atomic frequency standard analysis," 42th Annual Precise Time and Time Interval (PTTI) Meeting, Nov. 15-18, 2010, pp. 181-196.
- [8] F. Xu, Q. Hao, G. Ming, G.H. Mei, "A high signal to noise ratio physics package with a slotted-tube cavity for rubidium atomic clock", ACTA METROLOGICA SINICA (in Chinese), in press.
- [9] R.T. Dupuis, T.J. Lynch, J.R. Vaccaro, "Rubidium frequency standard for the GPS IIF program and modifications for the RAFSMOD program", 2008 IEEE International Frequency Control Symposium, 2011, pp. 655-660.
- [10] S.G. He, Q. Hao, F. Xu, F. Wang, F. Zhao, D. Zhong, G.H. Mei, "Study on self-absorption of spectral lines of rubidium spectral lamp", Chinese Journal of Magnetic Resonance (in Chinese), in press.
- [11] Q. Hao, S.G. He, F. Xu, F. Zhao, G.H. Mei, "Influence of lamp spectral profile on short-term stability and light shift of a rubidium atomic clock," China Satellite Navigation Conference (CSNC) 2015 Proceedings, Vol. III, pp. 387-397.

Non-destructive MEMS atomic vapor cells characterization by Raman spectroscopy and image analysis

Sylvain Karlen*, Jean Gobet, Thomas Overstolz and Jacques Haesler
 CSEM (Centre Suisse d'Électronique et de Microtechnique) SA
 Neuchâtel, Switzerland
 Email: *sylvain.karlen@csem.ch

Abstract—The use of innovative and non-destructive methods to characterize the content of MEMS atomic vapor cells for atomic devices is reported: Raman spectroscopy is used as a fast and quantitative method to estimate the Nitrogen pressure inside the cell cavity and image analysis is used to quantify the amount of metallic Rubidium. These techniques can be used for buffer gas pressure optimization and cell lifetime assessment.

I. INTRODUCTION

Chip-scale atomic clocks (CSAC) provide a high frequency accuracy and a long term stability at small size and low power consumption. They have found an increased interest for applications in telecommunication systems, global positioning and synchronization of communication networks. The heart of a CSAC consists of a microfabricated (MEMS) alkali vapor cell filled with Rubidium (Rb) or Cesium (Cs). Most often, a buffer gas is added inside the cell in order to reduce the resonance linewidth. This buffer gas however introduces a temperature-dependence of the hyperfine frequency due to the shift produced by the collisions with the alkali atoms. A common method to reduce the sensitivity of the clock frequency to temperature variations is to use a mixture of two buffer gases shifting in opposite directions such as Argon (Ar) and Nitrogen (N₂).

Among the different techniques used to fill micro-fabricated alkali vapor cells, the UV decomposition of Rubidium azide (RbN₃) into metallic Rb and gaseous N₂ is a very promising approach for low-cost wafer-level fabrication. We report here on the use of two innovative and non-destructive methods to characterize the decomposition yield and the buffer gas partial pressures (N₂ and Ar) of cells made with this technique: Raman spectroscopy is used as a fast and quantitative method to estimate the N₂ pressure inside the cavity; Image analysis is used to quantify the amount of metallic Rb in the cell.

II. MEMS ATOMIC VAPOR CELLS FABRICATION

CSEM wafer-scale cell fabrication process was presented in [1]. It is based on automated pipetting of small amounts of an aqueous RbN₃ solution into 1 mm thick and 2 mm wide cavities etched in a silicon wafer. The cavities are then hermetically sealed by anodic bonding of a glass cap under controlled Argon (Ar) pressure (see Figure 1). Metallic Rb and N₂ buffer gas are created in situ by UV irradiation of the RbN₃ following the decomposition reaction:



Fig. 1. MEMS atomic vapor cell: [left] Atomic vapor cell after dicing - [right] wafer-level view



This low-cost filling technique is compatible with wafer-level fabrication in a conventional clean room environment. Contrarily to other filling technique, which do not link the Rb and buffer gas partial pressure, the pipetting and the UV irradiation must be well controlled. Indeed, the N₂ partial pressure, which is linked to the reacted RbN₃ quantity, must be adapted such that the Ar/N₂ ratio matches the desired buffer gas frequency shift inversion temperature. Moreover, due to this stoichiometrical link between Rb and N₂, the total quantity of metallic Rb present in the cell is limited by the desired N₂ partial pressure. The two analytical techniques presented here were especially developed in order to quantify those two quantities.

III. RAMAN SPECTROSCOPY FOR N₂ PRESSURE MEASUREMENT

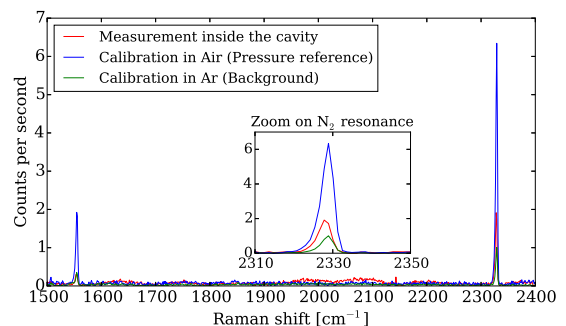


Fig. 2. Experimental μ -Raman spectra used for N₂ pressure measurement: Calibration in atmosphere, calibration in Ar and measurement inside a sealed MEMS cell cavity

Micro-Raman spectroscopy is a fast and non-destructive method that provides information about molecular vibrations. It has in particular the capability of measuring diatomic gases and was therefore proposed as a mean of analyzing gases in devices having an optical access to the sealed cavity [2]. In the present case, the N₂ buffer gas partial pressure inside the MEMS cells is measured with this technique. In gases, the Raman intensity of a band is proportional to the partial pressure of the considered gas:

$$I(\nu) \propto I_0 \sigma(\nu) p \quad (2)$$

Where $I(\nu)$ is the Raman intensity at the Raman shift ν , I_0 is the laser intensity, $\sigma(\nu)$ the Raman cross-section for the considered gas and p its partial pressure. The Raman vibrational mode of N₂ at $\nu = 2328\text{cm}^{-1}$ is considered here (see Figure 2). To calibrate the measurement, the chamber of the instrument is filled with N₂ atmospheric pressure $p_{\text{N}_2, \text{atm.}} = 761\text{mbar}$. The signal intensity $I_{\text{atm.}}$ is integrated over one hour. We repeat the measurement by filling the instrument's measurement chamber with Ar such that the partial pressure of N₂ is 0 and record I_{Ar} . The small N₂ Raman signal is resulting from the interaction of the laser with N₂ present in the instrument's atmosphere outside the measurement chamber filled with Ar. Finally, the Raman intensity is measured inside the cell cavity as I_{cell} . From equation 2, the pressure in the cell writes as:

$$p_{\text{N}_2, \text{cell}} = \frac{I_{\text{cell}} - I_{\text{Ar}}}{I_{\text{atm.}} - I_{\text{Ar}}} p_{\text{N}_2, \text{atm.}} \quad (3)$$

The results obtained by this Raman technique were compared with measurements made by Rb hyperfine frequency spectroscopy. In that case, the partial N₂ pressure is determined by the buffer gas shift of the Rb hyperfine frequency and its dependence to temperature. It is given by:

$$\Delta\nu_{BG} = \sum_{\text{Ar}, \text{N}_2} p_{\text{Ar}, \text{N}_2} [\beta_{\text{Ar}, \text{N}_2} + \delta_{\text{Ar}, \text{N}_2} (T - T_0) + \gamma_{\text{Ar}, \text{N}_2} (T - T_0)^2] \quad (4)$$

Where the β , δ , γ coefficients are given in [3]. In the present case, the shift from the unperturbed ⁸⁵Rb hyperfine frequency was measured in coherent population trapping (CPT) clock operation. The light shift was extrapolated to 0-light intensity (see Figure 3 - left) and the second order Zeeman shift was measured and subtracted. The partial pressure of Ar and N₂ were finally extracted by fitting of the temperature dependence of the hyperfine frequency shift (see Figure 3 - right).

The results of the two methods were compared for three cells and showed good agreement with an absolute difference below 2 mbar for all the three measurements, a Pearson correlation coefficient of $r = 0.99975$ and a 95% limit of agreement of -2.9 to 4.3mbar for the Raman measurement method (see Figure 4).

The Raman method allows to measure the N₂ partial pressure in a much wider pressure range than the hyperfine spectroscopy method, without presence of Rb and with a faster acquisition time.

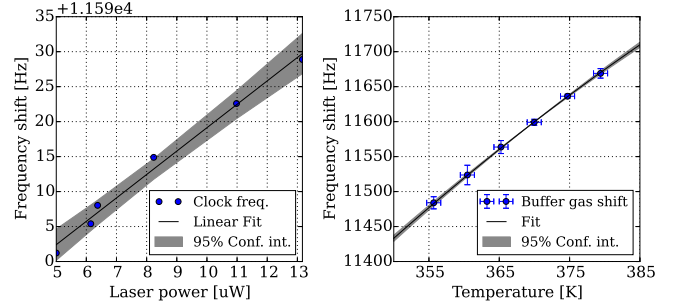


Fig. 3. Experimental determination of N₂ and Ar partial pressure by hyperfine frequency shift: [left] 0-light shift extrapolation of CPT clock frequency shift - [right] Fit of the temperature dependence of the buffer gas shift

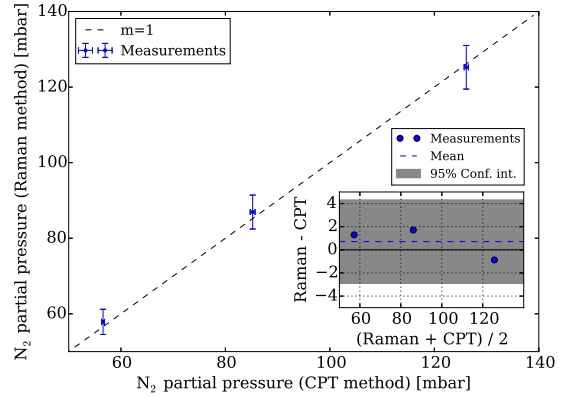


Fig. 4. Comparison between the N₂ partial pressure determined by Raman spectroscopy and the N₂ partial pressure determined by CPT spectroscopy - [insert] Tukey mean-difference plot

IV. RB QUANTITY ESTIMATION BY IMAGE ANALYSIS

The presence of metallic Rb in excess is required during atomic vapor cell operation in order to maintain the alkali vapor pressure. Observations in cells filled with low RbN₃ quantity showed that an initial consumption of Rb occurs before any Rubidium vapor can be detected in the cavity. Moreover, it was observed that the Rubidium quantity decreases over time, limiting the cell lifetime. The image analysis technique presented here was developed in order to quantify this initial consumption and allow a monitoring of the Rubidium quantity over the cell lifetime.

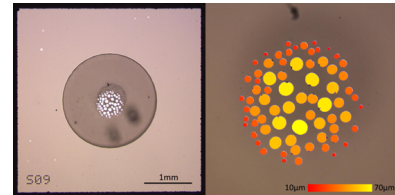


Fig. 5. Image recognition of Rb drops size in MEMS cell: [left] Microscope image of a cell - [right] Extraction of drop radius by image recognition software

To estimate the Rubidium quantity in the cell, the metallic Rb was migrated on the cell window by applying a thermal gradient. The condensed droplets were then imaged with a

microscope and the drops radius a was estimated using the image recognition software (see Figure 5).

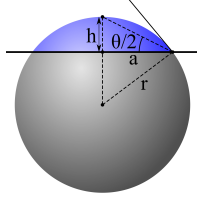


Fig. 6. Spherical cap used for Rb drop volume estimation

The drop volume can be estimated as the volume of a spherical cap in function of the contact angle θ (see Figure 6) :

$$V = \frac{\pi h}{6}(3a^2 + h^2); h \cong a \tan(\theta/2) \quad (5)$$

The contact angle is a priori not known but it can be estimated from the N_2 pressure measurements made by Raman (see above). Indeed, the amount of Rb created during the RbN_3 decomposition is directly linked to the N_2 pressure by the stoichiometrical relation (equation 1). A batch of cells was filled with different RbN_3 quantities, UV decomposed and measured with the two methods. No visible metallic Rb was observed in the cells with few RbN_3 quantity. The observed Rb mass $m_{mes.}$ can then be written as:

$$m_{mes.} = \begin{cases} m_{prod.} - m_{init. cons.} & \text{if } m_{prod.} > m_{init. cons.} \\ 0 & \text{if } m_{prod.} < m_{init. cons.} \end{cases} \quad (6)$$

Where $m_{prod.}$ is the the produced mass calculated by Raman and $m_{init. cons.}$ is the unknown initial consumed mass. From this equation, the contact angle θ can be adjusted such that the slope between $m_{meas.}$ and $m_{prod.}$ is 1 for the non-0 values of $m_{meas.}$. We found an experimental value of $\theta = 57 \pm 6^\circ$. This allows to estimate the initial consumed mass of Rb to $m_{init.cons.} = 0.50 \pm 0.08 \mu g$.

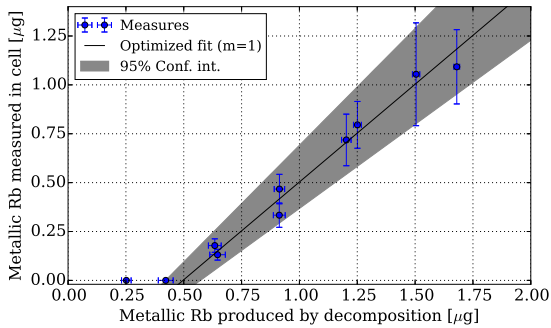


Fig. 7. Estimation of Rb initial consumption: The fit is realized only on the non-0 values of the measured Rb quantity. The contact angle θ is optimized such that the slope of this fit is 1

The reason of the initial consumption is still under investigation. A similar effect was observed in cm-sized cells[4], [5] but the quantities reported ($3 \cdot 10^{15}$ atoms per cm^2) only explain a small fraction ($\sim 10\%$) of the total consumed Rb in our cells. The image analysis method is currently being used to further explore the reasons of this initial consumption and

to monitor the Rb quantity over time in order to evaluate the cell lifetime.

V. CONCLUSION

Two characterization methods were developed for MEMS atomic vapor cells. Raman spectroscopy allow to measure the Nitrogen partial pressure inside the cell small volume at a precision below 5mbar. It can be used to optimize the RbN_3 filling and UV decomposition process and therefore to optimize the Ar/N_2 pressure ratio. Image analysis allows to measure the amount of Rubidium in a cell with a precision in the order of $0.1 \mu g$. This measurement relies on the contact angle between Rubidium and the borosilicate glass. A value of $\theta = 57 \pm 6^\circ$ was found. This technique was used to measure the amount of Rubidium initially consumed in the cell and a value of $0.5 \mu g$ was found. The reason for this initial consumption is still under investigation, as well as the cell lifetime by monitoring if the Rb quantity over time.

ACKNOWLEDGMENT

This work was supported by the European Space Agency (ESA) under the Networking and Partnering Initiative (NPI), ESA Contract No. 4000112650/14/NL/GLC and by CSEM's R&D activity financed the Canton of Neuchâtel. The authors would like to thank G. Mileti and S. Lecomte for their support on this project.

REFERENCES

- [1] T. Overstolz, J. Haesler, G. Bergonzi, A. Pezous, P.-A. Clerc, S. Ischer, J. Kaufmann, and M. Despont, "Wafer scale fabrication of highly integrated rubidium vapor cells," in *IEEE 27th International Conference on Micro Electro Mechanical Systems (MEMS)*, jan 2014, pp. 552–555.
- [2] W. H. Weber, M. Zanini-Fisher, and M. J. Pelletier, "Using Raman Microscopy to Detect Leaks in Micromechanical Silicon Structures," *Applied Spectroscopy*, vol. 51, no. 1, pp. 123–129, jan 1997.
- [3] J. Vanier, R. Kunski, N. Cyr, J. Y. Savard, and M. Têtu, "On hyperfine frequency shifts caused by buffer gases: Application to the optically pumped passive rubidium frequency standard," *Journal of Applied Physics*, vol. 53, no. 8, pp. 5387–5391, aug 1982.
- [4] J. Ma, A. Kishinevski, Y.-Y. Jau, C. Reuter, and W. Happer, "Modification of glass cell walls by rubidium vapor," *Physical Review A*, vol. 79, no. 4, p. 042905, apr 2009.
- [5] J. Brossel, J.-l. Mosser, and M. Winter, "Absorption du sodium par des parois de verre chauffées a $120^\circ C$," *J. Phys. Radium*, vol. 16, no. 10, pp. 814–815, 1955.

Experimental procedure to design stressed HBAR devices when the third-order elastic constants are not known

Baron Thomas, Bebon Ludovic, Petrini Valérie, Martin Gilles, Dulmet Bernard
Time & Frequency department,
FEMTO-ST, UMR CNRS-UFC-ENSMM-UTBM 6174,
26 Chemin de l'Épitaphe,
25030 Besançon Cedex, France
E-mail: thomas.baron@femto-st.fr

Lesage Jean-Marc
DGA – Information Superiority,
DGA, French MoD,
Bruz, France

Abstract— Vibration sensitivity is an important specification for oscillators dedicated to space or airborne systems. For some crystallographic material, some physical constant are not yet measured. So, computation of stress coefficients of frequency is not possible. This paper presents a simple experimentation which allows the determination of the six stress coefficients of frequency for each high-overtone bulk acoustic resonators configuration. The first three coefficient are α_{mn} are $-2.9 \times 10^{-12}/\text{Pa}$, $4.3 \times 10^{-10}/\text{Pa}$ and $9.4 \times 10^{-11}/\text{Pa}$. The relative standard deviation can be high due to experimental uncertainty.

Keywords— High-overtone Bulk Acoustic Resonators (HBAR) component; oscillator; vibration sensitivity; packaging.

I. INTRODUCTION

One of the challenges of frequency sources dedicated to space and airborne systems is the control of vibration sensitivity. Vibration sensitivity can be due to the resonator, the oscillator loop or non-oscillator components like wires, for instance. Commonly, the main source of acceleration sensitivity comes from the resonator. Active compensation can be used to decrease this effect, but such systems are not easily miniaturized.

Past papers at the EFTF conferences have focused on vibration sensitivity of High-overtone Bulk Acoustic Resonators (HBAR). Initial works have focused on the experimental results on HBAR with quartz or sapphire substrates [1] which present few $10^{-11}/\text{G}$ sensitivity. Further investigations focus on the implementation of theoretical aspects on modeling tools. These works were validated by comparison between the results of design and experimentation [2] in the case of quartz material. The agreement is around 50%.

Third-order elastic constants are mandatory requirements to compute stress sensitivity of HBAR. Thereby, most materials are not suitable to design low vibration sensitivity HBAR oscillator or pressure sensor. This work presents a new way to design such components when third-order elastic constants are not known. This approach is based on experimental measurements of stress sensitivity coefficients of HBAR. We

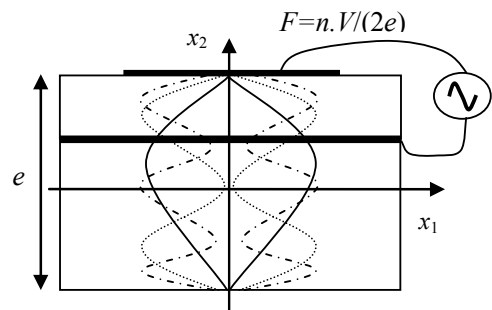
use LiNbO_3 (YXl)/163 piezoelectric layer on LiTaO_3 Z-cut substrate as example of this approach.

This paper described experimental approach to estimate the stress sensitivity coefficients of frequency of specific HBARs. Combined with the distinguishing features of HBAR resonator such as $Q \cdot f$ product and temperature coefficient of frequency [3], a complete oscillator design optimization can be done thanks to the six stress sensitivity coefficients. Similarly, it is possible to design a pressure sensor although the involved nonlinear elastic constants have not been determined yet.

II. HBAR

A. HBAR principle

HBARs combine the outstanding properties of the strong coupling coefficient of the deposited piezoelectric thin film and of the high intrinsic quality substrates. The piezoelectric film and the two electrodes on opposite sides are used as a transducer whereas the acoustic energy is mainly trapped in the substrate, Fig. 1. Resonance frequencies correspond to integer numbers of half wavelengths in the entire thickness. Unlike Film Bulk Acoustic Resonator (FBAR) and Solidly Mounted Resonator (SMR) in which only odd overtones exist, both odd and even overtones are compatible with resonance modes satisfying the electrical and mechanical boundary conditions. For more details, the reader can look at [4].



This work was partly supported by the RAPID project ORAGE under grant #092906659#.

This work was partly supported by the French RENATECH network and its FEMTO-ST technological facility.

This project has been performed in cooperation with the Labex ACTION program (contract ANR-11-LABX-0001-01).

COMSOL computations have been performed on the supercomputer facilities of the Mésocentre de calcul de Franche-Comté.

Fig. 1. Principle of a *HBAR*, showing possible harmonics distribution within the stack

B. *HBAR* features

For the experimentation, we use *HBAR* constituted by LiNbO_3 (YXl)/163 piezoelectric layer on LiTaO_3 Z-cut substrate. LiTaO_3 material presents low acoustic attenuation, so the Qf product can be high, as shown with the result presented in Fig. 2.

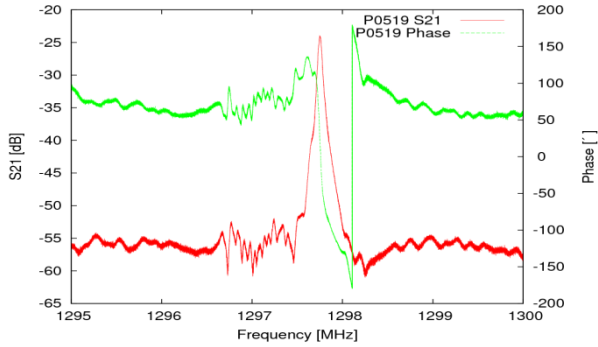


Fig. 2. Electrical response of *HBAR* with LiNbO_3 (YXl)/163° as piezoelectric layer and LiTaO_3 (YXl)/90° as substrate. This overtone exhibits Qf product around 3.7×10^{13} Hz.

Moreover, LiTaO_3 Z-cut is a cut orientation exhibiting a near zero frequency drift w.r.t. [5]. A turn-over point is found around 55°C and fifteenth consecutive overtones present the same behavior with the temperature. The figure 3 shows this result.

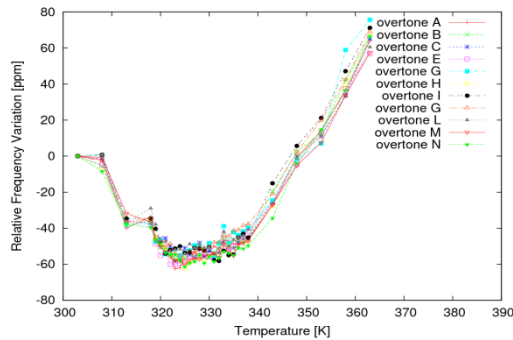


Fig. 3. Relative frequency variation versus temperature of several consecutive overtones of *HBAR* constituted by 150 nm of Aluminum, 1.8 μm of LiNbO_3 (YXl)/163°, 400 nm of Gold layer and 550 μm of LiTaO_3 (YXl)/90° substrate.

III. STRESS SENSITIVITY COEFFICIENTS OF FREQUENCY OF *HBAR*

A. Stress sensitivity coefficients of frequency

According to the following equations (1-3), introduced by Filler in [6], the measurement and the computation of vibration sensitivity of the acoustic resonator inside an oscillator loop is possible. Computation with the knowledge of the 14 non-linear coefficients for (3*m*) crystallographic material allows the determination of vibration sensitivity of the system in all-space directions (2-3). On the contrary, the measurement of different sensitivity in all-space direction (1) combined with the computation of stress tensor $\sigma_{ij,xi}$ is not sufficient to determine the 14 non-linear coefficients.

$$\Gamma_{x_i} = 10^{\left(\frac{L_f}{20}\right)} \frac{2\nu}{v_0 \sqrt{\gamma_{rms}^2 / BW}} \quad (1)$$

$$\Gamma = \sqrt{\Gamma_X^2 + \Gamma_Y^2 + \Gamma_Z^2}, \quad x_i = X, Y, Z \quad (2)$$

$$\Gamma_{x_i} = {}^s\alpha_{ij} \bullet \sigma_{ij,xi} \quad (3)$$

γ_{rms} is the root-mean-square value of vibration, Γ_{x_i} is the component of acceleration sensitivity vector in the i ($i=X, Y$ and Z) direction, ν and ν_0 are respectively the Fourier frequency and the frequency of the oscillator, BW is the bandwidth of vibration and L_f is the phase noise, ${}^s\alpha_{ij}$ is the stress sensitivity coefficients of *HBAR*.

B. Experimental principle

From the knowledge of nonlinear elastic constants, it is possible to calculate the *HBAR* stress sensitivity coefficients of frequency (${}^s\alpha_{mn}$) [2]. With the equation (3) above, the measurement of vibration sensitivity of *HBAR* oscillators in all-space direction allows to establish three equations. The six unknown coefficients ${}^s\alpha_{mn}$ oblige to determine three other equations from another package configuration.

Four package configurations were realized to determine the six stress sensitivity coefficients of *HBAR*. The configurations include two PCB configurations with hinges in two axis directions: vertical and horizontal. *HBAR* is glued on the PCB along vertical or horizontal orientations. Fig. 2 shows the configuration with vertical hinge and horizontal *HBAR* orientation. To prevent deterioration of acoustic wave inside the *HBAR*, the *HBAR* is glued on the alumina with hole. These four different configurations are realized twice to improve the accuracy of the coefficients determination.

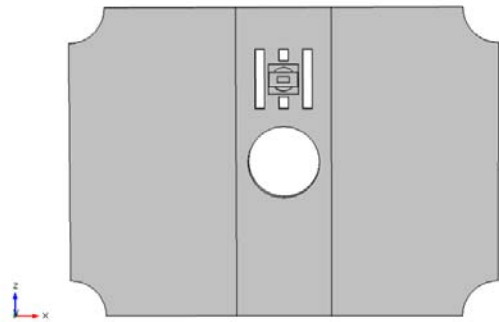


Fig. 4. Schematic view of *HBAR* of one the PCB one of the PCB of this paper. The orientation of *HBAR* or the hinges can be rotated of 90°.

The computation of the six stress sensitivity coefficients of frequency (${}^s\alpha_{mn}$) is possible due to the computation of the six stress coefficients in each configuration. The following table shows the six stress coefficients calculated with COMSOL for the configuration of Fig. 2 and for all three orientations. The stress coefficients were calculated in the active volume of the *HBAR*.

TABLE I. STRESS TENSOR APPLIED ON THE HBAR BASED ON (ZX) LiTAO₃ SUBSTRATE (THICKNESS EQUAL TO 500 μ m) WITH (YXL)/163 $^\circ$ LiNbO₃ LAYER OF 3 μ m THICKNESS WITH 1G IN ALL-SPACE DIRECTION

	X	Y	Z
σ_x	-57,811	-306,39	-175,4
σ_y	3,8604	29,081	6,0777
σ_z	-96,219	-628,36	-477,2
σ_{xy}	-2,4774	-6,3219	4,3319
σ_{xz}	-40,214	-130,24	-55,234
σ_{yz}	-3,1395	-18,372	-13,871

C. Experimental measurement

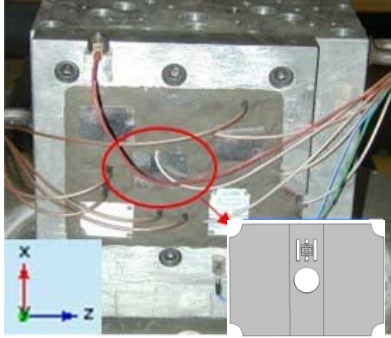


Fig. 5. Set-up for g sensitivity measurement. Rotation of 90 $^\circ$ is done to measure along Z axis, and resonators are put on the top of the bench to measure g sensitivity along Y axis.

The measurements of g-sensitivity have been achieved in all space directions on a test bench, shown in figure 5, applying random vibrations in the 10–2000 Hz frequency range with 20 G rms intensity levels respectively. Random vibrations are applied vertically, and the oscillators were rotated in different positions to achieve the three directions.

Even if the configuration is not done to realize low G-sensitivity oscillators, The figure 3 shows the PSD results provided by one oscillator exhibiting a sensitivity of 4.5 \times 10⁻¹¹/G.

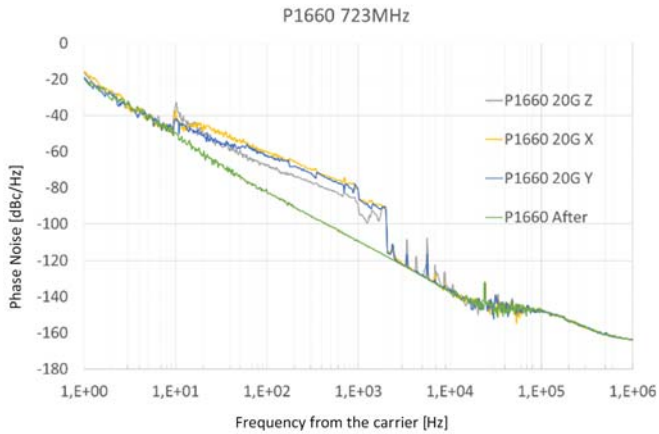


Fig. 6. Experimental phase noise density of an HBAR oscillator under vibration.

D. Determination of six stress sensitivity coefficient of HBAR

The four configurations are double, and each configuration is measured for all-space directions. So, the 24 linear equations (3) allow us to make several systems of six equations of six unknown variables. The redundancy of the equations, increase the accuracy of the coefficient estimation. Some mistakes are possible due to the inaccuracy of the stress coefficients, the parasitic vibrations, and the inaccuracy of the HBAR position on the PCB and on the position of oscillators on the test bench.

The six stress sensitivity coefficients of this specific configuration of HBAR have been computed. The following table summarizes the three first stress sensitivity coefficients of frequency of HBAR with an estimation of the relative standard deviation.

TABLE II. STRESS SENSITIVITY COEFFICIENTS OF FREQUENCY OF HBAR BASED ON (ZX) LiTAO₃ SUBSTRATE (THICKNESS EQUAL TO 500 μ m) WITH (YXL)/163 $^\circ$ LiNbO₃ LAYER OF 3 μ m THICKNESS WITH THE RELATIVE STANDARD DEVIATION

	Stress sensitivity coefficients of frequency (/Pa)	Relative standard deviation
$^s\alpha_x$	-2.9 \times 10 ⁻¹²	56.8
$^s\alpha_y$	4.3 \times 10 ⁻¹⁰	204.1
$^s\alpha_z$	9.4 \times 10 ⁻¹¹	47.7

The knowledge of the six stress sensitivity coefficients of frequency allows us to design different components like an optimized low vibration sensitivity oscillator or a pressure sensor. Moreover, the present work can be completed by all future measurements of components sensitive to stress, easily computed, to increase the accuracy of the coefficient.

IV. DISCUSSION

The knowledge of the non-linear coefficients allows the computation of the six stress coefficient sensitivity for all HBAR configurations. In the case of materials with not known non-linear coefficients, the determination of the six stress coefficients have to be done for each HBAR configuration. Moreover, this work allows the computation of different systems using the HBAR. It is possible to design an optimize oscillator presenting a low-G-sensitivity or a HBAR pressure sensor.

A. Oscillator design optimization procedure

The goal of this part is to propose a procedure to minimize the vibration sensitivity of HBAR oscillator realize on a PCB. The stress tensor on the PCB is easily computed by finite element software. From the equation (3), it is possible to calculate the effective vibration sensitivity of a virtual HBAR placed on each point of the PCB. The sum of these results time the six stress coefficients give us the optimal position of the HBAR.

The rotation of the HBAR on the PCB can also influence the vibration sensitivity. Fig. 5 shows this evolution; the orientations of 0 $^\circ$ and 180 $^\circ$ present the best configuration to minimize the vibration sensitivity and the technological drift.

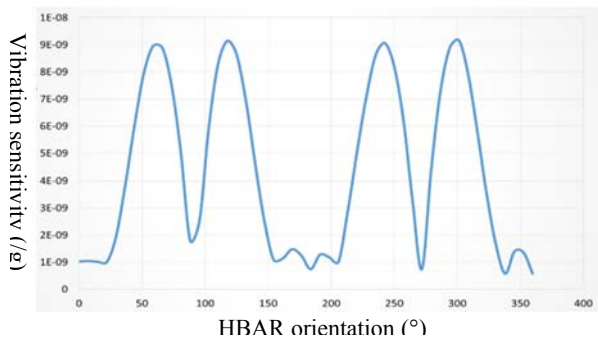


Fig. 7. Vibration sensitivity of HBAR with quartz substrate (/G) in function of its orientation.

Based on the stress sensitivity coefficients of frequency of the HBAR, it is possible to optimize the position of the HBAR in the oscillator to minimize the vibration sensitivity. To improve this sensitivity, it is possible to either pattern the PCB, as was done in the first part of this paper or to use active compensation.

B. HBAR pressure sensor

This part deals with the issue of pressure sensors based on HBAR. Previous works [7,8] presented the principle of HBAR pressure sensors and showed first experimental results. These first pressure sensors had not been designed due to lack of a software tool. The implementation of model allows us such design. So, the goal of this section is to give realistic dimensions of a HBAR pressure sensor based on quartz substrate. The dimension is determined based on the stress sensitivity coefficients of frequency of the HBAR.

The HBAR pressure sensor consists of a membrane with a cavity under the HBAR to confine the acoustic wave. For the specification of the sensor, we impose a maximum pressure of 5 bar and a resolution of 500 Hz at 434 MHz.

The size limitation of the membrane comes from the maximum stress admitted by the material. So, an experimental measurement to determine this maximal stress supported by the LiTaO₃ (ZX) cut material was done, and a value around 260MPa was found. Finally, the micro-fabrication based on bonding/lapping process gives us an acceptable thickness of 300μm for the membrane. A comparison between HBARs based on quartz and HBARs based on LiTaO₃ is done. Table III summarizes the results.

TABLE III. RESULTS OF HBAR PRESSURE SENSORS BASED ON (ZX) LiTaO₃ SUBSTRATE OR QUARTZ SUBSTRATE WITH (YXL)/163° LiNbO₃ AS PIEZOELECTRIC LAYER

Substrate of HBAR	Quartz	LiTaO ₃
Diameter (mm)	9000	3000
Sensitivity (Hz/Pa)	5.1×10^{-10}	1.5×10^{-9}
Resolution (Pa/Hz)	2.2×10^3	7.3×10^2

V. CONCLUSION

This paper presents an experimental procedure to determine the stress sensitivity coefficients of frequency of HBARs when the non-linear coefficients of material are not known. The first three coefficients are α_{mn} are $-2.9 \times 10^{-12}/\text{Pa}$, $4.3 \times 10^{-10}/\text{Pa}$ and $9.4 \times 10^{-11}/\text{Pa}$. From these stress sensitivity coefficients of frequency, a simple static study of the packaging allows us to determine the best position of each HBAR on the same PCB to minimize the vibration sensitivity.

REFERENCES

- [1] T. Baron, G. Martin, F. Bassignot, N. Chrétien, A. Reinhardt, P. Lassagne, J. Lesage, D. Rabus, L. Chommeloux, and S. Ballandras, "Low-G Sensitivity of HBAR Oscillator," *28th Eur. Freq. Time Forum*, pp. 431–434, 2014.
- [2] B. Thomas, P. Valerie, M. Gilles, C. Guillaume, C. Alexandre, D. Bernard, L. Jean-marc, L. Thierry, and B. Sylvain, "Stress sensitivity coefficients of HBAR," *Freq. Control Symp. Eur. Freq. Time Forum (FCS), 2015 Jt. Conf. IEEE Int.*, pp. 214–217, 2015.
- [3] B. Thomas, M. Gilles, C. Nicolas, P. Valérie, C. Guillaume, H. Fabien, B. Florent, R. David, C. Luc, R. Alexandre, L. Pierre-patrick, L. Jean-Marc, and B. Sylvain, "High-Q and low TCF HBAR based on LiTaO₃ substrate," *Freq. Control Symp.*, pp. 1–4, 2014.
- [4] T. Baron, E. Lebrasseur, F. Bassignot, G. Martin, V. Pétrini, and S. Ballandras, *Chapter 13 High-Overtone Bulk Acoustic Resonator. Modeling And Measurement Methods For Acoustic Waves And For Acoustic Microdevices*. 2013.
- [5] S. V. Krishnaswamy, B. R. McAvoy, J. H. L. Salvo, and R. A. Moore, "Temperature Frequency Characteristics of Selected high Q acoustic Materials," *Ultrason. Symp.*, pp. 421–423, 1984.
- [6] R. L. Filler, "The acceleration sensitivity of quartz crystal oscillators: a review.," *IEEE Trans. Ultrason. Ferroelectr. Freq. Control*, vol. 35, pp. 297–305, 1988.
- [7] T. Baron, J. Masson, J. P. Romand, L. Catherinot, M. Chatras, and S. Ballandras, "BAW pressure sensor on LiNbO membrane lapping.," *EFTF*, no. 1, 2010.
- [8] T. Baron, D. Gachon, J. P. Romand, S. Alzuaga, S. Ballandras, J. Masson, L. Catherinot, and L. Chatras, "A pressure Sensor based on a HBAR micromachined structure," *IFCS*, 2010.

Relativistic Effect Correction for Clock Transport

Takiguchi H, Gotoh T, Fujieda M, Nakagawa F, Narita H,
Matsubara K, Imamura K, Ito H, Amagai J, and Hanado Y

National Institute of Information and Communications Technology, Koganei, Tokyo, Japan
Email: htaki@nict.go.jp

Abstract—NICT carried out the first calibration of the GPS link between Koganei and Kobe by using GPS, TWSTFT and Clock Transport (CT). We presented the result of the calibration in EFTF 2015. The differential correction of GPS link by GPS, TWSTFT and CT were 102.5, 102.1 and 104.9 ns respectively. The CT result showed a discrepancy of 2 ns. By applying the relativistic effect correction for CT, we confirmed a good agreement of the results obtained by their three techniques.

Keywords—calibration; clock transport; relativistic effect

I. INTRODUCTION

The National Institute of Information and Communications Technology (NICT) has been establishing the second UTC generation station at Kobe city as part of our time scale UTC(NICT) decentralization project.

NICT is responsible for the generation, comparison and dissemination of Japan Standard Time UTC(NICT). The system is located at NICT headquarters only in Koganei city in Tokyo. After the 2011 off the Pacific coast of Tohoku Earthquake, NICT considered about the risk of this situation. Therefore, the decentralization of these tasks is proceeding to NICT's branch facilities in order to prepare for future disasters and to improve the reliability and accuracy of these tasks. At first, the Advanced ICT Research Institute, which is one of the NICT's branch institute, located at Kobe city was selected as the place for installing the second UTC(NICT) generation system (hereafter KOBE). The time transfer link using a real-time GPS common-view (GPSCV) was established between NICT headquarters and KOBE. If the emergency will occur at NICT headquarters, KOBE has to take over all the functions and tasks from NICT headquarters (hereafter KOGANEI), that is, KOBE performs the UTC(NICT) generation instead of NICT headquarters. At that moment, the time scale UTC(KOBE) which is generated at KOBE should be synchronized with the time scale UTC(NICT). Furthermore it is demanded that the time difference between them is enough small. Therefore, we need to calibrate the time transfer link to show the time difference between UTC(NICT) and UTC(KOBE), and then steer the difference to zero. From above reason, before the start of the operation officially, we carried out the calibration of the time transfer link in 2014.

In this calibration, we employed three time and frequency techniques which were GPS carrier phase (hereafter GPS), Two-Way Satellite Time and Frequency Transfer (TWSTFT) and Clock Transport (CT). The results of GPS and TWSTFT agreed well within their uncertainties. However, the CT result showed a discrepancy of 2 ns with respect to the results by

GPS and TWSTFT. We presented the result of the calibration in last EFTF 2015 [1]. By applying the relativistic effect correction for CT, we confirmed a good agreement of the results obtained by their three techniques.

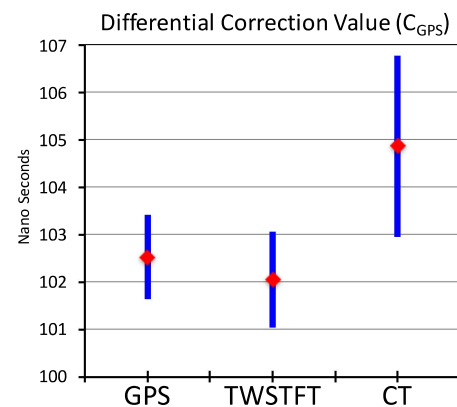


Fig. 1. The differential correction values of GPS link (UTC(NICT)-UTC(KOBE)) (previous results).

II. CALIBRATION PROCEDURE AND PREVIOUS RESULTS

The calibration measurements by GPS and TWSTFT were performed using a GPS travelling receiver and a portable TWSTFT station, respectively. The clock used in CT was consisted of a cesium atomic clock (Cs#42) equipped with AC/DC batteries and it was transported by a van between Koganei and Kobe. The CT measured the time difference between the UTC reference points at KOBE and KOGANEI and Cs#42 by using the time interval counter (SR620) directly. Table I shows the time difference measured by the CT.

TABLE I. MEASUREMENT DATA IN CT

Elapsed Time (s)	Time difference (ns)	
0	54118.4961	UTC(NICT) – Cs#42
33720	54013.5671	UTC(KOBE) – Cs#42
172740	54010.2174	UTC(KOBE) – Cs#42
207240	54114.1032	UTC(NICT) – Cs#42

The determined the differential correction value (C_{GPS}) of UTC(NICT)–UTC(KOBE) GPS link by GPS, TWSTFT and

CT were 102.5, 102.1 and 104.9 ns respectively. The calibration uncertainty of GPS, TWSTFT and CT were 0.9, 1.0 and 1.9 ns respectively. Fig. 1 shows the differential correction value of UTC(NICT)–UTC(KOBE) determined by each technique with the error bars which are the overall calibration uncertainties. There, we didn't apply the relativistic effect correction for CT. The details of the calibration procedure and the results of GPS and TWSTFT is described in [1] and [2].

III. RELATIVISTIC EFFECT CORRECTION

A. Theory

The relations arising from the application of the General Theory of Relativity to time transfer on the rotating Earth are defined in Recommendation ITU-R TF1010-1 [3] of the International Telecommunications Union. When a clock is transported from a point A to a point B, the coordinate time accumulated during transport can be written as,

$$dt = \int_A^B ds \left[1 + \frac{\Delta U(\vec{r})}{c^2} + \frac{V^2}{2c^2} \right] + \frac{2\omega}{c^2} A_E \quad (1)$$

where dt is the elapsed coordinate time, $\int ds$ is increment of proper time accumulated on the portable clock, ΔU is the gravitational potential difference between the location of the clock and the geoid, V is the velocity of the clock with respect to the ground, c is the speed of light, ω is the angular velocity of rotation of the Earth, A_E represents the equatorial projection of the area swept out during the transport of clock along its path [3], [4].

The first term in equation (1) is the gravitational redshift. ΔU can be approximated by the surface gravity which is the function of the latitude φ . The second term in equation (1) is the second-order Doppler shift. The third term in equation (1) is the Sagnac effect. The Sagnac effect is independent of the speed of the transport and depends on the form and direction of the transport path. The equation (1) can be re-written as,

$$dt = \int_A^B ds \left[\frac{(9.780 + 0.052 \sin^2 \varphi)h}{c^2} + \frac{V^2}{2c^2} \right] + \int_A^B d\lambda \frac{2\omega \pi a_1^2 \cos^2 \varphi}{c^2} \quad (2)$$

where φ is geographical latitude, h is distance above sea level, λ is longitude, a_1 is equatorial radius of the Earth.

B. Assumption

The Cs#42 was transported by a van. We used different driving routes in back and forth trips, which were the Tomei Expressway from Koganei (east) to Kobe (west) (hereafter west way), and the Chuo Expressway from Kobe (west) to Koganei (east) (hereafter east way). The Tomei Expressway is basically a flat road and is located at sea side. The Chuo Expressway is located at mountain area, so there are many steep slopes.

Unfortunately, we didn't record the position and velocity of the van. Therefore, we achieved the driving route information from a web service [5]. This web service provides the positions (longitude, latitude and altitude) of the road (Fig. 2). The distance between any two points is also provided by this web service. The total transport time (the elapsed time) was

estimated from Table I. About the velocity of the van, we determined the average velocity from the distance, the total transport time and the number of data. The assumed parameters were summarized in Table II.

TABLE II. SUMMARY OF THE ASSUMED PARAMETERS

Route (Number of Data)	Distance (km)	Elapsed Time (s)	Mean Velocity (km/h)
West Way (6245)	567.6	33720	60.6
East Way (8130)	579.8	34500	60.5

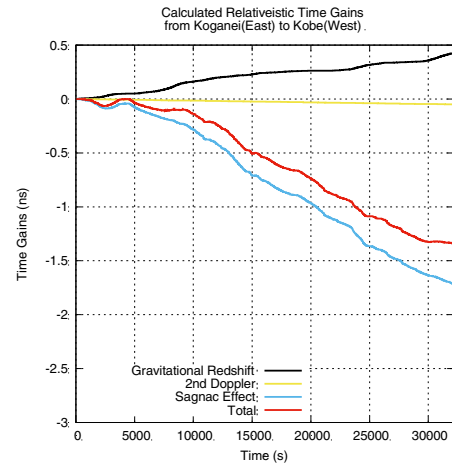


Fig. 3. Calculated relativistic time gains/losses for the portable clock for each of the contributing effects from Koganei (east) to Kobe (west).

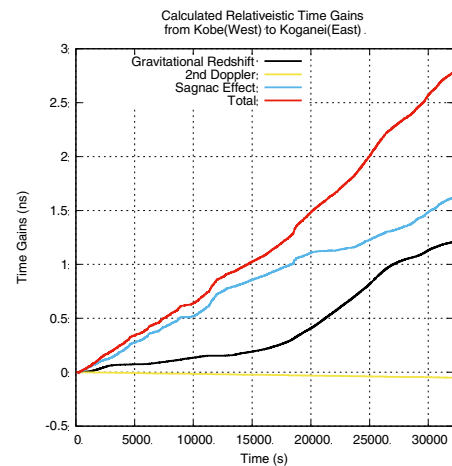


Fig. 4. Calculated relativistic time gains/losses for the portable clock for each of the contributing effects from Kobe (west) to Koganei (east).

C. Calculation and Results

We calculated the relativistic effect at every position data using the above assumption and the equation (2). The estimated total relativistic time gains/losses were -1.38 ns in the west way, 2.91 ns in the east way.

Fig. 3 and 4 show the calculated relativistic time gains/losses for the CT for each of the contributing effects, the gravitational redshift, the second-order Doppler shift and the Sagnac effect. The most contribution of the relativistic effect was the Sagnac effect and the next was the gravitational redshift. The second-order Doppler shift effect was about 200 ps. The Sagnac effect of the west way was loss and the east way was gain, because the Sagnac effect depends on the direction. The gravitational redshift effect of the east way was over 1 ns, because some of the route altitude were over 1000 m. Finally, we re-calculated the differential correction (C_{GPS}) of GPS link by the CT was 102.26 ns including the relativistic effect correction.

TABLE III. THE CALIBRATION UNCERTAINTY SOURCES OF CT

Uncertainty	Value (ns)	Description
U_{a1}	0.006	Jitter of the measurement (UTC(NICT)-Cs#42) 1 at NICT
U_{a2}	0.067	Jitter of the measurement (UTC(KOBE)-Cs#42) 1 at Kobe
U_{a3}	0.005	Jitter of the measurement (UTC(KOBE)-Cs#42) 2 at Kobe
U_{a4}	0.028	Jitter of the measurement (UTC(NICT)-Cs#42) 2 at NICT
U_{a5}	0.090	STD of the time difference of GPS link (NICT-KOBE)
U_a	0.116	The overall statistical uncertainty.
U_{b1} *	0.60	T.I.C. error at NICT 1
U_{b2} *	0.60	T.I.C. error at Kobe
U_{b3} *	0.60	T.I.C. error at NICT 2
U_{b4}	1.60	Time Instability of the Cs#42 at 2 days 9 hour 34 min.
U_{b5}	0.03	Relativistic Effect Correction error (west way)
U_{b6}	0.03	Relativistic Effect Correction error (east way)
U_b	1.91	The overall systematic uncertainty.
U	1.91	The overall uncertainty.

* According to the manufacture specifications the overall error of T.I.C (SR620) measurement is 0.60 ns (trigger level timing error, counter channel differential delay)

D. Uncertainty Estimation

We estimated the uncertainty of the CT again. The previously estimated the statistical uncertainty, the systematic uncertainty and the overall uncertainty were 0.12 ns, 1.91 ns and 1.91 ns, respectively [1] [2]. The all contributions are listed in Table III. As we described above, we introduced few assumptions and the data that came from the models (position, velocity, distance and interval time). The original of the position data that used in the web service is the digital maps which provided by the Geospatial Information Authority of Japan (GSI). The digital maps have errors, which of the horizontal position and the altitude are 18.5 m and 7.2 m, respectively [6]. We introduced 30 km/h as an error of the mean velocity. It seems that it's too much errors, but the effect of the velocity is negligible in the calculation of the relativistic effect in comparison to the ns-level uncertainty. Besides, the

distance error also does not affect so much the calculation. We calculated the systematic uncertainty of the relativistic correction by a velocity error of 30km/h for each ways. As a result, we obtained the systematic uncertainty of the west way and the east way were 51 ps (U_{b5}) and 80 ps (U_{b6}), respectively. The overall uncertainty for CT was concluded as 1.91 ns. Finally, we obtained the differential correction values of the GPS link by CT (C_{GPS}) was 102.26 ns with the uncertainty 1.91 ns. Fig. 5 shows the differential correction values of UTC(NICT)-UTC(KOBE) which were updated from Fig. 1. The CT result agreed well with those by GPS and TWSTFT within its uncertainty.

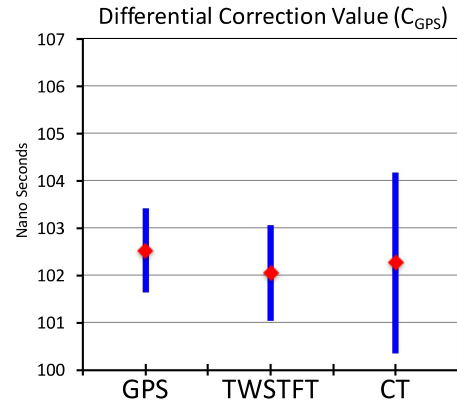


Fig. 5. The differential correction values of GPS link (UTC(NICT)-UTC(KOBE)).

IV. CONCLUSION

The total relativistic time gains/losses by the CT of the west way and the east way were estimated as -1.38 and 2.91 ns respectively. We applied these values for the CT data and re-estimated its uncertainty. Finally, we obtained the differential correction of GPS link by CT was 102.26 ns and the overall uncertainty was 1.91 ns. This result agreed with GPS and TWSTFT results within its uncertainty. This time, we introduced few assumptions and the data that came from models, but the results agreed very well. This suggests that CT still can be used for the remote calibration in the long distance when we apply the appropriate processing include the relativistic effect correction. For further accurate calculation, the appropriate record of the position and time during the transportation of clock is necessary.

In February 2016, we transported the Hydrogen maser from Koganei to Kobe. During the transportation, we carried out the GPS time transfer to record its time variation by feeding 10 MHz signal from H-maser as external reference (Fig. 6). We have not finished the data analysis yet. Further accurate analysis will be expected by the data.

ACKNOWLEDGMENT

We used IGS data and NRCan's PPP software. This experiment was supported by R. Ichikawa and R. Tabuchi. We would like to thank all these co-workers and institutes here.



Fig. 6. The photo of the truck which transported the H-maser while observing GPS

REFERENCES

- [1] H. Takiguchi et al., "Calibration of the NICT's 2nd UTC generation station KOBE by using GPS, TWSTFT and Clock Transportation", Abstract, 2014 IFCS-EFTF, B4P-H, 2014.
- [2] H. Takiguchi et al., "Calibration measurement for the UTC(NICT) decentralization". (*preparing*)
- [3] "Relativistic effects in a coordinate time system in the vicinity of the Earth", Recommendation ITU-R TF.1010-1.
- [4] J. A. Davis and J. McA Steele, "A Caesium Flying Clock Experiment between NPL and USNO", Proc. 11th EFTF, p. 306, 1997.
- [5] Latlonglab, <http://latlonglab.yahoo.co.jp/route/>.
- [6] H. Murakami, "Accuracy Estimation of Digital Map Series Data Sets Published by the Geographical Survey Institute", Geoinformatics, 6, 2, 59-64, 1995.

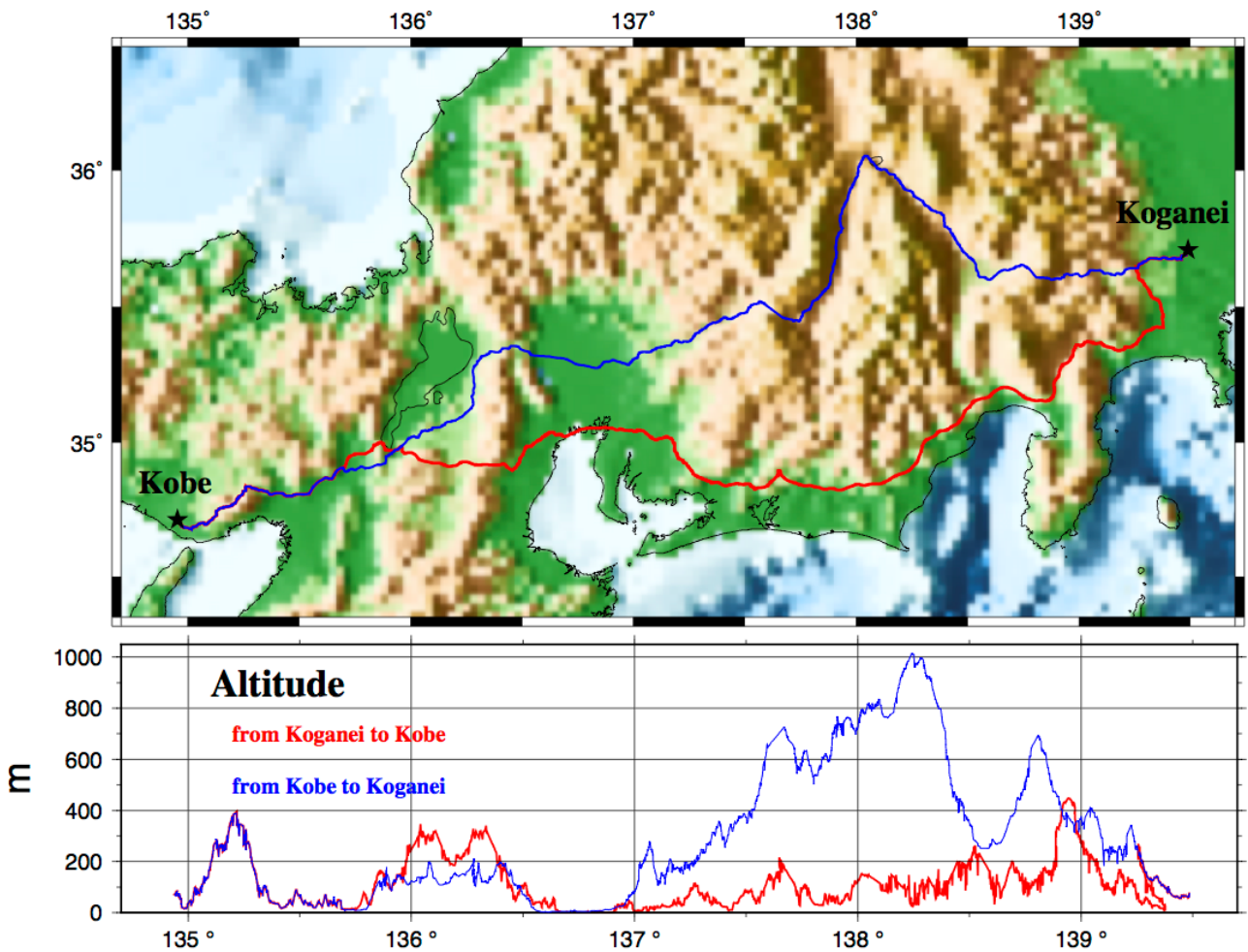


Fig. 2. The map of the driving route, and the altitude. Red line shows the route from Koganei to Kobe (west way). Blue line shows the route from Kobe to Koganei (east way).

S_0 Lamb wave resonators for in-liquid sensing: promising alternative to shear bulk acoustic wave devices

Teona Mirea, Enrique Iborra
GMME-CEMDATIC-ETSIT
Universidad Politécnica de Madrid
Madrid, Spain
teona@etsit.upm.es

Ventsislav Yantchev
Biophysical Technology Laboratory
Chalmers University of Technology
Gothenburg, Sweden

Q-Arts Consulting Ltd.
Sofia, Bulgaria

Abstract— Sensors capable of in-liquid operation are of primary importance not only for biosensors applications but also for liquid monitoring. Thin film electroacoustic (TEA) devices have emerged as promising choice for such applications. The most common TEA devices are the thin film bulk acoustic wave resonator (FBAR) and the Lamb wave resonator (LWR). FBAR operating on the shear mode have been widely studied in view of biosensors applications. A theoretical framework describing the in-liquid sensitivity features of LWR employing the S_0 mode (S_0 -LWR) has been experimentally proven recently. However, a comparison between both devices has not been performed yet. Here we theoretically and experimentally compare AlN-based S_0 -LWR and FBARs on their solidly mounted modality (SMR), in terms of their in-liquid sensitivity features at similar frequencies. S_0 -LWR prove to be slightly more sensitive to the density and viscosity of the liquids. Moreover, if a metallic bottom electrode is not deposited on their backside they can also sense variations in the dielectric permittivity of the liquid, which cannot be done with common SMRs.

Keywords— S_0 -Lamb wave resonator; solidly mounted resonator; AlN; In-liquid; Comparison.

I. INTRODUCTION

The thin film electroacoustic (TEA) [1] technology has gained considerable attention in the sensors field during the last decade. TEA sensors offer resolutions comparable and sometimes even better than their bulk crystal counterparts [2], while providing easier integration and compact sizes. Advances in the TEA field have been possible mainly owing to the successful growth of thin piezoelectric materials. The thin piezoelectric materials that stand out are the ZnO and the AlN. Recent trends have placed the latter as the preferred choice. The most studied devices within the TEA family are the thin film bulk acoustic wave resonator (FBAR) and the Lamb wave resonator (LWR) [2]. FBARs are based on bulk acoustic waves travelling through a piezoelectric film sandwiched between two electrodes. Their structure can be either in suspended form or containing an acoustic reflector (Fig. 1a). The latter is referred to as solidly mounted resonator (SMR). LWRs are also based on acoustic waves propagating within thin piezoelectric films, in this case membranes with thicknesses smaller than the acoustic wavelength; however, the acoustic waves generated in this case are laterally propagating Lamb waves.

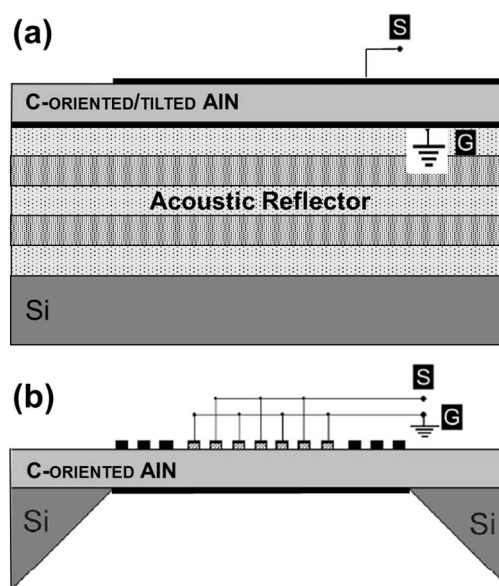


Fig. 1. Structures of (a) SMRs and (b) LWRs.

Although in LWRs motion follows an elliptical form as in typical Rayleigh surface acoustic waves, in thin plates the Lamb waves give rise to a series of symmetric and antisymmetric plate modes with different propagating characteristics. Lamb waves are excited by means of an interdigital transducer (IDT) and confined inside a resonant cavity either by a grating reflector (Fig. 1b) or by edge reflection, also known as contour mode resonators [3, 4].

Recently, shear mode FBARs have been developed in view of biosensors applications [5, 6]. Since these applications necessarily imply in-liquid operation, FBARs need to work on their shear mode, which requires piezoelectric deposition with tilted grains [7]. This technology is still facing challenges in view of uniformity and large scale applicability. On the contrary, Lamb wave resonators employing the S_0 mode (S_0 -LWR) have demonstrated great potential for gravimetric sensors and suitability for in-liquid operation [8] with the advantage of using commercial c -oriented piezoelectric technology. The in-liquid sensing mechanisms and performance of S_0 -LWRs have been thoroughly described only

recently [9, 10], however they have not been compared to their FBAR counterparts.

In this work we make use of a 2D finite element analysis (FEA) to study the in-liquid sensitivity features of AlN-based S_0 -LWRs and compare them to the ones of the commonly used shear mode FBARs, particularly SMRs. Further, with experimental measurements we prove the theoretical predictions. Both devices are studied at same resonant frequencies (~ 900 MHz), i.e. at comparable noise floors, presuming that device Q is dominated by the frequency dependent viscosity losses of liquids.

II. DEVICES AND FEA

The S_0 -LWR structure we employ in this work consists of an IDT composed of 79 Al strips, and two reflector gratings, each consisting of 53 Al strips. The strips width and gap is $3 \mu\text{m}$, which gives an acoustic wavelength of $12 \mu\text{m}$. All the Al strips have a thickness of 270 nm. The device is supported by an AlN membrane $2 \mu\text{m}$ -thick and it is studied with and without a 100 nm-thick Mo floating bottom electrode.

To theoretically assess the response of an S_0 -LWR to the varying properties of a contacting liquid, i.e. density (ρ), viscosity (η) and dielectric permittivity (ϵ), we consider a single cell (an IDT pair) with applied lateral periodic conditions, in contact with the liquid on its backside (Fig. 2). The liquid is modeled as a linear elastic and electric material, whose ρ , η and ϵ we vary. A piezoelectric PML is placed at the bottom of the liquid to absorb the outgoing waves. The model intends to account for the acoustic coupling to the liquid through shear stresses. A detailed description of the model can be found elsewhere [9, 10].

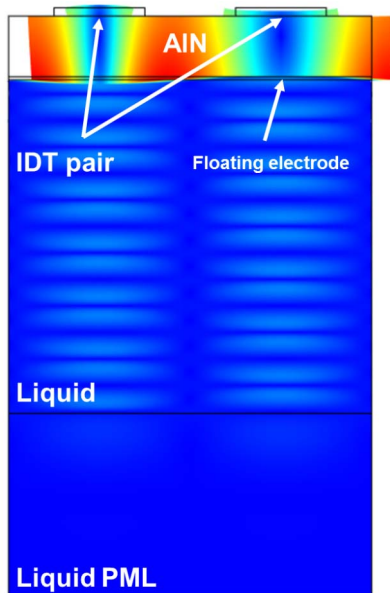


Fig. 2. FEA simulated displacements of the S_0 -LWR – liquid structure.

The structure of the SMR consists of a $1.6 \mu\text{m}$ -thick AlN film with tilted grains, sandwiched between a 160 nm-thick Ir bottom electrode and a 500 nm-thick Mo top electrode. All

these are placed onto an acoustic reflector composed of five 741 nm-thick SiO_x / 872 nm-thick Mo composites. This structure allows for an 889 MHz resonant frequency. As for the S_0 -LWR, the theoretical assessment is performed on a cell with applied lateral periodic conditions. However, in this case the liquid is placed on the top electrode, the AlN domain is defined using a rotated system with a 24° rotation about an out-of-plane axis, and a second PML needs to be placed at the bottom of the Si substrate (Fig. 3)

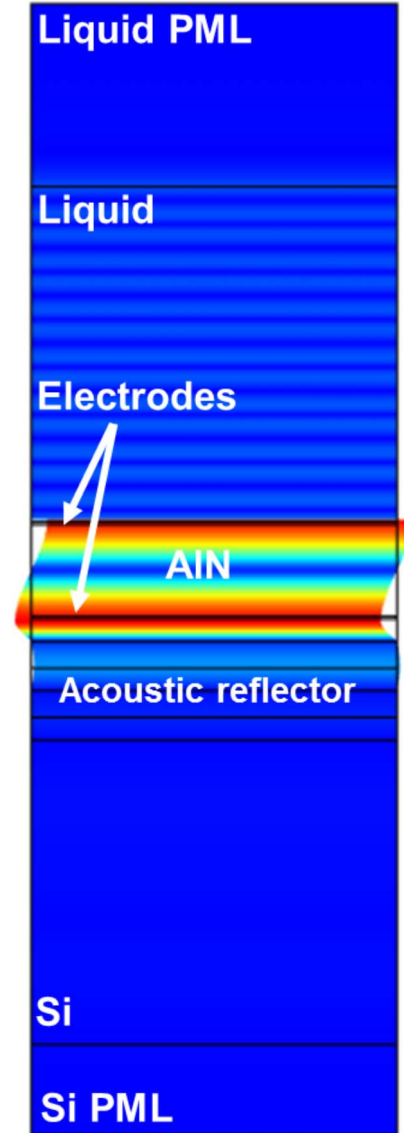


Fig. 3 FEA simulated displacements of the SMR – liquid structure.

III. EXPERIMENTAL METHODS

For both devices, AlN piezoelectric films are deposited in an ultra-high-vacuum system, pumped to a base pressure below 8×10^{-7} Pa. A high purity 150 mm Al target, located at a distance of 55 mm from the substrate, is sputtered in an Ar/ N_2 (40:60) mixture using a pulsed-DC source operating at 50 kHz. In order to optimize film stress, a low bias value (< -55 V) is applied to the substrate. To release the AlN membrane of the S_0 -LWR a

three step Bosch process is used. In the case of the SMR, AlN films are grown with tilted grains (with $\sim 24^\circ$ c -axis tilt) by using an initial AlN seed layer technique and subsequently an out of axis deposition [11]. A 1.6 μm -thick tilted AlN film is chosen to prevent peeling of the layer due to the high interfacial stresses associated with the tilted AlN growth. This necessarily implies the use of thick top Mo electrode to achieve about 900MHz resonance frequency. Thin film sputter deposition is used for Al, Mo and SiO_x layers, while Ir films are evaporated.

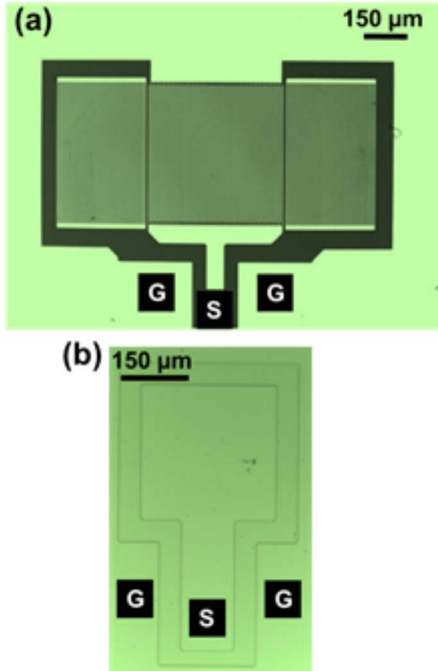


Fig. 4. Plain optical images of (a) an actual S_0 -LWR and (b) an SMR.

S_0 -LWRs (Fig. 4a) demonstrate resonant frequencies of about 850MHz and 870MHz, with and without floating Mo electrode respectively, Q factors in air of about 1200 and $k_{\text{eff}}^2 \sim 0.5\%$. At the same time, SMRs (Fig. 4b) demonstrate a shear resonant frequency of about 889 MHz, Q factors in air of around 350 and $k_{\text{eff}}^2 \sim 3.5\%$.

The testing liquids consist of ethylene glycol-water mixtures with ethylene glycol weight in water varying from 0% to 72%. ρ values are in the range of 995 kg/m^3 (H_2O) – 1087 kg/m^3 , η in the range of 0.972 mPa (H_2O) – 4.76 mPa, and ϵ from $80\epsilon_0$ (H_2O) to $55\epsilon_0$. Solutions are fed, by droplet dispensing, to the backside cavity of S_0 -LWRs and on the top electrode of SMRs.

IV. RESULTS AND DISCUSSION

In Fig. 5 we plot the theoretical and experimental frequency shifts of both, S_0 -LWRs and SMRs, vs the varying $(\rho\eta)^{0.5}$ of the ethylene glycol-water mixtures. Additionally, for S_0 -LWRs with open bottom surface, i.e. without a floating bottom electrode, we also represent the frequency shifts induced by the corresponding ϵ of each mixture (top axis).

Firstly, we indicate that the theoretical FEA predictions are in good agreement with the experimental results. Thus the developed FEA model [10] is valid not only for studying the interaction of S_0 -LWRs with liquids, but also for SMRs.

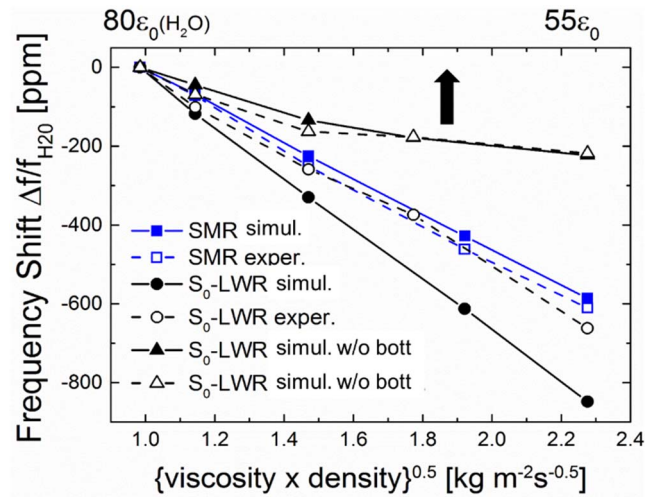


Fig. 5 Simulated and experimental frequency shifts of S_0 -LWR, with and without floating bottom electrode, and SMR, induced by the different $(\rho\eta)^{0.5}$ of the liquid mixtures. On the top axis the ϵ of the mixtures is indicated

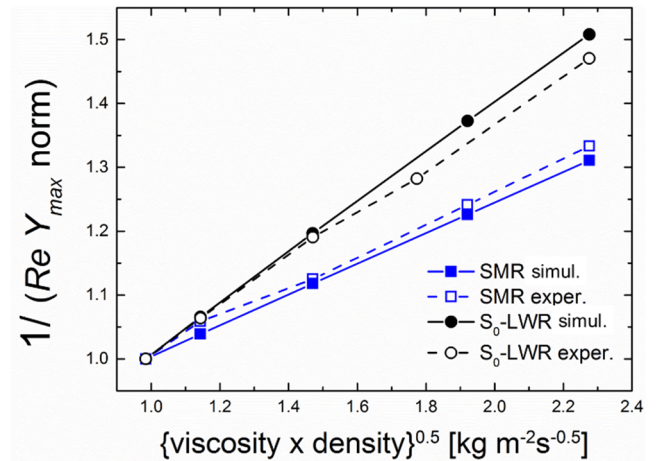


Fig. 6 Simulated and experimental losses induced on S_0 -LWR and SMR by the different liquid mixtures. Losses are represented by the inverse of the conductance maximum.

Secondly, that S_0 -LWRs with floating bottom electrode, that is, electrically shielded from the liquid, move in the same range of sensitivity than SMRs. The predicted higher sensitivity of S_0 -LWRs is in good agreement with Fig. 6, where we plot the losses induced on the devices (represented by the inverse of conductance maximum) by the liquids $(\rho\eta)^{0.5}$. Here it is seen that a higher sensitivity implies increased losses. In other words, the higher the sensitivity is the higher the energy losses are, since more energy is confined into the liquid. We attribute the deviation of the experimental results from S_0 -LWRs in Fig. 5 to marginal errors in the measurements. Moreover, the lower sensitivity of the SMRs was somehow expected since part of their energy is lost in the acoustic reflector and does not contribute to the sensing process.

Finally, if the S_0 -LWRs are not electrically shielded from the liquid (without floating bottom electrode) changes in the ϵ of the liquid also influence. In previous works [9, 10] it was

stated that the decrease in ε induces positive shifts in frequency due to variations in the k_{eff}^2 of the resonators. Since, $(\rho\eta)^{0.5}$ is increased with solute concentration and ε is decreased, what we see in Fig. 5 is a superposition of both influences. From results with and without floating bottom electrode, a sensitivity to ε can be extracted.

V. CONCLUSIONS

Several conclusions can be extracted from this work:

- A FEA model that was proved to correctly describe the in-liquid sensitivity features of S_0 -LWRs, has also been proven to work for SMR.
- The sensitivity to $(\rho\eta)^{0.5}$ is higher for S_0 -LWRs (with floating bottom electrode) than for SMRs. This is mainly due to the energy lost in the acoustic reflectors composing the SMR, while in S_0 -LWRs the energy is better confined inside the resonant cavity, contributing thus in a bigger proportion to the sensing mechanism.
- The higher sensitivity of S_0 -LWRs is also translated to increased induced losses.
- If a floating bottom electrode is not used in S_0 -LWRs, they also sense the variations of ε in the liquid, which cannot be done with SMRs.
- For an in-liquid shear operation with high performance, SMRs need AlN deposition with tilted grains, while S_0 -LWRs use c -oriented AlN films. The tilted grains technology is still facing challenges in terms of uniformity and scalability, while the c -oriented technology is already mature and industrialized.

ACKNOWLEDGMENT

This work was partially supported by the European Commission through the 7th Framework Programme by the RaptDiag project HEALTH-304814, by COST action IC1208, and by Ministerio de Economía y Competitividad del Gobierno de España through project MAT2013-45957-R.

REFERENCES

- [1] K.M. Laikin, "Thin Film Resonator Technology", IEEE Trans. Ultrason., Ferroelect., Freq. Control, Vol. 52, No. 5, pp. 707–716, 2005.
- [2] I. Katardjiev, V. Yantchev, "Recent developments in thin film electro-acoustic technology for biosensor applications", Vacuum, Vol. 86, pp. 520–531, 2012.
- [3] Chi-Ming Lin, V. Yantchev, Yung-Yu Chen and A. Pisano, "Micromachined One-Port Aluminum Nitride Lamb Wave Resonators Utilizing the Lowest-Order Symmetric Mode", IEEE J. Microelectromech. Syst., Vol. 23, No. 1, pp. 78–91, 2014
- [4] V. Yantchev and I. Katardjiev, "Thin film Lamb wave resonators in frequency control and sensing applications: a review", J. Micromech. Microeng., Vol. 23, pp. 043001-14, 2013.
- [5] J. Weber et al., "Shear mode FBARs as highly sensitive liquid biosensors", Sens. Actuators A Phys., Vol. 128, pp. 84–88, 2006.
- [6] G. Wingqvist, J. Bjurström, L. Liljeholm, V. Yantchev and I. Katardjiev, "Shear mode AlN thin film electro-acoustic resonant sensor operation in viscous media", Sens. Actuators B Chem., Vol. 123, pp. 466–473, 2007.

- [7] D.S. Ballantine, "Acoustic Wave Sensors; Theory, Design and Physicochemical Applications", Academic Press, 1997.
- [8] Lilia Arapan, Emil Anderås, Ilia Katardjiev and Ventsislav Yantchev, "Sensitivity Features of Thin Film Plate Acoustic Wave Resonators", IEEE Sensors J., Vol. 11, No. 12, pp. 3330–3331, 2011.
- [9] T. Mirea and V. Yantchev, "Influence of liquid properties on the performance of S_0 -mode Lamb wave sensors: a theoretical analysis", Sens. Actuators B Chem., Vol. 208, pp. 212–219, 2015.
- [10] T. Mirea, V. Yantchev, J. Olivares and E. Iborra, "Influence of liquid properties on the performance of S_0 -mode Lamb wave sensors II: Experimental validation", Sens. Actuators B Chem., Vol. 229, pp. 331–337, 2016.
- [11] J. Bjurström, G. Wingqvist and I. Katardjiev, "Synthesis of textured thin piezoelectric AlN films with a nonzero c -axis mean tilt for the fabrication of shear mode resonators", in Proc. 2005 IEEE Ultrasonics Symposium, pp. 321–324.

Sensitivity to a variation of m_e/m_p from splittings between $^{12}\text{C}_2\text{HD}$ reference frequencies

Florin Lucian Constantin
Laboratoire PhLAM, CNRS UMR 8523
Villeneuve d'Ascq, France

Abstract—The sensitivity to a variation of μ of the $2\nu_1$ and $\nu_1+\nu_3+\nu_5$ bands transitions of $^{12}\text{C}_2\text{HD}$ in the 193-199 THz spectral domain is calculated with an effective Hamiltonian for the Coriolis interaction between the $[200(00)^0_e]$ and $[101(01)^1_e]$ energy levels. The frequency splittings between near resonant transitions have sensitivity coefficients to a variation of μ of both signs in the range of 10^{-10} . The degeneracy is due to a cancellation of effective rotational intervals with frequency shifts associated to the vibrational band origins, the anharmonicity and the rotation-vibration interactions. The measurements of a temporal drift of a frequency splitting against the Cs hyperfine frequency may constrain the time variation of μ better than the time variations of α , g_{Cs} . The systematic frequency shifts are evaluated for intracavity saturated absorption spectroscopy measurements and constrain the measurement of a variation of μ at $\sim 10^{-10}$. The comparison between measurements of frequency splittings with sensitivity coefficients of both signs may discriminate a variation of μ at $\sim 8 \times 10^{-11}$.

Keywords— Proton-to-electron Mass Ratio Constant; Acetylene Reference Lines; Rovibrational Transitions; Rovibrational Interactions; Sensitivity to a Variation of the Fundamental Constants

I. INTRODUCTION

A possible variation of the fundamental constants has been addressed in the context of modern theories [1]. A variation of the quantum electrodynamics (QED) coupling constant, the fine structure constant α , would imply in the grand unification theories approaches a variation of the quantum chromodynamics (QCD) strength scale and quark masses. A variation of the proton-to-electron mass ratio leads to a change of the scale of masses in the QED and QCD. Nuclear g-factors changes are associated to variations of the QCD strength scale and quark masses. Atomic hyperfine spectra have been conveniently used to constraint a possible variation of α [2]. Fractional variation of the proton to electron mass ratio is expected to be higher [3]. Molecular spectra are intrinsically sensitive to $\mu=m_e/m_p$. A variation of μ has been probed by absolute frequency measurements of molecular clocks based, for example, on ammonia rotation-inversion transitions detected in a fountain [4], respectively rovibrational transitions of trapped molecular hydrogen ions [5] or diatomic molecules in optical traps [6] and on a two-photon transition on a molecular beam [7] which constraint μ at $5.6 \times 10^{-14} \text{ yr}^{-1}$ level. In addition, it has been pointed out that the splitting between near resonant molecular energy levels has an enhanced sensitivity to a variation of the constants (for a review see [8]).

Isotopic acetylene transitions provide frequency references in the spectral domain at 1.5 μm . The $2\nu_1$ band transitions of $^{12}\text{C}_2\text{HD}$ have been investigated by Fourier-transform spectroscopy [9], the rotational constants and band origins have been reported in [10], the high-resolution spectra have been investigated in [11] and a global fit has been reported in [12]. In addition, the small dipole moment of $^{12}\text{C}_2\text{HD}$ allows microwave spectra. Diode laser spectroscopy has been performed in with an accuracy of 10 MHz [13]. Absolute frequency measurements of $2\nu_1$ band transitions have been performed by Doppler-free spectroscopy with an accuracy of ~ 1 kHz [14]. This contribution presents calculations of the sensitivity of $^{12}\text{C}_2\text{HD}$ rovibrational transitions to a variation of μ located in the 193-199 THz spectral domain using a Hamiltonian accounting for the rovibrational couplings and an accurate set of molecular parameters. Near resonant transitions are identified in $^{12}\text{C}_2\text{HD}$ spectra and display small frequency splittings with enhanced sensitivity coefficients to a variation of μ . The absolute measurements of these frequency splittings may constrain better a variation of μ than variations of other fundamental constants.

II. MOLECULAR ENERGY LEVELS, TRANSITIONS AND SENSITIVITIES

The vibrational energy levels are described by normal vibrational modes $v=[v_1v_2v_3(v_4^{14}v_5^{15})^1]$, where v_s are vibrational quantum numbers, l_k quantum numbers of the degenerate modes $k=4,5$, $l_k=\pm v_k, \pm(v_k-2), \dots, \pm 1$ or 0 and $l=|l_4+l_5|$ the quantum number of the projection of the vibrational angular momentum on the molecular axis. The rotational energy levels are described in the basis of the rotational angular quantum number J . The parity of the vibrational levels is defined with labels e and f . The diagonal energy levels in the Hamiltonian are expressed in the Born-Oppenheimer approximation as the sum of a vibrational term and a rotational term. The vibrational term is expressed as:

$$G[v] = \sum_s \omega_s (v_s + g_s/2) + \sum_{ss'} x_{ss'} (v_s + g_s/2)(v_{s'} + g_{s'}/2) + \sum_{kk'} g_{kk'} l_k l_{k'} \quad (1)$$

in function of the normal mode frequency ω_s , degeneracy g_s , anharmonicity $x_{ss'}$, and anharmonic contribution of the degenerate vibrational modes $g_{kk'}$. Harmonic frequency is defined in terms of the normal mode frequency and first-order anharmonicities:

$$\omega_s^0 = \omega_s + x_{ss}g_s + \sum_{s' \neq s} x_{ss'}g_{s'}/2 \quad (2)$$

The rotational term is expressed as:

$$F_R[J, I] = B[v] \left[J(J+1) - I^2 \right] - D[v] \left[J(J+1) - I^2 \right]^2 + H[v] \left[J(J+1) - I^2 \right]^3 + L[v] \left[J(J+1) - I^2 \right]^4 \quad (3)$$

with the rotational constant $B[v]$ and centrifugal distortion constants $D[v]$, $H[v]$, $L[v]$. They are expressed in function of the rotation-vibration constants α_s , β_s and the rotational constants at equilibrium B_e , D_e , H_e , L_e , respectively in the ground state B_0 , D_0 , H_0 , L_0 :

$$B[v] = B_e - \sum_s \alpha_s (v_s + g_s/2) = B_0 - \sum_s \alpha_s v_s$$

$$D[v] = D_e + \sum_s \beta_s (v_s + g_s/2) = D_0 + \sum_s \beta_s v_s \quad (4)$$

$$H[v] = H_e \cong H_0, L[v] = L_e \cong L_0$$

The effective Hamiltonian matrix models the Coriolis interaction between $[20000] \Sigma$ and $[101(01)^{1c}] \Pi^e$ states:

$$\begin{pmatrix} E[20000] \langle 0^0 0^0 \rangle^0, JJ & \xi \sqrt{J(J+1)} \\ \xi \sqrt{J(J+1)} & E[101(01)^{1c}] \langle 0^0 1^1 \rangle^1, JJ \end{pmatrix}$$

$$E[20000] \langle 0^0 0^0 \rangle^0, JJ = v_\Sigma + B_\Sigma J(J+1) - D_\Sigma [J(J+1)]^2 + H_\Sigma [J(J+1)]^3 + L_\Sigma [J(J+1)]^4 \quad (5)$$

$$E[101(01)^{1c}] \langle 0^0 1^1 \rangle^1, JJ = v_\Pi + B_\Pi [J(J+1) - I] - D_\Pi [J(J+1) - I]^2 + H_\Pi [J(J+1) - I]^3 + L_\Pi [J(J+1) - I]^4$$

depending on the off-diagonal Coriolis constant ξ . There is an additional Fermi interaction between the levels $[110(02)^{0c}]$ and $[20000]$ levels with an off-diagonal term $W = (k_{1255}/4) \times 2^{3/2}$, depending on the anharmonic interaction constant, that leads a shift of the vibrational levels determined at the first-order of perturbation by $W^2/\Delta_{1255,11}$, where $\Delta_{1255,11} = G[20000] - G[110(02)^0]$. The energy levels are expressed at the first order in $J(J+1)$ leading to:

$$v_\Sigma = G[20000] + W^2/\Delta_{1255,11}$$

$$B_\Sigma = B[20000] - (W/\Delta_{1255,11})^2 (B[20000] - B[11002]) \quad (6)$$

Parameters used in the Hamiltonian have been derived by fitting experimental data [11,13,14] and are listed in Table 1 with their sensitivity coefficient to a variation of μ . Noteworthy, the Fermi interaction term can be expressed in function of molecular parameters that allows to derive its sensitivity coefficient of 1. The Fermi interaction shifts the $2\nu_1$ vibrational band frequency with the quantity $\delta v_\Sigma = W^2/\Delta_{1255,11} = 8934$ GHz estimated with the values of parameters from [12]. Its sensitivity coefficient $K_{W^2/\Delta_{1255,11}} = 2.23$ is calculated using the value of W and the dependence of $\Delta_{1255,11}$ on $\omega_{ss'}$, $x_{ss'}$. Similarly, the term $(W/\Delta_{1255,11})^2 = 3.66 \times 10^{-3}$ have a sensitivity coefficient of 2.45. The term $B[20000] - B[11002]$ is estimated with the values of α_s from [11] and have a sensitivity coefficient of 3/2. The contribution of the Fermi interaction to the effective rotational constant of the $2\nu_1$ vibrational band is therefore to add a term $\delta B_\Sigma = 38.7$ GHz with a sensitivity coefficient of 3.95. The

sensitivity coefficient for the fitted value of v_Σ , respectively v_Π , is calculated from its value [13] and the linear dependence on $\omega_{ss'}$, $x_{ss'}$, $g_{kk'}$ and, for v_Σ , on the supplementary term $W^2/\Delta_{1255,11}$. The sensitivity coefficient of the fitted value of B_Σ , respectively B_Π , is calculated from the its value [13] and the linear dependence on B_e , α_s and, for B_Σ , on the additional contribution of the term $W/\Delta_{1255,11}$. The contribution of the Coriolis interaction can be analogously discussed using the first-order of perturbation and expansion in power series of $J(J+1)$. The Coriolis interaction couples vibrational levels with a total difference between the quantum numbers $\Delta v = 4$ and the sensitivity coefficient for the Coriolis term is 3 from the dependence on the molecular parameters.

TABLE I. PARAMETERS FOR THE ROVIBRATIONAL HAMILTONIAN

Constant	Value (GHz)	K_A	Constant	Value (GHz)	K_A
B_0	29.725210	0.99809	ω_4^0	15511.193	0.49
$D_0 (\times 10^6)$	34.0468	2.006	ω_5^0	20268.6	0.49
$H_0 (\times 10^{12})$	37.2	3	x_{11}	-1570	1
$\alpha_1 (\times 10^3)$	145.6901	1.5	x_{12}	-188	1
$\alpha_2 (\times 10^3)$	128.7196	1.5	x_{13}	-163	1
$\alpha_3 (\times 10^3)$	200.8390	1.5	x_{14}	-143	1
$\alpha_4 (\times 10^3)$	-79.3056	1.5	x_{15}	-538.7	1
$\alpha_5 (\times 10^3)$	-44.5353	1.5	x_{22}	-171	1
$\beta_1 (\times 10^8)$	-30.0737	2.5	x_{23}	-604.1	1
$\beta_2 (\times 10^{10})$	-240	2.5	x_{24}	-110	1
$\beta_3 (\times 10^8)$	-188.26	2.5	x_{25}	-75.8	1
$\beta_4 (\times 10^8)$	107.3	2.5	x_{33}	-684.7	1
$\beta_5 (\times 10^8)$	44.762	2.5	x_{34}	-421.2	1
B_Σ	29.37764	0.99314	x_{35}	-85.1	1
$D_\Sigma (\times 10^6)$	34.713	1.9973	x_{44}	-6.4461	1
$H_\Sigma (\times 10^{12})$	39.45	3	x_{45}	25.618	1
$L_\Sigma (\times 10^{15})$	-48.9	4	x_{55}	-74.5851	1
B_Π	29.42610	0.99294	g_{44}	65.74524	1
$D_\Pi (\times 10^6)$	33.73	1.9804	g_{45}	20.9940	1
$H_\Pi (\times 10^{12})$	287	3	g_{55}	155.8845	1
$L_\Pi (\times 10^{15})$	-48.9	4	W	147.959	1
v_Σ	196946.1268	0.4718	$\Delta_{1255,11}$	2446	-0.23
v_Π	197010.2713	0.4811	$\delta v_\Sigma (\times 10^3)$	8934	2.23
ω_1^0	101550	0.49	$\delta B_\Sigma (\times 10^6)$	38.7	3.95
ω_2^0	55742.2	0.49	$\xi (\times 10^3)$	1384	3
ω_3^0	78120.8	0.49			

The Hamiltonian matrix is calculated for each J value and numerically diagonalized. That allows to predict transitions of the $2\nu_1$ and $\nu_1 + \nu_3 + \nu_5$ band transitions for J up to 45. The shift with the $2\nu_1$ band transitions measured in [14] up to $J=27$ with an accuracy of 1 kHz is less than 128 MHz and with the $\nu_1 + \nu_3 + \nu_5$ band transitions measured in [13] up to $J=47$ with an accuracy of 10 MHz is less than 0.4 GHz. For a given fractional variation of μ , the Hamiltonian parameters are incremented in proportion with their sensitivity coefficient and a set of μ -dependent frequencies are calculated. Sensitivity of these transitions is calculated as the slope of the frequency shift for a fractional variation of μ of 10^{-7} . Figure 1 displays the dependence of the sensitivity on the predicted rovibrational frequencies. The sensitivity coefficient of the frequency splitting between two transitions is the slope of the line between the corresponding data points in this plot. Although the frequency splitting is set positive and the sensitivity

coefficient may have positive or negative values (Figure 2) that is the frequency splitting increases or decreases for an increase of μ . At near resonance, the frequency splitting displays a highly enhanced sensitivity coefficient by $\pm 10^3$. The sensitivity coefficient varies rapidly when J changes by a unit for both transitions.

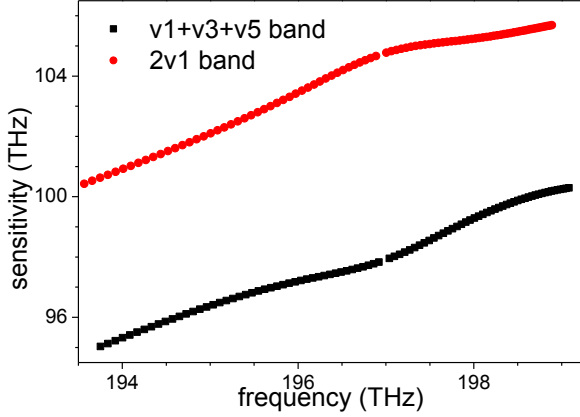


Fig. 1. Dependence of the sensitivity to a variation of μ on the frequency of $^{12}\text{C}_2\text{HD}$ rovibrational transitions

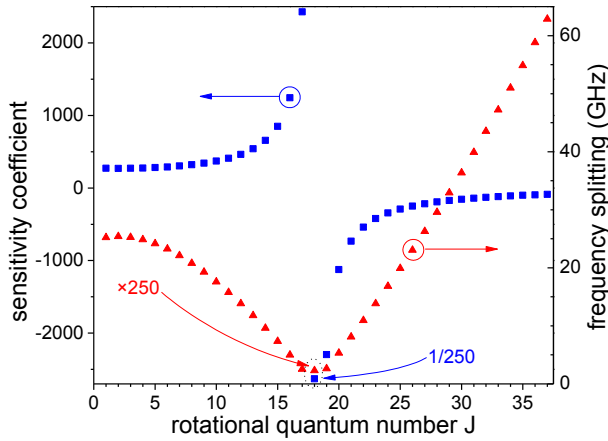


Fig. 2. Dependence on the rotational quantum number J of the sensitivity coefficient (blue squares, left axis) and of the frequency splitting (red triangles, right axis) of near resonant transitions P(J+1) of the $v_1+v_3+v_5$ band and P(J) of the $2v_1$ band.

III. EXPERIMENTAL APPROACH

Isotopic acetylene reference transitions are probed in a Fabry-Perot cavity for Doppler-free saturated absorption spectroscopy. The setup provides excellent metrological performances recognized by the *Comité International des Poids et Mesures* that recommended P(16) transition of the

$^{13}\text{C}_2\text{H}_2$ v_1+v_3 band as reference for absolute frequency [15]. Absolute measurements of $^{12}\text{C}_2\text{HD}$ lines of $2v_1$ band were performed with frequency combs techniques at National Research Council of Canada (NRC) [14]. The experimental setup is based on an extended cavity laser diode with external electro-optic modulation that is locked with the Pound-Drever-Hall method to a Fabry-Perot cavity filled with acetylene. The length of the cavity is modulated with a piezoelectric ceramic and the transmitted signal is demodulated at $3f$ to lock the cavity on the saturated absorption line. The short term (<1 s) laser linewidth is <50 kHz. The Allan fractional stability is 5×10^{-12} at 1 s and decreases to reach a floor of 5×10^{-13} at 100 s. Frequency reproducibility is 1 kHz on a day-to-day timescale.

Consider two similar laser systems locked on adjacent $^{12}\text{C}_2\text{HD}$ lines. The beatnote detected on a fast photodetector is counted against the Cs hyperfine frequency. The fractional time variation of the ratio between the frequency splitting and the Cs hyperfine frequency is expressed in terms of the fractional time variation of the fundamental constants as:

$$\frac{d \ln(X / f_{\text{Cs}})}{dt} = (d_{\mu} \ln X - 1) \frac{d \ln \mu}{dt} - (2 + A_{\text{HFS}}(\text{Cs})) \frac{d \ln \alpha}{dt} - \frac{d \ln g_{\text{Cs}}}{dt} \quad (7)$$

The fractional time variation of the Cs hyperfine frequency depends linearly on the fractional time variation of α with a sensitivity factor $A_{\text{HFS}}(\text{Cs})=0.83$ [16] and on the Cs g-factor g_{Cs} . A small linear time variation of the fundamental constants leads to a small linear time variation of the frequency ratio. The contribution of the fractional time variation of μ is amplified by the sensitivity coefficient $d_{\mu} \ln X$ comparing to the contributions of the fractional time variations of α , g_{Cs} . The measurement of a temporal drift leads to a tighter constraint on a possible variation of μ comparing to the constraints on α , g_{Cs} . Experimental evidence should be interpreted cautiously, by accounting the frequency drifts arising from the systematic effects.

The systematic frequency shifts have been measured for the reference P(16) line of $^{12}\text{C}_2\text{HD}$ $2v_1$ band [14]. It is anticipated that other lines from the $2v_1$ and $v_1+v_3+v_5$ bands have similar sensitivities to a variation of the experimental parameters. The power shift of -1.6 kHz/W leads to a frequency shift of -0.32 kHz and an uncertainty of 0.16 kHz. The pressure shift of 0.2 kHz/Pa leads to frequency shift of 0.4 kHz and an uncertainty of 0.14 kHz. The frequency shifts arising from the modulation technique and the offsets of the detection at $3f$ should be accounted cautiously because they depend on the laser system design. The modulation shift of 0.84 kHz/MHz_{pp} leads to a frequency shift of -1.51 kHz and an uncertainty of 0.17 kHz. The electronic offsets lead to an uncertainty estimated at 0.7 kHz. The systematic frequency shifts subtract for a frequency splitting. It displays therefore smaller systematic effects and uncertainties than that of a single line. They can be derived by extensive measurements of the systematic effects for the acetylene reference frequency grid. The systematic frequency shift for a frequency splitting is estimated here as that of the

reference P(16) line of the $2\nu_1$ band with a total uncertainty of 0.75 kHz.

IV. RESULTS AND DISCUSSION

Near resonant transitions arise in the rovibrational spectra at the lowest order of approximation from the compensation between effective rotational intervals with frequency splittings associated to the vibrational band origins, the anharmonicity or the rotation-vibration interactions.

Consider the measurement of the temporal drift of the P(16) line frequency of the $2\nu_1$ band with a sensitivity coefficient of 0.5274 against the Cs hyperfine frequency. The systematic uncertainties evaluated as above constrain the measurement of a possible variation of μ at 8.1×10^{-12} , if the variations of α , g_{Cs} are neglected. The measurement of a temporal drift of the frequency splitting between the P(20) line of the $\nu_1 + \nu_3 + \nu_5$ band and the P(19) line of the $2\nu_1$ band with a sensitivity coefficient of -2297 constrain a possible variation of μ at 1.2×10^{-10} , while possible variations of α , g_{Cs} are constrained at $\sim 10^{-7}$. Consider also the measurement of a temporal drift for near resonant transitions with a similar splitting and a sensitivity coefficient of opposite sign. The frequency splitting between the P(17) line of the $2\nu_1$ band and P(18) line of the $\nu_1 + \nu_3 + \nu_5$ band has a sensitivity coefficient of 2428. Comparison of the results of these measurements allows to discriminate the possible variation of μ . The systematic uncertainty increases by a factor of $\sim 2^{1/2}$ while the effective sensitivity coefficient increases by a factor of 2, that constrain a variation of μ at 8×10^{-11} .

V. CONCLUSION

This contribution presents the calculation of the sensitivity to a variation of μ for the $2\nu_1$ and $\nu_1 + \nu_3 + \nu_5$ bands transitions of $^{12}C_2HD$. These transitions may provide frequency references in the 193-199 THz spectral domain with an experimental setup based on intracavity saturated absorption spectroscopy with 0.75 kHz accuracy. Near resonant transitions arise in the molecular spectra from the compensation between effective rotational intervals with frequency shifts associated to the vibrational band origin, the anharmonicity and the rotation-vibration interactions. Their frequency splitting has an enhanced sensitivity coefficient to a variation of μ . The measurements of a temporal drift of a small frequency splitting against the Cs hyperfine frequency may constrain the time variation of μ better than the time variations of α , g_{Cs} . The systematic frequency shifts constrain the measurement of a variation of μ at $\sim 10^{-10}$. The comparison between measurements of frequency splittings with sensitivity coefficients of both signs may discriminate a variation of μ at $\sim 8 \times 10^{-11}$.

REFERENCES

[1] J. -P. Uzan, "The fundamental constants and their variation: observational and theoretical status," *Rev. Mod. Phys.* vol. 75, no. 2, pp. 403-455, Apr. 2003.

[2] S. N. Lea, "Limits to time variation of fundamental constants from comparisons of atomic frequency standards," *Eur. Phys. J. Special Topics* vol. 163, no. 5, pp. 37-53, May 2008.

[3] X. Calmet and H. Fritzch, "The cosmological evolution of the nucleon mass and the electroweak coupling constants," *Eur. Phys. J. C* vol. 24, no. 4, pp. 639-642, Jun. 2002.

[4] H. L. Bethlem, M. Kajita, B. Sartakov, G. Meijer, and W. Ubachs, "Prospects for precision measurements on ammonia molecules in a fountain," *Eur. Phys. J. Special Topics* vol. 163, no. 5, pp. 55-69, May 2008.

[5] S. Schiller and V. Korobov, "Tests of time independence of the electron and nuclear masses with ultracold molecules," *Phys. Rev. A* vol. 71, no. 3, pp. 032505-1-032505-7, Mar. 2005.

[6] M. Kajita, "Sensitive measurement of mp/me variance using vibrational transition frequencies of cold molecules," *New J. Phys.* vol.11, no. 5, pp. 055010-1-055010-19, May 2009.

[7] A. Shelkownikov, R. J. Butcher, C. Chardonnet, and A. Amy-Klein, "Stability of the proton-to-electron mass ratio," *Phys. Rev. Lett.* vol. 100, no. 15, pp. 150801-1-150801-4, Apr. 2008.

[8] P. Jansen, H. L. Bethlem, and W. Ubachs, "Perspective: Tipping the scales: Search for drifting constants from molecular spectra," *J. Chem. Phys.* vol. 140, no. 1, pp. 010901-1-010901-13, Jan. 2014.

[9] C. Latrasse, M. Breton, M. Tetu, N. Cyr, R. Roberge, and B. Villeneuve, " C_2HD and $^{13}C_2H_2$ absorption lines near 1530 nm for semiconductor-laser frequency locking," *Opt. Lett.* Vol. 19, no. 22, pp. 1885-1887, Nov. 1994.

[10] J. Lievin, M. A. Tamsamani, P. Gaspard, M. Hermann, "Overtone spectroscopy and dynamics in monodeuteroacetylene (C_2HD)," *Chem. Phys.* vol. 190, no. 2-3, pp. 419-445, Jan. 1995.

[11] L. Fusina, F. Tamassia, and G. Di Lonardo, "The infrared spectrum of $^{12}C_2HD$: the stretching-bending combination bands in the 1800-4700 cm^{-1} region," *Mol. Phys.* vol. 103, no. 19, pp. 2613-2620, Apr. 2005.

[12] M. Herman, C. Depiesse, G. Di Lonardo, A. Fayt, L. Fusina, D. Hurtmans, S. Kassi, M. Mollabashi, and J. Vander Auwera, "The vibration-rotation spectrum of $^{12}C_2HD$: new overtone bands and global vibrational analysis," *J. Mol. Spectr.* vol. 228, no. 2, pp. 499-510, Dec. 2004.

[13] J. L. Hardwick, Z. T. Martin, E. A. Schoene, V. Tyng, and E. N. Wolf, "Diode laser absorption spectrum of cold bands of C_2HD at 6500 cm^{-1} ," *J. Mol. Spectr.* vol. 239, no.2, pp. 208-215, Oct. 2006.

[14] J. Jiang, J. E. Bernard, A. A. Madej, A. Czajkowski, S. Drissler, and D. J. Jones, "Measurement of acetylene-d absorption lines with a self-referenced fiber laser frequency comb," *J. Opt. Soc. Am. B* vol. 24, no. 10, pp. 2727-2735, Oct. 2007.

[15] T. J. Quinn, "Practical realization of the definition of the metre, including recommended radiations of other optical frequency standards (2001)," *Metrologia* vol. 40, no. 2, pp. 103-133, Apr. 2003.

[16] V. V. Flambaum and A. F. Tedesco, "Dependence of nuclear magnetic moments on quark masses and limits on temporal variation of fundamental constants from atomic clock experiments," *Phys. Rev. C* vol. 73, no. 5, pp. 055501-1-055501-9, May 2006.

Utilising diffractive optics towards a compact, cold atom clock

James P. McGilligan, Rachel Elvin, Paul F. Griffin, Erling Riis and Aidan S. Arnold
Experimental Quantum Optics and Photonics Group University of Strathclyde
Glasgow, United Kingdom
Email: james.mcgilligan@strath.ac.uk

Abstract—Laser cooled atomic samples have resulted in profound advances in precision metrology [1], however the technology is typically complex and bulky. In recent publications we described a micro-fabricated optical element, that greatly facilitates miniaturisation of ultra-cold atom technology [2], [3], [4], [5].

Portable devices should be feasible with accuracy vastly exceeding that of equivalent room-temperature technology, with a minimal footprint. These laser cooled samples are ideal for atomic clocks. Here we will discuss the implementation of our micro-fabricated diffractive optics towards building a robust, compact cold atom clock.

I. INTRODUCTION

The continued research into atomic clocks in recent decades has lead to a considerable rise in the achievable accuracy and stability. This stability is most notable in the atomic fountain and lattice clocks, measuring frequencies at the $10^{-16}\tau^{-1/2}$ and $10^{-18}\tau^{-1/2}$ level respectively [6], [7], [8], [9]. This research has also lead to profound advancement of compact metrological devices, achieving frequency stabilities in the low $10^{-10}\tau^{-1/2}$ in package volumes measuring only a few tens of cubic centimetres [10], [11].

However, the majority of the current compact clocks are based around room temperature apparatus that use buffer gasses and cell wall coatings in order to minimise collisional spin flips, benefiting the system with increased contrast and interrogation times [12]. Ultimately, these coatings and buffer gasses limit the long term performance achievable in a clock due to cell degradation and temperature dependent pressure shifts.

To overcome this, a move towards cold atoms is favourable, with the benefit of long interrogation times and narrow linewidths. To date, attempts at miniaturising cold atom clocks remain confined to thousands of cubic centimetre packages. We begin by proposing the grating magneto-optical traps, GMOT, as a step closer to bridging the gap between high performance cold atom apparatus and the scale of a thermal package. This project aims at reaching a frequency stability better than $10^{-12}\tau^{-1/2}$ in a package on the scale of tens of cubic centimetres.

II. CPT INTERROGATION

Our study begins with the realisation of an atom chip that integrates the laser cooling apparatus into a compact device. The GMOT achieves equalised radiation pressure from balancing the intensities of a single incident beam by the diffracted orders from the grating surface [2], [3]. Previous optical tools for simplifying laser cooling and trapping have

been demonstrated [13], [14], [15], [16], however, as discussed in previous work, the GMOT out-performs these devices on size, reproducibility, robustness and trapping capabilities [5]. These properties make the GMOT the ideal candidate for a compact atomic clock.

To convert this device to a clock experimentally we propose to derive the ground state frequency splitting of ^{87}Rb by means of coherent population trapping, CPT [17]. The experimental set-up used is illustrated in Figure 1. We lock a home made external cavity diode laser, ECDL, to the cooling transition of ^{87}Rb and use an electro-optical modulator, EOM, to frequency modulate a sideband at the re-pumping frequency. An acousto-optical modulator, AOM, is used for switching on and off the cooling beam, that is fibre coupled and circularly polarised before reaching the diffraction grating. The magnetic field zero point, created by anti-Helmholtz coils, is centred on the light overlap volume for trapping the cold atomic sample. For an incident intensity of $\approx 40 \text{ mW/cm}^2$ in a 20 mm beam we trap 10^8 atoms. When sub-Doppler cooling mechanisms are introduced we bring 3×10^7 atoms down to $15 \mu\text{K}$.

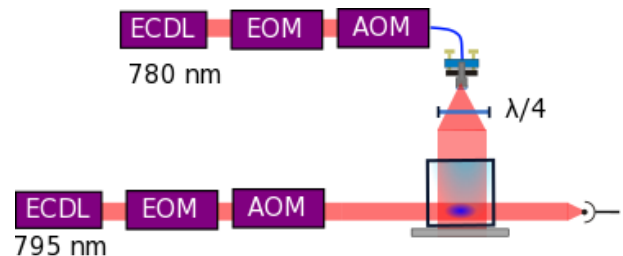


Fig. 1. Simplified grating MOT schematic for the cooling and probing beams. EOM: Electro-optical modulator. AOM: Acousto-optical modulator. ECDL: External cavity diode laser. $\lambda/4$: Quarter wave-plate.

When the cold atoms are free from external perturbation and in ballistic expansion, we apply a Raman probe beam to resolve the ground state clock transition. For this probe beam, a 795 nm laser is used to drive to the D1 states of ^{87}Rb . Once locked, an EOM is used to generate sidebands of equal amplitude to the carrier to couple the two ground states to the $F = 1$ excited state. With a small magnetic field is applied parallel to the clock beam, one can lift the degeneracy of the excited state enough to resolve CPT features of individual sub-levels, as can be seen in Figure 2. A few tens of μW 's of laser power is enough to resolve a full width half max, FWHM, of the $m_F = 0$ state to be 5 kHz.

To achieve a narrower clock feature we will convert the CPT procedure to a Raman-Ramsey sequence. The technique has been demonstrated to produce narrow fringes at higher

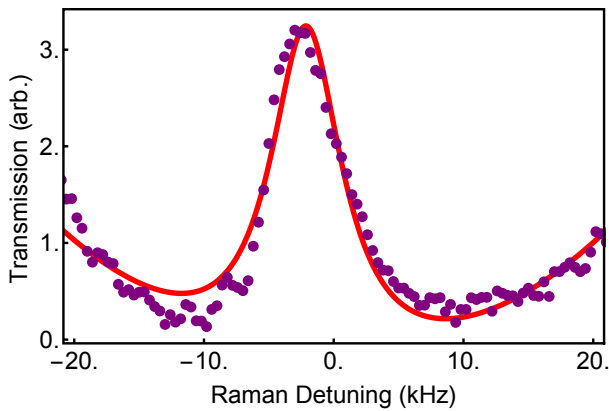


Fig. 2. Coherent population trapping transmission peak for the $m_F = 0$ sub-level of ^{87}Rb . Black line: The experimental data of the peak resolved with a Raman scan through the cold atomic medium. Red line: Lorentzian best fit to the experimental data

contrast than the original CPT feature, benefiting the measured frequency stability [18], [19].

III. CONCLUSION

The grating magneto-optical trap provides a compact means to cool and trap a large number of atoms, proving beneficial for precision measurements such as atomic clocks. With a coherent population trapping signal optimised to 5 kHz, the apparatus will be used to demonstrate Raman-Ramsey interrogation for a narrow clock reference.

ACKNOWLEDGMENT

The authors gratefully acknowledge financial support from the EPSRC (EP/M013294/1), DSTL (DSTLX-100095636R), and ESA (4000110231/13/NL/PA).

REFERENCES

- [1] G. Lamporesi, A. Bertoldi, L. Cacciapuoti, M. Prevedelli and G. M. Tino, "Determination of the Newtonian gravitational constant using atom interferometry" *Phys. Rev. Lett.* **100**, 050801 (2008)
- [2] J. P. McGilligan, P. F. Griffin, E. Riis, and A. S. Arnold, "Phase-space properties of magneto-optical traps utilising micro-fabricated gratings." *Opt. Express* **23**, 8948-8959 (2015)
- [3] J. P. McGilligan, P. F. Griffin, E. Riis, and A. S. Arnold, "Diffraction grating characterisation for cold atom experiments" *arXiv:1601.07431(2016)*
- [4] J. P. Cotter, J. P. McGilligan, P. F. Griffin, I. M. Rabey, K. Docherty, E. Riis, A. S. Arnold and E. A. Hinds "Design and fabrication of diffractive atom chips for laser cooling and trapping" *arXiv:1601.05548 (2016)*
- [5] C. C. Nshii, M. Vangeleyn, J. P. Cotter, P. F. Griffin, E. A. Hinds, C. N. Ironside, P. See, A. G. Sinclair, E. Riis and A. S. Arnold, "A surface-patterned chip as a strong source of ultracold atoms for quantum technologies" *Nat Nanotech.* **8**, 321-324 (2013)
- [6] T. P. Heavner, E. A. Donley, F. Levi, G. Costanzo, T. E. Parker, J. H. Shirley, N. Ashby, S. Barlow and S. R. Jefferts, "First accuracy evaluation of NIST-F2", *Metrologia* **51**, 174-182 (2014)
- [7] B.J. Bloom, T.L. Nicholson, J.R. Williams, S. Campbell, M. Bishof, X. Zhang, W. Zhang, S.L. Bromley, J. Ye, "An optical lattice clock with accuracy and stability at the 10^{-18} level", *Nature* **506**, 71-75 (2014)
- [8] M. Takamoto, F. L. Hong, R. Higashi and H. Katori, "An optical lattice clock" *Nature* **435**, 321-324 (2005)
- [9] N. Hinkley, J. A. Sherman, N. B. Phillips, M. Schioppo, N. D. Lemke, K. Beloy, M. Pizzocaro, C. W. Oates, A. D. Ludlow "An Atomic Clock with 10^{-18} Instability", *Science* **341**, 1215-1218 (2013).

- [10] P. D. D. Schwindt, S. Knappe, V. Shah, L. Hollberg, J. Kitching, L. A. Liew, and J. Moreland, "Chip-scale atomic magnetometer," *Applied Physics Letters*, **85**, (2004)
- [11] R. Lutwak, "The Chip-Scale atomic clock - recent developments", in *Proc. 2009 Joint Meeting IEEE Int. Frequency Control Symp. and EFTF Conf.*, Besancon, France, 2009, pp. 573-577.
- [12] X. Liu, J-M. Merolla, S. Guerandel, E. de Clereq and R. Boudot, "Ramsey spectroscopy of high-contrast CPT resonances with push-pull optical pumping in Cs vapor" *Opt. Express* **21**, 12451-12459 (2013)
- [13] S. Pollock, J. P. Cotter, A. Laliotis and E. A. Hinds, "Integrated magneto-optical traps on a chip using silicon pyramid structures", *Opt. Express* **17**, 14109-14114 (2009).
- [14] S. Pollock, J. P. Cotter, A. Laliotis, F. Ramirez-Martinez and E. A. Hinds, "Characteristics of integrated magneto-optical traps for atom chips", *New J. Phys.* **13**, 043029 (2011).
- [15] M. Vangeleyn, P. F. Griffin, E. Riis, and A. S. Arnold, "Single-laser, one beam, tetrahedral magneto-optical trap", *Opt. Express* **17**, 13601-13608 (2009).
- [16] M. Vangeleyn, P. F. Griffin, E. Riis, and A. S. Arnold, "Laser cooling with a single laser beam and a planar diffractor", *Opt. Lett* **17**, 3453-3455 (20010).
- [17] E. Arimondo, *Prog. Opt.* **35**, 257 (1996).
- [18] F. X. Esnault, E. Blanshan, E. N. Ivanov, R. E. Scholten, J. Kitching and E. A. Donley, "Cold-atom double Λ coherent population trapping clock", *Phys. Rev. A* **88**, 042120 (2013)
- [19] X. Chen, G-Q. Yang, J. Wang and M-S. Zhan, "Coherent Population Trapping-Ramsey Interference in Cold Atoms" *Chin. Phys. Lett.* **27**, 113201 (2010)

Light-Shift Coefficient in GPS Rubidium Clocks: Estimation Methods using Lamplight/Frequency Correlations

Valerio Formichella^{1,2}, James Camparo³, Patrizia Tavella¹

¹Department of Physical Metrology, INRiM, Torino, Italy

²Department of Electronics and Telecommunications, Politecnico di Torino, Torino, Italy

³Physical Sciences Laboratories, The Aerospace Corporation, El Segundo, CA, USA

E-mail: v.formichella@inrim.it

Abstract—The frequency of the Rubidium Atomic Frequency Standard (RAFS) used in Global Navigation Satellite Systems (GNSS) is affected by the light-shift effect, due to the optical-pumping light from the RAFS' rf-discharge lamp. As a consequence, lamplight intensity variations can induce RAFS output frequency variations, with lamplight stability setting a lower bound to RAFS frequency stability (i.e., to the eventual navigation performance of the GNSS). We study this effect by estimating the light-shift coefficient of an on-orbit RAFS and its possible variation in time using two different methods: the first makes use of large observed frequency jumps that are induced by lamplight jumps; the second uses the linear correlation between deterministic frequency and lamplight variations. We validate the methodology using GPS Block IIR RAFS data and present some preliminary results.

Keywords—rubidium clock; light shift; GNSS; frequency jumps; RAFS; GPS

I. INTRODUCTION

Rubidium Atomic Frequency Standards (RAFS) are a key technology for Global Navigation Satellite Systems (GNSS) like GPS, BeiDou and Galileo. However, their output frequency is affected by the light-shift effect [1], which is a shift of the nominal clock frequency due to the optical-pumping light from the RAFS' rf-discharge lamp. The contribution of the light-shift effect to the fractional frequency deviation of the clock is proportional to the lamplight intensity. The proportionality coefficient is the clock's light-shift coefficient α , depending on the spectrum of the lamplight reaching the resonance cell of the clock.

As a consequence of the light-shift effect, lamplight intensity variations can induce RAFS output frequency variations, degrading the stability of the clock. In general, the lamplight stability sets a lower bound to the RAFS frequency stability [2], depending on the magnitude of α . Hence, in order to uncover the effect of the lamp on the output frequency, it is necessary to characterize the RAFS' light-shift coefficient. Specifically, it is important to know if the light-shift coefficient for a particular RAFS can change over time, and it is important to know the RAFS-to-RAFS variability of α .

In the case of GNSS RAFS, little is known regarding the value of α and its stability over time. Moreover, measuring the light-shift coefficient of an on-orbit RAFS is not trivial, since one cannot simply adjust the lamplight's level and record a change in frequency as one might in the laboratory. In the present work we discuss two different methods for estimating the light-shift coefficient of an on-orbit GNSS RAFS; we validate the methodology using GPS Block IIR RAFS data, and we present some preliminary α generalities. We employ RAFS frequency data from the Information-Analytical Centre (IAC) and downloaded GPS RAFS lamplight telemetry data.

Section II provides the theoretical background and presents the two methods from a general point of view: the first makes use of large observed frequency jumps that are induced by lamplight jumps; the second uses the linear correlation between deterministic frequency and lamplight variations. The two methods are applied and validated on real data in Section III.

II. THEORY

A typical mathematical model for the fractional frequency deviation of an atomic clock is [3]

$$y(t) = y_0 + dt + \varepsilon(t) \quad (1)$$

where y_0 is the initial frequency deviation, d is the frequency drift and ε is the noise (taking $t_0 = 0$). The contribution of the light-shift effect to the clock fractional frequency deviation can be written as

$$y_{LS}(t) = \alpha i(t) \quad (2)$$

where α is the light-shift coefficient and i the normalized lamplight intensity, defined as $i(t) = I(t)/I_0$ with $I_0 =$ nominal intensity, $I(t) =$ intensity at the time t . We point out this term rewriting (1) as

$$y(t) = y'_0 + d't + y_{LS}(t) + \varepsilon'(t) \quad (3)$$

where y'_0 , d' , ε' summarize all the contributions to y_0 , d , ε independent of the light-shift effect. Ignoring the frequency's and the lamplight's trends, we find that the stability of the clock frequency has a lower bound fixed by the stability of the lamplight intensity and by the magnitude of the light-shift

coefficient. In other words, the Allan variance of the stochastic component of the frequency is

$$\sigma_y^2(\tau) = \alpha^2 \sigma_{y,i}^2(\tau) + \sigma_{y,\epsilon}^2(\tau) \Rightarrow \sigma_y^2(\tau) \geq \alpha^2 \sigma_{y,i}^2(\tau) \quad (4)$$

where $\sigma_{y,i}^2(\tau)$ is the Allan variance of the stochastic component of the lamplight. However, note that the measured lamplight instability could be higher than the intrinsic value $\sigma_{y,i}^2(\tau)$ because of the intensity's measurement noise, and this should be taken into account when one wants to find the lower bound to the clock stability.

Equation (2) means that lamplight intensity variations can induce RAFS output frequency variations. For instance, a linear drift of the lamplight intensity, d_i , would contribute to the linear drift of the frequency, $d = d' + \alpha d_i$. Unfortunately, the additional term d' is in general unknown and different from zero, hence this relation cannot be used to find α . Moreover, considering the GPS system, what we observe from the ground is not the original RAFS frequency, but the output of the on-board TKS (Time Keeping System): as described in [4] and [5], the drift of the output frequency can be changed by ground command, and no public information is available about the drift corrections made in the past.

If we want to estimate α , the first method we can use is based on large frequency jumps induced by lamplight jumps. Following (3), if an intensity jump has a certain duration and an amplitude A_i , the corresponding frequency jump has the same duration and an amplitude $A_y = \alpha A_i$. Hence, we can find an estimate of the light-shift coefficient as

$$\hat{\alpha} = \frac{\hat{A}_y}{\hat{A}_i} \quad (5)$$

where \hat{A}_y , \hat{A}_i are estimates of A_y , A_i . The larger the jump relative to the noise, the better the estimates of A_y , A_i , and hence the better the estimate of α . In the following, this first method will be called the ‘‘jumps method.’’

The second method is more general and makes use of any kind of deterministic lamplight fluctuation inducing a frequency fluctuation. First, we need to remove from the measured y and i any possible uncorrelated trend, mainly the linear drift discussed above. If the drift changes with time, we estimate and remove it for each time period over which it can be considered nearly constant. From (3) it follows that such detrended frequency and intensity data, y_D and i_D , satisfy

$$y_D(t) = \alpha i_D(t) + \epsilon(t) \quad (6)$$

where ϵ is the noise. Finally, equation (6) shows that there is a linear correlation between y_D and i_D , hence we can estimate α as the slope of the regression line fitting the data (y_D as a function of i_D). The closer to ± 1 the Pearson-product correlation coefficient r for this linear regression, the better the estimate of α . In the following, this second method will be called the ‘‘correlation method.’’

III. APPLICATION TO GPS RAFS DATA

Lamplight telemetry data from a number of Block IIR GPS RAFS were obtained, and in many cases the lamplight data

length for a single RAFS spanned more than a decade. These telemetry data are limited in resolution, however, by the bit-level quantization of the telemetry signal, and do not easily allow detection of the small lamplight variations that produce (for example) frequency jumps. Fortunately, the telemetry signal contains noise, so that averaging the lamplight telemetry signals over a 24 hour time interval allowed us to assess relative lamplight changes at the 0.1% level and below. (When a quantized signal has noise, the relative time that the signal spends at one level relative to the next quantized level allows one to get below the quantization limit by averaging.)

The clock phase offset data are obtained from IAC, one value every 300 seconds, then they are differentiated to obtain the corresponding frequency values. Finally, we compute daily averages of such frequency data, to be used in our analyses along with the daily-averaged lamplight data.

A. The case of GPS SVN 41 – The jumps method

Fig. 1 shows frequency and lamplight intensity data for the

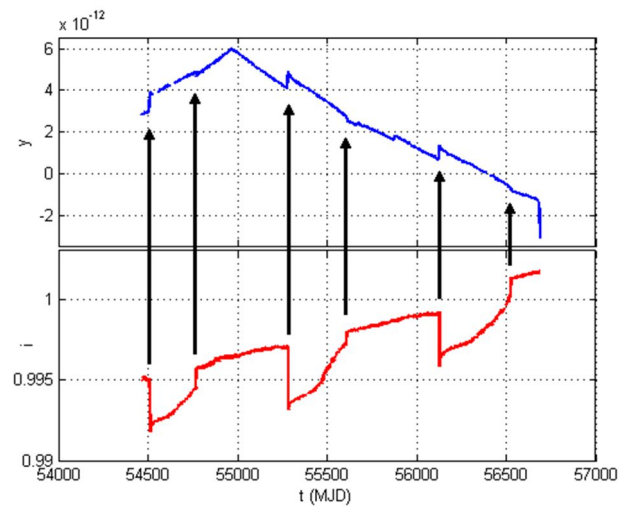


Fig. 1. Fractional frequency deviation (blue) and normalized lamplight intensity (red) of GPS SVN 41 with six common jumps (indicated by arrows), between 1 January 2008 and 30 January 2014.

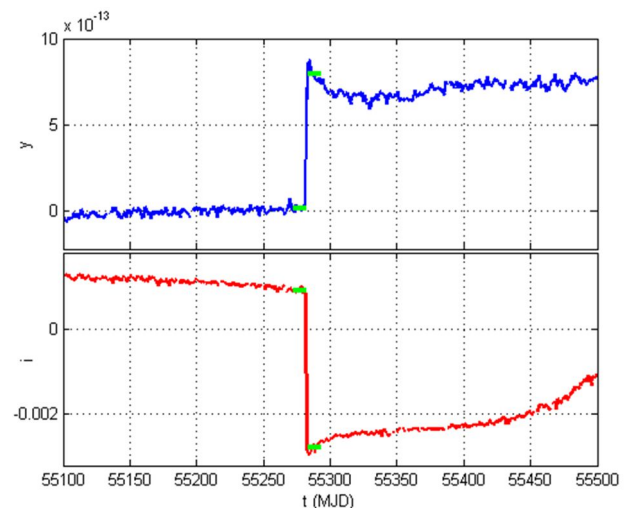


Fig. 2. Detrended fractional frequency deviation (blue) and normalized lamplight intensity (red) around the third jump of Fig. 1, with smoothed values delimiting the jump indicated in green.

operational RAFS on-board GPS Block IIR satellite SVN 41 for the period from 1 January 2008 to 30 January 2014. Six large common jumps are visible (indicated by arrows), which can be used to estimate the light-shift coefficient via the jumps method. In order to find the actual jump amplitudes, the first step is to estimate and remove the uncorrelated linear trends from both data series. Then, we compute two smoothed values, averaging the last ten values before the jump and the first ten values after the jump. (In case a residual linear trend is present, we use a linear fit instead of the simple average in order to give an estimate of the values delimiting the jump.) We take the standard deviation of the ten averaged values as a safe estimate of the uncertainty of the smoothed values. (If we use the linear fit instead of the average, we take the standard deviation of the residuals.) An example is given in Fig. 2, representing the detrended data around the third jump of Fig. 1. Finally, the jump amplitude is computed as the difference between the two smoothed values delimiting the jump; the corresponding estimate of α is computed according to (5), and its uncertainty follows from the law of uncertainty propagation. Fig. 3 reports the six estimates of α for this space vehicle along with 1-sigma error bars.

Reference [5] reports another ten frequency jumps for this RAFS and space vehicle in the years 2001 to 2005: we found that nine of them were caused by large lamplight jumps, and we obtained another nine estimates of the light-shift coefficient. The whole set of 15 estimates of α for this space

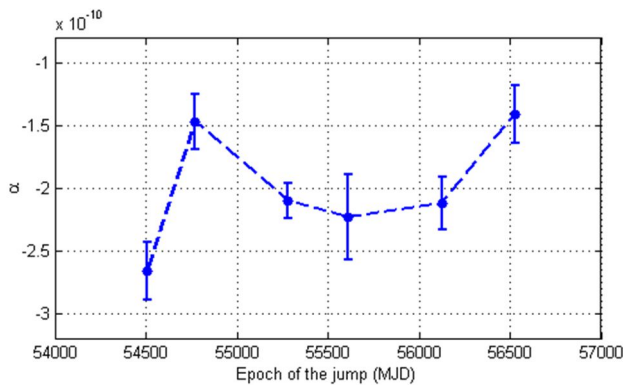


Fig. 3. The six estimates of the light-shift coefficient corresponding to the six common jumps represented in Fig. 1, along with their 1-sigma error bars.

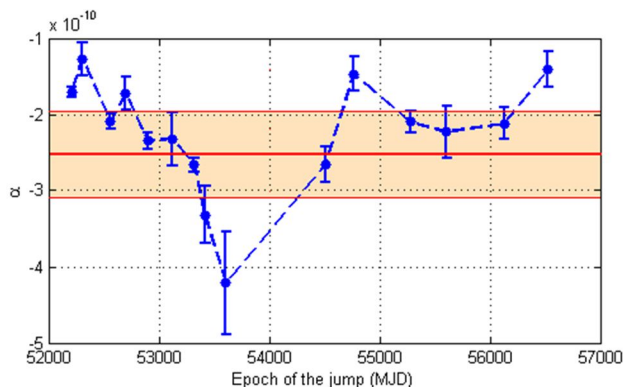


Fig. 4. The full set of 15 estimates of the light-shift coefficient. The red line in the middle is the arithmetic mean and the pink band marks the interval given by mean \pm one standard deviation.

vehicle's RAFS is reported in Fig. 4. We found no clear evidence of a possible variation of α with time, as also reported in [2]. Finally, we can give a single estimate of the light-shift coefficient of satellite SVN 41, averaging the 15 values obtained with the jumps method. We take the arithmetic mean and the standard deviation of the 15 values as a safe estimate of α and its uncertainty, obtaining: $\alpha_{41} = (-2.2 \pm 0.8) \times 10^{-10}$.

B. The case of GPS SVN 46 – The correlation method

Fig. 5 shows frequency and lamplight intensity data for the operational RAFS on-board GPS Block IIR satellite SVN 46 for the period from 1 January 2008 to 30 January 2014. Over the short term (10 days), the frequency and the lamplight show a similar periodic behavior (an example is visible in Fig. 7), which can be used to estimate the light-shift coefficient via the correlation method. Similar to the jump method, in this case the first step is to estimate and remove the uncorrelated linear trends. Then, we use the detrended data to search for periods of time with high correlation between lamplight variations and frequency variations. Specifically, we look for periods of time when the absolute value of the correlation coefficient r is larger than a preset threshold. (We chose our threshold as 0.5, as this is often taken as indicative of a large effect [6].) For each of these periods, we compute an estimate of α as the slope of the regression line (y_D as a function of i_D) and take the standard error of the slope as an estimate of the uncertainty in

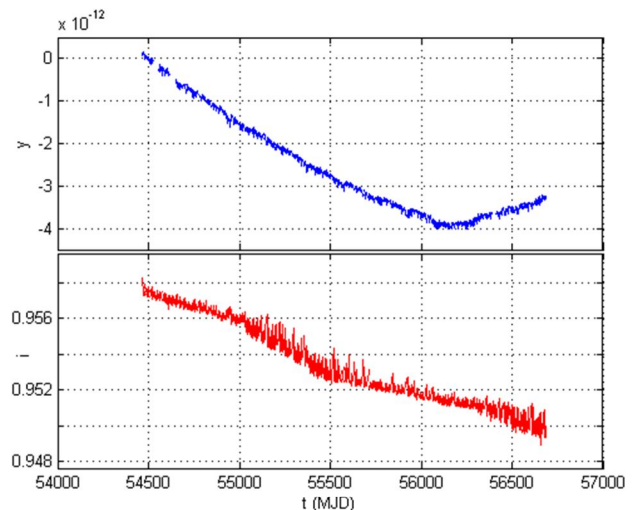


Fig. 5. Fractional frequency deviation (blue) and normalized lamplight intensity (red) of GPS SVN 46, between 1 January 2008 and 30 January 2014.

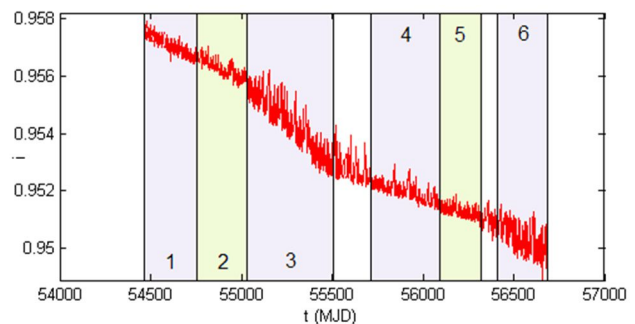


Fig. 6. The six periods with high correlation and acceptable estimates of the light-shift coefficient.

α . However, as a further check on accepting erroneous light-shift coefficient values, we only accept those estimates of α whose value is non-zero at a 95% confidence level. For the data of Fig. 5, we were able to find six periods satisfying our constraints, and these are highlighted in Fig. 6. As an example, lamplight and frequency correlated oscillations in the first part of the fourth period are represented in Fig. 7. Finally, the six estimates of α are reported in Fig. 8, with 1-sigma error bars.

It is interesting to note for this RAFS that the light-shift coefficient appears to change value when the lamplight periodicities change behavior. Specifically, looking at Figs. 8 and 6, we observe that the estimates of α obtained in periods 1, 2, 4, and 5 – periods in which the lamplight showed “small” variations – were all comparable with one another: for these periods the arithmetic mean yielded $\alpha_{46a} = -1.8 \times 10^{-10}$ with a standard deviation of $\sigma_{46a} = 0.2 \times 10^{-10}$. Alternatively, in the periods 3 and 6 – periods when the lamplight showed “large” variations – the arithmetic mean of the light-shift coefficients yielded $\alpha_{46b} = -0.70 \times 10^{-10}$ with a standard deviation of $\sigma_{46b} = 0.05 \times 10^{-10}$. Though this is clearly too small a data set from which to draw concrete conclusions, we nonetheless believe it an interesting observation, and one that should be archived for later more detailed consideration. Nevertheless, taking the data of Fig. 8 in whole, we arrive at a light-shift coefficient for this space vehicle: $\alpha_{46} = (-1.4 \pm 0.6) \times 10^{-10}$, which is consistent with

the value of α for the GPS Block IIR RAFS obtained with the jump method.

IV. SUMMARY

The light shift is one of the more important processes affecting the performance of RAFS used in GNSS systems. Here, we outlined two procedures by which the light-shift coefficient could be estimated using on-orbit data from GNSS RAFS: the jumps method and the correlation method. While the jumps method is more straightforward, and less ambiguous with regard to the causal relationship between RAFS frequency and RAFS lamplight, it requires the occurrence of lamplight jumps, which (as the data of Fig. 1 illustrate) can be few and far between. Alternatively, the correlation method can be employed even if lamplight jumps are not observed, but greater care is required in order to extract meaningful light-shift coefficients. Specifically, lamplight and frequency can change in a correlated fashion without a causal relation between the lamplight change and the frequency change.

In future work we intend to apply both of these techniques to a number of Block IIR GPS satellites for which we have data. In particular, we will be interested in addressing two fundamental questions:

1. What is the family-wide variance of light-shift coefficients for high-quality GNSS RAFS? Is the light-shift coefficient for one RAFS, built by the same manufacturer to the same specifications, widely different from another RAFS; or is the light-shift coefficient relatively constant for a particular family of RAFS?
2. Knowing the long-term behavior of a RAFS’ lamplight along with the RAFS’ light-shift coefficient, to what extent do lamplight variations affect the RAFS’ long-term frequency stability?

Knowing the answers to these questions will not only provide information on the ultimate timekeeping performance of GNSS, but the answers may point the way to improved RAFS for next generation GNSS.

ACKNOWLEDGMENT

V. F. thanks Giovanna Signorile and Ilaria Sesia for useful discussions during the writing of this work. J. Camparo’s efforts were funded by U.S. Air Force Space and Missile Systems Center under Contract No. FA8802-14-C-0001.

REFERENCES

- [1] B. S. Mathur, H. Tang, and W. Happer, “Light shifts in the alkali atoms”, *Phys. Rev.* 171(1), 11-19 (1968).
- [2] J. Camparo, I. Sesia, V. Formichella, G. Signorile, L. Galleani, P. Tavella, “Rubidium Clock Lamplight Variations and Long-Term Frequency Instability: First Analyses of Multiyear GPS Data”, in Proc. 2016 PTI Meeting, 150-156 (2016).
- [3] P. Tavella, “Statistical and mathematical tools for atomic clocks”, *Metrologia* 45 (2008) S183-S192.
- [4] M. Epstein, T. Dass, “Management of phase and frequency for GPS IIR satellites”, in Proc. 33th PTI Meeting, 481-492 (2001).
- [5] M. Epstein, T. Dass, J. Rajan, P. Gilmour, “Long-term clock behavior of GPS IIR satellites”, in Proc. 39th PTI Meeting, 59-78 (2007).
- [6] J. Cohen, “A power primer”, *Psych. Bull.* 112(1), 155-159 (1992).

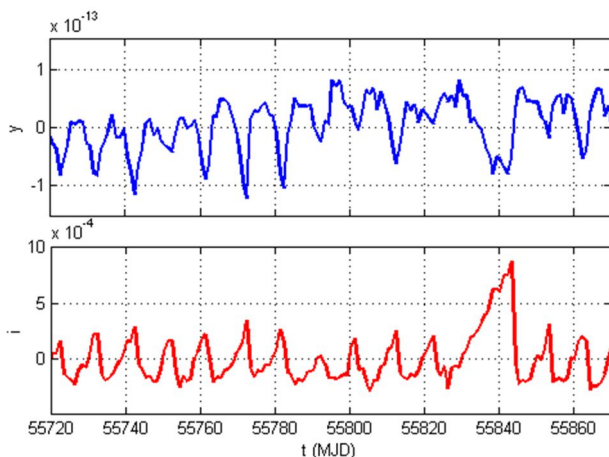


Fig. 7. Lamplight (red) and frequency (blue) in the first part of period number 4 (about 150 days). Correlated periodic oscillations are clearly visible.

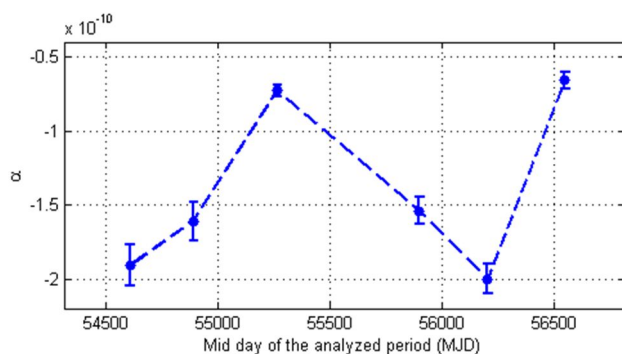


Fig. 8. The six estimates of the light-shift coefficient corresponding to the six periods represented in Fig. 6, along with their 1-sigma error bars.

Hydrogen plasma simulation for atomic clock lifetime assessment

Eleonie van Schreven, Marco Belloni

European Space Agency (ESA)

ESTEC, TEC-ETE

Noordwijk, Netherlands

Email: eleonie.van.schreven@esa.int, marco.belloni@esa.int

Abstract—In this paper we describe a plasma simulation done to understand aging phenomenon on dissociator bulb used on hydrogen masers. To the authors knowledge, this is the first time that CAE simulation is used for studying plasma related wear-out effects of atomic clocks.

Keywords—maser; plasma; simulation

I. INTRODUCTION

The Passive Hydrogen Maser (PHM) is one of the two clock technologies embarked on the Galileo navigation payload. PHM has showed outstanding stability performances both for short and long term. On the system side, it was demonstrated that the excellent stability of the PHM technology can be advantageously used by the ODTS process (clock modelling) to reduce significantly the orbit and clock errors. However, given the lack of statistic over lifetime, parallel activities are ongoing to analyse potential failure mechanisms and improve the robustness [1].

II. BACKGROUND AND MOTIVATION

The hydrogen gas dissociator has been identified as the most critical subsystem.

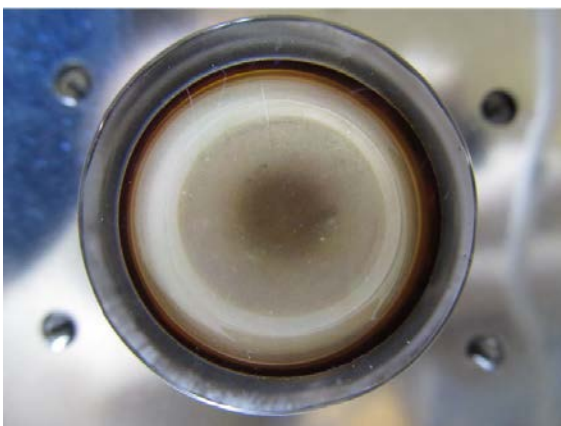


Fig. 1. White traces observed on the quartz surface of the hydrogen dissociator bulb due to aging.

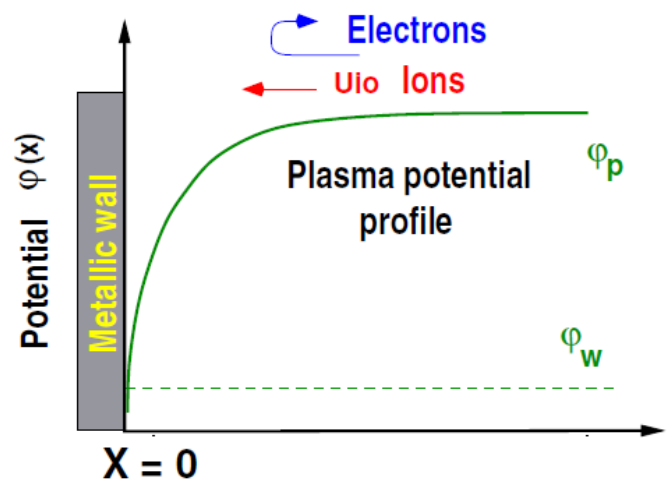


Fig. 2. Potential at the wall of a plasma cavity from [2]

A. Potential Failure Mechanisms

- **Wall erosion and recombination:** erosion of the vessel's walls increases the microscopic surface thus the recombination rate.
- **Wall sputtering:** silicon oxide release or other contaminants can affect the plasma reaction rates and thus the dissociation efficiency.

These mechanisms are induced by the sheath potential which increases the ion energy impacting the walls and therefore the sputtering yield.

B. Objective of the plasma simulation

To better understand the quartz vessel aging processes observed on lifestest models (Fig 1) the simulation needs to cover:

- A general characterization of the plasma behavior as function of dissociation parameters such as the gas pressure, the antenna electric field frequency and intensity, the distance between the antenna and the quartz bulb.

- Sheath phenomenon modelisation to identify its correlation with the wall surface erosions.
- Plasma interaction with the walls from a chemical prospective
- Modelisation of the actual dissociator design both in terms of geometry, materials and electromagnetic field distribution generated by the antenna.

III. SIMULATION MODEL

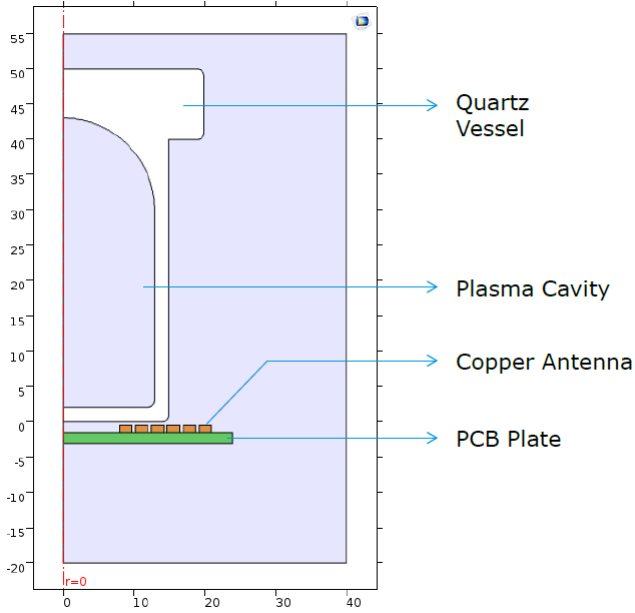


Fig. 3. 2D axisymmetric Geometry used in the simulation

COMSOL Multiphysics has been used to realize the simulation. A 2D Axisymmetric geometry around the z-axis was chosen for computational reasons. This affects both the geometry and the physics. The mesh includes boundary layers along the plasma walls and antenna surface to resolve skin effect.

The simulation of the Hydrogen Dissociator Bulb (HDB) can be separated into two sub-domains: the plasma and the electromagnetic components. The plasma is modeled using the Inductively Coupled Plasma interface within the Plasma Module, whereas the antenna and EM fields are solved with the Magnetic Formulation interface within the ACDC module. In order to create this model certain information about the problem are needed.

- Antenna parameters: power supplied to the antenna and frequency of interest.
- Gas parameters: initial pressure and initial temperature
- Particles present in the plasma: electron, ions, and neutrals
- Hydrogen reactions cross sections
- Cross sections or rate coefficients of the interactions between the hydrogen and the bulb walls.
- Reduced electron mobility
- Electron initial density and initial energy density

- Geometry of the bulb with the important surrounding elements
- Electrical conductivity, relative permittivity and dielectric constant of the materials involved in the simulation

Material properties are from the COMSOL database. Implemented reactions include:

- Elastic collisions
- Ionization
- Dissociation
- Recombination
- Excitation

In total 8 species were considered: 4 neutrals among which 3 excited states (i.e. H_2 , $H(n=2)$, $H(n=3)$, $H(n=4)$), 3 ions (H^+ , H_2^+ , H_3^+) linked to 24 volumetric reactions and 12 possible surface reactions.

Reactions	Rate coefficient [$m^3 s^{-1}$]
1. $e + H \rightarrow 2e + H^+$	$k_1 = 6.5023 \times 10^{-15} T_e^{0.48931} e^{-12.89365/T_e}$
2. $e + H_2 \rightarrow 2e + H + H^+$	$k_2 = 2.9962 \times 10^{-14} T_e^{0.44456} e^{-37.72836/T_e}$
3. $e + H_2^+ \rightarrow e + H + H^+$	$k_3 = 1.0702 \times 10^{-13} T_e^{0.04876} e^{-9.69028/T_e}$
4. $e + H_3^+ \rightarrow 2e + H^+ + H^+$	$k_4 = 2.1202 \times 10^{-15} T_e^{0.31394} e^{-23.29885/T_e}$
5. $H_2^+ + H \rightarrow H_2 + H^+$	$k_5 = 9.0 \times 10^{-16}$
6. $H_2 + H^+ \rightarrow H_3^+ + H$	$k_6 = 1.19 \times 10^{-28}$
7. $e + H_2 \rightarrow 2e + H_2^+$	$k_7 = 3.1228 \times 10^{-14} T_e^{0.17156} e^{-20.07734/T_e}$
8. $e + H_3^+ \rightarrow e + H + H_2^+$	$k_8 = 4.8462 \times 10^{-13} T_e^{-0.04975} e^{-19.16565/T_e}$
9. $e + H_2^+ \rightarrow H(n=2) + H$	$k_9 = 7.51371 \times 10^{-15} - 1.11516 \times 10^{-15} T_e + 1.03156 \times 10^{-16} T_e^2 - 4.14905 \times 10^{-18} T_e^3 + 5.85916 \times 10^{-20} T_e^4$
10. $H_2^+ + H_2 \rightarrow H_3^+ + H$	$k_{10} = 2.60 \times 10^{-15}$
11. $e + H_3^+ \rightarrow 3H$	$k_{11} = 4.19624 \times 10^{-15} + 1.50816 \times 10^{-15} T_e - 1.9022 \times 10^{-16} T_e^2 + 6.5554 \times 10^{-18} T_e^3 + 1.20816 \times 10^{-19} T_e^4$
12. $e + H_3^+ \rightarrow H_2 + H$	$k_{12} = 4.19624 \times 10^{-15} + 1.50816 \times 10^{-15} T_e - 1.9022 \times 10^{-16} T_e^2 + 6.5554 \times 10^{-18} T_e^3 + 1.20816 \times 10^{-19} T_e^4$
13. $e + H_2 \rightarrow e + 2H$	$k_{13} = 1.7527 \times 10^{-13} T_e^{-1.236668} e^{-12.59243/T_e}$

Fig. 4. H and H_2 reaction rates from [3]

A. Model limitation

Before presenting the results, the simulation model validity is discussed.

1) Comparison with Breakdown Theory

Fig. 5 describes the limits of the Breakdown Diffusion Theory [4] compared with the simulated conditions. The simulations are performed considering a gas pressure of $p_0 = 0.3$ mbar. This is the lowest gas pressure that results in an ignition of the plasma. However from experimental tests on representative test benches, a sustainable plasma is also achievable for lower pressures down to $p_0=0.1$ mbar and beyond. This discrepancy is a clear limit of the model. The simulation results obtained surveying different combinations between hydrogen pressure and electric field wavelength (λ) showed an area smaller than the one expected from the Breakdown Diffusion Theory, but with a similar shape (ref. to blue circles on Fig 5). The reason of these discrepancy is not understood yet and could be due to COMSOL Plasma Module solver assumptions related to the interaction between the electric field and the electrons. Another explanation could be linked to a not sufficient representativeness of the model, including the E-field distribution, as further discussed in the following section.

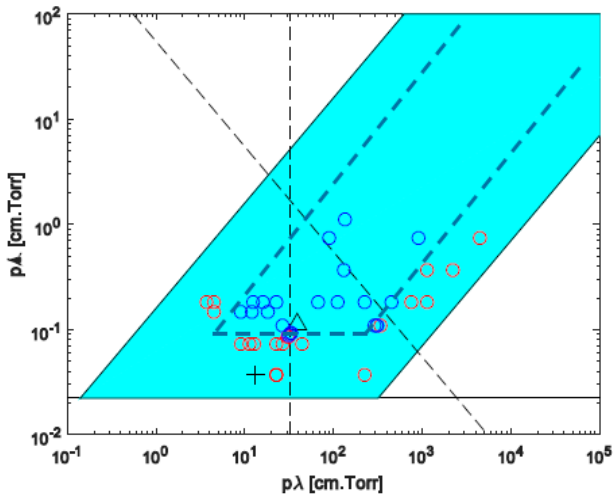


Fig. 5. Limit of the breakdown theory as described in [4]. The blue circles represent simulations that yield a sustained plasma whereas the red circles represent simulations with no ignition of the plasma. The black triangle is the condition used for most of the simulations. The black cross is a condition tested on a representative test-bench where a sustainable plasma is achievable.

2) Antenna Modeling

EM field distribution as effect of the antenna emission is obtained using the ACDC module of COMSOL and, more precisely, its magnetic formulation (MF). COMSOL works with interfaces inside modules which acts of interaction links with other modules. In this specific case the ICP (inductively coupled plasma) interface of the Plasma Module uses the MF interface of the ACDC Module to simulate the electromagnetic components of the model. The MF formulation uses certain assumptions, for instance it solves the problem for the in-plane magnetic field deducing from this the out-off-plane electric field. The adoption of a 2D axisymmetric geometry implies a cancellation of the electric field on the axis of symmetry. This is not representative of the actual field generated by a spiral antenna where the maximum of the electric field is exactly along the axis of symmetry of the bulb. To overcome this limitation several solutions were proposed by COMSOL, either using the MEF (Magnetic and Electric Field formulation) or using a Lumped Port to excite the antenna. However none of these possibilities can be used in combination with an ICP or in a 2D axisymmetric geometry.

In the current state, the antenna excitation as managed by the simulation, is thus not fully representative of the reality. Anyway this is not considered a major limitation given the primary objective to qualitatively analyze the behavior of the plasma as effect of the main dissociation parameters change.

IV. RESULTS

The following results are at $p_0=0.3$ mbar, $P_{\text{antenna}}=300$ W, $F_{\text{HDO}}=170$ MHz. The power to the antenna shall be considered indicative only given a full mismatch between the power source and the antenna. Electron density distribution in the plasma vessel shows a sustained stable plasma. It is worth noticing that the model allows to investigate the densities of all considered ions and neutral species (Fig. 7) and their

evolution in time. The stable plasma state is reached after about 50 milliseconds.

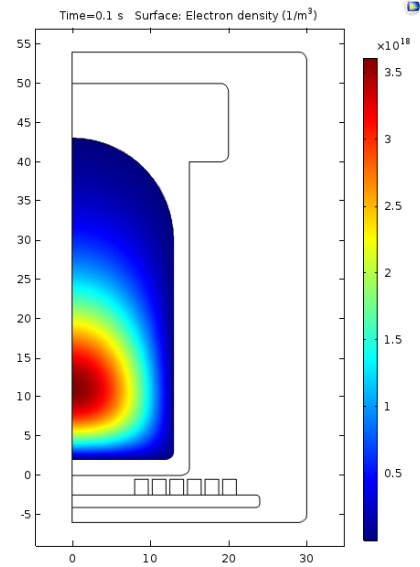


Fig. 6. Electron density ($1/m^3$) for a molecular hydrogen plasma.

More in depth, the results show that the ignition of the plasma starts close to the antenna where it is observable a maximum of the power deposition limited in depth by the skin effect of the plasma. Electrons then migrate and diffuse to the center of the dissociation bulb.

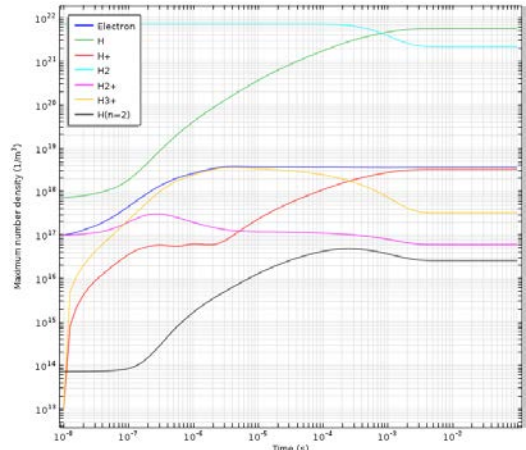


Fig. 7. Densities of all the considered specie over time.

Investigation of the molecular ion and electron fluxes (Fig. 8 and Fig. 11) show a preferred direction: the ions mainly impact the quartz surfaces close to the antenna, both on the surface parallel to the antenna and on the vessel side walls. This matches the observation done on aged bulbs (Fig. 10). The intensity of the ion flux is responsible for the vessel inner surface etching hence confirming sputtering to be one of the main aging effects of the quartz bulbs.

The simulation model has been used to study the sheath potential distribution and its dependence with the main dissociation parameters. The conclusions are briefly summarized hereafter:

- The sheath potential is stronger on the bulb surface close to the antenna.

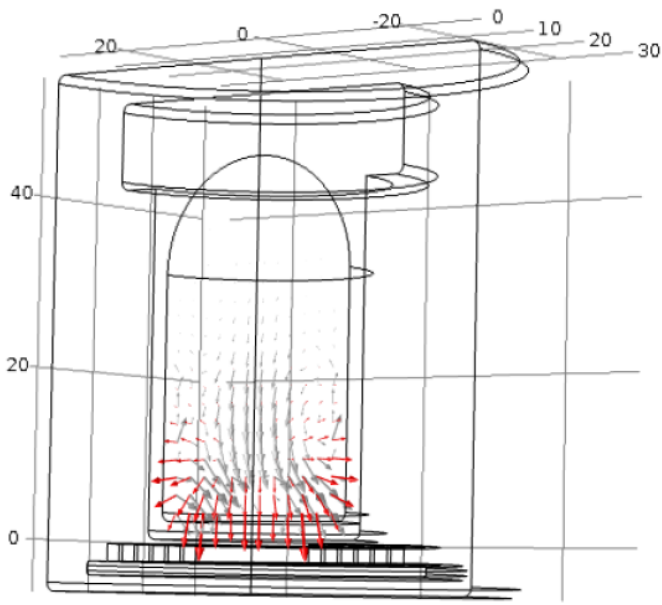


Fig. 8. Total Flux of H_2^+ (in red) and of electrons (in grey)

- The sheath potential is strongly influenced by the gas pressure inside the plasma and in a lesser quantity by the power and frequency used to excite the plasma. (Fig. 9).

The model requires still some refinements before to conclude on other aspects, like chemical plasma interaction with the vessel walls and the existence of dual or multi plasma modes which could affect the dissociation efficiency.

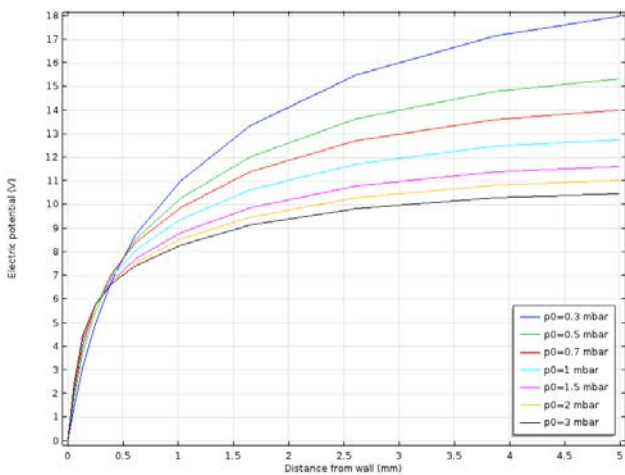


Fig. 9. Sheath potential for different initial gas pressure

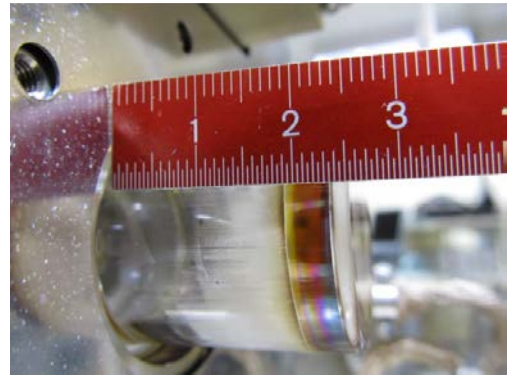


Fig. 10. Aging observed on the side to the quart bulb.

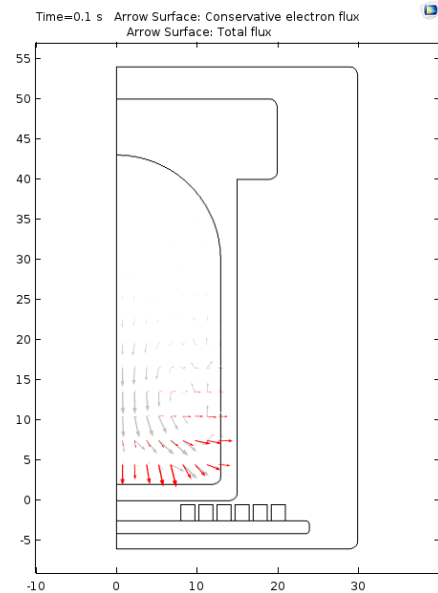


Fig. 11. Total Flux of H_2^+ (in red) and of electrons (in grey)

V. CONCLUSION

The developed simulation model allows to qualitatively assess the main phenomena which affect the aging of the dissociator bulb used in the hydrogen masers. This approach can be actively used for dissociation optimization and rf-dissociator improvement.

REFERENCES

- [1] A. E. Popa, H.T.M. Wang, W.B. Bridges, A.N. Chester, J.E. Etter, B.L. Walsh, "A Study to identify Hydrogen Maser Failures Modes", Hugues Research Laboratories, Malibu, California
- [2] L. Conde, "An Introduction to Plasma Physics and its Space Applications", Departement of Applied Physics, Universidad Politécnic de Madrid, March 5 2014.
- [3] I. Méndez, F. J. Gordillo-Vázquez, V. J. Herrero, I. Tanarro, "Atom and Ion Chemistry in Low Pressure Hydrogen DC Plasma", Instituto de Estructura de la Materia, Madrid, March 2006, J. Phys. Chem. A 2006, 110, 6060-6066
- [4] A. D. MacDonald, "Microwave breakdown in gases", Lockheed Palto Research Laboratory, John Wiley & Sons, 1966

Stress–Sensitivity of Wafer–Level Packaged SAW Delay Lines

Lilia Arapan, Guillaume Wong, Bernard Dulmet,
Thomas Baron, Jean-Michel Friedt, Vincent Placet
Time & Frequency Dpt,
FEMTO-ST, UMR CNRS-UFC-ENSMM-UTBM 6174,
26 Chemin de l’Épitaphe, 25030 Besançon, France
Email: lilia.arapan@femto-st.fr

Sébastien Alzuaga
SENSéOR, Besançon, France

Abstract—This paper presents the investigation of the influence of wafer-level packaging (WLP) on the stress–sensitivity of 100 and 200 MHz delay lines aimed to wireless sensing of stresses. The devices were fabricated on YXl/128° cut of lithium niobate. The investigated WLP achieves the assembly of two wafers by a 50 μm –thick layer of SU-8 photoresist. The delay line is micro-machined on top of the first wafer while the second wafer realizes the function of protective cap in a way that should not be detrimental to the stress-sensitivity of the device. The paper gives a comparison between the theoretical and experimental phase sensitivity of both packaged and raw devices submitted to a three–points bending test.

I. INTRODUCTION

Controlling the shift of parameters induced by the packaging is a key issue for the actual production of MEMS and SAW sensors initially developed in the laboratory. Here-studied devices are 100 MHz and 200 MHz delay lines on YXl/128° LiNbO₃. These devices are proof–of–concept samples close to higher–frequency sensors aimed to the wireless measurement of stresses in various kinds of structures. The actual wireless sensors are designed to operate in the 434 MHz and 2.45 GHz ISM bands. This circumstance puts significant constraints upon the microfabrication of the devices: wireless reading of SAW sensors is better achieved with high coupling piezoelectric substrate such as lithium niobate (LNO). The YXl/128° orientation, suitable for this purpose, fixes the Rayleigh wave velocity around 3990 m/s on a free surface, yielding a wavelength about 9 μm at 434 MHz and 1.6 μm at 2.45 GHz. Then the devices are fragile and must be encapsulated to protect them from external agents. Wafer Level Packaging (WLP) is a more efficient approach than Die Level Packaging (DLP), especially in view of stress sensing because standard ceramic enclosures used to encapsulate RF devices are essentially designed from electrical viewpoint, are not aimed to transmit the strain of the analyzed external structure to the SAW device, and induce strong thermally–induced differential stresses in the sensor. This issue is solved by the WLP technique consisting of assembling two wafers from the same material and dicing the chips at the very end of the fabrication process. The most common wafer-bonding techniques used in RF MEMS are direct surface bonding, glass frit and metallic layer bonding, achieving a rigid contact between the wafers. In case of bending, this features minimizes the extensional stresses at the interface, close to the neutral fiber of the assembly. Since

it coincides with the region of acoustic energy localization, such Wafer-Level Packaging (WLP) results into poor stress sensitivity of the sensors. Then, here–presented research was motivated by the need to reach a good compromise between the protection and the preservation of the stress sensitivity of the packaged delay lines.

II. DESIGN OF WAFER LEVEL PACKAGING

The most simple and generic WLP strategy relies on the assembly of 2 wafers of the same material and thickness. In such structure, traction-extension can be effectively transmitted along the entire cross-section of the assembly, but a flexural bending imposed by the monitored external structure has little chance to induce significant extensional strain and stress in the sensor if the surface acoustic wave propagates in the vicinity of the neutral fiber of the assembly. Conversely, by principle, the maximum longitudinal stress on the internal surface of a 2 wafers assembly is obtained when the sealing allows a perfect sliding between the wafers, as can be checked on Fig. 1 showing the FEA–computed distribution of the extensional strain ε_{xx} in the entire structure.

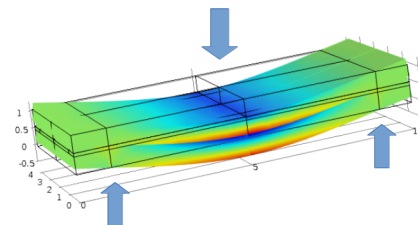


Fig. 1. Schematic distribution of extensional strain ε_{xx} for a three–points bending experiment applied to a typical two–wafers assembly with a sliding contact at the periphery. A 20 N net transverse force induces a value of ε_{xx} about $5.6 \cdot 10^{-4}$ at the upper surface of the base layer. Upon applying rigid contact conditions, the longitudinal strain drops to $1.8 \cdot 10^{-4}$.

We investigated the possibility to improve the stress–sensitivity of the packaged devices by realizing a soft polymer seal between the two wafers of the assembly. The moderate stiffness of the polymer joined with a sufficient thickness is expected to significantly soften the mechanical link between the two LNO layers, thereby increasing the longitudinal strain and stress at the free surface of the delay line wafer, in order

to improve the stress–sensitivity of the packaged device. In this purpose, a seal consisting of a $50\ \mu\text{m}$ –thick layer of SU–8 photoresist was found worth investigating, while eliminating the need of any additional etching operation to permit the free propagation of the SAW on top of the base wafer. The delay line systems consisted of one IDT transducer with 10 finger pairs plus two short reflectors on the measurement path and another one on the opposite side of the IDT for calibration of the time delay. The period of the IDT is $40\ \mu\text{m}$ for the test samples operating near 100 MHz, and $20\ \mu\text{m}$ for the samples operating near 200 MHz.

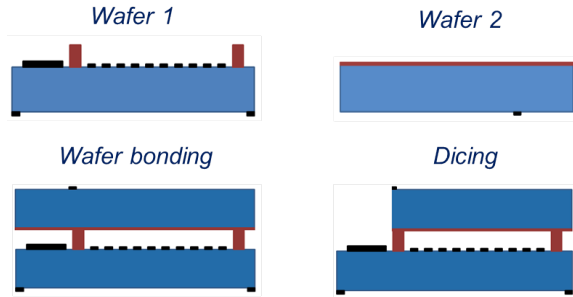


Fig. 2. Principle of soft polymer assembly for here–studied WLP design.

The fabrication process of the devices is illustrated on Fig. 2. Its main steps are the following:

a) Processing of Wafer 1 (device):

- Patterning the delay lines (Au deposit).
- Sputtering a thicker layer for the contact pads aimed to receive antennas after processing the WLP.
- Patterning of crosses to guide the dicing operation to separate the packaged die at the final step.
- Deposit and patterning of the $50\ \mu\text{m}$ –thick layer of SU–8 2075 polymer photoresist.

b) Processing of Wafer 2 (cap):

- Patterning dicing crosses (Au) to guide the dicing of the cap layer, aimed to provide access to the antennas contact pads.
- Spin-coat a thin layer of SU–8 2002 on the entire surface, in order to permit mutual adhesion by pressure and moderate heating.

c) Assembly and final operations:

- Wafers alignment and bonding.
- Dicing of wafer 2 to expose the contact pads.
- Dicing the entire thickness of the assembly in order to separate the chips.

III. PHASE-SHIFT MEASUREMENT UNDER 3-POINTS BENDING LOAD EXPERIMENT

Three–points bending tests were performed on both packaged and unpackaged chips with a traction machine of the



Fig. 3. Three–points bending experiment of a packaged chip (inside the ellipse mark).

Applied Mechanics Dpt. of FEMTO–ST. The electrical response was recorded during various transverse load cycles back and forth between 0 and $40\ \text{N}$. The packaged samples broke upon application of a transverse load threshold near $45\ \text{N}$. Fig. 4 shows typical response of a 200 MHz packaged device.

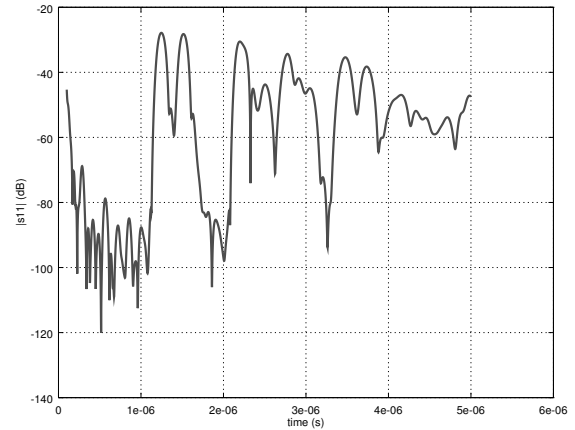


Fig. 4. $|s_{11}|$ electrical response of a 200 MHz packaged delay line.

The echoes correspond to the successive reflexions on the 3 reflectors present on the devices, including multiple reflexions along the acoustical path. The corresponding phase response is shown on Fig. 5. The phase behavior is altogether linear in the vicinity of the amplitude peaks. Then we selected the stress–induced phase change at $1.2\ \mu\text{s}$, $1.4\ \mu\text{s}$, $2.1\ \mu\text{s}$, and $2.7\ \mu\text{s}$ to plot the force–sensitivity characteristics shown on Fig. 6.

IV. ANALYSIS OF RESULTS

The relative phase shift is related to the bias–induced velocity shift and the time delay by the following chain of relationships:

$$\delta\varphi = \omega\delta\tau = \omega\delta\left(\frac{L}{V}\right) = -\frac{\omega L}{V^2}\delta V = -\omega\tau\frac{\delta V}{V} \quad (1)$$

where φ denotes the phase of the response at a fixed observation point, V denotes the phase velocity of the surface wave, τ is the time delay and L is the distance travelled by the wave. Since velocity is scalar and static strain and stress as well are

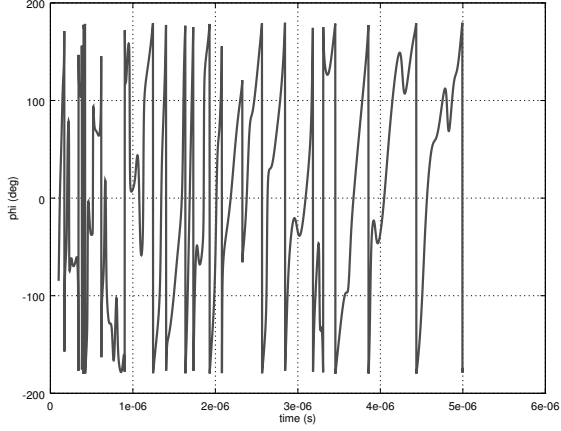


Fig. 5. Phase response of a 200 MHz packaged delay line.

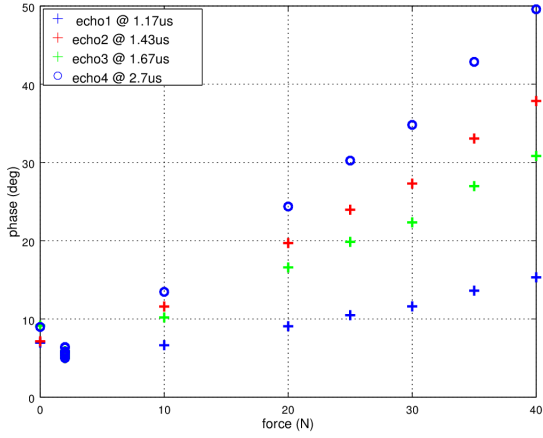


Fig. 6. Phase-shift v.s force characteristics of different echoes.

second rank tensors, the velocity shift is related to strain and stress by second rank pseudo-tensors¹, for instance:

$$\frac{\delta V}{V} = \alpha_{KL} \sigma_{KL} \text{ or } \frac{\delta V}{V} = \beta_{KL} \bar{E}_{KL} \quad (2)$$

where σ and \bar{E} respectively denote the static stress and strain, whereas α and β merely define the stress- and strain-sensitivity coefficients of the surface wave. These formulas hold only for uniform biases. The calculation of stress-sensitivity coefficients can be found in [1], [2] for the purely elastic problems but can also be derived for piezoelectric problems. Before proceeding further, we find enlightening and even necessary to consider the global context of the so-called acousto-elastic effect ruling the propagation of small-amplitudes elastic waves in a biased structure. Acousto-elastic effect and related problems were the subject of an

¹Although the value of the wave velocity is scalar, it is defined as the norm of the vector $\partial \bar{u} / \partial t$ where \bar{u} is the particular displacement. Then V depends on the orientation of the propagation on the semi-infinite substrate and this must be taken into account when calculating the stress-sensitivity coefficients. Thus α is not a tensor... unless we consider it is defined for the unique problem of the YX1-/128°SAW propagation in lithium niobate.

abundant literature in the second half of the 20-th century and constitute a particular application of the non linear theory of thermo-electro-elasticity in finite deformation. We illustrate below some of its aspects of interest for our purposes, while restricting here-presented formulas to the purely elastic case, for the sake of clarity and simplicity. Actually we performed all our numerical computations by taking into account the effect of the bias on the elastic part of the complete piezoelectric problem. In other words, we ignore bias-induced effects on the piezoelectric and dielectric behavior, although Rayleigh waves velocity is computed in the framework of piezoelectricity. Here we follow the well-established Lagrangian approach of small fields superimposed onto a bias [3], [4]. Then the propagation equations of surface waves [5] on a semi-infinite substrate of normal \bar{n}_2 in a current frame, rotated w.r.t crystallographic axes, can be mapped onto the set of fixed and known material coordinates (X_L) of the structure defined prior exertion of any bias:

$$\begin{aligned} \tilde{K}_{1\gamma,1} + \tilde{K}_{2\gamma,2} &= \rho_0 \ddot{u}_\gamma, \quad \gamma \in [1, 2, 3] \\ \tilde{K}_{L\gamma} &= G_{L\gamma 1\epsilon} u_{\epsilon,1} + G_{L\gamma 2\epsilon} u_{\epsilon,2} \\ G_{L\gamma M\epsilon} &= c_{L\gamma M\epsilon} + \hat{c}_{L\gamma M\epsilon}(w_{P,Q}) \\ \hat{c}_{L\gamma M\epsilon}(w_{P,Q}) &= \bar{T}_{LM} \delta_{\gamma\epsilon} + c_{L\gamma M\epsilon PQ}^3 \bar{E}_{PQ} \\ &\quad + c_{L\gamma MK}^2 w_{\epsilon,K} + c_{LKM\epsilon}^2 w_{\gamma,K} \\ \bar{T}_{LM} &= c_{LMNP} w_{N,P} = c_{LMNP} \bar{E}_{NP} \end{aligned} \quad (3)$$

where $\bar{u}(X_L, t)$ is the dynamic displacement field, $\bar{w}(X_L)$ is the static displacement field (bias) and ρ_0 is the mass density of the undeformed body since the problem is mapped onto the fixed material coordinates. Also $\tilde{K}_{L\gamma}$ denotes the first Piola-Kirchhoff stress tensor and $G_{L\gamma M\epsilon}$ indicates a component of the effective elastic coefficients in the so-called Lagrangian configuration. Then one should solve these equations together with the associated boundary conditions prescribed on the free surface of normal \bar{n}_2^0 that we consider located at $X_2 = 0$:

$$\tilde{K}_{2\gamma}(X_1, 0) = 0, \quad \gamma \in [1, 2, 3]. \quad (4)$$

Although Eq. (3) initially puts the bias-induced incremental elastic constant $\hat{c}_{LKM\epsilon}$ as a function of the static displacement gradients $w_{M,N}$ it is possible to reformulate \hat{c} as a function of the static strain

$$\begin{aligned} \hat{c}_{L\gamma M\epsilon} &= \bar{T}_{LM} \delta_{\gamma\epsilon} + c_{L\gamma M\epsilon AB}^3 \bar{E}_{AB} \\ &\quad + c_{L\gamma MN}^2 \bar{E}_{\epsilon N} + c_{LNM\epsilon}^2 \bar{E}_{\gamma N}. \end{aligned} \quad (5)$$

Because the static stress tensor is easily deduced from the static strain by inverting the tensor of second order elastic constants c^2 , it is easy to further rewrite the \hat{c} increment of elastic constants as a linear combination of the static stresses, which we find unnecessary to explicitly reproduce here. Because its linear expansion must be performed in terms of the displacement gradients which are non-symmetrical, instead of the classical strains which are symmetrical, the first Piola-Kirchhoff tensor $\tilde{K}_{L\gamma}$ is asymmetric by nature. Then it must be stored in a matrix of dimension $[9 \times 9]$. In case of stress-free bias such as free thermal expansion, it has been demonstrated that this matrix remains symmetric [6] provided that the notations be properly chosen. Nevertheless, the expression of the bias-induced increments $\hat{c}_{L\gamma M\epsilon}$ clearly

indicates that in case of a stress-generating or simply non-uniform bias, the resulting \mathbf{G} matrix is no more symmetrical. Then, two approaches can be followed to compute the velocity of the surface acoustic waves from the incremental equations of motion:

- For uniform biases and some cases of non-uniform but rather simple biases, it is still possible to directly solve the equations following the same procedure as in linear elasticity problems, as long as the $[9 \times 9]$ size of the $[\mathbf{G}]$ matrix and its eventual asymmetry induce relatively small changes in the classical procedure.
- A first order perturbation procedure [7] involving the computation of integrals relying on the knowledge of the partial derivatives of the unperturbed (unbiased) displacement field and of the static (biasing) displacement field.

The problem of SAW propagation in rectangular plates submitted to pure extensional or pure bending biases can be solved with either one approach. Ref. [5] provides with a detailed comparison of the direct and perturbation approaches to compute the velocity shift of Rayleigh waves in a purely bended structure. For here-presented work, we designed a computer program able to numerically determine the velocity of the SAW for the $YXl/128^\circ$ orientation of a LiNbO_3 plate submitted to a uniform bias, and in particular in the case of a pure longitudinal stress. Despite of the bias, the structure of the Rayleigh waves could still be assumed to comply with the classical combination obtained in case of propagation on a unbiased substrate:

$$u_i = \left(\sum_{n=1}^4 C_n \beta_i^{(n)} e^{j\omega s_2^{(n)} x_2} \right) e^{j\omega(s_1 x_1 - t)}, \quad (6)$$

where C_n represents the weight of a given partial wave in the combination, $\beta_i^{(n)}$ is a component of the normalized amplitude vector of the n -th partial wave, s_1 is the slowness of the guided propagation and $s_2(n)$ is the slowness of the partial wave in the vertical direction. We intend to provide more details about the direct approach in a further paper. The obtained value of the velocity-shift was found about 80% of the value provided by an earlier program elaborated at LPMO laboratory at the end of the nineties [1], [2]. The latter program is based on simplifications occurring in Tiersten's perturbation integral for the computation of Rayleigh velocity [8] in the case of uniform elastic bias. The perturbation formula for the two-dimensional problem of the proagation of Rayleigh waves of quasi-infinite aperture is the following:

$$\frac{\delta V}{V_0} \approx \frac{\int_{S_0} \hat{c}_{L\gamma M \varepsilon}(w_{M,N}) \mathcal{R}(u_{\varepsilon,M}^0 u_{\gamma,L}^{0*}) dS_0}{2\rho_0 \omega^2 \int_{S_0} \mathcal{R}(u_\alpha^0 u_\alpha^{0*}) dS_0}, \quad (7)$$

where \mathcal{R} denotes the real part, the superscript * denotes the complex conjugate, S_0 being the sagittal plane. In case of a uniform bias, the integrals can be reduced to simpler integrals

over the depth of the semi-infinite substrate:

$$\frac{\delta V}{V_0} = \frac{\hat{c}_{L\gamma M \varepsilon} \int_{-\infty}^0 u_{\varepsilon,M}^0 u_{\gamma,L}^{0*} dx_2}{2\rho_0 \omega^2 \int_{-\infty}^0 u_\alpha^0 u_\alpha^{0*} dx_2}. \quad (8)$$

Because of the exponential character and the convergence in the depth of the substrate of the partial waves (6) entering the structure of Rayleigh waves, the integrals are easily calculated, leading to the final result:

$$\frac{\delta V}{V_0} = \frac{\sum_{L=1}^2 \sum_{\gamma=1}^3 \sum_{M=1}^2 \sum_{\varepsilon=1}^3 \hat{c}_{L\gamma M \varepsilon} \sum_{n=1}^4 \sum_{m=1}^4 \frac{C_n C_m^* \beta_\varepsilon^{(n)} \beta_\gamma^{(m)*} s_M^{(n)} s_L^{(m)*}}{s_2^{(n)} - s_2^{(m)*}}}{2\rho_0 \sum_{\alpha=1}^3 \sum_{n=1}^4 \sum_{m=1}^4 \frac{C_n C_m^* \beta_\alpha^{(n)} \beta_\alpha^{(m)*}}{s_2^{(n)} - s_2^{(m)*}}} \quad (9)$$

The stress-sensitivity coefficients α_{LM} introduced at Eq. (2) are easily computed from both this expression and (5). Using the set of elastic constants provided by Ref. [9] gives the following value of σ_{xx} stress-sensitivity coefficient of Rayleigh wave velocity for the considered problem:

$$\alpha_{11} \approx -4.257 \cdot 10^{-11} / Pa \quad (10)$$

The FEA-computed stress for the 3 points bending test on top of the packaged delay line wafer was found close to $-3.2 \cdot 10^7 Pa$ when the net transverse force reached 20 N and assuming a rigid contact of the polymer with the 2 layers of niobate. Substituting this value together with (10) into (2) and the obtained result back into (1) yielded a phase-shift of 20° for the fourth echo ($\tau \approx 2.7 \mu s$) of the phase-response. The corresponding measurement of $\delta\varphi$ observed on Fig. 6 for this point was 23° . Then the agreement between theory and experiment was found good. Assuming that the polymer-niobate contact allows a free sliding, which corresponds to the "ideal" case of Fig. 1 yielded a FEA-computed value $\sigma_{xx} \approx 1.47 \cdot 10^8 Pa$ at the surface of the chip. Then the corresponding predicted sensitivity becomes nearly 5 times larger than the one that we actually observed. Nevertheless a further experiment was required, given the variability of results between direct and perturbation approach, the even larger variability induced by the values of elastic constants (nearly a factor 2 between the results calculated from [10] and [9]) and the expectable unaccuracy arising from the simplifying assumption of the essential contribution of the stresses near the surface. Then another three-points bending test was performed with a raw (unpackaged) chip. In that case the chip was flip-flopped in the traction apparatus in order to permit the free propagation of the SAW. The force had to be reduced since the chip broke at a much smaller transverse load (near 25 N), as expected. We performed the calculation for the same echo at $2.7 \mu s$ as previously and for a transverse force equal to 9 N , giving a FEA-computed longitudinal stress $\sigma_{xx} \approx 2.4 \cdot 10^8 Pa$. Then, using the same computation procedure as previously, we obtained a theoretical phase-shift close to -180° , whereas the measured value was found close to -195° . The similar agreement between theory and experiment for the cases of the packaged and the raw chips confirms to a large extent the validity of the approach and the conclusion drawn about the rather adhesive link between the polymer layer and the lithium niobate wafers.

V. CONCLUSION

Here-presented study indicated a satisfactory agreement between calculated and measured values of the phase-shift of the response of packaged and raw delay lines under a transverse load, assuming that the polymer used to perform the WLP assembly achieves a rigid link with the two wafers of lithium niobate. The loss of sensitivity between a firm contact and a sliding contact at the interfaces is about 5, and the sliding contact case would still represent a loss of a factor 2 with respect to the raw chip, which seems unavoidable if the two wafers have the same thickness, since two identical plates in parallel double the stiffness with respect to a single plate. Then a further optimization of the packaging is still needed to improve the stress-sensitivity of the device in case of bending imposed by the supporting structure. Nevertheless, this WLP design is promising since the stress-sensitivity is still largely measurable in case of pure bending of the chip. In addition, one must point out that the actual biasing states imposed to the SAW sensor by the monitored structures are combinations of bending and extension-compression rather than pure flexure.

ACKNOWLEDGMENT

The authors would like to thank the LAbEX ACTION for the postdoctoral support of L. Arapan through the ECCO project and the DGA for the support of the PhD of G. Wong through the ALCASAR/LANCASTER project.

REFERENCES

- [1] D. Hauden E. Bigler, G. Théobald. Stress-sensitivity mapping for surface acoustic waves on quartz. *IEEE Trans. on Ultrasonics, Ferroelectrics, and Frequency Control*, 36:57–62, 1989.
- [2] S. Ballandras E. Bigler. Stress sensitivity coefficients: a general approach for bulk, rayleigh and surface transverse waves. *Proc. of IEEE Int. Freq. Contr. Symp. (IFCS)*, pages 422–429, 1996.
- [3] H. F. Tiersten. On the nonlinear equations of thermo-electroelasticity. *Int. J. Engng Sci.*, 9:587–604, 1971.
- [4] J. C. Baumhauer and H. F. Tiersten. Non linear electroelastic equations for small fields superposed on a bias. *J. Acoust. Soc. Am.*, 54(4):1017–1034, 1973.
- [5] B.K. Sinha and H.F. Tiersten. On the influence of a flexural biasing state on the velocity of piezoelectric surface waves. *Wave Motion 1*, pages 37–51, 1979.
- [6] Bernard Dulmet and Roger Bourquin. Lagrangian effective material constants for the modeling of thermal behavior of acoustic waves in piezoelectric crystals. i. theory. *J. Acoust. Soc. Am.*, 110(4):1792–1799, 2001.
- [7] H. F. Tiersten. Perturbation theory for linear electroelastic equations for small fields superposed on a bias. *J. Acoust. Soc. Am.*, 64(3):832–837, 1978.
- [8] H. F. Tiersten and B. K. Sinha. A perturbation analysis of the attenuation and dispersion of surface waves. *J. Appl. Phys.*, 49(11):87–95, 1978.
- [9] M. Onoe A. Warner and G. Coquin. Determination of elastic and piezoelectric constants for crystals in class (3m). *J. Acoust. Soc. Am.*, 42:1223–1331, 1967.
- [10] Yasuo Cho and Kazuhiko Yamanouchi. Non linear, elastic, piezoelectric, electrostrictive, and dielectric constants of lithium niobate. *J. Appl. Phys.*, 61:875–887, 1987.

Progress on a pulsed CPT clock: Reduction of the main noise source contributions

F. Tricot, P. Yun, B. Francois¹, S. Mejri, J-M. Danet², M. Lours, S. Guerandel, E. de Clercq
LNE-SYRTE, Observatoire de Paris, PSL, Research University, CNRS, Sorbonne Universités, UPMC Univ. Paris 06
61 avenue de l'Observatoire, 75014 Paris – France

francois.tricot@obspm.fr

¹AR-Electronique, 16 rue la Fayette, 25000 Besançon - France

²Present address: SYRLINKS, ZAC des Champs Blancs, 28 rue Robert Keller, Cesson-Sevigne – France

Abstract— This paper reports on progress on a compact clock based on Coherent Population Trapping (CPT) using caesium vapour cell. The clock is working in a pulsed regime with two orthogonal linear polarizations made by two phase-locked lasers tuned to 895 nm and separated by 9.2 GHz. The short-term frequency stability is mainly limited by the Local Oscillator (LO) noise contribution and the laser relative intensity noise (RIN) at the level of 3.2×10^{-13} at 1 s. We present in this paper the work done to improve our experimental device by reducing the frequency noise source contributions.

Keywords— *atomic clock, vapour cell, coherent population trapping, frequency stability,*

I. INTRODUCTION

Many on-board applications (GNSS) needs compact and high stability clocks. As an example, the vapour cell atomic clock used in Galileo system has a frequency stability at the level of 5×10^{-12} at 1 s [1]. The next generations of compact atomic clocks based on Coherent Population Trapping (CPT) phenomenon offer a good alternative for this applications [2]: their simple scheme and high performance stability represent a promising candidate. In those clocks the atomic vapour cell is pumped and probed by two lasers separated by the microwave clock frequency.

In this paper we report investigations on the two main frequency noise sources of the SYRTE CPT clock prototype. In Section II we describe the experimental setup. Our prototype combines a high signal contrast and a narrow resonance width by using a so-called double Λ scheme and a Ramsey interrogation sequence [3]. It has been shown that the short-term frequency stability of our clock is limited by the Local Oscillator (LO) noise and the laser relative intensity noise (RIN) [4]. In Section III we present this two last stability contributions and the work in progress to improve them.

II. EXPERIMENTAL SETUP

Two extended cavity diode lasers (ECDL) are tuned to the D1 line of the caesium at 895 nm. The inset in Fig.1 shows the energy levels used to build the double Λ interrogation. The laser beams are orthogonally linearly polarized in order to get simultaneous $\sigma+$ and $\sigma-$ transitions. The Master laser is locked on the $F = 4 \rightarrow F' = 4$ transition thanks to a saturated absorption scheme. The laser beams are superimposed through a polarizing beam splitter (PBS), one path is used to produce a beat-note at

9.192 GHz. This 9.192 GHz optical beat-note is detected by the fast photodiode PD1 and compared to the frequency synthesis chain, then the error signal is integrated in the optical phase lock loop (OPLL) to phase-lock the slave laser.

On the other path, the superimposed laser beams are switched on-an-off by the Ramsey acousto-optic modulator (AOM_R) before crossing the Cs cell. The Cs cell, 5 cm long and 2 cm diameter, is also filled with a buffer gas (b.g.) mixture: N₂-Ar [5]. The transmitted power is recorded by the clock photodiode PD2. The signal is processed by the computer (PC) which drives simultaneously the AOM_R and a direct digital synthesizer in the frequency synthesis chain. The frequency synthesis chain is referenced by our laboratory H-maser. For more details, the synthesis chain is explained in [6].

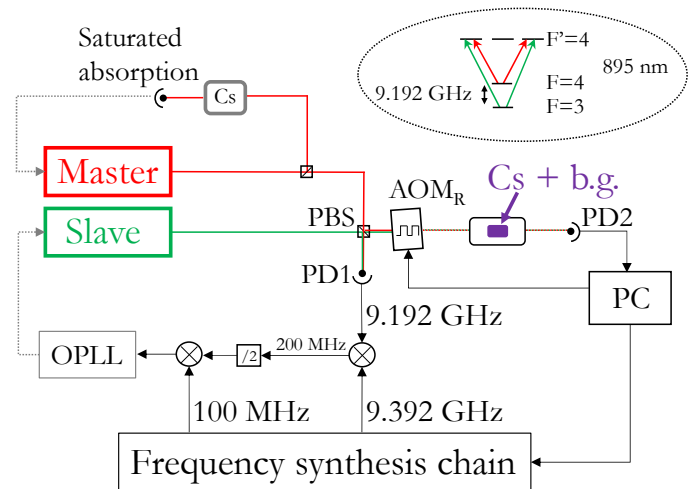


Fig. 1. Scheme of the experimental setup. The master laser is frequency locked by a saturated absorption scheme. The Slave laser is phase-locked on the master laser. PBS: polarizing beam splitter. PD1: fast photodiode. PD2: clock photodiode. OPLL: optical phase lock loop. AOM_R: the Ramsey acousto-optic modulator. The inset shows the Cs energy levels involved in the interrogation.

III. EXPERIMENTAL RESULTS

A. Estimation of the Dick effect contribution

The Dick effect originates from the down-conversion of the LO frequency noise at Fourier frequencies higher than the interrogation frequency [7]. The atomic response to a phase step

F. Tricot is supported by Thales Electron Devices and DGA. S. Mejri is supported by the CNES. The project is partly funded by ANR.

is given by the sensitivity function $g(t)$ [4,7]. In practical, a good estimation of the Dick effect contribution $\sigma_{yDick}(\tau)$ at the interrogation time τ is given by the formula:

$$\sigma_{yDick}^2(\tau) = \frac{1}{\tau} \sum_{m=1}^{\infty} \left(\frac{g_m}{g_0}\right)^2 S_y \left(\frac{m}{T_c}\right) \quad (1)$$

where g_m are the Fourier coefficients of the sensitivity function of $g(t)$ and S_y is the relative frequency power spectral density noise (PSD) of the LO at the modulation frequency harmonics m .

In order to improve our frequency synthesis chain, we implemented a better 100 MHz source (Pascall, OCXOF-E-100). We optimised the multiplication the chain and added an improved phase-lock loop circuit. The 9.392 GHz signal issued from the frequency synthesis chain has a Dick effect contribution at the level of $\sigma_{yDick} = 6.5 \times 10^{-14}$ at 1 s. This contribution is similar to the FEMTO-ST synthesis chain [8]. The OPLL has also been upgraded by optimizing the bandwidth and the electronic circuit itself. In Fig. 2, we clearly see that the microwave chain is no longer limiting the total Dick effect contribution.

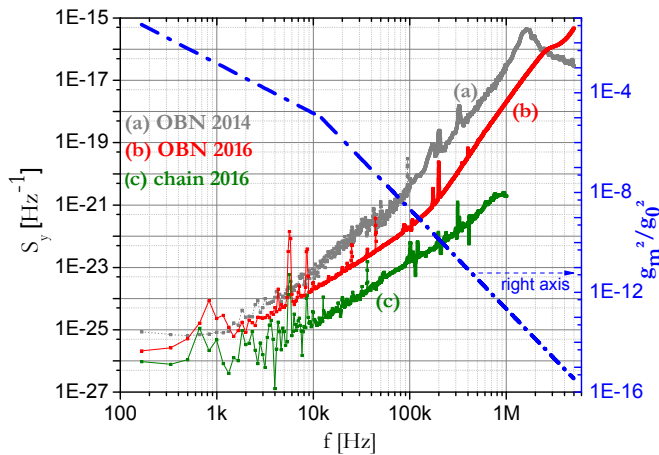


Fig. 2. Left axis: Relative frequency power spectral density noise of microwave signals at the frequency modulation harmonics. The total noise (a) and (b) measured on the 9.192 GHz optical beat-note (OBN) signal. The microwave chain noise (c) measured on the 9.392 GHz signal. Right axis: in blue the Fourier coefficients of $g(t)$.

B. Estimation of the intensity noise contribution

The second main noise source is the laser intensity noise. The fluctuations on the detected signal is directly proportional to the intensity fluctuation before the Cs cell [9]. This intensity noise is basically converted into a frequency noise σ_{yRIN} :

$$\sigma_{yRIN}(\tau) \sim \frac{\Delta\nu}{\nu_0} \frac{\sigma_{RIN}}{C} \sqrt{\frac{T_c}{\tau}} \quad (2)$$

where $\Delta\nu$ is the resonance width, ν_0 the resonance frequency, T_c the cycle time of interrogation, τ the averaging time, C is the resonance's contrast defined as the signal amplitude divided by the background and σ_{RIN} is the standard deviation related to the RIN filtered by the time detection window. From the measured

laser intensity we can estimate the intensity noise contribution to the clock stability. We use upgraded power lock circuit to decrease the intensity noise. In Fig. 3 we see the improvement of the RIN measured after the power lock, just before the AOM_R. By taking into account the degradation of the RIN caused by the AOM_R, and thanks to (2) we estimate the intensity noise contribution at the level of 1×10^{-13} at 1 s. This preliminary result will be confirmed and improved.

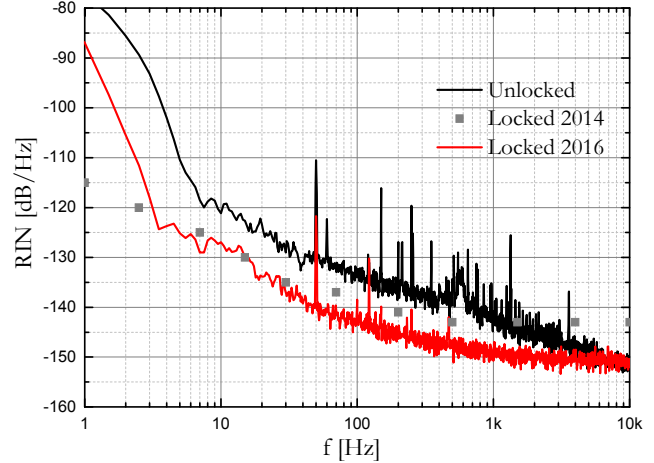


Fig. 3. Relative intensity noise of the laser beam measured before the AOM_R. Black: free running, grey: power locked in 2014, red: power locked in 2016.

CONCLUSION

We have presented a pulsed CPT clock prototype and work in progress in order to improve the short-term stability. The two main limiting noises, Dick effect and laser intensity, have been reduced. The preliminary results (TABLE I.) lead to an expected short-term stability of about $\sigma_y = 2 \times 10^{-13}$ at 1 s. Such a frequency stability would raise our clock prototype among other best vapour cell clocks [10-12].

TABLE I. FREQUENCY NOISE SOURCE AND ITS CONTRIBUTION

Frequency noise source		Estimated $\sigma_y(1\text{ s}) \times 10^{13}$	
		2014	2016
Dick effect	100 MHz	1.2	0.65
	Frequency chain	1.0	
	OPLL	2.1	1.7
Laser intensity		1.9	1.0
Total		3.2	2.1

ACKNOWLEDGMENT

We would like to thank the electronic team assistance. We also thank Rodolphe Boudot for helpful discussions. We are grateful to Pierre Bonnay for manufacturing Cs cells.

REFERENCES

- [1] P. Waller *et al.*, "The in-orbit performances of GIOVE clocks", IEEE Trans. Ultrason., Ferroelect., Freq. Contr. **57**, 738 (2010)
- [2] J. Vanier, "Atomic clocks based on coherent population trapping: a review", Appl. Phys. B **81**, 421-442 (2005)
- [3] T. Zanon, S. Guérandel, E. de Clercq, D. Holleville, N. Dimarcq, and A. Clairon, "High Contrast Ramsey Fringes with Coherent Population

- Trapping Pulses in a Double Lambda Atomic System”, *Phys. Rev. Lett.* **94**, 193002 (2005)
- [4] J.-M. Danet, M. Lours, S. Guerandel, E. de Clercq, “Dick effect in a pulsed atomic clock using Coherent Population Trapping”, *IEEE Trans. Ultrason., Ferroelect., Freq. Contr.* **61**, 547 (2014)
- [5] O. Kozlova, S. Guerandel, E. de Clercq, “Temperature and pressure shift of the Cs clock transition in the presence of buffer gases : Ne, N₂, Ar”, *Phys. Rev. A* **83**, 062714 (2011)
- [6] R. Boudot, S. Guerandel, E. de Clercq, “Simple-design low-noise NLTL-based frequency synthesizers for a CPT Cs Clock”, *IEEE Trans. Instrum. Meas.* **58**, 3659 (2009)
- [7] G. J. Dick, “Local oscillator induced instabilities in trapped ion frequency standards”, 19th PTTL, 133 (1987)
- [8] B. François, C. E. Calosso, J.-M. Danet, R. Boudot, “A low phase noise microwave frequency synthesis for a high-performance cesium vapor cell atomic clock”, *Rev. Sci. Instrum.* **85**, 094709 (2014)
- [9] J.-M. Danet, “Horloge atomique à piégeage cohérent de population du césium en cellule : limitations à la stabilité de fréquence”, PhD thesis (2014)
- [10] S. Micalizio, C. E. Calosso, A. Godone, F. Levi, “Metrological characterization of the pulsed Rb clock with optical detection”, *Metrologia* **49**, 425 (2012)
- [11] S. Kang, M. Gharavipour, C. Affolderbach, F. Gruet, G. Mileti, “Demonstration of a high-performance pulsed optically pumped Rb clock based on a compact magnetron-type microwave cavity”, *J. Appl. Phys.* **177**, 104510 (2015)
- [12] M. Abdel Hafiz and R. Boudot, “A coherent population trapping Cs vapor cell atomic clock base on push-pull optical pumping”, *J. Appl. Phys.* **118**, 124903 (2015)

Memory-efficient high-speed algorithm for multi- τ PDEV analysis

Magnus Danielson
R&D System Design
Net Insight AB
Stockholm, Sweden
Email: magda@netinsight.net

François Vernotte
Observatory THETA/UTINAM,
UBFC/UFC and CNRS
Besançon, France
Email: francois.vernotte@obs-besancon.fr

Enrico Rubiola
CNRS FEMTO-ST Institute,
Dept Time and Frequency
Besançon, France
Email: rubiola@femto-st.fr

Abstract—The Ω preprocessing was introduced to improve phase noise rejection by using a least square algorithm. The associated variance is the PVAR which is more efficient than MVAR to separate the different noise types. However, unlike AVAR and MVAR, the decimation of PVAR estimates for multi- τ analysis is not possible if each counter measurement is a single scalar. This paper gives a decimation rule based on two scalars, the processing blocks, for each measurement. For the Ω preprocessing, this implies the definition of an output standard as well as hardware requirements for performing high-speed computations of the blocks.

Index Terms—Least square methods, Phase noise, Stability analysis, Time-domain analysis.

I. PVAR AND Ω -COUNTERS

The concept of Ω -counter was formulated by Rubiola [1], based on Johansson [2], to achieve the optimal rejection of white phase noise for short term frequency measurement by using an estimator based on the least squares. Such methods was presented by Barnes [3], for the purpose of drift estimation under presence of white noise. The algorithms of [4] does not provide means of decimation of data while maintaining the least square properties, it rather states that there is no such method known. In [5] such method was presented, thus allowing for decimation.

The principle of this frequency estimation is to calculate the least squares slope over a phase sequence $\{x_k\}$ obtained at instants $t_k = k\tau_0$ with $k \in \{0, \dots, N-1\}$ where τ_0 is the sampling step and $\tau = (N-1)\tau_0$ the total length of the sequence. It is well known that the least squares provide the best slope estimate in the presence of white noise (i.e. white PM noise) [3]. It has been demonstrated that, in the presence of white PM, the variance of this frequency estimate is lower by a factor of $\frac{3}{4}$ than the MVAR. Moreover, since the least squares are optimal for white noise, the variance of the Ω -counter estimate is minimal. It is then an efficient estimator [6].

The Ω -counter weight functions for phase data as well as for frequency deviations are plotted in Figure 1. The shape of $w_c(t)$ (see Figure 1-B) explains the choice of the Greek letter Ω to name this counter [7], [1].

PVAR is then defined as $\text{PVAR}(\tau) = \frac{1}{2} \langle (\hat{y}_2^\Omega - \hat{y}_1^\Omega)^2 \rangle$ [4]. The weight function associated to PVAR for phase data is plotted in Figure 2.

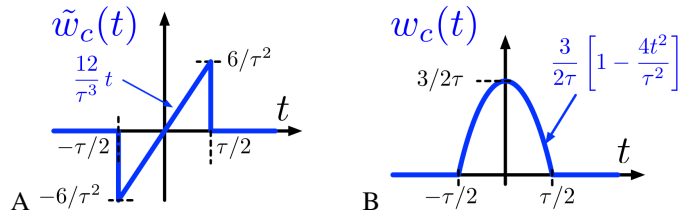


Fig. 1. weight functions of the Ω -counter computed from phase data (A, left) or from frequency deviations (B, right).

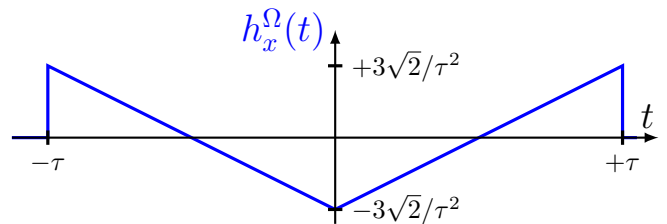


Fig. 2. weight function associated to PVAR for phase data.

PVAR, like MVAR, is intended to deal with short term analysis (and then white and flicker PM noises) whereas AVAR is preferred for the measurement of long term stability and timekeeping. The main advantage of PVAR regarding MVAR relies on the larger EDF of its estimates, and in turn the smaller confidence interval. The best of PVAR is its power to detect and identify weak noise processes with the shortest data record. PVAR is superior to MVAR in all cases, and also superior to AVAR for all short-term and medium-term processes, up to flicker FM included. AVAR is just a little better with random walk and drift. Therefore, PVAR should be an improved replacement for MVAR in all cases, provided the computing overhead can be accepted.

Thus, the only drawback of PVAR lies in the difficulty to find its decimation algorithm. In order to solve this problem, let us remind the basics of decimation.

II. LEAST-SQUARE FREQUENCY ESTIMATION

A. Linear system

The least square system producing the output vector \mathbf{x} of phase samples from the system state vector \mathbf{c} using the system matrix \mathbf{A} and assuming the error contribution of \mathbf{d} as defined in $\mathbf{x} = \mathbf{A}\mathbf{c} + \mathbf{d}$ having the least square estimation as given by

$$\hat{\mathbf{c}} = (\mathbf{A}^T \mathbf{A})^{-1} \mathbf{A}^T \mathbf{x} \quad (1)$$

For this system, a linear model of phase and frequency state is defined

$$\hat{\mathbf{c}} = \begin{pmatrix} \hat{x} \\ \hat{y} \end{pmatrix} \quad (2)$$

A block of phase samples, taken with τ_0 time in-between them, building the series x_n where n is in the range $\{0, \dots, N-1\}$ where by convention N is the number of phase samples. In the system model, each sample n has an associated observation time $t_n = \tau_0 n$. The matrix \mathbf{A} and the vector \mathbf{x} then becomes

$$\mathbf{A} = \begin{pmatrix} 1 & t_0 \\ \vdots & \vdots \\ 1 & t_n \\ \vdots & \vdots \\ 1 & t_{N-1} \end{pmatrix} = \begin{pmatrix} 1 & 0 \\ \vdots & \vdots \\ 1 & \tau_0 n \\ \vdots & \vdots \\ 1 & \tau_0(N-1) \end{pmatrix} \quad (3)$$

$$\mathbf{x} = \begin{pmatrix} x_0 \\ \vdots \\ x_n \\ \vdots \\ x_{N-1} \end{pmatrix} \quad (4)$$

B. Closed form solution

Inserting (3) and (4) into (1) results in

$$\hat{\mathbf{c}} = \left[\begin{pmatrix} \dots & 1 & \dots \\ \dots & \tau_0 n & \dots \end{pmatrix} \begin{pmatrix} \vdots \\ 1 \\ \vdots \end{pmatrix} \right]^{-1} \times \begin{pmatrix} \dots & 1 & \dots \\ \dots & \tau_0 n & \dots \end{pmatrix} \begin{pmatrix} \vdots \\ x_n \\ \vdots \end{pmatrix} \quad (5)$$

simplifies into

$$\hat{\mathbf{c}} = \begin{pmatrix} \sum_{n=0}^{N-1} 1 & \tau_0 \sum_{n=0}^{N-1} n \\ \tau_0 \sum_{n=0}^{N-1} n & \tau_0^2 \sum_{n=0}^{N-1} n^2 \end{pmatrix}^{-1} \begin{pmatrix} \sum_{n=0}^{N-1} x_n \\ \tau_0 \sum_{n=0}^{N-1} n x_n \end{pmatrix} \quad (6)$$

replacing the sums C and D

$$C = \sum_{n=0}^{N-1} x_n \quad (7)$$

$$D = \sum_{n=0}^{N-1} n x_n \quad (8)$$

becoming

$$\hat{\mathbf{c}} = \begin{pmatrix} N & \tau_0 \frac{N(N-1)}{2} \\ \tau_0 \frac{N(N-1)}{2} & \tau_0^2 \frac{N(N-1)(2N-1)}{6} \end{pmatrix}^{-1} \begin{pmatrix} C \\ \tau_0 D \end{pmatrix} \quad (9)$$

inverse can be solved as

$$\begin{pmatrix} N & \tau_0 \frac{N(N-1)}{2} \\ \tau_0 \frac{N(N-1)}{2} & \tau_0^2 \frac{N(N-1)(2N-1)}{6} \end{pmatrix}^{-1} = \frac{12}{\tau_0^2 N(N-1)(N+1)} \times \begin{pmatrix} \tau_0^2 \frac{(N-1)(2N-1)}{6} & -\tau_0 \frac{N-1}{2} \\ -\tau_0 \frac{N-1}{2} & 1 \end{pmatrix} \quad (10)$$

insertion of (2) and (10) into (9) resulting in the estimators

$$\hat{x} = \frac{6}{N(N+1)} \left(\frac{(2N-1)}{3} C - D \right) \quad (11)$$

$$\hat{y} = \frac{12}{\tau_0 N(N-1)(N+1)} \left(-\frac{N-1}{2} C + D \right) \quad (12)$$

these estimators have been verified to be bias free from static phase and static frequency, as expected from theory. Using these estimator formulas the phase and frequency can be estimated of any block of N samples for which the C and D sums have been calculated.

C. PVAR calculation

The PVAR estimator calculation is defined from the equations

$$\hat{\sigma}_P^2(\tau) = \frac{1}{M} \sum_{i=1}^M (\alpha_i)^2 \quad (13)$$

$$\alpha_i = \frac{1}{\sqrt{2}} (\hat{\mathbf{y}}_i^\Omega - \hat{\mathbf{y}}_{i+1}^\Omega) \quad (14)$$

inserting (12) and (14) into (13) produces

$$\hat{\sigma}_P^2(\tau) = \frac{72}{M \tau_0^2 N^2 (N-1)^2 (N+1)^2} \sum_{i=1}^M \left[(D_i - D_{i+1}) - \frac{N-1}{2} (C_i - C_{i+1}) \right]^2 \quad (15)$$

where (C_i, D_i) and (C_{i+1}, D_{i+1}) is two pairs of accumulated sums being consecutive. These may be either forms by the direct accumulation of (7) and (8) or through the decimation rule of (25) and (26), as long as N is the number of samples in each block (being of equal length) and that the block observation time $\tau = N\tau_0$. Using the decimation rules, any τ calculation can be produced and then their PVAR calculated using (15). Notice that M is the number of averaged blocks.

III. DECIMATION

A. Decimation of different sized blocks

The key idea in decimation is to form the (C, D) pair for a larger set of samples. Consider a block of N_{12} samples. The definition says

$$C_{12} = \sum_{n=0}^{N_{12}-1} x_n \quad (16)$$

$$D_{12} = \sum_{n=0}^{N_{12}-1} nx_n \quad (17)$$

but for practical reason processing is done on two sub blocks being N_1 and then N_2 samples long, giving

$$N_{12} = N_1 + N_2 \quad (18)$$

$$C_1 = \sum_{n=0}^{N_1-1} x_n \quad (19)$$

$$C_2 = \sum_{n=0}^{N_2-1} x_{N_1+n} \quad (20)$$

$$D_1 = \sum_{n=0}^{N_1-1} nx_n \quad (21)$$

$$D_2 = \sum_{n=0}^{N_2-1} nx_{N_1+n} \quad (22)$$

the C_{12} sum can be reformulated as

$$\begin{aligned} C_{12} &= \sum_{n=0}^{N_{12}-1} x_n \\ &= \sum_{n=0}^{N_1-1} x_n + \sum_{n=N_1}^{N_{12}-1} x_n \\ &= C_1 + \sum_{n=0}^{N_2-1} x_{N_1+n} \\ &= C_1 + C_2 \end{aligned} \quad (23)$$

where N_1 can be chosen arbitrarily under the assumption $0 \leq N_1 \leq N_{12}$ and then $N_2 = N_{12} - N_1$. Similarly the D_{12} sum can be reformulated as

$$\begin{aligned} D_{12} &= \sum_{n=0}^{N_{12}-1} nx_n \\ &= \sum_{n=0}^{N_1-1} nx_n + \sum_{n=N_1}^{N_{12}-1} nx_n \\ &= D_1 + \sum_{n=0}^{N_2-1} (N_1 + n)x_{N_1+n} \\ &= D_1 + \sum_{n=0}^{N_2-1} N_1x_{N_1+n} + \sum_{n=0}^{N_2-1} nx_{N_1+n} \\ &= D_1 + N_1 \sum_{n=0}^{N_2-1} x_{N_1+n} + D_2 \\ &= D_1 + N_1C_2 + D_2 \end{aligned} \quad (24)$$

Thus using (23) and (24) any set of consecutive blocks can be further decimated to form a new longer block. For each decimation, only the length N and sums C and D needs to be stored, thus reducing the memory requirements. In a pre-processing stage, these sums can be produced. The decimation rule thus allows for any length being a multiple to the pre-processed length to be produced, with maintained non-biased phase, frequency and PVAR estimator properties.

B. Decimation by N

The generalized decimate by N formulation follows natural from this realization and is proved directly though recursively use of the above rule. Consider that a preprocessing provides C and D values for block of length N_{pre} , then on first decimation block 0 and 1 is decimated, and block 1 needs to be raised with $N_{\text{pre}}C_1$ (as illustrated in Figure 4), as block 2 is decimated in the next round, $2N_{\text{pre}}C_2$ etc, and in general we find

$$C_{\text{tot}} = \sum_{i=0}^{N_2-1} C_i \quad (25)$$

$$D_{\text{tot}} = \sum_{i=0}^{N_2-1} D_i + iN_1C_i \quad (26)$$

for the observation time $\tau = \tau_0 N_1 N_2$ with $N_1 N_2$ samples, for use with the (11) and (12) estimators.

This decimation by N mechanism can be used together with the generic block decimation to form any form of block processing suitable, thus providing a high degree of freedom in how large amounts of data is being decimated.

C. Geometric representation

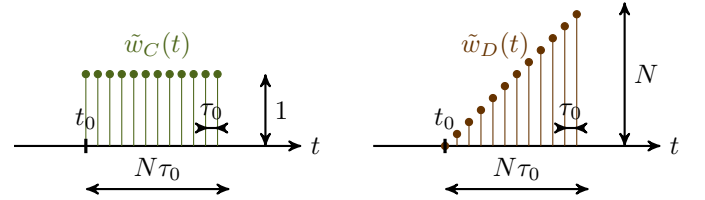


Fig. 3. weight functions of the C and D elementary block pair.

1) *Decimation rule:* Figure 3 represents the weight functions of the C and D elementary block pair that we will symbolize respectively with \square and \triangle .

In the same way as in § III-A, let us consider two consecutive sets of N_1 samples, beginning respectively at instants t_1 and t_2 , and the whole sequence of $N_{12} = 2N_1$ samples. We can form the blocks C_1 and D_1 over the first sub-sequence, C_2 and D_2 over the second one as well as C_{12} and D_{12} over the whole sequence (see left hand side of Figure 4). The right hand side of Figure 4 shows that $C_{12} = C_1 + C_2$ and $D_{12} = D_1 + N_1C_2 + D_2$ as demonstrated in (23) and (24).

2) *The Ω -counter weight function:* As stated in § I, the weight function of the Ω -counter for phase data $x(t)$ is given by [4]. Figure 5 shows that the estimate \hat{y}^Ω of the Ω -counter is:

$$\hat{y}^\Omega \propto D - \frac{N}{2}C.$$

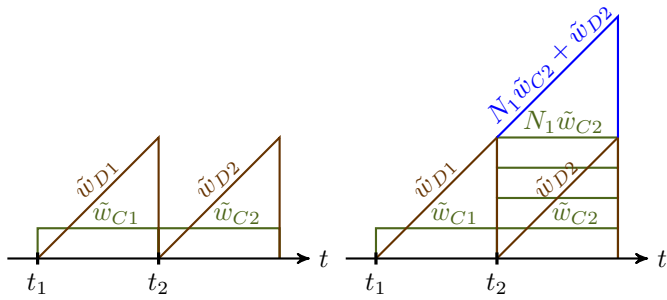


Fig. 4. Decimation rule of the (C_1, D_1) and (C_2, D_2) block pair weight functions over two adjacent sub-sequences for composing the (C_{12}, D_{12}) block pair weight functions over the whole sequence.

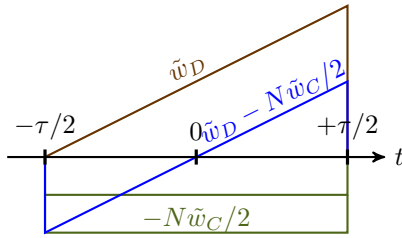


Fig. 5. Association of the (C, D) block pair weight functions for composing the Ω -counter weight function.

3) *The PVAR weight function:* Since $\text{PVAR}(\tau) = \frac{1}{2} \langle (\hat{y}_2^\Omega - \hat{y}_1^\Omega)^2 \rangle$, it comes

$$\text{PVAR}(\tau) \propto \left\langle \left(D_2 - \frac{N}{2} C_2 - D_1 + \frac{N}{2} C_1 \right)^2 \right\rangle$$

as illustrated by Figure 6.

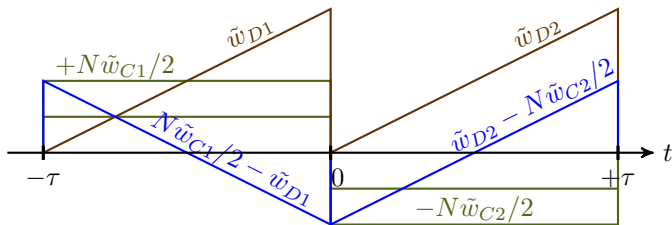


Fig. 6. Association of the (C_1, D_1) and (C_2, D_2) block pair weight functions for composing the PVAR weight function.

D. Decimation processing

It should be noted that the decimation process may be used recursively, such that it is used as high-speed preprocessing in FPGA and that the (C, D) pairs is produced for each N_1 samples as suitable for the plotted lowest τ . Another benefit of the decimation processing is that if the FPGA front-end has a limit to the number of supported N_1 it can process, software can then continue the decimation without causing a bias. This provides for a high degree of flexibility without suffering from

high memory requirements, high processing needs or for that matter overly complex HW support.

E. Multi- τ decimation

Another aspect of the decimation processing is not only that many τ can be produced out of the same sample or block sequence, but once a suitable set of τ variants have been produced, these can be decimated recursively in suitable form to create τ variants of higher multiples. One such approach would be to produce the 1 to 9 τ multiples (or only 1, 2 and 5 multiples which is enough for a log-log plot) of accumulates for τ being 1 s, thus producing the 1 to 9 s sums, and by recursive decimation by 10 produces the same set of points on the log-log plot, but for 10th multiple of time, for each recursive step. This will allow for large ranges of τ to be calculated for a reasonable amount of memory and calculation power.

IV. SUMMARY

Presented is an improved method to perform least-square phase, frequency and PVAR estimates, allowing for high speed accumulation similar to [8], but extending into any τ needed. It also provides for multi- τ analysis from the same basic accumulation. The decimation method can be applied recursively to form longer τ estimates, reusing existing calculations and thus saving processing. Thus, it provides a practical method to provide PDEV log-log plots, providing means to save memory and processing power without the risk of introducing biases in estimates, as previous methods have shown.

REFERENCES

- [1] E. Rubiola, M. Lenczner, P.-Y. Bourgeois, and F. Vernotte, "The Omega counter, a frequency counter based on the linear regression," *IEEE UFFC*, 2016, submitted (see arXiv:1506.05009).
- [2] S. Johansson, "New frequency counting principle improves resolution," *Proceedings of 37th PTTI*, 2005, <http://spectracom.com/sites/default/files/document-files/Continuous-timestamping-article.pdf>.
- [3] J. Barnes, "The measurement of linear frequency drift in oscillators," *Proceedings of 15th PTTI*, 1983, http://tycho.usno.navy.mil/ptti/1983papers/Vol_15_29.pdf.
- [4] F. Vernotte, M. Lenczner, P.-Y. Bourgeois, and E. Rubiola, "The parabolic variance (PVAR), a wavelet variance based on the least-square fit," *IEEE UFFC*, 2016, accepted (see arXiv:1506.00687).
- [5] M. Danielson, F. Vernotte, and E. Rubiola, "Least square estimation of phase, frequency and pdev," 2016, (see arXiv:1604.01004).
- [6] B. S. Everitt, "The cambridge dictionary of statistics," *Cambridge University Press*, 1998.
- [7] E. Rubiola, "On the measurement of frequency and of its sample variance with high-resolution counters," *RSI*, vol. 76, no. 5, May 2005, also arXiv:physics/0411227, Dec. 2004.
- [8] J. J. Snyder, "An ultra-high resolution frequency meter," *Proceedings of 35th Annual Frequency Control Symposium*, May, 1981.

Avoiding Aliasing in Fiber Link Data Analysis

Claudio Eligio Calosso, Cecilia Clivati, Salvatore Micalizio

Physics Metrology Division, Istituto Nazionale di Ricerca Metrologica, INRIM, Torino, Italy

e-mail: c.calosso@inrim.it

Abstract — A basic rule in signal analysis is to use an anti-aliasing filter before data decimation. Surprisingly, this fundamental rule is often missed in time and frequency community and this leads to problems when data are analyzed. They are particularly evident in case of fiber links, especially when the Allan variance is calculated. Here, we show that aliasing can be induced by the measurement instrument and, more subtly, by the variance algorithm itself. By properly setting the anti-aliasing filter, this problem can be eliminated. As an example, we apply this method to the experimental data we obtained on the 1284 km Italian coherent optical link.

Keywords — optical fiber link; atomic clock comparison; Allan variance; modified Allan variance; aliasing.

I. THE METHOD IN PRACTICE

Fiber links are intended to compare and disseminate distant clocks. Fig. 1 shows an example of remote comparison.

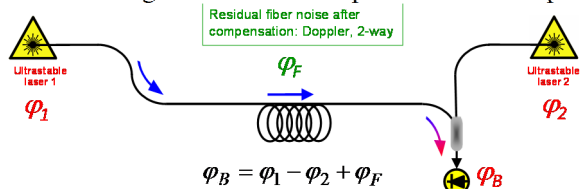


Fig. 1: Simplified block diagram of a remote optical clock comparison.

The result $(\varphi_1 - \varphi_2)$ is degraded by the residual noise of the link (φ_F) . Fig. 2.a shows the spectrum obtained in a hypothetical case where a microwave and an optical clock signals ($1 \times 10^{-13}/\sqrt{\tau}$ and $1 \times 10^{-16}/\sqrt{\tau}$ respectively) are transferred through a fiber link. The residual noise of the link is reported in Fig. 2.c. The fiber link degrades the spectrum of the microwave clock for $f > 5$ Hz and of the optical clock for $f > 25$ mHz. Since we are interested to clocks we filter out the fiber noise by closing the bandwidth at 5 Hz and 25 mHz respectively and then we calculate the Allan deviation (Fig. 2.b, in green). In this manner we retrieve the clock stability (red dashed) already at 100 ms and at 20 s respectively. This approach is optimum in terms of shortest averaging time and error. As a comparison, we calculate the full-bandwidth MDEV (Fig. 2.b, blue trace): it retrieves the microwave clock only at 400 ms and the optical clock only at 40 s. Moreover, it has a bias of -3 dB. To evaluate the residual noise of the fiber link, we close the bandwidth at 5 mHz, where the flicker PN begins. White PN, blue PN and the bump are filtered out and we get a frequency stability of 3×10^{-19} @ 1000 s (Fig. 2.d). In the end, the method is very simple: just filter out the fast noise components from fiber link data. The underlying reason is that they induce aliasing in the Allan variance computation. The rest of the paper shows where aliasing occurs and how to set the antialiasing filter. The latter requires a modelling of the bump. The interested reader will find more details in [1].

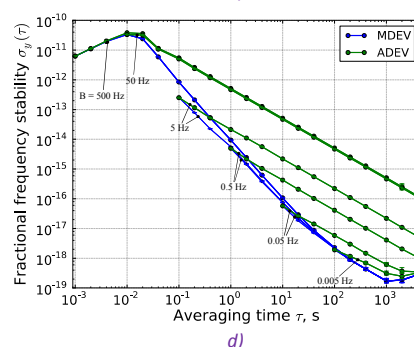
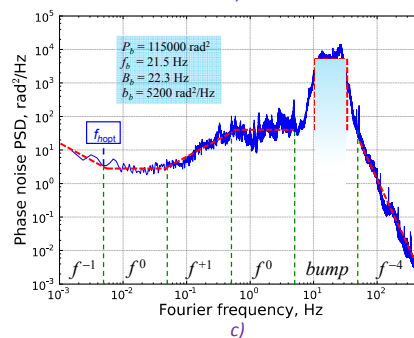
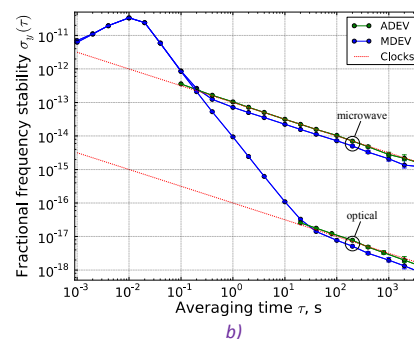
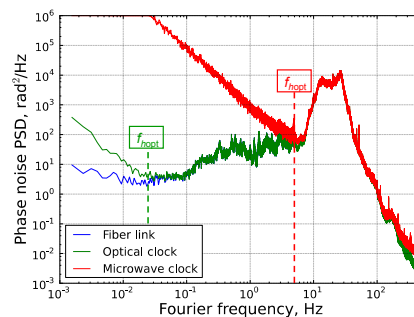


Fig. 2: Spectrum [a], [c] and frequency stability [b], [d] of a hypothetical clock comparison [a], [b] based on a real fiber link noise [c], [d]. The link is from Turin and Florence (Italy).

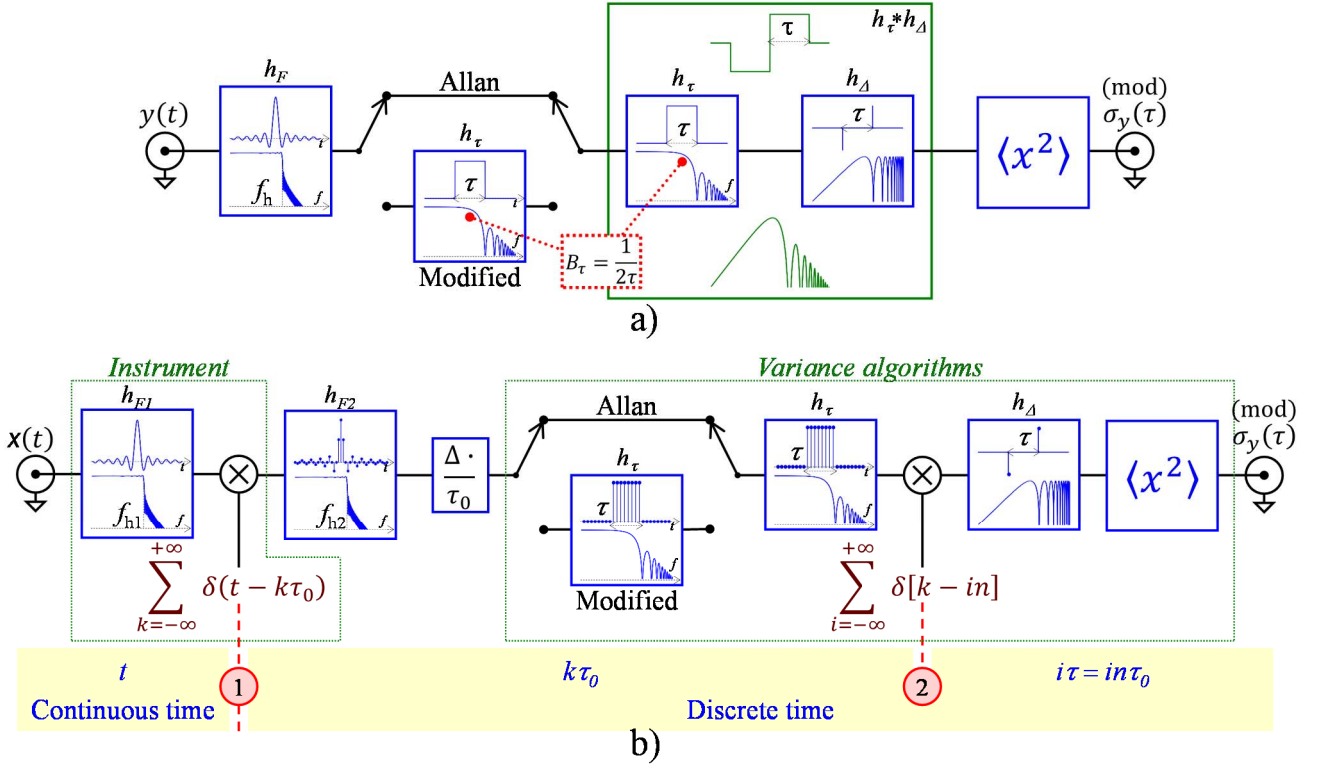


Fig. 3: Functional block diagram of AVAR and of MVAR. The switches allow selection between MVAR and AVAR, by enabling/disabling the additional moving average filter h_τ . a) highlights h_F that models the measurement bandwidth f_h ; b) shows the two stages where aliasing may occur: 1) the measurement instrument that samples the phase time $x(t)$ each τ_0 and 2) the AVAR and MVAR algorithms that decimate the average fractional frequency by n , reducing the data rate from $1/\tau_0$ to $1/\tau$. The Δ/τ_0 block differentiates the phase time to obtain the fractional frequency.

II. AVAR AND MVAR

A signal analysis interpretation

Equations (1) and (2) allow seeing the AVAR [2] and MVAR [3] as the power at the output of a filter chain.

$$\begin{aligned} \sigma_y^2(\tau) &= \frac{1}{2} \left\langle (\bar{y}(t) - \bar{y}(t - \tau))^2 \right\rangle \\ &= \left\langle (y(t) * h_F(t) * h_\tau(t) * h_\Delta(t))^2 \right\rangle \\ &= \int_0^\infty S_y(f) |H_F(f) H_\tau(f) H_\Delta(f)|^2 df \end{aligned} \quad (1)$$

$$\begin{aligned} \text{Mod } \sigma_y^2(\tau) &= \frac{1}{2} \left\langle \left(\frac{1}{n} \sum_{i=1}^n \bar{y}(t - i\tau_0) - \frac{1}{n} \sum_{i=1}^n \bar{y}(t - \tau - i\tau_0) \right)^2 \right\rangle \\ &\cong \left\langle (y(t) * h_f(t) * h_\tau(t) * h_\Delta(t))^2 \right\rangle \\ &= \int_0^\infty S_y(f) |H_F(f) H_\tau^2(f) H_\Delta(f)|^2 df \end{aligned} \quad (2)$$

h_F models the bandwidth f_h of the measurement system, h_τ is the average over time $\tau = n\tau_0$ and h_Δ is the difference between adjacent samples divided by $\sqrt{2}$. H_F , H_τ , H_Δ are the Fourier transforms of h_F , h_τ , h_Δ respectively. τ_0 is the acquisition period of the instrument. Fig. 3.a represents the equivalent block diagram of AVAR and MVAR. We can see that MVAR is

obtained from AVAR by means of the second averaging block h_τ . This provides the ability to analyze White Phase Noise (WPN) and Blue Phase Noise (BPN), but, on the other hand, it causes different estimation with respect to AVAR at all τ (i. e. -3 dB for White Frequency Noise WFN). Instead, the use of h_F to reject high frequency noise is advantageous, because h_F is more selective than h_τ and, having a fixed bandwidth, it does not affect the long-term estimation.

III. AVOIDING ALIASING

A. The Nyquist theorem

When a signal is sampled at a frequency $1/\tau_0$, the high frequency components are down-converted below the Nyquist frequency $1/(2\tau_0)$ and the Power Spectral Density (PSD) degrades. This phenomenon is called *aliasing* and is a loss of information. The Nyquist theorem [4] states:

1. to avoid aliasing, the signal must be sampled at least at twice its bandwidth B ($1/\tau_0 > 2B$);
2. if the sample rate $1/\tau_0$ is limited, the bandwidth must be reduced below one half of the sample rate [$f_h < 1/(2\tau_0)$]

In short, with fiber links, if the sampling rate is low, the anti-aliasing filter must be used.

Noise type	$S_\varphi(f)$	$\sigma_y^2(\tau)$	Mod $\sigma_y^2(\tau)$	$\frac{\text{MVAR}}{\text{AVAR}}$	$\frac{\text{MVAR}}{\text{AVAR}}, \text{ dB}$
Large bump $B_b > 1/\tau$	b_b $ f - f_b < \frac{B_b}{2}$	$\frac{3 P_b}{4\pi^2 v_0^2} \tau^{-2}$	$\frac{5 P_b}{8\pi^4 (f_b^2 - B_b^2/4) v_0^2} \tau^{-4}$	1.1×10^{-58}	-49.5^{\S}
Narrow bump $B_b < 1/\tau$	$P_b = b_b B_b$ $f_h > f_b + B_b/2$	$\frac{2}{\pi^2} \sin^4(\pi f_b \tau) \frac{P_b}{v_0^2} \tau^{-2}$	$\frac{2}{\pi^4 f_b^2} \sin^6(\pi f_b \tau) \frac{P_b}{v_0^2} \tau^{-4}$	-	-
Blue PN	$b_1 f^1$	$\frac{3 f_h^2 b_1}{8\pi^2 v_0^2} \tau^{-2}$	$\frac{9.643 + 10 \ln(\pi f_h \tau)}{16\pi^4} \frac{b_1}{v_0^2} \tau^{-4}$	$2.6 \times 10^{-5*}$	-45.9^*
White PN	b_0	$\frac{3 f_h b_0}{4\pi^2 v_0^2} \tau^{-2}$	$\frac{3 b_0}{8\pi^2 v_0^2} \tau^{-3}$	0.005^*	-23.0^*
Flicker PN	$b_{-1} f^{-1}$	$\frac{1.038 + 3 \ln(2\pi f_h \tau)}{4\pi^2} \frac{b_{-1}}{v_0^2} \tau^{-2}$	$\frac{3 \ln(256/27)}{8\pi^2} \frac{b_{-1}}{v_0^2} \tau^{-2}$	0.166^*	-7.8^*
White FN	$b_{-2} f^{-2}$	$\frac{1 b_{-2}}{2 v_0^2} \tau^{-1}$	$\frac{1 b_{-2}}{4 v_0^2} \tau^{-1}$	0.5	-3.0
Flicker FN	$b_{-3} f^{-3}$	$2 \ln(2) \frac{b_{-3}}{v_0^2}$	$\frac{27}{20} \ln(2) \frac{b_{-3}}{v_0^2}$	0.675	-1.7
Random Walk FN	$b_{-4} f^{-4}$	$\frac{2\pi^2 b_{-4}}{3 v_0^2} \tau$	$\frac{11\pi^2 b_{-4}}{20 v_0^2} \tau$	0.825	-0.8
Linear frequency drift \dot{y}	-	$\frac{1}{2} (\dot{y})^2 \tau^2$	$\frac{1}{2} (\dot{y})^2 \tau^2$	1	0

Table 1: AVAR and MVAR for several noise processes; these formulae hold for $f_h \tau \gg 1$ and $n \gg 1$. v_0 is the frequency of the optical carrier; f_h is the measurement bandwidth; the bump parameters: P_b, f_b, B_b and b_b are defined by (3). The ratio MVAR/AVAR has been calculated for $f_h \tau = 100$ (*) and for $f_b \tau = 100$ and $f_b = B_b$ (§);

B. Where aliasing occurs

Fig. 3.b is a more detailed equivalent block diagram of the two variances and shows that there are two points where the signal is sampled. This leads to what we call *instrumental* and *variance* aliasing. The first one is due to the measurement instrument, that each τ_0 samples the phase-time $x(t)$. Depending on the instrument bandwidth f_{h1} , there are two classes of instruments:

1. phasometers: $f_{h1} < 1/(2\tau_0)$. Usually, h_{F1} is selective and aliasing is avoided in the general case;
2. frequency counters: $f_{h1} > 1/(2\tau_0)$. In general, aliasing is avoided only if $\tau_0 < 1/(2B)$. Counters should require a more detailed discussion, but there is no space here.

The second type of aliasing is hidden in the variance algorithm itself. Each τ it samples the averaging frequency and reduces the data rate by a factor of n . A weak anti-aliasing filter is embedded in the variance algorithm:

1. in AVAR there is h_τ , a first order filter, effective up to WFN. With Flicker Phase Noise (FPN), aliasing is weak and AVAR can still be used, provided that f_h is

indicated. For WPN, Blue PN and bumps, aliasing is strong.

2. in MVAR there is $h_{\tau^*} * h_\tau$, a second order filter that is effective up to WPN. With BPN aliasing is weak, but with bumps also MVAR is dominated by aliasing, although less severely than AVAR.

h_{F2} is devoted to avoid variance aliasing, and must be used when the filter embedded in the variance is inadequate.

Tab. 1 reports the formulae of AVAR and MVAR for several noise types, including BPN and bumps. It is interesting to note, that variance aliasing is present each time the measurement bandwidth f_h appears in the formula.

C. The antialiasing filter

The antialiasing filter rejects instrumental and variance aliasing. We indicate it with h_F in Fig. 3.a or with h_{F1} and h_{F2} in Fig. 3.b. h_{F1} is embedded into the instrument, while h_{F2} is applied numerically to the acquired data. The antialiasing filter is specified completely by its cut-off frequency f_h and its average attenuation A_F . These two parameters depend on the PSD of the signal.

Fiber link PSD is characterized by the presence of BPN and bumps that need to be considered by our noise model:

$$S_\varphi(f) = \sum_{\alpha} b_{\alpha} f^{\alpha} + \text{bump} \quad -4 \leq \alpha \leq +1, f < B$$

We define the *equivalent bump*, characterized by a rectangular shape with the same power P_b , the same average frequency f_b , the same bandwidth B_b and the same amplitude b_b of the original bump, where

$$\begin{aligned} P_b &\stackrel{\text{def}}{=} \int_{f_l}^{f_u} S_\varphi(f) df \\ f_b &\stackrel{\text{def}}{=} \frac{1}{P_b} \int_{f_l}^{f_u} f S_\varphi(f) df \\ B_b^2 &\stackrel{\text{def}}{=} \frac{12}{P_b} \int_{f_l}^{f_u} (f - f_b)^2 f S_\varphi(f) df \\ b_b &\stackrel{\text{def}}{=} P_b / B_b \end{aligned} \quad (3)$$

Thanks to the equivalent bump, we are able to specify the two parameters of the antialiasing filter:

1. *Optimal measurement bandwidth f_{hopt} .* If f_h is too high, AVAR is overestimated a) due to high frequency noise. If f_h is too low, AVAR is underestimated b). With the optimal cut-off frequency f_{hopt} there is no estimation error on AVAR because the overestimation a) compensates exactly the underestimation b), that is

$$\int_0^{f_{\text{hopt}}} S_\varphi^{\text{link}}(f) \frac{f^2}{v_0^2} |H_A(f)|^2 df = \int_{f_{\text{hopt}}}^{\infty} S_\varphi^{\text{clock}}(f) \frac{f^2}{v_0^2} |H_A(f)|^2 df$$

where $H_A = H_\tau H_\Delta$ is the AVAR transfer function.

From a practical point of view, f_{hopt} is the frequency where the clock PSD crosses the fiber link PSD, or, in general, where the slope of the PSD changes from -2 to -1 (from -1 to 0 , in case weak aliasing is allowed).

2. *Average attenuation A_F .* The anti-aliasing filter has to attenuate the bump contribution to a negligible level

$$\int_{B_b} b_b \frac{f^2}{v_0^2} |H_A(f)|^2 |H_F(f)|^2 df \ll \int_0^{f_h} S_\varphi(f) \frac{f^2}{v_0^2} |H_A(f)|^2 df$$

For $\alpha \geq 0$, this simplifies in

$$P_b \frac{1}{A_F} \ll \int_0^{f_h} S_\varphi(f) df$$

$$\text{where } \frac{1}{A_F} \stackrel{\text{def}}{=} \frac{1}{B_b} \int_{B_b} |H_F(f)|^2 df.$$

Fig. 4.a shows in blue the required attenuation that filters out the bump of Fig. 4.b (blue curve) in case $f_h = 5$ Hz. It is clear that the truncated sinc filter (in green) is adequate, while the moving average filter (in red) is not. Fig. 4.b shows the effect of the two filters on the bump. The moving average provides a poor attenuation [b) curve] and still induces some aliasing as demonstrated by the d) curve (in purple) calculated after decimation.

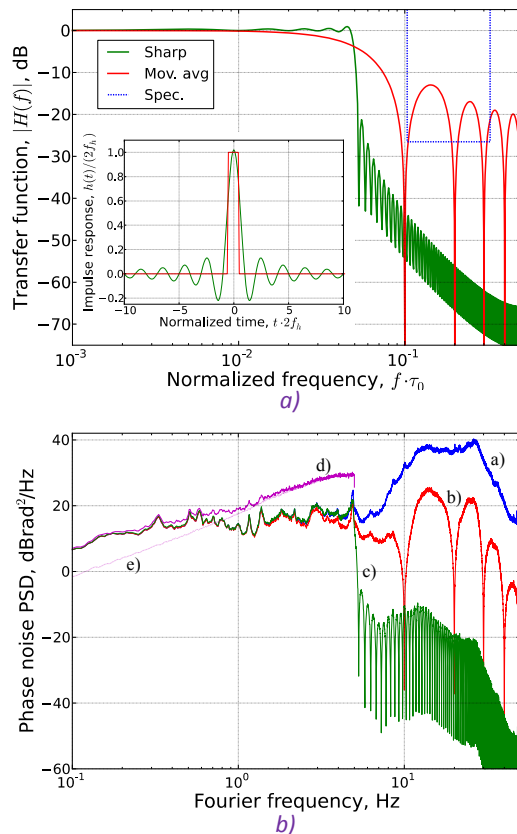


Fig. 4: bump filtering with two different filters: moving average (in red) and truncated sinc filter (in green). a) transfer function and impulse response; b) PSD before (in blue) and after filtering (in red and in green).

IV. CONCLUSIONS

In this work, we have shown how aliasing may affect AVAR and MVAR estimations and how to avoid it by setting properly the measurement bandwidth. This is particular important in fiber link data analysis because of the presence of blue phase noise and, mainly, of a significant bump. This method is optimal, because it retrieves the clock information at the shortest averaging time and without any bias. In this manner, we preserve the continuity with the existing literature, where the AVAR is used traditionally in clock uncertainty evaluation.

REFERENCES

- [1] Calosso C. E., Clivati C., Micalizio S., "Avoiding Aliasing in Allan Variance: an Application to Fiber Link Data Analysis" IEEE TUFFC, Vol. 63, Issue 4, pp. 1-10, April 2016.
- [2] D. W. Allan, "Statistics of Atomic Frequency Standards," Proc. IEEE V ol. 54, pp. 221-230, 1966.
- [3] D. W. Allan and J. Barnes, "A modified "Allan variance" with increased oscillator characterization ability," in Proceedings of the 35th Ann. Freq. Control Symposium, pp. 470-475.
- [4] H. Nyquist "Certain factors affecting telegraph speed", Bell Syst. Tech. Jour., vol. 3, pp. 324, 1924.

Development and spectral characterisation of ridge DFB laser diodes for Cs optical pumping at 894 nm

Renaud Matthey, Florian Gruet,
Christoph Affolderbach,
Gaetano Mileti
Laboratoire Temps – Fréquence,
Institute de Physique
Université de Neuchâtel
Neuchâtel, Switzerland
Email: renaud.matthey-de-
lendroit@unine.ch

Nicolas von Bandel,
Michel Garcia,
Michel Krakowski
III-V Lab
Palaiseau, France
Email: michel.krakowski@3-5lab.fr

Patrick Berthoud
Oscilloquartz SA
St-Blaise, Switzerland
Email: berthoud@oscilloquartz.com

Abstract—Optical pumping on the cesium (Cs) D1 transition at 894 nm, as compared to the Cs D2 line at 852 nm, can present advantages for e.g. Cs thermal beam atomic clocks or other atom-based sensors and instrumentation, due to its simpler hyperfine structure, larger atomic level splitting, and absence of cycling transitions. Here we report on the realisation and spectral characterisation of custom-made narrow-band DFB laser diodes emitting at 894 nm.

Keywords—laser diode; Cs atomic clock; frequency noise; linewidth; spectral characterisation

I. INTRODUCTION

A number of research fields and applications like spectroscopy, atom interferometry, laser cooling of atoms, magnetometers, atomic clocks and frequency standards make use of lasers to prepare, manipulate, pump or interrogate cesium (Cs) atoms. Distributed-feedback (DFB) lasers have proved to be convenient single-mode laser sources owing to their simplicity of use and control, frequency agility, reliability, low power consumption and compactness.

Due to the simpler hyperfine structure of the Cs excited state $6P_{1/2}$, four optical transitions from the ground state $6S_{1/2}$ exist for the D1 resonance line at 894 nm, while six are present for the excited state $6P_{3/2}$ at 852 nm (D2 line). No closed cycling transitions occur at 894 nm. The hyperfine level separations are also larger for $6P_{1/2}$ (1168 MHz) than for $6P_{3/2}$ (151-251 MHz). Consequently, the D1 transition shows a simpler spectrum and may offer advantages for some applications with respect to the D2 line, in particular for Cs vapour cell or thermal beam atomic clocks.

DFB lasers demonstrating sub-MHz linewidth, high intrinsic wavelength and optical power stabilities and low sensibility to optical feedback are presently commercially not available at 894 nm [1]. We report here on the characterisation results obtained from DFB laser devices developed to meet these goals, after having exposed their design and fabrication, which are based on a previous work by III-V Lab at 852 nm [2].

II. LASER DESIGN AND REALIZATION

A. Laser Epitaxial Structure

The vertical laser heterostructure was realized by metal organic vapour phase epitaxy (MOVPE) growth on an n-doped (100) GaAs buffer wafer. The active zone is composed of an 8-nm compressive-strained (+1%) InGaAsP quantum well embedded in a $\sim 1\text{-}\mu\text{m}$ GaInP large optical cavity (OC). The OC is surrounded by AlGaInP confining layers providing the refractive index gap for effective optical confinement. In a second-step regrowth, a $\sim 50\text{-nm}$ InGaAsP grating layer is inserted between the cladding and the OC, as illustrated in the sketched laser structure of Figure 1. The analysis of the photoluminescence wavelength of the quantum well on a calibration structure (2-inch wafer) showed that the emission is spectrally centered at 885 nm.

B. Internal Parameters and Ridge Design

Prior to the ridge laser fabrication, 100- μm multimode broad-area laser were design and processed to test materials' capabilities. Low values of internal losses (2 cm^{-1}) and transparency current density (93 A/cm^2) were measured together with high external differential efficiency (0.49 W/A per

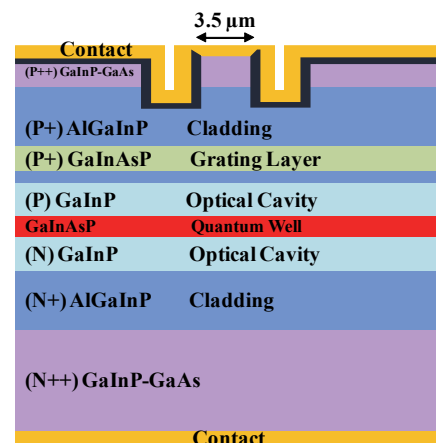


Fig. 1. Cut-view schematic of laser structure

This work is supported by the European Euripides project LAMA (grant EM 12-1307), the Swiss CTI agency (grant 14750.1), and the French DGE.

cleaved facet) and low threshold current density of 190 A/cm², for 2-mm lasers at 20°C. The emission of these lasers showed a gain maximum at 885 nm, 9 nm below the 894-nm value expected for this first try of fabrication. Nevertheless, the gain can be tuned to the desired wavelength by heating and operating the lasers around 65°C.

Adequately etching a few microns wide ridge in the laser layers can ensure lateral waveguide confinement, spatial single-mode emission and cutting of higher transverse modes.

C. DFB Design

Single longitudinal mode behaviour can be achieved using distributed-feedback effect, which consists in coupling the laser cavity to a nanoscale corrugation of periodic refractive index change (Bragg grating; see Fig. 2). In the present case, the coupling factor magnitude is evaluated to $\kappa = 8.5 \text{ cm}^{-1}$ yielding a normalized reflectivity of respectively $\kappa \cdot L = 1.3$ for device length of $L = 1.5 \text{ mm}$. This value is in line for DFB single mode operation. Also, the discrimination between the two DFB modes of the stop-band is favoured by applying reflecting coating to one cavity facet and anti-reflecting coating to the other.

The DFB single mode wavelength is given by Bragg's law. For an emission at 894.4 nm and an effective index of mode of $n_{\text{eff}} = 3.27$ at 25°C, a Bragg corrugation pitch of $\Lambda = 273.5 \text{ nm}$ is computed. Since optical gain at the desired wavelength was obtained at 65°, several pitches around the nominal computed value at 25°C have been implemented to reach a good accordance between the Bragg wavelength and the gain peak for effective single mode operation at D1 line at 65°C.

D. Bragg Grating and Ridge Processing Technology

After a first step of epitaxial growth of the heterostructure including the quantum well, a second-order Bragg grating with period Λ ranging from 272 nm to 275 nm is defined by e-beam lithography in the grating layers, followed by pattern etching by means of reactive ion etching. In a second step of growth ("regrowth") the nanostructure is buried up to the highly-doped top GaAs contact layer. Fig. 3 displays a scanning electronic microscope picture of a cut of the grating structure. Good grating definition is noticeable.

To obtain single transverse mode emission and lateral confinement in the cavity, a double-trench waveguide of $\sim 3.5\text{-}\mu\text{m}$

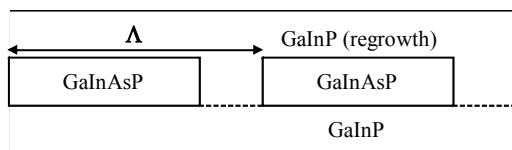


Fig. 2. Schematic of Bragg grating structure

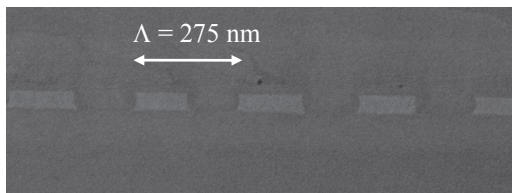


Fig. 3. Scanning electronic microscope view of the grating layer

width is defined by standard photolithography at the top of the heterostructure. This etch step is realized by inductively coupled plasma. An insulating SiO₂ layer is deposited on the surface by plasma enhanced chemical vapour deposition. On the top of the mesa, SiO₂ is removed to enable localized current injection. Top p-type ohmic contact is made of Ti/Pt/Au deposit. After reduction of the GaAs substrate thickness down to 100 μm , the Au/Ge/Ni/Au bottom n-type contact is deposited. Following an annealing at 400°C, a new deposit of Ti/Pt/Au is realized.

At the end of the process, the wafer is cleaved in bars of length $L = 1.5 \text{ mm}$ and $L = 2 \text{ mm}$ cavities. The facets are coated with dielectric mirrors. Standard 3% (front facet) and 95% (rear facet) reflectivity are achieved. The individual chips are separated and mounted p-side up on C-mount, equipped with a CuW heat dissipator, for lab characterisation.

III. LASER SPECTRAL CHARACTERISATION

Based on measurements of the optical power with respect to the injection current and of the optical spectrum with an optical analyser at chip level, a first screening of the produced DFB lasers diodes was realized. The non-rejected devices endured then further characterisation.

A. Spectral Test Bench Description

A dedicated test bench with emphasis on spectral analysis was assembled in LTF premises. In addition to usual parameters (threshold current, slope efficiency, tuning coefficients,

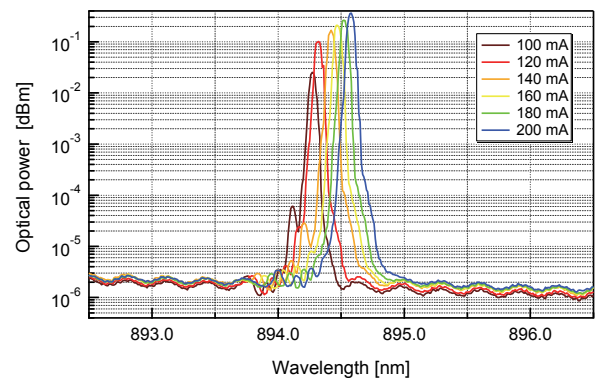


Fig. 4. Optical spectrum of a DFB laser sample operated at 67.5°C. The SMSR at Cs D1 transition (reached around 180 mA) is $> 47 \text{ dB}$.

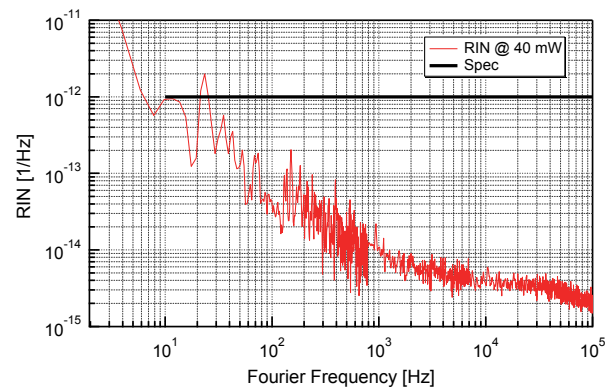


Fig. 5. RIN of a DFB laser sample operated at Cs D1 transition wavelength.

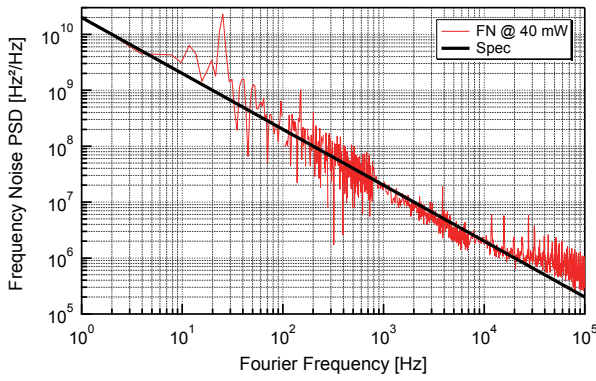


Fig. 6. Frequency noise of a DFB laser sample.

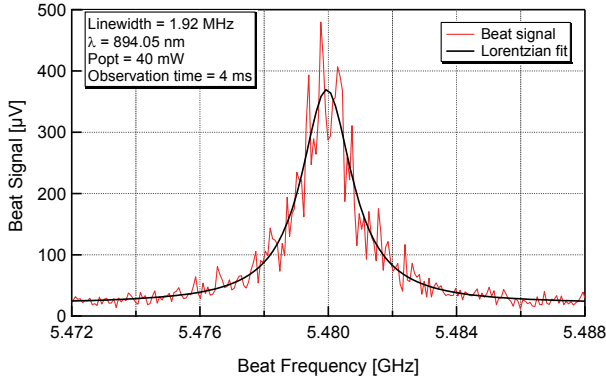


Fig. 7. Beat-note between two DFB laser samples. Averaging over 20 Lorentzian fits yields a beat linewidth of $1.9 \text{ MHz} \pm 0.2 \text{ MHz}$.

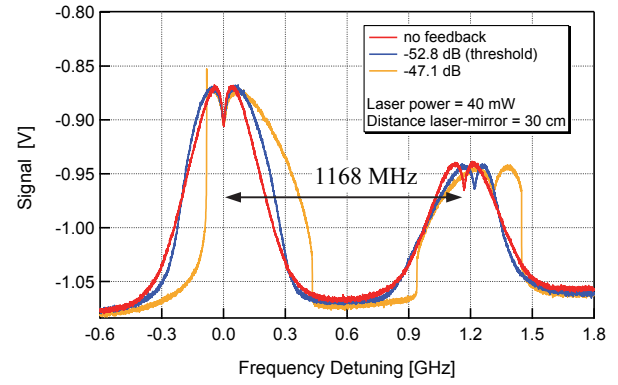


Fig. 8. Part of the Cs D1 spectrum (transitions from ground-state $F=4$) for different levels of optical feedback power into the DFB laser source, expressed as ratio to the laser emitted power (in dB).

the FN spectrum; in this case, the laser frequency is tuned to one of the slopes of the $F=4 \rightarrow F'=3$ transition. The linewidth was initially derived from the FN spectrum applying the β -separation line method [4]. In a further step, a heterodyne setup was also implemented, where the beat-note signal between two laser samples was measured.

To ensure sufficiently stable observational conditions to perform the sensitive spectral measurements, a dedicated thermally-controlled platform was designed that accommodates C-mount supports. Associated to a low-noise home-made digital laser controller, it guarantees sufficient passive thermal stability for a laser in free-running mode (below 10 mK, a value corresponding to laser frequency fluctuations of $< 250 \text{ MHz}$).

B. Test Results

For comparison purposes, the characterisation of each laser device under test was realised at current I_{Cs} and temperature T_{Cs} for which the laser reached the Cs D1 wavelength of 894.6 nm (more precisely at the transition from the ground state $F=4$) while delivering 40 mW of optical output power. Samples of different laser configurations in terms of laser length and ridge width were tested. The results of these tests are given in Table I. All samples reach the Cs D1 wavelength;

beam geometry and polarization) and side-mode suppression ratio (SMSR), two different types of laser noises that can limit the performance of a system like an optically-pumped atomic clock [3] are measured, the relative intensity noise (RIN) and the frequency noise (FN). The laser linewidth is also evaluated. A Cs vapour gas cell configured in a sub-Doppler absorption scheme serves as frequency reference to control that the laser under test reaches the Cs D1 transition of 894.6 nm. The same cell is used as frequency discriminator for the measurement of

TABLE I. SUMMARY OF LASER TEST RESULTS

Configuration no.	1	2	3	4
Configuration (length / ridge)	1.5 mm / 3.5 μm	1.5 mm / 4.0 μm	2.0 mm / 3.5 μm	2.0 mm / 4.0 μm
Threshold current (@ 25°C)	57 mA	59 mA	68 mA	72 mA
Slope efficiency (@ 25°C)	0.6 W/A	0.58 W/A	0.53 W/A	0.54 W/A
Laser temperature (= T_{Cs})	68.2°C @ λ Cs D1 and $P_{opt}=40 \text{ mW}$	66.4°C	70.3°C	67.5°C
Laser current (= I_{Cs})		160 mA	182 mA	186 mA
Opt. power versus temp. tuning (@ T_{Cs})	-0.40 mW/K	-0.15 mW/K	-0.15 mW/K	-0.23 mW/K
Freq. versus current tuning (@ T_{Cs})	-1.45 GHz/mA	-1.30 GHz/mA	-0.97 GHz/mA	-0.97 GHz/mA
Freq. versus temperature tuning (@ T_{Cs})	-20.5 GHz/K	-20.4 GHz/K	-20.9 GHz/K	-20.6 GHz/K
SMSR (= T_{Cs})	> 45 dB	> 50 dB	> 49 dB	> 47 dB
RIN ($f < 1 \text{ kHz}$) (@ T_{Cs}, I_{Cs})	$4 \times 10^{-12}/f \text{ Hz}^{-1}$	$5 \times 10^{-12}/f \text{ Hz}^{-1}$	$1.5 \times 10^{-11}/f^{1.05} \text{ Hz}^{-1}$	$5 \times 10^{-12}/f \text{ Hz}^{-1}$
RIN ($2 \text{ kHz} < f \leq 100 \text{ kHz}$) (@ T_{Cs}, I_{Cs})	$\leq 8 \times 10^{-15} \text{ Hz}^{-1}$	$\leq 6 \times 10^{-15} \text{ Hz}^{-1}$	$\leq 1 \times 10^{-14} \text{ Hz}^{-1}$	$\leq 8 \times 10^{-15} \text{ Hz}^{-1}$
Frequency noise ($f \leq 100 \text{ kHz}$) (@ T_{Cs}, I_{Cs})	$2.0 \times 10^{10} f^{1.08} \text{ Hz}^2/\text{Hz}$	$2 \times 10^{10} f^{1.08} \text{ Hz}^2/\text{Hz}$	$3.5 \times 10^{10} f^{1.08} \text{ Hz}^2/\text{Hz}$	$2 \times 10^{10} f^{1.07} \text{ Hz}^2/\text{Hz}$
Linewidth [2] (4-ms equival. obs. time) (@ T_{Cs}, I_{Cs})	1.02 MHz	797 kHz	929 kHz	639 kHz
Polarization (ellipticity) (@ T_{Cs}, I_{Cs})	Linear ($\leq 4.1^\circ$)	Linear ($\leq 2.5^\circ$)	Linear ($\leq \text{few } ^\circ$)	Linear ($\leq 0.9^\circ$)

however, they need to be operated at temperatures more elevated than the ambient, between 66.4°C and 70.3°C. The associated injection currents for delivering 40 mW of optical power amount to 160-186 mA. Under these conditions, the SMSR is always larger than 45 dB, as illustrated in Fig. 4. The RIN stays below 10^{-12} Hz⁻¹ at Fourier frequencies $f > 10$ Hz and follows an f^{-1} law up to $f = 1$ kHz, as shown in Fig. 5. For most of the lasers, the flicker noise of the FN spectral densities fits the function $2 \cdot 10^{10} / f^{1.08}$ (in Hz²/Hz) as evidenced in Fig. 6. Applying the β -separation line formalism with a cut-off frequency of 250 Hz, linewidths below 1 MHz down to 639 kHz are retrieved for equivalent observation time of 4 ms. The linewidth of the beat note between two samples was measured as 1.9 MHz (FWHM, see Fig. 7), confirming the 1-MHz value for a single laser.

During past activities, degradation of the frequency stability of an 852-nm optically-pumped thermal beam Cs atomic clock was observed depending on the DFB laser used as light source. Higher sensitivity to optical feedback of the laser diode was believed to cause this effect. Therefore a set-up for evaluating the sensitivity to optical feedback was assembled as functionality of the test bench. It consists in an intensity-controlled part of the emitted light reflected by a mirror and focused back into the DFB laser facet region of optical emission (optical confinement and active regions). The effect on the laser spectrum is indirectly appraised recording the Cs spectrum. Starting from a threshold feedback power level and above, the Cs spectrum is deformed (see Fig. 8). When the feedback is high enough, discontinuities in the spectrum are observed, associated to laser frequency mode hopping. Comparison with 852-nm laser diodes from other manufacturers is planned.

IV. CLOCK RESULTS

Two DFB lasers emitting at 852 nm (Cs D2 line) and packaged in TO3 housing have been integrated in an existing cesium thermal beam frequency standard [5]. Their design and fabrication process are fully similar to those of the 894-nm laser described previously. Only one laser module is operated at a time, while the second one is for redundancy purpose. Both lasers are frequency tuned to a specific pumping Cs optical transition by properly choosing their operating temperature and current.

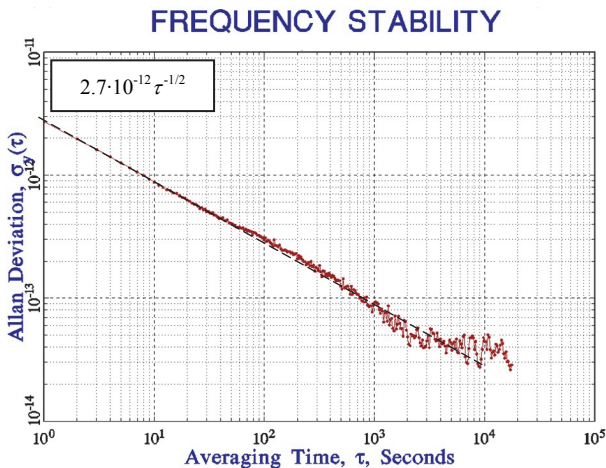


Fig. 9. Cesium clock frequency stability.

Compared to previously used lasers, the intrinsic narrower frequency linewidth of these new modules allows reducing the effective laser power before the used atomic transition reaches saturation. The consequence is a direct reduction of the background light level and its associated shot noise by a factor up to 3, what increases the clock frequency stability.

Fig. 9 shows the recorded clock frequency stability when its output frequency is compared to a passive hydrogen maser reference standard. The improvement of the background light level permits reducing the atomic beam flux and therefore increasing the clock lifetime while keeping the same high performance frequency stability ($\sigma_y(\tau) = 2.7 \cdot 10^{-12} \tau^{-1/2}$). Switching electronically the redundant laser source has also been demonstrated without affecting the clock frequency stability.

A second significant improvement of using these new laser modules is their very low sensitivity to optical feedback, which significantly improves the laser frequency stability and reliability on a long-term basis. In resume, tests and measurements at 852 nm with an existing clock have established that the newly conceived DFB lasers and associated technology meet the requirements to build and operate a high performance optical-pumped cesium beam clock.

V. CONCLUSIONS

We have presented the design, realisation, and spectral characterisation of custom-made DFB laser diodes emitting at 894 nm (Cs D1 line). The lasers reach the Cs D1 line at a temperature around 68°C, in single-mode operation. Laser properties tested at 40 mW of optical output power fulfil the design requirements for a Cs beam atomic clock with optical state selection. A good reproducibility of key parameters was found between the four evaluated laser dimensional configurations. In particular, narrow emission linewidths of ≤ 1 MHz is achieved for all samples. In a currently on-going second fabrication run, the parameters are adapted for the DFB lasers to reach emission at the Cs D1 line at ambient temperature.

ACKNOWLEDGMENT

The LTF authors thank M. Pellaton and S. Kang for their contributions to the design and setup of the laser characterisation bench.

REFERENCES

- [1] F. Gruet, D. Miletic, C. Affolderbach, G. Mileti, V. Vilokinen, P. Melanen, "Spectral characterization of aged and non-aged 894 nm DFB for their application in Cs atomic clocks," in Proc. of the Int. Sym. on Reliability of Optoelectronics for Space, Cagliari, Italy, 2009.
- [2] C. Cayron, et al., "High-power, high-reliability, narrow-linewidth, Al-free DFB laser diode, for Cs pumping (852 nm)," in Proc. SPIE 7230, 2009.
- [3] N. Dimarcq, V. Giordano, P. Cerez, "Statistical properties of laser-induced fluorescence signals," Appl. Phys. B, vol. 59, pp. 135-145, 1994.
- [4] G. Di Domenico, S. Schilt, P. Thomann, "Simple approach to the relation between laser frequency noise and laser lineshape," Appl. Opt., vol. 49, pp. 4801-4807, 2010.
- [5] P. Berthoud et al, "Development of a transportable optically-pumped cesium beam clock," Joint Meeting IEEE-IFCS and EFTF 2015, Denver, CO, USA, April 2015.

High coupling phononic SH-SAW resonators for in-liquid operation

V. Yantchev, A. Jesorka

Biophysical Tech. Lab., Dept. Chem. & Chemical Eng.
Chalmers University of Technology
Goteborg, Sweden
ventsi.yantchev@gmail.com

T. Mirea, E. Iborra

GMME-CEMDATIC-ETSIT
Universidad Politécnica de Madrid
Madrid, Spain
teona@etsit.upm.es

Abstract— In this communication we report on initial studies on the in-liquid operation of surface acoustic wave (SAW) phononic resonators employing shear (SH)-SAWs. The mode of operation is a SH-SAW with very high electromechanical coupling, propagating in the X-direction of Y-cut LiNbO₃ substrates. Measurements of the resonators immersed in ethylene glycol - water mixtures are presented along with an analysis of the underlying phenomena that determine device sensitivity. We found that the change of electromechanical coupling due to variations in the dielectric permittivity of the liquid becomes a leading contributing factor to device sensitivity. The results of this study are expected to enable the design of a novel class of phononic bio-sensors for lab-on-a-chip applications.

Keywords— SAW; Phononic; Liquid sensing; Bio-Sensors;

I. INTRODUCTION

Microacoustic Bio-sensors and sensors for in-liquid operation, which are well-established in various technological areas [1], are currently widely investigated with the aim to improve device performance when immersed in liquid, specifically to achieve sufficient mass and viscosity sensitivity. Only certain types of acoustic waves can satisfy the conditions needed for operation in fluids. These are the bulk shear waves [1, 2], the shear surface acoustic waves (SAWs) [3, 4], the lowest order asymmetric Lamb mode A_0 [5] and the lowest order symmetric Lamb mode S_0 [6]. So far, significant commercial success has been achieved only by the quartz crystal microbalance (QCM), employing shear bulk acoustic waves. A disadvantage of this approach is its poor electromechanical coupling and large dimensions unsuitable for implementation in sensor arrays. Recently, bio-sensor concepts based on shear horizontal SAWs (SH-SAWs) propagating on quartz and LiTaO₃ started to be investigated to alleviate some of the difficulties faced by the QCM approach [3, 4]. Alternatively, thin film bulk shear mode resonators and S_0 Lamb wave resonators are being studied as IC compatible in-liquid sensor platforms [6, 7].

Moreover, phononic crystals with high sensitivity to the liquid properties have recently entered the field on a macro scale, employing a planar substrate with an array of holes. External longitudinal wave transducers were used to measure the transmission spectra of the phononic crystal immersed in liquid media with changing physical properties. Sensitivity

towards changes in the liquid's speed of sound was demonstrated [8].

Here we describe our studies on SH-SAW based in-liquid sensors in combination with surface phononic gratings (SPG), integrated with interdigital transducers (IDT) (see Fig. 1) on top of an Y-cut LiNbO₃ crystal. The surface phononic grating consists of a 2D hexagonal array of W masses superimposed onto Al 1D periodic strip gratings. In detail, the distance between the W masses was chosen to be $a=10\mu\text{m}$ determining an Al grating pitch of $p=a*\text{Sin}(60)$ and a corresponding central wavelength of $\lambda=2p=17.32\mu\text{m}$. The diameter of the W masses was chosen to be $d=5.0\mu\text{m}$ ($d/p=0.58$), with a thickness of $H=720\text{nm}$ ($H/\lambda=4.15\%$). The Al strip thickness was $h=380\text{nm}$ ($h/\lambda=2.2\%$) with a metallization ratio of 0.46.

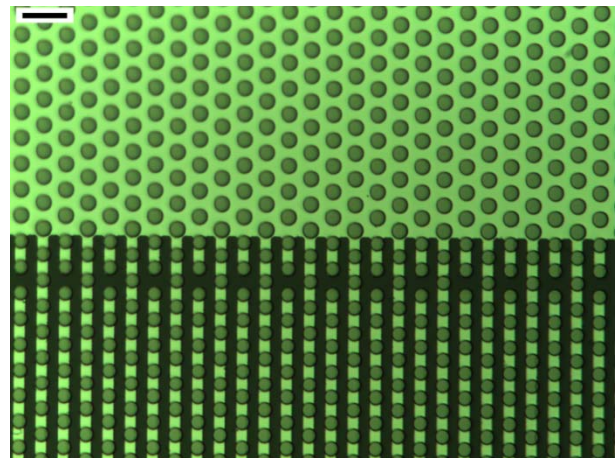


Fig. 1. Example of SPG integrated with the interdigital transducers [9], scale bar $17.32\mu\text{m}$.

The employed planar and optically transparent device format is highly compatible with typical lab-on-a-chip concepts. The phononic grating is based on heavy W masses integrated with Al IDT [9]. Within this configuration, velocity of the wave is slower than the bulk modes and the Rayleigh SAW in the structure, hence being well confined to the surface. Having a very high electromechanical coupling and high dielectric permittivity, the device can remain operational in relatively large dynamic ranges when loaded with liquids. In particular, this opens the possibility for non-conductive liquid measurement directly over the IDT.

The SPG structures have been recently reported in high Q SAW resonators with complete bandgap characteristics [9]. More specifically the use of surface phononic topology in classical SAW resonators was investigated in view of reducing losses from wave diffraction, bringing high performance resonators with narrow apertures for RF filter applications.

When considering SAW phononic gratings for in-liquid operation, the expected benefits are not related to the ability to achieve complete bandgap characteristics. Instead, the focus now is towards the increase of the effective surface, the increase of the energy confinement towards the surface and the employment of well guided modes with electromechanical coupling two orders of magnitude higher than that of the QCM approach. Further, the inclusion of a second dimension of the periodicity is thought to introduce new effects regarding the in-liquid sensitivity.

II. MEASUREMENTS

In Fig. 2a, the frequency responses of the SPG based SH-SAW resonator are shown for the resonators operating in air and water, respectively. When operating in air, the effective electromechanical coupling k_{eff}^2 is about 29% and the Rayleigh SAW resonance is positioned inside the resonator passband. When contacted with water, the latter vanishes completely, while the SH-SAW preserves a high performance having $k_{\text{eff}}^2 = 11.7\%$ and a quality factor Q at antiresonance of 165. Further, the anti-resonance frequency is showing much higher sensitivity than the resonance frequency.

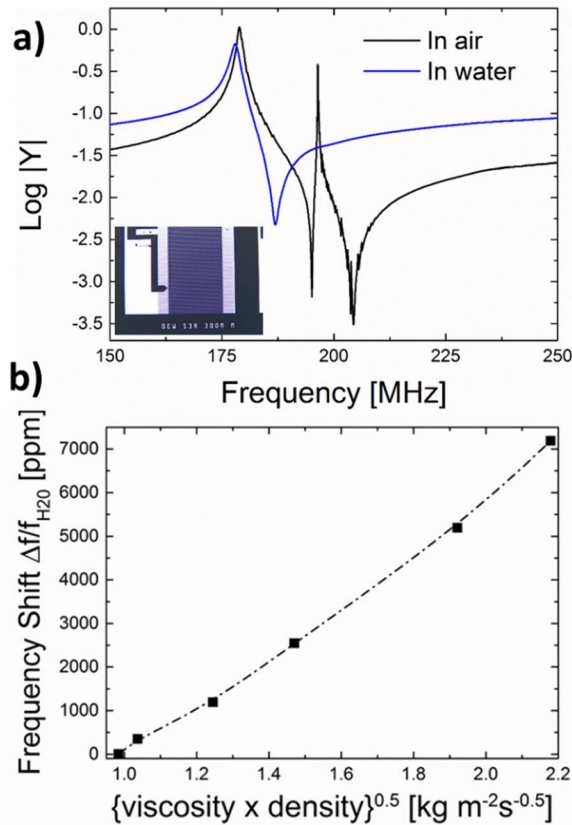


Fig. 2. In air and in water frequency responses of the device (a) and the sensitivity of the SH-SAW antiresonant frequency to ethylene glycol - water mixtures of different composition represented by $(\rho\eta)^{0.5}$ (b).

In Fig. 2b we present the frequency sensitivity of the antiresonance frequency for different water – ethylene glycol mixtures, which are represented by the square root of their density viscosity product $(\rho\eta)^{0.5}$. It can be observed a very high sensitivity of about 7200 ppm frequency shift for 1.2 units variation of the $(\rho\eta)^{0.5}$. Note that the frequency increases with the increase of the ethylene glycol concentration (proportional to $\rho\eta$). This results from the decrease of the dielectric permittivity of the liquid, which increases the electromechanical coupling varying in this measurement in the range of 11.7% - 13.5 % for the used mixtures. The Q factor at antiresonance drops from 165 to 80 for liquids with $(\rho\eta)^{0.5}$ ranging from 1 to 2.2, respectively.

We also observed very poor sensitivity at the resonant frequency. Measurements at the resonant frequency for the used mixtures of ethylene glycol and water have not revealed a clear tendency of the resonance shift, but remained hidden in the measurement error. This behavior is further clarified in the discussion below.

III. DISCUSSION

Y-cut LiNbO₃ was chosen as a base substrate here because it supports leaky SAW (LSAW) with predominantly shear polarization that exhibit electromechanical couplings higher than 25% [10]. A drawback of this wave is its relatively high losses through energy leaking into the crystal bulk. Within the SPG configuration, the LSAW velocity is decreased in comparison with the bulk modes, hence constituting well-confined SH-SAWs to the surface. This feature is clearly demonstrated in Fig. 3, where a frequency response analysis employing the finite element method with periodic boundary conditions over a primitive SPG cell is shown.

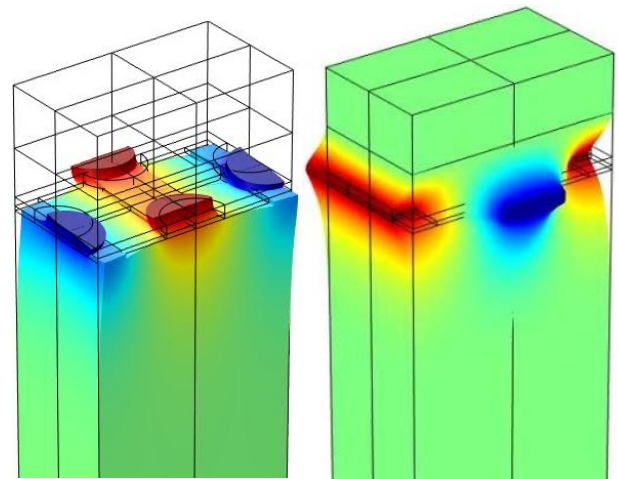


Fig. 3. SH-SAW displacement derived from COMSOL Multiphysics frequency response analysis of SPG SH-SAW loaded with liquid media.

The sensitivities of SH-SAW have been studied considering a uniform amplitude along the aperture (2D). These simple theoretical models based on the perturbation theory are suitable to identify in advance some basic characteristics of the phononic SH-SAWs. Accordingly, the mass sensitivity of the SH-SAW increases exponentially with the energy confinement towards the surface [11]. In this view, the very shallow energy confinement determined by the SPG is

expected to result in significantly improved mass sensitivity, making them promising for bio-chemical sensing applications based on surface-deposited reactants.

When immersed in liquids, SH-SAWs exhibit relative shift of acoustic wave velocity (i.e. frequency) proportional to the relative shift of the dielectric permittivity of the liquid [12]:

$$\frac{\Delta f}{f} = -K^2 \frac{\Delta \epsilon}{\epsilon + \epsilon_p}, \quad (1)$$

where K^2 is the SH-SAW electromechanical constant, $\Delta \epsilon$ is the shift of dielectric constant of the liquid, ϵ the nominal dielectric constant of the liquid and ϵ_p the effective permittivity of the crystal surface. Accordingly, waves with large K^2 are expected to demonstrate high sensitivities towards changes of the dielectric properties of the liquid. Note that when propagating under metal grating conditions, the above formula is not directly applicable. The metal strips and masses have a screening effect over part of the surface and also determine the existence of a frequency stopband caused by the grating reflectivity. In particular, part of the contribution to this reflectivity is provided by the charge distribution on the metal grating. For example, the improvement of dielectric permittivity leads to an overall slow-down effect on one hand, but on the other hand to a reduction of the stopband width (reflection). As a result, the lower edge of the frequency stopband may appear less sensitive to changes in dielectric properties than the upper stopband edge. This hypothesis has been confirmed by eigenfrequency COMSOL simulations, presuming relative dielectric constants of the liquid to be 50 and 80, respectively. The frequency downshift at the lower stopband edge was -255ppm (the resonant frequency), while at the upper stopband edge it was by an order of magnitude higher -2440ppm.

The viscosity sensitivity of SH-SAW is approximately given by [13]:

$$\frac{\Delta f}{f} = \frac{(\omega \eta)^2}{2(C_{EFF})^2}, \quad (2)$$

where $\Delta f/f$ is the relative frequency shift, ω the operating angular frequency, η the liquid viscosity and C_{EFF} the effective shear elastic modulus of the SH-SAW. Unlike QCM, the frequency shift is positive towards increase in viscosity, although for reasonable working frequencies (~ 100 MHz) the above quantity is very small $\sim 10^{-10}$, which indicates that the velocity of 2D SH-SAWs are practically insensitive to viscous properties of the liquids. SPG based SH-SAW differs from its uniform 2D counterpart by the specific energy (displacement) localization under the heavy W masses (see Fig. 4). This type of displacement distribution can effectively be represented by the interference of two SAW propagating in orthogonal directions. In X-direction, a plane wave SH-SAW harmonic is interfering with Z-direction propagating longitudinal SAW harmonic (see Fig. 4). Note that the polarization of both harmonics is towards Z-direction of the Y-cut LiNbO_3 , while its direction with respect to the propagation directions determine the modes as shear or longitudinal, respectively. The proposed SPG mode representation is equivalent to the representation by Bloch harmonics coupled in the structure [14], but is more intuitive. Following this representation we

consider now two SAW components interacting with the liquid.

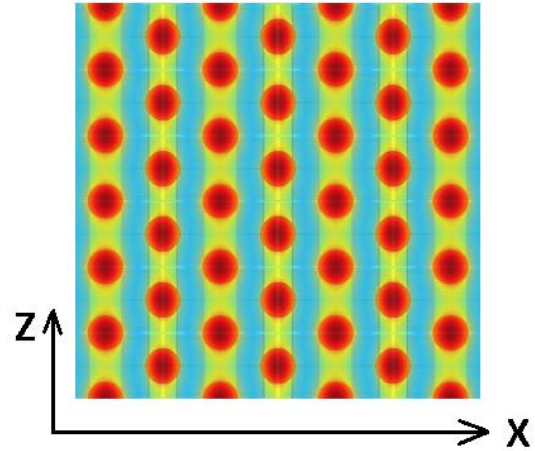


Fig. 4. SH-SAW displacement magnitude derived from COMSOL Multiphysics frequency response analysis.

The classical SH-SAW 2D harmonic is known to be insensitive to liquid viscosity and the orthogonally propagating longitudinal harmonic. The latter has been recently studied in view of in-liquid sensing applications and was found to exhibit sensitivity to $(\rho\eta)^{0.5}$ [6]. Thus, in contrast to uniform 2D SH-SAW, the phononic SH-SAW is expected to exhibit some sensitivity towards changes in the density–viscosity product of the liquid. Yet there is a need for further investigations to verify such a hypothesis.

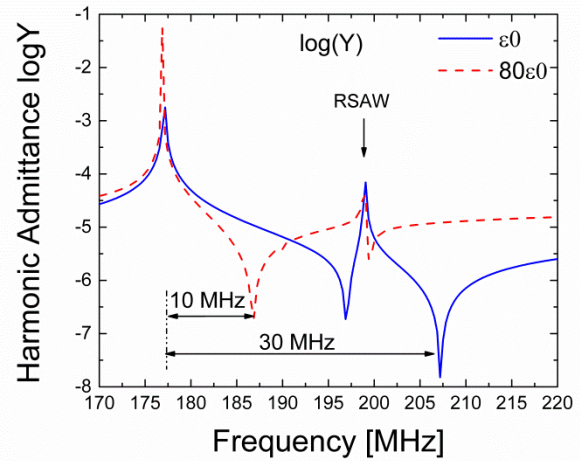


Fig. 5. Harmonic Admittance of the primitive SPG cell as simulated presuming dielectric permittivities $80\epsilon_0$ and ϵ_0 , respectively. The Rayleigh SAW is practically insensitive to changes in dielectric permittivity because of its significantly lower coupling.

Another sensitivity effect with respect to changes in liquid dielectric properties has been identified as the effect induced by the change of the electromechanical coupling itself. This effect must be considered for large values of K^2 . In Fig. 5, the harmonic admittance of the SPG cell is shown as calculated for two basic dielectric permittivities – the air (ϵ_0) and the water

($80\epsilon_0$), respectively. As seen, the significant shift of the parallel resonance determines a corresponding decrease of the effective electromechanical coupling, the latter determined by the relative shift between resonance f_R and antiresonance f_A frequencies $k_{\text{eff}}^2 \approx 0.25 \cdot \pi^2 (f_A - f_R) / f_R$. This effect differs from the loading effect described in eq. 1, which describes the impact over the SH-SAW velocity, while here the sensitivity is induced by the change of the electromechanical coupling. The impact of this effect is high and appears dominating in the sensitivity response at parallel resonance. Further it opens the way of using SPG SH-SAW resonators for in liquid sensing with the ability to discriminate mass loading versus dielectric loading effects, considering the fact that the antiresonance frequency shift is dominated by changes in dielectric properties, while resonant frequency shift is dominated by mass loading.

The above considerations are in very good agreement with the experimental measurements.

IV. CONCLUSION

In conclusion, some important features of the SPG SH-SAW immersed in liquid have been experimentally identified and theoretically grounded as follows:

- The resonance frequency is relatively insensitive to liquid mechanical properties (viscosity and density)
- The resonance frequency is relatively insensitive to liquid dielectric properties
- The antiresonance frequency exhibits high sensitivity towards changes in dielectric properties of the liquid
- Unlike the frequency shift, the Q factor at antiresonance decreases with the $(\rho\eta)^{0.5}$ product, thus being a measure for the viscous loading.

The study represents an early-stage attempt to understand the behavior of SH-SAW phononic resonators as in-liquid sensors. The interpretations given here are yet to be validated, and subsequently used in the design of application-oriented bio-sensor devices with boosted performance. Future research is needed to assess the mass sensitivity of the device immersed

in liquid in view of Bio-sensing applications. The clear potential of the phononic gratings in high performance in-liquid sensors remains to be fully unlocked.

REFERENCES

- [1] M. Rodahl, et. al., "Simultaneous frequency and dissipation factor QCM measurements of biomolecular adsorption and cell adhesion", *Faraday Discuss.*, vol. 107, pp. 229-246, 1997
- [2] M. Voinova, M. Jonsson and B. Kasemo, "On dissipation of quartz crystal microbalance as a mechanical spectroscopy tool", *Spectroscopy* vol. 18, pp. 537-544, 2004
- [3] K. Lange, B. Rapp, M. Rapp, "Surface acoustic wave biosensors: a review", *Anal Bioanal Chem* vol. 391, pp. 1509-1519, 2008.
- [4] Jun Kondoh, Yoshikazu Matsui and Showko Shiokawa, "New Biosensor Using Shear Horizontal Surface Acoustic Wave Device", *Jpn. J. Appl. Phys.*, Vol. 32, pp. 2376 – 2379, 1993
- [5] B. Martin, S. Wenzel, R. White, "Viscosity and density sensing with ultrasonic plate waves", *Sens. Actuat A: Physical*, Vol. 22, pp. 704-708, 1990
- [6] T. Mirea et. al., "Influence of liquid properties on the performance of S0 - mode Lamb wave sensors II: Experimental validation", *Sens. Actuat. B: Chemical*, vol. 229, pp. 331–337, 2016
- [7] I. Katardjiev and V. Yantchev, "Recent developments in thin film electro-acoustic technology for biosensor applications", *Vacuum* vol. 86, no. 5, pp. 520–531, 2012
- [8] R. Lucklum, "Phononic Crystal Sensors", in *Proc. European Frequency and Time Forum (EFTF)*, pp. 196 – 199, 2012
- [9] V. Yantchev, "Complete Bandgap SAW Phononic Resonators", in *Proc. 2014 European Frequency and Time Forum (EFTF)*, pp. 282 – 285, 2014
- [10] Ken-ya Hashimoto, *Surface Acoustic Wave Devices in Telecommunications, Modelling and Simulations*, Springer Berlin, 2000
- [11] V. Yantchev et al, "Theoretical and Experimental Mass-Sensitivity Analysis of Polymer-Coated SAW and STW Resonators for Gas Sensing Applications", *IEEE Sens. J.*, pp. 307-313, Aug. 2002
- [12] J. Kondoh, "A Liquid-Phase Sensor Using Shear Horizontal Surface Acoustic Wave Devices", *Electronics and Communications in Japan*, Vol. 96, No. 2, pp. 41 – 49, 2013
- [13] F. Josse Z. Shana, "Analysis of shear horizontal surface waves at the boundary between a piezoelectric crystal and a viscous fluid medium", *J. Acoust. Soc. Am.*, vol. 84, no. 3, pp. 978 – 984, 1998
- [14] V. Yantchev and V. Plessky, "Analysis of two dimensional composite surface grating structures with applications to low loss microacoustic resonators", *J. Appl. Phys.*, Vol. 114, Issue 7, art.no. 074902, 2013.

Optimization of Laser Radiation for CPT-based Miniature Frequency Standard

Konstantin Barantsev, Andrey Litvinov, Evgeniy Popov, Igor Sokolov
 Department of Quantum Electronics
 Peter the Great St.Petersburg Polytechnic University
 Saint-Petersburg, Russia
 Email: kostmann@yandex.ru

Abstract—The present work is dedicated to optimization of the laser radiation parameters and optical thickness of the gas cell for improvement of short-term stability of quantum frequency standard based on coherent population trapping effect in the cell with ^{87}Rb working gas and buffer gas. The effects associated with the optical density of the medium are investigated, such as laser spectrum distortion and appearance of the light shifts of the coherent population trapping resonance due to different absorption of frequency components.

I. INTRODUCTION

It is known that atoms, irradiated by multi-frequency laser field, can generate so-called "dark" states. Such states are a consequence of the coherent population trapping (CPT) effect [1]–[3]. In conditions of this effect occurs transparency window (CPT resonance), which significantly (by 3-4 orders) narrowly width than natural absorption line width. This allows using CPT effect in a wide variety of applications, one of which is using CPT effect as base for the developing miniature quantum frequency standards (QFS) [4], [5]. CPT effect advantage over the traditional QFS, which based on double radio-optical resonance [6], [7], is no need for using microwave resonator, which allows reducing both the overall dimensions and the energy consumption.

The CPT phenomenon in a gas cell is widely investigated. For example, works [8]–[10] are dedicated to the pseudo-resonance in the field of collinear waves. Optical pumping of Cs in perpendicular waves and the CPT effect in these atoms were considered theoretically and experimentally in [11]. In works [12]–[15] thoroughly studied diffusion-induced Ramsey narrowing in cells with buffer gas and in cells with anti-relaxation wall coating. Formation of the CPT resonance in the laser pumped coated cells was investigated in [16]–[18]. The influence of arbitrary polarization of the laser fields on the CPT resonance shape was described in [19], [20].

Summarizing, we can note, that CPT effect investigations are versatile and cover a very wide range of issues. However, conducted earlier investigations aim to identify influence of individual factors on the CPT resonance shape. Our work is dedicated to construction of the consistent theory, which describes propagation of the laser radiation with arbitrary polarization and spectrum shape in optically dense cell with working gas of alkali metal and buffer gas. On the base of this theory we make multifactorial optimization of the laser

radiation and gas cell parameters for developing CPT-based miniature quantum frequency standard.

II. THEORY

Let us consider the interaction between the laser radiation and saturated vapour of ^{87}Rb in gas cell at the temperature 30-70 $^{\circ}\text{C}$. The CPT-resonance detection scheme is shown in the Fig.1. In cell, besides ^{87}Rb , introduced buffer gas to decrease depolarization of atoms on the walls. If concentration of buffer gas is sufficient (usually 6-7 orders higher than ^{87}Rb concentration) then mean free path of ^{87}Rb becomes much smaller than the cell sizes and the frequency of collisions with the walls decreases. To avoid depolarization in collisions of ^{87}Rb atoms with buffer gas its selected so that spin-exchange cross section with ^{87}Rb is minimized [21], [22]. In our work we make the calculations for nitrogen N_2 as the buffer gas. Collisions between excited ^{87}Rb atoms and N_2 molecules with a high probability lead to quenching of ^{87}Rb atom. In this case the energy spent on vibrational-rotational motion of N atoms in the nitrogen molecule. Such quenching allows us to neglect fluorescent radiation.

Electromagnetic field with the vector

$$\mathbf{E}(z, t) = \mathbf{E}_1^0(z, t)e^{-i[\omega_1 t - k_1 z]} + \mathbf{E}_2^0(z, t)e^{-i[\omega_2 t - k_2 z]} + \text{c.c.} \quad (1)$$

is quasis resonant to D_1 -line of ^{87}Rb and contains two spectral components with the carrier frequencies ω_1 and ω_2 . The difference between these frequencies corresponds to the hyperfine

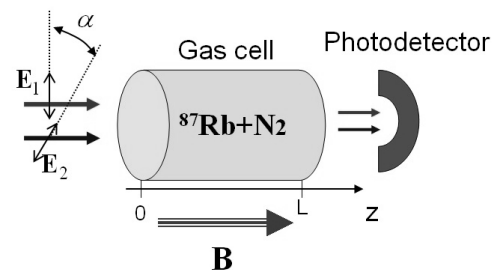


Fig. 1. Detection scheme of CPT signal, consisting of the gas cell with saturated steam of ^{87}Rb and buffer gas N_2 , irradiated by two frequency radiation with the components \mathbf{E}_1 and \mathbf{E}_2 , and photodetector. α is the angle between the planes of polarization. The cell is in a constant magnetic field \mathbf{B} .

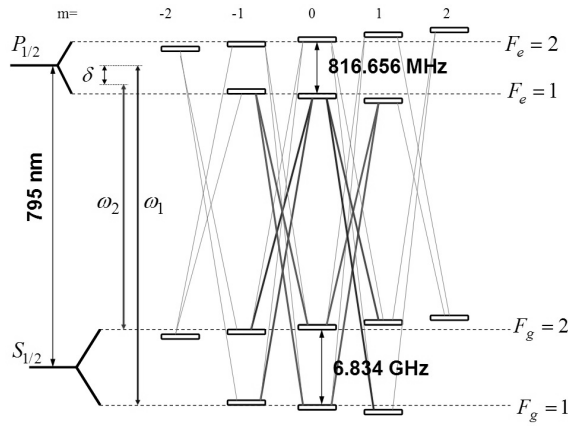


Fig. 2. Scheme of atomic levels for D₁-line of ⁸⁷Rb. Thick lines show the "magnetic-independent" CPT Λ -resonances schemes. The laser field contains two spectral components with the carrier frequencies ω_1 and ω_2 which have the intensities I_1 and I_2 respectively.

splitting of the S-state of the outer electron shell of ⁸⁷Rb atom (Fig.2). Complex amplitudes of both frequency components depend on the time due to amplitude and phase fluctuations with characteristic time $\sim \Gamma_{las}^{-1}$. It gives spectrum broadening of each frequency component by the value Γ_{las} . Propagation of field in the cell is described by the wave equation for complex amplitudes:

$$\left(\frac{\partial}{\partial z} + \frac{1}{c} \frac{\partial}{\partial t} \right) \mathbf{E}_n^0(z, t) = 4\pi i k_n \mathbf{P}_n^0(z, t), \quad n = 1, 2, \quad (2)$$

where k_n are the wave numbers, \mathbf{P}_n^0 are the slow amplitudes of the polarization, induced by the n-the carrier frequency.

We will describe the state of ⁸⁷Rb atoms using a density matrix $\hat{\rho}(v, z, t)$, where v is the projection of the velocity of atoms onto z axis. In a one-dimensional approximation quantum kinetic equation for the density matrix has the form:

$$\left(\frac{\partial}{\partial t} + v \frac{\partial}{\partial z} \right) \hat{\rho}(v, z, t) = -\frac{i}{\hbar} [\hat{H}, \hat{\rho}] + \hat{R}\{\hat{\rho}\} + \hat{S}\{\hat{\rho}\}, \quad (3)$$

where \hat{R} is the relaxation superoperator, \hat{S} is the collision integral. The Hamiltonian can be presented as the sum $\hat{H} = \hat{H}_0 + \hat{V}$, where \hat{H}_0 is the atomic Hamiltonian in the absence of the laser field and $\hat{V} = -\hat{\mathbf{d}}\mathbf{E}_1 - \hat{\mathbf{d}}\mathbf{E}_2$ is the interaction operator in the dipole approximation.

As noted above, the electromagnetic field fluctuates, therefore, the set of equations (2-3) is stochastic. We average it over statistics of the laser field. The solution of (3) after averaging will give us an expression for the atomic density matrix in terms of atomic-field correlation functions. We can decouple them on the field correlation functions of second order and average elements of the atomic density matrix assuming the Gauss noise statistics:

$$\langle E_m^{0*}(t) E_n^0(t') \rho(t') \rangle = \langle E_m^{0*}(t) E_n^0(t') \rangle \langle \rho(t') \rangle. \quad (4)$$

Pair correlation function of the field as a stationary stochastic process, is determined by the Wiener-Khinchin theorem through the energy spectrum J_{11} and J_{22} and the cross

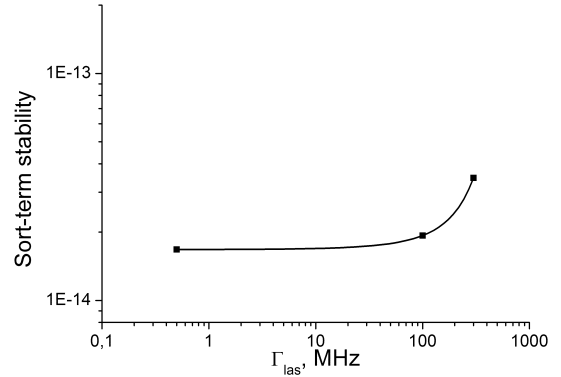


Fig. 3. Short-term stability of QFS depending on spectral width of the radiation entering the cell for averaging time $\tau = 1$ s. Laser spectrum at the cell input has the Lorentz profile. Field intensities are $I_1 = I_2 = 0.2 \text{ mW/cm}^2$, temperature $T=333\text{K}$, magnetic field $B=0.05\text{G}$, cell length $L=2\text{cm}$, cell radius $R=1\text{cm}$, concentrations $n_{Rb} = 1.15 \cdot 10^{11} \text{ cm}^{-3}$, $n_{N_2} = 2.9 \cdot 10^{17} \text{ cm}^{-3}$.

spectrum J_{12} :

$$\langle E_m^{0*}(t) E_n^0(t - \tau) \rangle = \int_{-\infty}^{\infty} J_{mn}(\omega) e^{-i\omega\tau} d\omega, \quad m, n = 1, 2. \quad (5)$$

In the short noise limit stability of QFS can be found as follows:

$$\sigma = \frac{\sqrt{j(\delta_c) e}}{S_j(\delta_c) \Gamma \omega_{hfs} \sqrt{\tau}}, \quad (6)$$

where $j(\delta_c)$ is the resonant photocurrent, e is the elementary charge, $S_j(\delta_c)$ is the absolute value of the second derivative of the photocurrent with respect to detuning δ at resonance, Γ is the width of the linear section of discriminator curve, τ is the averaging time of the discriminator signal, ω_{hfs} is the hyperfine splitting of the ground state. The photocurrent is proportional to the output intensity I :

$$j(\delta) = \frac{e\pi R^2}{\hbar\omega} I(\delta), \quad (7)$$

where R is the beam radius, ω is the frequency of the optical transition, δ is the two-photon detuning.

III. RESULTS AND DISCUSSION

For high contrast CPT resonance according to the scheme shown in Fig.1, it is necessary that the radiation is significantly absorbed in the cell at $\delta \neq 0$. Otherwise will happen "blinding" of the photodetector by the passing forward radiation and we will have low resonance contrast. Thus, the cell should have significant optical thickness and the mean free path of a photon is much less than the length of the cell (further we introduce the dimensionless parameter $n_{Rb}\lambda^2 L$ for optical thickness, where n_{Rb} is the concentration of ⁸⁷Rb, λ is the radiation wavelength, L is the length of the cell). In this work, we will consider mainly the effects associated with absorption of the radiation and distortion of the spectrum in an optically dense medium.

Let us consider CPT resonance excitation in two linear polarized waves. The angle α between the planes of polarization is equal to zero (lin || lin configuration). If the both

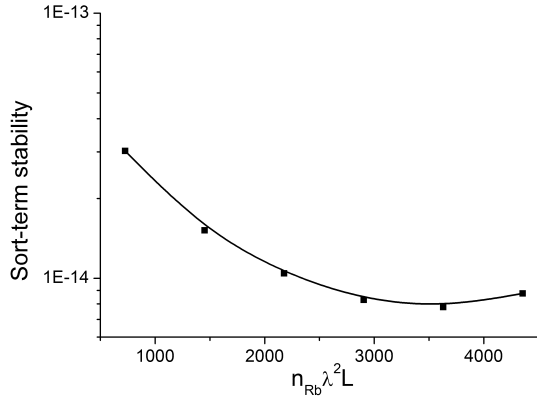


Fig. 4. Short-term stability for averaging time $\tau = 1s$ depending on optical thickness of the cell. Field intensities are $I_1 = 0.087 mW/cm^2$, $I_2 = 0.1 mW/cm^2$, spectral width of the radiation at the cell input $\Gamma_{las} = 500 kHz$, the other parameters are the same as in Fig.3.

frequencies are tuned to the level $F_e = 1$, two "magnetic-independent" CPT resonances are excited on transitions $|F_g = 1, m = \pm 1\rangle \leftrightarrow |F_g = 2, m = \mp 1\rangle$. Let us see how in this case the finite width Γ_{las} of the spectrum affects the short-term stability of QFS. If the spectrum width is much smaller than the Doppler broadening and hyperfine splitting of the excited level, the CPT signal is almost independent on the spectral width (horizontal section from 0.5 to 100 MHz in Fig.3). Stability begins to fall, when the spectral width exceeds the Doppler broadening (section from 100 to 300 MHz in Fig.3). In this case the spectral contour edges are absorbed weaker and "blind" the photodetector. It deteriorates the contrast of CPT resonance and QFS stability.

We now define what should be the optical thickness of the cell to achieve the maximal QFS stability. The short-term stability depending on the optical thickness is shown in Fig.4. If the optical thickness is small, then the passing forward radiation "blinds" photodetector that reduces the contrast of the CPT resonance. In contrary, very dense cell scatters the most part of radiation. As a result, the optimum optical thickness with the parameters presented in Fig.4, is $n_{Rb}\lambda^2L \approx 3600$. By increasing the total input intensity this optimum shifts towards large optical thickness.

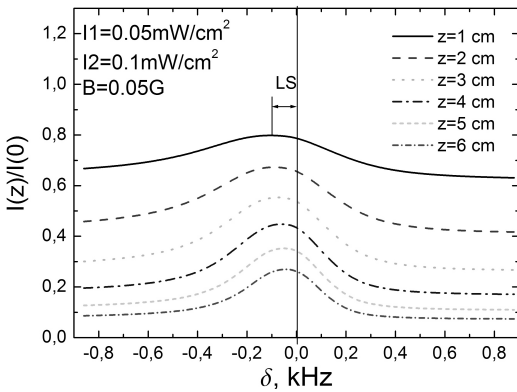


Fig. 5. CPT signal for the different cell lengths. $I_1 = 0.05 mW/cm^2$, $I_2 = 0.1 mW/cm^2$, $\Gamma_{las} = 500 kHz$. The other parameters are the same as in Fig.3.

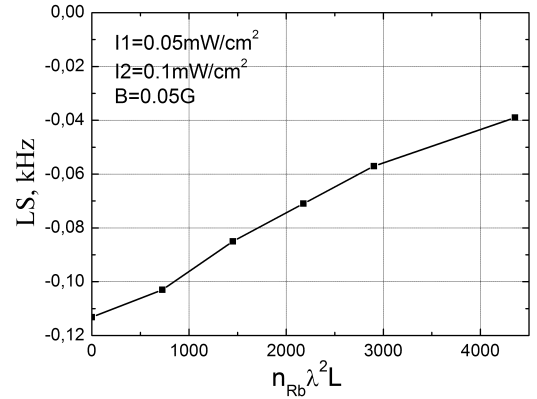


Fig. 6. Light shift of the CPT resonance depending on optical thickness of the cell. $I_1 = 0.05 mW/cm^2$, $I_2 = 0.1 mW/cm^2$, $\Gamma_{las} = 500 kHz$. The other parameters are the same as in Fig.3.

It is known that the electromagnetic radiation shifts an atomic transition, if it has detuning in the region of maximum of the dispersion curve [23], [24]. In the case of tuning to $F_e = 1$, interaction with the second hyperfine level $F_e = 2$ causes the light shift of transitions $|F_g = 1, 2\rangle \leftrightarrow |F_e = 2\rangle$, including levels $|F_g = 1, 2; m = \pm 1\rangle$, which form the dark state in CPT resonance. In general case these levels will be shifted differently, because intensities I_1 and I_2 can be not equal in the different points of the cell. It leads to the shift of transparency maximum - the light shift of CPT resonance.

Fig.5 shows how the light shift of CPT resonance changes at different points of the cell. The laser fields have different intensity at the input, so at the front edge of the cell there is a light shift (Fig.5, solid curve). Further, the difference between intensities of the fields becomes smaller because of different absorption coefficients on transitions $|F_g = 1, 2\rangle \leftrightarrow |F_e = 1\rangle$. This leads to a shift reduction (Fig.6). Thus, the CPT resonance light shift can be suppressed by adjusting the ratio I_1/I_2 of the intensities at the input of the cell that has been shown experimentally in [9].

Let us consider the dependence of the light shift of CPT resonance on the angle α between the planes of polarization (see the Fig.1). When the angle $\alpha \neq 0$, the "magnetic-

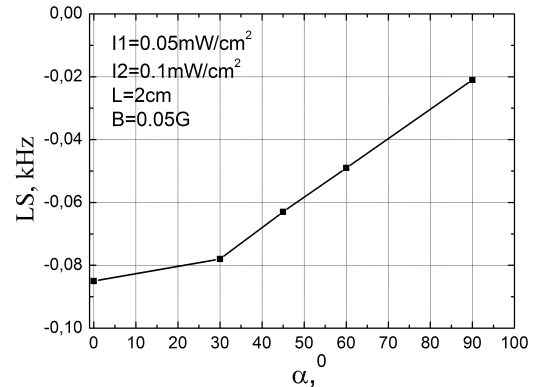


Fig. 7. Light shift of the CPT resonance depending on angle α between the planes of polarization. $I_1 = 0.05 mW/cm^2$, $I_2 = 0.1 mW/cm^2$, $\Gamma_{las} = 500 kHz$. The other parameters are the same as in Fig.3.

independent” resonance on transition $|F_g = 1, m = 0\rangle \leftrightarrow |F_g = 2, m = 0\rangle$ begins make a contribution in the CPT signal. It is susceptible to a light shift less much less than transitions $|F_g = 1, m = \pm 1\rangle \leftrightarrow |F_g = 2, m = \mp 1\rangle$, because field on this transitions forms only Λ -schemes and converts levels into the ”dark” state. One can see in Fig.7 that the light shift decreases when the lin || lin configuration is replaced by the lin \perp lin configuration.

IV. CONCLUSIONS

Mathematical model of the CPT effect which takes into account distortion of the light spectrum and changing in light polarization inside the gas cell due to selective absorption in optically dense medium has been constructed.

The short-term stability of quantum frequency standard was calculated for the linear polarized laser field which is tuned to level $F_e = 1$ of the $^{87}\text{Rb } D_1$ -line.

It was determined that optical thickness of the gas cell affects stability of the frequency standard. There is optimal optical depth of the atomic ensemble.

Decreasing in spectral width of the radiation improves contrast of the CPT resonance as well as the short-term stability of the CPT-based standard. On the contrary, wideband radiation with spectral width comparable with Doppler broadening or/and hyperfine splitting of the excited state causes noticeable depopulation of the working levels and deteriorates the stability.

The light shift of CPT-resonance, which is caused by different absorption of the frequency components, was investigated. The way of suppression of the light shift, which had been proposed in the work [9], was theoretically justified.

ACKNOWLEDGMENT

This work was supported by State Assignment in science activity for universities 2014/184 and 3.1446.2014/K, the Russian Foundation for Basic Research (grant No 14-02-31422, No 13-02-00944, No 16-32-00587), Scholarship of the Government of the Russian Federation, Russian President grant for young candidates of sciences (project MK-6530.2016.2).

The authors are grateful to M. Dushkina for the significant assistance.

REFERENCES

[1] G. Alzetta, A. Gozzini, L. Moi, and G. Orriols, *Nuovo Cimento B*, vol. 36, no. 5, 1976.
 [2] E. Arimondo and G. Orriols, *Nuovo Cimento Lett.*, vol. 17, 333, 1976.
 [3] B. D. Agapiev, M. B. Gorniy, B. G. Matisov, et al., *UFN*, vol. 163, no. 1, 1993.
 [4] M. Merimaa, T. Lindvall, I. Tittonen, and E. Ikonen, *JOSA B*, vol. 20, 273, 2003.
 [5] J. Vanier, *Appl.Phys. B*, vol. 81, p. 421, 2005.
 [6] A. S. Zibrov, A. S. Zhukov, V. P. Yakovlev, et al., *JETP Letters*, vol. 83, no. 168, 2006.
 [7] A. Litvinov, G. Kazakov, B. Matisov, I. Mazets., *J. Phys. B: At. Mol. Opt. Phys.*, vol. 41, 125401, 2008.
 [8] S. A. Zibrov, V. L. Velichanskiy, A. S. Zibrov, A. V. Taichenachev, V. I. Yudin, *JETP Letters*, vol. 82, no. 534, 2005.

[9] S. A. Zibrov, I. Novikova, D. F. Phillips, et al., *Phys. Rev. A*, vol. 81, 013833, 2010.
 [10] G. Kazakov, B. Matisov, I. Mazets, G. Mileti, and J. Delporte, *Phys. Rev. A*, vol. 72, 063408, 2005.
 [11] X. Liu, J. Mrolla, S. Gurandel, et al., *Phys. Rev. A*, vol. 87, 029903, 2013.
 [12] Y. Xiao, I. Novikova, D. F. Phillips, and R. L. Walsworth, *Phys. Rev. Lett.*, vol. 96, 043601, 2006.
 [13] E. Breschi, G.Kazakov, C. Schori, et al., *Phys.Rev. A*, vol. 82, 063810, 2010.
 [14] G. A. Kazakov, A. N. Litvinov, B. G. Matisov, et al., *Journal of Physics B*, vol. 44, 235401, 2011.
 [15] E. Kuchina, E. E. Mikhailov, and I. Novikova, *JOSA B*, vol. 33, no. 610, 2016.
 [16] G. Alzetta, S. Gozzini, A. Lucchesini, et al., *Phys.Rev. A*, vol. 69, 063815, 2004.
 [17] G. Kazakov, B. Matisov, A. Litvinov, I. Mazets., *J. Phys. B: At. Mol. Opt. Phys.*, vol. 40, 3851, 2007.
 [18] M. Klein, M. hohensee, D. F. Phillips, and R.L. Walsworth, *Phys. Rev. A*, vol. 83, 013826, 2011.
 [19] V. M. Datsyuk, I. M. Sokolov, D. V. Kupriyanov, and M. D. Havey, *Phys. Rev. A*, vol. 74, 043812, 2006.
 [20] V. M. Datsyuk, I. M. Sokolov, D. V. Kupriyanov, and M. D. Havey, *Phys. Rev. A*, vol. 77, 033823, 2008.
 [21] S. Brandt, A. Nagel, R. Wynands, and D. Meschede, *Rhys. Rev. A*, vol. 56, 2, 1997.
 [22] R. Wynands, A. Nagel, *Appl. Phys. B*, vol. 68, 1, 1999.
 [23] J. Barrat, C. Cohen-Tannoudji, *J. Phys. Radium*, vol. 22, no. 329, 1961.
 [24] C. Cohen-Tannoudji, J. Dupont-Roc, G. Grynberg, *AtomPhoton ”Interactions: Basic Processes and Applications”*, Wiley, New York, 1992.

Phase Locking an Atom Interferometer

Andrea Bartoldi^{*¶}, Ralf Kohlhaas^{*†}, Etienne Cantin^{*}, Alain Aspect[§], Arnaud Landragin^{||} and Philippe Bouyer^{*}

^{*}Laboratoire Photonique, Numérique et Nanosciences – Université Bordeaux – IOGS – CNRS: UMR 5298
rue Mitterrand, F-33400 Talence, France

[†]now at: SRON Netherlands Institute for Space Research, Sorbonnelaan 2 - 3584 CA Utrecht, The Netherlands

[‡]Quantel, 4 rue Louis de Broglie, Building D, F-22300 Lannion, France

[§]IOGS, LCF, Univ. Paris XI, F-91127 Palaiseau, France

^{||}LNE-SYRTE, Observatoire de Paris, CNRS and UPMC, 61 avenue de l'Observatoire, F-75014 Paris, France

[¶]Email: andrea.bartoldi@institutoptique.fr

Abstract—In atom interferometry the phase evolution of a quantum superposition state is measured with respect to a reference signal. The measurement has a limited unambiguous interval, since not the phase but its projection is measured as a population unbalance on two energetic levels. Resolving phase wrapping brings to a longer interrogation interval and hence instrument sensitivity. We extended the unambiguous probe interval using coherence preserving measurements and phase corrections, and demonstrated the phase lock of the clock oscillator to an atomic superposition state. On this basis we implemented a protocol to improve atomic clocks limited by local oscillator noise, which is the case of optical atomic clocks, nowadays the best frequency standard in terms of both accuracy and precision. The technique could be adopted to enhance the sensitivity of atomic gravimeters.

Measuring the phase evolution of a system is a radically different process in the classical and in the quantum case: whereas it is possible to follow continuously the phase evolution of, *e.g.*, a quartz oscillator, this is not the case for the phase evolution of an atomic superposition state. The remarkable differences are given by two features of the quantum measurement process: first, the extraction of information from the system modifies the system itself, changing its noise properties if the measurement is at the quantum projection noise level or beyond, and reducing its coherence. Standard destructive measurements reduce to zero the system coherence, and permit a single phase measurement on the system. Second, in the specific case of the atomic superposition state, the phase is not obtained directly, but via its trigonometric projection measured in terms of a population imbalance on two atomic levels; as a consequence the phase is known without ambiguity only if it stays within the interval $[\pi/2; \pi/2]$. Beyond such interval phase wraps occur, which determines readout errors.

Resolving phase wrapping is a common problem for which ingenious solutions have been devised in the classical case: in distant audio recovery, for example, laser Doppler vibrometers measure the phase of a reflected beam, as well as its Doppler shift to determine the velocity of the reflecting surface [1]. In atom interferometry [2,3] the phase evolution of a quantum superposition state is measured with respect to a reference, *e.g.* implemented with a local oscillatory signal in the case of an atomic clock and with the position of a retro-reflector for a Raman atom gravimeter. The standard approach is to avoid phase wraps by choosing an interrogation interval T short enough. This solution comes in detriment of the instrument sensitivity, which scales favorably with T , and notably linearly for an atomic clock and quadratically for a free fall atom

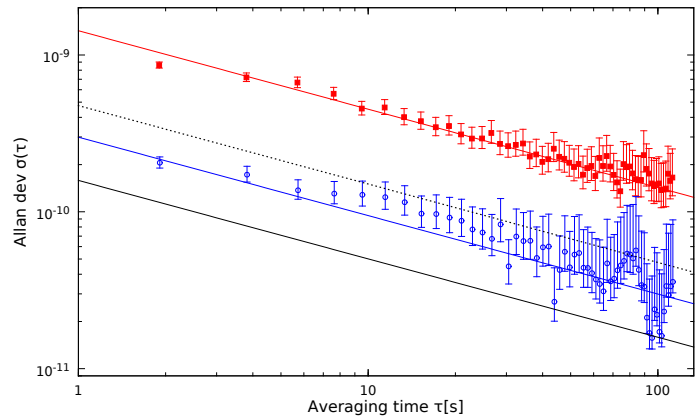


Fig. 1. Atomic clock implementing a phase lock. Allan frequency standard deviation for a normal Ramsey clock with interrogation time $T=1$ ms (red filled squares and red line) and for a clock implementing the phase lock between the LO and the atomic superposition state for nine successive, correlated interrogations on the same atomic ensemble, for a total interrogation time of $9 \times T=9$ ms (blue empty circles and blue line). The dead time is in both cases $T_D=1.9$ s. The red and blue lines are fits to the data, with a slope set to $\tau^{-1/2}$. The continuous black line lies a factor 9 below the red curve and represents the best achievable level of the phase lock sequence for the same number of interrogations. The dashed black line lies a factor 3 below the red curve and is the optimum level for nine consecutive uncorrelated Ramsey measurements with duration T each and the same total cycle time.

gravimeter. The improvement of the sensor performance relies thus on the development of references with less noise, *i.e.* an interrogation laser with a longer coherence time in the case of optical clocks [4-8] and a retro-reflecting mirror with an enhanced stabilization for a Raman atom gravimeter [9].

Conceptually different solutions have been recently proposed to extend the interrogation interval in atomic clocks [10,11] and demonstrated in atom interferometry based inertial sensing [12]; they use two or more ensembles interrogated simultaneously to monitor the relative phase evolution at different time scales so as to avoid phase wraps over a longer time interval. We combined this idea with the proposal of using weak measurement to monitor the phase evolution in a clock measurement [13], and extended the unambiguous interval to probe the evolution of an atomic ensemble using coherence preserving measurements and phase corrections. The experiment uses cold rubidium atoms trapped in a cavity enhanced optical potential and interrogated with a heterodyne detection on the D2 transition [14]. We first demonstrated the

protection of a quantum superposition state from external noise [14], and then the phase lock of the clock oscillator to an atomic superposition state [15]. On this basis we implemented a protocol based on the phase lock to improve atomic clocks limited by local oscillator (LO) noise, and demonstrated N successive, partially correlated Ramsey interrogations on the same clock cycle. The clock with the enhanced Ramsey interrogation sequence with effective duration $N \times T$ increases the sensitivity with respect to a clock with a single Ramsey cycle of duration T , as shown by the Allan frequency standard deviation. Notably, the enhancement factor is higher than \sqrt{N} , which proves the correlation - at least partial - between the successive measurements. In Fig. 1 we show the case $N=9$, for which we obtained an enhancement factor of 4.8(2) to be compared with the factor 3 expected in the case of uncorrelated measurements. We had similar results when N varied from 2 to 20. The systematic issues related to the repeated manipulations of the atomic state during the extended interrogation (namely: light shift induced by the probe; different effect of the LO noise during the measurement pulses of finite duration; accuracy of the actuator implementing the phase correction) can be bypassed using a two atomic systems interrogated with the same LO: the first system is used to implement the phase lock protocol for the LO; the second system uses the pre-stabilized LO for the coherent interrogation, and is operated in optimal conditions to minimize systematic uncertainty.

The best reported optical atomic clocks [16-18] have a sensitivity limited by the coherence time of the interrogation laser; they could gain from measurement and correction protocols like our, which reduce the effect of the oscillator noise. Remarkably, quantum non-demolition measurements of the clock state populations studied to implement spin squeezing on alkali-earth clocks [19] could serve to realize the coherence preserving manipulations for the phase lock sequence. More in general, the sensitivity enhancement given by correlating successive measurements could be combined with that given by engineering inter-particle correlations. Very recently, the ultimate bound on the Allan variance of an atomic clock implementing both solutions has been theoretically studied [20].

ACKNOWLEDGMENT

The authors acknowledge funding from Direction Gnrle de l'Armement, Centre National d'Etudes Spatiales, the European Metrology Research Programme (EMRP) (JRP-EXL01 QESOCAS), the European Union (EU) (iSENSE), Laser and Photonics in Aquitaine (APLL-CLOCK, within ANR-10-IDEX-03-02).

REFERENCES

- [1] S. J. Rothberg, J. R. Baker, and N. A. Halliwell, *Laser vibrometry: pseudo-vibrations*, *J. Sound and Vibr.* **135**, 516 (1989).
- [2] A. Cronin, J. Schmiedmayer, and D. E. Pritchard, *Optics and interferometry with atoms and molecules*, *Rev. Mod. Phys.* **3**, 1051 (2009).
- [3] B. Barrett, A. Bertoldi, and P. Bouyer, *Inertial quantum sensors using light and matter*, arXiv:1603.03246 [physics.atom-ph] (2016).
- [4] Y. Y. Jiang, A. D. Ludlow, N. D. Lemke, R. W. Fox, J. A. Sherman, L.-S. Ma, and C. W. Oates, *Making optical atomic clocks more stable with 10^{-16} -level laser stabilization*, *Nat. Photonics* **5**, 158 (2011).
- [5] T. Kessler, C. Hagemann, C. Grebing, T. Legero, U. Sterr, F. Riehle, M. J. Martin, L. Chen, and J. Ye, *A sub-40-mHz linewidth laser based on a silicon single-crystal optical cavity*, *Nat. Photonics* **6**, 687 (2012).

- [6] M. J. Thorpe, L. Rippe, T. M. Fortier, M. S. Kirchner, and T. Rosenband, *Frequency stabilization to 6×10^{-16} via spectral-hole burning*, *Nat. Photonics* **5**, 688 (2011).
- [7] G. D. Cole, W. Zhang, M. J. Martin, J. Ye, and M. Aspelmeyer, *Tenfold reduction of Brownian noise in high-reflectivity optical coatings*, *Nat. Photonics* **7**, 644 (2013).
- [8] S. Amairi, T. Legero, T. Kessler, U. Sterr, J. B. Wübena, O. Mandel, and P. O. Schmidt, *Reducing the effect of thermal noise in optical cavities*, *Appl. Phys. B* **113**, 233 (2013).
- [9] A. Peters, K. Y. Chung, and S. Chu, *High-precision gravity measurements using atom interferometry*, *Metrologia* **38**, 25 (2001).
- [10] T. Rosenband and D. R. Leibbrandt, *Exponential scaling of clock stability with atom number*, arXiv:1303.6357 (2013).
- [11] J. Borregaard and A. S. Sørensen, *Efficient atomic clocks operated with several atomic ensembles*, *Phys. Rev. Lett.* **111**, 090802 (2013).
- [12] F. Sorrentino, A. Bertoldi, Q. Bodart, L. Cacciapuoti, M. De Angelis, Y.-H. Lien, M. Prevedelli, G. Rosi, and G. M. Tino, *Simultaneous measurement of gravity acceleration and gravity gradient with an atom interferometer*, *Appl. Phys. Lett.* **101**, 114106 (2012).
- [13] N. Shiga and M. Takeuchi, *Locking the local oscillator phase to the atomic phase via weak measurement*, *New J. Phys.* **14**, 023034 (2012).
- [14] T. Vanderbruggen, R. Kohlhaas, A. Bertoldi, S. Bernon, A. Aspect, A. Landragin, and P. Bouyer, *Feedback control of trapped coherent atomic ensembles*, *Phys. Rev. Lett.* **110**, 210503 (2013).
- [15] R. Kohlhaas, A. Bertoldi, E. Cantin, A. Aspect, A. Landragin, and P. Bouyer, *Phase locking a clock oscillator to a coherent atomic ensemble*, *Phys. Rev. X* **5**, 021011 (2015).
- [16] C. W. Chou, D. B. Hume, J. C. J. Koelemeij, D. J. Wineland, and T. Rosenband, *Frequency comparison of two high-accuracy Al^+ optical clocks*, *Phys. Rev. Lett.* **104**, 070802 (2010).
- [17] N. Hinkley, J. A. Sherman, N. B. Phillips, M. Schioppo, N. D. Lemke, K. Beloy, M. Pizzocaro, C. W. Oates, and A. D. Ludlow, *An atomic clock with 10^{-18} instability*, *Science* **341**, 1215 (2013).
- [18] B. J. Bloom, T. L. Nicholson, J. R. Williams, S. L. Campbell, M. B. X. Zhang, W. Zhang, S. L. Bromley, and J. Ye, *An optical lattice clock with accuracy and stability at the 10^{-18} level*, *Nature* **506**, 71 (2014).
- [19] E. S. Polzik and J. Ye, *Entanglement and spin squeezing in a network of distant optical lattice clocks*, *Phys. Rev. A* **93**, 021404(R) (2016).
- [20] K. Chabuda, I. Leroux, and R. Demkowicz-Dobrzanski, *The quantum Allan variance*, arXiv:1601.01685 (2016).

Experimental time dissemination services based on European GNSS signals: the H2020 DEMETRA project

P. Tavella, I. Sesia, G. Cerretto, G. Signorile,
D. Calonico, R. Costa, C. Clivati, E. Cantoni,
C. De Stefano, M. Frittelli, V. Formichella
INRIM, Italy

P. Cerabolini, L. Rotiroli, E. Biserni,
V. Leone, E. Zarroli, D. Sormani
ANTARES, Italy

P. Defraigne, N. Ozdemir, Q. Baire.
Observatoire Royal de Belgique, ORB, Belgium

M. Gandara, V. Hamoniaux
Thales Alenia Space France, TAS-F, France

E. Varriale, Q. Morante
Thales Alenia Space Italy, TAS-I, Italy

T. Widomski, J. Kaczmarek, J. Uzycki, K. Borgulski,
P. Olbrysz, J. Kowalski
ELPROMA, Poland

M. Beccari, A. Cernigliaro, F. Fiasca,
A. Perucca, S. Mantero,
AIZOON, Italy

V. Dhiri, Telespazio VEGA UK Ltd, United Kingdom

M.T. Veiga, T. Suárez, J. Diaz
DEIMOS, Spain

M. Mangiantini, METEC, Italy

A.E. Wallin
MIKES Metrology, VTT Technical Research Centre of
Finland Ltd, Finland

L. Galleani, Politecnico di Torino, Italy

D. Hindley
National Physical Laboratory, NPL, United Kingdom

Abstract—DEMETRA aims to be a prototype of an European time dissemination service, based on the timing signal of the European Galileo system, adding particular features like – among the others - certification, calibration, or integrity, that could be of interest to a wide range of users belonging to different sectors as traffic control, energy distribution, finance, telecommunication, and scientific institutions. Nine time dissemination services are proposed. The paper will report about the development status and the first experimentation results of the system, showing potentialities and limits of the proposed time dissemination services, aiming to foster the exploitation of the European GNSS for timing applications.

Keywords— EGNSS; time dissemination; standardised time services; demonstrator; timing; H2020;

I. INTRODUCTION

During the last year an European Consortium of 15 scientific and industrial partners from Belgium, Finland, France, Italy, Poland, Spain, UK. worked on the DEMETRA (DEMonstrator of EGNSS services based on Time Reference

Architecture) project, funded by the European Union in the frame of the Horizon 2020 program, aimed at developing and experimenting time dissemination services based on the European GNSS and introducing important new features such as certified time stamping, improved accuracy, or integrity, not yet provided by GNSS systems. The consortium is also supported by the Czech metrological institution UFE, and the French space agency CNES

A. DEMETRA Project and Timing&Sync service

The overall concept of the DEMETRA Project [1] [2] is to realize a demonstrator that allows the development, testing, and validation of time dissemination services.

The need of time related products and the possibility to accurately synchronise a user clock is in fact crucial in different fields of application. The market analysis of the European GNSS Agency in 2015 [3] [3] reported for the first time the timing and synchronisation service available from the European GNSS and considered the main strategic markets

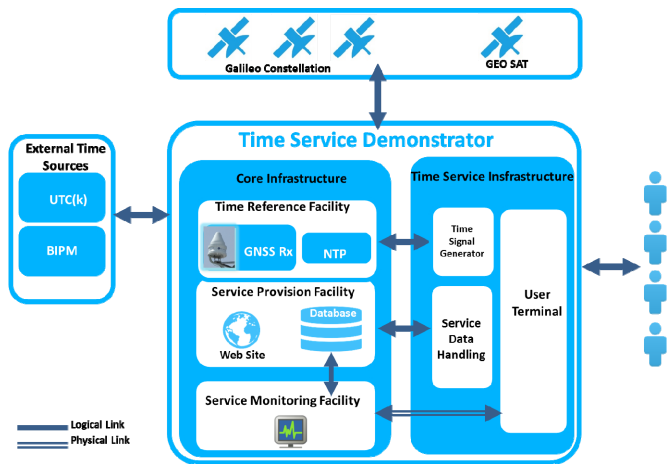


Fig. 1: DEMETRA Architecture

sectors of potential interest as Energy, Finance, Media, Science, Surveying, Telecommunications, and Transport

B. Overview of the Demonstrator

The demonstrator is designed to ensure a full operative architecture for the services delivery to final end users. As shown in Fig. 1, the demonstrator relies on external reference data, on the Galileo signal, and on a geostationary satellite.

It is composed of two infrastructures:

- The Time Service Infrastructures (TSI) corresponds to the nine DEMETRA services. Each service is composed of a Time Signal Generator, a Service Data Handling and a User Terminal(s).
- The Core Infrastructure is the hosting structure which provides common signals to the TSI and the final users. CI is composed of three main facilities:
 - Time Reference Facility, providing the reference time to be disseminated.
 - Service Provision Facility, a data base and a web page to interface the users.
 - Service Monitoring Facility, to measure, monitor, and validate the service.

The nine different time services are:

Service#1: Time broadcasting over TV/Radio links

This service allows the dissemination of time, by adopting the Radio and TV signals, conceiving analog and digital modulations [4].

Service#2: Certified Trusted Time Distribution using NTP

The service purpose is to implement a new innovative service to distribute authenticated NTP time and its back audit to end-users as well as deliver cryptographic time stamping service [5].

Service#3: Time and Frequency Distribution over Optical link

Time dissemination will be provided via the White Rabbit Optical Link, which was first developed for time transfer over relatively short fiber links: in the frame of the project, it will be experimented the Extended Range technology to cover wider

areas. A novel time signal based on Modulated Coherent Time will be tested [6] [7].

Service#4: Time and Frequency Distribution via GEO Satellite

The system disseminates time and frequency in real-time via geostationary satellite. This system is meant to work in parallel with GPS/GALILEO-based systems in order to reach full technological redundancy and it addresses those networks that require outstanding timing accuracy (~100ns provided) and high reliability.

Service#5: User GNSS Receiver Calibration

This Service aims at calibrating GNSS stations for timing applications, i.e. the hardware delays of the GNSS signals inside the antenna, the antenna cable and the receiver [8] [8]. Two methods can be used: absolute or relative.

Service#6: Certified Time Steering

Service 6 aims to disseminate precise and accurate time using GNSS Time Transfer techniques and a real-time internet link, allowing the real-time monitoring and certification of the time offset between the User Terminal and reference time.

Service#7: Time Monitoring and Steering

time scale in near real time at the nanosecond level, alerting the users about any abnormal phase or frequency jump of their clock or time scale. The system will be based on the Precise Point Positioning using the GNSS collected by the user receiver driven by its atomic clock. The service will additionally provide to the user daily information for the steering of his atomic clock or time scale to be aligned with UTC, as well as a prediction of the difference between its time scale and UTC during the next days [9] [10].

Service#8: Time Integrity

The Time Integrity Service aims to test the capability to deliver a time integrity service to the GNSS users providing integrity information to improve user timing accuracy as well as positioning [11], [12], [13].

Service#9: All-in-one Time Synchronization Solution.

Service 9 is based on SynchroNet, a Thales Alenia Space Italia patented system for high performance network synchronization. The Service is exploiting GNSS (GPS and GALILEO) synchronization algorithms and techniques into a higher level distributed infrastructure, matching critical systems requirements [14], [15], [16].

II. EXPERIMENTAL CAMPAIGNS

The DEMETRA experimentation includes two main phases named:

- Closed Loop campaign: all services components are installed and validated at INRIM DEMETRA Laboratory. In March 2016 the closed loop campaign is started. The User Terminals are collocated with the distributed reference time to perform a metrological characterization in best nominal conditions.
- End to End campaign: all services are validated in a real context. Starting from June 2016, the User Terminals will



Fig. 2: DEMETRA set up

be deployed at user premises to test the services in a real context.

Each campaign will include both nominal and stress tests in order to analyse the time services performance also in degraded conditions. A picture of the demonstrator is shown in Fig. 2.

III. FIRST EXPERIMENTAL TEST RESULTS

The experimental results are available and published in real time on the DEMETRA webpage (www.demetratime.eu). The webpage has a public page with general information, while the Key Performance Indicators, and the results of each service are available to registered users.

In the following some initial and recent test results are reported. In Fig. 3 - Fig. 5 the comparison between the Reference Time and the Time obtained at user level (UT-TRF) for *Service#2*, *3* and *4* is shown.

The detection of anomalies on the Galileo space clocks from *Service#8* is reported in Fig. 6 [17], while Fig. 7 reports the monitoring of time scales obtained by PPP solution of the *Service#7*.

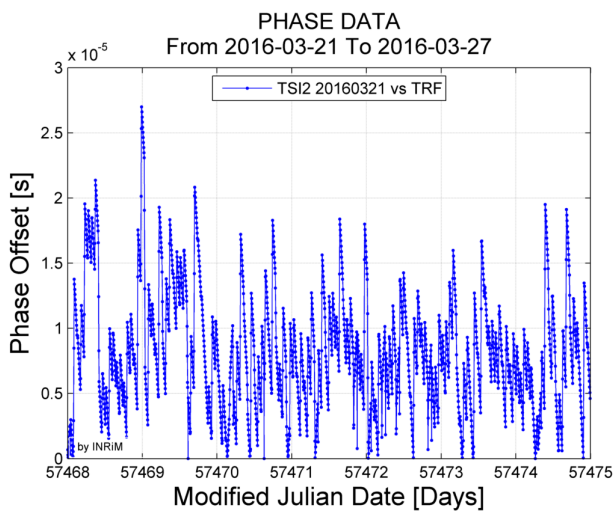


Fig. 3: Service#2 - Time Comparison UT2-TRF

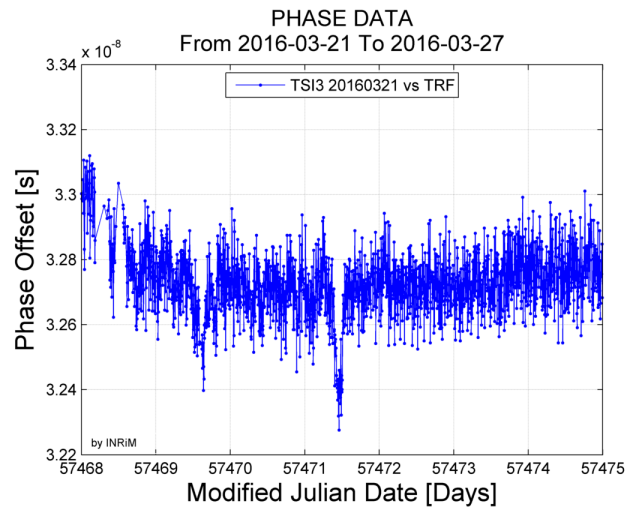


Fig. 4: Service#3 - Time Comparison UT3-TRF

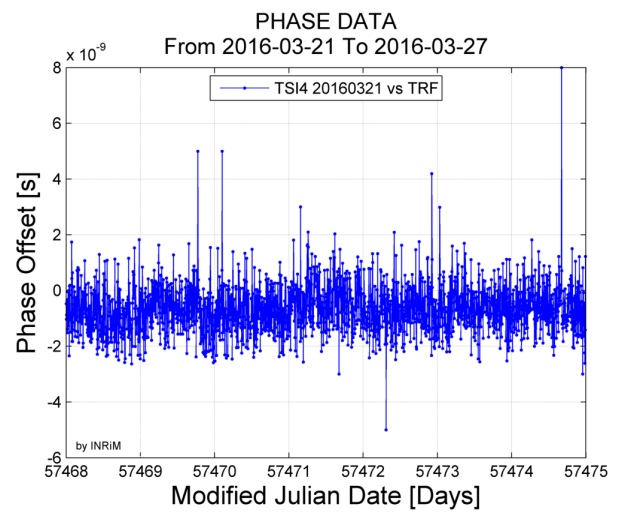


Fig. 5: Service#4 - Time Comparison UT4-TRF

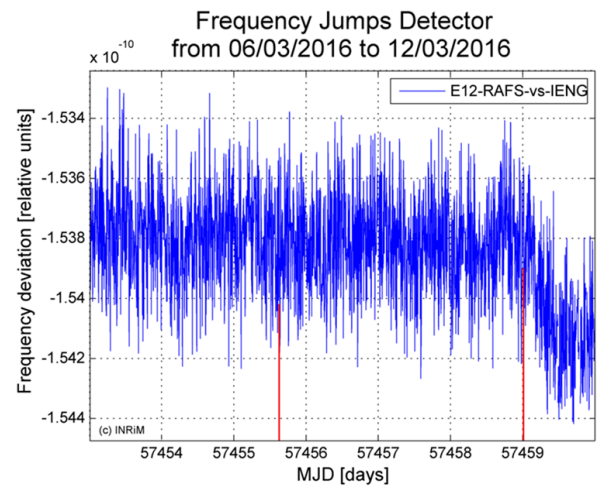


Fig. 6: Service#8 Frequency Jumps Detector

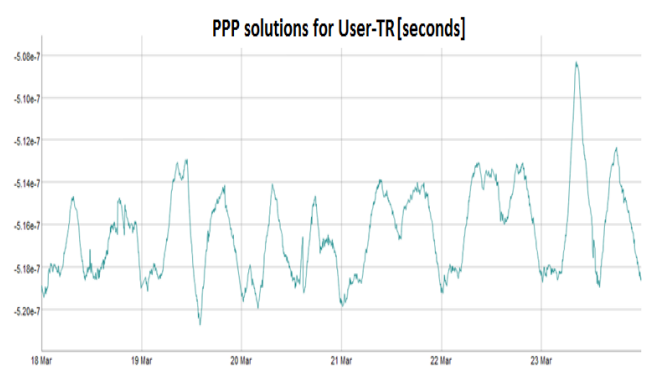


Fig. 7: Service#7 PPP solution Users wrt TRF

IV. CONCLUSIONS

The European funded project DEMETRA has been designed, developed, qualified and successfully integrated at INRIM. Currently, one of the two experimental phases is on-going, providing Key Performance Indicators of each service. The data are available on the web page. The time dissemination as well as the other services will still be tested for additional months to assess their capacity to fulfil the user needs and also to address the needs of the timing community in term of time scale monitoring, high accuracy time and frequency transfer, and calibration.

ACKNOWLEDGMENT

This project has received funding from the European GNSS Agency under the European Union's Horizon 2020 research and innovation programme under grant agreement No 640658.

REFERENCES

[1] P. Tavella and DEMETRA consortium, "The Horizon 2020 DEMETRA project: DEMonstrator of EGNSS services based on Time Reference Architecture", Metrology for Aerospace (MetroAeroSpace), 2015 IEEE Benevento 2015, <http://ieeexplore.ieee.org/xpl/articleDetails.jsp?arnumber=7180634>.

[2] P. Tavella and DEMETRA consortium "The European Project DEMETRA: Demonstrating Time Dissemination Services", in proc ION PTTI Precise Time and Time Interval meeting, Monterey CA, Jan 2016

[3] <http://www.gsa.europa.eu/2015-gnss-market-report>

[4] G. Cerretto et al, "INRIM Time and Frequency Laboratory: anupdate on the status and on the ongoing enhancement activities", in Proc. of the Precise Time and Time Interval Systems and Applications (PTTI), Boston, MA, USA, 1-4 December 2014.

[5] T. Widomski, J. Uzycki, K. Borgulski, J. Kowalski, R. Bender, P. Olbrysz, "Trusted Time Distribution with Auditing and Verification facilities Project TSI#2", submitted to Precise Time And Time Interval Systems And Applications Meeting January 2016, Monterey, California.

[6] E.F. Dierikx, A.E. Wallin, T. Fordell, J. Myyry, P. Koponen, M. Merimaa, T.J. Pinkert, J.C.J. Koelemeij, H. Peek and R. Smets, "White Rabbit Precision Time Protocol on Long Distance Fiber Links" (2015), TUFFC, <http://dx.doi.org/10.1109/TUFFC.2016.2518122>

[7] M. LIPINSKI et al., "White Rabbit: a PTP application for robust sub-nanosecond synchronization", IEEE ISPCS, 35-30, 2011.

[8] P. Defraigne, W. Aerts, G. Cerretto E. Cantoni and J.-M. Sleewaegen, "Calibration of Galileo signals for time metrology", IEEE transactions on UFFC, 12/2014 61(12):1967-75.

[9] P. Defraigne et al, "Advances on the use of Galileo signals in time metrology: calibrated time transfer and estimation of UTC and GGTO using a combined commercial GPS-Galileo receiver", in Proc. of the Precise Time and Time Interval Systems and Applications (PTTI), Bellevue, WA, USA, 3-5 December, 2013.

[10] P. Defraigne, W. Aerts, E. Pottiaux, Monitoring of UTC(k)'s using PPP and IGS real-time products, accepted in GPS solutions, 19 (1), p. 165-172, 2015. doi : 10.1007/s10291-014-0377-5.

[11] P.Waller, F.Gonzalez, S.Binda, I.Sesia, I.Hidalgo, G.Tobias, P.Tavella, "The In-orbit Performances of GIOVE Clocks", IEEE Transaction on Ultrasonics, Ferroelectrics, and Frequency Control, Volume 57, issue 3, March 2010, pp. 738-745.

[12] L. Galleani, P. Tavella, "Detection and identification of atomic clock anomalies", Metrologia, Vol. 45 Issue: 6, Pages: S127-S133, December 2008.

[13] I. Sesia, L. Galleani, P. Tavella, "Application of the Dynamic Allan Variance for the Characterization of Space Clock Behavior", IEEE Transactions on Aerospace and Electronic Systems, Volume 47, issue 2, April 2011, pp. 884-895.

[14] E.Varriale, D. Cretoni, F. Gottifredi, "SynchroNet: High Performance Clocks Network Synchronization System", European Navigation Conference '09, Naples, Italy.

[15] E. Varriale, D. Cretoni, F. Gottifredi, "SynchroNet: High Performance Network Synchronization System", InGRID '08, Ischia(NA) Italy.

[16] F. Gottifredi, E. Varriale, M. Gotta, "SynchroNet: A secure Network Synchronisation System", The Navigation Conference & Exhibition 2007, London (U.K.).

[17] I. Sesia, P. Tavella, G. Signorile, A. Cernigliaro, F. Fiasca, P. Defraigne, L. Galleani, "First steps towards a Time Integrity Service for EGNSS systems, in the DEMETRA project", in proceeding at the 30th European Frequency and Time Forum, April 2016.

Transfer of Stable Optical Frequency for Sensory Networks via 306 km Optical Fiber Link

Martin Cizek, Lenka Pravdova, Vaclav Hucl,
Simon Rerucha, Jan Hrabina, Bretislav Mikel,
Josef Lazar, Ondrej Cip
Department of Coherent Optics,
Institute of Scientific Instruments of the CAS,
Brno, Czech Republic

Vladimir Smotlacha, Josef Vojtech

CESNET, z. s. p. o.,
Prague, Czech Republic

Abstract - Optical fiber links for distribution of highly-stable optical frequencies were experimentally tested by many metrology laboratories in the past fifteen years. But recent development of new optical sensors for industrial application puts demands on a technology transfer of this high-end technology from laboratory experiments to the real industry. The remote calibration of interrogators of Fiber Bragg Grating strain sensory networks is one of important examples. We present a 306 km long optical fiber link established in the Czech Republic where a coherent transfer of stable optical frequency has been firstly demonstrated. The link between ISI CAS Brno and CESNET Prague uses an internet communication fiber where a window 1540 to 1546 nm in DWDM grid is dedicated for the coherent transfer and 1 PPS signal. The optical frequency standard at 1540.5 nm is used for the coherent transfer where compensation of the Doppler shift induced by the optical fiber is done by an acousto-optic modulator driven by a servo loop. The closed loop action is continuously recorded. This enables to compute changes in the transport delay introduced by external influences on the optical line. A comparison with a different measuring method based on analyzing the transport delay of a 1 PPS signal transmitted via the same DWDM window is done. This comparison is a subject of results of the paper.

Keywords—optical fiber link; stable optical frequency transfer; GNSS; DWDM; FBG sensory networks

I. INTRODUCTION

Fiber Bragg Grating (FBG) strain sensors are very promising measuring systems achieving resolution at a picometer level. The principle of the FBG sensor is based on measuring of the central optical frequency of the sensor reflective spectrum while it is illuminated by laser diodes through an optical fiber. FBG sensors became very popular in a nuclear power plant industry [1] for the long-term monitoring of the containment building conditions as long-term micro motions and creeps of pre-stressed concrete containment buildings. They have to operate with long-term stable parameters because only records of the measured parameters lasting months or years can identify the risk of possible loss of strength of the containment barrier. The concept of strain

measurement with FBG in containment buildings demands a high-resolution optical spectrum analyzer with the ultimate long-term absolute accuracy. The analyzer measures reflected optical frequencies from the sensory networks placed in the containment. The analyzer requires a real-time calibration with a stable optical frequency reference i.e. by a set of local optical frequency standards based on lasers with an absorption spectroscopy technique in the feedback [2]. But these local optical frequency standards need experienced operators for the periodical maintenance and this is quite a great problem in the industrial environment. Therefore there is a search for an alternative. The distribution of stable optical frequencies via optical fiber links becomes just the right solution for the real-time calibration. The operation scheme consists of a set of highly stable laboratory laser sources placed in a metrology laboratory and a distribution fiber optics telecommunication network delivering optical frequencies over long distances. Experimental transfer of highly-stable optical frequencies were researched and now experimentally operated by many metrology laboratories [3-6]. They use optical fiber links mainly for comparison measurement of experimental optical clocks to verify their ultimate relative stability but recent development is aiming to a technology transfer of this high-end technology from laboratory experiments to the real industry. Unlike laboratory comparison the optical clocks in the case of FBG sensory networks the main emphasis must be put on reliable long-term operation of the optical frequency transfer.

Our group has installed one FBG sensory network in Temelin nuclear power plant in Czech Republic. The demand is to calibrate the local optical frequency standard incorporated in the FBG interrogator. Thanks to uninterrupted monitoring the continuous measurement of the interrogator local optical frequency standard stability via optical fiber links is planned. We report on the first period of the remote-calibration effort in the Czech Republic which has been scoped to verification of the coherent transfer of the highly-coherent laser radiation over 306 km long fiber between the two largest cities in the Czech Republic - Brno and Prague. The optical fiber length is comparable with the fiber between Brno and Temelin where the transfer will be established later on.

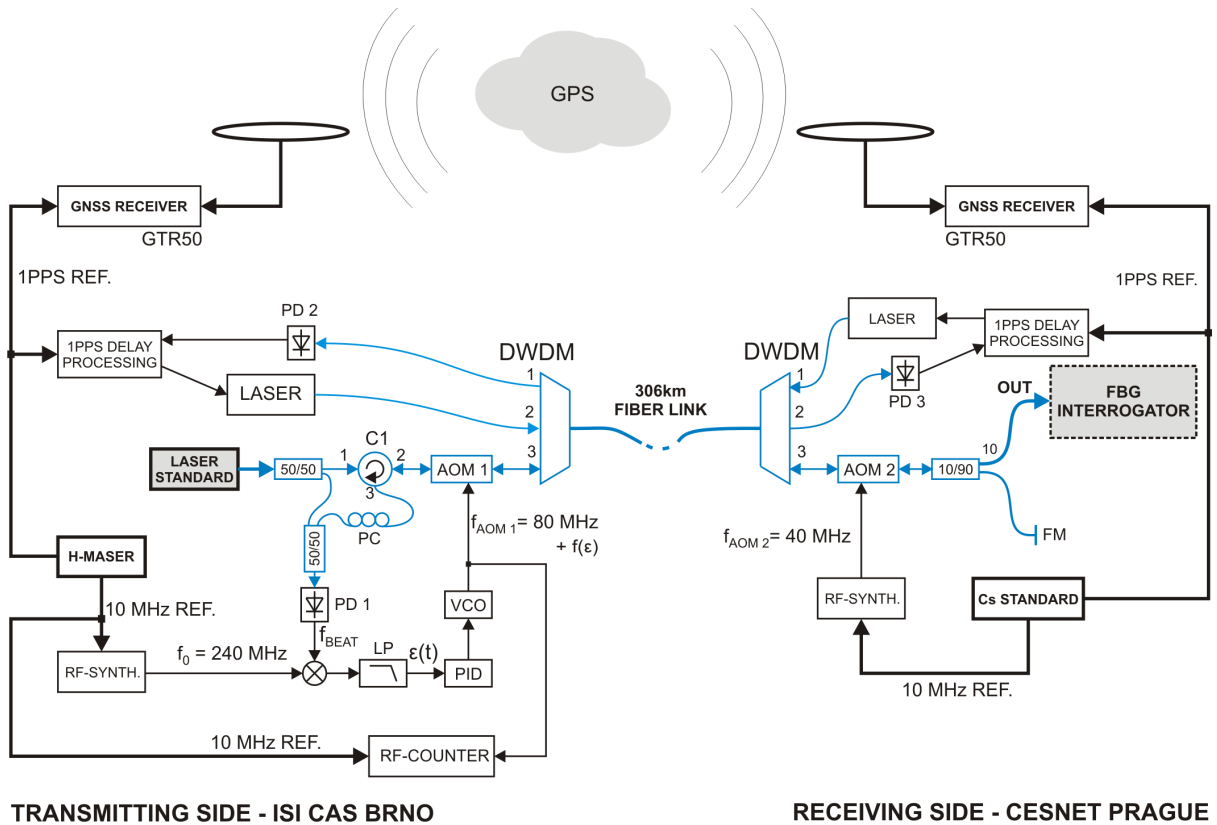


Fig. 1. The overall block diagram of the experimental optical frequency transfer setup. Legend: AOM 1, 2 – acousto-optic modulator; C 1 – optical circulator; DWDM – DWDM mux/demux.; FM – Faraday mirror; VCO – voltage-controlled oscillator; PD 1, 2, 3 – photodetector; PID – P-I-D controller; PC – polarisation controller.

II. COHERENT TRANSFER OF STABLE OPTICAL FREQUENCY

Highly-coherent laser Koheras Adjustik working at 1540.5 nm with a linewidth < 100 Hz is used as the optical frequency standard for the coherent transfer. The laser is frequency stabilized to Acetylene $^{13}\text{C}_2\text{H}_2$, P(13) transition with a saturation absorption spectroscopy technique [7].

The setup of link between ISI CAS Brno and CESNET Prague is shown in Fig. 1. An internet communication fiber with window 1540 to 1546 nm in DWDM grid is dedicated for the coherent transfer and 1 PPS transmission. The total length of the fiber is 306 km and it is equipped with 5 bidirectional EDFA amplifiers. The Doppler frequency shifts in the coherent transfer induced by the fiber link are suppressed using a closed-loop control system. The bandwidth of the control loop is limited by the roundtrip delay of the optical fiber link and it is 300 Hz approx. for 306 km link length [8].

To detect the optical frequency deviations a 50% portion of the light is sent back from the far end. At the near end the returned portion of the light is mixed with the light being transmitted and the beat note signal is detected by a photodetector PD1. In order to distinguish the unwanted reflections throughout the optical fiber link from the useful one originating from the far end and to move the detection outside from the $1/f$ noise region of PD1 the RF frequency translation is used. The first frequency translation happens as the coherent light passes AOM1 working at the nominal frequency of

80 MHz. At the far end the portion of the light that is returned back by FM has to pass AOM2 working at 40 MHz twice. Finally at the near end the returned light passes AOM1 once more and is again shifted by 80 MHz. As a result the RF output signal of PD1 contains a spectrum of components at various frequencies. The frequency components below the sum of all possible optical frequency shifts of 240 MHz originate from residual amplitude modulations by AOM1 and AOM2 (80 and 120 MHz) and from unwanted reflections of the light before reaching the far end. Only the beat-note centered on $f_0 = 240$ MHz is the product of mixing the transmitted coherent light with the returned portion that has passed all AOMs and the optical fiber link twice. Its instantaneous frequency is equal to $f_0 + v_e(t)$ where $v_e(t)$ is the current optical frequency shift induced by the optical link. This portion of the detected RF spectrum is preselected by a band-pass filter and processed by a servo-loop PID controller.

The selected beat note is phase locked to a reference signal 240 MHz by the PID controller detuning AOM1 the drive frequency f_{AOM1} generated by a voltage-controlled oscillator. As a result, the beat frequency is locked to the reference frequency $f_0 = 240$ MHz. Then Doppler optical frequency shifts $v_e(t)$ induced by the optical fiber link are suppressed. All RF equipment and electronics at the ISI Brno side is referenced from an active Hydrogen maser standard while at the CESNET Prague side has cesium standard used.

III. EXPERIMENTAL VERIFICATION AND DISCUSSION

For means of investigating the behavior of the fiber link the output frequency of the VCO is continuously measured by a zero dead-time RF counter. In the closed loop regime the controlled absolute deviations Δf_{AOM1} of f_{AOM1} from the nominal 80 MHz are equal to $-v_c(t)$. As shown in Fig. 2 a) by integrating these absolute deviations equal to the closed-loop action we can compute the changes in the transport delay in a non-compensated optical fiber link.

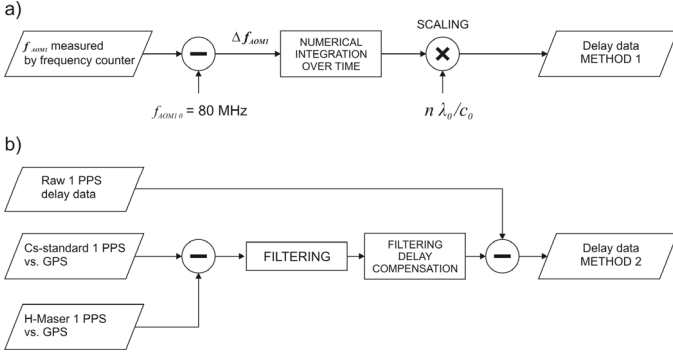


Fig. 2. The flowchart of delay data processing: a) the method based on numerical integration of the measured driving frequency of the AOM1; b) the method based on processing 1PPS transport delay data.

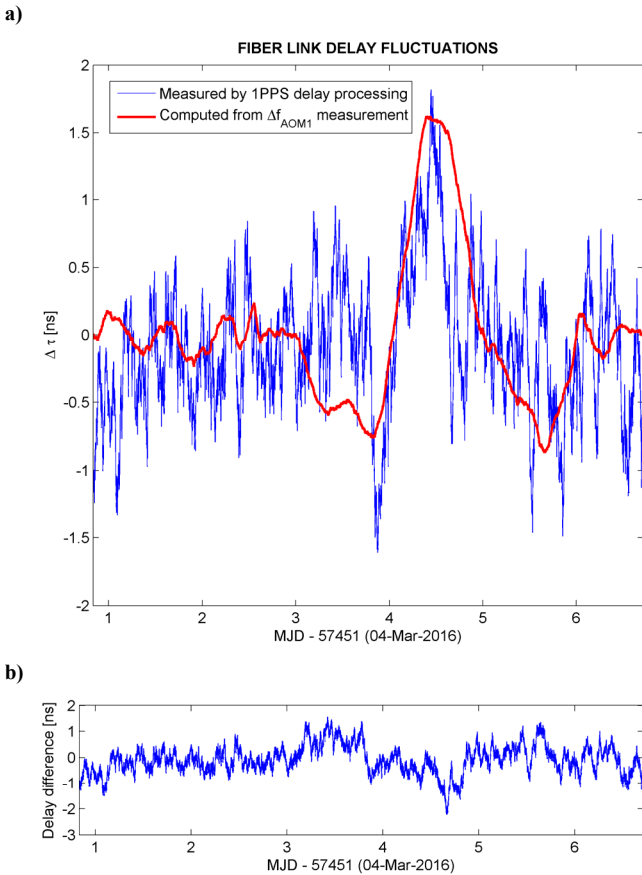


Fig. 3. a) The comparison of fiber link delay computed from closed-loop driving frequency of the AOM1 compensation and the delay measured directly by the 1 PPS delay processing system. b) The difference between the measured delays.

The fiber link delay computed by integrating the closed-loop action exhibits a good agreement with the moving average of the delay data computed from the 1 PPS transfer processing. From the comparison in Fig. 3 it is obvious that the delay measured by integrating the closed-loop action of the coherent transfer system exhibits less noise.

Fig. 4 shows the relative stability of the 1 PPS frequency transfer measured by both methods. The difference in short-term stability is probably caused by the uncertainties of the GPS time transfer but for integration times longer than one day Allan deviations agree. Thus the comparison method based on the 1 PPS two-way transfer device is useful mainly for long-term integration times (more than 10^5 seconds).

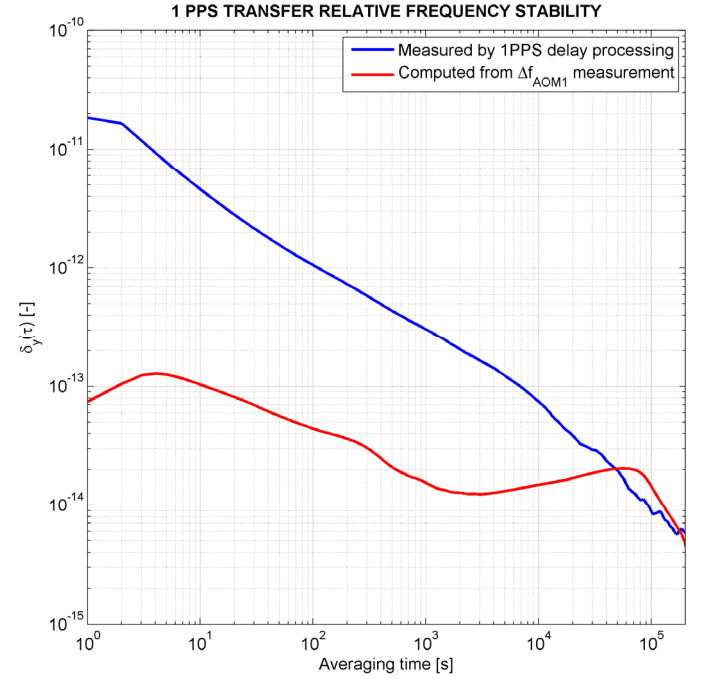


Fig. 4. The comparison of the 1 PPS transfer relative frequency stability computed from closed-loop driving frequency of the AOM1 compensation and the delay measured directly by the 1 PPS delay processing system.

IV. SUMMARY

We established the bidirectional optical fiber link with the length 306 km for demonstration of simultaneous transfer of the reference optical frequency and 1 PPS time signals from atomic clocks. The servo loop for suppression of Doppler shifts has been realized and experimentally compared with 1 PPS delay processing system. From the charts in Fig. 3 it is obvious that trends of long-term delay changes measured both systems are in accordance. This is good enough for the most of industrial applications like FBG sensory network interrogator remote calibrations. The long-term stability of the link is given by the fact that the most of its path is buried under the ground. Thus the main task of the presented Doppler frequency shifts suppression by AOM1 is to cancel fast short-term interference originating from external vibration especially in places the fiber link leads above ground.

ACKNOWLEDGMENT

The authors acknowledge the support from Technology Agency of CR (project TH01011254) for establishing long-haul fiber link. The issues with Doppler shift compensation have been supported by Grant Agency of CR (project GB14-36681G). The research infrastructure ALISI was funded by Ministry of Education, Youth and Sports of the Czech Republic and European Commission (project CZ.1.05/2.1.00/01.0017 and project LO1212) and by Czech Academy of Sciences (project RVO:68081731).

REFERENCES

- [1] A. Cusano et al., *Fiber Bragg Grating Sensors: Recent Advancements, Industrial Applications and Market Exploitation*, ISBN: 978-1-60805-343-8 (2011)
- [2] F. Riehle, *Frequency Standards: Basics and Applications*, ISBN: 978-3-527-60595-8 (2006)
- [3] Terra, O. et al., "Brillouin amplification in phase coherent transfer of optical frequencies over 480 km fibre," *Optics Express* 18, pp. 16102-16111 (2010).
- [4] C. E. Calosso, E. Bertacco, D. Calonico, C. Clivati, G. A. Costanzo, M. Frittelli, F. Levi, A. Mura, and A. Godone, "Frequency transfer via a two-way optical phase comparison on a multiplexed fiber network," *Opt. Lett.* 39, 1177-1180 (2014)
- [5] G. Grosche, M. Eggert, D. A. Humphreys, C. Campbell, J. C. Petersen, J. Henningsen, and B. Skipper, "Transmission of wavelength references via a commercial transparent optical network over 534 km," in *Conference on Lasers and Electro-Optics/International Quantum Electronics Conference and Photonic Applications Systems Technologies, Technical Digest (CD)* (Optical Society of America, 2004), paper CTuH4.
- [6] G. SANTARELLI, "Ultra-stable Long Distance Optical Frequency/Time Distribution Using the Internet Network," in *Frontiers in Optics 2013*, I. Kang, D. Reitze, N. Alic, and D. Hagan, eds., OSA Technical Digest (online) (Optical Society of America, 2013), paper FTh3B.1.
- [7] Hrabina, J., Sarbort, M., Acef, O., Du Burck, F., Chiodo, N., Hola, M., Cip, O. and Lazar, J., "Spectral properties of molecular iodine in absorption cells filled to specified saturation pressure," *Appl Optics* 53, p. 7435-7441, (2014).
- [8] Šmíd, R.; Čížek, M.; Mikel, B.; Číp, O. Frequency Noise Suppression of a Single Mode Laser with an Unbalanced Fiber Interferometer for Subnanometer Interferometry. *Sensors* 2015, 15, 1342-1353.
- [9] Smotlacha V., Kuna A., "Two-Way Optical Time and Frequency Transfer between IPE and BEV," *EUROPEAN FREQUENCY AND TIME FORUM 2012 Proceedings*, pp 375-378 (2012).

Hofstadter optical lattice for ultracold Ytterbium atoms

M. Scholl*[†], Q. Beaufils*, A. Dureau*, D. Döring*[†], M. Bosch Aguilera*,
R. Bouganne*, J. Beugnon* and F. Gerbier*

*Laboratoire Kastler Brossel,

Collège de France, CNRS, ENS-PSL Research University, UPMC-Sorbonne Universités,

11 place Marcelin-Berthelot, 75005 Paris

[†]FARO Scanner Production GmbH,

Lingwiesenstrasse 11/2, D-70825 Korntal-Münchingen

Abstract—Recently, a new generation of experiments with ultracold quantum gases has emerged where the many-body properties are probed and manipulated using ultra-narrow “clock” transitions. We describe here our experimental project, which aims at engineering a special kind of optical lattice realizing an effective magnetic field coupling to the atomic motion – the Hofstadter optical lattice. Our specific experimental scheme uses the ultra-narrow optical transition linking the ground state to a metastable excited state of ^{174}Yb atoms. We present the current status of the experiment, including the observation of coherent Rabi oscillations between the ground and excited states.

I. INTRODUCTION

Group II atoms (and atoms such as Ytterbium with a similar internal level structure) featuring ultra-narrow optical transitions are now routinely exploited in metrology laboratories worldwide to operate optical atomic clocks [1]. These atoms also provide new opportunities for quantum physics with atomic quantum gases, from quantum computing [2] to the realization of Kondo physics [3] or magnetism with many spin components and internal $SU(N)$ symmetry [4].

One particular line of research pursued in our laboratory is the realization of effective magnetic fields for neutral atoms, coupling to their motion in the same way as a real magnetic field couples to the motion of charged particles through the Lorentz force. This is currently a very active subject, looking to extend our understanding of orbital magnetism in quantum matter (see *e.g.* [5]–[7]). One major motivation to do so is to realize the atomic equivalent of two-dimensional electron systems exhibiting the fractional quantum Hall (FQH) effect [8]. Due to the massive degeneracy of single-particle (Landau) levels for electrons in strong magnetic fields, electron-electron interactions play a major role, and give rise to a zoo of exotic phases with intriguing properties. For instance, elementary excitations behave as “anyons” with fractional statistics intermediate between bosons and fermions [8]. It has been predicted theoretically that strongly correlated quantum phases, the atomic cousins of the electronic FQH states, should arise for interacting quantum gases in a strong effective magnetic field [9]. Observing these highly correlated liquids is one of the major goals in the field of quantum gases, and provides a strong motivation to explore schemes to “simulate” artificial gauge fields in optical lattices, where strong atom-atom interactions are a built-in feature [10].

The basic idea to generate such an effective magnetic field relies on the Aharonov-Bohm (AB) phase [11] $\bar{A}_{AB} = \frac{q}{\hbar} \int_C \mathbf{A} \cdot d\mathbf{l}$ accumulated by the wavefunction of a particle of charge q moving along a contour C in a region with non-zero vector potential \mathbf{A} . From a quantum mechanical point of view, the Aharonov-Bohm phase contains all the orbital effects associated with a magnetic field. In atomic physics, coherent atom-light interaction is a well-developed tool to manipulate the phase of an atom moving in a laser field coupling coherently two or more internal states. Under suitable conditions, this leads to a geometrical phase with the same properties as the AB phase. There is a large number of theoretical proposals building on this idea [12], [13].

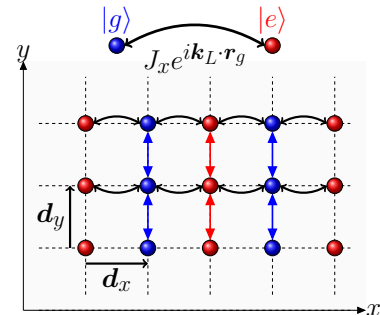


Fig. 1. Cartoon picture of the Hofstadter optical lattice. The blue (respectively, red) balls represent atoms in the g (resp. e) internal state, each trapped in a separate sublattice. The arrows show the microscopic tunneling processes, standard tunneling across the potential barriers within each sublattice (vertical straight lines) and laser-induced tunneling mediated by a clock laser (horizontal curved lines).

In this paper, we describe our experimental project aiming at realizing such an effective magnetic field for Ytterbium atoms in an optical lattice. The single-particle spectrum in such a lattice is fragmented into many sub-bands and organized in a fractal structure known as the Hofstadter butterfly [14], hence the nickname *Hofstadter optical lattice*. We present the proposal and its experimental implementation in Section II. We describe our experimental setup in Section III. In Section IV, we demonstrate Rabi oscillations on the clock transition for a Bose-Einstein condensate in a one-dimensional optical lattice (OL), and describe preliminary experiments to measure the scattering parameters in the excited state. We conclude in

II. REALIZING ARTIFICIAL MAGNETIC FIELDS FOR ULTRACOLD YTTERBIUM ATOMS IN OPTICAL LATTICES

In this Section, we describe the specific experimental scheme pursued in our experiment [15]. The basic settings, as in an earlier proposal by Jaksch and Zoller [16], is a state-dependent OL for the two clock states of Ytterbium atoms denoted g and e (see Figure 1). The atoms occupy the ground state of a strong confining potential along z , thereby freezing the atomic dynamics to the $x - y$ plane. In this plane, atoms are confined by a lattice potential formed by two independent standing waves at the “magic” wavelength $\lambda_m = 759$ nm (equal polarizabilities for g and e) and at an “antimagic” wavelength $\lambda_{am} = 617$ nm (opposite polarizabilities for g and e). The y lattice with period $\lambda_m/2$ traps atoms near the intensity maxima, irrespective of their internal state. The x lattice with period $\lambda_{am}/2$ traps atoms in g near the intensity maxima, but atoms in e near the minima. The combined potential thus consists of two separate sublattices, one for each internal state, shifted along x by $\mathbf{d}_x = (\lambda_{am}/4)\mathbf{e}_x$. We consider the “Hubbard regime”, where atoms occupy only the lowest Bloch band and are tightly localized around the trapping sites in each sublattice.

For a narrow transition connecting g and e (such that spontaneous emission is negligible), the two sublattices are essentially decoupled. An additional laser resonant with the clock transition between g and e is applied to induce hopping between the two sublattices (“laser induced tunneling”). An atom initially localized at \mathbf{r}_g in the g sublattice can absorb a laser photon and hop to one of its nearest neighbours at $\mathbf{r}_e = \mathbf{r}_g \pm \mathbf{d}_x$ in the e sublattice. The corresponding transition matrix element is [16]

$$J_x^\pm(\mathbf{r}_g) = -J e^{i\mathbf{k}_L \cdot \mathbf{r}_g} = -J e^{i2\pi\alpha \frac{y_g}{d_y}}, \quad (1)$$

with $\alpha = (k_L d_y)/2\pi$. The complex phase follows from the spatial dependence of the clock laser electric field, $\mathbf{E} \propto e^{i\mathbf{k}_L y}$.

The laser-induced phase is the key element allowing to realize an effective magnetic field. In a periodic potential and in a uniform magnetic field $\mathbf{B} = B\mathbf{e}_z$, the Hamiltonian for a particle of charge q is given in the tight-binding regime by [17]

$$H = -J \sum_{\mathbf{r}_i, \mathbf{d}_j} e^{i\bar{A}_{\mathbf{r}_i \rightarrow \mathbf{r}_i + \mathbf{d}_j}} |\mathbf{r}_i + \mathbf{d}_j\rangle \langle \mathbf{r}_i| + \text{h.c.} \quad (2)$$

Here $\mathbf{d}_j = \pm \mathbf{d}_x, \pm \mathbf{d}_y$ denote the discrete vectors linking one site to its nearest neighbours. The tunneling amplitudes are complex due to the broken time-reversal invariance, with an AB phase $\bar{A}_{\mathbf{r}_i \rightarrow \mathbf{r}_i + \mathbf{d}_j} = \frac{q}{\hbar} \int_{\mathbf{r}_i}^{\mathbf{r}_i + \mathbf{d}_j} \mathbf{A} \cdot d\mathbf{l}$. The Landau gauge choice $\mathbf{A} = B y \mathbf{e}_x$ leads to $\bar{A}_{\mathbf{r}_g \rightarrow \mathbf{r}_g \pm \mathbf{d}_x} = \pm(2\pi\phi/\phi_0) \times (y/d_x)$, where $\phi = B d_x d_y$ denotes the magnetic flux per unit cell, and $\phi_0 = h/|q|$ the quantum of flux.

The state-dependent optical lattice presented above leads to such a Hamiltonian, where the parameter α is equivalent to the AB phase for a particle of charge $q = 1$ and a density α of fictitious flux quanta. However, the equivalent magnetic field is not uniform. Whereas the AB phases for the transitions $\mathbf{r}_g \rightarrow \mathbf{r}_g \pm \mathbf{d}_x$ would be of opposite sign in a uniform field, the laser-induced phases in Eq. (1) are in fact the same. This follows

from the unitarity of the atom-light coupling Hamiltonian and is unavoidable if the same laser drives all transitions. This corresponds to a staggered magnetic flux alternating in sign from one column to the next, which can lead to interesting physics [18]–[20] but is far from the uniform Landau gauge we aim at. The staggered flux can however be rectified by using two different lasers propagating in opposite directions to drive neighboring $g \rightarrow e$ and $e \rightarrow g$ transitions independently. The sign change of the wavevectors compensates the sign change due to the staggered flux, resulting in the same phase $2\pi\alpha$ on every plaquette and a uniform flux configuration as desired. The main experimental question is how to drive independently one particular link without affecting the others. We plan to realize an experimental configuration involving a superlattice potential with double the period [21] superimposed to the main x lattice with a well-controlled relative phase ϕ_{SL} . The reader will find a detailed presentation in [15], [22].

III. EXPERIMENTAL SETUP

Laser cooling of Ytterbium atoms requires two resonant lasers. The first laser at 399 nm addresses the main dipole transition, and is used to slow an Yb atomic beam. The second laser at 556 nm addresses the narrower intercombination transition, whose linewidth is broad enough to capture relatively slow atoms (typical velocities in the m/s range) but narrow enough to allow Doppler cooling to very low temperatures (a few μK). In our experiment, both lasers are generated by frequency doubling two commercial infrared sources at 798 nm and 1112 nm, with around 100 mW power for the 399 nm laser and close to 1 W for the 556 nm laser.

We typically load about $2 \cdot 10^8$ atoms in a magneto-optical trap operating on the 556 nm transition at a temperature of about $10 \mu\text{K}$. We then transfer the atoms to a far-detuned optical dipole trap at 1070 nm, and transport the atoms from the primary ultra-high vacuum (UHV) chamber to a UHV science chamber where the final experiments are performed. The transport is done by displacing the laser focus by about 22 cm in 1 s. The trapped atoms follow this displacement with a moderate atom loss around 40% (half of which is compatible with free evaporation from the finite trap depth), and without measurable heating. In the science chamber, we add another dipole trap at 532 nm, crossing the 1070 nm trap at right angle. Atoms progressively accumulate in the crossing region as the 1070 nm power is reduced and temperature drops due to evaporative cooling. We finally lower the powers of both dipole traps to force evaporation of atoms in the crossing region. At the end of the evaporation ramp, we obtain a Bose-Einstein condensate of ^{174}Yb in the crossed dipole trap (CDT) containing a few 10^4 atoms with $> 80\%$ condensed fraction.

The core instrument of the experiment is an ultra-narrow laser used to drive the clock transition at 578 nm. We generate light at 578 nm by sum-frequency generation in a single-pass nonlinear crystal. We lock the laser frequency to a commercially available¹ ultrastable optical cavity made from ultra-low expansion glass. The cavity is held in vacuum and further isolated by an anti-vibration platform and several acoustic and thermal screens. Long term drifts have been reduced to a few

¹The cavity was made by Advanced Thin Films (Boulder, Co) and the cavity housing and temperature stabilization system by Stable Laser Systems (Boulder, Co).

tens of Hz per hour under optimized conditions [23]. So far we have not been able to estimate the laser linewidth from spectroscopy on ultracold atoms, since the resolution in the performed experiments has been limited by other broadening effects (see below).

IV. RABI OSCILLATIONS IN A ONE-DIMENSIONAL OPTICAL LATTICE

A. Rabi oscillations

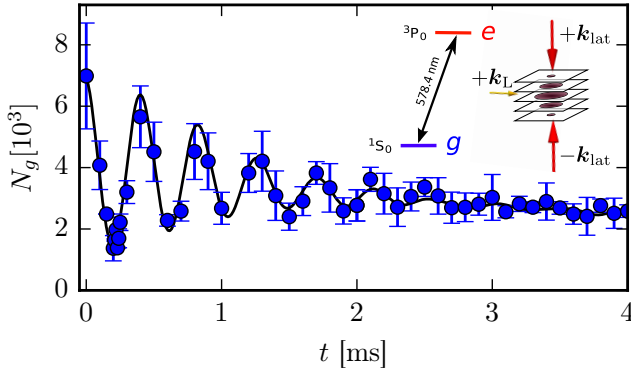


Fig. 2. Rabi oscillations between state g and e for a BEC of ^{174}Yb atoms. The inset shows the experimental geometry, where atoms are trapped in planes defined by a vertical optical lattice and where the coupling laser propagates horizontally. The solid line is a guide to the eye. The statistical error bars correspond to one standard deviation.

In a previous work, the clock laser was used for spectroscopy of expanding BECs released from the optical trap [23]. Here we report on a separate set of experiments performed on trapped atoms and after loading the BEC in a vertical standing wave (one-dimensional OL) at the magic wavelength $\lambda_m = 759\text{ nm}$. The optical lattice is derived from a Titanium-Sapphire laser, focused on the atoms with a waist $w \approx 150\ \mu\text{m}$. This results in an array of nearly-independent, disk-shaped traps, with angular frequencies $\omega_z \approx 2\pi \times 16\text{ kHz}$ along the lattice axis and $\omega_\perp \approx 2\pi \times 20\text{ Hz}$ in the transverse plane. We load approximately 10^4 atoms inside this OL.

We use a horizontally propagating laser to promote atoms to the excited state. We detect metastable e atoms through a decrease of the measured atom number in the ground state g . A vertical magnetic field of magnitude $B \approx 150\text{ G}$ is also applied, enabling a non-zero transition matrix element between g and e as described in [24]. For our parameters (power $\sim 10\text{ mW}$, beam waist $\sim 45\ \mu\text{m}$), this results in an effective $g-e$ Rabi frequency of $\Omega_L \approx 2\pi \times 2\text{ kHz}$.

We observe Rabi-like oscillations between the ground and metastable state, as shown in Fig. 2. This demonstrates the coherent nature of the excitation by the clock laser, and allows us to prepare a BEC in a coherent superposition of the ground state and of an optically excited state. To our knowledge this has not been reported before. The oscillation period is consistent with the expected Rabi frequency, with a contrast close to one but substantial damping. Many sources can contribute to this damping, including in particular phase fluctuations of the clock laser, motion of the recoiling e atoms in the harmonic

trap potential, and atom-atom interactions. Elastic atomic interactions occur predominantly in the s -wave regime, with strengths proportional to s -wave scattering lengths which differ in general for $g-g$, $g-e$ or $e-e$ interactions. Since the density distributions in the CDT or in the OL are not uniform, elastic interactions lead to a broadening of the resonance and to an apparent damping when recording the evolution of the total atom number. Scattering lengths in the ground state are well-known [25], but collisional parameters involving e atoms are not. Analysis of the experimental data is underway, and could allow us to extract experimental values for these parameters.

B. Inelastic losses in the excited state

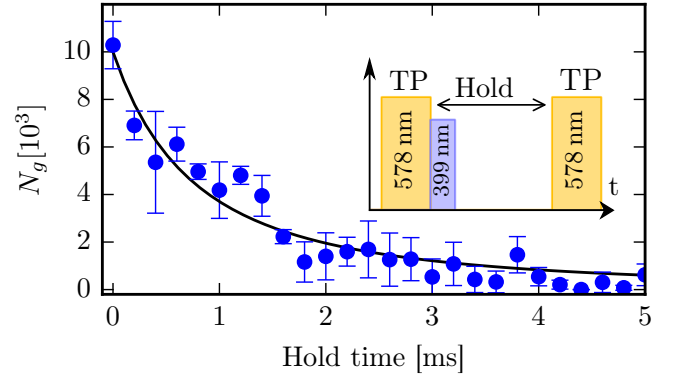


Fig. 3. Atom number versus hold time for a sample of atoms in the excited state e . The solid line is a fit to the data using Eq. (3) and the model explained in the main text. The inset details the experimental sequence. A transfer pulse (TP) at 578 nm first transfers about $\sim 80\%$ of the atoms to e , and is followed by a “cleaning” pulse at 399 nm that removes all remaining g atoms without affecting e . After a hold time another transfer pulse brings the atoms back to g where they are detected. The statistical error bars correspond to one standard deviation.

Two-body, inelastic collisions involving two e atoms or one e and one g atom can also contribute to the damping of the oscillations. Such collisions typically lead to a loss of both atoms from the trap, as the released internal energy converts into kinetic energy greatly exceeding the trap depth. Their occurrence was tested in a separate experiment (see Fig. 3), where a first pulse was applied for conditions leading to maximum transfer to e (apparent transfer efficiency $\eta \approx 80\%$). A pulse of resonant light at 399 nm was then applied, pushing g atoms away from the trap while leaving e atoms unaffected. After a variable hold time, another identical pulse returned η of the remaining e atoms back to g where they are detected. Assuming atom losses are dominated by $e-e$ inelastic collisions, the time evolution is governed by a rate equation of the form

$$\dot{n}_e = -\beta_{ee}n_e^2. \quad (3)$$

We have analysed our data using several assumptions to extract an estimate for β_{ee} . We model the initial state in terms of independent trap in each plane of the vertical OL, and assume that the population of each plane determined by the density profile of the BEC in the CDT. This determines the number of atoms per plane, the equilibrium Thomas-Fermi density profile in each plane, $n_g(\mathbf{r})$, and the number

of populated planes $N_z \approx 4Z_{\text{TF}}/\lambda_m \approx 10$, with Z_{TF} the Thomas-Fermi vertical size of the BEC in the CDT. We also assume that the laser pulses operate with a constant transfer efficiency η , which may not be the case in the presence of interactions and varying densities, and that atoms in the excited state keep the same density profile $n_g(\mathbf{r})$ at all times. Making these uncontrolled assumptions allows us to compute the decay of the total number as a function of hold time. Fitting this model to the experimental data yields an inelastic two-body loss coefficient $\beta_{ee} \approx 2 \times 10^{-11} \text{ cm}^3/\text{s}$, in line with other measurements for metastable triplet states of the fermionic isotopes of Ytterbium [26] or Strontium [27] atoms.

V. CONCLUSION

In conclusion, we have presented experimental results demonstrating the coherent excitation of a BEC of $^{174}\text{Ytterbium}$ atoms on the clock transition, observing in particular Rabi-like oscillations between the ground and excited state. Further analysis could allow to extract all relevant scattering parameters. Further work will concentrate on building a 3D lattice potential. Working with a lattice at the magic wavelength in all directions (“clock configuration”) and with well-defined filling factors in a Mott insulator state, different interaction parameters would result in a multiple-peak structure that could be resolved spectroscopically. This would represent an important step to assess the usefulness of bosonic optical atomic clocks.

ACKNOWLEDGMENT

We acknowledge many stimulating discussions with members of LKB and of the Frequency metrology group at SYRTE, in particular with Y. Le Coq, R. Le Targat and J. Lodewyck. We acknowledge financial support from the ERC under grant 258521 (MANYBO) and from the city of Paris and UPMC (Emergences programs).

REFERENCES

- [1] A. D. Ludlow, M. M. Boyd, J. Ye, E. Peik, and P. O. Schmidt, “Optical atomic clocks,” *Rev. Mod. Phys.*, vol. 87, pp. 637–701, Jun 2015.
- [2] A. V. Gorshkov, A. M. Rey, A. J. Daley, M. M. Boyd, J. Ye, P. Zoller, and M. D. Lukin, “Alkaline-earth-metal atoms as few-qubit quantum registers,” *Physical Review Letters*, vol. 102, no. 11, p. 110503, 2009.
- [3] A. V. Gorshkov, M. Hermele, V. Gurarie, C. Xu, P. S. Julienne, J. Ye, P. Zoller, E. Demler, M. D. Lukin, and A. M. Rey, “Two-orbital $SU(n)$ magnetism with ultracold alkaline-earth atoms,” *Nat Phys*, vol. 6, no. 4, pp. 289–295, Apr. 2010.
- [4] M. Hermele, V. Gurarie, and A. M. Rey, “Mott insulators of ultracold fermionic alkaline earth atoms: Underconstrained magnetism and chiral spin liquid,” *Phys. Rev. Lett.*, vol. 103, p. 135301, Sep 2009.
- [5] M. Aidelsburger, M. Atala, M. Lohse, J. T. Barreiro, B. Paredes, and I. Bloch, “Realization of the Hofstadter hamiltonian with ultracold atoms in optical lattices,” *Phys. Rev. Lett.*, vol. 111, p. 185301, Oct 2013.
- [6] G. Jotzu, M. Messer, R. Desbuquois, M. Lebrat, T. Uehlinger, D. Greif, and T. Esslinger, “Experimental realization of the topological Haldane model with ultracold fermions,” *Nature*, vol. 515, no. 7526, pp. 237–240, Nov. 2014.
- [7] C. J. Kennedy, W. C. Burton, W. C. Chung, and W. Ketterle, “Observation of Bose-Einstein condensation in a strong synthetic magnetic field,” *Nat Phys*, vol. 11, no. 10, pp. 859–864, Oct. 2015.

- [8] S. M. Girvin, “The quantum Hall effect: Novel excitations and broken symmetries,” in *Topological Aspects of Low Dimensional Systems*, A. Comtet, T. Jolicœur, S. Ouvry, and F. David, Eds. EDP Sciences and Springer-Verlag, 1999, arXiv:cond-mat/9907002.
- [9] N. Cooper, “Rapidly rotating atomic gases,” *Advances in Physics*, vol. 57, no. 6, pp. 539–616, 2008.
- [10] I. Bloch, J. Dalibard, and W. Zwerger, “Many-body physics with ultracold gases,” *Rev. Mod. Phys.*, vol. 80, no. 3, p. 885, 2008.
- [11] Y. Aharonov and D. Bohm, “Significance of electromagnetic potentials in the quantum theory,” *Phys. Rev.*, vol. 115, no. 3, pp. 485–491, 1959.
- [12] J. Dalibard, F. Gerbier, G. Juzeliūnas, and P. Öhberg, “Colloquium : Artificial gauge potentials for neutral atoms,” *Rev. Mod. Phys.*, vol. 83, pp. 1523–1543, Nov 2011.
- [13] N. Goldman, G. Juzelinās, P. hberg, and I. B. Spielman, “Light-induced gauge fields for ultracold atoms,” *Reports on Progress in Physics*, vol. 77, no. 12, p. 126401, 2014.
- [14] D. R. Hofstadter, “Energy levels and wave functions of Bloch electrons in rational and irrational magnetic fields,” *Phys. Rev. B*, vol. 14, no. 6, pp. 2239–2249, 1976.
- [15] F. Gerbier and J. Dalibard, “Artificial gauge potential for two-electron atoms in optical superlattices,” *New J. Phys.*, vol. 12, p. 033007, 2010.
- [16] D. Jaksch and P. Zoller, “Creation of effective magnetic fields in optical lattices: the Hofstadter butterfly for cold neutral atoms,” *New Journal of Physics*, vol. 5, p. 56, 2003.
- [17] P. G. Harper, “Single band motion of conduction electrons in a uniform magnetic field,” *Proceedings of the Physical Society. Section A*, vol. 68, no. 10, pp. 874–878, 1955.
- [18] Y.-F. Wang and C.-D. Gong, “Hofstadter butterflies in macroscopic time-reversal invariant systems: Tight-binding electrons under $n\sqrt{2} \times n\sqrt{2}$ staggered magnetic fields,” *Phys. Rev. B*, vol. 74, no. 19, p. 193301, 2006.
- [19] J.-M. Hou, W.-X. Yang, and X.-J. Liu, “Massless Dirac fermions in a square optical lattice,” *Phys. Rev. A*, vol. 79, no. 4, p. 043621, 2009.
- [20] M. Aidelsburger, M. Atala, S. Nascimbène, S. Trotzky, Y.-A. Chen, and I. Bloch, “Experimental realization of strong effective magnetic fields in an optical lattice,” *Phys. Rev. Lett.*, vol. 107, p. 255301, Dec 2011.
- [21] S. Fölling, S. Trotzky, P. Cheinet, M. Feld, R. Saers, A. Widera, T. Müller, and I. Bloch, “Direct observation of second-order atom tunnelling,” *Nature*, vol. 448, no. 7157, pp. 1029–1032, 2007.
- [22] M. Scholl, “Probing an ytterbium Bose-Einstein condensate using an ultra-narrow optical line,” PhD Thesis, ENS, 2014.
- [23] A. Dareau, M. Scholl, Q. Beaufils, D. Döring, J. Beugnon, and F. Gerbier, “Doppler spectroscopy of an ytterbium Bose-Einstein condensate on the clock transition,” *Phys. Rev. A*, vol. 91, p. 023626, Feb 2015. [Online]. Available: <http://link.aps.org/doi/10.1103/PhysRevA.91.023626>
- [24] Z. W. Barber, C. W. Hoyt, C. W. Oates, L. Hollberg, A. V. Taichenachev, and V. I. Yudin, “Direct excitation of the forbidden clock transition in neutral ^{174}Yb atoms confined to an optical lattice,” *Phys. Rev. Lett.*, vol. 96, p. 083002, Mar 2006.
- [25] M. Kitagawa, K. Enomoto, K. Kasa, Y. Takahashi, R. Ciurylo, P. Naidon, and P. S. Julienne, “Two-color photoassociation spectroscopy of ytterbium atoms and the precise determinations of s-wave scattering lengths,” *Phys. Rev. A*, vol. 77, no. 1, p. 012719, 2008.
- [26] A. D. Ludlow, N. D. Lemke, J. A. Sherman, C. W. Oates, G. Quéméner, J. von Stecher, and A. M. Rey, “Cold-collision-shift cancellation and inelastic scattering in a Yb optical lattice clock,” *Phys. Rev. A*, vol. 84, p. 052724, Nov 2011.
- [27] A. Traverso, R. Chakraborty, Y. N. Martinez de Escobar, P. G. Mickelson, S. B. Nagel, M. Yan, and T. C. Killian, “Inelastic and elastic collision rates for triplet states of ultracold strontium,” *Phys. Rev. A*, vol. 79, p. 060702, Jun 2009.

A compact setup for double-modulation coherent population trapping clock

Peter Yun, François Tricot, David Holleville, Emeric de Clercq, Stéphane Guérandel
 LNE-SYRTE, Observatoire de Paris, PSL Research University, CNRS, Sorbonne Universités, UPMC Univ. Paris 06,
 61 Avenue de l'Observatoire, 75014 Paris, France
 enxue.yun@obspm.fr

Abstract—We demonstrate an atomic clock based on double-modulation CPT. With a high contrast CPT signal observed in this scheme, we get a preliminary result of the frequency stability: 4×10^{-13} at 1 second. It shows the possibility to implement an atomic clock with a compact and robust setup while still maintaining its high performance.

Keywords—CPT; Liquid crystal polarization rotator; Atomic clock;

I. INTRODUCTION

A high performance passive coherent population trapping (CPT) clock [1,2] can be based on constructive polarization modulation CPT [3], in which a phase modulation is applied between the two optical components of the bichromatic laser synchronously with the polarization modulation. We call it double-modulation scheme. In this scheme, the two CPT dark states produced successively by the alternating polarizations add constructively, thus the atomic population no longer leaks to the end Zeeman states but to the desired clock states. The CPT signal of clock transition is detected with high contrast and narrow linewidth [4].

Compared with a different way to realize a high performance CPT clock based on PPOP [2,5,6], our scheme does not need a beam superposition alignment and the polarization modulation is less sensitive to vibration than a phase delay setup, thus it provides a compact and robust setup. Here we move a step further toward a more compact clock system, by replacing the electro-optic amplitude modulator (EOAM) used in our previous work [4] with a liquid crystal polarization rotator (LCPR). The polarization modulation frequency for the maximum CPT signal contrast is in the range of several kHz [4], allowing us to employ such liquid crystal based polarization switch. This low voltage driving and negligible size liquid crystal device would be an ideal choice for a compact CPT clock. We also demonstrated a promising frequency stability based on our CW double-modulation CPT clock.

II. EXPERIMENTAL SETUP

Our setup is depicted in Fig. 1, a DFB laser diode emits a monochromatic laser beam around 895 nm, the D1 line of Cesium. With the help of an electro-optic phase modulator (EOPM), which is modulated at 4.596 GHz with 26.5 dBm power, about 70% of the carrier power is transferred to the first sidebands, which form the wanted bichromatic laser.

The phase between the two optical sidebands, so called Raman phase, is further modulated through the driving 4.6 GHz microwave. By Combining with a synchronized polarization modulation, based on a LCPR, we get the double-modulated laser. The laser beam diameter is expanded to 15 mm before the vapor cell. The cylindrical Cs vapor cell, 20 mm diameter and 50 mm long, is filled with 21 Torr of mixed buffer gas (argon and nitrogen). The cell temperature is stabilized to about 38°C. In our experiment a uniform magnetic field of 3.44 μ T along the direction of cell axis is applied to remove the Zeeman degeneracy.

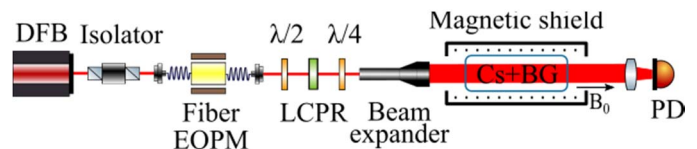


Fig. 1. Compact setup for double-modulation CPT.

III. EXPERIMENTAL RESULTS

We first study the response time of our LCPR as illustrated in Fig. 2(a), the measured rise (fall) time is about 100 μ s and the polarization extinction ratio is around 50. For a comparison, the EOAM [4] shows a response time of 2.5 μ s (limited by our high voltage amplifier) and polarization extinction ratio of 63. In the following, we will show the increase of switch time will not prevent us to observe high contrast CPT signal.

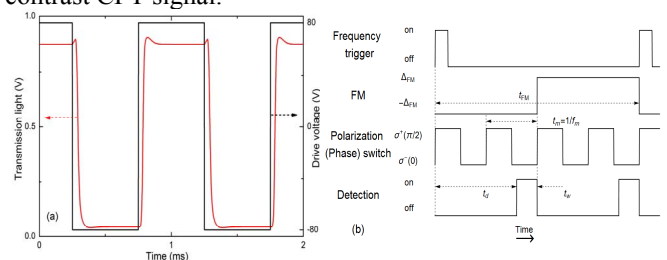


Fig. 2. (a) LCPR switch time. (b) Time sequence for double-modulation CPT.

As illustrated in Fig. 2(b), the polarization and phase modulation share the same modulation function, with a certain pump time to prepare the atoms into CPT states, we detect the CPT signal at t_d with a window of length t_w . To get an error signal to close the CPT clock loop, the microwave frequency is modulated with frequency FM. In our case, we choose FM = 125 Hz, which is a comprised between enough time for

This work is supported in part by ANR and DGA (ISIMAC project ANR-11-ASTR-0004). This work has been funded by the EMRP program (IND55 Mclocks). The EMRP is jointly funded by the EMRP participating countries within EURAMET and the European Union.

double-modulation to accumulate the atomic population into the clock states and the high operating frequency for lock-in amplifier to avoid low frequency noise.

A typical experimental CPT signal of clock transition is illustrated in Fig. 3, with a contrast (CPT amplitude divided by background) about 10% and a linewidth of 800 Hz.

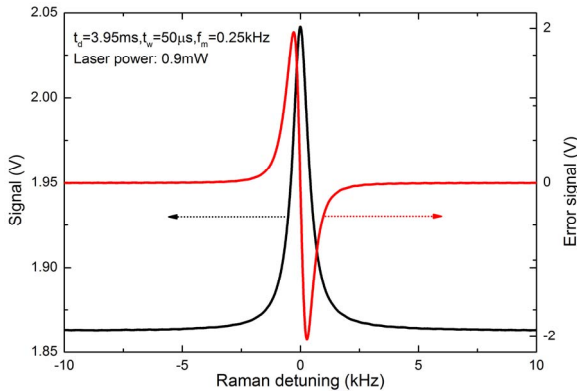


Fig. 3. CPT signal and error signal. Work parameters: $t_d = 3.95$ ms, $t_w = 50$ μ s, $f_m = 0.25$ kHz, $FM = 125$ Hz, modulation depth = 100 Hz. Laser power: 0.9 mW.

We measured the laser intensity noise after travelling across the atomic vapor cell, see Fig. 4. At the Fourier frequency of 125 Hz, we can see the laser intensity noise at Raman detuning (Δ) of 200 Hz, which is the lock position of our clock, is very close to the case of on resonance ($\Delta = 0$ Hz) and off resonance ($\Delta = 10$ kHz). The signal-to-noise (SNR) ratio in a 1 Hz bandwidth is about 2.8×10^5 . The short-term frequency stability can be estimated by the formula:

$$\sigma_y(\tau) \sim \frac{\Delta\nu}{\nu_c} \frac{1}{SNR} \tau^{-1/2}$$

which yields the frequency stability 3.1×10^{-13} at one second.

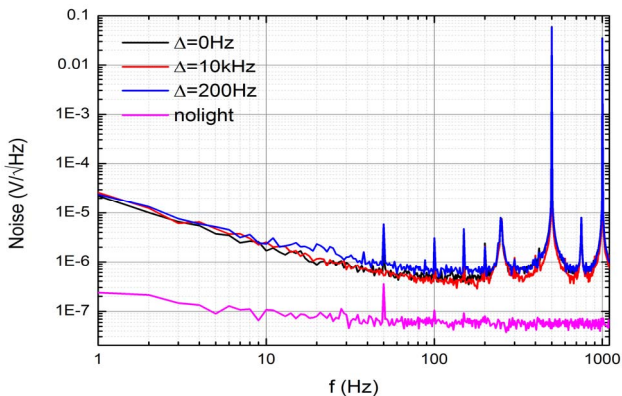


Fig. 4. Detection noise and the laser intensity noise after interaction with atomic cell at various Raman detuning. Work parameters: $f_m = 0.25$ kHz. Laser power: 0.9 mW.

The measured preliminary frequency stability is $4 \times 10^{-13}/\sqrt{\tau}$ (Fig.5), which is close to the expected SNR

limitation. Currently, the laser AM noise and the inter-modulation effect are the main contribution for the limitation of short-term frequency stability. The degradation of the mid-term frequency stability is believed due to the cell temperature fluctuation. Further study will focus on the improvement of the mid-term and long-term frequency stability.

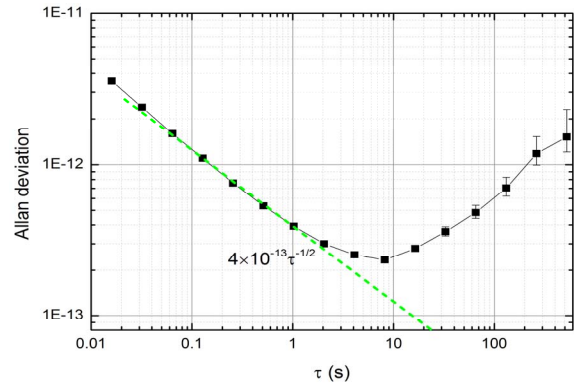


Fig. 5. Preliminary result of frequency stability.

IV. CONCLUSION

We implement a compact and robust CPT clock based on the double-modulation CPT, a short-term frequency stability of 4×10^{-13} at one second is demonstrated. This preliminary results show the possibility to offer a high performance and compact CPT clock based on the polarization modulation.

Acknowledgment

We would like to thank Rodolphe Boudot and Moustafa Abdel Hafiz for helpful discussions. We are grateful to José Pinto Fernandes for technical assistance and the realization of various electronic devices. We are also pleased to acknowledge Pierre Bonnay and Annie Gérard for manufacturing Cs cells.

References

- [1] J.-M. Danet, O. Kozlova, P. Yun, S. Guérandel and E. de Clercq, "Compact atomic clock prototype based on coherent population trapping," EPJ Web of Conferences, 77, 00017 (2014)
- [2] Abdel Hafiz M and Boudot R, "A coherent population trapping Cs vapor cell atomic clock based on push-pull optical pumping," J. Appl. Phys. 118, 124903 (2015)
- [3] P. Yun, J.-M. Danet, D. Holleville, E. de Clercq, and S. Guérandel, "Constructive polarization modulation for coherent population trapping clock," Appl. Phys. Lett. 105, 231106(2014)
- [4] P. Yun, S. Mejri, F. Tricot, M. A. Hafiz, R. Boudot, E. de Clercq, and S. Guérandel, "Double-modulation CPT cesium compact clock," 8th FSM, 2015.
- [5] Y.-Y. Jau, E. Miron, A. B. Post, N. N. Kuzma, and W. Happer, "Push-Pull Optical Pumping of Pure Superposition States," Phys. Rev. Lett., 93, p. 160802-1-4 (2004)
- [6] X. Liu, J.-M. Mérolla, S. Guérandel, C. Gorecki, E. de Clercq, and R. Boudot, "Coherent population trapping resonances in buffer-gas-filled Cs-vapor cells with push-pull optical pumping," Phys. Rev. A, 87, 013416 (2013)

State-of-the-art Ultra-low Phase Noise Photonic Microwave Generation

Bouchand Romain¹, Xie Xiaopeng¹, Nicolodi Daniele¹, Tremblin Pierre-Alain², Santarelli Giorgio², Alexandre Christophe³, Giunta Michele⁴, Lezius Matthias⁴, Haensel Wolfgang⁴, Holzwarth Ronald⁴, Shubhashish Datta⁵, Abhay Joshi⁵ and Le Coq Yann¹

¹LNE-SYRTE, Observatoire de Paris, CNRS, UPMC 61 avenue de l'Observatoire, 75014 Paris, France

²LP2N, Institut d'Optique Graduate School, Bordeaux University, Rue Francois Mitterand, 33400 Talence, France

³LNE-CNAM, CEDRIC Laboratory, 1 rue Gaston Boissier, 75015 Paris, France

⁴Menlo Systems GmbH, Am Klopferspitz 19a, D-82152 Martinsried, Germany

⁵Discovery Semiconductors, Inc. Ewing, NJ, USA

Abstract— Ultra-low phase noise microwave signals can be generated by photodetecting the train of pulses of an optical frequency comb locked to an ultrastable continuous laser reference. However the photodetection process itself is accompanied by some noise that is limiting the performance of this technique. We present how we overcome these limitations and combine different methods to generate, detect and characterize the lowest absolute phase noise microwave signal to date.

I. INTRODUCTION

Many applications such as telecommunication, radar, deep-space navigation systems and precision microwave spectroscopy are calling for ultrastable microwave signals [1]. The lowest noise microwave sources used today are cryogenic sapphire oscillator (CSO) and room temperature sapphire oscillator (RTSO) [2,3], however, photonic generation of microwave signals is of particular interest because it allows transferring the unsurpassed spectral purity of ultra-stable continuous wave lasers to the microwave domain and offers the opportunity of lowermost phase noise both close- and far-from-the-carrier [4].

In this technique, referred to as optical division, the conversion from optical to microwave is done by synchronization of the repetition rate of a femtosecond laser with an ultra-stable optical frequency reference. The advantage dwells in the fact that the reduction in the carrier frequency translates as a reduction in phase noise. The single sideband (SSB) phase noise is reduced by $20 \cdot \text{Log}(N)$, where N is the optical to microwave frequency ratio. In our setup we realize an optical division from 194 THz to 12 GHz, which implies 84 dB reduction in phase noise. For an ultra-stable optical reference exhibiting a stability of $\sigma_y \sim 5 \cdot 10^{-16}$ at one second, this theoretically means levels of phase noise lower than any other existing sources.

However, the photo-detection process itself introduces excess phase noise hereby limiting the stability of the optically generated microwave signal. The main limits on the purity of the microwave signal generated are:

- The amplitude-to-phase conversion ‘APC’ combined with the inevitable intensity noise of the femtosecond laser.
- Thermal and shot noise, due respectively to thermal agitation of the charge carriers in resistors and to the quantum nature of the photocurrent. The SSB phase noise they induce both scale down with the microwave power of the harmonics of interest in the photodetected electrical signal.

II. LIMITS AND ACHIEVEMENTS

A. Tackling the influence of amplitude modulation

Fiber combs exhibit levels of relative intensity noise (RIN) that are significantly higher than other lasers. This amplitude noise is a problem because it is converted to phase noise during photodetection *via* a process usually referred to as amplitude-to-phase conversion (or power-to-phase conversion or AMPM conversion) characterized by an amplitude-to-phase conversion coefficient.

The amplitude-to-phase conversion coefficient arises due to saturation of the photodiode and subsequent space charge effects. Therefore, it depends on the operational conditions of the photo-detector and it has been shown that it can be set to zero when operating at some ‘lucky spots’[1,5].

In the present work we combine a very low noise optical power servo and an active stabilization of the system at the zero APC point of a saturated fast photodetector to reject RIN-induced phase noise below -190dBc/Hz for frequencies above 1 kHz.

In order to measure the APC coefficient, The FPGA-based system operates modulating the intensity of the frequency comb output (*via* an AOM) and coherently demodulating the relative phase between the microwave signal obtained from the photodiode and a reference signal (CSO). The beatnote between the photo-detected microwave signal and the reference oscillator is digitized and phase measurement, demodulation, and control loop are implemented digitally, allowing for great flexibility in the choice of modulation

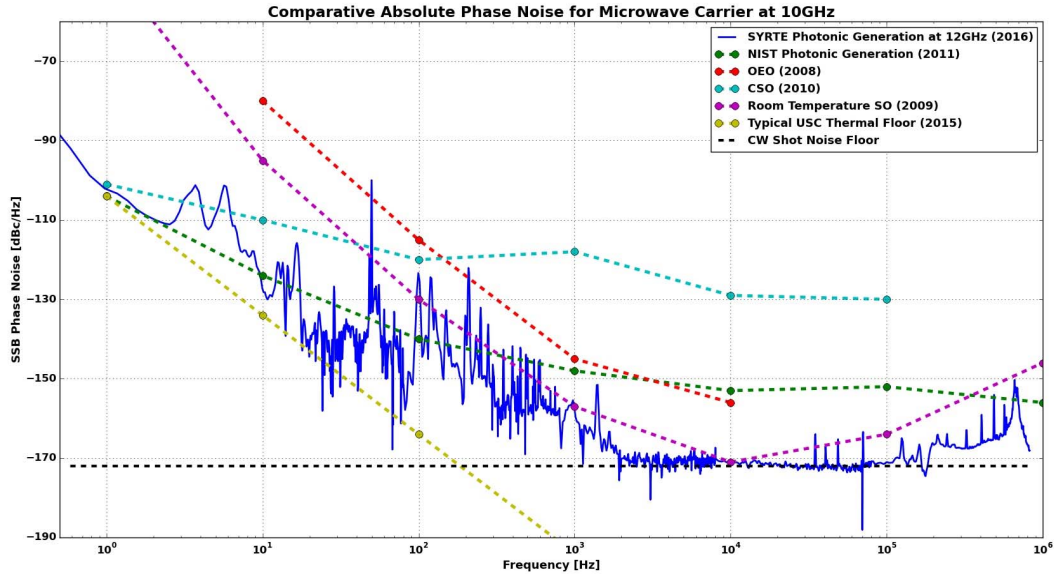


Fig. 1. Comparative single sideband phase noise for different low noise microwave sources [2,3,8].

parameters and control loop optimization. The sensitivity of the system to the amplitude-to-phase-conversion coefficient is limited by the phase noise of the reference oscillator and by the sensitivity of the digital phasemeter. However, adjusting the modulation frequency and amplitude, the sensitivity to the amplitude-to-phase conversion coefficient can be tuned, obtaining an arbitrary large rejection of the intensity noise.

B. Increasing microwave power

To reject the limits imposed by thermal and shot noises we increase the signal-to-noise ratio of the photodetected 12 GHz microwave signal. Firstly, the average optical power as such is increased by adding an EDFA ‘booster’ at the output of our Erbium fiber laser comb (Menlo Systems GmbH)¹. It reaches 300mW optical power at 1542 nm. Secondly, we increase the repetition rate of our comb from 250 MHz to 4 GHz using 4 cascaded Mach-Zehnder interferometers [6,7]. This redistributes the energy towards the high-order harmonics of the microwave signal and allows us to produce above 4dBm of power at 12GHz at the output of our photodetector (DSC40S, Discovery Semiconductors, Inc.).

III. HETERODYNE CROSS-CORRELATION

For ultra-precise characterization of the phase noise of the optically generated 12 GHz microwave signal, we mix our signal with two independent optically generated microwave references and perform a cross-correlation of the beat notes (~5 MHz) *via* a homemade FPGA-based heterodyne cross-correlator. To ensure consistency and fast convergence of the cross-correlation, the side microwave sources are coming from two other independent ultra-low phase noise stabilized

¹ The booster actually is a saturated EDFA and has the dual effect of rejecting more than 15 dB of RIN.

femtosecond lasers phase-locked to two additional distinct ultra-stable optical references.

IV. RESULTS AND FUTURE PROSPECTS

As can be seen on Fig. 1, our photonic generated 12 GHz microwave signal exhibits absolute levels of phase noise below -103 dBc/Hz at 1Hz and below -172 dBc/Hz at 10 kHz. This is lower than any existing sources and defines the new state-of-the-art.

We are now aiming at a further increase in microwave power to lower even more the noise limits. We consider using high-power handling capacities photodetectors (MUTC photodiodes...) and polarization-maintaining interleavers [9].

ACKNOWLEDGMENT

This work is funded by the DARPA Pulse program (PureComb project), the Eureka Eurostar program (STAMIDOF project) and the FIRST-TF Labex. We are grateful to Michel Lours, Jose Pinto, Jean-François Olivier and Alexandre Aristide for technical support.

REFERENCES

- [1] W. Zhang, T. Li, M. Lours, S. Seidelin, G. Santarelli, and Y. Le Coq, "Amplitude to phase conversion of InGaAs pin photo-diodes for femtosecond lasers microwave signal generation," *Appl. Phys. B* 106(2), 301–308 (2012).
- [2] S. Grop, P. Y. Bourgeois, R. Boudot, Y. Kersale, E. Rubiola, and V. Giordano, "10 GHz cryocooled sapphire oscillator with extremely low phase noise," *Electronics Letters*, vol. 46, pp. 420–422, Mar 2010.
- [3] E. N. Ivanov and M. E. Tobar, "Low Phase-Noise Sapphire Crystal Microwave Oscillators: Current Status", *IEEE Transactions on Ultrasonics Ferroelectrics and Frequency Control*, vol. 56, pp. 263–269, Feb 2009.

- [4] T. M. Fortier, F. Quinlan, A. Hati, C. Nelson, J. A. Taylor, Y. Fu, J. Campbell, and S. A. Diddams, "Photonic microwave generation with high-power photodiodes," *Opt. Lett.* 38(10), 1712–1714 (2013).
- [5] J. Taylor, S. Datta, A. Hati, C. Nelson, F. Quinlan, A. Joshi, and S. Diddams, B, "Characterization of power-to-phase conversion in high-speed P-I-N photodiodes" ,*IEEE Photon. J.*, vol. 3, no. 1, pp. 140–151, Feb. 2011.
- [6] A. Haboucha, W. Zhang, T. Li, M. Lours, A. N. Luiten, Y. Le Coq, and G. Santarelli, "Optical-fiber pulse rate multiplier for ultralow phase-noise signal generation," *Opt. Lett.* 36(18), 3654–3656 (2011).
- [7] H. Jiang, J. Taylor, F. Quinlan, T. Fortier, and S. A. Diddams, *IEEE Photon. J.*, vol. 8, 1004, (2011).
- [8] T. M. Fortier, M. S. Kirchner, F. Quinlan, J. Taylor, J. C. Bergquist, T. Rosenband, N. Lemke, A. Ludlow, Y. Jiang, C. W. Oates and S. A. Diddams, *Nature Photonics*, 5,425–429, (2011) and references therein.
- [9] E. Portuondo-Campa, G. Buchs, S. Kundermann, L. Balet, and S. Lecomte, *Opt. Express* 23, 32441 (2015).

Quartz Orientations for Optimal Power Efficiency in Wireless SAW Temperature Sensors

Alexander Shvetsov and Sergei Zhgoon
National Research University MPEI
Moscow, Russian Federation
Email: zhgoon@ieee.org

Ivan Antcev, Sergei Bogoslovsky, and Gennadiy Sapozhnikov
JSC "Radar mms"
St Petersburg, Russian Federation

Abstract—The efficiency of electromagnetic power re-radiation by a wirelessly interrogated passive sensor and its sensitivity to the measured value are the main factors defining the sensor performance. The analysis gives the relation between the re-radiation efficiency and the electromechanical coupling factor. Experimental resonator parameters demonstrate the relevance of this efficiency improvement. The calculation of the coupling factor simultaneously with the temperature coefficient of delay for all quartz orientations was carried out. The results of this calculation can help to select optimal trade-offs between the sensitivity and the efficiency of power re-radiation.

Keywords—temperature sensor; SAW sensor; wireless sensor

I. INTRODUCTION

Sensors based on surface acoustic waves (SAW) devices demonstrate promising features for wireless applications. Besides the large sensitivity of the sensor response informative parameter to a measured physical value, the power of sensor re-radiated response is the most important factor in wireless SAW sensors. The latter factor becomes especially critical when the sensor is placed in media with high electromagnetic loss such as in living objects [1]. Quartz gives the largest range of SAW temperature coefficient of delay (TCD) among the most useful piezoelectric crystals. This range spreads from about -90 ppm/°C to about 90 ppm/°C [2].

II. ACCUMULATION AND RADIATION OF ENERGY BY SAW RESONATOR WITH ANTENNA

A. Methods of Wireless Resonator Interrogation

Interrogation methods using continuous signal are appropriate in the case of quite strong coupling between the interrogator antenna and the antenna connected to a SAW device. In the case of weak coupling between these antennas the interrogation using impulse signal is preferable because the latter helps to separate the sensor response from electromagnetic wave reflections from obstacles by using the time gating method.

B. Equivalent Circuit Model

The analysis of energy accumulation and radiation based on an approximate equivalent circuit of a SAW device connected to an antenna provides results with restricted accuracy but it is very clear because of the model simplicity and thus it is useful

for understanding of the main tendencies. This equivalent circuit is shown in Fig. 1, where $e(t) = E_1 \cos(2\pi f_1 t)$ – the electromotive force that is created by the incident electromagnetic wave with the frequency f_1 . $Z_A = R_A + jX_A$ – is the impedance of the antenna, C_S – is the static capacitance of the SAW resonator; L , C , r – are the motional inductance, the motional capacitance, and the serial resonance resistance of the SAW resonator, respectively.

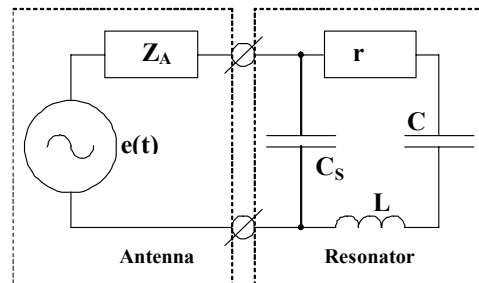


Fig. 1. Equivalent circuit of a SAW resonator with antenna.

More useful values for characterization of a SAW resonator are the quality factor $Q = \omega_r L / r$, where $\omega_r = (LC)^{-1/2} = 2\pi f_1$ is the resonance angular frequency, and the electrical coupling coefficient $K_C = C / C_S$. In respect to purposes of this analysis we assume $E_1^2 / R_A = \text{const}$ that means a constant value of incident wave power being received by antenna. This assumption helps to clearly understand the influence of the antenna impedance (although in fact the received power as well as the antenna impedance change with antenna design variation). Let us denote the maximal possible energy accumulated in the resonator in the stationary process conditions by W_{lim} (it is achieved if impedances are matched, so that Z_A equals to the complex conjugated impedance of the resonator). Taking into account the condition of impedance matching and the relation between accumulated and lost energy we obtain $W_{\text{lim}} = (E_1^2 Q) / (8R_A \omega_r)$.

The efficiency of energy re-radiation can be characterized by the ratio of the energy W_A lost in antenna during the free oscillation process (after the end of the excitation initial signal) to W_{lim} . W_A depends on f_1 , we will denote f_w the value of f_1 corresponding to the maximum of the function $W_A(f_1)$. Let us denote the ratio $W_A(f_1) / W_{\text{lim}}$ at $f_1 = f_w$ by $\eta = W_A(f_w) / W_{\text{lim}}$. The dependence of W_A on f_1 and on equivalent circuit parameters

This work was supported in part by the Ministry of Education and Science of the Russian Federation (123/14-544).

was investigated in details in case of $X_A = 0$. For the range of parameters that is relevant for quartz SAW resonators with the operation frequency from tenths of GHz to several GHz ($K_C < 0.25\%$ and $2000 < Q < 20000$) f_w and η can be described with a high accuracy by following expressions:

$$f_w = [(K_C/2)R_n^2/(1 + R_n^2) + 1]f_r, \quad (1)$$

$$\eta = 4[(R_n + 1/R_n)/(K_C Q)]/[1 + (R_n + 1/R_n)/(K_C Q)]^3, \quad (2)$$

where the normalized antenna resistance $R_n = R_A/(r \cdot K_C Q)$.

Fig. 2 demonstrates the dependence of η on R_n at different values of $K_C Q$. If $K_C Q > 4$, the maximal possible η approaching 0.6 is obtained at two points (they merge into a single point at $K_C Q = 4$). Values of R_n corresponding to maximums approach to $2/(K_C Q)$ and $K_C Q/2$ if $K_C Q$ is significantly larger than 4. If $K_C Q < 4$ the maximum of η located at $R_n = 1$ but the maximal possible value is not obtained. The maximal obtained value decreases with $K_C Q$ decreasing. Therefore, using of resonators with $K_C Q > 4$ is preferable (at least one needs to ensure that the $K_C Q$ that is not significantly smaller than 4).

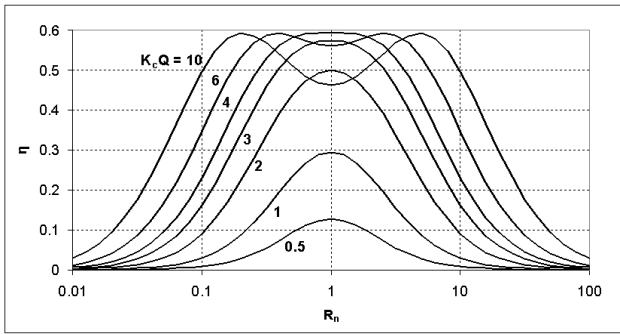


Fig. 2. Dependence of the energy re-radiation efficiency η on the normalized antenna resistance R_n .

C. Numerical Modeling Results

An alternative method of re-radiated energy calculation is the Fourier transform applied to the spectrum of the antenna current. This approach was realized using Mathcad™ software with a SAW resonator model based on the coupling-of-mode (COM) method. In this case, W_A is calculated as a time domain integral from the product of the square of the antenna current and the antenna resistance with integration range from the end of the excitation initial signal to maximal time that frequency discretization permits.

Fig. 3 shows the examples of W_A on R_n dependence for two particular resonators designed for different quartz orientations. The attenuation loss in the resonators model was adjusted in order to obtain the quality factor close to 5000. The parameters Q , K_C , and r for each resonator were extracted from the admittance frequency response. Dependencies calculated by numerical modeling are compared with those calculated analytically using (2) and expressions for η and W_{lim} . The frequency of the initial signal in the numerical calculation was

selected according to (1). It was proven that the frequency giving maximal W_A in numerical calculation is very close to f_w defined by (1). A sufficiently large duration of the initial signal was selected in such a way that no significant additional increase of W_A occurred with an additional increase of this duration. The relation $E_1^2/R_A = 1 \text{ V}^2/\text{Ohm}$ was used in calculations. The good agreement between the results obtained with these approaches shows that a simplest equivalent circuit model can be appropriate for this subject.

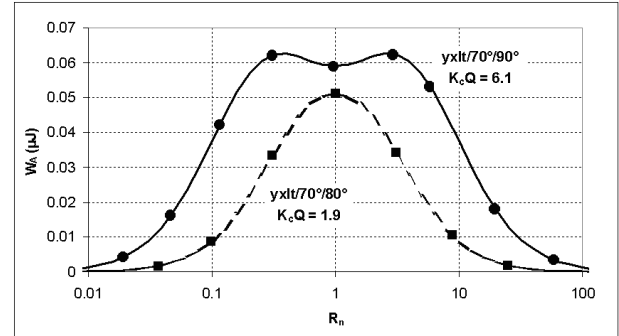


Fig. 3. Comparison of the analytical (lines) and numerical (markers) dependence of W_A on R_n at $E_1^2/R_A = 1 \text{ V}^2/\text{Ohm}$.

One of these resonators is designed for the substrate $YXlt/70^\circ/80^\circ$ with the effective electromechanical coupling factor for electrode structure [3] $K_{eff}^2 = 0.06\%$. It is characterized by $K_C = 0.04\%$ and $K_C Q = 1.9$. Another resonator for the substrate $YXlt/70^\circ/90^\circ$ with $K_{eff}^2 = 0.18\%$ is characterized by $K_C = 0.13\%$ and $K_C Q = 6.1$. Design details for these resonators are given in [2]. According to our experience in the design of SAW resonators this example reflects a general rule that the value of K_C is restricted by the value of K_{eff}^2 that is usually close to the value of the electromechanical coupling factor K^2 . Thus, the requirements to K_C affect the requirements to K^2 . Note that the resulting K_C is expected to be smaller due to the contact pads. Even more stringent requirements to K^2 appear in the case of connecting a pair of resonators to a single antenna. This connection results in a significant decrease of the electrical coupling factor in comparison to K_C of a single resonator (two times in case of two resonators with similar parameters).

III. QUARTZ ORIENTATIONS FOR HIGH TCD AND COUPLING FACTOR

A. Ranges of Orientations with Minimal and Maximal TCD

The evaluation of SAW parameters relevant to sensor applications was carried out with modified VCAL free software [4] using quartz constants from [5]. Properties of the lowest phase velocity SAW were calculated for all possible orientations. This choice of the wave guarantees the absence of energy leakage into the bulk. Also Blustain-Gulyaev-Shimizu (BGS) waves propagate without this type of energy leakage independently on the relation between their velocity and the velocities of other waves.

The global TCD minimum and its global maximum of non-leaky waves on quartz are obtained when BGS waves are used [2]. In both of the above cases, the velocity of the BGS wave exceeds the velocity of the bulk acoustic wave (BAW) propagating in the same direction. The energy leakage is absent if the wave propagates exactly perpendicularly to the axis X .

Alternative orientations with high TCD values exist around the local maximums of the TCD at Euler angles (30°, 90°, 105°) and (0, 170°, 90°). Alternative orientations with low TCD values exist around the local minimums of the TCD at Euler angles (30°, 90°, 170°), (0, 170°, 35°) and (30°, 40°, 165°).

The temperature coefficient of frequency (TCF) of a SAW resonator is mainly determined by the TCD of the SAW propagating along the free surface (namely the TCF is close to the TCD with opposite sign). For quite thick or quite dense electrodes this equality may be inadequate, so that the TCD of a SAW propagating in a structure with a corresponding layer of electrode material needs to be used instead of the free surface TCD as a simplest approximation in this case. The effective thickness of the layer to be used in calculations equals to the product of the electrode thickness and the metallization ratio. This model also can be used as a coarse guess for a coupling factor in the electrode structure. Taking into account electrode properties is especially important for BGS waves.

B. Coupling Factor of BGS Waves with Extremal TCD

The dependences of the calculated coupling factor of the BGS wave on 3°Y-cut quartz (with the maximal TCD) and Y-cut quartz (with the TCD that is close to the maximum) on Al film thickness h to wavelength λ ratio are shown in Fig. 4. Obtaining acceptable levels of K^2 requires quite thick aluminum or using of dense materials. Note that thick aluminum additionally increases the TCD and consequently it slightly improves this parameter.

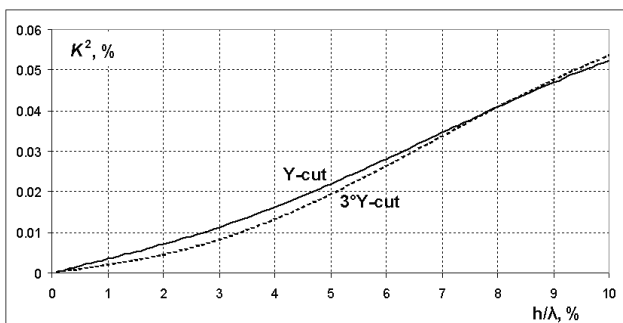


Fig. 4. Dependence of K^2 for a BGS wave on Al film thickness to wavelength ratio on 3°Y-cut and Y-cut quartz.

The dependence of the calculated coupling factor and of the calculated TCD of the BGS wave on 70°Y-cut on Al film thickness to wavelength ratio is shown in Fig. 5. The data on temperature behavior of the aluminum film mechanical properties [6] are taken into account in the TCD calculation. The absolute value of TCD drops with the thickness increase, but even obtaining the K^2 value close to 0.25 (that equals the

maximal value for other non-leaky SAWs on quartz) corresponds to the TCD value that is equal to -79 ppm/°C that is still smaller than the values for other non-leaky SAWs. Moreover very thick (or quite dense) electrodes allow us to exceed this limit. At the same time varying of the electrodes thickness as well as varying of the metallization ratio significantly changes the TCD at high thickness. This possibility can be used for producing of resonator pairs with high K_C and high TCF difference.

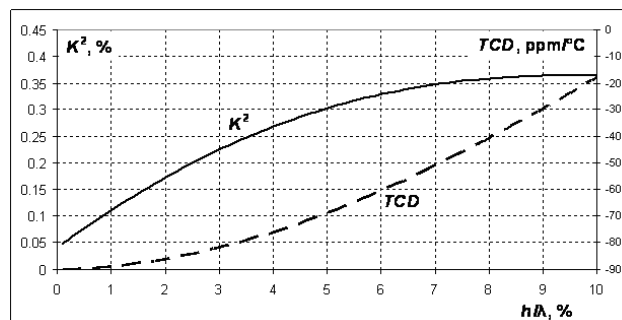


Fig. 5. Dependence of K^2 and TCD for a BGS wave on Al film thickness to wavelength ratio on 70°Y-cut quartz.

Using of thick or dense electrodes may restrict the achievable quality factor. Thus, alternative variants with improved K^2 without thick or dense electrodes are interesting for obtaining high $K_C Q$ value.

C. Maximum of the TCD Difference on a Single Substrate

Fig. 6 demonstrates the calculated maximal achievable TCD difference Δ_{max} as a function of the required coupling factor K^2_{req} . Δ_{max} is the maximum of Δ_{TCD} among all quartz cut orientations, where Δ_{TCD} is the difference between the maximal TCD and the minimal TCD for waves with $K^2 \geq K^2_{req}$ propagating on the same cut in different directions.

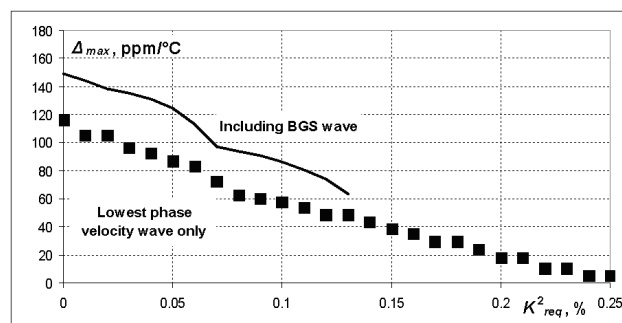


Fig. 6. Dependence of the maximal achievable TCD difference on the required coupling factor on quartz.

The dependence of Δ_{max} on K^2_{req} for alternative variants using only SAW with lowest phase velocity is shown on Fig. 6 as well as Δ_{max} for the variant using the BGS wave with a velocity that exceeds the velocity of the BAW. If K^2_{req} is smaller than 0.07% the cut with BGS wave is selected from the

range ($0, 167^\circ \pm 7^\circ, \psi$) and the propagation direction of the other wave (with larger TCD) ψ_{\max} varies from 77° to 90° that is quite close to the propagation direction of the BGS wave. If K^2_{req} varies from 0.07% to 0.14%, the cut is selected from the range ($0, 155^\circ \pm 5^\circ, \psi$) and ψ_{\max} varies from 0° to 33° .

In order to obtain larger levels of K^2_{req} cuts closer to the cut with global maximum of K^2 are appropriate. A SAW with maximal K^2 (about 0.26%) propagates on the cut with the orientation close to $(20^\circ, 55^\circ, 0)$ with the TCD about -38 ppm/ $^\circ\text{C}$. Smaller K^2 allow selecting a wave with slightly smaller TCD (it reaches -45 ppm/ $^\circ\text{C}$ with $K^2 = 0.14\%$) on the cuts that have similar orientations and with the propagation directions ψ_{\min} that vary from -15° to 0 . The propagation direction of the other wave (with larger TCD) ψ_{\max} varies from 0 to 20° .

Let us use for example two particular values of Q -factor: 4000 as an easily obtainable value and 10000 as a realistic improved value. In the first case $K_C Q > 4$ can be obtained simultaneously with Δ_{\max} up to 86 ppm/ $^\circ\text{C}$ (57 ppm/ $^\circ\text{C}$ without BGS waves). In the second case it can be obtained with Δ_{\max} up to 130 ppm/ $^\circ\text{C}$ (92 ppm/ $^\circ\text{C}$ without BGS waves).

D. Maximal TCD Difference on Separate Substrates

Fig. 7 demonstrates the calculated minimal and maximal TCD as a function of K^2_{req} (i. e. the minimum or the maximum of TCD for waves with $K^2 \geq K^2_{\text{req}}$). The distance between the maximum value and the minimum value corresponds to the maximal difference of TCD achievable on separate substrates depending on required K^2_{req} .

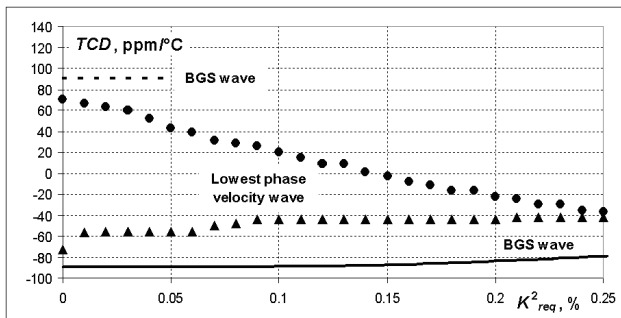


Fig. 7. Dependence of the minimal TCD and the maximal TCD on required coupling factor on quartz.

Using of separate substrates allows obtaining the TCD difference up to 180 ppm/ $^\circ\text{C}$. This value requires using a BGS wave with extremely high TCD as well as a BGS wave with extremely low TCD. Using a BGS wave with low TCD together with lowest phase velocity wave with high TCD on separate substrates allows obtaining the TCD difference that is 10 – 40 ppm/ $^\circ\text{C}$ larger than in case of a single substrate. $K_C Q > 4$ can be obtained with $Q = 4000$ simultaneously with a TCD range from -89 ppm/ $^\circ\text{C}$ (-44 ppm/ $^\circ\text{C}$ without BGS waves) to 20 ppm/ $^\circ\text{C}$. In case of $Q = 10000$ this condition can be obtained with a TCD range from -90 ppm/ $^\circ\text{C}$ (-56 ppm/ $^\circ\text{C}$ without BGS waves) to 52 ppm/ $^\circ\text{C}$.

IV. EXPERIMENTAL

Calculated and measured values of K_C as well as measured values of Q and $K_C Q$ product are summarized in Table I. These data demonstrate a typical range of $K_C Q$ for SAW resonators obtainable on quartz without special efforts for Q improving.

TABLE I. CALCULATED AND MEASURED PARAMETERS OF RESONATORS

Quartz Substrate	Electrical Coupling Coefficient K_C (%)		Measured Quality Factor Q	Measured $K_C Q$
	Calc.	Meas.		
YX	0.11	0.07	6500	4.3
YXl/-30°	0.08	0.05	5200	2.5
XYlt/32°/15°	0.1	0.08	5200	4.1
XYt/10°	0.13	0.07	5500	3.6
XYlt/78°/-62°	0.07	0.07	2600	1.7
YXl/70°/90° (BGS wave)	0.13	0.11	3500	3.8

V. CONCLUSION

Generally quartz orientations with extremal TCD values do not coincide with orientations presenting large coupling factors. The choice of SAW resonator substrates providing high sensitivity of resonance frequency to temperature in most cases results in $K_C Q < 4$. In this range of $K_C Q$ the efficiency of the power re-radiation depends on $K_C Q$, thus, the selection of substrates with larger K^2 allows obtaining larger efficiency. The selection of cuts with optimal trade-offs between sensitivity and efficiency of power re-radiation depends on requirements to a particular measurement system.

ACKNOWLEDGMENT

The use of K.-Y. Hashimoto's free software as the basis of our calculation tools is gratefully acknowledged.

REFERENCES

- [1] G. Martin, P. Berthelot, J. Masson, W. Daniau, V. Blondeau-Pâtissier, B. Guichardaz, S. Ballandras, and A. Lambert, "Measuring the inner body temperature using a wireless temperature SAW-sensor-based system," 2005 IEEE Int. Ultrasonics Symp., pp. 2089-2092.
- [2] S. Zhgoon, A. Shvetsov, I. Ancev, S. Bogoslovsky, G. Sapozhnikov, K. Trokhimets, and M. Derkach, "SAW temperature sensor on quartz," IEEE Trans. on UFFC, vol. 62, pp. 1066-1075, June 2015.
- [3] K. Hashimoto, Surface Acoustic Wave Devices in Telecommunications. Berlin: Springer, 2000.
- [4] K. Hashimoto and M. Yamaguchi, "Free software products for simulation and design of surface acoustic wave and surface transverse wave devices," 1996 IEEE International Frequency Control Symposium, pp. 300-306.
- [5] Y. Shimizu and Y. Yamamoto, "SAW propagation characteristics of complete cut of quartz and new cuts with zero temperature coefficient of delay," 1980 Ultrasonics Symposium, pp. 420-423.
- [6] S. Ballandras, E. Gavignet, E. Bigler, and E. Henry, "Temperature derivatives of the fundamental elastic constants of isotropic materials," Appl. Phys. Lett., vol. 71, No. 12, September 1997, pp. 1625-1627.

Digital Electronics Based on Red Pitaya Platform For Coherent Fiber Links

A. C. Cárdenas Olaya^{1,2,3}, S. Micalizio¹, M. Ortolano^{1,2},
C. E. Calosso¹

¹INRIM, Physics Metrology Division

²Politecnico di Torino, Electronic Engineering Department
Turin, Italy

E. Rubiola³, J-M. Friedt³

³CNRS/UFC, FEMTO-ST Institute, Department of Time
and Frequency
Besançon, France

Abstract— Recent improvements and continuous research on accurate clocks and frequency standards require the study of suitable tools and techniques for frequency transfer that minimize the added noise and allow fully exploiting these clocks in metrology applications. Different experiments performed during the last decade validated fiber links as the most performing tool for frequency transfer, reaching a statistical uncertainty of 10^{-20} for thousands kilometers links [1]. Recently, digital implementations have been used for metrological applications due to the flexibility, cost effective and compact solutions that can be achieved. In this paper, we propose a digital implementation for the detection and compensation of the phase noise induced by the fiber link. The beat note, representing the fiber length variations, is acquired directly with a fast Analog to Digital Converter (ADC) followed by a Tracking Numerical Controlled Oscillator (NCO). This reduces the component's latency and the communication delay between different blocks, increasing the tracking bandwidth. In addition, we report the characterization of the main components that allows foreseeing which are the limiting aspects and the expected performance of the complete implementation. The proposed system is being implemented on Red Pitaya, an open source platform driven by a Zynq, System on Chip (SoC) of Xilinx that contains a FPGA and an ARM processor embedded on the same chip.

Keywords—Digital Electronics; Fiber Link; FPGA; IIR filter; NCO; PLL; Time and Frequency transfer.

I. INTRODUCTION

The progress achieved on optical clocks along the last years, allowed reaching frequency stability in the 10^{-18} range. In order to exploit such a performance in metrological applications, fiber links are being widely used for frequency transfer and dissemination. However, mechanical and temperature stresses generate fiber length variations and therefore phase fluctuations that have to be compensated or cancelled if a degradation of the clock information is not desired. In this regard, different techniques exist: the classical, Doppler compensation [2] and the more recent, two-ways cancellation [3]. In the traditional analog configuration, the fiber noise is detected through, a tracking Voltage Controlled Oscillator (VCO) that cleans up the beat note of two lasers, and a frequency divider that increases the dynamic of the mixer. Afterward, a servo compensates the noise by acting on the frequency that drives the Acousto-Optic Modulator (AOM).

This kind of configuration demonstrated to work well [4, 5]. However, it has low flexibility and it is not predisposed naturally for efficient reconfiguration, monitoring and remote operation.

The advantages of a digital implementation on coherent fiber links were demonstrated, for the first time, by C. E. Calosso *et al.*, in [6]. There, the approach is based on the Tracking Direct Digital Synthesizer (DDS) technique, which detects the fiber phase noise directly. The flexibility of this system allowed demonstrating, a 6 dB improvement of the unsuppressed noise limit, and the two-ways scheme, with simple software reconfigurations. The system was usable only up to 47 km, limited by the serial communication of the DDS. For extending its usability to thousand-kilometer link it is necessary to increase the tracking bandwidth from 20 kHz to the megahertz region; that means to redesign the board with parallel communication components.

In this paper we propose an entirely digital implementation, from phase detection to fiber noise compensation. This alternative approach is based on a commercial board that integrates fast ADCs, DACs and a SoC. In addition to the advantages provided by the tracking DDS (monitoring and flexibility), here we exploit the reduction of the communication delay between components that leads to a tracking bandwidth increment, a key point for long links implementation. The work is focused on the critical aspects: latency and resources usage of each functional block implemented in the FPGA and residual noise of the main components. Based on these results, a tracking bandwidth of 2 MHz and a residual frequency stability of 10^{-18} at 1s are expected.

II. TRACKING DDS - PREVIOUS DIGITAL CONFIGURATION

Fig. 1 depicts the Doppler compensation technique using the Tracking DDS approach. A first DDS tracks the phase of the beat note and retrieves the fiber link noise directly. Then, a servo compensates for it by correcting the phase of a second DDS that drives the AOM. This implementation can reach a tracking bandwidth up to 1MHz using parallel communication with the DDS.

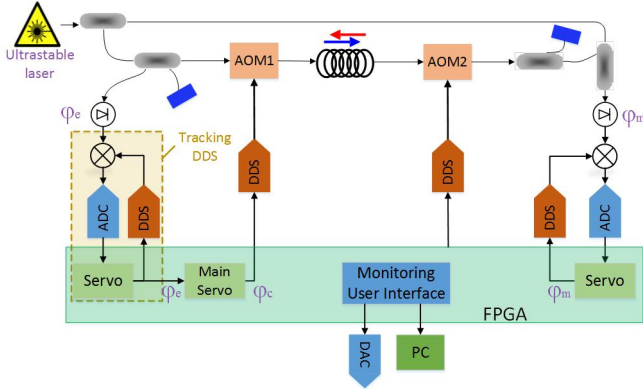


Fig. 1. Doppler compensation implemented by using tracking DDS.

III. TRACKING NCO DESCRIPTION

In the proposed implementation (Fig. 2), mixers and DDSs are replaced by digital blocks implemented on the FPGA, simplifying the hardware interconnection. DDSs are replaced by Numerical Controlled Oscillators (NCOs) and analog mixing is performed through a numerical multiplication. The phase is detected using digital I/Q demodulation having access to the quadrature and in-phase components of the beat note, allowing not only detecting phase but also amplitude fluctuations. The high frequency component is removed by a low pass filter, designed for avoiding the loop dynamic reduction.

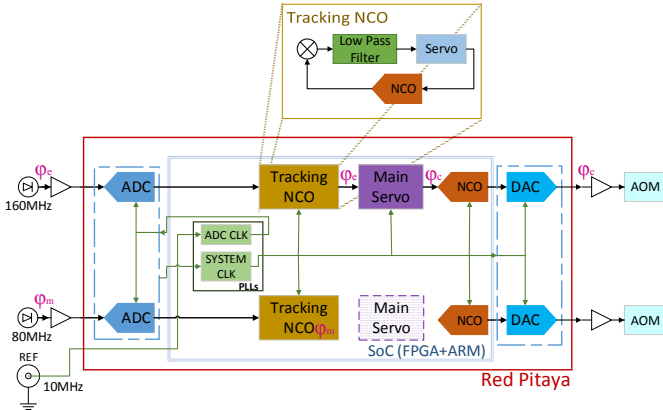


Fig. 2. Description of Tracking NCO block diagram. The phase detector and additional NCOs are implemented on the FPGA. The clock distribution is performed through one of the PLLs provided in the FPGA.

This scheme makes the tracking bandwidth independent of the ADC delay and the data more accessible for monitoring or for additional processing.

IV. IMPLEMENTATION AND CHARACTERIZATION

The implementation and characterization of the blocks was performed on Red Pitaya [7], the same platform currently in use for the complete system integration. Such a platform has two fast ADCs of 14 bits and 125MSPs, and two fast Digital to Analog Converters (DACs) of 14 bits and 125MSPs. The SoC, Zynq 7010, integrates in a single device a dual core ARM Cortex-A9 and an Artix-7 FPGA. Red Pitaya runs Linux, which provides, among other features, different protocols for remote connection.

The aim of this preliminary implementation is to characterize the main blocks: ADC, DAC, internal PLL, NCO and low pass filter, in order to test their suitability and contribution level to the performance of the complete system. Furthermore, it allows obtaining the necessary information to foresee the usage of the FPGA resources and to evaluate data latency that impacts directly on the maximum tracking bandwidth. Thereby, the complete system implementation feasibility is verified according to the application requirements.

The ADC characterization is reported in [8]. The parameter of main interest is the additive noise, which for a sinusoid at maximum amplitude results in a pure ϕ -type phase noise of -103 dB rad^2/Hz at 1 Hz (flicker) and of -152 dB rad^2/Hz at 1 MHz (white).

The tracking bandwidth is determined by the delay introduced by the blocks that belong to the tracking loop (Fig. 3), the low pass filter, the servo and the NCO. In order to keep the stability of the loop, the maximum bandwidth is given by (1).

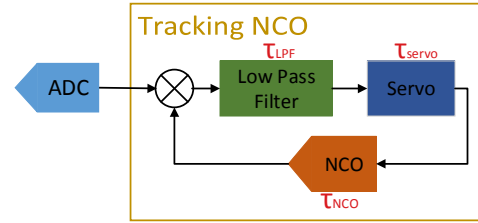


Fig. 3. Description of tracking NCO phase detector. The ADC delay is out of the loop and does not limit the tracking bandwidth.

$$B_{\max} = \frac{1}{8\tau_{\text{Tot}}}, \quad \tau_{\text{Tot}} = \tau_{\text{LPF}} + \tau_{\text{servo}} + \tau_{\text{NCO}} \quad (1)$$

The filter introduces not only delay due to the implementation, but also phase shift related to the filter typology. Both components will be taken into account as filter total delay (τ_{LPF}).

A. Clock Distribution - PLL

In the general scheme for frequency transfer and comparison, an Acousto-Optic Modulator (AOM) is used in the remote laboratory in order to separate reflections from the useful signal. A second AOM, placed in the local laboratory, corrects the fiber noise. In the proposed implementation, the AOMs are driven by the DACs, which in turn, are referred to the board time-base. The same time-base drives the ADCs that detect the phase of the beat notes. As a consequence, the phase noise of the internal time-base adds noise to the link. In this regard, the time-base is obtained from an external reference, taking advantage of the internal PLL of the FPGA.

B. Numerical Controlled Oscillator

The NCO implemented here is based on the DDS IP core provided by Xilinx. The block generates the sine and cosine signals, used for the detection of the quadrature (Q) and in-phase (I) components of the beat note, respectively. The configuration chosen minimizes latency and FPGA resources usage. The NCO has been sized taking into account that the

ADC has 11 effective bits (ENOB=11bits). In order not to degrade the information from the ADC, an output resolution of 16 bits was chosen. In addition, the NCO features 48 bits for phase and frequency, a latency $\tau_{NCO} = 2 T_{clk} = 16$ ns, and a maximum clock frequency of 460 MHz. It utilizes 72 configurable logic blocks (1.63%) and 54 kb RAM (1.66%).

C. Low Pass Filter

The filter plays an important role for what concerns the maximum tracking bandwidth achievable. Therefore, it was designed to minimize the phase shift and the delay on the signal and, at the same time, without excessive use of the FPGA resources. The typology chosen was an Infinite Impulse Response (IIR) elliptic of third order. The filter implemented has a total delay $\tau_{LPF} = 4.82 T_{clk} = 38.6$ ns and the transfer function depicted in Fig. 4. The filter specifications, guarantee the rejection of the high frequency component resulting from the multiplication. In this case, due to the sampling frequency this component will be at 70 MHz for φ_e and 90 MHz for φ_m . With respect to the Finite Impulse Response (FIR) implementation, it exhibits much smaller latency and -57% of resources usage. Particular attention has been paid on data resolution to ensure stability to the filter.

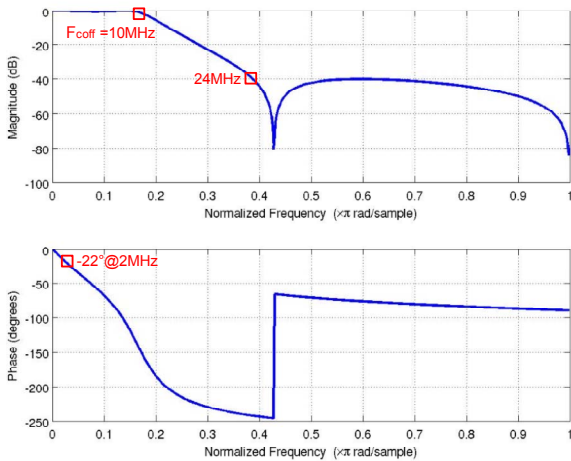


Fig. 4. Low pass filter design specifications. Cut off frequency: 10MHz, stop band attenuation: 40dB. Phase shift added at the desired frequency: 22°.

The features of the filter implemented are: Filter Order: 3, latency: 8 ns, phase shift at the desired tracking bandwidth (2MHz): 22°, output precision: 31 bits fixed point. FPGA Utilization: 0.53% Logic Cells, 12.5% DSPs (Multipliers).

D. Servo

The servo performs a Proportional and Integrative (PI) control in order to correct the phase of the NCO according to the beat note phase. The implementation is based on the architecture performed for the Tracking DDS. The latency added by this block is $\tau_{servo} = 1 T_{clk} = 8$ ns.

V. RESULTS

The residual phase noise of the two DACs was measured here. The DACs were driven by the NCO outputs at 40 MHz,

the value that will be used for driving the AOMs. The result is shown in Fig. 5. It is dominated by flicker noise ($b_{-1} = -97$ dB rad^2/Hz) that leads to a residual stability of 6.5×10^{-13} at 1s ($f_h = 50\text{Hz}$)

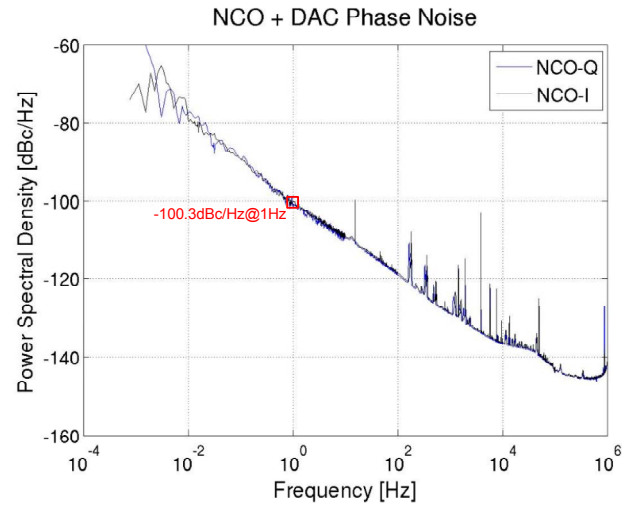


Fig. 5. The main phase noise contribution is added by the DAC.

The residual phase noise of the PLL embedded in the FPGA is shown in Fig. 6.

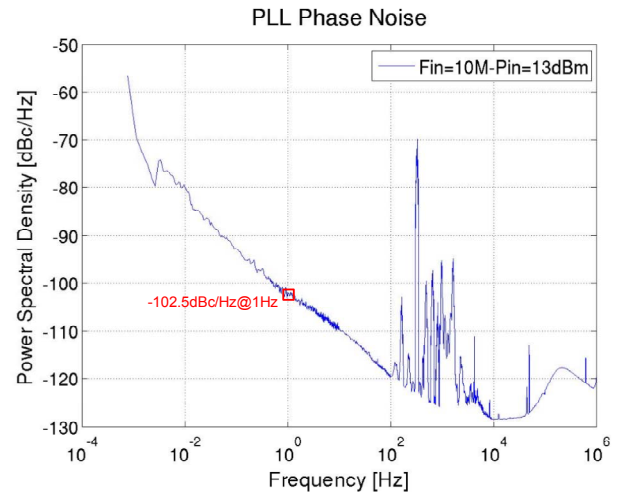


Fig. 6. PLL residual phase noise. Input frequency of 10MHz.

The flicker noise obtained is -99.5 dB rad^2/Hz at 1Hz referred to the reference (10 MHz). The residual stability is 8.8×10^{-13} at 1s ($f_h = 50$ Hz). It is the component with the highest noise and limits the overall performance. Nevertheless, we decided to privilege the compactness of the system and to avoid using external frequency multiplier. Thanks to the leverage between RF and optical frequencies, the system is expected to affect the fiber link performance at the level of 10^{-18} at 1s, allowing reaching the 10^{-21} region at 200 s.

Fig. 7 depicts the Allan deviation of the PLL phase noise. The frequency stability expected for the complete system is about 10^{-18} at 1s, close to the frequency stability obtained with the Tracking DDS approach.

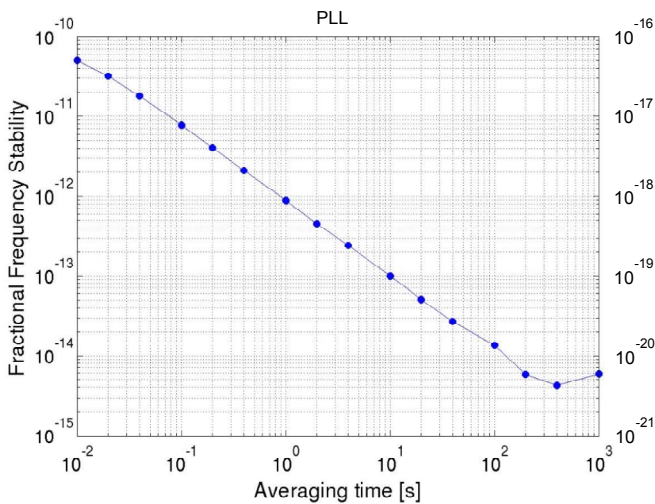


Fig. 7. Allan deviation of the PLL phase noise. Expected frequency stability of the completed system implementation.

The total bandwidth is expected to be 2 MHz according with the results obtained of each block implementation and characterization, compatible with thousand kilometers links.

Thanks to the NCO implementation, the system will have access to the in-phase component which allows performing automatic power compensation on the fiber.

The tracking NCO features a “dead frequencies range” due to the sampling frequency (125 MHz) used for this implementation. For input frequencies close to the sampling clock, the tracking bandwidth is faster than the information and therefore it can not be detected. This can be solved changing the sampling frequency. However, for the first approximation of the system the scheme will remain as it was shown here.

The implementation of the entire system is being performed currently. The electronics will be used on the Italian Link for Frequency and Time from Turin to Florence that is 642-km long [9].

REFERENCES

- [1] C. Lisdat, G. Grosche, N. Quintin, C. Shi *et al.* “A clock network for geodesy and fundamental science”, arXiv:1511.07735
- [2] C. E. Calosso, E. Bertacco, D. Calonico, C. Clivati, G. A. Costanzo, M. Frittelli, F. Levi, S. Micalizio, A. Mura, A. Godone, “Doppler-stabilized fiber link with 6 dB noise improvement below the classical limit”, *Opt. Lett.* 40, No. 2, 131 (2015).
- [3] C. E. Calosso, E. Bertacco, D. Calonico, C. Clivati, G. A. Costanzo, M. Frittelli, F. Levi, A. Mura, A. Godone, “Frequency transfer via a two-way optical phase comparison on a multiplexed fiber network”, *Opt. Lett.* 39 No.5, 1177-1180 (2014).
- [4] C. Clivati, A. Mura, D. Calonico, F. Levi, G. A. Costanzo, C. E. Calosso, A. Godone, “Planar-Waveguide External Cavity Laser Stabilization for an Optical Link with 10⁻¹⁹ Frequency Stability”, *IEEE Trans. Ultrason. Ferroelectr. Freq. Contr.*, 58, 2582-2587 (2011),
- [5] C. W. Chou, D. B. Hume, J. C. J. Koelemeij, D. J. Wineland, T. Rosenband, “Frequency Comparison of Two High-Accuracy Al⁺ Optical Clocks”, *Phys. Rev. Lett.* 104, 070802 (2010).
- [6] C. E. Calosso, E. K. Bertacco, D. Calonico, F. Levi, S. Micalizio, A. Mura *et al.*, “Tracking DDS for Coherent Optical Links”, *Proc. European Frequency and Time Forum & International Frequency Control Symposium (EFTF/IFC) 2013 Joint*, p. 885-888, Prague, 21-25 July 2013.
- [7] www.redpitaya.com
- [8] A. C. Cárdenas-Olaya, E. Rubiola, J.-M. Friedt, M. Ortolano, S. Micalizio, C. E. Calosso, “Simple Method for ADC Characterization under the Frame of Digital PM and AM Noise Measurement”. *Proc. 2015 Joint Conference of the IEEE International Frequency Control Symposium & the European Frequency and Time Forum*, p. 676-680, Denver, 12-16 April 2015.
- [9] F. Levi, D. Calonico, A. Mura, M. Frittelli, C.E. Calosso, M. Zucco *et al.*, “LIFT-the Italian link for time and frequency”, *European Frequency and Time Forum & International Frequency Control Symposium (EFTF/IFC) 2013 Joint*, p. 477-480, Prague 21-25 July 2013.

Frequency tripled 1.5 μm telecom laser diode stabilized to iodine hyperfine line in the 10^{-15} range

Charles Philippe¹, Rodolphe Le Targat¹, David Holleville¹, Michel Lours¹, Tuan Minh-Pham²,
Jan Hrabina², Frederic Du Burck³, Peter Wolf¹ and Ouali Acef¹
Email: charles.philippe@obspm.fr

¹LNE-SYRTE, Observatoire de Paris, PSL Research Univ., CNRS, Sorbonne Univ., UPMC Univ. Paris 06, 75014 Paris, France

²Institute of Scientific Instruments, Czech Academy of Sciences, Brno, Czech Republic

³Laboratoire de Physique des Lasers, Université Paris 13, Sorbonne Paris Cité, 93430 Villetaneuse, France

Abstract— We report on telecom laser frequency stabilization to narrow iodine hyperfine line in the green range of the optical domain, after a frequency tripling process using two nonlinear PPLN crystals. We have generated up to 300 mW optical power in the green ($P_{3\omega}$), from 800 mW of infrared power (P_{ω}). This result corresponds to an optical conversion efficiency $\eta = P_{3\omega}/P_{\omega} \sim 36\%$. To our knowledge, this is the best value ever demonstrated for a CW frequency tripling process. We have used a narrow linewidth iodine hyperfine line (component a_1 of the $^{127}\text{I}_2$ R 35 (44-0) line) to stabilize the IR laser yielding to frequency stability of $4.8 \times 10^{-14} \tau^{-1/2}$ with a minimum value of 6×10^{-15} reached after 50 s of integration time. The whole optical setup is very compact and mostly optically fibered. This approach opens the way for efficient and elegant architecture development for space applications as one of several potential uses.

Keywords—Optical frequency standards, measurement and metrology, Lasers, Laser stabilization, Visible lasers, Harmonic generation and mixing, High resolution spectroscopy.

I. INTRODUCTION

Coherent and powerful continuous wave (CW) lasers in the visible are widely needed for various applications such as laser cooling, medicine diagnostics, underwater optical communications, high resolution spectroscopy, etc. [1-5]. On the other hand, IR lasers, emitting around 1 μm , are currently proposed for many space applications such as gravitational wave detection, inter-satellites or ground to space optical communications, earth observations, etc. [6-8]. Nowadays, these lasers are successfully frequency stabilized against iodine transitions in the green, after frequency doubling process [8-9]. However, the optical setups devoted to these space applications are developed in free space configurations.

In this paper, we describe a new approach combining the use of frequency tripled Telecom laser sources (TLS) operating in the 1.5 μm range and one from thousands of narrow iodine hyperfine lines existing in the green part of the visible spectrum for the frequency stabilization purpose. Compared to other IR laser sources, the TLS exhibit unprecedented intrinsic phase noise before any electronic feedback (linewidth \sim kHz) associated to extremely small volume (\sim cm³) and optically fibered mode operation. On the other hand, iodine lines in the

green range of visible domain have remarkable quality factor ($Q > 2 \times 10^9$) [10], achievable with simple and compact experimental interrogation configurations.

II. EFFICIENT FREQUENCY TRIPLING PROCESS

Third harmonic generation (THG) of CW infrared lasers has been demonstrated in only few cases, with very poor efficiency $P_{3\omega}/P_{\omega}$ [11, 12]. In early 2002, a first attempt to observe iodine lines via a THG of a telecom laser has been described using two second order nonlinear processes in a unique crystal [13]. The two processes were operated in a single periodically poled Lithium Niobate crystal (PPLN) allowing a green power generation at level of few tens of nW. The associated optical conversion from IR to green $\eta = P_{3\omega}/P_{\omega}$ is in the range of $10^{-5}\%$. The main limitation is due to the difficulty to fulfill the quasi phase matching conditions for SHG and SFG simultaneously in the same nonlinear crystal. Recently, higher efficiency has been demonstrated at level of $\eta = P_{3\omega}/P_{\omega} = 0.25\%$, corresponding to 1.5 mW generated green light, with two independent crystals used to fulfill two cascaded second order steps: ($\omega + \omega \rightarrow 2\omega$) followed by ($\omega + 2\omega \rightarrow 3\omega$) [14].

Following this demonstration, we propose a new optical architecture using two fibered waveguide PPLN nonlinear crystals described in more details in ref. [15]. We utilize two optically fibered waveguide Zn doped PPLN crystals to achieve a second harmonic process (SHG) followed by a sum frequency generation (SFG) in an original optical arrangement as depicted in Fig. 1. We generate up to $P_{3\omega} = 300$ mW at 514 nm using $P_{\omega} = 200$ mW associated to red power $P_{2\omega} = 330$ mW achieved independently from PPLN1 with 600 mW at ω . Consequently, this maximum output green power was obtained from 0.8 W total IR power at 1.542 μm , corresponding to an optical conversion efficiency $\eta = P_{3\omega} / P_{\omega} \sim 36\%$. During our measurements, synthesized in Fig. 2, the total optical power incident onto the SFG crystal ($P_{\omega} + P_{2\omega}$) was intentionally limited to ~ 0.5 W in order to avoid possible optical damage. This new setup including the laser diode, the EDFA and all needed fibered optical components occupy a total volume of 4.5 liters

This work is supported by: Agence Nationale de la Recherche (ASTRID program ANR 11 ASTR 001 01), Labex FIRST-TF, Délégation Générale de l'Armement (DGA), SATT Lutech and AS-GRAM (CNRS/INSU).

C. Philippe PhD thesis is co-funded by Centre National d'Etudes Spatiales (CNES) and SODERN.

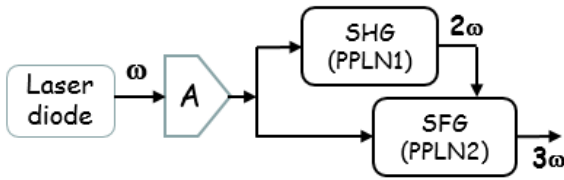


Fig. 1. Principle of the THG setup using two cascaded PPLN crystals: $(\omega + \omega \rightarrow 2\omega) + (\omega + 2\omega \rightarrow 3\omega)$. A= Erbium Doped Optical Fibre Amplifier, PPLN1 = Optical fibered PPLN crystal for SHG operation, PPLN2=optical fibered PPLN crystal for SFG operation.

The IR laser source used in this work is a butterfly type, narrow linewidth laser diode (linewidth ~ 2 kHz, power ~ 10 mW) followed by an erbium doped optical amplifier (EDFA) delivering up to 1 W over the full C band of the telecom range. All optical fibers, splitters and optical isolators used in this setup are polarization maintaining devices. Two homemade electronic control devices are used to fulfill in easy way the phase matching temperature conditions within 5 mK.

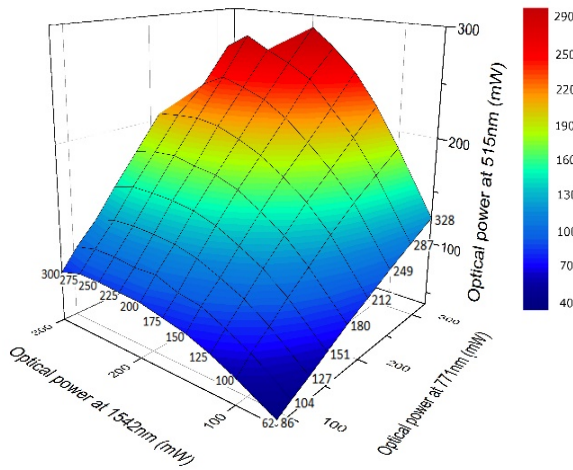


Fig. 2. Evolution of the generated green power (514 nm) versus variations of the red (771 nm) and the IR (1542 nm) powers.

III. FREQUENCY STABILIZATION SETUP

We use the well-known saturated absorption approach associated to the modulation transfer technique to frequency stabilize the 1.542 μm laser diode against an iodine hyperfine line in the green (Fig. 3). We have used the a_1 hyperfine component of the R 35 (44-0) $^{127}\text{I}_2$ line [16] at ~ 514.017 nm for a preliminary frequency stabilization evaluation.

The pump beam (respectively probe beam) is frequency shifted by 79 MHz (resp. 80 MHz) with acousto-optic modulators. A low frequency modulation (220 kHz) is applied to the pump beam thanks to an electro-optic modulator to detect the atomic saturation signal. The two optical laser beams of diameter ~ 2 mm are carefully collimated and overlapped in the 20 cm long iodine cell. The interaction length is extended up to 1.2 m thanks to 6 successive optical passes in the cell. Both internal and external faces of the cell windows are antireflection coated in the green [17]. The quartz cell is filled with highly pure iodine in Institute of Scientific Instruments in Czech Republic.

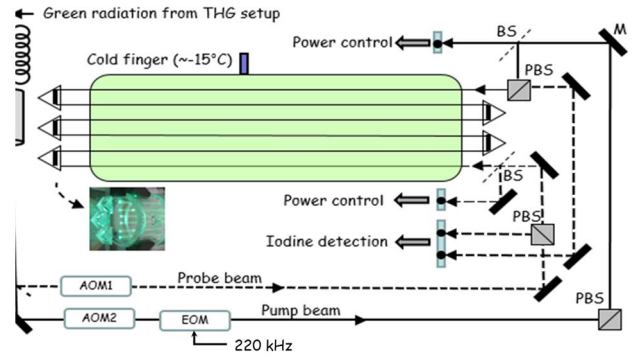


Fig. 3. Iodine stabilization optical setup. BS: beam splitter, M: Mirror, AOM: Acousto-optic modulator, EOM: electro-optic modulator, PBS: polarizing beam splitter.

The saturated absorption signal is detected by a balanced silicon photodiode. A part of the probe beam is split off before propagating in the cell in order to eliminate common noise of the laser probe beam. The probe and pump powers are stabilized with signals detected with two independent photodiodes. An additional photodiode (not shown in fig. 3) is used for a permanent control of the residual amplitude modulation (RAM) associated to the phase modulation of the pump beam. The cold finger temperature of the cell is regulated around -15°C within 1.5 mK as presented in Fig. 4, using a homemade electronic PID controller. The corresponding vapor pressure in the cell is estimated about 1 Pa.

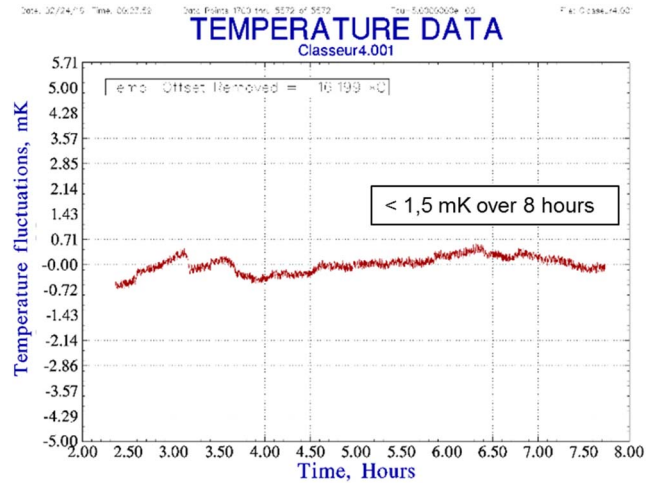


Fig. 4. Evolution of the cold finger temperature fluctuations over 8 hours

IV. FREQUENCY STABILITY MEASUREMENT

An independent stable frequency reference laser (FRL) is utilized to fulfill the frequency stability measurement of our 1.5 μm / iodine optical frequency standard. The FRL is based on another IR laser source frequency locked to an ultra-stable optical cavity described elsewhere [18]. It is located in a separate building and is connected to our experiment by a 200 meters optical fiber link, as seen in Fig. 5. During this preliminary measurement the frequency noise of this optical link was not

compensated, because its contribution together with the reference cavity instability exhibit an Allan deviation at level of $\sim 10^{-15}$ over the full integration time measurement. Subsequently, the frequency stability evaluation of our iodine stabilized laser is not affected. The beat note between our iodine frequency stabilized laser and the reference laser exhibits a linewidth smaller than 5 kHz (Fig. 5).

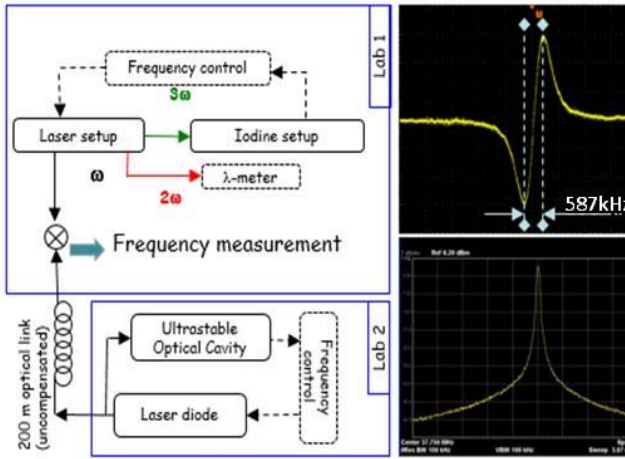


Fig. 5. Optical setup arrangement developed for the frequency stabilization measurement. Top right figure shows the line utilized to stabilize the laser. It corresponds to the a_1 hyperfine component of the R 35 (44-0) $^{127}\text{I}_2$ line at 514.017 nm. The figure bottom right reports the beat note in the infrared between the reference and the stabilized lasers (width ~ 5 kHz).

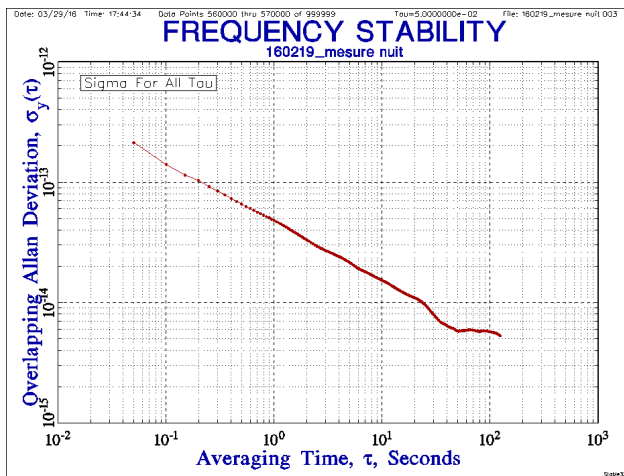


Fig. 6. Frequency stability of the iodine stabilized 1542 laser diode.

Fig. 6 reports the preliminary frequency stability measurement of the iodine stabilized laser diode. It shows an Allan deviation decreasing with a slope of $4.8 \times 10^{-14} \tau^{-1/2}$ with a minimum value of 6×10^{-15} for 50 s of integration time. During these preliminary measurements the residual amplitude modulation (RAM) was not compensated and could explain the behavior of the frequency stability observed for $\tau > 50$ s.

V. CONCLUSION

We have developed a compact and fibered optical setup for the generation of an intense continuous radiation (300 mW) in the green from 800 mW of IR. We have demonstrated the possibility of detecting very narrow transitions of molecular iodine around 514 nm and consequently the possibility to stabilize the laser diode frequency. Frequency stability in the range of 10^{-15} was demonstrated using a small part of the green power (< 10 mW).

REFERENCES

- [1] A. Hemmerich, D.H. McIntyre, D. Schropp Jr., D. Meschede, T.W. Hänsch, "Optically stabilized narrow linewidth semiconductor laser for high resolution spectroscopy", Optics Comm., Vol. 75, Issue 2, 15 February 1990, Pages 118-122
- [2] J. G. Fujimoto, C. Pitris, S. A. Boppart and M. E. Brezinski, "Optical Coherence Tomography: An Emerging Technology for Biomedical Imaging and Optical Biopsy", (2000) Neoplasia, Volume 2, Issue 1, 9 – 25.
- [3] F. Hanson, and St. Radic, High bandwidth underwater optical communication, Appl. Opt. 47(2), 277-283 (2008).
- [4] J. L. Hall, Nobel Lecture: Defining and measuring optical frequencies, Rev. Mod. Phys. 78, 1279-1294 (2006).
- [5] B. Woodward, & H. Sari, "Underwater speech communications with a modulated laser", Appl. Phys. B 91, 189–194 (2008).
- [6] Missions P. L. Bender, J. L. Hall, J. Ye, W.M. Klipstein, "Satellite-Satellite Laser Links for Future Gravity missions", Space Science Reviews July 2003, Volume 108, Issue 1, pp 377-384.
- [7] M. Shao and D. H. Staelin, "Long- baseline optical interferometer for astrometry", Journal of the Optical Society of America Vol. 67, Issue 1, pp. 81-86 (1977).
- [8] K. Doringshoff, K. Mohle, M. Nagel, E. V. Kovalchuk, A. Peters, "High performance iodine frequency reference for tests of the LISA laser system," in Proceedings of EFTF-2010 24th European Frequency and Time Forum pp.1-6, 13-16 April 2010, and references therein.
- [9] E. J. Zang, J. P. Cao, Y. Li, C. Y. Li, Y. K. Deng, and C. Q. Gao, "Realization of Four-Pass I2 Absorption Cell in 532-nm Optical Frequency Standard", IEEE Trans. on Instrum. And Meas. V. 56, N°. 2, April 2007.
- [10] W.-Y. Cheng, L. Chen, T. H. Yoon, J. L. Hall, and J. Ye, Sub-Doppler molecular-iodine transitions near the dissociation limit (523–498 nm), Opt. Lett. 27(8), 571-573 (2002).
- [11] B. Corcoran, C. Monat, C. Grillet, D. J. Moss, B. J. Eggleton, T. P. White, L. O'Faolain, and T. F. Krauss, "Green light emission in silicon through slow-light enhanced third harmonic generation in photonic-crystal waveguides", Nat. Photonics 3, 206 (2009).
- [12] S. Sederberg and A. Y. Elezzabi, "Coherent Visible-Light-Generation Enhancement in Silicon-Based Nanoplasmonic Waveguides via Third-Harmonic Conversion", Phys. Rev. Lett. 114, 227401 –June 2015
- [13] R. Klein and A. Arie, Observation of iodine transitions using the second and third harmonics of a 1.5- μm laser, Appl. Phys. B 75, 79-83 (2002).
- [14] N. Chiodo, F. Du-Burck, J. Hrabina, M. Lours, E. Chea, and O. Acef, Optical phase locking of two infrared continuous wave lasers separated by 100 THz, Opt. Lett., 39(10), 2936-2939 (2014).
- [15] C. Philippe, To be published
- [16] S. Gerstenkorn, and P. Luc, Atlas du spectre d'absorption de la molécule d'iode, Editions du C.N.R.S., Paris, France, 1978.
- [17] J. Hrabina, M. Šarbot, O. Acef, F. Du Burck, N. Chiodo, M. Holá, O. Číp O, J. Lazar, "Spectral properties of molecular iodine in absorption cells filled to specified saturation pressure", Appl Opt. 53(31):7435-7441, Nov. 2014.
- [18] B. Argence, E. Prevost, T. Leveque, R. Le Goff, P. Lemonde, S. Bize and G. Santarelli, "Prototype of an ultra-stable optical cavity for space applications » Optics Express 20 (23) pp. 25409-25420 (2012).

Metrological Characterization Of INRIM's Yb Lattice Clock

Benjamin Rauf*[†], Marco Pizzocaro*, Pierre Thoumany*, Gianmaria Milani*[†], Filippo Bregolin*[†], Michele Gozzelino*, Davide Calonico*, Giovanni Antonio Costanzo*, Cecilia Clivati* and Filippo Levi*

*Istituto Nazionale di Ricerca Metrologica (INRIM), Physical Metrology Division

Strada delle Cacce 91, 10135 Torino, Italy

Email: b.rauf@inrim.it

[†]Politecnico di Torino, Dipartimento di Elettronica e Telecomunicazioni

C.so duca degli Abruzzi 24, 10125 Torino, Italy

Abstract— We present the results of a preliminary metrological characterization of our neutral ^{171}Yb -atoms lattice clock at INRIM. During one clock cycle we cool and trap the atoms utilizing 399 nm laser light for the first stage magneto-optical trap (MOT), followed by a cooler 556 nm 2nd stage MOT. Atoms are then transferred in a one-dimensional, horizontal lattice adjusted to the magic wavelength (759 nm). Subsequently the clock transition at 578 nm is excited by a laser stabilized to an ultra-stable cavity, followed by repumping and state-detection. We obtain $2 \cdot 10^3$ atoms in the lattice after 150 ms of loading time. The laser radiation at 399 nm, 556 nm and 578 nm is produced via infrared lasers and non-linear crystals, whereas the lattice features a Titanium-Sapphire laser. A detailed description of the laser light generation and stabilization as well as of the physics package is given. We locked the clock laser to the atoms and achieved a first metrological characterization through optical fiber-comb based comparison with INRIM's primary frequency standard, the IT-CsF2 cryogenic fountain clock [1]. The reported frequency of the clock transition agrees to the value recommended by the BIPM [2] within the stated uncertainty.

I. INTRODUCTION

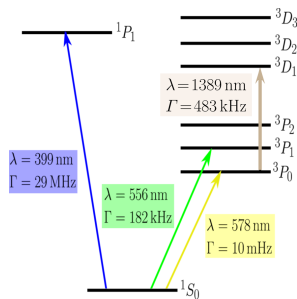


Fig. 1. The relevant atomic transitions in Yb for clock operation

and therefore long-living $^1S_0 \rightarrow ^3P_0$ transition in neutral ^{171}Yb . The relevant atomic levels and transitions for cooling, trapping and interrogation of Yb are shown in Fig. 1. The fermionic ^{171}Yb isotope has a nuclear spin of $I=1/2$ leading to a hyperfine structure which makes it an interesting candidate not only as frequency standard, but also for quantum computing and quantum simulation. It's sensitivity to possible variations of the fine-structure constant make it also an interesting proposal for fundamental science. We are

In recent years atomic clocks based on optical transitions in ions or neutral atoms have surpassed the current standard for the SI-second, Cesium fountain clocks, by more than one order of magnitude in accuracy as well as in stability [3] and have therefore been recognised by the BIPM [2] as secondary representations of the second. Among these atomic frequency standards is the spin and angular-momentum forbidden

$^1S_0 \rightarrow ^3P_0$ transition in neutral ^{171}Yb . The relevant atomic levels and transitions for cooling, trapping and interrogation of Yb are shown in Fig. 1.

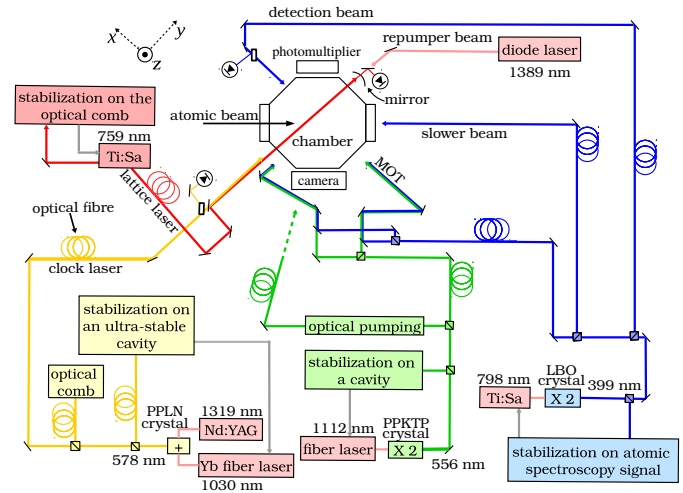


Fig. 2. Drawing of the vacuum chamber and optical composition

operating a ^{171}Yb based optical clock in the laboratories of INRIM. The cooling takes place in a two-stage MOT that utilizes the strong (linewidth 29 MHz) $^1S_0 \rightarrow ^1P_1$ transition at 399 nm for trapping and the weaker $^1S_0 \rightarrow ^3P_1$ transition (linewidth 182 kHz) subsequently cooling further down the atoms to few microkelvins. The atoms are then transferred to an optical lattice operating at the 759 nm magic wavelength. Excitation of the 578 nm $^1S_0 \rightarrow ^3P_0$ clock-transition with a natural lifetime of more than 100 s is reversed by exploiting repumping through driving of the $^3P_0 \rightarrow ^3D_1$ 1389 nm (linewidth 483 kHz) transition. With the experimental setup completed we have obtained locking on the spin-polarized clock transition and, by comparing to INRIM's IT-CsF2 Cs atomic fountain clock, received a preliminary characterization of our clock.

II. EXPERIMENTAL SETUP

A. Physics package

Fig. 2 displays the vacuum chamber and its surrounding optical assembly for atomic spectroscopy. The atoms are emitted in a collimated beam by an effusion oven (Temperature 400°C). Instead of implementing a Zeeman-slower for maximum capture efficiency here the distance between atoms source

and trapping chamber is kept minimal for increased atomic flux. The atoms are trapped inside the custom aluminum chamber designed for wide optical access with indium-sealed viewports. 10 thermistors are distributed all over the chamber for precise blackbody-shift evaluation and it is being kept at ultra-high vacuum (pressure $< 10^{-9}$ mbar) by two ion pumps and one non-evaporable getter pump. The MOT coils are vertically arrayed outside the vacuum chamber. Three pairs of Helmholtz coils are compensating the stray magnetic field.

B. Laser ensemble

All lasers are spatially separated from the vacuum chamber and are delivered to it by means of polarization-maintaining (PM) optical fibers. The radiation at 399 nm acting on the $^1S_0 \rightarrow ^1P_1$ transition is produced via 2nd harmonic generation (SHG) from a 798 nm Titanium-Sapphire (Ti:Sa) laser by means of a nonlinear lithium-triborate (LBO) crystal inside an enhancement cavity [4]. The Ti:Sa laser delivers an output power of about 1.1 W with an 8 W solid state pump laser at 532 nm with the typical total power of 399 nm radiation set to 0.5 W. The laser is locked to the $^1S_0 \rightarrow ^1P_1$ transition through transverse spectroscopy of an auxiliary atomic beam. The 2nd stage MOT and the spin-polarizing beam are generated via SHG of an amplified 1112 nm Yb-doped fiber laser passing through a single-pass periodically-poled potassium titanyl phosphate (PPKTP) crystal. About 10 mW of 556 nm radiation are obtained from 1.0 W of infrared light. The laser is referenced to a stable cavity made out of Corning Ultra-Low Expansion glass (ULE). About 1 W of lattice power is provided by a Ti:Sa laser with an initial output of about 2 W. The 578 nm laser acting upon the clock transition is generated by sum-frequency-generation (SFG) in a waveguide periodically-poled lithium niobate (PPLN) crystal combining the 1319 nm emission line of a neodymium-doped yttrium aluminium garnet (Nd:YAG) laser with an erbium fiber laser at 1030 nm [5]. The generated 578 nm radiation amounts to about 7 mW. The frequency is actively stabilized employing the Pound-Drever-Hall (PDH) method on a 10 cm ultra-stable ULE cavity featuring fused-silica mirrors with ULE compensation rings. The cavity is equipped with a two-stage temperature control using Peltier elements to keep the cavity at the point of vanishing coefficient of thermal expansion (zero CTE). The temperature control system is a digital implementation of the Active Disturbance Rejection Control (ADRC) technique [6]. The radiation is distributed by means of phase-noise cancelled PM optical fiber links with one path going to the ultra-stable cavity, one to the vacuum chamber for spectroscopy and one to a fiber-based optical comb for comparison with the IT-CsF2 SI-second standard. The repumper laser is a commercial pigtail distributed feedback laser emitting at 1389 nm. The output beam focused on the atoms contains 10 mW of light power, broadening the $^3P_0 \rightarrow ^3D_1$ transition to 300 MHz, while having a frequency stability better than 100 MHz. Therefore active frequency stabilization is not required.

C. Clock cycle

During a single spectroscopy cycle we use around 150 ms of time for cooling and trapping followed by another 100 ms of clock-transition spectroscopy and detection. First atoms are slowed down by counter-propagating a 399 nm light beam

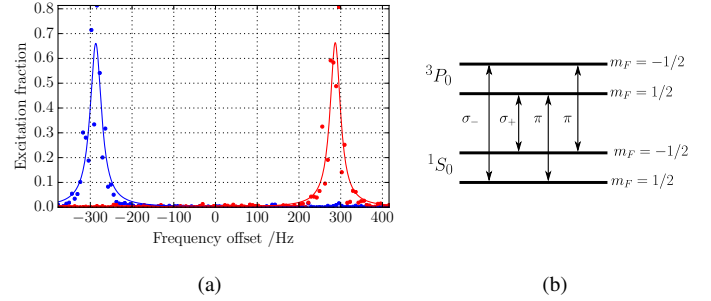


Fig. 3. a) Scan of the clock transition in the presence of a magnetic field with spin-polarization to the $m_F = -1/2$ (red) or $m_F = +1/2$ (blue) hyperfine state b) The hyperfine structure of the $^1S_0 \rightarrow ^3P_0$ transition in ^{171}Yb

(slower-beam), which is having a power of about 50 mW and a detuning from resonance of -360 MHz. We dispense of a varying magnetic field needed for a Zeeman-slower, but exploit the leaking field of the MOT coils. The six laser beams of the 1st stage MOT add up to about 30 mW of light power with an $1/e$ radius of 1 cm each and a detuning of -20 MHz. The magnetic field gradient is 0.4 T/m along the z-axis. The duration of slower and 1st stage MOT is 50 ms. The 2nd stage MOT at 556 nm is loaded from the blue MOT with up to 70% efficiency. The six green 2nd stage MOT laser beams amount to a total power of 2 mW with each having an $1/e$ radius of 0.5 cm. The green MOT is divided in three sub-stages with different frequencies and magnetic field gradients. The first stage (30 ms) is designed for maximum atoms transfer from the blue MOT, implementing a magnetic field gradient of 0.25 T/m. The following 2nd stage (20 ms) utilizes less red-shift and a reduced magnetic field gradient of 0.18 T/m to lower the atomic temperature further. The last stage MOT (10 ms and 0.25 T/m) then only serves to provide an enhanced transfer efficiency of atoms to the lattice. The lattice is formed by a horizontally aligned, retro-reflected and focused 759 nm beam. The laser power on the atoms reaches 1 W in a waist of $45 \mu\text{m}$. During on cycle we trap about $2 \cdot 10^3$ atoms with an atomic lifetime in the lattice of 2.7 s. Connected with a dimension of the trapping-area of estimated 0.5 mm we assume an occupation of 1.5 atoms per lattice site. Spin-polarization of the ground state with more than 98% efficiency is then applied by a vertically aligned 1 ms green pulse with a magnetic field of $4.12 \cdot 10^{-4}$ T along the same axis. Spectroscopy of the clock transition at 578 nm is executed by a $200 \mu\text{m}$ focused laser beam collinear to the lattice (laser power about 70 nW) with pulse durations between 50 ms and 100 ms. The resulting clock-level occupation is then determined with 3 resonant 399 nm probe pulses. The first one measures the atoms left in the ground state, the second one reveals the signal background from scattered light and excited hot background gas atoms. The repumper laser at 1389 nm (beam power 10 mW and duration 12 ms) subsequently pumps the excited atoms over the short-lived 3D_1 level back to the ground state, where they are detected by the third probe pulse.

III. RESULTS

A. Spectroscopy

Fig. 4 shows the spectra of a single scan over the spin-polarized clock-transition with a Full-Width-Half-Maximum

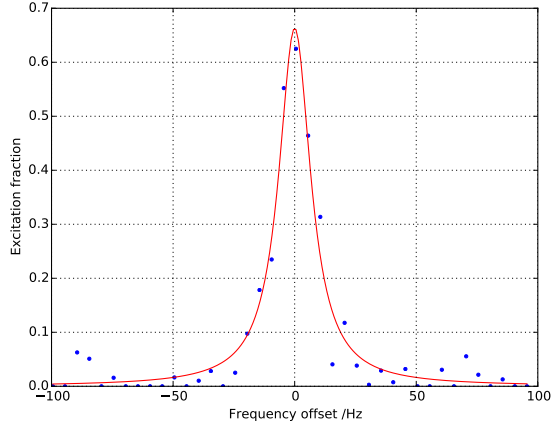


Fig. 4. A single scan (FWHM 16 Hz) over the spin-polarized resonance in the presence of a small magnetic field

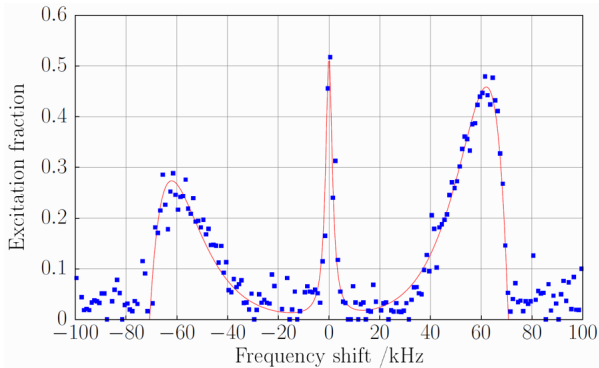


Fig. 5. From the frequency of the red-and blue-sideband's sharp edge the trap depth can be calculated, whereas their shape reveals the thermodynamic temperature and motional state distribution of the atoms

(FWHM) of 16 Hz. During clock-operation the line is typically between 20 Hz and 30 Hz FWHM. In Fig. 5 we observed the spectroscopic signal (blue dots) obtained by interrogation of $1 \cdot 10^4$ atoms in the lattice with 100 μ W of light power and a pulse duration of 100 ms. From the fit of the sidebands shape (red curve) we can deduce (for the details of the calculation see [7]) a horizontal trap frequency of 70 kHz corresponding to a trapping depth of 300 Er and an atomic temperature of 4.5 μ K. The effect of spin-polarization is shown in Fig. 3a) and a scheme of the clock-transition Zeeman-splitting in Fig. 3b).

In order to measure the clock transition frequency we apply a small vertical magnetic field at the position of the atoms, leading to a Zeeman-shift of ca. 300 Hz for each m_F substate.

B. Absolute Frequency Measurement

We obtain the frequency of the unshifted line by alternately locking to the $\pm 1/2$ spin-state. In this way the first order Zeeman-shift is sufficiently suppressed by averaging in our measurements. The clock laser is locked to each hyperfine-state atomic resonance by consecutive measurement and stabilization of the excitation fraction in equal distances on the left and right flanks of the transition. Therefore one full clock cycle consists out of four complete spectroscopic cycles and accordingly lasts about one second. We determined the

absolute frequency of our clock by using an optical frequency comb that is referenced to a H-maser. The maser on the other hand is being read by our IT-CsF2 fountain clock. We determined the magic wavelength by interleaving clock cycles with different lattice powers. The stability (Allan-deviation) of one of these measurements is shown in Fig. 6. The measured magic wavelength is 394798228(10) MHz. We determined the linear lattice light shift coefficient to $b = -0.0225(3)$ Hz/(GHz \cdot E $_r$), in agreement with previous results from other groups [8]. Hyperpolarizability effects were estimated by applying data from [9] and [10] to our situation. With 1.5 atoms per lattice site density shifts need careful evaluation. We determined the density shift by interleaving clock cycles with different blue MOT capture times (45 ms vs. 150 ms). The blackbody-radiation

(BBR) shift was calculated by applying the reading of the 10 thermistors to a simple model of the vacuum chamber consisting out of the oven, hot window and aluminum vacuum chamber. The chamber is taken into account as a thermistor-reading adequate environmental temperature with an uncertainty. The

Effect	Shift $\times 10^{-16}$
Zeeman	0.8
Collision	1
Blackbody	0.1
Microwave	1
Redshift	0.1
Total	2.4

TABLE I. IT-CsF2 UNCERTAINTY BUDGET

oven ($400 \pm 10^\circ\text{C}$) and hot window ($230 \pm 10^\circ\text{C}$) are modeled as BBR-sources within a certain irradiation angle, which is given by the dimensions of the stainless-steel-junctions to the aluminum chamber. This angle is expanded to an effective angle by including reflections inside the junctions. The greatest contribution to the BBR-shift uncertainty in this calculation originates from the hot window, since its effective angle has a high uncertainty. The first order Zeeman-shift is sufficiently suppressed by reason of averaging in our measurements. Nevertheless higher order effects do appear and need to be evaluated. The magnetic field induced separation of the two m_F states during our clock operation accounts typically to 300(10) Hz in our measurements. We take the results from [9] and apply them to our situation. We determine the magnetic field through the 1st order Zeeman-shift by using $\Delta_{B1} = \alpha_B \cdot B$ and $\alpha_B = 2.10 \cdot 10^3$ Hz/mT to obtain $B = 150(5)$ μ T. The 2nd order Zeeman effect is therefore, together with $\gamma_B = -7(1)$ Hz/mT 2 , given by: $\nu_{B2} = \gamma_B \cdot B^2 = 0.14(2)$ Hz or $2.8(4) \cdot 10^{-16}$ in relative units. The gravitational potential in respect to the geoid at the atoms position is 2336.48(27) m 2 /s 2 , as determined by a Global Navigation Satellite System/geoid approach [11]. This results in a redshift of 13.474(2) Hz or $2.5997(2) \cdot 10^{-14}$. The probe light shift was evaluated taking the sensitivity given in [12]. The current uncertainty evaluation of our Yb clock is given in Tab. II. For measuring the absolute frequency of our clock transition we used a working lattice frequency of 394798238 MHz and corrected the ac stark shift accordingly. Preliminary measurements agree with the recommended value established by the BIPM given the current measurement uncertainty. The uncertainty-budget of the Cs-fountain is given in Tab. I.

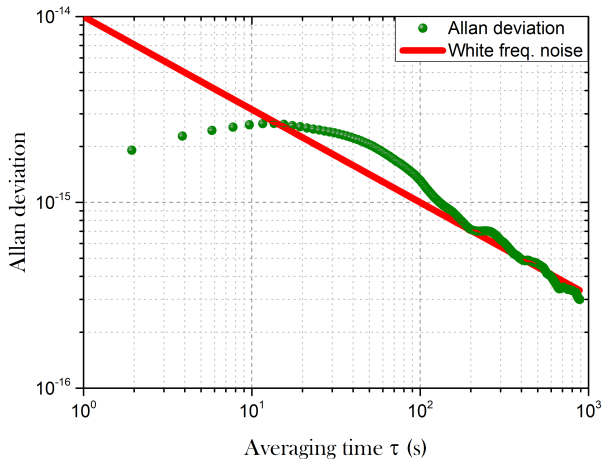


Fig. 6. Allan-deviation of an interleaved measurement featuring alternating low- and high-power lattice to determine the magic wavelength having a stability of about $1 \cdot 10^{-14}/\sqrt{\tau}$

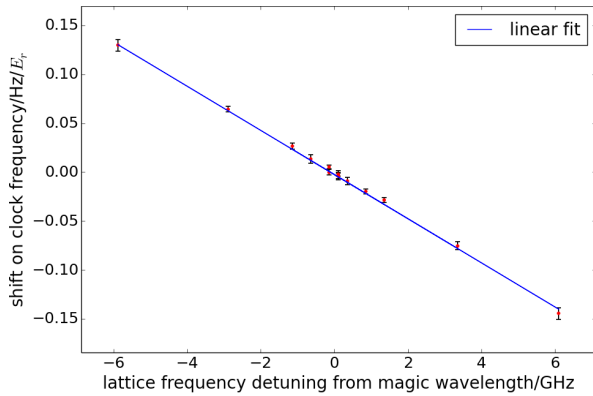


Fig. 7. Determination of magic wavelength. Each point was measured by interleaving high and low light power in the lattice beam. The linear lattice light shift sensitivity coefficient b results as $b = -0.0225(3) \text{ Hz}/(\text{GHz} \cdot E_r)$

IV. CONCLUSION

We have completed the Yb clock's physical setup and achieved highly efficient spin-polarization. The characterization of the clock has shown first promising results and a full absolute frequency measurement by comparison towards the IT-CsF2 fountain clock is under way with preliminary results agreeing to the BIPM-recommended value within the stated uncertainty. We have lately replaced the hot window with a cold intra-vacuum mirror. This enables us to reduce the BBR shift uncertainty into the 10^{-17} region and ultimately the full uncertainty below the 10^{-16} -level. We will also improve

Effect	Shift /Hz	Unc. /Hz	Shift $\times 10^{-16}$	Unc. $\times 10^{-16}$
Quadratic Zeeman shift	-0.14	0.02	-2.8	0.4
Lattice Polarizability	-0.16	0.06	3.1	1.2
Hyperpolarizability	0.06	0.02	1.2	0.3
Blackbody shift	-3.2	0.3	-62	6.0
Collisional shift	0.01	0.09	0.2	1.7
Probe light shift	0.0027	0.0012	0.05	0.02
Gravitational red shift	13.474	0.002	259.97	0.02
Total	10.1	0.3	200	6.4

TABLE II. PRELIMINARY UNCERTAINTY BUDGET FOR THE YB LATTICE CLOCK

our clock laser to raise stability. Our clock will take part in remote as well as local comparisons with other optical clocks within the ITOC (International Timescales with Optical Clocks) project and in stable reference signal distribution via the national fiber link developed under AQUASIM (Advanced Quantum Simulation and Metrology).

ACKNOWLEDGMENT

The authors acknowledge funding from the EMRP Project SIB55-ITOC, MIUR Project PRIN2012 AQUASIM and ITN Marie Curie Project FACT. The EMRP is jointly funded by the EMRP participating countries within EURAMET and the European Union.

REFERENCES

- [1] F. Levi, D. Calonico, C. E. Calosso, A. Godone, S. Micalizio, and G. A. Costanzo, "Accuracy evaluation of itsf2: a nitrogen cooled caesium fountain," *Metrologia*, vol. 51, no. 3, p. 270, 2014. [Online]. Available: <http://stacks.iop.org/0026-1394/51/i=3/a=270>
- [2] BIPM, *The International System of Units (SI)*, 8th ed. BIPM, 2006.
- [3] I. Ushijima, M. Takamoto, M. Das, T. Ohkubo, and H. Katori, "Cryogenic optical lattice clocks," *Nat Photon*, vol. 9, no. 3, pp. 185–189, Mar. 2015. [Online]. Available: <http://dx.doi.org/10.1038/nphoton.2015.5>
- [4] M. Pizzocaro, D. Calonico, P. C. Pastor, J. Catani, G. A. Costanzo, F. Levi, and L. Lorini, "Efficient frequency doubling at 399 nm," *Appl. Opt.*, vol. 53, no. 16, pp. 3388–3392, Jun 2014. [Online]. Available: <http://ao.osa.org/abstract.cfm?URI=ao-53-16-3388>
- [5] M. Pizzocaro, G. A. Costanzo, A. Godone, F. Levi, A. Mura, M. Zoppi, and D. Calonico, "Realization of an ultrastable 578-nm laser for an Yb lattice clock," *IEEE Trans. Ultrason., Ferroelect., Freq. Cont.*, vol. 59, no. 3, pp. 426–431, march 2012.
- [6] M. Pizzocaro, D. Calonico, C. Calosso, C. Clivati, G. A. Costanzo, F. Levi, and A. Mura, "Active disturbance rejection control of temperature for ultrastable optical cavities," *IEEE Trans. Ultrason., Ferroelect., Freq. Cont.*, vol. 60, no. 2, pp. 273–280, february 2013.
- [7] S. Blatt, J. W. Thomsen, G. K. Campbell, A. D. Ludlow, M. D. Swallows, M. J. Martin, M. M. Boyd, and J. Ye, "Rabi spectroscopy and excitation inhomogeneity in a one-dimensional optical lattice clock," *Phys. Rev. A*, vol. 80, p. 052703, Nov 2009. [Online]. Available: <http://link.aps.org/doi/10.1103/PhysRevA.80.052703>
- [8] Z. W. Barber, J. E. Stalnaker, N. D. Lemke, N. Poli, C. W. Oates, T. M. Fortier, S. A. Diddams, L. Hollberg, C. W. Hoyt, A. V. Taichenachev, and V. I. Yudin, "Optical lattice induced light shifts in an Yb atomic clock," *Phys. Rev. Lett.*, vol. 100, p. 103002, Mar 2008. [Online]. Available: <http://link.aps.org/doi/10.1103/PhysRevLett.100.103002>
- [9] N. D. Lemke, A. D. Ludlow, Z. W. Barber, T. M. Fortier, S. A. Diddams, Y. Jiang, S. R. Jefferts, T. P. Heavner, T. E. Parker, and C. W. Oates, "Spin-1/2 optical lattice clock," *Phys. Rev. Lett.*, vol. 103, no. 6, p. 063001, Aug 2009.
- [10] N. Nemitz, T. Ohkubo, M. Takamoto, I. Ushijima, M. Das, N. Ohmae, and H. Katori, "Frequency ratio of yb and sr clocks with 51017 uncertainty at 150seconds averaging time," *Nat Photon*, vol. advance online publication, pp. –, Feb. 2016. [Online]. Available: <http://dx.doi.org/10.1038/nphoton.2016.20>
- [11] H. Denker, C. Voigt, and L. Timmen, "Private communication," 2016.
- [12] N. Poli, Z. W. Barber, N. D. Lemke, C. W. Oates, L. S. Ma, J. E. Stalnaker, T. M. Fortier, S. A. Diddams, L. Hollberg, J. C. Bergquist, A. Bruschi, S. Jefferts, T. Heavner, and T. Parker, "Frequency evaluation of the doubly forbidden $^1S_0 \rightarrow ^1P_3$ transition in bosonic ^{174}Yb ," *Phys. Rev. A*, vol. 77, no. 5, p. 050501, May 2008. [Online]. Available: <http://pra.aps.org/abstract/PRA/v77/i5/e050501>

System of formation of reference frequency for modern data conversion

Anatoly V. Kosykh, Konstantin V. Murasov, Sergey A. Zavyalov, Rodion R. Fakhrutdinov, Ruslan A. Wolf
 Omsk State Technical University
 Omsk, Russia.
 E-mail: avkosykh@omgtu.ru

Abstract— The paper presents reference frequency formation system implementation for modern data conversion systems in manufacturing process of 180 nm. The system is based on integer PLL, with VCO being tunable widely. The clock generator forms of nonoverlapping pulses used in ADC. A possibility of loop bandwidth filter program tuning permits usage of a broad frequency comparison range of a detector.

Keywords: VCO; PLL; CMOS; delay line oscillator; divider

I. INTRODUCTION

High speed analog to digital converters have been widely spread in the radio communication systems of complicated modulation types, different types of medical equipment, data acquisition and processing systems and so on lately. The increase of bit capacity of conversion and the number of converters on one crystal lead to a great increase in the number of outputs, required for parallel digital interfaces of data conversion realization. An alternative approach is based on implementation of high-speed serial interface, serving all ADC channels simultaneously. On the other hand implementing external clock source on several GHz frequencies is difficult. The most technological version of solution to the problem is placing high frequency clock signal forming unit directly on ADC crystal having external low frequency clock signal. The forming signals provide clock both of ADC and high-speed serial interface. Thermo-compensated and oven-controlled crystal oscillators, having greater frequency stability of clock signal and little phase noise level, are applied as an external source of reference frequency.

II. THE ARCHITECTURE OF THE SYSTEM

The architecture of PLL is shown in Fig. 1. The clock signal generated by external oscillator is buffered by an input buffer. The division coefficient of an input divider is assigned by loading the division coefficient in register *divP*. The value of charge pump unit current and filter configuration are programmed by loading the corresponding code in register *filt_prog*. The division coefficient of the output frequency VCO is assigned by loading the division coefficient in register *divN*.

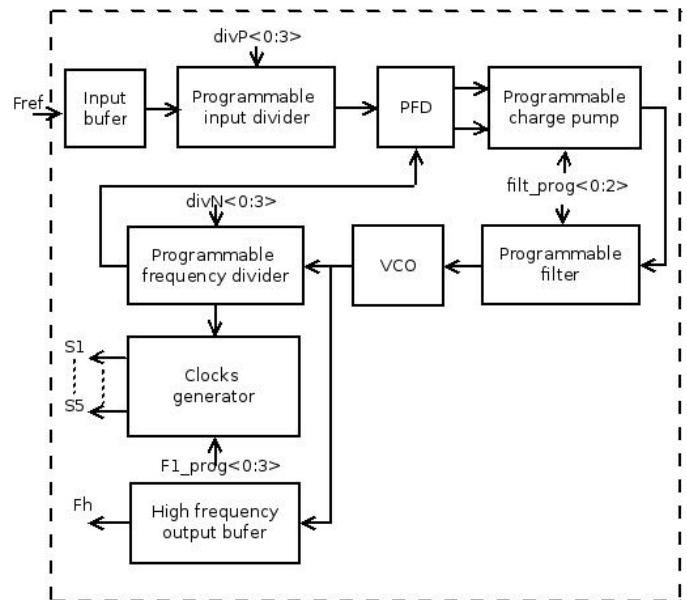


Fig. 1 PLL architecture

The clock signal generator forms the set of non-overlapping pulses used for ADC units to be clocked. A high frequency output buffer is used to minimize the effect of loading on VCO. An input for reference frequency signal and all output interfaces are designed according to a differential circuit.

III. THE VOLTAGE CONTROLLED OSCILLATOR

The manufacturing process being used possesses several constraints. In particular, an inductance coil is not available here. The usage of differential circuits of VCO [1] is restricted by frequency of 1,5 GHz that is a maximum accessible frequency for such VCOs. Therefore, using delay line VCOs also known as ring oscillators is favorable [2, 3]. The maximum frequency of such oscillator is defined by signal propagation delay through inverters. The maximum number of inverters is defined by the necessity to ensure maintenance of steady-state oscillations. Generally, not less than 5 inverters are used. The time required for switching from one mode to another is specified by recharging input and output capacitances of inverter transistors drains.

$$C_{in} = \frac{3}{2} C'_{ox} (W_p L_p + W_n L_n)$$

$$C_{out} = C'_{ox} (W_p L_p + W_n L_n)$$

$$C_{tot} = C_{in} + C_{out}$$

The time necessary for charging the resultant capacitance from 0 to V_o is specified by constant current I_{Dp} :

$$t_1 = C_{tot} \cdot \frac{V_o}{I_{Dp}}$$

The time needed for discharge of resultant capacitance from supply voltage up to V_o is determined by constant current I_{Dn} :

$$t_2 = C_{tot} \cdot \frac{VDD - V_o}{I_{Dn}}$$

Making currents $I_D = I_{Dp} = I_{Dn}$ equal, it is possible to determine the of inverter switching time:

$$t_1 + t_2 = \frac{C_{tot} \cdot VDD}{I_D}$$

The frequency of the annular generator is defined by the expression:

$$f_{osc} = \frac{I_D}{N \cdot C_{tot} \cdot VDD}$$

It is possible to control the frequency of the generator by controlling recharge current magnitude. The circuit of VCO is shown in Fig. 2.

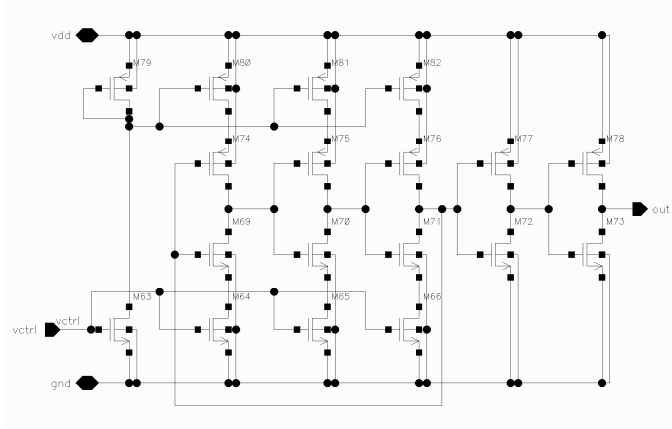


Fig. 2 Current-starved VCO

The annular VCO is designed on three inverters, their current being assigned by current sources. Current magnitude is defined by control voltage V_{GS} applied to input vctrl:

$$I_D = \frac{1}{2} \mu_n C_{ox} \frac{W}{L} (V_{GS} - V_{th})^2 (1 + \lambda V_{DS})$$

The output of VCO is buffered by the two in-series inverters. The dependence of VCO frequency on control voltage is shown in Fig. 3.

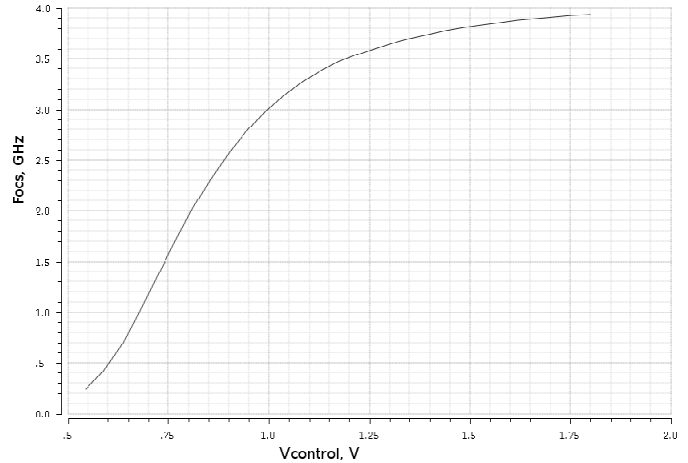


Fig. 3 VCO frequency dependence on control voltage

The output frequency changes in the range of 500 MHz to 3.85 GHz under the control voltage excursion from 600 mV to 1600 mV. The control characteristic is of quadratic character, this being explained by corresponding dependence of current on control voltage. The control characteristic in the middle of the control voltage range possesses slope of 4 GHz/V.

IV. THE PROGRAMMABLE CHARGE PUMP

Tuning the charge pump and filter system is required due to the control slope change of VCO and the change of the dividers division coefficients [4, 5]. The charge pump circuit is shown in Fig. 4.

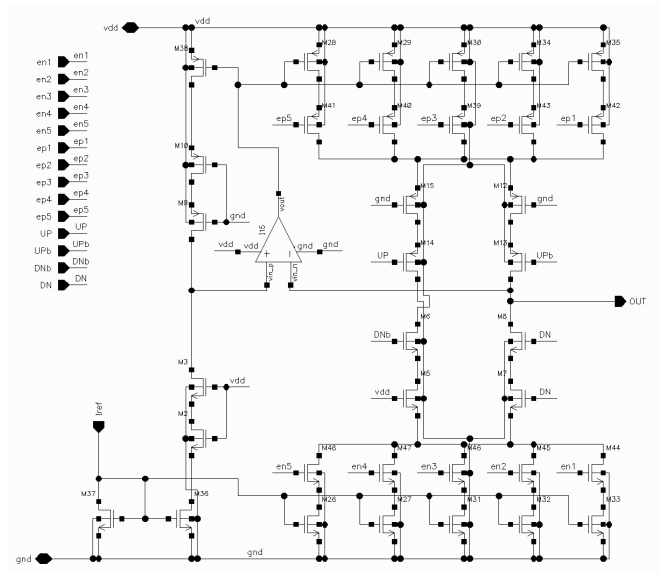


Fig. 4 Tuning circuit representation

The charge pump circuit is designed in the form of 5 bit binary weighted structure which consists of pluggable current

sources. The charge current can take 32 discrete values in the range of 20 uA to 640 uA. Charge pump current change linearity leads to the increase of loop filter tuning accuracy. The realization of the filter is shown in Fig. 5. Software-configurable filter resistance consists of parallel-series resistors of the same value. This enables to apply a matching technique in developing topological representation and, thus, to minimize the manufacturing tolerance of each resistance of the array.

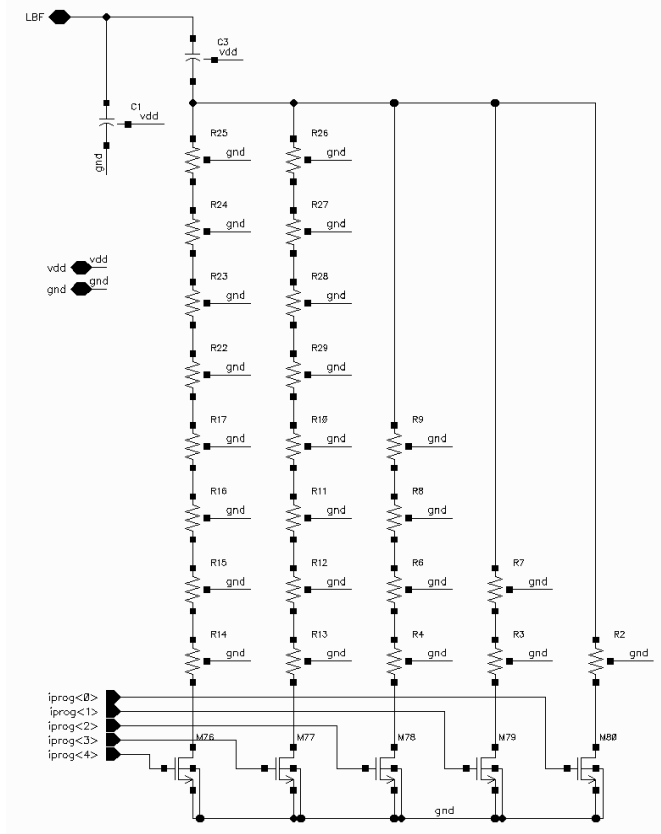


Fig. 5 Loop bandwidth filter

The loop filter resistance value is programmed depending on the set charge pump current value. The filter bandwidth is approximately defined by the expression:

$$\omega_{LBW} \approx R \cdot \frac{I_{CP}}{2\pi} \cdot \frac{K_{VCO}}{N}$$

where R - filter resistance, I_{CP} - charge pump current, N - common division coefficient of PLL.

V. PRACTICAL IMPLEMENTATION

The system of reference frequency formation for modern data conversion system has been implemented based on CMOS 180nm process. In Fig. 6 the fragment of the topology of the crystal containing the designed system is presented. The active area of system is 0.0726 mm^2 ($459 \times 495.4 \mu\text{m}^2$).

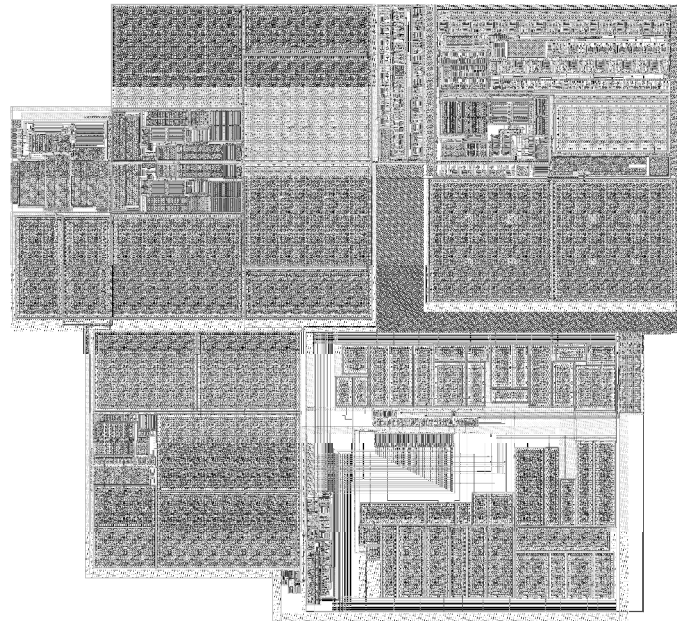


Fig. 6 System layout

VI. RESULTS

The developed system of reference frequency formation for modern data conversion based on PLL was used in the development of high resolution pipeline ADC. Current consumption of the unit does not exceed 4.5 mA. Supply voltage is 1.8 V. Frequency of the reference frequency external source can be within 10...128 MHz. The frequency divider of VCO can be programmed to values from 1...128. Phase-frequency detector frequency comparison can be done on frequencies from 625 kHz to 10 MHz. The output frequency setting time does not exceed 3 μs. The jitter value of an output signal of VCO does not exceed 2.1 ps. Clock signals of different relative pulse duration and non-overlapping areas, being essential for pipeline operation, are formed in output of a clocks generator unit (Fig. 1).

REFERENCES

- [1] A. Kral, F. Behbahani, and A. A. Abidi, "RF-CMOS oscillators with switched tuning," in Proc. IEEE Custom Integrated Circuits Conf., May 1998, pp. 555–558.
- [2] R. Jacob Baker, "CMOS Circuit Design, Layout, and Simulation. Third Edition", New Jersey, 1177 p., 2010.
- [3] B. Razavi, "RF Microelectronics. Second Edition", New York, 916 p., 2011.
- [4] J. Shin, H. Shin, "A 1.9–3.8 GHz Delta-Sigma Fractional-N PLL Frequency Synthesizer With Fast Auto-Calibration of Loop Bandwidth and VCO Frequency", *Proceedings, IEEE JOURNAL OF SOLID-STATE CIRCUITS*, VOL. 47, NO. 7, pp. 665 – 675, March. 2012.
- [5] F. M. Gardner, "Phaselock Techniques Third Edition." New York: John Wiley & Sons Inc., 2005.

Transparent thin film bulk acoustic wave resonators

Mario DeMiguel-Ramos, Girish Rughoobur and
Andrew Flewitt

EDM, Electrical Engineering Division, Department of
Engineering
University of Cambridge
Cambridge, UK
md647@cam.ac.uk

Teona Mirea, Bárbara Díaz-Durán, Jimena Olivares,
Marta Clement and Enrique Iborra

GMME-CEMDATIC, ETSI de Telecomunicación
Universidad Politécnica de Madrid
Madrid, Spain

Abstract— Transparent electronic devices have interesting applications in a wide range of fields, such as wearables, intelligent windows, new concepts of smartphones and sensors. In this work we present fully transparent AlN-based thin film bulk acoustic wave solidly mounted resonators. We have used indium-tin oxide as the transparent material for the electrodes and a transparent acoustic reflector consisting of alternating layers of SiO₂ and Ta₂O₅ or WO₃, to ensure an adequate acoustic confinement while keeping a high transparency. The fabricated devices display an electromechanical coupling coefficient up to 4% and a quality factor Q of 100. The measured transmittance in the visible spectrum (450 – 750 nm) is 75%.

Keywords— *Transparent electronics; AlN BAW resonator; SMR; acoustic reflector*

I. INTRODUCTION

Transparent electronic devices have become increasingly popular in the last few years. They have interesting applications in a wide range of areas, such as wearables, intelligent windows, new concepts of smartphones and sensors [1]. A large number of transparent electronic components have already been fabricated, such as transistors [2], batteries [3] and optical circuits [4]. Thin film bulk acoustic wave resonators (FBARs) are used in the communications industry for the fabrication of filters and duplexers [5]. The application of FBARs in gas and biological sensing has also been widely reported in the last years [6, 7]. Both fields could benefit from the fabrication of transparent resonators. In case of communications, it will enable the development of a new concept of devices, integrated in windshields or windows. Regarding the area of sensing, transparent FBAR sensors offer the interesting possibility of performing analysis using simultaneous optical and gravimetric techniques to detect targeted species.

The confinement of the acoustic energy in FBARs is critical for their optimum performance. Two different structures are currently used to achieve this. The free-standing FBAR uses an air-gap below the piezoelectric stack that ensures the reflection of the wave [8]. In case of solidly mounted resonators (SMRs), an acoustic reflector is used to confine the wave. The reflector consists of a stack of alternated layers of high acoustic impedance and low acoustic impedance materials with $\lambda/4$ thicknesses (Bragg mirror) [9].

To achieve transparent devices, the substrate and all the films composing the solidly mounted resonator should have a high light transmittance. There is a wide choice of transparent substrates, for example glass or even polymers such as polyamide [10]. However, obtaining transparent materials for the electrodes and the acoustic reflector is not straightforward. Transparent acoustic Bragg mirrors have already been developed [11-13] but transparent electrodes for piezoelectric AlN have not been extensively studied. The growth of AlN thin films with good crystal quality and high piezoelectric performance requires specific surface properties, which are usually only displayed by metallic layers (Ir, Ru, Pt, W or Mo) [14]. Depositing AlN films on amorphous substrates or conductive oxides results in AlN films with very poor performances, although some attempts to deposit AlN on SiO₂ have been successful [15]. The particular case of AlN deposition on ITO films has been barely investigated and usually the piezoelectricity of AlN is not considered [16].

In this work we present the development of transparent AlN-based SMRs. We chose glass as the substrate and ITO as the material for the transparent electrodes. The acoustic reflector is made of alternating layers of high acoustic impedance oxides (Ta₂O₅ or WO₃) and low acoustic impedance oxides (SiO₂), that ensure a high confinement of the acoustic wave and high optical transparency. We have studied the effect of using an insulating AlN seed layer to prevent the contact of the piezoelectric AlN layer with the ITO bottom electrode and we have characterised the transparent acoustic resonators both electrically and optically.

II. EXPERIMENTAL

To fabricate the transparent FBARs, we used 0.6 mm-thick Corning 7059 Glass[®] as the substrate. To achieve both transparency and acoustic confinement, the acoustic reflector consisted of 7 alternated layers of Ta₂O₅ [11] or WO₃ [13], and porous SiO₂ [12], 559 nm thick or 511 nm thick and 592 nm thick respectively. These layers were deposited using a Leybold Z-550 system by pulsed-DC reactive magnetron sputtering of 150 mm Ta, W and Si targets in Ar-O₂ admixtures. We used 250 nm thick ITO layers for both the bottom and top electrodes, deposited using Precision Atomic[®] Metal Sputterer from a 100 mm ITO compound target under the following conditions: 25 W power and 0.35 Pa. AlN films were deposited in an ultra-high-vacuum system pumped to a

base pressure below 8×10^{-7} Pa. A high purity (99.9995 %) 150 mm Al target was sputtered in Ar/N₂ (40:60) atmosphere between 0.27 Pa and 0.39 Pa using a pulsed-DC source (MKS-ENI RPG-50) operating at a frequency of 250 kHz and 1.2 kW of power. During deposition, the substrate was kept at 400 °C and biased to a DC voltage that was adjusted between -50 V and -65 V to control the stress of the film. Figure 1 displays a schematic of the structure. We measured the impedance of the devices as a function of the frequency (between 300 MHz and 3 GHz) using an Agilent E5062A network analyser. The resulting spectra were fitted using the Mason’s model [17] to obtain the electromechanical coupling factor (k^2) and the quality factor (Q) of the devices for the longitudinal mode. We assessed the optical transmittance of the samples between 250 nm and 1100 nm using a Perkin-Elmer Lambda- “UV-VIS-NIR” spectrophotometer. The average value in the visible range was assessed by using an incandescent bulb lamp as illuminator and measuring the total light transmittance using a Si PIN photodiode (Osram SFH 203) to assess the light intensity with and without the sample between them.

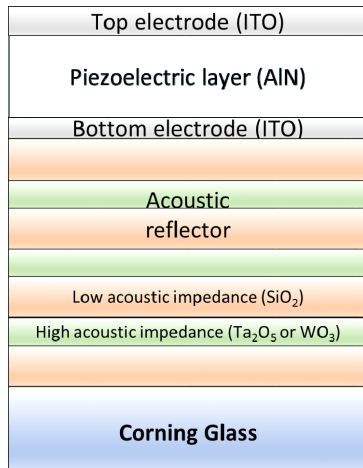


Fig. 1. Structure of the transparent devices with the ITO electrodes, the oxide-based acoustic reflector and the piezoelectric layer.

III. RESULTS AND DISCUSSION

We varied two main parameters of the AlN layer deposition process to influence the piezoelectric quality of the films: pressure and bias DC voltage. The pressure was varied between 0.27 Pa and 0.39 Pa without observing any significant improvement in the performance of the resonators. On the other hand, the bias DC voltage applied to the transparent stack does have a significant influence on the stress of the films. The bias was varied between -50 V and -65 V. In this range we have not observed any significant variation in the performance of the devices. However, for values outside this range the AlN layer is too stressed and the sample delaminates.

Figure 2 displays the response in frequency of one of the fabricated resonators. The longitudinal resonant frequency of the device is 1800 MHz and it shows a $k^2 \approx 4\%$ and a $Q \approx 100$. This device was fabricated using a SiO₂/Ta₂O₅ acoustic reflector and the AlN piezoelectric layer was 1.8 μm thick,

deposited at 0.27 Pa and applying -55 bias DC voltage. We fabricated additional samples with resonators operating at higher frequencies (up to 2300 MHz) by reducing the thickness of the AlN piezoelectric layer, without observing any other significant improvement in the performance of the devices. The use of SiO₂/WO₃ reflectors also does not seem to increase the figures of merit of the transparent FBARs.

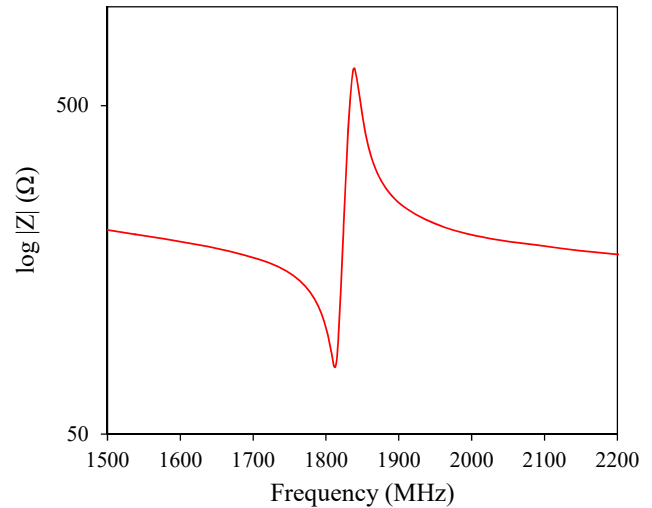


Fig. 2. Response in frequency of a transparent resonator with its longitudinal resonant frequency at 1800 MHz, a $k^2 \approx 4\%$ and a $Q \approx 100$. The device was fabricated on top of a SiO₂/Ta₂O₅ acoustic reflector.

AlN deposition on materials containing oxygen usually has a detrimental effect on the properties of the AlN film and results in low quality layers. ITO thin films are not an exception to this rule. However, previous studies [18] showed that titanium oxide could be a good seed layer for AlN growth. Therefore, improvements of these results could be possible by adding an intermediate seed layer between the ITO electrode and the AlN film. To try to avoid the negative effect of the oxygen we have deposited a 100 nm thick AlN seed layer on top of the electrode prior to the deposition of the active AlN piezoelectric layer. The purpose of this seed layer is to prevent the contact of the oxygen with the active layer in order to increase its piezoelectric quality. However, this method does not seem to improve the performance of the resonators. We could attribute this to the fact that such a thin layer of sputtered AlN lacks adequate crystalline structure to enhance the growth of a high quality AlN on top of it.

To obtain an accurate optical characterization of the devices we have performed UV-visible spectroscopy measurements in the 250 nm – 1100 nm range. The result is shown in figure 3, along with the spectrum of a bare glass as comparison. It should be note that the spectrum of the transparent stack presents several peaks and troughs. This is caused by the variation of the refractive indexes of the materials of the structure. The acoustic reflector consists of alternated layers of two oxides with thicknesses equal to $\lambda/4$, which is the acoustic equivalent of an optical Bragg mirror. In this case, since the stack is transparent and its visible spectrum can be measured, we can observe and characterise the actual effect of the reflector in the optical domain.

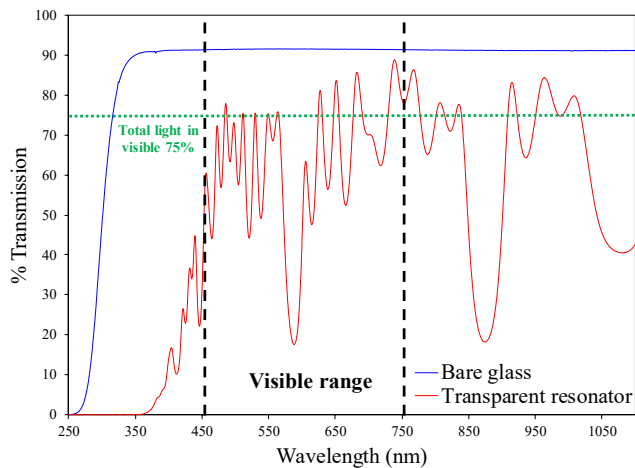


Fig. 3. UV-visible spectra between 250 nm and 1100 nm of bare glass (blue) and a transparent resonator (red). The visible range (450 nm to 750 nm) is delimited by dashed black lines. The presence of lobes in the spectrum of the transparent stack is caused by the effect of the Bragg mirror structure used as acoustic reflector. The total light measured in the visible range is 75% based on a photocurrent measurement (horizontal dashed green line).

The resulting transmittance measured by using an incandescent bulb lamp and a silicon PIN photodiode was around 75%. This value was obtained by dividing the total photocurrent given by the photodiode with and without the sample placed perpendicularly to the light-path. When placed on top of a retro illuminated display the sample keeps a high transparency, as it can be seen in figure 4. The image behind the transparent resonator substrate is clear, with sharp edges and fully distinguishable, and only a 25% reduction of its brightness is remarkable.

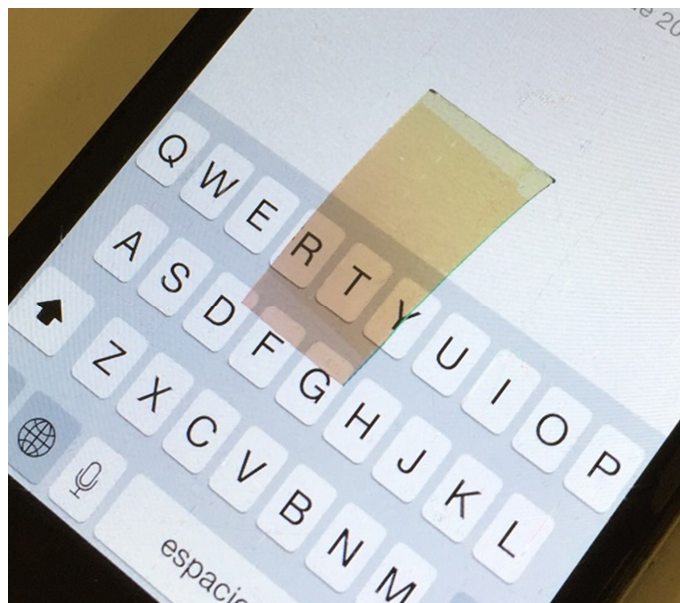


Fig. 4. The sample with transparent resonators placed on top of a retro illuminated smartphone screen.

Another interesting feature of these transparent resonators is that their surface can be observed under the microscope even when looking from the back of the substrate, along with samples placed below the devices. An example of this can be seen in figure 5. The picture has been taken from the back of the glass substrate, and the active area of the resonator and a human hair below it are simultaneously visible. This is potentially interesting to perform simultaneous gravimetric and optical analysis of samples and could have additional applications for the alignment of microfluidics and FBAR sensors.

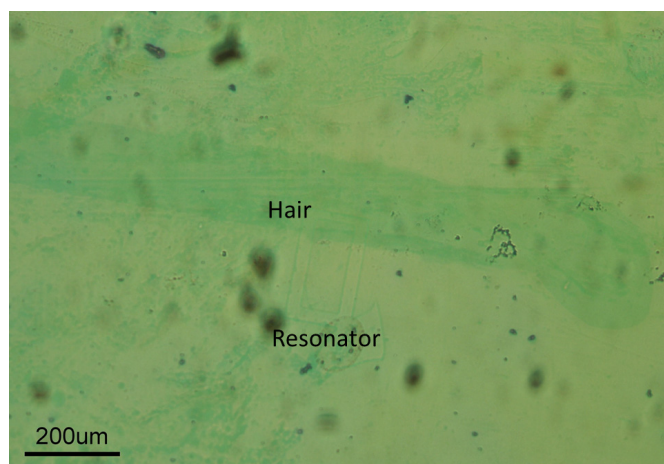


Fig. 5. Transparent resonator observed under the microscope from the back of the substrate. A human hair placed below the active area can be simultaneously distinguished.

IV. CONCLUSION

We have fabricated transparent SMRs on glass substrate using AlN as piezoelectric layer and ITO as electrodes. The acoustic reflector consists of alternated layers of a low acoustic impedance oxide (porous SiO₂) and a high acoustic impedance oxide (Ta₂O₅ or WO₃), to ensure both acoustic confinement and transparency. The devices display a longitudinal resonance at 1800 MHz, a $k^2 \approx 4\%$ and a $Q \approx 100$. The spectral assessment of the stack in the visible range shows the typical transmittance of a Bragg optical mirror with deep and narrow reflecting bands, although the total-light transmittance in the visible region of the light spectrum shows an average transparency of 75%. The devices look highly transparent and with no distortion when placed on a retro illuminated display. Even though the figures of merit of the resonator need to be improved in order to fabricate commercially viable devices, this results are a promising first step into the integration of transparent FBARs, with potential applications in wearables, communications and sensing.

ACKNOWLEDGMENT

This work was partially supported by the European Commission through the COST action IC1208 and by the Ministerio de Economía y Competitividad del Gobierno de España through project MAT2013-45957-R.

REFERENCES

- [1] J. F. Wager, "Applied physics. Transparent electronics.," *Science*, vol. 300, no. 5623, pp. 1245–6, May 2003.
- [2] S. Ju, A. Facchetti, Y. Xuan, J. Liu, F. Ishikawa, P. Ye, C. Zhou, T. J. Marks, and D. B. Janes, "Fabrication of fully transparent nanowire transistors for transparent and flexible electronics.," *Nat. Nanotechnol.*, vol. 2, no. 6, pp. 378–84, Jun. 2007.
- [3] Y. Yang, S. Jeong, L. Hu, H. Wu, S. W. Lee, and Y. Cui, "Transparent lithium-ion batteries.," *Proc. Natl. Acad. Sci. U. S. A.*, vol. 108, no. 32, pp. 13013–8, Aug. 2011.
- [4] Z. Wu, Z. Chen, X. Du, J. M. Logan, J. Sippel, M. Nikolou, K. Kamaras, J. R. Reynolds, D. B. Tanner, A. F. Hebard, and A. G. Rinzler, "Transparent, conductive carbon nanotube films.," *Science*, vol. 305, no. 5688, pp. 1273–6, Aug. 2004.
- [5] M. Clement, E. Iborra, J. Olivares, N. Rimmer, S. Giraud, S. Bila, and A. Reinhardt, "DCS Tx filters using AlN resonators with iridium electrodes.," *IEEE Trans. Ultrason. Ferroelectr. Freq. Control*, vol. 57, no. 3, pp. 518–23, Mar. 2010.
- [6] D. Chen, Y. Xu, J. Wang, and L. Zhang, "Nerve gas sensor using film bulk acoustic resonator modified with a self-assembled Cu²⁺/11-mercaptopundecanoic acid bilayer.," *Sensors Actuators B Chem.*, vol. 150, no. 1, pp. 483–486, Sep. 2010.
- [7] M. Nirschl, A. Blüher, C. Erler, B. Katzschner, I. Vikholm-Lundin, S. Auer, J. Vörös, W. Pompe, M. Schreiter, and M. Mertig, "Film bulk acoustic resonators for DNA and protein detection and investigation of in vitro bacterial S-layer formation.," *Sensors Actuators A Phys.*, vol. 156, no. 1, pp. 180–184, Nov. 2009.
- [8] R. Ruby, M. Small, F. Bi, D. Lee, L. Callaghan, R. Parker, and S. Ortiz, "Positioning FBAR technology in the frequency and timing domain.," *IEEE Trans. Ultrason. Ferroelectr. Freq. Control*, vol. 59, no. 3, pp. 334–45, Mar. 2012.
- [9] K. Lakin, "Solidly mounted resonators and filters.," *Proc. IEEE Int. Ultrason. Symp.*, vol. 2, pp. 905–908, 1995.
- [10] G. Chen, X. Zhao, X. Wang, H. Jin, S. Li, S. Dong, A. J. Flewitt, W. I. Milne, and J. K. Luo, "Film bulk acoustic resonators integrated on arbitrary substrates using a polymer support layer.," *Sci. Rep.*, vol. 5, p. 9510, Jan. 2015.
- [11] J. Capilla, J. Olivares, M. Clement, J. Sangrador, E. Iborra, and A. Devos, "High-acoustic-impedance tantalum oxide layers for insulating acoustic reflectors.," *IEEE Trans. Ultrason. Ferroelectr. Freq. Control*, vol. 59, no. 3, pp. 366–72, Mar. 2012.
- [12] J. Olivares, E. Wegmann, J. Capilla, E. Iborra, M. Clement, L. Vergara, and R. Aigner, "Sputtered SiO₂ as low acoustic impedance material for Bragg mirror fabrication in BAW resonators.," *IEEE Trans. Ultrason. Ferroelectr. Freq. Control*, vol. 57, no. 1, pp. 23–9, Jan. 2010.
- [13] M. DeMiguel-Ramos, B. Diaz-Duran, J. Munir, M. Clement, T. Mirea, J. Olivares, and E. Iborra, "Tungsten oxide layers of high acoustic impedance for fully insulating acoustic reflectors.," *IEEE Trans. Ultrason. Ferroelectr. Freq. Control*, vol. PP, no. 99, pp. 1–6, 2015.
- [14] S. Inoue, K. Okamoto, T. Nakano, and H. Fujioka, "Characteristics of single crystalline AlN films grown on Ru(0001) substrates.," *J. Cryst. Growth*, vol. 297, no. 2, pp. 317–320, Dec. 2006.
- [15] A. Artieda, C. Sandu, and P. Mural, "Highly piezoelectric AlN thin films grown on amorphous, insulating substrates.," *J. Vac. Sci. Technol. A Vacuum, Surfaces, Film.*, vol. 28, no. 3, p. 390, Mar. 2010.
- [16] H.-D. Kim, H.-M. An, Y. Seo, and T. G. Kim, "Transparent Resistive Switching Memory Using ITO/AlN/ITO Capacitors.," *IEEE Electron Device Lett.*, vol. 32, no. 8, pp. 1125–1127, Aug. 2011.
- [17] J. Rosenbaum, *Bulk Acoustic Wave Theory and Devices*, 1st ed. Boston: Artech House, 1988.
- [18] J. Olivares, J. Capilla, M. Clement, J. Sangrador, and E. Iborra, "Growth of AlN oriented films on insulating substrates.," in 2011 IEEE International Ultrasonics Symposium, 2011, pp. 1716–1719.

Long-Term Frequency Stability Improvement of OCXO using CSAC

Tomas Bagala¹, Adam Fibich¹, Vladimir Stofanik^{1,2}

¹Institute of Electronics Photonics FEI STU;

²Institute of Physics, Slovak Academy of Sciences; Bratislava, Slovak Republic

Email: tomas.bagala@stuba.sk, adam.fibich@stuba.sk, vladimir.stofanik@savba.sk

Abstract — In this paper we introduce long-term frequency stability improvement of Oven Controlled Crystal Oscillator (OCXO) using Chip Scale Atomic Clock (CSAC). Compared to OCXO, the main disadvantage of the CSAC is their higher phase noise; however the CSAC features with better long-term frequency stability, much lower power consumption and much faster warm-up.

Keywords— OCXO, CSAC, FPGA, long-term frequency stability, phase noise

I. INTRODUCTION

Nowadays, the Chip scale atomic clock (CSAC) gives great potential for wide range of commercial, industrial and especially military and aerospace systems requiring superior long-term frequency stability. Compared to OCXO, the main disadvantage of the CSAC is their higher phase noise (Fig. 1); however the CSAC features with better long-term frequency stability, much lower power consumption and much faster warm-up [1], [2].

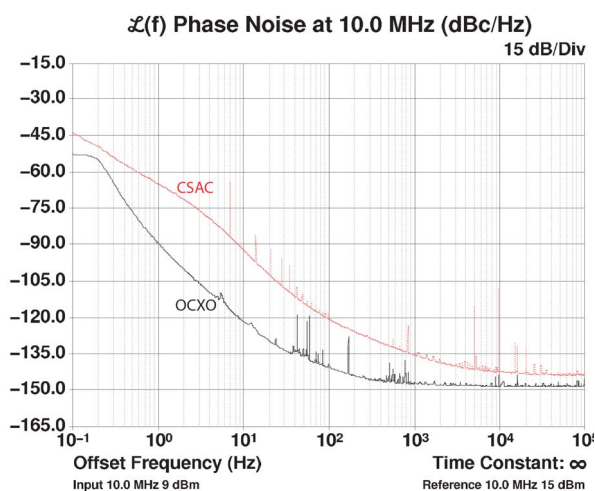


Fig. 1: Phase noise comparison of OCXO (MTI 230-0827) and CSAC (SA.45s)

In this connection, it can easily occur an idea to build a system that will benefit from both types of oscillators. By this way, the superior behavior of the CSAC can be incorporated to many existing strategic RF and microwave systems requiring low phase noise level as well.

II. COMPARISON OF THE CSAC AND OCXO

Firstly, we compare characteristics of the selected 10-MHz OCXO MTI 230-0827 and the 10-MHz CSAC SA.45s (Symmetricom) we obtained experimentally [3], [4].

Figure 2 illustrates behavior the both oscillators after power-up. During warm-up of the OCXO, occurred anomalies in frequency characteristic, which can be seen evidently in the Fig. 2. Frequency settling of the CSAC takes much shorter time in compare to the OCXO's. According to the specification, the warm-up time of the CSAC takes less than 180 s [4].

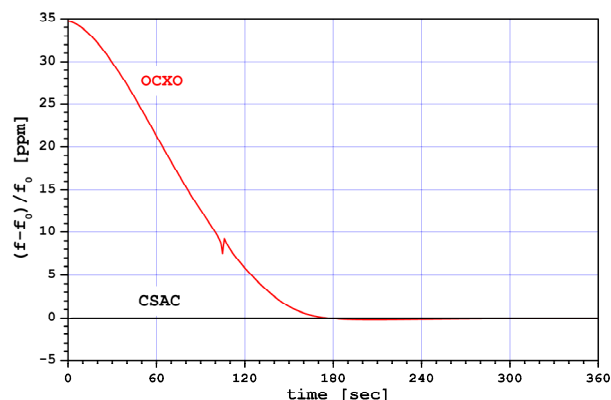


Fig. 2 Measured frequency transient of the CSAC SA.45s and of the OCXO MTI 230-0827 after power-on

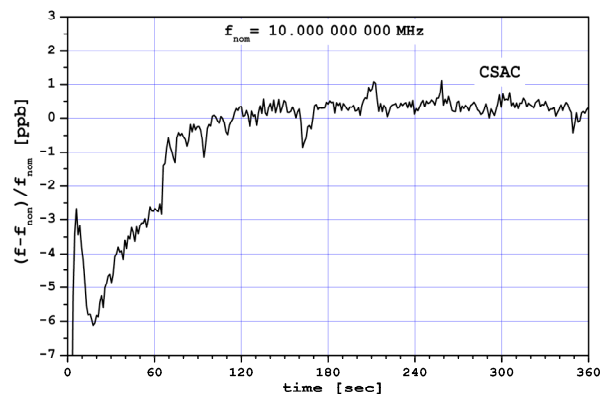


Fig. 3 Measured power-up frequency transient of the CSAC SA.45s after power-on

This research was supported by the Ministry of Education of Slovak Republic under the grants VEGA No. 1/0921/13 and VEGA No. 1/0664/14

The CSAC frequency changes after power-up are too small and are not visible in Fig. 2. Thus, we have measured power-up frequency transient of the CSAC with increased resolution; the result is shown in Fig. 3. One minute after power-up, the frequency deviations of the CSAC are below ± 1 ppb. Comparing with the CSAC, the OCXO requires much longer warm-up time, which extends requirements for initial delay when the system is powering-up.

Besides warm-up characteristics, we measured frequency instabilities of the oscillators for longer time period. Figure 4 shows instability of both oscillators over six-hour interval. The OCXO's frequency tends to rise evidently without any external frequency tuning. It uses only the inner feedback frequency tuning. Deviation $(f - f_0) / f_0$ are at least 10 ppb per 180 minutes interval. Its frequency has better stabilized only after at least ten hours of operation, however short term frequency instability is comparable with CSAC which shows not variable character during over six-hour interval and more.

Allan deviations of the two compared oscillators we measured are shown in Fig. 5 and Fig. 6; it proves a difference in the tendency with increasing averaging time.

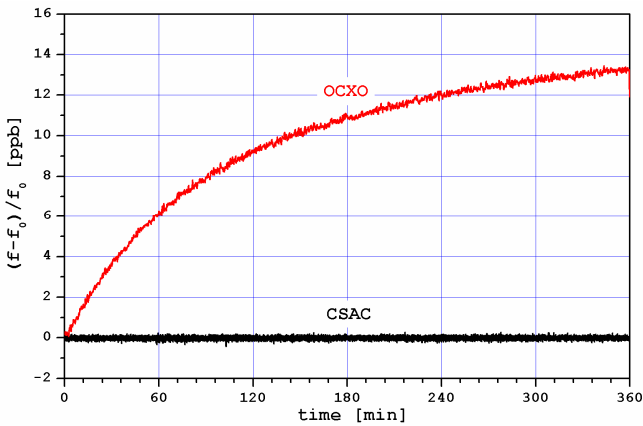


Fig. 4 Measured frequency instability of the CSAC SA.45s and of the OCXO MTI 230-0827 over six-hour interval after warm-up

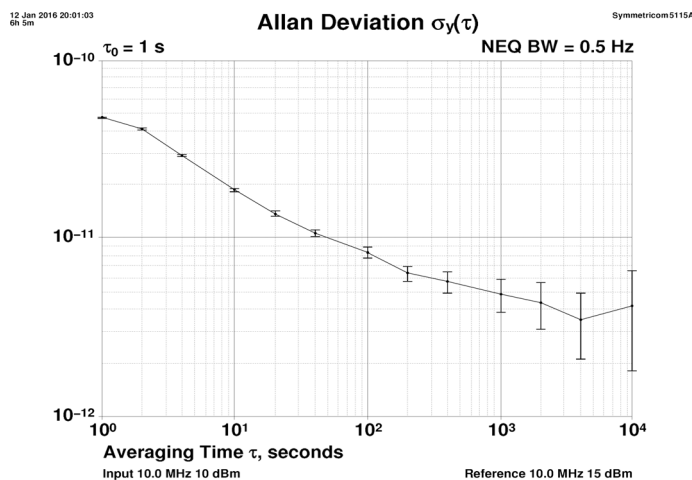


Fig. 5 Measured Allan deviation of the CSAC SA.45s

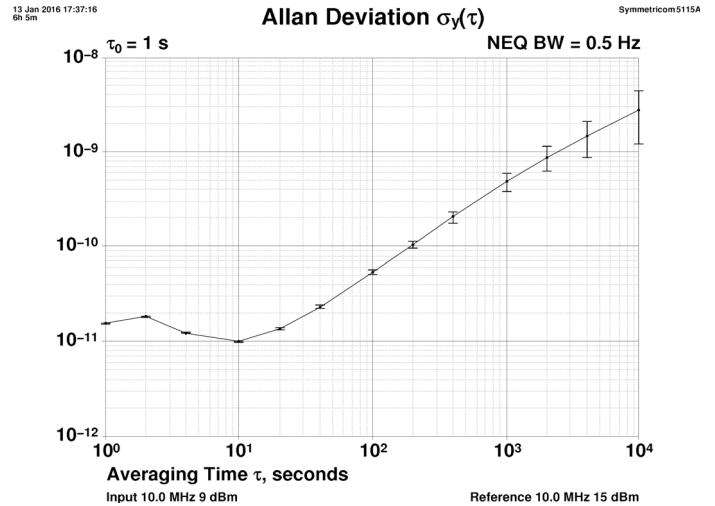


Fig. 6 Measured Allan deviation of the OCXO MTI 230-0827

III. SYSTEM IMPLEMENTATION

Based on the advantages of both oscillators, we have designed the closed loop system of long-term frequency stability improvement of OCXO using the CSAC, FPGA, microcontroller and D/A converter. Principle is based on periodical evaluation of an actual OCXO frequency during defined integration interval, followed with the OCXO frequency tuning to eliminate the frequency deviations of the OCXO. The integration interval determines the resolution of the evaluated OCXO frequency, as well as the system reaction time. It is important to choose the integration time as a compromise between the resolution and the system reaction time.

Basic logic-cell of used FPGA XC3S200 (any device from the Spartan-3 family; Xilinx Inc.) contains two elementary four-bit look-up tables, which may be alternatively utilized as the 16-stage shift register (SRLC16E block). Figure 7 shows the internal structure of the SRLC16E elementary block. The inputs include: common clock CLK, clock enable input CE and first stage data input D. In addition, four input address lines: A0, A1, A2 and A3 determine the stage to be accessed on the output Q. The output of the last register Q15 is available as well, to help cascading more SRLC16E elements. The INIT property of the SRLC16E defines the initial content of the sixteen internal stages after the FPGA configuration sequence. Utilization of the SRLC16E primitives leads to significant reduction of resource utilization when compared with alternative flip-flop only utilization [5].

Simplified block diagram of the OCXO long-term frequency stability improvement system is shown in Fig. 8. Long-term stable reference frequency 10 MHz is derived from the CSAC output.

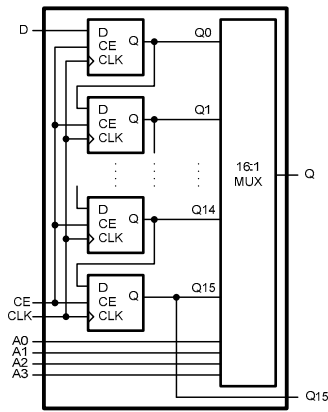


Fig. 7. Internal structure of SRLC16E element in Spartan-3 devices.

The output of this register forms the clock enable signal of the SRLC16E block, which acts as the least significant part of the binary counter used to accumulate the clock pulses related to the actual frequency of the OCXO. The output Q15 of the SRLC16E block is connected to the microcontroller's internal counter clock input. The frequency of this clock signal is nominally 7.5 MHz. More significant part of the accumulating binary counter has been implemented within the microcontroller.

During the integration time interval, the clock pulses of frequency proportional to actual OCXO frequency are accumulated in the binary counter. To increase the frequency measurement resolution, we utilized the frequency multiplication (i.e. DCM block within the FPGA multiplies the OCXO frequency by 24, i.e. nominally to 240 MHz). If we consider one-second integration time interval, for example, we have to obtain nominally 240 000 000 pulses; and digital resolution ± 1 LSB then represents relative frequency uncertainty equivalent to ± 4.167 ppb. Longer integration time interval, naturally leads to better resolution. Implemented algorithm within the microcontroller flexibly varies this integration interval, to balance the resolution and the control feedback response time.

The microcontroller alternatively can communicate with the PC via the standard UART or USB interface.

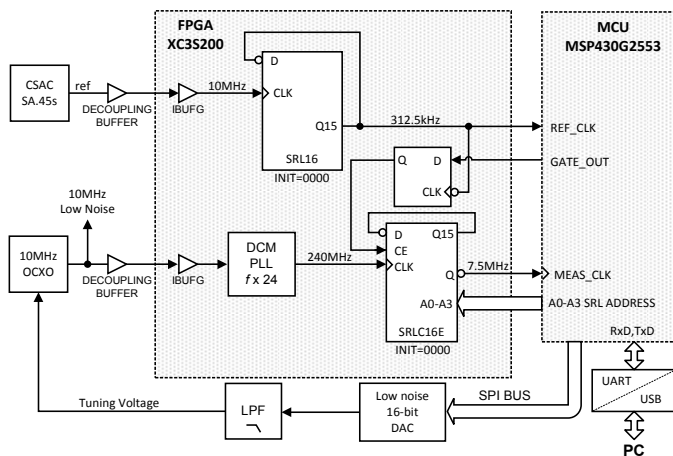


Fig. 8. Block diagram of the OCXO long-term frequency stability improvement system

The microcontroller (MSP430G2553) executes in the loop the following tasks:

- defines integration time interval of the control loop;
- evaluates an actual frequency deviation of the OCXO;
- derives the appropriate feedback control (tuning) voltage for the OCXO;
- transmits digital serial representation of the feedback voltage to the low noise 16-bit DAC.

The microcontroller manages the integration time interval related to the CSAC reference frequency 10 MHz. At first, the reference frequency from CSAC is divided by 32, with assistance of simple SRL16 block within the FPGA. The resulting REF_CLK signal has accurate frequency 312 500 Hz; it is processed further by the microcontroller. During selected number of the REF_CLK signal periods the microcontroller activates the frequency measurement (i.e. sets the GATE_OUT signal). The GATE_OUT signal is synchronized internally within the FPGA on falling edge of the REF_CLK signal using simple flip-flop register.

IV. CONCLUSION

Simple implementation of OCXO long-term frequency stability improvement utilizing CSAC SA.45s we designed and verified. In this way, the superior behavior of the CSAC can be incorporated to many existing strategic RF and microwave systems, requiring low phase noise as well.

REFERENCES

- [1] Thomas H. Lee, and Ali Hajimiri, "Oscillator Phase Noise: A Tutorial", IEEE Journal of Solid-State Circuits, vol. 35, no. 3, March 2000, pp. 326-336.
- [2] J.F. DeNatale, R.L. Borwick, C. Tsai, P.A. Stupar, Y. Lin, R.A. Newgard, R.W. Berquist and M. Zhu, "Compact, Low-Power Chip-Scale Atomic Clock", Position, Location and Navigation Symposium, 2008 IEEE/ION, May 5-8 2008, pp. 67-70.
- [3] 230 SERIES OCXO - MTI-Milliren Technologies Inc.: www.mti-milliren.com/pdfs/230.pdf.
- [4] Microsemi (Symmetricom) SA.45s QUANTUM Chip Scale Atomic Clock http://www.microsemi.com/document-portal/doc_download/133305-quantum-sa-45s-csac.
- [5] Vladimír Štofanič, Anel E. Sam, Igor Baláž, and Marian Minárik, "Direct Digital Synthesizer Clock Frequency Versus Temperature Dependency Compensation Using Two Look-Up Tables", in Proceedings of the 2004 IEEE International Ultrasonics, Ferroelectrics, and Frequency Control Joint 50th Anniversary Conference 2004, pp. 770-774.

The LNE-SYRTE cold atom gravimeter

P. Gillot, B. Cheng, A. Imanaliev, S. Merlet, F. Pereira Dos Santos
LNE-SYRTE, Observatoire de Paris, PSL Research University
CNRS, Sorbonne Universités, UPMC Univ. Paris 06
61 avenue de l'Observatoire, 75014 Paris, France
Email: franck.pereira@obspm.fr

Abstract—We present results on the evaluation of the metrological performances of our second generation cold atom gravimeter, operating since 2009. This instrument uses free falling ^{87}Rb cold atoms, whose acceleration is measured thanks to atom interferometry techniques. This allows for a sensitive and absolute determination of the gravity acceleration. We present the results of various comparisons of our atomic sensor with high performance absolute or relative gravimeters based on other technologies.

I. INTRODUCTION

Gravimeters are vertical accelerometers used to measure the local gravity acceleration or variations in the gravity field. They find applications in many fields, such as geophysics and geodesy, navigation, exploration of natural resources, detection of underground infrastructures and monitoring of reservoirs. The absolute measurement of gravity is obtained from the measurement of the motion of a free falling body. State of the art commercial absolute gravimeters are based on a free falling corner cube whose trajectory is tracked using a laser interferometer. These instruments have accuracies of a few μGal ($1 \mu\text{Gal} = 10^{-8}\text{m/s}^2$) and their sensitivity depends on the environmental conditions, as they are usually limited by residual ground vibrations, despite the use of a sophisticated vibration isolation system based on the use of a super spring. They operate at a measurement cycle time of a few seconds, and require regular maintenance because of the wear of their mechanical parts.

Atomic sensors offer an attractive alternative to corner cube gravimeters. In these instruments, the test mass is an atom and its acceleration is measured by means of an atom interferometer realized with laser beamsplitters. Because the interaction with the lasers imprints the atoms position with respect to the lasers onto the atomic phase, the phase at the output of the interferometer finally allows for the measurement of the acceleration of the free falling atoms with respect to the setup (and to be more precise, in most cases, to the position of a mirror that reflects the interferometer laser beams). They have the great advantage of not suffering from mechanical wear and thus offer the possibility of performing continuous and high rate measurements over extended periods of time. Such continuous measurements are usually realized thanks to relative instruments, such as spring or superconducting gravimeters. But, these instruments need to be calibrated and suffer from drifts (of order of hundreds of μGal per day for spring gravimeters, to a few μGal per year only for superconducting gravimeters).

In this paper, we describe the cold atom gravimeter (CAG) we have developed and its measurement principle. We give de-

tails on its level of performance, and present the results of the various comparisons it participated to with other instruments, either absolute or relative gravimeters.

II. DESCRIPTION OF THE GRAVIMETER

In our experiment, ^{87}Rb atoms from a 2D-Magneto-Optical Trap (MOT) load a 3D-MOT for 80 ms [1]. Next, a molasses phase cools atoms down to a temperature of about $2 \mu\text{K}$. The molasses beams are then switched off within $100 \mu\text{s}$ with a fast mechanical shutter. The atomic cloud is thus simply let to freely fall, over a distance of about 20 cm, before being detected at the bottom of the vacuum chamber.

The atoms are then velocity selected [2] along the vertical direction in the $|F = 1, m_F = 0\rangle$ state thanks to a combination of microwave, pusher and Raman pulses. After the selection, we drive a Mach-Zehnder interferometer, using a $\pi/2\text{-}\pi\text{-}\pi/2$ Raman pulse sequence, to respectively separate, redirect and finally recombine the two partial wave packets [3]. The two-photon Rabi frequency of the Raman pulse is of order of $2\pi \times 25 \text{ kHz}$ at maximum. The single-frequency detuning of the Raman lasers is of order of -1 GHz , and the $1/e^2$ radius of the Raman beams is 12 mm. The first pulse of the interferometer occurs about 16 ms after the release from the molasses.

We exploit the state labelling of the Raman process [4] to measure the populations in the two output states, thanks to a fluorescence detection performed on the internal state. From the measurement of the populations N_1 and N_2 in the two hyperfine states, we calculate the transition probability $P = N_1/(N_1 + N_2)$. This transition probability P is given by $P = (1 + C \cos(\Delta\Phi))/2$, where C is the interferometer contrast and $\Delta\Phi$ the phase difference between the two different arms. In our geometry, with vertically aligned Raman lasers, this interferometer phase shift is given by $\Delta\Phi = k_{eff}gT^2$ [5]. k_{eff} is the effective Raman wavevector, given by the difference between the wavevectors of the two counter-propagating Raman lasers. g is the gravity acceleration and $T = 80 \text{ ms}$ is the time separation between consecutive pulses. The cycle time in our experiment is 380 ms.

The figure 1 displays a picture of the instrument. At the forefront, the drop chamber, enclosed in a cylindrical two layer magnetic shield, is installed on a thick aluminium plate. This plate lies on a passive isolation platform, which we use to reduce the impact of parasitic vibrations. A low noise seismometer is installed on top of the chamber, which measures the residual vibration noise not filtered by the platform. At the back, the electronic control system and the power supplies are installed in a rigid frame made of aluminium bars. The laser breadboard is placed at the top of this frame, in a



Fig. 1. Picture of the instrument. At the forefront, the drop chamber. Behind, the control electronics and laser system.

dedicated aluminium box. The two parts, vacuum chamber and electronic-optics frame, are connected via optical fibres and electrical cables. Both the drop chamber and the frame can be equipped with wheels, so that they can be moved out separately from the laboratory, be placed in a truck and be transported to a dedicated measurement site. In the normal conditions of operation, the wheels under the drop chamber are removed, so that the isolation platform rests on the floor.

III. MEASUREMENT PRINCIPLE

Usually, the absolute measurement of g is performed in our experiment by alternating measurements in four different configurations [1]. This protocol allows removing many of the systematic effects, except Coriolis acceleration and phase shifts due to wavefront distortions. It comprises two pairs of configurations in which the wave-vector k_{eff} is reversed (k_{\uparrow} and k_{\downarrow}). The half difference of a single pair of configuration (k_{\uparrow} and k_{\downarrow}) provides a $g_{\uparrow\downarrow}$ measurement in which most of the effects related to hyperfine frequency shifts and from radio-frequency phase shift are suppressed [6]. The second pair is performed with half the Raman power, which allows correcting for the two-photon light shift [7].

IV. LONG TERM MEASUREMENTS AND COMPARISON WITH A SUPERCONDUCTING GRAVIMETER

We start by presenting in figure 2 continuous measurements of the gravity acceleration performed in April 2015, for almost a month, with two different instruments operating simultaneously, the CAG and an iGrav superconducting gravimeter installed in the same laboratory, just a few meters away. The superconducting gravimeter uses as a test mass a superconducting sphere which is levitated using a magnetic force that exactly balances the force of gravity. The CAG and iGrav data points are both averaged over the same duration of about 3 minutes. Both instruments record the expected fluctuations of gravity of order of a few hundreds of μGal which are due to Earth tides. For these measurements, which are performed in an industrial area in Trappes, the short term sensitivity is $10\mu\text{Gal}$ at 1s. We have obtained at best a short term sensitivity twice better when operating in the more quiet environment of

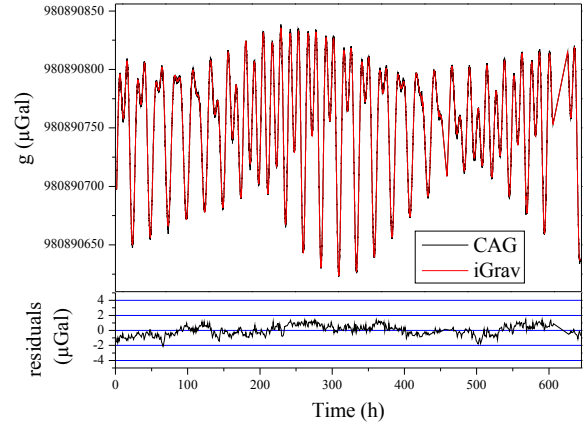


Fig. 2. Continuous measurement over 25 days of the CAG and the superconducting gravimeter iGrav, and the residuals of the difference between the two signals.

the underground laboratory at Walferdange [8], where the 2011 and 2013 comparisons took place.

The bottom plot on figure 2 displays the residuals obtained by subtracting the two signals. Note that in order to obtain these residuals, one has to have a precise determination of the calibration factor of the iGrav, ie the link between a change in its output current and the change of gravity, and also to account for eventual time delays in its response. This is in fact realized by correlating the two signals. Once this calibration is done, we are left with residuals which fluctuate by about $\pm 1\mu\text{Gal}$. We attribute these residuals to uncontrolled fluctuations of the systematic effects of the CAG.

V. ACCURACY BUDGET AND COMPARISONS WITH ABSOLUTE GRAVIMETERS

TABLE I. ACCURACY BUDGET

Systematic effect	Correction μGal	U μGal
Alignment	1.2	0.5
Frequency reference	3.2	0.1
RF phase shifts	0	< 0.1
Gravity gradient	-13	< 0.1
Self gravity effect	-2.1	0.1
Coriolis	-5.3	1
Wavefront distortions	0	4
1 photon Light shift	0	< 0.1
Zeeman	0	< 0.1
2 photon Light shift	-7.7	0.4
Detection offset	0	0.5
Optical power	0	1.0
Refraction index	0.4	< 0.1
Cold collisions	0	< 0.1
TOTAL	-23.2	4.3

Table I displays the accuracy budget of our instrument. The inaccuracy of our measurement, of order of $4\mu\text{Gal}$ is

dominated by our imperfect knowledge of the effect of wave-front distortions. This accuracy budget has been validated by comparing our instrument with state of the art corner cube gravimeters.

We have participated to three international comparison campaigns of absolute gravimeters. They took place at BIPM in Sèvres in 2009, and in the Underground Laboratory for Geodynamics in Walferdange, Luxembourg, in 2011 and 2013. The 2009 comparison at BIPM was the first Key Comparison (KC) as defined by the CIPM MRA, organized by the Consultative Committee for Mass and Related Quantities (CCM) and designated as CCM.G-K1. Our instrument has been the first and remains so far the only atomic sensor which has ever participated to such official comparisons. In addition, we have organized a few comparisons in our laboratory, located in the Watt balance (WB) laboratories of the Laboratoire National de Métrologie et d'Essais, in Trappes, a city in the suburb of Paris (France).

Table II summarizes the results of these comparisons. Our instrument was in agreement within our claimed uncertainty with the reference value provided by the other sensors, this value being, depending on the comparison, an average over many, a few, or a single instrument.

TABLE II. RESULTS OF THE COMPARISONS WITH OTHER ABSOLUTE GRAVIMETERS

Date	Place	Number of Instruments	$g(\text{CAG})-g(\text{other})$ (μGal)
2009	BIPM	22	-1.6(7.8)
2009	Trappes	2 FG5-220	-4.3(6.4)
2010	Trappes	3 FG5-209, IMG-C02	+11(6.5)
2011	LUX	22	+5.4(5.7)
2013	LUX	25	+6.2(5.5)
2014	Trappes	2 FG5X-220	0(5)

VI. GRAVITY MEASUREMENTS AT THE WB LABORATORY

Finally, we display in figure 3 the results of repeated gravity measurements performed at Trappes for the last 7 years. The red points correspond to measurements performed after changing the orientation of the experiment by 180 degrees. The difference of 15-20 μGal between two opposite orientations is due to Coriolis acceleration. The dispersion of the data decreases with time, which reflects the improvement of the long term stability and of our control of the systematic effects. Note that the measurements over the first three years were not taken for identical measurement parameters (such as Rabi frequency, power in the MOT beams, interferometer duration $2T$...), so that the dispersion is partly linked to these changes, which were necessary to investigate the systematic effects. Since 2012, we have tried to repeat the measurements with a set of fixed parameters. During the last year, we have implemented a lock of the power in the Raman beams and in the cooling beams, which improves even further the repeatability. The rms fluctuations of the gravity value over the last year is 2.5 μGal .

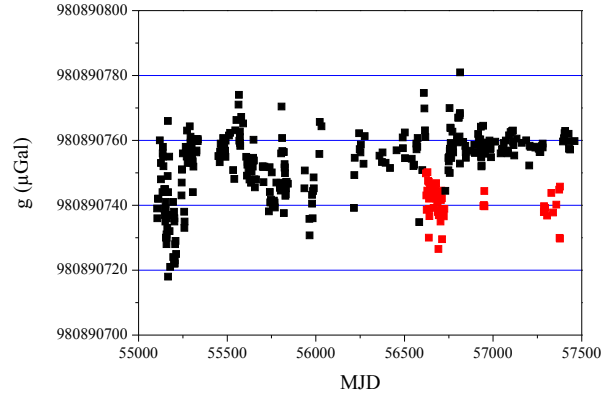


Fig. 3. Gravity measurements performed with the CAG in the Watt balance laboratory in Trappes since 2009.

VII. CONCLUSION

We have presented the main features our cold atom gravimeter and its level of performances. Limits on its long term stability and its accuracy have been identified. They are related to the fluctuations of the initial position of the atomic source and its residual expansion in the profile of the Raman beams. To reduce these effects, we plan to use a source of ultracold atoms produced by evaporative cooling in a crossed dipole trap, which will provide a better stability of the atoms initial position and a reduced expansion. We expect to push the accuracy and long term stability below the μGal level.

ACKNOWLEDGMENT

The authors would like to thank Q. Bodart, T. Farah, A. Louchet-Chauvet and C. Guerlin for early contribution to the present work, and A. Landragin for useful discussions.

REFERENCES

- [1] A. Louchet-Chauvet, T. Farah, Q. Bodart, A. Clairon, A. Landragin, S. Merlet, and F. P. Dos Santos, "The influence of transverse motion within an atomic gravimeter," *New Journal of Physics*, vol. 13, no. 6, p. 065025, 2011.
- [2] K. Moler, D. Weiss, M. Kasevich, and S. Chu, "Theoretical analysis of velocity-selective Raman transitions," *Phys. Rev. A*, vol. 45, pp. 342–348, 1992.
- [3] M. Kasevich and S. Chu, "Atomic interferometry using stimulated raman transitions," *Physical Review Letters*, vol. 67, no. 2, pp. 181–184, 1991.
- [4] C. Bordé, "Atomic interferometry with internal state labeling," *Phys. Lett. A*, vol. 140, pp. 110–112, 1989.
- [5] C. Bordé, "Theoretical tools for atom optics and interferometry," *Comptes Rendus de l'Académie des Sciences - Series {IV} - Physics*, vol. 2, no. 3, pp. 509 – 530, 2001.
- [6] A. Peters, K. Y. Chung, and S. Chu, "High-precision gravity measurements using atom interferometry," *Metrologia*, vol. 38, pp. 25 – 61, 2001.
- [7] A. Gauguier, T. E. Mehlstäubler, T. Lévêque, J. Le Gouët, W. Chaibi, B. Canuel, A. Clairon, F. Pereira Dos Santos, and A. Landragin, "Off-resonant raman transition impact in an atom interferometer," *Phys. Rev. A*, vol. 78, p. 043615, Oct 2008.
- [8] P. Gillot, O. Francis, A. Landragin, F. P. D. Santos, and S. Merlet, "Stability comparison of two absolute gravimeters: optical versus atomic interferometers," *Metrologia*, vol. 51, p. 5, 2014.

On temporal correlations in high-resolution frequency counting

Tim Dunker
Justervesenet
P.O. Box 170
2027 Kjeller, Norway
E-mail: tdu@justervesenet.no

Harald Hauglin
Justervesenet
P.O. Box 170
2027 Kjeller, Norway
E-mail: hha@justervesenet.no

Ole Petter Rønningen
ICTEC AS
Drammensveien 127
0277 Oslo, Norway
E-mail: ole.petter@ictec.com

Abstract—We analyze noise properties of time series of frequency data from different counting modes of a Keysight 53230A frequency counter. We use a 10 MHz reference signal from a passive hydrogen maser connected via phase-stable Huber+Suhner Sucoflex 104 cables to the reference and input connectors of the counter. We find that the high resolution gap-free (“CONT”) frequency counting process imposes long-term correlations in the output data, resulting in a modified Allan deviation $MDEV \sim \tau^{-1/2}$ -characteristic of random walk phase noise. Equally important, the CONT mode results in a frequency bias. In contrast, the counter’s undocumented raw continuous mode (“RCON”) yields unbiased frequency stability estimates with white phase noise characteristics, $MDEV \sim \tau^{-3/2}$, and of a magnitude consistent with the counters 20 ps single-shot resolution. Furthermore, we demonstrate that a 100-point running average filter in conjunction with the RCON mode yields resolution enhanced frequency estimates with flicker phase noise characteristics, $MDEV \sim \tau^{-1}$. For instance, the counter’s built-in moving-average function can be used. The improved noise characteristics of the averaged RCON mode versus the CONT mode imply that the former mode yields frequency estimates with improved confidence for a given measurement time.

I. INTRODUCTION

Rubiola [1] and Dawkins et al. [2] described frequency counting methods and averaging processes, as well as their uncertainties. We investigate the CONT and RCON measurement modes of a widely used frequency counter—the Keysight 53230A. We measure a 10 MHz reference signal against itself with this counter, and analyze the resulting frequency offset and autocorrelation function. We compare the different measurement modes to each other and determine which mode provides the most reliable frequency estimate. Furthermore, we measure the same signal with a Pendulum CNT-91 frequency counter and compare the results to those obtained with the Keysight counter’s CONT and RCON modes.

The CONT measurement mode “configures the counter for continuous, resolution-enhanced, gap-free measurements” [3, p. 71]. According to Keysight, the CONT mode is required to achieve the best accuracy with respect to the Allan deviation calculated from frequency measurements [3, p. 206]. However, we do not know exactly how the CONT mode operates. The RCON measurement mode is an undocumented, raw continuous frequency measurement mode.

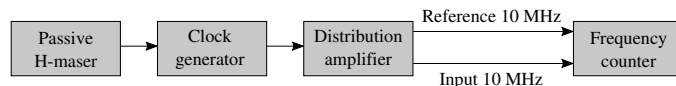


Fig. 1. Experimental setup

The Keysight 53230A is a Π -counter if it operates in RCON mode. If it operates in RCON mode with internal averaging, the counter is a Λ -counter [4]. Different frequency counters use different techniques to reduce the influence of phase noise on frequency estimates [4]. One such method is internal averaging over a given time interval. We therefore look at different sampling intervals, and also apply a moving average to see how averaging affects the frequency estimates and the temporal correlations of the frequency measurements.

Temporal correlations in frequency measurements can be induced by a measurement mode, and may not be representative of the device under test. In particular, the autocorrelation function [5, e.g.] is a suitable tool to analyze the dependence between consecutive frequency measurements.

II. EXPERIMENTAL SETUP

Figure 1 is a sketch of our experimental setup. We connected a 10 MHz signal from a passive hydrogen maser (Vremya-Ch VCH-1008) to a TimeTech 10274 distribution amplifier via SpectraDynamics HROG-10 clock generator. We coupled this 10 MHz signal with phase-stable Huber+Suhner Sucoflex 104 cables to the reference and input connectors of a Keysight 53230A frequency counter [3].

We measured the frequency with the Keysight 53230A counter in CONT mode at time resolutions of 10 s and 0.1 s, and in the undocumented RCON mode with a time resolution of 0.1 s. We also computed a 100-point moving average of the RCON data measured with a time resolution of 0.1 s. We used the internal storage option provided by the Keysight 53230A counter, except for the CONT 10 s data, which we acquired remotely with TimeLab [6]. When data are acquired with TimeLab, the default driver of the Keysight 53230A counter in TimeLab sends a “READ?” SCPI command to the counter, which triggers a new measurement, resulting in frequency measurements that are not gap-free. Instead, the “R?” SCPI command should be used, which does not trigger

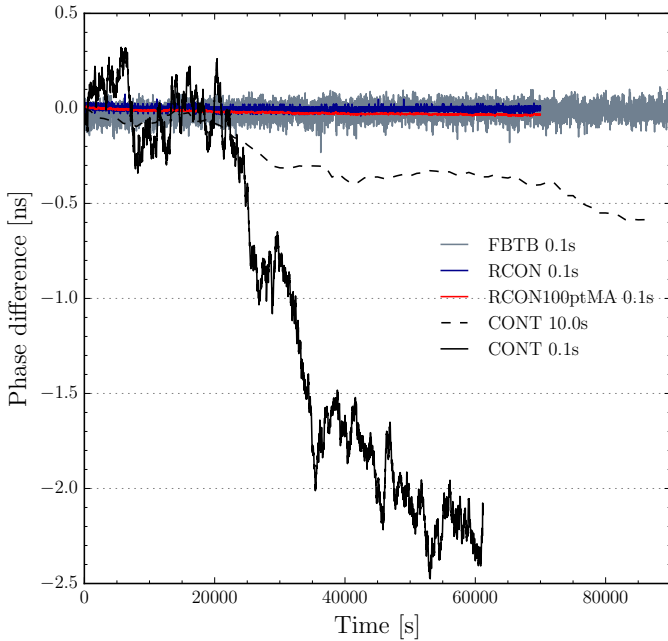


Fig. 2. Phase difference measured with the same experimental setup (Fig. 1) and different counters and modes: CONT 0.1 s (black, solid), CONT 10.0 s (black, dashed), RCON 0.1 s (blue), RCON 0.1 s with a 100–point moving average (red), and CNT–91 in frequency back–to–back mode and a temporal resolution of 0.1 s (grey). Only every 100th value is shown here. The CONT 10.0 s data were acquired with TimeLab.

a new measurement. We could not detect any systematic difference between data acquired with TimeLab and those stored internally in the counter.

For comparison, we repeated the measurement at a sampling interval of 0.1 s with a Pendulum CNT–91 frequency counter in frequency back–to–back (FBTB) mode [7].

III. RESULTS AND DISCUSSION

A. Frequency estimates

Because we measure the reference signal at 10 MHz against itself, the measured relative frequency offset should be 0 in any measurement mode and at any sampling interval for a sufficiently long measurement period. From frequency measurements in different modes of a Keysight 53230A counter, we computed the phase difference. The results are shown in Fig. 2. For comparison, we also show a similar measurement made with a Pendulum CNT–91 counter in frequency back–to–back mode. As we expect from the specifications [3], the Keysight counter exhibits less noise than the Pendulum CNT–91 [7].

We have fitted a least–squares linear regression to the phase difference data to obtain the relative frequency offset. We summarized these values in Table I. Surprisingly, the CONT mode measurements yield a frequency bias at both sampling intervals. These are much larger than the relative frequency offsets measured in RCON mode or with the CNT–91 frequency counter. It is important to note that we cannot ascertain that the relative frequency offsets measured

TABLE I
RELATIVE FREQUENCY OFFSET, $\Delta f/f$, COMPUTED FROM FREQUENCY MEASUREMENTS IN FIVE DIFFERENT MEASUREMENT MODES.

Instrument	Measurement mode	$\Delta f/f$
Keysight 53230A	CONT 10.0 s	-6.1×10^{-15}
Keysight 53230A	CONT 0.1 s	-5.0×10^{-14}
Keysight 53230A	RCON 0.1 s	-1.0×10^{-16}
Keysight 53230A	RCON100ptMA 0.1 s	-4.9×10^{-16}
Pendulum CNT–91	FBTB 0.1 s	1.6×10^{-16}

in RCON, RCON100ptMA, and FBTB mode are significantly different from 0.

The results from the frequency offsets (Table I) show that the RCON mode yields a better frequency estimate than the CONT mode, even if we increase the sampling interval in CONT mode from 0.1 s to 10 s.

If we increase the sampling interval from 0.1 s to 10.0 s in CONT mode, we obtain a smaller relative frequency offset, but is still different from 0. In particular, the RCON mode yields better results, with and without a moving–average filter.

B. Autocorrelation function

Riley [8, pp. 45 to 46] pointed out that the dominant noise process in a time series of fractional frequency data can be identified using the lag 1 autocorrelation, ρ_1 . If the data have not been differenced, white phase noise yields $\rho_1 = -1/2$, flicker frequency noise yields $\rho_1 = 1/3$, and white frequency noise yields $\rho_1 = 0$ [8].

An autocorrelation of $\rho_1 = -1/2$ at lag 1 can be interpreted as there being a 50 % chance of measuring a value smaller than average at $t = 1$ if one measured a larger–than–average value at $t = 0$.

For the RCON 0.1 s and CNT–91 FBTB 0.1 s measurements, the autocorrelation at lag 1 is $\rho_1 = -1/2$ (not shown). Thus, the dominating process is white phase noise. This is what we expect. The autocorrelation functions of the CONT 10.0 s, CONT 0.1 s, and RCON 0.1 s (with 100–point moving average) time series are shown in Fig. 3. The behaviour of the CONT mode is surprising. We see that the CONT mode results in temporal correlations at lag 1, which clearly are not due to white phase noise. In addition, the autocorrelation does not vanish for lags 2 and 3. Judging from the values of ρ_1 , the dominant noise process seems to be a combination of flicker phase noise and random–walk phase noise.

When we apply a 100–point moving average to the RCON data with 0.1 s time resolution, the characteristics of the autocorrelation function do not change (Fig. 3, bottom panel). We now get an autocorrelation of $\rho_{100} = -1/2$. A finite averaging window does not lead to long temporal correlations that we see in CONT mode.

C. Allan deviation

Figure 4 shows the Allan deviation of the frequency measurements, and Fig. 5 shows the modified Allan deviation.

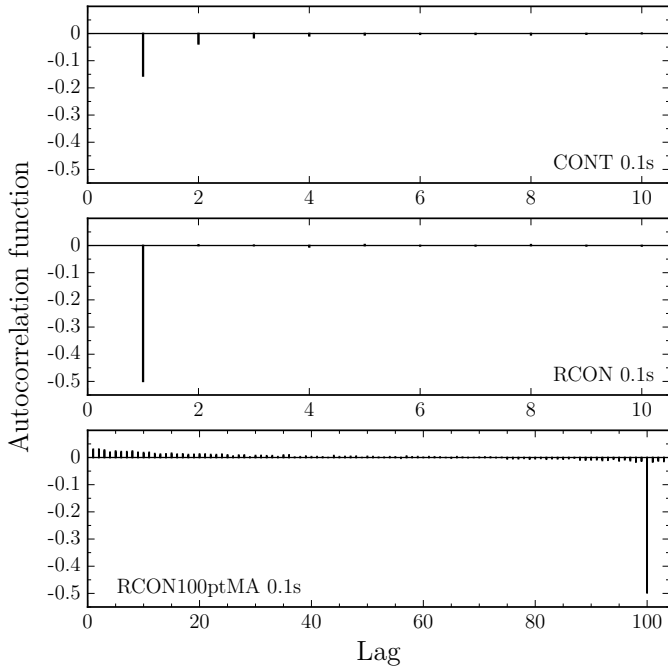


Fig. 3. Autocorrelation function for the measurement in different modes, made with a Keysight 53230A frequency counter. Top panel: CONT mode with 0.1 s time resolution. Middle panel: RCON mode with 0.1 s time resolution. Bottom panel: RCON mode with a time resolution of 0.1 s and a 100–point moving average. Note the different scales for the lag.

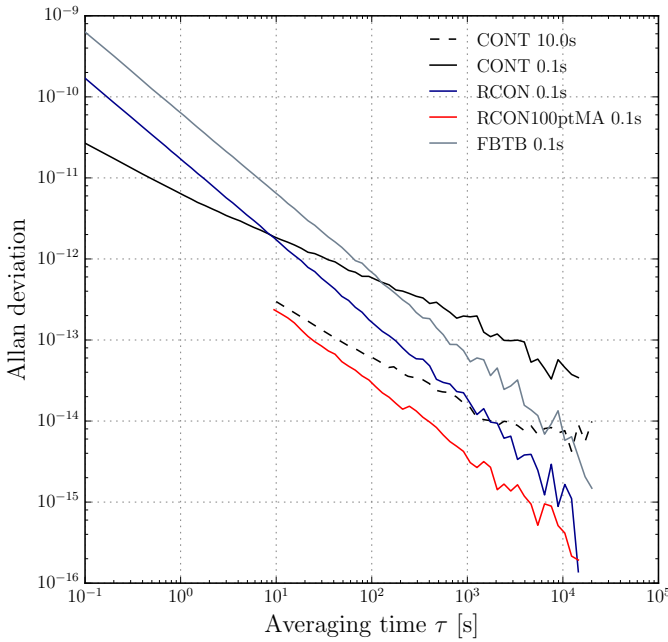


Fig. 4. Allan deviation of the time series shown in Fig. 2: CONT 0.1 s (black, solid), CONT 10.0 s (black, dashed), RCON 0.1 s (blue), RCON 0.1 s with a 100–point moving average (red), and CNT–91 in frequency back–to–back mode and a temporal resolution of 0.1 s (grey).

From Fig. 4, we see that the RCON 100–point moving average time series with 0.1 s temporal resolution is approxi-

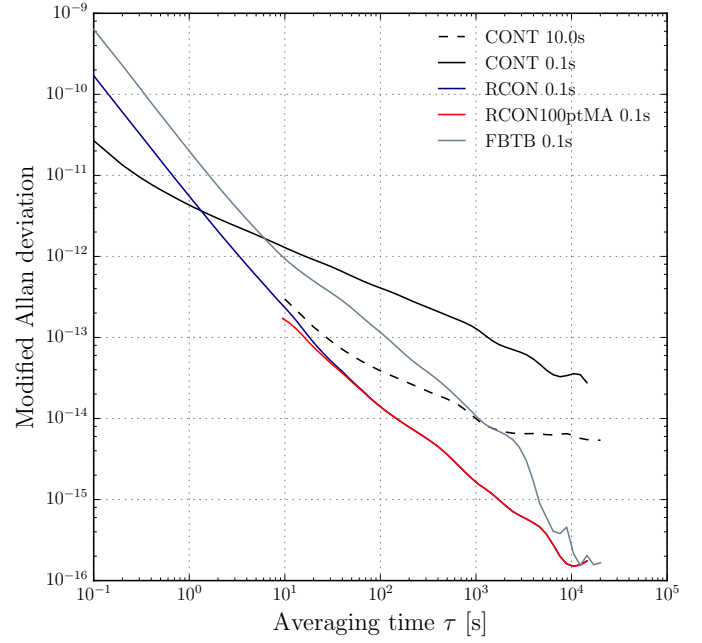


Fig. 5. Modified Allan deviation of the time series shown in Fig. 2: CONT 0.1 s (black, solid), CONT 10.0 s (black, dashed), RCON 0.1 s (blue), RCON 0.1 s with a 100–point moving average (red), and CNT–91 in frequency back–to–back mode and a temporal resolution of 0.1 s (grey).

mately one order of magnitude better than RCON 0.1 s without moving average. This is consistent with the central limit theorem. We also see that, for averaging times $\tau \gtrsim 10$ s, the RCON mode provides a frequency estimate with better stability than the CONT mode.

The CONT mode frequency measurements result in a modified Allan deviation with an approximate slope of $\tau^{-1/2}$, which is characteristic of random–walk phase noise. We confirmed this result by calculating the first differences of the CONT 0.1 s time series and computing its autocorrelation (not shown). We obtained $\rho_1(d=1) = -1/2$, which corresponds to random–walk phase noise [8].

The undocumented RCON mode exhibits white phase noise characteristics, as does the Pendulum CNT–91 in frequency back–to–back mode. The modified Allan deviation of these measurements follows a slope of $\tau^{-3/2}$.

When we apply a 100–point moving average to the RCON 0.1 s–measurements, the modified Allan deviation follows a τ^{-1} slope. That is, we obtain resolution–enhanced frequency estimates with flicker phase noise characteristics. This is also true if we use the Keysight counter’s built–in function for a 100–point moving average (not shown).

IV. CONCLUSIONS

To characterize a Keysight 53230A frequency counter, we measured a 10 MHz reference signal against itself, using the counter’s different measurement modes (CONT and RCON). We compared these measurements to frequency back–to–back measurements made with a Pendulum CNT–91 counter.

We find that the Keysight 53230A's CONT mode, which is a "resolution-enhanced, gap-free" [3] frequency measurement mode, yields a frequency bias (error), even for measurement periods of roughly one day. The CONT mode exhibits random-walk phase noise, and the autocorrelation at lag 1 is not $-1/2$, as is typical for white phase noise. The autocorrelation for lag 2 does not vanish, leading to a temporal correlation in the frequency measurements. The frequency bias is present also for longer sampling intervals (10.0 s instead of 0.1 s).

In contrast, the undocumented RCON mode does not show any frequency bias, and shows no temporal correlation at lag ≥ 2 . The modified Allan deviation exhibits white phase noise characteristics. The results are consistent with measurements made with a Pendulum CNT-91 frequency counter.

Using the undocumented RCON mode, we can obtain frequency estimates with better stability and without bias. The resolution can be enhanced using the counter's built-in moving-average function.

ACKNOWLEDGMENTS

We used the Python package "allantools" by Anders Wallin, Danny Price, Cantwell G. Carson, and Frédéric Meynadier. We also used TimeLab by John Miles, whom we thank for his helpful advice.

REFERENCES

- [1] E. Rubiola, "On the measurement of frequency and of its sample variance with high-resolution counters," *Rev. Sci. Instrum.*, vol. 76, no. 5, 2005, 054703.
- [2] S. T. Dawkins, J. J. McFerran, and A. N. Luiten, "Considerations on the measurement of the stability of oscillators with frequency counters," *IEEE T. Ultrason. Ferr.*, vol. 54, no. 5, pp. 918–925, 2007.
- [3] Keysight, *The 53230A frequency counter*, accessed: April 5, 2016. [Online]. Available: www.keysight.com/en/pd-1893420-pn-53230A/
- [4] E. Benkler, C. Lisdat, and U. Sterr, "On the relation between uncertainties of weighted frequency averages and the various types of allan deviations," *Metrologia*, vol. 52, no. 4, pp. 565–574, 2015.
- [5] R. H. Shumway and D. S. Stoffer, *Time Series Analysis and Its Applications*, 3rd ed. New York: Springer, 2011, ISBN (print): 978-1-4419-7864-6.
- [6] J. Miles, "TimeLab." [Online]. Available: <http://www.ke5fx.com/timelab/readme.htm>
- [7] Spectracom, *User's Manual, Timer/Counter/Analyzer CNT-90, CNT-91; Frequency Calibrator/Analyzer CNT-91R, CNT-91R/AF; Microwave Counter/Analyzer CNT-90XL*, 2014, rev. 8; accessed: April 5, 2016. [Online]. Available: <http://spectracom.com/documents/users-manual-timercounteranalyzer-cnt-90-cnt-91-frequency-calibratoranalyzer-cnt-91r-cnt>
- [8] W. J. Riley, "Handbook of frequency stability," NIST Special Publication 1065, National Institute of Standards and Technology, Boulder, CO, USA, 2008, available online: tf.boulder.nist.gov/general/pdf/2220.pdf.

Influence of induced stress on AlN-solidly mounted resonators

A. Delicado, M. Clement, J. Olivares, T. Mirea, B. Díaz-Durán, and E. Iborra

GMME-CEMDATIC-ETSIT
Universidad Politécnica de Madrid
Madrid, SPAIN
mclement@etsit.upm.es

Abstract— The frequency variation of solidly mounted resonators made with AlN thin films operating in longitudinal and shear acoustic modes with induced in plane mechanical strain is presented. The induced deformation range is in the hundreds of microstrains and the frequency variations in the hundreds of kHz, giving coefficients of resonant frequency with deformation in the order of 56% per unit strain. The influence on this parameter of the resonant mode, coupling factor and frequency is analyzed.

Keywords—AlN resonator; mechanical strain; frequency variation

I. INTRODUCTION

Sensors based on thin film piezoelectric resonators are currently more widely used in industrial and consumer electronic devices than ever. Gyroscopes, accelerometers, as well as temperature, pressure, and chemical sensors are being developed as application of such devices. Strain sensors mainly based on SAW devices are being investigated as well. If an electroacoustic resonator is strained, its resonant frequency shifts due to two main reasons. First, the strain causes a variation resonator geometry by changing the thickness of the layers and the area of the surfaces, which affects directly the resonant frequency. Additionally, some of the properties of the materials composing the device (density, elastic constants and dielectric permittivity) may also experience variations, directly influencing the resonator behavior. The properties of the stressed materials do not necessarily vary in the same direction. Depending of the geometry and applied forces, their effects on the resonant frequency can be partially compensated or enhanced. Therefore, for each kind of device and particular use, the response to an applied stress must be analyzed individually. Many examples of mechanically excited sensors based on the sensitivity of the resonant frequency to strain.

Pressure sensors have been manufactured with film bulk acoustic resonators (FBAR) [1, 2], Lamb wave resonators [3], and thin film surface acoustic wave (SAW) resonators [4, 5]. Strain sensors, intended for harsh environments or exhibiting very high response speed (for crash experiment, for example) can be achieved using SAW devices [6-9]. However, membrane-based sensors are not robust enough to be used in applications where the pressure is very high, like common rail fuel injection engines. In these cases, solidly mounted resonators (SMR) made of thin film piezoelectric capacitors built on top of acoustic mirrors are more adequate, because their mechanical

resistance is set by the chosen substrate, usually consisting in silicon wafer or a steel or plastic plate. SMRs also allow reducing the influence of temperature variations, as the thermal conductivity of the mirror is larger than that of air or any other fluid.

In this paper, we investigate the variations in the resonant frequency, electromechanical coupling factor (k^2) and quality factor (Q) of AlN-based SMRs when the substrate is deformed.

II. EXPERIMENTAL

A. Device fabrication

We fabricated AlN-based SMRs using (100)-oriented silicon substrates covered with an acoustic reflector that alternated five sputtered layers of porous SiO₂, as low acoustic impedance material [10], and Mo, as high acoustic impedance material. The thickness of the layers was adjusted to achieve maximum reflectance for the longitudinal mode at a frequency of 2.5 GHz. As bottom electrode a continuous iridium thin film 130 nm thick was deposited on the uppermost SiO₂ layer of the reflector covered by a 10 nm-thick Ti adhesion layer.

The AlN film was deposited in an ultra-high-vacuum system pumped to a base pressure below 8×10^{-7} Pa. A high purity (99.9995 %) 150 mm in diameter Al target was sputtered in an Ar/N₂ (40:60) atmosphere at 0.27 Pa using a pulsed-DC source (MKS-ENI RPG-50) operating at a frequency of 50 kHz and a power of 1.2 kW. Two types of resonators were fabricated and characterized. Resonators of type I consisted in single longitudinal mode resonators made with perfectly c-axis oriented AlN films. Resonators of type II consisted in mixed shear and longitudinal mode resonators, fabricated with AlN thin films containing uniformly tilted grains, achieved using a procedure described elsewhere [11]. During deposition, the substrates were kept at 400°C and biased to a DC voltage of -55 V to adjust the residual stress of the AlN films to values below 200 MPa. The films were grown to a thickness of around 1 μm, yielding resonators operating at around 2.5 GHz for longitudinal mode and at around 1.4 GHz for shear mode. The top electrode was made of 200 nm thick Mo thin film patterned by conventional photolithography followed by a wet etching. The contact to the bottom electrode was achieved by capacitive coupling using an extended contact lying in the same plane than the top electrode. This way, no patterning of AlN film was required. Fig. 1 shows a picture of a typical device.

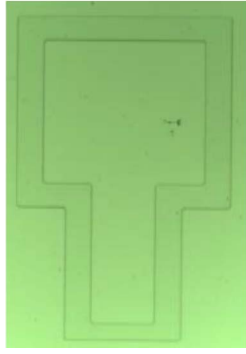


Fig. 1. Photograph of one of the fabricated devices.

B. Controlled strain generation

For generating a known and controlled strain in the devices, we used two experimental arrangements. The first one consisted in a 20 cm- long, 2 cm-wide and 3 mm-thick stainless steel cantilever clamped at one of its edges and actuated with a micrometer screw in the free edge. A 1.5 cm × 2 cm silicon die containing several resonators was glued on top of the cantilever with a two-component high-strength epoxy. The in-plane strain of the top surface (ε) of the test wafer was calculated from the typical formula [11].

$$\varepsilon = \frac{t}{R} \quad (1)$$

where t is the distance of the surface to the neutral fiber, located in the middle of the cantilever and R the radius of curvature of the cantilever, which can be calculated from:

$$R = \frac{(1 + (\frac{dy}{dx})^2)^{3/2}}{\frac{d^2y}{dx^2}} \quad (2)$$

being x the coordinate parallel to the cantilever and y the deflection at x . The deflection at x is:

$$y(x) = \frac{-P}{6EI} (3Lx^2 - x^3) \quad (3)$$

with P force applied on the cantilever edge, E the elastic constant, I the momentum of inertia and L the total length of the cantilever. See Fig. 2 for details.

The main issue concerning this method is the bonding strength. Although we tried to reduce the thickness of the glue layer between the silicon sample and the steel to its minimum value, the desired deformation might not be generated on top of the sample owing to some compliance of the glue layer. To verify this issue, we performed tests by gluing 3 mm-long standard strain gauges atop the silicon sample to measure the actual deformation of its surface. The measurements of the gauge were always in a $\pm 10\%$ band around the calculated strain for the whole measurement range and no hysteresis was found after repeating the measurements several times. Only deflections of the free beam edge greater than 1 cm yielded departures of measurements from theoretical values, due to the glue layer compliance. Therefore, to guarantee that the strain values were correct, we limited the displacements of the free edge of the steel bar to 5 mm, corresponding, in our geometry, to maximum strains of 800 $\mu\varepsilon$.

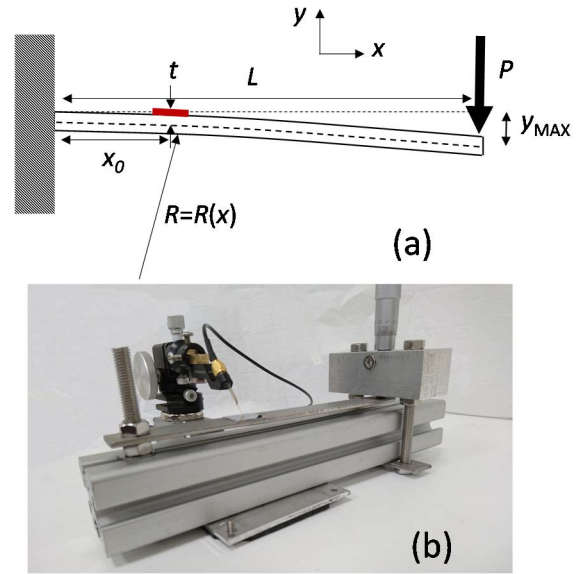


Fig. 2. First deformation method. One-fixed-side bar with punctual excitation at its edge. a) scheme with notation, b) picture of the apparatus.

The second technique for generating a controlled deformation consisted in clamping the silicon die containing the resonators by its edges, and pushing the bottom of the substrate with a steel bar. Fig. 3 show the experimental arrangement. The micrometer screw pushes down a lever, which transmits the fourth of the displacement to a very rigid steel punch in contact with the bottom surface of the silicon sample (see Fig. 3 for details).

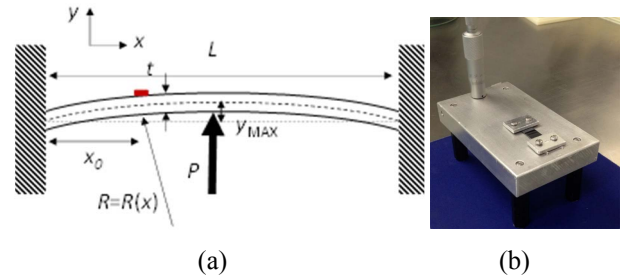


Fig. 3. Second deformation method. Two-fixed-side silicon bar with punctual excitation in the midpoint. a) scheme with notation, b) photo of the apparatus.

In this case, the profile of the distorted silicon beam is given by

$$y(x) = \frac{-P}{48EI} (3Lx^2 - x^3) \quad (4)$$

for $x < L/2$, being symmetric the other half. In this case, the measurement of the strain on the silicon surface at the middle of the beam with a conventional strain gauge departs around 15% with respect to the calculated values.

C. Device characterization

The electrical response of the resonators was measured with an Agilent 5230A network analyzer between 10 Mhz and 10 Ghz by using a large density of data points around the resonances. Samples were contacted with RF probes (Picoprobe from GCB

Industries). For accurately determining the resonant frequency, the real part of the admittance spectrum around the resonance was fitted with an eight-degree polynomial, which was subsequently differentiated with respect to the frequency to obtain its root corresponding to the resonant frequency. Using this method, the value of the measured resonant frequency was determined an uncertainty of less than 5 kHz (less than 2 ppm). A continuous adjustment of the pressure applied to the probes leaning on the contact pads as the sample is deformed is needed to ensure a reproducible electrical contact. Additional measurements of the impedance spectra of samples operating in the longitudinal mode with a DC biasing were performed. For these measurements an Agilent 4991A impedance analyzer was used instead of the network analyzer.

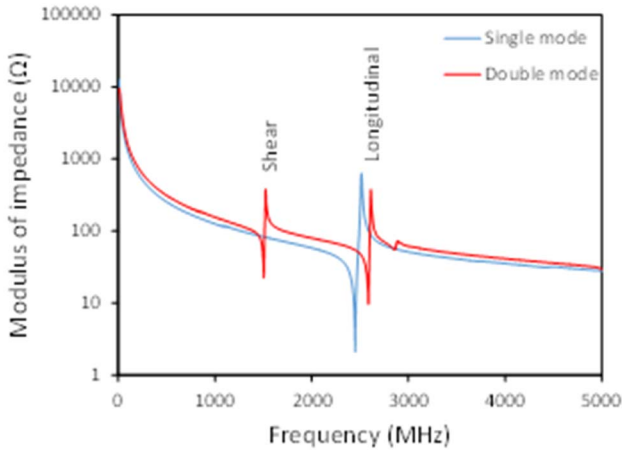


Fig. 4. Modulus of impedance spectra of typical samples with single and double resonant modes.

III. RESULTAS AND DISCUSSION

Fig. 4 shows a typical spectrum of the frequency response of a resonator showing a single longitudinal mode along with that of a resonator exhibiting shear and longitudinal modes. The quality factor for the single mode at both resonant and antiresonant frequencies was around 600 and 400 respectively and the value of electromechanical coupling around 6.4 %. For double mode samples the quality factor of shear mode was 300 and 200 at the resonant and antiresonant frequencies, respectively, and the electromechanical coupling was 2.8% and 2.4% for shear and longitudinal modes, respectively.

We measured several samples of the two types with both deformation methods finding reasonably good reproducibility of the measurements. Generally, samples first measured under the pushing bar deformation scheme and then glued and measured in the cantilever show similar behaviors, with discrepancies of around 20%.

Fig. 5 shows the variations of the resonant frequency of the longitudinal mode of two representative samples with different values of k^2 subjected to deformation using both the cantilever beam and with the pushing bar, as a function of the calculated induced strain. The sensitivity of the resonant frequency to strain for the longitudinal mode is always negative and larger (in modulus) for resonators with higher k^2 values in both types of samples, single and mono mode. This result is independent of the method used for deforming the samples.

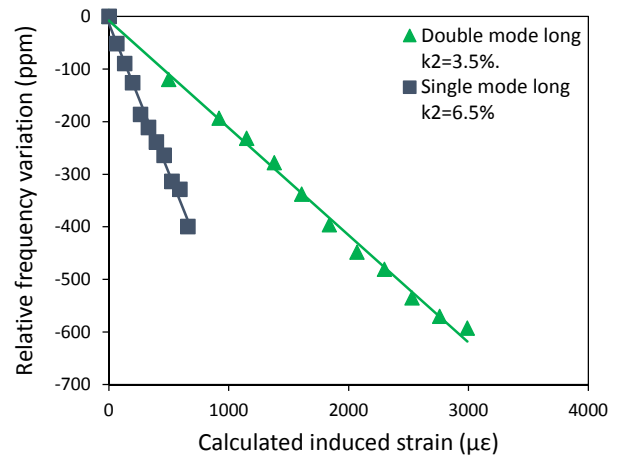


Fig. 5. Relative variations of resonant frequencies for a single mode resonator (■) and double mode one (▲) longitudinal and (●) shear.

Sensitivity to strain of the shear modes is always lower than that of the longitudinal modes, even if the values of the k^2 are comparable. For some samples, shear mode showed a slightly positive sensitivity as shown in Fig. 6. This effect seems to be dependent on the value of the resonant frequency but cannot be explained at this moment.

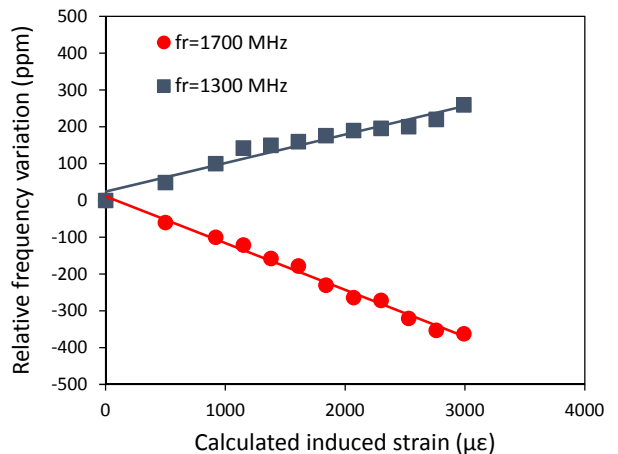


Fig. 6. Relative variations of resonant frequencies for shear mode in double mode resonators at two different resonant frequencies of 1300 MHz (■) and 1700 MHz (●).

As analyzed by Weber et al. [12], the frequency variations with strain are due to the variation of the thicknesses of the films owing to the Poisson effect, the variations of the material densities and to the variations of the elastic constants when a stress is applied to them. All these magnitudes directly affect the resonant frequency. The relative influence of these factors is variable depending on the geometry (particular thicknesses) and, apparently, strongly dependent of the quality of the materials. It is worth noting that, generally, we have found that the resonances of lower values of the electromechanical coupling factor show are less sensitive to the induced strain, regardless of the resonant mode nature (shear and longitudinal). On the other hand, while variations of the resonant frequency of longitudinal modes are always negative, the variation of shear modes can be positive and, for very low coupling factors, near zero. A careful

analysis of the phenomena is needed to explain the observed behavior. Finite element analysis could be a very good tool for doing it.

An alternative method to generate a controlled strain in AlN films by virtue of the piezoelectric effect is to apply a continuous voltage superimposed to the measurement test signal. We have biased the sample using a DC voltage varying from 0 to 40 V while measuring the impedance spectrum of the resonators. In order to compare these measurements we have calculated the field-induced strain (s) as:

$$s = \frac{V \cdot d_{33}}{t \cdot \nu} \quad (5)$$

where V is the applied DC voltage, d_{33} is the piezoelectric coefficient in the c-axis direction, t is the thickness of the AlN film and ν is the Poisson coefficient for AlN.

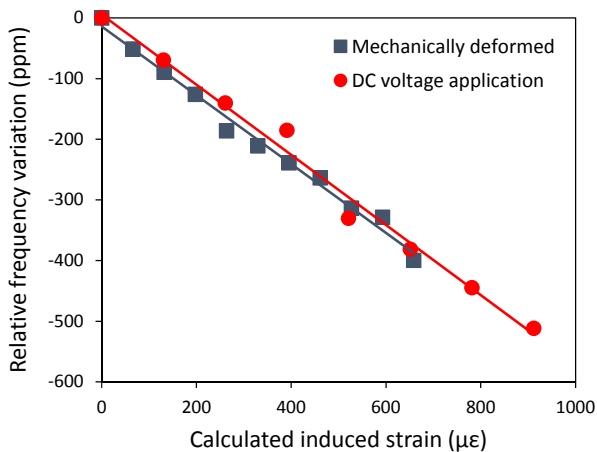


Fig. 7. Relative variations of resonant frequencies for a single mode resonator when mechanically deformed (■) and when a DC bias voltage is applied during measurement (●).

The particular values chosen for the strain calculation were $d_{33} = 4.1$ pm/V and $\nu = 0.28$. Fig. 7 shows the frequency variations of the single mode resonator shown in Fig. 5 as a function of deformation arising from the application of a DC voltage during the measurement.

Regarding the quality factors Q and electromechanical coupling k^2 , although not all the tested devices exhibit exactly the same behavior, the trend of the quality factor at the antiresonant frequency is to remain invariable under strain. The Q at resonant frequency shows a more scattered evolution, probably because of the variation of the series resistance introduced by adjusting the pressure of the RF probes differently. As for the values of k^2 , only a slight increase is observed in devices of large k^2 values (6.5% for longitudinal mode). This is attributed to the fact that the antiresonant frequency is less sensitive to strain than the resonant one. This effect is not appreciable for devices with the lowest k^2 tested (around 3%)

IV. CONCLUSIONS

The variations of the resonant frequencies of the longitudinal and shear modes in mechanically strained AlN-based SMRs have been investigated. The frequency shifts are greater when the mechanical coupling factor is greater. Values up to -0.71 ppm/ $\mu\epsilon$ have been measured for longitudinal modes. For shear modes the sensitivity of the resonant frequency appears to be lower (for comparable values of k^2), changing the sign in some cases. The effects of the strain in Q is not significant. Only devices of high k^2 values show a slightly increase of k^2 with the increasing strain. Numerical simulations, taking into account all the effects caused by the deformation of the device are needed to account for all this phenomena.

ACKNOWLEDGMENT

This work was partially supported by Ministerio de Economía y Competitividad del Gobierno de España through project MAT2013-45957-R.

REFERENCES

- [1] Chiu, G., H. Chen, and R. Huang. "FILM BULK ACOUSTIC-WAVE RESONATOR PRESSURE SENSOR." Eurosensors Conf., Gotenburg. 2006.
- [2] X.L. He, L. Garcia-Gancedo, P.C. Jin, J. Zhou, W.B. Wang, S.R. Dong, J.K. Luo, A.J. Flewitt, and W.I. Milne "Film bulk acoustic resonator pressure sensor with self temperature reference". J. Micromech. Microeng. 22 (2012) 125005 (6pp)
- [3] E. Anderås, L. Arapan, I. Katardjiev, V. Yantchev, "Thin Film Plate Wave Resonant Sensor for Pressure and Gravimetric Measurements" Procedia Engineering 25 (2011) pp. 571-574.
- [4] Wang, Tao, et al. "Diaphragm shape effect on the sensitivity of surface acoustic wave based pressure sensor for harsh environment." Applied Physics Letters 107.12 (2015) pp. 123501.
- [5] Rodriguez-Madrid, J. G., et al. "High precision pressure sensors based on SAW devices in the GHz range." Sensors and Actuators A: Physical 189 (2013) pp. 364-369.
- [6] B. Donohoe, D. Geraghty, and G.E. O'Donnell, "Wireless Calibration of a Surface Acoustic Wave Resonator as a Strain Sensor", IEEE Sensors Journal, 11 (2011) pp. 1026-1032.
- [7] Z. Bao, M. Hara, and H. Kuwano. "Highly sensitive strain sensors using surface acoustic wave on aluminum nitride thin film for wireless sensor networks", 18th Int. Conf. on Solid-State Sensors, Actuators and Microsystems (Transducers2015) (2015) pp. 1239-1242.
- [8] T. Konno, M. Hara, and H. Kuwano. "Oscillator-based strain gauges employing surface acoustic wave resonators for wireless sensor network", 2013 Joint UFFC, EFTF and PFM Symposium. (2013), pp. 1930-1933.
- [9] R. Stoney, D. Geraghty, and G.E. O'Donnell. "Characterization of differentially measured strain using passive wireless surface acoustic wave (SAW) strain sensors". IEEE Sensors Journal. 14, (2014) pp. 722-728.
- [10] J. Olivares, E. Wegmann, J. Capilla, E. Iborra, M. Clement, L. Vergara, R. Aigner, "Sputtered SiO₂ as low acoustic impedance material for Bragg mirror fabrication in BAW resonators", IEEE T. Ultrasonics Ferroelectrics and Frequency Control 57 (1) (2010) pp. 23-29
- [11] M. DeMiguel-Ramos, T. Mirea, M. Clement, J. Olivares, J. Sangrador, E. Iborra "Optimized tilted c-axis AlN films for improved operation of shear mode resonators". Thin Solid Films 590 (2015) 219-223.
- [12] S.P. Timoshenko, J.N. Goodier, "Theory of Elasticity", McGraw-Hill International Editions, Third Edition, 1970.
- [13] J. Weber, M. Link, R. Primig, D. Pitzer, M. Schreiter, "Sensor for ambient pressure and material strains", 2005 IEEE Ultrasonics Symposium (2005) 1258-1261.

Ultra-low-noise optoelectronic oscillator at 10 GHz based on a short fiber delay

Oriane Lelièvre, Vincent Crozatier, Ghaya Baili, Perrine Berger, Loïc Morvan, Grégoire Pillet, Daniel Dolfi
Thales Research and Technology
1 Avenue Augustin Fresnel
91767 Palaiseau, France

Olivier Llopis
Laboratoire d'Analyse et
d'Architecture des Systèmes, CNRS,
Université de Toulouse,
7 Avenue du Colonel Roche,
31077 Toulouse, France

Fabienne Goldfarb, Fabien Bretenaker
Laboratoire Aimé Cotton, CNRS,
Université Paris Sud 11,
ENS Cachan,
Université Paris-Saclay,
91405 Orsay Cedex, France

Abstract— We report on an optoelectronic oscillator (OEO) at 10 GHz based on a single 1 km long fiber delay, and exhibiting simultaneously an ultra-low close-in phase noise (-94 dBc/Hz @100 Hz) and a low spurious level (below -110 dBc/Hz). These results are well predicted by a model taking into account the frequency and intensity noise from the laser source that are converted into phase noise.

Keywords— optoelectronic oscillator, fiber delay line, phase noise.

I. INTRODUCTION

OEOs are known to deliver ultra-low phase noise microwave signals at high frequency with a quite easy setup [1]. As expected from a simple feedback model considering the microwave amplifiers as the main noise source, the phase noise level of an OEO can be reduced by lengthening the fiber delay. But this is true only up to few kilometers, where other noise sources start to dominate, such as the conversion of laser frequency noise to microwave phase noise [2], and nonlinear effects in the fiber [3]. Moreover, a long fiber delay leads to a high level of spurs at multiples of cavity free spectral range, and to a large volume, both criteria being detrimental for demanding applications. In this paper, we report on an optoelectronic oscillator (OEO) at 10 GHz based on a short fiber delay, and exhibiting simultaneously an ultra-low close-in phase noise and a low spurious level.

II. EXPERIMENTAL SETUP AND RESULTS

The setup of our optoelectronic oscillator is described on Fig.1. The laser source is a high-power semiconductor DFB laser at 1.55 μm driven by a low-noise current source, in order to reduce its low-frequency intensity and frequency noises. Indeed, we aim at reducing the laser noise conversion into RF phase noise photodiode nonlinearity and through fiber dispersion [2]. The laser is modulated by a Mach-Zehnder Modulator exhibiting an ultra-low half-wave voltage of 1.6 V at 10 GHz, followed by a 1 km long delay line based on a standard G652 fiber. The signal is detected by a high-speed PIN photodiode, and amplified by two ultra-low phase noise RF amplifiers (12 dB gain, flicker phase noise -157 dBc/Hz at 100 Hz). After amplification, the signal is filtered by a custom

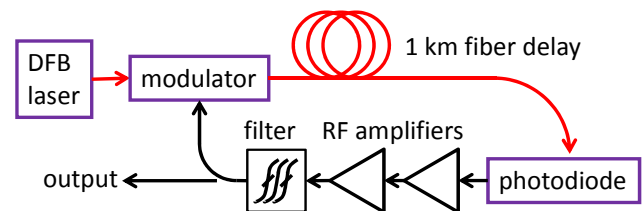


Fig. 1. Phase noise at 10 GHz.

RF filter based on a high-Q dielectric ceramic resonator. The filter is centered at 10 GHz and exhibits a 4.4 MHz FWHM bandwidth, and 3.8 dB of insertion losses, corresponding to a loaded quality factor Q of 2280. A 10 dB RF coupler is inserted between the filter and the modulator to get the useful output of the oscillator. To further reduce the noise, we modulate the laser current at 2.5 MHz through the driver in order to reduce the effects of Rayleigh backscattering [3].

A stable RF oscillation is observed when the photocurrent reaches 6.5 mA. We then measure a close-in phase noise of -94

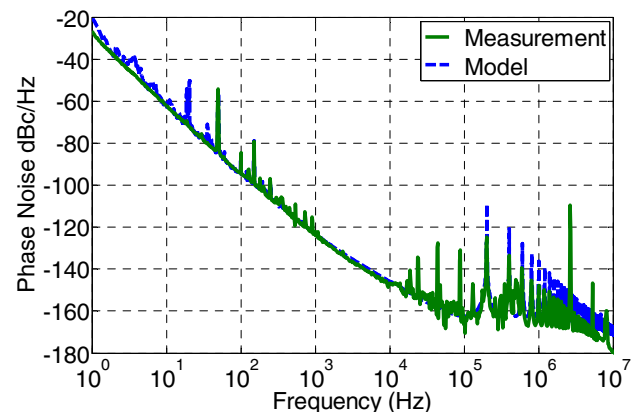


Fig. 2. Phase noise at 10 GHz. The peak at 2.5 MHz is due to the laser current modulation. The peaks below 100 kHz are measurements spurious.

dBc/Hz at 100 Hz from the carrier, and a low spurious level, below -110 dBc/Hz (Fig. 2).

As seen on Fig.2, these performances are well predicted by a model adapted from [2], including the standard noise source of a microwave photonic link (photodetection and thermal

This work has been partly funded by Direction Générale de l'Armement (DGA) through European Defense Agency (EDA) project HIPMOMOS.

noises), and also (i) the laser frequency noise converted through fiber chromatic dispersion and (ii) the laser intensity noise converted by photodiode nonlinearity. The RF amplifier phase noise is modeled by a $1/f$ phase noise contribution and a noise figure. The actual laser noises and photodiode nonlinearity are measured and fed to the model.

From this model, we deduce that our oscillator is limited at low frequency (below 1 kHz offset) by the conversion of laser frequency noise into phase noise through the fiber dispersion, suggesting that an increase of the fiber length would not lead to a significant improvement of the phase noise.

III. CONCLUSION

We have assembled an optoelectronic oscillator based on a short fiber delay. By properly choosing the components and their operating conditions, our oscillator exhibits an ultra-low

close-in phase noise of -94 dBc/Hz at 100 Hz from the carrier, and a low spurious level, below -110 dBc/Hz. To the best of our knowledge, these noise and spurs level are the lowest for such a short delay, these performances exceeding the ones of OEOs using up to 4 km fiber length.

REFERENCES

- [1] X. S. Yao and L. Maleki, "Converting light into spectrally pure microwave oscillation," *Opt. Lett.*, Vol. 21, p. 483-485, 1996.
- [2] K. Volyanskiy et al., "Contribution of Laser Frequency and Power Fluctuations to the Microwave Phase Noise of Optoelectronic Oscillators," *J. of Light. Tech.*, Vol. 28, p. 2730-2735, 2010.
- [3] A. Docherty et al., "Rayleigh-Scattering-Induced RIN and Amplitude-to-Phase Conversion as a Source of Length-Dependent Phase Noise in OEOs," *IEEE Phot. J.*, Vol. 5, p. 5500514-5500514, 2013.

Build-Up Detection and Level Monitoring by Using Capacitive Glocal Technique

F. A. Khan, A. Yousaf, L. M. Reindl
Laboratory for Electrical Instrumentation
IMTEK, University of Freiburg
Freiburg, Germany
khanf@tf.uni-freiburg.de

Abstract—This paper presents a proof of concept of continuous level monitoring and build-up detection by developing an innovative capacitive E-fields approach “Glocal” (global and local). The change in the sensitivity of the sensor to detect the build-up on the sensor probe is increased by using local E-fields. An initial prototype sensor with a length of 89.5 mm is developed and tested on various fluids. Finite element method (FEM) analysis is also performed in order to investigate the sensitivity of the proposed sensor in liquids with various dielectric constants. An analytical model is also presented which estimates the electric field strength between the capacitive elements as a function of level for a single segment.

Keywords—Continuous level monitoring; glocal E-fields; build-up; dielectric permittivity; analytical model.

I. INTRODUCTION

Fluid level monitoring in various industrial and commercial applications is being performed by using several measurement approaches [1-3]. These approaches are generally based on contact and contactless methods. Contactless methods include optical and ultrasound approaches. Optical approach is based on a camera and an image signal processor to calculate the liquid level by detecting the edge of the image. Ultrasound works on time of flight principle by using the reflected waves. Contact based measurement includes mechanical, electrical and pressure approaches. Float type mechanical device is the most common approach used to detect the level by switching between the upper and lower limits. Pressure sensing technique works on the basis of detecting change of pressure increasing or decreasing the liquid level from a container [4-5].

Among all the contactless approaches, capacitive measurement approach is more robust and economical approach. One of the challenges for the capacitive measurement approach is to measure liquid level continuously with accuracy and high sensitivity [6].

The detection of build-up effect is one of the serious problems in level monitoring because build-up directly affect the sensor’s sensitivity and introduces error in liquid monitoring. Build-up is created, when the level sensing probe is immersed into a liquid for long time duration and later used to measure another fluid level in the different permittivity. Manufactures

used different contact and contactless approaches to overcome build-up effects. An acoustic principle based material coating detection sensor was also reported in [7] which operates on the principle of lamb wave’s mode conversion. Due to the presence of material’s coating in the container wall, the propagation time of waves are changed, resulting in the alteration of the waves properties and is detected by implementing two receivers on the outer side of the container wall. In RF impedance technique, special electronic circuitry is designed to produce 4 - 20 mA current which is evaluates the level by measuring their capacitance and impedance [8-9]. However, in presence of build-up, the current is reduced below 4 mA which is blocked or ignored. Vibrating tuning fork point level detection is also useful technique to detect the build-up problem. It is designed with the specific resonant frequency which is excited by the piezoelectric method from the fork. The oscillating signal (frequency and amplitude) is changed in the presence of build-up on the probe [10].

II. MOTIVATION AND CONCEPT

To examine the build-up problem, a concept of global and local E-fields is developed by using the specific arrangement of copper plates in capacitive level monitoring. The copper plates having less separation distance between them, creates strong local E-fields E_{local} which can detect the effect of build-up as shown in figure 1. On the other hand, global E-fields E_{global} as generated by the large distances between the copper plates are used for level monitoring. This allows to detect the build without any additional electronic circuitry at the same time continuously monitoring the level. Furthermore the presented sensor is cost effective, easy to manufacture and more robust as compare to other fluid level approaches.

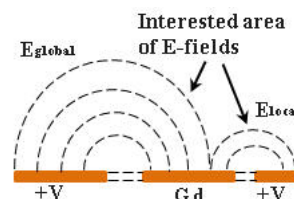


Figure 1: Concept of global and local electric fields

III. SENSOR DESIGN

The designed sensor probe is composed of multi segments capacitive elements. This 1 m probe with a diameter of 16 mm is divided into 11 segments and each segment has 89.5 mm in length.

The comparison of two designs of CLS segment (basic and mixed model, each one having the specific arrangement of copper plates) is investigated to obtain the optimized sensitivity with respect to different permittivity of liquids as well as the detection of build-up problem as shown in figure 2. The difference between these two models is the global and local fields' concept.

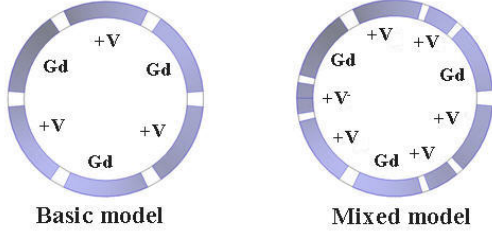


Figure 2: Arrangement of copper plates in basic and mixed model of CLS segments, where +V is active voltage and Gd is ground

The reason of splitting the copper plates into this specific arrangement is to evaluate improvement in sensitivity of a CLS segment by applying opposite polarity in between them.

FEM simulations in COMSOL Multiphysics were performed to optimize the specific distances between the plates and their arrangements as this is one of the important parameter to differentiate between the global and local capacitance. A 2D simulation design model of the CLS segment is shown in figure 3 with polypropylene (PP) material used as insulation.

A PCB based prototype of a single segment of mixed model of CLS is developed by dividing the sensor into the three strips of copper having specific distances of 1 mm and 0.5 mm respectively in between (figure 4). Two strips of copper are active with the central strip being grounded. The length and height of a segment are 89.5 mm and 35 μm respectively.

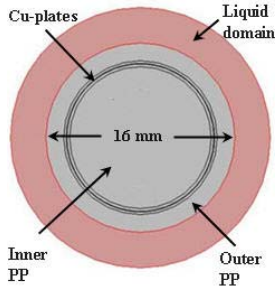


Figure 3: 2d design of a CLS segment

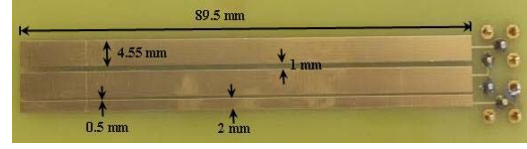


Figure 4: Dimension of single segment of CLS

IV. ANALYTICAL MODEL

The local and global capacitance can be calculated by using the approach as given [11-12]. Here, the two plates are having a positive voltage (V) and third one with zero voltage. The global capacitance (C_g) and local capacitance (C_l) can be calculated for finite gap as:

$$C_g = \frac{2\epsilon_0\epsilon_r L}{\alpha} \ln\left[\left(1 + \frac{2w_g}{a_g}\right) + \sqrt{\left(1 + \frac{2w_g}{a_g}\right)^2 - 1}\right] \quad (1)$$

$$C_l = \frac{2\epsilon_0\epsilon_r L}{\alpha} \ln\left[\left(1 + \frac{2w_l}{a_l}\right) + \sqrt{\left(1 + \frac{2w_l}{a_l}\right)^2 - 1}\right] \quad (2)$$

Where ϵ_0 is the vacuum permittivity, ϵ_r is the permittivity of liquid, α is the angle between the copper plates, a is the distance between the copper plates, L is the level of liquid. The penetration depth of E-fields in liquids is considered as $\epsilon_r > 1$ and calculated by the width of global (w_g) and local plates (w_l). From equation (3), the build-up effect can also be determined by evaluating the value of local capacitance (C_l). The value of C_l without build-up is represented as $C_{l_{nob}}$. In presence of a coating on the sensor, the value of C_l will change and represented as C_{lb} . By taking the ratio of C_{lb} and $C_{l_{nob}}$ the presence or absence of a build-up can be expressed as:

$$C_l = \frac{C_{lb}}{C_{l_{nob}}} \quad (3)$$

If $C_l \approx 1$ (no build-up effect), or $C_l \neq 1$ (build-up effect). The level can be analytically represented as

$$X = \frac{2\epsilon_0\epsilon_r}{\alpha} \ln\left[\left(1 + \frac{2w_g}{a_g}\right) + \sqrt{\left(1 + \frac{2w_g}{a_g}\right)^2 - 1}\right]$$

$$L = \frac{C_g}{X} \quad (4)$$

V. MEASUREMENT AND RESULTS

The measurements are performed in liquids having dielectric permittivity (2 to 80) with in a non-conductive tank. The measurements were conducted using a vector network analyzer (Agilent 8753ES) by applying a frequency sweep from 0.3 MHz to 20 MHz as shown in figure 5. The global and local

capacitances in presence of fluids are extracted from the measured data [13] (S_{11} and S_{22}) of vector analyzer at 1 MHz as this is the maximum frequency at which a stabilized impedance signal was measured. Theoretically dielectric constant is directly proportional to the capacitance with respect to level in capacitive level, if the effect of insulation layer is negligible. On the other hand, insulation layer produces saturation effects in sensitivity of sensor with respect to different dielectric constants.

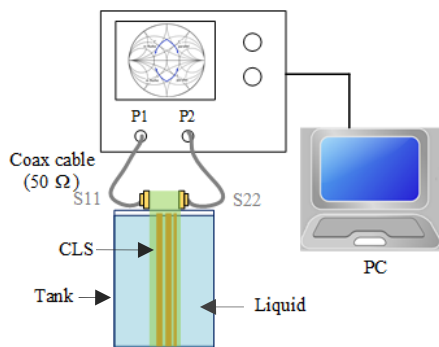


Figure 5: Measurement setup

A. Finite Element Method (FEM)

The 3D FEM analyses of a single segment of CLS models were performed in COMSOL Multiphysics to evaluate and compare different models with the basic model. In this paper, the comparison between the basic (case 1) and mixed (case 5) model are presented as shown in table 1. Polypropylene (PP) is used for insulation between the copper plates and liquid which has a permittivity of $\epsilon_r = 2.2$ and suitable material properties e.g. highly chemical resistant, stable and easy to clean etc. An input signal of 1 V with a frequency of 1 MHz is applied on the sensor when the tank (diameter = 11 mm) is non-conductive.

Table 1: Comparison between the case 1 and case 5.

Cases	Cond.	Level: Local S [fF/mm]	Level: Global S [fF/mm]	Build-up: Local S [fF/mm]	Build-up Global S [fF/mm]
1	Water	-	43.9	-	32.4
	Oil	-	7.70	-	1.45
5	Water	16.6	41.0	12.6	30.5
	Oil	2.34	7.26	0.89	1.22

Column 5 and 6 represents the build-up for oil and water effect when there is no liquid in the tank. The sensitivity (S) is calculated as follows:

$$S\left[\frac{fF}{mm}\right] = \frac{\Delta C}{L_{segment}} = \frac{C_{liquid} - C_{air}}{L_{segment}} \quad (5)$$

Where ΔC is the difference between the liquid capacitance (C_{liquid}) and air capacitance (C_{air}), $L_{segment}$ is the length of single segment of CLS.

The results concluded that the sensitivity is highly influenced by build-up effects, so mixed model (case 5) has an advantage to detect build-up effect by local E-fields with the global E-fields.

B. Evaluation

The measurements were performed by using the single segment CLS (see figure 4) in non-distilled water without insulation material. The build-up effects are evaluated by changing the slope of the capacitance with respect to liquid level and by adding parafilm material. Firstly, all capacitance measurements are studied in air environment, then the position where the liquid level contacts the copper strips is marked, which represents a zero level or offset value of liquid as shown in figure 6. The global and local capacitances are 4.92 pF and 28.81 pF. The water level sensitivities of 0.87 pF/mm and 0.92 pF/mm for global and local fields were evaluated at the room temperature.

The build-up effect is analyzed by varying the parafilm thickness on a segment at different positions. Where, parafilm is a known flexible thermoplastic, having a dielectric constant of $\epsilon_r = 2.3$. The effect of build-up slightly changes the air capacitances of the sensor. In the following experiment, 127 μm and 254 μm thickness of parafilm is used and it is wrapped on a specific area of the sensor, one area is covered from 0 to 40 mm and second area is covered from 40 to 89.5 mm of CLS.

From figure 6, result concluded that the influence of build-up is significant in the local capacitance because of confine E-fields of local plate. The variations in slopes are clarifies the effect of build-up at different area of a segment.

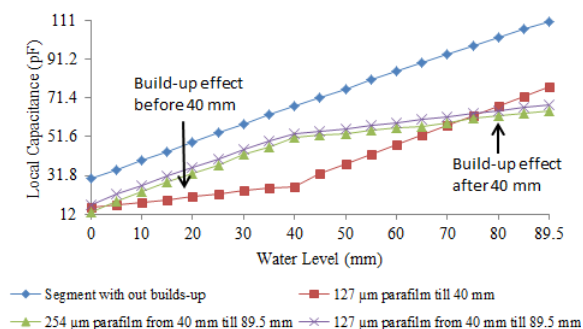


Figure 6: Effect of local capacitances of a CLS

The global and local sensitivity's impacts of parafilm thickness on CLS segment in water are as follow:

$$S_{127\mu m(local_build-up)} = 0.43 \frac{pF}{mm}, S_{254\mu m(local_build-up)} = 0.40 \frac{pF}{mm}$$

$$S_{127\mu m(global_build-up)} = 24.76\%, S_{254\mu m(global_build-up)} = 28.98\%$$

In the end, the insulation material is tested for the examination of capacitance behavior of conductive

and non-conductive liquids at the room temperature. In the initial measurements, a transparent tape is used for insulation, having a dielectric constant of more than water ($\epsilon_r = 80$). Table 2 contains the calculated sensitivity (S) of the liquids with respect to length of the segment.

Table 2: Calculated global and local sensitivities of various

Liquids	ϵ_r	S_g [pF/mm]	S_l [pF/mm]
Oil	2.53	0.022	0.072
Ethanol	24.3	0.244	0.179
Methanol	33.6	0.344	0.275
Glycol	41.2	0.713	0.653
Water	80.0	1.869	1.366
Salt water	> 80.0	2.163	1.387

Where S_g and S_l represent the global and local sensitivities of a sensor.

The local and global sensitivity's impacts of parafilm thickness on CLS segment with insulation material in water are as follow:

$$S_{127\mu m(local_build-up)} = 0.86 \frac{pF}{mm}, S_{254\mu m(local_build-up)} = 0.83 \frac{pF}{mm}$$

$$S_{127\mu m(global_build-up)} = 37.99\%, S_{254\mu m(global_build-up)} = 41.82\%$$

Result concluded that the sensor's sensitivity is directly affected by increasing the thickness of build-up because of the limitation of E-fields.

VI. CONCLUSION

Within the presented work, FEM simulation is used to analyze the concept of global and local E fields generated by specific arrangement of multi elements (copper plates) based on a CLS segment. The mixed model demonstrated the highest sensitivity for detecting the build-up effect as compared with the simple model.

Moreover, a PCB based prototype of a single segment CLS is use to detect the build-up or coating effect by incorporating local E-fields and global E-fields for level monitoring. Various parameters like segment dimensions, arrangement of copper plates and separation distance between them were taken into account to optimize the sensitivity. Moreover an analytical model is also presented which evaluates the build-up presence.

In future work, a multi segment CLS will be developed. Moreover, a self-calibrating algorithm would be implemented and will tested on an automated measurement setup

ACKNOWLEDGMENT

The authors would like to thank the SICK AG for the technical support and DENE for financing the research work.

REFERENCES

- [1] Y. Dou, J. Qin and X. Chang, "The study of a capacitor sensor and its system used in measuring ice thickness, sedimentation and water level of a reservoir.", IEEE, International forum on IT and applications 2009.
- [2] S. Das, T. S. Sarkar and B. Chakraborty "A semi-cylindrical capacitive sensor used for soil moisture measurement", Int. Journal of Electrical, Robotics, Electronics and Comm. Engg. vol: 8 No:1, 2014.
- [3] H. Conbolat, "A novel measurement technique using three capacitive sensors for liquids", IEEE Trans. Instrum. Meas., vol. 58, nr. 3, Oct. 2009.
- [4] T. Nakagawa, A. Hyodo, K. Kogo, H. Kurata, K. Osada and S. Oho, "Contactless liquid-level measurement with frequency-modulated millimeter wave through opaque container", IEEE Sensor Journal, vol. 13, nr. 3, Mar. 2013.
- [5] S. Pal and R. Barik, "Design, development and testing of a semi cylindrical capacitive sensor for liquid level measurement", Sensors & Transducers Journal, vol. 116, nr. 5, May 2010.
- [6] S.E. Woodard and B.D. Taylor, "A wireless fluid-level measurement technique", NASA Tech. Memo. 19271, 2006.
- [7] M. Schmitt, K. Schmidt, S. Olfert, J. Rautenberg, G. Lindner, B. Henning, L. M. Reindl, "Detection of coating within liquid-filled tubes and containers by mode conversion of leak Lamb waves", Journal of Sensors and Sensors Systems, 2, pg 73-84, 2013.
- [8] G. Vass, "Leak/level the principles of level measurements", Sensors Online Report, Princo Instruments, Oct 2000.
- [9] "Technology review point level monitoring of powder and solids", Monitor Technologies LLC, 2005.
- [10] J. E. Edwards, D. W. Otterson, "Applying liquid level measurement", Contributed paper, Meas. and Control, vol 7, nr. 5, pg 153-157, June 2014.
- [11] J. Z. Chen, A. A. Darhuber, S. M. Troian, S. Wagner, "Capacitive sensing of droplets for microfluidic devices based on thermocapillary attuation", Journal Royal Society of Chemistry, pg 473-480, 2004.
- [12] M. N. Alam, "Application of electromagnetic principles in the design and development of proximity wireless sensors", Dissertation, University of South Carolina – Columbia, 2014.
- [13] A. Yousaf, F. A. Khan, L. M. Reindl, "Passive Wireless Sensing of Micro coil parameters in fluidic environments", Journal of Sensors and Actuators A, pg. 69 – 79, 2012.

Planar Angle Metrology: G-LAS, the INRIM - INFN Ring Laser Goniometer

Jacopo Belfi^{*}, Nicolò Beverini^{**†}, Angela Di Virgilio^{*}, Enrico Maccioni^{**†}, Milena Astrua[‡], Marco Pisani[‡],
Marco Santiano[‡]

Email: {jacopo.belfi,angela.divirgilio}@pi.infn.it {nicolo.beverini,enrico.maccioni}@unipi.it
{m.astrua,m.pisani,m.santiano}@inrim.it

^{*}INFN, sezione di Pisa, Pisa, Italy

[†]Department of Physics, University of Pisa, Pisa, Italy

[‡]Istituto Nazionale di Ricerca Metrologica, INRIM, Torino, Italy

Abstract—Precision mechanical industry, geodetic measurements, astronomy and experimental physics require accurate measurement of angles down to the nanoradian level. A collaboration between INRIM and INFN is developing a new transportable goniometer (G-LAS, GyroLaser Angular Standard) that makes use of a ring laser gyroscope mounted on a precision turntable with a target accuracy of 10 nrad, being the accuracy of the most precise existing angular encoders at the level of some 100 nrad. The apparatus will consist in a square optical cavity of about 0.5 m in side, equipped with the last generation dielectric super-mirrors that are employed in the large gyroscopes for application in seismology and geodesy.

Keywords—angular metrology; laser gyroscopes; Sagnac effect

I. INTRODUCTION

Ring lasers (RL) gyroscopes exploit the Sagnac effect to provide inertial measurements of rotation rate. The rotational motion of their reference frame determines a differential length of the effective optical path of the two oppositely travelling beams and by consequence a relative frequency shift (Sagnac frequency). For a ring cavity of area vector \vec{A} , perimeter p acting at an emission wavelength λ , this frequency is

$$f_{\text{Sagnac}} = |f_{\text{CW}} - f_{\text{CCW}}| = \frac{4\vec{A} \cdot \vec{\Omega}}{\lambda p} = \frac{4A}{\lambda p} \Omega \cos\theta = K \Omega \quad (1)$$

being $\vec{\Omega}$ the angular speed vector of the cavity frame. This frequency difference can be efficiently observed by beating on a photodetector the two beams emitted from the laser cavity [1]. The factor K (i.e. the ratio between the angular speed and the Sagnac frequency) is defined as the RL gyroscope sensitivity factor. Laser gyroscopes with perimeter-length of tens of centimetres are commonly used for inertial navigation applications while larger systems (side-length larger than one meter), rigidly fixed to the ground, provide precise measurements of the Earth rotation rate and of the small superimposed local rotations coming from geophysical and geodetic phenomena.

Applications of RL's in Angular Metrology have been foreseen since the end '60s. The basic idea is to use the interference fringes by the two counter-propagating modes as an ultra-fine angular scale dividing the full angle into a number

of $N=P/\lambda$ intervals. The most effective realization of such kind of goniometer is the apparatus developed by Yu. V. Filatov and collaborators since the end of '70s. It consists in a monolithic RL, 11 cm in side-length, mounted on a turntable. The RL is equipped with total reflection prisms in optical contact with a Zerodur cavity frame [2]. The typical resolution of this instrument is at the level of 100 nrad, limited by the errors due to the influence of environmental parameters on the ring laser dynamics.

In this paper we will describe the state-of-art of G-LAS, the prototype of a transportable goniometer based on a RL that is under construction at the Italian National Institute for Metrologic Research (*Istituto Nazionale di Ricerca Metrologica* – INRIM) with the collaboration of the Italian Institute for Nuclear Physics (*Istituto Nazionale di Fisica Nucleare* – INFN).

This project exploits the large expertise on RL gyroscope acquired in the recent years by the group operating at the section of Pisa of INFN and at the Pisa University Department of Physics [3,4] with the purpose of building a gyroscope having the very high sensitivity that needs for detecting in a terrestrial laboratory the thin effect foreseen by the general relativity equations, due to the distortion of the space-time metrics induced by the rotating Earth mass (the so called Lense-Thirring effect), which is expected to give a correction of the order of 1 ppb over the Earth rotation speed [5,6].

Precision mechanical industry, geodetic measurements, astronomy and experimental physics require accurate measurement of angles down to the nanoradian level. The target of the present prototype is to build a goniometer with an angular accuracy of the order of 0.002 arcsec (equivalent to 10 nrad), being the accuracy of the most precise angular encoders working in the world at the level of some 100 nrad in spite of a resolution more than one order of magnitude better.

II. THE RL GONIOMETERS

The realization of the angular scale is made by subdividing the circle into a number of equal intervals in fact implemented with the circular grating of angle encoders. The resolution in the encoder performance in the present state-of-art measurement apparatus has achieved nanoradian level, but the accuracy is limited by technological factors to the microradian

level. Absolute calibration of such instruments is today an open issue of angle metrology.

A RL mounted on a continuously rotating table can act as an ideal angular encoder. The measure of a rotation angle ϕ can be evaluated as $\phi = 2\pi N_\phi / N_{2\pi}$, being N_ϕ and $N_{2\pi}$ the number of fringes counted by beating the two counter-rotating laser beams, respectively, when the table rotates by ϕ and the full 2π angle.

As a fact, the number of fringes observed in the time $t_1 - t_0$ when the table rotates by an angle ϕ is:

$$N_\phi = \frac{1}{2\pi} \int_{t_0}^{t_1} f(t) dt = \frac{K}{2\pi} \int_{t_0}^{t_1} \Omega(t) dt = \frac{K}{2\pi} \phi \quad (2)$$

while the number observed in the period T , correspondent to a full a 2π rotation is:

$$N_{2\pi} = \frac{1}{2\pi} \int_{t_0}^{t_0+T} f(t) dt = \frac{K}{2\pi} \int_{t_0}^{t_0+T} \Omega(t) dt = K \quad (3)$$

By (3) it appears that RL sensitivity factor K can be accurately determined each time a measure is performed, providing an accurate self calibration of the apparatus without any a priori knowledge of the exact geometry of the instrument.

While angle encoders have very high sensitivity, RL has high intrinsic accuracy. A transportable RLG goniometer can consequently provides an ideal apparatus to make the intercalibration of encoders in use in the different metrological Institutes.

III. ACCURACY OF RL GONIOMETER

In a previous paper [7] we presented a simplified analysis of the different sources of inaccuracy that can affect a RL goniometer. A more complete analysis can be found in [8].

Up today, the only existing goniometer based on RL gyroscope is the apparatus EUP-1L, developed at the St. Petersburg Electrotechnical University [2]. The ring laser consists in a Zerodur monolithic cavity 44 cm in perimeter-length, equipped with total reflection prisms in optical contact with the cavity frame [9]. The cavity is filled by a He-Ne mixture and is lasing on the classical red line at 632.8 nm. The laser is fixed on a turntable, and a counter measures the number of fringes corresponding to the rotation angles. Specimens of EUP-1L are in use in some metrological institutions in the world. Its typical resolution is limited to 0.1'' (0.5 μ rad) by the influence of the environmental parameters on the ring laser dynamics (birefringency induced by spurious magnetic fields on the corner prisms, mechanical instabilities of the rotator, non-optimization of the geometrical parameters of the laser cavity). The resolution of the prototype active in St. Petersburg has been pushed down to 100 nrad through a careful (and quite cumbersome) analysis of all these systematic errors [10].

Finally, the performances are limited by the RL dimension. Statistical noise on the angle definition is dominated by shot noise. In a RL with the optical cavity quality factor Q for a single measurement it is given by:

$$\delta\Omega_{shot\ noise} = \frac{c}{LQ} \sqrt{\frac{h\nu\tau}{P_{out}}} \quad (4)$$

where P_{out} is the detected radiation power, c is the light speed, and τ is the measuring time, which corresponds to the period of the turntable. Thanks to the fact that the scale constant K is self-calibrated every complete turn of the table, quantum noise can be further reduced averaging over many measurements.

Both the ratio A/p and Q increase linearly with the side dimension. Thus, increasing the RLG dimension can be very effective in reducing shot noise. Considering a mirror reflectivity of the order of 99,999%, $\tau \approx 5$ s, and typical value of laser operation, the shot noise in a single measurement amounts to 330 nrad/s for a square ring cavity with side $L = 11$ cm (as in Filatov's instruments), while is 15 nrad/s for $L = 50$ cm (as in present prototype).

Other possible sources of errors are related to change in the scale factor K during the measuring time τ (around 10 s). An accuracy target of 0.002 arcsec (equivalent to 10 nrad) requires a temperature stability of the structure of a few mK. Also the wobble of the rotating table and the rotational speed stability must be controlled at 10^{-4} level. Moreover, (1) is only a first order approximation of the actual relation between the observed Sagnac frequency and the rotational speed. In a more complete analysis, it is necessary to take into account the coupling between the two counter-propagating laser beams due to the back-scattering on the mirrors and the possible effect of non-reciprocity in the two optical paths. Also these effects are strongly reduced by enlarging the RL dimensions.

From all these considerations it is evident that larger ring dimensions will provide better performances. But this has a price: longer optical path means smaller free spectral range of the optical cavity that eventually become smaller than the laser homogeneous linewidth, making more and more difficult to achieved stable single longitudinal mode laser operation. The experience with large frame RL demonstrates that this problem can be partially bypassed by increasing the pressure of the gas in the active medium (then, enlarging the homogeneous linewidth by pressure broadening) and by operating the laser very close to its threshold. Moreover, when the target is to build a transportable instrument, weight and dimensions



Fig. 1. Picture of the carbon fibre board mounted on the turntable. Three corner tower and two sides of the ring vacuum chamber has been already fixed on the board .

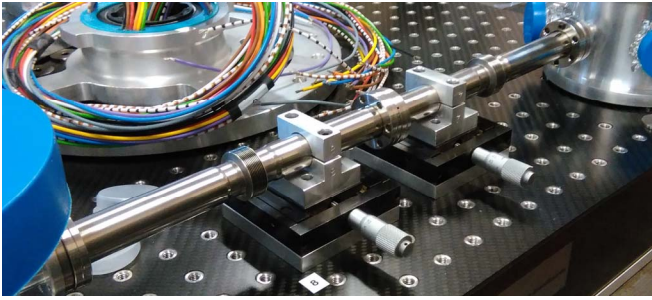


Fig. 2. The sliding stages to position the diaphragm. The diaphragm is inserted in the gasket connecting the two ConFlat flanges between the two stages.

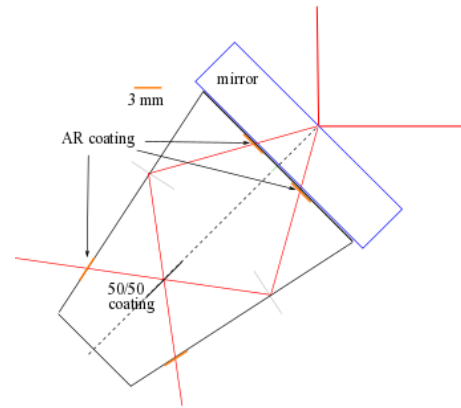


Fig. 3. The combining prism (Koester prism). It consists in two symmetric quartz prism glued together. On the contact region of the two prisms a semitransparent 50/50 coating allows beams combining

become obviously critical parameters.

IV. THE INRIM-INFN GONIOMETER

The design of our RL goniometer is based on a square RL mounted on a precision turntable. The optical cavity is delimited by the four mirrors, without any physical confinement of the active medium on the optical path, so that the intra-cavity losses are limited only by mirrors reflectivity. Then, all the cavity is filled with the He-Ne mixture.

The ring optical cavity, with the side of 50 cm, is mounted on a 90×90 cm² board realized by a carbon fibre honeycomb, closed between two layers of carbon fibre panels. Board material had chosen for its properties of stiffness and lightness and for its moderate thermal expansion coefficient ($2.5 \cdot 10^{-6}$ K⁻¹). The board is fixed on one side to the rotating table and on the other side to the ring laser vacuum chamber through stainless steel inserts. (Fig. 1). The vacuum chamber consists in four corner towers, connected together by pipes enclosing the optical path. Thermal stability of the cavity must be provided by the carbon fibre board. Bellows provides the needed elasticity to the connections of the pipes to the towers. In the middle of one of the pipes is joint a pyrex capillary, where external electrodes can excite by radiofrequency the laser discharge. The four angular towers host the mirrors with their mechanical mounting and present openings for electrical feedthroughs, windows for the output of the single beam and interference signal and for visual inspection. To reduce the weight of the structure, they are worked on Aluminium that is much lighter than the usual stainless steel. The connections between the vacuum chamber components are all realized with UHV ConFlat standard. A valve allows the connection to the vacuum pumps and to the gas reservoir for initial operation of filling the He-Ne mixture. A getter pump keeps the purity of the gas in the time.

The turntable, produced by Aerotech (model ABRS-300MP), is an air bearing, with integrated direct driving motor and high accuracy optical encoder. By the high accuracy manufacturing it achieves sub-microradian rotation errors and a resolution in angle position better than $0.2 \mu\text{rad}$. The most important feature for our application is that the table is capable of rotating at a constant speed Ω with a relative error $\Delta\Omega/\Omega$ of the order of 10^{-5} . A hole placed in the centre of the table allows inserting a sliding contact assembly used to connect the RL signals, controls and power supplies to the laboratory.

The optical cavity is closed by two flat and two concave mirrors. The radius of the concave mirrors is 4 m. The pipe with the discharge is placed between the two concave mirrors. With this geometry, the optical cavity is stable, with a waist in the discharge region and one in the middle of the opposite side with the dimensions (4 times the $1/e^2$ beam intensity radius) of 2.17×2.41 mm² and 1.64×2.17 mm², respectively. In order to favour laser operation on TEM₀₀ mode, a diaphragm will be inserted in the pipe at the second waist (Fig. 2). The exact

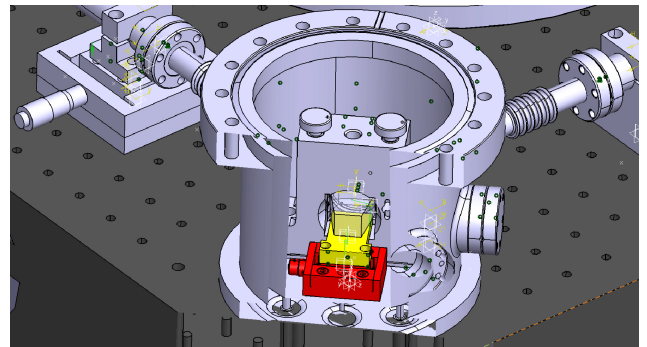


Fig. 4. Sketch of the corner tower accommodating a curved mirrors and the combiner prism. The mechanical and the sliding share stage are highlighted in yellow and in red, respectively,

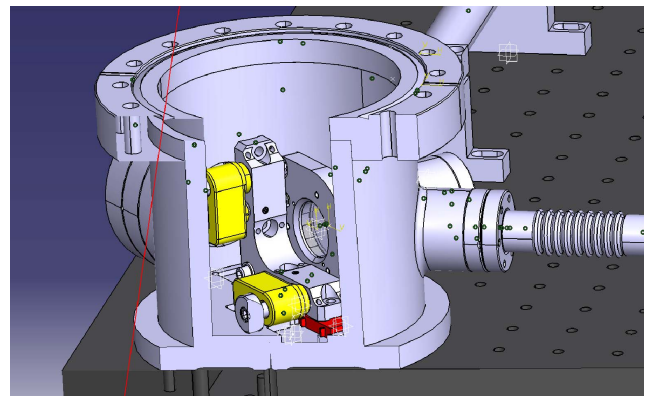


Fig. 5. Sketch of one corner tower that accommodate the flat mirrors. The motorized tilt controls and the sliding share stage are highlighted in yellow and in red, respectively,

position of the diaphragm will be adjusted by moving the pipe through linear travel stages. The mirrors are top-quality mirrors, with the best available surface roughness ($< 1 \text{ \AA}$) and a reflectivity R near to 99.999%, in order to increase the cavity quality factor and to minimize the coupling between the counter-rotating traveling beams due to backscattering. Beside one of the two concave mirrors, a specially designed prism (Koester prism) combines the two counter-rotating laser beams (Fig. 3 and 4). The interference signal exits the vacuum chamber through a window and is detected by a photodiode. The laser beams transmitted by the second concave mirror are detected by other photodiodes for the diagnostics of the laser operation and to provide the stabilization of the laser wavelength. The two flat mirrors orientation can be fine adjusted under vacuum by motorized tilt regulations, while PZT driven linear share stages can shift the mirrors in the direction orthogonal to its surface (Fig. 5).

The mirror's coating is extremely delicate and requires the respect of a high cleanness level. Then the mirrors will be mounted inside the structure, operating in clean room. There, we will perform also the rough alignment of the optical cavity, adjusting the mirror mechanical controls and the combiner prism with the help of an auxiliary external green laser beam injected through a mirror. The laser chamber is then filled with the He-Ne gas mixture and is sealed off, closing the valve of connection with the vacuum system. A getter pump, which is active for molecular gases and not to noble gases, keeps the purity of the mixture in the time. Further fine alignment will be performed through the motorised controls of the flat mirrors. For a reasonable range of perturbation, this set of control is able to fully control the optical cavity. In particular the system is robust against thermal dilatations that will not affect the alignment of the two curved mirrors, the discharge tube and the combiner prism.

The active medium is excited by a radiofrequency discharge through external electrodes. Radiofrequency excitation is chosen to avoid plasma cathoporesis that would perturb the Sagnac signal. As stated before, the RL will operate near to threshold, in order to have stable operation condition without mode jumping. For this purpose, it is important to stabilise the optical cavity length, keeping the laser emission wavelength on the maximum of the gain profile. Thermal optical cavity shift can be corrected acting on the PZT stages translating the flat mirrors. Moving the two mirrors together, the length of the two sides of the ring that connect the concave to the flat mirrors will change of the same amount.

This operation does not affect neither the position of the beam spot on the two curved nor the alignment of the discharge capillary and of the combiner prism. The stabilisation of the optical length to the maximum laser output power will be implemented by a servo lock, superimposing a small sinusoidal dithering on the PZT drivers voltage and detecting in-phase on a photodiode the single beam output.

ACKNOWLEDGMENTS

We have to thank Filippo Bosi for its support in the use of the clean room facility. We thanks also dr. Giorgio Carelli and dr. Andreino Simonelli for the useful discussions.

Present project is funded by the Italian *Ministero dell'Istruzione, dell'Università e della Ricerca* in the frame of "*Progetti premiali*".

REFERENCES

- [1] K.U. Schreiber, and J-P. R. Wells, "Large ring lasers for rotation sensing", *Rev Sci Instrum* vol. 84 041101, 2013
- [2] Yu. V. Filatov, D. P. Loukianov and R. Probst, "Dynamic angle measurement by means of a ring laser ", *Metrologia* vol. 34 pp. 343-351, 1997.
- [3] J. Belfi, N. Beverini, F. Bosi, G. Carelli, A. Di Virgilio, E. Maccioni, A. Ortolan, and F. Stefani: "A 1.82 m² ring laser gyroscope for nano-rotational motion sensing", *Appl Phys B* vol. 106, pp.271–281, 2012
- [4] J.Belfi, et al.: "Performance of G-Pisa ring laser gyro at the Virgo site", *J. Seism. vol. 16*, pp. 757-766. 2012
- [5] F. Bosi, et al., "Measuring Gravito-magnetic Effects by Multi Ring-Laser Gyroscope", *Phys Rev D* vol. 84 122002, 2011
- [6] A. Di Virgilio, et al.: "A ring lasers array for fundamental physics", *C. R. Physique* vol. 15, pp. 866–874, 2014
- [7] M. Astrua, J. Belfi, N. Beverini, A. Di Virgilio, G. Carelli, E. Maccioni, A. Ortolan, M. Pisani, and M. Santiano *The INRIM - INFN ring laser gyroscope for planar angle metrology application*, *Fotonica 2015 Proceedings*, AEIT Italian Conference on Photonics Technologies, Torino, 6-8 May 2015
- [8] V.E. Primalov and Yu. V. Filatov, "Investigation of the output characteristic of a rotating ring gas laser", *Sov. J. QE* vol. 7 pp. 802-806, 1977.
- [9] E. N. Zhuravleva, V. N. Kuryatov, and B. N. Semenov, 2nd Saint Petersburg Int. Conf. Gyroscopic Technology and Navigation, Part 2, St Petersburg, SCRI 'Electropribor', pp. 57-59, 1995.
- [10] M. N. Burnashev, P. A. Pavlov, and Yu. V. Filatov, "Development of precision laser goniometer systems", *Quantum Electronics* vol. 43 pp. 130 – 138, 2013.

Optimized 1f-2f Actively Compensated Frequency Synchronization

Xi Zhu^{1,3}, Bo Wang^{1,2}, Chao Gao^{1,2}, Yibo Yuan^{1,3}, Jingwen Dong^{1,2}, and Lijun Wang^{1,2,3}

¹ Joint Institute for Measurement Science, State Key Laboratory of Precision Measurement Technology and Instruments, Tsinghua University, Beijing 100084, China

² Department of Precision Instruments, Tsinghua University, Beijing 100084, China

³ Department of Physics, Tsinghua University, Beijing 100084, China
Email: bo.wang@tsinghua.edu.cn

Abstract—We proposed a 1f-2f actively compensated frequency synchronization system with phase noise compensation function placed at the receiving site. During the application, we found that this system is sensitive to ambient temperature of fiber link so that the phase fluctuation cannot be completely compensated. It is caused by the nonlinear effect of RF components in the system. We optimize the 1f-2f frequency synchronization scheme and improve its robustness to complicated working environment.

Keywords—square kilometer array; frequency synchronization; nonlinear effect

I. INTRODUCTION

The SKA project is an international effort to build the world's largest radio telescope. It provides over a million square meters of collecting area through many thousands of antennas. In order to ensure imaging fidelity, the SKA demands high precision frequency synchronization for all antennas. In accordance with the features and needs of it [1-3], we proposed a 1f-2f actively compensated frequency synchronization system with phase noise compensation function placed at the receiving site [4]. As to practical applications, the robustness of the system to complicated working environment should be taken into consideration. The South African SKA site was selected in the desert regions. In order to capture a variety of meteorological parameters such as temperature and wind data, SKA South Africa Project Office has built a weather station at the South Africa core site since 2005. According to statistical analysis on the temperature data in the period January 1, 2005 to March 31, 2011, the difference between the absolute maximum and minimum temperature over the days of the month is nearing 40 degree centigrade. And the site sometimes meet thunderstorms and gales with temperature changed rapidly. At present, overhead fiber links are used by SKA South Africa site to realize frequency synchronization between antennas. They are easily affected by ambient temperature change. Whether use overhead or buried fiber links in the future is not determined.

To test the performance of the frequency synchronization system working on overhead fiber links and the topology specifications, the system was shipped to South African SKA site to perform a trial test in September 2015. We found that it

is sensitive to ambient temperature of fiber link so that the phase fluctuation cannot be completely compensated.

In this paper, we optimize the 1f-2f frequency synchronization scheme and perform a comparing test of the original and optimized schemes on 50 km fiber spools. The spools are placed in a temperature-controlled box with temperate fluctuating 40 degrees in 12 hours. In the optimized scheme, the significantly worse on the Allan variance plot of dissemination stability at the averaging time between 10s and 1000s diminish. Relative frequency stabilities of $3.8 \times 10^{-14}/s$ and $3.1 \times 10^{-16}/10^4s$ are obtained. Detailed experimental results will be shown during the conference.

II. THERMAL TESTING OF 1F-2F ACTIVELY COMPENSATED FREQUENCY SYNCHRONIZATION SYSTEM

A. 1f-2f Actively Compensated Frequency Synchronization System

We have proposed a 1f-2f actively compensated frequency synchronization system with phase noise compensation function placed at the receiving site [4]. Figure 1(a) shows the schematic diagram of transmitting site (TX). A 100 MHz signal from H-maser is working as reference signal. A 2 GHz signal from phase-locked dielectric resonant oscillator (PDRO) is phase locked to the reference signal to enhance the signal-to-noise ratio. It can be expressed as:

$$V_0 = \cos(\omega_0 t + \varphi_1). \quad (1)$$

V_0 is used to modulate the amplitude of a 1547.72 nm diode laser. Then the modulated laser light is divided into several equal light beams and we take two for example. After passing through a fiber coupler and an optical circulator, the two light beams are coupled to a 50 km fiber link respectively. To improve the utility of frequency synchronization system and further reduce the influence of environment, TX is integrated into a prototype module, as Fig. 1(b) shows. It comprises one main control card, two transmitting cards and eight scalable transmitting cards. The prototype module can work together with ten receiving sites (RXs) simultaneously at most. The functions of main control card are modulating and broadcasting modulated laser lights to transmitting cards. The transmitting card is used to couple laser light to fiber link. Scalable transmitting card is empty and replaceable.

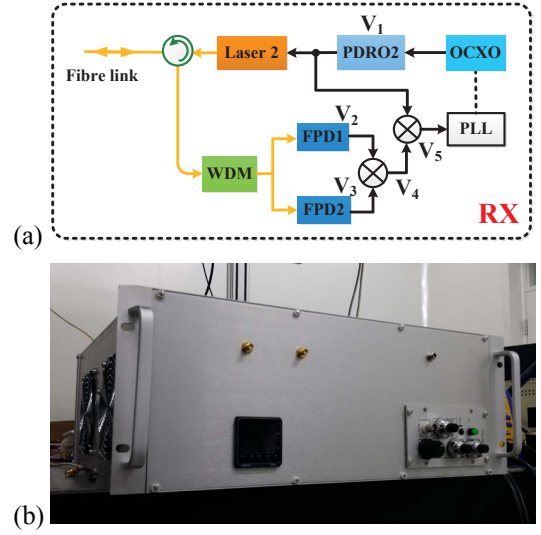
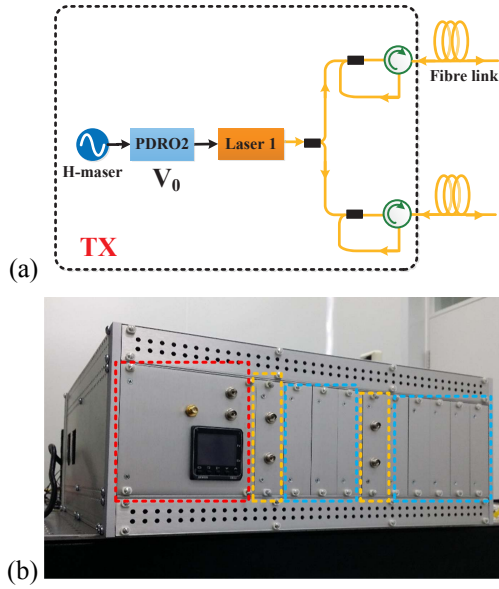


Fig. 2. (a) Schematic diagram of receiving site (RX). (b) Prototype module.

Fig. 1. (a) Schematic diagram of transmitting site (TX). (b) Prototype module, main control card is shown in red box; transmitting cards are shown in yellow boxes; scalable transmitting cards are shown in blue cards.

Figure 2(a) shows the schematic diagram of receiving site (RX). An oscillator containing a 100 MHz oven-controlled crystal oscillator (OCXO) and a 1 GHz PDRO generates a 1 GHz signal that can be expressed as:

$$V_1 = \cos(\omega_1 t + \phi_1). \quad (2)$$

It is used to modulate the amplitude of a 1548.53 nm diode laser and disseminated via the same fiber link from RX to TX then back. After separating by a wavelength-division multiplexer (WDM) and detecting by two fast photodiodes (FPD), the disseminated 2 GHz and 1 GHz signals are respectively expressed as

$$V_2 = \cos(\omega_0 t + \phi_0 + \phi_p); \quad (3)$$

$$V_3 = \cos(\omega_1 t + \phi_1 + \phi'_p), \quad (4)$$

where ϕ_p is the phase fluctuation accumulated during the 50 km fiber dissemination and ϕ'_p is that of 50 km round-trip dissemination. One-way phase fluctuation of 2 GHz frequency signal is the same as round-trip accumulated phase fluctuation of 1 GHz frequency signal, namely $\phi_p = \phi'_p$. By mixing signals V_2 and V_3 , we obtain

$$V_4 = \cos[(\omega_0 - \omega_1)t + \phi_0 + \phi_p - \phi_1 - \phi'_p]. \quad (5)$$

Then V_4 is mixed with V_1 . An error signal

$$V_5 = \cos[(\omega_0 - 2\omega_1)t + \phi_0 + \phi_p - 2\phi_1 - 2\phi'_p] \quad (6)$$

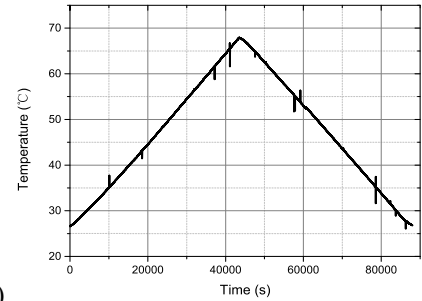
is obtained. V_5 is used for phase locked loop (PLL) to feedback-control the phase of OCXO. With the relations of $\omega_0 = 2\omega_1$ and $\phi_p = \phi'_p$, V_5 can be expressed as

$$V_5 = \cos(\phi_0 - 2\phi_1). \quad (7)$$

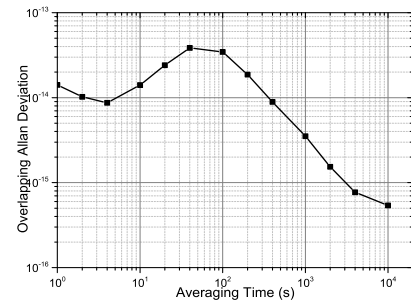
When PLL is closed, the 100 MHz OCXO at RX is phase locked to the reference signal at TX, namely $\phi_0 = 2\phi_1$. Thus the reference signal is reproduced at RX. Figure 2(b) is the photo of RX prototype module.

B. Thermal Testing

TX and RX module are connected by 50 km fiber spool which is placed in a temperature-controlled box. And the temperature fluctuation is set as 40 degrees with a period of 24 hours, as Fig. 3(a) shows. Relative frequency stabilities between 100 MHz reference signal and recovered signal are as Fig. 3(b) shows. From the results, when the ambient temperature of fiber link fluctuated, the relative frequency stabilities get worse, namely there is a bump on the Allan variance plots of dissemination stability at the averaging time between 10s and 1000s.



(a)



(b)

Fig. 3. (a) Temperature fluctuation of fiber link. (b) Result of relative frequency stability measurement.

It is caused by the nonlinear effect of RF components in the system. As previously mentioned, we ignore the nonlinear effect of RF mixer in the system when 1 GHz and 2 GHz signals mixing. The mixing will be influenced by ultra-harmonics of signals. The down-converted 1 GHz signal is consisted of ideal target signal, the 1 GHz leakage and the 1 GHz which is produced by 3 rd. harmonic of transferred 1 GHz mixing with transferred 2 GHz. Namely, V_4 can be expressed as

$$\begin{aligned} V_4 = & \cos [(w_0 - w_1) t + \varphi_0 + \varphi_p - \varphi_1 - \varphi'_p] \\ & + \xi \cos (w_1 t + \varphi_1 + \varphi'_p) \\ & + \zeta \cos [(3w_0 - w_1) t + 3\varphi_1 + 3\varphi'_p - \varphi_0 - \varphi_p] \end{aligned} \quad (8)$$

Here, ξ and ζ are small quantities. Accordingly, V_5 can be expressed as

$$V_5 = \cos (\varphi_0 - 2\varphi_1) + \xi \cos \varphi_p + \zeta \cos (3\varphi_1 - \varphi_0 + 2\varphi_p). \quad (9)$$

The error signal contains φ_p which cannot be eliminated. When the ambient temperature of fiber link fluctuated, φ_p will change with it. For V_4 , when the cumulative variable quantity of φ_p catch up with half the period of 1 GHz, there will be a periodism of V_4 caused by the change of φ_p . Thus V_5 will show periodic.

III. OPTIMIZED 1F-2F ACTIVELY COMPENSATED FREQUENCY SYNCHRONIZATION SYSTEM

In optimized scheme, TX is the same as the original scheme. And the schematic diagram of RX is shown in Fig. 4. The 1 GHz PDRO is replaced by PDRO2 and PDRO3 (with frequencies of 1 GHz+130Hz and 1 GHz-130Hz, respectively) which are phase locked to the same OCXO. Then V_1 can be expressed as:

$$V_1 = \cos [(w_1 + 130 \text{ Hz}) t + \varphi_1]. \quad (10)$$

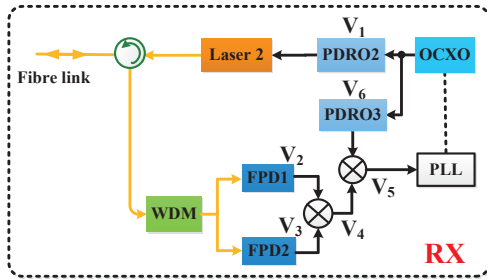


Fig. 4. Schematic diagram of optimized receiving site (RX).

After round-trip dissemination in 50 km fiber link, we obtain:

$$V_3 = \cos [(w_1 + 130 \text{ Hz}) t + \varphi_1 + \varphi'_p]. \quad (11)$$

V_0 is the same as the previous, namely (1). After dissemination from TX to RX, V_2 is also the same as (3). Then V_2 is mixed with V_3 , the down-conversion signal can be expressed as:

$$V_4 = \cos [(w_0 - w_1 - 130 \text{ Hz}) t + \varphi_0 + \varphi_p - \varphi_1 - \varphi'_p]$$

$$+ \xi \cos [(w_1 + 130 \text{ Hz}) t + \varphi_1 + \varphi'_p] \quad (12)$$

$$+ \zeta \cos [(3w_0 - w_1 + 390 \text{ Hz}) t + 3\varphi_1 + 3\varphi'_p - \varphi_0 - \varphi_p]$$

The signal from 1 GHz-130Hz PDRO can be expressed as:

$$V_6 = \cos [(w_1 - 130 \text{ Hz}) t + \varphi_1]. \quad (13)$$

V_6 is mixed with V_4 . An error signal

$$\begin{aligned} V_5 = & \cos (\varphi_0 + \varphi_p - 2\varphi_1 - 2\varphi'_p) \\ & + \xi \cos (260 \text{ Hz} \times t + \varphi'_p) \\ & + \zeta \cos (390 \text{ Hz} \times t + 3\varphi_1 + 3\varphi'_p - \varphi_0 - \varphi_p) \end{aligned} \quad (14)$$

is obtained. The 260 Hz and 390 Hz signal components can be filtered. In the optimized scheme, the relations of $(1 + 1.3 \times 10^{-7}) w_0 = 2w_1$ and $(1 + 1.3 \times 10^{-7}) \varphi_p = \varphi'_p$ are satisfied. Then V_5 can be expressed as:

$$V_5 = \cos (\varphi_0 - 2\varphi_1 - 1.3 \times 10^{-7} \varphi_p). \quad (15)$$

When the PLL is closed, we have:

$$\varphi_0 = 2\varphi_1 + 1.3 \times 10^{-7} \varphi_p. \quad (16)$$

For a little part of φ_p is brought into the phase of PDRO2, the frequency stability will be little affected.

For 50 km distance dissemination, with the temperature of fiber link fluctuating 40 degrees as previous, the bump on the Allan variance plot of dissemination stability at the averaging time between 10s and 1000s almost diminished, and relative frequency stabilities of $3.8 \times 10^{-14}/s$ and $3.1 \times 10^{-16}/10^4s$ are obtained.

ACKNOWLEDGMENT

This work is being carried out for the SKA Signal and Data Transport (SaDT) consortium as part of the Square Kilometre Array (SKA) project. The SKA project is an international effort to build the world's largest radio telescope, led by SKA Organisation with the support of 10 member countries. Fourteen institutions from eight countries are involved in the SaDT consortium, led by the University of Manchester. We acknowledge financial support from the National Key Scientific Instrument and Equipment Development Project (No. 2013YQ09094303).

REFERENCES

- [1] P. Dewdney, "Baseline Design document version2," <https://www.skatelescope.org/key-documents/>. (January 2016).
- [2] R. McCool, S. Garrington, and R. Spencer, "Signal transport and networks for the SKA," In General Assembly and Scientific Symposium, IEEE, 2011, pp. 1-4.
- [3] W. Turner, "SKA phase 1 system (level 1) requirements specification," <https://www.skatelescope.org/key-documents/>. (January 2016).
- [4] B. Wang, X. Zhu, C. Gao, Y. Bai, J. W. Dong, and L.J. Wang, "Square Kilometre Array Telescope - Precision Reference Frequency Synchronisation via 1f-2f Dissemination", Scientific Reports, 5, 2015.

Very High Sensitivity Laser Gyroscopes for General Relativity Tests in a Ground Laboratory

J. Belfi, F. Bosi, A. Di Virgilio
INFN Pisa, Pisa, Italy
Email: belfi@pi.infn.it

N. Beverini, G. Carelli,
U. Giacomelli, E. Maccioni, A. Simonelli
Dip. di Fisica, Università of Pisa, Pisa, Italy

A. Beghi, D. Cuccato,
A. Donazzan, G. Naletto
Dip. Ingegneria dell'Informazione,
Università di Padova, Padua, Italy

A. Ortolan
Laboratori Nazionali INFN,
Legnaro, Padua, Italy

M. G. Pelizzo
CNR-IFN and INFN Sezione di Padova, Padua, Italy

A. Porzio
CNR-SPIN, and INFN Napoli,
Naples, Italy

C. Altucci, R. Velotta
Dip. di Fisica, Università di Napoli Federico II
and INFN Napoli, Naples, Italy

A. Tartaglia
Dip. di Scienza Applicata e Tecnologia
Turin, Italy

Abstract—Two ring laser gyroscopes are being developed by the INFN in view of fundamental Physics applications. The scope of this activity is to 'fill the gap' between the present state of the art technology and the requirements in sensitivity and accuracy needed for general relativity tests. The first prototype, called GP2 and located at INFN Pisa, is dedicated to the interferometric control of the ring laser cavity form factor. The second prototype, called GINGERino, is a larger ring laser located deep underground (INFN LNGS) and has the scope of characterizing the low frequency rotational noise of the site. We show the most recent results of the two experiments.

I. INTRODUCTION

Large frame helium neon ring lasers are unique instruments for geophysics and geodesy since they monitor the instantaneous angular velocity of their reference frame with an extremely high resolution, detecting both local ground rotations and global effects. Recently the Gross Ring "G" at the Wettzell Geodetic Observatory has reached the outstanding resolution on the Earth rotation rate of 3×10^{-9} (about 0.25 prad/s with few hours of integration time [1]). This level is less than one order of magnitude far from the requirement, in term of resolution, for the direct observation of the effects induced by General Relativity on the local measurement of the Earth rotation rate [2]. The GINGER (Gyroscopes IN General Relativity) project ([3],[4]) aims at developing a rotations detector capable to probe General Relativity effects on ground. We consider two independent estimates of the Earth angular velocity vector: one performed in the Earth-based laboratory reference system with a ring laser array, say it $\vec{\Omega}$, and the other performed with respect to an inertial reference frame (distant observer), say it $\vec{\Omega}'$. According to the Einstein's Relativity predictions, to the leading order, the difference $\delta\vec{\Omega} = \vec{\Omega} - \vec{\Omega}'$ between the two measurements is given by:

$$\delta\vec{\Omega} \sim \frac{GM}{c^2 R} \Omega_E \sin \theta \hat{e}_\theta + \frac{G}{c^2 R^3} J_E [\hat{j} - 3\hat{J}_E \cdot \hat{e}_r] \quad (1)$$

where G is the gravitational constant, R is the Earth mean radius, c is the speed of light, Ω_E is the Earth's angular

velocity, M is the Earth mass, J_E is the Earth's angular momentum, θ is the laboratory colatitude, \hat{j} is the direction of the Earth rotation vector, \hat{e}_r and \hat{e}_θ are respectively the radial and the tangential directions in the local meridian plane. The first term is related to the Earth mass only and corresponds to the geodetic effect. The second term is related to the rotation of the Earth mass and corresponds to the frame dragging or Lense-Thirring effect. The order of magnitude of the different relativistic terms depends on the latitude, but always below 1 part per billion of the Earth's rotation rate. The main issues to approach for achieving such an ambitious goal are connected to:

- Reduce the light shot-noise level: this can be obtained by increasing the size of the ring cavity (for a given set of mirrors the sensitivity scales as L^α with $\alpha \sim 5$ [5]).
- Improve the long-term stability: laser parameters and the environmental parameters drifts can be reduced respectively by means of active controls and by selecting a properly isolated installation. A deep underground sensor location seems necessary to reduce surface noise due to changing weather patterns and local hydrological effects.
- Correction of the nonlinear laser dynamics. Intracavity dynamics introduces nonreciprocal effects consisting in a null-shift term in the laser gyroscope response. To achieve the required accuracy, an estimate of these contributions must be implemented [6].

In the following we will describe the mechanical and optical properties of the two INFN prototypes and their recent performance.

II. GP2 RING LASER

Resolving the Earth rotation rate below the level of one part per billion, requires to control the ring laser geometrical

scale factor K_s to the same level of accuracy. Being $K_s = \frac{4A}{\lambda P}$, the stabilization of the only laser cavity perimeter P , directly related to the ring laser optical frequency emission, is not sufficient. In fact, also the area A enclosed by the beam path must be controlled. The aim is to reduce the fluctuation associated with the deformation of the optical cavity, stabilizing with a sub-nanometer accuracy the variation of the mirror inter-distances.

More specifically, the beam circulating inside a cavity with four spherical mirrors has 12 degrees of freedom in space, corresponding to the 3 coordinates in space of each of the four mirrors. Tracing out the three rigid translations and rotations, we have 6 remaining degrees of freedom determining the cavity shape. Our basic idea is to constrain these degrees of freedom by exploiting the symmetry properties of a closely regular square shape. In particular, we proposed [7] an active stabilization approach. This is done by injecting the two diagonal Fabry-Pérot resonators, formed by the two couples of opposite cavity mirrors with the same ultra-stable reference laser, and correct the position of the cavity mirrors by means of piezoelectric nanometric transducers. In this way the stability of the laser wavelength is transferred to the square diagonals and the cavity is affected only to the second order by the perturbations on the mirrors positions along the residual 4 degrees of freedom. These last can be eventually optimized by controlling the cavity perimeter length. In fact, once the fixed diagonals length constraint is considered, the regular square configuration corresponds to a saddle point for the perimeter length function. The experimental setup installed at the INFN in Pisa is shown in Fig. 1.

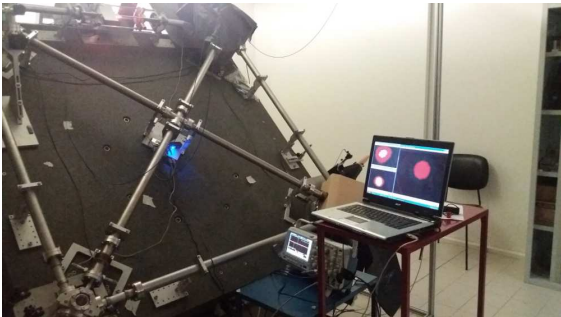


Fig. 1: GP2 ring laser is a $1.6 \times 1.6 \text{ m}^2$ square cavity and is oriented at the maximum kinematical Sagnac signal, i.e. with the laser plane perpendicular to the Earth's rotation axis. Three webcams are used for monitoring the beam profiles of three laser beams: the two modes resonating in the diagonals and the ring laser emission itself.

The experimental technique for the diagonal cavities control is based on the multi-frequency phase modulation of a reference laser, and is described in detail in [8]. This provides the estimate of both the cavity resonance frequency and the free-spectral range of the two resonators, so that an absolute length measurement can be achieved. In Fig. 2 the optical scheme of the geometry control apparatus is reported. A sub-nanometer length stabilization of the diagonals cavities has been obtained with a signal integration time of few hundred seconds. The feedback signals controlling the two diagonal cavity lengths are reported in Fig. 3. Both signals follow the

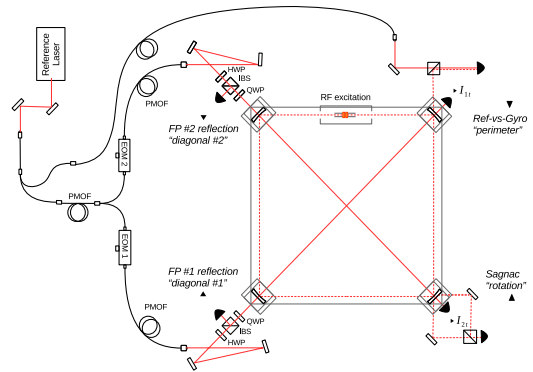


Fig. 2: Optical setup for the interrogation of the two diagonal resonators. EOM: Electro-Optic Modulator. PBS: Polarizing Beam Splitter. IBS: Intensity Beam Splitter. PMOF: Polarization Maintaining Optical Fiber. HWP: Half Wave Plate. QWP: Quarter Wave Plate. PZT: Piezoelectric Transducer. F: neutral filter. FP: Fabry Pérot cavity.

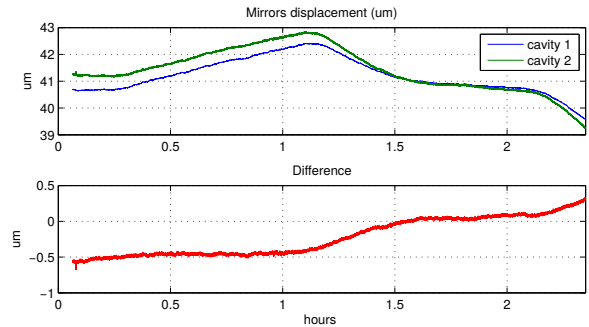


Fig. 3: Closed-loop corrections to the two couples of opposite mirrors forming the GP2 diagonal cavities.

room temperature fluctuation in the laboratory, that to date is not provided by a temperature stabilization system. The switch off of the air-conditioning/heating, is visible and clearly affect the trend of the two signals. The difference between the two signal corrections, plotted in the same graph, accounts for time-dependent temperature gradients in the laboratory, differential mechanical relaxations, and also slightly different mechanical responses of the piezoelectric translator stages. The square cavity length (perimeter) is the other quantity that is estimated. Two methods provide precise cavity length measurements: the beat frequency between the ring laser and the reference laser and the ring laser longitudinal mode spacing between different longitudinal modes emitted by the ring laser. The second method requires to operate the laser in multi mode regime and provides an absolute value of the ring laser round-trip time.

III. GINGERINO RING LASER

A comparison between a local measurement of the Earth's rotation rate with a measurement provided by the IERS system (based on the VLBI network) requires a strong rejection of the local rotational noise. This is mainly given by surface geo-

physical phenomena connected to atmospheric load variations caused by changing weather patterns and local hydrology. The LNGS deep underground laboratory is a possible candidate location, being located underneath more than thousand meters of solid rock. GINGERino ring laser gyroscope is located inside the LNGS lab, in an isolated area, outside the principal experimental rooms. Its aim is to perform high resolution local measurements of the vertical component of the Earth rotation rate, and analyze the different noise contributions by comparing them with the measurement provided by seismic instrumentation installed on top of the ring laser rigid structure: one tilt-meter with nrad resolution (2-K High Resolution Tiltmeter (HRTM), Lipmann) and two high performance seismometers (Trillium 240s and Guralp CMG 3T 360s). GINGERino uses the mechanics of G-Pisa [9] which is made up of 4 mirror boxes connected by vacuum pipes. The optical resonator is a square cavity 3.6 m in side-length equipped with four spherical mirrors 4 m in radius of curvature. Each mirror box can be independently tilted with micrometric screws, so to align the optical cavity. The ring laser (Fig. 4) is tightly attached to a cross structure made of black African granite, composed by a central octagonal massive block (3 tons), and four lightened arms each weighting ~ 800 kg. The granite structure is screwed

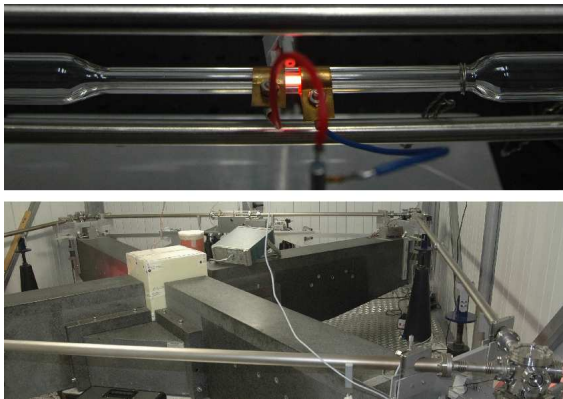


Fig. 4: Upper picture: detail of the ring laser excitation system. A radio-frequency discharge generates a He-Ne plasma inside a pyrex tube, 4 mm in diameter. Lower picture: the GINGERino vacuum chamber, containing the square cavity.

to a reinforced concrete block integral to the underneath bedrock. The African black granite has been chosen because it can be machined with high precision and has a low thermal expansion coefficient ($7\text{ppm}/^\circ\text{C}$). The installation area was at a temperature of about 8°C with a relative humidity close to the dew point all the year round. The whole installation is now protected by a large anechoic chamber. Infrared lamps are used to increase the temperature inside the box, thus reducing the relative humidity from more than 90% down to 50 – 60%. Typical environmental parameters trends inside the chamber are shown in Fig. 5.

The optical apparatus allowing us to run the laser continuously and observe the Earth induced Sagnac frequency is much simpler than the setup under study for the GP2 ring laser. The four cavity mirrors are spherical mirrors with 4 meters of radius of curvature. Presently, the ring down time of resonant light inside the ring is about $150\ \mu\text{s}$, corresponding to

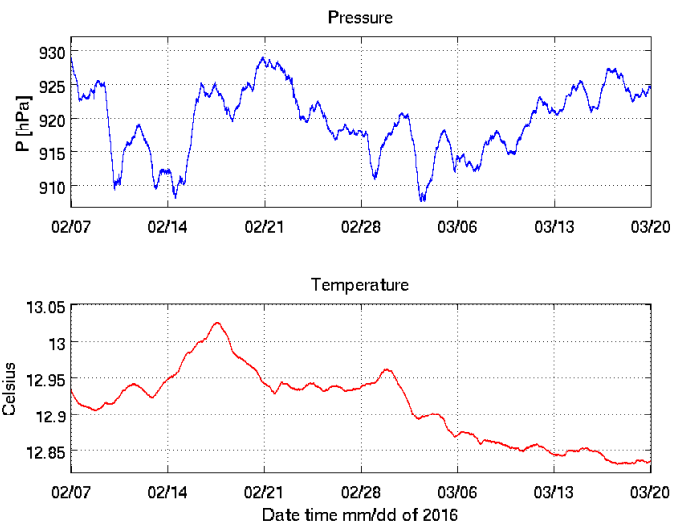


Fig. 5: Environmental parameters inside the GINGERino experimental chamber inside the Gran Sasso laboratory.

an average reflectivity of 99.98%, mainly limited by scattering losses. This is definitely a low level performance for a set of supermirrors and we expected to achieve the level of 99.999% with a new set of mirrors to be installed before summer 2016.

The Sagnac frequency recorded by GINGERino running without any frequency stabilization system is shown in Fig. 6. The noise level evaluated from the power spectral density is shown in Fig.7

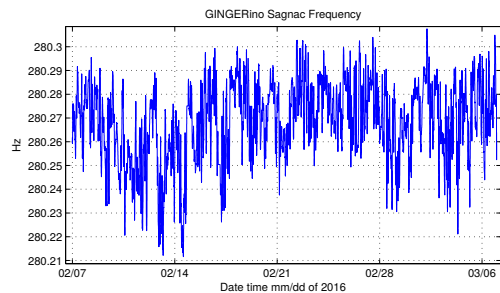


Fig. 6: Raw data time series of 29 days of continuous acquisition of the Earth’s induced Sagnac frequency. The instrument duty cycle is approximately 100%. Sampling interval of this time series is 1 sample per hour.

IV. CONCLUSION

The present status of the experimental activity toward General Relativity tests with ring lasers has been discussed. Two prototypes GP2 and GINGERino are operating respectively at INFN Pisa and inside the LNGS deep underground laboratories. The GP2 control system is under study and the diagonal resonators length control has been demonstrated with a precision at the nanometric level. Next steps toward the demonstration of an enhanced stability Sagnac interferometer, controlled both in diagonals and perimeter, are ongoing.

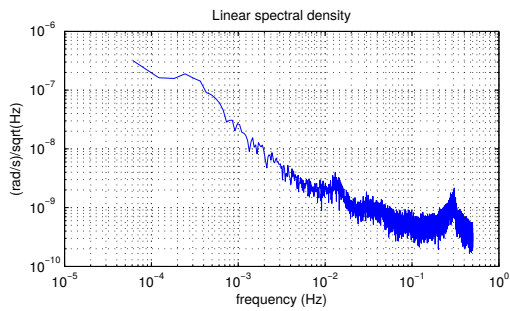


Fig. 7: Raw data linear spectral density of the rotational signal of GINGERino.

GINGERino is taking data in free running mode (without any active stabilization system up to now). The passive stability of the environment makes it possible to perform continuous acquisition of the Sagnac frequency on the monthly timescale. The present performances of GINGERino are limited by the large amount of backscattered light coming from the low quality set of mirrors. Large improvements are expected after the installation of a new set of mirrors and the implementation of the perimeter length stabilization.

REFERENCES

- [1] K. U. Schreiber and J-P. R. Wells, *Rev. Sci. Instrum.* **84**, (041101), (2013).
- [2] F. Bosi et al., *Phys. Rev. D* **84**, 1220022, (2011).
- [3] <https://web2.infn.it/GINGER>
- [4] <http://arxiv.org/abs/1601.02874>
- [5] K. U. Schreiber et al., *Phys. Rev. Lett.*, **107**, 173904, (2011).
- [6] D. Cuccato et al., *Metrologia* **51**, 97107, (2014).
- [7] R. Santagata et al., *Class. Quantum Grav.* **32**, 055013, (2015).
- [8] J. Belfi et al., *Class. Quant. Grav.* **31**, 22500, (2014).
- [9] J. Belfi et al., *Appl. Phys. B*, **106**, 271-281, (2012).

A Rotating Fan-Beam Radiation Model for the Pulse Duration and Frequency Spectrum of Pulsar Radiation

Michael J Underhill

Underhill Research Limited

Lingfield, UK

Email: mike@underhill.co.uk

Abstract— The assumption of a rotating fan-beam of broadband RF radiation appears to fit the observed pulse length to period ratio and pulse amplitude statistics of some pulsars. Here an electromagnetic (EM) mechanism is proposed for the generation of the fan-beam. The radiation pattern is assumed to arise from coupled standing wave components at harmonics of the pulsar spin frequency in radiating layers of (ionospheric) plasma above and around the equator of the pulsar neutron star. The conductive plasma carries current which circulates the magnetic axis of the pulsar. The particle beams emitted from the poles can also act as secondary radiators for the pulse radiation generated by the equatorial layer currents. In this model the radiation is not directed along the magnetic pole axis but is at right angles to it. The frequencies of the multiple layers form a comb spectrum with components spaced at harmonics of the pulsar rotation frequency. The pulse length to period ratio can be argued to be related to the fundamental EM coupling coefficients first presented in [6].

Keywords—pulsar time and frequency, pulse length to period ratio; pulse occurrence statistics

I. INTRODUCTION

A continuous 77GHz signal from a ‘phase-coherent’ CW radar, when reflected from a smooth or rough spinning cylinder, is converted into a pulse train with a repetition frequency equal to the cylinder spin frequency [1, 2, 3, 4]. The pulses look like those from a pulsar. Here we examine the possibility that the same pulse generation mechanism holds for both situations.

The explanation proposed for the spinning cylinder pulse-train generation process is that several layers of standing waves are created above the surface of the cylinder each having an integer number of wavelengths around its circumference. The forward and reflected wave components have different velocities depending on the spin rate and the distance of the given layer from the spinning surface. The ‘local ether drag’ decreases to zero at a distance inversely proportional to the square root of carrier frequency. In this case amounting to no more than 40 component layers Doppler shifted at harmonics of the spin frequency.

We find that the pulse period to pulse length ratio the number of layers divided by $1/2\pi$ and demonstrate this by simulation as shown in Fig. 3. This shows the fan 3dB-thickness of about 10° where the phases of the six components used in the simulation all add up. Thus measured pulsar pulse widths can determine the

number of layer components or at least the spectrum width seen on the spin frequency ‘carrier’.

The pulse *modulation* spectrum width always determines the reciprocal of the pulse length, even for the of the broad band of EM light wave radiation components from a pulsar. In this case we postulate that this is determined by the EM coupling observed between components of different frequency mode layers in the same or adjacent space [5]. This is related to the ‘EM coupling coefficient of $1/2\pi$ [6].

II. ESTABLISHED PULSAR RADIATION MODELS

Fig. 1 shows nine pulses from a Pulsar BB0329+54 observed with the Lovell telescope at Jodrell Bank at a VHF frequency [7]. Such records present measured pulse width and amplitude statistics of radiation from a given pulsar.

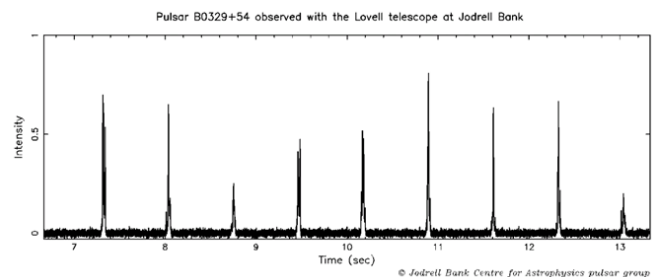


Fig. 1. Sequence of received pulses from Pulsar BB0329+54 observed with the Lovell telescope at Jodrell Bank. Intensity versus time (sec)

Fig. 2 shows established rotating pencil beam models of pulsars together with magnetic field lines and beams of highly energetic (charged) particles being emitted from the magnetic poles [8]. The assumptions are that the pulsed EM radiation is emitted most strongly in the direction of the poles, and the magnetic axis is substantially offset from the spin axis of the pulsar.

Here we propose that most of the pulsar EM radiation is in the direction orthogonal to the magnetic axis and the particle beams and the radiation is in the shape of a fan beam. This would appear to be better in accordance with what is known about electromagnetic radiation from currents in loop antennas. Furthermore, most if not all EM and antenna simulation methods operate on the basis that “the current radiates orthogonally”.

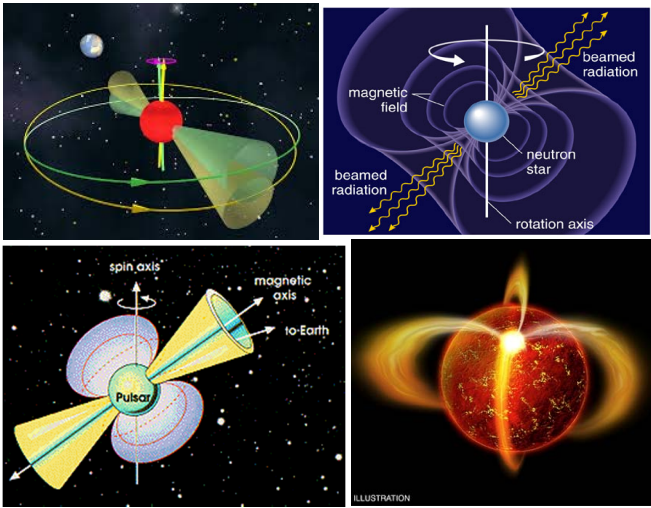


Fig. 2. Images for Pulsars [8]. Top left and right, and bottom left: Spinning pencil beams from magnetic poles offset from spin axis. Bottom right: Magnetic field lines with particles can radiate and rotate with the pulsar.

III. GENERATION OF THE FAN BEAM RADIATION PATTERN

To simulate the generation of a fan beam we postulate that a conductive plasma or ionosphere surrounding the magnetic equator supports many wavelengths of EM wavelengths in the form of layers of standing waves with components travelling at the speed of light circumferentially in opposing directions.

The rotation of the massive pulsar through the action of its local gravitational dragging of the ether in the region that supports surface wave layers means that the standing wave components see differing ether velocities in each direction. The speed of light is slightly different in each direction. It is this that causes each standing wave layer to be dragged in the direction of the pulsar rotation.

But we postulate that ether drag is local and the drag velocity rapidly decays with distance like the Casimir Effect [9]. Thus the layers are Doppler shifted less as the radial distance increases. In fact, the layers occupy stable positions for which the Doppler shifts are integer values of the pulsar spin frequency.

For the Mathcad simulation six components only at carrier frequencies spaced by the pulsar spin frequency are assumed. We find that these combine to form a double fan beam. In Fig. 3 we simulate outward radiation only by a simple two element Yagi pattern.

This simple idealized model does in fact generate a fan beam with a shape of the right general form as can be seen in Fig. 3.

Also we find experimentally (and confirmed by hindsight theory) that the pulse period to pulse length ratio is the number of components divided by $1/2\pi$. In Fig.3 we find a fan beam 3dB-thickness of about 10° where the phases of the six components used in the simulation are the same so that all their amplitudes add up to give a short pulse. Measured pulsar pulse widths thus can determine the number of layer components or at least the spectrum width seen on the spin frequency 'carrier'.

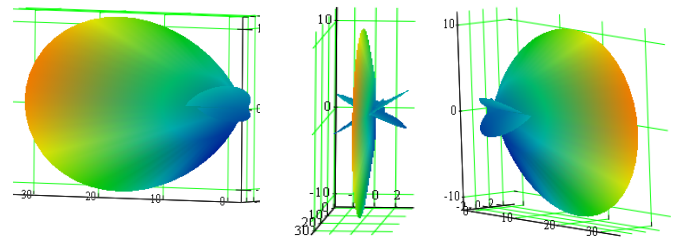


Fig. 3. Fan-beam rotating about vertical axis, with three positions shown. Mathcad simulation adding six equal amplitude components, with frequencies spaced at rotation frequency. Unidirectional fan simulated by two element phased array (Yagi). Note small unwanted side-lobes.

The measurements shown Fig. 4 show that visible pulse side lobes can exist for some pulsars. This picture was provided in a private communication [10] the provenance of this data is currently being traced).

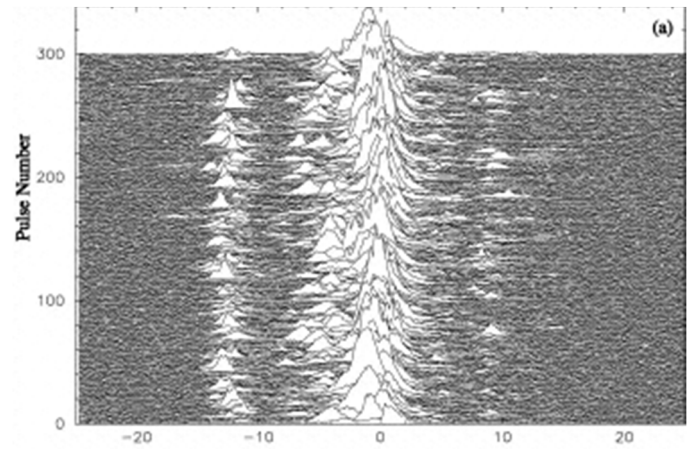


Fig. 4. Successive pulses stacked in a time waterfall showing pulse sidelobes and jitter on the pulse positions

IV. DOUBLE FAN BEAM RADIATION PATTERN

Fig. 5 shows a double fan beam radiation simulation. If we assume a small varying offset angle between the two fan beams in opposite directions, we can model alternating pulse with offset timings as in the measurements shown in Figure 6.

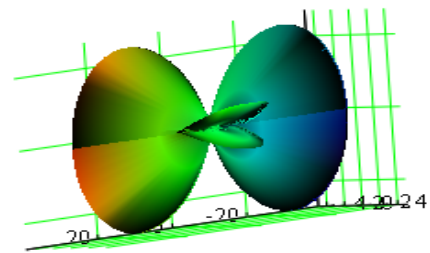


Fig. 5. Mathcad simulation of six frequency components giving a double fan-beam. The spurious sidelobes are smaller if more components are used in the model. The alternating pulse timings shown in Figure 5 correspond to a small varying misalignment of the oppositely directed fan-beams.

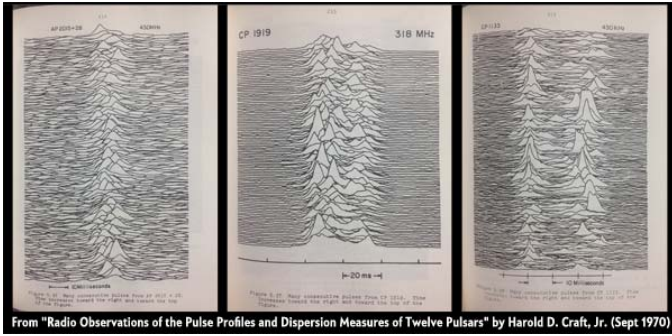


Fig. 6. Successive pulses stacked in time waterfalls alternating in time position indicating a double fan-beam radiation pattern as shown in Figure 6. (Reference at bottom of photocopy.) Successive pulses stacked in time waterfalls alternating in time position indicating a double fan-beam radiation pattern as shown in Figure 6. (Reference at bottom of photocopy.)

Once again in Fig.5 notice the presence of side-lobes. But in this case these would only occasionally generate longer low level pulses between the main pulses that would be easy to factor out.

V. DE-DISPERSION OF PULSES

Possibly there is a fundamental problem in the measurement of pulsar pulse lengths. Measurement frequencies typically lie between 100MHz and a few GHz. Fig. 7 shows that a pulse arrival time is progressively delayed as the measurement frequency is lowered [11].

The ‘dispersion’ coefficient can easily be measured for the frequency measurement range shown, and then the pulses can be ‘de-dispersed’ as shown and explained in Fig. 8 [12]. In this way the signal-to-noise-ratio of the pulse is greatly enhanced.

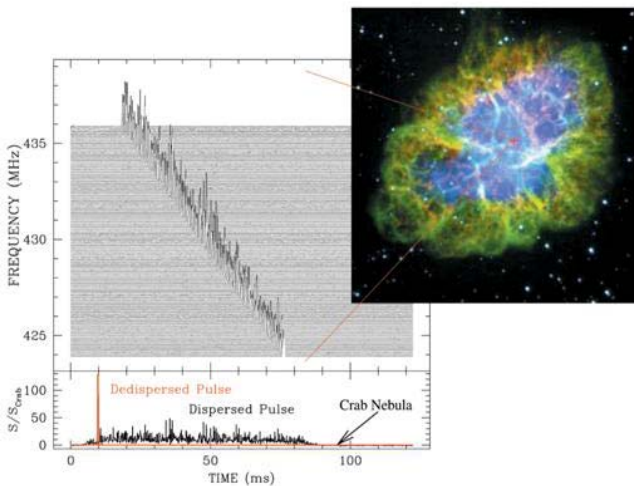


Fig. 7. A bright giant pulse from the Crab Nebula pulsar PSR B0531+21 from Arecibo observations at 430 MHz; the dispersed and dedispersed pulses are also shown. This giant pulse is $\sim 2 \times 10^4$ times stronger than typical normal pulses. Right: Palomar image of the Crab nebula that hosts the pulsar. Such bright, very steep spectrum giant pulses can potentially be detected with the MWA demonstrator out to ~ 1 Mpc. Credit: (R. Bhat (MIT Haystack), P. Scowen (Palomar/ASU) [11].

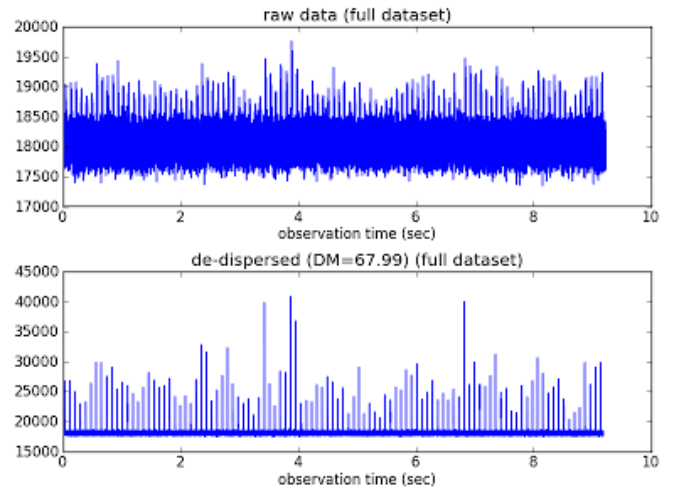


Fig. 8. The so-called “de-dispersed” time series signal is shown in the lower plot above. This is what you get once you have corrected for the dispersion i.e. effectively straightened the curves in the time-frequency plot. Clearly the Vela pulses are now much stronger relative to the noise (the base part) of the signal. This can also be appreciated by listening to the de-dispersed signal and comparing with the dispersed raw signal as discussed previously for the upper plot. Note now that the pulsar pulses can be clearly heard due to the major increase in the signal-to-noise ratio brought about by the de-dispersion operation. How cool is that! [12]

It is arguable that the measurements are showing that over the distance between the pulsar and earth there is not only time dispersion of the pulse but a continuous and progressive red-shift [13] of the original pulses presumably originally generated at optical frequencies. If so it could represent a ‘Landau damping’ process in free space, not just in plasmas [14]? In turn is this the same as a progressive red-shift as a result of fluctuations in the gravitational potential casing small variations in the gravitational field in free space [15]? Would this be an alternative explanation for Hubble’s Law [16] but calling into question the age of the universe?

VI. CONCLUSIONS

For some pulsars a EM fan-beam radiation model would appear to give a more accurate match to the measured short and long term pulse amplitude and pulse width statistics of the pulsar when compared with the spot beam model.

The fan-beam model can be argued to comply better with the principles of electromagnetic radiation (from antennas). It would appear that a better electromagnetic explanation for the pencil beam model is needed in any case. What this may be is not immediately obvious.

The next step is to determine whether the measured pulse amplitude statistics in each case are a better fit to this new ‘fan-beam’ model or the conventional ‘pencil-beam’ model. It may be a case that both models are needed?

There remains the problem of finding the fundamental cause of the ‘dispersion’ of pulsar pulses. A possible explanation is being sought using extensions of fundamental electromagnetic

concepts used to explain the formation of a fan-beam radiation pattern for pulsars.

Another problem to be addressed is to formulate a similar electromagnetic model for the radiation from binary pulsars [17].

REFERENCES

- [1] J. K. Christensen, and M. J. Underhill, , “Analysis of the PM and AM associated with the natural eigen-frequencies of spinning metallic and dielectric cylinders illuminated at high frequencies“, 18th EFTF 2004, pp. 334 – 338. .
- [2] J. K. Christensen and M. J. Underhill, “Phase coded pulse Doppler and continuous wave 77 GHz radar measurement and analysis facility”, Radar, Sonar and Navigation, IEE Proceedings 2004, vol. 151 no.6, pp 365-374
- [3] M. J. Underhill, “More fundamental instabilities in oscillators?”, *15th EFTF 09: IEEE-FCC’09*, Besancon, France, 20-24 April 2009, pp 334-337.
- [4] M. J. Underhill, “The phase noise spectrum and structure of photons?” Proc. 16th EFTF-2010, Noordwijk, Netherlands, 13-16 April 2010, 8 pages.
- [5] M. J. Underhill., “Coupling Theory for Fluctuating Spurs in Oscillators”, *Proceedings*, 2014 IEEE Int. Frequency Control Symp., Taipei, Taiwan, 19-22 May 2014, pp. 1-5.
- [6] M. J. Underhill, “A Physical Model of Electro-magnetism for a Theory of Everything”, *PIERS Online*, Vol.7, No. 2, 2011, pp. 196 -200. Also in *Proc. PIERS 2011*, March 20-23, Marrakesh, Morocco, pp. 1665 – 1669.
- [7] Jodrell Bank pulsar records
<http://www.jb.man.ac.uk/~reatough/sounds.htm>
- [8] Images for pulsars:
https://www.google.co.uk/search?q=pulsars&biw=1280&bih=648&tbo=isch&tbo=u&source=univ&sa=X&ved=0ahUKewjbnP3G_-XLAhUHsxQKHTi1CKsQsAQISg
- [9] M. J. Underhill, “The Casimir Force and Heat Conduction Viewed as Exclusion of Natural Spatial Energy and Lateral EM Coupling between the Walls of a Waveguide”, *Proc. PIERS 2014* August 25-28, Guangzhou, China, pp. 274 - 278.
- [10] Private communication from P. W. East, February 2016. Provenance being investigated.
- [11] <http://www.haystack.mit.edu/mwa/Science%20Goal/ScienceOpportunities/opportunity.html>
- [12] <http://public.ska.ac.za/kat-7/kat-7-data-reduction/pulsars-and-transients>
- [13] M. J. Underhill, “Discovery of Ionospheric ‘Hubble’ Frequency Shifts and Impact on Gravity Wave Detection and the Age of the Universe?,” *Proc. PIERS 2015*, Prague, 6-9 July 2015, pp.
- [14] “Landau damping”, http://en.wikipedia.org/wiki/Landau_damping
- [15] “Gravitational redshift”,
http://en.wikipedia.org/wiki/Gravitational_redshift
- [16] “Hubble’s Law”, http://en.wikipedia.org/wiki/Hubble's_law
- [17] “Binary Pulsar”, https://en.wikipedia.org/wiki/Binary_pulsar

Sequential measurement of optical frequency difference of semiconductor lasers for time transfer system

Ł. Buczek

Department of Electronics
AGH University of Science and Technology
Kraków, Poland
Email: lbuczek@agh.edu.pl

Abstract—This paper describes the concept of differential wavelength measurement of two semiconductor lasers with better resolution and accuracy than offered by a typical optical spectrum analyzer. In a two-way fiber-optic transfer system the knowledge of difference of wavelength is used to calibrate of time transfer. Applying this solution allows to calibrate time transfer system with lower uncertainty.

Keywords—differential wavelength measurement; time transfer system; sequential measurement

I. INTRODUCTION

The stability and accuracy of optical time transfer system (OTTS) depends, among other factors, on optical frequency difference between forward and backward direction laser transmitters [1]. The OTTS system exploits two lasers working in two different ITU channels and their optical frequency difference is 100 GHz ($\approx 0,8$ nm). In principle, measurement of optical frequency difference could be made using typical optical spectrum analyzer (OSA), but its resolution and accuracy may be insufficient in this application. This problem concerns in particular long-haul fiber optic link with high value of accumulated chromatic dispersion (D). The difference of propagation delay ($\Delta\tau$) caused by the lasers working in two different ITU channels ($\Delta\lambda$) is:

$$\Delta\tau = D \cdot \Delta\lambda \quad (1)$$

Letting for example $D = 10000$ ps/nm and $\Delta\lambda = 100$ GHz (0,8 nm), the delay difference is about 8000 ps. This difference of propagation delay must be take into account during calibration process of OTTS system. Assuming the standard uncertainty of measurement of optical frequency difference equal to 3 pm (375MHz). It introduces additional about 13 ps to uncertainty budget of OTTS system calibration [2]. The concept proposed herein assumes the use of two auxiliary adjustable semiconductor lasers and three high-speed photodiodes and three channels frequency meter and microcontroller with control algorithm. This method allows measurement with the estimated standard uncertainty equal to about 5MHz (0.04 pm).

II. THE CONCEPT OF SEQUENTIAL MEASUREMENT

The idea of sequential measurement of optical frequency difference is presented in Fig 1. This method uses two auxiliary

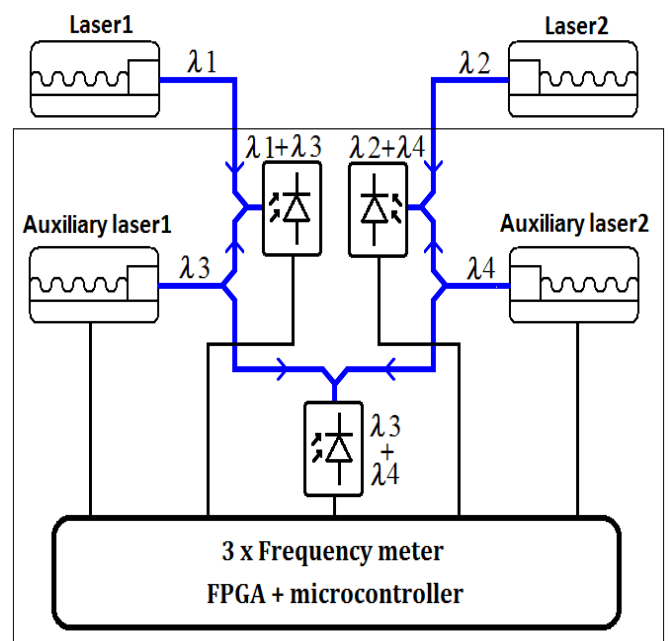


Fig. 1. An idea of measuring the difference of semiconductor lasers carrier frequencies using beatnote signal and two auxiliary adjustable semiconductor lasers.

semiconductor lasers. Each of auxiliary lasers must be tunable and its tuning range involves wavelengths of measured lasers. The method requires three different optical signals:

- sum of the optical signals from Laser1 and first auxiliary laser
- sum of the optical signals from Laser2 and second auxiliary laser
- sum of the optical signals from first and second auxiliary lasers

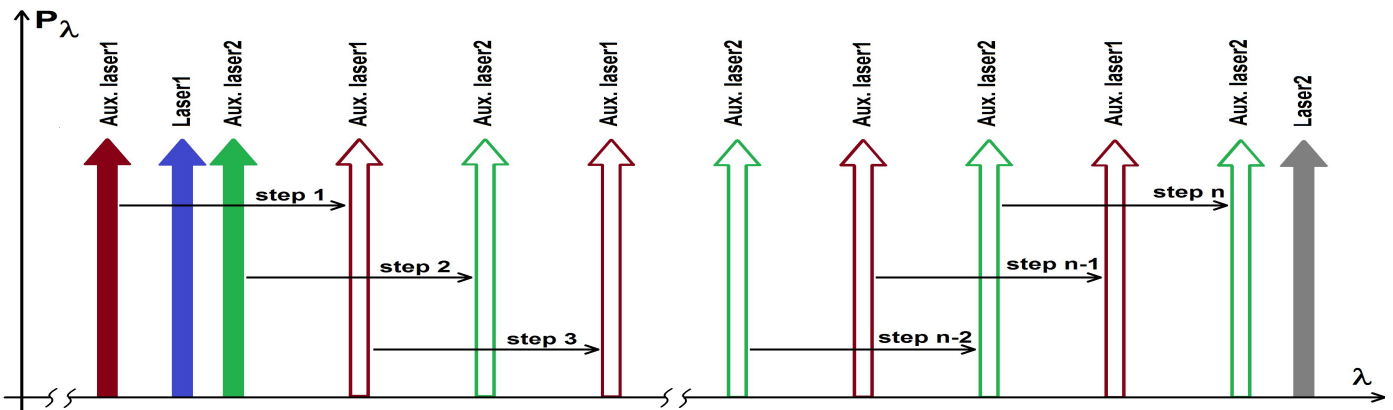


Fig. 2. Sequential tuning of two auxiliary adjustable semiconductor lasers.

The three optical signals are supplied to three high-speed photodiodes. Resulting beatnotes with the frequency equal to the difference of the lasers carriers are further measured. A single measurement of optical frequency difference of lasers requires sequential tuning of auxiliary lasers and frequency measurement in three channels. This sequence is shown in Fig 2. The measurement start requires tuning of the auxiliary lasers close to the Laser1. Maximum detuning of lasers in this and each successive step can't be greater than photodiode bandwidth. During consecutive steps wavelengths of auxiliary lasers are increased and beatnote signals from three photodiodes are recorded. The record of frequency beatnote signals from photodiodes during single measurement of optical frequency difference of two DFB lasers is presented in Fig 3. Tuning of auxiliary lasers continues until one of them will be close to the Laser2. Final result of the measurement of optical frequency difference between the two lasers is a sum of partial measurements of frequency from three photodiodes. The number of steps depends on difference of measured laser wavelength and auxiliary laser tuning range in single step. The laser tuning range in the single step depends on the photodiode

bandwidth and the range of frequency meter. The standard uncertainty of final result depends on standard uncertainty of single frequency measurement and short-time stability of the wavelength of auxiliary lasers. The estimated standard uncertainty of the whole measurement is about 5 MHz.

III. CONCLUSION

The advantage of the proposed solution compared with the conventional spectrum analyzer measurement is much lower standard uncertainty. This solution can also be part of another device because it is easy to use. The disadvantage of this solution may be however longer measuring time compared to the conventional method but in many situations this is not relevant.

IV. REFERENCES

- [1] Ł. Śliwczyński, P. Krehlik, and M. Lipiński, "Optical fibers in time and frequency transfer", *Meas. Sci. Technol.* **21** (2010) 075302, 2012.)
- [2] Ł. Śliwczyński, P. Krehlik, A. Czubla, Ł. Buczek and M. Lipiński, "Dissemination of time and RF frequency via a stabilized fibre optic link over a distance of 420 km", *Metrologia* **50** 133–145, 2013.

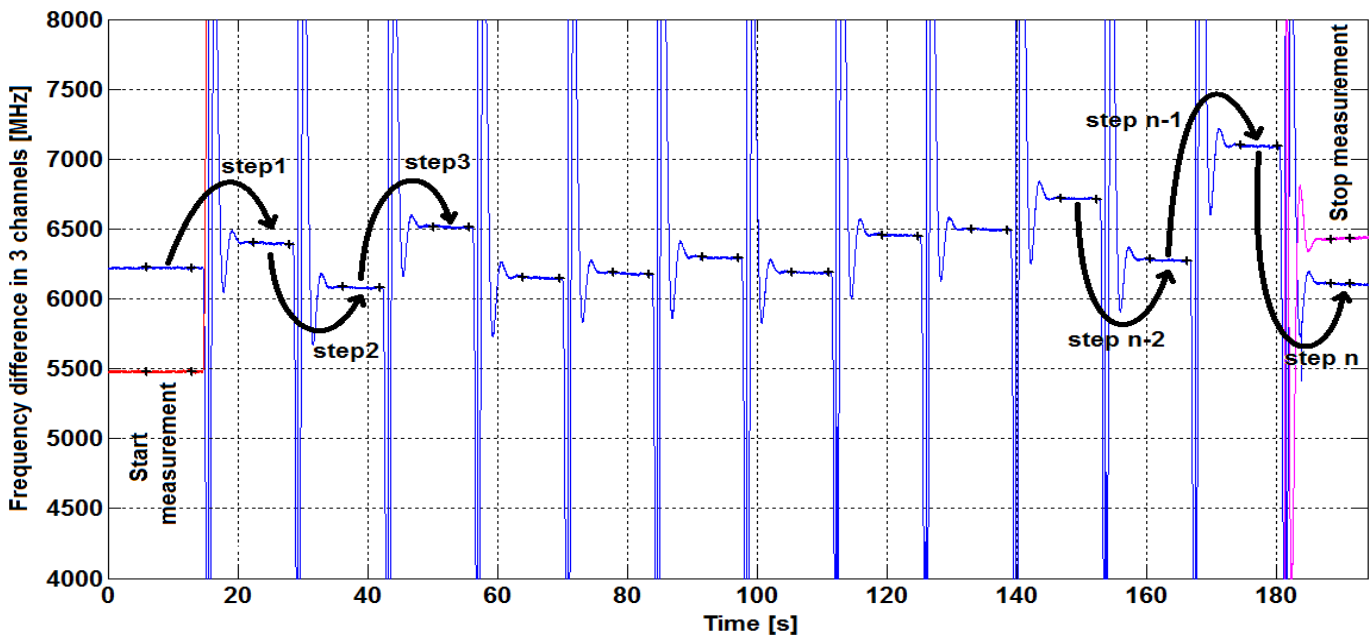


Fig. 3. The record of beatnote signals from three photodiodes during single measurement

Behavior of Quartz Crystal Resonators at Liquid Helium Temperature

Serge Galliou*, Philippe Abbé*, Maxim Goryachev†, Eugene N. Ivanov†, Michael. E. Tobar†, and Roger Bourquin*

*Time and Frequency Department,
FEMTO-ST Institute (UMR 6174, CNRS, UBFC), Besançon, France.
serge.galliou@femto-st.fr

† ARC Centre of Excellence for Engineered Quantum Systems,
School of Physics, the University of Western Australia, Crawley, WA, Australia.
maxim.goryachev@uwa.edu.au, michael.tobar@uwa.edu.au

Abstract—Bulk acoustic wave (BAW) quartz crystal resonators working at liquid helium temperature are an exciting topic of interest. Indeed, high-quality devices can exhibit quality factors of a few hundreds of millions, from tens of megahertz to hundreds of megahertz, and can reach a few billions for the best ones. As a consequence they are good candidates to various applications ranging from frequency references to fundamental physics. A brief review is first proposed regarding Q-factor properties of BAW SC-cut resonators within the temperature range 3K - 12K. The A, B and C mode behaviors are also examined in terms of frequency versus temperature, as well as the frequency dependence with the excitation power. Finally measurements on Nyquist noise are presented.

I. INTRODUCTION

The behavior of bulk acoustic wave (BAW) quartz crystal resonators at liquid helium temperature has been a real topic of interest in the 1960's-1970's, in the theoretical domain as well as experimentally [1], [2], [3], [4], [5], [6]. Some studies have continued a few years later [7], [8], [9], and have been developed again from 2008 [11], [12]. Up to 2008, the operating temperature was reached by means of helium cryostats. From 2008, pulse-tube cryo-refrigerators have been used instead of cryostats, enabling longer experiments without needing helium supply. From these first experiments with cryo-refrigerators, measurements often revealed better results than those previously published in terms of quality factors, probably due to an improvement of the quartz crystal quality. More recently, it has been demonstrated that quality factors greater than 1 billion can be reached by the best units of bulk acoustic wave quartz crystal resonators working below 6 K [13]. Such low-loss resonators are good candidates for various applications including potentially very stable frequency sources but also experiments in fundamental physics involving acoustic cavities in quantum hybrid systems for example [14], [15], [16], [17], [18]. The devices tested in the frame of this paper are mainly doubly-rotated SC-cut quartz resonators. By means of their slowly varying thickness, these spherically contoured resonators look like plano-convex disks where the

acoustic energy is trapped, according to Tiersten and Stevens theory [19]. They are initially optimized to work at room temperature on the 3rd overtone of the C-mode, one of both quasi-pure thickness shear modes, at 5 or 10 MHz. After a short review of theoretical basis, some collected data are shown to illustrate the behavior of such resonators in the vicinity of 4 K, in terms of quality-factor, temperature, and power dependence versus frequency.

II. BACKGROUND

When operating at low temperature typically lower than 20 K, lower mechanical losses than at room temperature can be expected just because of the thermal phonon reduction. Nevertheless, this can be achieved provided that the engineered losses of the acoustic resonator are minimized. These engineered losses obviously include energy losses inside the holders because of a certain lack of trapping, scattering due to the surface roughness depending on lapping and polishing quality, but also absorption due to impurity and/or defect density according to the material quality. In short, the resulting loss $1/Q$ can be expressed as a sum of individual losses $1/Q_i$. Ideally, when all the engineering losses are minimized, the remaining losses are intrinsic losses due to phonon-phonon interaction and thermoelastic effect. Actually, the latter do not exist for shear modes (B and C modes) and even in the case of the extensional mode - the A mode- it can be shown that losses are no longer significant for frequencies typically greater than a few megahertz.

Regarding the interaction of the acoustic phonon with thermal phonons, mechanisms at cryogenic temperatures are different from those at 300 K. Indeed, the thermal phonon lifetime τ_{ph} increases as the temperature goes down below 10 Kelvins, and achieves the condition $2\pi f\tau_{ph} > 1$. Thus, the absorption coefficient $\alpha(f)$ of the propagating wave is changed, and in turn, the Q-factor which is proportional to $\frac{f}{\alpha(f) \times V}$ where f is the frequency, and V the corresponding acoustic wave velocity. At room temperature, $\alpha(f)$ is proportional to f^2 whereas at

liquid-helium temperature, it becomes proportional to $T^4 \times f$ according to the Landau-Rumer theory [20]. It turns that the product $Q \times f$ is a constant at room temperature - a feature of the so-called Akheiser regime [21] - whereas Q does not depend on f anymore at liquid helium temperature. In addition, it behaves as $1/T^n$ with $1 < n < 9$ depending on whether the mode is a longitudinal or transverse one [4], [20], [22]. Fig. 1 shows a set of results at low temperature for resonators exhibiting a $Q \times f$ product slightly greater than $1 \cdot 10^{13}$ at room temperature. For temperature lower than about 6 K, it can be noticed that the slope decreases towards $1/T^{1/3}$, which could be attributed to a two-level-dependency (TLS) effect [23] due to the presence of impurities [9] (see also [10]). Another feature that may be highlighted from Fig. 1 is that Q-values of the A mode are always greater than those of the B-mode which are themselves greater than those of the C-mode. It has been demonstrated that this is the result of the energy trapping whose efficiency can be sorted exactly like the observed losses [24] [11]. At least, it should be mentioned that a special attention should be paid to the high-Q measurements. The experimental set-up and the corresponding measurement procedure have already been described (see for example references [11] [25]). It can simply be reminded that three coaxial cables similar to that feeding the device under test (DUT) are ended at their cold ends by a 50-ohms load, a short-circuit, and an open-circuit respectively. Thus, the calibration procedure of the network analyzer can easily be used for measuring efficiently the impedance modulus and phase of the DUT, and then, the requested Q-value.

III. OTHER EXPERIMENTAL DATA

A. Quality factors versus frequency

When plotting the quality factor of a given mode against the frequency of its overtones, a constant Q-value would be expected according to Landau-Rumer theory, as mentioned above. Actually, as illustrated in Fig. 2, from low frequency values, Q-values usually increase as the frequency increases before being a constant up to the vicinity of 100 MHz from which Q-values decrease with frequency. At lower frequencies, this trend, hiding the expected constant value of the quality factor, can easily be explained: the higher the overtone order, the better the energy trapping. On the other end of the explored frequency range, the Q-value decrease at higher frequencies can be explained by scattering due to the surface roughness and/or the amorphous layer resulting from lapping and mechanical polishing [13].

B. Frequency versus temperature

Typical frequency-temperature behaviors are shown in Fig. 3. As expected at low temperature, one can observe that the frequency to temperature sensitivity decreases with the temperature like most material properties. Nevertheless, when taking into account the measurement uncertainty, there is no turning point seemingly. The latter would be needed for using a cryogenic acoustic resonator as the heart of a frequency standard.

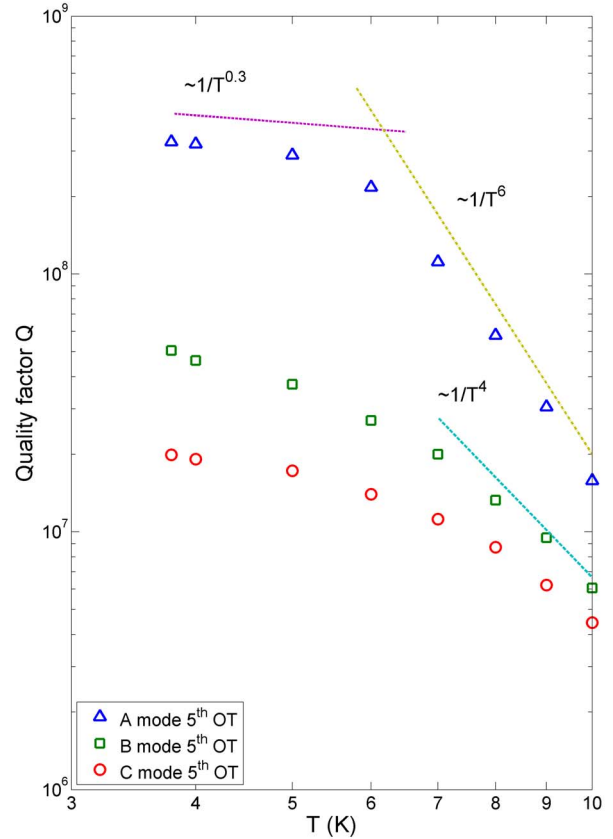


Fig. 1. Quality factor versus temperature for a 13 mm-diameter BVA-type resonator optimized to work at 5 MHz on the 3rd overtone of the C-mode at room temperature. The frequencies of the 5th OT are about 8.400 MHz, 9.197 MHz and 15.597 MHz for the C, B and A mode respectively.

IV. NONLINEARITIES

Wrong values of Q-factors may result of an excess of feeding power. As an example, plots of the impedance modulus and phase shown in Fig. 4 demonstrate that slopes strongly depend on the excitation power.

Beyond this mishandling, the issue of the dissipated power inside the resonator becomes relevant because of the high quality-factors Q . Indeed, the energy stored inside the resonator can be expressed as: $E_{stored} = Q \times p \times 1/\omega_0$, where p is the power dissipated inside the resonator (i.e. in the motional resistance), and ω_0 the resonance angular-frequency. So, the excitation power should be very weak to avoid nonlinearities as well as an excessive dissipation, and justifies values typically in the order of one nano-watt (see Fig. 4). It can also be noticed that a "high" excitation power can lead to a visible frequency shift during the measurement, resulting from an increase of the resonator temperature.

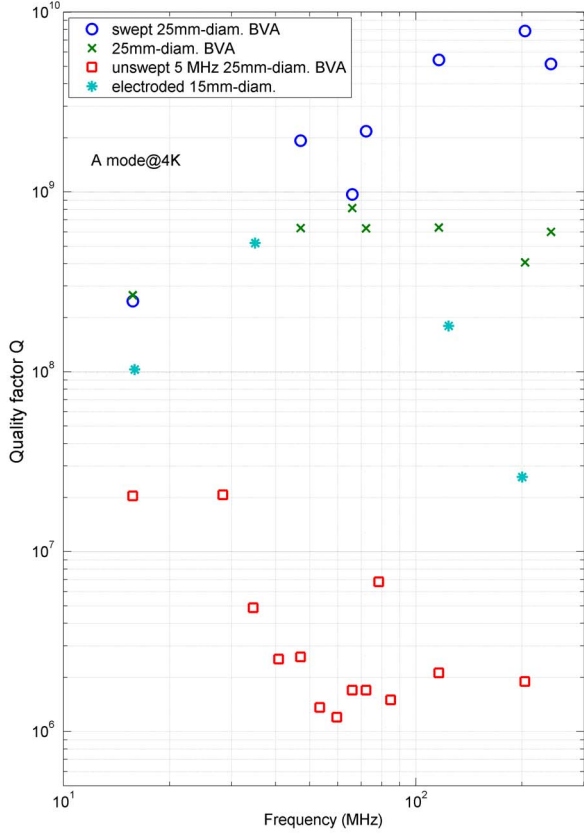


Fig. 2. Q-values versus frequencies of A-mode overtones at 4 K for various type of resonators originally optimized to work at 5MHz on their 3rd overtone at room temperature. The best resonator is seemingly an exceptional unit. Conversely, an unswept material can provide a very bad resonator in terms of Q-values at low temperature, even if at room temperature this resonator exhibits Q-values very similar to that of a premium-quality resonator.

V. NYQUIST NOISE

Recently, thermal Nyquist noise fluctuations of a high-Q BAW resonator have been observed at cryogenic temperatures [26]. The device was coupled with a DC superconducting quantum interference device (SQUID) amplifier. One of the goals of this step was to confirm whether or not BAW devices are dominated by intrinsic Nyquist noise due to quantum or thermal fluctuations when the carrier is not present. Actually, this observation is an important step towards the preparation of a BAW resonator in the quantum ground state which would be one the ultimate aim. Moreover, this work is obviously one step towards a frequency source based on very high Q-factor mechanical resonator. It combines the benefit of high-Q resonators to low-noise superconducting technology. Fig. 5 illustrates one of the measurement result. Data can be fitted by a lorentzian plot as a function of the motional resistance, from which the Nyquist noise originates. The integral of this Lorentzian fit is proportional to the power p dissipated

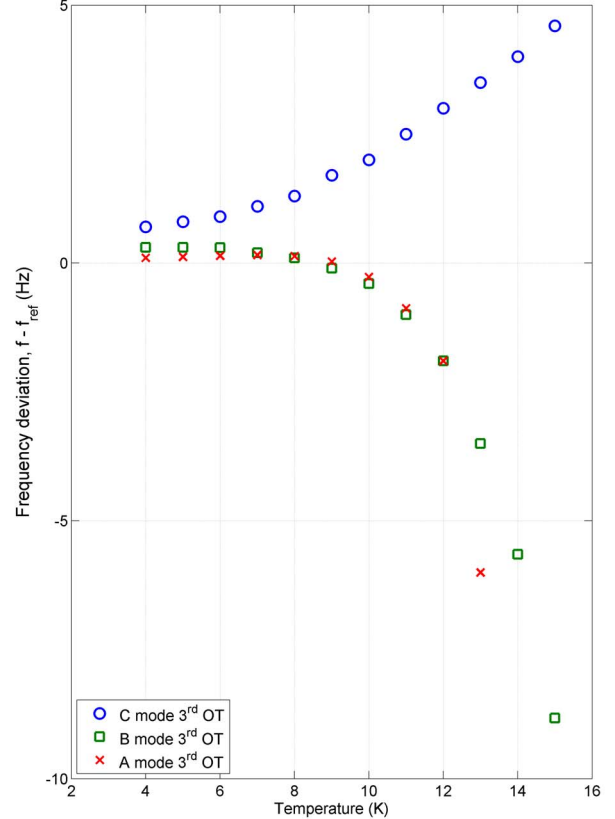


Fig. 3. Frequency deviation versus Temperature. The reference frequencies f_{ref} are 4993048.0 MHz, 5505583.0 MHz, and 9410720.0 MHz for the 3rd overtones of the C-mode, B-mode and A-mode respectively. Temperature uncertainty is about ± 0.1 K whereas frequency uncertainty is ± 0.05 Hz.

inside the resonator (see section "Nonlinearities" above), when assuming a constant SQUID transfer function within the analyzed frequency range. Details are given in ref [26].

VI. CONCLUSION

This digest on features of cryogenic BAW resonators highlights properties of matter related to these specific operating conditions. For example, quality factors can increase from one million at room temperature to hundreds of millions at cyogenic temperature. Some applications can obviously take advantage of these outstanding features such as ultra-stable frequency sources, but also experiments of fundamental physics [15], [18]. Regarding frequency source the next step will be to look for a temperature compensated cut. Measurements of the elastic coefficients of quartz at liquid helium temperature are currently in progress.

ACKNOWLEDGMENT

The authors would like to thank the Conseil Régional de Franche Comté for its financial support, as well as the Embassy of France, Canberra, Australia. Special thanks are given

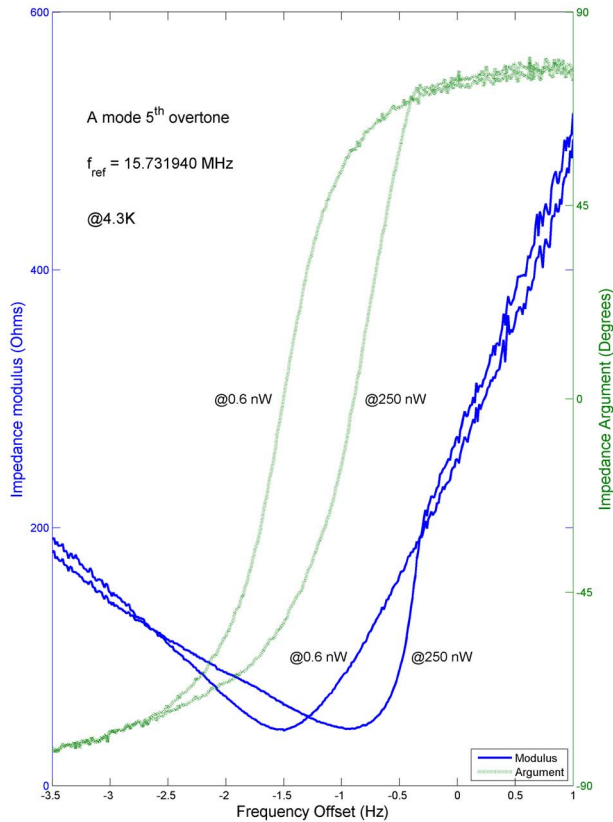


Fig. 4. Impedance argument and phase versus frequency offset (with respect to 15.731940 MHz) for two different feeding powers, when the resonator is at 4.3 K.

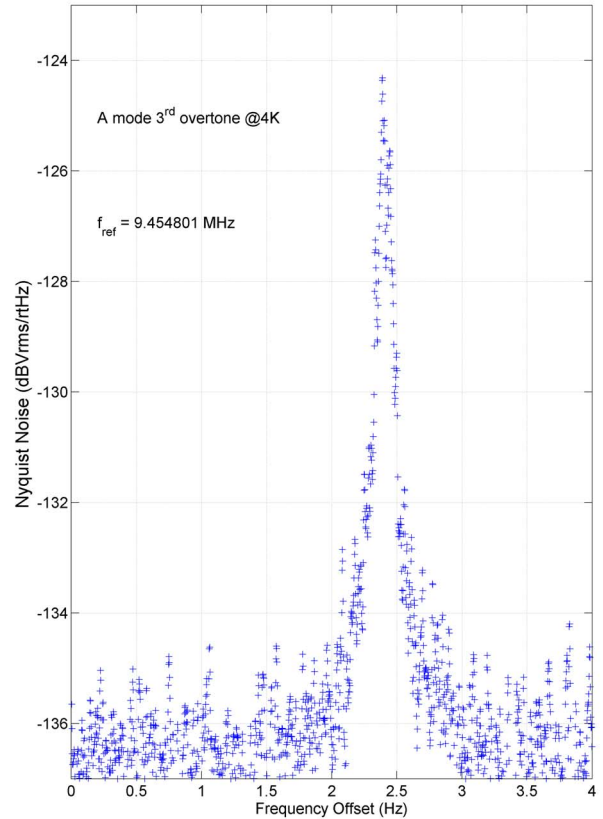


Fig. 5. Nyquist noise around the 3rd overtone of the A-mode at 9.454801 MHz.

to *Oscilloquartz SA*, Neuchatel, Switzerland for providing resonators, and especially Isabelle Lozach, Jean-Pierre Aubry, and Luc Schneller. MG is thankful to the Australian Research Council under grant CE110001013.

REFERENCES

- [1] A. W. Warner, "Ultra-precise quartz crystal frequency standards" *IRE Transactions on Instrumentation*, 1958.
- [2] N. Smagin, "Quartz crystal resonators with quality factors of about $120 \cdot 10^6$ at 2 K" *Izmeritel Tekh. SSSR N9*, 1960.
- [3] D. B. Fraser, "Impurities and anelasticity in crystalline quartz" *Physical Acoustics, vol. V*, pp. 59-110, Academic Press, 1968.
- [4] H. J. Maris, "Interactions of sound with thermal phonons in dielectric crystals" *Physical Acoustics, vol V*, pp. 279-345, Academic Press, 1968.
- [5] J. J. Gagnepain, "Non linear mechanisms in quartz crystal resonators" *Thesis, University of Franche Comte' (UFC)*, France, March 1972.
- [6] G. Mossuz, "Study and achievement of a quartz crystal oscillator at very low temperature" *UFC PhD*, July 1975.
- [7] G. Robichon, J. Gros Lambert, J.J. Gagnepain, "Frequency stability of quartz crystal at very low temperatures: preliminary results" *38th Annual frequency Control Symposium*, 1984, pp. 201-205.
- [8] M. Planat, J. J. Gagnepain, "1/f noise in quartz crystal resonator in relation with losses and frequency dispersion" *Appl. Phys. Lett. Vol. 50, N 9*, pp. 510-512, March 1987.
- [9] A. El Habti, F. Bastien, "Low temperature limitation on the quality factor of quartz resonators" *IEEE Trans. on Ultrasonics Ferroelectrics and Frequency Control, Vol. 41, N2*, pp. 250-255, 1994.
- [10] M. Goryachev, D. L. Creedon, S. Galliou, and M. E. Tobar, "Observation of Rayleigh phonon scattering through excitation of extremely high overtones in low-loss cryogenic acoustic cavities for hybrid quantum systems," *Phys. Rev. Lett.* 111, 085502, August 2013.
- [11] S. Galliou, J. Imbaud, R. Bourquin, N. Bazin, P. Abbé, "Outstanding Quality Factor of Bulk Acoustic Wave Resonators at Cryogenic Temperature," *Proc. 22nd European Freq. Control Symp.*, 2008.
- [12] S. Galliou, J. Imbaud, R. Bourquin, N. Bazin, and Ph. Abb, "Quartz crystal resonators exhibiting extremely high Q-factors at cryogenic temperatures," *Electronics Letters, Vol. 44, no 14*, p. 889-890, Juillet 2008.
- [13] S. Galliou, M. Goryachev, R. Bourquin, Ph. Abbé, J. P. Aubry, and M. E. Tobar, "Extremely Low Loss Phonon-Trapping Cryogenic Acoustic Cavities for Future Physical Experiments," *Nature: Scientific Reports*, 3, 2132, 2013. <http://www.nature.com/srep/2013/130704/srep02132/full/srep02132.html>
- [14] M. Aspelmeier, T. J. Kippenberg, and Florian Marquardt, "Cavity optomechanics", *Rev. Mod. Phys.*, 86, 1391, 2014.
- [15] M. Goryachev and M. E. Tobar, "Gravitational wave detection with high frequency phonon trapping acoustic cavities," *Physical Review D* 90, 102005, 2014.
- [16] M. Goryachev and M. E. Tobar, "Effects of geometry on quantum fluctuations of phonon-trapping acoustic cavities," *New Journal of Physics* 16, 083007, 2014.
- [17] M. Goryachev, "Cryogenic Quartz BAW Resonator Technology," *8th Symposium on Frequency Standards and Metrology, Potsdam, Germany*, October 2015.

- [18] A. Lo, P. Haslinger, E. Mizrachi, L. Anderegg, H. Mller, M. Hohensee, M. Goryachev, M.E. Tobar, "Testing the isotropy of space using rotating quartz oscillators," *Phys. Rev. X*, in press, 2016; arXiv:1412.2142 [gr-qc].
- [19] D. S. Stevens and H. F. Tiersten, "An analysis of doubly rotated quartz resonators utilizing essentially thickness modes with transverse variation," *J. Acoust. Soc. Am.* 79 (6), pp. 1811-1826, June 1986.
- [20] L. Landau and G. Rumer, *Phys. Z. Sowjetunion* 11, 18, 1937.
- [21] A. Akheiser, *J. Phys. USSR*, 1, 277, 1939.
- [22] M. F. Lewis and E. Patterson, "Microwave phonon-attenuation measurements in quartz" *Physical Review* 159, 3, pp. 703-711, 1967.
- [23] C. Seoanez, F. Guinea, A. H. Castro Neto, "Dissipation due to two-level systems in nanomechanical devices," *Europhysics Letters* 78, 60002, 2007.
- [24] S. Galliou, J. Imbaud, M. Goryachev, R. Bourquin, Philippe Abbé, "Losses in high quality quartz crystal resonators at cryogenic temperatures," *Appl. Phys. Lett.* 98, 091911, 2011.
- [25] M. Goryachev, S. Galliou, Ph. Abbé, P.-Y. Bourgeois, S. Grop, B. Dubois, "Quartz Resonator Instabilities Under Cryogenic Conditions," *IEEE Trans. on UFFC*, vol. 59, No. 1, pp. 21-29, 2012.
- [26] M. Goryachev, E. N. Ivanov, F. Van Kann, S. Galliou, and M. E. Tobar, "Observation of the fundamental Nyquist noise limit in an ultra-high Q-factor cryogenic bulk acoustic wave cavity" *Applied Physics Letters* 105, 153505, 2014.

Towards an Engineering Model of Optical Space Cs Clock

R.Schmeissner, A.Douahi,
I.Barberau, P.Dufreche, N.Mestre
M.Baldy
Department of Atomic Clocks
Thales Electron Devices
Vélizy, France

N. von Bandel, O.Parillaud,
M.Garcia, M.Krakovski
III-V Lab
Palaiseau, France

K.Kudielka, F.Loiseau, A.Romer,
C.Roth, W.W.Cooppolse
RUAG AG
Zurich, Switzerland

Abstract— Thales Electron Devices and RUAG currently develop the engineering model of the Optical Space Cs Clock (OSCC) in the framework of an ESA/CNES project. Recent progress of the project is reported. Emphasis is put on the performance tests using new laser sources delivered by III-V Lab. The implementation of an isolator-free optics subsystem and the space evaluation of the laser and photodiode are discussed.

Keywords *Optically pumped Cs clock, DFB laser diodes, space evaluation*

I. INTRODUCTION

The optical pumping of the Cs hyperfine state was identified many years ago as a suitable technology candidate for an atomic clock to operate in GNSS, and in particular in Galileo. Related industrial activities currently develop this technology with focus on ground applications [1, 2]. Based on their heritage in the domains of Cs clock development and space electronics, Thales Electron Devices (TED) and RUAG currently develop the engineering model (EM) of the Optical Space Cs Clock (OSCC). The current project phase started in 2015 and will end in 2017.

II. FORMER DEVELOPMENTS AND DESIGN TARGET

In end of the previous development phase in 2013, a short-term frequency stability of $3E-12\tau^{-1/2}$ was demonstrated. The target of the present phase is $1E-12\tau^{-1/2}$. Further new design constraints are: 12 liter volume, 10kg mass, 30W power consumption and 12 years lifetime in medium earth orbit.

III. PRELIMINARY DESIGN

The preliminary design of the engineering model has been completed in spring 2016.

A. Functional Architecture

The functional architecture was consolidated in former development phases. As shown in Fig. 1, the clock is composed by the Laser and Optics (L&O) sub-system (s/s), the Atomic Resonator (AR) s/s and the Electronic Package (EP) s/s.

The preliminary design of the housing of the engineering model is shown in Fig. 2. It demonstrates the theoretical feasibility of a highly integrated clock. Small size AR (target

The Cs clock development is supported by the European Space Agency under European GNSS Evolution Program (activity ID-98) and CNES under contract n° 150920. The DFB laser diode development project LAMA is supported by Euripides/CTI grant No. 14750.1 PFNM-NM

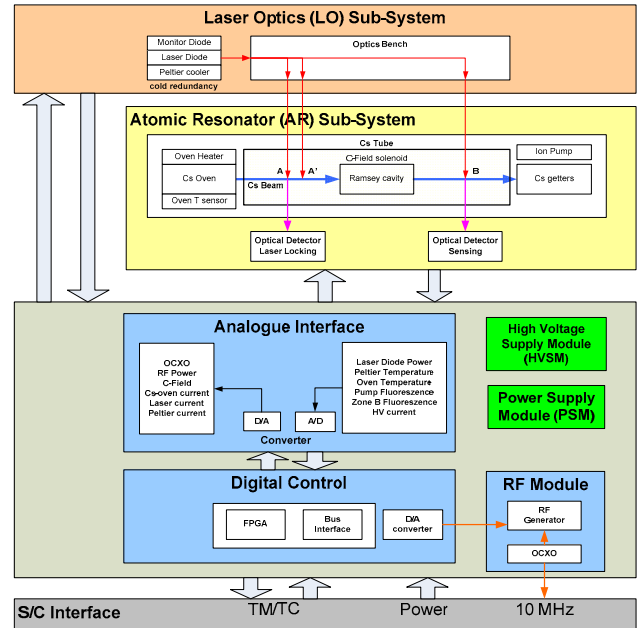


Fig. 1. Functional Architecture of the optically pumped Cs clock

5kg, 6 liters) and L&O s/s (target 500g, 1liter) were re-designed to fit with weight and volume constraints. The concept of the EP was modified using multiplexing technologies to reduce the number of components. Oversampling approaches are implemented to reach the necessary signal conversion resolutions while maintaining low power consumption through low bit-number AD/DA converters. The over-all housing is optimized in order to withstand the vibrational constraints at satellite launch while still providing the necessary thermal conductivity.

IV. TEST OF A NEW DFB LASER DIODE SOURCE

During the former development phase of the industrial, optically pumped Cs clock, the laser diode has been evaluated as the most critical technology. The reach of optimal linewidths below 1 MHz [6] was historically linked to the use of external cavity diode lasers. Although this technology is well known, it appears to add a significant amount of complexity to a commercial clock. Today, even two European suppliers provide T03 packaged DFB sources with a specified

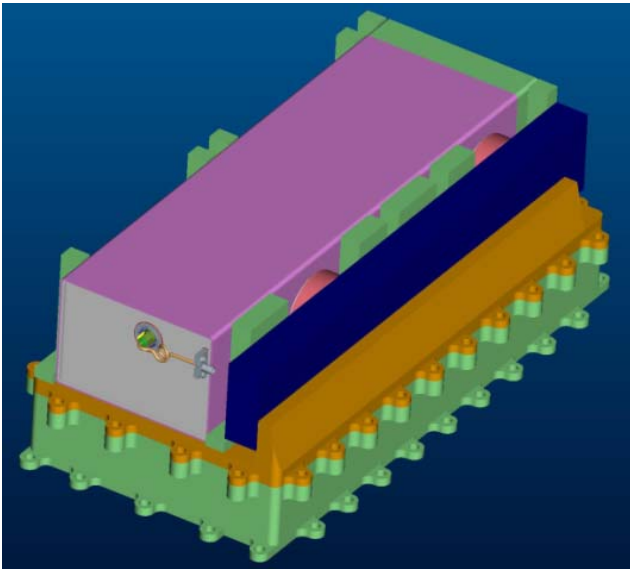


Fig. 2. Preliminary design of the housing of the engineering model. The Atomic Resonator is on the top, the Laser and Optics s/s on the right, the Electronics Package is integrated in the housing below.

B. Performance comparison to former developments

The following table II summarizes former developments of optically pumped Cs clocks in single optical frequency configuration. The value Q is the quality factor of the atomic resonator and $1/Q \cdot \text{SNR}$ is proportional to the theoretical achievable clock stability assuming $\sigma(t) \sim [Q \cdot \text{SNR}]^{-1} t^{-1/2}$.

TABLE II. COMPARISON OF SIMILAR FORMER DEVELOPMENTS

Clock (year)	Oven temp °C	Transition	Laser	SNR (typ)	$1/Q \cdot \text{SNR}$
Tekelec (2000)	110	D2 3-3' σ	DBR	> 4500	< 1E-11
Cs4 (2000)	90	D2 3-3' σ	DBR	11800	6E-12
PHACS	110	D1 3-4' π	ECDL	9200	2.5E-11
ECO	95	D2 4-4' dp	DFB	13500	6.1E-12
OSCC (2013)	95	D2 4-4' dp	DFB	17000	4.8E-12

dp...depolarized,

Indeed, the Cs D1 transition has not been studied so far using a readily applicable DFB laser. In addition, the quality factor of the PHACS atomic resonator did not permit to reach the OSCC target stabilities.

C. Test of a new DFB laser diode

For Cs clock application and in the frame of the European Euripides LAMA project, III-V Lab has recently developed an active region Aluminum-free DFB laser diode emitting at Cs D1 line 894nm. The implementation is based on previous results at Cs D2 line 852nm [4]. The laser is a Separate Confinement Heterostructure (SCH) made of a single compressive-strain 8 nm thick GaInAsP quantum-well embedded in a GaInP 1 μm wide cavity, surrounded by AlGaInP cladding layers, see Fig. 3. Such structure has low transparency current density $J_0=93\text{A}/\text{cm}^2$ and low internal losses $\alpha_i=2\text{cm}^{-1}$. The cavity single transverse mode behavior is enabled by etching a few μm wide ($\sim 3.5\mu\text{m}$) ridge waveguide in the layers. On the other side, the single longitudinal mode operation is ensured by definition: Ebeam lithography and etching of a second-order Bragg grating above the active zone, followed by an epitaxial re-growth to bury the diffraction pattern up to the top contact layer. When the two laser facets are coated with, respectively, antireflective and high reflectivity dielectric mirrors (3%-95%), the laser shows

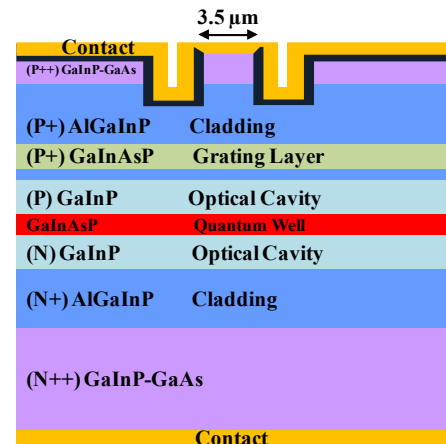


Fig. 3. III-V Lab laser structure. The active region is Al free.

linewidth below 2 MHz as a standard product. They can be readily implemented in a clock. Nevertheless, a clock performance comparison using these sources was so far not available and will be presented here.

A. Suitable atomic transitions

The theoretically achievable clock performance is proportional to the product of the signal to noise ratio of the detected Rabi-Ramsey Signal Fringe. The following table I recalls the optical pumping/read-out transitions which are theoretically the most suitable for clock operation and highest SNR [3]. Therein, the value Δn is the theoretically achievable Cs atom hyperfine level population difference which can be achieved by optical pumping. All the mentioned transitions are subject to the Hanle effect [5]. This coherent population trapping during pumping is circumvented by the known principle of spatial depolarization of the laser beam. In the ideal case, the highest product of population difference Δn and photons per atom will provide the highest SNR. In conclusion, the D1 4-3' and the D2 3-3' transitions are theoretically the most suitable for clock operation. In the previous phase of OSCC, the D2 4-4' transition has been used according to the exclusive availability of a Cs D2 DFB laser source.

TABLE I. RECALL OF SUITABLE CS TRANSITIONS

Line	Transition	Δn in %	Photons/atom
D1	4-3' σ	16.5	4
D2	3-3' σ	12.2	4
D2	4-4' σ	15.5	2,4

single mode behavior at Cs D1 line. The Side Mode Suppression Ratio (SMSR) is more than 45dB at the operation temperature of $\sim 65^\circ\text{C}$ (at Cs D1). For a 2 mm laser bar, the threshold current at such temperature is in the range of 90 mA, with 0.5W/A of external efficiency. An output power of 40mW at 185 mA bias is obtained in such conditions. The laser linewidth was measured by two different methods: with the self-heterodyne setup (2 km delay line and 4 ms integration time) and by derivation from the frequency noise characteristic from 250Hz to the high frequencies [4]. Both methods show that the linewidth lies in the range of 0.7 to 1MHz. Ongoing developments aim at DFB Cs D1 line at ambient chip temperature. They concern an improvement of the threshold current and the external laser diode efficiency. All chips are integrated into a TO3 can, monitored and controlled in temperature. Table III compares the III-V Lab laser diode to the eagleyard [8]. Although the thermal/electro-optical tuning coefficients are nearly identical, the III-V provides a significantly smaller linewidth.

TABLE III. LASER DIODE COMPARISON – TYPICAL PERFORMANCES

DFB Laser	GHz/K	GHz/mA	$\Delta\nu$ MHz	SMSR dB
eagleyard	24	1.2	2	> 30
III-V Lab	25	1.1	0.7 to 0.9	> 45

D. Signal To Noise Ratio Measurements

Table IV shows the measured SNR performance of the OSCC Cs tube using three different laser sources, an eagleyard DFB at 852nm and two III-V Lab DFB emitting at 852nm and 894nm respectively. They are the key results of the present paper. All measurements were carried out with a HP35670A FFT Spectrum Analyzer. All three laser diodes were packaged in TO3. They were implemented on a dedicated optics test bench seeding the Cs Atomic Resonator with identical geometric properties independent to the laser used. The beam intensities were optimized for each laser. This approach permits a quantitative comparison of the maximum achievable SNR. An impact of the optical linewidths on the SNR is expected according to [6], but its level is driven by the part of un-pumped Cs atoms in the signal detection [7].

TABLE IV. CS-CLOCK/LASER DIODE COMPARISON – TYPICAL PERFORMANCES

SNR in $1/\text{Hz}^{1/2}$ on OSCC tube at 96°C Cs oven measurement uncertainty $500\text{Hz}^{-1/2}$			
DFB Laser	D1 4-3'	D2 4-4'	D2 3-3'
eagleyard	n/a	15000	15500
III-V Lab	20000	15000	16500

The ratio un-pumped atoms for the experiments considered here is lower than $5\text{E-}3$. At this level, a small impact of the laser diode linewidth on the detected noise level is expected. This is confirmed by the measurement results shown in table IV. In line with the theoretical expectation, the highest SNR is obtained with the D1 4-3' transition.

V. SMALL SIZE LOW WEIGHT OPTICS BENCH

A key design challenge on the design of the OSCC clock are the mass and volume constraints. In order to minimize the respective budgets of the laser and optics s/s (500g, 1liter), a simplified optics bench has been designed. Despite a cold laser diode redundancy, it contains only the minimum number of optical elements and no optical isolator.

A. Prototype implementation

In order to verify the functionality of this optics design, a partially representative prototype was implemented together with a dedicated Cs tube. The latter is nearly identical to the OSCC one. It uses the concept of tilted optical windows in order to reduce the amount of back-reflected light into the laser diode. Both tubes show the same SNR performances on the optics test bench.

B. Performance validation

With this new atomic resonator and optics bench, a typical SNR of 24500 was measured using the III-V lab DFB laser diode on the Cs D1 4-3' transition. The Cs oven temperature was 100°C and all optical beam properties were optimized. This level of SNR corresponds to a theoretical clock stability of better than $2\text{E-}12\tau^{-1/2}$. The maximum Cs oven temperature for OSCC is 100°C in order to limit the Cs consumption over 12 years target lifetime.

The Fig. 4 shows the clock stability when measured against an OSCILLOQUARTZ BVA 8607BM quartz reference oscillator and using the electronics hardware from previous OSCC breadboard development. A short term stability of better than $2.8\text{E-}12\tau^{-1/2}$ is measured at 20s integration time. The slight stability degradation for longer integration times might be due to thermal drift of the reference oscillator. The discrepancy to the expected $2\text{E-}12\tau^{-1/2}$ is attributed to non optimal parameters of the clock electronics. In summary, the stability shown in Fig. 3 demonstrates the applicability of the III-V Lab 894nm DFB laser diodes for optical clock application. Their functionality is validated in a setup without an optical isolator.

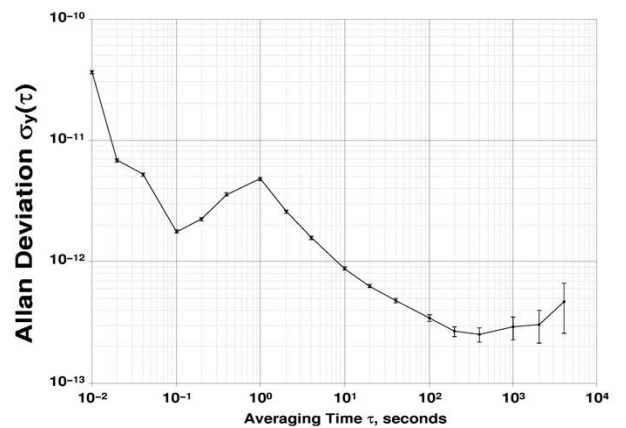


Fig. 4. Validation of the simplified optics bench using Cs D1 4-3' transition. The clock loop resonance is at 1Hz. The Quartz reference oscillator limits the measurement precision above 200s. Data obtained with a Timing Solutions TSC5110A time interval counter.

TABLE V. CS-CLOCK NOISE BUDGET AND TYPICAL CONTRIBUTIONS

Typical noise levels in $\mu\text{Vrms}/\text{Hz}^{1/2}$ at 40Hz (pre-amplified signal)			
Clock Signal at Full Width Half Peak Valley Ramsey Fringe	Photodiode dark noise and pre-amplifier	Stray Light	Atomic Signal Noise
54	21	30	41

Table V shows the over all noise budget of the measurement. The detected noise is limited by the noise in the atomic fluorescence signal. This is in line with the consolidated design of the photodetector signal amplification and the optimized properties of the interrogating laser beam. Nevertheless, improvements in the atomic resonator optics design can still reduce the amount stray light and improve clock performance.

VI. SPACE EVALUATION OF OPTOELECTRONIC COMPONENTS

Being conceived for a lifetime of 12 years in medium earth orbit, all components of the clock will have to be space-qualified at a later development phase. The current project phase aims to reduce the associated risk. The latter is essentially driven by the space-qualification of the optoelectronic components: the laser diode and the light detecting photodiode. In a pre-evaluation phase in 2015, the most critical properties and degradation modes of the two components were identified based on supplier heritage and expertise of THALES, CNES and ESA. To reduce the remaining qualification risks, a respective space-evaluation program was defined and will be implemented starting 2016.

A. Laser Diode

The design baseline is a TO3 packaged DFB laser diode as an off-the-shelf product with modifications. Lifetime and component construction have been identified as most critical issues. They will be evaluated in detail in the current project phase. In contrast and based on return on experience from former laser diode qualifications, radiation induced damage (100krad over 12years) was evaluated to be a minor risk. The same holds for the hermeticity of the TO3 packaging which benefits from longstanding industrial heritage.

B. Photodiode

The OSCC development was so far based on a Hamamatsu S1337 large area, low noise photodetector. Former CNES evaluations demonstrated that this off-the-shelf detector cannot be space qualified mostly due to hermeticity issues of the packaging. In early 2016 TED conceived with First Sensor a customized detector for a space evaluation. It is an off-the-shelf product with modifications and shall even slightly increase the detected clock signal level (clock stability) due to a higher light collection efficiency. The foreseen detector chip is similar to a quadrant detector which is currently qualified for the use in a space sun-sensor application. Indeed, the photodetector dark noise could be increased by the total

ionizing dose above the acceptable margins. This aspect will be verified in the space-evaluation program 2016-2017. A dedicated test campaign will be implemented concerning the photodiode substrate types (n-type or p-type). The impact of ionizing radiation is known to depend on this parameter. The customized TO packaging will benefit from supplier heritage on a similar packaging for EUCLID mission.

VII. CONCLUSIONS

The preliminary design of the OSCC engineering model is reported. In addition to mechanical and electronic design improvements, a new laser diode source and a new optics bench were developed and tested successfully. Using a III-V Lab 894nm DFB laser diode on the Cs D1 4-3' transition, a clock stability of better than $3\text{E-}12\tau^{-1/2}$ was demonstrated. The implemented optics s/s is of minimized complexity and does not contain an optical isolator. As a first step towards space qualification, possible degradation modes of the laser diode and the photodiodes were evaluated. To reduce the remaining qualification risks, a dedicated space evaluation program was developed and will be implemented starting 2016.

Acknowledgment

The authors acknowledge European Space Agency (ESA), the Centre National d'Etudes Spatiales (CNES), EURIPIDES and Thales Electron Devices for financial support of the project. The authors are grateful for helpful discussion and technical support to V.Hermann, G.Corrador and G.Gauthier at Thales Electron Devices, S.Guérandel at SYRTE, Paris, and G.Baily and L.Morvan at Thales Research and Technology, Palaiseau, G.Guibaud at Thales Communication and Security, Toulouse, J.Delporte, F-X Esnault, O.Gilard and J.Mekki at CNES, Toulouse, C.Bringer and P.Waller at ESA-ESTEC, Noordwijk. The authors acknowledge support from the suppliers First Sensor and eagleyard Photonics.

References

- [1] Progress in the Development of Commercial Optically Pumped Cs Atomic Clock, Yuanhong Cao, et al., International Frequency Control Symposium IFCS 2014
- [2] Development of a transportable optically pumped atomic Cs beam clock, P.Berthoud et al. EFTF 2015
- [3] Comparison of pumping a cesium beam tube with D1 and D2 lines, N. Dimarcq, V. Giordano, G. Theobald, and P. Cérez, J.Appl Phys 69 (3), 1991
- [4] N. Von Bandel et al., SPIE Photonics West 2016, Quantum Sensing and Nano Electronics and Photonics XIII, paper 9755-90
- [5] G.Théobald, N.Dimarcq, V.Giordano, P.Cérez, Ground state zeeman coherence effects in an optically pumped cesium beam, Opt.Comm. 71 (5) 1989
- [6] N.Dimarcq, V.Giordano, P.Cérez, G.Théobald, Analysis of the Noise sources in an optically Pumped Cesium Beam resonator, IEEE Trans. Instr. and Meas., 42 (2) 1993
- [7] G.Lucas-Leclin, P.Cérez, N.Dimarcq, Laser-induced noise contribution due to imperfect atomic state preparation in an optically pumped caesium beam resonator. J.Phys.B, At. Mol. Opt. Phys 32 (1999)
- [8] Part No. EYP-DFB-0852-00150-1500-TOC03-0005

The optical feedback spatial phase driving perturbations of DFB laser diodes in an optical clock

R.Schmeissner¹, N. von Bandel², A.Douahi¹, O.Parillaud², M.Garcia², M.Krakovski², M.Baldy¹

¹Department of Atomic Clocks, Thales Electron Devices, Vélizy-Villacoublay, France

²III-V Lab, Palaiseau, France

Abstract— Frequency perturbations of a laser seeding an optically pumped Cs clock are likely to reduce the achievable clock stability. They can be induced by residual back reflections in the optical system. It is shown here that the sensitivity of DFB laser diodes to low-level back-reflections significantly depends on the spatial phase of the reflected beam, i.e. the surface roughness of the reflecting element.

Keywords: *Optically pumped Cs clock, DFB laser diodes, optical feedback*

I. INTRODUCTION

The optical pumping of the Cs hyperfine level is currently developed by Thales Electron Devices as a possible clock technology for Galileo 2nd generation [1]. Related industrial activities also consider this technology for ground applications [2, 3]. The concept of the physics package of such a clock is re-called in Fig.1. A laser diode is locked on the Cs D1 or D2 electronic transition. Subsequently it is used to pump a hyperfine level of the Cs ground state in a thermal beam by iterative absorption and spontaneous recombination. After resonant interaction with a radio frequency in a Ramsey Cavity and spin transfer to the other hyperfine level, the state of the atoms is detected via fluorescence measurement. To that aim, the same laser optical frequency is used as in the hyperfine pumping. Finally, fluorescence is observed as a function of the injected radio frequency, the so-called Rabi-Ramsey fringes. Their local structure permits to lock a quartz oscillator on the Cs hyperfine transition and as such to create a clock [4]. In the current Optical Space Cs Clock (OSCC) development, the target clock stability is 1 to $3E-12\tau^{-1/2}$ [1].

II. THE POSSIBLE IMPACT OF BACK-REFLECTIONS

The design of the clock signal read out is fluorescence detection in saturated regime. Due to the presence of stray light, optimized clock performance is typically measured for optical intensities in the detection zone which are close to saturation. As such, a variation of the optical signal spectral power density of the laser at the selected D1 or D2 transition can still have an impact on the detected signal level and the clock stability. For that reason, an important Side Mode Suppression Ratio (SMSR) of larger than 30 dB is required to

The DFB laser diode development and back-reflection analysis is supported by Euripides grant n° 12-1307 and internal funding of Thales Electron Devices. Synergies are obtained with ongoing Cs clock development being supported by the European Space Agency under European GNSS Evolution Programme (activity ID-98) and CNES under contract n° 150920.

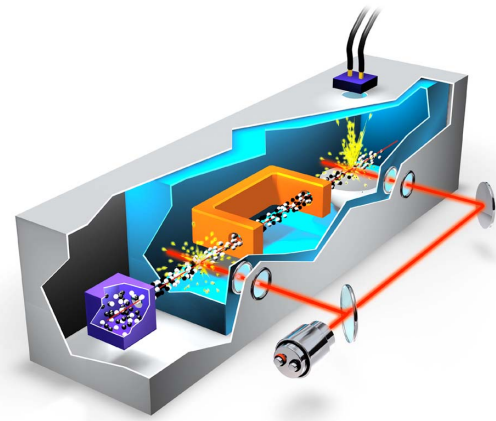


Fig. 1. Visualization of the “physics package” of the optically pumped Cs clock. A thermal beam of Cs atoms inside a vacuum tube interacts with laser radiation and a RF signal. A fluorescence signal is measured.

the used DFB laser diode. Nevertheless, although the laser diode SMSR may be compliant with the requirement, the presence of residual back reflections into the DFB laser may lead to additional side modes and perturb the clock operation. The impact of low level feedback into DFB laser diodes has been studied intensively since more than three decades [5]. Back-reflection into DFB lasers induces notably mode competition [6] and the self-mixing phenomenon [7]. Both perturb either the free running optical frequency or the carrier band power if the laser frequency is locked. Here, the so far not considered spatial phase profile of back-reflections is identified as a key driver for the perturbation strength.

III. III-V LAB LASER DIODE DEVELOPMENT

In order to secure procurement of the OSCC key technologies, Thales Electron Devices is investigating DFB laser diodes currently developed by III-V Lab [1]. In early 2015, a new generation of laser diode chips was manufactured by III-V Lab at 894nm and implemented on C-mount, see Fig. 2. The TO3 packaged lasers were delivered after the completion of the here presented experiments. C-mount implementation typically allows early performance assessment and semiconductor design risk reduction. The laser is based on a Separate Confinement Hetero-structure and does not contain Aluminium in the active zone. The gain is provided by a

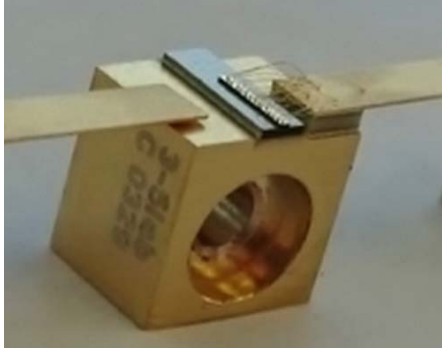


Fig. 2. III-V Lab DFB laser diode (in the middle on the top) on a C-mount

compressively strained GaInAsP quantum well. The laser structure provides low internal losses, high internal quantum efficiency and low transparency current density. A ridge structure provides lateral confinement in the waveguide. The laser emission linewidth is below 1MHz at Cs D1 line [8].

IV. BACK REFLECTION ANALYSIS

In order to mitigate the risk associated with back reflections, an optical isolator of up to 60dB reflection attenuation is typically integrated into the clock optics setup. Nevertheless, based on return on experience from former OSCC development phases, it was so far supposed that residual back reflections might still be present in the optics part of the clock.

A. Qualitative assessment

The setup shown in Fig. 3 was implemented in order to verify the presence of back reflections on an optics bench representative for the OSCC implementation. The fluorescence signal of the first light-atom interaction zone of the clock Cs vacuum tube is considered. In clock operation, the latter is used to lock the laser diode on either Cs D1 or D2 transition. In the setup Fig. 3 the laser diode optical frequency is continuously swept in the vicinity of the Cs D1 4-3'

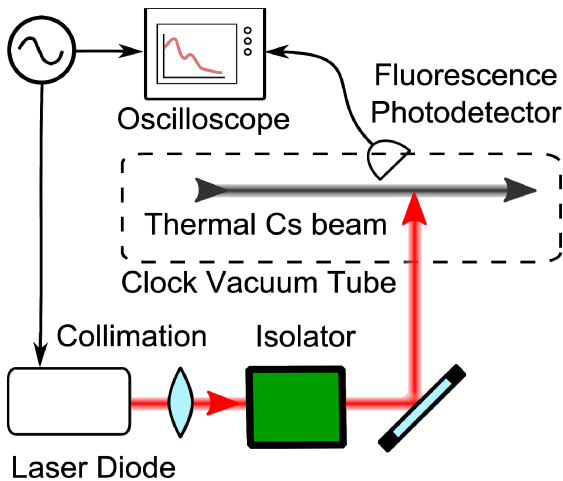


Fig. 3. Experimental scheme to qualitatively evaluate the perturbation of a DFB laser diode by feedback of an optical isolator. The clock vacuum tube is part of the OSCC development.



Fig. 4 Fluorescence of the Cs D1 4-3' transition (yellow curve) observed on the setup Fig.3. Left: without optical isolator. Right: with optical isolator

transition. Figure 4 shows the observed fluorescence as a function of the presence (fig.4 right) or not (fig.4 left) of the optical isolator (ISOWAVE, -60dB). In the system containing the optical isolator, numerous fluorescence side-peaks are observed. This behavior has been called “shadow resonances“ in former developments. These resonances are not present when the optical isolator is removed. Referring to former studies of back-reflection induced semiconductor laser dynamics [5, 6, 7] these resonances can be attributed to the presence of additional frequency modes in the laser emission. The residual reflection generating these effects is supposed to be the AR coated entrance aperture of the optical isolator. Indeed, even high quality AR coatings are still subject to ppm reflection. It is in addition observed that the presence and dynamics of the “shadow resonances” depends strongly on the position dynamics of the reflecting object, i.e. the optical isolator. In practice, even tiniest variations of its position induce strong variations on the structure of the “shadow resonances”. These resonances correspond to additional frequency modes in the laser and mode competition dynamics is induced. Under the constant gain of the DFB active zone, this competition is likely to induce variation of the optical power of the carrier frequency. It is this variation that is suitable to perturb the stability of the optically pumped Cs clock.

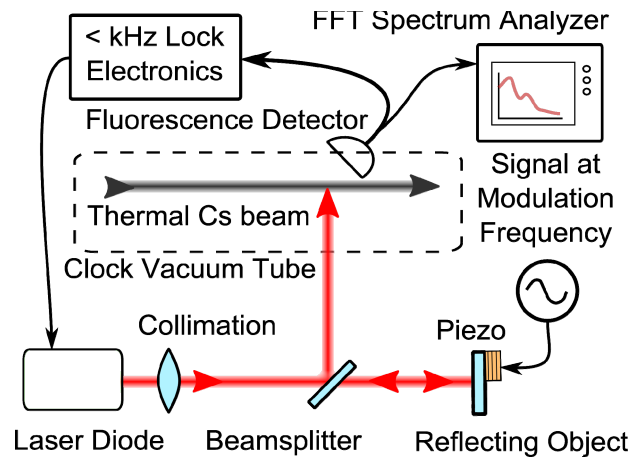


Fig. 5 Experimental scheme to quantitatively evaluate the perturbation of a DFB laser diode by feedback of a reflecting mirror of different surface roughnesses. The out of lock bandwidth error error signal is analyzed.

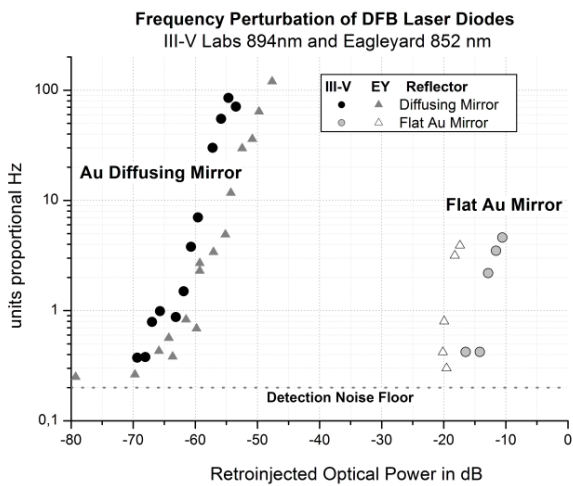


Fig. 6 DFB laser diode frequency perturbation depending on retroinjected optical power, the surface roughness of the reflecting element and the supplier. The uncertainty of the retroinjected power estimation is ± 3 dB.

B. Quantitative assessment

In order to evaluate the presence and impact of back reflections on the frequency locked laser diode, the measurement shown in Fig. 5 is considered. The laser diode is frequency locked in the same way as for clock operation: A current dither at 50kHz is applied to generate the error signal for frequency locking based on fluorescence detection and synchronous demodulation. The applied PI gain is of a bandwidth below 1kHz. Based on the return on experience from the qualitative analysis above, the feedback is generated by a continuously position modulated, piezo-mounted mirror. The amount of feedback is tuned by absorptive filters and calibrated on a separate measurement. The out-of-feedback bandwidth error signal of the laser diode frequency lock loop, at the piezo modulation frequency of 5kHz, is used as a measurement of the frequency perturbation of the laser diode. DFB laser diodes from eagleyard are considered for comparison [9]. The emission wavelengths of the compared laser diodes are different: eagleyard at Cs D2 852nm and III-V Lab at Cs D1 894nm. Nevertheless, the approaches developed individually by each supplier for the laser structure and for the laser coating are valid for both wavelengths 852nm and 894nm. The results discussed below are consequently suitable for quantitative comparison. For the measurements presented here, the eagleyard DFB lasers are TO3 packaged whereas the III-V lab chip is implemented on a C-mount.

C. Results of the quantitative analysis

The results of the quantitative analysis are shown in Fig. 6. At first, the laser diodes are exposed to feedback of -10 to -20dB originated from a flat mirror. A perturbation signal is measured and proportionality between the perturbation strength (error signal deviation proportional to frequency deviation) and the retro-injected power is observed. Second, a diffusing mirror of rough surface is used in the same experiment. Compared to the perturbation strength induced by the reflections from the flat mirror, the same level of perturbation is observed at approximately 40 dB less back-

reflected optical power. In this configuration the impact of optical feedback down to -70dB is measurable. Within the measurement uncertainty, the perturbation strength is the same for the eagleyard and the III-V laser diode. The used of the III-V lab laser does consequently not bring any disadvantage for the concern of the possible presence of residual back reflections on the Cs clock optics sub system.

V. CONCLUSIONS

In conclusion, even lowest levels of back-reflections significantly perturb laser diode operation and likely the performance of the optically pumped Cs clock. The here identified necessary conditions are that the reflection transverse phase-profile is inhomogeneous and that the reflection geometry changes slightly (due to e.g. thermal drifts in the setup). The structure of the transverse phase profile of the reflection was demonstrated to drive the laser perturbation significantly. The results presented here are helpful for the design of the optics sub-system of the OSCC: they provide a qualitative criterion on the presence of residual reflections and a design baseline for any directly reflecting element.

Complementary measurements will have to quantitatively assess the impact of back reflections on the clock stability itself.

Acknowledgment

The authors acknowledge EURIPIDES and Thales Electron Devices for financial support. The European Space Agency (ESA) and the Centre National d'Etudes Spatiales (CNES) are acknowledged for financial support of the related OSCC project. The authors are grateful for helpful discussion to F.Gruet, R.Matthey and G.Mileti of Laboratoire Temps-Fréquence (LTF) Neuchatel, V.Hermann at Thales Electron Devices, S.Guérandel at SYRTE, Paris, G.Baily and L.Morvan at Thales Research and Technology, Palaiseau, J.Delporte and F-X Esnault at CNES, Toulouse, P.Waller at ESA-ESTEC, Noordwijk and eagleyard Photonics, Berlin.

References

- [1] Towards an Engineering Model of Optical Space Cs Clock, R.Schmeissner et al., EFTF 2016, Contribution 1218
- [2] Progress in the Development of Commercial Optically Pumped Cs Atomic Clock, Yuanhong Cao, et al., International Frequency Control Symposium IFCS 2014
- [3] Development of a transportable optically pumped atomic Cs beam clock, P.Berthoud et al. EFTF 2015
- [4] C.Audoin and J.Vanier, The Quantum Physics of Atomic Standards, Bristol U.K., Adam Hilger 1989
- [5] Regimes of Feedback Effects in 1.5 μ m DFB Lasers, R.W.Tkach et al., J. Lightwave Technology 4 (11) 1986
- [6] Mode Selection and Stability of a Semiconductor Laser with Weak Optical Feedback, J.O.Binder, G.D.Cormack, IEEE J.Quantum Electron 25 (11) 1989
- [7] Laser diode self-mixing technique for sensing applications, G.Giuliani et al., J. Optics A, 4, 2002
- [8] N. Von Bandel et al., DFB-ridge laser diodes at 894 nm for Cesium atomic clocks, Proc. SPIE 9755, Quantum Sensing and Nano Electronics and Photonics XIII, paper 9755-90 (February 18, 2016)
- [9] Part No. EYP-DFB-0852-00150-1500-TOC03-0005

Iodine Absorption Cells Quality Measurements

Jan Hrabina, Martin Sarbort, Miroslava Hola,
Ondrej Cip, Josef Lazar
Institute of Scientific Instruments, CAS
Brno, Czech Republic
hrabina@isibrno.cz

Ouali Acef
LNE-SYRTE, Observatoire de Paris
Paris, France

Massimo Zucco
Istituto Nazionale Di Ricerca Metrologica
Torino, Italy

Frederic Du-Burck
Laboratoire de Physique des Lasers
Universite Paris 13, Sorbonne Paris Cite
Paris, France

Abstract— This work is oriented to comparison of methods for iodine absorption cells quality evaluation. Optical frequency references based on molecular iodine represent one of the most used references for stabilization of laser standards working at visible spectral range. Unfortunately iodine is a media with very high sensitivity to contamination so the chemical purity of iodine cells must be precisely controlled. Traditional methods for iodine absorption cells quality checking have several difficulties and disadvantages, these problems complicate their common using in labs. Due to this reason we propose an alternative method of spectral linewidths measurement, which overcomes these difficulties of traditionally used approaches and which serves as a tool for iodine cells quality evaluation. In this work we present the results of comparison of two laser induced fluorescence setups (with and without the compensation for the laser source spectral mode-hops) with proposed method of selected hyperfine transition linewidth measurements and we discuss advantages and limitations of these methods for practical using.

Keywords—absorption cells; molecular iodine; laser spectroscopy; spectral linewidth; frequency stability

I. INTRODUCTION

The molecular iodine represents one of the most used reference absorption media for the laser frequency stabilization. It offers a rich spectra of very strong and narrow transitions covering visible and near infrared spectral range. Thanks to its spectral properties, the molecular iodine is also an absorption medium recommended by the Comité International des Poids et Mesures (CIPM) for the realization of primary standards of length at several wavelengths [1]. The frequency doubled Nd:YAG laser ($\lambda=532$ nm) frequency stabilized by methods of saturation spectroscopy in molecular iodine represents the most stable conventional laser standard with relative frequency stabilities at 10^{-14} or better level [2].

The main drawbacks of molecular iodine used as an absorption media are its extreme sensitivity for contamination by foreign molecules and impurities and its very high corrosivity with many of substances. Presence of impurities in iodine absorption cells causes frequency shifting of absorption

spectra, spreading of absorption lines and finally reduction of achievable frequency stability of realized laser standard [3]. Due to this reason a special care must be taken on appropriate iodine filling during the cells manufacturing process and quality of finished cells must be precisely controlled. This work describes the most often used methods for iodine cells purity evaluation and compare their properties with proposed method of spectral transitions linewidth measurement.

II. IODINE CELLS TECHNOLOGY AND PROGRESS

The iodine cells intended for the most demanding scientific applications (ultra-stable laser standards) are traditionally made of a fused silica glass, a material which is inert to the iodine media and which allows to achieve a high iodine chemical purity. The critical points of iodine cell manufacturing are perfect cleaning and proper evacuation of the cell body, followed by several steps of iodine chemical purification and finally filling of iodine into the cell. The absorption cells made at ISI usually use welding approach of optical windows to the cell body, so the iodine is in contact just with the pure fused silica. The optical windows can be equipped with antireflection coatings at both sides to suppress unwanted backreflections and losses. Another challenges of optical contacting of rectangular optical windows were passed in project of custom design internal multi-pass iodine cell of rectangular shape intended for laser standard at orbital station operation, where compact design and robustness play a crucial role [2]. Less demanding applications (stable laser sources for industrial laser interferometry, lasers stabilized by linear absorption spectroscopy) can be based on cells of alternative material, for example a borosilicate glass. With great care taken during the manufacturing process, the borosilicate glass cells can also achieve a very high purity of absorption media which is suitable for these applications. These cells carry an advantage of cost reduction and simplification of manufacturing process (needs lower welding temperatures, cheaper material). Next way to simplify these references is to

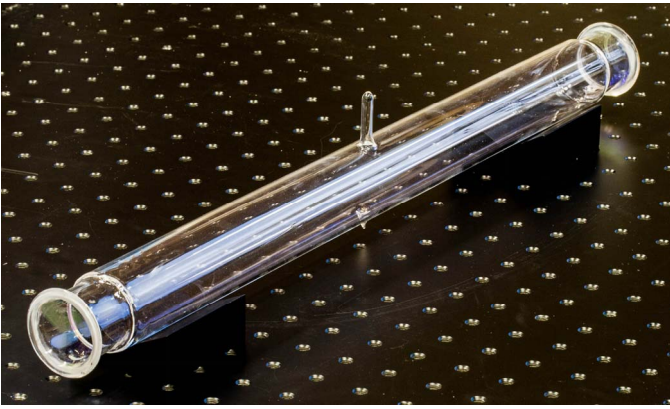


Fig. 1. Photo of standard design ISI iodine absorption cell.

fill the cells with absorption media under exact saturation pressure [4]. Current research also covers investigation of absorption cells based on filled hollow-core photonics crystal fibers (HC-PCF) which should lead into all-fiber laser standards [5,6]. Although several groups have realized cells based on this approach (filled with different gases), in case of molecular iodine a non-contaminating technology is still not satisfactorily solved (speak nothing about measurement of these fiber-cells iodine purity) [7].

III. METHODS FOR IODINE CELLS QUALITY EVALUATION

A. Laser induced fluorescence (LIF) method

One of the traditionally used techniques for iodine cells quality evaluation is method of laser induced fluorescence (LIF). Presence of chemical impurities in absorption media causes collisions between iodine molecules and molecules of impurities which ends in non-radiative transitions of the excited iodine molecules to the basic state and in reduction of excited state lifetime. By the selection of a transition where this effect is strong enough we are able to check the iodine chemical contamination. The dependency between iodine vapor pressure and the level of relative laser induced fluorescence is expressed through the Stern-Volmer formula and coefficient [8]. Unfortunately a practical realization of the LIF method uses quite rare Ar-ion laser operated at 502 nm wavelength where this collisional-quenching effect is strong enough. Next drawbacks of this method are impossibility to measure highly-pure cells thanks to the method sensitivity and resolution limits and also problems of straight and backscattered light especially in case of cells without AR coatings on their optical windows.

B. Absolute frequency shifts measurement

The second usually used method for iodine cells purity evaluation is iodine-stabilized laser standards absolute frequencies measurement [9]. It utilizes an effect of frequency shifting of absorption spectra due to the contamination of the iodine media. Unfortunately this technique needs relatively complicated experimental setup of saturated absorption

spectroscopy method with the precise counting of the laser absolute frequency (i.e. a beat-note measurement between laser stabilized by tested iodine cell and well known optical frequency reference/standard or stabilized frequency comb). This method also has relatively low sensitivity for the iodine chemical purity (it brings difficulties especially for cells with high iodine purity) and it needs a precise measurement and control of several intricately controllable parameters [3].

C. Spectral linewidths measurement

Due to mentioned drawbacks and limits of above described methods we propose an alternative technique for iodine cell purity evaluation based on measurement of hyperfine transitions linewidths [4]. The linewidth of selected spectral line is very strongly dependent on iodine purity and this method allows to measure the cells of different mechanical dimensions and designs. The experimental setup is based on locking of the exciting laser to selected transition in reference cell and scanning of hyperfine spectra in tested cell with the help of acousto-optics modulator/shifter tuning. The measurement is performed for different saturation power intensities and iodine pressure levels to obtain zero-power broadening and zero-pressure broadening values and the recorded hyperfine profiles/spectra are post-processed by the inverse 3f algorithm to obtain the Lorentzian profiles and computing natural linewidths. This setup was originally used for investigation of iodine hyperfine spectra structures in region of 515 nm and testing of spectral properties of iodine cells made of borosilicate glass, filled to certain saturation pressure [4]. The method shows a very high sensitivity to the iodine contamination so its suitable also for high-quality cells, it can be applied on cells with different opto-mechanical designs and it has a very good reproducibility (the repeated measurements of the 8 cells set made after 1 year from the first test shows the deviations at only few kHz levels) [4]. Main disadvantage of this method is in fact, that it can be only hardly used in cases of cells with very poor quality (very bad signal-to-noise ratio of the hyperfine transition spectral profile).

D. Quality of iodine cells set

A comparison of laser induced fluorescence and spectral linewidth measurement methods was performed on a iodine cells set (8 pcs of different iodine media purity and different mechanical designs), particularly developed and manufactured at BIPM (Paris, France) and at ISI AS CR (Brno, Czech Republic) institutes. The measurement of Stern-Volmer coefficients was done at two independent experimental setups, firstly at original BIPM design (currently operated at INRIM, Torino, Italy) and at second at ISI setup which was equipped with several modifications (1. for overcoming of a tendency of the exciting laser to mode-hops and multimode regime, the setup was amended with the reference cell hold at constant iodine pressure – the signal from this reference cell shows the spectral condition of the laser; 2. the system was equipped with the laser power stabilization stage; 3. the measuring procedure

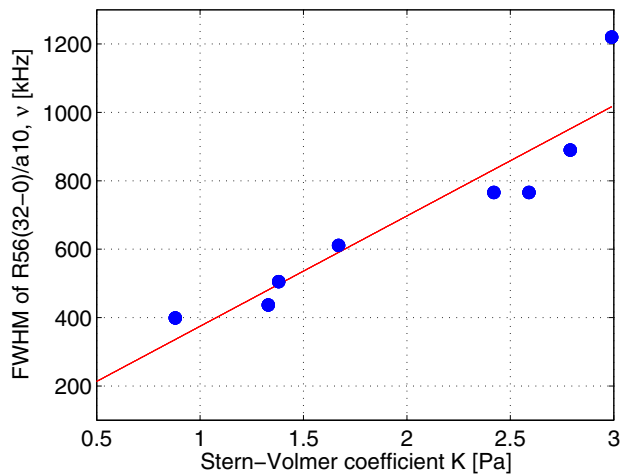


Fig. 2. Measurement of Stern-Volmer coefficients (laser induced fluorescence method) and natural linewidth measurement of tested set of iodine absorption cells.

includes measurement of the level of background and scattered light – the cell is cooled down to the liquid nitrogen temperature level, where no iodine fluorescence can be observed and the level of background light is measured in reference and also measured cells. These data are then used for compensation of the results). This two systems comparison confirmed possibility of using lower quality Ar-ion laser (laser with mode-hops) as a exciting source and moreover it shows a significant improvement (at better than half order level) in term of measurement uncertainty with using ISI compensated system.

The hyperfine transitions linewidth measurement was performed on experimental system based on frequency doubled Nd:YAG laser at 532 nm wavelength and saturated absorption spectroscopy setup (with detection by 3f technique). The cells evaluation was processed on a well known R56(32-0) line, component a_{10} hyperfine transition.

Each cell was measured several times for different iodine media pressures, different modulation depths and different saturating power intensities and zero-pressure and zero-power broadening linewidths values were computed by inverse 3f algorithm.

The dependency between LIF (Stern-Volmer coefficients measured by ISI setup) and natural linewidth measurements at selected iodine transition is shown at Fig. 2. The graph shows a very high sensitivity of the transition linewidth to the absorption media purity (the linewidth increases by 100% for Stern-Volmer coefficients from 1 Pa to 2.5 Pa). Thanks to this excellent sensitivity, the linewidth method shows its very high potential especially for measurements of clean iodine cells, where LIF and absolute frequency shifts measurement methods bump into their resolution and sensitivity limits. Not at all, the linewidth method can be used for evaluation of HC-PCF based optical frequency references, where the obtained results can inform about expectable frequency stability of the fiber based reference stabilized laser. On

opposite side, the measurements show difficulties in case of highly contaminated cells, where signal-to-noise ratio of recorded hyperfine spectral profiles decreases and proper processing and computing of the linewidth can not be easily done.

IV. CONCLUSION

We compared traditionally used methods for iodine absorption cells quality evaluation based on laser induced fluorescence and absolute frequency shifts measurements with proposed method of hyperfine linewidth scanning and drawbacks and advantages of each approach were described. It was shown that proposed method of linewidths measurements overcomes difficulties of traditional approaches and that it allows a precise measurement of iodine cells quality especially in case of very clean absorption media. This method is suitable also for absorption cells with non-standard opto-mechanical designs, where commonly used LIF and frequency shifts method bump their limits. The main drawback and limit of the linewidth method can be seen in affecting of signal-to-noise ratio and accuracy for highly contaminated cells.

ACKNOWLEDGMENT

The research was supported by Grant Agency CR, project GA15-18430S. The infrastructure for the research was funded by Ministry of Education, Youth and Sports CR, projects LO1212, CZ.1.05/2.1.00/01.0017, and by Academy of Sciences CR, project RVO:68081731.

REFERENCES

- [1] T. J. Quinn, "Practical realization of the definition of the metre, including recommended radiations of other optical frequency standards (2001)," *Metrologia*, 40(2), 2003, p.103-33.
- [2] K. Doringshoff, M. Reggentin, E. V. Kovalchuk, M. Nagel, A. Keetman, T. Schuldt et al., "Iodine based optical frequency reference with 10(-15) stability," 2012 European Frequency and Time Forum (EFTF), 2012, p. 419-421.
- [3] J. Lazar, J. Hrabina, P. Jedlicka and O. Cip, "Absolute frequency shifts of iodine cells for laser stabilization," *Metrologia*, 46(5), 2009, p. 450-456.
- [4] J. Hrabina, M. Sarbort, O. Acef, F. Du Burck, N. Chiodo, M. Hola, O. Cip, and J. Lazar, "Spectral properties of molecular iodine in absorption cells filled to specified saturation pressure," *Applied Optics* 53, 2014, p. 7435-7441.
- [5] P. T. Marty, J. Morel, and T. Feurer, "All-fiber frequency-stabilized erbium doped ring laser," *Optics Express* 18, 2010, p. 26821-26827.
- [6] J. Henningsen, J. Hald, and J. C. Petersen, "Saturated absorption in acetylene and hydrogen cyanide in hollow-core photonic bandgap fibers," *Optics Express* 13, 2005, p.10475-10482.
- [7] P. S. Light, J. D. Anstie, F. Benabid, and A. N. Luiten, "Hermetic optical-fiber iodine frequency standard," *Optics Letters* 40, 2015, p.2703-2706.
- [8] S. Fredin-Picard, "A Study of Contamination in I-127(2) Cells Using Laser-Induced Fluorescence," *Metrologia* 26, 1989, p. 235-244.
- [9] M. Zucco, L. Robertsson, and J. P. Wallerand, "Laser-induced fluorescence as a tool to verify the reproducibility of iodine-based laser standards: a study of 96 iodine cells," *Metrologia* 50, 2013, p. 402-408.

Optical-to-microwave synchronization with sub-femtosecond daily drift

Aram Kalaydzhyan^{1,*}, Michael Y. Peng², Ming Xin^{1,2}, Kemal Shafak^{1,3}, Wenting Wang¹ and Franz X. Kärtner^{1,2,3}
¹Center for Free-Electron Laser Science, Deutsches Elektronen-Synchrotron DESY, D-22607 Hamburg, Germany
²Research Laboratory of Electronics, Massachusetts Institute of Technology, Cambridge, MA 02139, USA
³Department of Physics, University of Hamburg and the Hamburg Center for Ultrafast Imaging, D-22761 Hamburg, Germany
 *Email: aram.kalaydzhyan@cfel.de

Abstract—We demonstrate a balanced optical-microwave phase detector (BOMPD) showing robust long-term optical-RF synchronization characteristics with sub-femtosecond residual timing drift over 24 hours under laboratory conditions without active temperature control of optical and electronic paths. Using this BOMPD, a 10.833 GHz Sapphire-loaded cavity oscillator (SLCO) was successfully disciplined by the pulse train from a 216.66 MHz femtosecond laser oscillator with a relative RMS jitter below one femtosecond integrated from 1 Hz to 1 MHz.

I. INTRODUCTION

Optical frequency combs provide a coherent link between optical and radio-frequency (RF) standards [1] and are outstanding tools for precision optical and microwave frequency measurements. In particular, they find a place in ultra-low phase noise microwave generation based on direct detection of the pulse train emitted by a mode-locked laser (MLL) [2]. Such systems can achieve sub-femtosecond short-term stability of the generated multi-GHz signals [3]. However, nonlinear effects during photo detection may degrade long-term phase stability of the extracted microwave signals. One way out of this problematic is by making the photo detection insensitive to optical power fluctuations and environmental drifts [4]. However, this forces to study the electro-optical properties of each particular photo detector used in the experiment to find its optimal operating conditions and minimize the influence of non-linear effects.

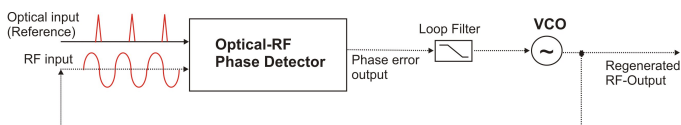


Fig. 1. Schematic diagram of an opto-electronic phase-locked loop.

There is a workaround for these issues - one should utilize the pulse train directly as a frequency reference in a RF phase-locked loop (PLL) that is insensitive to the input optical power fluctuations. Narrowband voltage-controlled oscillators (VCOs) can be disciplined by an optical pulse train generated by a femtosecond MLL to significantly improve its long-term stability. However, such a perfect marriage requires a match-maker who translates directly frequency and phase stability from optical domain to electronic domain, a hybrid optical-microwave phase detector (see Fig. 1). Various schemes for such phase detectors were successfully implemented to achieve

hybrid PLLs [5], [6], however their sensitivity to temperature and humidity drifts still have not allowed for sub-1-fs RMS stability over many hours of operation.

II. EXPERIMENT

Here, we are using a hybrid balanced optical-microwave phase detector (BOMPD) to connect a 216 MHz MLL (One-Five Origami) and a 10.8 GHz Sapphire-loaded cavity oscillator (PSI SLCO) together in an optoelectronic PLL. The BOMPD operation principle is based on balanced optical heterodyne detection of the output of a fiber Sagnac interferometer [7]. In addition to the last modifications of the BOMPD scheme [5] with multi-GHz modulation and, therefore, unidirectional phase modulation of the optical pulses in the Sagnac loop, we have implemented an independent RF demodulation arm for the error signal (see Fig. 2). The signal demodulation is performed at the lowest possible frequency (half of the MLL repetition rate) to maximize SNR at photodetection and to minimize thermally- and humidity-induced phase drifts in the electronic and optical paths for long-term stability.

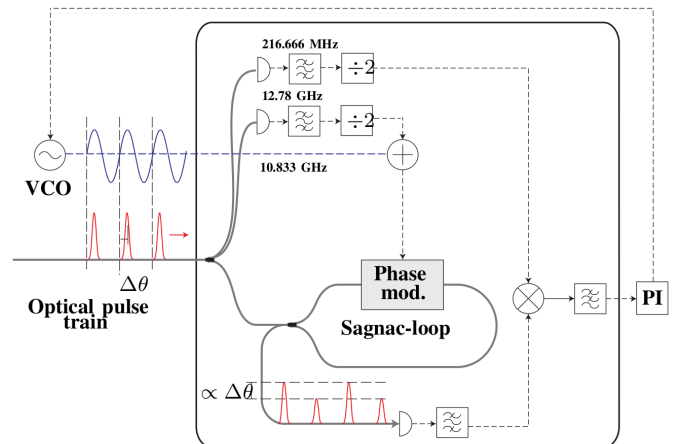


Fig. 2. Scheme of the BOMPD with an additional independent reference path down-mixing of the modulated pulse train at the output of Sagnac-loop interferometer. Much lower operating frequency of this reference path makes possible further suppression of the photodetection noise floor without limiting of the PLL's operating bandwidth.

Microwave phase trimmers in the RF paths were replaced by free-space optical delay lines to eliminate spurious losses

and to improve precision of phase tuning. Low power consumption low noise RF amplifiers (Micran) have eliminated the need of active cooling of electronics and, as consequence, improved the thermal stability of the setup.

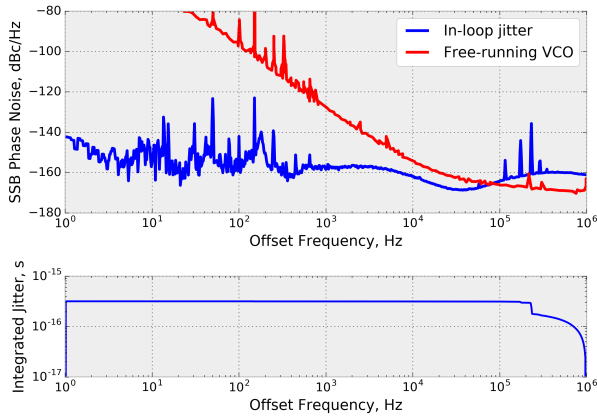


Fig. 3. *Top*: Variation of the single-sideband (SSB) phase noise of the free-running SLCO (red) and residual in-loop phase noise of the locked PLL (blue) at 10.833 GHz carrier frequency with offset frequency. *Bottom*: Integrated RMS in-loop jitter of the locked PLL.

As one would expect, the phase noise performance of the VCO improves dramatically after switching on of the PLL (see Fig. 3). The SSB phase noise curve of the 10.833 GHz carrier stays mainly below -140 dBc/Hz level except several sharp spikes at 50 Hz, 150 Hz and others which are induced by external noise sources, such as 50 Hz power lines, air conditioning system, EMI and others. However, they don't influence much the RMS jitter integrated from 1 Hz to 1 MHz which remains on the level of about 500 as.

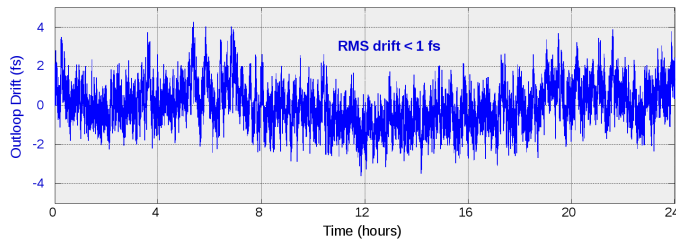


Fig. 4. Long-term drift of the system. The RMS value stays slightly below 1 fs during the 24 hour experiment ($ADEV < 1.15 \times 10^{-20}$ for 1 day).

Due to the greatly reduced power consumption of the RF paths of the BOMPD and, therefore, reduced heat generation, it became possible to place the whole setup into a thermo-insulating housing without the danger of running out of the operating temperature ranges of power RF amplifiers. After a warm-up process the temperature of most system components is passively stabilized within a range of 0.1 K, while the value of relative humidity could drift by about 2% per day. The result of the long-term out-of-loop measurement, captured by a second identical BOMPD, is shown in Fig. 4. There is still a small day-night cycle oscillation visible, because some components of the PLL are still placed outside the thermo-insulating housing. However, the RMS drift of the regenerated

10.833 GHz signal stays below 1 fs over one day of operation.

III. CONCLUSION

We have achieved optical-to-RF synchronization of a 10.833 GHz SLCO with a 216.66 MHz pulse train from a femtosecond laser with a residual RMS jitter of about 0.5 fs integrated from 1 Hz to 1 MHz and sub-femtosecond daily drift. The new scheme of the hybrid phase detector will be used in future FEL timing distribution systems. To make the design of the BOMPD more compact and even more robust, all RF paths will be placed on a single ceramic PCB in the near future.

REFERENCES

- [1] J. Ye, H. Schnatz and L. W. Hollberg, *Optical frequency combs: from frequency metrology to optical phase control*, IEEE J. Sel. Top. Quantum Electron. **9**(4), pp. 1041-1058, 2003.
- [2] T. M. Fortier, M. S. Kirchner, F. Quinlan, J. Taylor, J. C. Bergquist, T. Rosenband, N. Lemke, A. Ludlow, Y. Jiang, C. W. Oates and S. A. Diddams, *Generation of ultrastable microwaves via optical frequency division*, Nature Photonics **5**, pp. 425-429, 2011.
- [3] T. Fortier, F. Quinlan, A. Hati, C. Nelson, J. Taylor, Y. Fu, J. Campbell and S. Diddams, *Photonic microwave generation with high-power photodiodes*, Opt. Lett. **38**, pp. 1712-1714, 2013.
- [4] K. J. Williams, R. D. Esman and M. Dagenais, *Nonlinearities in p-i-n microwave photodetectors*, J. Lightwave Technol. **14**(1), pp. 84-96, 1996.
- [5] M. Y. Peng, A. Kalaydzhyan and F. X. Kärtner, *Balanced optical-microwave phase detector for sub-femtosecond optical-RF synchronization*, Opt. Express **22**, pp. 27102-27111, 2014.
- [6] K. Jung and J. Kim, *Long-term stable sub-femtosecond synchronization of microwave signals with mode-locked Er-fiber lasers*, Frequency Control Symposium (FCS), 2012 IEEE International, Baltimore, MD, 2012, pp. 1-4.
- [7] J. Kim and F. X. Kärtner, *Attosecond-precision ultrafast photonics*, Laser Photon. Rev. **4**(3), pp. 432-456, 2010.

Local Clocks Quality Evaluation Subsystem

Szplet Ryszard, Rózyc Krzysztof, Kwiatkowski Paweł, Jachna Zbigniew

Department of Electronics
Military University of Technology
Warsaw, Poland
rysard.szplet@wat.edu.pl

Abstract—This paper presents the design, operation and test results of a Clocks Evaluation Subsystem (CES) developed for the EUREKA’s research project called Legal Time Distribution System (LTDS). The main aim of the CES is to gather information about time drift of the tracked clocks, then to evaluate their stability, and finally to select the most stable one as a local reference clock. The CES contains three main functional blocks: 3-channel time interval counter [1], distribution amplifier and set of three local clock sources, i.e. low noise chip scale atomic clocks (LN CSAC, *Microsemi*)

Keywords—multichannel time counter, time-to-digital converter, programmable device, clock quality evaluation

I. INTRODUCTION

In a modern networked society, an excellent timing synchronization is commonly required to enable various activities into a global framework of data and information exchange. Time has evolved from a physical quantity to a matter of legal and financial importance, crossing the classical boundaries of physics and astronomy into the realm of everyday life, in applications as diverse as finance, traffic control, synchronous telecommunications networking and utilities such as power generation and distribution.

Generation of a time scale is primarily carried on by institutions known as National Metrological Institutes (NMIs) that, however, are not responsible for time scale distribution. Typical way to achieve the legal time outside the NMI is based on synchronization of locally created time scale to the national time scale. However, if the local clock at the user premises is stable enough, it may be taken into consideration during a creation of the national or even global time scale, improving their quality. Quality of a local time scale can be verified through the measurement of clock’s drift performed with the use of a precise time counter. In the proposed LTDS system the data gathered at the user premises are transferred to the NMI and processed to compute instantaneous timing and frequency parameters (frequency drift, time and frequency offsets), and long-term characterization of the remote clocks. Such information allows to control remote clocks by steering each clock toward the legal time reference, as needed. In this way users can keep their local clocks synchronized to the legal time, and generate its local replica to adapt to particular applications, while the NMI can monitor the users clocks and can track their behavior with respect to the legal time.

This work was supported by the Polish National Centre for Research and Development under contract no. E1/8727/LTDS/1/2014.

In this paper we propose a Clock Evaluation Subsystem (CES) for continuous verification of parameters of local reference clocks. The CES is a part of the End User Unit (EUU) designed and developed within EUREKA’s research project named Legal Time Distribution System (LTDS). Simplified block diagram of the EUU is shown in Fig. 1.

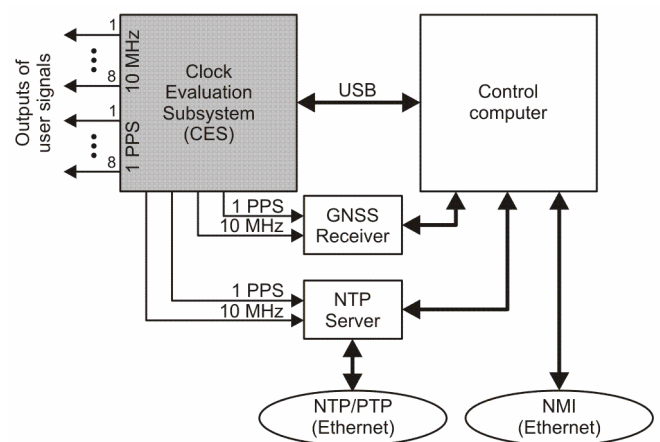


Fig. 1. Simplified block diagram of the EUU.

Apart from the CES, the EUU includes control computer, GNSS receiver and NTP (or PTP) server. The computer sends/receives data to/from NMI via Ethernet and also controls other modules of the EUU. The GNSS receiver determines the phase difference between the local clock signal and the reference signal synchronized to GPS/Galileo system. The phase difference data can optionally be used to adjust the frequency and synchronize the phase of a local clock. Finally, on the basis of the local reference clock, the NTP server distributes the time information using the NTP (or the PTP) protocol. The unit EUU provides also direct output signals, 1PPS and 10 MHz, which are available to the local user.

The CES (Fig. 2) contains three main functional blocks: (1) three-channel precise time interval counter (TIC), (2) set of three local clock sources and (3) multichannel signal distributor that allows for selecting signals from the currently most stable source as a local reference clock. The TIC measures simultaneously the time relations between 1PPS pulses generated by three local clock sources. The counter provides the high measurement precision (below 15 ps) and wide range (above 1 sec) [1]. It is implemented in a Field Programmable Gate Array (FPGA) device. Functions of the

multichannel signal distributor are performed by a digital switch implemented in FPGA device and low-jitter multi-output buffer (with reference to 1PPS pulses), and by a programmable analog high-speed crosspoint switch (with reference to 10 MHz sine wave signals). Three low noise chip scale atomic clocks (LN CSAC) were applied as local clock sources and integrated with the whole system on a single PCB board. Another chip scale atomic clock (CSAC) was used as a reference clock for the TIC. The local controller allows for transferring information from TIC to the control computer and receiving the steering data from the computer.

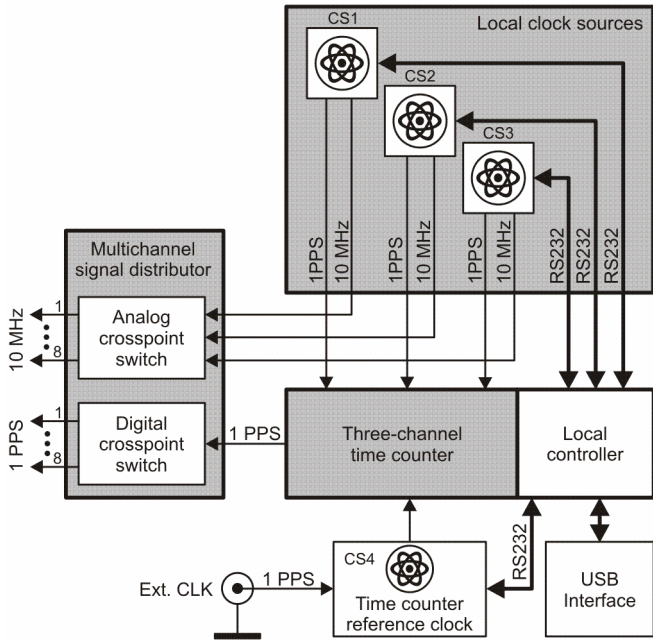


Fig. 2. Simplified block diagram of the CES (CS1, CS2, CS3 - LN CSAC, CS4 - CSAC and low-noise synthesizer).

II. TIME INTERVAL COUNTER

As high-precision, continuous registration of 1PPS pulses from three independent clock sources is needed, the three-channel time counter operates based on timestamps method combined with double interpolation [1]. The simplified block diagram of the TIC is shown in Fig. 3.

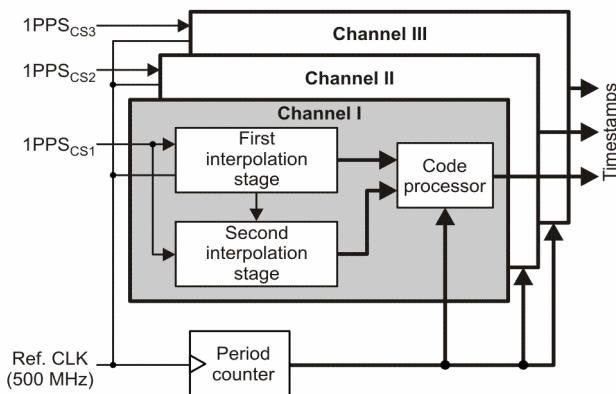


Fig. 3. Simplified block diagram of the TIC.

The idea of timestamps method is to register time of appearance of any input events (leading pulse edges) on a common time scale [2]. Such a scale is created by continuous counting of the reference clock periods (T_0) by a period counter. Since the 29-bit binary counter operates with 500 MHz clock signal, then it provides 1.07 sec time scale range. When the counter overflows, it starts counting from the beginning. Taking into account that the input signals are 1PPS pulses, the period counter is sufficiently wide.

In case of a simple timestamps method the measurement resolution is limited by the clock period T_0 to 2 ns (500 MHz signal frequency). Thus, two-stage interpolation is applied within a single clock period to get finer time scale. The first interpolation stage identifies in which segment of the four-phase clock the 1PPS pulse appeared. Then the second interpolation stage accurately quantizes time interval between neighboring edges of the four-phase clock. The use of time coding delay line [3, 4] in this stage allows to get several picoseconds resolution of the time scale. Double interpolation increases time counter precision by applying the more and more precise time-to-digital converters in each stage.

When 1PPS pulse appears at an input of the TIC, the current state of period counter is collected together with results from both interpolation stages in a code processor. Then the code processor performs calculation to create timestamp value as:

$$TS = N \cdot T_0 + T_{int},$$

where N is the content of period counter and T_{int} is combined result from the first and second interpolation stages. Time relation between subsequent timestamps from the same channel may be used to determine a single clock stability while differences between channels to observe the time drift between atomic clocks.

The time counter was built as integrated module implemented in a low-cost XC6SLX9-3TQG144 Spartan-6 FPGA device manufactured by *Xilinx*. A timebase reference clock signal of 500 MHz frequency is generated outside integrated time counter module with the use of 10 MHz chip scale atomic clock SA45S (*Microsemi*) and low-noise synthesizer Si5326 (*Silicon Labs*).

A local controller is implemented in the same FPGA chip as three-channel time counter. The controller is responsible for communication between the CES and a control computer via USB interface (Fig. 1).

III. LOCAL CLOCK SOURCES

The quality of local clock sources is verified through the permanent measurement of their time drifts in relation to the reference clock. The obtained data transferred to NMI are then used to compute timing and frequency parameters and long-term characterization of each clock. It allows tuning each clock to minimize time and frequency offsets and time drift in relation to the NMI reference clock.

According to system assumptions the local clock sources have to provide 1PPS pulses and 10 MHz sine wave signals with ability to adjust output frequency. Thus, the LN CSACs (*Microsemi*) [4] were applied in the design. The LN CSAC

combines the accuracy of an atomic clock with a compact size and low power (below 275 mW). It provides the 1PPS pulses and 10 MHz sine wave signal with short-term stability $ADEV < 2E-11 @ 1 \text{ sec}$. The clock generator is equipped with a standard RS-232 serial interface typically used to control and calibrate the unit. It also allows for adjusting the output frequency within the range of $10 \text{ MHz} \pm 0.2 \text{ Hz}$. Additionally, the LN CSAC accepts 1PPS pulses that may be used to synchronize the unit to an external more stable reference clock.

The 1PPS pulses created by each generator are connected to inputs of the three-channel time counter, while a selected one (from the most stable clock) is transmitted to the input of the digital crosspoint switch. The 10 MHz generators output signals are connected directly to inputs of the programmable multichannel signal distributor.

IV. MULTICHANNEL SIGNAL DISTRIBUTOR

Since the output signals of the CES are 1PPS pulses and 10 MHz sine wave, then the programmable multichannel signal distributor includes two independent outputs: an analog and digital, controlled by the local controller.

Choosing a valid 1PPS signal from local clock sources is accomplished through the 3x1 multiplexer built in the FPGA device. The FPGA output signal is then connected to digital part of a signal distributor, designed with 1x8 fanout buffer and 8 independent 3-state TTL standard buffers.

The 10 MHz sine wave signals from local clock sources are connected directly to analog part of the signal distributor. It is accomplished with the use of a programmable high-speed analog crosspoint switch. All input signals are initially conditioned by a tunable amplifiers in order to obtain the amplitude of output signals equaled to 1V (rms) at the load of 50Ω , at all outputs of the distributor. The output buffers are made with the aid of low-noise operational amplifiers.

V. MEASUREMENT TESTS

The parameters and implementation aspects of the designed CES were verified in series of tests aimed at evaluation of: (1) precision of measurements of 1PPS pulses from the built-in local clock sources, (2) delay time introduced by CES to 1PPS and 10 MHz signals.

The integrated time counter precision reported in [1] is below 15 ps within the measurement range up to 100 ms and increases to about 33 ps for time interval of 1 s. However, the outputs of LN CSACs have limited current efficiency and have to be buffered before connecting to the three-channel time counter. That adds extra jitter to the measured signal. Therefore the time relations between subsequent 1PPS pulses from LN CSACs are evaluated with precision of about 115 ps. The histograms obtained for tested clocks are shown in Fig. 4.

The next tests of the CES was aimed at evaluation of the spread of delays introduced by outputs of analog and digital parts of the signal distributor. All measurements were performed using an oscilloscope DSA90804A (*Keysight*) that offers very low noise floor ($\sim 1.5 \text{ ps}$). The spread of delays observed for 1PPS signals is below 160 ps. It mainly comes

from non-uniformity of delays (propagation times) of output buffers. In analog part of the distributor, the spread of delays of 10 MHz sine wave signals is below 250 ps. It is a sum of non-uniformity of delays of output buffers and signal paths inside the analog crosspoint switch.

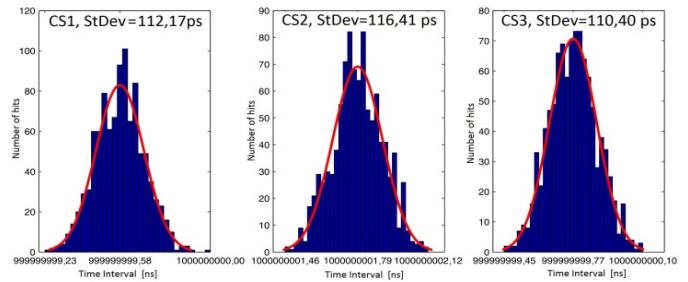


Fig. 4. Precision of measurements of 1PPS pulses from three built-in local clock sources (CS1-CS3).

The value of the delay between active edges of 1PPS and 10 MHz signals does not exceed 1.9 ns. It is mainly due to the non-uniformity of delays of paths inside the FPGA device introduced for 1PPS pulses.

VI. CONCLUSION

A local clock quality evaluation subsystem is described. It is designed for continuous verification of parameters of local clock sources in the end user unit of the Legal Time Distribution System.

Due to the use of compact atomic clocks, the whole subsystem including an integrated three-channel time counter, low-noise power supplier, 1PPS and 10 MHz signal distributors, is encased in a single 19" Rack 2U case. Measurements performed by the time counter provide data to calculate the clock signals stability and drift, and to choose the one that is the closest to the legal time scale. The user of the system obtains two groups of highly stable ($ADEV < 2E-11 @ 1 \text{ sec}$) output signals:

- 8 x 1PPS (TTL standard, 100 μs pulse width),
- 8 x 10 MHz sine wave (1 V rms @ 50Ω load).

The designed subsystem allows the users to keep their local clock synchronized to the legal time, and also generate its local replica for employing in own applications.

REFERENCES

- [1] Szplet R., Kwiatkowski P., Jachna Z., Rozyc K., "Precise Three-Channel Integrated Time Counter", Proc. Joint Conference of the IEEE IFCS-EFTF 2015, Denver, USA, April 12-16, 2015.
- [2] M. Zieliński, D. Chaberski, M. Kowalski, R. Frankowski, S. Grzelak, "High-resolution time-interval measuring system implemented in single FPGA device", Measurement vol. 35, 2004, pp 311-317.
- [3] Szplet R., "Time-to-Digital Converters", Chapter 7 in: Carbone P., Kiaei S., Xu F. (eds), Design, Modeling and Testing of Data Converters, Springer, 2014, pp 211-246.
- [4] Klepacki K., Szplet R., Pelka R., "A 7.5 ps single-shot precision integrated time counter with segmented delay line", Review of Scientific Instruments, vol. 85, 034703, 2014, 10 pp.
- [5] "Quantum LN CSAC", Data Sheet, Microsemi Corporation, 2014.

Brillouin lasing in a LiF whispering-gallery mode resonator and application to microwave generation.

Souleymane Diallo
Femto-St Institute,
15 B Avenue des Montboucons,
25030, Besancon CEDEX, France
Email: souleymane.diallo@femto-st.fr

Guoping Lin
Center for Gravitational Experiments,
Luoyu Road 1037,
430074, Wuhan, Hubei province, China,
Email: guoping.lin@hust.edu.cn

Jean-Pierre Aubry
Femto-St Institute,
15 B Avenue des Montboucons,
25030, Besancon CEDEX, France
Email: jp.aubry@femto-st.fr

Yanne K. Chembo
Femto-St Institute,
15 B Avenue des Montboucons,
25030, Besancon CEDEX, France
Email: yanne.chembo@femto-st.fr

Abstract—We report the excitation of single Stokes Brillouin lasing using an-ultra high-quality (Q) lithium fluoride crystalline resonator pumped above given threshold. The home-made resonator has a quality factor above hundred million at 1550 nm. This is, to the best of our knowledge, the first demonstration of Brillouin lasing in a monofluoride crystal. Combined with the narrow linewidth of the Brillouin gain, the low threshold for oscillations, offers great potential for ultra-stable microwave generation.

I. INTRODUCTION

The topic of Whispering Gallery Mode (WGM) resonators has been widely explored since the very first attempt to propose a theory to unveil their physical nature (Lord Rayleigh, 1871 [1]). In the optical domain, these resonators are used for various purposes such as laser stabilization, biosensing, microwave photonics applications and more [2]–[5]. The interesting point about these WGM resonators is the strong enhancement of nonlinear effects within the resonator due to the small mode volume and the ultrahigh Q factor. In fact, in the ray-optics point of view, light propagates in such resonators by total internal reflexion with a photon lifetime that can be as high as few microseconds. The inner periphery of the resonator becomes the host of strong light confinement that enhances various nonlinear effects. Amongst them, we can cite Raman [6], Kerr [7] but also Brillouin effects [8]–[13], all triggered with very low pump power.

Stimulated Brillouin Scattering (SBS) has been reported in optical fibers, amorphous but also crystalline resonators. It is a nonlinear process resulting from the interaction between a strong laser beam and acoustic phonons. The scattering process is mediated by electrostriction that leads to the formation of a refractive index grating travelling at an acoustic wave velocity. This grating scatters incident photons with a Doppler downshift corresponding to acoustic phonon frequencies, which can be calculated from the elastic constants of the material. Brillouin scattering is known to allow for laser linewidth narrowing in fiber lasers [14]. H. Lee and *al.* have reported SBS using a chemically etched

ultra-high Q Silica wedge WGM resonators [10]. J. Li and *al.* from the same team have reported a cascaded SBS with up to 9th order with cascaded lines presenting a Schawlow-Townes noise $< 0.1 \text{ Hz}^2 \text{ Hz}^{-1}$. They have demonstrated in their work a microwave synthesizer with performance in an open loop configuration of -90 dBc/Hz at 10 kHz offset and -110 dBc/Hz at 100 kHz offset of a 21.7 GHz carrier [13]. Their system has also a record low-white-phase-noise floor of -160 dBc/Hz in the closed loop configuration. However, to the best of our knowledge, Brillouin lasers based on crystalline resonators have only been reported in difluoride crystals such as calcium fluoride and barium fluoride [9], [12].

Difluoride crystals with ultrahigh Q factors can be obtained using mechanical polishing [15]–[17], but it is much more difficult to polish monofluoride crystals [18]. We present here the fabrication of a monofluoride crystalline WGM resonator made of lithium fluoride (LiF) with a quality factor above 10^8 at the wavelength of 1550 nm. The quality factor is measured using the cavity ringdown spectroscopy technique. We demonstrated Brillouin lasing in LiF and analyze the key mechanisms leading to this phenomenology.

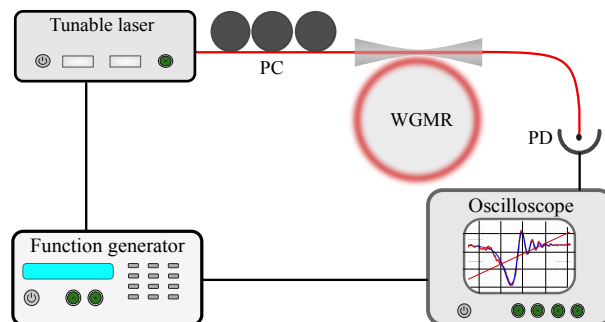


Fig. 1. Experimental setup for the WGM resonator characterization. PC: polarisation controller, PD: photodiode; WGMR: whispering gallery mode resonator

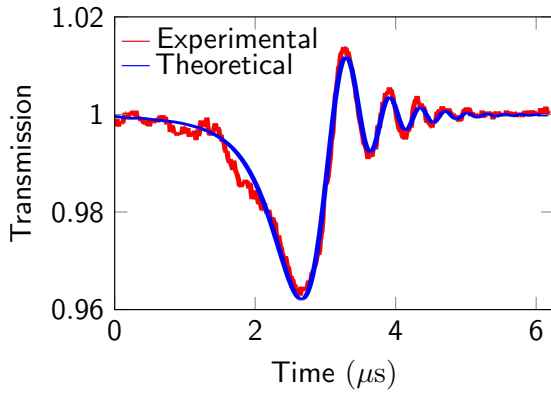


Fig. 2. Ring down transmission spectrum. A theoretical fit gives an intrinsic quality factor of 3.35×10^8 , an extrinsic quality factor of 2.58×10^8 and a loaded quality factor of 1.45×10^8

II. FABRICATION AND CHARACTERIZATION OF THE ULTRA-HIGH Q LiF DISK RESONATOR

Lithium fluoride is a cubic crystal with a wide transparency window ranging from the ultra-violet (UV) to the mid-infrared (IR). It has a very high transmission in the UV but also in the X-ray domain [19]. The Q factor above 10^8 is achieved using a commercially available crystalline LiF WGM disk resonator, and after several steps of grinding and polishing, thanks to an air-bearing spindle motor that spins the disk at a very high velocity [17], [18]. The grinding step is performed using a decreasing abrasive-coated support to preform the resonator rim into a sharp "V" edge necessary to trap the photons within the resonator. The Mohs hardness of LiF is equal to 4, and it is lower than the one of MgF_2 . It makes the grinding step shorter (less than an hour) than the one of MgF_2 , but also more delicate. The polishing step is performed repeatedly using decreasing size abrasive particles down to 100 nm. Once this step achieved, the resonator is placed under a microscope equipped with a $40\times$ magnification Mirau objective. The purpose of this process is to obtain a 3D reconstruction of an area of the resonator in order to determine his surface roughness.

In order to avoid thermal effects occurring during linewidth measurement, we have used the so-called cavity-ring-down spectroscopy technique to determine the quality factor of the resonator. We can therefore obtain the intrinsic, extrinsic and loaded quality factors: $1/Q_{\text{load}} = 1/Q_{\text{in}} + 1/Q_{\text{ext}}$ where Q_{int} corresponds of the contribution of the material absorption, his surface diffusion and diffraction [20]. To do so, we fast scan the laser frequency across the resonance and measure the output timetrace which gives the pertinent information with regards to the loss mechanisms in the resonator. The experimental setup is made of sub-kHz continuous wave laser that is swept at a scanning speed of 1.2 GHz/ms and is used to couple light in the resonator through the evanescent field of a tapered silica fiber. The recorded transmission corresponds to the interference between the laser input and output signal from the resonator. An analytical fit using a formula which is presented in [20] allows us to obtain at 1550 nm an intrinsic quality factor of 3.35×10^8 , an extrinsic quality factor of 2.58×10^8 , and a loaded quality factor of 1.45×10^8 .

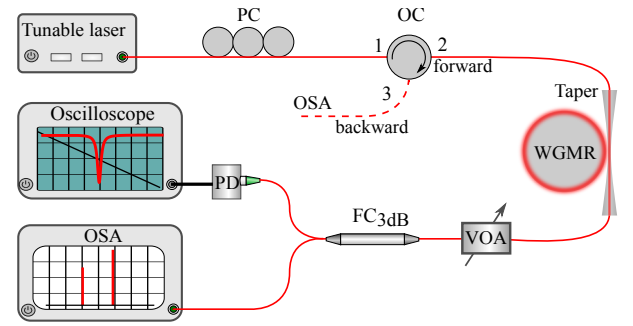


Fig. 3. The experimental setup for the WGM scattering process characterization. PC: fiber polarization controller; L1, L2: GRIN lenses; VOA: Variable optical attenuator; FC_{3dB}: 3dB fiber coupler. PD: photodetector; OSA: Optical spectrum analyzer; fw: forward, bw: backward.

III. BRILLOUIN SCATTERING IN WGM RESONATORS

Stimulated Brillouin scattering is a well known nonlinear effect resulting from the interaction between light and an acoustic wave traveling at a given speed. The generation of the scattered wave is therefore associated to a frequency shift due to Doppler effect. A Stokes wave is generated when light and the acoustic wave travel in the same direction and an anti-Stokes wave is generated in the opposite case. In optical fibers, when the pump power is high, the acoustic wave becomes strong and act as a Bragg mirror that is backscattering the injected power. For this reason, Brillouin effect is a power limiting factor in optical fiber telecommunications. However, fiber based Brillouin lasers feature linewidth narrowing effect where the Stokes line becomes narrower than the pump by a factor that can be as high as 10^4 . Therefore, SBS can find applications in several domains such as fiber lasers, microwave generation and rotation sensing. Brillouin effect has been reported in several difluoride crystals such as calcium fluoride CaF_2 and barium fluoride BaF_2 . Chemically etched ultrahigh-Q-silica-on-silicon wedge resonators have been used to demonstrate narrow linewidth Brillouin microcavity laser but also an ultra-low-phase-noise microwave synthesizer [10].

Our aim is, in this contribution, to report Brillouin lasing at 1550 nm using lithium fluoride resonator with a quality factor beyond 10^8 . The pump and scattered signals are separated by a frequency shift $\nu_B = \Omega_B/2\pi = 2n_{\text{eff}}V_a/\lambda_p$ where n_{eff} is the effective refractive index of the WGM optical mode, λ_p is the optical wavelength in vacuum, and V_a the phase velocity. The latter is calculated using the following expression: $V_a = [(C_{11} + C_{12} + 2C_{44})/2\rho]^{0.5}$ where $C_{11} = 1.3197 \times 10^{11} \text{ N.m}^{-2}$, $C_{12} = 0.4767 \times 10^{11} \text{ N.m}^{-2}$, $C_{44} = 0.6364 \times 10^{11} \text{ N.m}^{-2}$ represent the elastic constants of LiF and $\rho = 2.639 \text{ g.cm}^{-3}$ his volumic mass. We obtain an acoustic speed of 7.62 km.s^{-1} and a Brillouin frequency shift of 13.61 GHz. This value is in excellent agreement with the 13 GHz shift measured in Fig. 4.

In order to measure the spectra of the forward and backward waves, we have designed the experimental setup displayed in Fig. 3. The measurements display proof of Brillouin lasing as shown in Fig. 4, where the Brillouin shift is in excellent agreement with the theoretically predicted value ν_B .

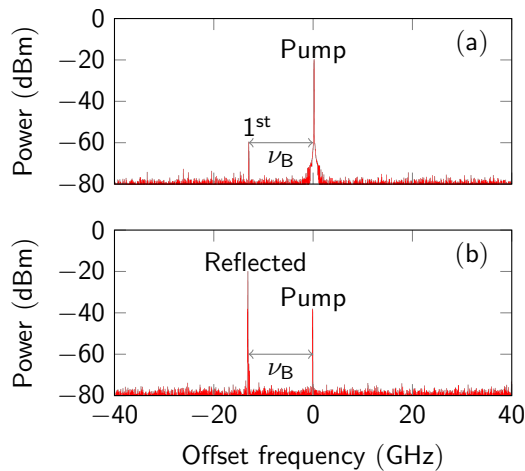


Fig. 4. Experimental spectra of the intra-cavity fields. The frequency ν_B corresponds to the Brillouin frequency shift, (a) Forward direction, (b) Backward direction. Note that the Brillouin signal in the forward direction and the pump signal in the backward direction are induced by parasitic Rayleigh backscattering.

During the experiment, the Brillouin mode is interacting with a mode belonging to another eigenmode family with regards to the pump. This means that if the pumped mode belongs to the eigenmode family $n = n_1$, then the Brillouin excited mode belongs to an eigenmode family mode $n_2 \neq n_1$. This explains how Brillouin scattering is possible in WGM resonators even when the Brillouin shift does not match a multiple of the FSR. We hope by this contribution to enlarge the possibilities to generate new frequencies in microwave photonics applications using WGM resonators since the Brillouin shift is material-specific. The interesting advantage of LiF in this regard is the fact that its transparency goes down to the deep ultra-violet, thereby allowing for applications in that wavelength range.

IV. CONCLUSION

We have reported a LiF WGM resonator with an intrinsic quality factor of three hundred millions at telecom wavelength. We have also demonstrated the excitation of a Stokes wave with this resonator, thereby evidencing for the first time Brillouin lasing in a monofluoride crystal to the best of our knowledge. Further research will be devoted to the exploration of the various applications that can be powered by this phenomenon with an emphasis on ultra-stable microwave generation. We also expect nonlinear phenomena in LiF to display a wide range complex frequency conversion mechanisms which might find applications in various areas of nonlinear optics and microwave photonics [25]–[37]

February 26, 2016.

ACKNOWLEDGMENT

The authors acknowledge support from the European Research Council (ERC) through the projects NextPhase (StG 278616) and Versyt (PoC 632108), from the Centre National d'Études Spatiales (CNES) through the project SHYRO, from the Région de Franche-Comté through the project CORPS, from the Labex ACTION and from the Labex First-TF.

REFERENCES

- [1] L. Rayleigh, J. W. S. B. *The Theory of Sound*, vol. 1, 1894.
- [2] M. C. Collodo, F. Sedlmeir, B. Sprenger, S. Svitlov, L. J. Wang, and H. G. L. Schwefel, *Sub-kHz lasing of a CaF₂ whispering gallery mode resonator stabilized fiber ring laser*, *Opt. Exp.*, vol. 22, no. 16, 282 pp. 1927719283, Aug. 2014.
- [3] A. A. Savchenkov, A. B. Matsko, V. S. Ilchenko, N. Yu, and L. Maleki, *284 Whispering-gallery-mode resonators as frequency references. II. Stabilization*, *J. Opt. Soc. Amer. B*, vol. 24, no. 12, pp. 29882997, 286 Dec. 2007.
- [4] F. Vollmer and S. Arnold, *Whispering-gallery-mode biosensing: Label-free detection down to single molecules*, *Nature Methods*, vol. 5, no. 7, 289 pp. 591596, Jul. 2008.
- [5] A. A. Savchenkov, E. Rubiola, A. B. Matsko, V. S. Ilchenko, and L. Maleki, *Phase noise of whispering gallery photonic hyper parametric microwave oscillators*, *Opt. Exp.*, vol. 16, no. 6, pp. 41304144, 275 Mar. 2008.
- [6] I. S. Grudinina and L. Maleki, *Efficient Raman laser based on a CaF₂ resonator*, *J. Opt. Soc. Amer. B*, vol. 25, no. 4, pp. 594598, Mar. 2008.
- [7] T. Herr et al., *Universal formation dynamics and noise of Kerr-frequency combs in microresonators*, *Nature Photon.*, vol. 6, pp. 480487, Jun. 2012.
- [8] A. Chiasera et al., *Spherical whispering-gallery-mode micro-resonators*, *Laser Photon. Rev.*, vol. 4, no. 3, pp. 457482, pp. 2010.
- [9] I. S. Grudinina, A. B. Matsko, and L. Maleki, *Brillouin lasing with a CaF₂ whispering gallery mode resonator*, *Phys. Rev. Lett.*, vol. 102, no. 4, pp. 043902-1043902-4, Jan. 2009.
- [10] H. Lee et al., *Chemically etched ultrahigh-Q wedge-resonator on a silicon chip*, *Nature Photon.*, vol. 6, no. 6, pp. 369373, May 2012.
- [11] M. Tomes and T. Carmon, *Photonic micro-electromechanical systems vibrating at X-band (11-GHz) rates*, *Phys. Rev. Lett.*, vol. 102, no. 11, pp. 113601-1113601-4, Mar. 2009.
- [12] G. Lin et al., *Cascaded Brillouin lasing in monolithic barium fluoride whispering gallery mode resonators*, *Appl. Phys. Lett.*, vol. 105, no. 23, p. 231103, 2014.
- [13] J. Li, H. Lee, and K. J. Vahala, *Microwave synthesizer using an on-chip Brillouin oscillator*, *Nature Commun.*, vol. 4, no. 2097, pp. 17, Jun 2013.
- [14] Z. Ou, X. Bao, Y. Li, B. Saxena, and L. Chen, *Ultrannarrow linewidth Brillouin fiber laser*, *IEEE Photon. Technol. Lett.*, vol. 26, no. 20, pp. 20582061, Oct. 15, 2014.
- [15] A. A. Savchenkov, A. B. Matsko, V. S. Ilchenko, and L. Maleki, *Optical resonators with ten million finesse*, *Opt. Exp.*, vol. 15, no. 11, pp. 6768-6773, May. 2007.
- [16] A. A. Savchenkov, V. S. Ilchenko, A. B. Matsko and L. Maleki, *Kilohertz optical resonances in dielectric crystal cavities*, *Phys. Rev. A*, vol. 70, no. 5, pp. 051804-1-051804-4, Nov. 2004.
- [17] G. Lin, S. Diallo, R. Henriët, M. Jacquot, Y. K. Chembo, *Barium Fluoride Whispering-Gallery Mode Disk-Resonator with one Billion Quality-Factor*, *Opt. Lett.*, vol. 39, no. 20, pp. 6009-6012, Oct. 2014.
- [18] R. Henriët, A. Coillet, K. Saleh, L. Larger and Y. Chembo, *Barium Fluoride and lithium fluoride whispering-gallery mode resonators for photonics applications*, *Opt. Eng.*, vol. 53, no. 7, pp. 071821-1-071821-3, Jul. 2014.
- [19] M. J. Weber, *Handbook of optical materials*, CRC Press, vol. 19, 043828, 2002.
- [20] Y. Dumeige, S. Trebaol, L. Ghisa, T. K. Nguyen, H. Tavernier, and P. Feron, *Determination of coupling regime of high Q resonators and optical gain of highly selective amplifiers*, *J. Opt. Soc. Am. B*, vol. 25, no. 12, pp. 2073-2080, Dec. 2008.
- [21] G. Agrawal, *Nonlinear Fiber Optics*, Acad. Press, vol. 5, pp. 1-629. 2003.
- [22] A. B. Matsko, A. A. Savchenkov, D. Strekalov, V. S. Ilchenko, and L. Maleki, *Review of applications of whispering-gallery mode resonators in photonics and nonlinear optics*, *IPN Prog. Rep.*, vol. 42, no 162, pp. 1-51, Aug 2005.
- [23] A. B. Matsko and V. S. Ilchenko, *Optical resonators with whispering gallery modes Part II: Applications*, *IEEE J. Sel. Topics Quantum Electron.*, vol. 12, no. 1, pp. 1532, Jan./Feb. 2006.

- [24] A. B. Matsko and V. S. Ilchenko, *Optical resonators with whispering gallery modes Part I: Applications*, IEEE J. Sel. Topics Quantum Electron., vol. 12, no. 1, pp. 1532, Jan./Feb. 2006.
- [25] K. Saleh, P. Merrer, O. Llopis and G. Cibiel, *Millimeter wave generation using Brillouin scattering in a high Q fiber ring resonator*, in Proc. Int. Topical Meeting Microw. Photon. (MWP), pp. 164167, Sep. 2012.
- [26] Y. K. Chembo and C. R. Menyuk, *Spatiotemporal Lugiato-Lefever formalism for Kerr-comb generation in whispering-gallery-mode resonators*, Phys. Rev. A, vol. 87, no. 5, p. 053852, May, 2013.
- [27] R. Henriët, et al. *Kerr optical frequency comb generation in strontium fluoride whispering-gallery mode resonators with billion quality factor*, Opt. Lett., vol. 40, no. 7, pp. 1567-1570, Apr., 2015.
- [28] A. Coillet, et al. *Azimuthal Turing Patterns, Bright and Dark Cavity Solitons in Kerr Combs Generated With Whispering-Gallery-Mode Resonators*, IEEE Photonics J., vol. 5, no. 4, p. 6100409, Aug., 2013.
- [29] A. Coillet, R. Henriët, K. P. Huy, M. Jacquot, L. Furfaro, I. Balakireva, L. Larger, and Y. K. Chembo *Microwave photonics systems based on whispering-gallery-mode resonators*, Journal of Visualized Experiments 78, e50423, doi:10.3791/50423 (2012).
- [30] G. Lin, S. Diallo, R. Henriët, M. Jacquot, and Y. K. Chembo, *Barium fluoride whispering-gallery-mode disk-resonator with one billion quality-factor*, Opt. Lett. 39, 6009 (2014).
- [31] A. Coillet and Y. K. Chembo, *On the robustness of phase-locking in Kerr optical frequency combs*, Optics Letters 39, 1529 (2014).
- [32] A. Coillet, J. Dudley, G. Genty, L. Larger and Y. K. Chembo, *Optical rogue waves in whispering-gallery mode resonators*, Phys. Rev. A 89, 013835 (2014).
- [33] A. Coillet, and Y. K. Chembo, *Routes to spatiotemporal chaos in Kerr optical frequency combs*, Phys. Rev. A 89, 013835 (2014), A.I.P 24,013313 (2014).
- [34] Y. K. Chembo, Ivan S. Grudinin, and N. Yu, *Spatiotemporal dynamics of Kerr-Raman optical frequency combs*, Phys. Rev. A 92, 043818 (2015).
- [35] J. Pfeifle, A. Coillet, R. Henriët, K. Saleh, P. Schindler, C. Weimann, W. Freude, I. V. Balakireva, L. Larger, C. Koos, and Y. K. Chembo, *Optimally Coherent Kerr Combs Generated with Crystalline Whispering Gallery Mode Resonators for Ultrahigh Capacity Fiber Communications*, Phys. Rev. Lett. 114, 093902 (2015).
- [36] Y. K. Chembo, *Quantum dynamics of Kerr optical frequency combs below and above threshold: Spontaneous four-wave mixing, entanglement, and squeezed states of light*, Phys. Rev. A. 93, 033820 (2016).
- [37] G. Lin and Y. K. Chembo, *On the Dispersion management of Fluorite Whispering-Gallery Mode Resonators for Kerr Optical Frequency Comb Generation in the Telecom and Mid-Infrared Range*, Opt. Express 23, 1594 (2015).

High-bandwidth large-dynamic frequency control of an optical comb by tuning polarization state

Yanyan Zhang^{1,2}, Lulu Yan¹, Songtao Fan^{1,2}, Maoqiang Chen^{1,2}, Wenge Guo^{1,3}, Shougang Zhang¹ and Haifeng Jiang¹

¹Key Laboratory of Time and Frequency Primary Standards, National Time Service Center, Xi'an, China

²University of Chinese Academy of Sciences, Beijing, China

³School of Science, Xi'an Shiyou University, Xi'an, China

Email: haifeng.jiang@ntsc.ac.cn

Abstract—we report a new method to precisely control carrier-envelope frequency (f_{ceo}) of a nonlinear-polarization-rotation mode-locked Er: fiber optical frequency comb. The f_{ceo} is phase-locked onto an RF reference frequency by rotating polarization state with a special home-made intra-cavity electro-optic modulator (EOM). The EOM is inserted right after the PBS of a well-known ring mode-locked laser's loop and rotates polarization state with a coefficient of about 1.2×10^{-4} rad/v in ellipticity. The frequency control range of the EOM is two orders of magnitude larger than the traditional ones. Benefiting from fast response of the EOM, in-loop frequency stabilities of the f_{ceo} is below 2×10^{-17} at 1 second, and the corresponding timing jitter is about 0.16 rad.

Keywords—optical comb; frequency control; polarization state; electro-optic modulator

I. INTRODUCTION

High-performance optical frequency combs have been indispensable tools in many applications, including optical spectroscopy [1], optical frequency standards [2], ultra-fast science research [3], ultra-stable microwave generation [4] and distance measurement [5]. To match requirement of these applications, scientists and engineers develop optical frequency combs with more precise control of repetitive rate (f_r) and f_{ceo} . Typically, the f_r is stabilized by tuning the cavity length with a Piezotransducer (PZT) or/and the optical length of the cavity with an EOM [6, 7]; while the f_{ceo} is controlled by tuning the pump power of the laser [8]; new techniques [9, 10], such as cavity power modulation and extracavity frequency shift have been invented to stabilize the f_{ceo} . However, these existing frequency control methods have low bandwidth or small dynamic range limited by various reasons.

In this paper, we present a servo control method to stabilize f_{ceo} by changing polarization state of the laser with a home-made intra-cavity EOM. By controlling the EOM, the f_{ceo} is stabilized with 1.8 MHz feedback bandwidth in the range of several hundred megahertz.

II. EXPERIMENTAL SETUP AND MEASUREMENT RESULTS

Figure 1 shows the experimental setup of the frequency-stabilized optical comb. The oscillator shown in the left side of the figure is a home-made Er: fiber ring laser employing nonlinear polarization rotation (NPR) mechanism for mode locking. It is pumped through a wavelength division multiplexing (WDM) with two 750mW 976nm pigtailed diode lasers. Its cavity contains three types of fibers: 48 cm SMF-28 fiber, 41 cm highly Erbium-doped fiber (Liekki 110-4/125) and 5 cm HI1060 fiber. The free-space components include collimators, 4 wave plates on both sides of a polarization beam splitter (PBS), a PZT and a 3-mm thick home-made EOM. The PZT is mounted in the cavity to compensate the long-term frequency drift caused by temperature change. The maximum dynamic range of PZT is about 1 kHz. The EOM has been placed right after the PBS to control the f_{ceo} by steering the polarization state of the laser. Net dispersion of the laser cavity is about -5000 fs^2 at 1550nm. Setting the pumping power at 1 watt, a mode-locking state has been found by setting wave plates in proper angles. The repetition rate is ~ 193 MHz. Direct output power is ~ 140 mW. The center wavelength of the optical spectrum is at ~ 1575 nm and the bandwidth is ~ 20 nm.

The EOM is a $3(x) \times 5(y)$ mm² and 3(z)-mm thick LiNbO₃ crystal. The direction of the laser passing is the crystal optical axis (z-axis), and the external electric field is parallel to the x axis. By using the refractive index ellipsoid theory and stokes vectors [11], we calculate polarization rotation induced by external electric field in theory. For the incident light with the polarization perpendicular to x axis, the theoretical date for polarization state as a function of voltage on the EOM by verifying the voltage in the range of -200 v to 200 v is shown in fig. 2 (dashed lines). The EOM rotates polarization state with a coefficient of ~ 0.14 mrad/v in ellipticity and null in azimuth, in almost agreement with the experimental result of 0.12 mrad/v as shown in fig. 2 (points).

This work was supported by NSF of China under Grants Nos. 91536217, 91336101, 61127901, and the key project fund of the CAS "Light of West China" Program under Grant No. 2013ZD02.

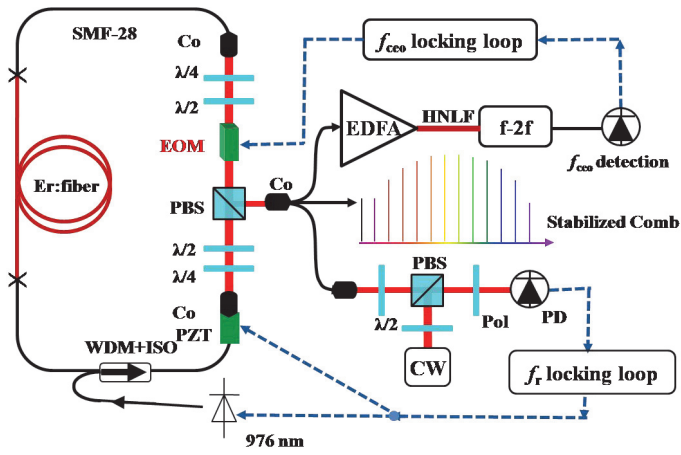


Fig. 1. The setup of the Erbium fiber laser frequency comb. $\lambda/2$: Half-wave plate; $\lambda/4$: Quarter-wave plate; WDM: Wavelength division multiplexer; ISO: Isolator; PBS: Polarization beam splitter; CO: Collimator; PD: Photodetector; PZT: Piezoelectric transducer; EOM: Electro-Optic Modulator; EDFA: Erbium-Doped fiber amplifier; HNLF: Highly nonlinear fiber; CW: Continuous laser.

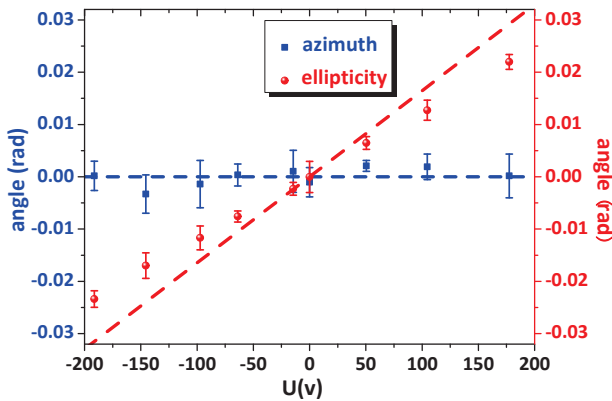


Fig. 2. The relation between the polarization state tuning and the voltage on the EOM (theoretical data: dashed line, experimental data: points)

The output of the laser is separated into three branches as shown in the right half of Fig. 1. One branch is the optical frequency comb output for utilization; the other two are used for produce an f_{cco} signal and a beat note with a 1550 nm continuous wave (CW) laser, respectively. The f_{cco} signal detected by an inline $f-2f$ interferometer at ~ 1000 nm after amplifying ~ 30 mW output power from the laser. The signal-to-noise ratio (SNR) of the detected f_{cco} signal is about 40 dB under 300 kHz resolutions.

We record the variation of the f_{cco} to the voltage on the EOM using a counter when the laser operates in a certain state. The frequency control dynamic range of f_{cco} is about 400 MHz, as shown in Fig. 3. Comparing to the traditional intro-cavity EOM with the same size, the frequency sensitivity of f_{cco} to voltage is ~ 50 times larger. We propose that the corresponding large frequency control dynamic range because it benefits from birefringence of the whole cavity fiber instead of only index change of an EOM crystal driven by tunable electric-field. Polarization state tuning of the laser can lead to a group-velocity shift while the phase velocity keeps relatively stable in

the mode-locked laser. Hence, f_{cco} , representing difference between group velocity and phase velocity, is sensitive to polarization state of the fiber laser. Note that the EOM in our system, only tuning the polarization state in ellipticity, may not represent the maximum frequency dynamic range. However, we can conclude that a relatively large dynamic frequency steering (at least a few of 10^{-7}) can be achieved by tuning lasers polarization state. And we also note that no side effect is observed during experiment by monitoring the optical spectrum and the relative intensity noise of the laser.

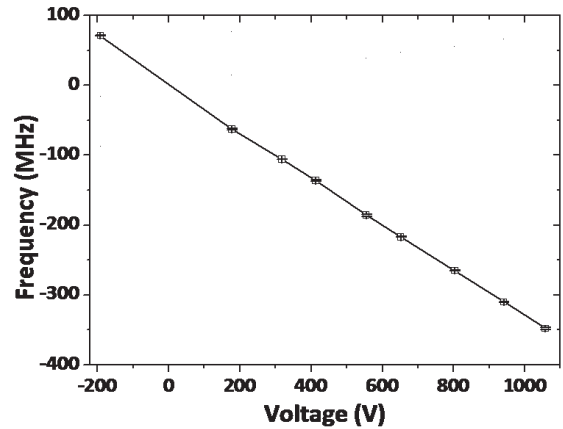


Fig. 3. Frequency variation of f_{cco} as a function of voltage for certain operation state.

To investigate the ability of the special home-made EOM, we used it to stabilize f_{cco} onto a RF reference signal. The signal at 245.5 MHz is flitted and enters a double-balance mixer to produce an error signal by comparing with the RF reference signal. The error signal is then fed back to the EOM with a home-made loop filter. On the other hand, we stabilize a comb tooth onto a CW laser at 1550 nm by controlling both pumping power and the PZT.

Fig. 4(a) shows frequency spectra of the phase stabilized the f_{cco} . We observe servo gain bumps at ~ 650 kHz and ~ 1.8 MHz by optimizing loop filter parameters, indicating that f_{cco} control loop has a broad servo bandwidth. In this state of the system, we measured that the phase noise of f_{cco} is generally in the range of -75 dB rad^2/Hz \sim -85 dB rad^2/Hz expect some noise bumps from 1 Hz to 100 kHz, and the corresponding phase jitter is about 0.16 rad, as shown in fig. 4(b). Down-converted frequency of f_{cco} at 30 MHz is recorded with a Π -type counter (made by K&K company). Fig. 4(c) shows the relative in-loop frequency stability of f_{cco} (normalized with the optical frequency of ~ 192 THz) is about 2×10^{-17} at 1 s and scales down with a slope of $1/\tau$ for short term. The peak-to-peak fluctuation is about 20 mHz. Note that the in-loop frequency stability of a comb tooth is about 10 times higher due to the limitation of the pumping power. We also note that the power fluctuation caused by f_{cco} control with our home-made EOM is only $1/270^{\text{th}}$ of the pumping power control method [12].

III. CONCLUSION

In summary, we demonstrate a servo control method for f_{ceo} stabilization of an Er: fiber optical frequency comb system with a home-made EOM by tuning polarization state of the laser. This approach can be used to control f_{ceo} in broad bandwidth and a large dynamic range by taking the birefringence of the laser cavity fiber. We obtain the phase noise of the stabilized f_{ceo} is 0.16 rad from 1 Hz to 100 kHz. And the in-loop frequency stability of f_{ceo} is about 2×10^{-17} at 1 s and roll down to 10^{-19} at 10^3 s. The EOM in our system tunes polarization state only in ellipticity. We plan to design a new EOM to rotate the laser's polarization state in azimuth or/and in ellipticity, which may obtain a larger frequency controlling dynamic.

References

- [1] S. A. Diddams, L. Hollberg, and V. Mbele. "Molecular Fingerprinting with the Resolved Modes of a Femtosecond Laser Frequency Comb." *Nature* 445, 7128 (2007): 627-30.
- [2] B. J. Bloom, T. L. Nicholson, J. R. Williams, S. L. Campbell, M. Bishof, X. Zhang, W. Zhang, S. L. Bromley, and J. Ye. "An Optical Lattice Clock with Accuracy and Stability at the 10-18 Level." *Nature* 506, 7486 (2014): 71-75.
- [3] A. Wirth, M. T. Hassan, I. Grguras, J. Gagnon, A. Moulet, T. T. Luu, S. Pabst, *et al.* "Synthesized Light Transients." *Science* 334, 6053 (2011): 195-200.
- [4] J. J. McFerran, E. N. Ivanov, A. Bartels, G. Wilpers, C. W. Oates, S. A. Diddams, and L. Hollberg. "Low-Noise Synthesis of Microwave Signals from an Optical Source." *Electronics Letters* 41, 11 (2005): 650-51.
- [5] I. Coddington, W. C. Swann, L. Nenadovic, and N. R. Newbury. "Rapid and Precise Absolute Distance Measurements at Long Range." *Nature Photonics* 3, 6 (2009): 351-56.
- [6] J. Rauschenberger, T. M. Fortier, D. J. Jones, J. Ye and S. T. Cundiff, "Control of the frequency comb from a mode-locked Erbium-doped fiber laser." *Optics Express* 10, 24 (2002):1404-10.
- [7] D. D. Hudson, K. W. Holman, R. J. Jones, S. T. Cundiff, J. Ye, and D. J. Jones. "Mode-Locked Fiber Laser Frequency-Controlled with an Intracavity Electro-Optic Modulator." *Optics Letters* 30, 21 (2005): 2948-50.
- [8] B. R. Washburn, R. W. Fox, N. R. Newbury *et al.* "Fiber-laser-based frequency comb with a tunable repetition rate." *Optics Express* 12, 20 (2004):4999-5004.
- [9] C. C. Lee, C. Mohr, J. Bethge, S. Suzuki, M. E. Fermann, I. Hartl, and T. R. Schibli. "Frequency Comb Stabilization with Bandwidth beyond the Limit of Gain Lifetime by an Intracavity Graphene Electro-Optic Modulator." *Optics Letters* 37, 15 (2012): 3084-86.
- [10] S. Koke, C. Grebing, H. Frei, A. Anderson, A. Assion, and G. Steinmeyer. "Direct frequency comb synthesis with arbitrary offset and shot-noise-limited phase noise." *Nature Photonics* 4, (2010): 462-465.
- [11] M. Nakazawa, K. Kikuchi and T. Miyazaki. "High spectral density optical communication technologies." Ch 2 (Springer, New York, 2010).
- [12] Y. Y. Zhang, L. L. Yan, W. Y. Zhao, *et al.* "A Long-Term Frequency-Stabilized Erbium-Fiber-Laser-Based Optical Frequency Comb with an Intra-Cavity Electro-Optic Modulator." *Chin. Phys. B* 24, 6 (2015): 64209-064209.

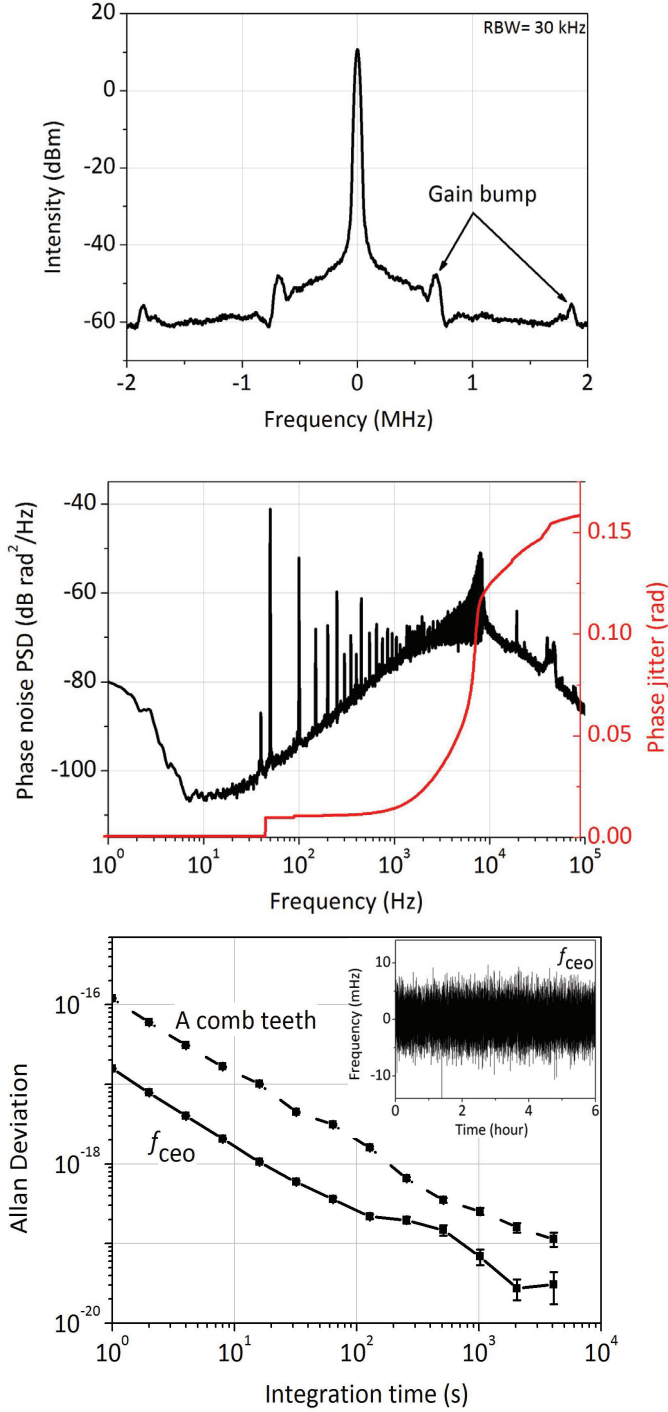


Fig. 4. (a) frequency spectrum of in-loop f_{ceo} ; (b) phase noise and phase jitter of in-loop f_{ceo} ; (c) In-loop frequency stability of f_{ceo} (solid black square) and a comb tooth @ 1550 nm (solid black square).